Coastlab 20

Dec 9-12 Zhoushan, China

Proceedings

The 8th International Conference on the Application of Physical Modelling in Coastal and Port Engineering and Science

Dec 9-12, 2020, Zhoushan, China

Editors:

Pengzhi Lin | Zhiguo He | Dezhi Ning

ISSN: 2710-1509

ISBN: 978-90-824846-5-6

The papers included in this volume were all of 8th International Conference on the Application of Physical Modelling in Coastal and Port Engineering and Science cited on the cover and title page. Papers were selected and subject to review by the editors and International Scientific Committee. The papers published in these proceedings reflect the work and thoughts of the authors and are published herein as submitted. The publisher is not responsible for the validity of the information or for any outcomes resulting from reliance thereon.

Proceedings of the 8th International Conference on the Application of Physical Modelling in Coastal and Port Engineering and Science

Dec 9-12, 2020. Zhoushan, China

Editors: Pengzhi Lin, Zhiguo He, Dezhi Ning

Published by:

International Association for Hydro-Environment Engineering and Research -IAHR-

Pª Bajo Virgen del Puerto, 3 28005 Madrid, SPAIN

A-1 Fuxing Road, Haidian District, 100038, Beijing, CHINA

ISSN: 2710-1509

ISBN: 978-90-824846-5-6

IAHR publications follow the Ethical Guidelines and Codes of Conduct provided by the Committee of Publication Ethics (COPE).

IAHR, founded in 1935, is a worldwide independent member-based organisation of engineers and water specialists working in fields related to the hydro-environmental sciences and their practical application. Activities range from river and maritime hydraulics to water resources development and eco-hydraulics, through to ice engineering, hydroinformatics, and hydraulic machinery.
IAHR consists of two offices: Madrid Office, Spain and Beijing Office, China.

CONFERENCE PROCEEDINGS

Contents

APPENDIX: ABSTRACTS

Contents

Preface

We are very pleased to introduce the Conference Proceedings of the 8th International Conference on the Application of Physical Modelling in Coastal and Port Engineering and Science (Coastlab2020), which contain the full papers and abstracts of the presentations delivered at the conference. Coastlab is an important conference series under the supervision of the Committee of Coastal and Maritime Hydraulics of International Association of Hydro-Environment Engineering and Research (CMH-IAHR). This year's event, from December 9th to 12th, 2020 in Zhoushan, China, was hosted by Zhejiang University, Dalian University of Technology, Sichuan University, Zhejiang Ocean University, and co-organized by other 5 universities and institutions.

Coastlab2020 aimed for gathering the latest developments and applications of laboratory, numerical and field measurement technologies in port and coastal engineering. The conference organized 7 parallel sessions and 5 special sessions covering the following topics:

- Wave, tidal and wind energy
- Coastal and ocean structures, breakwaters, and revetments
- Coastal hydrodynamics and coastal processes
- Estuary and coastal environment and eco-hydraulics
- Laboratory techniques and measurement systems
- Field measurement, floating bodies, wave generation and analysis
- Sediment transport, erosion, and sedimentation
- Coastal reservoirs
- Marine aquaculture engineering
- Evolution and modeling of the yellow river estuary
- Coastal hazards and integrated management options
- Marine geotechnics

Centering around the topics, Coastlab2020 received 272 abstracts and 51 full papers. The scientific committee of Coastlab2020 managed all the submissions and coordinated the peer-review process to a very high standard. The final results of the quality submissions contributed by the authors, reviewers, and scientific committee members are reflected in the proceedings, which provide a comprehensive record of the theories and technologies presented in the conference and serve as important references to researchers and practitioners in relevant areas.

Due to the Covid-19, Coastlab2020 was running in the combination of on-site and online. This was challenging, but achieved unexpected great successes. The Coastlab 2020 was considered as the part of celebration programs of IAHR 85th anniversary. We were pleased to have the president of IAHR, Prof. Joseph H.W. Lee, given a very encouraging and inspiring opening speech. The conference gathered 176 informative oral presentations, including 7 plenary speeches and 49 session invited talks; among these, 123 presentations were delivered on-site and 53 online. The presentations not only stimulated inspiring discussions among ~240 attendees on-site but also made a profound impact among ~13,000 attendees online. The online participants were from over 60 countries/regions on six continents.

We would like to express our sincerest appreciations to all the presenters who shared your wisdom and insights graciously, to the reviewers who provided insightful comments in enhancing the quality of the conference

proceedings, to the local organizing committee and volunteers who made considerate arrangements of the conference, to the editors and secretariat members who have participated in reviewing and editing the proceedings. We would like to particularly appreciate the following organizations: Zhejiang University, Dalian University of Technology, Sichuan University, Zhejiang Ocean University, Bureau of Science and Technology of Zhoushan, Hohai University, Nanjing Hydraulic Research Institute, Ningbo University, Journal of Marine Science and Engineering, Key Laboratory of Offshore Geotechnics and Material of Zhejiang Province, International Joint Research Center for Offshore Civil Engineering (Ministry of Science and Technology of the People's Republic of China), and Engineering Research Center of Oceanic Sensing Technology and Equipment (Ministry of Education of the People's Republic of China). We would also like to thank the conference sponsors (i.e., CHANGMU Ltd., SINFOTEK Co., Ltd., and YICHEN Ltd.) who generously provided financial supports to the conference. Your great contributions and efforts were essential factors of the successful Coastlab2020 and the informative conference proceedings.

We are looking forward to the next gathering of Coastlab, the proposal call of which is already open.

CHAIRS of Coastlab2020**:**
Professor Pengzhi Lin, Sichuan University
Professor Zhiguo He, Zhejiang University
Professor Dezhi Ning, Dalian University of Technology

16th January 2021

Coastlab 20

Dec 9-12 Zhoushan, China

Proceedings

8th International Conference on the Application of Physical Modelling in Coastal and Port Engineering and Science
Dec. 9th - 12th, 2020, Zhoushan, China

LOCAL SCOUR AROUND POROUS SUBSEA CUBIC CAISSONS IN STEADY CURRENT

FAN YANG1*, LILI QU1, CHENG FAN1, GUOQIANG TANG1, LU LIN1

1State Key Laboratory of Coastal and Offshore Engineering, Dalian University of Technology, Dalian, 116024, China

ABSTRACT

Local scour around porous subsea cubic caissons has been studied experimentally in a water flume. The parameter, streamwise porosity (two-dimensional porosity P2D), was investigated on the development of scour. The scour profiles, time history, equilibrium scour depth as well as time scale were studied. In the present study, the horseshoe vortex plays a fare less role than the velocity amplification on the corners of the cubic caisson. The development of scour depth is weakened as P2D further increase. The equilibrium scour depth can be up to 35% decrease of results of the solid one. Empirical formulae and correction factor Kp for predicting the equilibrium scour depth was derived by an exponential correlation.

1 INTRODUCTION

As one of the key features leading to the structure failure in the offshore engineering, investigations on the local scour around subsea structures attracts substantial interest in the past decades. Horseshoe vortex in front of the slender piles and the velocity contractions at two sides of the piles lead to the local scour at the junctions of the pile and seabed. And the vortex shedding further contributes to the scour in the wake.

Time scale of local scour development around subsea structures has been well predicted through a series of empirical formulas. Sumer et al. (1992a) and Whitehouse (1998) used exponential function to describe the development of the scour depth at the front most upstream point of a vertical circular or rectangular pile. The formula is

$$S(t) = S_0(1 - exp^{-t/T}) \quad (1)$$

where S is the scour depth, S_0 is the equilibrium scour depth, t is the time and T is defined as the time scale of scour. Sumer et al. (1992a) found that time scale of scour around a vertical slender pile follows

$$t = \frac{D^2}{[g(s-1)d_{50}^3]^{1/2}} t^* \quad (2)$$

$$t^* = \frac{\delta}{2000D} \theta_s^{-2.2} \quad (3)$$

where D is the representative dimension of the vertical pile (diameter for a circular pile or dimension perpendicular to flow for a rectangular cylinder), δ is the boundary layer thickness and t^* is the non-dimensional time scale of scour.

Briaud et al. (1999) proposed a hyperbolic function:

$$S(t) = S_0 \frac{t}{t+T_0} \quad (4)$$

in which T_0 the equilibrium time scale for the hyperbolic equation.

The focus of the previous investigations is on the local scour and global scour around subsea structures. However, it is not clear that how the flow permeability may influence the scour depth and time scale. The existence of porosity in surfaces of the structures is believed to largely change the development of scour, whilst the study on this topic is rare due to the best knowledge of the author. The present work reports a systematical experimental study of scour around a cubic caisson. Some questions about the scour of a cubic caisson will be answered including (1) what is the flow mechanism of the influence of Porosity on the scour depth and time scale; (2) does the horseshoe vortex still play a dominant role in the scour process; (3) how does the attack angle of the steady flow affect the scour.

2 EXPERIMENTAL SETUP

Investigations on scour around porous subsea cubic caissons in steady current were carried out through experimental apparatus. The present tests were conducted in the Non-linear Water Flume. As shown in Figure

1, a sand basin of 8m in length is built in the water flume. Tests were carried out in the downstream part of the sand basin where the depth of the sand is 0.3m. The upstream area where the sand depth is 0.1m was designed to provide sand supply to the test section in order to avoid excessive loss of sand in the test area.

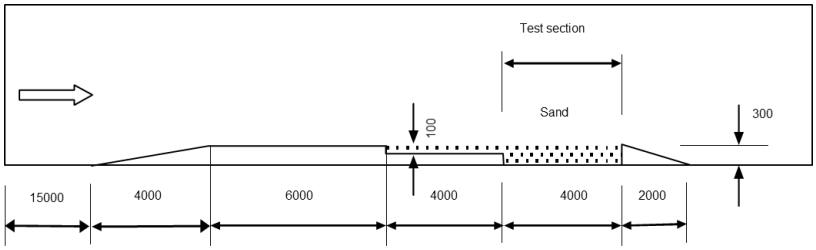

Figure 1. Test flume and setup for experiments

The square-shaped porous caissons were made of acrylic material in the present work. The porous model has a dimension of 20cm × 20cm × 20cm in width × length × height with a square shape in plane. A new parameter, Porosity, *P*, was applied in the current work, which was defined by (1):

$$P = \frac{A_p}{A_{cross}} \quad (5)$$

in which A_p is the total area of permeable parts in the cross-section surface, and A_{cross} is the area of the cross section of the cubic caisson. Porosity, *P*, was denoted as the ability that the water flows through the cubic caisson. The scenario of two-dimensional porosity P_{2D} is where the porous sections were only located in the cross section of the cubic caisson in the front and back surfaces as shown in Figure 2. The scour depth in the current study is normalized by the horizontal dimension in the cross-flow direction D^* (= *D*).

Only one type of the sand was used. The water depth and depth averaged flow velocity were kept constant at 0.5m and 0.353m/s in all tested cases. The critical Shields parameter θ_{cr} was calculated by the improved empirical formula by Soulsby (1997) and Soulsby and Whitehouse (1997),

$$\theta_{cr} = \frac{0.30}{1+1.2D_*} + 0.055[1 - exp(-0.020D_*)] \quad (6)$$

where the non-dimensional particle size D_* is defined as

$$D_* = [g(s-1)/\upsilon^2]^{1/3} d_{50} \quad (7)$$

The Shields parameter due to total friction was obtained according to the measured velocity profile. And the Shields parameter θ_s due to skin friction is defined as

$$\theta_s = \frac{\tau_s}{\rho g(s-1)d_{50}} = \frac{U_{fs}^2}{g(s-1)d_{50}} \quad (8)$$

where τ_s is the shear stress due to the skin friction experienced by the sea bed from the flow, ρ is the water density, g is the acceleration due to the gravity, s is the specific gravity of sand, d_{50} is the median particle size of sand as shown in Figure 3, υ is the kinematical viscosity of water, and $\mathrm{U_{fs}}$ is the friction velocity associated with skin friction defined by

$$U_{fs} = (\tau_S/\rho)^{1/2} \quad (9)$$

in which the shear stress due to skin friction τ_s can be calculated by the empirical formula for flat and surface by Soulsby (1997)

$$\tau_s = \rho C_D \overline{U}^2 \quad (10)$$

where the logarithmic relationship for C_D is

$$C_D = \left\{\kappa / \left[ln\left(\frac{z_{0s}}{h}\right) + 1\right]\right\}^2 \quad (11)$$

in which κ is the Karman constant equaling 0.4, $\overline{U}$ is the depth averaged flow velocity, $z_{0s}(= d_{50}/12)$ is the roughness height due to the skin friction and h is the water depth. The skin friction Shields parameter is used to judge whether a test is under live-bed or clear water condition. As θ_s/θ_{cr} >1, the live-bed water condition is observed, while as θ_s/θ_{cr} ≤1, it is recognized as the clear-water condition. Table 1 shows the summary of the parameters used in the tests. In the present work, θ_s/θ_{cr} = 1.28, which indicates a live-bed water condition.

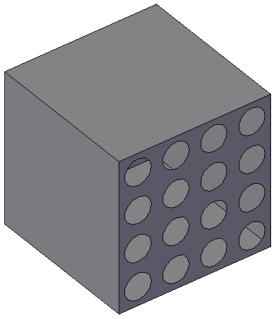

Figure 2. Subsea structures used in the current experiments.

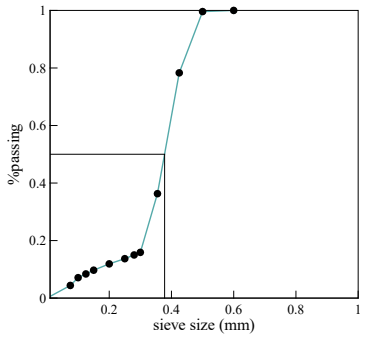

Figure 3. Parameters of sediments used in the current experiments.

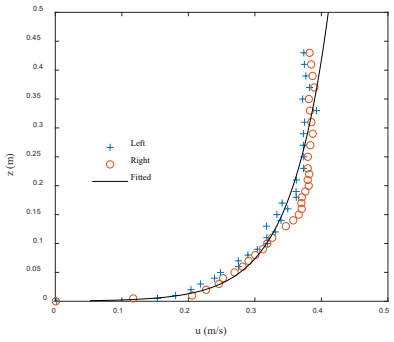

Figure 4. Measured distribution of velocity in water depth.

The velocity was measured after the generating flow was stable. A fitted curve according to the measured velocities below z = 0.4m was also plotted in Figure 4. The fitted curve follows the logarithmic law described by

$$u(z) = \frac{U_{ft}}{\kappa} ln\left(\frac{z}{z_{0t}}\right) \quad (12)$$

where U_{ft} is the friction velocity associated with the total shear stress, z_{0t} is the total roughness. Through curve-fittings obtained by the measured velocity profiles using least square method, the total friction velocity and total roughness can be achieved as shown in Table 1 (Soulsby, 1997).

Table 1. Parameters used in the current tests.

Median particle size of sand d_{50} (mm)	0.378
d_{85}(mm)	0.449
d_{15} (mm)	0.28
Uniform parameter of sand $(d_{85}/d_{15})^{0.5}$	1.266
Specific gravity s	2.67
Critical Shields parameter θ_{cr}	0.0336
Water depth h (m)	0.5
Depth averaged velocity U (m/s)	0.353
Shields parameter due to skin friction θ_s	0.0429
Total Shields parameter θ_t	0.077
Total roughness length z_{0t} (m)	4.05×10^{-4}
Roughness length for skin friction z_{0s} (m)	3.15×10^{-4}

In order to approximately understand the duration required for the scour test, δ = 0.4 m is applied to Eq. (2) and (3), and the time scale for D = 0.2m is T = 1.02h. By substituting $S(t)/S_0$ = 0.95 and the above the calculated time scales into Eq. (1), the time taken for scour reaching 95% of equilibrium scour depth for D = 0.2m is estimated as t = 1.02h. In this study, the durations of the scour tests were set in the range of 6h ~ 10h. Tests applied in the present work are summarized in Table 2.

Table 2. List of tests.

Test	Diameter of hole in face AB and face AC (cm)	Porosity of face AB and face AC (%)	Diameter of hole in face BC and face AD (cm)	Porosity of face BC and face AD (%)	Horizontal dimension length in the crossflow direction D* (cm)	Angle between flow direction and long boundary of models α (°)
A1	0	0	0	0	20	0
A2	1	3.14	0	0	20	0
A3	2	12.57	0	0	20	0
A4	3	28.27	0	0	20	0
A5	3.5	38.49	0	0	20	0
A6	4	50.27	0	0	20	0

3 RESULTS AND DISCUSSIONS

Results

As shown in Table 2, Test A1-A6 have been applied in the present work for quantifying the influence of stream porosity (two-dimensional porosity, P_{2D}). P_{2D} is ranging from 3.14% to 50.27% and the solid cubic caisson with P_{2D} = 0 is set as the reference as Test A1. Figure 1 (a), (b) and (c) shows contours of sand bed level after 10min, 1h and 6h of scour for Test A3 with P_{2D} = 12.57%, and the instants of 6h for Test A1 is presented at Figure 1 (d). The initial seabed level after leveling is set as z = 0 in the current coordinate system. As shown in Figure 1(a) for 10min after scour, scour initiates from two upstream corners for around 30 mm induced by the velocity amplifications at two upstream corners A and D. The sand in the upstream is washed out to form two sand ridges which are located around two downstream corners B and C and the height is around 50 mm. Scour at the central part of the upstream surface is not observed at t = 10min. This indicates that the horseshoe vortex is not strong enough to cause erosion in front of the structures. This is validated by investigations of Zhao et al. (2010) and Yao et al. (2018), in which the influence of horseshoe vortex is largely weakened by the small height of the cubic caisson. At the start of Test A3, the suspended sand was observed to flow over the top of the cubic caisson, which is also an indication of the weakness of the horseshoe vortex in the front. At t = 1h, two sand ridges in the wake is further accumulating and pushed towards the further downstream. The height achieves at 85 mm. Scour didn't reach the middle section of the upstream surface until t = 1h in Figure 1(b). The range of scour holes around the cubic caisson is further widened to -400 mm in the streamwise direction and -300 to 300 mm in the spanwise direction. Large amount of the sand was washed out by the flow to the downstream, and some suspended sand deposits were observed at the top of the cubic caisson, leading to two sand ridges in the wake merging with each other to form a new pile-up. The new forming pile-up has a height of 95 mm and extends its range to further downstream at 700mm in streamwise direction. The scour continued after 1h, whilst the scour propagation rate was observed to be obviously slow. At 6h of scour in Figure 1(c), scour holes at two upstream corners extended to 120 mm which is 60% of the height of the cubic caisson. Scour depth at the middle section of the front boundary keeps almost unchanged at -200mm, and the range of scour hole is observed to be rarely widened. The amalgamating pile-up in the wake grew up quickly and the maximum height is up to 105 mm, which is 51% of the height of the cubic caisson. Comparing with results of Test A1 in Figure 1 (d), the depth of the scour holes is smaller and the pile-up in the wake reduces its dimension.

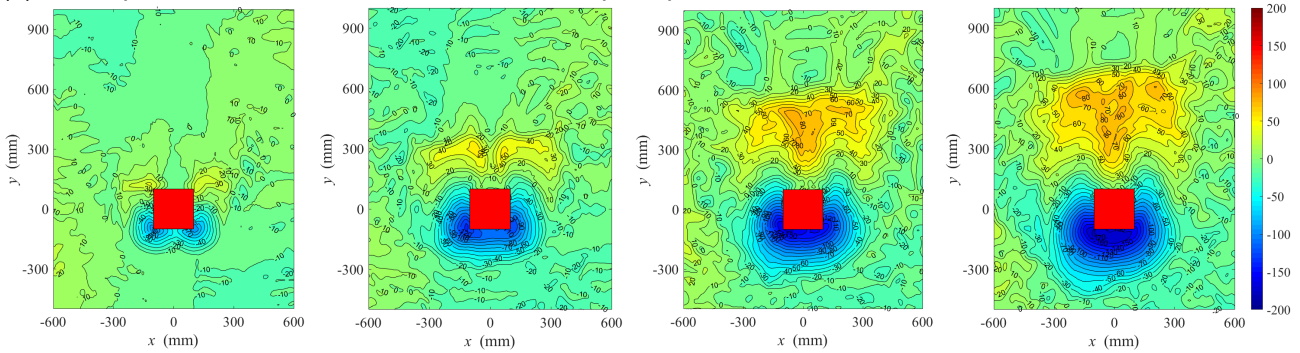

Figure 1. Contours of bed level at three instants during scour for Test A3 with P_{2D} = 12.6% (unit: mm). (a) t = 10min, (b) t = 1h, (c) t = 4h and (d) t = 6h for Test A1 with P_{2D} = 0.

Figure 2 presents the contours of bed levels at four different instants during the scour for Test A5 with P=38.5%. The scour phenomena for Test A5 is very similar to that for Test A3 in Figure 1, while the scour rate is much

slower. It seems that the scour didn't extend to the middle section of the front boundary from the two upstream corners until t = 4h. And sand ridges at two downstream corners start to collapse till t = 4h. Through comparing with results in Figure 1, scour depths at two upstream corners is about 10%~23% smaller than their counterparts in Test A3 for t = 10min and 1h. However, this reduction increases to 32% after t = 4h. The amalgamating pile-up in the wake also reduces its height to about 810 mm at t = 6h, up to 20% smaller than the counterpart in Test A3.

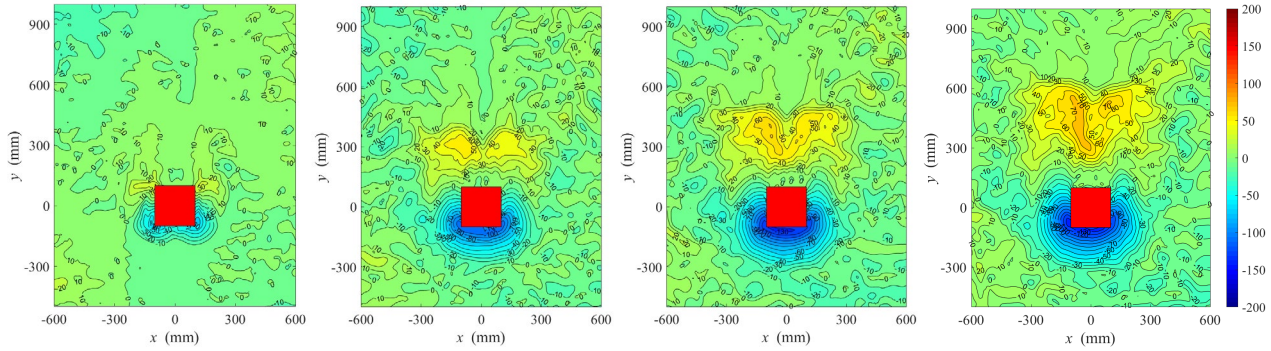

Figure 2. Contours of bed level at three instants during scour for Test A5 with P_{2D} = 38.5% (unit: mm). (a) t=10min, (b) t=2h, (c) t=4h, (d) t=6h

Through the contours of bed levels in Figure 1 and Figure 2, the velocity amplifications at two upstream corners govern the flow mechanism of the scour rather than the horseshoe vortex. It is believed that the existence of the porosity in the front and back boundaries results in a divergent flow rate through the inside of the cubic caisson. Increases of porosity, P_{2D}, would increase the flow rate through the cubic caisson and decrease the flow rate outside the caisson. Therefore, the velocity amplification at two upstream corners is believed to be weakened, which would lead the weakening of the local shear stress and further reduce the local scour.

Different from the surface-piercing structures, the sand ridges and amalgamating pile-up in the present work are quite unique. Typical scour holes induced by the Von Karman vortex street for surface-piercing structures are not observed. Tsutsui (2012) visualized an arc-shaped tip vortex forming at the top and side for a cylinder with height-to-width smaller than 1 rather than the typical vortex street in the lee wake. And this can be explained the formations of pile-ups in the present work. Similar phenomena are also observed by Zhao et al. (2012) and Yao et al. (2018) for low height-to-width structures.

It is worthwhile to indicate that the present results reported is based on the relatively low flow intensity (θ_s/θ_{cr} = 1.28). Yao et al. (2018)'s results show that the equilibrium scour depth does not vary monotonically with the flow intensity, and the equilibrium scour depth experiences a sudden drop as θ_s/θ_{cr} >1 and then increase again for further increasing θ_s/θ_{cr}. This phenomenon is most pronounced for the caisson with the height-to-width ratio smaller than 1 due to the influence of the upstream sediment transport and bed ripples. It is suspected that with further increase of the flow intensity, the development of scour for the porous cubic caisson will be changed. Though the scour propagation in the two upstream corners is expected to be larger, the scour could be initiated at the center of the upstream surface. The size and range of amalgamating pile-ups could experience an extraordinary reduction.

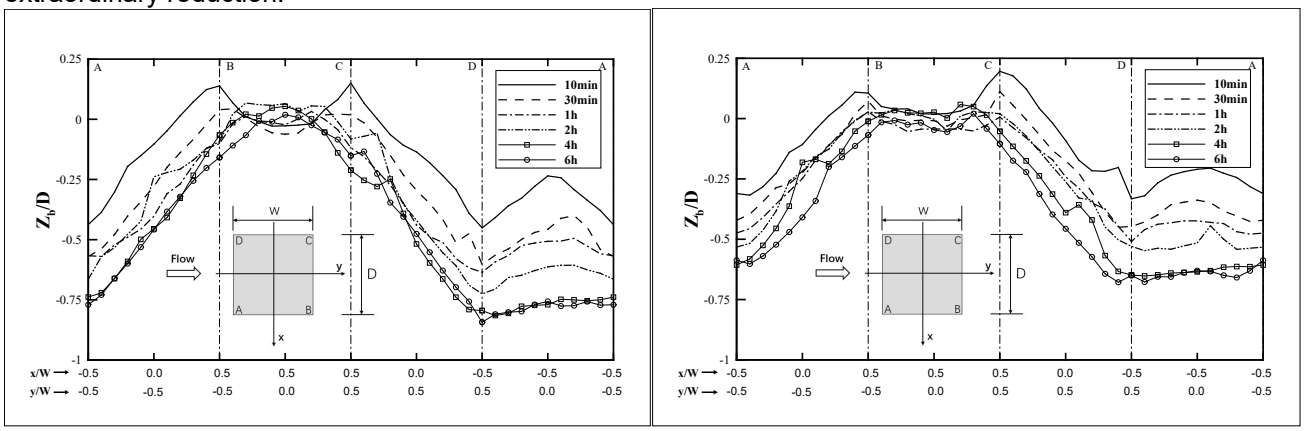

Figure 3. Distributions of sea bed level along the boundary of the cubic caisson for (a) Test A3 with P_{2D} = 12.6% and Test A5 with P_{2D} = 38.5%.

Figure 3 shows the distributions of non-dimensional level of bed surface (Z_b/D) along the boundary of the cubic caisson for Test A3 and A5. The level of bed surface is normalized by the cross-flow dimension of the cubic

caisson. Sketches for the model cubic caisson are also attached in Figure 3 with four corners labeled by A, B, C and D. *x/W* and *y/D* marked below the horizontal axis indicate multiple positions along the boundary of the cubic caisson. As presented in Figure 3(a), the scour initiates from two upstream corners A and D, propagating towards the downstream corners and central part of the upstream. The sediments eroded from corners A and D deposit themselves at the two downstream corners B and C, corresponding to the observed sand ridges in Figure 1. The maximum scour depth occurs at the two upstream corners A and D. And scour finally extends to the middle section of surface BC for Test A3 in Figure 3(a).

The distributions of non-dimensional level of bed surface for Test A5 in Figure 3(b) is similar to observations of Test A3. However, the scour does not reach the central section of the surface BC at t = 6h, whilst the scour at two upstream corners A and D has already reach the equilibrium state. On the other hand, the scour propagation rate towards the downstream is much slower than it of Test A3. At t = 4h, as the scour for Test A3 has already extended to the central section, the scour for Test A5 just passes corners B and C for about 0.2D. The scour propagation rate towards the upstream is very similar. The scour extends to the central section of the surface AD at t = 4h for both Test A3 and A5.

4 Development of Scour

Figure 8 shows the development of the scour depth at the two upstream corners of the cubic caissons for Test A1-A6. The dot symbols represent the averaged values of measured scour depth at the upstream corner D, which has the maximum scour depth. Fitting curves are employed through hyperbolic equations Eq. (4) by solid lines. As in Figure 9, the fitted curve using hyperbolic equation agrees better with the measured data, comparing with fitted curves using exponential equations. The fitted data by using hyperbolic equations are believed to be more conservative which is in agreement with the results by Zhao et al. (2010) and Yao et al. (2018). The fitting hyperbolic equation Eq. (4) has been applied to the development of the equilibrium scour depth and the time scale in the remainder of the present work.

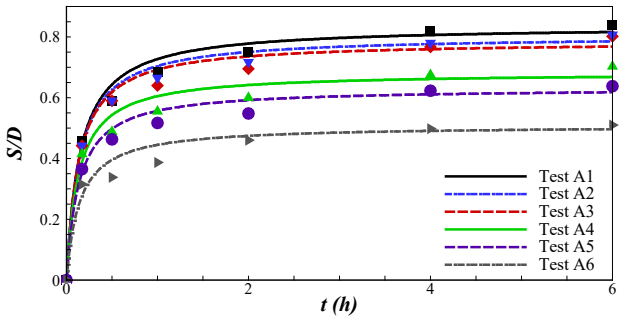

Figure 8. Development of the non-dimensional scour depth at the two upstream cornners of the casssions with different P_{2D} ranging from 0 to 50.3%. Fitted curves are based on the exponential equation Eq. (4).

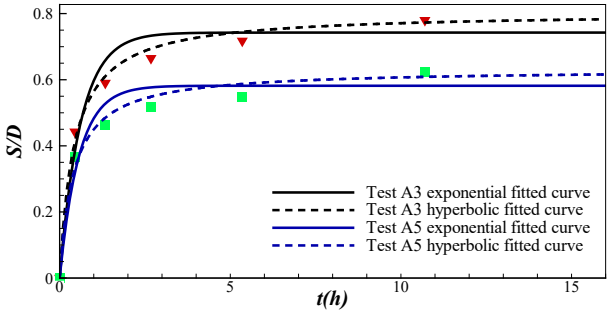

Figure 4. Development of scour depth at the two upstream corners of the subsea structures for Test A3 and A5. Symbol, averaged values of measured scour depth at the two upstream corners; dashed line, fitted curve according to exponential equations; solid line, fitted curve according to hyperbolic equations.

Test A2 has run for 10h until the equilibrium state is achieved as shown in Figure 9, in which the scour depth at t = 6h reaches 90% of the equilibrium scour depth. Therefore, the instant with the scour depth at t = 6h ~ 8h can be regarded as an approximation closing to the equilibrium stage for local scour. The approximation provides a reliable way to predict the equilibrium scour depth and the time scale by the fitted mathematical expression, which is widely used by Sumer and Fredsoe (2002), Zhao et al. (2010) and Yao et al. (2018). According to Figure 8, it can be seen that the scour depth increases rapidly after the initiation of the local scour at two upstream corners. The influence of two-dimensional porosity P_{2D} is observed to be presented at $t \geq$ 10min. The scour depth with a larger P_{2D} is always smaller. At the end of the tests at t = 6h, the scour depth decreases monotonically with the increases of P_{2D}. The equilibrium scour depth S_0 achieves at 0.79D for P_{2D} = 3.1%, while its counterpart for P_{2D} = 50.3% achieves at 0.5D. And it is apparent that the variations of S_0/D are not linear to P_{2D}. As discussed in Figure 1, the increase of porosity results in the decrease of velocity amplifications at two upstream corners, which would reduce local shear stress and sediment transport. It is also believed that the increase of porosity leads the decrease of adverse pressure gradient, which further weaken the flow concentrations due to the contraction of streamlines (Sumer and Fredsøe, 1997).

Figure presents the equilibrium scour depth for the porous cubic caisson of Test A1-A6. It should be noted that as P_{2D} = 1, which means no structures in the test section, the local scour would not exist and S_0 = 0. It can be seen that in Figure that the equilibrium scour depth decreases with increase of P_{2D}, and this correlation is not

on linear. S_0/D for P_{2D} = 3.1% and 12.6% are very close and as P_{2D} increases to P_{2D} = 28.3%, S_0/D sharply decrease around 15%.

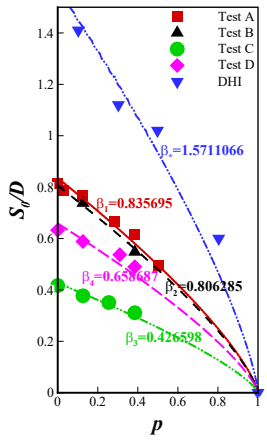

Figure 10. Fitted curves for the non-dimensional equlibrium scour depth S_0/D with different P_{2D} through exponetial equations Eq. (13).

To better quantify the correlation between P_{2D} and S_0/D, the data plotted in Figure are fitted in the curve by an exponential equation with the exponent of 0.75. The fitting exponential equation can be written as:

$$S_{0_{2D}}/D = \beta_1(1 - P_{2D})^{0.75} \quad (13)$$

in which β_1 is a fitting-in-curve coefficient, which is β_1= 0.835695 for the current square model with the flow intensity (θ_s/θ_{cr}=1.28) and height-to-width ratio (h/D = 1). It should be noted that the flow intensity and height-to-width ratio would have influence on the local scour accounting for the porosity effect. The fitting exponential equation based on the current data however provides an insightful and quantitative way to collapse the experimental results for the equilibrium scour depth into a correction as a function of two-dimensional porosity, P_{2D}.

Data of square porous structures in DHI and Snamprogetti (1992) are also plotted for comparison. Despite values of S_0/D is quite larger comparing to the results in the present work, the trend that the larger the porosity is, the smaller the equilibrium scour depth achieves is very similar. The data of DHI agrees quite well with the predicting exponential equations with β_* = 1.5711066 as shown in Figure . The difference of values may be due to the different testing setups, where Sumer and Fredsoe (2002) gives very limited details. One reason ascribed to the difference is the flow intensity. The present results were conducted in the live-bed flow condition with θ_s/θ_{cr}= 1.28, whilst Sumer and Fredsoe (2002) present the shields number θ_s around the critical values (θ_s/θ_{cr}= 1). It is known that the equilibrium scour depth S_0/D doesn't vary monotonically with the flow intensity (θ_s/θ_{cr}), instead has a local peak at around θ_s/θ_{cr}= 1, which is expected to due to the influence of the upstream sediment transport and the bed ripples. As discussed in Yao et al. (2018), for a low height-to-width structure (h/D = 1), the equilibrium scour depth S_0/D for θ_s/θ_{cr}= 1 is around 30% larger than S_0/D for θ_s/θ_{cr}= 1.28. On the other hand, it is suspected that the water depth for DHI and Snamprogetti (1992) is larger than the present work. The water depth for present work is up to around 2.5 times of the effectiveness diameter. And as illustrated in Melville and Sutherland (1988), the scour depth would be reduced largely at the shallow water whose depth is smaller than 2.6 times of the effectiveness diameter. As the water depth is up to 4 times of the effectiveness diameter, Yao et al. (2018) recorded a 80% higher of the equilibrium scour depth S_0/D comparing with the results of Zhao et al. (2012) with 1.77-2.6 times of the effectiveness diameter for cubic caissons.

5 CONCLUSION

Scour around porous subsea cubic caissons has been investigated through experimental tests in the present work. Systematic analysis on the influence of streamwise porosity (two-dimensional porosity P_{2D}), spanwise porosity (three-dimensional porosity P_{3D}) and attack angle α on the development of scour has been launched. The scour profiles, time history, equilibrium scour depth as well as time scale were studied. The results can be summarized as follows:

1) In the current dimension of subsea cubic caissons with height to width ratio equaling 1, horseshoe vortex plays a fare less role than the velocity amplification at the corners of the cubic caisson. The development of scour depth is weakened as P_{2D} further increase. The equilibrium scour depth can be up to 35% decrease of results of the solid one. It is believed that the existence of P_{2D} will lead more flow coming through the cubic caissons, which will reduce the velocity amplifications at corners.

2)Empirical formulae for predicting the equilibrium scour depth at the upstream corners of a cubic caisson were derived based on the experimental data for Test A1-A6. An exponential correlation of the equilibrium scour depth is achieved along with a new governing parameter K_p.

ACKNOWLEDGEMENTS

The authors would like to acknowledge the support from the National Key R&D Program of China (Project ID: 2016YFE0200100 and 2017YFC1404202).

REFERENCE

[1] SOULSBY, R. 1997. Dynamics of marine sands: a manual for practical applications, Thomas Telford.
[2] SOULSBY, R. & WHITEHOUSE, R. Threshold of sediment motion in coastal environments. Pacific Coasts and Ports' 97: Proceedings of the 13th Australasian Coastal and Ocean Engineering Conference and the 6th Australasian Port and Harbour Conference; Volume 1, 1997. Centre for Advanced Engineering, University of Canterbury, 145.
[3] SUMER, B., CHRISTIANSEN, N. & FREDSOE, J. Time scale of scour around a vertical pile. The Second International Offshore and Polar Engineering Conference, 1992a. International Society of Offshore and Polar Engineers.
[4] SUMER, B. M. & FREDSOE, J. 2002. The Mechanics of Scour in the Marine Environment.
[5] SUMER, B. M. & FREDSØE, J. 1997. Hydrodynamics around cylindrical structures, World Scientific.
[6] SUMER, B. M., FREDSOE, J. & CHRISTIANSEN, N. 1992b. SCOUR AROUND VERTICAL PILE IN WAVES. Journal of Waterway Port Coastal and Ocean Engineering-asce, 118, 15-31.
[7] TSUTSUI, T. 2012. Flow around a cylindrical structure mounted in a plane turbulent boundary layer. Journal of wind engineering and industrial aerodynamics, 104, 239-247.
[8] WHITEHOUSE, R. 1998. Scour at marine structures: A manual for practical applications, Thomas Telford.
[9] YAO, W., AN, H., DRAPER, S., CHENG, L. & HARRIS, J. M. 2018. Experimental investigation of local scour around submerged piles in steady current. Coastal Engineering, 142, 27-41.
[10] ZHAO, M., CHENG, L. & ZANG, Z. 2010. Experimental and numerical investigation of local scour around a submerged vertical circular cylinder in steady currents. Coastal Engineering, 57, 709-721.

Coastlab 20
May 25-29, Zhoushan, China

8th International Conference on the Application of Physical Modelling in Coastal and Port Engineering and Science
Dec. 9th - 12th, 2020, Zhoushan, China

EXPERIMENTAL STUDY ON HYDRODYNAMIC CHARACTERISTICS OF DUAL-PONTOON BREAKWATER IN TRANSIENT WAVES

XIAOTONG SUN, CHONGWEI ZHANG* & DEZHI NING

State Key Laboratory of Coastal and Offshore Engineering, Dalian University of Technology, Dalian 116024, China,
*Corresponding author. Email: chongweizhang@dlut.edu.cn

ABSTRACT

This study considers a dual-pontoon breakwater that is damaged with open channels regularly distributed along the pontoons. Physical experiments are conducted in the wave flume at Dalian University of Technology to investigate the wave protection effectivity of the remaining part of the breakwater. Effects of the pontoon space on the wave reflection and transmission coefficients of the breakwaters are first investigated. The reflection coefficient of the damaged breakwater generally shows a decreasing trend for larger wave periods, indicating a failure of its wave protection capability for longer waves. Then, the wave height between two pontoons corresponding to different wave periods are discussed. Compared with undamaged cases, the wave height between two damaged pontoons seems insensitive to the wave periods under consideration. Finally, the evolution of wave profiles between two damaged pontoons is further investigated. For short-wave cases, the wave profile along the pontoon has spatial variation, indicating the occurrence of a transverse standing wave.

Keywords: Breakwater, dual-pontoon, water wave, reflection coefficient, transmission coefficient

1 INTRODUCTION

Breakwaters are widely used for the creation of a calm water area from attacking waves. For the deep-water condition or temporary purposes, floating breakwaters are preferred rather than conventional rubble mound ones in terms of the economic cost, construction process and environmental impact. Among various types of floating breakwaters, the single-pontoon type has been most widely studied (e.g. Drimer et al. 1992; Sannasiraj et al. 1998; Abul-Azm & Gesraha 2000; Christensen et al. 2018). However, for certain sea states especially long wave conditions, the wave transmission through the breakwater is non-neglectable. An intuitive solution is to deploy multiple floating breakwaters in parallel, so that transmitted waves behind the front breakwater can be further blocked by the rear one.

Many studies have focused on the dual-pontoon breakwaters. For example, Abul-Azm (1994) investigated dual flexible floating breakwaters in two dimensions, using an eigenfunction expansion technique. William & Abul-Azm (1997) studied hydrodynamic properties of a dual pontoon floating breakwater by using boundary integral equation method. Syed & Mani (2006) considered a three-pontoon floating breakwater with the boundary integral equation method. The spaces between neighbor pontoons showed obvious effect on the wave reflection and transmission coefficients. Peña et al. (2011) studied various designs of breakwaters which included single and double pontoons, aiming to test the coastal protection function. Tan et al. (2016) captured reflection and transmission coefficients to measure dissipative energy in the gap under different edge configuration of floating dual-pontoons. Ji et al. (2016) took four types of floating breakwaters into consideration. The 2D experiment was conducted. Ji et al. (2019) experimentally compared the hydrodynamic performance of single and dual floating breakwaters, whose results indicated that the dual-pontoon floating breakwater has a smaller transmission coefficient compared with the single case for short-period wave conditions.

This study also considers the dual-pontoon breakwater. A special situation is investigated when the breakwater is damaged with open water channels regularly distributed along the pontoons, as an extended investigation of Ning et al. (2018). Physical experiments are conducted to investigate the wave protection effectivity of the remaining part of the breakwater. The reflection and transmission coefficients are compared between undamaged and damaged cases. Wave profiles between damaged pontoons are also analyzed.

2 EXPERIMENTAL SET-UPS

Physical experiments are carried out in the State Key Laboratory of Coastal and Offshore Engineering, Dalian University of Technology. Figure 1 illustrates set-ups of the experiment. Two sets of dual-pontoon models are tested in a 60m long and 3m wide wave flume, corresponding to undamaged and damaged breakwaters,

respectively. The initial water depth is *d*=0.6m. For the damaged situation, water channels on each pontoon are considered to distribute regularly. Taking advantage of the geometric symmetry, we can consider the pontoons as infinitely long. As in Figure 1 (a) and (b), three parameters (i.e. the length *A*, breadth *B*, and draught *h*) are used to represent the geometry of pontoons. We use *A*=3m, *B*=0.6m and *h*=0.3m for the undamaged situation, and *A*=1.4m, *B*=0.6m and *h*=0.3m for the damaged one. Three spaces *L*=0.026, 0.029, and 0.036m between two pontoons will be tested. Five wave gauges (G1 to G5) are located between two pontoons, whose relative locations are marked out in Figure 1(c). The distance between the wave gauges and the front pontoon is 0.145m. Three wave gauges (G6, G7, G8) are located in the weather side of the front ponton to separate incident and reflected waves. Their distances from the front pontoon are *A1*=1m, *A2*=0.5m and *A3*=1.5m, respectively. G9 is on the lee side of the back pontoon to test transmitted waves with *A4*=1.5m. A series of regular waves with periods ranging from 0.7s to 2.0s are generated in the wave flume. For each test, over 50 incident waves were generated to capture the fully developed waves. The incident wave height is constantly set as H_i=0.04m for all cases.

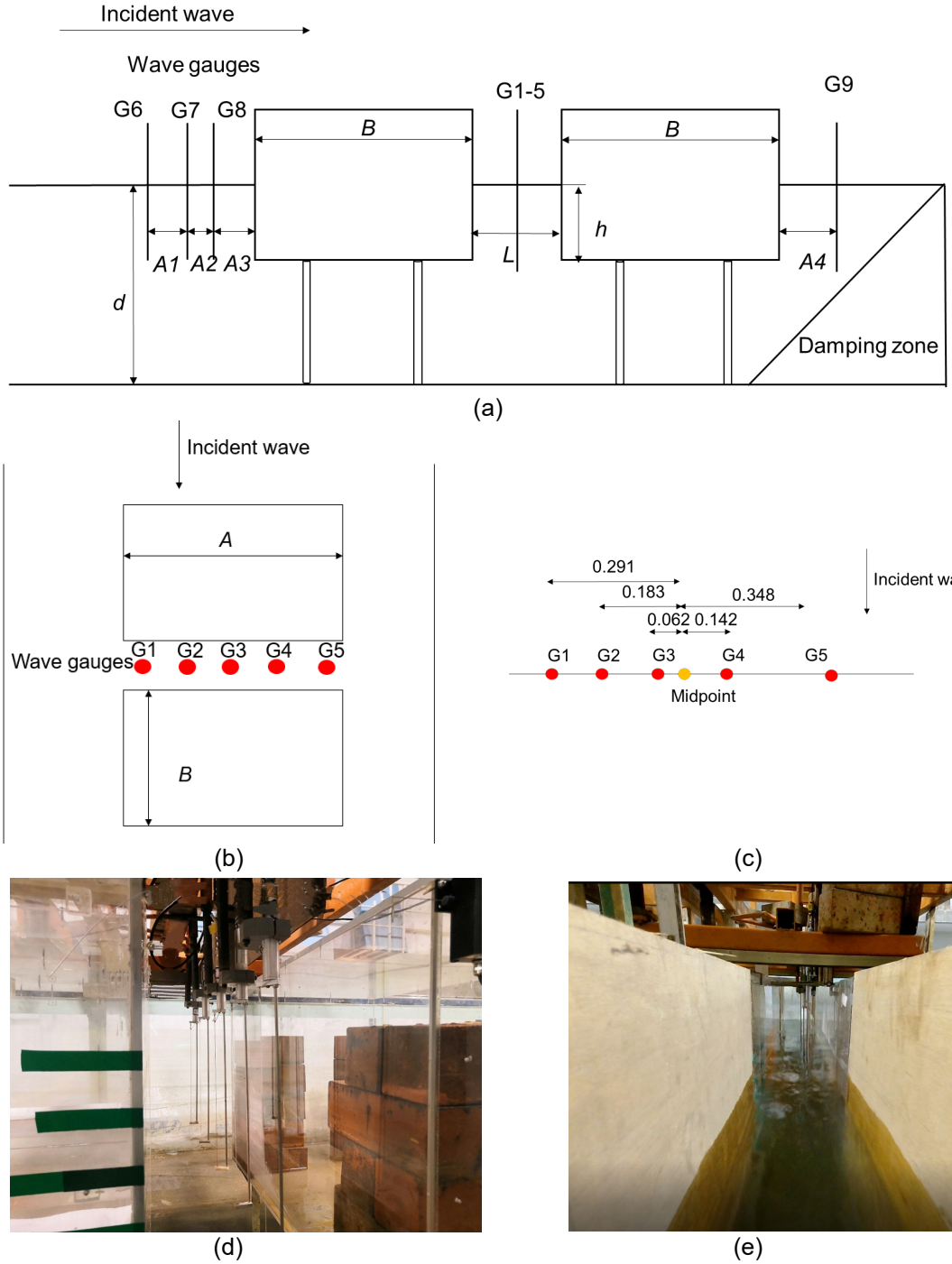

Figure 1 Overview of experimental set-up: (a) side view; (b) top view; (c) layout of wave gauges between two pontoons; (d) physical model when *L*=1.4m and (e) physical model when *L*=3m

3 RESULTS AND DISCUSSIONS

3.1 Wave reflection and transmission coefficients

This subsection will compare the wave reflection and transmission coefficients of undamaged and damaged dual-pontoon breakwaters. The coefficients are obtained by the method proposed in Goda & Suzuki (1976). Figure 2 gives both coefficients corresponding to different wave periods. From subfigure (a) to (c), the pontoon space is set as L=0.22m, 0.29m and 0.36m, respectively. The subscript r and t denote the reflection of transmission coefficients, respectively. The undamaged breakwater is denoted by the length of the pontoon as A=3m, and the damaged one by A=1.4m.

For the undamaged situation, the problem in fact is two-dimensional. In each subfigure, the trend of the K_r curve shows a valley within the consider range of wave period. To be specific, as the pontoon space increases from 0.22m to 0.29m and further 0.36m, the minimum reflection coefficient occurs at about T=1.7s, 1.8s and 1.95s, respectively. The transmission coefficient K_t generally has the opposite trend. This confirms the fact that the pontoon space can apparently influence the reflection and transmission coefficients of the dual-pontoon breakwater.

For the damaged situation, corresponding to the same wave period, the reflection coefficient K_r is always lower than the undamaged one, which can be expected easily. The K_r curve generally shows a decreasing trend for larger wave periods, which means that the damaged breakwater is losing its wave protection capability for longer waves. However, for the transmission coefficient K_t, the value for all wave periods is around 1.0 indicating a nearly complete wave transmission. This incredibly large value of K_r may be caused by the methodology. The wave field around the breakwater is three-dimensional. The calculated K_r is only based on the wave gauge at G9, where three-dimensional wave effects from other directions also contribute.

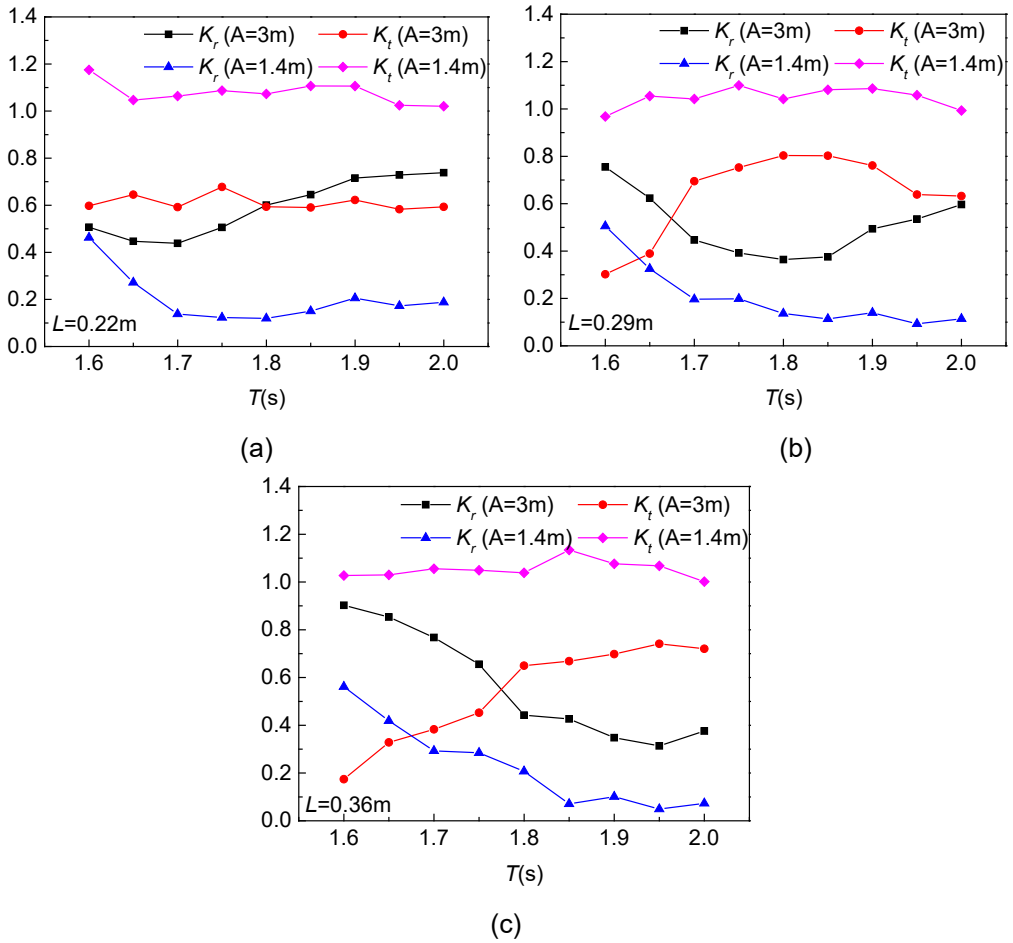

Figure 2 Reflection and transmission coefficients of undamaged and damaged dual-pontoon breakwaters with (a) L=0.22m; (b) L=0.29m; and (c) L=0.36m

3.2 On wave height between two pontoons

Figure 3 further compares the wave height between two pontoons based on the measurement at G3. For the undamaged situation, the largest wave height is around 3.3, 3.1 and 2.5 times H_i for L=0.22m, L=0.29m and

L=0.36m, respectively. In Figure 3(a), the curve peaks occur at the wave period *T*=1.65s, 1.8s and *T*=1.9s, very close to wave conditions of the largest wave transmission or the smallest wave reflection in Figure 2. We may give a physical explanation that the large amplitude oscillation of water column between two pontoons can further disturb the downstream wave field and increase the wave transmission. For the damaged situation, the wave heights between pontoons are smaller than those in undamaged cases. Compared with the undamaged breakwaters, the wave height between two damaged pontoons seems insensitive to the wave period for these considered cases.

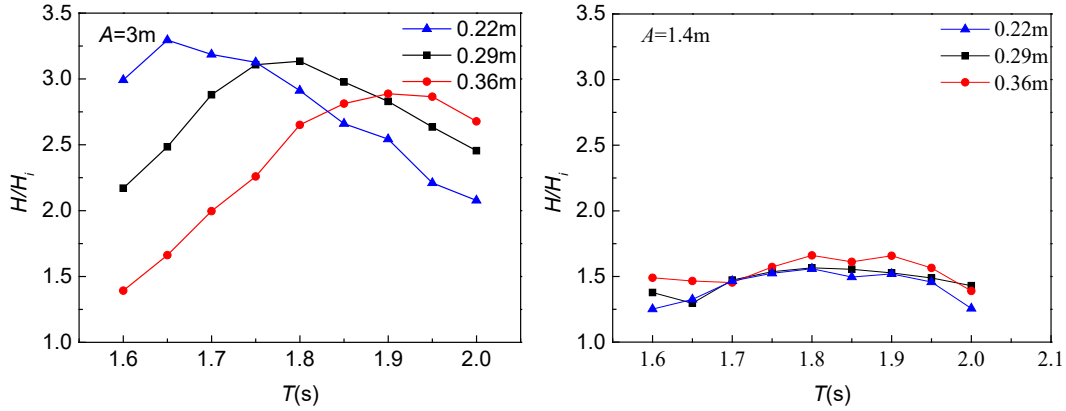

(a) (b)

Figure 3 Wave height of the middle of gap, for (a) *A*=3m; and (b) *A*=1.4m

3.3 Wave profiles between two pontoons of the damaged breakwater

This subsection further considers the evolution of wave profiles between two pontoons of the damaged breakwater. The instantaneous wave profiles between two pontoons are obtained through a cubic interpolation of wave elevations measured at G1 to G5. To help increase the interpolation accuracy, another five image wave gauges can be introduced due to the physical symmetry of the wave field about the middle plane of the wave flume. Figure 4 shows the evolution of wave profiles between two pontoons for the wave period of *T*=1.6, 1.8, and 2.0. Along the length of the pontoon, the wave profiles are nearly constant, without evident three-dimensional wave effect. We further shorten the period of incident waves, and give the evolution of wave profiles for *T*=0.7s, 0.8s, and 0.9s in Figure 5. For these short-wave cases, the wave profile along the pontoon has spatial variation. This means that the waves can get into the gap between two pontoons and influence the wave motion inside. Corresponding to a smaller period of incident waves, the wave-length of the wave profile along the pontoon is also smaller, as an evidence of stronger three-dimensional wave effects. The evolution of these wave profiles indicates that a transverse standing wave may exist along the pontoon, whose properties deserve further investigation.

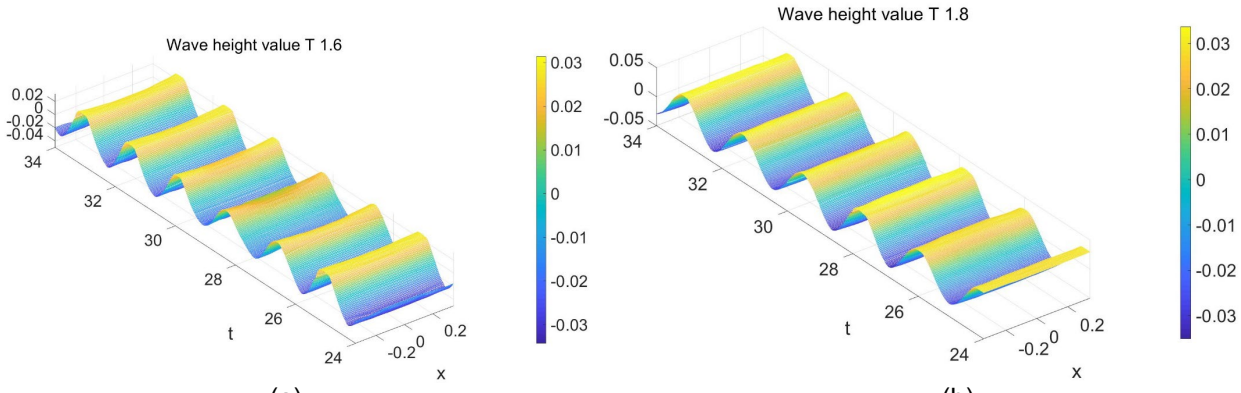

(a) (b)

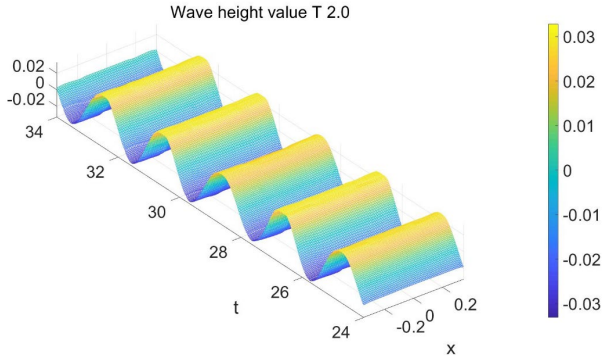

(c)

Figure 4 Evolution of wave profile between pontoons in transient waves for *T*= (a) 1.6s; (b) 1.8s; and (c) 2.0s

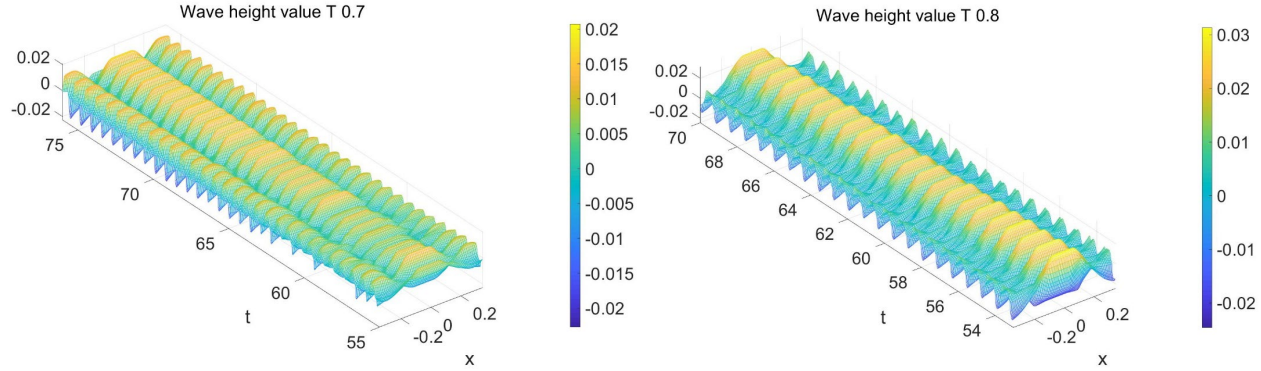

(a)

(b)

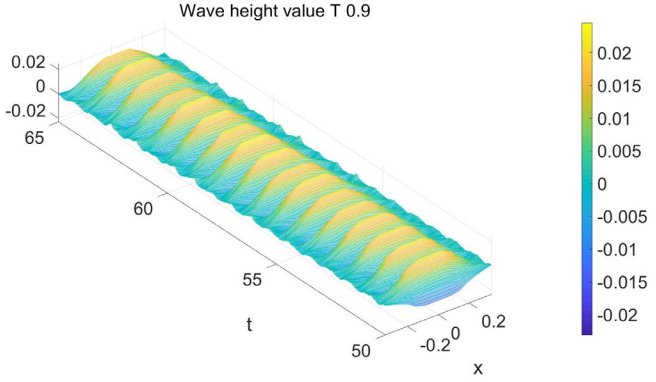

(c)

Figure 5 Evolution of wave profile between pontoons in transient waves for *T*= (a) 0.7s; (b) 0.8s; and (c) 0.9s

4 CONCLUSIONS

This study considers the dual-pontoon breakwater. A special situation is investigated when the breakwater is damaged with open water channels regularly distributed along the pontoons. Physical experiments are conducted to investigate the wave protection effectivity of the remaining part of the breakwater. Effects of the pontoon space on the wave reflection and transmission coefficients of the breakwaters are investigated. The wave height between two pontoons corresponding to different wave periods are discussed. The evolution of wave profiles between two pontoons of the damaged breakwater is investigated.

It is found that the reflection coefficient of a damaged breakwater generally shows a decreasing trend for larger wave periods. This means that the damaged breakwater is losing its wave protection capability for longer waves. Meanwhile, the wave heights between two damaged pontoons are smaller than those in undamaged cases. Compared with undamaged breakwaters, the wave height between two damaged pontoons seems insensitive to wave periods under consideration. For a larger wave period, the wave profile along the pontoon is nearly constant, without evident three-dimensional wave effects. However, for short-wave cases, the wave profile along the pontoon has spatial variation, indicating the occurrence of a transverse standing wave. The three-dimensional wave field around a damaged breakwater deserves further investigation.

ACKNOWLEDGEMENT

This study is supported by the National Key R & D Program of China (Grant No. 2018YFB1501904), the National Natural Science Foundation of China (Grant Nos. 51709038 and 51739010), and the Project funded by China Postdoctoral Science Foundation (No. 2018M630289 and 2019T120209).

REFERENCES

Abul-Azm, A.G. (1994). Wave diffraction by double flexible breakwaters. *Applied ocean research*, 16 (2), 87-99.

Abul-Azm, A.G., & Gesraha, M.R. (2000). Approximation to the hydrodynamics of floating pontoons under oblique waves. *Ocean Engineering*, *27* (4), 365-384.

Christensen, E.D., Bingham, H.B., Friis, A.P.S., Larsen, A.K., & Jensen, K.L. (2018). An experimental and numerical study of floating breakwaters. *Coastal engineering*, 137, 43-58.

Drimer, N., Agnon, Y., & Stiassnie, M. (1992). A simplified analytical model for a floating breakwater in water of finite depth. *Applied Ocean Research*, 14 (1), 33-41.

Goda, Y., & Suzuki, Y. (1977). Estimation of incident and reflected waves in random wave experiments. In *Coastal Engineering* 1976 (pp. 828-845).

Ji, C. Y., Chen, X., Cui, J., Yuan, Z. M., & Incecik, A. (2015). Experimental study of a new type of floating breakwater. *Ocean Engineering*, 105, 295-303.

Ji, C., Deng, X., & Cheng, Y. (2019). An experimental study of double-row floating breakwaters. *Journal of Marine Science and Technology*, 24 (2), 359-371.

Ning, D., Zhu, Y., Zhang, C., & Zhao, M. (2018). Experimental and numerical study on wave response at the gap between two barges of different draughts. *Applied Ocean Research*, 77, 14-25.

Peña, E., Ferreras, J., & Sanchez-Tembleque, F. (2011). Experimental study on wave transmission coefficient, mooring lines and module connector forces with different designs of floating breakwaters. *Ocean Engineering*, 38 (10), 1150-1160.

Sannasiraj, S.A., Sundar, V., & Sundaravadivelu, R. (1998). Mooring forces and motion responses of pontoon-type floating breakwaters. *Ocean Engineering*, *25* (1), 27-48.

Syed, S.A., & Mani, J.S. (2006). Performance of Multiple Pontoons Floating Breakwater–A Numerical Approach. In *Civil Engineering in the Oceans VI* (pp. 342-355).

Tan, L., Lu, L., Tang, G. Q., & Cheng, L. (2016). Experimental Study of Wave Resonance in a Narrow Gap with Various Edge Shapes. In *Proceedings of the 20th Australasian Fluid Mechanics Conference, Perth, Australia* (pp. 5-8).

Williams, A.N., & Abul-Azm, A.G. (1997). Dual pontoon floating breakwater. *Ocean Engineering*, 24 (5), 465-478.

8th International Conference on the Application of Physical Modelling in Coastal and Port Engineering and Science
Dec. 9th - 12th, 2020, Zhoushan, China

EXPERIMENT ON VORTEX-INDUCED VIBRATION AND WALL IMPACT OF SUBMARINE FLEXIBLE PIPELINE NEAR SEABED

HONGJUN ZHU[1,2], HONGLEI ZHAO[3] & NARAKORN SRINIL[4]

[1] State Key Laboratory of Oil and Gas Reservoir Geology and Exploitation, Southwest Petroleum University, Chengdu, China, zhuhj@swpu.edu.cn
[2] State Key Laboratory of Coastal and Offshore Engineering, Dalian University of Technology, Dalian, China
[3] Petroleum Engineering School, Southwest Petroleum University, Chengdu, China, 201811000091@stu.swpu.edu.cn
[4] Marine, Offshore & Subsea Technology Group, School of Engineering, Newcastle University, United Kingdom

ABSTRACT

In this paper, VIV of a flexible pipeline span is experimentally investigated in a water flume. The pipeline made of silica gel has an aspect ratio of about 87 and fixed supports, subject to approaching flow with an angle of attack of 30°. A non-intrusive measurement with high-speed cameras is employed to simultaneously capture the space-time varying oscillations in the in-line and cross-flow directions for a reduced normal velocity range of U_r=3–15, corresponding to a Reynolds number range of 650-2780, with G/D=0.2 and 0.5. Cross-flow response is asymmetric about the initial position and the new equilibrium position deviates against the plane wall. For a certain segment of the flexible pipeline, the impact occurs when the difference between the oscillation amplitude and the new equilibrium position is equal to the initial gap ratio. In view of the dominant response mode and the collision spatial distribution, six distinct solid-pipe impact patterns are observed for G/D = 0.2 and 0.5, including FS (the first dominant response with a short segment impact), FL (the first dominant response with a long segment impact), SA (the second dominant response with two segments alternating impact), SS (the second dominant response with a single segment impact), T1 (transition mode 1), T2 (transition mode 2).

Keywords: vortex-induced vibration; pipeline; pipe-wall impact; impact pattern; non-intrusive measurement

1 INTRODUCTION

Offshore oil and gas flows are commonly transported by submarine pipelines that are generally laid on or shallowly buried in the seafloor. Free spans are easily formed due to the complex topographic conditions and local scour, posing a risk to the safety of pipelines. In the past decades, significant research efforts have been devoted to investigating the scour process beneath submarine pipelines and the forces exerted on pipeline surface. A gap between the pipeline and the seabed was observed to be a key parameter determining the hydrodynamic lift/drag forces and the pipe vibration response.

Experimental studies by Bearman and Zdravkovich (1978), Grass et al. (1984), Taniguch and Miyakoshi (1990), Buresti and Lanciotti (1992), Lei et al. (1999), Price et al. (2002) and He et al. (2017) as well as numerical investigations of Lei et al. (2000) have found that the existence of plane wall significantly affected the vortex-shedding characteristic and the hydrodynamic loading of a near-wall cylinder. These studies shown that the critical gap ratio G/D (G is the gap between the wall and the bottom of the circular cylinder and D is the cylinder diameter) for vortex shedding suppression is about 0.2-0.3.

Nevertheless, the cylinder can still vibrate even though the regular vortex shedding does not take place when the initial gap between the cylinder and the plane wall is extremely small (Wang et al., 2013). Numerous numerical studies by Tham et al. (2015), Li et al. (2017), Chern et al. (2017), Chen et al. (2019) and Gao et al. (2020) have been observed that the single vortex or asymmetrical vortex was discovered and the XY-trajectory is regularly an oval-shape due to the wall proximity at low Reynolds numbers.

Moreover, if the gap is sufficiently small, the pipeline may collide with the seabed and bounce back after the collision, influencing the vibration characteristics due to the time-varying gap. However, quite a few studies in the literature have investigated the solid-pipe impact phenomenon between the cylinder with the plane wall. The influence of close proximity of wall was experimentally studied (Yang et al., 2006), where a laser displacement transducer was employed in a water flow channel to record the vertical displacements of the near-boundary pipeline. It was found that the displacements of the near-wall pipe were asymmetrical and the periodical collisions between the test pipe and the rigid boundary were observed with G/D=0.28.

Zhao and Cheng (2011) numerically studied the vibration response of cylinder close to a plane boundary with G/D=0.002. It indicated that the cylinder will impact with the plane boundary and the vibration amplitude is related to the bouncing back coefficient, which is between zero and one. Chung (2016) observed the beating

phenomenon at a lager gap of 0.06*D* and 0.3*D*, where the impact has no obvious effect on the amplitude and frequency of VIV. Zang and Zhou (2013) showed that the vibration equilibrium position away from the bottom wall and the impact between cylinder and the plane wall lead to the non-symmetric oscillation. Afterwards, Zang and Zhou (2017) found that the vortex shedding pattern of "vortex-shedding-after-bounce-back mode", which is defined by Zhao and Cheng (2011). The effects of the plane boundary on the vertical response of a near-wall cylinder have been experimentally studied in a water flume (Barbosa et al., 2017). It was shown that the critical gap ratio which the cylinder impacts the wall is 0.75. For gaps smaller than 0.75 diameters, the cylinder will collide with the plane wall, resulting in the associated asymmetric vibration response. Recently, the particle image velocimetry (PIV) has been employed to capture the wake vortex shedding from the near-wall cylinder (Daneshvar and Morton, 2020). It was observed that P or P_0 vortex shedding pattern may be introduced, owing to the intensive interaction between the near-wall side shed vortices with the wall boundary layer, when the impact occurs. The impact branch (or bounce back branch) of the amplitude response was determined by Chung (2016), Zang and Zhou (2017) and Daneshvar and Morton (2020), for which the vibration amplitude is equal to the gap ratio.

The aforementioned studies are mainly concerned the VIV and wall impact of rigid cylinders near a plane boundary. The dynamic behavior of long flexible cylinders in the presence of a wall is fairly different from that of rigid ones. Therefore, in this work, the dynamic responses and pipe-solid impact of a long flexible pipeline near a bottom are experimentally investigated via a non-intrusive measurement.

2 TITLE, AUTHORS AND AFFILIATIONS

The experiments were performed in a water flume with a test section of 1m × 0.5m × 2m (height × width × length) at the Offshore Oil and Gas Laboratory of Southwest Petroleum University. As depicted in Figure 1, the water depth was kept constant of 0.6m and the coming flow velocity was measured by an Acoustic Doppler Velocimetry (ADV), with the maximum normal velocity generated by the water flume of 0.46m/s. The pipe model was fixed through two supporting rods, which can be adjusted so that the gap between the flexible pipe and the bottom wall can meet the gap ratios (G/D=0.2 and G/D=0.5) considered in the present study. Besides, a horizontal oblique angle θ=30° between the coming flow direction and the pipe cross-sectional plane is considered. A non-intrusive measurement was employed to capture the pipeline response, with a total of twenty-six measurement points marked along the pipe. The in-line and cross-flow vibration displacements of the flexible pipe were measured by two high-speed cameras, which were placed underneath the flume and beside the flume, respectively.

The main experimental parameters are summarized in Table 1, where the pipe model is made of a silica gel tube with the elasticity modulus E=3.59MPa. The aspect ratio was L/D=87, where L is the length and D is the diameter of this pipe. The mass ratio of the pipe was calculated to be $m^*=4m/\pi\rho D^2L$=1.02, where m is the total mass of the pipe filled with water and ρ is the water density. The normal Reynolds number range of Re_n=650-2780, corresponding to the normal reduced velocity range of U_r=3.40-14.43. The first natural frequency f_1 and the damping ratio ζ were determined with the free decay test by placing the flexible pipe in still water and giving an initial displacement. In this study, the first natural frequency is 5.34Hz and the damping ratio is 0.072.

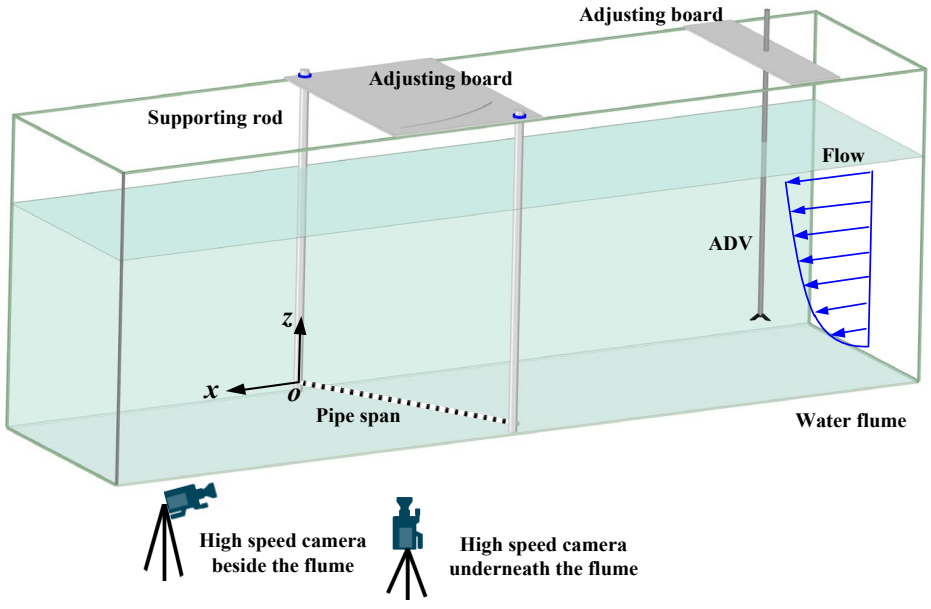

(a)

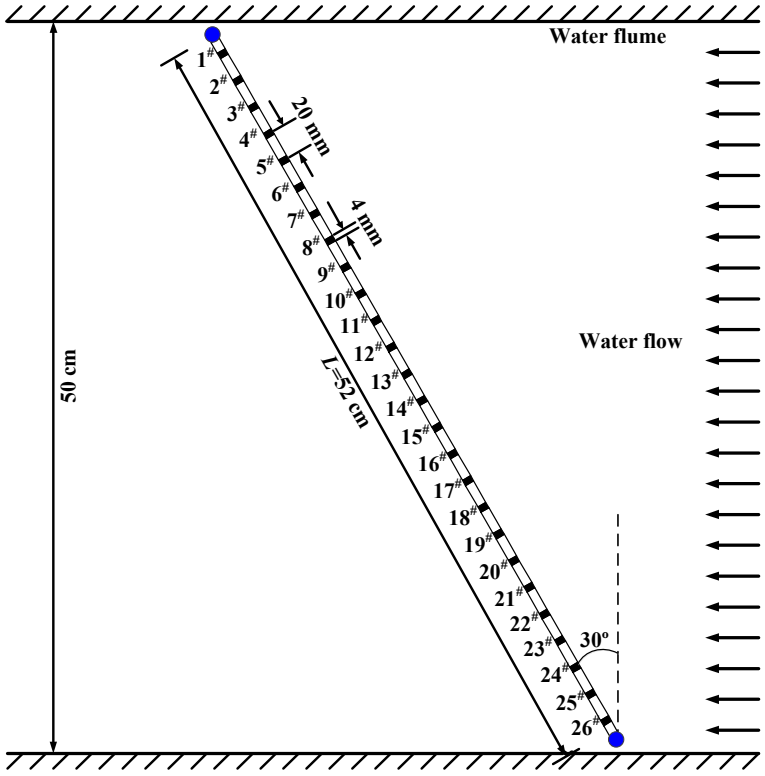

(b)

Figure 1. Experimental set-up.

Table 1. Experimental flow-pipe parameters.

Parameters	Value	Unit
Length, L	52	cm
Outer diameter, D	6	mm
Pipe thickness, δ	1	mm
Aspect ratio, L/D	87	/
Gap ratio, G/D	0.2, 0.5	/
Young's modulus, E	3.59	MPa
Mass ratio, m^*	1.02	/
Damping ratio in water, ζ	0.072	/
Normal flow velocity, U_n	0.11-0.46	m/s
Normal Reynolds number, Re_n	650-2780	/
Normal reduced velocity, U_r	3.40-14.43	/

3 SAMPLE IMPACT PATTERN

Figure 2(a) presents crossflow displacement envelope curves at U_r=6.06, for G/D=0.2, for which the dashed lines of Z/D=-0.2 represent the plane wall position. It is seen that the crossflow vibration of the submarine flexible pipeline is not symmetric about the initial equilibrium position (Z/D=0), which is in accordance with findings reported by Zang et al. (2013). Both the wall proximity and collision affect the pipe vibration response, resulting in the new equilibrium positions deviate away from the bottom boundary. When the impact between the pipe and the solid wall occurs, the maximum crossflow displacement in the downward direction is equal to -0.2, which is the same as the pipe-to-wall gap ratio. Figure 2(b) shows the inline amplitude profile envelope, appearing to be a shuttle shape. Figure 2(c, d) presents the dimensionless vibration amplitudes and the new equilibrium positions for both the cross-flow and in-line directions. It is clear that the responses are first-mode excitation both in the CF and IL directions, and the amplitude is basically symmetrical about the middle span so that the maximum amplitude is primarily at the mid-span. A key feature of the in-line response is that the pipe will be driven downstream because of the drag forces acting on the flexible pipe. Nevertheless, it is worth noting that the CF equilibrium position has a distribution of CF response amplitude. The impact appearance is attributed to the response amplitude over the total of the equilibrium position and the plane boundary. For the first-mode dominant responses in crossflow and inline directions, the

impact occurs with a short segment in middle span: this case is termed FS (the first dominant response with short segment impact).

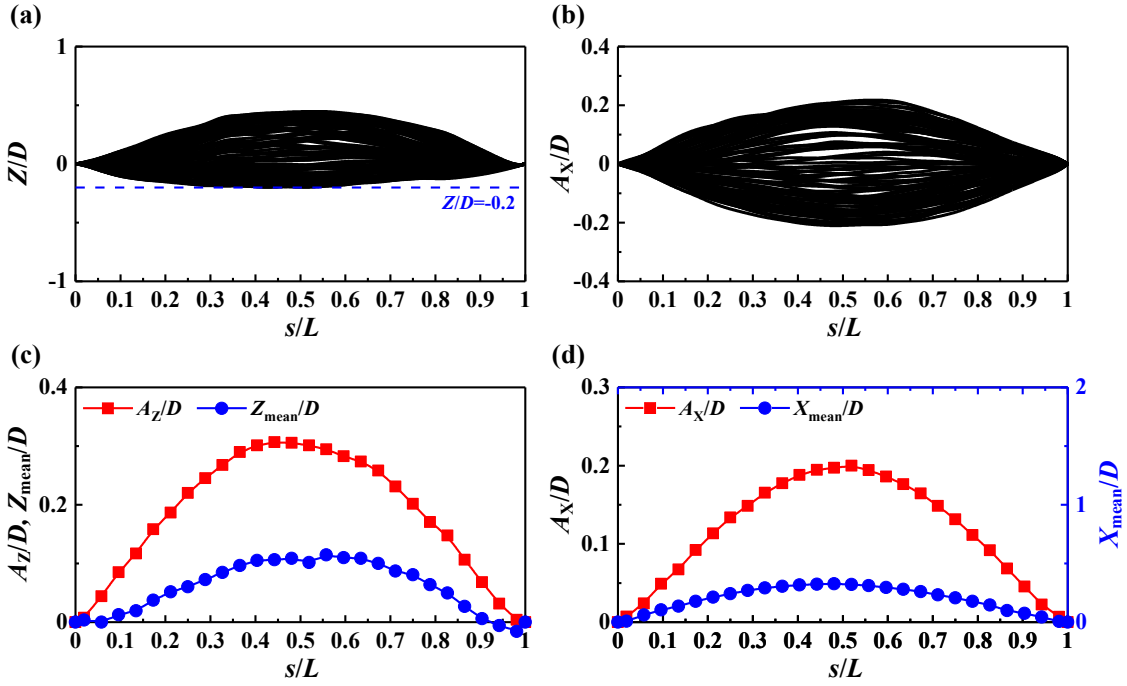

Figure 2. Response profile envelopes in (a) crossflow and (b) inline directions; response amplitude and equilibrium positions in (c) crossflow and (d) inline directions, all at U_r=6.06 of G/D=0.2.

Figure 3 shows the same plots as Fig. 2, but for U_r=7.38 and G/D=0.5. Compared to the previous case, the 1st mode in the CF direction and 2nd mode in the IL direction were excited. There are a long pipe-segment impact with the plane wall, which is termed FL (first dominant response with long segment impact).

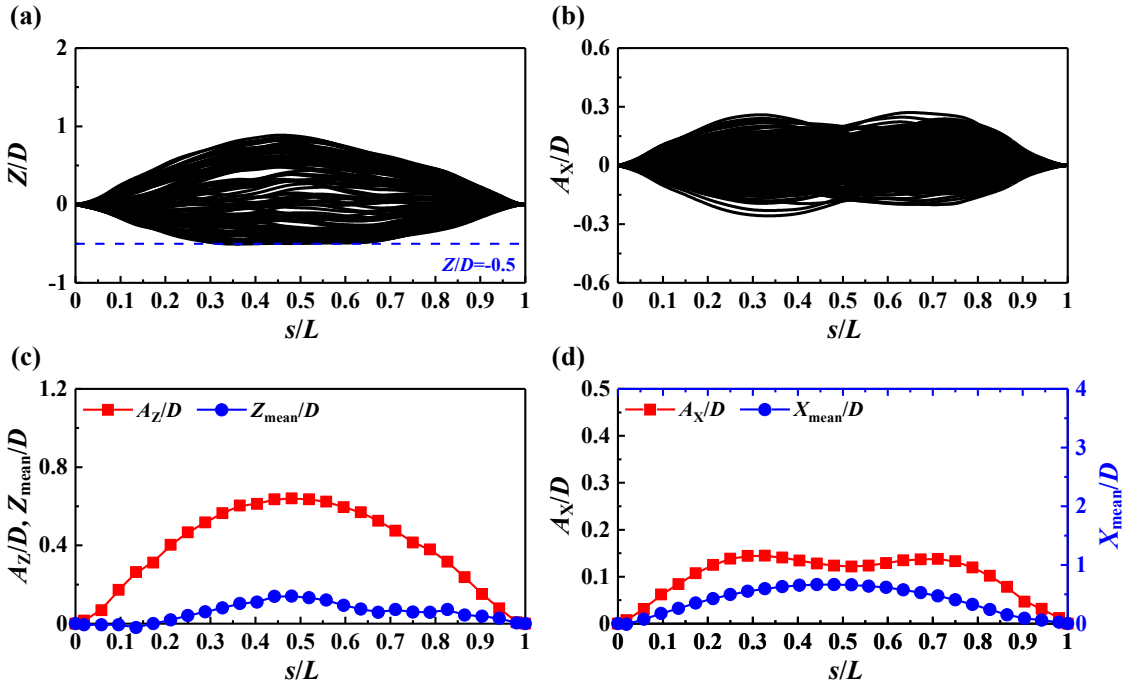

Figure 3. Response profile envelopes in (a) crossflow and (b) inline directions; response amplitude and equilibrium positions in (c) crossflow and (d) inline directions, all at U_r=7.38 of G/D=0.5.

The response of flexible submarine at a normal reduced velocity of U_r=14.43 with G/D=0.2 is chosen as a representative response, where the CF response has been completely translated to the second mode, and the IL response was in transition from the second to the fourth mode. There are two alternate pipe-segment impact parts with the plane wall, and this is termed SA (the second dominant response with two segments alternating impact).

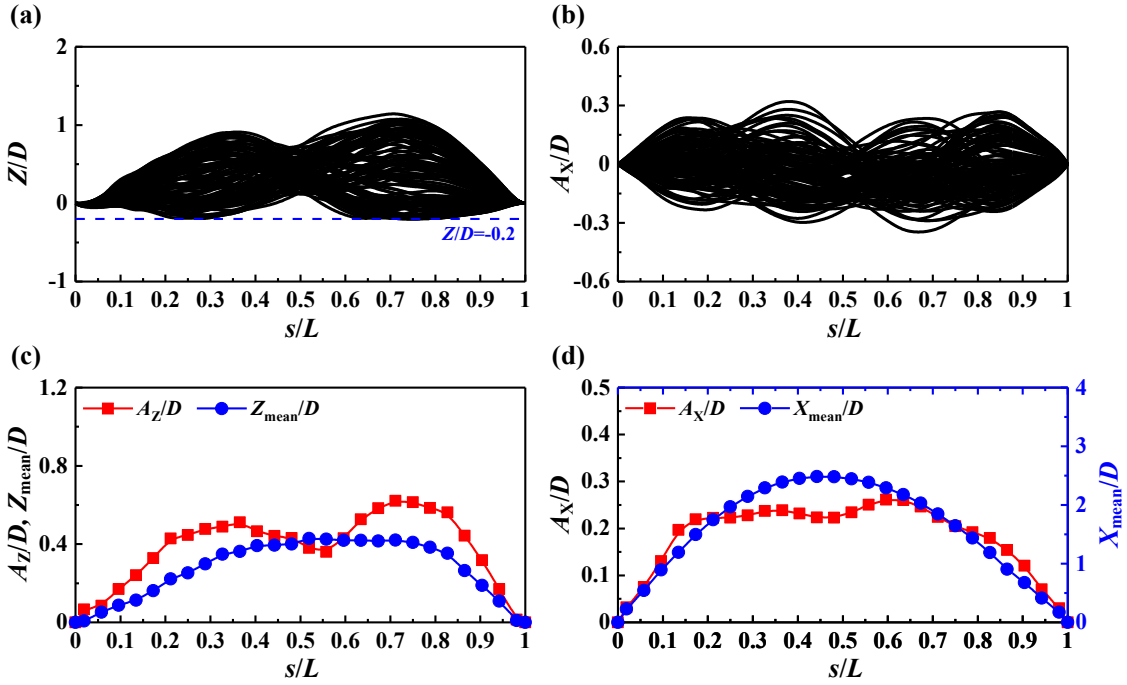

Figure 4. Response profile envelopes in (a) crossflow and (b) inline directions; response amplitude and equilibrium positions in (c) crossflow and (d) inline directions, all at U_r=14.43 of G/D=0.2.

Similar to Figure 4, the near-wall pipe response in CF was still dominated by the second mode, while the third-mode shape was observed in the inline direction at U_r=13.85 of G/D=0.5. The smaller peak of vibration amplitude is less than the summation of new equilibrium position and initial gap ratio as show in Figure 4, indicating that the impact does not occur, which is termed SS (the second dominant response with single segment impact).

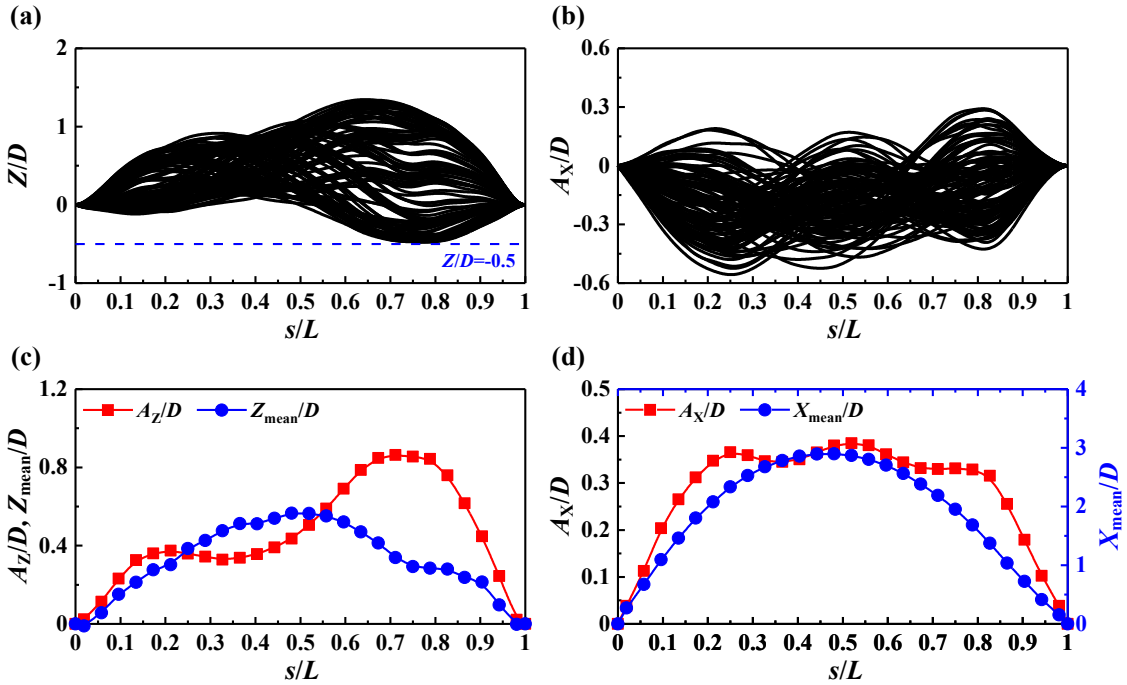

Figure 5. Response profile envelopes in (a) crossflow and (b) inline directions; response amplitude and equilibrium positions in (c) crossflow and (d) inline directions, all at U_r=13.85 of G/D=0.5.

As displayed in Figures 6 and 7, a multimode dynamic response and transition from the lower first-mode excitation to a higher second-mode excitation in the crossflow direction of the flexible pipe were observed. For U_r=9.36 and G/D=0.5, the multi-mode (first mode and second mode) response, dominated by the first mode, was excited in the crossflow direction, whereas the inline excitation was dominated by the third mode as shown in Figure 6. Figure 7 shows that the transition from the first mode to the second mode in the crossflow

direction was still incomplete for U_r=10.83 and G/D=0.5. Nevertheless, the CF response was dominated by the second mode compared to Figure 6. Two different impact patterns were defined as T1 (transition mode 1) and T2 (transition mode 2), respectively.

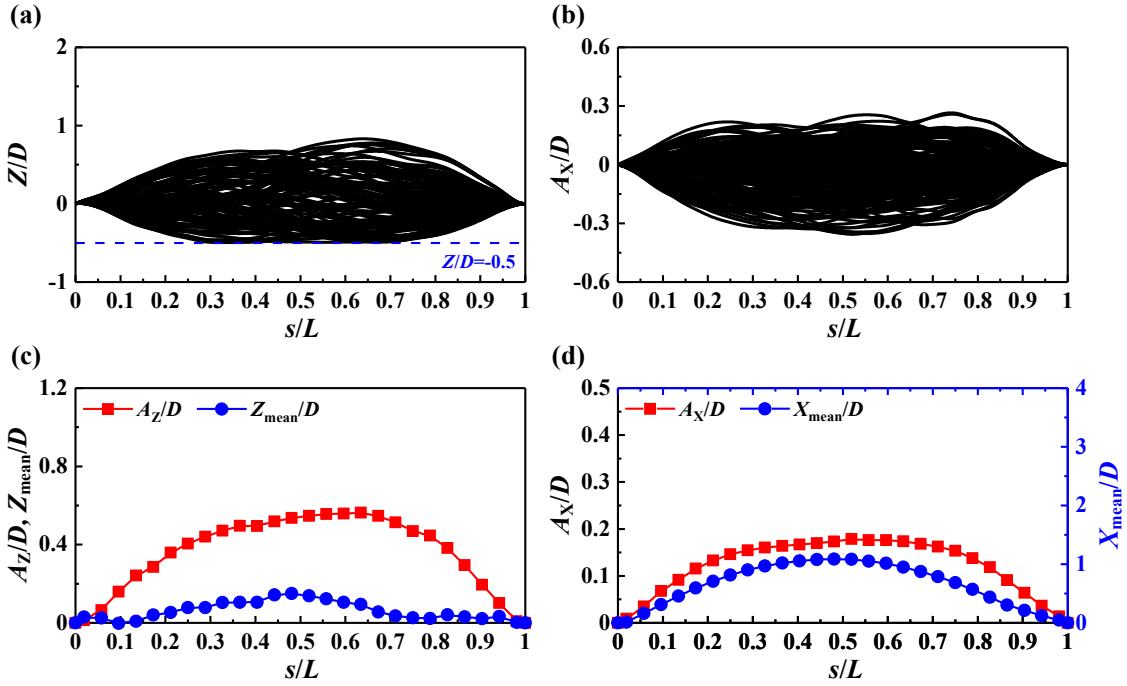

Figure 6. Response profile envelopes in (a) crossflow and (b) inline directions; response amplitude and equilibrium positions in (c) crossflow and (d) inline directions, all at U_r=9.36 of G/D=0.5.

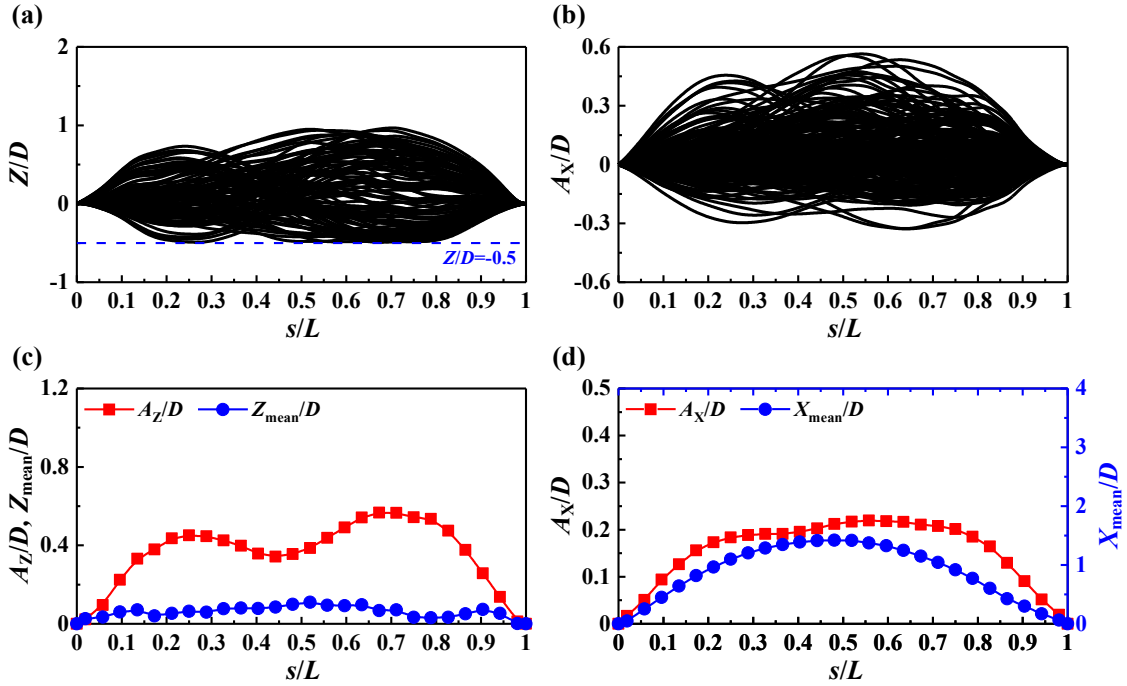

Figure 7. Response profile envelopes in (a) crossflow and (b) inline directions; response amplitude and equilibrium positions in (c) crossflow and (d) inline directions, all at U_r=10.83 of G/D=0.5.

Figures 8 and 9 show the solid-pipe impact pattern and the collision spatial distribution for two different gap ratios G/D=0.5 and G/D=0.2, respectively. Based on the above discussion, the collision occurs as a result of the difference between the vibration amplitude and the new equilibrium position being equal to the initial gap ratio, and the impact pattern and the dominant transverse vibration mode are interrelated. It is notable that there is no second mode dominant for the two segment alternating impact at G/D=0.5. The two vibration peaks of the second-order dominant vibration mode are not equal, and the smaller peak vibration amplitude could be less than the summation of the new equilibrium position and the initial gap ratio. Meanwhile, only four

impact patterns have been discovered at G/D=0.2, without mode transition, indicating that the increase with U_r of vibration amplitude and the new equilibrium position are inconsistent.

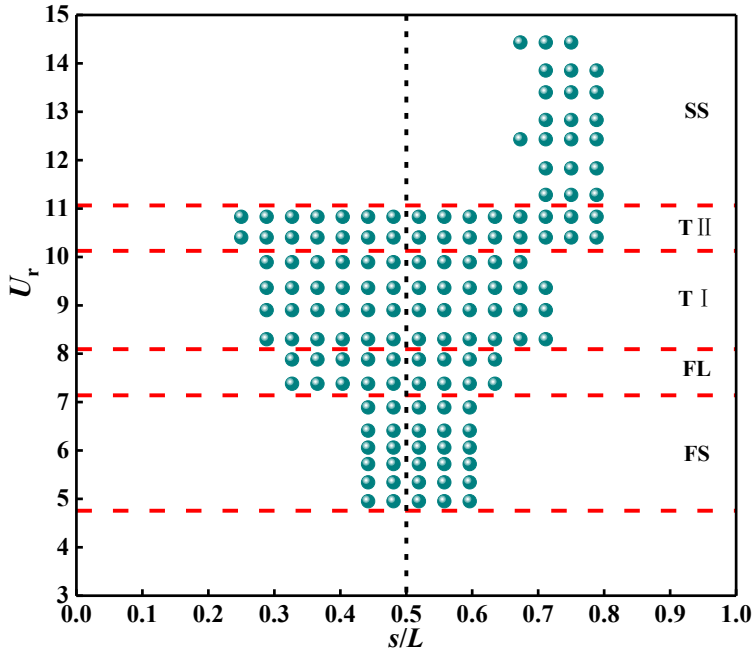

Figure 8. Variations of solid-pipe impact pattern distribution and impact position with U_r of G/D=0.5

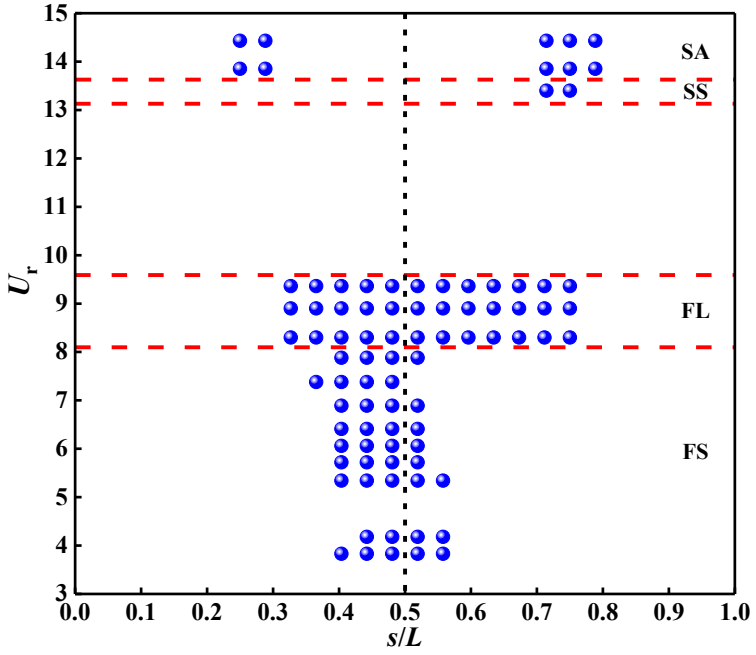

Figure 9. Variations of solid-pipe impact pattern distribution and impact position with U_r of G/D=0.2.

4 CONCLUSIONS

This work focuses on the response and pipe-wall impact of the flexible pipeline exposed to shear flow in a water flume and located near a solid wall. A non-intrusive measurement with high-speed cameras is employed to simultaneously capture the space-time varying oscillations in the inline and crossflow directions for a reduced normal velocity range of U_r=3–15, corresponding to a Reynolds number range of Re=650-2780, with G/D=0.2 and 0.5. The major conclusions from this study can be drawn as follows:

(1) Crossflow response is asymmetric about the initial position and the new equilibrium position deviates from the plane wall. The impact occurs due to the difference between the oscillation amplitude and the new equilibrium position being equal to the initial gap ratio.

(2) In view of the dominant response mode and the collision spatial distribution, six distinct solid-pipe impact patterns have been observed for G/D = 0.2 and 0.5: FS (the first dominant response with a short segment impact), FL (the first dominant response with a long segment impact), SA (the second dominant

response with two segments alternating impact), SS (the second dominant response with a single segment impact), T1 (transition mode 1), T2 (transition mode 2).

ACKNOWLEDGEMENTS

The research work was supported by National Nature Science Foundation of China (No. 51979238) and the Open Research Fund of State Key Laboratory of Coastal and Offshore Engineering, Dalian University of Technology (No. LP1930). The authors also gratefully acknowledge the Offshore Oil and Gas Laboratory at Southwest Petroleum University for the support to this work.

REFERENCES

Barbosa, J.M.D.O., Qu, Y., Metrikine, A.V., & Lourens, E.M. (2017). Vortex-induced vibrations of a freely vibrating cylinder near a plane boundary: Experimental investigation and theoretical modelling. Journal of Fluids and Structures, 69, 382–401.

Bearman, P.W., Zdravkovich, M.M. (1978). Flow around a circular cylinder near a plane boundary. Journal of Fluid Mechanics, 89, 33-47.

Buresti, G., Lanciotti, A. (1992). Mean and fluctuating forces on a circular cylinder in cross-flow near a plane surface. Journal of Wind Engineering and Industrial Aerodynamics, 41-44, 639–650.

Grass, A.J., Raven, P.W.J., Stuart, R.J. & Bray, J.A. (1984). The influence of boundary layer velocity gradients and bed proximity on vortex shedding from free spanning pipelines. Journal of Energy Resources Technology, 106, 70-78.

Chen, W.L., Ji, C.N., Xu, D., & Williams, J. (2019). Two-degree-of-freedom vortex-induced vibrations of a circular cylinder in the vicinity of a stationary wall. Journal of Fluids and Structures, 91, 102728.

Chern, M.J., Lu, G.T., Kuan, Y.H., Chakraborty, S., Nugroho, G., Liao, C.B., & Horng, T.L. (2017). Numerical study of vortex-induced vibration of circular cylinder adjacent to plane boundary using direct-forcing immersed boundary method. Journal of Mechanics, 34, 177–191.

Chung, M.H. (2016). Transverse vortex-induced vibration of spring-supported circular cylinder translating near a plane wall. European Journal of Mechanics B/Fluids, 55, 88–103.

Daneshvar, S., Morton, C. (2020). On the vortex-induced vibration of a low mass ratio circular cylinder near a planar boundary. Ocean Engineering, 201, 107109.

Gao, Y., Zhang, Z.Z., Zou, L., Liu, L.M., & Yang, B. (2020). Effect of surface roughness and initial gap on the vortex-induced vibrations of freely vibrating cylinder in the vicinity of a plane wall. Marine Structures, 69, 102663.

He, G.S., Wang, J.J., Pan, C., Feng, L.H., Gao, Q., & Rinoshika, A. (2017). Vortex dynamics for flow over a circular cylinder in proximity to a wall. Journal of Fluid Mechanics, 812, 698–720.

Lei, C., Cheng, L., & Kavanagh, K. (1999). Re-examination of the effect of a plane boundary on force and vortex shedding of a circular cylinder. Journal of Wind Engineering and Industrial Aerodynamics, 80, 263–286.

Lei, C., Cheng, L., Armfield, S., & Kavanagh, K. (2000). Vortex shedding suppression for flow over a circular cylinder near a plane boundary. Ocean Eng., 27(), 1109–1127.

Li, Z., Jaiman, R.K., & Khoo, B.C. (2017). Coupled dynamics of vortex-induced vibration and stationary wall at low Reynolds number. Physics of Fluids, 29, 093601.

Price, S.J., Sumer, D. Smith, J.G., Leong, K., & Paidoussis, M.P. (2002). Flow visualization around a circular cylinder near to a plane wall. Journal of Fluids and Structures, 16(2), 175-191.

Taniguchi, S., Miyakoshi, K. (1990). Fluctuating fluid forces acting on a circular cylinder and interference with a plane wall. Experiments in Fluids, 9, 197–204.

Tham, D.M.Y., Gurugubelli, P.S., Li, Z., & Jaiman, R.K. (2015). Freely vibrating circular cylinder in the vicinity of a stationary wall. Journal of Fluids and Structures, 59, 103–128.

Wang, X.K., Hao, Z., & Tan, S.K. (2013). Vortex-induced vibrations of a neutrally buoyant circular cylinder near a plane wall. Journal of Fluids and Structures, 39, 188–204.

Yang, B., Gao, F.P., Wu, Y.X., & Li, D.H. (2006). Experimental Study on Vortex-Induced Vibrations of Submarine Pipeline near Seabed Boundary in Ocean Currents. China Ocean Engineering, 20(1), 113–121.

Zang, Z., Gao, F.P., & Cui, J.S. (2013). Physical modeling and swirling strength analysis of vortex shedding from near-bed piggyback pipelines. Applied Ocean Research, 40, 50–59.

Zang, Z., Zhou, T. (2017). Transverse vortex-induced vibrations of a near-wall cylinder under oblique flows. Journal of Fluids and Structures, 68, 370–389.

Zhao, M., Cheng, L. (2011). Numerical simulation of two-degree-of-freedom vortex induced vibration of a circular cylinder close to a plane boundary. Journal of Fluids and Structures, 27, 1097–1110.

8th International Conference on the Application of Physical Modelling in Coastal and Port Engineering and Science
Dec. 9th - 12th, 2020, Zhoushan, China

A BOTTOM-SITTING WAVE ENERGY CONVERTER: LOCAL SCOUR AND THE CHARACTERISTICS OF LOCAL FLOW FIELD

ZHENHUA HUANG [1], SHIJIE HUANG [2] , YING-MIN LOW [3], ZHIXUAN ZHANG [4] & JUNCHENG CHEN [5]

[1,2] Department of Ocean and Resources Engineering, School of Ocean and Earth Science and Technology, University of Hawaii at Manoa, Honolulu HI, USA,
zhenhua@hawaii.edu

[3,4,5] Department of Civil and Environmental Engineering, National University of Singapore, Singapore,
ceelowym@nus.edu.sg

ABSTRACT

Most existing studies on wave energy converters (WECs) focused on the hydrodynamics and conversion efficiency of various designs. For the foundation safety of a bottom-sitting WEC, wave-induced scour around the WEC is an important factor to consider. There is a rich literature in wave or current induced scour around circular cylinders or bridge piers; however, published results on the local scour around WECs are scarce. Compared to circular cylinders or bridge piers, bottom-sitting WECs have much more complicated geometry and near-field flow patterns. This study will focus on a bottom- sitting WEC, which is a circular oscillating-water-column (OWC) integrated with a C-shaped support. A wave-flume test was performed to study the wave-induced local scour around the WEC. Development of the scour hole depth and the final scour hole profile around the bottom-sitting OWC-type WEC are presented. Two-phase (air-water) flow simulations were also performed to reveal the local flow structure and understand the experimental results. Numerical results show that the vortices shed from the two ends of the C- shaped support are responsible for the formation of the scour holes observed around the two ends of the C-shaped support.

Keywords: Wave energy conversion, OWC, CFD

1 INTRODUCTION

There is an increasing interest in utilizing ocean wave energy as a major and promising renewable resource (McCormick and Kraemer, 2001). For example, the University of Hawaii at Manao maintains a testing site for wave energy converters (WECs), providing berthing for as many as three WECs in the 10 to 1000 kW range Most existing studies focused on the following areas: the characterization of the wave energy resource, experimental, theoretical and numerical studied of various designs of wave energy converters (WECs) with an emphasis on wave energy conversion efficiency, power-takeoff (PTO) devices, and the mooring system for floating WECs, and construction and deployment into real sea of prototypes (Falcao 2010).

In terms of installation methods, there are two types of WECs: bottom- sitting WECs and floating WECs. To design and deploy bottom-sitting WECs, wave loading and foundation safety also need to be considered in addition to the efficiency of wave energy conversion. Detailed knowledge of the flow field around a bottom-sitting WEC is needed to calculate the loading on the WEC and understand possible scour around the WEC. Only recently have studies on wave loading, flow characteristics, and local scour been reported in the literature. For example, López et al. (2015) measured the flow field inside a rectangular OWC-type WEC by means of particle imaging velocimetry; Huang et al. (2019) performed a numerical study of wave loading on a bottom-sitting oscillating water column (OWC); Huang et al. (2020) reported a numerical study of the characteristics of the flow around a bottom-sitting WEC; and Lancaster et al. (2020) conducted an experimental study of the 3D scour process around a gravity based OWC-type WEC.

Existing numerical studies of flow fields around marine structures such as piles, pipes or WECs assume that the effect of the permeability on the water flow is negligible. For example, when simulating the local scour around a vertical cylinder, one most-used approach is to separate the simulation of the hydrodynamics from the simulation of sediment transport and scour process (Liang and Cheng, 2005). In this approach, the flow field at a given time step is first obtained by assuming that the bed is impermeable, next sediment transport rate is calculated using empirical equations with the obtained flowfield, and then the bed form is updated based on the calculated sediment transport rate for simulating the flow field at next time step (Baykal et al., 2017a)..

In this study, one set of experimental results of wave-induced scour around a bottom sitting oscillating water column is presented. To understand the observed scour pattern, the flow field around a bottom sitting

oscillating water column with the same dimensions was simulated using OpenFOAM (Jacobsen et al., 2012a). The relation between the flow field and the sour pattern is discussed.

2 METHODS

A wave-flume test was performed to study the wave-induced scour around a bottom-sitting OWC-type WEC. An OpenFOAM-based CFD numerical simulation was performed to understand the flow field around the bottom- sitting OWC-type WEC.

2.1 Experimental setup and methods of measurement

The wave flume used in this study had the following dimensions: 2 m (wide) x 1.3 m (high) x 36 m (long). The wave flume was equipped with a piston-type wave generator which is capable of generating regular and irregular waves. The water depth at the wave generator was fixed at 0.45 m in the experiment.

An OWC model was fabricated using a PVC pipe, which has an inner diameter of 0.089 m, and a pipe-wall thickness of 0.006 m. The orifice plate also had a thickness of 0.006 m and the orifice had a diameter of 0.0089 m, which results in an opening ratio of 1.0%.

The OWC model was installed in middle of a sand pit, which was constructed in the middle of the wave flume using two wedges, each with a slope of 1:7. The length of the sand pit was 2 m, and the depth of the sand pit was 0.15 m so that the water depth at the OWC model was 0.30 m. The size of the sand was D50 = 0.28 mm, and the specific gravity was 2.61.

Three wave gauges were used to measure the surface displacements at three locations: the first one was placed 4 m away from the paddle of the wave generator, the second one was place on the up-wave side of the OWC model, the third one was placed on the down-wave side of the OWC model. Both the second and the third wave gauges were above the sand pit. The air pressure inside the OWC chamber was not measured.

Figure 1 shows the model tested in the wave-flume tests, the model installed in the wave flume, and the devices used to measure the waves and local scour. The conversion efficiency of this OWC-type WEC has been studied by Xu et al. (2016) and Xu and Huang (2019).

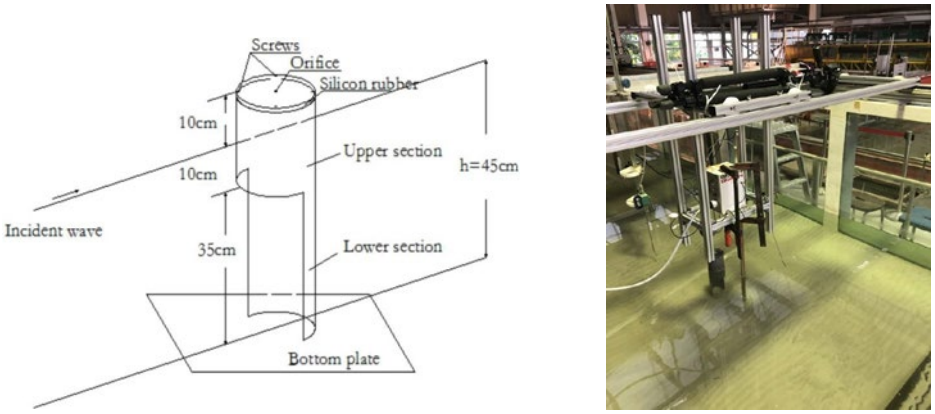

Figure 1. The left panel shows the model tested in the wave-flume tests, and the right panel shows the model installed in the wave flume.

The bed level was measured using sand profiler, Profile Indicator PV-09. The instrument has a servomechanism-driven gauge with a thin rod-shaped tip forming the actual probe. When the bed under the probe develops, the gauge can continuously follow changes in bed level. When measuring the bed levels on the concave side of the C-shaped supported, the orifice plate was removed. The bed levels at locations very close to the inner surface of the C-shaped support were not measured due to the difficulty of positing the probe at those locations.

2.2 Numerical methods

Waves2foam, an open source CFD library (Jacobsen et al., 2012a), is adopted in this study to perform two-phase flow simulations of wave interaction with a bottom-sitting, circular WEC. For completeness, the key equations in this two-phase flow model are summarized here.

The air is assumed to be in-compressible, and a mixture of air and water is used to describe the flow of air and water, which is governed by the incompressible Reynolds-Averaged Naiver-Stokes equations (RANS) (Rusche, 2003). A VOF method is used to track and locate the air-water interface by using a volume-fraction function s: s = 0 when a cell is occupied by air alone, s = 1 when a cell is occupied by water alone, and 0 < s <

1 when a cell is occupied by a mixture of air and water (Rusche, 2003). Anywhere in the flow, the density ρ and the dynamic viscosity μ_{lam} of the air-water mixture are calculated by

$$\rho = s\rho_w + (1-s)\rho_a, \quad [1]$$

$$\mu_{lam} = s\mu_w + (1-s)\mu_a, \quad [2]$$

where the subscripts w and a refer to water and air, respectively.

When 0 < s < 1, the volume-fraction function s is governed by a transport equation:

$$\frac{\partial s}{\partial t} + \nabla \bullet [s\vec{u}] + \nabla \bullet [\vec{u}_r s(1-s)] = 0, \quad [3]$$

where $\vec{u}$ is the velocity of the mixture, and $\vec{u}_r$ is a ``compression velocity", which is applied in the direction normal to the local air-water interface. The purpose of using a proper ``compression velocity" is to maintain a sharp air- water interface by compressing the volume-fraction field (Rusche, 2003).

The continuity equation for the air-water mixture is

$$\nabla \bullet \vec{u} = 0, \quad [4]$$

and the momentum equations is

$$\frac{\partial \rho \vec{u}}{\partial t} + \nabla \bullet [\rho \vec{u}\vec{u}^T] = \rho \vec{g} - \nabla p + \nabla \bullet [\mu \nabla \vec{u}], \quad [5]$$

where $\vec{g}$ is the gravitational acceleration, *p* is the total pressure of the air- water mixture. The total viscosity μ is

$$\mu = \mu_{lam} + \mu_t, \quad [6]$$

where μ_{lam} is the dynamic viscosity of the fluid and μ_t is the dynamic turbulent eddy viscosity determined by

$$\mu_t = \rho \frac{k}{\tilde{\omega}}, \quad [7]$$

and

$$\tilde{\omega} = \max\left\{\omega, C_{\lim}\sqrt{\frac{2S:S}{\beta^*}}\right\}, S = \frac{1}{2}\left(\nabla \vec{u} + (\nabla \vec{u})^T\right), \quad [8]$$

with ω being the specific dissipation rate (or a characteristic eddy frequency). Both C_{lim} and β^* are model parameters.

To obtain the turbulent kinetic energy *k* and the specific dissipation rate ω, the following k-ω SST turbulence model (Wilcox, 1993) is adopted :

$$\frac{\partial \rho \omega}{\partial t} + \nabla \bullet [\rho \vec{u} \omega] = \alpha p_\omega - \beta \rho \omega^2 + \frac{\sigma_d}{\omega}\rho \nabla k \bullet (\nabla \omega)^T + \nabla \bullet \left[\left(\mu_{lam} + \sigma_\omega \rho \frac{k}{\omega}\right)\nabla \omega\right], \quad [9]$$

and

$$\frac{\partial \rho k}{\partial t} + \nabla \bullet [\rho \vec{u} k] = \alpha p_k - \beta \rho \omega k + \nabla \bullet [(\mu_{lam} + \sigma_\omega \mu_t)\nabla k], \quad [10]$$

where the terms p_k and p_ω represent the productions of k and ω, respectively. To suppress possible abnormal growths in the turbulent viscosity and turbulent kinetic energy across the air-water interface, the following expressions for p_k and p_ω are employed (Mayer and Madsen, 2000; Jacobsen et al., 2012b):

$$p_k = \mu_t (\nabla \times \vec{u}) \bullet (\nabla \times \vec{u})^T, \quad p_\omega = \frac{\omega}{k} p_k. \quad [11]$$

Note that the expressions for p_k and p_ω relate the production of turbulent kinetic energy to the vorticity of the fluid motion (not the shear rate in the flow), a desired feature for flows like water waves. It is remarked that expressions given in Eq. [11] are slightly different from the original expressions for the turbulence production terms suggested by (Wilcox, 1993, 2008). This study adopted the following values suggested by Wilcox (2008) for the model parameters in the k-ω model: α = 13/25, β= 0.072, β^*= 0.09, σ_ω = 0.5, σ^*= 3/5 and C_{lim} = 7/8.

Two-phase (air-water) flow simulations were performed on XSEDE's Stampede2 supercomputers.

3 RESULTS

The characteristics of the flow field around the OWC structure affects the local sediment transport and scour at the structure. Near bed flow field is directly related to the bed load transport and the flow field away from the bed affects mainly the transport of suspended load. The common practice in numerical simulations of wave-induced scour around a bottom sitting structure is to assume that the effects of the permeability of the bed on the water flow can be ignored. For numerical simulations of wave-interaction with bot- tom sitting OWCs, existing studies all assumed that the permeability of the bed has negligible influence on the performance of the OWC's wave energy extraction.

In this section, results of the characteristics of the flow around the bottom- sitting OWC model and the local scour are presented. Wave-induced local sour was studied in the wave flume study, but not included in the numerical study. The two-phase flow simulation was performed without the top orifice plate.

3.1 Experimental results

As waves pass the OWC model installed on the sandy bed, vortex flow around the model cause locally-enhanced sediment transport, resulting in a local scour around the model. In the present experimental study, in addition to local scour, sand ripples were developed as shown in Fig. 2. These sand ripples migrate in time (Barr et al., 2004).

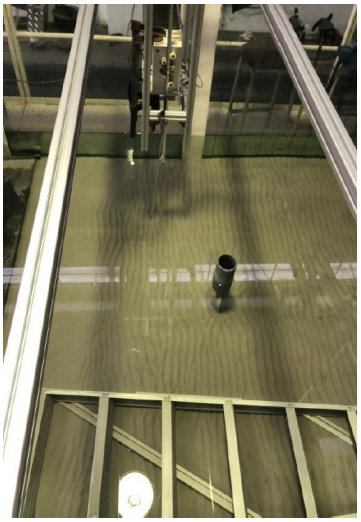

Figure 2. A view of the final bed form. The orifice plate was removed for measuring the bed levels under the OWC chamber.

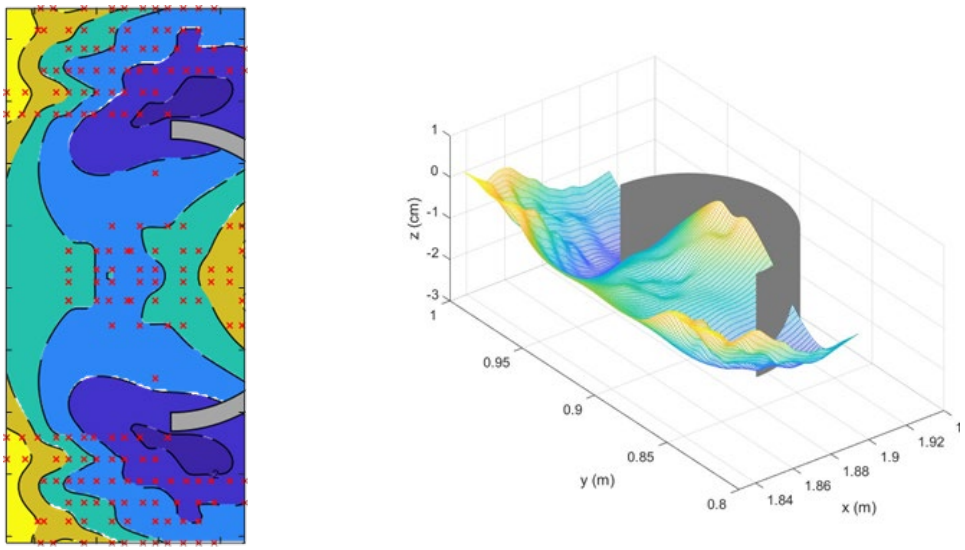

Figure 3. Experimental results showing the scour profile in the vicinity of a cylindrical OWC. The left panel shows the locations where bed levels were measured and the interpolated contour lines. The right panel shows a 3D view of the interpolated bed surface. Label is missing for the levels the contour lines

Fig. 3 shows the measured bed profile for wave period=0.9 s and incident wave height=0.101 m. Two scour holes can be observed next to the two ends of the C-shaped support. Due to the limitations of the method used to measure the bed profile, the bed elevations in locations where the measurements were not taken are obtained using a surface interpolation method. In the left panel of Fig. 3, the marks show the locations where measurements were taken; most measurements were taken underneath the OWC chamber and close to the edges of the C-shaped support. It is believed that the interpolated bed profiles near the tow edges and underneath the OWC chamber are reliable.

It can be seen that the scour hole is more or less symmetric about the plane of symmetry, and the maximum scour depth occurred next to the edges of the C-shaped support. Based on the measured bed level changes, a slight sand accretion is expected on the plane of the symmetry right in front of the inner surface of the C-shaped support.

Two scour holes were developed in the vicinity of the two ends. The maximum depths of these two scour holes are more or less the same. The development of the maximum scour depth measured at one end is shown in Fig. 4 for wave period=0.9 s and wave height=0.101 m. It can be seen that it takes about 400 waves to reach the equilibrium. The maximum scour depth at the equilibrium is about 0.23 times the outer diameter of the C-shaped support.

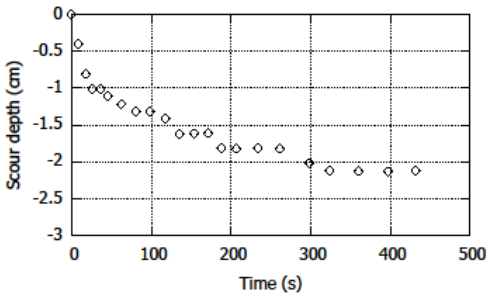

Figure 4. The development of the maximum scour depth.

It is remarked that the experimental data will be used in the future to verify and validate a three-phase (solid-gas-liquid) flow model developed to study sediment transport in geophysical flows and sediment transport around marine structures.

3.2 Numerical results

Simulated velocity fields in horizontal and vertical planes are used to understand the observed change of bed profile.

3.2.1 Velocity field in the plane of symmetry

Fig. 5 shows four snapshots of the velocity field in the plane of symmetry of the OWC model. The four instants at which the four snapshots are taken are marked on the time series of the cross-sectional average of the surface elevations inside the OWC chamber. The velocity of the water inside the OWC chamber is on the order of 10^{-1} m/s.

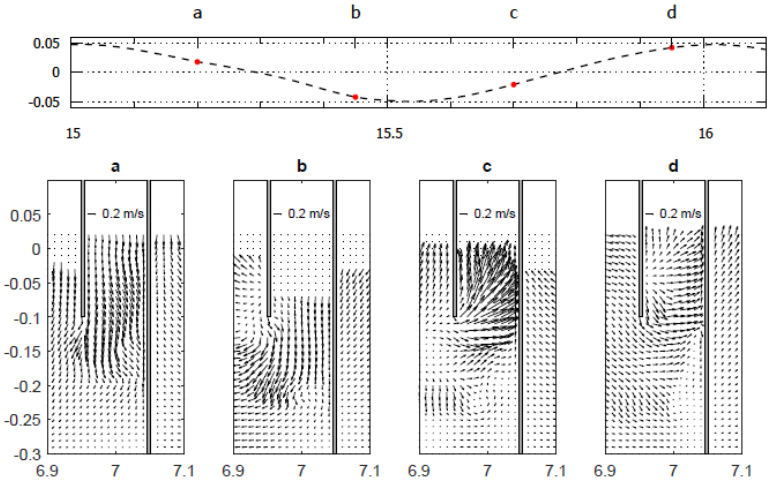

Figure 5. Four snapshots of the velocity field in the plane of symmetry. The top plot shows the cross-sectional average of the surface elevations inside the OWC chamber. All lengths are in meters.

Fig. 6 shows four snapshots of the velocity field in a plane connecting the two ends of the C-shaped support. Due to the vortex shedding from the two ends of the C-shaped support and the lower edge of the OWC chamber skirt, the flow field is not exactly symmetric about the plane of symmetry.

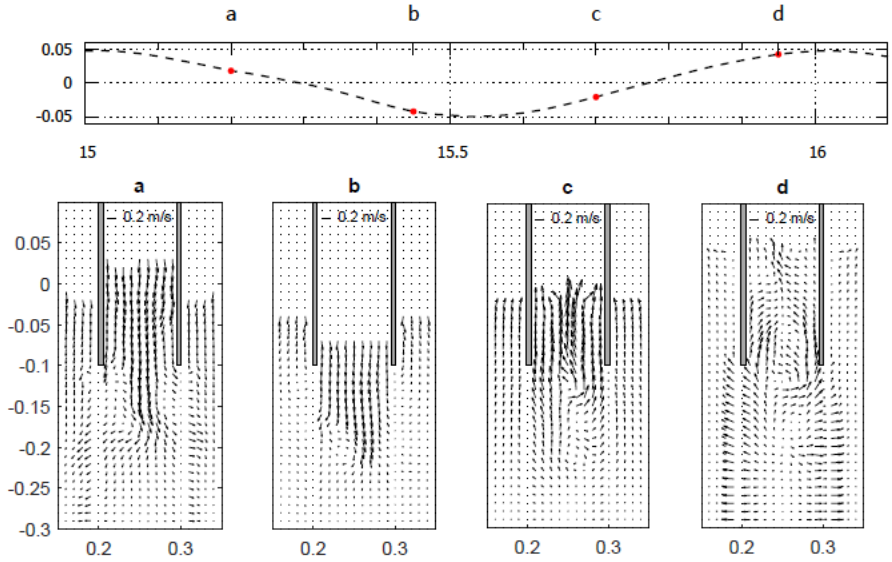

Figure 6. Four snapshots of the velocity field in the vertical plane connecting the two ends of the C-shaped support. The top plot shows the cross-sectional average of the surface elevations inside the OWC chamber. All lengths are in meters. Only velocity in water is shown, air velocity is set to be 0 and denoted with dots

3.2.2 Velocity field in a horizontal plane 5 mm above the bed

Four snapshots of the instantaneous velocity field in a horizontal plane 0.005 m above the seabed (i.e., 0.295 m beneath the still water level) are shown in Fig. 7. The four instants at which the four snapshots of the velocity field are taken are marked on the curve for the surface elevation.

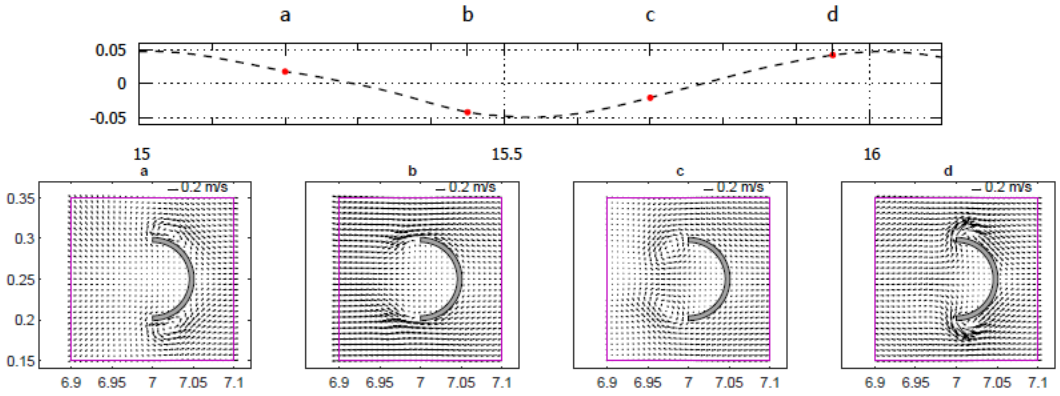

Figure 7. Four snapshots of the velocity field in a horizontal plane located at 5 mm above seabed. All lengths are in meters.

Next to the outer side of each end of the C-shaped support, one vortex can be observed at the instant either ‘a’ or ‘d’. The two vortices are counter- rotating. At the instant ‘c’, two counter-rotating vortices can be observed on the up-wave side of the C-shaped support; however, the strength of these two vortices is weaker compared to that at the instant either ‘a’ or ‘d’.

Fig. 8 shows the mean velocity field in a horizontal plane 5 mm above the bed. The mean flow field is obtained by averaging the instantaneous velocity fields within one wave period.

3.2.3 On simulating the porous bed

A separate numerical simulation was performed, by modifying the momentum equation by including a sink/source term to mimic the force between water flow and an artificial porous media[1]. It was found that that

[1] A porous multiphase flow toolbox for OpenFOAM, presented by Horgue, Pierre and Soulaine, Cyprien and Franc, Jacques and Guibert, Romain and Gerald, Debenest at the 9th OpenFOAM Workshop. Zagreb, Croatia. 23-26 June, 2014

the bed porous bed did not significantly affect the flow velocity and pressure inside the OWC chamber. However, the simulated kinetic energy was found to be much larger if the artificial porous bed was included in the simulation. The numeral results for the artificial porous bed are not included in this paper because it is not clear whether or not the kinetic energy enhanced by the artificial porous bed in the simulation is due purely to numerical artifacts.

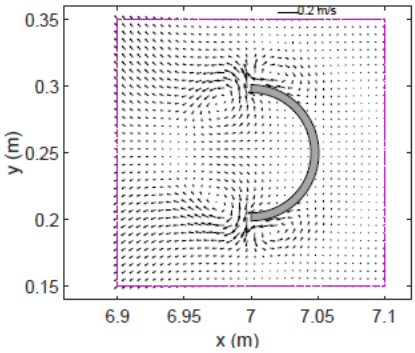

Figure 8. The mean velocity field in a horizontal plane located at 5 mm above seabed.

4 DISCUSSION

Vortex flows are erosive and responsible for local scour at the bottom- sitting WEC. For the bottom-sitting OWC-type WEC studied here, strong vortices are shed from the two edges of the C-shaped support and the lower tip of the OWC chamber skirt during each half period.

When a wave trough passes the OWC model, two vortices are shed into the up-wave side of the C-shaped support from the two ends of the support. Since there is no boundary to confine the flow on the up-wave side, the formation of these vortices is due to a sudden expansion of the flow. These two vortices grow in size and move toward the plane of symmetry.

When a wave crest passes the OWC model, two vortices are shed next to the two ends into the down-wave side of the C-shaped support. Since the forward flow is confined by the outer surface of the C-shaped support, these vortices are formed due to the flow separation from the outer surface. Since the size of these vortices is confined by the outer surface of the C-shaped support, the strength of these vortices is stronger than that found on the up-wave side, and thus more erosive.

The instantaneous vortices shed from the two edges of the C-shaped support (see Fig. 7) correlate well with the regions where local scour was observed in the experiment (see Fig. 3). In particular, the strong vortices shed from the two ends when a wave crest passes the OWC model are responsible for the maximum scour-hole depths observed next to the two ends.

In their study of wave-induced scour at the round head of a rubble-mound breakwater, Fredsøe and Sumer (1997) found that the steady streaming is responsible for the scour hole on the up-wave side of the breakwater. By comparing the mean velocity field (see Fig. 8) and the measured bed profile (see Fig. 3), four vortices can be found in the mean flow field, while only two scour holes can be found in the measured bed profile. There seems to exist a correlation between the locations of the observed maximum scour depths and the locations of the two vortices in the mean flow field on the down-wave side of the C-shaped support.

Even though there are also vortices shed from the lower tip of the OWC chamber skirt, the strength of these vortices decrease with the distance from the tip. As a result, they are not likely to affect the flow pattern near the bed and the scour holes next to the two ends of the C-shaped support.

For a rigid bed, numerical simulations have shown that the horseshoe vortex can increase the near bed turbulent stresses upstream of the obstacle (Kirkil et al., 2005). The formation of horseshoe vortex begins when the incoming flow encounters an obstacle, causing the flow velocity to direct downwards in front of the obstacle. The horseshoe vortex system is believed to be a direct cause of local scour around vertical piles (Roulund et al., 2005; Baykal et al., 2015, 2017b). For the present problem, our numerical results do not show the existence of a horseshoe vortex system on the up-wave side of the C-shaped support, possibly because of the influence of the strong vortices shed from the two ends of the C-shaped support.

5 CONCLUSIONS

This study examines a bottom-sitting OWC-type WEC. a three-dimensional CFD simulation was used to study the characteristics of the flow around the WEC, and a wave-flume test was used to study the wave-induced local scour at the WEC. Two scour holes were observed in the vicinity of the two ends of the C-shaped support. The simulated velocity field suggests that the observed scour holes are related to the vortices shed from the two end of the C-shaped support. There are four vortices in the mean flow field, but there are

only two scour holes at the OWC model. Effects of the bed permeability on the development of the scour holes need further studies.

DATA AVAILABILITY STATEMENT

The datasets generated and/or analyzed during the current study are available from the corresponding author on reasonable request.

AUTHORSHIP CONTRIBUTION STATEMENT

Zhenhua Huang conceived of the presented idea, supervised the project, contributed to the interpretation of the results, were in charge of overall direction and planning, and wrote and approved the manuscript. Shijie Huang performed the numerical simulations, prepared the figures, and contributed to the manuscript. Zhenhua Hunag and Ying-min Low planned the experiments. Zhixuan Zhang and Juncheng Chen carried out the experiments.

ACKNOWLEDGEMENTS

This work was partially supported by the US National Science Foundation under grant no. CBET-1706938. The National University of Singapore is acknowledged for supporting the experimental work reported here through a MSc student project under the supervision of Dr. Low. Extreme Science and Engineering Discovery Environment (XSEDE) is also acknowledged for providing computing resources through two grants (OCE170015 and ENG180008). Any opinions, findings, and conclusions or recommendations expressed in this material are those of the author(s) and do not necessarily reflect the views of the National Science Foundation.

REFERENCES

Barr, B.C., Slinn, D.N., Pierro, T., Winters, K.B., 2004. Numerical simulation of turbulent, oscillatory flow over sand ripples. Journal of Geophysical Research: Oceans 109, C09009.

Baykal, C., Sumer, B., Fuhrman, D., Jacobsen, N., Fredsøe, J., 2017a. Numerical simulation of scour and backfilling processes around a circular pile in waves. Coastal Engineering 122, 87 – 107.

Baykal, C., Sumer, B.M., Fuhrman, D.R., Jacobsen, N.G., Fredsøe, J., 2017b. Numerical simulation of scour and backfilling processes around a circular pile in waves. Coastal Engineering 122, 87–107.

Baykal, C., Sumer, B.M., Fuhrman, D.R., Jacobsen, N.G., Fredsøe, J., 2015. Numerical investigation of flow and scour around a vertical circular cylinder. Philosophical Transactions of the Royal Society A: Mathematical, Physical and Engineering Sciences 373, 20140104.

Falcao, A.F.d.O., 2010. Wave energy utilization: A review of the technologies. Renewable and Sustainable Energy Reviews 14, 899 – 918.

Fredsøe, J., Sumer, B., 1997. Scour at the round head of a rubble-mound breakwater. Coastal Engineering 29, 231 – 262.

Huang, Z., Huang, S., Xu, C., 2020. Characteristics of the flow around a circular OWC-type wave energy converter supported by a bottom-sitting c-shaped structure. Applied Ocean Research 101, 102228.

Huang, Z., Xu, C., Huang, S., 2019. A CFD simulation of wave loads on a pile-type oscillating-water-column device. Applied Ocean Research 31, 41–49.

Jacobsen, N., Fuhrman, D., Fredsøe, J., 2012. A wave generation toolbox for the open-source CFD library: OpenFOAM. International Journal for Numerical Methods in Fluids 70, 1073–1088.

Kirkil, G., Constantinescu, G., Ettema, R., 2005. The horseshoe vortex system around a circular bridge pier on equilibrium scoured bed, in: Proceedings of World Water and Environmental Resources Congress 2005, Anchorage, Alaska, United States. pp. 1–12.

Lancaster, O., Cossu, R., Baldock, T.E., 2020. Experimental investigation into 3d scour processes around a gravity based oscillating water column wave energy converter. Coastal Engineering 161, 103754.

Liang, D., Cheng, L., 2005. Numerical model for wave-induced scour below a submarine pipeline. Journal of Waterway, Port, Coastal, and Ocean Engineering 131, 193–202.

López, I., Castro, A., Iglesias, G., 2015. Hydrodynamic performance of an oscillating water column wave energy converter by means of particle imaging velocimetry. Energy 83, 89 – 103.

Mayer, S., Madsen, P.A., 2000. Simulation of breaking waves in the surf zone using a Naiver-Stokes solver, in: 27th International Conference on Coastal Engineering, ASCE. pp. 928–941.

McCormick, M., Kraemer, D., 2001. Wave energy, in: Steele, J.H. (Ed.), Encyclopedia of Ocean Sciences (Second Edition). second edition. Academic Press, Oxford, pp. 300 – 303.

Rusche, H., 2003. Computational fluid dynamics of dispersed two-phase flows at high phase fractions. Ph.D. thesis. Imperial College London (University of London).

Wilcox, D.C., 1993. Turbulence modeling for CFD. volume 2. DCW industries La Canada, CA.

Wilcox, D.C., 2008. Formulation of the k-ω turbulence model revisited. AIAA Journal 46, 2823–2838.

Xu, C., Huang, Z., 2019. Three-dimensional CFD simulation of a circular owc with a nonlinear power-takeoff: Model validation and a discussion on resonant sloshing inside the pneumatic chamber. Ocean Engineering 176, 184 – 198.

Xu, C., Huang, Z., Deng, Z., 2016. Experimental and theoretical study of a cylindrical oscillating water column device with a quadratic power take-off model. Applied Ocean Research 57, 19 – 29.

8th International Conference on the Application of Physical Modelling in Coastal and Port Engineering and Science
Dec. 9th – 12th, 2020, Zhoushan, China

APPROACH COASTAL CHANGE ANALYSIS AT THE NORTHERN CUA DAI RIVER MOUTH BY ADOPTING DIGITAL SHORELINE ANALYSIS SYSTEM

VU HUONG NGAN[(1)], NGUYEN NHAT MINH[(2)], NGUYEN KHANH LINH[(3)], DINH NHAT QUANG[(2,*)], HO SY TAM[(2)] & NGUYEN TRUNG VIET[(2)]

[(1)] International Center of Tropical Agriculture, Pham Van Dong, Hanoi, Vietnam
vuhuongngan235@gmail.com

[(2)] Thuyloi University, 175 Tay Son, Dong Da, Hanoi, Vietnam
minhnn6nk@wru.vn; quang.dinh@tlu.edu.vn, tamhs.cttl@tlu.edu.vn, nguyentrungviet@tlu.edu.vn

[(3)] Former student, Thuyloi University, 175 Tay Son, Dong Da, Hanoi, Vietnam
linhnk5nk@wru.vn

ABSTRACT

Coastal change analysis is one of the controversial issues in water resources fields since this greatly impacts coastal management. The case study of this research is the coastline at the Northern Cua Dai river mouth, where witnessed the significant morphological change in recent years. To approach coastal change analysis in this region, the authors adopted DSAS - Digital Shoreline Analysis System, an addi-in to ArcGIS software, to calculate rate-of-changes statistics in the long-term process. Satellite scenes in 1990, 1995, 2000, 2005, 2010, 2015, 2017 and 2019 were collected and processed to extract representative coastlines, which were the inputs to implement DSAS calculation. The results indicate the case study experience both erosion and accretion phenomenon, where 8 km coastline in Hoi An had been eroded most seriously with the highest rate reached to -45 m/yr and retreat distance was more than 1 km. Importantly this methodological approach provides not only visual coastline change information (Net Shoreline Movement, End Point Rate, Linear Regression Rate) but also relating indicators (Uncertainty, Standard Error, Correlation Coefficient and Confidence Interval) for checking the accuracy of the application. Three primary reasons leading to the severe situation of erosion and accretion in the Northern Cua Dai river mouth are natural factors, constructions and tourism industry. The local authorities can base on the results of this research to offer suitable and optimal methods in cover the damage in this area.

Keywords: coastal change analysis, satellite images, Digital Shoreline Analysis System, Quang Nam province.

1 INTRODUCTION

Coastal change analysis plays a vital role during coastal region management when coastlines are dynamic features over time (Maiti and Bhattacharya, 2009). Morphological attributions of these features are paid great attention by both local authorities and researchers since they have a direct relationship with erosion and accretion in coastal zones (Bird, 1996). The majority of worldwide coasts witness the severe consequences of erosion, where the eroding rate increases significantly in recent years (Hergarten and Kenkmann, 2018). Moreover, the process of erosion and accretion also contributes major parts in the movement of coastline position, which leads to river mouths' morphological changes in the same areas (Abessolo Ondoa et al., 2018). As a consequence, human activities, e.g. exploitation, aquaculture and tourism, can be influenced detrimentally if sustainable solutions are not given (Magoon et al., 2012). Furthermore, without sustainable methods to remain the balance between exploitation and maintenance, the ecosystem in coastal region would witness degradation, with the increasingly severe occurrence of flood inundation, salinity and sea level rise (Nichols et al., 2019).

For the above reasons, enormous methods are studied and implemented to approach coastal change analysis (Dobson et al., 1995; Li et al., 2008; Webb, 2006), and Digital Shoreline Analysis System (DSAS) is an effective extension tool in analysing coastal change (Chakraborty and Pal, 2020). As an add-in to ArcGIS software, this tool is adopted widely due to its ability to analyse geographic information and calculate shoreline rate-of-change then illustrate through statics in time series (Thinh and Hens, 2017). Thus, DSAS users need to collect excessive input data to process, and satellite images become essential and valuable sources because of their spatial and temporal range (Sheeja and Ajay Gokul, 2016). The two most common satellite scene sources for coastal change analysis are Landsat series and Sentinel-2 for their spatial resolution and availability (Mitri et al., 2020). As the mission of Sentinel-2 is to combine with other satellites and provide global coverage, users can obtain satellite scenes continuously after every 5-10 days (Huang et al., 2018).

The objective of this research is to approach coastal change analysis in the Northern Cua Dai river mouth in spatial and long-term scopes by adopting DSAS to calculate rate-of-change statistics. This region has potential factors in developing the economic in the Central Coast of Vietnam; however, the residents are experiencing

the negative influences of natural hazards, e.g. erosion and accretion. Since managing operations have not been markedly effective, the coastal morphology fluctuates year by year, leading to the extreme situation of coastal erosion, accretion and disappearance of sand spits (Anh, 2020). From the results of this research, local authorities can have a better understanding of coastal change in this region, as well as obtain sustainable managing methods in coastal regions.

2 CASE STUDY

The case study of this research is the pelagic coastline fronting the open ocean that is located in Son Tra, Ngu Hanh Son, Dien Ban (Da Nang city) and Hoi An (Quang Nam province) districts (**Figure 1**a). As having beautiful landscape and pure beaches, local authorities attempt to promote tourism development and many accommodating facilities have been constructed along this coastline. Moreover, aquaculture, especially fisheries sectors, sees a considerable contribution on Da Nang and Quang Nam's economic development in recent years, providing enormous benefits and job opportunities for residents (Vietnam Briefing, 2019). Nevertheless, the studied coastline is suffering severe damages of natural hazards, which affect directly coastal and river mouth regions. Coastlines around Cua Dai estuary are eroded significantly over the last few years, coming with extreme accretion, unexpectedly extensive sand islands, and sea level rise (Mau et al., 2018) (

Figure **1**b.). These can be explained through the high intensity of annual floods, tidal-induced water level fluctuation and hurricane-driven regime shift, and anthropic activities in coastal areas, such as beach nourishment, port construction and tourism development.

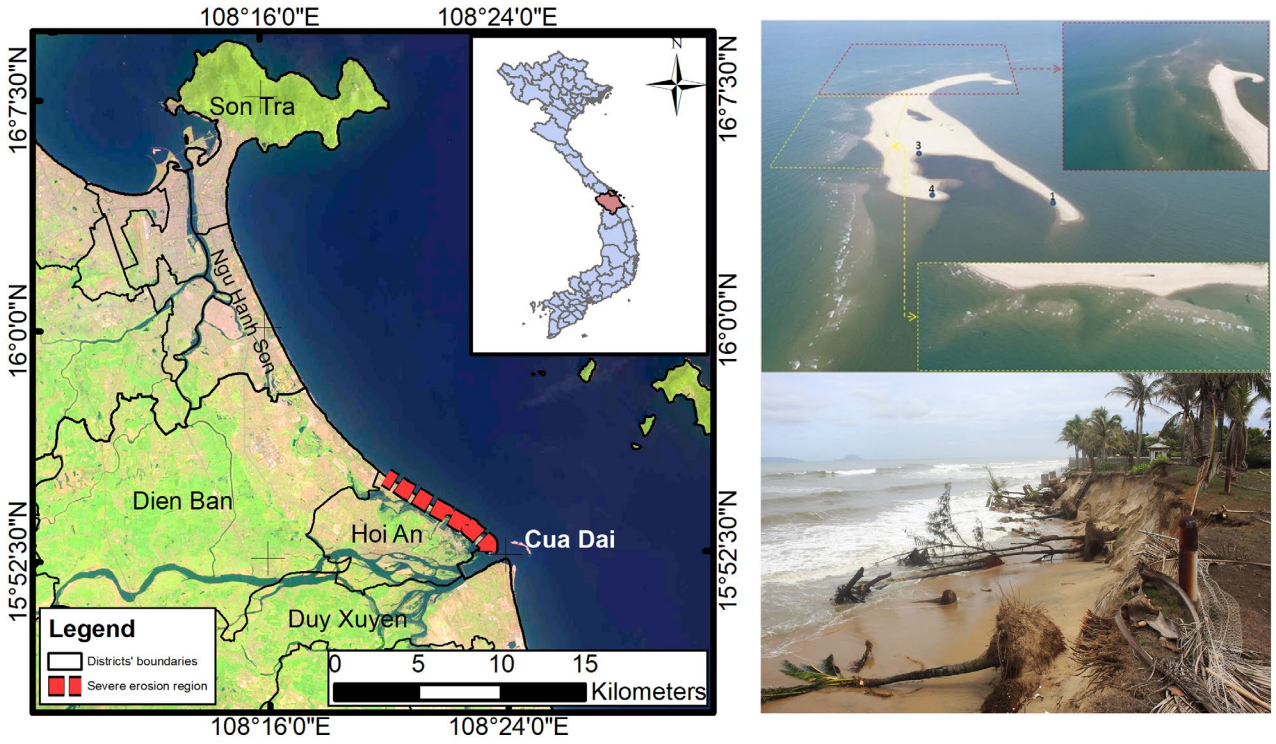

Figure 1. (a) Northern coastline of Cua Dai river mouth; (b) erosion and accretion at the study site (SGGPO, 2019; Thanh, 2020)

3 DATA COLLECTION

Satellite scenes of Landsat series and Sentinel-2 were collected for 8 years (1990, 1995, 2000, 2005, 2010, 2015, 2017 and 2019). To obtain favorable images for further process, only the scenes that have cloud cover below 20% were collected. To make accuracy assessment, the authors compare the results obtained from DSAS tool with coastline variation along Cua Dai's Northern part from 2018 field survey (red dashed line in Figure 1a). The geological map in 1996 by Geological Survey was used to explain the erosion and accretion phenomenon of the case study.

In decades, Quang Nam, Da Nang provinces and the Central region have suffered the most intense series of tropical storms, resulting in great casualties and property losses (Figure 2a). For example, typhoon Molave with a minimum pressure of 950 hPa hit this area in October 2020, that caused extensive damage with significant storm surge, devastating flooding and landslides across the area (Figure 2b).

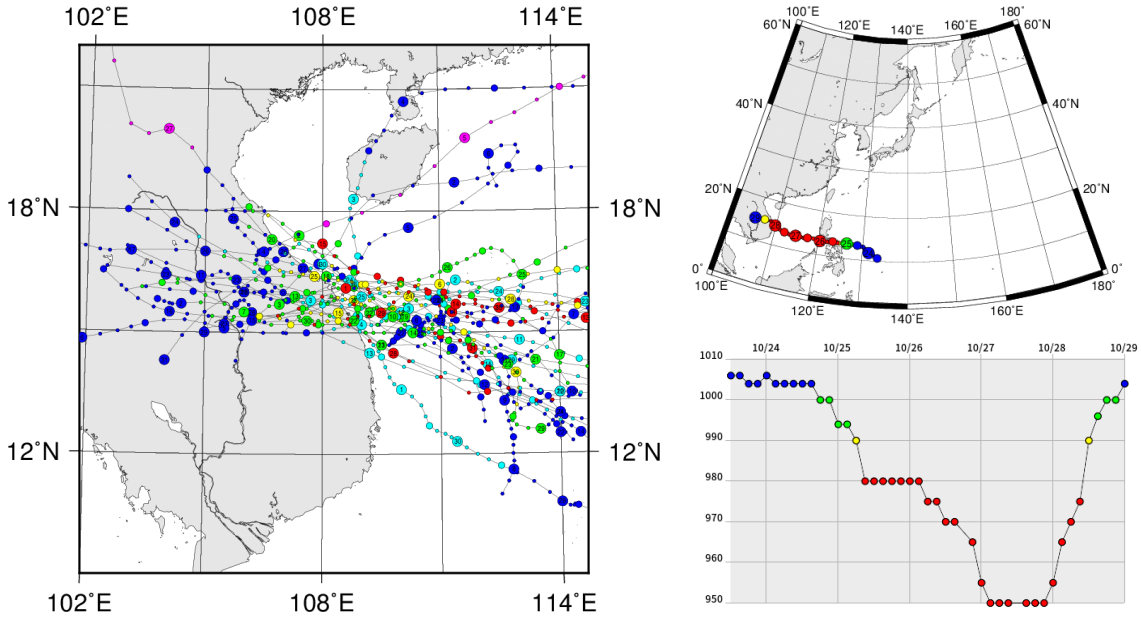

Figure 2. (a) Series of tropical stroms hit Quang Nam and Da Nang in decades; (b) Best track map and Central Pressure Chart of typhoon Molave

4 METHODOLOGY

In this research, the authors extracted representative coastlines in 1990, 1995, 2000, 2005, 2010, 2015, 2017 and 2019 from the computation of modified Normal Different Water Index (mNDWI) and Water Frequency Index (WFI). Then, rate-of-change statistics and spatio-temporal changes of the studied coastline were calculated and clarified through DSAS tool. The overall methodology and steps to implement this research are shown in Figure 3.

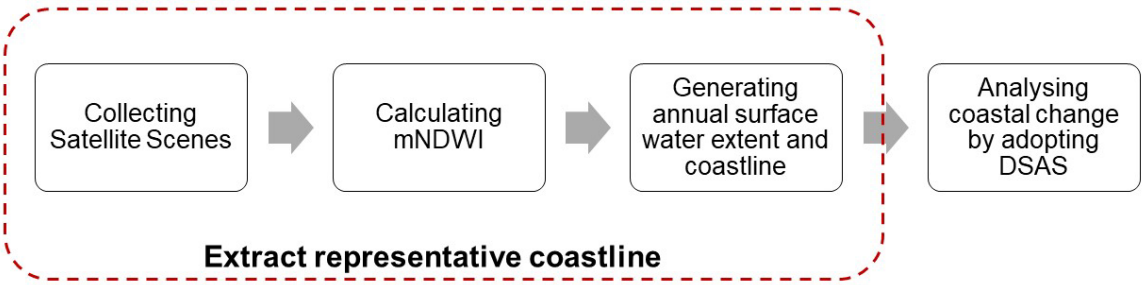

Figure 3. Overall methodology

4.1. Representative coastline extraction

Several stages were processed to extract the representative coastline for the study area. Firstly, mNDWI, which was introduced by Xu (2006) and considered to have relatively higher accuracy in surface water extraction than other water indices (Huang et al., 2018), was computed from Green and Mid-infrared (MIR) bands of each satellite scene:

$$mNDWI = \frac{Green - MIR}{Green + MIR} \quad [1]$$

The results of equation [1] have the range from -1 to 1, where the positive value can discretize water bodies from other land covers. Since the authors considered the representative coastline for a year (e.g. the annual coastline), mNDWI results calculated for all scenes within each studied year were then used as the input to calculate WFI, which can highlight the locations where water appears most (Xu, 2018):

$$WFI = \frac{N_{water}}{N_{water} + N_{land}} \quad [2]$$

where N_{water} and N_{land} are the numbers of time that a pixel at a fixed location is counted as water or land respectively in a year. The WFI value ranges from 0 to 1, where the threshold larger than 0.5 corresponds to annual water surface and the lower threshold represents annual other land covers. After delineating water

regions, annual surface water extent was extracted and shown through pixels having a value greater than 0.5 (see Figure 4). The representative coastline for that year was identified as the boundary (the green line) between land-water at coastal regions, and it was smoothed by Cartography tool in ArcGIS software with smoothing tolerance of 150 m.

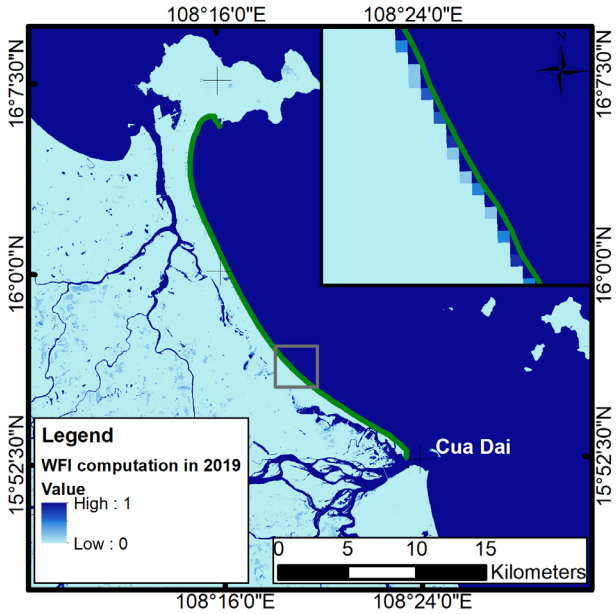

Figure 4. WFI map and annual coastline in the year 2019

4.2. Coastal change analysis by adopting DSAS

DSAS application has the potential to give insight into the rates of spatial-temporal changes of coastal morphology since it creates perpendicularly transects to historical shorelines from baseline and comes with statistical computations used in assessing the coastline (Otoo, 2018). Then, the points of intersection between the transects and shorelines are used to calculate metrics of shoreline change. In this study, coastlines were extracted for 7 years of 1990, 1995, 2000, 2005, 2010, 2015 and 2019. The baseline was constructed manually by buffering all coastlines entirely with a distance of 1000 meters, and transects were spaced 100 m apart.

Three statistical parameters functioned in DSAS, namely End Point Rate (EPR), Linear Regression Rate (LRR) and Net Shoreline Movement (NSM), were quantified to make the comparison and perform erosion/accretion rates. Since EPR has well-performance with only two coastlines, this parameter is frequently applied to compare the newest and oldest lines (Sutikno et al., 2015). To enhance the performance as well as mitigate unexpected errors, LRR was adopted for the cases having more than two lines (O'Rourke, 2017). Combining these parameters can provide vital information to assess the robustness of the computed regression rates (Nassar et al., 2019). The authors also computed the distance of coastlines between the investigated and base year (i.e. 2019) through the average of NSM. As a result, the rates of coastline changes along the case study were performed in the following part.

5 RESULTS AND DISCUSSION

Based on the results of mNDWI and WFI computation, a dataset of 8 extracted annual coastlines for the study area was generated (Figure 5a). To access coastal change along 31 km at the Northern Cua Dai river mouth, 307 individual transects were generated perpendicularly to the extracted coastlines by applying DSAS, where the distance between two transects is 100 m (see Figure 5b). Then DSAS uses the intersection points (measurement point) and the information contained in the shoreline attribute table to calculate rate of change statistics (Irrgang et al., 2018). The long-term coastal changes in rates and distances were shown through EPR, LRR and NSM statistical parameters. The positive values of these parameters stipulate deposition towards the sea, while their negative values show the degradation. In Figure 4a, the location of coastline variation of erosion/accretion was shown through 7 color ramps, which correspond to 7 levels from very high erosion (red color) to very high accretion (blue color). Interestingly, the region where is indicated to be high or very high erosion from LRR computation is relatively similar to the one identified from 2018 field survey (red dashed line in Figure 4b).

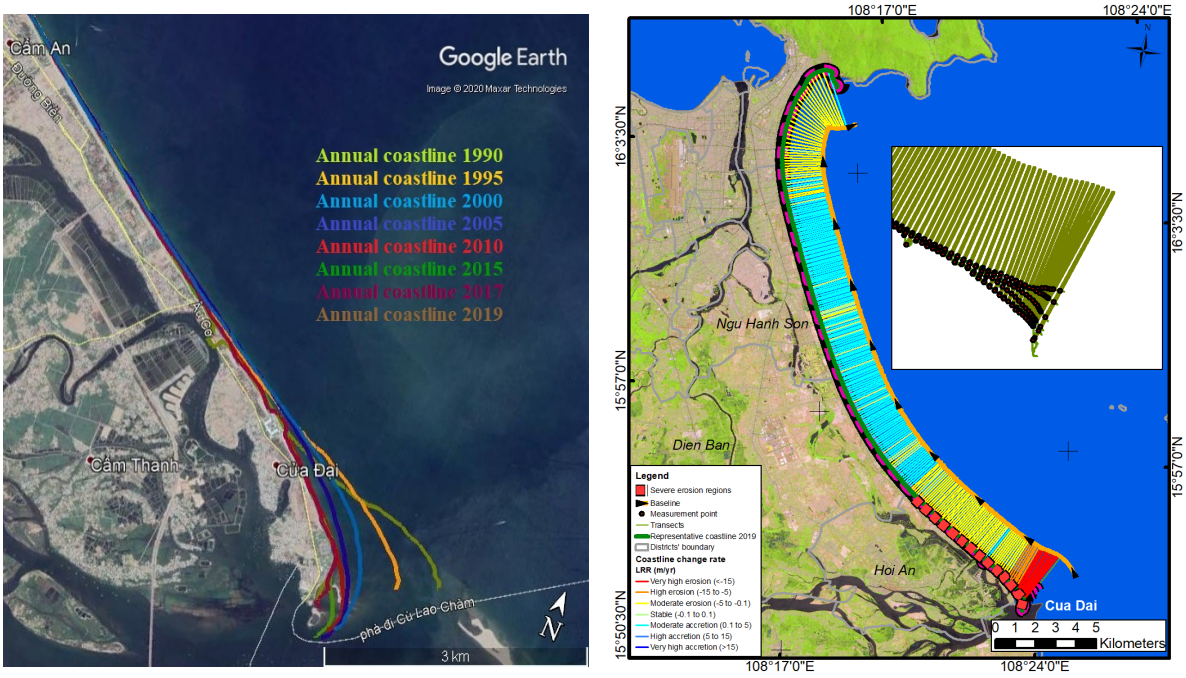

Figure 5. (a) 8 extracted coastlines with Google Earth image in 2019; (b) Results of coastline change analysis in the North of Cua Dai estuary using DSAS

The calculated parameters from DSAS in Figure 5 and Table 1 indicated that the coastline in the North of Cua Dai river mouth experienced both erosion and accretion phenomenon over the last three decades. More precisely, the furthest distance of coastline, which moved toward inland (NSM) from 1990 to 2019, was more than 1 km, while the longest distance of accretion only recorded at 183.02 m. The EPR results revealed that 135 transects (accounted for 43.97% of the coastline) were in the erosional regime and observed mainly in Hoi An and Son Tra; the average retreat value was -2.37 m/yr; and the rate-of-change fluctuated from -45.92 m/yr to 6.31 m/yr. Accretion took place mostly at Dien Ban and Ngu Hanh Son districts, with a moderate level at an averagely 0.41 m/yr for the entire coastline. Since EPR parameter is only capable of comparing two coastlines, LRR parameter was also calculated and compared with the results obtained from EPR. The rates of coastline position changes calculated by the LRR indicate that the accretion transects made up 51.14% of the coastline, while the figure for erosion transects was 48.86%, despite of the high and very high rates of eroding transects. Specifically, the most serious erosion was observed along 8 km coastline from Cua Dai estuary, where transects from 1 (i.e. the segment nearest to Cua Dai river mouth) to 30 were eroded at a very high rate, of more than 40 m/yr for the first few transects near Cua Dai.

Table 1. Highlights of coastline change analysis results

		NSM (m)	EPR (m/yr)	LRR (m/yr)
Erosion	Number of transects		135	150
	Average	-68.73	-2.37	-2.61
	Maximum value	-1126.55	-45.92	-42.41
Accretion	Number of transects		172	157
	Average	11.98	0.41	0.43
	Maximum value	183.02	6.31	2.88

The variation of the coastline from Cua Dai estuary to Son Tra over the studied period, obtained by EPR and LRR parameters, was presented in Figure 6a. Noticeably, transects 1 to 80 witnessed significant increase in rate of change, corresponding to 8 km coastline of the Northern Cua Dai river mouth. For the remained path, these rates were nearly unchanged since their values fluctuated slightly around the line of zero change (dashed green line in Figure 6a). It is worthwhile noting that the rates of change computed by the LRR and EPR show similar results, where average and maximum rates of erosion from LRR computation were -2.61 and -42.41

m/yr, respectively; and the corresponding figures from the EPR were -2.37 and -45.92 m/yr (**Table 1**). Figure 6b illustrated a great correlation between these two parameters with the obtained R^2 value of 0.981.

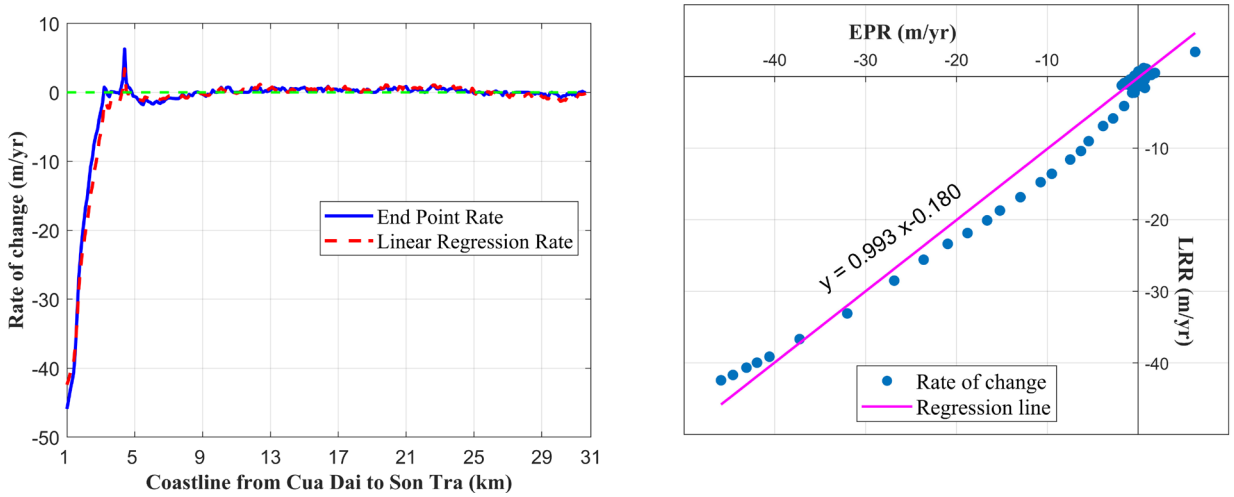

Figure 6. (a) Quantified coastline change rate by EPR and LRR along the Northern coastline of Cua Dai; (b) comparison of coastline rates obtained by EPR and LRR

The uncertainty associated with the computation of the EPR, denoted as EPRunc, indicates the confidence of the EPR calculation and is automatically calculated in DSAS application. According to Irragang et al. (2018), the more reliable of EPR value, the lower the EPRunc is. From the output of DSAS application, the uncertainty of the average EPR rate is 0.49, which is the acceptable value. Additionally, the supplemental statistics, i.e. Standard Error, Correlation Coefficient (LR2) and Confidence Interval (LCI) were also calculated for the LRR method. The standard error of estimate (LSE) is one of the metrics that tells us about the fit of the line to the data, in other words, the LSE is the standard deviation of the errors (or residuals). The formula of LSE is shown as:

$$LSE = \sqrt{\frac{\sum (y - y')}{n - 2}} \qquad [3]$$

Where: y is known distance from baseline for a measurement point (Figure 5a), y' is predicted value based on the equation of the best-fit regression line, and n is number of coastlines used.

Figure 7a plotted data as distance from baseline (meters) versus the coastline date (years) to highlight the calculation of the LRR and LSE statistics, i.e. -36.91 m/yr and 80.46 m, respectively. It means that LSE gives the average distance of about 80 m of the estimated to the actual value. In the example illustrated in Figure 7b, the 95-percent confidence interval of the slope (LCI95) is 0.64. More precisely, the band of confidence around the reported rate of change is -36.91 ±0.64. In other words, it can be 95-percent confident that the true rate of change is between -36.27 and -37.55 m/yr, leaving only a 5 percent chance that the true line is outside those boundaries. Correlation Coefficient (LR2) for each transect is computed and given the results that closet to 1.0 to describes how much the rate of each transect is "reliable" according to linear regression (Cenci et al., 2013). According to Alemayehu (2015), the LR2 statistic has a dimensional index that ranges from 0 to 1, in which the smaller the variability of the residual values around the regression line, the better the prediction. The LR2 results obtained from DSAS are evaluated and shown in Table 2, more than 61% of transects used for coastline evolution analysis are characterized by LR2 > 0.7. This result and interpolation functions of the time series associated with coastline positions suggest that coastline changes follow a near linear trend.

Table 2. Thresholds and proportion of transects corresponding to LR2 value

LR2 values	% of transects
< 0.5	15.8 %
>0.5 and <0.7	22.9 %
>0.7	61.3 %

There is no doubt that these additional statistics provide information that is helpful in assessing the robustness of the computed regression rates. Furthermore, it also proves that DSAS has really productive and systematic functions in evaluating coastline change, as well as producing various parameters automatically for every transects of entire coastline, no matter the distance of coastline. Therefore, these results are very important to incorporate in the coastal management master plan and different purposes of investigation.

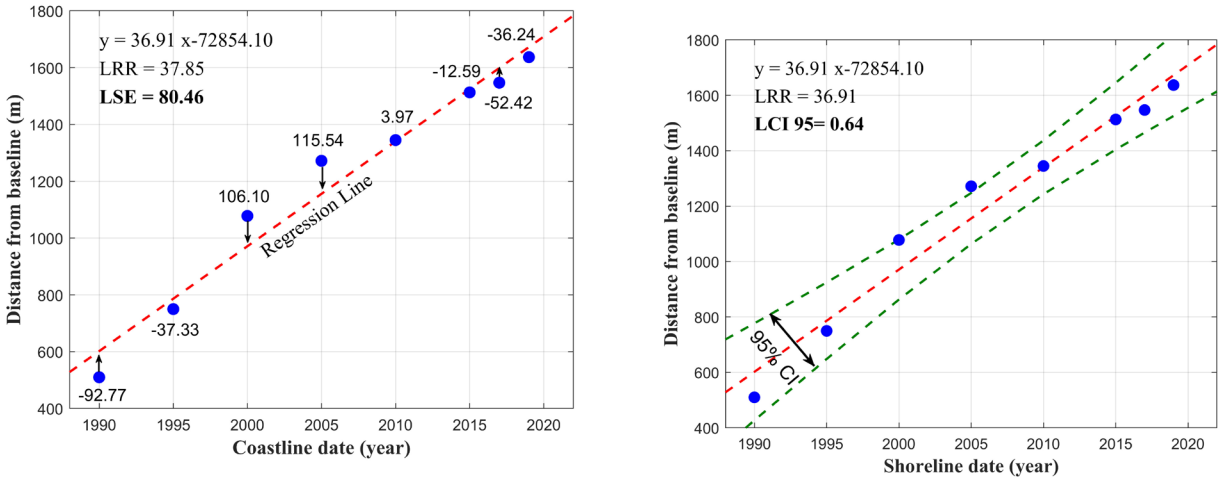

Figure 7. (a) Standard error of the estimate (LSE); (b) Confidence interval of LRR

Through both DSAS results and field surveys, coastlines in the Northern Cua Dai river mouth saw a significant rate of erosion and accretion by times. Enormous factors contribute to the more severe situation of these phenomena, and the authors considered three main factors: natural factors, coastal construction and tourism industry.

In term of natural factors, the Northern Cua Dai river mouth has succumbed to change. According to Geological Survey map in 1996 (Figure 8), the geomorphology, created by medium to fine sand, cobble, humus of plant, had caused the vulnerability in variation of this area. The continuously temporal changes in coastline can derive from several processes, e.g. seasonal variation, sea level fluctuation, etc. (ref). In this case study, since the river mouth move from North to South gradually as being impacted by a new ebb shoal, the long-term morphological change of this area has established as a non-periodic cyclic process for last decades (Do et al., 2018). Moreover, the Northern Cua Dai river mouth is also dominated by ENE waves in winter months, which create significant influences on the northern coastline. Since floods mostly appears in winter months with increasing intensity, erosion levels in the Northern Cua Dai river mouth tend to rise, and with human intervention, this situation becomes worse (Do et al., 2019). Thus, the obtained parameters to indicate the serious erosion/ accretion in this research can be clarified through the above statements, which are also similar to other previous studies of Quang Tuan et al (2017), Mau et al (2018) and JICA (2018).

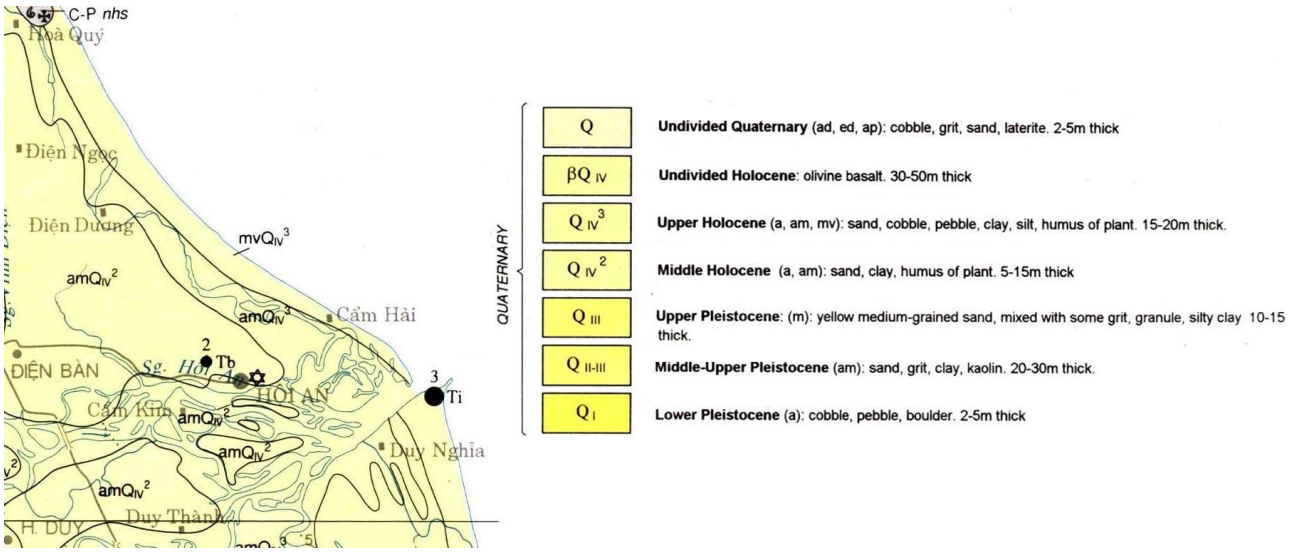

Figure 8. Geological Survey map in 1996 for study case

Constructions are also the major culprits, which lead to the extremely severe morphological change in the case study. To specify, Cua Dai bridge, which crosses the upstream of Thu Bon river at 1.5 km, has an abutment on the left of the bank (yellow point in Figure 4b). This construction narrowed down the river cross-section, diverting the mainstream to the right bank and creating a reduction of sediment to the left of Cua Dai coastline. Thus, the quantity of sediment distributing on the right hand side of coastline could rise significantly (JICA,

2018). As losing the balance in longshore sediment transportation, sand spits' formation and serious erosion take place, threatening flood safety and causing land loss (Do et al., 2020) .

Since the facilities for tourism activities along the Northern Cua Dai coastline were established, erosion has occurred with the more extremely severe situation. A series of hotel/resorts have been constructed along the coast near estuary with high density, e.g. Vinpearl, Victoria, Golden Sand, Sunrise. In 2015, several embankments were constructed to reduce the sediment discharges, including Shore and geotextile shore protection (position 3 – **Figure 9**), rock formations for tiled roofs by Golden Sand resort (position 4 – **Figure 9**), etc. These structures have a great influence on the sediment exchange, with the decrease of serious erosion trend in the North part of Cua Dai, especially 8 km coastline near the river estuary (**Figure 10**). Therefore, the result from DSAS application for the period 2015-2019 performs that 8km coastline along Hoi An city was no longer suffered from exacerbated erosion. Even though about 100m coastline closest the estuary still witnessed high landslides, the highest value by using EPR was decreasing to -29 m/yr, compared to about 40 m/yr of the period 1990-2019. The other segments remained stable or only experienced moderate erosion (**Figure 10**)

Figure 9. Protection constructions along North side of Cua Dai. Source: JICA REPORT (2018)

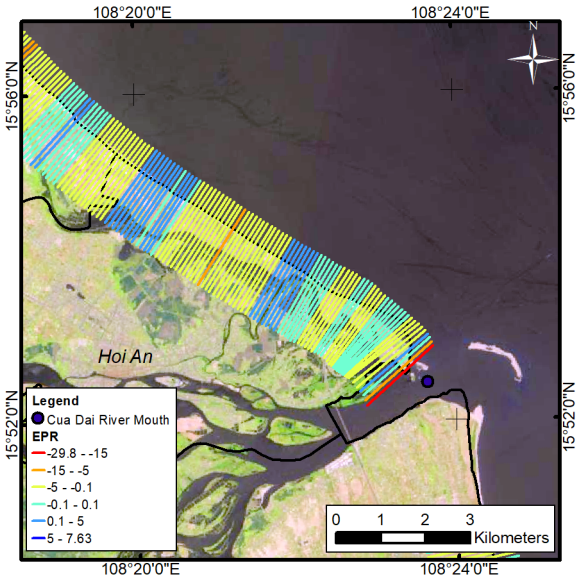

Figure 10. Rate-of-change along 8 km closest to Cua Dai estuary from 2015 to 2019

6 CONCLUSION

The coastal variability assessment is a qualitative value that was achieved in the study so that it would be possible to identify areas with more or less predisposition to erosion and accretion phenomena (Pérez-Alberti et al., 2013). The actual methods to measure the change of coastline recently such as field survey or collecting historical materials, but the drawbacks might have when the coastline currently is under pressure of climate change, outputs from actual surveys could not be up-to-date and might influence on giving decisions. The using of satellite images and DSAS application to investigate the variation of North Cua Dai coastline for the period from 1990 to 2019 were effective and truthful methodology for both saving survey time and giving fast and detailed results. Conversely The study revealed that North Cua Dai coastline suffered from both erosion and accretion. The long-term mean erosion rate using EPR and LRR statistics are -45 m/yr and -42 m/yr respectively. The coastline segment that moved landward furthest is measured by NSM at the value of 1126

km, and the longest measured distance at the seaward movement segment of the coastline was 183.02m. Most of the serious regression was centered around 8 km nearest to the estuary. DSAS application also has outstanding and scientific features in terms of providing secondary indicators in addition to erosion and accretion pattern computation of the coastal areas. The investigation of coastline change could form a background for further analysis of reasons as well as effective solutions.

ACKNOWLEDGEMENT

This research is supported by a bilateral program between Vietnam and Japan (code: HNQT/SPĐP/16.19) and in part by a Research Environment Links grant, ID 527612186, under the Newton Programme Vietnam partnership. The grant is funded by the UK Department of Business, Energy and Industrial Strategy (BEIS) and delivered by the British Council. For further information, please visit http://www.newtonfund.ac.uk. The authors would like to express their sincere gratitude for these supports.

REFERENCES

Abessolo Ondoa, G., Onguéné, R., Eyango, M., Duhaut, T., Anselme, C., Angnuureng, D., Almar, R., 2018. Assessment of the Evolution of Cameroon Coastline: An Overview from 1986 to 2015. J. Coast. Res. 81, 122–129. https://doi.org/10.2112/SI81-016.1

Alemayehu, F., Richard, O., Kinyanjui, M.J., V, W.O., 2015. Assessment of Shoreline Changes in the Period 1969-2010 in Watamuarea, Kenya. Glob. J. Sci. Front. Res.

Anh, L., 2020. Salinisation in Quang Nam Coastline. Electr. News Vietnam. Minist. Nat. Resour. Environ.

Bird, E.C.F., 1996. Coastal Erosion and Rising Sea-Level, in: Milliman, J.D., Haq, B.U. (Eds.), Sea-Level Rise and Coastal Subsidence: Causes, Consequences, and Strategies, Coastal Systems and Continental Margins. Springer Netherlands, Dordrecht, pp. 87–103. https://doi.org/10.1007/978-94-015-8719-8_5

Cenci, L., Disperati, L., Sousa, L., Phillips, M., Alves, F., 2013. Geomatics for Integrated Coastal Zone Management: Multitemporal shoreline analysis and future regional perspective for the Portuguese Central Region. J. Coast. Res. https://doi.org/10.2112/SI65-228.1

Chakraborty, R., Pal, S., 2020. Application of numerical models to simulate the charland area from Rajmahal to Farakka barrage of the Ganga river of eastern India. Spat. Inf. Res. 28, 683–698. https://doi.org/10.1007/s41324-020-00327-9

Do, A., Kralli, V., Vries, S., Viet, N., Stive, M., 2020. Morphodynamics of a Seasonal Inlet: A Case Study Using Remote Sensing and Numerical Modelling for Cua Dai Inlet, Central Vietnam. pp. 417–425. https://doi.org/10.1007/978-981-15-0291-0_58

Dobson, J., Bright, E., Ferguson, R., Field, D., Wood, L., Haddad, K., III, H., Jensen, J., Klemas, V., Orth, R., Thomas, J., 1995. NOAA Coastal change analysis program (C-CAP): Guidance for regional implementation.

Hergarten, S., Kenkmann, T., 2018. Has erosion globally increased? Long-term erosion rates as a function of climate derived from the impact crater inventory. Earth Surf. Dyn. Discuss. 1–17. https://doi.org/10.5194/esurf-2018-59

Huang, C., Chen, Y., Zhang, S., Wu, J., 2018. Detecting, Extracting, and Monitoring Surface Water From Space Using Optical Sensors: A Review. Rev. Geophys. 56, 333–360. https://doi.org/10.1029/2018RG000598

Irrgang, A., Lantuit, H., Manson, G., Günther, F., Grosse, G., Overduin, P., 2018. Variability in Rates of Coastal Change Along the Yukon Coast, 1951 to 2015. J. Geophys. Res. Earth Surf. 123. https://doi.org/10.1002/2017JF004326

JICA, 2018. Data Collection Survey on Basin-based Comprehensive Sediment Management in River Systems of the Central Region in Vietnam (Final report).

Li, R., Deshpande, S., Niu, X., Lee, I.-C., Wu, B., 2008. Multi-dimensional geospatial data integration for coastal change analysis.

Magoon, O.T., Edge, B.L., Stone, K.E., 2012. The Impact of Anthropogenic Activities on Coastal Erosion 3934–3940. https://doi.org/10.1061/40549(276)308

Maiti, S., Bhattacharya, A.K., 2009. Shoreline change analysis and its application to prediction: A remote sensing and statistics based approach. Mar. Geol. 257, 11–23. https://doi.org/10.1016/j.margeo.2008.10.006

Mau, L.D., Trung, P.B., Binh, T.V., 2018. EROSION FEATURES ALONG CUA DAI BEACH, HOI AN CITY, QUANG NAM PROVINCE, VIETNAM. Vietnam J. Mar. Sci. Technol. 18, 21–31. https://doi.org/10.15625/1859-3097/18/4A/13634

Mitri, G., Nader, M., Abou Dagher, M., Gebrael, K., 2020. Investigating the performance of sentinel-2A and Landsat 8 imagery in mapping shoreline changes. J. Coast. Conserv. 24. https://doi.org/10.1007/s11852-020-00758-4

Nassar, K., Mahmod, W.E., Fath, H., Masria, A., Nadaoka, K., Negm, A., 2019. Shoreline change detection using DSAS technique: Case of North Sinai coast, Egypt. Mar. Georesources Geotechnol. 37, 81–95. https://doi.org/10.1080/1064119X.2018.1448912

Nichols, C.R., Zinnert, J., Young, D.R., 2019. Degradation of Coastal Ecosystems: Causes, Impacts and Mitigation Efforts, in: Wright, L.D., Nichols, C.R. (Eds.), Tomorrow's Coasts: Complex and Impermanent, Coastal Research Library. Springer International Publishing, Cham, pp. 119–136. https://doi.org/10.1007/978-3-319-75453-6_8

O'Rourke, M., 2017. Archaeological Site Vulnerability Modelling: The Influence of High Impact Storm Events on Models of Shoreline Erosion in the Western Canadian Arctic. Open Archaeol. 3, 1–16. https://doi.org/10.1515/opar-2017-0001

Otoo, D.A., 2018. Shoreline Change Analysis of the Coastline of Teshie in Accra. (Thesis). University Of Ghana.

Pérez-Alberti, A., Pires, A., Freitas, L., Chaminé, H., 2013. Shoreline change mapping along the coast of Galicia, Spain. Proc. Inst. Civ. Eng. - Marit. Eng. 166, 125–144. https://doi.org/10.1680/maen.2012.23

Quang Tuan, N., Cong Tin, H., Quang Doc, L., Anh Tuan, T., 2017. Historical Monitoring of Shoreline Changes in the Cua Dai Estuary, Central Vietnam Using Multi-Temporal Remote Sensing Data. Geosciences 7, 72. https://doi.org/10.3390/geosciences7030072

SGGPO, 2019. 50 meters more in Cua Dai sand spit's accretion [WWW Document]. Báo Sài Gòn Giải Phóng. URL https://www.sggp.org.vn/content/NTMzMjM5.html

Sheeja, P.S., Ajay Gokul, A.J., 2016. Application of Digital Shoreline Analysis System in Coastal Erosion Assessment 6. https://doi.org/10.4010/2016.1848

Sutikno, S., Murakami, K., Handoyo, D., Fauzi, M., 2015. Calibration of Numerical Model for Shoreline Change Prediction Using Satellite Imagery Data. Makara J. Technol. Search Search 193, 113–119. https://doi.org/10.7454/mst.v19i3.3042

Thanh D., 2020. Serious erosion occurring in Cua Dai coastline [WWW Document]. vnexpress.net. URL https://vnexpress.net/bo-bien-cua-dai-sat-lo-4164076.html (accessed 11.17.20).

Thinh, N., Hens, L., 2017. A Digital Shoreline Analysis System (DSAS) applied on mangrove shoreline changes along the Giao Thuy Coastal area (Nam Dinh, Vietnam) during 2005-2014. Vietnam J. Earth Sci. 39, 87–96. https://doi.org/10.15625/0866-7187/39/1/9231

Vietnam Briefing, 2019. Investing in Quang Nam's Province - 3 Competitive Factors [WWW Document]. Vietnam Brief. News. URL https://www.vietnam-briefing.com/news/investing-vietnams-quang-nam-province-3-competitive-factors.html/

Webb, A., 2006. Coastal change analysis using multi-temporal image comparisons – funafuti atoll.

Xu, H., 2006. Modification of normalised difference water index (NDWI) to enhance open water features in remotely sensed imagery. Int. J. Remote Sens. 27, 3025–3033. https://doi.org/10.1080/01431160600589179

Xu, N., 2018. Detecting Coastline Change with All Available Landsat Data over 1986–2015: A Case Study for the State of Texas, USA. Atmosphere 9, 107. https://doi.org/10.3390/atmos9030107

8th International Conference on the Application of Physical Modelling in Coastal and Port Engineering and Science
Dec. 9th - 12th, 2020, Zhoushan, China

EFFECTIVENESS OF DUMMY WATER LEVELS IN PHYSICAL MODELS TO OPTIMIZE THE TOE AND THE CREST LEVELS

D.P.L. RANASINGHE [1], I.G.I.K.KUMARA [2], N.L.ENGILIYAGE [3], K.RAVEENTHIRAN [4]

[1] Engineering Manager, Lanka Hydraulic Institute Ltd., Sri Lanka, prasanthiranasinghe@gmail.com
[2] Research Engineer, Lanka Hydraulic Institute Ltd., Sri Lanka, indika.kumara@lhi.lk
[3] Research Engineer, Lanka Hydraulic Institute, Sri Lanka, nalika.engiliyage@lhi.lk
[4] Senior Engineering Manager, Lanka Hydraulic Institute, Sri Lanka, ravi@lhi.lk

ABSTRACT

Physical models can save a substantial amount from the actual construction coat even though the procedure is cost and time consuming than the other design techniques. The objective of this study was to use the constructed physical model to represent the different toe and the crest levels by adjusting the water levels during the model testing. Application of dummy water levels for toe optimization has been adopted for the various 2D models done in Lanka Hydraulic institute Ltd (LHI) and the outcome of two of them are (shallow and deep water coastal structures) presented in this paper. The crest optimization has been done for a deep breakwater by changing the water levels to represent the effective freeboard for the overtopping. The same design waves were applied for different water levels as deep water wave conditions are not much varying at the adjacent water depths. Since the toe stability is assessed by considering maximum wave height that can be generated at the critical low water level, effective water depth at the toe has been considered while optimizing the toe elevation using adjusted water levels. This paper includes the discussion on toe stability for deep and shallow water sections as well as the suitability of dummy water levels for engineering judgments while optimizing the crest and toe levels of the coastal structures. The results concluded that the dummy water levels can be used as an alternative method for crest and toe level optimization instead of having structural modifications of the model.

Keywords: Crest level, Dummy water levels, Physical models, Toe stability

1 INTRODUCTION

1.1 Background

To design a stable coastal structure, empirical equations would be sufficient if the design parameters are well defined and fully obtained. However, coastal structures are to be built in a very complex coastal environment in which its parameters are also varying in time and the location. Further, those structures need to withstand against dynamic forces for at least 50 or 100 years. Therefore, the designers must consider the stability and the durability of the structure, material availability and the construction methodology while designing them. Especially, the designers want to make sure the stability of the structure before they build on site. If the structure is failed, rehabilitation cost is too high. Hence, physical models are necessary to assess the hydraulic performance of the structures and to optimize them.

1.2 Utilizing a constructed physical model

The physical models can save a substantial amount from the actual construction as it reproduces the actual phenomenon on a small scale without any schematization (Ranasinghe et al., 2018). However, the model tests scaling is the key factor on physical model testing and it has been proven correct by several studies in which prototype damage has been re-created in a scale model (Hughes, 1993). However, the cost and time consuming for a physical model study are comparatively higher than the other design techniques. Therefore, the designers are very much keen on the utilizing of the built physical model to obtain a various output which would be beneficial to optimize the structure. Furthermore, determine the effects that a proposed modification might have on an existing structure's stability and performance is also an objective of the physical model testing (IAHR, 2011). On the other hand, some modifications that have to be done during the model testing requires considerable time as well as the manpower which may lead to higher the testing cost. Hence, limited no of modifications is recommended in the physical model study. Therefore, this study aimed to identify the alternative method to test different crest levels and toe levels without doing any structural modifications in a constructed 2D model. Figure 1 illustrates the similarity of the structural modification and the water level adjustment to

achieve the toe and the crest levels in a model. However, no reference has been found on such an alternative method. Further, a study on the water level adjustment instead of the structural modification in the 2D model has not been previously done to the best of our knowledge. Therefore, the objective of this study was to use the constructed physical model to represent the different toe and the crest levels by adjusting the water levels during the 2D physical model testing.

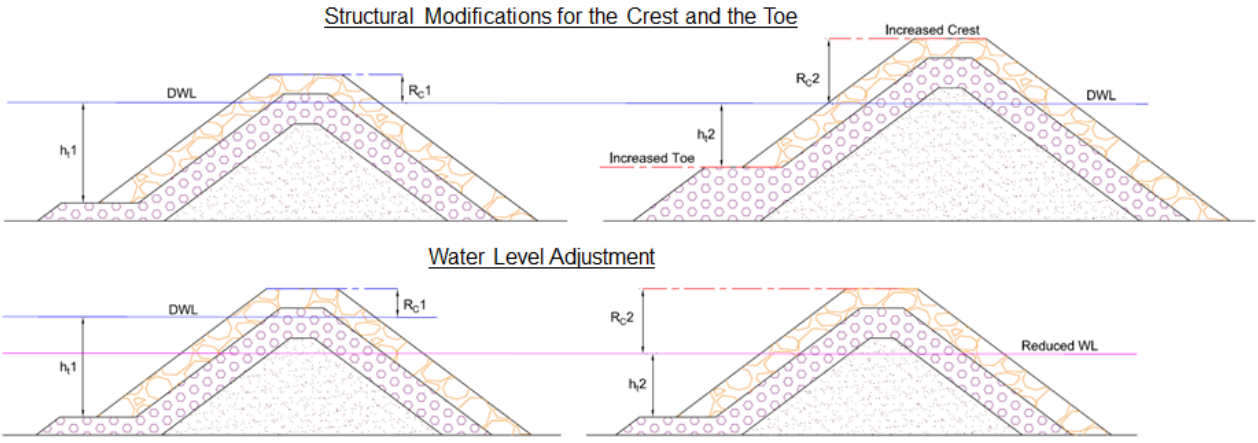

Figure 1. Details of the modifications done for the deep-water section

2 PROJECT SPECIFIC DETAILS

Two breakwaters which have been tested in the LHI's 2D flume were considered for this study.

The proposed fishery harbour consists of a 400 m long land rooted breakwater which ends up at -20.0 m CD with the deepest trunk section (Section B) located at -26.5 m CD depth. The selected rouble mound rock armoured section includes the core (1-1000 kg), the underlayer (60-300kg) the main armour (1-3 T). The initial crest was at +5.0 m CD while a berm is located at -6.30 m CD (Figure 2). The 2D physical model study was carried out to assess the hydraulic performance of the selected deep-water section concerning the armour stability and wave transmission. Since the total height of the structure is 31.5 m and water depth at the structure is 30.45 m, structural dimensions and water depths were considered as key factors while selecting the model scales for this trunk section. Therefore, a length scale of 1:50 was found as the maximum possible scale for the proposed section.

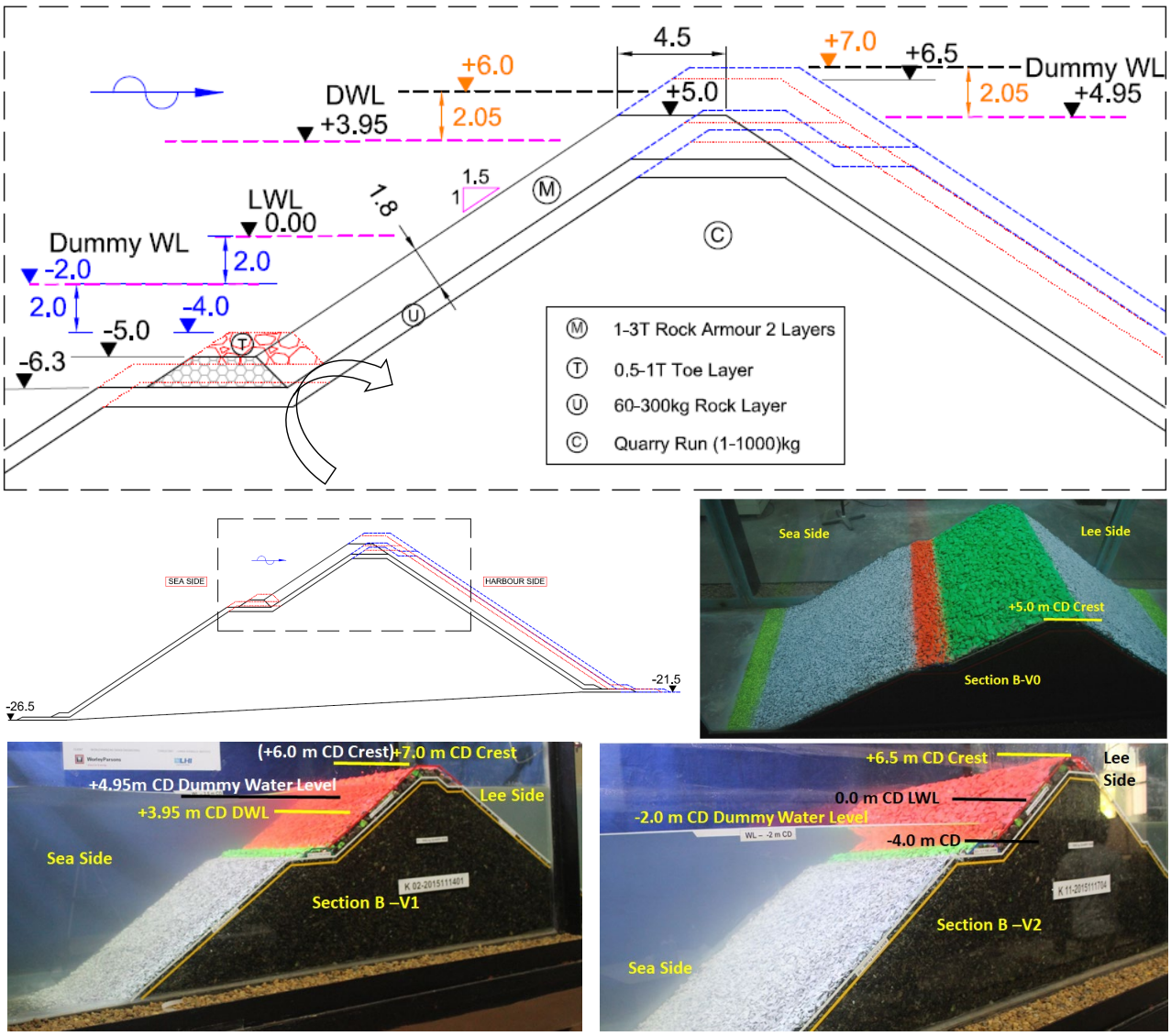

Figure 2. Details of the modifications done for the deep-water section

The second breakwater that has been considered for this study is a 2025 m long shallow breakwater. Two cross sections (Section E and Section D) were tested in the 2D flume to assess the hydraulic performance of the sections by evaluating the armour stability and overtopping. Since both sections are located at very shallow depths toe stability was one of the key focus (Figure 3). 1 m^3 CORE-LOC units have been used as the single layer main armour for the sea side while rock has been utilized for the other layers (Toe: 1-3 T, Harbour Side Main Armour: 0.3-1.0 T, Under Layer_Seaside: 0.2-0.4 T, Under Layer_Harbour Side: 60-300 kg and the Core: 1-1000 kg). The length scale of 1:26.5 was selected by considering the available flume length and the armour unit sizes.

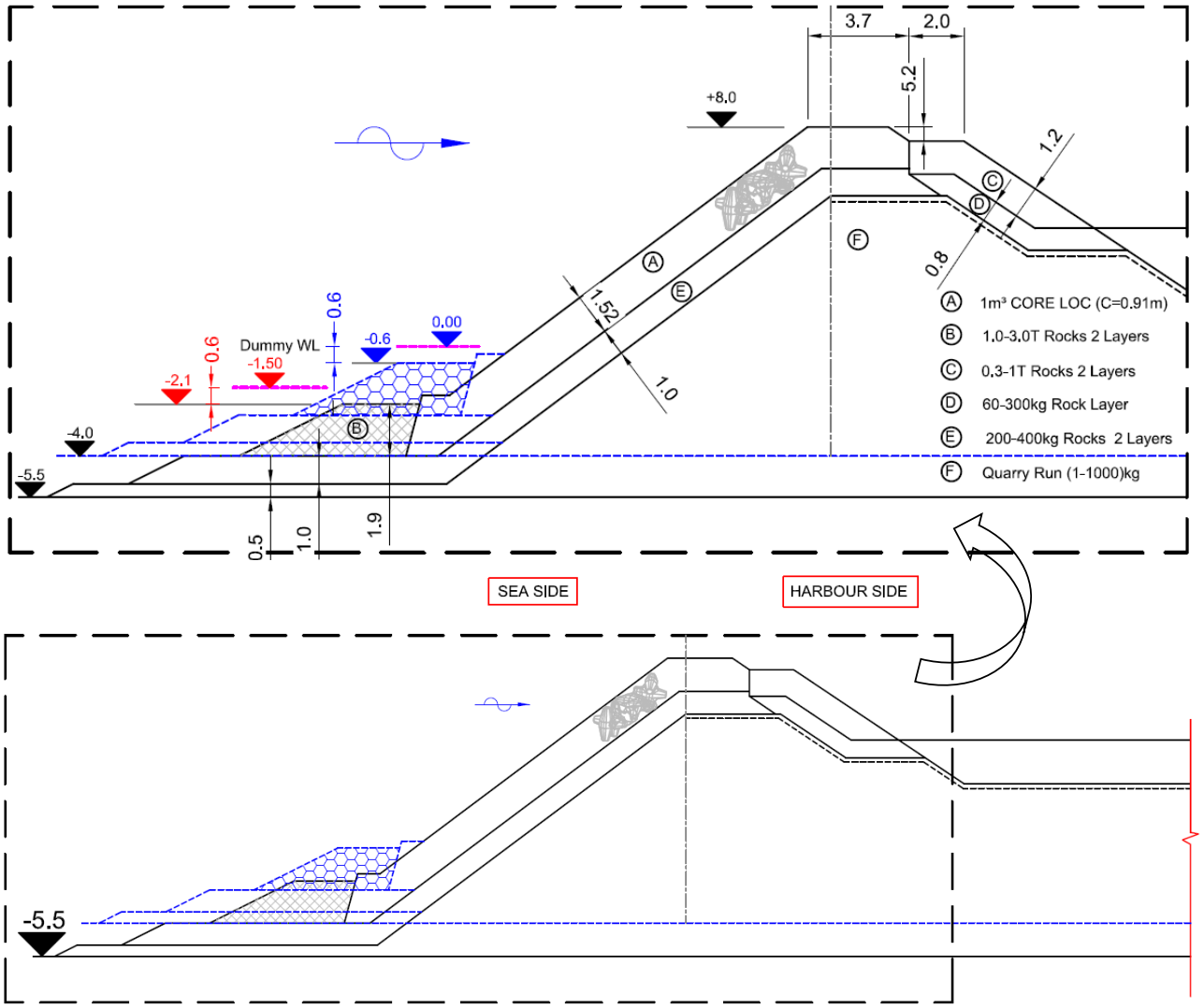

Figure 3. Details of the modifications done for the shallow-water section

3 PHYSICAL MODEL SETUP

The 2D model testing has been carried out at LHI laboratory wave flume which is 30 m long, 0.8 m wide and 1.0-1.6 m deep. The wave is generated by a hydraulically operated paddle and controlled by a PC based Wave Synthesiser Software. The interface between the software and Active Wave Absorption Control System (AWACS) is established through the wave generator/receiver unit which enables wavemakers to simultaneously generate the desired waves and to absorb reflected waves online. In the wave generation process, wave parameters of wave height and wave period were specified and the JONSWAP spectrum based on these parameters was used to create input water level time series. Resistance type wave gauges which comprise of two thin, parallel stainless steel electrodes were used to measure the water surface elevation. Three wave gauge system has been utilized to measure the water surface elevation in the view of separation of the incident and reflected waves from the outputs (Mansard and Funke, 1980). Three sets of multi-gauge arrays, each consisting of three wave gauges were used near the wavemaker, near the structure as well as at the middle of above mentioned locations in the flume. Prior to executing the actual test runs, a series of calibration runs were carried out to establish input wave conditions for the wave generation software to obtain required design wave conditions in front of the paddle. Apart from that, one wave gauge was placed at the lee breakwater to assess the wave transmission. Waves were generated in the flume without any breakwater sections and a wave absorption system placed at the end of the flume to reduce the reflection. After calibration, a set of verification tests were also done to ensure the design wave conditions are achieved at the paddle.

4 BREAKWATER DESIGN

Since this study is focused on the optimization of the crest and the toe design consideration, only those aspects are described in this section.

4.1 Design of the Crest

The vertical height above the SWL to which water from an incident wave will run upon the face of the breakwater determines the required breakwater height (Crest level). The wave run-up depends on the incident wave height and steepness, interaction with the preceding reflected wave, slope angle, surface roughness and permeability and porosity of the slope (CEM, 2006). Wave overtopping occurs when the highest of the run-up levels exceed the crest of the breakwater and it is mostly given as an average discharge Q per unit width (in m^3/s per m run). Following formula gives the mean overtopping discharge for the probabilistic design of rubble mound breakwater (EurOtop, 2007).

$$\frac{q}{\sqrt{gH_s^3}} = 0.2\exp\left[\frac{-2.6R_c}{H_s\gamma_f\gamma_\beta}\right] \qquad [1]$$

Where;

q = mean overtopping discharge
H_{m0} = significant wave height calculated from the spectrum
R_c = free board
g = acceleration due to gravity
γ_f = reduction factor for roughness (0.55 for Rocks,2 layers, impermeable core and 0.44 for CORE-LOC)
γ_β = *Reduction factor for influence of angle of incidence(β) of the waves(1 for* $0^\circ < \beta < 10^\circ$*)*

It is evident that mean overtopping discharge depends on the freeboard (R_c) and the significant wave height if all the properties of the structure slope remain unchanged. Hence, the crest level optimization of the deep-water could be done by changing the R_c for a particular wave condition.

4.2 Design of the Toe

Generally, a toe bund is required, if the water depth is less than 2Hs and/or if a structure slope is less than 1 in 3. The function of toe berm is to support the main armour layer and to prevent damage resulting from scour. In the shallow water condition, the bottom of the breakwater can be exposed to breaking wave action. However, this scouring effect depends on founding soil properties. The formula for estimation of the mean nominal diameter of the toe rock is given as follows (Van der Meer et.al, 1995, CIRIA RM, 2007)

$$N_{od}^{0.15} = \frac{H_s}{\left(2+6.2\left(\frac{h_t}{h}\right)^{2.7}\right)\Delta D_{n50}} \qquad [2]$$

Where;

ht = water depth at the toe of the structure
h = water depth in front of the structure
Δ = relative buoyant density of the material
D_{n50} = median normal diameter of armour unit at the toe
Hs = significant wave height at the toe of the structure
N_{od} = damage number

Range of applicability; The limitations of the above equation are as follows:

$0.4 < ht/h < 0.9$
$3 < ht / Dn50 < 25$
$0.28 < Hs / h < 0.8$

The interpretation of the damage level is made as follows:

$N_{od} = 0.5$: start of damage
$N_{od} = 2.0$: some flattening out of the toe
$N_{od} = 4.0$: complete flattening out of the toe

As the waves at high water levels are hardly created an effect on the toe, the Critical Low Water Level (CLWL) is considered while assessing the toe stability and the CLWL could be calculated as below.

CLWL = {Sea bed level + (Design wave height / 0.78) + Thickness of scour protection + Thickness of toe foundation layer} [3]

The purpose of this is to assess the toe stability in the worst-case scenario which has the maximum possible wave height at the lowest possible water depth at the toe.

5 USAGE OF DUMMY (ALTERED) WATER LEVELS

The normal practice is to change the breakwater height to achieve the different R_c values while keeping the same water levels and the wave parameters in the 2D wave flume. Similarly, the adjustment to the toe level has been done to achieve different effective water depths at the toe. Therefore, usage of dummy water levels (altered water levels) could fulfil both the requirements while keeping the built structure as it is. In other words, it would be possible to change the water level to achieve the required R_c and the effective water depth at the toe.

Design water level for the deep-water section was +3.95 m CD while 0.00 m CD was taken as the lowest water level. Two dummy water levels of +4.95 m CD and -2.00 m CD have been used to optimize the crest level and the toe level respectively. Similarly, 0.00 m CD was used to assess the toe stability of the shallow-water section while -2.00 m CD altered water level was utilized to assess the same. Table 1 illustrated the details of the simulated test conditions concerning the actual and dummy water levels.

Table 1. Simulated test condition for deep-water (top) and shallow-water (bottom) sections

Test No.	Return Period	Water Level (m CD)	H_s (m)	T_p (Sec)	Section	Crest Level (m CD)	Crest Free Board (m)	Toe Level (m CD)	Effective WD (m)
K-04(0)	100	+3.95	1.60	6.33	B-V0	+5.0	1.05	-5.0	8.95
K-04(1)	100	+3.95	1.60	6.33	B-V1	+7.0	3.05	-5.0	8.95
K-04(2)	100	+3.95	1.60	6.33	B-V2	+6.5	2.55	-4.0	7.95
K-05(0)	Overload	+3.95	1.92	6.5	B-V0	+5.0	1.05	-5.0	8.95
K-05(1)	Overload	+3.95	1.92	6.5	B-V1	+7.0	3.05	-5.0	8.95
K-05(2)	Overload	+3.95	1.92	6.5	B-V2	+6.5	2.55	-4.0	7.95
K-09(1)	100	+4.95*	1.60	6.33	B-V1	+7.0	2.05	-5.0	9.95
K-10(1)	Overload	+4.95*	1.92	6.50	B-V1	+7.0	2.05	-5.0	9.95
K-06(1)	100(LWL)	0.00	1.60	6.33	B-V1	+7.0	7.00	-5.0	5.00
K-06(2)	100(LWL)	0.00	1.60	6.33	B-V2	+6.5	6.50	-4.0	4.00
K-11(2)	100(CLWL)	-2.00*	1.60	6.33	B-V2	+6.5	8.50	-4.0	2.00
ME-06	100 (LWL)	0.00	2.76	17.3	E-V0	+8.0	8.00	-2.1	2.10
MD-06	100 (LWL)	-1.50*	2.55	17.3	D-V0	+8.0	9.50	-0.6	0.60
ME-08	Overload(LWL)	0.00	3.05	16.0	E-V0	+8.0	8.00	-2.1	2.10
MD-08	Overload(LWL)	-1.50*	2.47	16.0	D-V0	+8.0	9.50	-0.6	0.60

Note: *-Dummy Water Level; CD-Chart Datum; WD-Water Depth; CLWL-Critical Low Water Level

6 DISCUSSION ON THE RESULTS

6.1 Deep-water Section

Initially, the deep-water breakwater section was designed with +5.0 m CD crest and -5.0 m CD of toe berm (B-V0). Even though the structure was tested for the full set of wave series including 1, 10, 50, 100 YRP and overload waves as well as design high and design low water levels, only 100 YRP and overload waves are discussed in this study. The overtopping is negligible over the structure even for higher return periods. However, the wave transmission through the main armour was observed even for lower return period waves as the water level is higher than the top of the under layer. Hence, the disturbance at the harbour was the main concern while optimizing the section. Therefore, modifications (Figure 2) were introduced in terms of structure height (as B-V1 with +7.0 m CD crest and B-V2 with +6.5 m CD crest) to achieve the tolerable disturbance at the harbour with a hydraulically stable structure. Furthermore, optimizing of toe berm level was also considered as a key factor as it correlated with the area covered with main armour. Hence, the hydraulic stability of the structure is discussed along with wave transmission and toe stability separately.

As far as wave measurements at the lee side of the structure are concerned maximum recorded wave height is 0.39 m in section B-V0 (+5.0 m CD crest) which is slightly above the acceptable limit of 0.3 m of harbour tranquillity. However, observed damage at main armour was depicted that the front side is sable with the larger rocks while it is loosening its stability at the rear side against the overtopped and transmitted water through the armour layer (Figure 4). The rear side of section B-V1 (+7.0 m CD crest) was perfectly stable even for the high waves, as there was a significant reduction in wave transmission (maximum of 0.04m wave height at the harbour) through the main armours. In each test run, the main armours at the crest were not even affected by

the waves, hence kept stable (Figure 5). As the +7.0 m CD crest was shown over stability, the possibility of the reduction of breakwater height has been considered to have an economical section.

Two tests of 100 YRP and the overload condition for +7.0 m CD crest section were carried out with raised water level of 4.95 m CD to represent the dummy section of +6.0 m CD crest with 3.95 m CD water level (Figure 2). The rear side armours were found to be stable (Figure 6) and the wave height at the harbour was 0.1 m.

Considering the stability condition for the above three crest levels (+5.0, +7.0 and +6.0 m CD crest), structure height was adjusted to +6.5 m CD. The testing carried out for higher return periods (100YRP and Overload) depicted that the whole structure was hydraulically stable when its crest raised above the +6.0 m CD (Figure 7). However, it has been observed that the maximum wave height at the harbour was reduced to 0.04 m when the crest level was raised to +6.5 m CD or more.

Figure 4. Before 100 YRP (Left), After 100 YRP (Middle) and After the Overload (Right) Condition (B-V0)

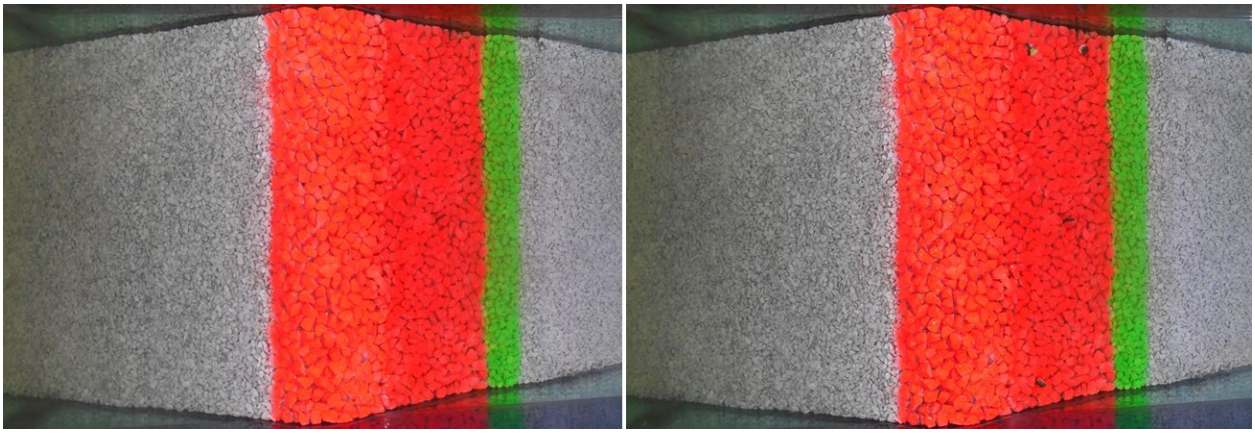

Figure 5. Before 1 YRP (Left) and After the Overload YRP (Right) Condition (B-V1)

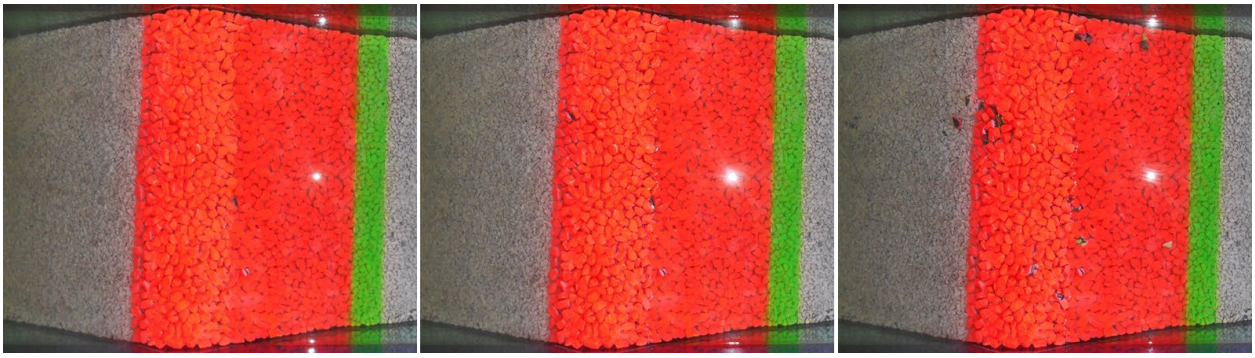

Figure 6. Before 100 YRP (Left), After 100 YRP (Middle) and After the Overload (Right) Condition (B-V1 with Dummy Water Level)

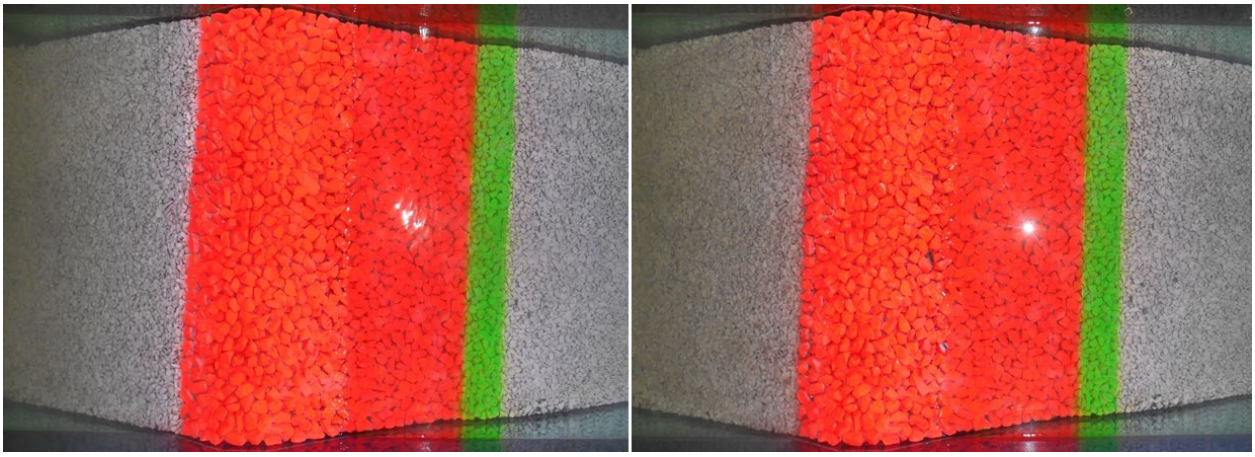

Figure 7. Before 100 YRP (Left) and After the Overload (Right) Condition (B-V2)

The calculated CLWL for the 100 YRP waves at the deep-water section was -4.25 {=-6.3 + (1.6/.78)} m CD Hence, the minimum possible depth (Theoretical) at the toe was 2.05 m {=-6.3 - (4.25)} and actual depth at the toe is 6.3 m for LWL (0.00 m CD). The toe stability results depicted that the front toe was perfectly stable for both sections of B-V0 and B-V1 with -5.0 m CD toe level even for higher waves since the wave action has not been even reached to the toe. Therefore, the toe level was raised by 1.0 m so that the toe level in section B-V2 is -4.0 m CD. However, the toe was kept stable for section B-V2 as well (Figure 7). Considering minimum water depth that can be allowed on top of the toe, the water level has been lowered by 2 m (at -2.0 m CD) for section B-V2 in order to represent the effective toe level of -2.0 m CD with 0.0 m CD LWL. The test results were proven that toe could be stable with the minimum water depth of 2.0 m at the toe for 100YRP waves (Figure 8).

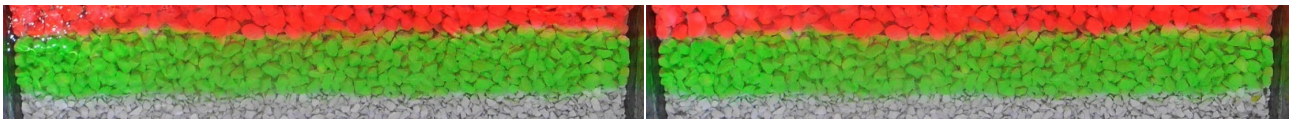

Figure 8. Before 100 YRP (Left) and After the Overload (Right) Condition (B-V2 with Dummy Water Level)

6.2 Shallow-water Section

Even though section E-V0 and D-V0 are located at -5.5 m CD and -4.0 m CD depths, the geometry of both sections are same. Therefore, toe stability of section D-V0 was assessed by using section E-V0 and the dummy water level of -1.5 m CD which represents the 0.00 m CD at section D-V0. CLWL for section E-V0 was found as -0.46 m CD for 100 YRP waves and respective water depth at the toe was 3.5 m (Theoretical). As the lowest water level was given as 0.00 m CD the actual water depth at the toe was 4.0 m. The front toe was perfectly stable for both sections of E-V0 (with -2.1 m CD toe level top) and D-V0 (-0.6 m CD toe level top) even for higher waves. It has been observed that the toe armours are strong enough to withstand the wave action though the toe was exposed occasionally during the test (Figure 9 and 10).

Figure 9. Before 50 YRP LWL (Left) and After the Overload LWL (Right) Condition (E-V0)

Figure 10. Before 50 YRP LWL (Left) and After the Overload LWL (Right) Condition (D-V0)

7 CONCLUSIONS AND RECOMMENDATIONS

The results obtained using the dummy water levels were successfully verified at LHI's 2D flume as they well agree with similar tests done using structural modifications and actual water levels. Further, the results obtained using the dummy water level were sufficient enough to pre-assess the effectiveness of the structural modification in a 2D flume. Following conclusions were made based on the 2D model results done with dummy water levels to optimize the crest and toe levels of the deep and shallow water structures.

7.1 Crest Optimization of the Deep-Water Section

As far as wave measurements at the lee side of the structure are concerned maximum recorded wave height is 0.39 m and 0.09 m for the crest level of +5.0 m CD and +6.0 m CD while it is 0.04 m for the crest level more than 6.5 m CD.

The hydraulic stability criterion in each element of the structure including main armour, under layer, toe and scour protection layer is within the limit for all the sections of B-V0, B-V1 and B-V2. Even though the structure could be hydraulically feasible to construct when the structure crest is raised more than +6.0 m CD, the structure with +7.0 m CD crest has been shown the over stability even for the overload condition.

Therefore, the wave transmission and stability condition of the armours obtained for the +6.0 m crest with dummy water levels are well in line with the value obtained for +5.0 m CD, +6.5 m CD and +7.0 m CD crest with actual water levels and the structural modifications.

7.2 Toe Optimization of the Deep-Water and Shallow-water Sections

Optimizations of the toe berm level of the deep-water section were considered using actual and dummy water levels. The front toe is perfectly stable for both toe levels of -5.0 and -4.0 m CD done with actual water levels. Further, the critical low water level test done with dummy water has been revealed the possibility of raising the toe level to -2.0 m CD.

The stability assessment of the front toe of section E-V0 of the shallow water section was done using actual water levels. Since the geometry and the crest level is similar in both sections of E-V0 and D-V0, the toe stability of section D-V0 has been done using the dummy water level at section E-V0. The results indicated that the front toe is perfectly stable in both the sections of E-V0 with -2.1 m CD and D-V0 with -0.6 m CD toe level (Top).

The results obtained using the dummy water level on the constructed model has generated reasonably accurate results which comply with results obtained using structural modifications with actual water levels. Therefore, the dummy water levels can be used as an alternative method for crest and toe level optimization instead of having structural modifications of the model.

8 ACKNOWLEDGEMENT

The authors wish to acknowledge all the team members of above two physical model studies at Lanka Hydraulic Institute Ltd for their enamours support during the studies. Further, the authors' gratitude also extended to Ms. D. Pathiranage and Ms. K. P. M. Fernando at Lanka Hydraulic Institute for their various supports while preparing this paper. Finally, the authors convey their special thanks to anonymous reviewers as well as all other colleagues who support this study.

9 REFERENCES

CIRIA, CUR, CETMEF (2007): The Rock Manual, use of rock in hydraulic engineering (2nd edition), C683, CIRIA, London.

D. P. L. Ranasinghe, I. G. I. K. Kumara, H. P. G. M. Caldera, N. L. Engiliyage (2018): Adaptation of Directional Wave Measurement in 3D Physical Model to Eliminate the Reflection Component in Uni-Directional Waves, Proceedings of the Twenty-eighth International Ocean and Polar Engineering Conference, Sapporo, Japan, pp 868-875.

EurOtop (2007) Wave Overtopping of Sea Defences and Related Structures: Assessment Manual, Authors: Pullen, T., Allsop, N.W.H., Bruce, T., Kortenhaus, A., Schüttrumpf, H., Van Der Meer, J.W. (2007): www.overtopping-manual.com

Hughes, S.A. (1993): Physical models and laboratory techniques in coastal engineering, Advanced Series on Ocean Engineering, Vol. 7, World Scientific Publishing, Singapore.

IAHR. (2011): Design Manual-Users Guide to Physical Modelling and Experimentation-Experience of the HYDRALAB Network, International Association for Hydro-Environment Engineering and Research.

Mansard, E.P.D. And Funke, E.R. (1980): The measurement of Incident and Reflection spectra using a Least square method, Proceedings of the 17th International Conference of Coastal Engineering, ASCE, Sidney, Australia, pp 95-96.

U.S. Army Corps of Engineers (2006.) Coastal Engineering Manual. Engineer Manual 1110-2-1100, U.S. Army Corps of Engineers, Washington, D.C. (in 6 volumes).

Van Der Meer, J.W., D'angremond, K. And Gerding, E. (1995): Toe structure stability of rubble mound breakwaters, In: J.E. Clifford (ed), Advances in coastal structures and breakwaters, Thomas Telford, London, pp 308-321.

8th International Conference on the Application of Physical Modelling in Coastal and Port Engineering and Science
Dec. 9th - 12th, 2020, Zhoushan, China

NUMERICAL SIMULATION OF HYDRODYNAMIC AND SEDIMENT TRANSPORT AT CUA LO INLET, QUANG NAM PROVINCE, VIETNAM

NGUYEN QUANG DUC ANH[1], DUONG CONG DIEN[2], HO SY TAM[3], NGUYEN TRUNG VIET[4], HITOSHI TANAKA[5]

[1, 3,4] Thuyloi University, 175 Tay Son, Dong Da, Hanoi, Vietnam
ducanh.cte@gmail.com; tamhs.cttl@tlu.edu.vn; nguyentrungviet@tlu.edu.vn
[2] Institute of Mechanics, 264 Doi Can, Lieu Giai, Ba Dinh, Ha Noi
duongdienim@gmail.com;
[5] Tohoku University, 6-6-06 Aoba, Sendai 980-8579, Japan
hitoshi.tanaka.b7@tohoku.ac.jp;

ABSTRACT

In recent decades, Cua Lo Inlet in Quang Nam province of Vietnam is experienced serious problems of deposition and erosion. Based on the long-term analysis of the satellite images, it has been figured out that one of the main causing mechanisms for this problem is the elongation of up-drift sand spit which leads to the severe erosion of the south bank of the river mouth. In this study, detailed numerical simulations of hydrodynamic and sediment transport at Cua Lo Inlet are conducted using the DELFT3D model. The ebb current and wave-induced current during the Northeast monsoon season are the main dynamic factors for sand spit elongation and inlet morphological changes.
Key Words: Cua Lo River Mouth, long-shore sediment transport rates, river discharges, tidal currents, nearshore wave parameters.

1 INTRODUCTION

Tidal inlets are highly dynamic due to the influence of wave climate and seasonal river flow (Lam *et al.*, 2007). On the central coast of Vietnam, the hydrodynamic regime and morphology of the tidal inlet will change seasonally. During the dry season, the tidal current through the inlet has maintained the opening of the inlets against the closure tendency due to wave-driven long-shore sediment transport. During this period, the long-shore currents and sediment transport along the coast are caused by prevailing winter monsoon and are much larger than the flow and sediment transport from rivers to the coast through the inlet which leads to the closure of the river mouth and the sand spits elongation phenomenon. On the other hand, in the flood seasons, the hydrodynamic regime and morphology of a tidal inlet are subjected to dominance by flood flows. Strong river floods erode the sand spit and widen the cross-section of the inlet (de Swart & Zimmerman, 2009). Furthermore, when the sand spit is elonged due to sediment accumulation on the up-drift side, breaching will occur at the original location of the inlet opening to create a more efficient pathway for the water behind the sand spit (FitzGerald *et al.*, 2000). However, there are a number of distinct cases of elongation phenomenon, most notably in the case of Cua Lo inlet, Quang Nam, Vietnam. Based on the remote sensing analysis techniques, Duy et al., (2018) point out that the breach of the sand spit in the Cua Lo inlet is not going to happen due to the changing of its hydrodynamic modification. However, the hydrodynamic mechanism of the Cua Lo inlet that accompanies sand spit elongation is not yet fully understood. Therefore, this study has been conducted by using the numerical models and observed data to address the hydrodynamic mechanism and their influence on the morphology of the inlets.

1.1 Study area

Cua Lo is a natural tidal inlet of the Truong Giang River, which has a river basin area of 436 km^2 and a length of 70 m (Figure 1). This tidal inlet is also a part of the littoral system extending from Da Nang to An Hoa cape, across the Cua Dai river mouth. In recent decades, the elongating development of the sand spit from the North of this inlet not only narrows the river mouth but also causes severe erosion in the South, making it difficult for ships to go through Cua Lo Inlet. This area is considered as the “hot-spot” of erosion and acceleration issues, having detrimental influences on sustainable management and development for the inlet area.

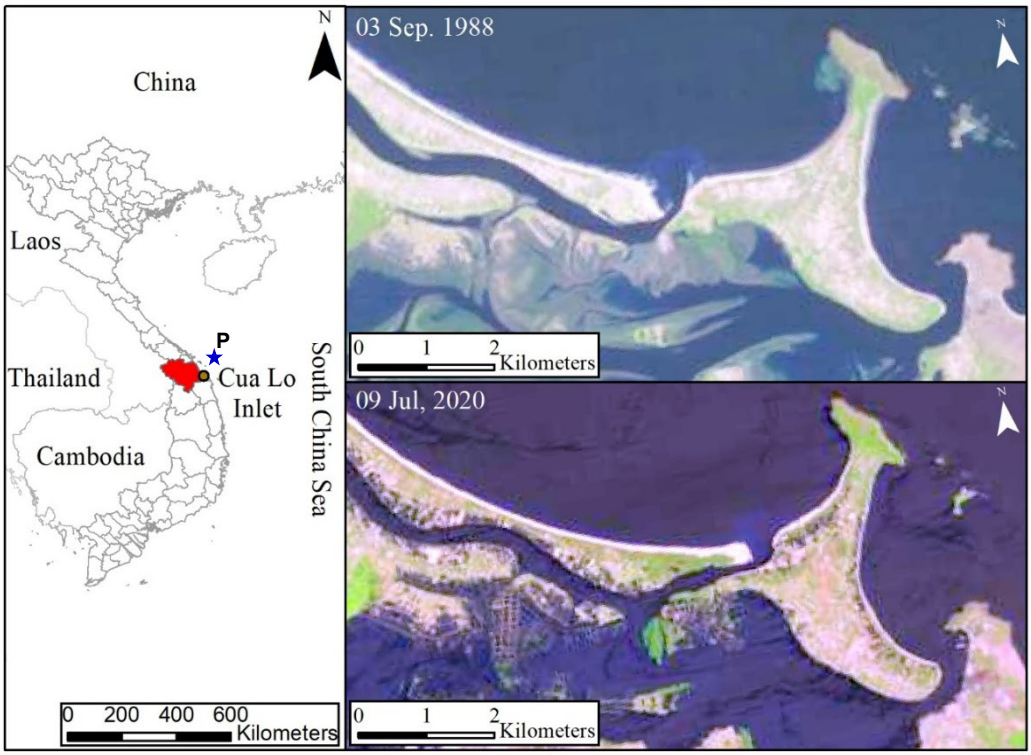

Figure 1. Cua Lo Inlet and its morphology

1.2 Data collection for numerical simulation

The collected data to set up the boundary conditions for the numerical model are as follows:

(a) Bathymetry

The bathymetry data for the numerical model was combined from several sources including the measurement data from the previous projects by the local government, General Bathymetric Chart of the Ocean data, and Vietnam Bathymetry data.

(b) Wind data

There are two major seasons in a year: the winter monsoons and the summer monsoons and the calm wind account for 28÷43%. The highest average wind speed is 6.1 m/s. The strongest wind speed in months is less varied, ranging from 5.3÷6.5 m/s. The wind rose at the Quang Nam region is shown in Figure 2.

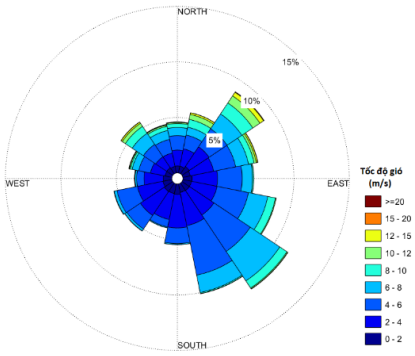

Figure 2. Wind rose

(c) River discharge

Truong Giang River downstream depends on the Tam Ky flow and the tidal regime. There are no hydrological stations on the Truong Giang river basis. In this study, the river discharge was collected from the results of the rainfall-runoff model for setting up the boundary condition.

(d) Wave

Offshore wave conditions of Cua Lo Inlet were modeled at an offshore point (Figure 1, point P), located approximately 80 km to the east coast.

(e) Tide

The simulation for hydrodynamics, waves, and sediment transport for the long-term period will normally require a lot of computational effort. To reduce the computational time, a morphological factor proposed by (Roelvink, 2006) is applied. In which, the morphological tide is determined from 3 main tidal wave components, including M2, K1, and O1. The O1 and K1 tidal components are aggregated into a C1 component according to Eq. [1]. The tidal boundary conditions used for the model as shown in Figure 4.

$$\text{Amplitude: } C_1 = \sqrt{2O_1 + K_1} \text{ ; and Phase: } C_1 = \frac{\varphi_{O1} + \varphi_{K1}}{2} \quad [1]$$

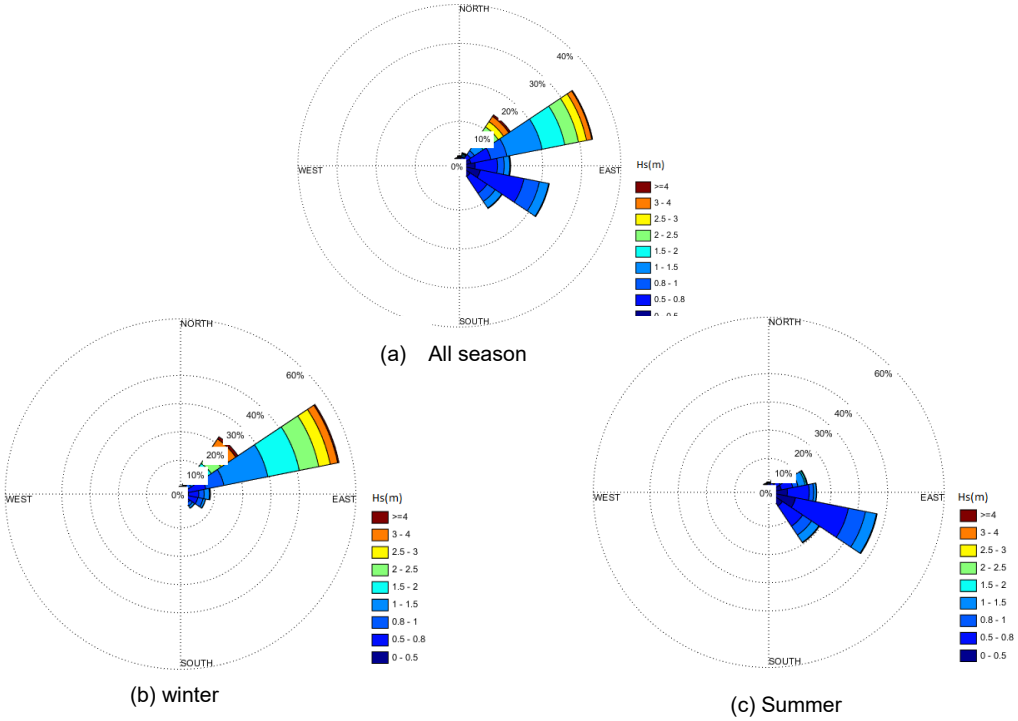

(a) All season

(b) winter

(c) Summer

Figure 3. Wave roses in Quang Nam coast (from 1995 to 2019)

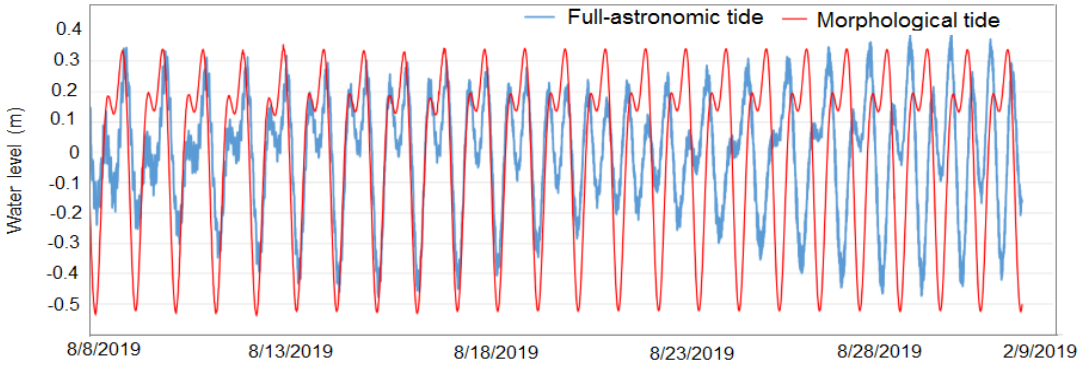

Figure 4. Tidal water levels, full-astronomic tide (blue), and morphologic tide (red)

2 NUMERICAL MODELING

To investigate the sediment transport process in the Cua Lo inlet, a process-based numerical model Delft3D) is used, which is an open-source code and developed by Deltares in Delft, the Netherlands (research version, September 2017). It is integrated from the wave module Delft3D-WAVE and the hydrodynamic module Delft3D-FLOW modules and the sediment transport module Delft3D-SED. The Delft3D-FLOW module solves the depth-averaged or 3D shallow water equations on a rectilinear or curvilinear grid. In the Delft3D-WAVE module, the wave transformation is computed by the third-generation wave model SWAN (Booij *et al.*, 1999; Ris *et al.*, 1999). It includes wave propagation, generation by wind, nonlinear wave-wave interaction, and dissipation. The WAVE and FLOW modules are coupled online at regular intervals to account for the effects of waves on the flow and to provide flow boundary conditions for the wave transformation.

2.1 Computational grids and bathymetries

The calculated grid system and boundary positions for the integrated models are shown in Figure 5. The larger domain was set up for the wave model, and the small one was used for the flow and sediment transport models. The wave grid size was chosen larger than the flow one to prevent lateral boundary effects. The flow domain consists of an area of 35×12.5 km^2 from the grid are coarser offshore and finer near shore and in the inlet area. The large grids consist of 10738 grid cells with sizes vary from 300 to 600 m, including the entire Quang Nam Coast from the Northern bank of Cua Dai Inlet to the end of Dung Quat Bay with an area of 80 × 30 km^2.

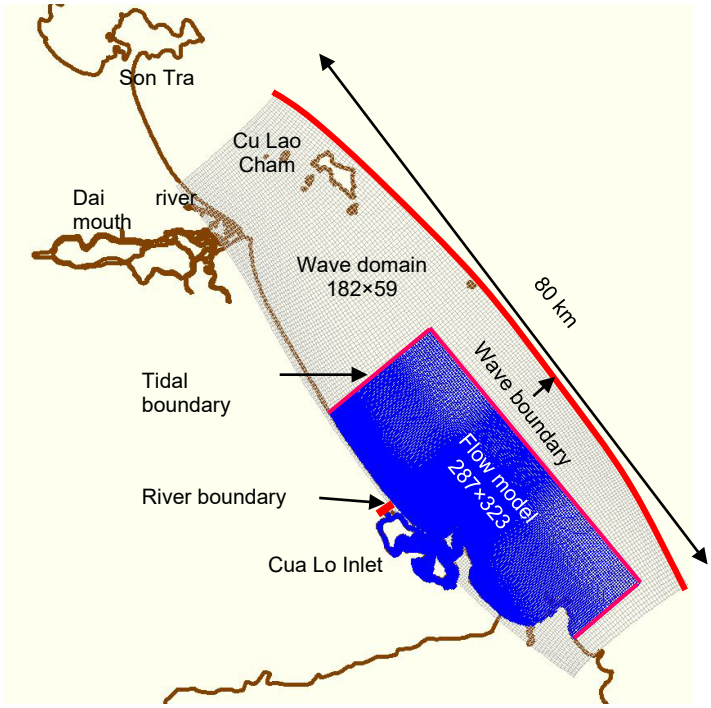

Figure 5. Grid systems for Delft 3D-Flow and Delft 3D-Wave modes

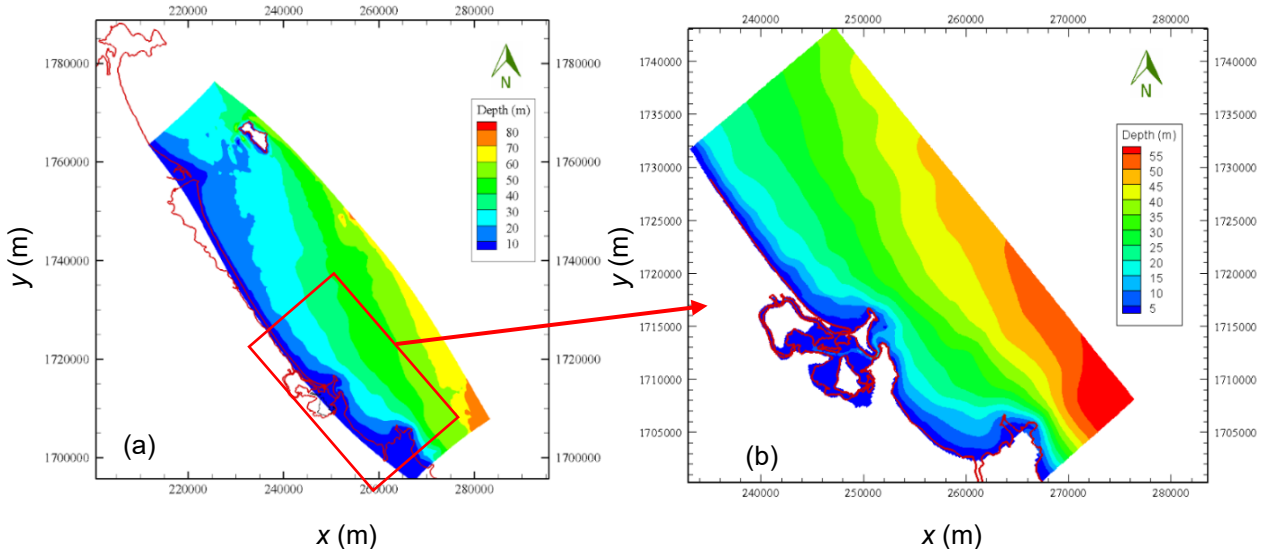

Figure 6. Bathymetry for Flow and Wave model: (a) big domain, and (b) detail domain

2.2 Model calibration and validation

In this study, the surveyed water level, and wave parameters during the summer period (August 2019) and the winter period (November 2019) were used to calibrate the hydrodynamic model. The locations of the measuring stations for model calibration are shown in Figure. The root–mean–square error (RMSE) was used to assess the model accuracy of the model. These criteria are defined as Eq. [2]:

$$\mathrm{RMSE} = \sqrt{\frac{\sum(M-D)^2}{n}} \qquad [2]$$

where D is the observational data, M is the corresponding modeled data, n is total number of pairs.

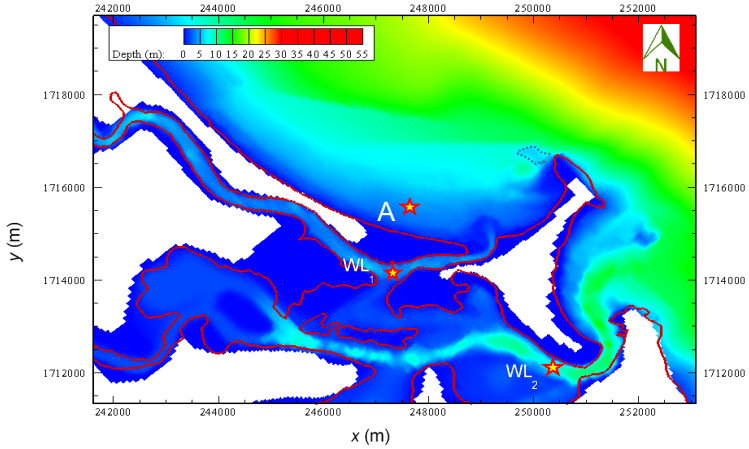

Figure 7. Locations of hydraulic measurement stations for model calibration: (A)- the wave station, WL_1 and WL_2 - water level stations

Figure 8 shows the results of comparing water levels, and wave parameters at measuring stations. The obtained RMSE values for water levels are 0.04 m, 0.05 m, and 0.036 m, for wave height and wave period 0.11 m and 0.77 s, respectively. These small differences indicated that the model achieved excellent performance.

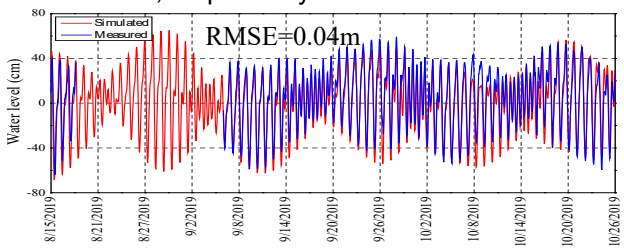

(a) Calibration result of the water level at W1 station

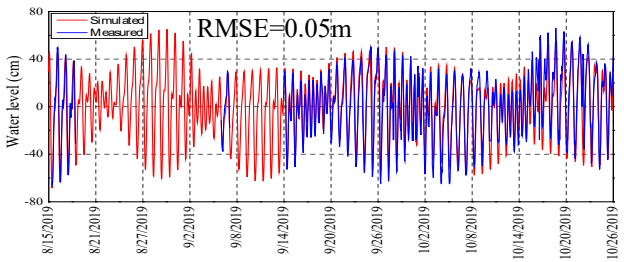

(b) Calibration result of the water level at W2 station

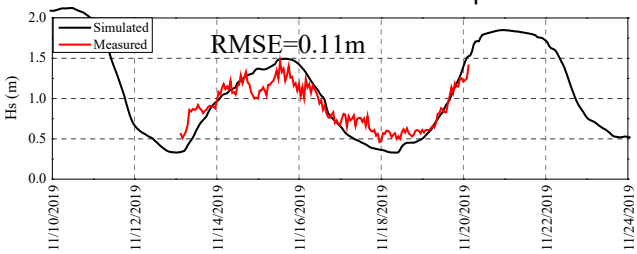

(c) Calibration result of the significant wave height at A station

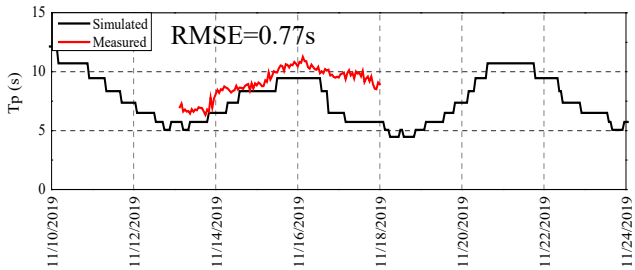

(d) Calibration result of the significant wave period at A station

Figure 8. Model calibration and validation

3 RESULT AND DISSUCSS

In this study, the authors evaluate the hydrodynamic regime and sediment transport in the Cua Lo area based on the effects of winter monsoons, summer monsoon waves, and effects of 5% river flood frequency.

3.1 The hydrodynamic and sediment transport

Figure 9 (a) shows the distribution of wave height in the Cua Lo area in winter monsoon. The nearshore wave height in the Cua Lo area is large, in a range from 1.5 m to 1.8 m. After the wave propagates over the coral reefs to the Cua Lo area, the wave height decreases due to the shallow water effects. Since being protected by the coral reefs and Ban Than cape, when reaching the Cua Lo area, the waves seem are divided into three areas with quite different wave heights: (a) in the Northern beaches of Cua Lo Inlet, the wave height is much higher than the two above areas, from 1.0 to 1.5m (b) at Cua Lo Inlet, the wave height is between 0.2 and 1.0 (m); (c) Southern beaches of Cua Lo Inlet, the wave height is only about 0.2 ÷ 0.8 m; In contrast, the wave height in Cua Lo area during the summer is very small because the direction of the wave incoming is in the Eastern and Southeastern direction, so when the waves pass through the coral reefs and Ban Than cape, it almost releases all energy through the wave breaking process (as shown in Figure 9(b)).

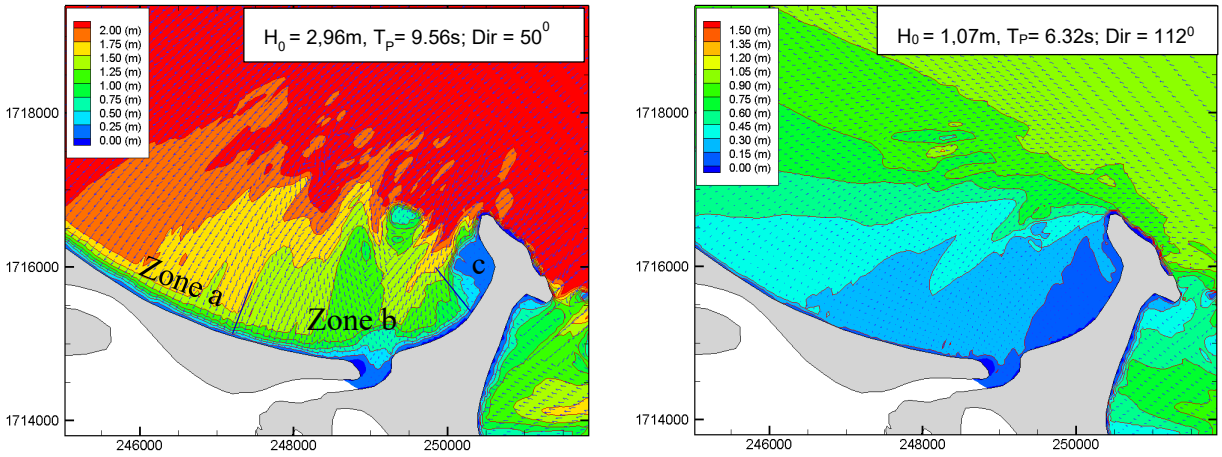

(a) Wave height and wave vectors in winter (b) Wave height and wave vectors in summer

Figure 9. Distribution of wave height for NE and SE waves

Figures 10(a) and 10 (b) show the velocity flow field during the high tide and the ebb tide that is influenced by monsoon waves in the winter season. Inside the inlet, the ebb current is divided into two directions, one moving into Cua Lo Inlet then flowing into the sea and the other one moves to An Hoa lagoon and Ky Ha Inlet. The former interacts with the wave-induced current by the very strong waves in winter create a very strong turbulent current in front of the sand spit tip. It is interesting that always exists current forming backward vortices in the sand spit tip that cause the sediment transport to the South. This current is formed by the difference in water levels between the current convergence points when wave-induced current and the ebb current during the winter monsoon time. This current reaches from 0.2 ÷ 0.4 m/s and bring sediment deposit at the head of the sand spit.

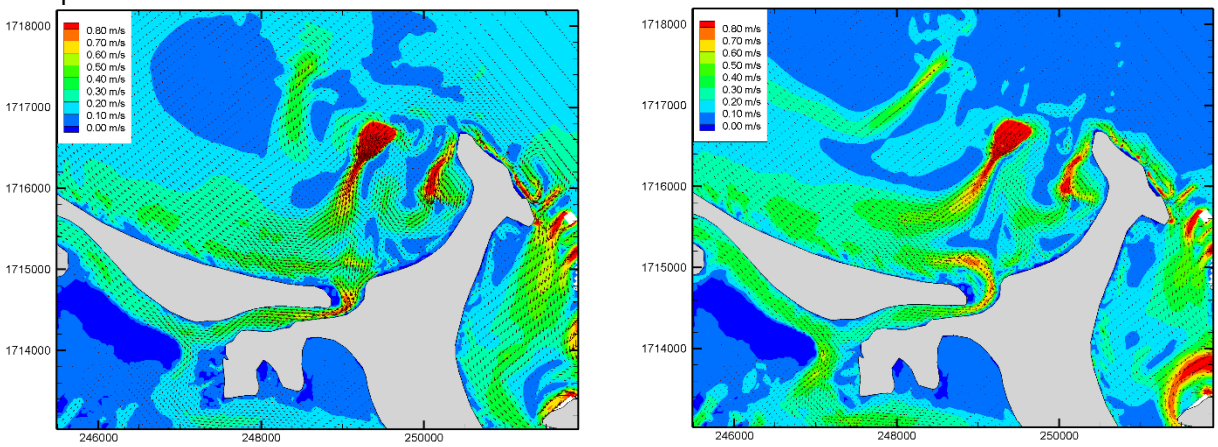

(a) Velocity flow field during high tide phase (b) Velocity flow field during ebb tide phase

Figure 10. Distribution of the current during winter monsoon affected

Figures 11 shows the velocity flow field in the Cua Lo area when the study area is influenced by waves to the Southeast direction. In this case, it can be seen that the wave interaction on the hydraulic regime in the Cua Lo area is not as great as the above situation.

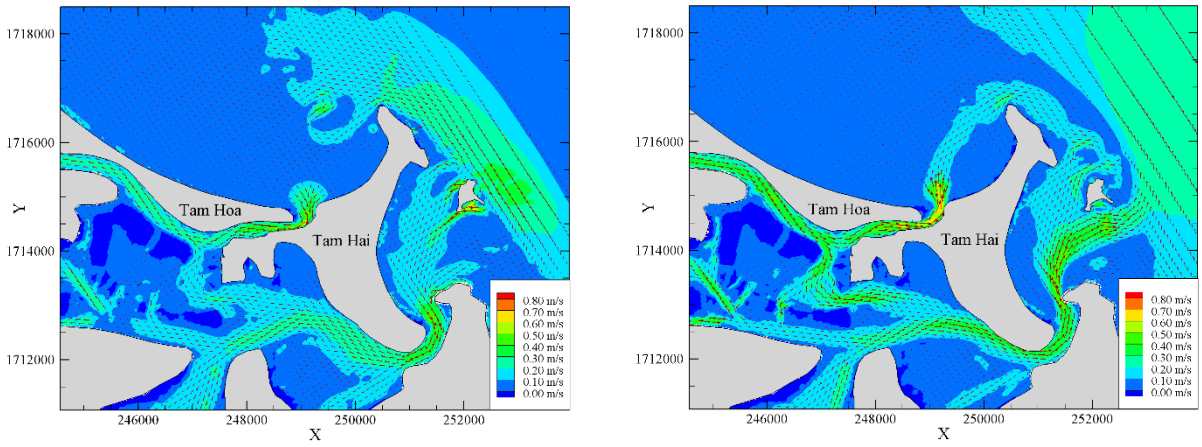

(a) Velocity flow field during high tide phase (b) Velocity flow field during ebb tide phase

Figure 11. Distribution of the velocity flow field influenced by summer monsoon

Figure 12(a) shows the bed level changes when the Cua Lo area is influenced by Northeast monsoon waves. The impact of waves during Northeast monsoon causes significant morphological fluctuations in the coastal and estuary areas. In the north beach area, there are separated sand bars with a northward direction because the current has a south-north direction. In the estuary area, the total current brings sediment deposited at the inlet and caused the sand spit elongation. Meanwhile, Figure 12 (b) bed level changes of the Cua Lo area when the area is influenced by Summer Monsoon. Because waves to the Cua Lo area during the summer period are very small, the topographic change due to the wave influence during this period is also almost negligible.

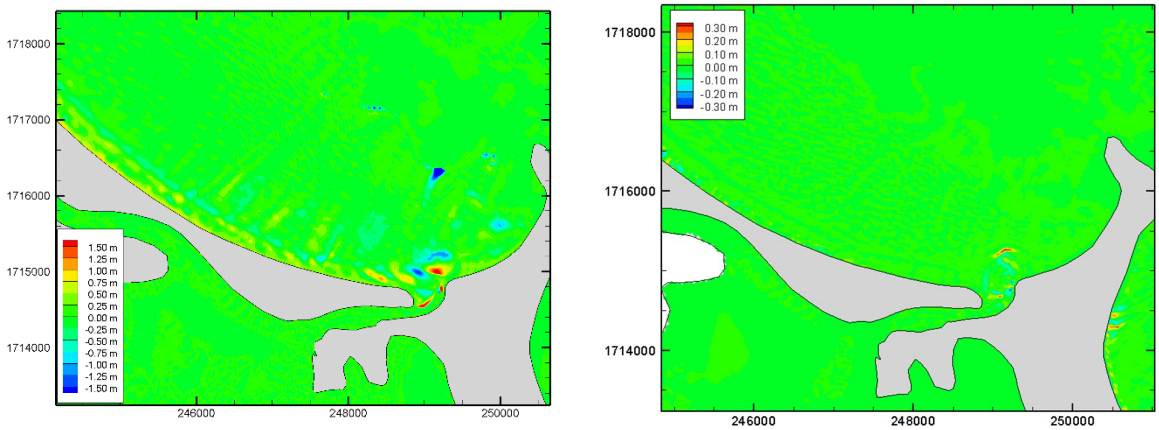

Figure 12. Map of morphological changes under the impact of Northeastern waves

Figure 13 and 14 shows the flood flow field in Cua Lo area when it is subjected to 5% floods and cross-sections extraction. The hydraulic simulation results clearly show that the flood transmission process from the Tam Ky and Truong Giang river system is very clear, the river flow is divided into two branches, one is from Nui Thanh to An Hoa lagoon into the sea through Ky Ha estuary; the other branch flows into Tam Hoa, then a part leads to An Hoa lagoon, and a part flows into the sea through Cua Lo. This shows that the direct impact of the flood flow in the Tam Ky and Truong Giang river system to Cua Lo is not large. During the flood peak period, the largest discharge through Cua Lo Inlet during 5% flood event is only about 650 m^3/s; meanwhile, the average discharge in term of the normal condition through Cua Lo section in normal conditions is about 450 m^3/s as reported by Tam et al. (2019).

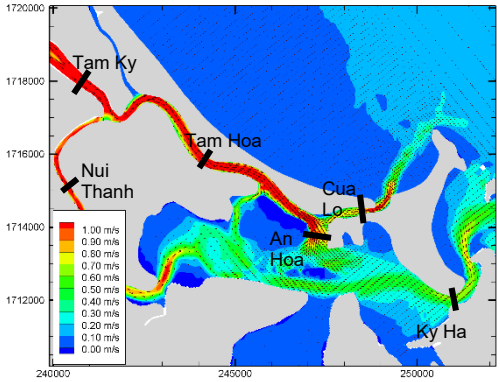

Figure 13. The 5% flood flow field in Cua Lo area and location of the cross-sections profiles

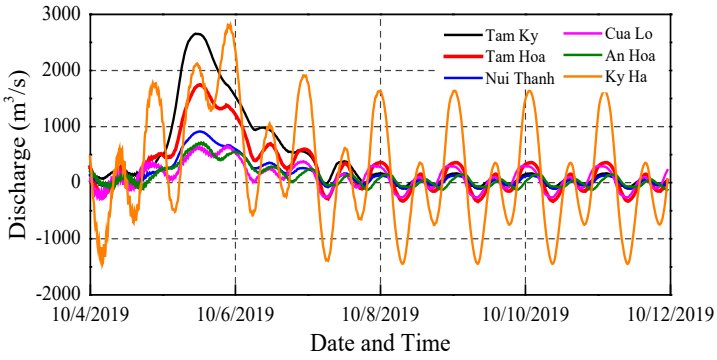

Figure 14. River discharge through cross-sections under 5% flood of Tam Ky and Truong Giang river

3.2 Annual average sediment transport direction

Figure 8 is the map of the annual average sediment transport direction in Cua Lo Inlet and the surrounding area, in which areas in red are in a higher sediment transport rate, areas in yellow and in green are in a smaller sediment transport rates. Thus, the northern beaches in the area where sediment transport rate fluctuations are very large during the year, similar to the shallow water in front of Cua Lo and the head of the sand spit. Interestingly, the inverse currents at the head of the sand spit are produced by the difference in water level, which is caused by the convergence of currents generated by waves and the ebb current will tend to accrete at the sand spit.

Through the map of the annual average sediment transport direction, it can be seen that the morphological change is enormous by the wave impacts. The erosion occurs on the right side of the inlet then the ebb current brings the material erosion to move to the area in front of the inlet, which becomes the main source for ebb shoal regeneration. In the presence of large waves, a portion of sediment at these ebb shoal will follow the current forming backward vortices providing for sand spit elongation and the remaining portion of sediment supply to beaches.

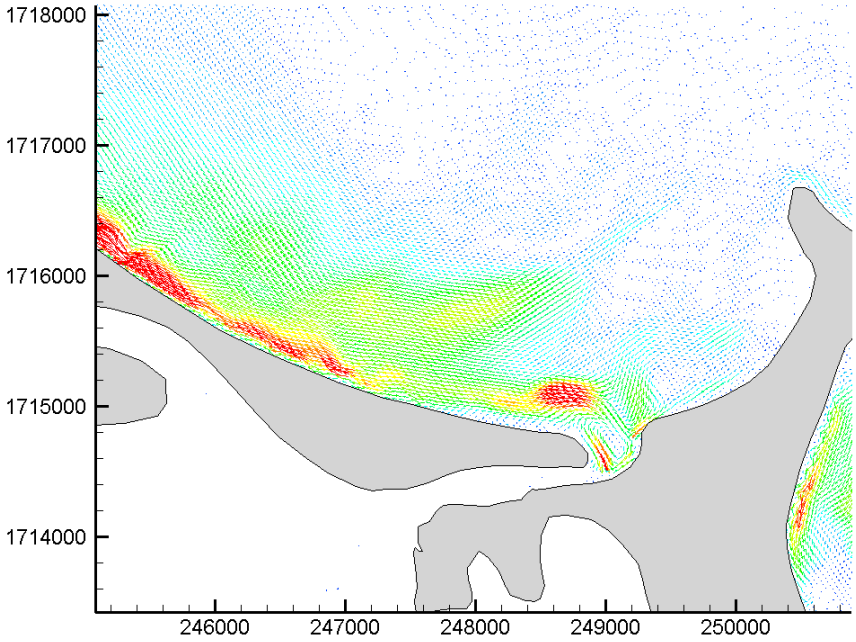

Figure 15: Map of the annual average sediment transport direction

4 CONCLUSION

In this study hydrodynamics and bed level change of the Cua Lo Inlet have been analyzed for different conditions as monsoon wind waves and flood with an application of the physical-based simulation model Delft3D. The simulation model has taken into account the processes of waves, tides, river flows, sediment transports, and bed level change using observed data of the area. Although the observed data is limited, the model has allowed analyzing the fundamental mechanisms of morphological changes of Cua Lo Inlet.

The simulation model results show that the main reason for sand spit elongation and inlet morphological is

the wave impacts and the strong turbulent currents in front of sand spit head which is a current formed by a combination of ebb current and wave generated current in winter. The stronger ebb tidal currents and river flows flush the sediment out to maintain the inlet but the sediment transported out by ebb currents and river flows are too small compared to the turbulent currents at the inlet.

ACKNOWLEDGEMENTS

This research is supported by a bilateral program between Vietnam and Japan (code: HNQT/SPĐP/16.19) and in part by a Research Environment Links grant, ID 527612186, under the Newton Programme Vietnam partnership. The grant is funded by the UK Department of Business, Energy and Industrial Strategy (BEIS) and delivered by the British Council. For further information, please visit www.newtonfund.ac.uk. The authors would like to express their sincere gratitude for this support.

REFERENCES

Booij, N., Ris, R. C. & Holthuijsen, L. H. (1999). *J. Geophys. Res. Oceans*. 104, 7649–7666.
Duy, D. V., Tanaka, H., Mitobe, Y., Anh, N. Q. D. & Viet, N. T. (2018). *J. Coast. Res.* 81, 32–39.
FitzGerald, D. M., Kraus, N. C. & Hands, E. B. (2000). 10.
Lam, N. T., Stive, M. J. F., Verhagen, H. J. & Wang, Z. B. (2007). *Fourth Int. Conf. Port Dev. Coast. Environ.* 4, 10.
Ris, R. C., Holthuijsen, L. H. & Booij, N. (1999). A third-generation wave model for coastal regions, 1, Model description and validation American Geophysical Union.
Roelvink, J. A. (2006). *Coast. Eng.* 53, 277–287.
de Swart, H. E. & Zimmerman, J. T. F. (2009). *Annu. Rev. Fluid Mech.* 41, 203–229.
Tam, H. S., Tanaka, H., Viet, Nguyen T., Tinh, N. X., Quang, D. N. & Anh, N. Q. D. (2019). Investigation of countermeasures to the overall stabilization of Truong Giang River, Nui Thanh District in order to satisfy the economic requirement for sustainable development in the study area and its neighbors.

8th International Conference on the Application of Physical Modelling in Coastal and Port Engineering and Science
Dec. 9th - 12th, 2020, Zhoushan, China

PIEZOELECTRIC NANOGENERATORS-ENABLED BY MECHANICAL METAMATERIALS FOR ENERGY HARVESTING IN OCEAN ENGINEERING

LUQIN HONG(1), HAIPENG WANG(1), KINGJAMES IDALA EGBE(1), ALI MATIN NAZAR(1), YANG YANG(1), FANG HE(1), PENGCHENG JIAO(1), (2)

(1) Institute of Port, Coastal and Offshore Engineering, Ocean College, Zhejiang University, Zhoushan 316021, Zhejiang, China
(2) *Engineering Research Center of Oceanic Sensing Technology and Equipment, Zhejiang University, Ministry of Education, China*
Email: pjiao@zju.edu.cn

ABSTRACT

Here, we develop a novel energy harvesting technique under quasi-static excitations using piezoelectric materials (PENG) enhanced by mechanical metamaterials (MM). The MM are fabricated in the plate shape using the photolithography and atomic layer deposition (ALD) techniques, and the piezoelectric layer is grown by the PVDF-TrFE material using the spin-coating technique. A sliding cell is designed to convert low-frequency excitations into high-frequency motions through postbuckling mode transitions of the piezo-MM. As a consequence, the PVDF-TrFE is triggered to generate electrical power. In this process, the environmental input (<1Hz) is transformed into mechanical energy, which is then converted into electrical power. Fabrication and testing of the MM-PENG are conducted at the microscale, and the numerical models are developed to validate the experimental results with satisfactory agreements. The MM-PENG is outlooked for the green energy by generating electrical power for multifunctional applications. The fluctuation of the ocean surface, for example, provides periodically vibrated waves. Increasing the MM-PENG to millimeter-scale and placing in the ocean, the periodic wave can be used as an axial excitation to trigger the energy harvester to generate electrical power.

1 INTRODUCTION

Piezoelectric nanogenerator (PENG) has been reported as a sustainable energy solution that converts mechanical energy into electrical power (Xie et al., 2017; Wang et al., 2018; Ali et al., 2019). The first Piezoelectric nanogenerator by means of piezoelectric zinc oxide nanowire (NW) arrays was demonstrated in 2006 (Wang et al., 2006). To improve the performance of PENG, for example, various PDMS pattern arrays are fabricated to enhance the friction effect such that the power generation density is improved (Fan et al. 2012), chemical doping and interfacial modification strategy were applied (Liu et al., 2016), and paper was proposed to serve as the starting material of origami triboelectric nanogenerators innovatively (Yang et al., 2015). Since the technique is vibration-based, the mechanical characteristics of PENG significantly affect the output performance, especially when the input is low-frequency excitation (e.g., ~1Hz (Pi et al., 2014)). Given the preponderant mechanical characteristics of the mechanical metamaterials (MM), e.g., significant stiffness enhancement and complete deformation recovery to the original shape, studies have been conducted to exploit the promising behaviors of MM using the geometric strategies such as lattice structures (Lantada et al., 2016), and the material strategies such as 3D printed multimaterials （Janbaz et al., 2018）. This study develops a novel energy harvesting technique using piezoelectric materials (PENG) enhanced by mechanical metamaterials (MM). In this study, the concept and design principles of the MM-PENG are proposed. The piezo layer (e.g., PVDF-TrFE (Pi et al., 2014)) is envisioned to be grown on the Plate-like MM that is used to tune the mechanical response of the energy harvester. Figure 1 shows the concept and design of the MM-PENG. The piezo-MM plates are fixed at both ends in the rigid MM-PENG container. The plates are placed between the bilateral constraints (i.e., the sliding cell) that can freely move in the longitudinal direction. Due to the bilateral constraints, the piezo-MM plates experience postbuckling snap-through, which can be used to activate the piezo layer to generate electrical power. The external excitations from quasi-static to high-frequency motions are enhanced by the postbuckling response of the piezo-MM plates. When placing the axially loaded piezo-MM plates between the walls, quasi-static excitations can be transformed into the dynamic snap-through of the plates. Therefore, the dynamic response can stimulate the piezo layer mechanically. The reported MM-PENG addresses the inadequacy under low-frequency excitations by maneuvering postbuckling mode transitions of the piezo-MM (Jiao et al., 2017; Jiao et al., 2017). Consequently, the MM-PENG is a green way to generate electrical energy for broader applications.

2 DESIGN PRINCIPLE OF MM-PENG

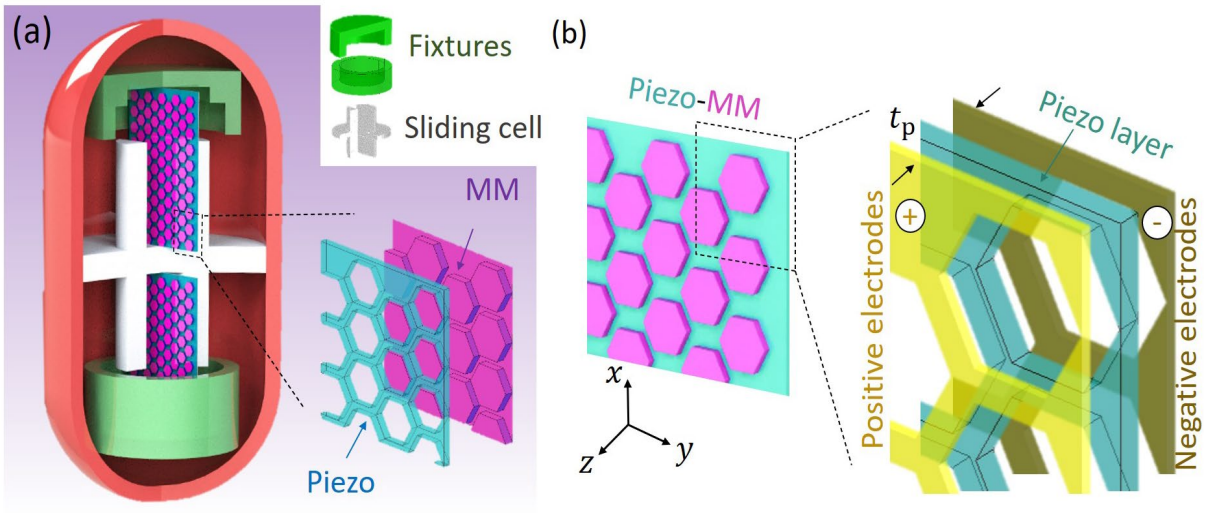

Figure 1. (a) Schematics of the design principle and components of the MM-PENG, including the fixtures, sliding cell and MM plates. (b) Fabrication procedures of the MM-PENG using the photolithography and atomic layer deposition (ALD) techniques.

The design principle and fabrication of the MM-PENG are shown in Figure 1 (Jiao et al., 2020). Low-frequency excitation is collected and then converted into electrical energy, as shown in Figure 1(a). The MM with hexagonal corrugations is placed in the sliding cell, which can freely move in the longitudinal direction and fixed at both ends. Note that the piezoelectric layer (e.g., PVDF-TrFE) can be grown on the hexagonal MM (Pi et al., 2014). The piezo-MM is buckled due to the inertia force caused by the low-frequency excitation. The design principle includes the mechanical process and the electrical process. In the mechanical process, restricting the displacement in the transverse direction, the piezo-MM behaves postbuckling response, which converts the environmental excitation into mechanical energy. The postbuckling behavior of the described piezo-MM can be divided into loading and unloading phases, and the area between the force-displacement curve is equal to the mechanical energy. In the electrical process, the postbuckling response causes severe deformation to the piezo layer, which transforms the mechanical energy into electrical energy. Figure 1(b) presents the schematic diagrams that the PVDF-TrEE layer is coated on the patterned MM plate.

Figure 2 demonstrates the nanoscale fabrication of the MM-PENG using the photolithography and atomic layer deposition (ALD) techniques (Jiao et al., 2020). Figure 2(a) shows the three processes (i.e., photolithography, alumina coating, and sample releasing) to fabricate the hexagonal MM sample. In the photolithography process, the MM samples were fabricated from a mold on silicon wafers. Prime n-doped (100) silicon wafers were spin-coated with HMDS, and the ribs were etched into the silicon with a deep reactive ion etching to a depth of about 10 μm. The photoresist was subsequently removed with sonication in a 60 °C bath of acetone, followed by rinsing with acetone, methanol, and isopropanol, and then ashed with oxygen plasma. In the alumina coating process, the patterned wafers were conformally coated with aluminum oxide via atomic layer deposition with tetramethyl aluminum and water. The thickness was measured after deposition with spectral reflectometry. In the sample releasing process, the aluminum oxide material on the surface was released by first etching away the majority of the silicon wafer in a small 10-30 mm2 area. The backside of the wafer was laser micromachined until ~50 μm of the silicon remained adjacent to the aluminum oxide. The remainder of the silicon was etched away in XeF2 vapor. After completing etching, evident by the absence of visibly opaque areas of silicon, small aluminum oxide samples were cut from the silicon frame using a knife. The proposed MM-PENG is realized by the piezo-MM assembled with the sliding cell. The piezo-MM consists of an MM plate and PVDF-TrFE plate that can be obtained by the spin-coating technique through three processes, i.e., *depositing*, *coating*, and *cooling* (Pi et al., 2014). In the depositing process, a thin layer of silicon dioxide (e.g., $\frac{1}{5}$ of the MM's thickness) can be deposited on the MM by thermal evaporation to ensure good adhesion with a gold electrode. Physical vapor deposition (PVD) can be used to grow the gold layer as a bottom electrical contact. In the coating process, PVDF-TrFE 75/25% mol powder form can be dissolved in diethyl carbonate (DEC) solution. The PVDF-TrFE copolymer solution can be repeatedly spin-coated on the substrate to reach the designed thicknesses such as 20 nm in this study. The top gold electrode can then be grown directly on the copolymer film surface. Thermopoling is conducted to polarize the PVDF-TrFE by subjecting the electrodes to a field of 0.5–0.8 MV/cm in the thickness direction at 100 °C for approximately 30 mins. In the cooling process, the piezo-MM will be cooled to room temperature in the presence of the electric field, which will stabilize the polar alignment and lead to a virtually permanent polarization. Figure 2(b) demonstrates the fabricated MM-PENG samples.

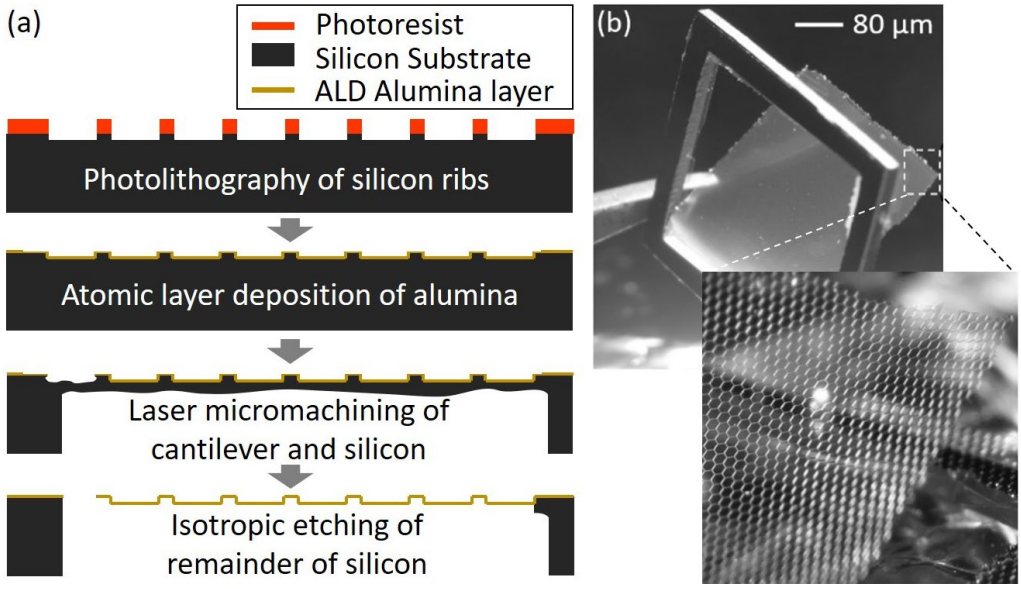

Figure 2. (a) Schematic diagrams of PVDF-TrFE thin film grown on the MM for the piezo-MM plates. (b) Corrugated alumina MM with nanoscale thickness.

3 NUMERICAL SIMULATION

Numerical simulation was conducted to validate the feasibility of the proposed design. To obtain the post-buckling response of the metastructure and then investigate the generated electrical power of the MM-PENG, two types of simulations (i.e., buckling and postbuckling) were carried out in Abaqus. The methods in the buckling and postbuckling analysis were linear perturbation/buckle and dynamic, implicit with Nlgeom, respectively. The contact interaction between layers was defined as “hard” contact without friction that allowed separation in normal and tangential directions. Figure 3 illustrates the meshed FE models of the piezo-MM. The MM was modeled using the shell elements (S4R), while the linear piezoelectric brick elements (C3D8E) was used in the piezo layer’s simulation. The rigid constraints on both ends were simulated with rigid analytical elements. The contact interfaces between the MM and piezo layers were tie-constrained in case of debonding. To generate the electrical potential difference, ground electric potential boundary conditions were set on the piezo layer. The geometric and material properties, the corresponding mesh type, and size of the FE models, are listed in Table 1.

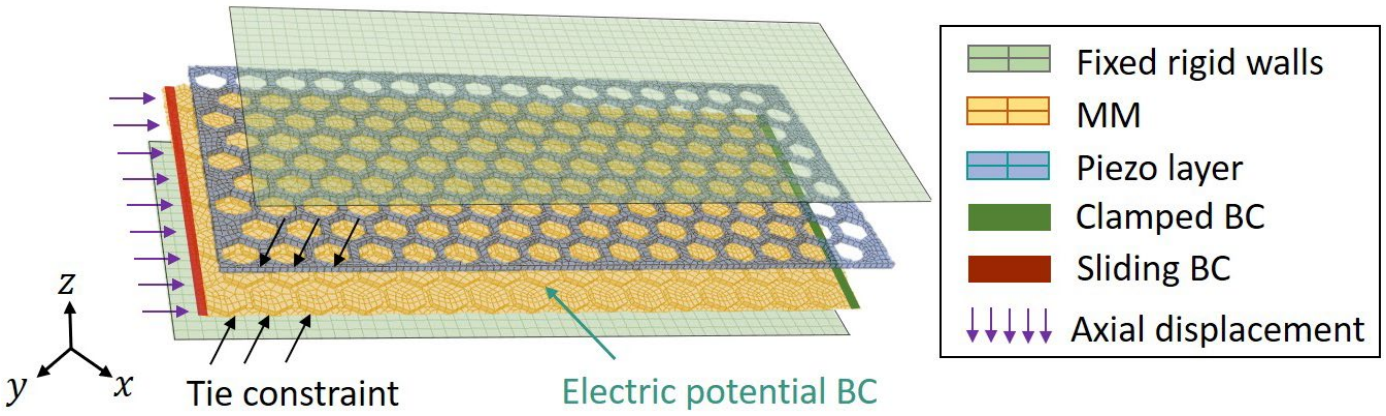

Figure 3. Loading, boundary conditions and meshing of the piezo-MM plate subjected to the axial motion.

Table 1. Geometric and material properties of the MM-PENG.

Geo. property	Overall MM-PENG	Length L (mm)	1
		Width b (mm)	0.5
		Thickness t (nm)	55
		Height h (μm)	50
		Cell gap g (μm)	40
	Hex. MM & Piezo (μm)	Diameter D_{hex}	300
		Rib width g_{hex}	20
		Thickness of piezo t_{p}	25
Material property	Material of MM (Alumina)	Young's modulus E_{mm} (GPa)	120
		Poisson's ratio v_{mm}	0.22
	Piezo (PVDF-TrFE) (Pi et al., 2014)	Young's modulus E_{p} (GPa)	7.5
		Density ρ_{p} (g/cm^3)	1.78
		Strain constant d_{31} (pC/N)	20
		Strain constant d_{33} (pC/N)	-30
		Electrical permittivity (pF/m)	115

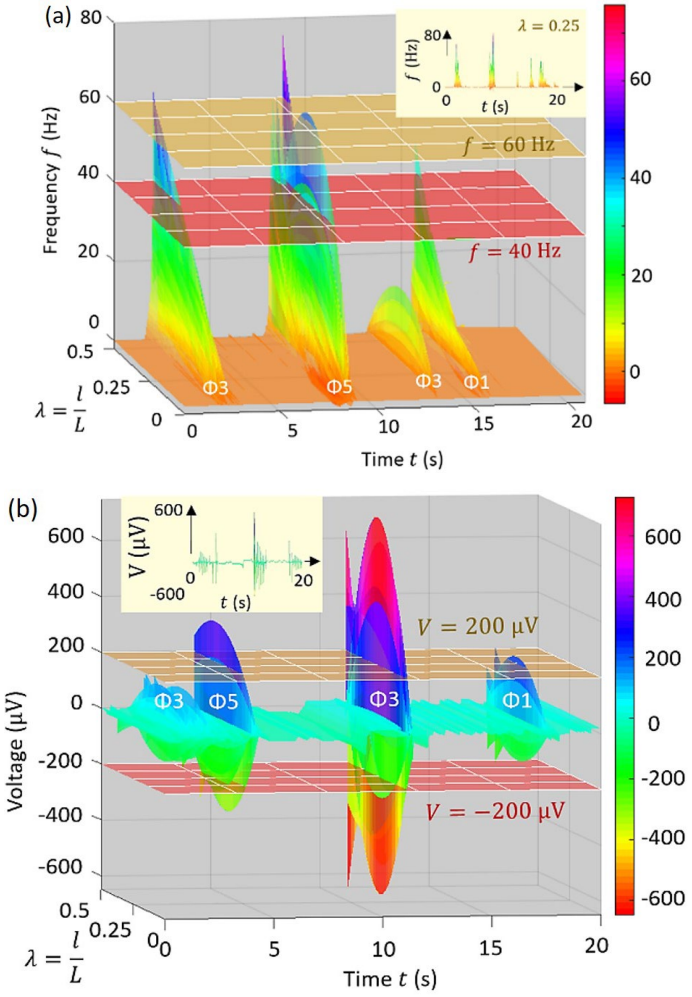

Figure 4. (a) Peak frequency and (b) output voltage of the MM-PENG at the postbuckling mode transitions with respect to different $\lambda = \frac{l}{L}$ (Φ3 and Φ5 denote the snap-throughs of the piezo-MM plates in the 3rd and 5th postbucking modes during the loading and unloading phases, respectively).

Figure 4 presents the peak frequency and output voltage of the MM-PENG with respect to different $\lambda = \frac{l}{L}$. Figure 4(a) shows the peak frequency happened at Φ1, Φ3 and Φ5. It can be seen that higher buckling snap-throughs are likely to provide higher frequencies for the MM-PENG. Figure 4(b) presents the output voltage of the MM-PENG resulted in the postbuckling snap-throughs. It can be seen that the proposed postbuckling design (i.e., placing MM plates between the sliding, bilateral constraints) effectively trigger the piezoelectric plates, and therefore, generate electrical power under low-frequency excitations.

4 VISION OF POTENTIAL APPLICATIONS OF THE MM-PENG NETWORK

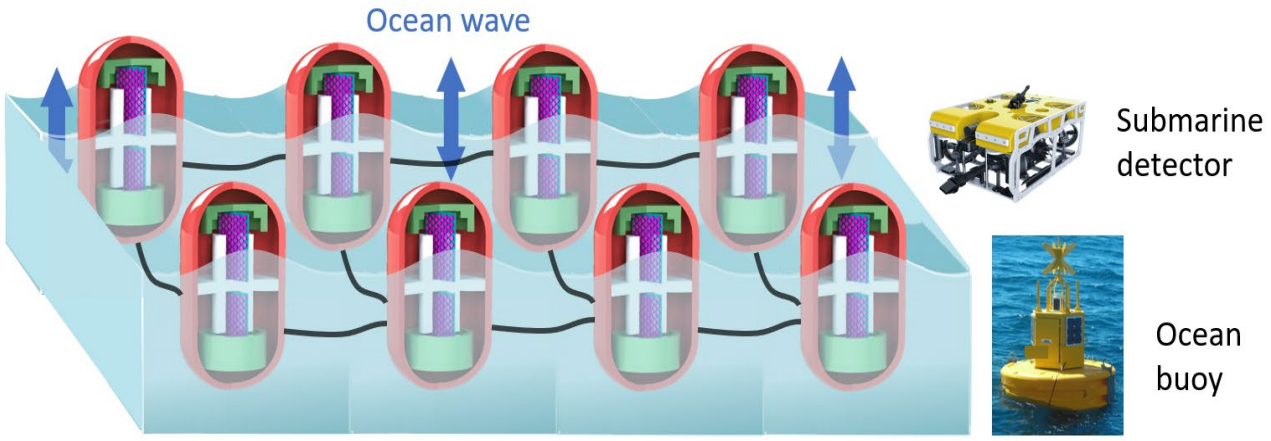

Figure 5. Vision of the potential applications of the MM-PENG network for wave monitoring sensor, submarine wireless detector, or ocean buoy.

Figure 5 outlooks the application of the MM-PENG in ocean engineering. The electrical power of ocean devices is likely to be severely reduced and difficult to be charged in the traditional ways. Therefore, it is significant to automatically charge those devices. Taking advantage of the periodic wave resulted in the fluctuation of the ocean surface, the MM-PENG network can be triggered to generate power. The MM-PENG network can be installed in the devices such as tiny marine wireless detectors or ocean buoys, such that the network can generate electrical power while the devices are working in the ocean. It is worth pointing out that the MM-PENG can serve as wave sensors according to the generated voltage signals subject to the fluctuation and a kind of devices integrated with energy collecting and monitoring will have further applications in ocean engineering.

5 CONCLUSIONS

This study proposed a novel type of MM-PENG with hexagonal corrugations. The sliding cell was applied innovatively to trigger the postbuckling response of the piezo-MM under low-frequency excitation. Therefore, the MM-PENG effectively generated electrical power under quasistatic ambient excitations. Plate-shaped MM with hexagonal corrugations was fabricated and tested to investigate the mechanical response, and the PVDF-TrFE was introduced as the possible piezo layer grown on the MM. Numerical simulations were carried out to verify the feasibility of this novel design. In the end, we envisioned the multiscale applications of the MM-PENG. The reported mechanical energy generator in this study opens a green new path of generating electricity from the environmental excitations for multifunctional applications.

Acknowledgements

This work is partially supported by the Natural Science Foundation of Zhejiang Province (No. LY19E090007).

References

Ali, F., Raza, W., Li, X., Gul, H., Kim, K.H.(2019). Piezoelectric energy harvesters for biomedical applications. Nano Energy, 57, 879-902.

Fan, F.R., Lin, L., Zhu, G., Wu, W., Zhang, R., Wang, Z.(2012). Transparent Triboelectric Nanogenerators and Self-Powered Pressure Sensors Based on Micropatterned Plastic Films. Nano Letters, 12(6), 3109-3114.

Janbaz, S., McGuinness, M., Zadpoor, A.A.(2018). Multimaterial control of instability in soft mechanical metamaterials. Physical Review Applied, 9 (6), 064013.

Jiao, P., Borchani, W., Hasni, H., Lajnef, N.(2017). Enhancement of quasi-static strain energy harvesters using non-uniform cross-section post-buckled beams. Smart Materials and Structures, 26, 085045.

Jiao, P., Borchani, W., Alavi, A.H., Hasni, H., Lajnef, N.(2017). An energy harvesting and damage sensing solution based on postbuckling response of nonuniform cross-section beams. Structural Control and Health Monitoring, e2052, 1-19.

Jiao, P., Hasni, H., Lajnef, N., Alavi, A.H.,(2020). Mechanical metamaterial piezoelectric nanogenerator (MM-PENG): Design principle, modeling and performance. Materials & design, 187, 108214.

Lantada, A.D., Romero, A.B., Schwenenwein, M., Jellinek, C., Homa, J.(2016). Lithography-based ceramic manufacture (LCM) of auxetic structures: present capabilities and challenges. Smart Materials and Structures, 25 (5).

Liu, C., Yu, A., Peng, M., Song, M., Liu, W., Zhang, J.,Zhai, J.(2016). Improvement in the Piezoelectric Performance of a ZnO Nanogenerator by a Combination of Chemical Doping and Interfacial Modification. The Journal of Physical Chemistry C, acs.jpcc.6b00069.

Pi, Z., Zhang, J., Wen, C., Zhang, Z.B., Wu, D.(2014). Flexible piezoelectric nanogenerator made of poly (vinylidenefluoride-co-trifluoroethylene) (PVDF-TrFE) thin film. Nano Energy, 7 (2014), 33-41.

Wang, J., Zhou, S., Zhang, Z., Yurchenko, D.(2018). High-performance piezoelectric wind energy harvester with Y-shaped attachments. Energy Conversion and Management, 181, 645-652.

Wang, Z., Song, J.(2006). Piezoelectric Nanogenerators Based on Zinc Oxide Nanowire Arrays. Science, 312(5771).

Xie, X.D., Wang, Q. (2017). A study on an ocean wave energy harvester made of a composite piezoelectric buoy structure. Composite Structures, 178, 447-454.

Yang, P.K., Lin, Z.H., Pradel, K.C., Lin, H., Li, X., Wen, X., He, J.H., Wang, Z.(2015). Paper-Based Origami Triboelectric Nanogenerators and Self-Powered Pressure Sensors. Acs Nano, 9(1), 901-7.

Coastlab 20
May 25-29, Zhoushan, China

8th International Conference on the Application of Physical Modelling in Coastal and Port Engineering and Science
Dec. 9th - 12th, 2020, Zhoushan, China

PHYSICAL MODELING OF REGULAR WAVE INDUCED HORIZONTAL CIRCULATION OVER A REEF-LAGOON-CHANNEL SYSTEM

SHUBIN CHEN[1], SONGGUI CHEN[2] JIAN SHI[3], YU YAO[4], QIMING ZHANG[5], JINHAI ZHENG[6]*

[1,2,3,6] Hohai University, Nanjing, P.R. China, 181303020029@hhu.edu.cn; jianshi@hhu.edu.cn, chensg05@163.com
[2] Tianjin Research Institute of Water Transport Engineering, Tianjin, P.R. China, chensg05@163.com
[4,5]Changsha University of Science and Technology, Changsha, Hunan 410114, P.R China, yaoyu821101@163.com

ABSTRACT

Based on the on-site observation of the topography of Bubble Bay in French Bolivia, a generalized three-dimensional physical model of coral reef-lagoon-channel system was established in the wave basin. Velocity meters and surface velocity measurement system were used to analyze current field characteristics at different locations under regular wave condition. Over the coral reefs, the mean current direction is mainly cross-shore, and there is a tendency of increasing first and then decreasing. In the lagoon, the mean current is mainly a longshore one that points symmetrically to the channel. The velocity increases from the two sides to the rip channel first and then decreases. The mean current flows offshore in the chanenl, and increases first and then decreases. Based on the data collected by SVM system, the vorticity diagram of current field is drawn, it proves that the direction that the direction of velocity changes at both sizes of the channel, and wave induced current transforms into longshore current at the back part of reef.

Keywords: reef-lagoon-channel; wave induced current; SVM system; three dimensional experiment

1 INTRODUCTION

The horizontal circulation on the coral reef has a profound impact on the ecology, environment, geomorphology and engineering construction of the area. The wave induced setup and circulation allow nutrients to pass through the coral reef and remove the metabolic wastes of the organisms, which is helpful for the survival of coral insects and plays an important role in maintaining the ecological balance of coral (Hearn, Atkinson & Falter, 2001). The circulation also affects the sediment transport in the coral reef system, changes the distribution of coral reef organisms, the formation of coral reef landforms and the stability of the coastline (Kench & Brander, 2006).

A large number of field observations (Hench et al., 2008; Lowe, Falter et al., 2009; Symonds et al., 2011; Taebi et al., 2011;Monismith et al., 2013) have reported the horizontal circulation pattern of the reef-lagoon-channel system.The waves travel from the open sea to the edge of the reef flat.After wave breaking, the mean water level increases from the breaking point to the end of the breaking zone. Then the mean water level decreases along the reef and reaches near zero in the lagoon, The pressure gradient caused by wave setup drives the water to generate wave induced currents perpendicular and parallel to the coast. On the other hand, coral reefs are usually discontinuous, with some channels connected to the open sea. Therefore, the uneven distribution of water setup along the coast drives the longshore currents in the lagoon and returns to the open sea through the channel.

The physical model experiments of coral reef hydrodynamics in the literature are mainly focused on the problems of wave propagation, deformation, breaking and wave setup. Early studies of this subject can be found in Gerritsen (1980). Using generalized coral reef model, Mei and Gao (2013) simulated two kinds of wave conditions, the annual wave and the wave of 50 years reappearing period, studied the propagation of wave propagation on the reef flat after breaking. Yao et al. (2013) using a fringing-reef profile, conducted laboratory experiments to systematically study the characteristics of breaking wave types, the location and the width of the breaking zone, then gave empirical formulas that affected the characteristics of breaking waves. The law of wave deformation, the wave forces and overtopping on the coral reef with seawall were studied by Chen Songgui et al. (2018,2019). Liu et al. (2015) analyzed the influence of wave height on the position of wave breaking. Gourlay (1996) reported a series of laboratory experiments with idealized reef models to study wave setup. He showed that wave-induced setup on the reef flat increased with reducing reef-flat water depth or increasing deep-water wave height. Demirbilek et al. (2007) conducted laboratory experiments to study combined effects of wind and waves on wave setup and runup, and the effect of wind was found insignificant on the measured maximum wave runup. More recently, Buckley et al. (2015) conducted high-resolution wave measurements in their laboratory experiment, which were designed to investigate the dynamics of wave setup

over a smooth or rough reef flat.

Reef-lagoon-channel horizontal circulation systems have been rarely studied at present. Only Yao et al. (2018) established an approximate theoretical model of the reef-lagoon-channel system using momentum and mass conservation equations. However, experimental study of the reef-lagoon-channel physical model has not been reported so far. To achieve breakthroughs in this respect, the wave basin test must be used to simulate the 2DH reef-lagoon-channel system. Therefore, in this paper, through the physical model experiment in the wave basin, the spatial distribution of wave current in Coral Coast was measured in detail by single point velocity meter and surface velocity measurement system (SVM), and then the distribution characteristics of horizontal circulation system were analyzed.

2 Experimental setup

- Experimental setup

The laboratory experiments were conducted in the wave basin of Tianjin Research Institute for Water Transport Engineering (TIWTE), which is 60 m long, 42 m width and 1m deep, as shown in Figure 1. Nine servo-controlled wave-makers were placed at one end of the basin to generate the designed waves. Follow the Froude similarity criterion, the physical model of coral reef was conducted according to the prototype of field observation (Monismith et al., 2013), as shown in Figure 2, and the scale of the model is 1:50. The reef profile has a slope of 1:8, which joins a horizontal platform (reef flat). The toe of the slope is 34 m from the wavemaker, and the reef flat is 0.40 m above the bottom. Both reef flats are 14 m long and 15 m wide. There is a 6 m wide channel in the middle of the two reefs, and a 5 m wide lagoon behind the reefs. Finally, a 1:3.3 slope was set behind the lagoon. The physical model was filled with sand and the surface was plastered with cement, as shown in Figure 3.

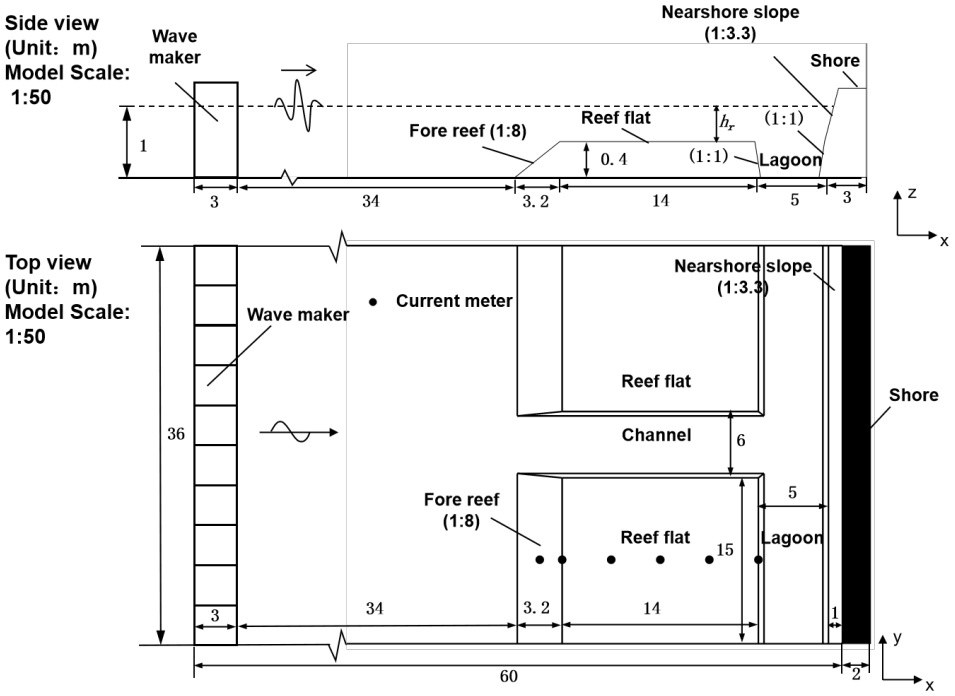

Figure 1. Experimental set-up

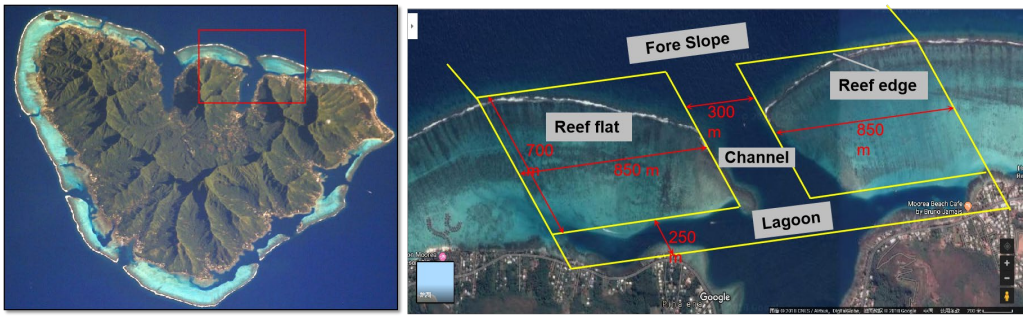

Figure 2 Field observation prototype

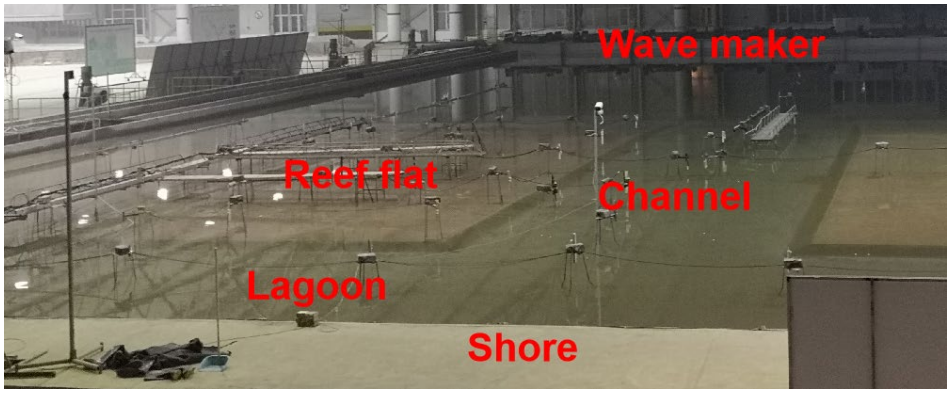

Figure 3 Experimental area

- Measuring method

The current field in this experiment was measured by 6 propeller current meters(Kenek, Japan). The arrangement of the instruments is shown in Figure 1. At the same time, the surface velocity measurement system was used to measure the surface velocity by tracking a 2 cm diameter drifter in the current field. The motion of the drifter is recorded by a high-resolution industrial camera 13 m above the basin, with a resolution of 20 million pixels. The acquisition frequency of the camera is 10 frames/s, the camera range is 36 m×42 m, and the image is shown in Figure 4. In order to transform the pixel coordinates to the real spatial coordinates, two steps are used to determine the relationship between the pixel coordinates and the real spatial coordinates, that is, to first determine the distortion coefficients of camera, and then convert the pixel coordinates to the real spatial coordinates. After correction of distortion coefficient, the relationship between the pixel coordinates and the spatial coordinates is as followed.

$$\begin{bmatrix} L_1 - L_3 X_c & L_2 - L_7 X_c \\ L_5 - L_3 X_c & L_6 - L_7 Y_c \end{bmatrix} \begin{bmatrix} X_w \\ Y_w \end{bmatrix} = \begin{bmatrix} X_c - L_4 \\ Y_c - L_8 \end{bmatrix} \quad [1]$$

Where (X_c, Y_c) is the pixel coordinate captured by the camera, (X_w, Y_w) is the real spatial coordinate. $L_1 \sim L_8$ are 8 pending coefficients. In this experiment, 4 spatial locations are measured by total station, and their coordinates and corresponding pixel coordinates are substituted into equation (1) to determine the coefficient $L_1 \sim L_8$. Then the corresponding spatial coordinates (X_w, Y_w) can be calculated from any pixel coordinates (X_c, Y_c) by equation [1].

Images are import into the FPTM (fluid pattern tracking Master) software for processing. By identifying the drifter position in the adjacent frame image, the grid current field can be obtained, and data file with '.dat' name postfix can be output. The wave height, velocity and surface current field were collected synchronously, and all the velocity analyzed were the average velocity in one period.

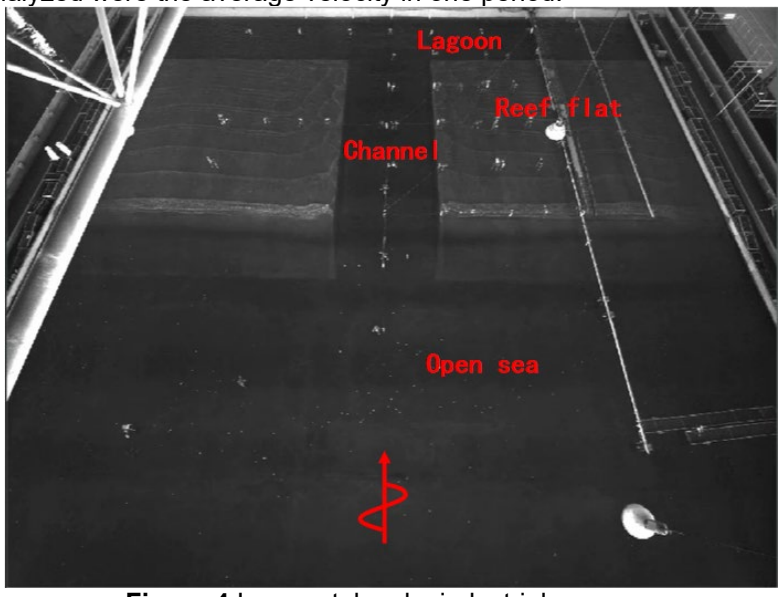

Figure 4 Images taken by industrial cameras

In order to verify the accuracy of velocity distribution obtained by surface velocity measurement system

(SVM), we compared the measurement data of this method with the data of the current meters. In this experiment, there were 6 current meters, which were arranged on the middle line of reef. Comparisons of measurement results between SVM system and current meter with different incident wave height are shown in Figure 5. It can be seen that the results of current meter measurement are in good agreement with those of SVM system. Thus, the experimental results by SVM method have good credibility, and the surface velocity measured is reasonable and feasible.

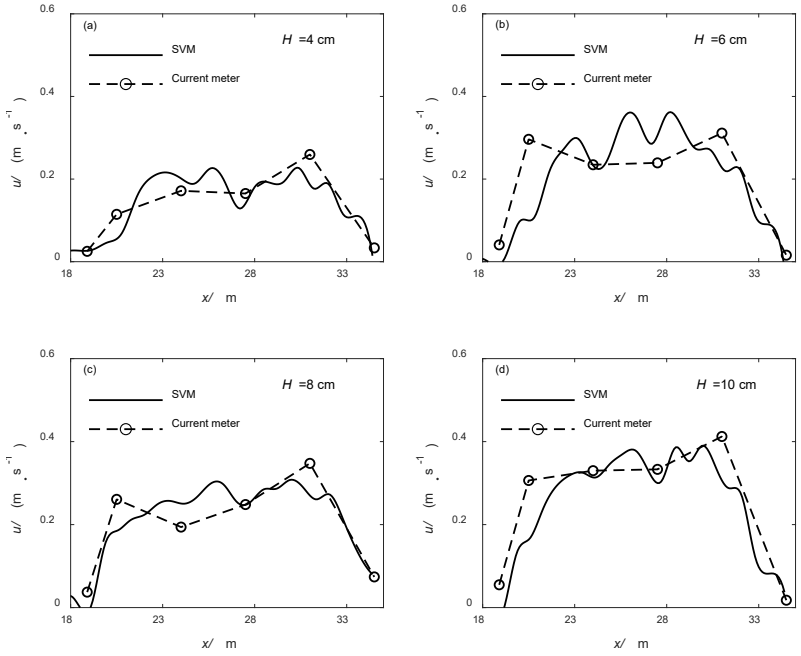

Figure 5 Comparison of measurement results between SVM system and current meter

- Experimental condition

The test condition is determined according to the field observation data (Hench, 2008; Monismith, 2013), in which the water depth of reef is slightly larger than the data given in two articles considering the extreme wave conditions. The water depth in front of the reef is 44cm, 4cm on the reef flat, the incident wave height is 0.08m, and the wave period is 2s. During the experiment, each wave condition was repeated three times to ensure repeatability. Based on our tests, each wave duration time is 20 minutes, and data is collected from 5 minutes after the wave is stable. Sufficient waiting time between two consecutive runs was imposed to avoid possible effects of residual waves and currents in the basin. The wave trains and velocity time series of two repeated experiments at several different location are compered in Figure 6., and it can be seen that the experimental repeatability is good.

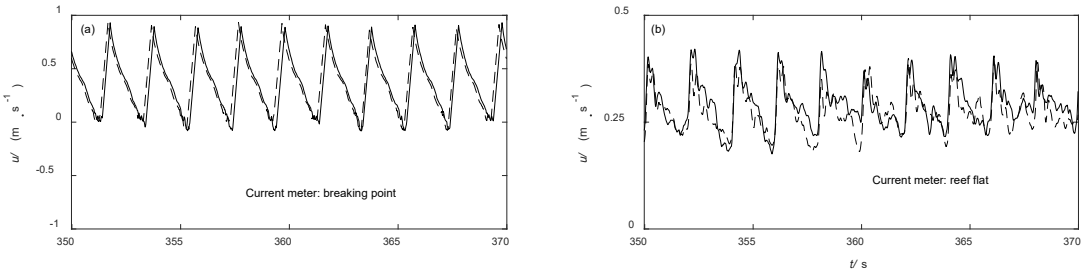

Figure 6 Comparison of two repeated velocity at different positions

3 Results analysis

- Circulation patterns

The vectors of mean current and streamline respectively are shown in Figure 7 and Figure 8. The cross-shore direction is defined as the *x* direction, the current velocity is recorded as *u*, longshore direction is defined as the *y* direction, and the current velocity is described as *v* (the same applies hereinafter).

In general, the slope in front of the reef is dominated by cross-shore current with small intensity, and symmetrical circulation is generated near the channel due to the impact of channel. The onshore current on the reef flat is relatively strong, and there is no obvious velocity into the channel. The velocity near the side wall in the lagoon is onshore direction, and the longshore current from both sides to the channel is generated,

which makes up the compensating current of the circulation system. There is mainly offshore current in the channel, which will extend to a certain distance beyond the front reef slope and rotate in direction. Therefore, a horizontal circulation system of open sea-reef-lagoon-channel is formed.

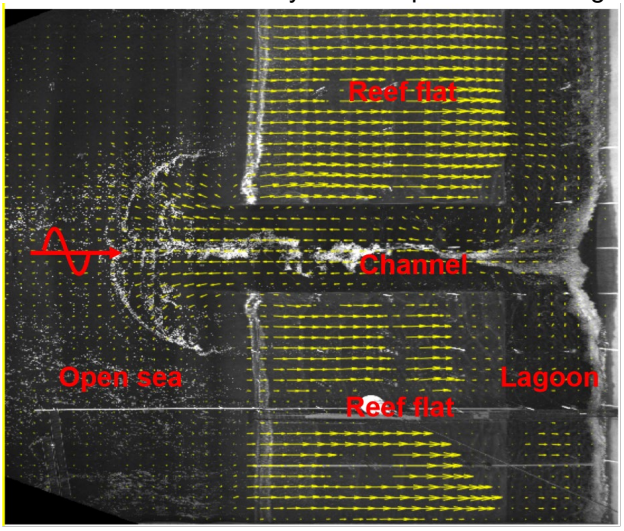

Figure 7 Velocity vector diagram

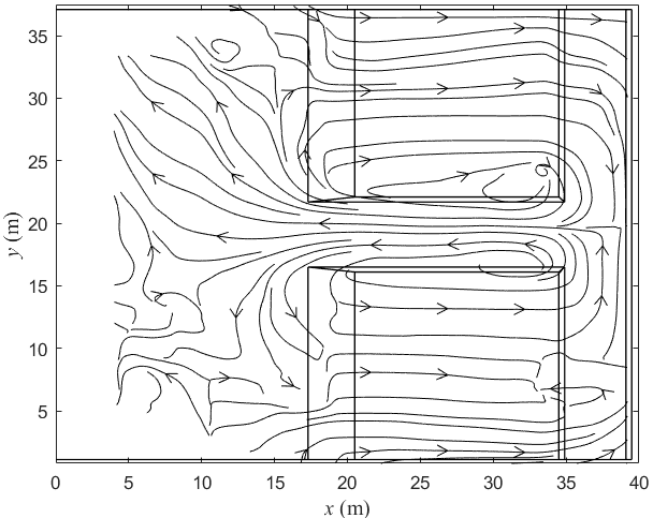

Figure 8 Streamline diagram

- Spatial distribution of velocity

The contour of the onshore velocity on the reef flat is shown in Figure 9. In the cross-shore direction, u increases first and then decreases as it propagates to the lagoon. Namely, *u* increases rapidly after wave breaking, reaches the maximum in the front part of reef flat and keeps stable, while in the back part of reef flat, the velocity decreases rapidly.

In the longshore direction, the velocity in the middle of the reef is larger, while it's smaller near the side wall than in other locations. The reason is that the mean water level (MWL) changes rapidly in the center of the reef, but not much in the side wall (as shown in Figure 9), which makes the pressure gradient of wave surface various at different locations, resulting in the velocity distribution.

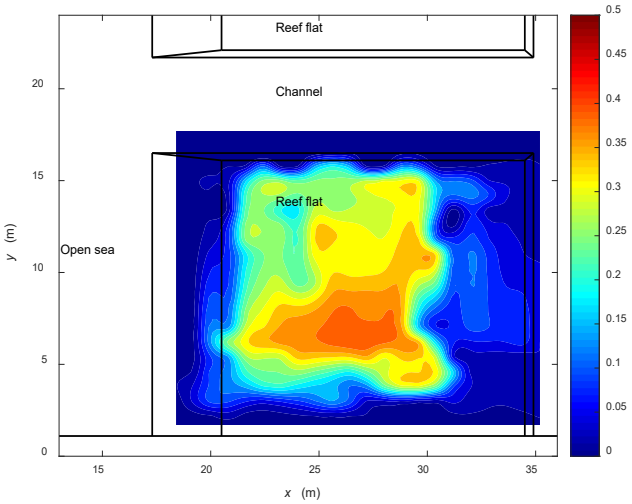

Figure 9 Contour of velocity *u* on reef flat

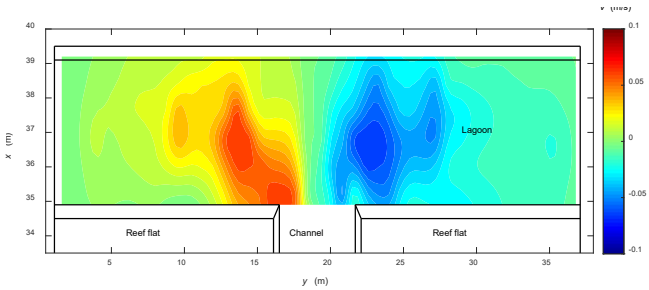

Figure 10 Contour of velocity *v* in channel

The spatial distribution of longshore velocity in lagoon is shown in Figure 10. In the cross-shore direction, the velocity *v* is smaller near the shoreline (*x*=38.4 m), but larger in the reef edge. In the longshore direction, the current changes direction at the center of the channel (*y*=19.1 m), and it first increases and then decreases from side wall to the channel. The general direction is to converge to the channel, then provides compensation current for the offshore current in the channel, which becomes a part of two circulations around the reef. The current velocity in the middle of the lagoon can reach a maximum value of 0.086 m/s.

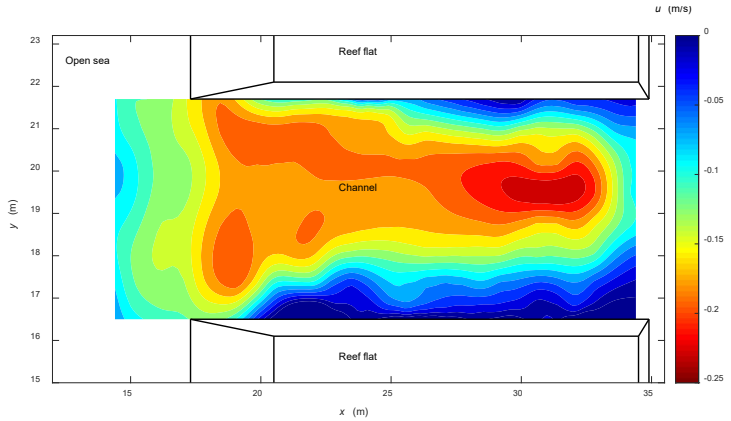

Figure 11 Contour of velocity *u* in lagoon

The variation of offshore current velocity along the channel is shown in Figure 11. This figure indicates that the offshore current is the largest in the middle section (*y*=19.5 m), and it reaches the maximum value of 0.18 m/s near the lagoon (*x*=29.5 m). Subsequently, the current velocity decreased along the channel, the outflow distance of the current can reach around *x*=17m. At the tail of the offshore current(*x*=17 m), the velocity is larger on both sides while smaller in the middle, because there is a longshore current pointing to the reef flat at this place(see Figure 9), which leads to the generation of a secondary circulation system at the outer reef edge.

- Vorticity distribution of current field

Vorticity is usually used to measure the strength and direction of a vortex, which is the curl of the velocity field. Vorticity is defined as

$$\vec{\Omega} = 2\vec{\omega} = \nabla \vec{V} \qquad [2]$$

Its projection in the plane coordinate system is

$$\Omega = \frac{\partial v}{\partial x} - \frac{\partial u}{\partial y} \qquad [3]$$

By interpolating the collected velocity data and substituting it into Eq. [3], the vorticity distribution can be obtained, as shown in Figure 12.

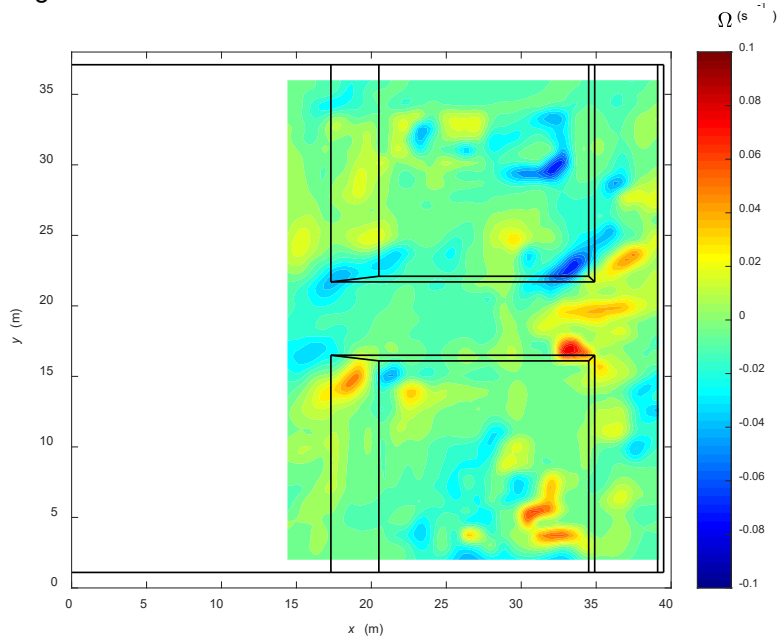

Figure 12 Contour of vorticity

According to the right-hand rule, positive value in the vorticity graph represents the anticlockwise vortex, and negative value represents the clockwise vortex. It can be seen that there are two large-scale circulation opposite to each other on the two reef flats, and the value of vortices at the junctions of the channel with open sea and lagoon is numerically opposite. It is proved that there is a large angular velocity and the direction of

the current changes at these positions. When the wave-induced current reaches the back part of the reef flat, there is large vorticity in these positions. In other words, the direction of velocity will deflect here and turn to the longshore current in the lagoon.

4 CONCLUSIONS

Based on the on-site observation of the topography of Bubble Bay in French Bolivia, a 1:50 size three-dimensional physical model of coral reef-lagoon-channel system was established in the wave basin. Velocity meters, and surface velocity measurement system were used to analyze wave and current field characteristics at different locations under regular wave condition.

Through the analysis of velocity diagram, it is found that the wave breaks after reaching the fore slope of the reef, and the current on the reef flat is mainly towards the shore, with the trend of increasing first and then decreasing. When the current reaches the lagoon, it rotates for the first time, and turns into the longshore current which points symmetrically to the channel. The current velocity increases first and then decreases from both sides to the channel. The longshore current converges near the channel and rotates for a second time in the direction, thus forming an offshore current in the channel. The current velocity also increases first and then decreases. After arriving at the reef edge, the offshore current continues to propagate to the open sea for a certain distance and rotates for the third time simultaneously, forming the longshore current from the channel to both sides.

The vorticity diagram of the current field proves that the direction of velocity changes at both sizes of the channel, and wave induced current transforms into longshore current at the back part of reef.

• ACKNOWLEDGEMENTS

This study was supported financially by the National Science Fund for Distinguished Young Scholars (51425091), Young Elite Scientist Sponsorship Program by the China Association for Science and Technology (Grant No. 2018QNRC001), Research Funds for the Central Universities (Grant No. TKS190201, TKS20200402)

•

• REFERENCES

Hearn, C., Atkinson, M., & Falter, J. (2001). A physical derivation of nutrient-uptake rates in coral reefs: effects of roughness and waves. *Coral Reefs*, 20(4), 347-356.

Kench, P. S., & Brander, R. W. (2006). Wave processes on coral reef flats: implications for reef geomorphology using australian case studies. *J. Coast. Res.*, 221(1), 209-223.

Hench, J. L., Leichter, J. J., & Monismith, S. G . (2008). Episodic circulation and exchange in a wave-driven coral reef and lagoon system. *Limnol. Oceanogr.*, 53(6), 2681-2694.

Lowe, R. J., Falter, J. L., Monismith, S. G., & Atkinson, M. J. (2009). Wave-driven circulation of a coastal reef-lagoon system. *J. Phys. Oceanogr.*, 39(4), 873-893.

Symonds, G., Zhong, L., & Mortimer, N. A. (2011). Effects of wave exposure on circulation in a temperate reef environment. *J. Geophys. Res.-Oceans*, 116: C09010.

Taebi, S., Lowe, R. J., Pattiaratchi, C. B., Ivey, G. N., Symonds, G., & Brinkman, R. (2011). Nearshore circulation in a tropical fringing reef system. *J. Geophys. Res.-Oceans*, 116: C02016.

Monismith, S. G., Herdman, L. M. M., Ahmerkamp, S., & Hench, J. L. (2013). Wave transformation and wave-driven flow across a steep coral reef. *J. Geophys. Res.-Oceans*, 43(7), 1356-1379.

Gerritsen F. (1980). *Wave attenuation and wave set-up on a coastal reef*. Doctoral Dissertation. Unversity of Trondheim, Trondheim.

Mei T, Gao F. (2013). Flume experiment research on law of wave propagation in reef flat (in Chinese). *J. Waterw. Harbor.*, 34, 13-18.

Yao, Y., Huang Z.H., Monismith, S. G., et al. (2013). Characteristics of monochromatic waves breaking over fringing reefs. *J. Coast. Res.*, 286(1), 94-104.

Chen S. G., Zhang H. Q., Chen H. B., et al. (2018). Experimental study of irregular wave transformation on reefs with seawalls in large wave flume (in Chinese). *Mar. Sci. Bull.*, 2018, 37(05), 99-105.

Chen S. G., Wang Z. M., Zhang C., et al. (2019). Experiment on wave overtopping of a vertical seawall on coral reefs in large wave flume (in Chinese). *Chin. Sci. Bull.*, 64(Z2), 3049-3058

Chen S. G., Chen H. B., Zhao H. B., et al. (2019). Experimental study of wave forces on seawalls over coral reefs in large wave flume (in Chinese). *J Hohai Univ.(Natural Sci.)*, 47(1), 65-70.

Liu S. X., Liu N., Li J. X., et al. (2015). Experimental researches on wave propagation characteristics on reefs terrain (in Chinese). *Ocean. Eng.*, 33: 42-49.

Gourlay M R. (1996) Wave set-up on coral reefs. 1. Set-up and wave-generated flow on an idealised two dimensional horizontal reef. *Coast. Eng.*, 27(3-4),161-193.

Demirbilek Z., Nwogu O.G., Ward D.L. (2007). *Laboratory Study of Wind Effect on Runup over Fringing Reefs. Report 1: Data report.* Coastal and Hydraulics Laboratory Technical Report ERDC/CHL-TR-07-4, U.S.

Army Engineer Research and Development Center, Vicksburg, MS.

Buckley M. L., Lowe R. J., Hansen J. E., et al. (2016). Wave setup over a fringing reef with large bottom roughness[J]. *J. Phys. Oceanogr.*, 46,2317-2333

Yao Y., Huang Z.H., He W., et al. (2018) .Wave-induced setup and wave-driven current over Quasi-2DH reef-lagoon-channel systems. *Coast. Eng.*, 138,113-125.

8th International Conference on the Application of Physical Modelling in Coastal and Port Engineering and Science
Dec. 9th - 12th, 2020, Zhoushan, China

MAPPING TIDAL CURRENTS AT A TIDAL CHANNEL JUNCTION USING FLUVIAL ACOUSTIC TOMOGRAPHY SYSTEM

CONG XIAO[1], KIYOSI KAWANISI[2], MOHAMAD BASEL AL SAWAF[3]

1 Department of Civil and Environmental Engineering, Graduate School of Engineering, Hiroshima University, Higashi-Hiroshima, Japan, d180047@hiroshima-u.ac.jp

2 Department of Civil and Environmental Engineering, Graduate School of Engineering, Hiroshima University, Higashi-Hiroshima, Japan, kiyosi@hiroshima-u.ac.jp

3 Department of Civil and Environmental Engineering, Graduate School of Engineering, Hiroshima University, Higashi-Hiroshima, Japan, mbasel@hiroshima-u.ac.jp

ABSTRACT

In a tidal channel network, there are many branches/junctions that are commonly bifurcated asymmetrically. Investigations of hydrodynamics at the tidal channel junction related to the interaction between the tidal waves, upstream river discharge, and the geometrical shape of branches has been carried out. The Fluvial Acoustic Tomography (FAT) System developed by Hiroshima University is able to measure tidal currents in shallow waters and continuous visualize 2D flow pattern. Herein, the hydrodynamics of tidal junction are presented by an array of FAT system with numerical inversion schemes. The horizontal distributions of the tidal currents and the residual currents were well calculated by inverse analysis of FAT data. Although the salt-wedge intrusion had a strong effect on sound propagation patterns that led to a multitude of arrival times, the reconstructed flow patterns agreed favorably with ADCP data. Moreover, we analyzed the main dynamic processes responsible for the residual currents using the averaged horizontal momentum equation. The predominant terms in balancing the momentum equation of the residual currents are the advection of the tidal currents, the horizontal pressure gradient, and the horizontal mixing of the residual currents.

Key Words: Shallow-water acoustic tomography, tidal channel junction, tidal current, residual current

1 INTRODUCTION

Ocean acoustic tomography (OAT) is a powerful oceanographic technique for mapping mesoscale oceanic phenomena (Munk et al., 1995). Coastal acoustic tomography (CAT) was proposed as an application of OAT to the coastal area, aiming at the continuous monitoring of tidal currents in bays, straits, and inland seas (Kaneko et al., 1994; Yamaguchi et al., 2005; Yamoaka et al., 2002). The main idea behind the Fluvial Acoustic Tomography (FAT) system (Kawanisi et al., 2010) is extending the applications of CAT to extremely shallow waters, in order to investigate shallow flows ranging from mountainous rivers (~ 0.5 m) to the mouth of estuaries (~ 10 m).

Previous studies had already demonstrated a lot of applications by using only two crossing paths to reconstruct flow velocity magnitude and direction, such as, the measurement of dam flush in a mountainous river (Kawanisi et al., 2013) and the measurement of tidal flow in a shallow estuary (Razaz et al., 2013). Furthermore, Razaz et al. (2015, 2016) positioned an array of eight FATs in a shallow mountainous river and in the upper reach of a tidally dominated channel to map the depth-averaged flow pattern. In the case of the mountainous river, though the boundary is meandering, there is no salt-wedge intrusion effect on sound propagation patterns. In the case of tidal channel, the salt-wedge intrusion effect should be considered. An investigation of hydrodynamics at the tidal channel junction related to the interaction between the tidal wave, upstream river discharge, and the geometrical shape of branches has been carried out by a few researchers.

Here are the results of reciprocal transmission among 5 acoustic stations placed at a shallow tidal junction. The survey was performed for about 18 hours during 18-19 June of 2019 and includes one flood and ebb of a semidiurnal tide. The surveyed zone is characterized by unsteady and complex flow distribution patterns generated by the frequent intrusion of saline water, the freshwater discharge, and irregular bathymetry.

2 SURVEY SITE AND DATA ACQUISITION

The Ota River is a network of several tide-dominated river branches that flow through Hiroshima City, Japan. The Ota river divides into two main branches nearly 9 km upstream from the river mouth. Rows of Gion sluice gates control the volume of the runoff in the Otagawa floodway, whereas the runoff in Kyu Ota River is controlled by two different gates at Oshiba (Figure 1a): the fixed weir is 86 m wide, and three sluice gates control the width of 13.33 × 3 m, and are always open throughout the year. The studied junction is in the middle part of the Ota River network channel, approximately 2.5 km downstream from the Oshiba gates and approximately 5.8 km from the mouth, as shown in Figure 1a. The tidal channel junction consists of three branches: the northern branch (upstream Kyu Ota River), the eastern branch (downstream Kyu Ota River), and the western branch (Tenma River). The saltwater intrusion in the Ota River can reach 11.5 km upstream from the river mouth.

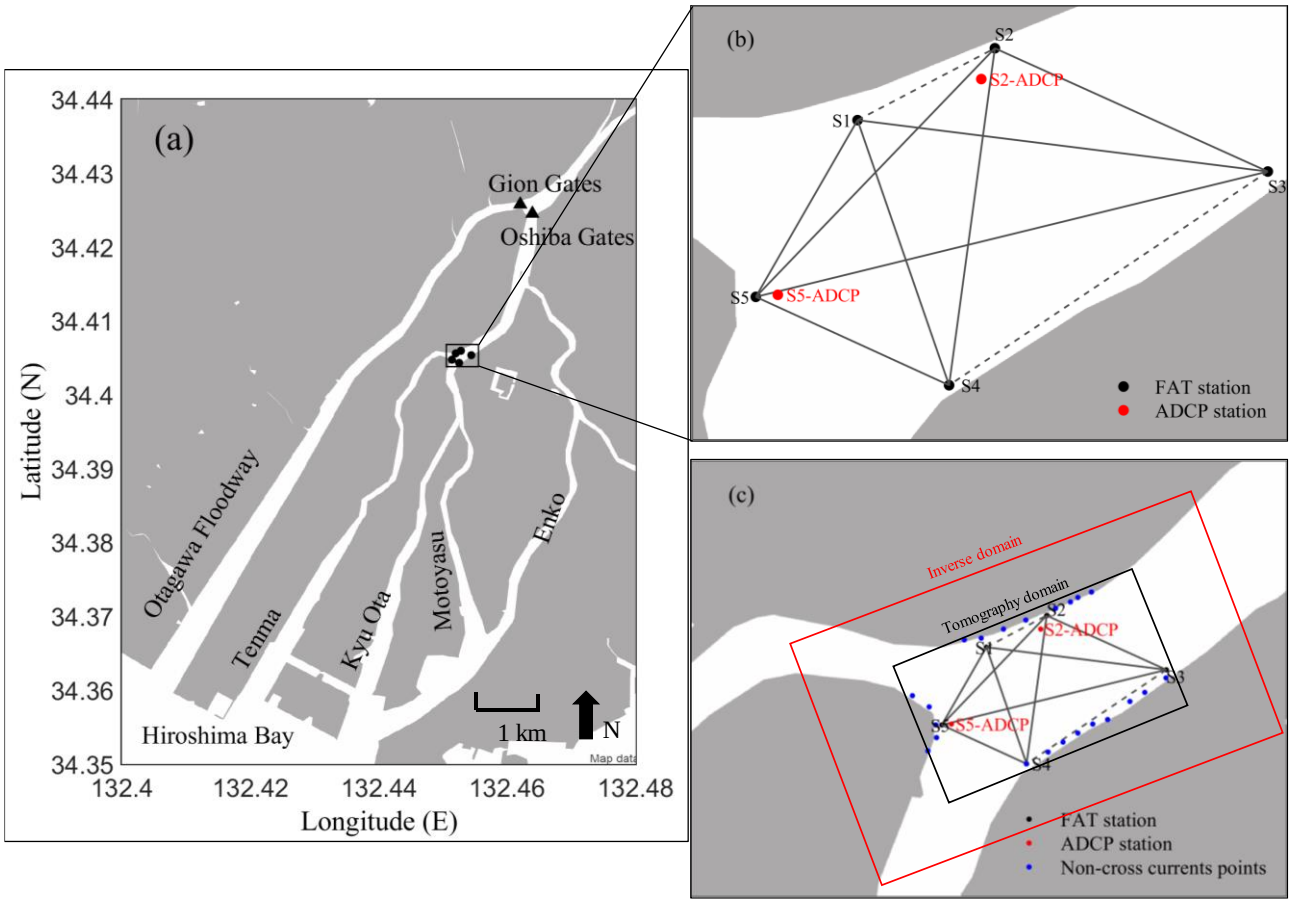

Figure 1. Location maps of the experiment site. The positions of the FAT stations (S1 to S5) and ADCP stations are indicated by black and red dots, respectively. The solid lines connecting the FAT stations indicate the sound transmission lines.

The FAT measurement campaign was carried out between 19:00-14:30 JST on 18-19 June 2019 (Spring tide). As shown in Figure 1, an array of FAT comprised of 5 acoustic stations was installed along the shallow banks of the channel in an area approximately 310 m long by 170 m wide. In total simultaneous reciprocal transmissions were conducted along 8 ray paths. Every 30 second, a signal with 30 kHz central frequency was generated simultaneously from each source and received by the other stations. Signals were modulated by an M-sequence of order 9 to increase the processing gain by about 27.1 dB. M-sequence is a type of pseudorandom signals by which the phase shift of in the carrier is generated with irregular time intervals. The successful acquisition rates of sound transmission data varied from 70% to 94.2% (Figure 2). The cable at S1 had some problems from 9: 30 JST on 19 June, the data related to S1 were missed (S1-S3, S1-S4, S1-S5). The missing data during the other period were mainly caused by the shallow region.

As shown in Figure 1, two 2 MHz ADCP (Aquadopp Profiler, Nortek) were installed between 20:00-14:00 JST on 2-3 August 2019 (Spring tide) to measure the 3D velocities in the water column, with a 1 min sampling interval and average interval of 30 s. The bin size was set as 0.1 m, the bin number was 50, and the blank distance was 0.1 m.

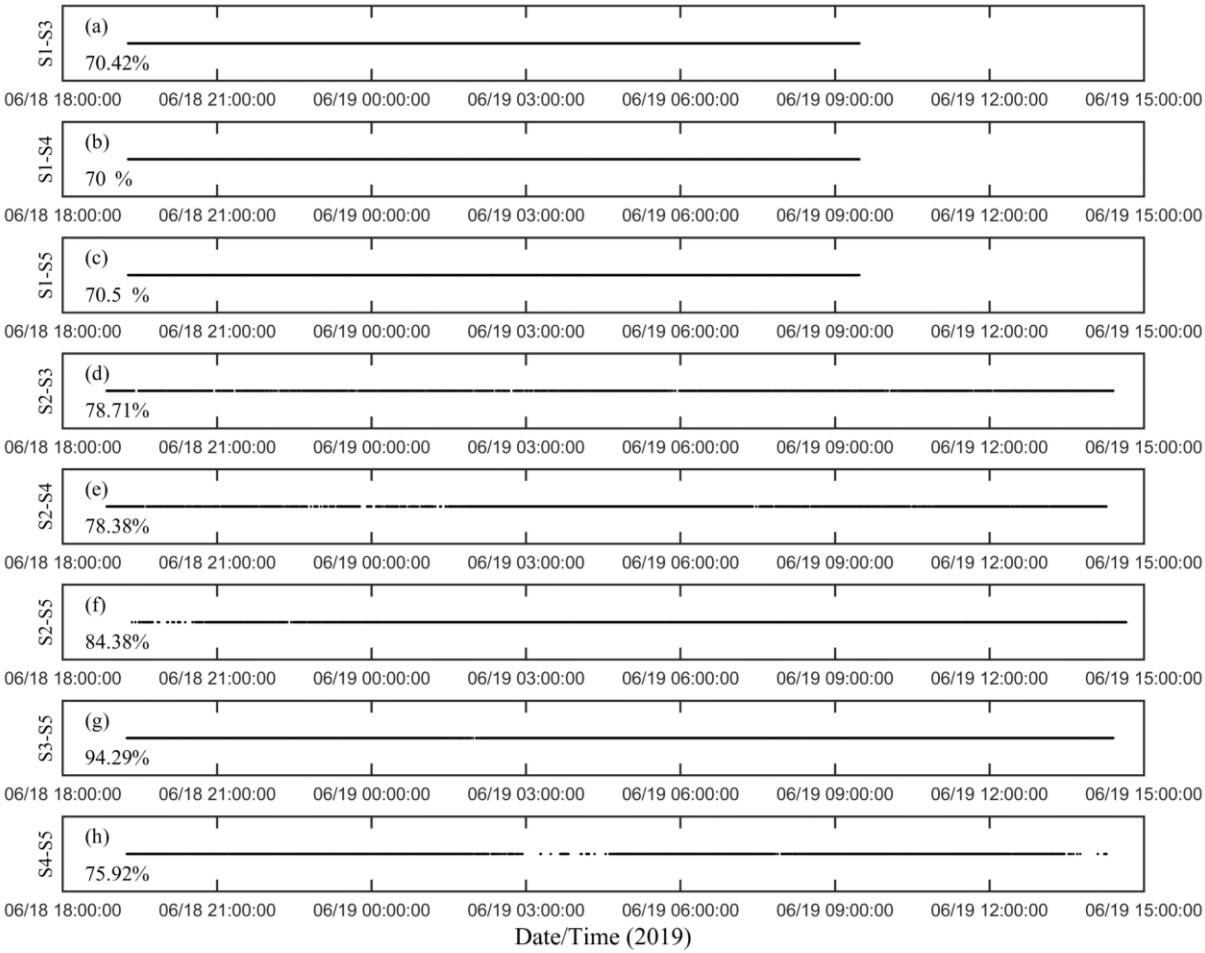

Figure 2. The acquisition rates of sound transmission data during the observation period.

3 METHODOLOGY

3.1 Forward problem

The sound travel time along the reciprocal ray path $\Gamma^{\pm}$ between two acoustic transceivers can be expressed:

$$t_i^{\pm} = \iint_{\Gamma_i^{\pm}} \frac{ds}{C_m + \delta C(x,y) \pm u(x,y)\cdot n_i} \quad [1]$$

where +/– represent the direction of sound propagation. C_m is the averaged sound speed, δC represents the sound speed deviation relative to C_m, ds represents the increment of arc length measured along the ray, u is the current velocity, n_i is the unit vector along the ray. The path integrals are taken along the ray. We assume that the two-way path geometry is reciprocal and $\Gamma^{\pm} \approx \Gamma$ in order of $|u|/C_m << 1$ and $\delta C/C_m << 1$. The two-way travel time difference may be expressed by:

$$\Delta t_i = \frac{1}{2}(t_i^+ - t_i^-) = -\int_{\Gamma_i} \frac{u\cdot n}{C_m^2} ds \quad [2]$$

The above equation is a kind of integral equation with unknown variable u and can be solved with the inverse analysis.

3.2 Inverse problem

In the Cartesian coordinate system, we expand the stream function ψ (x, y) into a truncated Fourier series:

$$\psi(x,y) = c_0 x + d_0 y + \sum_{k=0}^{N}\sum_{l=0}^{N}\left\{C_{kl}\cos 2\pi\left(\frac{kx}{L_x}+\frac{ly}{L_y}\right) + D_{kl}\sin 2\pi\left(\frac{kx}{L_x}+\frac{ly}{L_y}\right)\right\} \quad [3]$$

where (L_x, L_y) is the size of inversion domain and N is the truncated number of the Fourier series.

In the present analysis, the inversion domain was taken larger than the tomography domain for reducing the periodicity effect in the solution (Figure 1c) (Park and Kaneko, 2001). We select L_x = 340 m, L_y = 620 m for the size of inversion domain and N = 3. Here the unknown values $\boldsymbol{u}$ (x, y) were replaced by a set of Fourier coefficients after the spatial derivative $\boldsymbol{u}$ (x, y) = $\nabla \times \psi$ (x, y) $\boldsymbol{k}$ of Eq. [3] is substituted into Eq. (2). The $\boldsymbol{k}$ is the unit vector in the vertical direction.

In matrix notation, Eq. [2] can be written in the form of a general inverse problem as,

$$y = Ex + e \qquad [4]$$

where the travel time difference data are put into the column vector y of order M and the unknown variables into the column vector x of order N. e denotes the observation errors.

The method to consider the riverbank condition in the inverse analysis is to introduce a liner equation 0 = $\boldsymbol{u}$ (x_b, y_b)·$\boldsymbol{m}$ (x_b, y_b), where (x_b, y_b) is the position at the riverbank and $\boldsymbol{m}$ the unit vector perpendicular to the riverbank. This linear equation is rewritten by using the stream function, and the resulting equation is added to the row of Eq. [4]. The riverbank condition is given at the 22 points, distributed over each riverbank as seen in Figure 1c.

The expected solution of Eq. [4] is obtained by the damped least-squares method described by Yamoaka et al. (2002) and Yamaguchi et al. (2005).

4 RESULTS AND DISCUSSION

4.1 Ray simulation

Figure 3 shows the ray patterns obtained between the shortest station pairs (S4-S5) and the longest station pairs (S3-S5) by the ray-tracing method. Figure 3a shows the typical vertical profile of temperature, salinity and sound speed recorded by CTD at the upstream. Owing to saltwater intrusion, deeper water had a higher salinity and temperature. At high water level, owing to the weak mixing, the water column was divided into two separate layers. In the upper layer, which is characterized by cold freshwater, the sound speed remained constant at ~ 1470 m/s. Then, it increased sharply to ~1500 m/s at the interface between the freshwater and salt wedge, before remaining constant in the deeper layer.

The rays released within large launch angles make multiple bottom and surface reflections and cannot reach to the receiver due to large reflection losses. Then, only the rays within small angles were traced to simulate traveling sound. The first peak points with positive launch angles are used as input data in the inversion analysis in this work (Figure. 3).

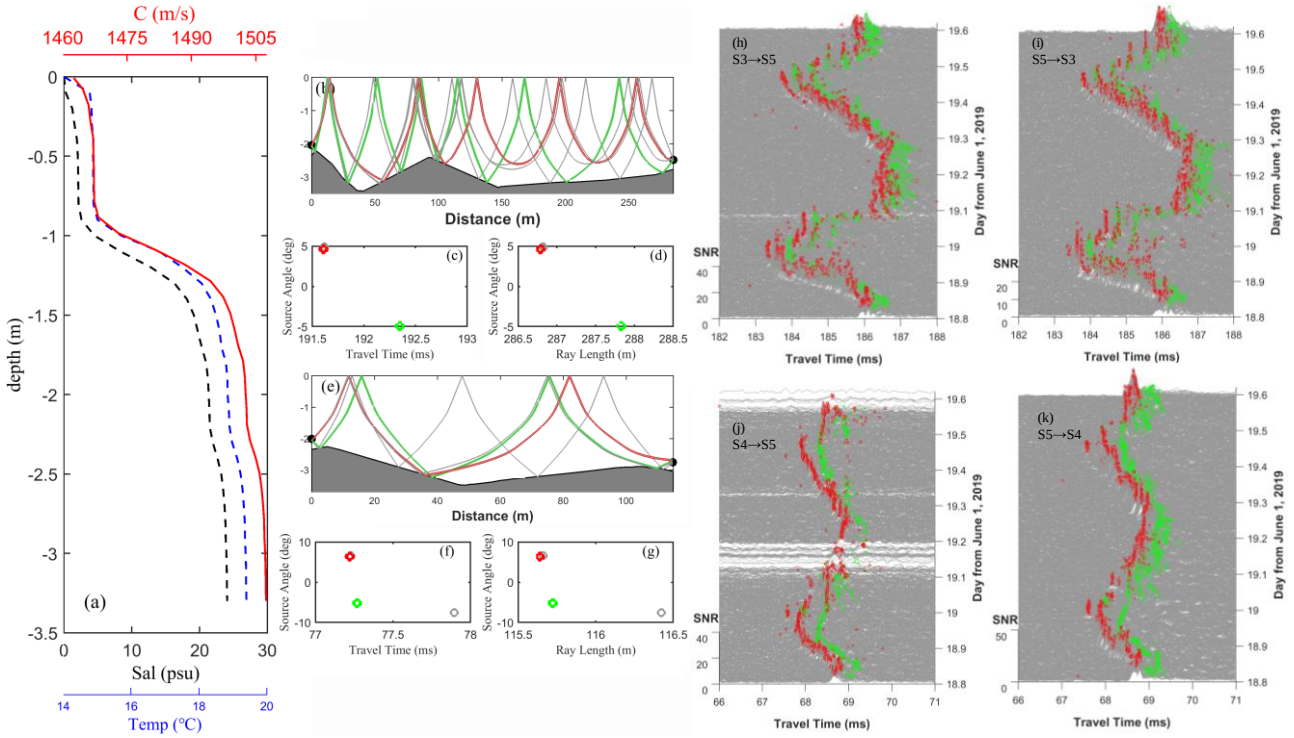

Figure 3. (a) Typical vertical profile of water temperature (blue dashed lines), salinity (black dashed lines), and calculated sound speed (red solid lines). (b) – (d) and (e) – (g) are results of ray tracing along the longest and shortest transmission lines S3S5 and S4S5. (h), (i), (k) and (k) Stack diagrams of the received correlation patterns plotted with the time axis along the longest and shortest transmission lines S3S5 and S4S5.

4.2 Tidal Currents and residual currents distribution

The horizontal distribution of the hourly interval depth-averaged tidal current (Figure 4) was reconstructed by using the inverse method. Flow distribution pattern varied favorably with the tide, the velocity directions and magnitudes for the FAT inverse results, which are closest to ADCP, showed good agreement with that measured by the fixed ADCP near S2 and S5. During flood tide, a significant upward current flowed with a maximum speed of 0.35 m/s, the currents were originated from the Hiroshima Bay owning to the saltwater intrusion. Otherwise, significant downward currents during ebb tide, with a maximum speed of 0.4 m/s. Velocity distribution in the tidal junction shows that tidal currents during ebb tide are higher than during flood tide.

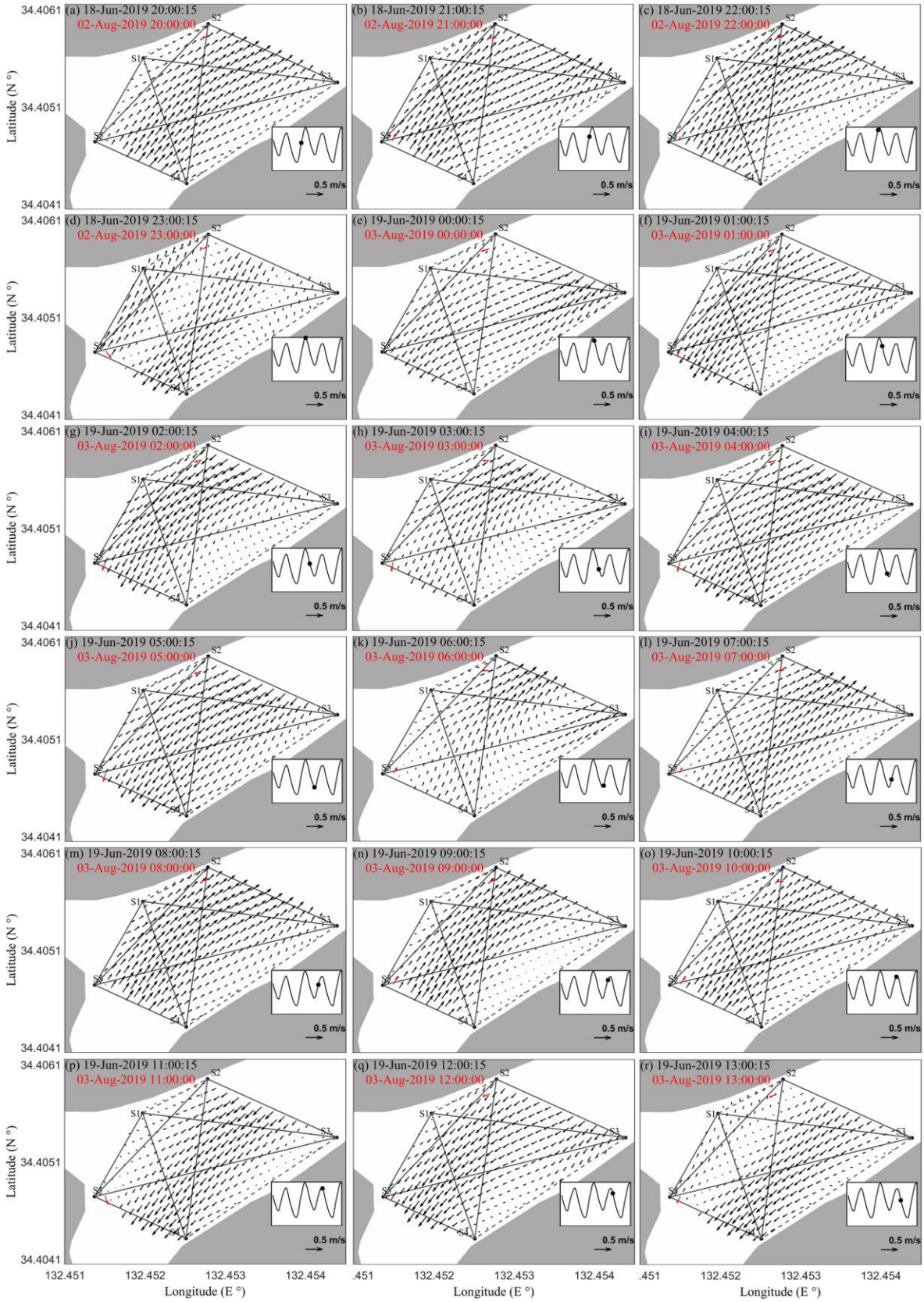

Figure 4. Depth-averaged current structures from 20:00 JST on June 18 to 13:00 JST on June 19, 2019, at an hourly interval reconstructed by inverse analysis. The black dots denote the FAT station, and the solid lines connecting the acoustic stations represent transmission rays. The black and red arrows indicate the velocity obtained by FAT and ADCP, respectively.

Figure 5a shows the horizontal distribution of the residual currents. In the present analysis, residual current is a constant term that is separated from the tidal current by using harmonic analysis within 12.48 hours. The

residual currents were stronger along the east branch, the maximum residual current in the upstream reached 0.4 m/s. The residual current along the west branch was relatively small, with a mean residual current of 0.03 m/s.

As shown in Figure 5b, the amplitudes and phases of M_2 tidal current constituent were obtained by using harmonic analysis within 12.48 hours. The semi-major axes of the M_2 tidal ellipses were extended in a northeast-southwestward direction, and the ellipses were northeast-southwestward direction in the tomography area.

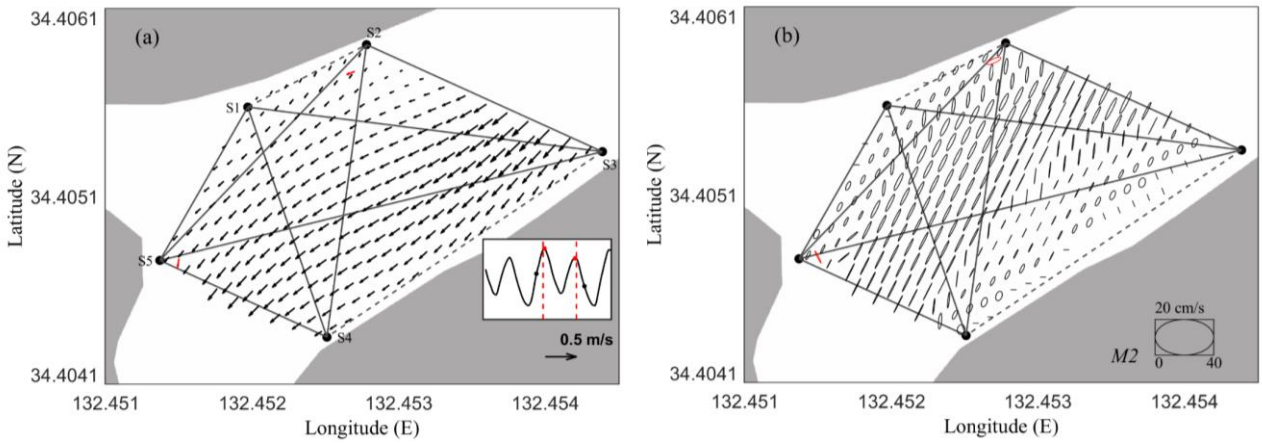

Figure 5. (a) The residual current obtained by harmonic analysis. (b) Distribution of tidal current ellipses for M_2 tidal constituent. The black arrows and ellipses are from FAT results, and the red arrow and ellipse indicate ADCP results

4.3 Evaluation of the inversion results

Following the damped least-squares method, a damping factor α was used to stabilize the solution. The estimated error covariance matrix U (uncertainty) of solution for the damped least squares method may be expressed as:

$$U = I - E^T(EE^T + \alpha^2 I)^{-1}E \quad [5]$$

U can be transformed into S in a physical space by multiplying the vector P composed of the harmonic functions appearing in the Fourier series:

$$S = P^T UP \quad [6]$$

The diagonal elements of S display the uncertainties of solution in the physical space. The uncertainties depend on the number and arrangement of successful transmission ray and furthermore the values of α determined by the L curve method. Most of the time, the uncertainties are less than 0.1 m/s in the tomography domain (Figure 6). The higher uncertainties are always exhibited around S4 and at the center of the tomography domain (Figure 6).

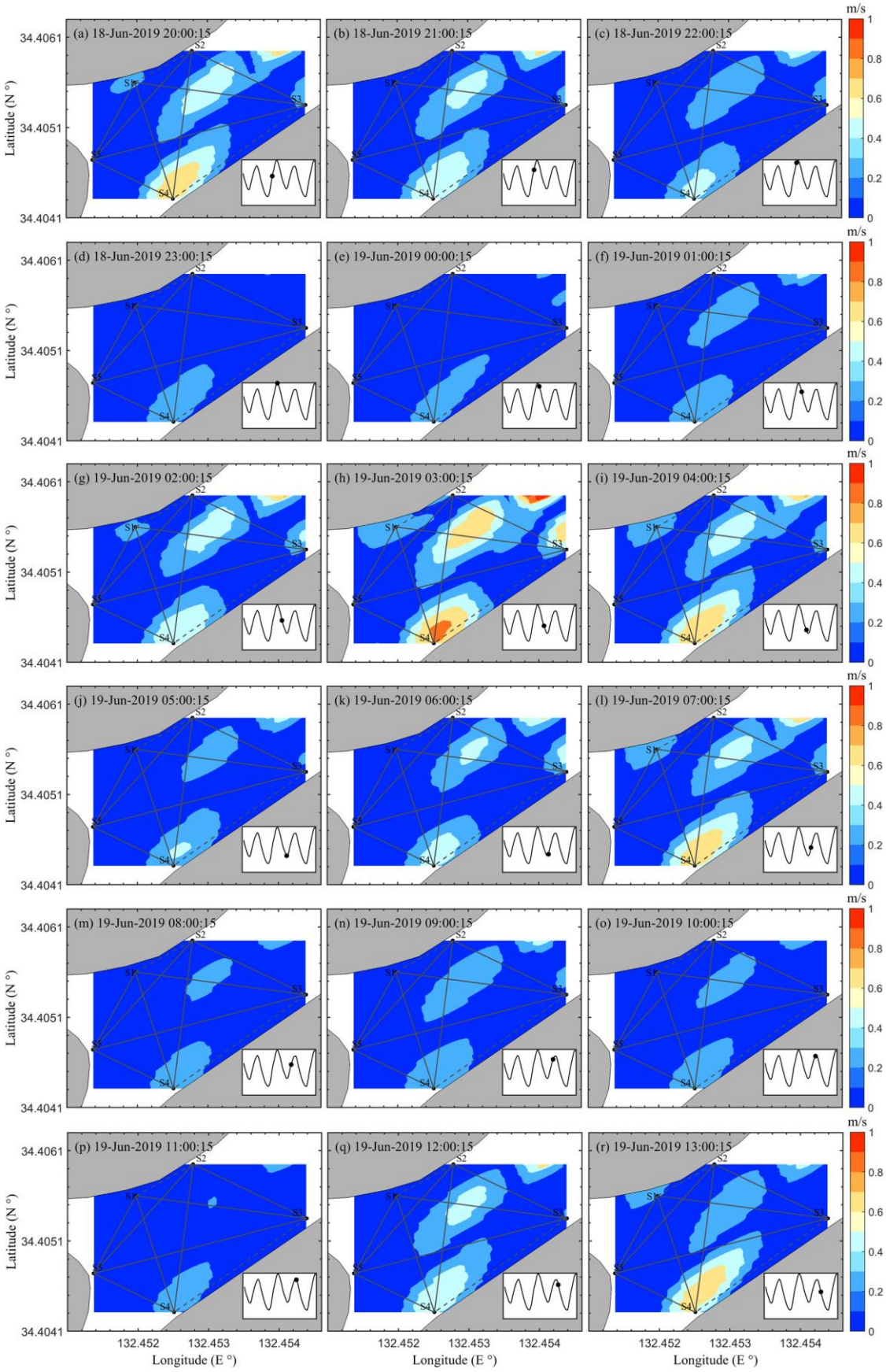

Figure 6. Uncertainty maps for the inverse solution of the horizontal currents from 20:00 JST on June 18 to 13:00 JST on June 19, 2019 corresponding to the horizontal current distribution of Figure 4.

4.4 Dynamic mechanisms of residual currents

To comprehend the main dynamic processes of the residual currents at the junction, we decomposed the depth-averaged currents ($\vec{u} = u\vec{\imath} + v\vec{\jmath}$) observed by FAT into two parts: the tidal currents ($\overrightarrow{u'} = u'\vec{\imath} + v'\vec{\jmath}$) and the residual currents ($\vec{U} = U\vec{\imath} + V\vec{\jmath}$). The momentum equation, integrated from the bottom to the surface and averaged over one tidal cycle is written in Sheng and Wang (2004). The term on the left-hand side of the equation is known as the tidally averaged advection of the tidal currents ($\nabla_h\overline{\overrightarrow{u'}\overrightarrow{u'}}$) (Sheng and Wang, 2004). It is the forcing term for the residual flow and is part of the tidal stress. It is balanced by the six terms on the righthand side of the equation. They are the pressure gradient of residual water level ($-g\nabla_h\bar{\eta}$); advection of the residual currents ($\nabla_h(\vec{U}\vec{U})$); horizontal mixing of residual currents ($A_m\nabla_h\cdot(\nabla_h\vec{U})$); time mean wind stress ($\frac{\overrightarrow{\bar{\tau}_w}}{\rho h}$); time mean bottom stress ($\frac{\overrightarrow{\bar{\tau}_b}}{\rho h}$); Coriolis term ($-\overrightarrow{fk}\times\vec{U}$).

The horizontal distributions of four terms in the equation are shown in Figure 7. Unfortunately, we did not have the horizontal distribution of water depth, the terms of time mean wind stress and time mean bottom stress are only calculated one site. Figure 7a shows that the tidally averaged advection term of the tidal currents is large in the downstream. The horizontal distribution of the residual current advection term gradually increased from the riverbank to the center of the channel. The spatial distribution of the horizontal mixing of the residual current term is similar to the Coriolis term. The approximate ratios of temporally and spatially averaged values of these terms were $T_{\nabla_h\overline{\overrightarrow{u'}\overrightarrow{u'}}} : T_{\nabla_h(\vec{U}\vec{U})} : T_{A_m\nabla_h\cdot(\nabla_h\vec{U})} : T_{\frac{\overrightarrow{\bar{\tau}_w}}{\rho h}} : T_{\frac{\overrightarrow{\bar{\tau}_b}}{\rho h}} : T_{-\overrightarrow{fk}\times\vec{U}}$ = 100% : 0.38% : 58.0% : 0.28% :7.85%: 0.31%.

Therefore, the momentum equation of the residual currents at the junction is mainly balanced by the tidally averaged advection of the tidal currents, the averaged horizontal pressure gradient, and the horizontal mixing of the residual currents. In this region, the bottom friction plays relatively less important roles, the advection of the residual currents, the wind stress, and the Coriolis force are negligible.

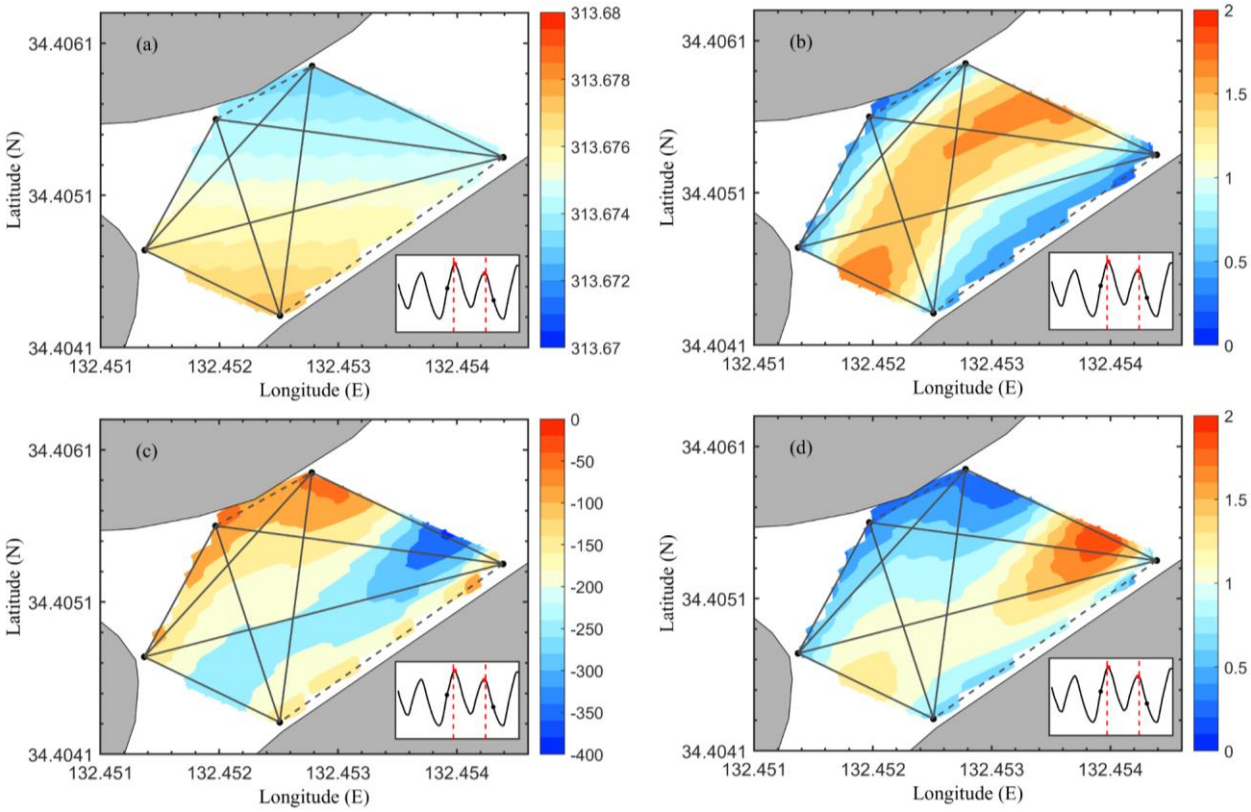

Figure 7. Horizontal distribution for terms in equation (in units of 10^{-6} m s^{-2}): (a) The tidally averaged advection of the tidal currents ($\nabla_h\overline{\overrightarrow{u'}\overrightarrow{u'}}$). (b) Advection of the residual currents ($\nabla_h(\vec{U}\vec{U})$). (c) Horizontal mixing of residual currents ($A_m\nabla_h\cdot(\nabla_h\vec{U})$). (d) Coriolis term ($-\overrightarrow{fk}\times\vec{U}$).

5 CONCLUSIONS

The horizontal structure and the temporal variation of the tidal velocities at the junction were observed by the FAT system composed of five fixed acoustic stations during 18-19 June 2019. Simultaneous reciprocal transmissions of high-frequency sound pulses were carried out for 18 hours along 8 ray paths. The horizontal

tidal velocities and residual currents estimated by inverse analysis agreed well with ADCP. It is demonstrated that the application of FAT in conjunction with inversion schemes provides an effective tool to determine the depth-averaged currents in a shallow tidal junction. The averaged horizontal momentum equation of the residual currents reveals that the predominant terms in balancing the momentum equation of the residual currents are the advection of the tidal currents, the horizontal pressure gradient and the horizontal mixing of the residual currents, while the wind stress, the bottom friction, and the Coriolis force terms contribute less.

ACKNOWLEDGEMENTS

The author (CONG XIAO) gratefully acknowledges the financial support provided by the China Scholarship Council (CSC) for his Ph.D. studies at Hiroshima University. The authors acknowledge the students who participated in the observations and obtained valuable data for this work. The author would like to thank Dr Chuanzheng Zhang (State Key Laboratory of Satellite Ocean Environment Dynamics, Second Institute of Oceanography, State Oceanic Administration, China) and Professor Arata Kaneko (Department of Transportation and Environmental Systems, Graduate School of Engineering, Hiroshima University, Japan,) for their suggestions in analyzing the data. This work was supported by the Japan Society for the Promotion of Science (JSPS) KAKENHI grant number JP17H03313.

REFERENCES

Kaneko, A., Yuan, G., Gohda, N. and Nakano, I., 1994. Optimum design of the ocean acoustic tomography system for the sea of japan. Journal of Oceanography, 50(3): 281-293.

Kawanisi, K., Razaz, M., Kaneko, A. and Watanabe, S., 2010. Long-term measurement of stream flow and salinity in a tidal river by the use of the fluvial acoustic tomography system. Journal of Hydrology, 380(1-2): 74-81.

Kawanisi, K., Razaz, M., Yano, J. and Ishikawa, K., 2013. Continuous monitoring of a dam flush in a shallow river using two crossing ultrasonic transmission lines. Measurement Science and Technology, 24(5): 055303.

Munk, W., Worcester, P. and Wunsch, C., 1995. Ocean acoustic tomography, cambridge univ. Pr., Cambridge UK.

Park, J.-H. and Kaneko, A., 2001. Computer simulation of coastal acoustic tomography by a two-dimensional vortex model. Journal of oceanography, 57(5): 593-602.

Razaz, M., Kawanisi, K., Kaneko, A. and Nistor, I., 2015. Application of acoustic tomography to reconstruct the horizontal flow velocity field in a shallow river. Water Resources Research, 51(12): 9665-9678.

Razaz, M., Kawanisi, K., Nistor, I. and Sharifi, S., 2013. An acoustic travel time method for continuous velocity monitoring in shallow tidal streams. Water Resources Research, 49(8): 4885-4899.

Razaz, M., Kawanisi, K., Nistor, I. and Zedel, L., 2016. Depth-averaged flow reconstruction in an extremely shallow estuary. Coastlab16.

Sheng, J. and Wang, L., 2004. Numerical study of tidal circulation and nonlinear dynamics in lunenburg bay, nova scotia. Journal of Geophysical Research: Oceans, 109(C10).

Yamaguchi, K. et al., 2005. A continuous mapping of tidal current structures in the kanmon strait. Journal of oceanography, 61(2): 283-294.

Yamoaka, H. et al., 2002. Coastal acoustic tomography system and its field application. IEEE Journal of Oceanic Engineering, 27(2): 283-295.

8th International Conference on the Application of Physical Modelling in Coastal and Port Engineering and Science
Dec. 9th - 12th, 2020, Zhoushan, China

NUMERICAL INVESTIGATION OF THE LOCAL SCOUR PROCESS AROUND ROUND-ENDED BRIDGE PIERS

YIZHOU XIAO(1), GUILIN PAN(2) & XIANDAO FENG(3)

(1,2,3) CCCC Second Harbor Engineering Company LTD, Key Laboratory of Large-span Bridge Construction Technology China, Research and Development Center of Transport Industry of Intelligent Manufacturing Technologies of Transport Infrastructure, CCCC Highway Bridge National Engineering Research Centre Co. LTD, Wuhan, China,
xiao_yizhou@163.com; 1368539596@qq.com; 1403438483@qq.com

ABSTRACT

Scour of sediments around bridge piers by the flow is the most significant contributing factor for bridge failures. The aim of this study is to assess the simulation and prediction of scour processes, both hydrodynamically and morphologically, around vertical round ended piers. The RNG $k-\varepsilon$ turbulent model is employed to capture turbulent performances. Firstly, the simulations at previous experimental flow conditions in the literatures are conducted, and results obtained from simulations agree well with the experimental data, thus validating the numerical reliability. The hydrodynamic and morphological characteristics are acquired, including the velocity distributions and bed shear stress. Additionally, the instantaneous scour process around piers are evaluated. This study indicated that a 3D hydromorphological model can predict effectively the scour depth around bridge piers.

Keywords: scour of bridge piers; numerical simulation; scouring-depth

1 INTRODUCTION

Local scour around the pier is a common phenomenon that proposes practical problems for structural integrity of bridges. Therefore, an accurate prediction of the local scour around a pier is an engineering question worthy of study and exploration.

Aiming at the question of local scour around the pier, many scholars have made researches on field prototype observation, physical model experiments and numerical simulations (Bozkus and Yildiz, 2004; Bozku and Cesme, 2010; Ehteram and Mahdavi, 2015; Zhang and Shi, 2016; Vaghefi et al., 2016). Graf and Yulistiyanto (1998) employed an Acoustic Doppler Velocity Profiler to obtain instantaneously the three directions of the velocity in the flow, and results of the experiments showed that a horseshoe-vortex system was established, existing of a measurable vortex with underneath a return flow of negative vorticity. Zu (2009) used an Acoustic Doppler Velocimetry to capture the three-dimensional velocity field near the pier experimentally, ensuring the relationship between the turbulent width and Froude number. Vaghefi et al. (2016) experimentally investigated scour around circular bridge piers with two different diameters and different inclination angles toward downstream, revealing that increase in the inclination angle decreased the scour depth. Khosronejad et al. (2012) carried experiments and numerical simulations to study clear-water scour around the three bridge piers with cylindrical, square, and diamond cross-sectional shape, respectively. This work revealed that the predictive capability of the URANS morphodynamic model improved dramatically for the diamond shape pier for which sediment transport was driven primarily by the shear layers shed from the pier sharp edges. Omara et al. (2019) have assessed and validated the accuracy of the numerical model both hydrodynamically and morphologically.

In this paper, numerical simulations of the local scour around the round-ended pier is performed to determine the impact of a round-ended pier on hydrodynamical and morphological characteristics. A comparison of the simulated results and experimental data reported in the literature by Mou et al. (2017) is conducted. The erosion processes are successfully reproduced in simulations. Furthermore, the characteristics of mean flow field and bed shear stress are also investigated.

2 Mathematical approaches

2.1 Governing equations

The Navier-Stokes equations for incompressible and viscous flow are as follows (Xiao et al., 2016):

$$\frac{\partial \rho}{\partial t}+\frac{\partial(\rho u_i)}{\partial x_i}=0 \quad [1]$$

$$\frac{\partial\left(\rho u_i\right)}{\partial t}+div\left(\rho u_i \mathbf{u}\right)=-\frac{\partial p}{\partial x_i}+div\left(\mu \mathbf{grad} u_i\right)+F_i \quad [2]$$

where ρ is the flow density, p is the dynamic pressure, ui is the component of the local time-average flow velocity, u is the velocity vector, t is time, μ is coefficient of dynamic viscosity, Fi is the body force of a microelement.

The sediment scour model used here is based on Mastbergen and Van den Berg (2003). The Soulsby-Whitehouse Equation (2014) is used to predict the critical shields $\theta_{\mathrm{cr},i}$:

$$\theta_{\mathrm{cr},i}=\frac{0.3}{1+1.2d_{*,i}}+0.055\left[1-\exp\left(-0.02d_{*,i}\right)\right] \quad [3]$$

$$d_{*,i}=d_i\left[\frac{\rho_f\left(\rho_i-\rho_f\right)\|g\|}{\mu_f^2}\right]^{\frac{1}{3}} \quad [4]$$

where ρ_{i} is the density of the sediment species (i), ρ_{f} is the fluid density, d_i is the grain size diameter, μ_{f} is the dynamic viscosity of fluid, and g is the magnitude of the acceleration of gravity.

The local shields parameter is computed based on the local bed shear stress (τ):

$$\theta_{\mathrm{i}}=\frac{\tau}{\|g\| d_i\left(\rho_i-\rho_f\right)} \quad [5]$$

where τ is calculated using the law of the wall by considering bed surface roughness.

The entrainment coefficient (0.005) is used to scale the scour rates and fit the experimental data. The settling velocity controls the Soulsby deposition equation. The volumetric sediment transport rate per width of the bed is calculated using Equation (6):

$$\Phi_i=\beta_{VR,i}d_{*,i}^{-0.3}\left(\frac{\theta_i}{\theta_{cr,i}'}-1\right)^{2.1}c_{b,i} \quad [6]$$

$$\Phi_i=\beta_{MPM,i}\left(\theta_i-\theta_{cr,i}'\right)^{1.5}c_{b,i} \quad [7]$$

$$\Phi_i=\beta_{\mathrm{Nie},i}\theta_i^{0.5}\left(\theta_i-\theta_{cr,i}'\right)c_{b,i} \quad [8]$$

where $\beta_{MPM,i}$, $\beta_{\mathrm{Nie},i}$ and $\beta_{VR,i}$ are coefficients that are typically equal to 8.0, 12.0 and 0.053, respectively; $c_{b,i}$ is the volume fraction of species (i) in the bed material, and Φ_i is the dimensionless bed load transport rate, which is assumed to be 0.05. The volumetric bed load transport rate ($q_{b,i}$) is expressed as follows:

$$q_{b,i} = \Phi_i \left[\|g\| \left(\frac{\rho_i - \rho_f}{\rho_f} \right) d_i^3 \right]^{0.5} \quad [9]$$

The law of the wall for the mean velocity, as modified for roughness, is expressed by Equation 10:

$$\frac{u_p}{u} = \frac{1}{k} \ln \left[E \frac{\rho c_\mu^{1/4} k_p^{1/2} z_p}{\mu} \right] - \Delta B \quad [10]$$

where u_p is the main flow velocity at point p, k is von Karman's constant (0.418), u is the shear velocity related to the bottom shear stress ($\tau = \rho u^2$), ρ is the fluid density, c_μ is the constant, k_p is the turbulent kinetic energy at point p, and ΔB is the roughness function.

2.2 Flow configuration and boundary condition

The flow configuration is based on those used in the experiments conducted by Mou et al. (2017) as illustrated in Figure 1. The origin of the Cartesian coordinates is set at the bottom of the apex of the upstream round-ended pier. The diameter of the end of the cylinder is D= 0.09 m, and the middle rectangle of the pier has a length of 0.2 m and a width of 0.09 m. Sediment with a thickness of 0.23 m is used to simulate the sediment state on the bed surface, and the fine sand is used with a median particle size of 0.24 mm. The simulated domain of the rectangular flume had a length, width, and height of 3 m, 0.5 m and 0.5 m, respectively. This paper simulates three working conditions as Table 1.

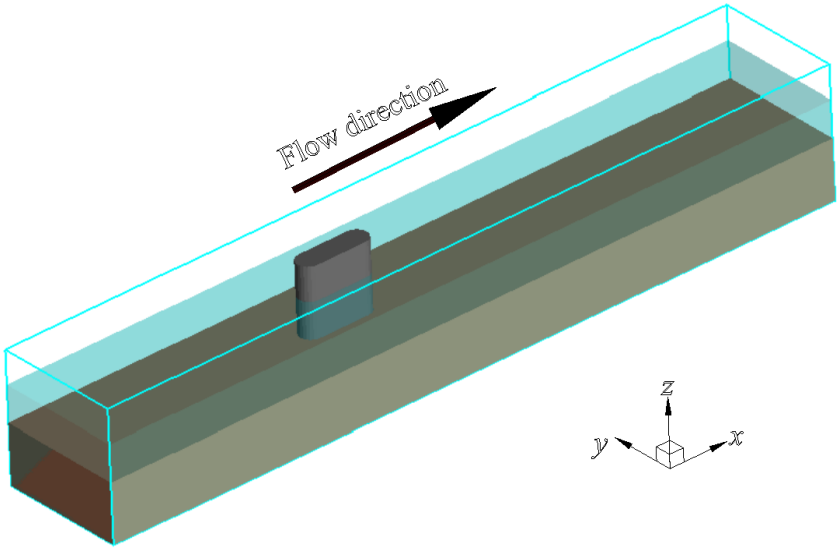

Figure 1. Schematic of the computational domain.

Table 1. Calculated conditions.

Case	Mass flow rate Q(m^3/s)	Water depth H(m)	Ambient velocity Ua(m/s)
1	0.028	0.14	0.3968
2	0.032	0.16	0.3990
3	0.036	0.18	0.4012

The volume flow rate boundary condition is adopted at the inlet boundary condition of the flume. The pressure outlet boundary condition is set as the outlet boundary condition. The wall condition is set at the baseboard and the side walls of the flume. Furthermore, the air inlet at the top of the flume was set as a symmetry boundary condition, which was the default that no fluid flows through the boundary.

2.3 Computational method

The numerical solution is used to calculate the Reynolds-averaged Navier-Stokes (RANS) equations. The RNG $k-\varepsilon$ model is selected to provide an accurate estimation of the near-wall shear stresses. The TruVOF

method, which only computed the unit of the fluid, not the unit of the air, was adopted to reduce the time of convergence. Meshes were generated by the FAVOR (Fractional Area Volume Obstacle Representation) method, which used the finite difference method to simulate complicated models. Additionally, the FAVOR method used fewer hexahedron grid units to smoothen and eliminate the rough regions, which build a mesh model without any distortion. The simulations were considered convergent when the residual was less than 1×10^{-5} for the governing equations.

3 RESULTS

3.1 Validation of morphological characteristics

The experiments data by Mou et al. (2017) are used to validate the numerical model. The erosion processes result in the emergence of the groove, which occurred at the base of the scour hole in front of the pier. Figure 2 shows the results of the numerical model for the clear-water scour hole around the round-ended pier. The results indicate terrain elevation around the pier. The maximum depth of erosion in the simulation is 8.8 cm, which agrees well with the experimental data (9.2cm). Additionally, the maximum width of erosion in the simulation is 18.5 cm, which is consistent with experimental data (16.8 cm).

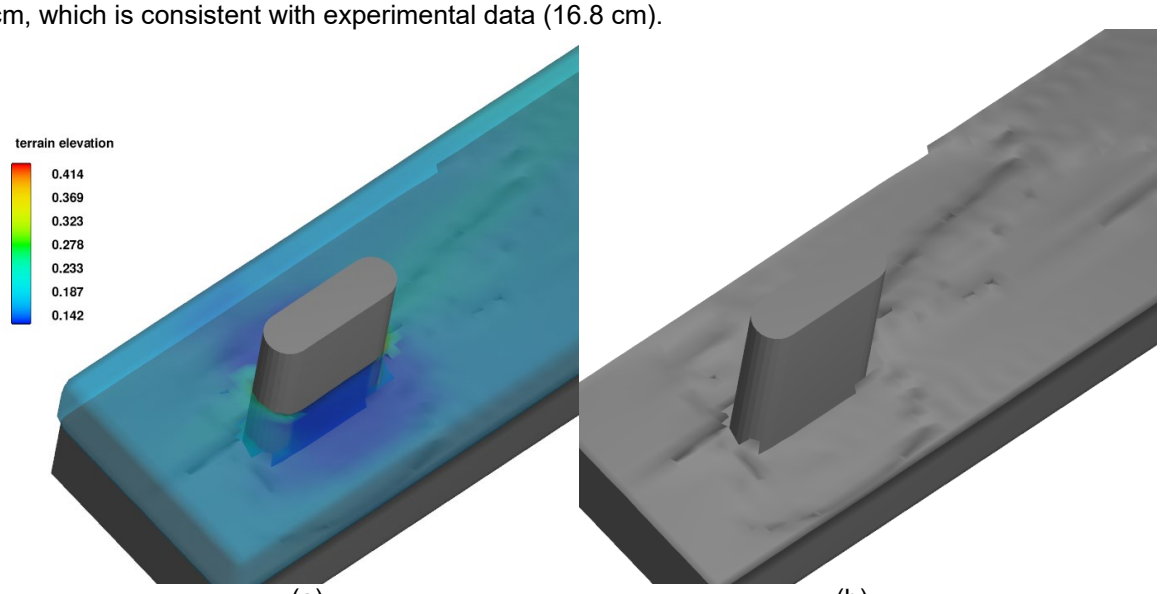

(a) (b)

Figure 2. The scour hole shape in Case 2: (a) terrain elevation, (b) shape of local scour around the pier.

The scouring process was captured by numerical simulations, as shown in Figure 3. The scouring process begins at the side of the pier, after which the scour emerges at the nose of the pier. The sediment in front of the scour groove collapses by the upstream currents, eventually carries around the pier, and forms the long sand ridges behind the pier. The model effectively simulates the scour hole, erosion and sediment.

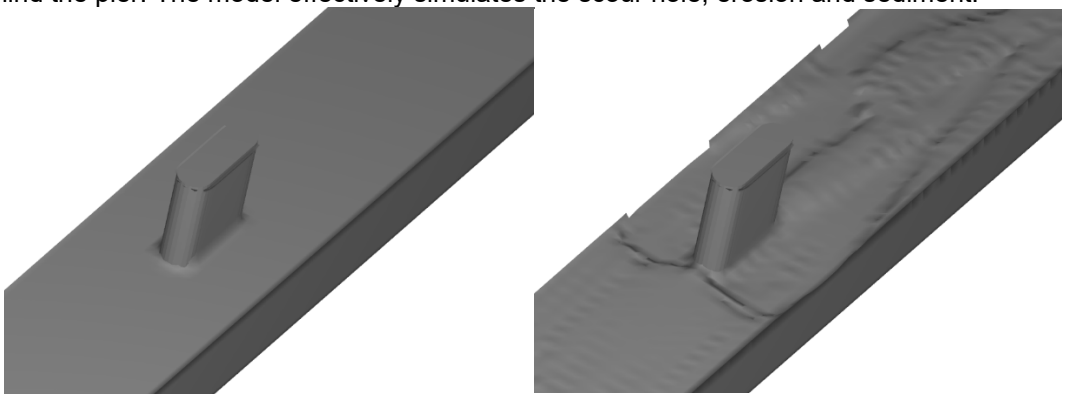

(a) (b)

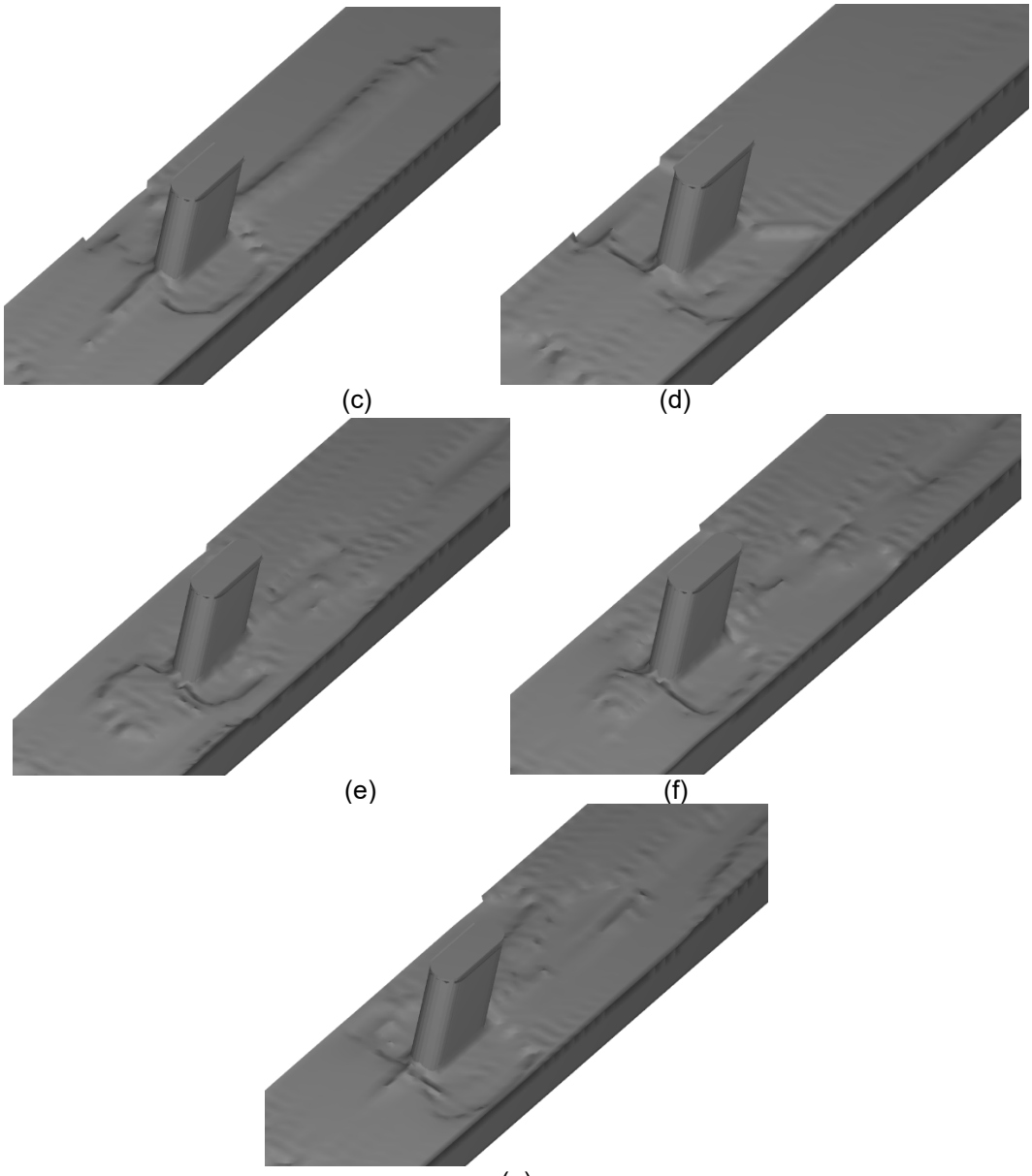

Figure 3. Erosion process, the time interval is 886.7 *D*/*Ua*.

3.2 Mean flow

The flow field around the pier plays an important role in the stability of the pier. The contours of the velocity are shown in Figure 4. The results indicate that the lower velocity regions exist in front and behind the pier, while the velocity increases sharply beside the pier. As the inlet mass flow rate increases, so does the velocity in the flow field. What's more, with the mass flow rate increasing, the length of vortex forming region of pier's wake gradually shortens.

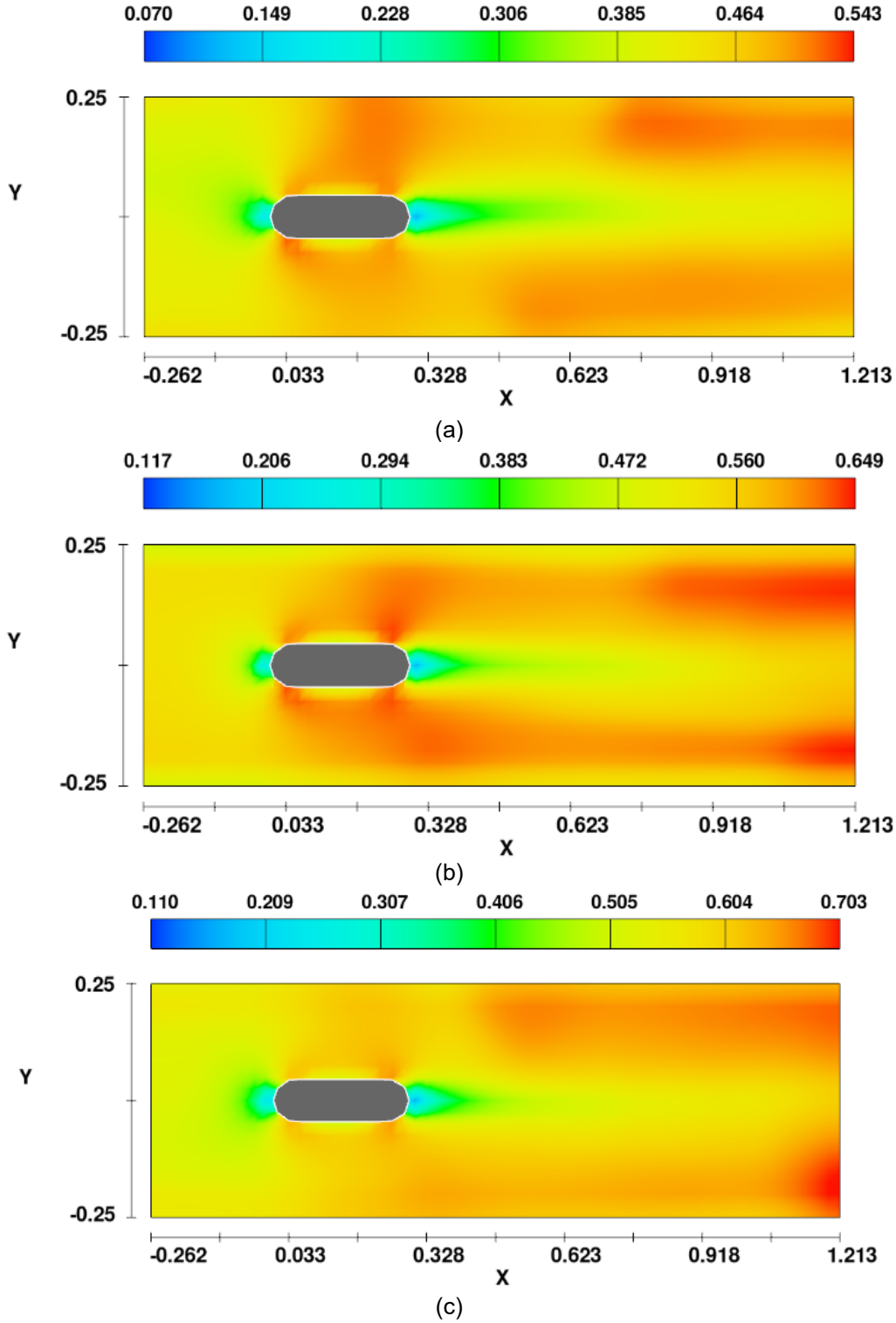

Figure 4. Velocity distribution in the horizontal plane: (a) Case 1, (b) Case 2, (c) Case 3.

3.3 Bed shear stress

Bed shear stress influences important benthic processes such as sediment transport. Bed shear stress is calculated from:

$$\tau = \frac{1}{2}\rho C_f U_d^2 \qquad [11]$$

in which U_d is the depth-averaged velocity and C_f is the skin friction coefficient. Figure 5 shows the distributions of bed shear stress along the flow in Case 2. The results reveal that the bed shear stress decrease in front of

the pier, while it increase beside and behind the pier. This is mainly due to the acceleration and separation of the water flow on the sides of the pier.

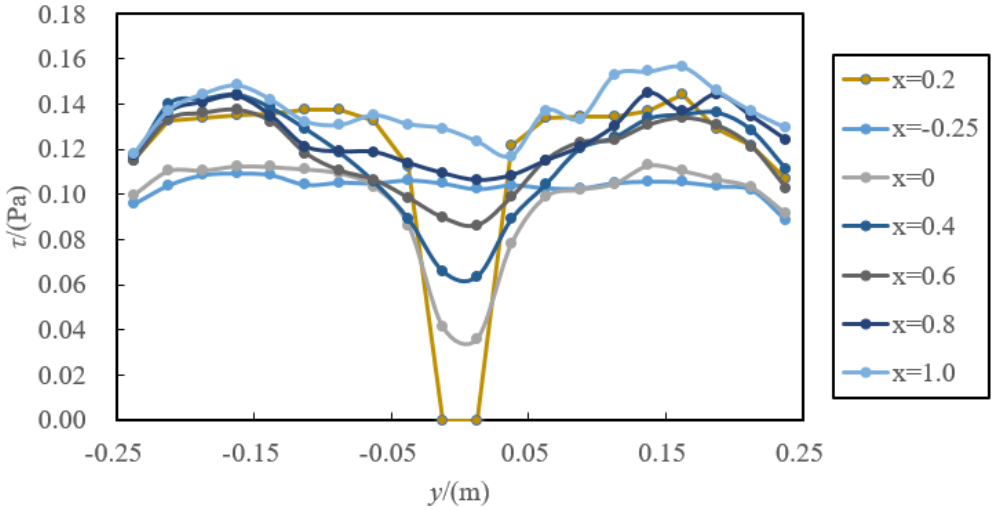

Figure 5. Distributions of bed shear stress along the flow in Case 2.

4 CONCLUSIONS

In this study, the local scour around the round ended pier is simulated and predicted, both hydrodynamically and morphologically. The RNG $k-\varepsilon$ turbulent model is employed to capture turbulent performances. The results have agreed well with the experimental data, thus validating the numerical reliability. The hydrodynamic and morphological characteristics are acquired, including the velocity distributions and bed shear stress. Furthermore, the instantaneous scour process around piers are evaluated. This research provides a good understanding of the local scour around round ended piers through the RANS, and the protective effect of pier protection measures can be explored in a further study.

ACKNOWLEDGEMENTS

The numerical calculation in this paper have been done on the workstation in the CCCC Second Harbor Engineering Company LTD.

REFERENCES

Bozkus, Z., Yildiz, O. (2004). Effects of inclination of bridge piers on scouring depth. *Journal of Hydraulic Engineering*, 130, 827-832.

Bozkus, Z., Çesme, M. (2010). Reduction of scouring depth by using inclined piers. *Canadian Journal of Civil Engineering*, 37, 1621–1630.

Ehteram, M., Mahdavi, A. (2015). Numerical modeling of scour depth at side piers of the bridge. *Journal of Computional and Applied Mathematics*, 280:68–79.

Graf, W.H., Yulistiyanto, B. (1998). Experiments on flow around a cylinder, the velocity and vorticity fields. *Journal of Hydraulic Research*, 36(4): 637-653.

Khosronejad, A., Kang, S., Sotiropoulos, F. (2012). Experimental and computational investigation of local scour around bridge piers. *Advances in Water Resources*, 37:73-85.

Mastbergen, D.R., Van Den, Berg. J.H. (2003). Breaching in fine sands and the generation of sustained turbidity currents in submarine canyons. *Sedimentology*, 50(4):625–637.

Mou, X.Y., Wang, D., Ji, H.L., Li, C.J., Qiao, C.L. (2017). Resistance capability and hydraulic characteristics of ring-wing plates against local scour of round-ended piers. *South-to-North Water Transfers and Water Science & Technology*, 15(5): 146-155. (in Chinese)

Omara, H., Elasyed, S.M., Abdeelaal, G.M., Abd-Elhamid, H.F., Tawfik, A. (2019). Hydromorphological numerical model of the local scour process around bridge piers. *Arabian Journal for Science and Engineering*, 44:4183-4199.

Vaghefi, M., Ghodsian, M., Salimi, S. (2016). Scour formation due to laterally inclined circular pier. *Arabian Journal for Science and Engineering*, 41, 1311–1318.

Vaghefi M, Ghodsian M, Salimi S. The effect of circular bridge piers with different inclination angles toward downstream on scour. Sadhana, 2016, 41:75-86.

Wei, G., Brethour, J., Grünzner, M., Burnham, J. (2014). Report sedimentation scour model. *Flow Science Incprporated Report*, 03-1–29.

Xiao, Y.Z., Wang, W.E., Hu, X.T., Zhou, Y. (2016). Experimental and numerical research on portable short-throat flume in the field. *Flow Measurement and Instrumentation*, 47: 54-61.

Zhang, Z., Shi, B. (2016). Numerical simulation of local scour around underwater pipeline based on FLUENT software. *Journal of Applied Fluid Mechanics*, 9:711–718.
Zu, X.Y. (2009). Experimental study of turbulent flow width and the characteristic of the turbulence around round-ended pier. Changsha: *Changsha University of Science & Technology*. (in Chinese)

8th International Conference on the Application of Physical Modelling in Coastal and Port Engineering and Science
Dec. 9th - 12th, 2020, Zhoushan, China

FREQUENCY DOMAIN ANALYSIS OF HYDRODYNAMIC CHARACTERISTICS OF MARICULTURE SHIP WITH TRUSS AND PLATE FRAME HYBRID STRUCTURE

SHAO MIN WANG(1), XIE QIU YANG(2) & TAI PING YUAN(3)

(1,2,3) South China Sea Fisheries Research Institute, Chinese Academy of Fishery Sciences, Guangzhou, China
wangshaomin2013@163.com; yangxieqiu@163.com; ytp0720@163.com

ABSTRACT

In recent years, mariculture in deeper and farther waters has attracted much attention, and the optimal design and development of large-scale aquaculture facilities has become an urgent need. To study the hydrodynamic performances of a mariculture ship composed of truss structure and several floating bodies with plate and frame structures, we analyzed the hydrodynamic characteristics of the ship based on three-dimensional potential flow theory and Morison theory. Through the analysis of hydrodynamic parameters and motion responses, we get the changing trend of the main performance of mariculture ship. The results show that the added mass and radiation damping of mariculture ship are sensitive to the change of frequency, and the sensitivity is obviously different in all motion directions. The added mass and radiation damping of rotational motion are larger than those of plane motion, which are closely relate to the structural type of mariculture ship. Under the action of incident waves in different directions, the first-order wave force on mariculture ship increases at first and then decreases with the increase of frequency, and the first-order wave force curve in high frequency section tends to be stable under the action of incident waves in different directions. There is a great difference in the medium and low frequency section. Under the conditions of high frequency and low frequency, the ship motion is small, but it resonates when encountering medium and short period waves. The surge and pitch of mariculture ship are the main motion modes in head or follow wave condition, and the roll and heave are the main modes of motion in the beam wave. This study lays the theoretical basis for optimal design of subsequent mariculture ship and the safe implementation of marine aquaculture facilities afterwards.

Keywords: Truss and plate frame hybrid structure; mariculture ship; hydrodynamic performance; Motion response

1 INTRODUCTION

Truss and plate are two commonly used main structures in marine engineering, such as semi-submersible drilling platform and SPAR platform. Because of their small wave area, small motion response and long inherent period (Birk et al., 2001; Nallayarasu et al., 2012), They have excellent hydrodynamic performance (Du et al., 2013; Chakrabani et al., 2007). To meet the work requirements in versatile sea environment, large-scale mariculture ship (also known as platform or fish farm) in the aquaculture industry has been developed drawing lessons from the relevant structural forms. Its watertight floating body with bow and stern plate structure is adopted to ensure sufficient buoyancy, and the floating body is rigidly connected by steel pipe truss structure to satisfy the demand of water exchange in the process of mariculture. Due to such special structural form, which is obviously different from conventional ships and offshore platform not only in shape, weight distribution, but also in physical properties, it is necessary to study its hydrodynamic characteristics.

Based on potential flow theory and Morison theory, this paper attempts to calculate and study the hydrodynamic parameters and motion response of mariculture ship composed of truss structure and plate structure. Firstly, the main theories and the solution method of related parameters are presented. Then the hydrodynamic characteristics of free floating mariculture ship are calculated by using the general radiation / diffraction potential calculation program, and the changing trends of different hydrodynamic parameters are analyzed and discussed. The hydrodynamic performance of the mariculture ship is gained and the main conclusions are drawn. This work would lay the theoretic basis for optimal design, in-depth study and safe implementation of marine mooring and mariculture ship.

2 MAIN THEORY

The Cartesian coordinate system *OXYZ*, fixed on the earth is used as the reference coordinate system. As shown in figure 1, the coordinate origin *O* is located in the still water surface, the *Z* axis is vertical, and the

coordinate system follows the right-handed rule. At the same time, the satellite coordinate system *oxyz*, is established on mariculture ship, in which the coordinate origin o is located at the stern baseline, *x* points to the bow, and the initial coordinate axes are parallel to those of the reference coordinate system. *α* is the angle between the propagation direction of the incident wave and the positive direction of the *OX* axis.

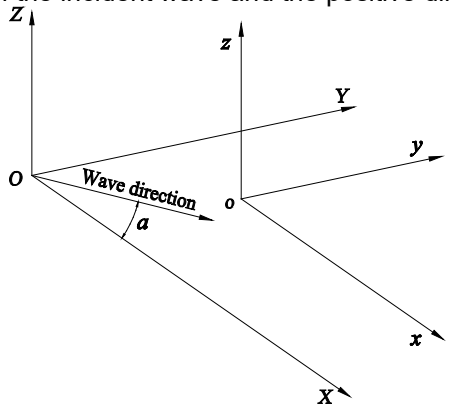

Figure 1. The coordinate system

Assuming that the fluid in the flow field of the aquaculture farm is inviscid, irrotational and incompressible, and the free surface is a micro-amplitude wave, the motion of the fluid can be described by the three-dimensional potential flow theory. According to this theory, there is an unsteady velocity potential Φ in the flow field, which can be decomposed into incident wave velocity potential Φ^I, diffracted wave velocity potential Φ^D and radiation wave velocity potential Φ^R, where:

$$\begin{aligned}\Phi(x,y,z,t) &= \emptyset(x,y,z)e^{-i\omega t} = [\emptyset^I(x,y,z) + \emptyset^D(x,y,z) + \emptyset^R(x,y,z)]e^{-i\omega t} \\ &= \left[\emptyset^I(x,y,z) + \emptyset^D(x,y,z) + \sum_{j=1}^{6} i\omega\overline{x}_j\emptyset^j(x,y,z)\right]e^{-i\omega t}\end{aligned} \quad [1]$$

According to the Bernoulli equation, the radiation force acting on the mariculture ship can be expressed as follows:

$$\begin{aligned}F_{jk} &= -\int_S P_k\, n_j dS = -\int_S i\omega\rho\emptyset_k x_k\, n_j dS \\ &= \omega\rho x_k \int_S \mathrm{Im}(\emptyset_k)\, n_j dS - i\omega\rho x_k \int_S \mathrm{Re}(\emptyset_k)\, n_j dS \\ &= -\mu_{jk}\ddot{x}_k - \lambda_{jk}\dot{x}_k\end{aligned} \quad [2]$$

Where, F_{jk} is the radiation force in *j* direction due to the motion in *k* direction under the action of the unit amplitude. x_k is the amplitude of motion in *k* direction of the mariculture ship. μ_{jk} is added mass. λ_{jk} is radiation damping coefficient.

The first-order wave force on the aquaculture ground consists of incident wave force (Froude-Krylov force) and diffracted wave force. The incident potential and diffraction potential can be calculated by substituting the incident potential and diffraction potential into the Bernoulli equation, as follows:

$$F_j = -i\omega\rho \int_S (\emptyset^I + \emptyset^D)\, n_j dS \quad [3]$$

In the mariculture ship, the ratio of the equivalent diameter of the truss columns to the wavelength of the incident wave is much less than 0.2, so the wave force is calculated by the Morison formula based on the diffraction theory, as follows:

$$F' = 0.5C_d\rho A V_x|V_x| + C_M\rho\Delta\frac{dV_x}{d_t} \quad [4]$$

Where, n_j is the component of the normal vector on the surface of the mariculture ship in the *j* direction. C_d is the resistance coefficient of the cylinder, C_M is the inertia force coefficient, and Δ is the volume of a unit column. V_x and ($\mathrm{d}V_x/\mathrm{d}t$) are the horizontal velocities and accelerations of wave particles at any position on the axis of the cylinder.

Since Morison resistance is nonlinear, it is usually not calculated directly in frequency domain statistical analysis. Nevertheless, the contribution of the Morison element of truss structure to the static force, hydrostatic resilience, added mass and wave force is calculated in the hybrid model in this paper.

In the frequency domain analysis, the motion characteristics under the action of waves are generally expressed with the frequency response function, that is, the response amplitude operators (RAOs).

$$\mathrm{RAO} = \frac{x_k}{\xi} \quad [5]$$

Where, ξ is the amplitude of incident wave at a certain frequency.

3 CALCULATION OBJECT

The mariculture ship investigated in this paper is mainly composed of a large number of truss structures located in the middle and three independent watertight floats with one in the bow and the other in the stern as displayed in figure 2. The principal parameters of the ship are list in Table 1. In the hydrodynamic characteristics study, the water depth is set as 20m to calculate the frequency domain of mariculture ship. The ship

hydrodynamic model is shown in figure 3, in which the grid number of the whole hydrodynamic model is 13032 and the total number of nodes is 20500. The ship motion model in the waves is shown in figure 4.

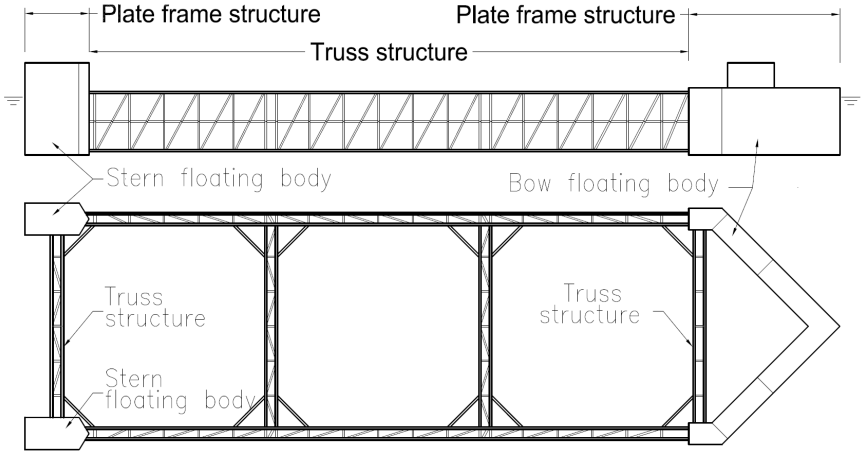

Figure 2. The mariculture ship

Table 1. Parameters of the mariculture ship

Parameters	Value
Length overall /m	91.3
Width /m	27.6
Depth /m	7.5
Draught /m	6.5
Full load displacement /t	1073
Center of gravity （*x*，*y*，*z*）	（51.9，0，3.35）
Rolling inertia radius/m	9.7
Pitching inertia radius /m	62.8
Yaw inertia radius /m	63.3

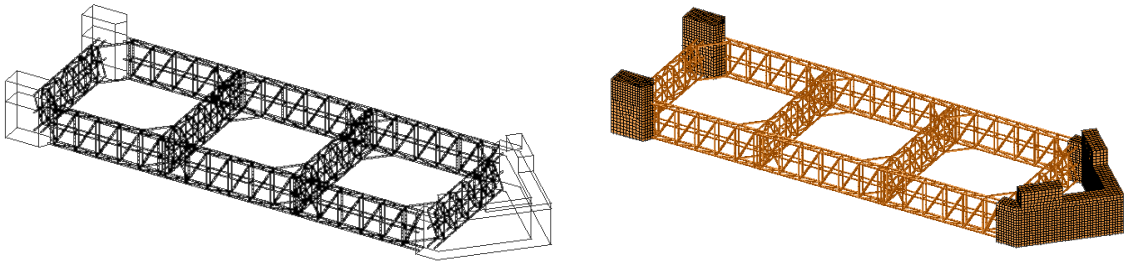

（a）Geometrical model （b）Spatial discretization

Figure 3. The mariculture ship hydrodynamic model

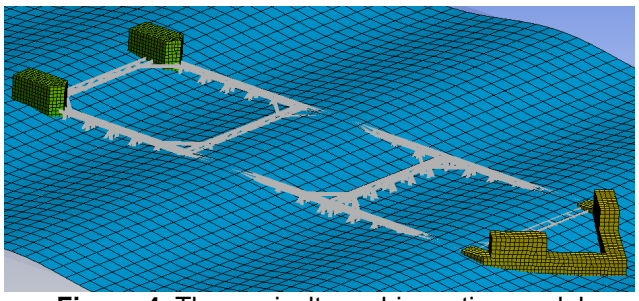

Figure 4. The mariculture ship motion model

4 RESULTS AND ANALYSIS

4.1 Added mass and radiation damping coefficient

Figure 5 shows the added mass generated by the mariculture ship during its surge, sway, heave, roll, pitch and yaw motions, which is represented by μ_{11}, μ_{22}, μ_{33}, μ_{44}, μ_{55} and μ_{66}, respectively. It can be seen that the

added mass is sensitive to the change of frequency on the six degrees of freedom, and a significant difference of added mass exists among each direction of motion. Especially, The added mass varies greatly when the frequency ranges from 0.5 rad/s to 2 rad/s, showing peak and trough values, and tends to be stable when the frequency is more than 3 rad/s. Moreover, the added mass is larger in rotating motion than that in plane motion, and is relatively smaller in heave, roll and pitch than that in surge, sway and yaw, in which the heave of the mariculture ship has the minimum added mass and the yaw has the largest one. The relationship between the added mass of translation and shaking is $\mu_{11} > \mu_{22} > \mu_{33}$ and $\mu_{66} > \mu_{55} > \mu_{44}$, respectively.

The ship response curves of radiation damping coefficient during surge, sway, heave, roll, pitch and yaw motion are displayed in figure 6, which is represented by λ_{11}, λ_{22}, λ_{33}, λ_{44}, λ_{55} and λ_{66}, respectively. It shows that the damping coefficient is very sensitive to the frequency's changing as well, and the degree of sensitivity is obviously different for all motions. The variation trend of damping coefficient in surge, sway and yaw motion is consistent, which is small in high frequency band as well as in low frequency band, and has a peak value frequency is between 1 rad/s and 2 rad/s. However, the change of the other three motion directions is not significant. The radiation damping coefficients of the rotating motions are larger than those of the plane motions. When the yaw motion occurs, the added damping will reach the maximum value, resulting in a larger radiation wave. Like the added mass, during heave, roll and pitch, the radiation damping coefficients are very small and tend to be zero.

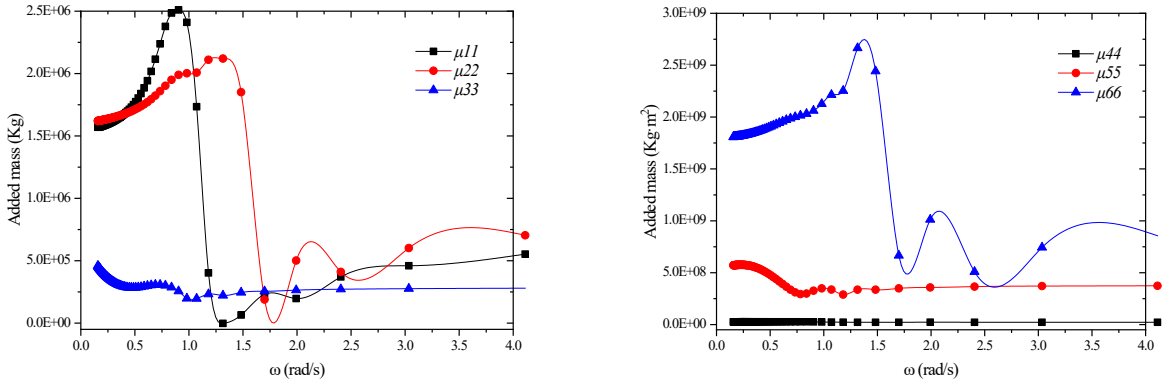

（a）plane motions （b）rotational motions

Figure 5. Added mass of mariculture ship

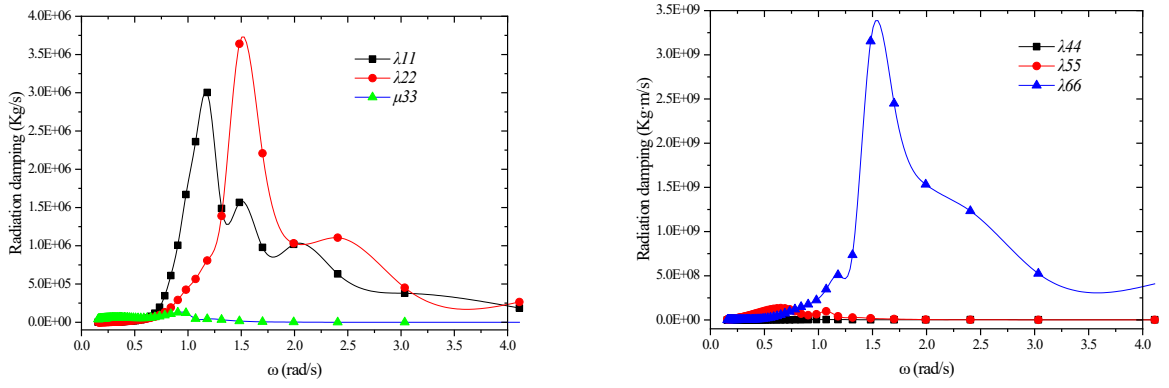

（a）plane motions （b）rotational motions

Figure 6. Radiation damping of mariculture ship

4.2 First-order wave force

As shows in figure 7, under the action of incident waves in all directions, the first-order wave force response curve of the mariculture ship under each degree of freedom is similar except of heave. With the increase of frequency in other motions, the curves increase at first and then decreases, and finally tends to be 0, but in the heave case, the curve does not show an increasing trend and on the contrary decreases first. When the incident angles are 30 °and 150 °, 60 °and 120 °respectively, the corresponding first-order wave force response curve basically coincides in the low frequency band (less than 0.75 rad/s). Moreover, the curves oscillate obviously when frequency ranging from 0.5 rad/s to 2 rad/s, resulting in an extreme value, and at the same time, they decrease gradually and tend to be 0 in the high frequency band.

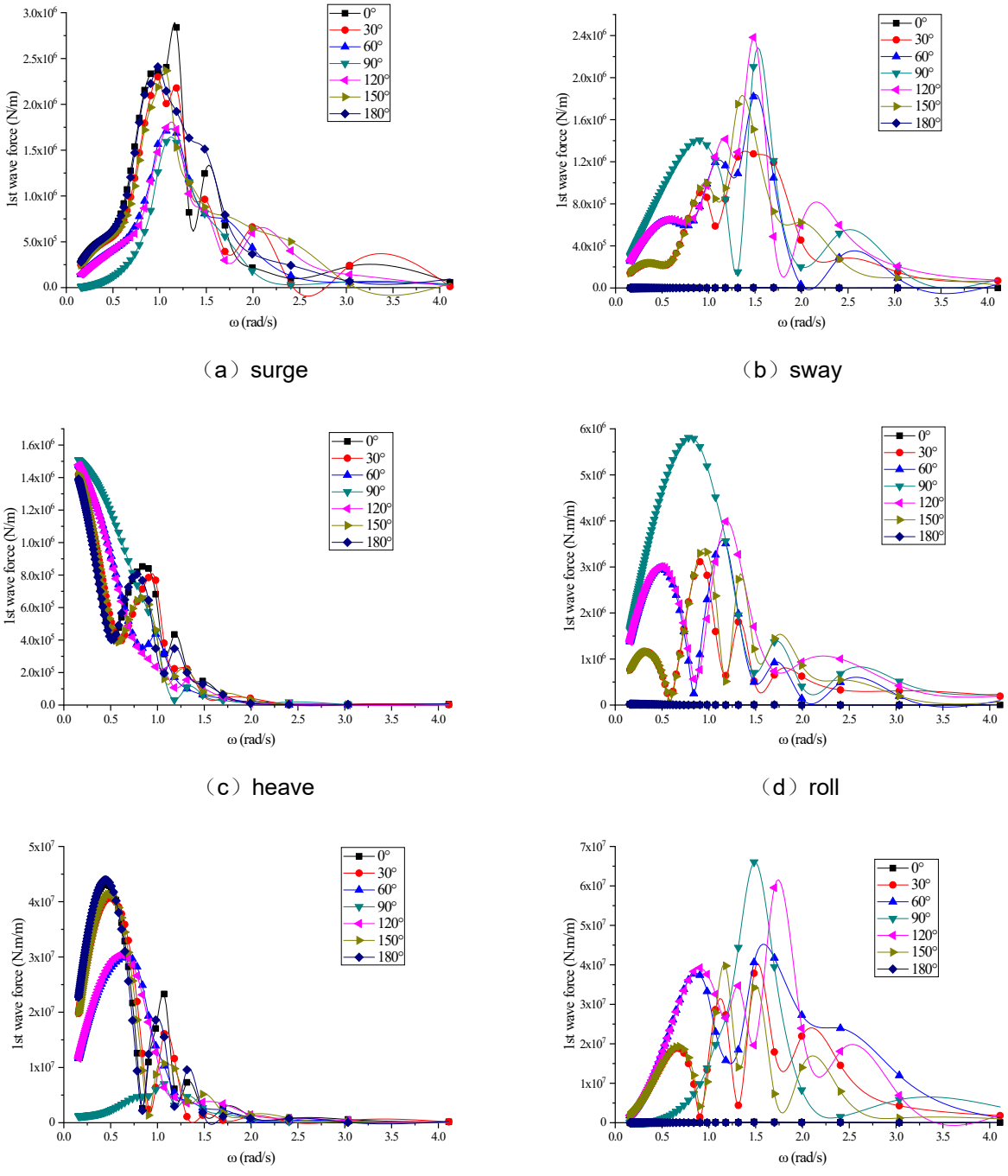

Figure 7. First order wave forces/moments of mariculture ship in different wave directions

4.3 Motion response

Figure 8 shows the RAOs curves of the mariculture ship during its surge, pitching, rolling and heave motions in different wave directions. It can be seen that the response trend of the two rotational motions of the ship is similar, showing a trend of rising first and then descending, which is due to the x-axis symmetry of the ship structure. If the heave motion is not taken into account, the response of the ship is small and its performance is good in both high and low frequency bands, but the resonance occurs in the range of 0.5 rad/s to 1.5 rad/s. When the ship in follow wave (α = 0 °) or head wave (α = 180 °) condition, the surge and pitch are the main motion modes, while in the 90 ° bean wave, the roll and heave are the main motion modes.

For the surge motion, because the horizontal force of the mooring system is not taken into account in the frequency domain analysis, the surge RAO curves vary significantly with the incident angle and frequency in the low frequency band, which is much larger than the wave frequency response, showing very obvious low frequency characteristics. Moreover, the mariculture ship generates response extremes at 0.75 rad/s, 1.0 rad/s

and 0.95 rad/s in pitch, roll and heave motions, respectively, so the ship has obvious wave frequency motion near these frequencies and leads to resonance.

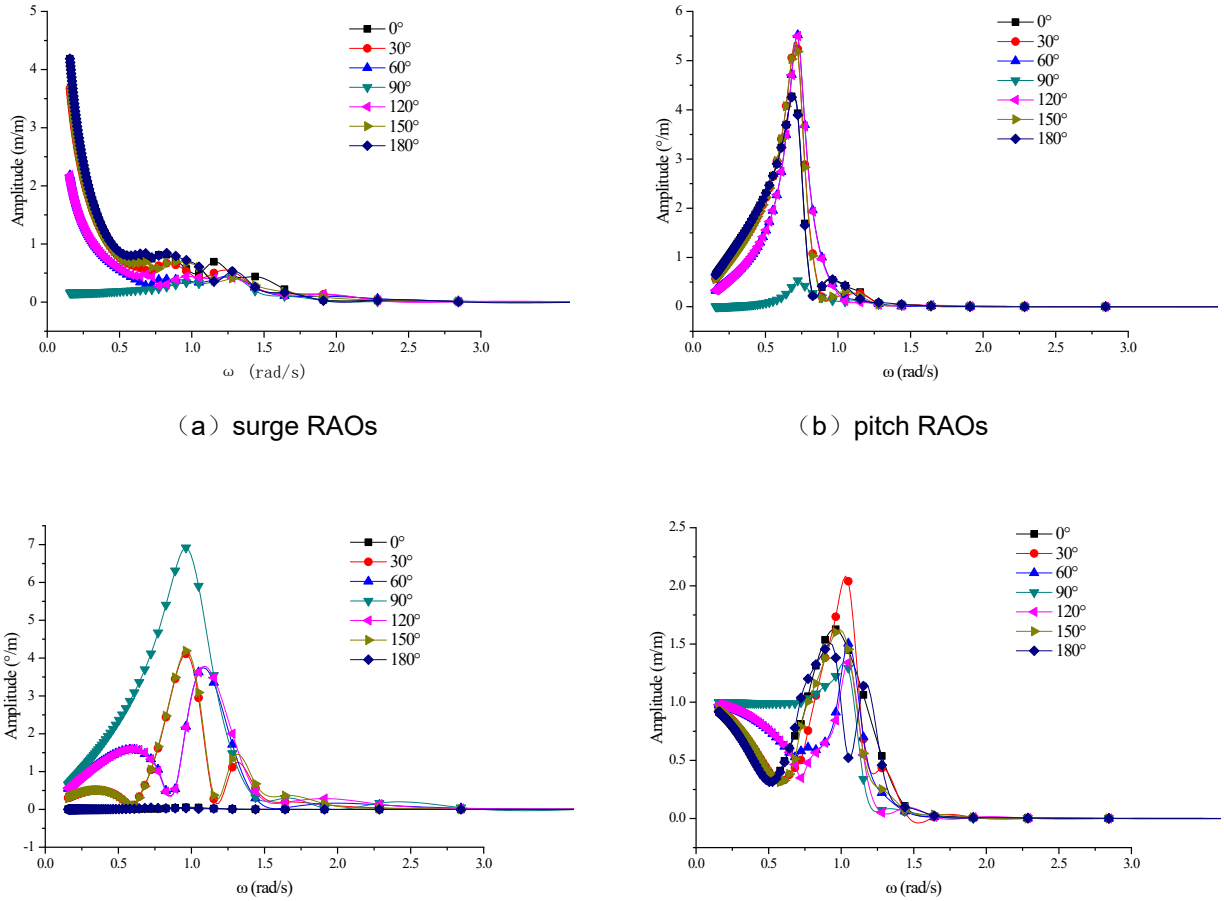

（a）surge RAOs　　（b）pitch RAOs

（c）roll RAOs　　（d）heave RAOs

Figure 8. Motion response of mariculture ship in different wave directions

5 CONCLUSIONS

(a) The added mass and radiation damping of the mariculture ship are sensitive to the change of frequency, and the sensitivity is obviously different in all directions. The calculation results of the rotational motions are larger than the plane motions, and this is closely related to the structural shape of the mariculture ship.

(b) The force and motions curves of the mariculture ship have obvious wave frequency characteristics, and are sensitive to the excitation frequency.

(c) Under high frequency or low frequency excitation, the motion response of the mariculture ship is small, but the resonance occurs when it moves in the medium and short-period regular waves.

ACKNOWLEDGEMENTS

The research reported herein is supported by the National Key R&D Program of China (Grant No. 2019YFD0900903), also supported by the National Natural Science Foundation of China (Grant No. 31772897 & 31902424).

REFERENCES

Birk L, Clauss G F. (2001) Automated hull optimisation of offshore structures based on rational seakeeping criteria. *Proceedings of the Eleventh International Offshore and Polar Engineering Conference*. Stavanger, Norway, *ISOPE2001*, 382-389.

Chakrabani S, Barnett J, Kanchi H, et al. (2007) Design analysis of a truss pontoon semi-submersible concept in deep water. *Ocean Engineering*, 34, 621-629.

Du Q G，FENG W，YAN S Z, et al. (2013).The research to the towage resistance of the pontoons with different shapes of a semi-submersible drilling platform, *China Offshore Platform*, 28(2), 39-44.

Nallayarasu S, Prasad P S. (2012). Hydrodynamic response of spar and semi-submersible interlinked by a rigid yoke-Part I: regular waves. *Ships and Offshore Structures*, 7(3), 297-309.

8th International Conference on the Application of Physical Modelling in Coastal and Port Engineering and Science
Dec. 9th - 12th, 2020, Zhoushan, China

MESO NUMERICAL SIMULATION OF CHLORIDE ION DIFFUSION IN CONCRETE BASED ON STOCHASTIC CONVEX POLYGON COARSE AGGREGATE MODEL

YUANZHAN WANG[(1)], ZHEHUI ZHOU[(1)], ZHEN LIU[(1)]&DUO WANG[(2)]

[(1)]State Key Laboratory of Hydraulic Engineering Simulation and Safety and Collaborative Innovation Center for Advanced Ship and Deep-Sea Exploration, Tianjin University, Tianjin, China,
yzwang@tju.edu.cn;472195343@qq.com;zliu@tju.edu.cn

[(2)] China Academy of Building Research, Beijing, China,
duowang1994@163.com

ABSTRACT

In the marine environment, the corrosion of steel in the reinforced concrete (RC) structure caused by chloride ion diffusion is one of the most significant factors affecting the durability of RC structures. Using physical model experiment method to explore the natural diffusion of chloride ion in concrete not only needs a lot of manpower, material resources, financial resources and time, but also is difficult to carry out long-term experimental research. Numerical simulation method is an efficient method to save a lot of physical experiment costs. In this paper, the concrete is regarded as a three-phase composite material composed of cement mortar, coarse aggregate and interfacial transition zone (ITZ) and a meso numerical model of chloride ion diffusion in concrete is established. Compared with the widely used extended convex algorithm, a more computationally efficient method, namely interpolation sorting algorithm, is proposed. This method can consider the influence of ITZ and generate convex polygon coarse aggregate randomly. The accuracy and reliability of the numerical model are verified by physical test, and the effect of coarse aggregate volume fraction on chloride ion diffusion was studied.

Keywords: concrete, chloride ion diffusion, meso numerical model, interpolation sorting algorithm

1 INTRODUCTION

In the marine environment, the durability damage of reinforced concrete (RC) structure is an important problem threatening its service life. The main factors that cause the durability damage of the RC structure are steel corrosion, concrete carbonization, concrete freeze-thaw cycle damage and so on (Lu, 1997). Among them, the steel corrosion caused by chloride ion diffusion is considered to be the most important factor. Therefore, it is significant to study the transport and diffusion characteristics of chloride ion in concrete in the marine environment for delaying the steel corrosion and improving the durability of RC structure.

At present, the research of chloride ion diffusion in concrete mostly adopts the physical model experiment method (Delagrave et al. 1997; Yang et al., 2002; Wang et al., 2014), it not only needs a lot of manpower, material resources, financial resources and time, but also the research cycle and research conditions have great limitations. In recent years, with the development of computer technology, some scholars began to establish numerical models to simulate the chloride ion diffusion in concrete (Wang L.C et al., 2008; Xiao J et al., 2012; Li L.Y et al., 2012). Compared with physical model, it is an efficient method which can save a lot of physical experiment costs and facilitate long-term research.

There are two kinds of numerical models: macro model and meso model (Bitaraf et al., 1997). The macro model considers that the concrete is a homogeneous material, and does not consider the influence of internal aggregate and interfacial transition zone (ITZ). However, the macro model ignores the composite material characteristics of concrete, and it is difficult to reveal the influence of each phase composition in concrete on the chloride ion diffusion characteristics clearly. The meso model considers that concrete is a three-phase composite material composed of cement mortar, coarse aggregate and ITZ (Duan et al., 1991). It is assumed that coarse aggregate is not available for chloride ion transport, and it have dilution effect and zigzag effect, which will hinder the chloride ion diffusion. On the contrast, ITZ has high porosity, which will accelerate the chloride ion diffusion (Shah et al., 2000). Therefore, the algorithm of stochastic generation and placement of coarse aggregate and ITZ is of great significance to the meso numerical simulation of chloride ion diffusion in concrete.

In the study of numerical simulation of chloride ion diffusion, Peng et al. (2009) used finite element method to study the influence of two-dimensional octagonal aggregate area fraction on chloride ion diffusion. Du et al. (2013) established two-dimensional meso models of concrete with different aggregate shapes, such as circle, regular quadrilateral and ellipse, and discussed the influence of different volume fraction of coarse aggregate, water cement ratio and other factors on chloride ion diffusion. Liu et al. (2015) established a circular aggregate model to study the ITZ and role of ion binding in chloride ion diffusion. Wang et al. (2018) used a spherical aggregate meso model to simulate the chloride ion diffusion, and established a long-term

prediction model in the marine tidal environment. In addition, some scholars also put forward the concrete models of irregular aggregate. Gao et al. (2003) put forward extended convex algorithm to build the model based on circle. Zheng et al. (2018) established the model based on the stochastic walk algorithm.

At present, most scholars simplify the coarse aggregate into regular shapes such as circle and regular polygon. However, in the actual project, the concrete coarse aggregate is mostly crushed stone, whose shape is closer to polygon. Therefore, numerical simulations using regular aggregates are quite different from actual ones. For irregular aggregate model established by a small number of scholars, the model generation and placement efficiency is low, and ITZ is not considered. In this paper, from the meso level, a new interpolation sorting algorithm is proposed to generate coarse aggregate, which is closer to actual ones. This method can consider the effect of ITZ, aggregate position and particle size distribution. The accuracy and reliability of the numerical model are verified by the comparison between the model calculation data and the experimental data.

2 Meso model of concrete stochastic convex polygon aggregate

The concrete is composed of cement mortar, coarse aggregate and ITZ the meso model, as shown in Figure 1. In this paper, a new interpolation sorting algorithm is used to develop stochastic convex polygon aggregate generation and placement, and a three-phase meso model of concrete is established for numerical simulation of chloride ion diffusion in concrete.

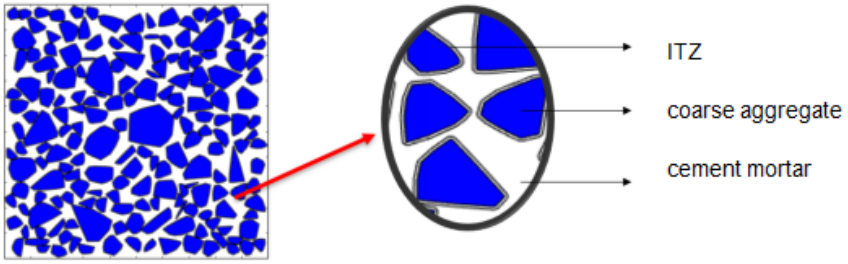

Figure 1. Meso model of concrete stochastic convex polygon aggregate

2.1 The generation of concrete stochastic convex polygon aggregate

The steps for generating aggregate randomly are as follows:

(1) Input the initial conditions.

They include the length and width dimensions *X* and *Y* of the concrete specimen, the volume fraction *V* of the aggregate, the minimum particle diameter d_{min}, the maximum particle diameter d_{max}, and the thickness of the interface transition zone *ITZ*. The particle diameters are the diameters of the smallest circumscribed circles of the convex polygon aggregates.

(2). Generate convex polygon aggregate particle size d_i randomly.

In order to make concrete have ideal workability and compactness, the particle size distribution of aggregate should meet the W.B.Fuller's grading curve. The aggregate cumulative frequency expression is given in Eq. [1]:

$$P_{(d)} = 1 - \frac{d_{\min}^2 (d_{\max}^2 - d_i^2)^{1.5}}{d_i^2 (d_{\max}^2 - d_{\min}^2)^{1.5}} \quad [1]$$

Where $P_{(d)}$ is the cumulative frequency of aggregate particle size larger than d_i.

(3). Take the circle with diameter d_i, and take any three points on the circle to form a triangle as the aggregate basic structure.

In order to ensure that the circumscribed circle is the smallest circumscribed circle, it is necessary to determine that the triangle is an acute-angled triangle. Otherwise, perform step 3 again.

(4). Store the triangle point and line information and calculate the aggregate area *s*.

(5). Insert a point in a circle as a new vertex of the convex polygon randomly. The following decisions are made simultaneously:

(a) Ensure that the point is outside the polygon. If it is inside, a new vertex is regenerated.

(b) Ensure that the new polygon formed by the combination of the vertex and the old polygon is a convex polygon (Beddow et al., 1980).

If the above conditions are met at the same time, go to step6, otherwise go to step5.

The convex polygon judgment method is as follows:

First, the triangle area formula in linear algebra is given in Eq. [2]:

$$S = \frac{1}{2} \begin{vmatrix} x_1 & y_1 & 1 \\ x_2 & y_2 & 1 \\ x_3 & y_3 & 1 \end{vmatrix} \quad [2]$$

Where (x_1, y_1), (x_2, y_2), and (x_3, y_3) are the coordinates of the three vertices of the triangle, and these three points are ordered counterclockwise. As shown in Figure 2, the new point P and the adjacent points are combined in a counterclockwise order to form two triangles PA_iA_{i+1} and $PA_{i-2}A_{i-1}$. The area of the two triangles is calculated according to Eq. [2]. When the obtained results are all greater than 0, it can be guaranteed that the newly generated polygon is a convex polygon, and if it is less than 0, it is a concave polygon.

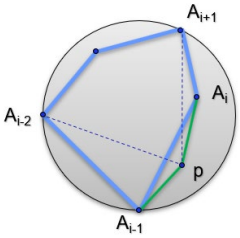

Figure 2. Discrimination of aggregate convexity

(6). Set the number of sides of convex polygon aggregate n.

Generally, the number of sides of crushed aggregate is 4~12(Hu et al., 2017). In order to reduce the sharp angle of the aggregate and make the stochastic characteristics of aggregates prominent, set n=12. Reorder and record the coordinates of each vertex of the new point, and add the new triangle area d_s to the current aggregate area s. When n = 12, stop and save aggregate information data into the cell array.

The above is a new interpolation sorting algorithm for generating concrete stochastic convex polygon aggregate. The process is repeated until the total aggregate content is greater than the set aggregate volume fraction, that is $s \geq X \times Y \times V$, the cycle is stopped.

The interpolation sorting algorithm proposed in this paper uses Monte Carlo method to generate stochastic convex polygon aggregates that conform to the W.B.Fuller's grading curve. Compared with the traditional extended convex algorithm, it has higher computational efficiency.

2.2 The placement of concrete stochastic convex polygon aggregate

The steps for placing aggregate randomly are as follows:

(1). Sort d in descending order.

When the aggregates are placed from large to small, it is easier to put small aggregates into the gap of large aggregates, which improves the placement capacity and efficiency.

(2). Place the aggregate i.

Generate the aggregate center coordinates (x_i, y_i)in the concrete specimen area $x_i \in (d_i/2, X - d_i/2)$, $y_i \in (d_i/2, Y - d_i/2)$.

(3). Determine whether the aggregate i overlaps the aggregate j (j=1, 2,⋯, i-1). The overlap situation is shown in Figure 3. The overlap discrimination steps are as follows:

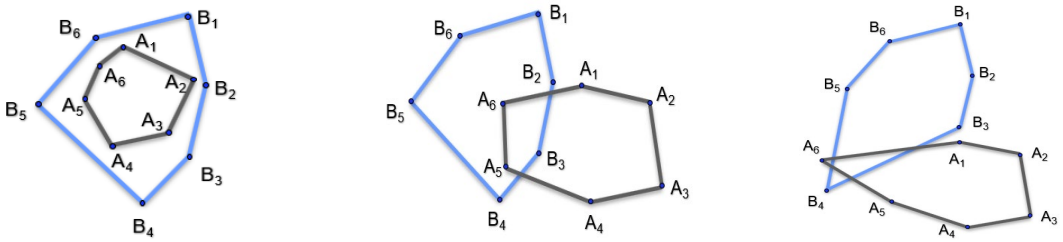

(a) Points included completely (b) Points included incompletely (c) No point included

Figure 3. Overlapping discrimination

(a) Determine whether the distance L_{ij} between the center of the aggregate i and the center of the aggregate j is greater than the sum of the radii of the two aggregates, if $(d_i/2 + d_j/2) < L_{ij}$, the two aggregates will not overlap and return to step2 to place the aggregate i+1. Otherwise, proceed to the next step.

(b) Determine whether each vertex position of the aggregate i is inside the aggregate j. If it is, it overlaps and returns to step2. If it is not, it performs the next step judgment

(c) Determine whether there is an intersection between the aggregate i and the aggregate j. If there are intersection points, overlap, and return to step2. If not, the aggregates do not intersect, and the delivery is successful. Return to step2 to place the aggregate i+1.

(4) If all generated aggregates are put into operation, stop circulation. Otherwise, return to step2 to place the aggregate i+1.

The interpolation sorting algorithm proposed in this paper sorts the aggregate particle diameter in descending order before putting, which improves the efficiency of overlapping discrimination greatly.

2.3 The generation of ITZ

The ITZ is due to the hydration reaction of the cement, which results in the micro structure between the concrete aggregate and the cement base. It has a greater calcium hydroxide content and porosity which is different from the cement. In meso studies, ITZ can be thought of as a film of uniform thickness wrapped around the outside of the aggregate.

Based on the above assumptions, after the convex polygon aggregates are generated and placed randomly, the vertices of each aggregate are translated a distance to the outside, and this distance is the thickness of ITZ. Subsequently, the translated points are connected in a counterclockwise direction, so that an ITZ with a customizable thickness can be obtained. The effect is shown in Figure 4.

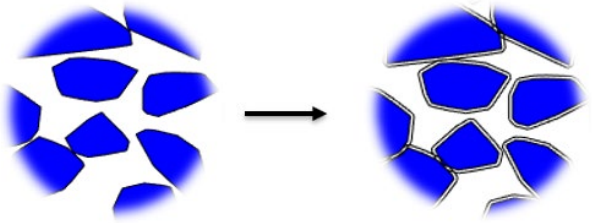

Figure 4. ITZ generation schematic diagram

The ITZ is soft and can be overlapped, so there is no need to distinguish the overlaps between the ITZ. On this basis, the aggregate, mortar and ITZ are treated separately in this paper. Based on the concept of "layer" in COMSOL, the coarse aggregate is located on the top of ITZ directly. Therefore, there is no need to distinguish the overlap between the ITZ and the coarse aggregate, which can improve the generation and calculation efficiency of the model.

2.4 Interaction between concrete model and numerical simulation software

This paper generates and places convex polygon aggregate randomly, and through the reference and modification of some main functions in DXFLlib function library, the model file is converted into DXF format file, as shown in Figure 5, which is convenient for subsequent import into COMSOL for further research.

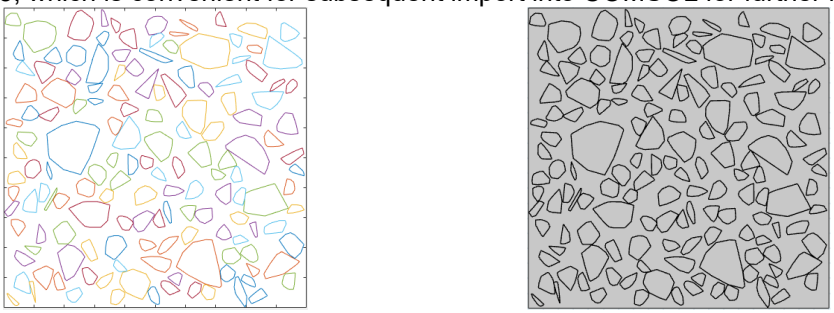

(a) generated model image (b) Effect of dxf file in COMSOL

Figure 5. Model transformation effect

In this paper, the meso model of the stochastic convex polygon aggregate is close to the actual concrete. Compared with the concrete models of other scholars, the numerical simulation method has the following advantages:

(a) the algorithm is concise and clear, the calculation efficiency is high, and the non-overlap effect of aggregates is considered.

(b) Based on the concept of "layer" in COMSOL, it is possible to generate a micron-thick ITZ around the coarse aggregate.

(c) Through the interaction between concrete model and numerical simulation software, the concrete model established can be converted into a dxf file and imported into COMSOL to calculation directly, greatly improving the overall efficiency of the numerical simulation process.

3 Model validation

3.1 Model calculation results verification

Lv (2017) made concrete test block with cross-section dimensions of 100×100×100mm^3 and coarse aggregate volume fractions of 20%, 30%, and 40%. Epoxy resin was used to seal chloride ion transmission on the other five surfaces except the eroded surface. The artificial marine environment tidal zone automatic simulation device was used to determine the chloride ion concentration of each group of concrete test block at

different depths under different tidal cycle times (60d, 100d, 140d, and 180d) to explore the influence of coarse aggregate on chloride ion diffusion in concrete.

In order to verify the rationality of the calculation results of the numerical model in this paper, COMSOL was used for numerical simulation. The chloride ion diffusion model is considered based on Fick's second law considering time-varying effects.

Based on the research conditions of the above-mentioned physical experiments, a meso model of stochastic convex polygonal aggregates of concrete with the same size and coarse aggregate volume fraction was established. The models are shown in Figure 6. Numerical simulations were performed on 10 groups with different coarse aggregate volume fractions. The surface chloride concentration is taken as the boundary condition, and the numerical simulation parameter settings are shown in Table 1. The concentration distribution of chloride ion along the depth at different diffusion times was calculated, and the mean value of ten groups was taken as the result for data analysis.

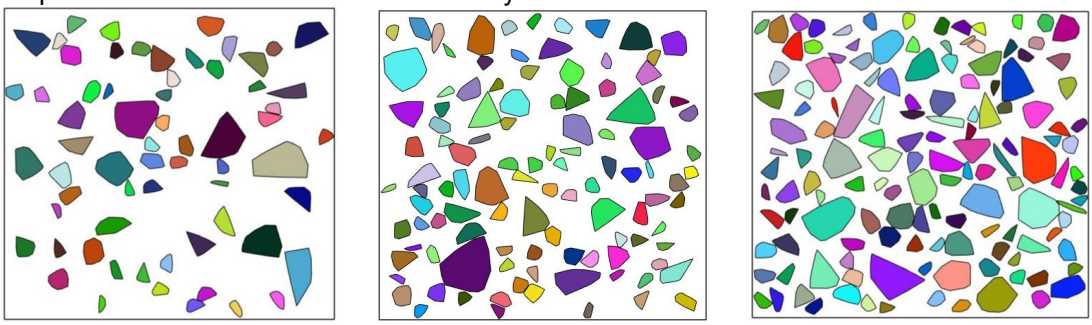

(a) V=20% (b) V=30% (c) V=40%

Figure 6. Stochastic model of concrete with different coarse aggregate volume fractions

Table 1. Numerical model calculation parameters.

Initial chloride ion concentration C_0(%)	Surface chloride concentration C_S(%)	Coarse aggregate diffusion coefficient D_a(m²/s)	mortar diffusion coefficient D_0(m²/s)	Age decay coefficient m	Thickness of ITZ h(um)	Diffusion coefficient multiple of ITZ r
0	0.6047ln(t)-1.6433	0	6.423×10^{-12}	0.333	30	30

The chloride ion concentration results obtained by numerical simulation calculation under different aggregate volume fractions are compared with the physical test results, and a three-dimensional comparison chart is drawn as shown in Figure 7. In the Figure 7, SM denotes the result of numerical simulation calculation and PM denotes the result of physical model test.

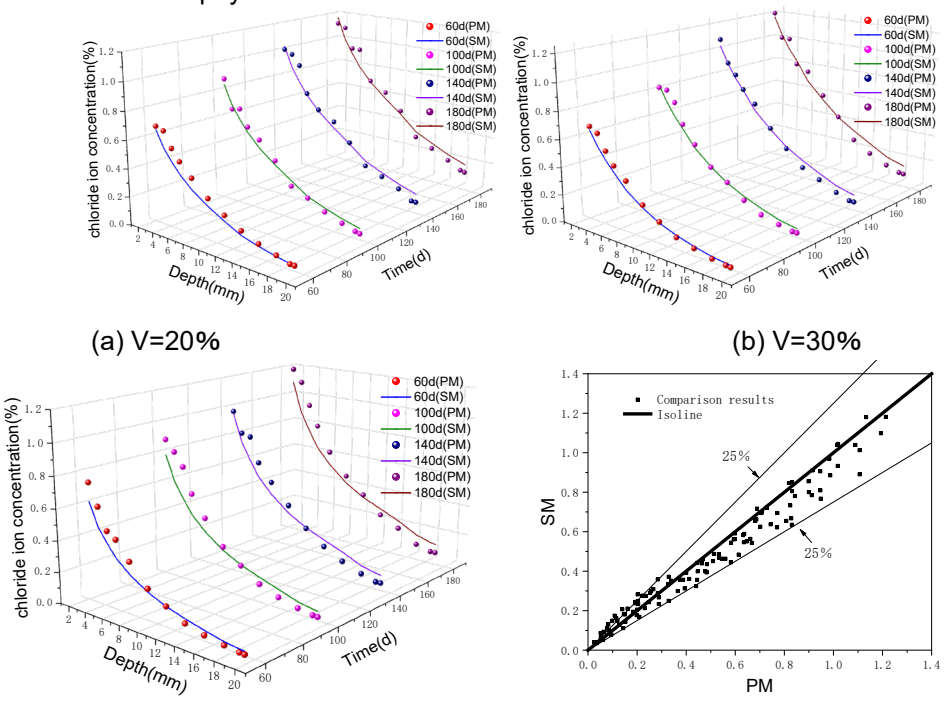

(a) V=20% (b) V=30%

(c) V=40% (d) error analysis

Figure 7. Comparison of chloride ion concentration at different coarse aggregate volume fractions

It can be found that the concentration distribution trends are similar. The chloride ion concentration decreases with increasing depth, and the curve forms are similar, and the concentration approaches 0 at deeper depths. The error is basically controlled within 25%, at larger depths, numerical simulation results are higher than the results of physical tests. The main reason can be attributed to the lack of sensitivity of the instrument for measuring the concentration of chloride ions during the test. To sum up, the chloride ion diffusion results obtained by the numerical calculation of the stochastic concrete model established in this paper fit well with the physical test results and have high reliability.

4 Effect of coarse aggregate volume fraction on chloride ion diffusion

According to the meso model of concrete stochastic convex polygonal aggregate introduced in Chapter 2, the models with coarse aggregate volume fractions of 0 (only containing cement mortar), 10%, 20%, 30%,40% and 50% are established. The initial conditions, boundary conditions and other settings are shown in Table 1. Set the solution step size to 5d and the total solution time to 1800d. The numerical simulation method proposed in this paper was used to study the effect of coarse aggregate volume fraction on the diffusion characteristics of chloride ion. Due to the large number of groups, only the chloride ion concentration cloud in the concrete with a volume fraction of 50% of coarse aggregate at t=1800d is shown in Figure. 8.

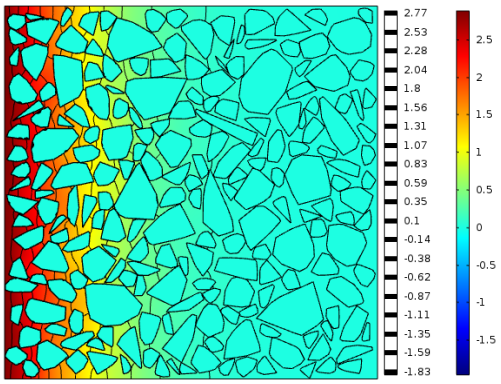

Figure 8. Chlorine ion concentration calculation cloud

It can be seen from the Figure 8. that chloride ion is concentrated near the front of the coarse aggregate, which shows that the presence of coarse aggregate will hinder the chloride ion diffusion. The blocked chlorine ion will gather at the front of the aggregate, and the corresponding chloride ion concentration at the back of the aggregate will be relatively reduced.

In order to reduce the error caused by the randomness of the model, the ten groups of numerical models with coarse aggregate volume fraction of 0, 10%, 20%, 30%, 40%, 50% were calculated. The calculation results of 10 groups of models are averaged, and the distribution curve of the chloride ion concentration along the depth at different times is shown in Figure 9.

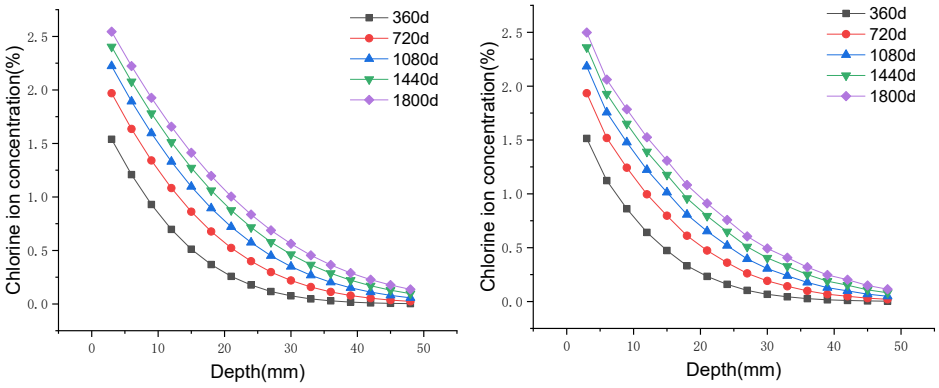

(a) V=0%　　(b) V=10%

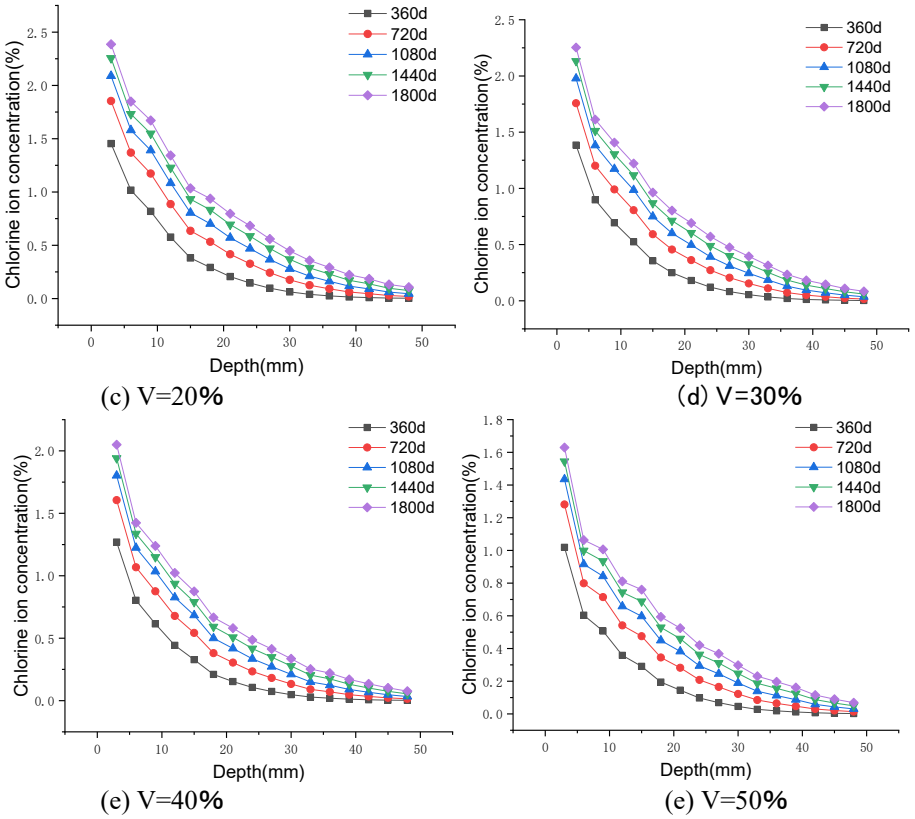

Figure 9. Concrete chloride ion concentration distribution along depth

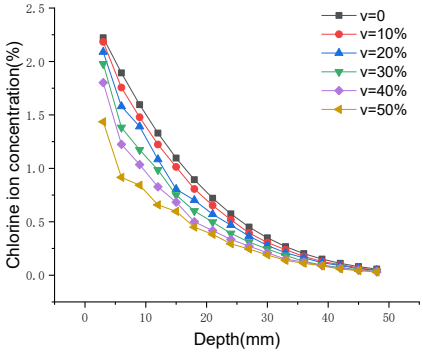

Figure 10. Chloride ion concentration along depths for different coarse aggregate volume fractions

It can be seen from Figure.9 that the chloride ion content in concrete will increase with diffusion time, and the chloride ion concentration at the same depth will increase accordingly. In order to observe the influence of coarse aggregate volume fraction on chloride ion diffusion, the chloride ion concentration of different coarse aggregate volume fractions at the diffusion time t=1080d was analyzed, as shown in Figure. 10. With the increase of coarse aggregate volume fraction, the chloride ion concentration at the same depth decreases significantly. This shows that although the ITZ will accelerate the diffusion of chloride ion, it is weaker than dilution effect and zigzag effect of coarse aggregate which hinder the chloride ion diffusion.

5 CONCLUSIONS

In this paper, concrete chloride ion diffusion model based on concrete stochastic convex polygon coarse aggregate and ITZ is established. COMSOL was used to perform numerical simulation analysis in the established model. The specific research results are as follows:

(a) Considering the characteristics of three-phase meso of concrete, a meso model of concrete chloride ion diffusion including cement mortar, coarse aggregate, and ITZ was established. The model with interpolation sorting algorithm is simple and clear, and the calculation efficiency is high, which meets the requirements of non-overlapping aggregate. At the same time, the randomness of the aggregate particle size and location distribution is well considered, so that the generated model is more similar with actual concrete.

(b) The stochastic concrete model of the same size, initial and boundary conditions as physical tests is established for numerical simulation. The calculated results of chloride ion concentration distribution were compared with the results of physical experiments, which verifies the reliability of the numerical simulation method of chloride ion diffusion based on the concrete stochastic convex polygonal aggregate model.

(c) Concrete models with different coarse aggregate volume fractions were established to investigate the influence of coarse aggregate content on the chloride ion diffusion. It is found that the concentration of chloride ion decreases with the increase of the coarse aggregate volume fraction. Compared with the ITZ effect, the dilution effect and zigzag effect of coarse aggregate play a leading role.

(d) The numerical simulation method of stochastic convex polygon aggregate proposed in this paper has high calculation efficiency, and its calculation results are relatively reliable, which can be used as an important method for studying the chloride ion diffusion problem of concrete.

ACKNOWLEDGEMENTS

This research was supported by the National Key Research and Development Program of China (2016YFC0802204, 2016YFC0802201), the National Natural Science Foundation of China (51979191).

REFERENCES

Beddow, John K. (1980). *Testing and characterization of powders and fine particles*. London, Heyden, 59-64.

Bitaraf M, Mohammadi S. (2008) Analysis of chloride diffusion in concrete structures for prediction of initiation time of corrosion using a new meshless approach. *Construction & Building Materials*, 22(4):546-556.

Caré S. (2003). Influence of aggregates on chloride diffusion coefficient into mortar. *Cement & Concrete Research*, 33(7):1021-1028.

Delagrave A, Bigas J.P, Ollivier J.P, et al. (1997). Influence of the Interfacial Zone on the Chloride Diffusivity of Mortars. *Advanced Cement Based Materials*, :86-92.

Du X.L, Jin L, Ma G.W. (2013). A meso-scale analysis method for the simulation of nonlinear damage and failure behavior of reinforced concrete members. I*nternational Journal of Damage Mechanics*,22(6):878-904.

Duan S.J. (1991). Brief introduction of the durability design criteria for concrete structures (Trial) in Japan. *Journal of North China University of Water Resources and Electric Power*, 1:56-60.

Gao Z.G, Liu G.Y. (2003). Two-dimensional random aggregate structure for concrete. *Journal of Tsinghua University (Science and Technology)*, 43(5):135-139.

Hu D.L, Zhang L.X, Chen D.S. (2017). The establishment and application of two-dimensional meso-random concrete model. *Journal of Chang'an University (Natural Science Edition),* 37(3):53-63.

Kwiatek G. MATLAB library for creating 2D/3D dxf files. [EB/OL]. http://www.induced.pl/projects/dxflib.

Li L.Y, Xia J, Lin S.S. (2012). A multi-phase model for predicting the effective diffusion coefficient of chlorides in concrete. *Construction & Building Materials*, 26(1):295-301.

Liu Q.F, Easterbrook D, Yang J, et al. (2015). A three-phase, multi-component ionic transport model for simulation of chloride penetration in concrete. *Engineering Structures*, 86:122-133.

Lu M. (1997). Recent study and research directions of concrete durability. *Industrial Construction*, 27(5):1-6.

Lv Y.W. (2017). *Experimental Study on Chloride Diffusion of Concrete Members Considering the Coaction of Coarse Aggregate and Steel Bar*. Tianjin University.

Peng G.J, Zheng J.J, Zhou Y.Q. (2009). A numerical method for predicting the chloride diffusion coefficient of concrete with aggregate shap. *Advances in Science and Technology of Water Resources*, 29(6):13-16.

Shah S.P. (2000). *High Performance Concrete, Past, Present and Future*. Hong Kong University of Science and Technology, Book, 3-29.

Wang L.C, Wang Z.J. (2008). Mesoscopic simulation for chloride diffusion in concrete. *Journal of Building Structures*, 29(s1):192-196.

Wang Y.Z, Lin C.A.P, Cui Y.Q. (2014). Experiments of Chloride Ingression in Loaded Concrete Members under the Marine Environment. *Journal of Materials in Civil Engineering*, 26(6):1-7.

Wang Y.Z, Wu L.J, Wang Y.C, et al. (2018). Prediction model of long-term chloride diffusion into plain concrete considering the effect of the heterogeneity of materials exposed to marine tidal zone. *Construction & Building Materials*, 159:297-315.

Wittmann F.H, Roelfstra P.E, Sadouki H. (1985). Simulation and analysis of composite structures. *Materials Science & Engineering*, 68(2):239-248.

Xi Y.P, Willam K, Frangopol D.M. (2000). Multiscale Modeling of Interactive Diffusion Processes in Concrete. *Journal of Engineering Mechanics*, 126(3):258-265.

Xiao J.Z, Ying J.W, Shen L.M. (2012). FEM simulation of chloride diffusion in modeled recycled aggregate concrete. *Construction & Building Materials*, 29:12-23.

Yang C.C, Su J.K. (2002). Approximate migration coefficient of interfacial transition zone and the effect of aggregate content on the migration coefficient of mortar. *Cement & Concrete Research*, 32(10):1559-1565.

Zheng J.J, Zhang J, Zhou X.J, et al. (2018). A numerical algorithm for evaluating the chloride diffusion coefficient of concrete with crushed aggregates. *Construction & Building Materials*, 171:977-983.

8th International Conference on the Application of Physical Modelling in Coastal and Port Engineering and Science
Dec. 9th - 12th, 2020, Zhoushan, China

DERIVATION OF FORMULAS FOR SEDIMENT CARRYING CAPACITY AND EROSION AND DEPOSITION STRENGTH APPLICABLE TO CHANNEL SILTATION CALCULATION ON SILTY MUD COAST

XIAOTIAN DONG(1), WENJIN ZHU(2)*, CONGYING KONG(3), NA WANG(4)

(1,2,4)Jiangsu Ocean University, Lianyungang, China
dongxt@jou.edu.cn; zhucius@jou.edu.cn; 1098577677@qq.com
(3)Tianjin Port Engineering Institute Co., Ltd. of CCCC First Harbor Engineering Co., Ltd., Tianjin, 300222,China;
CCCC First Harbor Engineering Company Ltd., Tianjin, China
kongcongying@tpei.com.cn

ABSTRACT

Silt siltation is an important problem in channel construction. Sediment transport in channel had been a research hotspot because of its uniqueness. Based on the cross-section characteristics of channel, and in view of the problem that most of the existing formulas are semi-empirical and semi-theoretical, with assumption and simplification of the motion of sediment-laden flow, this paper deduces the formulas for calculating the flow carrying force and seabed scouring and silting strength from the perspective of hydrodynamic equilibrium of sediment-laden flow.

Keywords: sediment carrying capacity; seabed erosion and deposition; sediment-laden flow; silty mud coast.

1 INTRODUCTION

An important problem in waterway engineering construction is silt siltation. The shoal of silty mud coast has a gentle slope, and generally has a deep silt layer. Under the great excavation depth of channel, the channel slope has poor stability. For deepwater channel dredging in shoal, there is abundant sediment source on both sides of the channel. The shear strength of the channel slope is slightly lower because of mechanical damage on the seabed surface layer structure caused by dredging, which constitutes the main factor of silt siltation in deepwater channel of silty mud coast. Silt siltation in open channel is more complicated: smaller channel cover area, stronger wave power, worse extreme sea conditions, which usually trigger sediment deposition during long-term or sudden siltation, occuring in Tianjin Port, Huanghua Port, Jingtang Port, Lianyungang Port, Hangzhou Bay and Changjiang Estuary channel.

The research methods of sediment deposition mainly include the analysis of measured data, empirical and semi-empirical formula calculation, numerical simulation, physical model test and so on. Among them, the empirical and semi-empirical sediment calculation formula shows good applicability and ease of use in the application (Cao et al., 2010; Wang et al.,2000; Liu et al., 1990). Many researchers have put forward semi-theoretical and semi-empirical formulas for channel silt siltation calculation and seabed erosion and deposition in silty mud coast, such as Liu Jiaju formula, Cao Zude formula, Yu Yi-jin formula, Le Pei-Jiu formula, Luo Zhao-sen formula and Li Wang-sheng formula, etc. Among them, Liu Jiaju's formula are widely applicable. Based on approach channel under equilibrium between scouring and deposition, considering the angle between channel trend and flow direction, assuming suspended sediment falls evenly from water body to the channel, Liu established the widely used formula for channel silt siltation strength calculating (Liu et al., 1990), which became recommended formula on "Code of Hydrology for Harbour and Waterway".

2 DERIVATION OF DYNAMIC BALANCE EQUATION OF SEDIMENT-LADEN FLOW

It is assumed that the x-axis and the flow velocity of sediment-laden flow V are parallel to the interface of seawater and sediment-laden flow, the flow velocity of seawater is $\bar{U}_1$, and the positive direction is consistent with the direction of sediment-laden flow, so a motion model of sediment-laden flow is constructed, as shown in Figure 1.

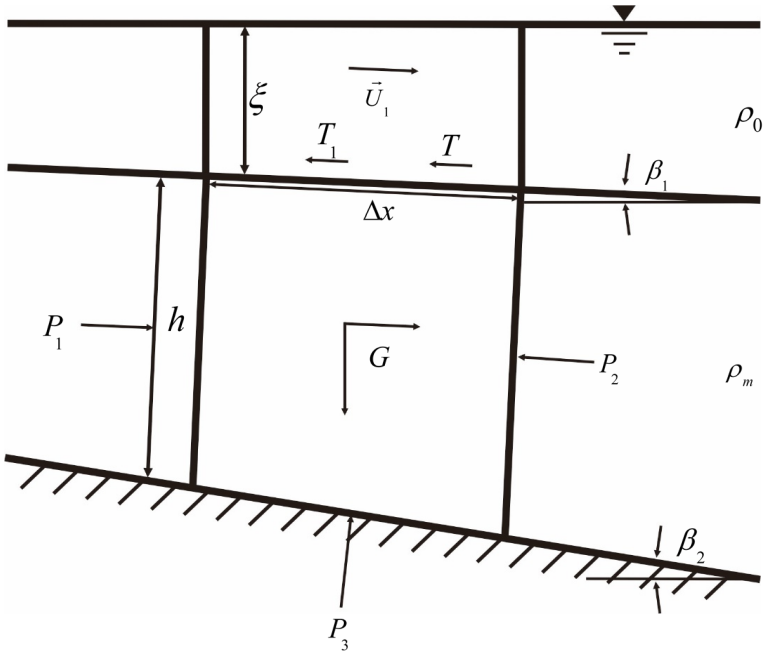

Figure. 1 Force analysis schematic diagram of sediment-laden flow

Considering the sediment-laden flow with *a* width, Δx length and J_0 slope as the research object, the force on the flow direction of this section of sediment-laden flow includes the following parts:

Pressure on sediment-laden flow

$$P_1 = a\int_0^h \left(\rho_0 g\xi + \int_z^h \rho_m g\mathrm{d}z\right)\mathrm{d}z \quad [1]$$

$$P_2 = a\int_0^{h+\frac{\partial h}{\partial x}\Delta x}\left[\rho_0 g\left(\frac{1}{\Delta x}\int_{x_0}^{x_0+\Delta x}\xi\mathrm{d}x\right) + \int_z^{h+\frac{\partial h}{\partial x}\Delta x}\rho_m g\mathrm{d}z\right]\mathrm{d}z \quad [2]$$

$$P_3\sin\left(\beta_2-\beta_1\right) = \left[\frac{1}{\Delta x}\int_{x_0}^{x_0+\Delta x}\rho_0 g\xi\mathrm{d}x + \frac{1}{\Delta x}\int_{x_0}^{x_0+\Delta x}\left(\frac{1}{h}\int_0^h\rho_m\mathrm{d}z\right)gh\mathrm{d}x\right]\frac{a\Delta x}{\cos\left(\beta_2-\beta_1\right)}\sin\left(\beta_2-\beta_1\right) \quad [3]$$

In equation [3], ξ is the depth of seawater; h is sediment-laden flow depth; ρ_m, ρ_s and ρ_0 are the bulk density of sediment-laden flow, sediment and seawater, respectively.

The gravity of the research object is

$$G\sin\beta_2 = a\frac{1}{h+\frac{\partial h}{\partial x}\Delta x}\int_0^{h+\frac{\partial h}{\partial x}\Delta x}\left[\int_{x_0}^{x_0+\Delta x}\rho_m gh\mathrm{d}x\right]\mathrm{d}z\sin\beta_2 \quad [4]$$

The total resistance of the research object T includes bed resistance T_b, seawater resistance at the interface T_1 and side resistance T_c

$$\begin{aligned} T = T_b\cos\left(\beta_2-\beta_1\right)+T_1+T_c &= \frac{f_0'}{8}\rho_{ma}V^2a\Delta x + \frac{f_1'}{8}\rho_{m0}V^2a\Delta x \\ &+ 2\frac{f_c}{8}V^2\int_{x_0}^{x_0+\Delta x}h\mathrm{d}x\frac{1}{h}\int_0^h\rho_m\mathrm{d}z \end{aligned} \quad [5]$$

In equation [5], $f_0^{'}$ and $f_1^{'}$ are bed resistance coefficient, resistance coefficient of sediment-laden flow and seawater interface, respectively. f_c is side resistance coefficient, ρ_{ma} is sediment-laden flow density at reference height, and ρ_{m0} is sediment-laden flow density at sediment-laden flow and seawater interface.

The inertia force of sediment-laden flow due to acceleration or deceleration is

$$I = \frac{1}{\Delta x}\int_{x_0}^{x_0+\Delta x}\int_0^h\rho_m\mathrm{d}z\mathrm{d}x\Delta xa\frac{dV}{dt} \quad [6]$$

The density of sediment-laden flow is $\rho_m = \rho_0 + \frac{\rho_s - \rho_0}{\rho_s} S$. Because the integration along water depth of suspended sediment distribution is very complex, in order to simplify the derivation process and reveal the movement law of sediment-laden flow model, the vertical variation of sediment-laden flow density is simplified as follows

$$k_1 = \frac{\int_0^h \left(\int_z^h \rho_m \mathrm{d}z \right) \mathrm{d}z}{\rho_m \frac{h^2}{2}} = \frac{\int_0^{h+\frac{\partial h}{\partial x}\Delta x} \left(\int_z^{h+\frac{\partial h}{\partial x}\Delta x} \rho_m \mathrm{d}z \right) \mathrm{d}z}{\rho_m \frac{\left(h + \frac{\partial h}{\partial x}\Delta x \right)^2}{2}} \quad [7]$$

$$k_1' = \frac{\int_0^h \rho_m \mathrm{d}z}{h\rho_m} = \frac{\int_0^{h+\frac{\partial h}{\partial x}\Delta x} \rho_m \mathrm{d}z}{\left(h + \frac{\partial h}{\partial x}\Delta x \right)\rho_m} \quad [8]$$

$$k_2 = \frac{\rho_{ma}}{\rho_m} \quad [9]$$

$$k_2' = \frac{\rho_{m0}}{\rho_m} \quad [10]$$

In equation [7] ~ equation [10], k_1, k_1', k_2 and k_2' are coefficients to correct the uneven distribution of sediment-laden flow density along the water depth.

Then equation [1] ~ equation [6] can be reduced to

$$P_1 = \left(\rho_0 g \xi h + k_1 \rho_m g \frac{h^2}{2} \right) a \quad [11]$$

$$\begin{aligned} P_2 &= a\left[\rho_0 g \left(\xi + \frac{\partial \xi}{\partial x}\Delta x \right)\left(h + \frac{\partial h}{\partial x}\Delta x \right) + k_1 \frac{\rho_m g}{2}\left(h + \frac{\partial h}{\partial x}\Delta x \right)^2 \right] \\ &= \left[\rho_0 g \xi h + k_1 \rho_m g \frac{h^2}{2} + \left(\rho_0 g \xi + k_1 \rho_m g h \right)\frac{\partial h}{\partial x}\Delta x + \rho_0 g h \frac{\partial \xi}{\partial x}\Delta x \right] a \end{aligned} \quad [12]$$

$$\begin{aligned} P_3 \sin\left(\beta_2 - \beta_1\right) &= \left[\rho_0 g \left(\xi + \frac{\partial \xi}{\partial x}\frac{\Delta x}{2} \right) + k_1' \rho_m g \left(h + \frac{\partial h}{\partial x}\frac{\Delta x}{2} \right) \right] \frac{a\Delta x}{\cos\left(\beta_2 - \beta_1\right)} \sin\left(\beta_2 - \beta_1\right) \\ &= \left(\rho_0 g \xi + k_1' \rho_m g h \right)\frac{\partial h}{\partial x} a \Delta x \end{aligned} \quad [13]$$

$$G \sin\beta_1 = k_1' \rho_m g \left(h + \frac{\partial h}{\partial x}\frac{\Delta x}{2} \right)\Delta x \sin\beta_1 a = k_1' \rho_m g h \frac{\partial \xi}{\partial x}\Delta x a \quad [14]$$

$$\begin{aligned} T = T_b \cos\left(\beta_2 - \beta_1\right) + T_1 + T_c &= k_2 \frac{f_0'}{8}\rho_m V^2 a \Delta x + k_2' \frac{f_1'}{8}\rho_m V^2 a \Delta x \\ &+ 2k_1' \frac{f_c}{8}\rho_m V^2 h \Delta x \end{aligned} \quad [15]$$

$$I = k_1' \rho_m \left(h + \frac{\partial h}{\partial x}\frac{\Delta x}{2} \right)\Delta x \frac{\mathrm{d}V}{\mathrm{d}t} a = k_1' \rho_m h \Delta x a \left(\frac{\partial V}{\partial t} + V \frac{\partial V}{\partial x} \right) \quad [16]$$

In addition, the additional stress T' caused by the reverse flow of the upper layer of sediment-laden flow at velocity V_1 can be written as

$$T' = \tau' \Delta x a \quad [17]$$

In equation [17], τ' is additional stress.

Therefore, the equilibrium equation of force on sediment-laden flow is

$$P_1 - P_2 + P_3 \sin(\beta_2 - \beta_1) + G \sin \beta_1 - T - T' = I \quad [18]$$

By substituting equation [11] ~ [17] into equation [18] and assuming $k_1 = k_1'$, the force balance equation is simplified as

$$\begin{aligned}(k_1\rho_m - \rho_0) gh \frac{\partial \xi}{\partial x} - \frac{\left(k_2 f_0' + k_2' f_1'\right)}{8} \rho_m V^2 - \frac{h}{a} k_1 \frac{f_c}{4} \rho_m V^2 - \tau' \\ = k_1 \rho_m h \left(\frac{\partial V}{\partial t} + V \frac{\partial V}{\partial x} \right)\end{aligned} \quad [19]$$

Because of the following relationship between bed elevation and sediment-laden flow depth

$$\frac{\partial \xi}{\partial x} = -\frac{\partial (Z_0 + h)}{\partial x} = J_0 - \frac{\partial h}{\partial x} \quad [20]$$

By substituting equation [20] into equation [19] and making the comprehensive resistance coefficient $f = k_2 f_0' + k_2' f_1'$, equation [19] can be simplified as

$$J_0 - \frac{\partial h}{\partial x} - \frac{f}{8} \frac{V^2}{\frac{k_1\rho_m - \rho_0}{\rho_m} gh} - \frac{f_c}{4a} \frac{V^2}{\frac{k_1\rho_m - \rho_0}{k_1\rho_m} g} - \frac{\tau'}{h(k_1\rho_m - \rho_0) g} = \frac{1}{\frac{k_1\rho_m - \rho_0}{k_1\rho_m} g} \left(\frac{\partial V}{\partial t} + V \frac{\partial V}{\partial x} \right) \quad [21]$$

Equation [21] is the dynamic balance equation of sediment-laden flow. In the next section, the sediment carrying capacity formula will be derived from the dynamic balance equation of sediment-laden flow under the condition of stable and uniform state.

3 DERIVATION OF SEDIMENT CARRYING CAPACITY FORMULA

According to the derived dynamic balance equation of sediment-laden flow, if it is extended to the whole depth range, in equation [21], h is water depth and V is vertical average velocity of sediment-laden flow.

Under the condition of stable and uniform sediment-laden flow, equation [21] is transformed into

$$J_0 - \frac{f}{8} \frac{V^2}{\frac{k_1\rho_m - \rho_0}{\rho_m} gh} - \frac{f_c}{4a} \frac{V^2}{\frac{k_1\rho_m - \rho_0}{k_1\rho_m} g} - \frac{\tau'}{h(k_1\rho_m - \rho_0) g} = 0 \quad [22]$$

Multiply both sides of the equation by $\frac{k_1\rho_m - \rho_0}{\rho_m}$, equation [22] is reduced to

$$\frac{k_1\rho_m - \rho_0}{\rho_m} J_0 - \frac{f}{8} \frac{V^2}{gh} - k_1 \frac{f_c}{4a} \frac{V^2}{g} - \frac{\tau'}{\rho_m gh} = 0 \quad [23]$$

(1) Suppose $k_1 = 1$, sediment-laden flow density is $\rho_m = \rho_0 + \frac{\rho_s - \rho_0}{\rho_s} S$, ρ_0 is seawater density, ρ_s is sediment density, S is sediment concentration (kg/m^3), then equation [23] is transformed into

$$J_0 \left(\frac{\rho_m - \rho_0}{\rho_m} \right) = \frac{f}{8} \frac{V^2}{gh} + \frac{f_c}{4a} \frac{V^2}{g} + \frac{\tau'}{\rho_m gh} \quad [24]$$

Let $\chi_1 = \frac{f}{8} \frac{V^2}{gh} + \frac{f_c}{4a} \frac{V^2}{g} + \frac{\tau'}{\rho_m gh}$, then equation [24] can be written as

$$J_0 \left(\frac{(\rho_s - \rho_0) S}{(\rho_s - \rho_0) S + \rho_0 \rho_s} \right) = \chi_1 \quad [25]$$

Reduction to get

$$S = \frac{\rho_0 \rho_s \chi_1}{(\rho_s - \rho_0)(J_0 - \chi_1)} \quad [26]$$

Equation [26] is the sand carrying capacity formula applicable to rivers and nearshore sea area. When the sediment-laden flow is extended to the full depth, the resistance at the interface between sediment-laden flow

and seawater is $\frac{f_1'}{8}\frac{V^2}{gh}=0$. In the nearshore sea area, if the side boundary is nearly infinite, the side resistance is $\frac{f_c}{4a}\frac{V^2}{g}=0$, there it is $\chi_1=\frac{k_2 f_0'}{8}\frac{V^2}{gh}$, equation [26] can be simplified as follows

$$S=k_2 C_D\frac{\rho_0\rho_s}{\rho_s-\rho_0}\frac{1}{(J_0-\chi_1)}\frac{V^2}{gh} \quad [27]$$

In equation [27], the resistance coefficient is $C_D=\frac{f_0'}{8}$; k_2 is the coefficient to correct the non-uniform bulk density of sediment-laden flow along water depth. When it is assumed that the density of sediment-laden flow is uniform along water depth, there is $k_2=1$. Equation [27] is sediment carrying capacity formula that suited for offshore waters.

It can be seen from equation [27] that when $\chi_1=o(J_0)$, equation [27] can be written in a more concise form

$$S=k_2\frac{C_D}{J_0}\frac{\rho_0\rho_s}{\rho_s-\rho_0}\frac{V^2}{gh} \quad [28]$$

Equation [28] is consistent with the general formula of sediment carrying capacity (Li et al., 2014).

(2) If $\chi_2=\frac{f}{8}\frac{V^2}{gh}+\frac{f_c}{4a}\frac{V^2}{g}$, then equation [23] can be written as

$$J_0\left(\frac{(\rho_s-\rho_0)S}{(\rho_s-\rho_0)S+\rho_0\rho_s}\right)-\frac{\rho_s}{(\rho_s-\rho_0)S+\rho_0\rho_s}\frac{\tau'}{gh}=\chi_2 \quad [29]$$

Reduction to get

$$S=\frac{\rho_0\rho_s\chi_2+\rho_s\frac{\tau'}{gh}}{(\rho_s-\rho_0)(J_0-\chi_2)} \quad [30]$$

In equation [30], τ is the surface wind stress.

Equation [30] is the sediment carrying capacity formula which can be applied to offshore waters considering the effect of surface wind stress. Similarly, if the sediment-laden flow is extended to the full depth, the resistance of the interface between sediment-laden flow and seawater is $\frac{f_1'}{8}\frac{V^2}{gh}=0$; in nearshore sea area, the side resistance is $\frac{f_c}{4a}\frac{V^2}{g}=0$ if the side boundary is nearly infinite, so $\chi_2=\frac{k_2 f_0'}{8}\frac{V^2}{gh}$, equation [26] can be simplified as

$$S=k_2 C_D\frac{\rho_0\rho_s}{\rho_s-\rho_0}\frac{1}{(J_0-\chi_2)}\frac{V^2}{gh}+\frac{\rho_s}{\rho_s-\rho_0}\frac{1}{(J_0-\chi_2)}\frac{\tau'}{gh} \quad [31]$$

In equation [31], the resistance coefficient is $C_D=\frac{f_0'}{8}$. Equation [31] is sediment carrying capacity formula considering the effect of surface wind stress.

(3) In general, $k_1\neq 1$, it corresponds to the second case

Let $\chi_3=\frac{1}{k_1}\left(\frac{f}{8}\frac{V^2}{gh}+k_1\frac{f_c}{4a}\frac{V^2}{g}\right)$, then equation [23] can be written as

$$J_0\frac{k_1\left[(\rho_s-\rho_0)S+\rho_0\rho_s\right]-\rho_0\rho_s}{(\rho_s-\rho_0)S+\rho_0\rho_s}-\frac{\rho_s}{(\rho_s-\rho_0)S+\rho_0\rho_s}\frac{\tau'}{gh}=k_1\chi_3 \quad [32]$$

Reduction to get

$$S=\frac{k_1\rho_0\rho_s\chi_3+\rho_s\frac{\tau'}{gh}-J_0\rho_0\rho_s\left(k_1-1\right)}{k_1\left(\rho_s-\rho_0\right)\left(J_0-\chi_3\right)} \quad [33]$$

Equation [33] is sediment carrying capacity formula applicable to rivers and coastal waters, which considering the effect of surface wind stress. Similarly, if the sediment-laden flow is extended to all water depths, the resistance at the interface between sediment-laden flow and seawater is $\frac{f_1'}{8}\frac{V^2}{gh}=0$; in coastal waters, if the side boundary is nearly infinite, then the side resistance is $\frac{f_c}{4a}\frac{V^2}{g}=0$. Therefore $\chi_3=\frac{k_2f_0'}{8k_1}\frac{V^2}{gh}$, equation [32] can be simplified as

$$S=\frac{k_2}{k_1}C_D\frac{\rho_0\rho_s}{\rho_s-\rho_0}\frac{1}{\left(J_0-\chi_3\right)}\frac{V^2}{gh}+\frac{1}{k_1}\frac{\rho_s}{\rho_s-\rho_0}\frac{1}{\left(J_0-\chi_3\right)}\frac{\tau'}{gh}-\frac{\left(k_1-1\right)}{k_1}\frac{\rho_0\rho_s}{\rho_s-\rho_0}\frac{1}{\left(J_0-\chi_3\right)}J_0 \quad [34]$$

In equation [34], the resistance coefficient is $C_D=\frac{f_0'}{8}$. Equation [34] is sediment carrying capacity formula suited in coastal waters, with the effect of surface wind stress is considered.

4 KEY PARAMETERS

According to the three sediment carrying capacity formulas [27], [31] and [34] which are applicable to the nearshore sea area, it can be seen that the relevant undetermined parameters of the three formulas are the flow resistance coefficient C_D and the slope J_0.

4.1 Slope

Generally, the channel section is designed as inverted trapezoid, and the channel slope is determined according to the soil properties and hydrodynamic conditions. The dredged slope will be adjusted to be a stable slope within a certain period of time. The stable slope is related to the thickness of dredged mud layer, dredging depth, wave, current, geological topography and time. In silty mud coast, the channel slope is generally between 1:3 and 1:50.

The energy dissipation rate of the system is the minimum under the condition of water flow and bed surface. Based on the theory and the measured data, Yang Zhida (Yang et al., 1984) deduced that

$$\frac{VJ_0}{\omega_s}=\text{const} \quad [35]$$

In equation [35], Φ is the flow rate.

Then, in the equilibrium state, the above equation can be written as $J_0=K\frac{\omega_s}{V}=K\frac{\upsilon}{Vh}\frac{\omega_s d}{\upsilon}\frac{h}{d}=K\frac{1}{d/h}\frac{\mathrm{Re_d}}{\mathrm{Re}}$, indicating that the energy slope is related to the relative roughness, the Reynolds number of sand particles and the Reynolds number of water flow.

According to minimum energy dissipation rate theory (Xu et al., 2003), the equation [35] can be substituted into equation [36]

$$S=k_3C_D\frac{\rho_0\rho_s}{\rho_s-\rho_0}\frac{V^3}{\omega_s gh} \quad [36]$$

In equation [36], k_3 is the coefficient.

Equation [36] is consistent with Li Ruijie's general form of sediment carrying capacity formula (Li et al., 2014), which also confirms the rationality of the derived sediment carrying capacity formula.

Through numerical flume simulation test, Chang (Chang et al., 2013) have concluded that under different inflow and sediment conditions, the flow and sediment conditions and riverbed boundary conditions before and after riverbed adjustment change, and the corresponding minimum energy dissipation rate is also different.

4.2 drag coefficient

The resistance coefficient C_D is related to the turbulence intensity, relative roughness of bed surface and pressure density, especially with Reynolds number. It reflects the resistance of boundary to flow, which is an important part of the turbulent structure of open channel and pipeline, and also the foundation of building the mathematical model of tidal current sediment. Generally, C_D is difficult to be obtained by theoretical calculation, and it is determined by experiments.

Many scholars have obtained the calculation formula of resistance coefficient of pipeline and open channel from theory or experiment. Poisson, Posilex, Schiller and Newman (Li et al., 2007), Prandtl, think that it is only related to Reynolds number; Carmen and soulsby (Soulsby, 1997) think it is related to bed roughness length. Dou Guoren (Dou, 1980) analyzed the random structure of turbulent flow, combined with the near wall flow structure, theoretically derived the unified calculation formula of resistance coefficient of open channel flow in turbulent rough area, smooth area and transition area; Dai Lu (Dai et al., 2016) built the index of resistance coefficient and Reynolds number in different flow areas by fitting the experimental data of pipeline resistance, according to the turbulent characteristics of flow Relationship.

5 VERIFICATION OF SEDIMENT CARRYING CAPACITY FORMULA

In the verification process of formula [28], the concept of effective velocity is adopted, and the calculation formula is (Li et al., 2013)

$$V = \left(\frac{1}{T} \int_0^T \left(u^2 + v^2 \right) \mathrm{d}t \right)^{\frac{1}{2}} \qquad [37]$$

In this paper, the sediment carrying capacity formula [28] is verified and analyzed by using river hydrological and sediment data, coastal water hydrological and sediment data. The comparative verification is shown in Figure. 2. The hydrologic and sediment data of the rivers used include the measured data of 3570 stations in about 20 rivers of the Yellow River (Shihohara et al., 1959; Chitales, 1966), the Yangtze River (Cobly et al., 1955; Simons, 1957) and (Hubbel et al., 1968; Totffaleti, 1968; Chaudhry et al., 1970; Culbertson et al., 1972; Mahmood et al., 1984; Nakato, 1990; Yang, 1998) abroad; the hydrological and sediment data of coastal waters cover Liaoning, Shandong, Fujian, Jiangsu, Zhejiang, including TongZhou Bay, Sanmen Bay, Zhoushan, Dayu Bay, Taizhou and Oujiang Estuary, with a total of 70 bays. The grain size of river sediment is 0.01mm ~ 8.0mm, and that of nearshore is 0.0007mm ~ 0.1mm.

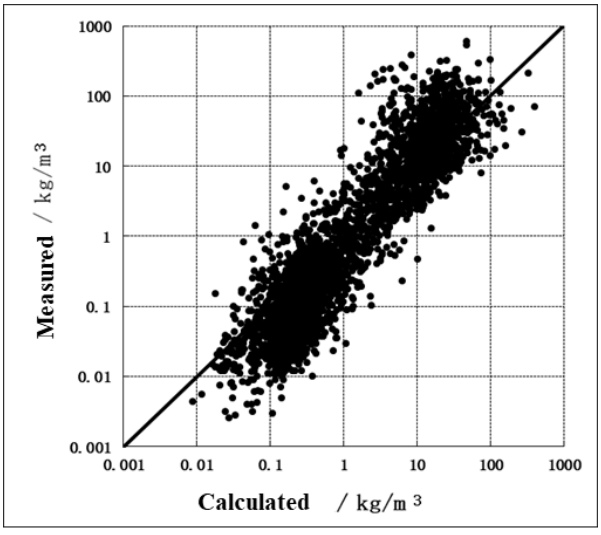

Figure.2 Verification chart of sediment carrying capacity formula

Based on the measured data of rivers and coastal waters, the derived sediment carrying capacity formula is verified and analyzed. The results show that the sediment carrying capacity formula [28] can be applied to the calculation of sediment carrying capacity of river and offshore area.

6 DERIVATION OF SEABED EROSION AND DEPOSITION FORMULA

The basis of the calculation of the sediment deposition is the mechanism of sediment erosion and deposition in the bottom bed. Considering the suspended movement, the mechanism of sediment deposition can be understood as the difference between the sediment content of the water body and the sediment carrying capacity of the water. When the sediment content of water body is equal to the sediment carrying capacity of water body, the seabed is in the state of balance of scour and deposition; when the sediment content of water body is greater than the sediment carrying capacity of water body, the seabed will deposit; when the sediment content of water body is less than the sediment carrying capacity of water body, the

seabed will be scoured. In this case, the fluxes of scour and deposition of seabed are related to the difference between sediment content and sediment carrying capacity of water. In this section, based on formula [28] and formula [36] of water flow carrying capacity obtained by combining minimum energy dissipation rate, the formula of seabed erosion and deposition strength is derived.

The equation of sediment unit width motion can be expressed as follows

$$\frac{\partial(qS)}{\partial x}+\alpha\omega(S-C_s)=0 \qquad [38]$$

In equation [38], x is the coordinate along the flow direction; q is the unit width discharge and α is the probability of sediment settlement.

The seabed deformation equation is

$$\frac{\partial(qS)}{\partial x}+\gamma_0\frac{\partial Z}{\partial t}=0 \qquad [39]$$

In equation [39], Z is bed elevation and t is time coordinate.

By subtracting equation [39] from equation [38], the calculation formula of seabed erosion and deposition can be obtained

$$\Delta z_0=\frac{\alpha\omega_s\Delta t}{\gamma_0}(S-C_s) \qquad [40]$$

In equation [40], Δz_0 is the corresponding thickness of erosion and deposition, and Δt is the duration of erosion and deposition.

If the bed thickness change at time t is recorded as Δz_1 and that at time $t+\Delta t$ as Δz_2, the erosion and deposition intensity during Δt can be written as

$$P=\Delta z_2-\Delta z_1=\frac{\alpha\omega_s\Delta t}{\gamma_0}\left[(S_2-C_{s2})-(S_1-C_{s1})\right] \qquad [41]$$

In equation [41], the intensity of erosion and deposition is positive for sedimentation and negative for erosion.

Assuming that the local seabed erosion and deposition changes do not change the incoming sediment conditions, as S_2=S_1, there is

$$P=\frac{\alpha\omega_s\Delta t}{\gamma_0}(C_{s1}-C_{s2})=\frac{\alpha\omega_s C_{s1}\Delta t}{\gamma_0}\left(1-\frac{C_{s2}}{C_{s1}}\right) \qquad [42]$$

By substituting equation [28] and equation [36] into the above formula, two forms of seabed erosion and deposition strength formula can be obtained

$$P=\frac{\alpha\omega_s C_{s1}\Delta t}{\gamma_0}\left[1-\frac{C_{D2}}{C_{D1}}\frac{J_1}{J_2}\left(\frac{V_2}{V_1}\right)^2\left(\frac{h_1}{h_2}\right)\right] \qquad [43]$$

$$P=\frac{\alpha\omega_s C_{s1}\Delta t}{\gamma_0}\left[1-\frac{C_{D2}}{C_{D1}}\left(\frac{V_2}{V_1}\right)^3\left(\frac{h_1}{h_2}\right)\right] \qquad [44]$$

Considering the relationship between seabed erosion and deposition and flow resistance, combined with the ocean resistance coefficient equation [45] obtained by Soulsby and the roughness height calculation equation [46] given by Colebrook, the resistance coefficient ratios of the following different flow regions (laminar flow area, turbulent smooth area, turbulent rough area and turbulent transition area) can be obtained, as shown in Table 1.

$$C_D=\left[\frac{1}{7}\left(\frac{12z_0}{h}\right)^{\frac{1}{7}}\right]^2 \qquad [45]$$

$$z_0=\frac{k_s}{30}+\frac{\nu}{9u_*} \qquad [46]$$

In equation [46], k_s is the height of Nikuradse roughness.

Table 1 resistance coefficient ratios for different flow regions

Flow area	C_{D2}/C_{D1}
Laminar flow region	$\frac{V_1 h_1}{V_2 h_2}$
Turbulent smooth region	$\left(\frac{V_1 h_1}{V_2 h_2}\right)^{1/4}$
Turbulent transition zone	$\left(\frac{V_1 h_1}{V_2 h_2}\right)^{m}$, $m \in (-\frac{1}{4}, 0)$
Turbulent rough area	$\left(\frac{h_1}{h_2}\right)^{2/7}$

The ratio of resistance coefficient in different flow areas is shown in Table 1, and the equation [43] and equation [44] are used to calculate the seabed erosion and deposition formula for different flow areas.

α is the saturation coefficient of sediment recovery or sediment movement parameter, which is related to dynamic conditions and sediment settling velocity. In the application of tidal current and sediment model, the empirical values of sediment restoration saturation coefficient are mostly between 0.25 and 1.0. It is generally believed that the sediment restoration saturation coefficient during scouring is greater than that of sediment deposition. Li Ruijie ,Dou Guoren and Li Wangsheng gave the empirical value of saturation coefficient

7 CONCLUSIONS

In this paper, based on the derivation of the hydrodynamic balance equation of sediment-laden flow and considering the steady and uniform state, new formulas of sediment carrying capacity [27], [31] and [34] are derived, and two simplified forms of equation [27], as [28] and [36] are given. Equation [27] is verified by a large number of measured data. The equation [27] is the formula of sand carrying capacity without considering the surface wind effect, and the equation [31] and equation [34] are the formula of sand carrying capacity considering the surface wind effect, and the three formulas are applicable to the offshore area.

Based on the derived equations [28] and [36], two kinds of seabed erosion and deposition formulas [43] and [44] under different flow regions are derived by combining the sediment single width motion equation and the bed deformation equation.

Because the formula of sediment carrying capacity and seabed erosion and deposition intensity contain slope, there are some advantages in the calculation of channel sedimentation. The calculation formula of seabed erosion and deposition strength derived from this paper will be discussed in the next paper.

REFERENCES

Cao Zude, Xiao Hui. (2010). Seabed evolution forecast by hydrologic data[J]. Port& Waterway Engineering, 39(2): 20-22.

Wang Yigang, Lin Xiang, Feng Weibing. (2000). A simple method for calculating long-term deposition rate afterconstruction of warping bank in estuary[J]. Journal of Hohai University, 28(6): 100-102.

Liu Jiaju, Yu Guohua. (1990). Calculation and forecast of the beach protection and accretion acceleration on the siltbeach [J]. The Ocean Engineering, 8(1): 51-59.

Li Ruijie, Zheng Jun, Zhang Wenhu, etc. (2014). A general formula of sediment carrying capacity and its analysis. [J]. Journal of Sediment Research, 39(1): 1-7.

Yang C T. (1984). Unit stream power equation for gravel[J]. Journal of Hydraulic Engineering, 110(12): 1783-1797.

Xu Guobin, Lian Jijian. (2003). Theories of the minimum rate of energy dissipation and the minimum entropy production of flow (Ⅱ)[J]. Journal of Hydraulic Engineering, 34(5): 43-47.

Chang Mei, Xu Guobin. (2013). Numerical simulation of fluid motion in flume based on theory of minimum rate of energy dissipation [J]. Journal of Sediment Research, 38(2): 67-71.

Li Yong, Yu Xiping. (2007). Numerical study on suspended sediment transport in oscillatory flows [J]. Journal of Hydrodynamics, 22(4): 420-426.

Soulsby R. (1997). Dynamics of marine sands: a manual for practical applications[M]. Thomas Telford.

Dou Guoren. (1980). Generalized laws of turbulent flow in open channels and pipes for various regions[J]. Hydro-Science and Engineering, 1:1-12.

Dai Lu, Li Ruijie, Feng Qing, etc. (2016). A general formula of resistance coefficient and its application in sediment carrying capacity computation [J]. Journal of Sediment Research, 41(2): 7-13.

Li Ruijie, Zheng Jun, Feng Qing, etc. (2013). Sediment carrying capacity and erosion rate of nearshore sediment [J]. Journal of Sediment Research, 38(4): 21-25.

Shihohara K,Tsuhaki T. (1959). On the characteristic of sand waves formed upon beds of the open channels and rivers[R]. Reports of Research Institute of Applied Mechanics, Kyushu University.

Chitales S V. (1966). Hydraulics of stable channels[R]. Government of India, Ministry of Irrigation and Power, Central Water and Power Commission.

Cobly B R, Hembree C H. (1955).Computation of total sediment discharge, Niobrara River near Cody, Nebraska[R]. U.S. Geol. Surv., Water-Supply Pap.1 357.

Simons D B. (1957). Theory and design of stable channels in alluvial materials[D].Ph.D. Thesis, Colorado State University, Fort Collins, Colorado.

Hubbell D W, Matejka D Q. (1968). Investigations of sediment transportation, Middle Loup River at Dunning, Nebraska[R]. U.S. Geol. Survey, Water-Supply Pap.1 476.

Totffaleti F B. (1968). A procedure for computation of the total river sand discharge and detailed distribution, bed to surfaee[R]. Technical Report No.5, Committee of Channel Stabilization, Corps of Engineeriug,U.S. Army, November.

Chaudhry H M, Smith K V N and Vigil H. (1970). Computation of sediment transport in irrigation canals[R]. Proc. Institution of Civil Engineering.

Culbertson J K, Scott C H, Bennett J P. (1972). Summary of alluvial-channel data from Rio Grande conveyance channel, New Mexico,1965-1969[R]. Professional Paper 562-J, United States Geological Survey, Washington D.C..

Mahmood K, Haque M I, Choudri A M, Malik M A. (1984). ACOP canals equilibrium data, vol. x: summary of 1974-1980 data[R]. Civil, Mechanical and Environmental Engineering Department, George Washington University.

Nakato T. (1990). Tests of selected sediment-transport formulas[J]. Journal of Hydraulic Engineering, 116(3): 362-379.

Yang C T. (1998). Sedimentation, river morphology, and modeling[R]. Technical Service Center, U.S. Bureau of Reclamation, Denver Colorado, July.

8th International Conference on the Application of Physical Modelling in Coastal and Port Engineering and Science
Dec. 9th - 12th, 2020, Zhoushan, China

A THEORETICAL MODEL FOR DESCRIBING CHANNEL AXIS DEVIATION AND CROSS-SECTION CHANGE UNDER THE ACTION OF CROSS FLOW IN COASTAL REGION

WENJIN ZHU[1], NA WANG[2], XIAOTIAN DONG[3*]

[(1,2,3)]*Jiangsu Ocean University , china*
zhucius@jou.edu.cn ; 1098577677@qq.com; dongxt@jou.edu.cn(Corresponding author)*

ABSTRACT

The mechanism of coastal sediment transport is that wave stirs up sediment and current transports the sediment. The waterway of the coastal region is subject to current and waves. Usually, currents are perpendicular to the longitudinal axis of the waterway. The currents are called as cross flow. The phenomenon of channel axis deviation and cross-section change will occur under the action of the cross flow. The velocity of cross flow comprises the residual velocity and main tidal constituents velocity. It is assumed that waves only act as stirring when the channel axis deviate and cross-section change. Moreover, it is also assumed that the morphological time is much larger compared to the tidal period. The seabed deformation equations caused by the motion of bed load and suspended load are averaged over the tidal period separately. For the bed load, Bagnold transport formula is used for bottom boundary condition. For the suspended load, the bottom net sediment flux equation is used and the reference concentration is proportion to the square velocity. The higher order terms are retained for the results, while lowed order terms are neglected. Then, a theoretical model is established for describing the law of channel axis deviation and cross-section change in the coastal region. The new theoretical model has the form of one-dimensional convection-diffusion equation which has constant convection-diffusion coefficients. The Gauss function is used to describe the waterway cross-section. According to the theoretical solution of the one-dimensional convection-diffusion equation, the quantitative description of channel axis deviation and cross-section change under the action of cross flow is obtained. The channel axis deviation and cross-section change is a function of residual velocity. The new method is applied to the channel of Lianyungang Port in the Southern Yellow Sea. Under present hydrodynamic conditions, the migration rate of channel axis in Lianyungang Port is about 5m yr^{-1}, and the change rate of cross-section is 292.69m^2 yr^{-1}. In addition, it is also applied to the waterway of the Port of Haian at Qiongzhou Strait. The migration rate of channel axis in Haian Port is about 10m yr^{-1}, and the change rate of cross-section is 294.22m^2 yr^{-1}. This research has important engineering value for designing channel and dredging maintenance.

Key Words:cross flow, residual velocity, one-dimensional convection-diffusion equation, Gauss function, migration rate

1 INTRODUCTION

The sediment transport near the open channel in the coastal region is subject to current and wave. The mechanism of coastal sediment transport is that wave stirs up sediment and current transports the sediment. The hydrodynamics condition will cause the deviation of channel longitude axis and the change of cross-section. The channel of Rotterdam port and Amsterdam port in the Nether-land have found channel axis deviation and cross-section change. The similar phenomena have been also found in the Chinese Haian port located in the northern of Qiongzhou strait and channel of Lianyungang Port in the Southern Yellow Sea.

Nearshore current is generally a reciprocating flow parallel to the shoreline or isobath. In coastal region, many harbor channels axis have an intersection angle with the current direction, sometimes even reaching 90^0. Many scholars(Batteen, M.L. et al.,2007; Xu, D. et al.,2013; Xie, M.X. et al.,2009; Xiong, W.,2017) have studied the strength characteristics of the cross flow and magnitude of the maximum cross flow.With the deepening of research, more and more scholars(Xie, M.X.et al.,2015; Zhang, W.et al.,2012; Zhang, W.et al.,2014) are researching the relationship between cross-flow magnitude and tidal-level range, or the methods for calculating magnitude of cross-flow. Some researchers are focusing on the establishment, verification and prediction of the coastal channel deposition formula under the cross-flow. Another scholars use the method of hydrodynamics and sediment transport numerical model to calculate deposition rate. Although these methods can reproduce the process of channel axis deviation and cross-section change, its understanding of the

influencing factors of channel axis deviation and cross-section change is not deep enough.

In order to understand the evolution law of the channel axis deviation and cross-section change under the action of cross current for long time, a theoretical model of the evolution of open channel in the coastal region is established. The new theoretical model has the form of one-dimensional convection-diffusion equation which has constant convection-diffusion coefficients. By analyzing the new equation, the migration rate of channel axis and the law of channel cross-section change under the action of cross flow are obtained. The quantitative description is applied to channel of Lianyungang Port in the Southern Yellow Sea and the channel of Haian port in the northern side of Qiongzhou strait.

2 ASSUMPTION

2.1 Cross-section

While the water depth increases, the cross-section area increases and the flow velocity decreases. It is assumed that the current velocity inside the channel is U and the current velocity outside the channel is u. According to the continuity equation

$$U(h+a)=uh \qquad [1]$$

Where h is the depth of water and a the dredging depth relative to the original seabed.

In general, cross-section shape of the coastal channel is similar to Gaussian distribution(Jacobus van de, K. et al.,2002). In order to quantitatively describe cross-section shape, Gauss function is adopted to describe the channel section shape. The equation for the initial cross-section shape is

$$a=\frac{A}{\sqrt{2\pi}\sigma_0}e^{-x^2/2\sigma_0^2} \qquad [2]$$

Where A is the area of channel dredging region and σ_0 is 1/2 of channel width. Initial cross-section describing by Gaussian distribution is shown in the following figure 1.

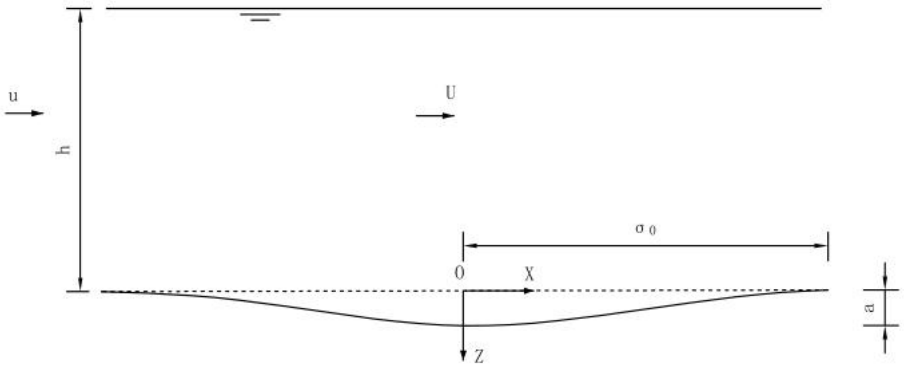

Figure 1. Initial cross-section describing by Gaussian function

2.2 Cross flow

Because the tidal current oscillates in period and the main tidal constituent is considered only, the current velocity is expressed as

$$u=u_0+u_1\cos\omega t \qquad [3]$$

Where, u_0 is residual velocity and u_1 the maximum velocity of the main tide constituent, ω the frequency of main tidal constituent. Equation [3] is time-averaged in tidal period

$$\bar{u}=u_0 \qquad [4]$$

$$\overline{u^2}=\overline{u_0^2+2u_0u_1\cos\omega t+u_1^2\cos^2\omega t}=u_0^2+\frac{1}{2}u_1^2\approx\frac{1}{2}u_1^2 \qquad [5]$$

$$\overline{u^3} = \overline{u_0^3 + 3u_0^2u_1\cos\omega t + 3u_0u_1^2\cos^2\omega t + u_1^3\cos^3\omega t} = u_0^3 + \frac{3}{2}u_0u_1^2 \approx \frac{3}{2}u_0u_1^2 \quad [6]$$

Considering residual velocity u_0 is a small number on the order of the main tide constituent maximum velocity u_1, thus u_0^2 and u_0^3 are neglected in the expressions.

3 APPROACH

3.1 Bed load transport

The sediment transport in the coastal region is mainly composed by bed load and suspended load. Equation of seabed deformation caused by bed load transport

$$\frac{\partial a}{\partial t} = \frac{\partial q}{\partial x} \quad [7]$$

Where, q is the sediment transport rate of unit width, and Bagnold formula(Bagnold, R.A.,1966)is adopted

$$q = fu^3\left(1 + \lambda\frac{\partial a}{\partial x}\right) \quad [8]$$

Among them, $\lambda = 1.7$, $f = 1.6\times10^{-5}$ m^{-1} s^{-2}. Because of $U(h+a) = uh$, it can be eliminated q between equation [7] and [8]. The equation for the bed deformation

$$\frac{\partial a}{\partial t} = -\frac{3fh^3u^3}{(h+a)^4}\frac{\partial a}{\partial x} - \frac{3fh^3u^3}{(h+a)^4}\left(\frac{\partial a}{\partial x}\right)^2 + \frac{fh^3u^3}{(h+a)^3}\lambda\frac{\partial^2 a}{\partial x^2} \quad [9]$$

In general, the dredging depth is much smaller than the original water depth. Assuming $h \approx h + a$. The coefficient of the first term on the right-hand side $-\frac{3fh^3u^3}{(h+a)^4} = -\frac{3fu^3}{h}$ .The assumptions are also adopted for the remaining coefficients of the other terms. $(\frac{\partial a}{\partial x})^2$ is a small quantity order under slow slope topography. Equation [9] can be simplified as follows

$$\frac{\partial a}{\partial t} = -\frac{3fu^3}{h}\frac{\partial a}{\partial x} + fu^3\lambda\frac{\partial^2 a}{\partial x^2} \quad [10]$$

Equation [10] is a typical one-dimension convection-diffusion equation. It can be understood that the cross-section migrates with a speed $\frac{3fu^3}{h}$ in the x direction, and the shape of cross-section is deformed by diffusion coefficient $fu^3\lambda$. In order to comprehend more clearly channel section change and axis deviation with time, equation [10] is time-averaged in tidal cycle and simplified to get equation [11]

$$\frac{\partial a}{\partial t} + v\frac{\partial a}{\partial x} = K\frac{\partial^2 a}{\partial x^2} \quad [11]$$

In the formula $v = \frac{3f\overline{u^3}}{h} = \frac{9fu_0u_1^2}{2h}$, $K = \lambda f\overline{u^3} = \frac{3\lambda fu_0u_1^2}{2}$. Equation [11] means that, from a longer time scale, the cross-section is convected with velocity v in the x direction, and section shape is changed owing to diffusion coefficient K .

According to the theoretical solution of equation [11] and initial section form of equation [2] (when $t=t_0$), the cross-section form of the channel at any time t can be expressed as

$$a = \frac{A}{\sqrt{2\pi}\sigma} e^{-(x-v(t-t_0))^2/2\sigma^2} \qquad t \geq t_0 \qquad [12]$$

3.2 Suspended load transport

Equation of seabed deformation caused by suspended load

$$\frac{\partial(h+a)c}{\partial t} + \frac{\partial(h+a)Uc}{\partial x} - \varepsilon(h+a)\frac{\partial^2 c}{\partial x^2} = E - D \qquad [13]$$

$$\frac{\partial a}{\partial t} = \frac{E-D}{\rho_s(1-p)} \qquad [14]$$

$$\frac{\partial(h+a)c}{\partial t} + \frac{\partial(h+a)Uc}{\partial x} - \varepsilon(h+a)\frac{\partial^2 c}{\partial x^2} = \rho_s(1-p)\frac{\partial a}{\partial t} \qquad [15]$$

Where, c is suspended sediment concentration, p seabed porosity, ε suspended sediment diffusion coefficient in the x direction, ρ_s sediment density, $E - D = w(c_a - c)$ (Julien,P.Y.,2010; Li, R.J. et al.,2009), $wc_a = \beta u^2$ (Schuttelaars, H.M. et al.,1996), c_a the reference point concentration, β scour coefficient, E the erosion rate and D the deposition rate. By referring to the equation [11] of seabed deformation caused by bed load, the high-order small quantities are ignored after joining equations [13], [14] and [15]. Time-averaged equation in tidal cycle of seabed deformation are obtained

$$\frac{\partial a}{\partial t} + v\frac{\partial a}{\partial x} = K\frac{\partial^2 a}{\partial x^2} \qquad [16]$$

where $v = \frac{3\beta u_0 u_1^2}{\rho_s(1-p)w}$, $K = \frac{\varepsilon\beta u_1^2}{\rho_s(1-p)w}$.

The theoretical solution of equation [16] is similar to the bed load. The channel section at any time t is expressed as

$$a = \frac{A}{\sqrt{2\pi}\sigma} e^{-(x-v(t-t_0))^2/2\sigma^2} \qquad t \geq t_0 \qquad [17]$$

4 Application

4.1 Channel of Lianyungang Port

4.1.1 Basic information

The project of 300000-ton deep-water channel of Lianyungang Port is 52.9km long. The site-plan is shown in the figure above. The effective width of the designed channel is 280m(Huang, W.M, et al.,2012). The origin seabed elevation of the open channel is -19m(based on the lowest theoretical low water level locally). The designed slope of the channel is changing from 1:5 to 1:10(Ying, M., et al.,2017). The cross-section form of 300000-ton deep-water channel in Lianyungang Port is shown in the figure 2. In this study, water depth $h = 19$ m, depth $a = 3$ m, effective width of channel 280m and slope 1:8 are used for calculation, then $\sigma_0 = 164$ m.

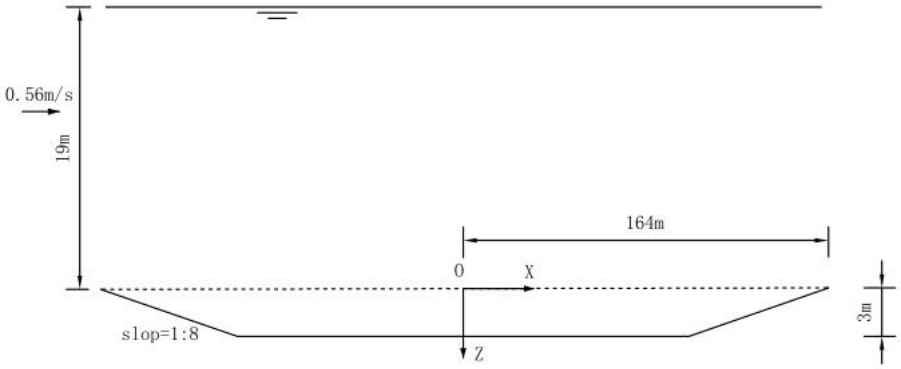

Figure 2. Schematic diagram of channel cross-section of Lianyungang Port

The tidal current velocity of the coastal region near the open channel of Lianyungang is between 0.48m/s and 0.56m/s in the spring tide, and between 0.24m/s and 0.32m/s in the neaps. The the maximum velocity of flood current is slightly higher than the maximum velocity of ebb current. The direction of the flood tide is southwest while the ebb tide is northeast. Channels axis is perpendicular with the current direction and $u_1 = 0.56$ m/s will be used.

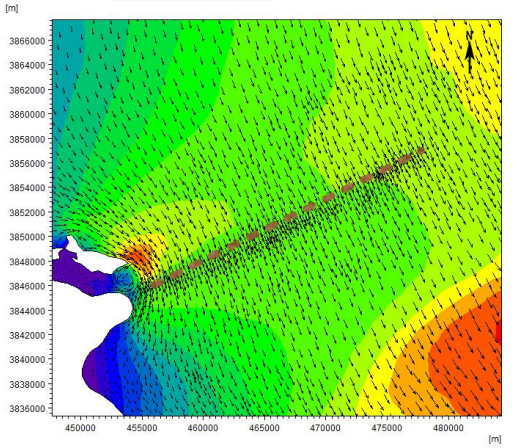

Figure 3. Axis direction and flood current of spring tide

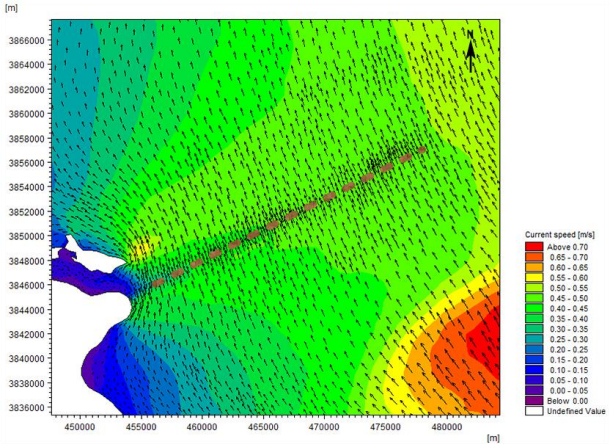

Figure 4. Axis direction and ebb current of spring tide

The residual current is affected by many factors. According to the existing literature, it is concluded that residual current in Lianyungang open channel is about $u_0 = 0.07$ m/s, and the direction of the residual current is perpendicular with the channels axis. The median grain size D_{50} of deposited sediment in the Lianyungang open channel is between 0.005 and 0.009mm.The portion of clay is generally between 25% and 55%. The density of deposited material is about 1.45 ~1.60t/m^3.In this study, the density of deposited material is taken as 1.5t/m^3, and $p = 0.43$, and $\varepsilon = 10$ m^2 s^{-1}and $\beta = 10^{-4}$ kg s m^{-4}.

4.1.2 Theoretical application

The parameters v and K can be obtained from equations [12] and [17]. The computed value can be listed as follows

Table 1. Results calculated of *v* and *K*

	v(m/yr)	*K*(m^2/yr)
bed load（*BL*）	2.62	161.74
suspended load（*SL*）	2.75	130.95
total（*TO*）	5.37	292.69

Note: BL represents the only consideration of bed load.
SL represents the only consideration of suspended load.
TO represents the consideration of bed load and suspended load.

When bed load is only considered, the equation of channel cross section can be expressed as $a_{t=t_0} = \frac{912}{164\sqrt{2\pi}} e^{-(x-2.62)^2/(2\times 164^2)}$. In the same way, the equation of channel cross section with different influencing factors for the years can be obtained. These equations can be plotted and analyzed.

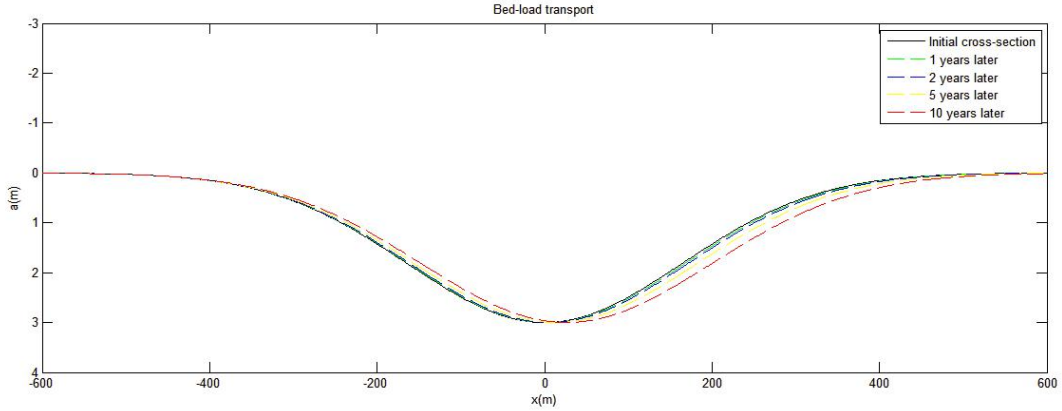

Figure 5. Evolution process of channel only with bed load transport

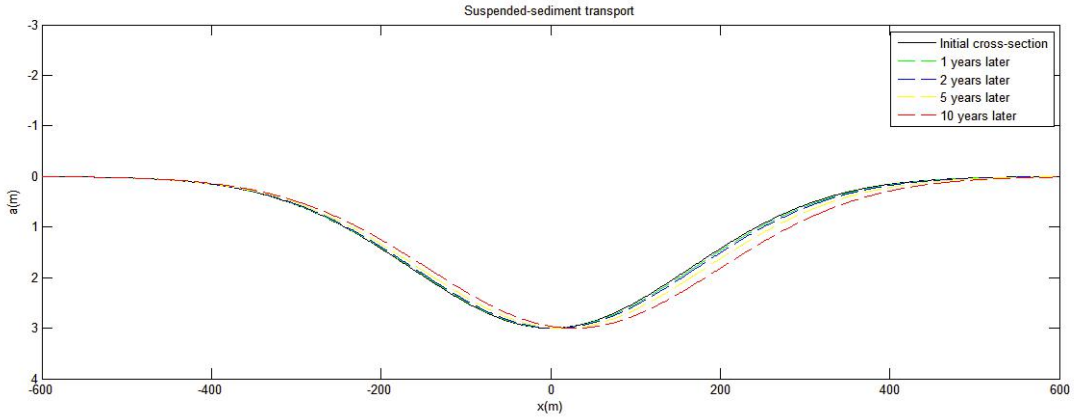

Figure 6. Evolution process of channel only with suspended load transport

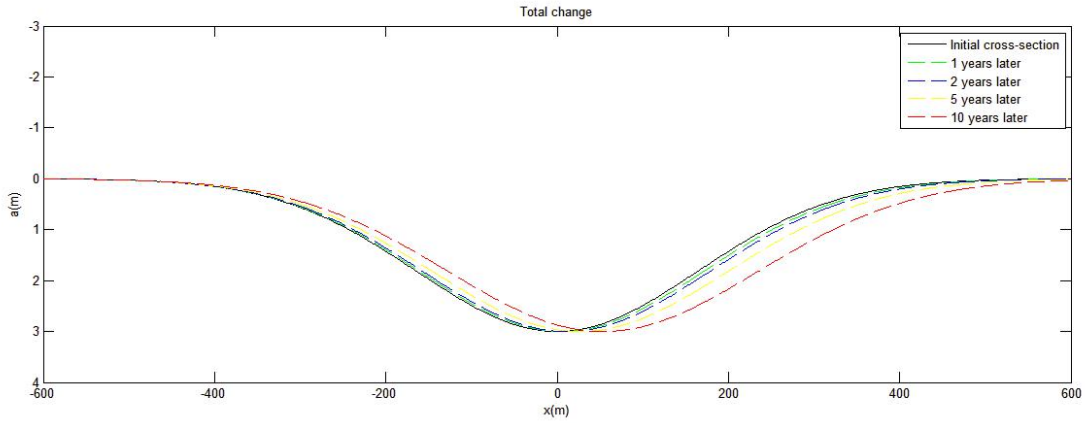

Figure 7. Evolution process of channel with both bed load and suspended load transport

It is shown that for both transport models, the cross-section of channel is governed by an advection-diffusion equation with constant coefficients. The channel deviation is accompanied by the elevation change on both sides of the channel.According to bed load and suspended load transport modes are taken into consideration, the annual shifting distance of channel axis in Lianyungang Port is about 5 m yr^{-1}, and the change rate of waterway cross-section shape is 292.69m^2 yr^{-1}.

4.2 Channel of Haian Port

4.2.1 Basic information

Haian port located in Qiongzhou Strait is at the southern of the Chinese mainland.The sediment transport in the coastal channel of Haian port is mainly affected by waves and current.In this study, $h = 4.1$ m, $a = 1$ m and slope 1:10 are taken. The designed effective width of channel is 180m and then the initial state $\sigma_0 = 100$ m, as shown in figure 8.

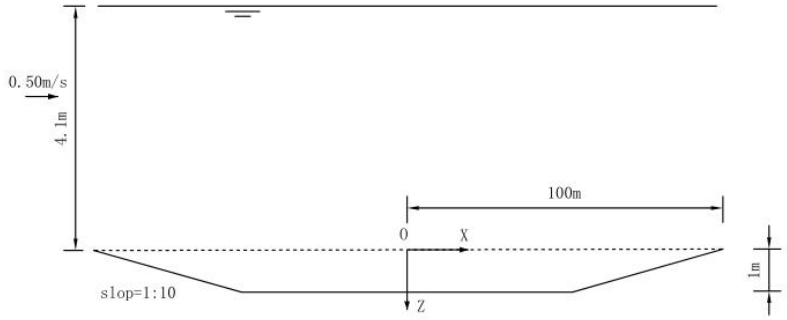

Figure 8. Schematic diagram of channel cross-section of Haian Port

In order to analyze the hydrodynamic and sediment transport of Haian port, six observation stations were set up to measure hydrodynamic conditions.According to the fields data,channels axis is perpendicular with the current direction and $u_1 = 0.50$ m/s will be used.The residual current directions of the six observations are also perpendicular with channels axis, and the magnitude are as follow

Table 2. The residual current velocity

	V1#	V2#	V3#	V4#	V5#	V6#
spring tide(m/s)	0.090	0.082	0.084	0.091	0.032	0.092
neap tide(m/s)	0.060	0.010	0.021	0.025	0.016	0.050

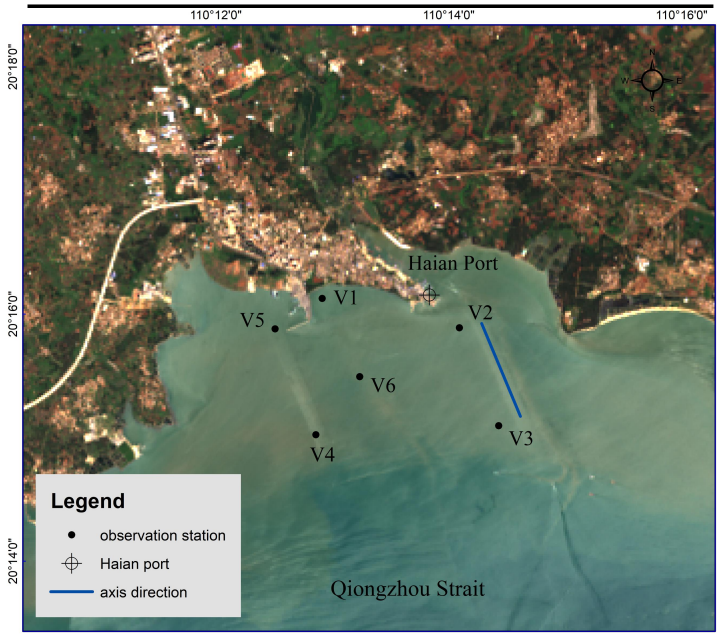

Figure 9. Schematic diagram of observation stations

By tracking and measuring sea bed topography of the coastal region near Haian channel in January 2002, October 2003, July 2006 and November 2007, it is found that channel axis has shifted to the west. Sediment in the bottom bed of Haian coastal region is easily suspended under the disturbance of ships. Suspended sediment is transported to the surrounding coastal region under the action of hydrodynamics. The parameters are taken as $p = 0.64$, $\varepsilon = 10$ m^2/s, $\alpha = 10^{-4}$ kg s m^{-4}.

4.2.2 Theoretical application

The values of v and K can be obtained from equations [12] and [17], which can be listed as follows:

Table 3. Results calculated of *v* and *K*

	v(m/yr)	*K*(m^2/yr)
total（*TO*）	9.59	294.22

Note:TO represents the consideration of bed load and suspended load.

The initial cross-section can be described

$$a_{t=t_0} = \frac{251}{100\sqrt{2\pi}} e^{-x^2/(2\times 100^2)} \qquad [18]$$

In the same way, the equation of channel cross section with different influencing factors for the years can be obtained. The following results can be obtained by drawing images and arranging and analyzing these equations.

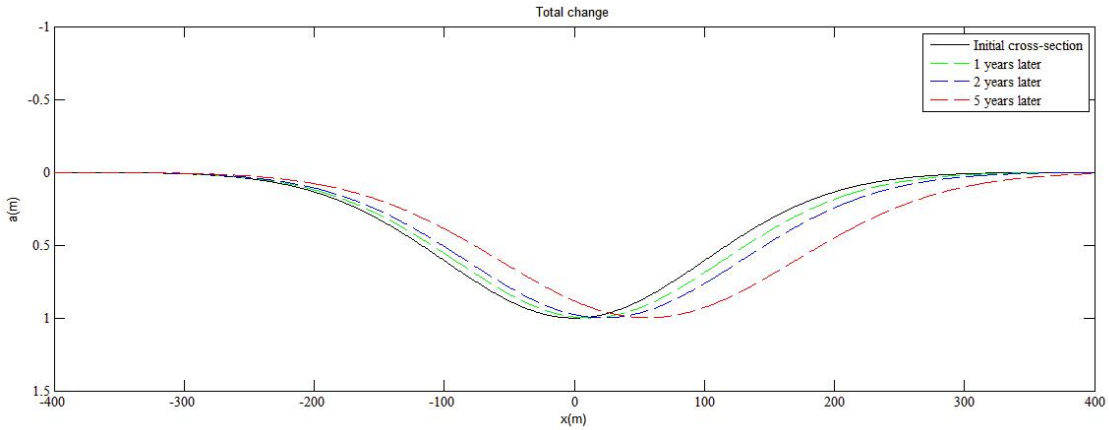

Figure 10. Evolution process of channel with both bed-load and suspended load transport

The channel axis deviation is accompanied by the elevation change on both sides of the channel. According to bed load and suspended load transport are taken into consideration, the annual migration distance of the channel axis of Haian port is about 10m and the change rate of waterway cross-section shape is 294.22m^2 yr^{-1}.

5 Conclusion

Seabed deformation equation caused by the bed load and suspended load movement takes the average over the tidal period respectively in tidal cycle and omits higher order a small amount. Seabed deformation equation of time-averaged in tidal cycle is relatively similar with the traditional form of convection diffusion equation. By analyzing the new seabed deformation equation, the evolution law of the channel axis deviation and cross-section change under the action of cross current are obtained.The Gaussian distribution is used to describe cross-section shape. According to the theoretical solution of one-dimensional convection and diffusion equation, the quantitative description of channel cross-section change and axis derivation are obtained.

The new method is applied to evaluate channel axis deviation and cross-section change under the action of cross flow in the 300000-ton deep-water channel of Lianyungang Port in the Southern Yellow Sea. Under present hydrodynamic conditions, the shifting distance of channel axis in Lianyungang Port is about 5 m yr^{-1}, and the change rate of waterway cross-section shape is 292.69m^2 yr^{-1}. In addition, it is also applied to the waterway of the Port of Haian at Qiongzhou Strait. The shifting distance of channel axis in Haian Port is about 10 m yr^{-1}, and the change rate of waterway cross-section shape is 294.22m^2 yr^{-1}. This research has important engineering value for designing channel and dredging maintenance.

REFERENCES

Bagnold, R.A.(1966). An approach to the sediment transport problem from general physics. *Geological Survey Professional Paper 422- Ⅰ.*

Batteen, M.L., Martinho, A.S., Miller, H.A.& McClean, J.L.(2007). A process-oriented modelling study of the coastal Canary and Iberian Current system. *Ocean Modelling*, 18(1): 1-36.

Huang, W.M, Wang W.H., Zhang W.S.&Zhang, J.S.(2012). Analysis of Characteristics of the Tides and the Tidal Currents in Adjacent Waters of Lianyungang. *Zhejiang Hydrotechnics, (3): 1-5, 14.*

Julien, P.Y.(2010). *Erosion and sedimentation*. Cambridge University Press.

Jacobus van de, K., Sander, E.H., Martin, V.(2002). An analytical model for the morphodynamics of a trench in the presence of tidal currents. *Continental Shelf Research,22(11-13).*

Li, R.J., Luo, F., Zhu, W.J(2009). The suspended sediment transport equation and its near-bed sediment flux. *Science in China Series E: Technological Sciences,52(2).*

Soulsby, R.(1997). *Dynamics of marine sands: a manual for practical applications.* Thomas Telford.

Schuttelaars, H.M., Deswart, H.E.(1996). Anidealized long-term morphodynamic model of a tidal embayment. *European journal of mechanics. B, Fluids, 15(1): 55-80.*

Xu,D, Malanotte,R.P.(2013). The seasonal variation of the upper layers of the South China Sea (SCS) circulation and the Indonesian through flow (ITF): An ocean model study. *Dynamics of Atmospheres and Oceans*,63:103-130.

Xiong, W.(2017). Study on 3D Cross-flow Characteristics of Deepwater Channel in Estuarine Shoal of

Lianyungang Main Port Area. *Pearl River*, 38(11): 50-54.

Xie, M.X., Yao, S.S., Li, W.D., Zhao, H.B.&Gao, Z.L.(2015). Investigation of the Movement Characteristics of West Guangdong Longshore Ocean Current System, China. *Journal of Coastal Research,73(sp1): 364-369.*

Xie, M.X., Zhang, W., Li, G.C.(2009). Three dimensional features of cross flow in approach channel and its effect on navigation. *Journal of Wuhan University of Technology(Transportation Science & Engineering)*,33(5): 968-971.

Ying, M., Zhao, Y., Ma, X.H.&Ding, Q.(2017). Observation and research on perennial channel siltation of Lianyun port 250000 DWT waterway and xuwei port 50000 DWT waterway. *Port and waterway engieering, (11): 86-91, 103.*

Zhang, W., Li, Z., Liu, R.&Qian, W.(2014). Research on three-dimensional characteristics of cross-flow in approach channel at entrance of encircle breakwater. *The Ocean Engineering, 32(1): 91-98.*

Zhang, W., Zhang, J., Li, Z., Qian, W.(2012). Research on Cross Flow in Approach Channel at Entrance of Breakwater-encircled Harbor in Lianyungang. *China Harbour Engineering, (6): 4-7.*

8th International Conference on the Application of Physical Modelling in Coastal and Port Engineering and Science
Dec. 9th - 12th, 2020, Zhoushan, China

NUMERICAL SIMULATION OF WINTER WAVE FIELD IN THE SOUTH CHINA SEA FIELD BASED ON SWAN

ZOU LI[1,2], WANG WEI[1], JIANG SHENGCHAO[1], WANG PEIZHENG[1] & ZHAO JIAN[1]

[1]School of Naval Architecture, State Key Laboratory of Structural Analysis for Industrial Equipment, Dalian University of Technology, Dalian 116024, PR China
zoulidut@126.com

[2]Collaborative Innovation Center for Advanced Ship and Deep-Sea Exploration, Shanghai 200240, PR China

ABSTRACT

Studying the wave fields in the South China Sea is of great significance for maritime shipping and energy development in the South China Sea. Under the influence of the winter monsoon, the change of the wave field in the South China Sea becomes more complicated. This paper utilized the internationally advanced third-generation wave model SWAN (Simulating Waves Nearshore) on the numerical simulation of the South China Sea wave field for two months from December 1, 2014 to January 31, 2015, adopting nested grid technology and unstructured grid respectively. The numerical simulation results of significant wave heights and mean periods were compared with the observations from the local buoy. Overall, the numerical simulation results using the nested grid technology agreed better with the observations than unstructured grid, and the error statistics of significant wave height and mean period was within a reasonable range. Therefore, using the nested grid technology of the SWAN wave model can more accurately simulate the winter wave field in the South China Sea, which is of great significance to the numerical prediction of long-term wave field in the South China Sea.

Keywords: South China Sea; SWAN; nested grid technology; winter wave field; observations.

1 INTRODUCTION

The South China Sea is located in the low latitudes south of 23°37' north latitude and is dominated by the northeast or northwest monsoon in winter. Under the influence of the winter monsoon, the wave field in the South China Sea becomes more complicated. Numerical simulation of the winter wave field in the South China Sea is of great significance for maritime shipping and energy development in the South China Sea. Marine scientists began studying ocean waves in the 1850s, and wave numerical models have evolved into the third generation, such as WAM model, SWAN model and WAVEWATCH Ⅲ model. Xu et al. (2017) studied three typhoon waves in the South China Sea by using the third-generation wave model SWAN and WAVEWATCH Ⅲ , respectively, and compared them with the observations, and discussed the importance of nonlinear wave-wave interaction to the formation of the spectrum. Zhou et al. (2014) numerically simulated the wave field in the South China Sea from 1976 to 2005 using WAVEWATCH Ⅲ model, and summarized the seasonal law of wave direction. Wang et al. (2014) simulated the typhoon waves in the South China Sea and its adjacent areas with the third-generation wave model WAVEWATCH Ⅲ, the numerical simulation results agreeing well with the observations, and utilized the Spectrum Integration Method and the Spectrum Partitioning Method to separate the wind wave and swell in the one-dimensional and two-dimensional wave Spectrum. Kim et al. (2018) compares wave parameters calculated by SWAN and WAVEWATCH Ⅲ during Typhoon Bolaven passing through the East China Sea and the Yellow Sea with observations at ocean tower station and buoys. Akpınar et al. (2016) numerically simulated the wave field in the black sea from 1979 to 2009 by using the SWAN model, and systematically analyzed the wind and wave characteristics.

This paper, adopting the nested grid technology and unstructured grid respectively, utilized the internationally advanced third-generation wave mode SWAN to simulate the winter wave field in the South China Sea. By comparing the numerical simulation results with the buoy data, it was found that the numerical results calculated by nested grid technology were in better agreement with the buoy data than unstructured grid, which verified the feasibility of numerical simulation of winter wave field in the South China Sea by SWAN nested grid technology.

2 INTRODUCTION TO SWAN MODEL

SWAN model is a third generation wave model based on the action density balance equation and linear random surface gravity wave theory, developed by the department of civil engineering of Delft University in the Netherlands. The SWAN model can describe wave propagation processes as follows: wave propagation in geographic space, shallowness and refraction caused by the changes of current and water depth, wave set-up, diffraction and other processes.

The SWAN model (Ris et al., 1999; Booij et al., 1999; Zijlema et al., 2005) adopts the action density balance equation as the governing equation to describe the waves， the governing equation of the SWAN model in the Cartesian coordinate system as in Eq.[1].

$$\frac{\partial}{\partial t}N+\frac{\partial}{\partial x}C_xN+\frac{\partial}{\partial y}C_yN+\frac{\partial}{\partial \sigma}C_\sigma N+\frac{\partial}{\partial \theta}C_\theta N=\frac{S}{\sigma} \quad [1]$$

Where, the first term on the left shows the rate of change of the action density with time. N represents the action density. The second and third terms represent the propagation of the action density in geometric space. C_x and C_y represent the propagation velocity in x and y directions respectively. The fourth term represents the frequency shift caused by the current and the water depth change. The fifth term represents refraction and shallowness due to the current and the water depth change. C_σ and C_θ represent the propagation velocity in spectral space (σ,θ). The S on the right side of the equation represents the source terms (Booij et al., 1999; Akpınar et al., 2012), which is used to represent various physical processes, including wave growth due to wind input, dissipations due to whitecapping, bottom friction, depth-induced wave breaking, non-linear triad wave-wave interaction and quadruplet wave-wave interactions.

3 COMPUTATIONAL DOMAINS AND GRID

There are two computational domains in this paper. Region Ⅰ is the South China Sea and region Ⅱ is the Yongle Atoll area of the South China Sea.

In SWAN mode, there are the rectangular grid, the curve grid and the triangular grid to choose from. In this paper, rectangular grid and triangular grid were used. SWAN mode can also be nested with a variety of modes, including self-nesting with SWAN mode, and nesting with WAVEWATCH Ⅲ and WAM mode. In this paper, what the nested grid technology adopted was self-nesting with SWAN mode.

3.1 Computational domains

The computational domain Ⅰ is the South China Sea, with a range of 105°E-125°E and 9°N-24°N, with a resolution of about 0.0083°, as shown in figure 1. The computational domain Ⅱ is the Yongle Atoll, with a range of 111.49°E-111.805°E and 16.4198°N-16.618°N, resolution of about 0.0009 °, as shown in figure 2. The terrain documents were provided by China Ship Scientific Research Center. Buoy information was shown in table 1.

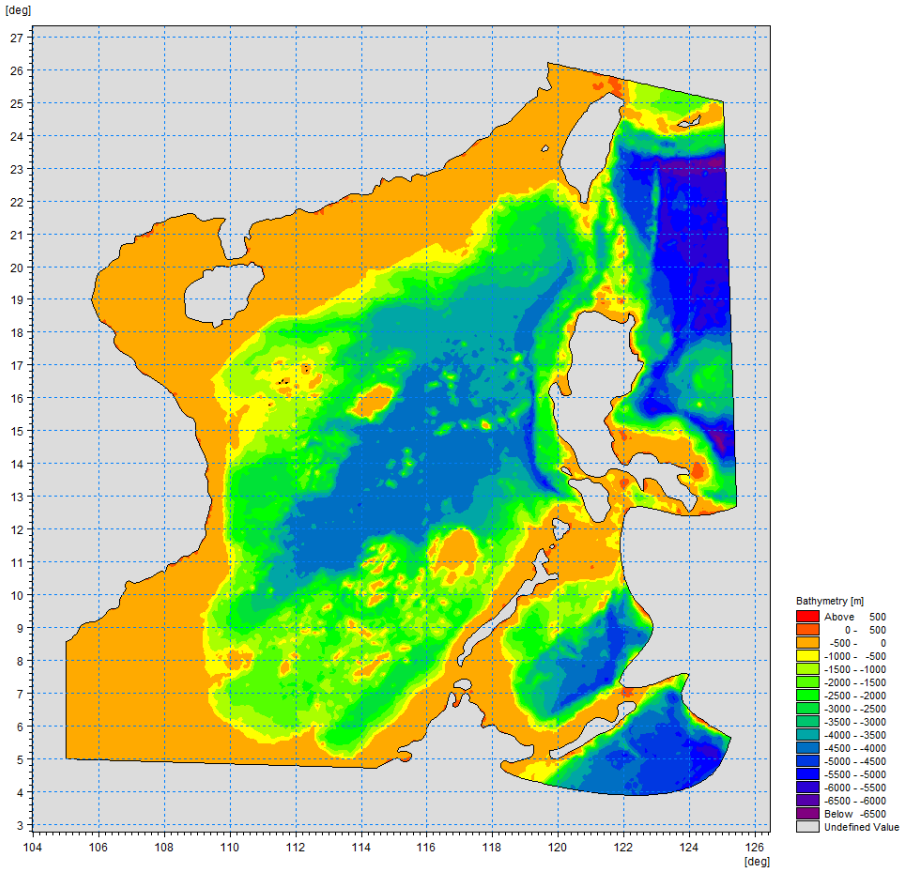

Figure 1. Topographic map of computational domain Ⅰ

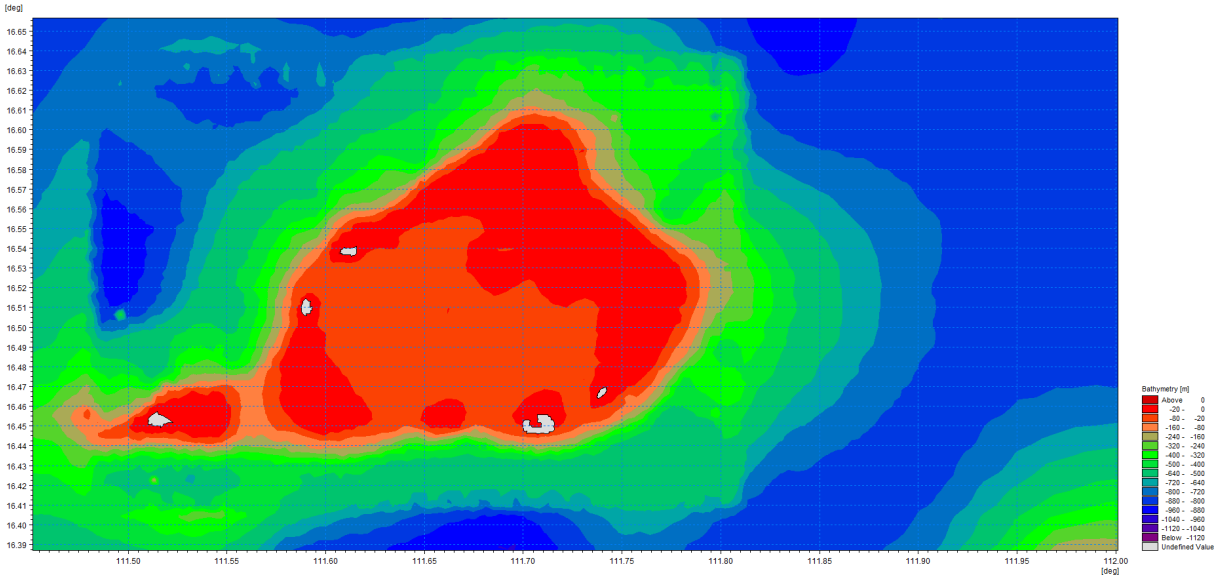

Figure 2. Topographic map of computational domain Ⅱ

Table 1. Buoy information

Buoy name	Lon (°E)	Lat (°N)	Water depth (m)
Ocean wave direction measurement system	111.73825	16.47468	20

3.2 Nested grid technology

The nested grid technology adopted in this paper is the two-layer rectangular grid nesting. That is, the rectangular grids are used in the computing regions Ⅰ and Ⅱ. The number of grids in the computing region Ⅰ is 600×600, and the resolution in the longitude direction is 0.033° and the latitude direction is 0.025°. The number of grids in the computing region Ⅱ is 350×220, and the resolution in the longitude direction is 0.0009° and the latitude direction is 0.0009°. The wave field simulated in the computing region Ⅰ is used as the boundary

conditions of the wave field in region Ⅱ. That is, the boundary conditions of wave field in region Ⅰ are generated by numerical simulation of region Ⅱ.

3.3 Unstructured grid

The unstructured grid used in this paper is triangular grid, and the computing region is region Ⅰ, with a range of 105°E-125°E and 9°N-24°N. This type of grid can control the terrain resolution by controlling the size of the distance between the grid points. As shown in figure 3, in the islands and reefs areas, the minimum grid points are separated by 300 meters, while in the outer open sea, the maximum grid points are separated by 0.167° (about 3.5km). The triangular grids were provided by South China Sea Institute of Oceanology, Chinese Academy of Sciences.

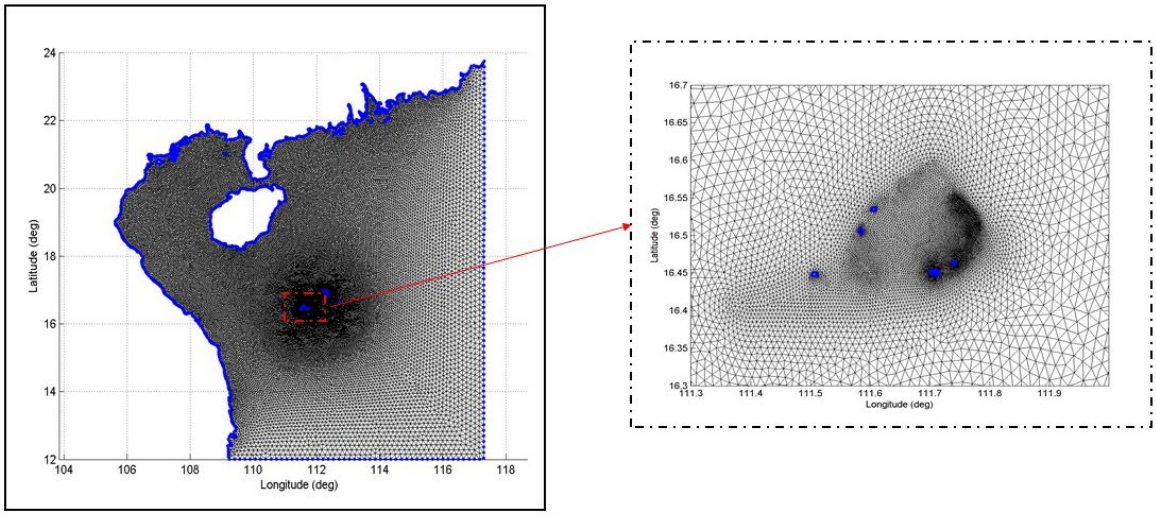

Figure 3. Triangular grids

4 NUMERICAL SIMULATION OF WINTER WAVE FIELD IN THE SOUTH CHINA SEA

4.1 Wind field

The wind field files were provided by China Ship Scientific Research Center. The wind field is the wind speed at 10 meters. The spatial resolution of the wind field is 0.1°, and the temporal resolution is 1 hour. Figure 4 compares the inputted wind speed and the observations during December 2014, which shows good agreement between the two datasets.

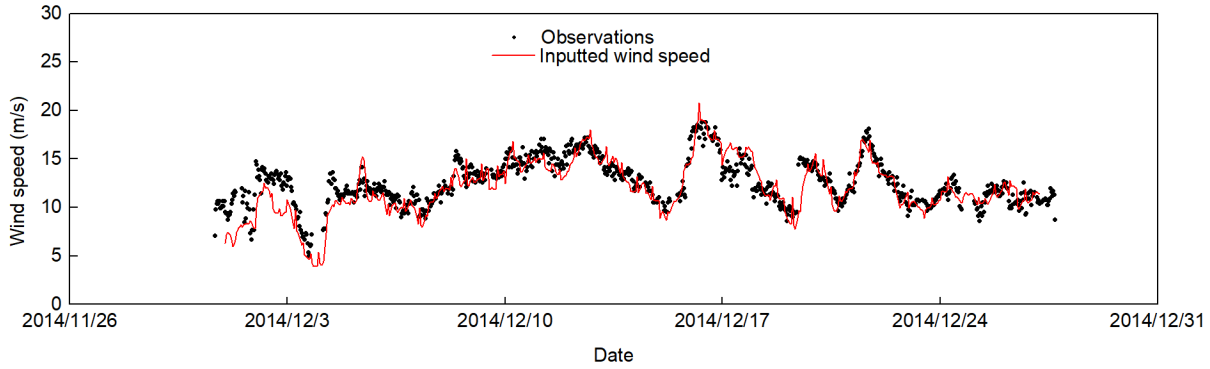

Figure 4. Comparison of inputted wind speed with observations

4.2 Model setup

The time step length of the numerical simulation is 10min, and the discrete frequency range is 0 to 1.5Hz. During the calculation, the triad wave-wave nonlinear interaction, quadruplet wave-wave nonlinear interaction, wave breaking, whitecapping dissipation and bottom friction source term were turned on, and all coefficients were default values.

5 RESULTS ANALYSIS

5.1 Significant wave height time series

The time series of significant wave height was shown in figure 5. The numerical simulation results of the two grid models agreed well with the overall variation trend of the observations in general, but the significant wave heights simulated using the triangular grids were a little higher than observed. The significant wave heights simulated using the nested grid technology were in good agreement with the observations, but at the peaks, the numerical simulation results were lower than the observations. Through calculation, the mean relative error between the simulated using the triangular grids and the observed was 28.52%, and the root-mean-square error (RMSE) between the assimilated using the triangular grids and observed was 0.1388m. The mean relative error between the simulated using the nested grid technology and the observed was 13.48%, and the RMSE between the assimilated using the nested grid technology and observed was 0.0763m. Apparently, the significant wave heights simulated using the nested grid technology came closer to the observations.

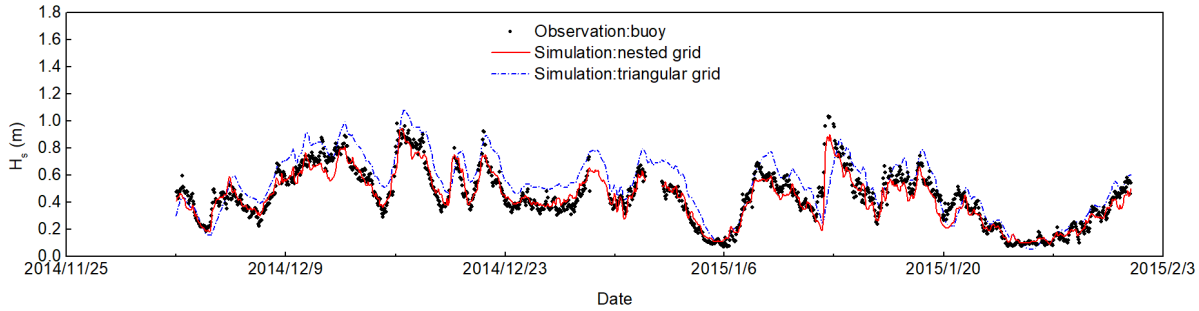

Figure 5. Comparisons of calculated significant wave heights with observations

5.2 Mean period time series

The mean period time series was shown in figure 6. The variation trend of the numerical simulation results was basically consistent with observations, but the numerical simulation results were significantly lower than the observations, especially, the numerical simulation results calculated by the nested grid technology. Through calculation, the mean relative error between the simulated using the triangular grids and the observed was 11.33%, and the RMSE between the assimilated using the triangular grids and observed was 0.4357s. The mean relative error between the simulated using the nested grid technology and the observed was 18.97%, and the RMSE between the assimilated using the nested grid technology and observed was 0.5965s. The mean periods simulated using the triangular grids obviously came closer to the observations.

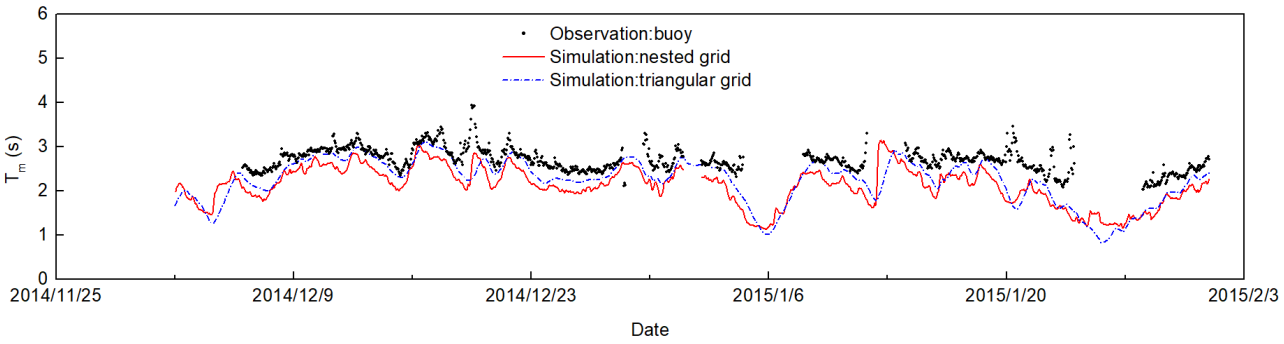

Figure 6. Comparisons of calculated mean periods with observations

6 CONCLUSIONS

This paper utilized the internationally advanced third-generation wave model SWAN on the numerical simulation of the South China Sea wave field for two months from December 1, 2014 to January 31, 2015, adopting nested grid technology and unstructured grid respectively. By comparing the numerical simulation results with the observations, the mean relative error between the simulated using the triangular grids and the observed significant wave heights was 28.52%, and the RMSE was 0.1388m. The mean relative error between the simulated using the nested grid technology and the observed significant wave heights was 14.48%, and the RMSE was 0.0763m. The mean relative error between the simulated using the triangular grids and the observed mean periods was 11.33%, and the RMSE was 0.4357s. The mean relative error between the simulated using the nested grid technology and the observed mean periods was 18.97%, and the RMSE was 0.5965s. The error analysis shows that the significant wave heights simulated using the nested grid technology came closer to the observations and the mean periods simulated using the triangular grids came closer to the observations. But in the numerical simulation of wave field, the main concern is the wave height, so the numerical simulation results calculated by the nested grid technology are better than the triangular grids. Therefore, we can think using the

nested grid technology of the SWAN wave model can more accurately simulate the winter wave fields in the South China Sea, which is of great significance to the numerical prediction of long-term wave fields in the South China Sea.

ACKNOWLEDGEMENTS

This research was funded by Ministry of Industry and Information Technology of China ([2016]22), and National Key Research and Development Program of China (2019YFC0312400) & (2017YFE0132000). The authors would like to thank the China Ship Scientific Research Center for providing the terrain documents and wind field files, and the South China Sea Institute of Oceanology, Chinese Academy of Sciences for providing the triangular grids and observations.

REFERENCES

Xu, Y., He, H.L., Song, J.B., Hou, Y.J., and Li, F.N. (2017). Observations and Modeling of Typhoon Waves in the South China Sea. *Journal of Physical Oceanography*, 47 (6), 1307-1324.

Zhou, L.M., Li, Z.B., Mou, L., and Wang, A.F. (2014). Numerical simulation of wave field in the South China Sea using WAVEWATCH Ⅲ. *Chinese Journal of Oceanology and Limnology*, 32 (3), 656-664.

Wang, J.C., Zhang, J., and Yang, J.G. (2014). Numerical simulation and preliminary analysis on ocean waves during Typhoon Nesat in South China Sea and adjacent areas. *Chinese Journal of Oceanology and Limnology*, 32 (3), 665-680.

Kim, T.R., and Jae Lee, H. (2018). Comparison of High Wave Hindcasts during Typhoon Bolaven (1215) using SWAN and WAVEWATCH Ⅲ Model. *Journal of Coastal Resear*

ch, 85 (sp1), 1096-1100.

Akpınar, A., Bingölbali, B., and Van Vledder, G.P. (2016). Wind and wave characteristics in the Black Sea based on the SWAN wave model forced with the CFSR winds. *Ocean Engineering*, 126, 276-298.

Ris, R.C., Holthuijsen, L.H., and Booij, N. (1999). A third-generation wave model for coastal regions: 2, verification. *Journal of Geophysical Research*, 104 (C4), 7667–7681.

Booij, N., Holthuijsen, L.H., and Ris, R.C., (1999). A third-generation wave model for coastal regions. Model description and validation. *Journal of Geophysical Research*, 104 (C4), 7649–7666.

Zijlema, M., and Van der Westhuysen, A.J., (2005). On convergence behaviour and numerical accuracy in stationary SWAN simulations of nearshore wind wave spectra. *Coastal Engineering*, 52 (3), 237–256.

Akpınar, A., van Vledder, G.P., Kömürcü, M.İ., Özger, M., (2012). Evaluation of the numerical wave model (SWAN) for wave simulation in the Black Sea. *Continental Shelf Research*, 50–51, 80–99.

8th International Conference on the Application of Physical Modelling in Coastal and Port Engineering and Science
Dec. 9th - 12th, 2020, Zhoushan, China

PRELIMINARY RESULTS ON THE DYNAMICS OF A PILE-MOORED FISH CAGE WITH ELASTIC NET IN CURRENTS AND WAVES

ZITTI GIANLUCA(1), NOVELLI NICO&BROCCHINI MAURIZIO

Dipartimento Ingegneria Civile, Edile e dell'Architettura
Università Politecnica delle Marche, Ancona, Italy
(1)e-mail: g.zitti@univpm.it

ABSTRACT

Over the last decades the aquaculture sector increased significantly and constantly, moving fish-farm plants further from the coast, and exposing them to increasingly high forcing due to currents and waves. The performances of cages in currents and waves have been widely studied in literature, by means of laboratory experiments and numerical models, but virtually all the research is focused on the global performances of the system, i.e. on the maximum displacement, the volume reduction or the mooring tension.
In this work we propose a numerical model, derived from the net-truss model of Kristiansen and Faltinsen (2012), to study the dynamics of fish farm cages in current and waves. In this model the net is modeled with straight trusses connecting nodes, where the mass of the net is concentrated at the nodes. The deformation of the net is evaluated solving the equation of motion of the nodes, subjected to gravity, buoyancy, lift and drag forces. With respect to the original model, the elasticity of the net is included. In this work the real size of the net is used for the computation mesh grid, this allowing the numerical model to reproduce the exact dynamics of the cage.
The numerical model is used to simulate a cage with fixed rings, based on the concept of mooring the cage to the foundation of no longer functioning offshore structures. The deformation of the system subjected to currents and waves are studied.

Keywords: Fish cage, Cage dynamics, Deformable net, Numerical model, Current and Waves.

1 INTRODUCTION

The aquaculture sector has been characterized by a significant increase in production and revenues over the last decades. The latest FAO report on fish consumption (Food and of the United Nations, 2017) showed that fish-farming provides more than 40% of the fish production in 2015. Further, while fish capture amount remained constant in the period 2008-2015, fish farming was characterized by a constant rise. This trend required fish-farm plants to be larger and located in offshore sites, where they are exposed to stronger actions (Klebert et al., 2013).

The performances of fish-farm cages have been analyzed both experimentally and numerically, with a large focus on the determination of the hydrodinamic coefficients of the net, forced by currents or waves. For example, Lader and Fredheim (2006) evaluated experimentally the drag and lift forces onto a net in uniform flow, while Tsukrov et al. (2011) provided empirical values for the normal drag coefficients of copper nets. On the other hand, numerical models (validated experimentally) have been applied to the study and design of real fish cages, including floating top rings, mooring elements, or coupling multiple cages.

Among the different numerical models used in literature to simulate the dynamics of fish-farm net in currents and waves, the most used are the lumped-mass method, the net-truss model, the spring-mass model and finite elements models. The large number of models and applications testifies the capability of these models to reproduce the nets behaviours, subjected to different loads. The lumped-mass method, proposed by Tsukrov et al. (2003), modeled included the effects of drag, inertia, weight, buoyancy and net elasticity. The model was validated and applied to several fish farm configurations with different environmental forcing (Li et al. 2006 , Zhao et al. 2007, Dong et al. 2010, Xu et al. 2011, Chen et al. 2012, Zhao et al. 2013, Xu et al. 2013, Cui et al. 2013, Huang et al. 2018, Huang et al. 2019). The net-truss model, originally presented by Bris and Marichal (1998) simulated the net with straight trusses connecting nodes. The model was improved and applied by Kristiansen and Faltinsen (2012, 2015), who introduced the screen model for the viscous forces

and applied the method for the study of an aquaculture net cage with floaters in currents and waves. The net-truss model is at the basis of the super-elements model (Lader and Fredheim, 2001; Lader et al., 2001, Lader et al. 2002, Lader and Fredheim, 2006; Klebert et al., 2015), where net mesh is grouped into super-elements, composed by consistent and diagonal trusses, characterized by lumped-masses and nonlinear springs. The spring-mass model, proposed by Lee et al. (2008,2015) approximated the net mesh to virtual mathematical mesh with size larger than the real one. Finite elements methods (FEM) were also used, exploiting the implementation in commercial software, such as Ansys Aqwa (DeCew et al. 2010) and Abaqus (Li et al. 2013a,b). In most of these models the computational cost is reduced by lumping the properties of the large number of cage nodes into a small number of panels. This approximation does not affect the efficiency of the methods in terms of mooring tension and volume reduction (Klebert et al., 2015). However, the coarser mesh reduces the capability of these models to represent the actual deformation of the cages. For example, Moe-Føre et al. (2015) compared three different approximated numerical models, finding them good for the design process, but overpredicting the loads acting on the structures for high solidity ratio.

In the present paper we use a deformable net-truss model, based on the model proposed by Kristiansen and Faltinsen (2012), to study the dynamics of a specific, but emblematic, fish cage as forced by both sea currents and waves. In particular, the net elements are not grouped into a coarser mesh, therefore the computational resolution corresponds exactly to the real-life net grid. Hence, in contrast to other recent applications of net models, the application here proposed simulates accurately the dynamics of each point of the net. The cage considered for the simulations is a cylindrical cage fixed to a top ring and a bottom ring, which are moored to a central pillar (see the sketch of Fig. 1). This structural concept derives from the idea of exploiting the foundation of dismissed offshore structures as structural elements of the cage.

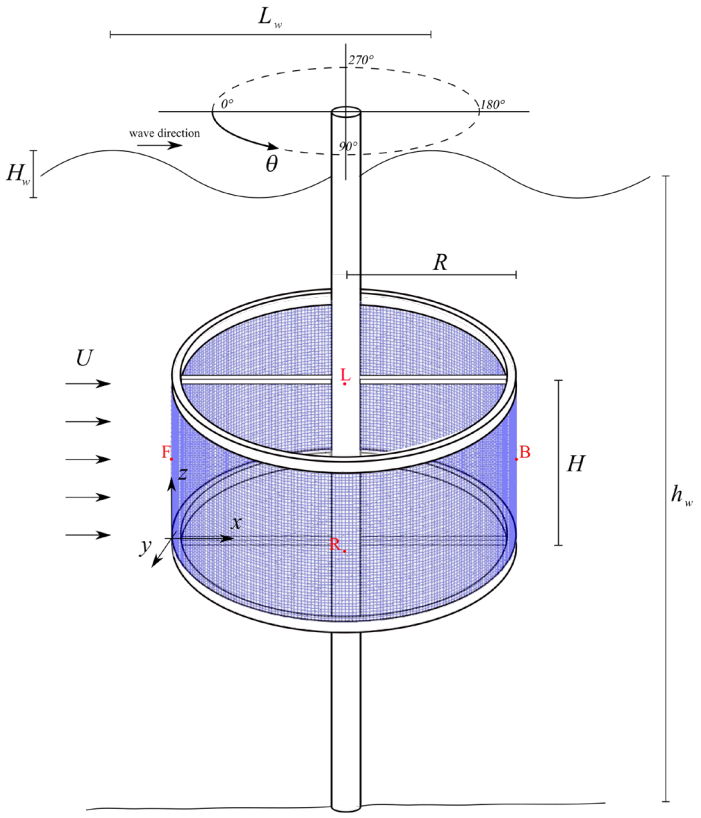

Figure 1. Sketch of a cylindrical cage fixed to two rings moored to a central pillar. Red points are reference locations for the analyses.

The geometry of the cage is characterized by the cage radius R=1 m, the cage height H=1 m, and the cage is located at water depths between 2 m and 4 m from the free surface. The net mesh is squared, with twine length being l_0=0.02 m and the twine diameter (or thickness) d_{twine}=0.0015 m. Hence, the solidity ratio can be calculated, following Kristiansen and Faltinsen (2012), $S_n=2(d_{twine}/l_0)-(d_{twine}/l_0)_2$~0.144. The material of the net is assumed to be elastic and isotropic, with Young modulus $E=81\cdot10^6$ N/m^2.

The dynamics of the net is simulated with two loading conditions: a steady current with velocity U=0.5 m/s, and a monochromatic wave with height H_w=1 meter and length L_w=25 meters in deep water (time averaged water depth h_w=20 m). These are taken as representative of typical working conditions at sea.

2 METHODS

The numerical model used in this work to reproduce in detail the deformation of the net is inspired by the net-truss model proposed by Kristiansen and Faltinsen (2015), where the net is represented by nodes connected by straight trusses. Each *ij*-node, representing a net knot, is described by the vector $\boldsymbol{x}_{ij}$, collecting its spatial coordinates. Trusses represent the net twines and the *ijhk*-truss, linking nodes *ij* and *hk*, is described by its length l_{ijhk} and by its direction vector $\boldsymbol{s}_{ijhk}$. The displacements of the nodes were solved by means of the time-discretized motion equation. Time is discretized in steps of size Δt. Hence, the position of the *ij*-node at the time step *n+1* is evaluated from the position of the *ij*-node at the time step *n* using the velocity of the *ij*-node at the time step *n+1*:

$$\boldsymbol{x}_{ij}^{n+1} = \boldsymbol{x}_{ij}^{n} + \boldsymbol{u}_{ij}^{n+1}\Delta t \quad [1]$$

where the velocity of the *ij*-node at the time step *n+1* is evaluated from the velocity of the *ij*-node at time step *n* using the acceleration of the ij-node at the time step n:

$$\boldsymbol{u}_{ij}^{n+1} = \boldsymbol{u}_{ij}^{n} + \boldsymbol{a}_{ij}^{n}\Delta t \quad [2]$$

The acceleration is evaluated using the dynamic equilibrium principle:

$$M_{ij}\boldsymbol{a}_{ij}^{n} = \boldsymbol{f}_{int\,ij}^{n} + \boldsymbol{f}_{ext\,ij}^{n} \quad [3]$$

Where M_{ij} is the mass of the net concentrated at *ij*-node, while $\boldsymbol{f}_{int\,ij}^{n}$ and $\boldsymbol{f}_{extij}^{n}$ are the internal and external contributions to the force acting on the node *ij* at time step *n*.

The concentrated mass of each node M_{ij} is calculated by the product of the twines volume by the polyamide density ρ_{PA6}=1140 kg/m^3, equally divided between the two contact nodes. The obtained mass was multiplied by a coefficient equal to 1.5, to include the added mass effect (see e.g. Dong et al. (2010) and Lee et al. (2015)).

Differently from the model of Kristiansen and Faltinsen (2015), in our model the kinematic constraint of the constant truss length is not imposed. Hence, the internal force contribution is evaluated using a linear elastic relation between the deformation and tension of the trusses.

The internal forces on a node are given by the force contributions of all the trusses insisting on the node. Since the net is squared, the internal forces is given by the tensile contribution of four twines σ_{ijhk}^{n}, multiplied by the cross sectional area of the truss A_{twine}, which is constant because the twine diameter variation is assumed negligible during the deformation:

$$\boldsymbol{f}_{int\,ij}^{n} = A_{twine}\left(\boldsymbol{\sigma}_{ijij+1}^{n} + \boldsymbol{\sigma}_{iji+1j}^{n} + \boldsymbol{\sigma}_{ijij-1}^{n} + \boldsymbol{\sigma}_{iji-1j}^{n}\right) \quad [4]$$

The internal tensions act in the direction of the corresponding truss and vanish when the trusses are compressed:

$$\boldsymbol{\sigma}_{ijhk}^{n} = \begin{cases} E\varepsilon_{ijhk}^{n}\boldsymbol{s}_{ijhk}^{n} & \text{if} \quad \varepsilon_{ijhk}^{n} > 0 \\ \mathbf{0} & \text{if} \quad \varepsilon_{ijhk}^{n} < 0 \end{cases} \quad [5]$$

where *E* is the material Young modulus and ε_{ijhk}^{n} is the elongation of the *ijhk*-truss at time step *n*, defined as:

$$\varepsilon_{ijhk}^{n} = \frac{l_{ijhk}^{n} - l_{ijhk}^{0}}{l_{ijhk}^{0}} \quad [6]$$

The external forces $\boldsymbol{f}_{ext\,ij}^{n}$ on the *ij*-node at time step *n* are composed by gravity, buoyancy and viscous forces and can be expressed as:

$$\boldsymbol{f}_{ext\,ij}^{n} = M_{ij}\left(1 - \frac{\rho_{PA6}}{\rho_w}\right)\mathbf{g} + \boldsymbol{f}_{V\,ij}^{n} \quad [7]$$

The first term includes gravity and buoyancy, where *g* is the gravitational acceleration vector and ρ_w is the water density. The second term $\boldsymbol{f}_{\boldsymbol{V}\,\boldsymbol{ij}}^{\boldsymbol{n}}$ represents the viscous force, due to the interaction of the net with the fluid. It has been evaluated using the screen model proposed by Kristiansen and Faltinsen (2012).

Since both the internal and external forces can be calculated from the coordinates and velocity of the nodes at time step *n*, the acceleration at such time step *n* can be evaluated directly from Equation [3]. This set of equations, together with the boundary conditions of zero displacement (i.e. zero acceleration) given at the nodes of the top and bottom rings, is a set of algebraic equations that can be solved in terms of the acceleration. The evaluated acceleration can be substituted into Equations [2] and [1], to update the velocity and the position of the nodes at time step *n+1*.

2.1 Validation

The numerical model here proposed has been validated by simulating the experimental test reported in Section 3.2 of Bi et al. (2014). A square panel of flexible net with size 0.30 × 0.30 m, fixed at the free surface and weighted at the bottom with two steel bars, was subjected to a water current with four different velocities U=0.058, 0.113, 0.170 and 0.226 m/s, using the method above reported. The net was characterized by trusses with length l^0=0.02 m and diameter d_{twine}=0.0026 m, composed by polyethylene (with density ρ_{PE}=880 kg/m^3 and Young modulus $E_{PE}=6\cdot10^{-8}$ N/m^2). The four experiments have been simulated with the proposed numerical model, using the net material characteristics reported above and a time step size of Δt = 0.0025 in the two test with the lowest velocities and Δt = 0.001 in the two test with the highest velocities. The grid used for the simulation is exactly the geometry of the net, characterized by a squared net with initial truss length l^0=0.02 m. The two support steel bars, at the net top edge and the other mounted on the bottom of the net as a sinker system, were 0.3 m long, 6 mm in diameter, and with mass of 73 g. The two bars are implemented in the numerical simulations introducing the additional weight and the additional drag force, with drag coefficient of C_D=2, applied proportionally to the nodes where the two bars are attached. In Fig 2 the drag evaluated with numerical simulations is compared with the corresponding experimental results of Bi et al. (2014). Here, also the results of the numerical model proposed by the same benchmark reference is reported. The results obtained with the proposed model highlight the capability of the code to reproduce the drag force measured in the experiments with good accuracy. In particular, the simulation characterized by the highest current velocity show a better accuracy than the simulation proposed by Bi et al. (2014).

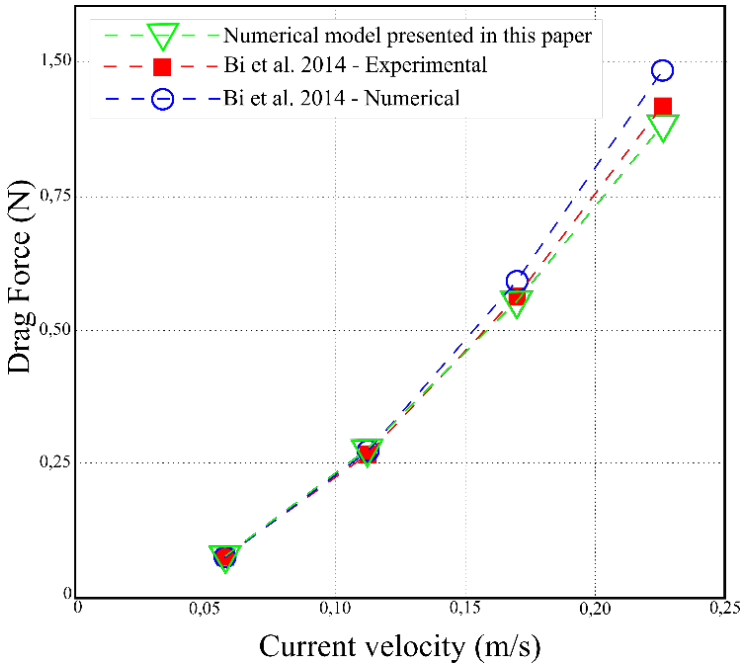

Figure 2. Comparison of the drag forces measured experimentally (red dashed line and red squares) and evaluated numerically (blue lines and blue circles) by Bi et al. (2014), and the drag forces evaluated numerically with the proposed method (green line and triangles).Modified figure from Bi et al. (2014).

3 RESULTS

The model has been applied to two cases: one with forcing due to a steady sea current only, and one with forcing due to a linear wave only. The initial condition was the undeformed condition, with zero motion. The total time of simulation has been set to 4 s for the simulation with the sea current and to 32 s for the simulation with the waves. The total run time has been discretized in time steps of size Δt = 0.00005 s.

The results are reported in dimensionless form. The displacement $\boldsymbol{\delta}_{ij}^{n} = \boldsymbol{x}_{ij}^{n} - \boldsymbol{x}_{ij}^{0}$is made dimensionless using the height of the cage *H* for the vertical displacement and the undisturbed radius of the cage *R* for the horizontal displacement:

$$\boldsymbol{\delta}_{ij}^{n} \rightarrow \boldsymbol{\delta}_{ij}^{n*} = \begin{cases} \dfrac{\boldsymbol{\delta}_{ij}^{n}}{R} & \text{for horizontal components} \\ \dfrac{\boldsymbol{\delta}_{ij}^{n}}{H} & \text{for vertical components} \end{cases} \quad [8]$$

For the simulation forced by a sea current, the time scale is taken equal to $\sqrt{R/g}$, while for the simulation forced by the waves, the time scale is the wave period *T*:

$$t \rightarrow t^{*} = \begin{cases} \dfrac{t}{\sqrt{R/g}} & \text{for the sea current test} \\ \dfrac{t}{T} & \text{for the wave test} \end{cases} \quad [9]$$

In the following, results are reported for four significant points at the mid-height nodes of the cage upstream (point F at *z*=0.5 m and *θ*=0° in Fig. 1), downstream (point B at z=0.5 m and *θ*=180° in Fig. 1) and at the two lateral sides (points L and R at z=0.5 m and θ=90° and θ=270°, respectively, in Fig. 1).

3.1 Cage dynamics in steady sea currents

The simulation for the steady current case starts from an undeformed configuration. Hence, the first phase of the simulation reproduces the transient. This is evident from the time evolution of the displacement of the four significant nodes, reported in Fig.3. After t*=0.5, the steady condition is attained. The displacement in the flow direction (top panel in Fig.3) is obviously the largest one, with a maximum displacement of about δ_x^*~0.05 in the back point and about δ_x^*~0.04 in the frontal and lateral points. Further, displacement of the lateral points is evident in the cross-flow direction (middle panel in Fig.3). The magnitude of this displacement is of about $|\delta_y^*|$~0.005 and it is positive (i.e. toward the right direction) for the point on the left side L, and negative (i.e. toward the left direction) for the point on the right side R. Finally, the displacement in the vertical direction (bottom panel in Fig.3) is negligible at the four check points.

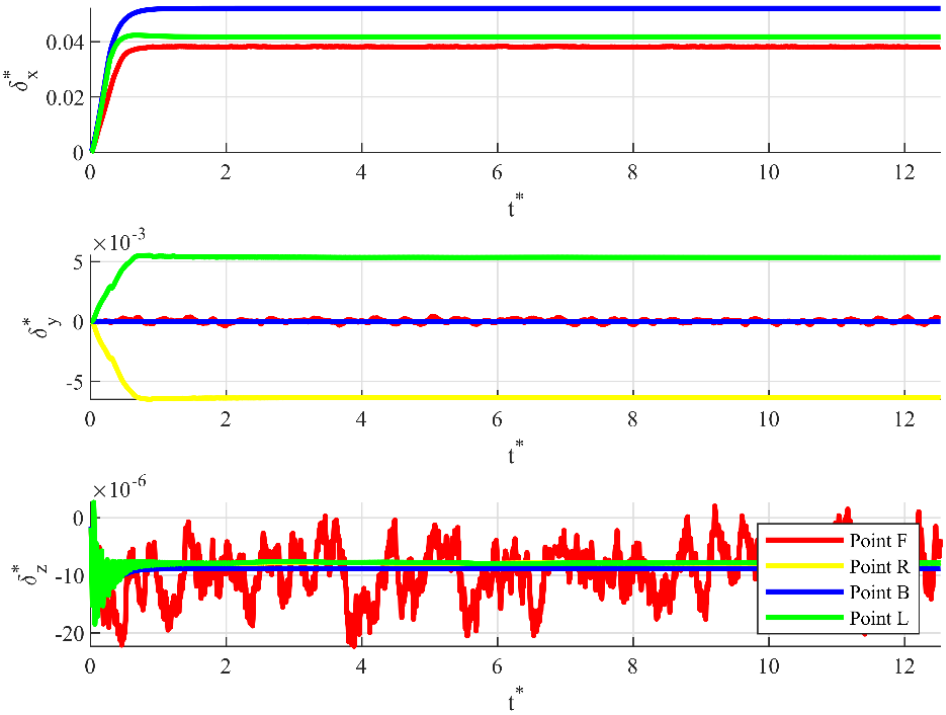

Figure 3. Displacements at the four reference mid-height nodes (points F, B, R and L in Fig. 1) in the flow direction (top panel), cross-flow direction (middle panel) and vertical direction (bottom panel), for the steady current test.

3.2 Cage dynamics in sea waves

Also the simulation with waves starts from an undeformed configuration and displays an initial transient phase, after which the time evolution of the displacement is quasi-steady. The simulation reproduces two periods (see the time evolution of the displacement in the three directions of the significant nodes reported in Fig4). The maximum and minimum displacements in each direction of the reference points in the first reproduced period after the transient phase, i.e $0.25 \leq t^* \leq 1.25$, with the corresponding time, are reported in Table 1.

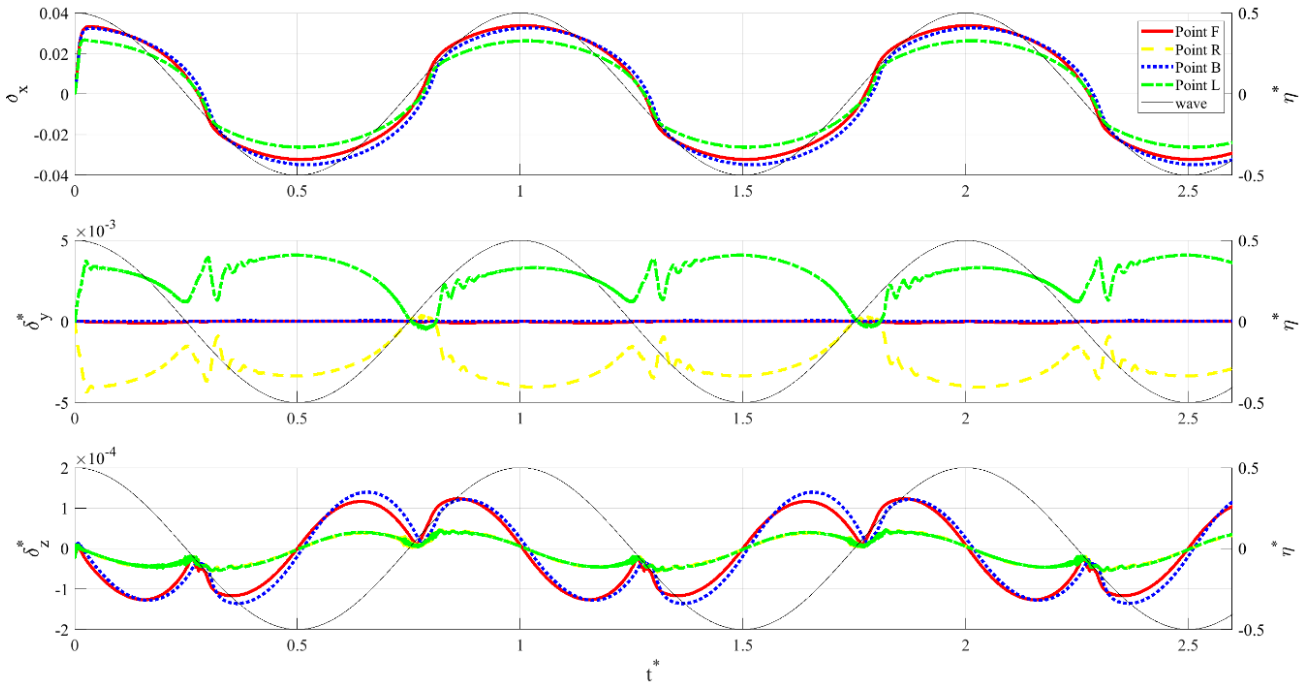

Figure 4. Displacements of the four significant mid-height nodes in the wave direction (top panel), cross-flow direction (middle panel) and vertical direction (bottom panel), for the linear wave test. The black dashed line represents the water elevation above the front of the cage $\eta^*=\eta/H$.

Table 1. Maximum and minimum displacements in each direction of the reference points, with the corresponding time, in the first simulated period after the transient phase ($0.25 \leq t^* \leq 1.25$).

	$\delta^*_{x\,max}$	t^*	$\delta^*_{y\,max}$ [m 10^-3]	t^*	$\delta^*_{z\,max}$ [m 10^-3]	t^*
F	0.034	1.00	2.708	0.44	123.340	0.86
B	0.033	1.01	47.298	0.67	139.640	0.65
L	0.026	1.01	4085.900	0.49	45.534	0.81
R	0.026	1.01	370.190	0.77	47.086	0.82
	$\delta^*_{x\,min}$	t^*	$\delta^*_{y\,min}$ [m 10^-3]	t^*	$\delta^*_{z\,min}$ [m 10^-3]	t^*
F	-0.032	0.503	-0.084	0.164	-0.126	1.147
B	-0.035	0.516	-0.012	0.782	-0.136	0.363
L	-0.026	0.505	-0.488	0.783	-0.055	0.323
R	-0.026	0.505	-4.043	1.027	-0.056	0.308

The displacement in the wave direction (top panel in Fig.4) is very similar to the wave profile evolution, even if some sharp-cornered inflection points appears after every zero-upcrossing and zero-downcrossing point. The amplitude of the displacements of the frontal and back points (about δ^*_x~ 0.035) is larger than the amplitude of the displacements of the lateral points (about δ^*_x~ 0.025). Instead, the displacement in the cross-flow direction (middle panel in Fig4) is characterized by a more complicated behaviour. It is smaller than 10−3 at the frontal and back points, while the displacement of the lateral points are complex specular functions, toward the right direction for the left point L and toward the left direction for the right point R. These displacements resemble positive wave functions, whose amplitude reaches a maximum displacement of about δ^*_y~0.004 and occurs when the forcing wave is in its crest and trough conditions. Further, higher frequency

oscillations of the crossflow displacement of the lateral point occur during the zero-downcrossing and zero-upcrossing of the forcing wave. Finally, the displacement in the vertical direction (bottom panel in Fig4) shows a complex evolution, characterized by a quasi-steady evolution, significantly different from the wave oscillation. Oscillations of frontal and back points show larger amplitudes than those of the lateral points, but the values are always smaller than 10−3 at the four check points.

Comparison of the sea wave forcing signal with the displacement of the reference points in the wave direction, reported in Fig 4, reveals a difference in phase, the cage displacement been delayed to the sea wave forcing. Such delay is evaluated as the difference between the zero upcrossing/downcrossing time of the sea wave η(t) and the zero upcrossing/downcrossing time of the reference point displacement. Delays are reported, for each zero upcrossing/downcrossing and each reference point in Table 2. The delay ranges between t*=0.025 and t*=0.032 for the frontal and lateral reference points, while is higher for the back point, where it ranges between t*=0.037 and t*=0.039.

Table 2. Timing of zero down crossing (0-DC) and zero up crossing (0-UC) of the wave and of the cage displacement and delay.

	1st 0-DC	1 st 0-UC	2nd 0-DC	2nd 0-UC	3rd 0-DC
t*(η=0)	0.250	0.750	1.250	1.750	2.250
t*(δ_x^*=0)in F	0.278	0.775	1.278	1.775	2.278
delay for F	0.028	0.025	0.028	0.025	0.028
t*(δ_x^*=0) in B	0.287	0.789	1.287	1.789	2.287
delay for B	0.037	0.039	0.037	0.039	0.037
t*(δ_x^*=0) in L	0.279	0.781	1.279	1.782	2.279
delay for L	0.029	0.031	0.029	0.032	0.029
t*(δ_x^*=0) in R	0.279	0.781	1.279	1.782	2.279
delay for R	0.029	0.031	0.029	0.032	0.029

4 DISCUSSION AND CONCLUSIONS

The proposed numerical solver is based on a model currently available in the literature, but the application is characterized by an accurate representation of the net. In fact, the net grid is reproduced by an exact reproduction of the physical mesh (without any grouping procedure), and the net elastic response is included in the model using a tension-deformation relation. In this manner, the proposed numerical model is suitable for simulating accurately the behaviors of a fish-farm cage. It can provide the displacement, the deformation and the tension of each truss of the net. In this manner it is possible to evaluate important design parameters, such as the maximum displacement and specific evolution of the net displacement. The numerical model is used to reproduce the dynamics of a pile-moored fish cage with a simple cylindrical shape. The variation in space of displacement are accurately reproduced in both the forcing conditions of current and linear wave (typical forcing for marine deep waters). The capability of the numerical model in representing complex behaviors is evident from the analysis of the results of the simulation where the cage is forced by the wave. In fact, the model can track in time the displacement of each node. For example, the complex oscillations in time of the displacements of the reference points were accurately described and reported in Fig 4.

As expected, the maximum displacements of the net occur at the location where the net is perpendicular to the flow, i.e. at the frontal and back points. In particular, the maximum displacements due to wave forcing occur in the wave direction during the crest stage and in the opposite direction during the trough stage. Further, in both configurations, with sea current forcing and wave forcing the displacement in the cross-flow direction of the lateral points (where the net is parallel to the flow) is always toward the center of the net.

4.1 Conclusions and outlooks

- We used an accurate numerical model to describe carefully the reaction of a cylindrical pile-moored fish cage in sea currents and waves, representative for a possible application in the overall re-use strategy of an offshore platform foundation.

- We investigated the response of a fish farm new with respect to those treated so far in the sector, represented by a net cage fixed at the top and at the bottom, to two rigid rings).
- Simulations show expected major displacements of the frontal and back points of the net in the sea current and wave direction (at crest and trough stages), while unexpected displacements of the lateral points have been found in the crossflow direction, toward the center of the net.
- Beyond evaluating the significant parameters of the net displacement, the numerical model can also provide an accurate description of the distribution of deformation and tension in space and a more detailed description of the complex changes in shape of the net.
- In the future, a grouping method will be implemented in the numerical model, for the study of realistic pile-moored fish cage forced by realistic sea states.

ACKNOWLEDGEMENTS

This study was carried out in the framework of the project PLaCE (PON Ricerca e Innovazione 2014–2020, project code: ARS01_00891), co-funded by the European Union.

REFERENCES

Bi, C.-W., Zhao, Y.-P., Dong, G.-H., Xu, T.-J., Gui, F.-K., (2014). Numerical simulation of the interaction between flow and flexible nets. Journal of Fluids and Structures 45, 180–201.

Bris, F. L., Marichal, D., (1998). Numerical and experimental study of submerged supple nets: Applications to fish farms 3, 161–170.

Chen, C. P., Zhao, Y. P., Li, Y. C., Dong, G. H., Zheng, Y. N., (2012). Numerical analysis of hydrodynamic behaviors of two net cages with grid mooring system under wave action. China Ocean Engineering 26 (1), 59–76.

Cui, Y., Guan, C.-T., Wan, R., Huang, B., Li, J., sep 2013. Numerical simulation of a flatfish cage system in waves and currents. Aquacultural Engineering 56, 26–33.

DeCew, J., Tsukrov, I., Risso, A., Swift, M., Celikkol, B., (2010). Modeling of dynamic behavior of a single-point moored submersible fish cage under currents. Aquacultural Engineering 43 (2), 38–45.

Dong, G.-H., Xu, T.-J., Zhao, Y.-P., Li, Y.-C., Gui, F.-K., (2010). Numerical simulation of hydrodynamic behavior of gravity cage in irregular waves. Aquacultural Engineering 42 (2), 90–101.

Food, of the United Nations, A.O. (2017). FAO Yearbook of fishery and aquaculture statistics 2015. FAO.

Huang, X.-H., Guo, G.-X., Tao, Q.-Y., Hu, Y., Liu, H.-Y., Wang, S.-M., Hao, S.-H., (2018). Dynamic deformation of the floating collar of a net cage under the combined e_ect of waves and current. Aquacultural Engineering 83, 47–56.

Huang, X., Liu, H., Tao, Q., Hu, Y., Wang, S., Yuan, T., (2019). Numerical analysis of the dynamic response of a single-point mooring fish cage in waves and currents. Aquaculture Studies 19 (1).

Klebert, P., Lader, P., Gansel, L., Oppedal, F., jan (2013). Hydrodynamic interactions on net panel and aquaculture fish cages: A review. Ocean Engineering 58, 260–274.

Klebert, P., Patursson, Ø., Endresen, P.C., Rundtop, P., Birkevold, J., Rasmussen, H.W., (2015). Three-dimensional deformation of a large circular flexible sea cage in high currents: Field experiment and modeling. Ocean Engineering 104, 511–520.

Kristiansen, T., Faltinsen, O.M., (2012). Modelling of current loads on aquaculture net cages. 34, 218–235

Kristiansen, T., Faltinsen, O. M., (2015). Experimental and numerical study of an aquaculture net cage with floater in waves and current. Journal of Fluids and Structures 54, 1–26.

Lader, P., Fredheim, A., (2001). Modeling of net structures exposed to 3d waves and current. Open Ocean Aquaculture IV.

Lader, P., Fredheim, A., Lien, E., (2001). Dynamic behavior of 3d nets exposed to waves and current. In: The 20th International Conference on Offshore Mechanics and Arctic Engineering.

Lader, P. F., Enerhaug, B., Fredheim, A., Johnsen, S. G., Krokstad, J. R., (2002). Hydroelastic modelling of net structures exposed to waves and current.

Lader, P.F., Fredheim, A., (2006). Dynamic properties of a flexible net sheet in waves and current - a numerical approach. Aquacultural engineering 35 (3), 228–238.

Lee, C.-W., Kim, Y.-B., Lee, G.-H., Choe, M.-Y., Lee, M.-K., Koo, K.-Y., (2008). Dynamic simulation of a fish cage system subjected to currents and waves. Ocean Engineering 35 (14-15), 1521–1532.

Lee, C.W., Lee, J., Park, S., (2015). Dynamic behavior and deformation analysis of the fish cage system using mass-spring model. China Ocean Engineering 29 (3), 311–324.

Li, Y.-C., Zhao, Y.-P., Gui, F.-K., Teng, B., (2006). Numerical simulation of the hydrodynamic behaviour of submerged plane nets in current. Ocean Engineering 33 (17-18), 2352–2368.

Li, L., Fu, S., Xu, Y., (2013a). Nonlinear hydroelastic analysis of an aquaculture fish cage in irregular waves. Marine Structures 34, 56–73.

Li, L., Fu, S., Xu, Y., Wang, J., Yang, J., (2013b). Dynamic responses of floating fish cage in waves and current. Ocean Engineering 72, 297–303.

Moe-Føre, H., Christian Endresen, P., Gunnar Aarsæther, K., Jensen, J., Føre, M., Kristiansen, D., Fredheim, A., Lader, P., Reite, K.-J., (2015). Structural analysis of aquaculture nets: Comparison and validation of different numerical modeling approaches. Journal of Offshore Mechanics and Arctic Engineering 137 (4).

Tsukrov, I., Eroshkin, O., Fredriksson, D., Swift, M. R., Celikkol, B., (2003). Finite element modeling of net panels using a consistent net element 30, 251–270.

Tsukrov, I., Drach, A., DeCew, J., Swift, M. R., Celikkol, B., (2011). Characterization of geometry and normal drag coefficients of copper nets. Ocean Engineering 38 (17-18), 1979–1988.

Xu, T.-J., Dong, G.-H., Zhao, Y.-P., Li, Y.-C., Gui, F.-K., sep 2011. Analysis of hydrodynamic behaviors of gravity net cage in irregular waves. Ocean Engineering 38 (13), 1545–1554.

Xu, T.-J., Zhao, Y.-P., Dong, G.-H., Li, Y.-C., Gui, F.-K., may 2013. Analysis of hydrodynamic behaviors of multiple net cages in combined wave–current flow. Journal of Fluids and Structures 39, 222–236.

Zhao, Y.-P., Li, Y.-C., Dong, G.-H., Gui, F.-K., Teng, B., (2007). Numerical simulation of the e_ects of structure size ratio and mesh type on three-dimensional deformation of the fishing-net gravity cage in current. Aquacultural Engineering 36 (3), 285–301.

Zhao, Y.-P., kun Gui, F., Xu, T.-J., Chen, X.-F., Cui, Y., (2013). Numerical analysis of dynamic behavior of a box-shaped net cage in pure waves and current. Applied Ocean Research 39, 158–167.

8th International Conference on the Application of Physical Modelling in Coastal and Port Engineering and Science
Dec. 9th - 12th, 2020, Zhoushan, China

EXPERIMENTAL STUDY ON THE EVOLUTION OF EROSION AND DEPOSITION IN THE YELLOW RIVER ESTUARY

XIANG ZHAO(1), ZUWEN JI(1), ANJUN DENG(1) & DANGWEI WANG(1)

(1) State Key Laboratory of Simulation and Regulation of Water Cycle in River Basin, China Institute of Hydropower & Water Resources Research, Beijing, China
zx_sedi@163.com

ABSTRACT

The Yellow River estuary has the characteristics of less water and more sediment, and the distribution of water and sediment is uneven. The flow path swings frequently and has experienced 3 stages and 11 times major avulsions since 1855. Therefore, maintaining the stability of the Yellow River estuary flow path and prolonging the service life of the current flow path are important for the construction of the Yellow River Delta Highly Efficient Ecological Economic Zone. Based on the generalized model of the Yellow River estuary, the evolution of erosion and deposition of the Yellow River delta under different dynamics and boundary conditions are studied. For the problem of large test area topographic survey, the traditional measurement methods are time-consuming and labor-intensive. 3D laser scanning technology was adopted to measure the test terrain, and the test data statistics and analysis such as contour drawing and erosion and deposition calculation were made by ArcGIS software. The result shows that the runoff dynamic plays a dominant role in the evolution of erosion and deposition in the Yellow River delta, while the marine dynamics is relatively weak. In addition, the relationship between the distribution of erosion and deposition and the avulsion is discussed. The avulsion of the Yellow River estuary is not only related to the dynamic conditions, but also important to the boundary conditions, and the formation of boundary conditions is mainly related to the dynamic conditions. Therefore, the study on the evolution of erosion and deposition under different dynamic conditions and boundary conditions can provide some references for the breeding process of the avulsion of the Yellow River estuary.

Keywords: Yellow River estuary, Physical model, 3D laser scanning technology, evolution of erosion and deposition, avulsion

1 INTRODUCTION

The natural geographical position of the Yellow River estuary is very special, so it is very difficult for the field measurement. Therefore, there is often a lack of observational data in the study of the Yellow River estuary. We can only through the model to simulate the evolution of the estuary. Considering the complexity of the dynamic factors, it is difficult for the mathematical model to truly and comprehensively simulate its evolution, so the physical model is necessary.

Wang (2004) put forward specific suggestions on the planning and construction of the physical model of the Yellow River estuary. The variation of suspended sediment composition and sediment concentration along the river channel were studied by using the generalization physical model (Ren et al., 2013). Cao (2002) studied the effect of flushing the Yellow River estuary by physical model test. The research on the evolution law of erosion and deposition in the Yellow River estuary is mainly based on the measured data and remote sensing image analysis.

This paper analyzes the evolution of erosion and deposition in the Yellow River estuary by using the generalized physical model, in order to provide some references for the comprehensive treatment of the Yellow River estuary flow path.

2 THE TEST

2.1 Study area

The Yellow River estuary is located in Kenli District, Dongying City, Shandong Province, between 119° 12′ ~ 119° 18′ east longitude and 37° 46′ ~ 37° 52′ north latitude. The north is the Bohai Sea and the east is near Laizhou Bay. The modern Yellow River estuary delta was deposited after the diversion of the Tongwaxiang in Lankao County, Henan Province in August 1855 (Wang et al., 2007). According to the estuary classification index, the Yellow River estuary belongs to a typical weak tidal continental estuary. Its tidal effect is relatively weak, and its evolution characteristics are mainly determined by the characteristics of water and sediment. The inflow and sediment from the Yellow River estuary is mainly concentrated in the flood season. The gradient of the river channel at the tail reach is relatively small, and there is a sand bar hindering the discharge at the estuary, which leads to the instability of the flow path, and presents the basic laws of deposition, extension, swing and diversion. According to different dynamic conditions, the model generalization area is

divided into three parts: the section from the Xihekou to the T-junction is the runoff dynamic simulation area, the T-junction to the estuary is the runoff dynamic and marine dynamic simulation area, and the area outside the current flow path is the marine dynamic simulation area.

2.2 Model similar scale

The model horizontal scale is 500 and the vertical scale is 500. The model mainly includes two parts: channel area and sea area. The river area is a 25m-long compound channel for simulating runoff dynamic. The sea area is a rectangular area with a width of 15m. The delta area is a simulation area of runoff dynamics and marine dynamics. Outside is the marine dynamic simulation area. For the test sand, the fly ash from power plant was selected for its stable physicochemical properties and appropriate specific gravity. The model similarity criterion considers the similarity of water flow motion, sediment transport, wave motion, erosion and deposition.

2.3 Model arrangement

The water is supplied by a small reservoir and a mixing pool. The small reservoir is responsible for providing the model with clean water and recycling the model water, and the mixing pool is responsible for providing the model with muddy water. Two one-way pumps simulate the fluctuation of tide level, and one two-way pump simulates the tidal current. A number of water level indicator, pitometers, flowmeters and concentration meters were installed on the model to observe the characteristics of water and sediment. The test control system was written in Java and realized the wireless connection and feedback control of the model device through WIFI technology, and realized the integration of the imported water automatic control subsystem, the muddy water automatic control subsystem, the tidal current automatic control subsystem and the wave automatic control subsystem. The layout of the model is shown in figure 1.

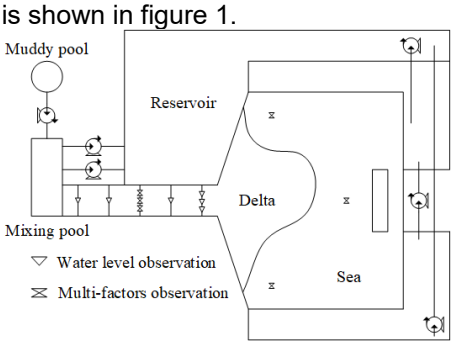

Figure 1. Model arrangement

2.4 Experiment scheme and design

A total of 19 model tests were carried out according to different runoff dynamics, tides, tidal currents and boundary conditions as shown in table 1. Through the grid division of the test area, the variation of erosion and deposition in different areas was counted into blocks to explore the law characteristics of erosion and deposition evolution in the Yellow River estuary. The meshing scheme is shown in the figure 2.

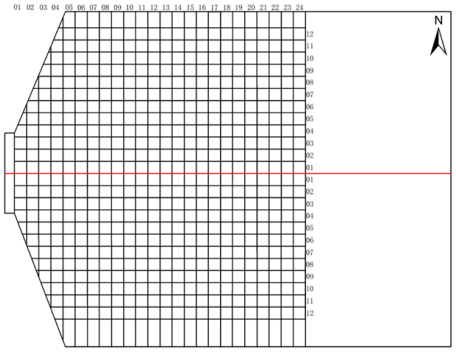

Figure 2. Meshing diagram

Table 1. Testing program

Testing program	runoff dynamic	tide	tidal current	Underlying surface
A-1	A-1 flow and sediment progress	I/A	I/A	initial terrain
A-2	A-2 flow and sediment progress	I/A	I/A	initial terrain
A-3	A-3 flow and sediment progress	I/A	I/A	initial terrain
A-4	A-4 flow and sediment progress	I/A	N/A	initial terrain
A-5	A-5 flow and sediment progress	I/A	N/A	initial terrain
B-1	B-1 flow and sediment progress	I/A	N/A	initial terrain
B-2	B-2 flow and sediment progress	I/A	N/A	initial terrain
B-3	B-3 flow and sediment progress	I/A	N/A	initial terrain
B-4	B-4 flow and sediment progress	I/A	N/A	initial terrain
B-5	B-5 flow and sediment progress	I/A	N/A	initial terrain
C-1	C-1 flow and sediment progress	I/A	N/A	initial terrain
C-2	C-2 flow and sediment progress	I/A	N/A	initial terrain
C-3	C-3 flow and sediment progress	I/A	N/A	initial terrain
C-4	C-4 flow and sediment progress	I/A	N/A	initial terrain
C-5	C-5 flow and sediment progress	I/A	N/A	initial terrain
D-1	D-1 flow and sediment progress	I/A	I/A	initial terrain
D-2	D-2 flow and sediment progress	I/A	I/A	initial terrain
D-3	D-3 flow and sediment progress	I/A	I/A	initial terrain
D-4	D-4 flow and sediment progress	I/A	I/A	initial terrain

3 METHODS

3.1 3D laser scanning technology

There are two main topographic survey methods in traditional river model test: manual needle survey and topographic instrument survey. Both rely on the bridge to measure the elevation data of each point in the measured cross section. Measurement accuracy is limited and time consuming. Considering that the test area is large and the accuracy requirement is high, the traditional measurement method is not applicable, so the 3D laser scanning technology is adopted to complete the test topography measurement.

3D laser scanning technology is a kind of automatic and high-precision stereo scanning technology, also known as ‘real scene replication technology’(Mei et al., 2010). 3D laser scanning technology is an emerging technology developed in recent years, which is praised as ‘another technological revolution in surveying and mapping field after GPS technology’. The laser pulse transmitter periodically fires laser pulses at the object under test, which generates a reflected signal back to the laser scanner. The distance S between the laser scanner and the measured point was calculated by recording the time difference between the emission and return of the laser pulse, and the observed value at the transverse scanning angle φ and at the longitudinal scanning angle θ for each laser pulse was measured(Cui et al., 2015). The three-dimensional coordinates of the measured point P can be obtained by calculation, as in Eq. [1] and figure 3.

$$\begin{cases} x = S\cos\varphi\cos\theta \\ y = S\sin\varphi\cos\theta \\ z = S\sin\theta \end{cases} \quad [1]$$

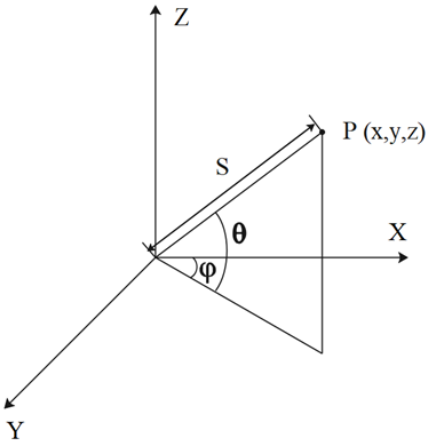

Figure 3. Schematic diagram of three-dimensional coordinate measurement

3.2 Data collection

3.2.1 Field data acquisition

Firstly, the position of 3D laser scanner should be determined. Considering the working principle of the 3D laser scanner, the 3D laser scanner should be set in a good field of vision, so that the whole test area can be observed and the blind area can be avoided. Then, set up 3D laser scanner, and make sure the position and level of the instrument. Customize the scan mode before measurement, and determine the horizontal and vertical range of the scan, and select the accuracy. Ensure the stability of the instrument to avoid interference of other factors to the measurement results.

3.2.2 Preprocessing of test data

The terrain data obtained by the 3D laser scanner is point cloud data, which cannot be directly processed and analyzed. It needs to be preprocessed by professional software Riscan Pro. The purpose of preprocessing is to eliminate redundant point cloud data and reduce the workload of subsequent data processing. Although the scanning range has been set during the scanning, there are still a lot of terrain data outside the test area. The point cloud data outside the test area is manually eliminated through the deletion function of Riscan Pro.

3.2.3 3D terrain construction

The point cloud data obtained through pre-processing still cannot be directly analyzed. Although Riscan Pro provides some functions of geographic data processing, considering the limitations of its functions, it needs to be combined with other professional software to extract and analyze terrain data. This paper compares and selects ArcGIS to extract and analyze experimental terrain data.

The point cloud data is exported to TXT format, which contains the three-dimensional coordinates of each measuring point in the instrument's own coordinate system. Point cloud data is imported into ArcGIS, and create TIN (Triangle Irregular Network). TIN is a kind of representation of digital elevation model. It forms a triangle by a series of points and is connected by the edges to form a triangular net. TIN's data storage mode is more complicated than raster surface model. It not only stores the elevation of each point, but also stores its plane coordinates and topological relations between nodes. Therefore, the efficiency of TIN processing is lower than that of raster surface model. Considering that some tools in ArcGIS cannot use TIN model, TIN model is transformed into a raster surface model.

3.2.4 Coordinate system conversion

In the river model, the actual river is reduced according to the scale. Therefore, the measured terrain data need to be converted into prototype data in the subsequent data analysis. The transformation of coordinate system is carried out by geographic registration and raster calculator in ArcGIS. In plane XOY, coordinates of known control points are input and corrected through the geographic registration function, while in elevation, terrain elevation is converted to prototype elevation through a grid calculator. The elevation conversion formula is in Eq. [2].

$$H_{PB} = 100H_{MB} + K \quad [2]$$

Where, H_{PB} is the base point elevation of prototype, H_{MB} is the base point elevation of model. And K is the offset between prototype and model in the vertical direction.

3.2.5 Analysis of terrain data

After the prototype raster surface model is obtained, the measured test terrain can be analyzed through the terrain analysis tool provided in ArcGIS. The most common one is the generation of contour lines, which can be directly generated by the tool of contour lines in ArcGIS. In addition, the longitudinal profile of the river and the cross section of each measured section can also be extracted.

When studying the evolution of scouring and deposition, it is often necessary to analyze the topography changes. ArcGIS can easily obtain the change characteristics of terrain and distribution of erosion and deposition.

4 RESULTS AND ANALYSIS

4.1 Plane characteristics of erosion and deposition evolution

The distribution map of erosion and deposition and contour map are superimposed and analyzed, as in figure 4. It can be seen that there is an obvious phenomenon that concave bank erodes and convex bank deposits in the section near the entrance. There is a erosion phenomenon at the concave bank with the maximum erosion depth reaching 5m, and deposition phenomenon at the convex bank, with the maximum deposition depth reaching 5m. Because of circulating current in curved channels, the surface flow with a small sediment concentration flows to the concave bank, while the bottom flow with a large sediment concentration deposits to the convex bank, which makes the concave erodes continuously, the convex bank deposits continuously, and the bending degree of the bend increases gradually and moves to the downstream.

The whole area was in a state of deposition, among which the deposition was mainly concentrated in the front of mouth, and the shoreline extends forward considerably. While the amount of deposition on both sides was small. This indicates that the evolution of erosion and deposition in the Yellow River estuary is mainly related to the characteristics of runoff dynamics.

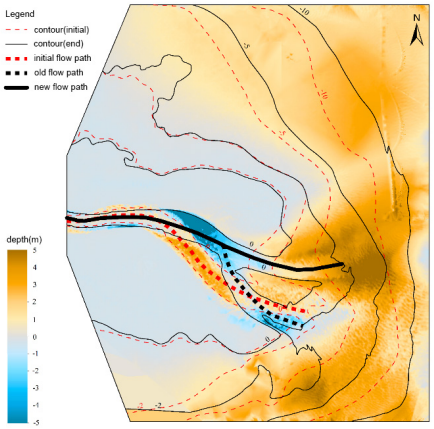

Figure 4. Distribution of erosion and deposition

4.2 Vertical characteristics of erosion and deposition evolution

The vertical character of erosion and deposition evolution is mainly reflected in the change of river longitudinal profile. It can be seen from the longitudinal profile diagram that the longitudinal profile gradient in river channel is always large and the variation is small. With the deposition in the delta, the longitudinal profile gradient in the estuary gradually decreases, forming a longitudinal profile like a step. Negative gradient and sand bar appear, which hinder the flow.

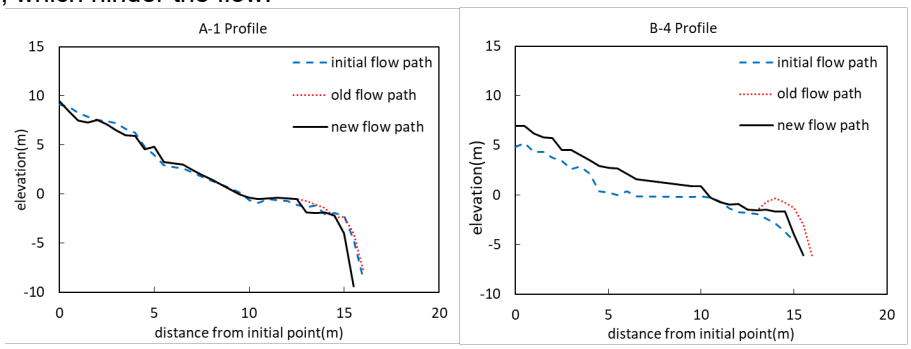

Figure 5. Typical channel profile

The formation of negative gradient and sand bar is due to the combined effect of runoff and marine dynamics at the estuary, which reduces the runoff velocity at the estuary, and sediment falls and deposits. When the tide rises, the runoff into the sea is uplifted by the tide, and the sediment deposits to form a relatively gentle

longitudinal profile. When the tide falls, the runoff and the tide together make the longitudinal profile steepen, eventually forming the longitudinal profile like a step.

4.3 Relationship between estuary evolution and avulsion

There is a certain relationship between the estuary evolution and avulsion, which is usually accompanied by the erosion and deposition. The degree of deposition in different parts is not balanced. Count the location of the avulsion and the maximum deposition part on the plane grid. There is a good linear correlation as in figure 6. It shows that the distribution of the erosion and deposition will affect the position of the avulsion. The maximum deposition position is usually located near the estuary. When the deposition reaches a certain level, the runoff will be obstructed and overland. Runoff looks for shortcuts to the sea and avulsion.

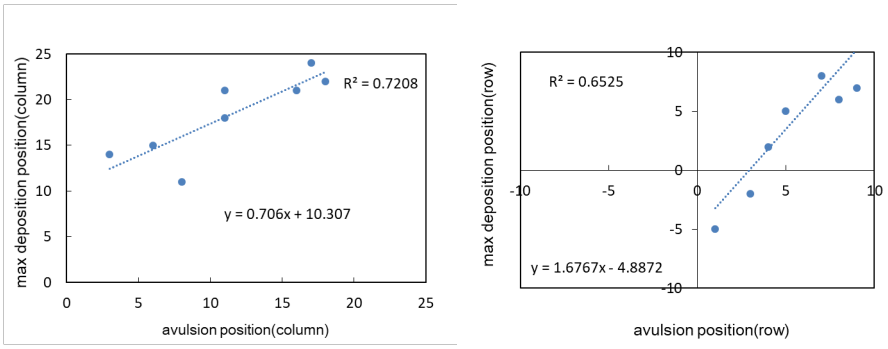

Figure 6. Typical channel profile

5 CONCLUSIONS

3D laser scanning technology can be used to realize high precision, large range and rapid measurement of river model topographic survey. Combined with ArcGIS, 3D model of experimental terrain can be constructed with high precision and various types of topographic elements can be extracted. The experiment shows that this technique can acquire the topographic data efficiently and has a good prospect.

The evolution of erosion and deposition in the Yellow River estuary is mainly influenced by the combined effects of runoff and marine dynamics, with the latter playing a dominant role. With the combined action of the two, the channel often forms a stepped longitudinal profile, and there are negative gradient or sand bar to hinder the discharge. When the overbank flow meets the weak bank, it erodes and forms a branch. There is a certain linear correlation between the location of avulsion and the max deposition part.

ACKNOWLEDGEMENTS

It was supported by National Key Research and Development Program of China (grant No.2017YFC0405501) and the Open Research Fund of State Key Laboratory of Simulation and Regulation of Water Cycle in River Basin, China Institute of Water Resources and Hydropower Research(grant No. SKL2018ZY07) and the National natural science foundation of China(grant No. 51879282).

REFERENCES

Wang, K.R., Li, Z.G, Wang, J.T., Zhao, J., Tang, M.Y. and Li, S. G. (2004). Planning and construction of solid model for Yellow River estuary. *Yangtze River,* 3, 28-29.

Ren, Y.F., Zhang, L.B and Wu, G. Y. (2013). Experimental study on the generalized model of the Yellow River estuary. *Yangtze River,* 44(21), 90-92+103.

Cao, W.H., Hu, C.H and Jiang, N. S. (2002). Experimental study on the flushing of Yellow River estuary by seawater. *Journal of Sediment Research,* 6, 31-38.

Wang, K.R., Yu, Y. and Wang, K. C. (2007). Research and management of Yellow River estuary. *Yellow River conservancy press,* book, chapter C1.

Mei, W.S., Zhou, Y.F, Wang and Zhou, J. (2010). Fine topographic mapping based on three-dimensional laser scanning. *Bulletin of surveying and mapping,* 01, 53-56.

Cui, Y.F., Ding, S.L, Shi, P. and Chen, X. L., (2015).Application of 3D laser scanning in the hydraulic engineering topographic survey and mapping. *Beijing surveying and mapping,* 3, 28-29.

8th International Conference on the Application of Physical Modelling in Coastal and Port Engineering and Science
Dec. 9th - 12th, 2020, Zhoushan, China

AMPLIFICATION OF INFRAGRAVITY WAVES INDUCED BY UNDERWATER SHOALS

Z. L. LIAO[1], S. W. LI[2], Y. LIU[3]

1 State Key Laboratory of Hydraulic Engineering Simulation and Safety, Tianjin University, Tianjin, China, tju_lzl@tju.edu.cn
2 State Key Laboratory of Hydraulic Engineering Simulation and Safety, Tianjin University, Tianjin, China, lishaowu@tju.edu.cn
3 State Key Laboratory of Hydraulic Engineering Simulation and Safety, Tianjin University, Tianjin, China, liuye2009@tju.edu.cn

ABSTRACT

Infragravity waves (IGWs) are waves with frequencies remarkably lower than short waves (SWs), typically between 0.004 and 0.04 Hz in prototype, and have important effects on many aspects of coastal hydrodynamics, such as beach and dune erosion, nearshore sediment transport, and short-wave groupiness on coral-reef flat. Utilizing the non-hydrostatic wave model SWASH, the previously reported phenomenon of IGWs being amplified in the presence of an underwater shoal was investigated in detail under non-breaking conditions. Nonlinear energy transfer from SWs to IGWs was found to consistently occur in the shoal region, and the effect was more significant on a milder bottom slope. Energetic free IGWs that are weakly correlated with the wave group were found to transmit behind the shoal, constituting a potential source of nearshore IGWs.

Key Words: infragravity waves, shoal, non-hydrostatic model

1 INTRODUCTION

Infragravity waves (IGWs) are waves with frequencies remarkably lower than short waves (SWs), typically between 0.004 and 0.04 Hz. *Munk* [1949] and *Tucker* [1950] are the pioneers in recognizing such a low-frequency motion outside the surf zone from field observations and termed it as 'surf beat'. Since then, the important contributions of IGWs have been recognized in many aspects of coastal hydrodynamics and engineering problems, such as resonance in the harbor [*Maa et al.*, 2010; *Okihiro et al.*, 1993; *Thotagamuwage and Pattiaratchi*, 2014b], beach and dune erosion [*Roelvink et al.*, 2009], nearshore sediment transport [*De Bakker et al.*, 2016a], and short-wave groupiness on coral reef flat [*Liu and Li*, 2018]. The bound long wave theory of *Longuet-Higgins and Stewart* [1962] (hereinafter referred to as LHS62) suggests that the nonlinear subharmonics in equilibrium with the wave group are the key mechanism of IGWs generation. This theory has been widely verified by field observations [*Elgar et al.*, 1992; *Masselink*, 1995], numerical studies [*List*, 1992; *Van Dongeren et al.*, 2002], and laboratory investigations [*Baldock et al.*, 2000; *Kostense*, 1984]. As waves shoal on nearshore sloping beaches, however, group-bounded IGWs lag behind the group forcing [*Battjes et al.*, 2004; *De Bakker et al.*, 2015; *De Bakker et al.*, 2013; *De Bakker et al.*, 2016b; *Herbers et al.*, 2000; *Inch et al.*, 2017] so that the LHS62 theory does not apply. As a consequence, nonlinear energy transfer from SWs to IGWs occurs, leading to a shoaling rate higher than the Green's Law [*Eldeberky and Battjes*, 1995; *Herbers and Burton*, 1997].

Apart from the local generation on nearshore beaches, IGWs could also be amplified by offshore underwater shoals. For instance, recently *Paniagua-Arroyave et al.* [2019] reported from field observation that a cap-related isolated shoal with gentle slopes on both sides is a potential source of IGW energy flux when the direction of the incident wave is normal to the orientation of the shoal. Another example is the Chengmai Bay in Hainan Province, China, where the mooring condition of a harbor basin is worsened by an underwater shoal located in the bay mouth roughly parallel to the coastline. *Li et al.* [2018] found from numerical simulations that the IGW energy is greatly enhanced after propagating across the shoal, which may account for the observed substantial long period oscillations in the harbor. IGW energy growth and harbor resonance, independent of the offshore wave conditions, were also observed in Two Rocks Marina of Australia with an offshore-submerged reef system [*Thotagamuwage and Pattiaratchi*, 2014a]. Unlike waves propagating over a straight sloping beach, waves propagating over a shoal change from shoaling to de-shoaling. However, up until now most of the literature in the past decades focused on wave evolutions in the shoaling and surf zones

(see the comprehensive review of *Bertin et al.* [2018]) with little attention to the de-shoaling zone.

In the present work, the evolutions of SWs and IGWs across an idealized trapezoidal shoal of various slopes were investigated using the non-hydrostatic wave model SWASH (Simulating WAves till SHore) [*Zijlema et al.*, 2011]. The bispectral analysis was used to quantify the nonlinear energy exchange between IGWs and SWs. In particular, contributions of nonlinear triad interactions to the IGW energy evolution on the plateau, and combined effects of nonlinear triad interaction and de-shoaling on the rear slope of the shoal were investigated. The paper is organized as follows: Section 2 introduces the SWASH model, model set-up, and descriptions of the bispectral analysis; The energy balance between IGWs and SWs and the influences of the bottom slope is illustrated in Section 3; Section 4 discusses the composition of IGWs behind the shoal. Conclusions are given in Section 5.

2 METHODOLOGY

2.1 Numerical experiment

2.1.1 Numerical model

The multilayer non-hydrostatic model SWASH was used to calculate the time series of water surface elevations in the computational domain. The 2-D governing equations are the momentum and mass conservation equations without any viscosity effect. The SWASH model is essentially a RANS equation solver capable to describe the processes of wave motion with strong nonlinearity [*Kirby*, 2017]. The model has been extensively validated against both laboratory [*De Bakker et al.*, 2016b] and field data [*Dirk Pieter Rijnsdorp et al.*, 2015] of nearshore wave evolution with strong nonlinearity.

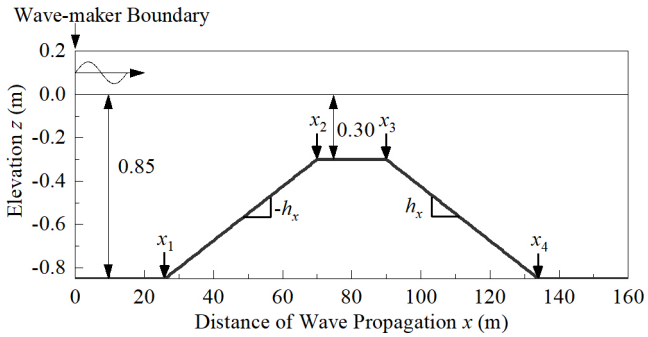

Figure 1. Sketch of idealized shoals in all runs of test. The original of the x coordinate was fixed at the wave-maker boundary. x_1 and x_4 are different for different test runs depending on the bottom slope; x_2 and x_3 are fixed to 70 m and 90 m, respectively.

2.1.2 Model set-up

The numerical test runs were conducted in a 2-D vertical numerical wave flume with an efficient computational domain of 160 m long (Figure 1). A series of isosceles trapezoidal shoal with four different slopes of 1/100, 1/80, 1/60, and 1/40 (see Figure 1 and Table 1) were placed in the middle of the flume. In all cases, the top of the shoal was fixed between 70 m ≤ x ≤ 90 m at a water depth of 0.3 m, which was slightly deeper than the critical water depth of wave breaking, and the bottom of the shoal is at a water depth of 0.85 m.

The incident significant wave height and the peak period for all test cases were 0.1 m and 2.25 s. The enhancement factor γ of the incident JONSWAP spectrum was set to 20 to obtain a relatively narrow band condition. The wave conditions in the present study are identical to that of Run A3 in the experiment of the GLOBEX project for an energetic swell [*Ruessink et al.*, 2013] in the nearshore region to drive a typical pattern of IGWs evolution.

At the inlet boundary on the left side of the flume, a second-order wave theory was prescribed to suppress the generation of spurious free IGWs, and a weakly reflective condition was adopted to prevent re-reflections [*D. P. Rijnsdorp et al.*, 2014]. A Sommerfeld condition, in combination with a 20 m long sponge layer (not shown in Figure 1), was used to absorb the outgoing waves at the outlet boundary on the right side of the

domain.

Six layers were adopted in the vertical direction to ensure the accuracy of dispersion and nonlinearity in the simulations according to *Smit et al.* [2014] and *De Bakker et al.* [2016b]. Water surface elevations were sampled at a frequency of 10 Hz at each grid point. The horizontal grid size and computational time step of 0.02 m and 0.002 s were selected. Each model run lasts 65 min, including a 5 min warming-up. Since the present study focuses on the energy transfer due to nonlinear triad interaction, the bottom friction that may complicate the analysis, therefore, is ignored by adopting a zero friction factor.

Table 1. Slope conditions of the numerical tests

Run ID	Slope	x_1 (m)	x_4 (m)
1	1/100	15	145
2	1/80	26	134
3	1/60	37	123
4	1/40	48	112

2.2 Bispectral analysis and nonlinear energy transfer

Since introduced by *Hasselmann et al.* [1963], bispectral analysis has been applied widely to study the nonlinear processes of waves, including breaking, shoaling, and nearshore dissipation of IGWs [*De Bakker et al.*, 2015; *De Bakker et al.*, 2016b; *Eldeberky and Battjes*, 1995; *Elgar*, 1989; *Herbers and Burton*, 1997; *Herbers et al.*, 2000].

Given a discrete time-series of signal with finite length, the discrete bispectrum is defined as

$$B_{f_1,f_2} = \mathbf{E}\left[A_{f_1} A_{f_2} A^*_{f_1+f_2} \right] \tag{1}$$

where **E**[•] is the ensemble average of the triple product, A is the complex Fourier coefficients of the signal and the asterisk denotes complex conjugation.

To obtain a comprehensive biphase $\beta_{\mathrm{IGW,SW}}$ that represents the phase coupling between SWs and IGWs, the biphase was integrated over the intersection frequency band of SWs and IGWs as follows

$$\beta_{\mathrm{IGW,SW}} = \mathrm{Arg}\left(\sum_{f_2=0.22\,\mathrm{Hz}}^{0.5 f_N} \sum_{f_1=0}^{0.22\,\mathrm{Hz}} B_{f_1,f_2} \right) \tag{2}$$

where f_N = 5 Hz is the Nyquist frequency.

The formula for calculating irregular wave energy evolution in the weakly dispersive regime was proposed by *Herbers and Burton* [1997] based on the Boussinesq theory as

$$\frac{dP_f}{dx} = R_{sh} + R_{nl} = -\frac{1}{2h}\frac{dh}{dx} P_f + \frac{3\pi f}{h\sqrt{gh}} \sum_{f'=-\infty}^{+\infty} IM\left(B_{f',f-f'} \right) \tag{3}$$

where h is the water depth, IM(•) denotes the imaginary part of a complex number. The first term on the *right hand side* of Eq. (3), R_{sh}, represents the linear shoaling term and the second term, R_{nl}, is the contribution of nonlinear triad interactions. The direction of nonlinear energy transfer is determined by the sign of the bispectrum imaginary part. A negative imaginary part indicates an energy transfer from the sum frequency $f_3 = f_1+f_2$ to f_1 and f_2 and vice versa.

3 MODEL RESULTS

3.1 Evolution of wave energy

Figure 2a shows the evolution of normalized SW energy over a trapezoid shoal with a slope of 1/80 (Run 2). The SW energy increases over the front slope (26 m ≤ x ≤ 70 m) due to shoaling, and then hardly change over the horizontal plateau. At the rear end of the plateau, wave reflection occurs and causes a slight fluctuation of the SW energy. During de-shoaling on the rear slope, the SW energy decreases at a faster rate than the rate of increase in SW energy while shoaling over the front slope, and achieves approximately 10% increment in total at the end of the rear slope.

Figure 2b shows the cross-shoal evolution of normalized IGW energy. The IGW energy increases throughout the front slope and continues so over the plateau at a constant rate despite the uniform depth. On the rear slope, interestingly the IGW energy increases slowly in the first half of the slope and then decreases slowly over the rest of the slope despite the fast decaying SW energy. After propagating across the whole shoal, the IGW energy is amplified by nearly 18 times. It must be stressed that the water depths on the two sides of the shoal are the same.

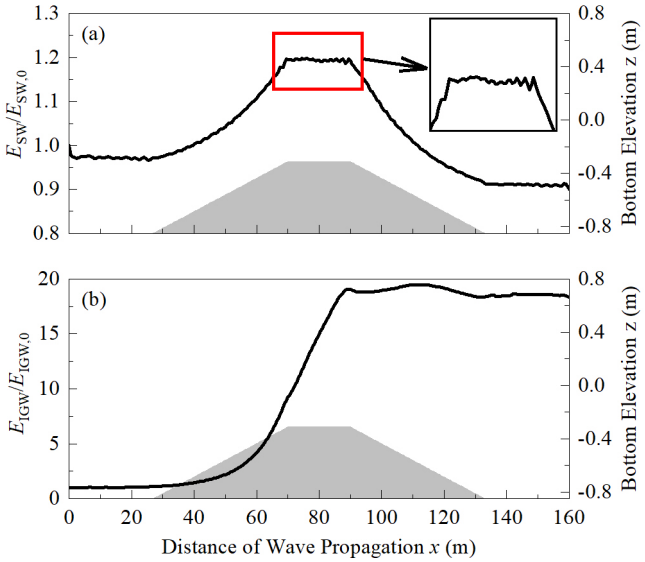

Figure 2. Spatial evolutions of normalized wave energy for Run 2 (bottom slope 1/80). (a) SW, and (b) IGW. The subscript 0 denotes quantities at the incident boundary.

3.2 Nonlinear wave energy transfer

Figure 3 presents a quantitative analysis of the nonlinear energy transfer between SWs and IGWs, in which the shoaling term $R_{IG,sh}$ and the nonlinear interaction term $R_{IG,nl}$ of the IGW energy on the *right hand side* of Eq. (3) were obtained by applying Eq. (3) to each component of the IGWs and then integrating over the infragravity frequency band (0-0.22 Hz). The gradient of the IGW energy was obtained through linear regression of the simulated IGW energy over twice the peak wavelength. Figure 3a shows a good agreement between the sum of source terms ($R_{IG,sh}$+$R_{IG,nl}$) and the linear regression. Cross-shoal variations of $R_{IG,sh}$ and $R_{IG,nl}$ in Figure 3b indicates that $R_{IG,sh}$ follows the gradient of the water depth, keeps positive and increases over the front slope, decays to zero over the plateau and then becomes negative over the rear slope. Meanwhile, $R_{IG,nl}$ remains positive across the shoal, implying that the IGWs gain energy from the SWs through nonlinear interactions, which is the mechanism for the amplification of IGW energy, as indicated in Figure 2b. $R_{IG,sh}$ and $R_{IG,nl}$ have the same sign over the front slope but opposite signs over the rear slope with comparative magnitudes. The constructive sum leads to the fast growth of IGW energy over the front slope while the counteraction of the nonlinear energy transfer and de-shoaling effects causes slow variation over the rear slope.

3.3 Influence of bottom slope

A comparison among the IGW energy of test runs at x = 152 m is illustrated in Figure 4. It is evident that the amplification of IGWs becomes greater over a milder bottom slope. Besides, the IGWs at this position are

far stronger than the bound IGWs for all the slopes. Taking the result of test Run 4 (bottom slope 1/40) as an example, the significant wave height of IGWs at x = 152 m is evaluated to be 0.0217 m, whereas that of bound IGWs is predicted to be only 0.0074 m. Note that the wave conditions in the present study follow the laboratory scale counterpart of the GLOBEX experiment [*Ruessink et al.*, 2013]. If transformed into field condition with a geometric scaling factor of 1:20, the significant wave heights of the free IGWs and the bound IGWs would be 0.408 m and 0.148 m, respectively.

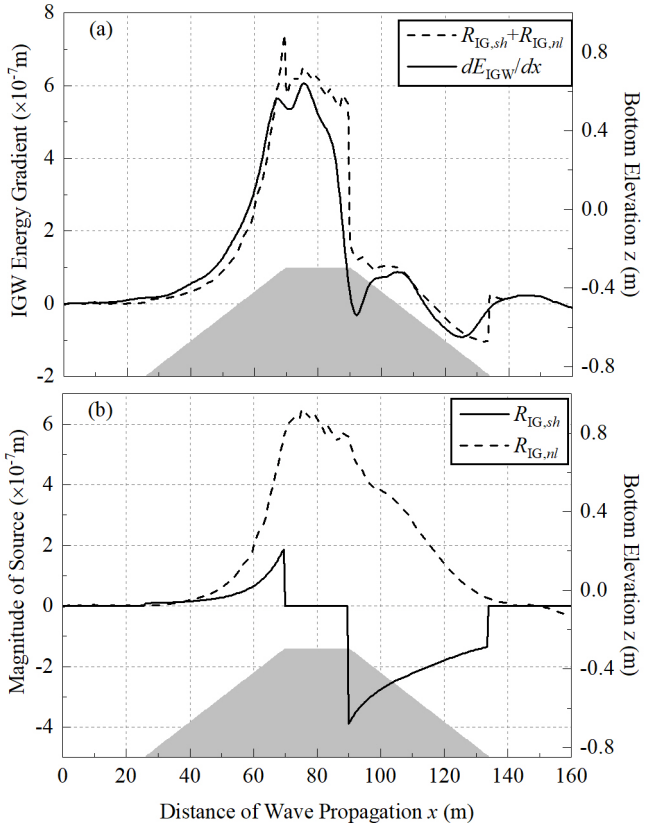

Figure 3. Spatial evolutions of (a) sum of the two source terms ($R_{IG,sh}$+ $R_{IG,nl}$) and gradient of IGW energy E_{IGW} from numerical simulation, (b) source terms of IGW energy E_{IGW} due to shoaling ($R_{IG,sh}$) and nonlinear interactions ($R_{IG,nl}$) of Run 2 (bottom slope 1/80).

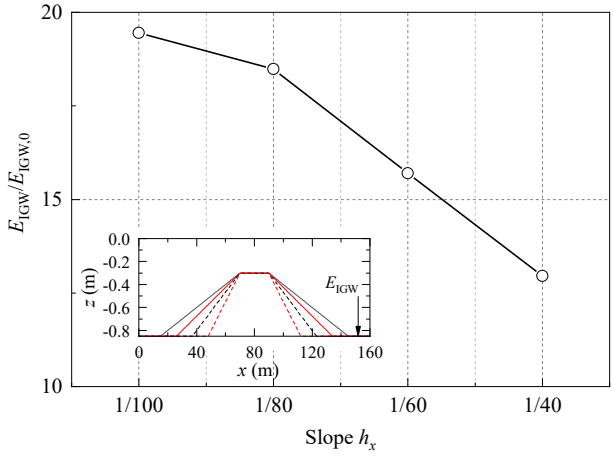

Figure 4. IGW energy relative to the incident IGW energy at leeward of the shoal for all test runs of different bottom slopes.

4 DISCUSSION

4.1 Composition of IGWs behind the shoal

Behind the shoal, the IGW energy is considerably amplified while a little drop of the SW energy occurs despite the resume of water depth. The SWs over the rear slope of the shoal are no longer capable of driving strong bound IGWs. The nonlinear second-order finite-depth theory of *Hasselmann* [1961] can be employed to calculate the bound IGWs that travel over the horizontal bottoms on both sides of the shoal. Taking Run 2 (bottom slope 1/80) as an example, although the bound IGWs dominate the low frequencies of the incident IGWs, the IGW departs significantly from the bound IGW theory (not shown). In order to shed some light on this phenomenon, an additional simulation was conducted by extending the length of the computational domain (sponge layer not included) from 160 m to 320 m.

In the extended region (160 m ≤ x ≤ 320 m), free IGWs were detected. As shown in Figure 5, in the region of 0 m ≤ x ≤ 264 m, only one extremum is recognized in the correlation coefficients between the local IGWs and the wave group envelope; in the region of 264 m ≤ x ≤ 320 m, however, two local extrema are identified in the correlation coefficients, which correspond to two time lags τ_1 and τ_2 ($|\tau_1| < |\tau_2|$). The time lag τ_2 indicates the occurrence of free IGWs propagating at a different speed of $\sqrt{gh}$ from SWs. The release of bound IGWs can explain why the free IGWs are negatively correlated with the group envelope (Figure 5) since the bound IGWs, from which the free IGWs originate, are negatively correlated with the group envelope. Although this explanation seems to contradict with the traditional breaking-induced IGWs theory, *Baldock* [2012] argued that the bound IGWs may be released only if they satisfy the same dispersion relationship as free IGWs wave, *i.e.* the shallow-water resonance condition, regardless of wave breaking. They also stated that bound IGWs will be released if SWs propagate in shallow waters prior to breaking. Note that the water depth on the plateau in the present work is close to shallow water for the primary wave ($k_p h$ = 0.51 and $c_g/\sqrt{gh}$ = 0.89, where k_p is the wavenumber at the peak frequency) as to reach the near-resonance state, the present model results are consistent with the argument of *Baldock* [2012]. This result also highlights the fact that wave breaking is not necessarily the only trigger for the release of bound IGWs.

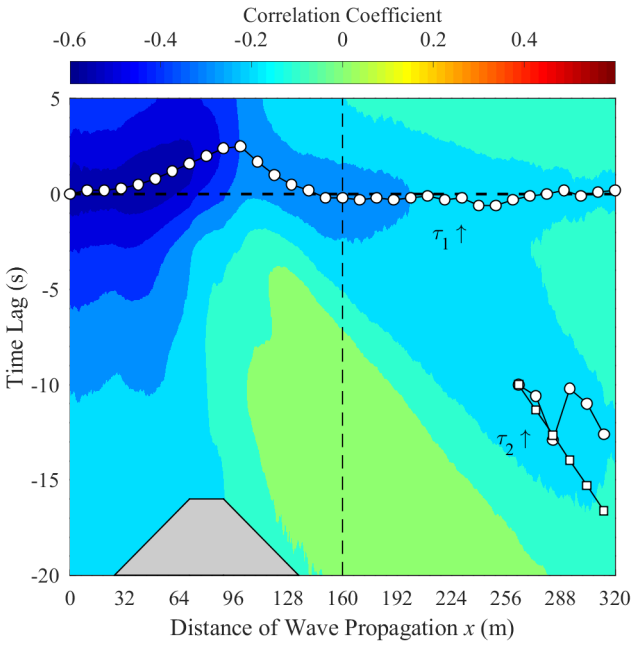

Figure 5. Cross-correlation between the local surface elevation of IGWs and wave height history for Run 2 (bottom slope 1/80) with the flume extended 160 m longer. The circled line denotes time lags of the local minima of the cross-correlation function; the squared line is calculated with the free long wave speed and group speed evaluated with linear theory; the horizontal dash line separates the domain of Run 2 and the extended region. The gray trapezoid is a sketch of the topography.

5 CONCLUSIONS

A series of numerical experiments were conducted using the SWASH model to investigate the evolution of the IGW energy over a symmetric trapezoidal shoal with different bottom slopes. It was found that the incident bound IGWs can be significantly amplified due to the nonlinear energy transfer from SWs to IGWs when SWs propagate over uneven topography at a finite water depth. Without wave breaking, the IGW energy always increases over the front slope and the subsequent plateau but may increase or decrease over the rear slope, depending on the relative importance of the de-shoaling and nonlinear energy transfer.

The nonlinear energy transfer from SWs to IGWs can be evaluated based on the phase lag between local IGWs and SW group envelope, which increases during shoaling over the front slope, continues to increase over the plateau and during the early stage of de-shoaling over the rear slope. This effect and the resultant amplification of IGWs across the shoal is greater when the bottom slope of the shoal becomes milder.

Strong free IGWs were detected on the leeward side of the shoal through cross-correlation analysis. The free IGWs may be generated by the release of the additional bound IGWs after propagating across the shoal. The results support the hypothesis that bound IGWs can be released by topographical change without wave breaking. The released free IGWs on leeward of the shoal are stronger for milder slopes. For the wave conditions of the present study, these free IGWs have a significant wave height at the order of decimeters in prototype scale, which may have significant impacts on nearshore sediment and pollutant transport and mooring condition in the harbor behind the shoal.

REFERENCES

Baldock, T. E. (2012), Dissipation of incident forced long waves in the surf zone-Implications for the concept of "bound" wave release at short wave breaking, *Coastal Engineering*, *60*(1), 276-285, doi:10.1016/j.coastaleng.2011.11.002.

Baldock, T. E., D. A. Huntley, P. A. D. Bird, T. O'Hare, and G. N. Bullock (2000), Breakpoint generated surf beat induced by bichromatic wave groups, *Coastal Engineering*, *39*(2), 213-242, doi:https://doi.org/10.1016/S0378-3839(99)00061-7.

Battjes, J. A., H. J. Bakkenes, T. T. Janssen, and A. R. van Dongeren (2004), Shoaling of subharmonic gravity waves, *Journal of Geophysical Research: Oceans*, *109*(C2), doi:10.1029/2003jc001863.

Bertin, X., et al. (2018), Infragravity waves: From driving mechanisms to impacts, *Earth-Sci. Rev.*, *177*, 774-799, doi:10.1016/j.earscirev.2018.01.002.

De Bakker, A. T. M., J. A. Brinkkemper, F. V. D. Steen, M. F. S. Tissier, and B. G. Ruessink (2016a), Cross-shore sand transport by infragravity waves as a function of beach steepness, *Journal of Geophysical Research*, *121*(10), 1786-1799.

De Bakker, A. T. M., T. H. C. Herbers, P. B. Smit, M. F. S. Tissier, and B. G. Reussink (2015), Nonlinear infragravity–wave interactions on a gently sloping laboratory beach, *Journal of Physical Oceanography*, *45*(2), doi:10.1175/JPO-D-14-0186.1.

De Bakker, A. T. M., M. Tissier, V. Marieu, N. Sénéchal, A. Ruju, J. Lara, and B. G. Ruessink (2013), Infragravity wave propagation and dissipation on a low-sloping laboratory beach, *Proc. Seventh Int. Conf. on Coastal Dynamics, Bordeaux*, 443-452.

De Bakker, A. T. M., M. F. S. Tissier, and B. G. Ruessink (2016b), Beach steepness effects on nonlinear infragravity-wave interactions: A numerical study, *Journal of Geophysical Research Oceans*, *121*(1), 554-570, doi:10.1002/2015JC011268.

Eldeberky, Y., and J. A. Battjes (1995), Parameterization of triad interactions in wave energy models, paper presented at Coastal Dynamics.

Elgar, S. (1989), Bispectra Of Shoaling Ocean Surface Gravity Waves, paper presented at The Workshop on Higher-Order Spectral Analysis.

Elgar, S., T. H. C. Herbers, M. Okihiro, J. Oltman-Shay, and R. T. Guza (1992), Observations of infragravity waves, *Journal of Geophysical Research: Oceans*, *97*(C10), 15573-15577, doi:10.1029/92jc01316.

Hasselmann, K. (1961), On the non-linear energy transfer on a gravity-wave spectrum. Part 1. General Theory, *Fluid. Mech.*, *12*, 481-500, doi:10.1017/S0022112062000373.

Hasselmann, K., W. Munk, and G. MacDonald (1963), *Bispectra of ocean waves*, John Wiley, New York.

Herbers, T. H. C., and M. C. Burton (1997), Nonlinear shoaling of directionally spread waves on a beach, *Journal of Geophysical Research Oceans*, *102*(C9), 21101-21114, doi:10.1029/97JC01581.

Herbers, T. H. C., N. R. Russnogle, and S. Elgar (2000), Spectral energy balance of breaking waves within the surf zone, *Journal of Physical Oceanography*, *30*(11), 2723-2737, doi:10.1175/1520-0485(2000)030<2723:sebobw>2.0.co;2.

Inch, K., M. Davidson, G. Masselink, and P. Russell (2017), Observations of nearshore infragravity wave dynamics under high energy swell and wind-wave conditions, *Continental Shelf Research*, *138*, 19-31, doi:http://dx.doi.org/10.1016/j.csr.2017.02.010.

Kirby, J. T. (2017), Recent advances in nearshore wave, circulation, and sediment transport modeling, *Journal of Marine Research*, *75*(3), 263-300, doi:10.1357/002224017821836824.

Kostense, J. K. (1984), Measurements of surf beat and set-down beneath wave groups, paper presented at 19th International conference on Coastal Engineering, American Society of Civil Engineers, Houston, Texas, United States.

List, J. H. (1992), A model for the generation of two-dimensional surf beat, *Journal of Geophysical Research Oceans*, *97*(C4), 5623-5635, doi:10.1029/91JC03147.

Liu, Y., and S. Li (2018), Variation of wave groupiness across a fringing reef, *J Waterw Port Coast*, *144*(6), 14, doi:10.1061/(asce)ww.1943-5460.0000475.

Longuet-Higgins, M. S., and R. W. Stewart (1962), Radiation stress and mass transport in gravity waves with application to 'surf beats', *Journal of Fluid Mechanics*.

Maa, P. Y., C.-H. Tsai, W.-J. Juang, and H.-M. Tseng (2010), A preliminary study on Typhoon Tim induced resonance at Hualien Harbor, Taiwan, *61*(4), 411-423.

Masselink, G. (1995), Group bound long waves as a source of infragravity energy in the surf zone, *Continental Shelf Research*, *15*(13), 1525-1547, doi:https://doi.org/10.1016/0278-4343(95)00037-2.

Munk, W. H. (1949), Surf beats, *Eos Transactions American Geophysical Union*, *30*(6), 849–854.

Okihiro, M., R. T. Guza, and R. J. Seymour (1993), Excitation of seiche observed in a small harbor, *Journal of Geophysical Research: Oceans*, *98*(C10), 18201-18211, doi:10.1029/93jc01760.

Paniagua-Arroyave, J. F., P. N. Adams, S. M. Parra, and A. Valle-Levinson (2019), Observations of surface-gravity-wave scattering and dissipation by an isolated shoal related to a cuspate foreland, *Continental Shelf Research*, *173*, 43-55, doi:https://doi.org/10.1016/j.csr.2018.12.004.

Rijnsdorp, D. P., G. Ruessink, and M. Zijlema (2015), Infragravity-wave dynamics in a barred coastal region, a numerical study, *Journal of Geophysical Research Oceans*, *120*(6), 4068-4089, doi:10.1002/2014JC010450.

Rijnsdorp, D. P., P. Smit, and M. Zijlema (2014), Non-hydrostatic modeling of infragravity waves under laboratory conditions, *Coastal Engineering*.

Roelvink, D., A. Reniers, A. R. van Dongeren, J. van Thiel de Vries, R. McCall, and J. Lescinski (2009), Modelling storm impacts on beaches, dunes and barrier islands, *Coastal Engineering*, *56*(11), 1133-1152, doi:https://doi.org/10.1016/j.coastaleng.2009.08.006.

Ruessink, B. G., H. Michallet, P. Bonneton, D. Mouaze, J. Lara, P. A. Silva, and P. Wellens (2013), Globex: wave dynamics on a gently sloping laboraty beach, paper presented at 7th International Conference on Coastal Dynamics.

Smit, P. B., T. T. Janssen, L. Holthuijsen, and J. J. Smith (2014), Non-hydrostatic modeling of surf zone wave dynamics, *Coastal Engineering*, *83*, 36-48, doi:10.1016/j.coastaleng.2013.09.005.

Thotagamuwage, D. T., and C. B. Pattiaratchi (2014a), Influence of offshore topography on infragravity period oscillations in Two Rocks Marina, Western Australia, *Coastal Engineering*, *91*(91), 220-230.

Thotagamuwage, D. T., and C. B. Pattiaratchi (2014b), Observations of infragravity period oscillations in a small marina, *Ocean Engineering*, *88*, 435-445, doi:https://doi.org/10.1016/j.oceaneng.2014.07.003.

Tucker, M. J. (1950), Surf Beats: Sea Waves of 1 to 5 Min. Period, *Proceedings of the Royal Society A*, *202*(1071), 565-573.

Van Dongeren, A. R., H. J. Bakkenes, and T. T. Janssen (2002), Generation of long waves by short wave groups, in *Coastal Engineering 2002*, edited, pp. 1093-1105, doi:10.1142/9789812791306_0093.

Zijlema, M., G. Stelling, and P. Smit (2011), SWASH: An operational public domain code for simulating wave fields and rapidly varied flows in coastal waters, *Coastal Engineering*, *58*(10), 992-1012, doi:10.1016/j.coastaleng.2011.05.015.

8th International Conference on the Application of Physical Modelling in Coastal and Port Engineering and Science
Dec. 9th - 12th, 2020, Zhoushan, China

EXTRACTION OF HIGHER HARMONICS IN A FOCUSED WAVE GROUP BY A PHASE MANIPULATION APPROACH

XINGYA FENG [1,2], WEI BAI [3] & DEZHI NING [4]

[1] Southern University of Science and Technology, Shenzhen, China,
fengxy@sustech.edu.cn
[2] Southern Marine Science and Engineering Guangdong Laboratory (Guangzhou), Guangzhou, China,
[3] Manchester Metropolitan University, UK,
w.bai@mmu.ac.uk
[4] Dalian University of Technology, China,
dzning@dlut.edu.cn

ABSTRACT

In this work we aim at extracting the higher harmonic wave profiles of nonlinear focused wave groups based on the assumption of a 'Stokes-type' harmonic structure. We present a methodology to generate high-quality nonlinear wave groups of a narrow-banded wave spectrum in a wave tank. The methodology manipulates the wave group phases by an active control of the wave paddle. Four phases with 90-degree shift each are prescribed – four runs for each case, in order to extract the harmonics up to fourth order. The input focused wave group is generated by the NewWave model, which represents an extreme wave in a random sea state. A fully nonlinear potential flow model is also employed to replicate the experiments carried out in the Kelvin Tank in Glasgow, UK. The results show clean separation of the first four harmonics in the elevation spectra. Comparisons between the experimental data and the fully nonlinear model show remarkably good agreements for the higher harmonics. We confirm the Stokes-type underlying nonlinear structure of the harmonic elevations in wave groups. This is concluded by simulating wave groups with varying wave steepness and calculating the corresponding elevation coefficients of the higher harmonics. The harmonic coefficients are found almost constant against varying steepness. We extract wave profiles of higher harmonics in space in the numerical simulation and the evolution of the higher harmonics is clearly demonstrated.

Keywords: Focused wave group, Higher harmonics, Stokes expansion, Nonlinear simulation

1 INTRODUCTION

Extreme waves are usually the most critical to the survival of offshore structures. Measurement of those giant waves from instruments in the ocean, for example, the well-known Draupner wave described in Walker et al. 2004, has driven extensive research on the scientific explanation of the formation of them and understanding their characteristics (Adcock et al., 2015; Wang and Balachandran, 2018). Attempt to recreate similar extreme waves in the laboratory using a deterministic wave energy spectrum has also been made in recent years in Buldakov et al. (2017). Extreme waves in the ocean are believed to form when the wave components associated with a large number of wave frequencies in a random sea come into phase, see a detailed explanation in Fedele et al. (2016). That is the focusing of a transient wave group.

The focused wave group has been demonstrated to be the average shape of large waves in a random sea Whittaker et al. (2016). Mathematically, the representation of the focused wave group is the scaled autocorrelation function as reported in Lindgren (1970). The simplest linear model for a focused wave group might be the NewWave presented originally in Tromans et al. (1991). The ability of the NewWave model to represent an extreme wave has been shown in a few field data in deep, intermediate and shallow water depths (Walker et al., 2004; Whittaker et al., 2016). Meanwhile, for tests or simulations in a tank, an obvious advantage of using a focused wave group against a random sea state is the time savings because the focusing occurs in a very short period of time. In addition, in such a short period the near field wave is free from contamination of possible reflection from the far end of the tank.

Most of the research work mentioned above investigate the general shape of a focused wave group in the linear, or at most second order regime. It is well known that higher harmonics can be expected resulting from the strong nonlinear wave-wave interactions among the frequencies components. The nonlinear Schrodinger equation provides a good approximation for the nonlinear evolution of the wave group in deep water (Lo and Mei, 1985; Adcock and Taylor, 2016). Modulation of wave surface profile was identified in these studies.

Nonetheless, the properties of those individual higher harmonics (than the second) remains almost

unexplored due to the difficulty in accurately extracting the individual higher harmonics. There are two reasons. The first is because the higher harmonic components could be very small, for experiments possibly below the accuracy of confidence of the instruments. The second is that the higher harmonic components cannot be easily and cleanly isolated from the total nonlinear wave field due to the spectrum overlap between neighbouring harmonics. Therefore, further study has to be conducted to extract cleanly the higher harmonics and to understand the nonlinear behaviour of the harmonics in an extreme wave.

Since capturing the small higher harmonic elevations might be difficult in a tank test, it becomes practical to employ numerical models to replicate the process of the formation of the extreme wave. A numerical model that can simulate all nonlinearities associated with the wave group might be the time-domain fully nonlinear numerical wave tank (NWT). The NWT model we employed in this work basically represents a rectangular physical tank and simulates the wave generation and absorption. Without any assumption to the wave propagation and evolution (except for fluid viscosity), the fully nonlinear simulation will retain any higher harmonic components arising from wave-wave interactions. Innovative approach needs to be implemented in the NWT to cleanly extract the harmonics, since we are concerned with the properties of each harmonic.

The method used in this study for decomposing higher harmonic components from a focused wave group is the phase manipulation recently presented in Adcock et al. (2019). Fitzgerald et al. (2014) generalized a four-phase method. The first four harmonics can be separated by combining the four waves groups of 90° phase apart. The approach assumes a Stokes-type harmonic structure of the wave elevations for a narrow-banded wave group. The regular wave amplitude A can be generalized to a time-varying amplitude $A(t)$ for the focused wave group owing to the fact that the amplitude $A(t)$ is modulated and slowly varying near focusing.

This work presents a fully nonlinear potential flow model for simulating unidirectional focused wave groups in a rectangular tank. Inviscid fluid and irrotational flow is assumed following the potential flow theory. The fully nonlinear free surface boundary conditions are fulfilled during the time-domain simulation, with the exact free surface captured in time marching. A higher order boundary element method is adopted to solve the boundary value problem enclosing the fluid of interest. We generate the focused wave group from a given wave energy spectrum. Phase control is implemented at the wavemaker in order to set apart the desired wave phases. The primary purpose of this work is to investigate the characteristics of the higher harmonics in a focused wave group via clean harmonic decomposition, and to confirm the underlying structure of these harmonics.

2 MATHEMATICAL FORMULATION

2.1 Model description

We employ a numerical tank technique to simulate the focused wave groups. The rectangular numerical wave tank is defined in Figure 1. Similar to a physical tank, a narrow long tank is modelled. The schematic figure consists of a wavemaker at the left boundary of the tank and a numerical beach placed on the surface at the far end of the tank. The coordinate system $Oxyz$ has its origin on the undisturbed water surface in the centre of the tank, with z-axis pointing upward. The computational domain includes all the wetted boundaries. In particular, S_{WM} and S_F represent the wavemaker and the free water surface, respectively. It is a three-dimensional tank and the two side walls are not shown in the diagram.

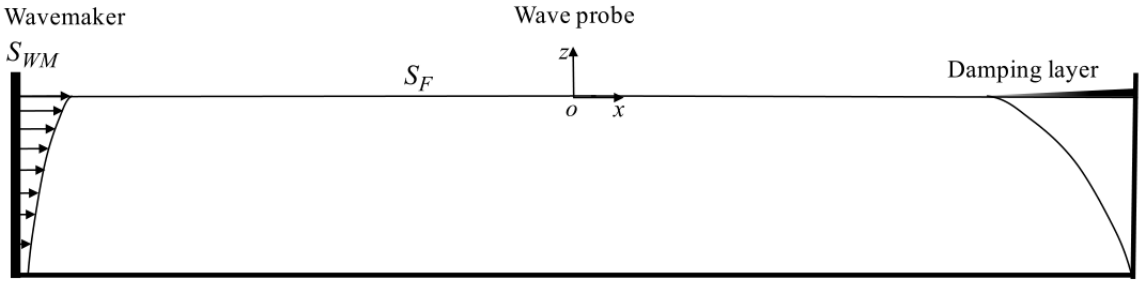

Figure 1. Schematic diagram of a wave tank.

2.2 Wave group generation

The key to the work here is to generate high-quality focused wave groups, as an extension of the numerical tank designed for regular waves (Bai et al., 2014; Feng and Bai, 2017). We generate a focused wave group by prescribing the proper phases of each frequency component. For a given wave energy spectrum $S(\omega)$, the free surface elevation and the velocity potential based on the linear NewWave model can be calculated as

$$\eta_I(x,t) = \sum_{n=1}^{N} A_n \cos[k_n(x - x_c) - \omega_n(t - t_c)] \qquad [1]$$

$$\phi_I(x,z,t)=\sum_{n=1}^{N}A_n\frac{\omega_n}{k_n}\frac{\cosh k_n(z+h)}{\sinh k_n h}\sin[k_n(x-x_c)-\omega_n(t-t_c)] \quad [2]$$

where A_n is the wave amplitude, ω_n the wave frequency, k_n the wavenumber of the n th component. The water depth is h. The focused time is set as t_c and focused position x_c. The total number of components N should be large enough to reproduce the desired spectrum and $N = 200$ is adopted in this study. The amplitude $A_n(\omega)$ of each wave component is calculated by

$$A_n(\omega)=A\cdot\frac{S(\omega_n)\Delta\omega}{\sum_{n=1}^{N}S(\omega_n)\Delta\omega} \quad [3]$$

where $A=\sum_{n=1}^{N}A_n$ is defined as the linearized wave group amplitude. The NewWave profile is simply the scaled autocorrelation function, i.e. the Fourier transform of the energy density spectrum for the underlying sea state, and the amplitude components are proportional to $S(\omega_n)\,\Delta\,\omega/\sigma^2$. The sum $\sigma^2=\sum_{n=1}^{N}S(\omega_n)\,\Delta$ is the variance of the wave elevation.

In the numerical tank as in a physical tank, to make the desired wave group, a proper transfer function $f_T(\omega)$ has to be applied to the prescribed displacement and velocity for the wavemaker. Therefore, the desired free surface elevation at the wavemaker is $\eta_I(x_{WM},t)/f_T(\omega)$ and the velocity distribution on the wavemaker becomes $U(t)=\frac{\partial\phi_I(x_{WM},z,t)}{\partial x}/f_T(\omega)$ with x_{WM} the position of the wavemaker. For the piston-type wavemaker used in the model, there is a $\pi/2$ phase difference between its displacement and the wave elevation on the wavemaker. The above equations will generate waves focusing at x_c at the time instant t_c, according to linear wave theory. However, as the wave group evolution is nonlinear in this model, both the focusing location and time would slightly shift due to nonlinear dispersion and wave-wave interactions.

A classic linear transfer function proposed by Ursell et al. (1960) has been used in the wave generation problems for decades. The function based on linear wave theory is expressed as

$$f_T(\omega)=\frac{2\sinh^2 kh}{\sinh(kh)\cosh(kh)+kh} \quad [4]$$

In our model, we compute the numerical transfer functions by carrying out numerical tests. For a particular depth, regular waves of very low amplitude ($kA<0.01$) are generated and the transfer function is then estimated from the steady-state surface elevations. The linear transfer function is used in the numerical model, however it might introduce errors of elevations at the second or higher orders.

2.3 Phase-manipulation approach

A good model for the nonlinear harmonic elevations appears to be that they follow a 'Stokes-like' form

$$\begin{aligned}\eta_{total}=&AS_{11}\cos\varphi+A^2(S_{20}+S_{22}\cos 2\varphi)+A^3(S_{31}\cos\varphi+S_{33}\cos 3\varphi)\\&+A^4(S_{40}+S_{42}\cos 2\varphi+S_{44}\cos 4\varphi)+O(A^5)\end{aligned} \quad [5]$$

up to fourth order of the amplitude A. The coefficients S_{mn} represent the coefficients corresponding to super/sum ($m=n$) and sub/difference ($m-n=2$) harmonics and $\varphi=\omega t+\varphi_0$ is the phase of the linear component of the wave. The φ_0 is the initial phase to be prescribed at the wavemaker. In the case of a wave group, it is assumed the time varying amplitude is modulated such that it is slowly changing near the focus time. This requires the wave spectrum is narrow-banded (Mei et al., 2005).

To extract the different harmonics we use a phase-manipulation technique following Fitzgerald et al. (2014) who studied the wave forces on a surface-piercing column. We alter the phase at the wavemaker in certain increments. This allows us to combine different phase results in order to separate different harmonics. In particular, we make the incoming waves with a phase shift of $\varphi_0=0,90,180,270\ degrees$. We then submit them into Eq.[5]. By linearly combining the four corresponding responses $\eta_0,\eta_{90},\eta_{180}and\eta_{270}$, the first four separated harmonics read

$$\begin{aligned}(\eta_0-\eta_{90}^H-\eta_{180}+\eta_{270}^H)/4&=(AS_{11}+A^3S_{31})\cos\omega t,\\(\eta_0-\eta_{90}+\eta_{180}-\eta_{270})/4&=(A^2S_{22}+A^4S_{42})\cos 2\omega t,\\(\eta_0+\eta_{90}^H-\eta_{180}-\eta_{270}^H)/4&=A^3S_{33}\cos 3\omega t,\\(\eta_0+\eta_{90}+\eta_{180}+\eta_{270})/4&=A^2S_{20}+A^4S_{40}+A^4S_{44}\cos 4\omega t.\end{aligned} \quad [6]$$

where the accuracy is truncated to fourth order and the superscript H denotes the Hilbert transform of the time signal. Clearly, to separate the harmonics up to fourth order using this approach, we have to repeat each simulation four times. In a relative simpler model the odd and even harmonics can be separated using only the η_0 and η_{180} signals. The averaged difference and sum of these two signals give, up to 4th harmonic.

2.4 Modified Dalzell model for a wave group

The mathematical model of second-order wave-wave interaction for two regular waves was presented by Dalzell (1999). We modify it for a focused wave group in a random sea state. This is done by considering every pair of two components in a wave group and summing up all the possible pairs. The formulation in Dalzell (1999) considers directional spreading. Here we set up the direction of all the wave component as zero, making it unidirectional.

The regular wave-wave interaction resulting from two components in uni-direction has the second-order sum elevation

$$\eta^{(22)} = \frac{A_1^2 k_1}{4\tanh k_1 h}\left[2+\frac{3}{\sinh^2(k_1 h)}\right] + \frac{A_2^2 k_2}{4\tanh k_2 h}\left[2+\frac{3}{\sinh^2(k_2 h)}\right] + A_1 A_2 B_p \quad [7]$$

$$B_p = \frac{\omega_1^2+\omega_2^2}{2g} - \frac{\omega_1\omega_2}{2g}\left[1-\frac{1}{\tanh k_1 h \tanh k_2 h}\right] \times \left[\frac{(\omega_1+\omega_2)^2 + g(k_1+k_2)\tanh(k_1 h + k_2 h)}{D_p}\right] + \frac{\omega_1+\omega_2}{2gD_p}\left[\frac{\omega_1^3}{\sinh^2(k_1 h)} + \frac{\omega_2^3}{\sinh^2(k_2 h)}\right] \quad [8]$$

$$D_p = (\omega_1+\omega_2)^2 - g(k_1+k_2)\tanh(k_1 h + k_2 h) \quad [9]$$

where the subscript 1 and 2 stand for the quantities associated with the two wave components. $A_{1,2}$ are the amplitudes, $\omega_{1,2}$ the frequencies, g the gravitational acceleration and h the water depth. Each wavenumber $k_{1,2}$ still satisfies the linear dispersion equation $\omega_{1,2}^2 = gk_{1,2}\tanh(k_{1,2}h)$. Note that here only the second harmonic elevation is resolved from Dalzell's result. The difference term and the mean elevation term are not included.

In the focused wave group, as the phases of all components are aligned, the amplitude of the second-order wave elevation will be the summation of the elevations resulting from interactions between every two components. We have the following second harmonic elevation for the wave group

$$\eta_{group}^{(22)} = \sum_{j=1}^{N}\sum_{k=j}^{N}\eta_{jk}^{(22)} \quad [10]$$

where N is the total number of components in the wave group and j,k are the indexes of any two components.

3 HIGHER HARMONIC ANALYSIS

3.1 Harmonic decomposition

We now apply the four-phase based method to extract the harmonics. The purpose is to explore the detailed underlying structure of the higher harmonic wave elevations. We set up a tank of 15 m long and 0.2 m wide, and the water depth is 1.8 m. A narrow-banded JONSWAP spectrum is used. Its peak frequency is $f_p = 0.429$ Hz. The input wave frequency cutoff is $0.5f_p - 3.0f_p$. The JONSWAP spectrum in this range is discretized into 200 frequency components. For a focused wave group, we use the peak wave frequency and wavelength as its characteristic property when referring to a regular wave theory. The water depth is intermediate with $k_p h = 1.48$. Note that the Stokes wave theory breaks down at a shallow water depth. Various wave amplitudes are simulated. The setup of the case corresponds to the recent experiments conducted at the Kelvin Hydrodynamic Laboratory in the University of Strathclyde. Details about the setup of the experiments are described in the recent conference paper in Adcock et al. (2019). The numerical tank is modelled shorter than the physical tank to minimize the computational effort.

Applying the linear combinations according to Eq.[6], the resulting four time histories of the first four harmonics are shown in Fig. 2. The corresponding spectra in log scale are shown in Fig. 3. The frequency is non-dimensionalized by the peak frequency. The separation of the first four harmonics, $\eta^{(1)}, \eta^{(2)}, \eta^{(3)}, \eta^{(4)}$, is very successful. No overlap is present among the four. The second subharmonic or difference $\eta^{(2-)}$ covering $0 - 2.0f_p$ can be easily extracted from the fourth harmonic (the blue dot-dash line), as their frequency ranges are largely apart. The linear component covers the input frequency range. Higher harmonic frequencies are

slightly broadened. For instance, the second sum covers the range of $1.0f_p - 5f_p$. The peak frequency of each harmonic corresponds to nf_p.

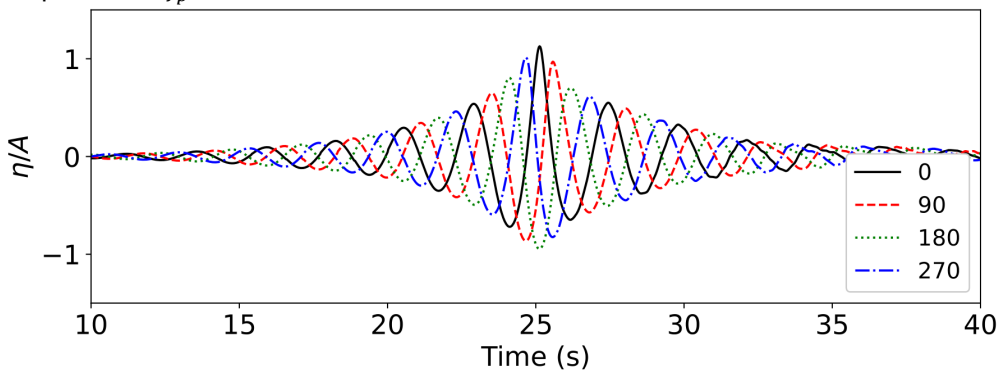

Figure 2. Time histories of the wave elevations of four phases for $A = 0.213$ m. Te wave group has a JONSWAP spectrum with $H_S = 0.426$ m and $f_p = 0.429$ Hz.

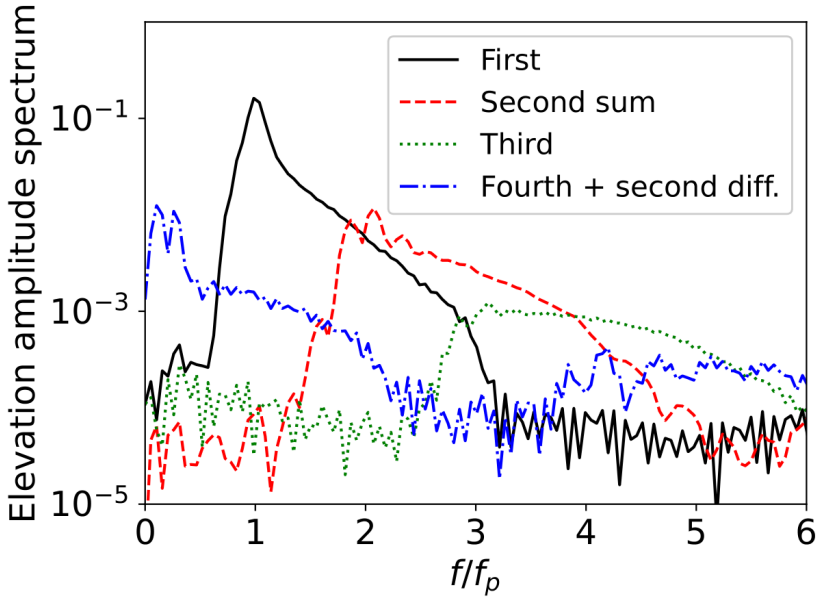

Figure 3. Decomposed elevation spectra for $A = 0.213$ m from the four-phase method. Input wave frequency is $0.5f_p - 3.0f_p$.

Direct comparisons of the elevations, particularly the higher harmonics, are made with the experimental results. The same approach was used in the experiments to obtain the harmonics. The results for $A = 0.213$ m are shown in Fig. 4. We shift the time histories such that the focusing time is at $t = 0.0$ s. The nth harmonics are normalized by $\mathrm{A^n}$. For both cases, the linear elevations agree very well, as in many other studies. The second difference $\eta^{(2-)}$ shows a significant set-down of the wave group. The numerical result in Fig. 4 shows the typical set-down at focusing, which is a long but smooth component. The overall agreement is good.

Very good agreements are also observed in the second sum harmonics, except after the time $t = 7.0$ s when a large component appears in the numerical result. This is believed to be due to the presence of the second-order error wave generated at the wavemaker. The presence and effect of error wave is extensively discussed in Orszaghova et al. (2014). The source of the error wave could be the linear transfer function used in the model. Nevertheless, the error wave is much delayed to the main wave group as higher frequency waves travel slower. It will not affect the magnitude of the main group. The phase modification due to third-order resonant wave-wave interactions, see recently Bonnefoy et al. (2016), could be the explanation for the delay in the focused wave group. However, the discrepancy is not observed for $A = 0.213$ m in Fig. 4. Note that the third harmonic elevation is very small in value. From the above very scrutiny comparisons at higher harmonics, we are confident that the numerical tank is highly accurate in predicting the higher harmonics of focused wave groups. Therefore, the four-phase decomposition approach is quite successful for the extraction of higher harmonics.

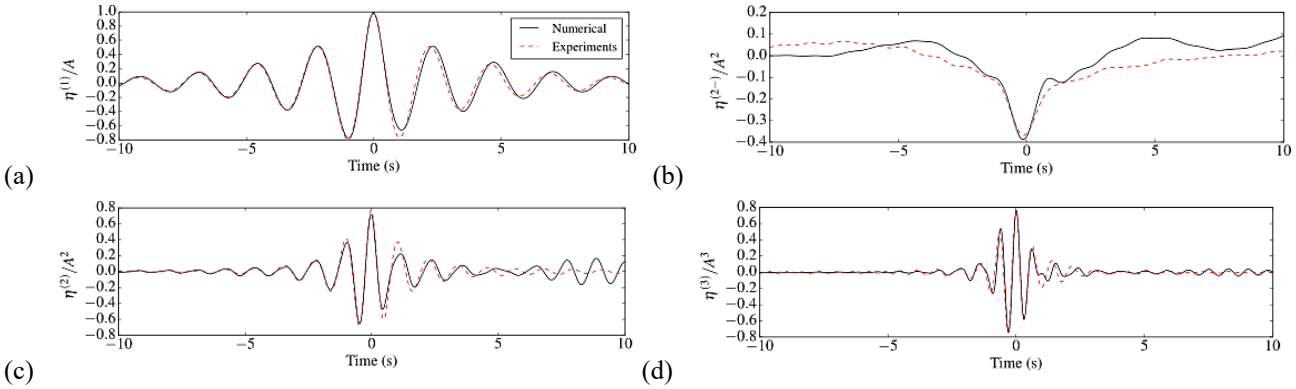

Figure 4. Time histories of the harmonic wave elevations at the centre of the tank for $A = 0.213$ m.

Further insight can be revealed from the time evolution of the wave profile of each harmonic along the tank in Fig. 5 where the first three harmonics are shown. This is obtained by recording the wave elevation at every point along the tank. Applying the four-phase combination method to each point gives the responses at each harmonic in the time domain. We then plot the wave profile of each harmonic along the tank at every time step. This post-processing could be time consuming, depending on the resolution of the free surface mesh. In the figures, each line shows the wave profile at a certain time step. The bold red line shows the profile at the focused time. Note that the time steps for the three harmonics are different as they evolute at different time scales. The linear wave profile in Fig. 5(a) covers a time period more than three times longer than that in Fig. 5(c). We see that the linear wave group has a smooth focusing and de-focusing process with a relatively long wavelength. In Fig. 5(b) the error wave behind the main group is visible, in the top left triangular zone. Generally the phase speed of the second harmonic is stable. In contrast, the third harmonic profile shows some randomness of its phase over the focusing and de-focusing time period. As explained, the reason might be the underlying third-order resonant wave-wave interactions causing energy transfer between different frequency components. It is also noticed that the third harmonic component only becomes significant near the focused time and near the focused location, i.e. it is compactly localized.

3.2 Harmonic coefficients

In view of the `Stokes-like' harmonics of a focused wave group in Eq. [5], we can treat the time-varying amplitude as the envelope of the time series. Using the peak value of the envelope, we are able to compute the corresponding n th harmonic coefficient as $S_{nn} = \frac{\max\{E(\eta^{(n)})\}}{A^n}$, where $E()$ is the envelope of the time series. The envelope is computed by $E(\eta^{(n)}) = \sqrt{(\eta^{(n)})^2 + (\eta_H^{(n)})^2}$. The superscript H represents its Hilbert transform.

To resolve the coefficient and the underlying structure of the harmonics, it is necessary to perform simulations using various wave amplitudes. Figure 6 shows the second and third harmonic coefficients S_{22} and S_{33} against the wave steepness $k_pA = 0.05 - 0.25$. The cross is the experimental result. The short lines represent some theoretical predictions which are independent on the wave steepness. In Fig. 6 the solid black line is the prediction using the method presented by Dalzell (1999) with modification for a wave group. The original Dalzell model considers the wave-wave interaction of two waves. We extend the model for the wave group by considering the interactions between each possible pair of wave components in the group. The modified formulation for the second-order elevation is presented previously. The dot line is simply the regular wave Stokes second-order coefficient and the dot-dash line is the Stokes coefficient in deep water. The numerical second harmonic coefficient S_{22} shows more or less a constant value about 0.72 over the steepness range. There is slight increment when the wave is steep near $k_pA = 0.20$. This trend is consistent with the experimental results, where there is minor scattering. It should be borne in mind that in the tests the actual value of the second harmonic peak is in the level of millimetre or smaller, which is to the accuracy of wave gauges. For the numerical model, probing the small wave elevations is not an issue. The averaged numerical S_{22} agrees very well with modified Dalzell model, and both are about 10% higher than the Stokes coefficient. The deep-water Stokes coefficient is much lower. This is expected since the wave nonlinearity typically weakens with increasing water depth.

The third harmonic coefficient S_{33} of the experiments is more scattering than the second. The scattering seems to occur either at low steepness or high steepness ranges. For the very mild wave, possibly the wave gauges could not capture the tiny component at the third harmonic. For the relatively steep wave, the third-order resonant wave-wave interaction would occur, breaking down the `Stokes-like' nonlinear structure. Nonetheless, the numerical results are still constant against the steepness. Again, the averaged numerical coefficient S_{33} is close to that of the experiments. The regular wave Stokes third-order coefficient underestimates the test results

by about 30%. Though close, in any case the focused wave group is different from a regular wave. The nonlinear wave-wave interaction could play an important role in modifying the peak or trough of a focused wave group, especially the third harmonic.

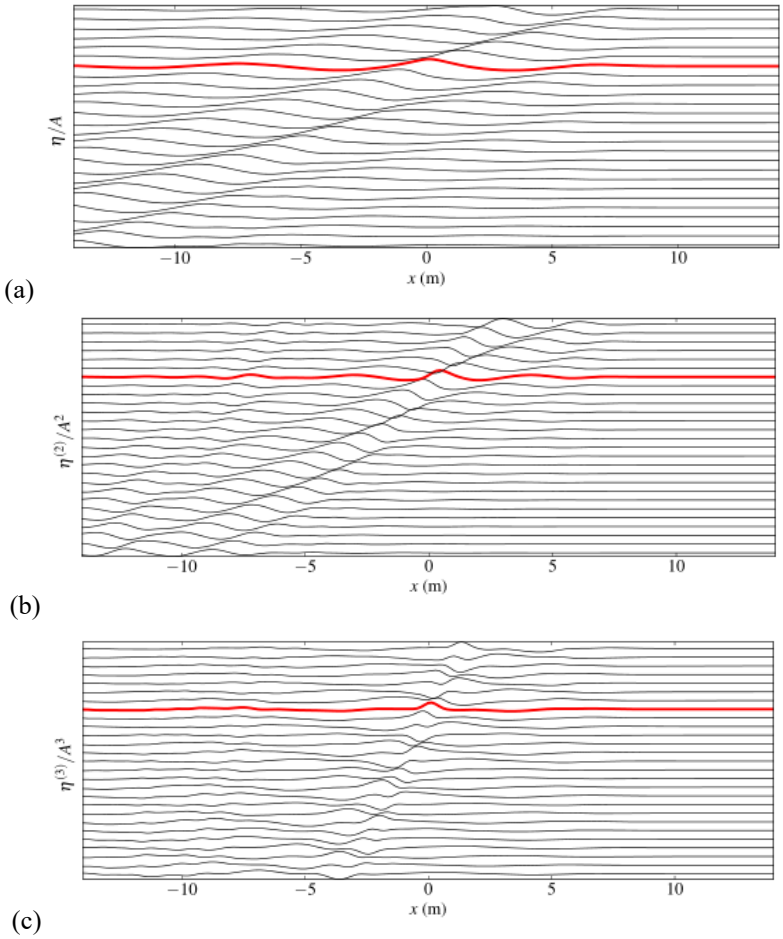

Figure 5. Evolution of the decomposed free surface elevations along the tank with $A = 0.213$ m for (a) first harmonic; (b) second harmonic; (c) third harmonic. Each line shows the wave profile at a certain time step. The bold red line shows the profile at the focused time.

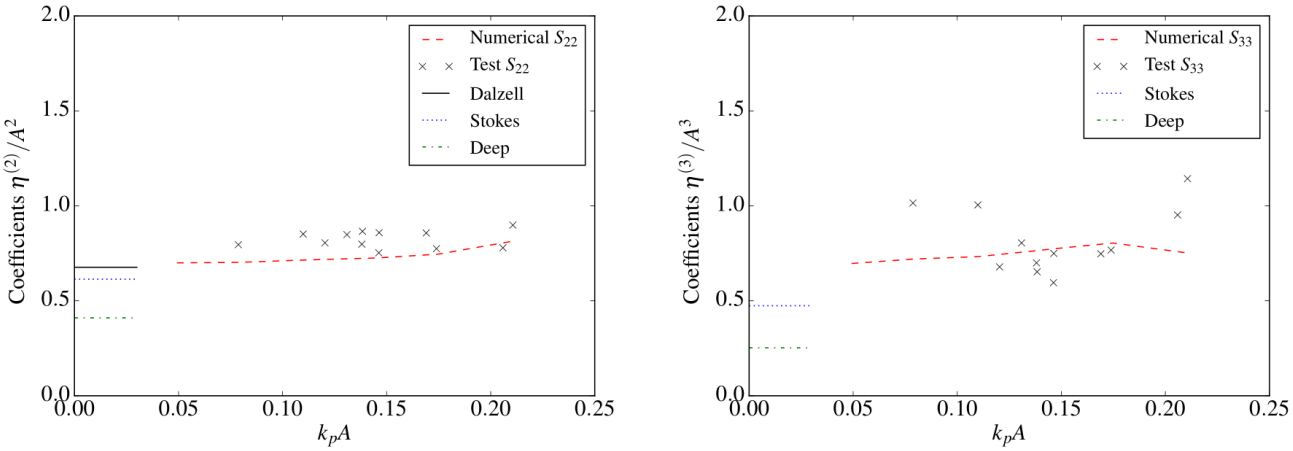

Figure 6. Evolution of the Harmonic coefficients of wave elevations for focused wave groups for $f_p = 0.429$ Hz with comparison against tests.

4 CONCLUSIONS

We present a fully nonlinear potential flow model with implementation of generation of focused wave groups. A phase-manipulation method is adopted to decompose the harmonic components of the nonlinear wave elevation. The four-phase method is demonstrated successful for separating the higher harmonics in the

nonlinear wave group. Direct comparison of the harmonic time histories is made with the recent experiments. The agreement is generally good. Small discrepancies are observed in the third harmonic elevation. While the third harmonic peak values are close for the numerical and experimental results, there exists a slight phase difference. This is explained by the phase modification resulting from resonant third-order wave-wave interactions.

The evolution of the decomposed higher harmonic wave profile is illustrated. Both the linear and second harmonics show smooth profiles along the tank. The third is localized and wavy due to its short wave length and possible phase modification.

We simulate the wave groups with varying amplitudes. Comparisons of the harmonic coefficients are made with the tests and the theory at increasing wave steepness. The second-order coefficient S_{22} is almost constant against the steepness for the numerical results. The second-order wave-wave interaction model by Dalzell (1999) is extended for a focused wave group. The modified Dalzell model shows good prediction, while the Stokes second-order model (for regular waves) slightly under-predicts the second-order coefficient. For the third-order coefficient S_{33}, the numerical results are almost constant with increasing wave steepness while the variation in the test data is considerable.

ACKNOWLEDGEMENTS

The authors appreciate the support from the Key Special Project for Introduced Talent Team of Southern Marine Science and Engineering Guangdong Laboratory (Guangzhou) (GML2019ZD0503).

REFERENCES

Adcock, T.A., Taylor, P.H., (2016). Non-linear evolution of uni-directional focussed wave-groups on a deep water: A comparison of models. *Applied Ocean Research* 59, 147–152.

Adcock, T.A.A., Feng, X., Tang, T., van den Bremer, T.S., Day, A.H., Dai, S., Li, Y., Lin, Z., Xu, W., Taylor, P.H., (2019). Application of phase decomposition to the analysis of random time series from wave basin tests, in: *Proceedings of the ASME 2019 38th International Conference on Ocean, Offshore and Arctic Engineering*.

Adcock, T.A.A., Taylor, P.H., Draper, S., (2015). Nonlinear dynamics of wave-groups in random seas: unexpected walls of water in the open ocean. *Proceedings of the Royal Society A: Mathematical, Physical and Engineering Sciences* 471.

Bai, W., Feng, X., Eatock Taylor, R., Ang, K.K., (2014). Fully nonlinear analysis of near-trapping phenomenon around an array of cylinders. *Applied Ocean Research* 44, 71–81.

Bonnefoy, F., Haudin, F., Michel, G., Semin, B., Humbert, T., Aumaitre, S., Berhanu, M., Falcon, E., (2016). Observation of resonant interactions among surface gravity waves. J*ournal of Fluid Mechanics* 805, R3

Buldakov, E., Stagonas, D., Simons, R., (2017). Extreme wave groups in a wave flume: Controlled generation and breaking onset. *Coastal Engineering* 128, 75–83

Dalzell, J., (1999). A note on finite depth second-order wave-wave interactions. *Applied Ocean Research* 21, 105–111

Fedele, F., Brennan, J., Ponce de Len, S., Dudley, J., Dias, F., (2016). Real world ocean rogue waves explained without the modulational instability. *Scientific Reports* 6, 27715

Feng, X., Bai, W., (2017). Hydrodynamic analysis of marine multibody systems by a nonlinear coupled model. *Journal of Fluids and Structures* 70, 72–101.

Fitzgerald, C.J., Taylor, P.H., Taylor, R.E., Grice, J., Zang, J., (2014). Phase manipulation and the harmonic components of ringing forces on a surface-piercing column. *Proceedings of the Royal Society of London A: Mathematical, Physical and Engineering Sciences* 470.

Lo, E., Mei, C.C., (1985). A numerical study of water-wave modulation based on a higher-order nonlinear Schrodinger equation. *Journal of Fluid Mechanics* 150, 395–41

Mei, C.C., Stiassnie, M., Yue, D.K.P., (2005). Theory and applications of ocean surface waves. Volume 23. World Scientific.

Orszaghova, J., Taylor, P.H., Borthwick, A.G.L., Raby, A.C., (2014). Importance of second-order wave generation for focused wave group run-up and overtopping. *Coastal Engineering* 94, 63–79.

Tromans, P.S., Anaturk, A.R., Hagemeijer, P., (1991). A new model for the kinematics of large ocean waves application as a design wave, in: *The First International Offshore and Polar Engineering Conference*.

Ursell, F., Dean, R.G., Yu, Y.S., (1960). Forced small-amplitude water waves: a comparison of theory and experiment. *Journal of Fluid Mechanics* 7, 33–52.

Walker, D.A.G., Taylor, P.H., Eatock Taylor, R., (2004). The shape of large surface waves on the open sea and the Draupner New Year wave. *Applied Ocean Research* 26, 73–83.

Whittaker, C., Raby, A., Fitzgerald, C., Taylor, P., (2016). The average shape of large waves in the coastal zone. *Coastal Engineering* 114, 253–264.

8th International Conference on the Application of Physical Modelling in Coastal and Port Engineering and Science
Dec. 9th - 12th, 2020, Zhoushan, China

NUMERICAL STUDY OF BRISBANE RIVER ESTUARY AND MORETON BAY AUSTRALIA: PROPOSED COASTAL RESERVOIR FOR FLOOD ADAPTATION AND WATER RESOURCE DEVELOPMENT

USMAN KHALIL[1], SHUQING YANG [2] & MUTTUCUMARU SIVAKUMAR [3] MARIAM SAJID [4]

[1,2,3] University of Wollongong, Australia; [4]University of Engineering and Technology Lahore, Pakistan
[1]uk998@uowmail.edu.au [2]shuqing@uow.edu.au.com [3]siva@uow.edu.au.com [4]maryamsajidmalik@hotmail.com

ABSTRACT

This study selects the region of Brisbane, River to analyse the adaptation measures against the 2011 flood and water resource development through a Coastal Reservoir (CR) technique. Extreme weather events are one of the significant aspects of South East Queensland (SEQ). The floods history starts from 1806 to recent 2011, after a decade-long drought, the Brisbane River catchment experienced an extreme rainfall event during January 2011 that gave rise to the so-called '2011 Brisbane flood'. A numerical model based on MIKE-21 is used to investigate the feasibility of the proposed CR after being calibrated and validated. The results show that the flood level at the Brisbane city can be reduced to 0.58 m (13%) by the gate operation of the CR and can be reduced to 1.13 m (28%) by the joint operation of Wivenhoe dam, which can safeguard infrastructure damage. Further, the study found that a150 m^3/sec discharge can flushed salinity up to the mouth and water can be store in CR for water supply. This study could provide useful information on flood management for the regional community.

Keywords: Flood mitigation, Freshwater, Coastal Reservoir, Salinity, MIKE-21,

1 INTRODUCTION

Flooding and droughts being the major impacts of climate change causing a substantial risk to the coastal area living. Flooding is a worldwide prevalent catastrophe which poses a severe threat to lives and properties (Liu and Lim, 2017). Floods are the most destructive among all the natural calamities in the world (Khalil and Khan, 2017). Similarly, drought ranks second in terms of economic impacts, afar direct economic impacts, drought can extremely influence drinking water supplies and ecosystems, and can even contribute to amplify food prices.

Australia has a long history of flood and drought. The floods history starts from 1806 to recent 2017. The Brisbane River, Queensland, Australia along with its main tributaries have a recorded flood history of almost two centuries with 1974 and the recent flood of 2011 are the most severe floods (van den Honert and McAneney, 2011). Australia is also among one of the driest country and continent (Donohue et al., 2009). Australia, during the last two centuries i.e. 1803 to 2010, has been experienced by ten spells of severe droughts. The period for each drought varies between 2 to 8 years. From 2000 to 2013, considerable southern and central inland has experienced nearly seven years of extreme drought, and few places remained 10 years in drought; it is identified as the Millennium Drought of Australia (BCC, 2012), where the South East Queensland (SEQ) dams water was reduced to 20 % in 2007(Seqwater, 2015).

Adaptation and mitigation to climate change are an important feature to lessen and avert the influence of floods and droughts (Ghozali et al., 2016). Flood management is a serious issue, coastal floods are viewed as the most hazardous and damaging of all-natural catastrophes affecting urban areas adjacent to the coastlines (Tsoukala et al., 2016). Further, flood forecast and climate change perspective have directed the needs of hydrodynamic models (Di Baldassarre et al., 2017; Gilles and Moore, 2010; Middelkoop et al., 2004; Patro et al., 2009). Adapting to climate change is an enormous challenge for major cities, particularly those in coastal areas. A low-lying locality, urban development and extreme weather events connected to climate change make Brisbane predominantly vulnerable to flooding and droughts. The region required 500 GL additional water supply for future needs (Yang, 2015), the region needs to look for other water resource options, (Seqwater, 2016) region require new water resources and flood mitigation options (Davidson et al., 2013). It is therefore essential to evaluate the flood mitigation options at the downstream catchment of the Wivenhoe dam and forecast water resources in current and future conditions for long-term sustainable development in this Brisbane river basin.

Analyzing and adaptation of future flooding risks in Brisbane Australia is essential for coastal planning and management (Pellikka et al., 2018). Coastal Reservoir technique is used for flood adaptation in Brisbane River Estuary (BRE) (Khalil et al., 2020) and may be used to store water for Brisbane City water supply.

2 PROJECT SITE

The study area is lower Brisbane River and the Moreton Bay, Australia (Figure 1). The Brisbane River is the longest in sub-tropical SEQ, having a length of 344 km and a catchment area of 13,600 km2 (Eyre et al., 1998). The Brisbane River estuary (BRE) has a tidal range of 2.8 m and it's a meso-tidal estuary (Yu et al., 2014). However, (Wolanski, 2014) defines it as a micro-tidal estuary, with a mean spring and neap tidal range of 1.8 and 1 m respectively. The BRE tidal section is more than 80 km from the river mouth and with 60 km upstream saltwater intruding length from the river mouth during the maximum time of the year (Ecosystem Health Monitoring Program, 2007). The Oxley Creek and Bremer River join the estuary at 34 and 73 km respectively, upstream from the river mouth, and the depth varies along the estuary from 15 m at the river mouth to about 4 m at the Bremer River junction at Moggill point.

The Moreton Bay is semi-closed situated in sub-tropical Southeast Queensland, Australia. The bay ranges from 27.05o to 27.5 o S and 153.1o to 153.3o E and covers an area of 1500 km2, with a depth of water range from 2 to 27 m. It is categorized as the bay with several islands (e.g. from north to south next to the river mouth is Mud Island, St, Helena Island, and Greed Island) and shallow average water depth of 6.8 m and it is described by semi-diurnal tides, with a range of 1-2 m (Dennison and Abal, 1999).

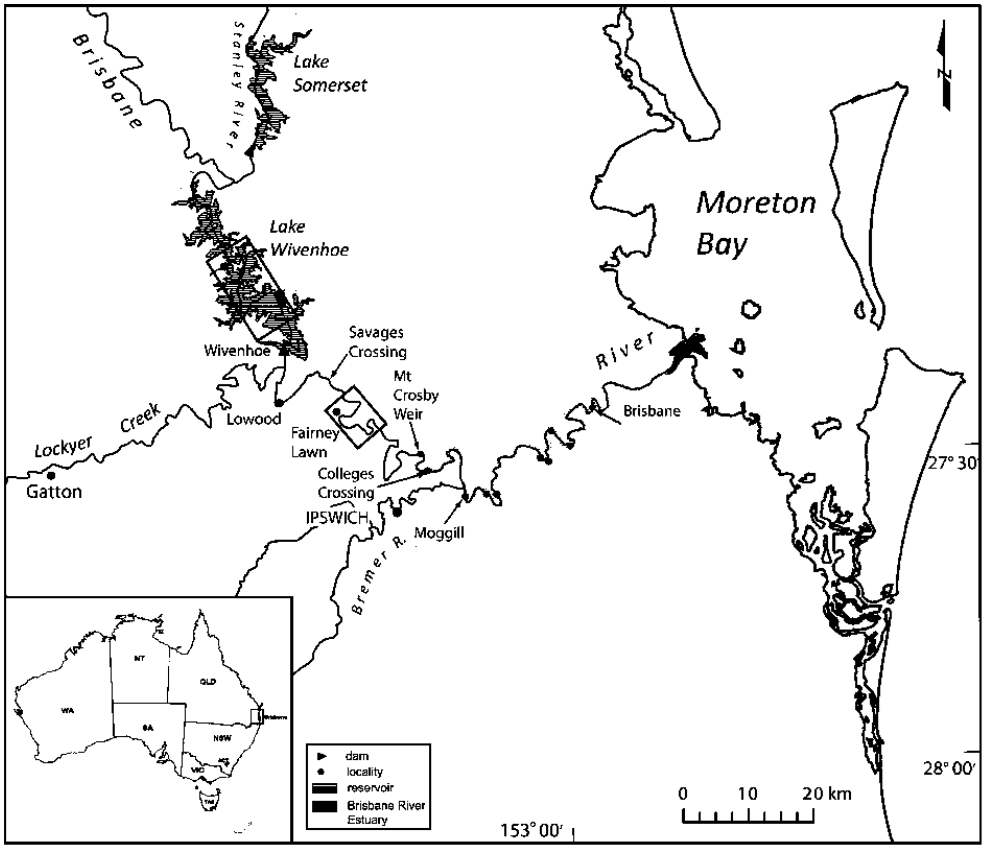

Figure 1. The Brisbane River, Queensland, Australia and Moreton Bay

3 DATA AND METHODS

The Flow Model FM of MIKE 21 was used for hydrodynamic and salinity change simulation in the BRE. In MIKE 21, an unstructured grid offers an optimum degree of flexibility in the illustration of composite geometries and allows smooth demonstrations of boundaries. The modelling domain is change to small elements where more detail is desired, and larger elements are used where less detail is required to optimize information for a specific quantity of computational time.

The MIKE 21 FM hydrodynamic model is set up with topographic data, Manning's roughness coefficients, water level and tidal data for the year 2011. The model is calibrated and validated well to match flood levels.

Coastal Reservoir area is selected based on available bathymetry and has a storage capacity of 900GL (surface area 75 km^2 and the water depth approximately 12 m). The reservoir dike with hydraulic gates to regulate the river flows into CR as shown in Figure 2.

Gate location and size is optimized according to the width of the river mouth. Gate A and B operation is optimized to allow water inside the CR and to stop the tidal water entering the estuary as shown in Figure 2. During a high flood, water could be diverted into the CR, which will cause a decrease in upstream flood level as there will be no resistance from tidal water and all flow will move to CR. While during low flow season, water will be discharged towards the Brisbane bar by closing the CR gate without storage.

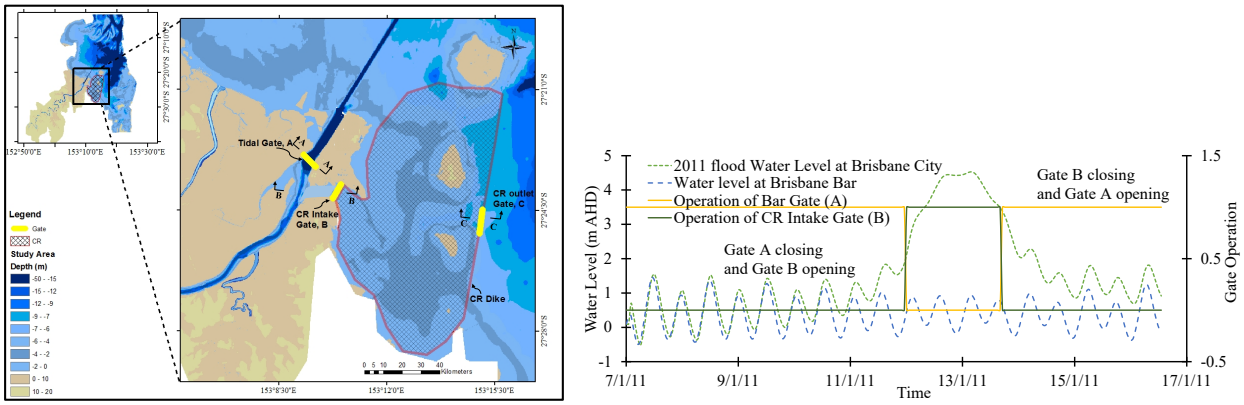

Figure 2. Coastal Reservoir Layout and operation of gates for the 2011 flood mitigation

3.1 Salinity

Monthly interval salinity data across BRE and Moreton bay from 2002-2018 were collected from Ecosystem Health Monitoring Program (EHMP). EHMP has been conducted water sampling at the ebb tides at 16 monitoring sites as shown in Figure. 3a. Salinity data is taken by using YSI 6920 conductivity sensor (Yu et al., 2014) and it is expressed using practical salinity unit (PSU). The measured monthly depth-averaged salinity data in BRE is plotted as shown in Figure. 3b.

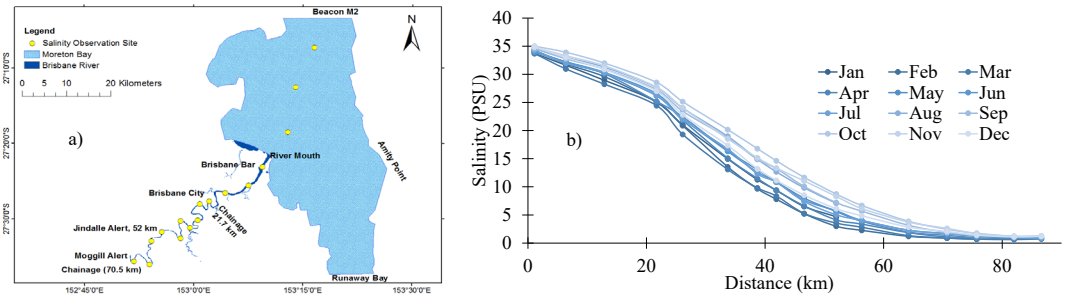

Figure 3. a) The Brisbane River estuary (BRE), Queensland, Australia, and locations of observation sites along the estuary; b) Observed monthly averaged Salinity Data in BRE over 16 years from 2002 to 2018

4 RESULTS AND DISCUSSION

The model is calibrated and validated well to match flood inundation extent with 85% accuracy as shown in Figure 4.

The simulated salinity compared well with the measured salinity measurements in BRE with a correlation coefficient of 0.90 (Figure 5). Since the results indicate that the MIKE 21 model is suitable for simulating BRE hydrodynamic and salinity intrusion, the calibrated parameters were, therefore, used for scenario analyses.

The water level remains unaffected before the gate operation. As the gate start operating at 12 January 2011 12:05 am, the water level starts decreasing in the Brisbane River and it reduces the peak water level at Brisbane city gauge from 4.46 m AHD to 3.95 m AHD, with overall 0.51 m reduction in peak water level as shown in Figure 6. This reduction in water level will save the infrastructure damage. Further, with improved flood management of the Wivenhoe Dam, the releases will be controlled and the water level at Brisbane city would be reduced below the major flood level.

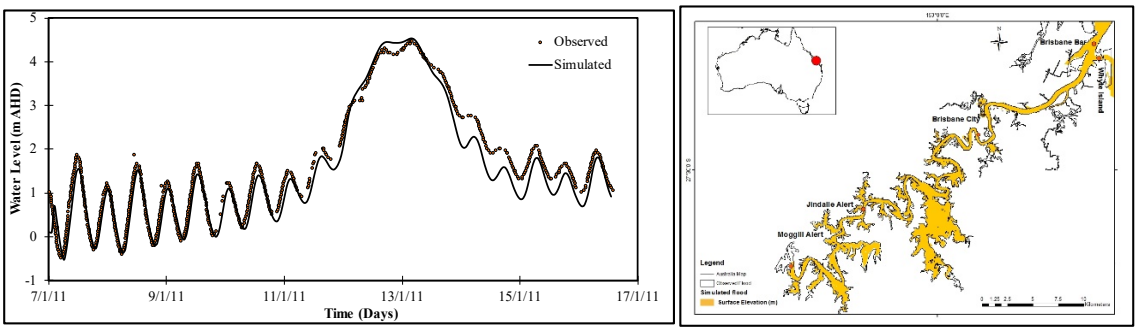

Figure 4. Simulated and observed water levels at Brisbane City; and simulated and observed inundation area

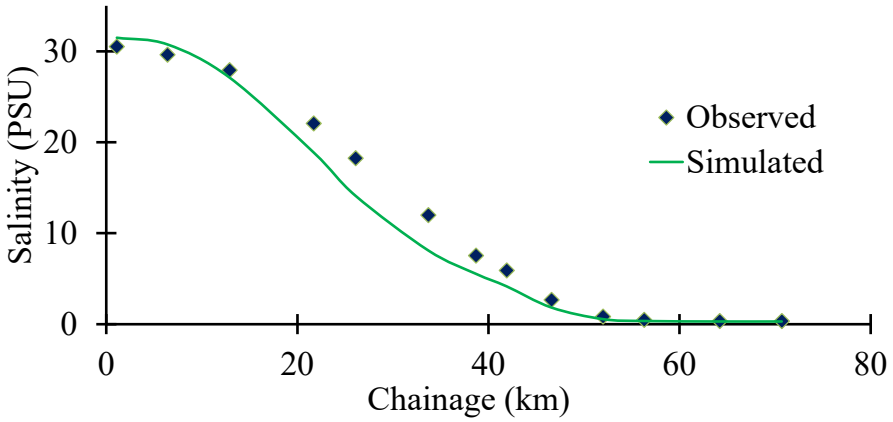

Figure 5: Comparison of observed and simulated salinity, 2011

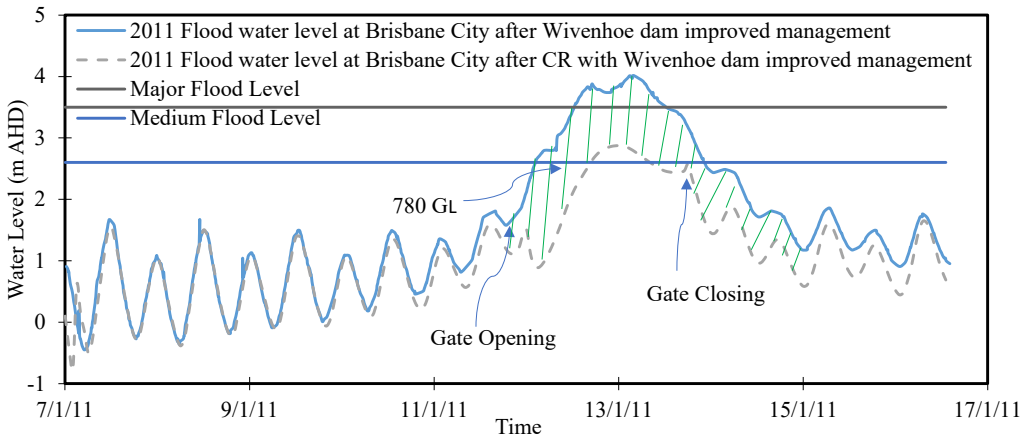

Figure 6. The water level during the 2011 flood in BRE with and without CR.

The salinity distribution in BRE under tidal response freshwater flow 150 m^3/sec is shown in Figure 7. Simulation results demonstrate that 150 m^3/sec of freshwater discharge purged salinity up to BRE mouth, with freshwater and saltwater interface (FSI) value taken to be the less than 1% PSU.

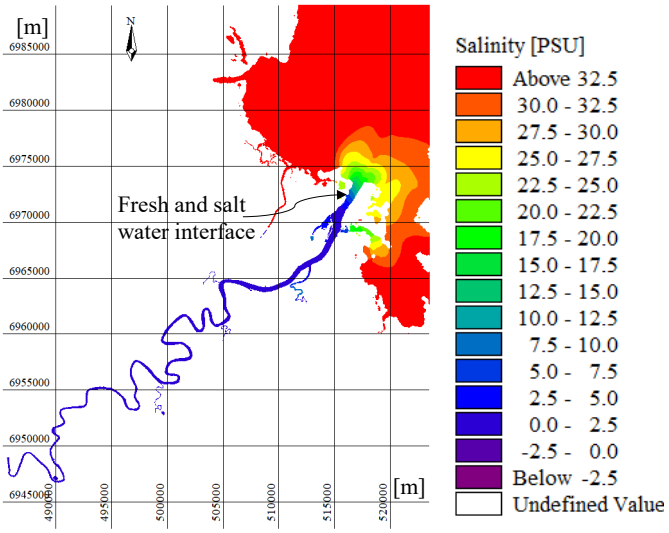

Figure 7: Freshwater and saline water interface under 150 m^3/sec discharge.

4 CONCLUSIONS

To enhance flood disaster mitigation in BRE, we analyzed the feasibility of a proposed CR at the river mouth. The major flood of 2011, was simulated and CR operation was analyzed using MIKE 21. The operation of the CR intake gate shows that the 2011 observed flood level (4.46 m AHD) can be reduced to 3.88 m AHD (13% reduction). While under the improved management of Wivenhoe dam, flood level will be (4 m AHD), by suitable operation of CR gate, flood level can be reduced to 2.87 m AHD (28.3% reduction) at the Brisbane city, The CR has great prospects to adapt to the flood of the Brisbane catchment and thus to mitigate BRE the flood disaster. Further, CR can intake and store high-quality water when the discharge is more than 150 m^3/sec.

ACKNOWLEDGEMENTS

The authors would like to thank the Queensland Government Departments for providing all necessary input data. We are also thankful to DHI for providing the MIKE 21 license.

REFERENCES

BCC, B.C.C., 2012. Brisbane Economic Development Plan.
Davidson, J. et al., 2013. SEQ WATER FUTURES.
Dennison, W.C., Abal, E.G., 1999. Moreton Bay study: a scientific basis for the healthy waterways campaign. South East Qld Regional Water Quality Management Strategy Team.
Di Baldassarre, G., Martinez, F., Kalantari, Z., Viglione, A., 2017. Drought and flood in the Anthropocene: feedback mechanisms in reservoir operation. Earth System Dynamics, 8(1): 225-233. DOI:10.5194/esd-8-225-2017
Donohue, R.J., McVICAR, T.R., Roderick, M.L., 2009. Climate-related trends in Australian vegetation cover as inferred from satellite observations, 1981–2006. Global Change Biology, 15(4): 1025-1039.
Ecosystem Health Monitoring Program, E., 2007. Ecosystem Health Monitoring Program 2005-2006 Annual Technical Report.
Eyre, B., Hossain, S., McKee, L., 1998. A suspended sediment budget for the modified subtropical Brisbane River estuary, Australia. Estuarine, Coastal and Shelf Science, 47(4): 513-522.
Ghozali, A., Sukmara, R.B., Aulia, B.U., 2016. A comparative study of climate change mitigation and adaptation on flood management between Ayutthaya City (Thailand) and Samarinda City (Indonesia). Procedia-Social and Behavioral Sciences, 227: 424-429.
Gilles, D., Moore, M., 2010. Review of hydraulic flood modeling software used in Belgium, The Netherlands, and The United Kingdom. International Perspectives in Water Resources Management, Iowa City, IA.
Khalil, U., Khan, N.M., 2017. Floodplain Mapping for Indus River: Chashma–Taunsa Reach. Pakistan Journal of Engineering and Applied Sciences.
Khalil, U. et al., 2020. Investigating an Innovative Sea-Based Strategy to Mitigate Coastal City Flood Disasters and Its Feasibility Study for Brisbane, Australia. Water, 12(10). DOI:10.3390/w12102744
Liu, X., Lim, S., 2017. Flood Inundation Modelling for Mid-Lower Brisbane Estuary. River Research and Applications, 33(3): 415-426.
Middelkoop, H. et al., 2004. Perspectives on flood management in the Rhine and Meuse rivers. River research and applications, 20(3): 327-342.

Patro, S., Chatterjee, C., Mohanty, S., Singh, R., Raghuwanshi, N., 2009. Flood inundation modeling using MIKE FLOOD and remote sensing data. Journal of the Indian Society of Remote Sensing, 37(1): 107-118.

Pellikka, H., Leijala, U., Johansson, M.M., Leinonen, K., Kahma, K.K., 2018. Future probabilities of coastal floods in Finland. Continental Shelf Research, 157: 32-42. DOI:10.1016/j.csr.2018.02.006

Seqwater, 2015. Water for life.

Seqwater, 2016. Water for life South East Queensland's Water Security Program 2016-2046.

Tsoukala, V.K. et al., 2016. An integrated wave modelling framework for extreme and rare events for climate change in coastal areas–the case of Rethymno, Crete. Oceanologia, 58(2): 71-89.

van den Honert, R.C., McAneney, J., 2011. The 2011 Brisbane floods: causes, impacts and implications. Water, 3(4): 1149-1173.

Wolanski, E., 2014. Estuaries of Australia in 2050 and Beyond. Springer.

Yang, S.-Q., 2015. A preliminary feasibility study for a backup water supply-coastal reservoir in Southeast Queensland, Australia. Journal of Water Supply: Research and Technology-Aqua, 64(4): 470-485.

Yu, Y., Zhang, H., Lemckert, C., 2014. Salinity and turbidity distributions in the Brisbane River estuary, Australia. Journal of hydrology, 519: 3338-3352.

8th International Conference on the Application of Physical Modelling in Coastal and Port Engineering and Science
Dec. 9th - 12th, 2020, Zhoushan, China

EFFECT OF THE WAVE RESONANCE IN THE GAP ON THE HYDRODYNAMICS CHARACTERISTICS OF A WEC DEVICE

Jing Geng(1), Yang Zhang(2), Xuanlie Zhao(3), Lars Johanning(4), Mingwei Li(5)

(1,2,3,5) *College of Shipbuilding Engineering, Harbin Engineering University, Harbin, China, gengjing@hrbeu.edu.cn, zhyangchanges@hrbeu.edu.cn, xlzhao@hrbeu.edu.cn, limingwei@hrbeu.edu.cn.*
(4) *College of Engineering, Mathematics and Physical Sciences, Exeter University, Cornwall TR10 9FE, UK, L.Johanning@exeter.ac.uk*

ABSTRACT

The Comb-Type Breakwater-WEC (Wave Energy Converter) system is characterized by a gap between the device and the flange. In this paper, an analytical model based on the linear potential flow theory is built to investigate the effect of the wave resonance in the gap on the hydrodynamics characteristics of a WEC device. The Galerkin approximation method is used to solve the singularity in the velocity near the tip of the flange. The analytical model is validated with the published results. Results show that wave resonances (including piston and sloshing mode) modify the hydrodynamic performance of the system significantly. It mainly reflected in that an increase in the capture width ratio of the device accompanies the occurrence of the piston mode response. When the sloshing mode resonance occurs, the device is located at the antinode of superposition of the incident and reflected waves from the flange, which can improve the efficiency of the device.

Keywords: Comb-type breakwater; capture width ratio; wave resonance; analytical method.

1 INTRODUCTION

Owing to large reserves and low carbon emissions, many engineers and researchers pay more attention to the ocean wave energy. Many kinds of wave energy converters (WECs) include oscillating water column, point absorber and overtopping device (Falcão, 2010). However, high cost and low energy conversion efficiency hinder the commercialization of WECs (Melikoglu, 2018). Integrating WECs with marine structures potentially enhances economic viability through dual-functionality (Mustapa et al., 2017; He et al., 2019), including breakwater-WEC integration (Zhang et al., 2020; Zhang et al., 2020; Zhao et al., 2019), floating wind turbine-WEC integration (Pérez-Collazo et al., 2015), et al. Functions of the wave attenuation and energy utilization can be realized simultaneously for a hybrid breakwater-WEC system.

The Comb-Type Breakwater (CTB) has dual functions of wave attenuation and water exchange, which has been successfully applied in the port area of Da-yao, Dalian, China, consisting of an array of rectangle caissons connected with thin walls (Niu et al., 2003). Zang et al. (2018) had invesitgated hydrodynamic characteristics of CTB numerically and experimentally, with a focus on the flow mechanism of impulsive wave forces. Wang et al. (2018 and 2019) developed an analytical solution to estimate the hydrodynamic qualities, including reflection and transmission coefficients, total wave force and wave surface elevation. The CTB can realize the better wave attenuation performance, but the wave amplitude between adjacent caissons can be amplified, which results in an increase in wave energy flux desity. Saadat et al. (2013 and 2016) proposed an integration system called Helmholtz wave energy converter comprosed of a contraction channel and a basin. The performance of WECs in a basin was improved owing to the wave energy gathering characteristics.

Considering the wave amplification of the CTB, a novel integrated system consisting of an oscillating body WEC and a CTB was proposed in this study. The vertical pile-constraining bodies with power take-off (PTO) system are arranged in the wave chamber composed of adjacent caissons. The oscillating buoy moves in heave motion under the constraining of the vertical pile. The working mechanism of the WEC is similar to that in Ning et al. (2016). Due to the dual effect of wave energy absorbing of the WEC and the wave reflection of the CTB, the integrated system is anticipated to work effectively as a breakwater.

The paper aims to build an analytical model to investigate the hydrodynamic performance of the integrated system. The velocity singularity at the tip of the flange was solved. The analytical model is validated with the published results. Meanwhile, the effect of the device location on hydrodynamic characteristics of the integrated system is conducted. Finally, the conclusion can be drawn.

2 MATHEMATICAL MODEL

The integrated system consists of heaving body-WECs and the Comb-Type Breakwater. In order to absorb the wave energy effectively, the width of the heaving body is identical to that of the wave chamber. The

geometry of the integrated system and 3D Cartesian coordinate system are shown in Fig. 1. Due to the periodicity of the integrated system, the problem can be reduced to an analogous channel problem with impermeable side walls. The integrated system array can be simplified as the unit without loss of generality. The origin is located at the cross-point of the still water surface and the medial axis of the heaving body. The *z*-axis is positive in the vertically upward direction. The water depth is *h*. The incident wave amplitude, wavelength and period are *A*, *L* and *T*, respectively.

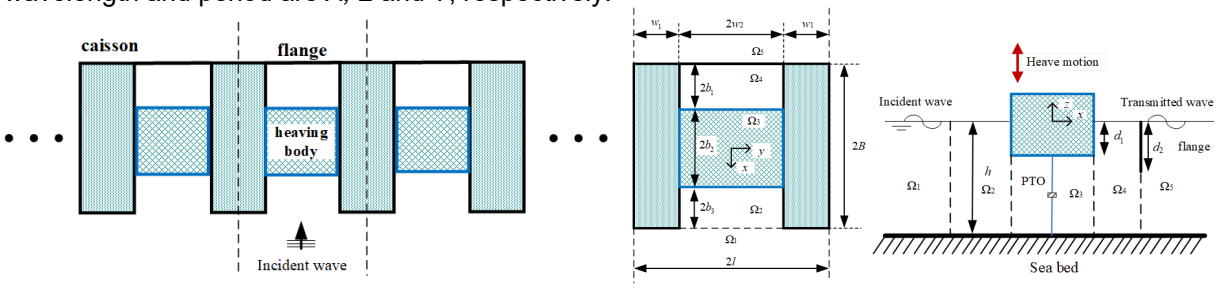

(a) (b) (c)

Fig. 1. (a) a linear array of heaving bodies integrated with the comb-type breakwater, (b) the section of the integrated system unit and (c) the top view of the integrated system unit.

2.1 Governing equation and boundary conditions

As indicated in Fig. 1(b) and (c), the fluid is divided into five subdomains, which are defined as the exposed side of caissons Ω_1: $-l \le y \le l$, $B \le x \le +\infty$ and $-h \le z \le 0$; the domain between adjacent caissons in front of a heaving body Ω_2: $-w_2 \le y \le w_2$, $b_2 \le x \le B$ and $-h \le z \le 0$; the domain below a heaving body Ω_3: $-w_2 \le y \le w_2$, $-b_2 \le x \le b_2$ and $-h \le z \le -d_1$, the domain between adjacent caissons in back of a heaving body Ω_4: $-w_2 \le y \le w_2$, $-B \le x \le -b_2$ and $-h \le z \le 0$ and the lee side of caissons Ω_5: $-l \le y \le l$, $-\infty \le x \le -B$ and $-h \le z \le 0$. The fluid motion in the whole fluid domain is depicted by the spatial velocity potential:

$$\Phi(x,y,z,t) = \mathrm{Re}\{\phi(x,y,z)\exp(-\mathrm{i}\omega t)\} \quad [1]$$

where the spatial velocity potential $\phi(x, y, z)$ satisfies the 3D Laplace Equation:

$$\frac{\partial^2\phi}{\partial x^2} + \frac{\partial^2\phi}{\partial y^2} + \frac{\partial^2\phi}{\partial z^2} = 0 \quad [2]$$

Based on the consideration of the heave motion, ϕ is decomposed as

$$\phi = \phi_\mathrm{I} + \phi_\mathrm{D} + \phi_\mathrm{R} \quad [3]$$

where ϕ_I and ϕ_D represents the incident wave and the diffracted potential, and ϕ_R denotes the radiated potential, which can be expressed as

$$\phi_\mathrm{R} = -\mathrm{i}\omega\xi\varphi_\mathrm{R} \quad [4]$$

where ξ denotes the heave response amplitude of the heaving body, and φ_R is the spatial complex potential.

The spatial complex velocity potential satisfies the free surface boundary condition and non-penetration condition of the seabed. Furthermore, $\phi(x, y, z)$ must satisfy the non-penetration boundary conditions on the solid wall and the heaving body, as well as the far-field radiation conditions.

2.2 Solutions of wave diffraction and radiation

The velocity potentials for different regions can be derived based on the above-described boundary problems using the matching eigenfunction expansion method. The diffracted and radiated potentials satisfy the continuity conditions for both the normal velocity and pressure at the interfaces between adjacent subdomains. This system can be truncated into a finite number of coefficients and solved with the employment of standard eigenfunction matching methods at the interfaces between adjacent subdomains. However, there exist strong singularities at the sharp edges of the flange, the convergence of the system with increasing the number of the truncated terms was found rather slow. To reduce this problem to the solution of a small number of algebraic equations, we adopted the Galerkin approximation method proposed by Evans and Porter (1995) to handle the singularities. The following auxiliary functions are introduced to express the water velocities below the flange.

$$U^{(l)}(y,z) = \sum_{m=1}^{\infty}\overline{C}_m(y)\sum_{q=0}^{\infty}A_{mq}^{(l)}u_q(z) \quad [5]$$

where l=1 and 2, corresponding to the diffraction and radiation problem. $U^{(l)}(y,z)$ represents the velocity under the flange. $\overline{C}_m(y)$ denotes the y-direction eigenfunction, can be expressed as

$$\overline{C}_m(y) = \cos\overline{\gamma}_m(w_2 - y) \quad [6]$$

The function of $U_q(z)$ can be written as

$$u_q(z)=\frac{2(-1)^q}{\pi\sqrt{(h-d_2)^2-(z+h)^2}}T_{2q}\left(\frac{z+h}{h-d_2}\right) \quad [7]$$

where T_{2q} can be considered as a Chebyshev polynomial.

$$S_{qn}=\int_{-h}^{-d_2}u_q(z)Z_n(z)\mathrm{d}z=\frac{J_{2q}\{k_n(h-d_2)\}}{\cos k_n h} \quad [8]$$

where J_{2p} is the Bessel function of order 2q.
The velocity continuity conditions of radiation and diffraction problem x=-B can be written as

$$\frac{\partial\phi_D^4}{\partial x}=\begin{cases}U^{(1)},-w_2<y<w_2,-h<z<-d_2\\-\dfrac{\partial\phi_1}{\partial x},-w_2<y<w_2,-d_2<z<0\end{cases} \quad [9]$$

$$\frac{\partial\varphi_R^4}{\partial x}=\begin{cases}U^{(2)},-w_2<y<w_2,-h<z<-d_2\\0,-w_2<y<w_2,-d_2<z<0\end{cases} \quad [10]$$

$$\frac{\partial\phi_D^5}{\partial x}=\begin{cases}-\dfrac{\partial\phi_1}{\partial x},(-l<y<-w_2)\cup(w_2<y<l),-h<z<0\\U^{(1)},-w_2<y<w_2,-h<z<-d_2\\-\dfrac{\partial\phi_1}{\partial x},-w_2<y<w_2,-d_2<z<0\end{cases} \quad [11]$$

$$\frac{\partial\varphi_R^5}{\partial x}=\begin{cases}0,(-l<y<-w_2)\cup(w_2<y<l),-h<z<0\\U^{(2)},-w_2<y<w_2,-h<z<-d_2\\0,-w_2<y<w_2,-d_2<z<0\end{cases} \quad [12]$$

where ϕ^5_D, φ^5_R and ϕ^4_D, φ^4_R denote the diffraction and radiation potential of subdomain Ω_5 and Ω_4.

2.3 hydrodynamic coefficients
The wave exciting force F_z acting on the bottom of a heaving body can be expressed as

$$F_z=\mathrm{i}\omega\rho\int_{S_b}(\phi_I+\phi_D)n_z\mathrm{d}s \quad [13]$$

where S_b is the bottom surface of a heaving body and n_z is the unit normal vector in the positive z-direction. The added mass μ and radiation damping λ in the heave motion subjected to a unit forced motion of a heaving body can be written as

$$\mu=\rho\int_{S_b}\mathrm{Re}[\varphi_R]n_z\mathrm{d}s \quad [14]$$

$$\lambda=\rho\omega\int_{S_b}\mathrm{Im}[\varphi_R]n_z\mathrm{d}s \quad [15]$$

where Re[ ] and Im[ ] denote the real and imaginary part of a complex.

According to the motion equation in the frequency domain, the heave response amplitude ξ can be expressed as

$$\xi=\frac{F_z}{-\omega^2(M+\mu)-\mathrm{i}\omega(\lambda+\lambda_{PTO})+K} \quad [16]$$

where λ_{PTO} is the Power Take-Off (PTO) damping, M and K represent mass and stiffness term, respectively. Therefore, the capture width ratio (CWR) η can be expressed as $\eta=P_{capture}/P_{incident}$, where $P_{capture}$ is the absorbed power of a WEC with the PTO damping λ_{PTO}, and $P_{incident}$ represents the incident wave power with incident wave width 2l.

$$P_{capture}=0.5\lambda_{PTO}\omega^2|\xi|^2 \quad [17]$$

$$P_{incident}=\frac{1}{2}\frac{\rho g A^2\omega l}{\kappa_1}\left(1+\frac{2\kappa_1 h}{\sinh 2\kappa_1 h}\right) \quad [18]$$

The reflection coefficient and transmission coefficients can be expressed as

$$K_r=\lim_{x\to+\infty}\left|\frac{\phi_D+\phi_R}{\phi_I}\right| \quad [19]$$

$$K_t=\lim_{x\to-\infty}\left|\frac{\phi_I+\phi_D+\phi_R}{\phi_I}\right| \quad [20]$$

3 COMPARSION WITH THE PUBLISHED RESULTS

Since the law of energy conservation is satisfied within the frame of the linear potential flow theory, the

relation of $K_r^2+K_t^2+\eta=1$ is used to validate the present analytical model. Fig. 2 showed the variations of the K_r, K_t, η and $K_r^2+K_t^2+\eta$ with the dimensionless wavenumber for geometrical parameters of B/h=1, d_1/h=1/3, b_2/h=1/3, b_1/b_2=1/4, w_1/h=1/3 and l/h=2/3. The PTO damping is chosen as $\lambda_{optimal}$. Based on the numerical convergence analysis, the terms of the *z*- and *y*-direction eigenfunctions are truncated at 100 and 10, as well as the velocity expansion number q=6. As indicated in Fig. 2, the relation of energy conservation is satisfied, which verifies the accuracy of the present analytical model.

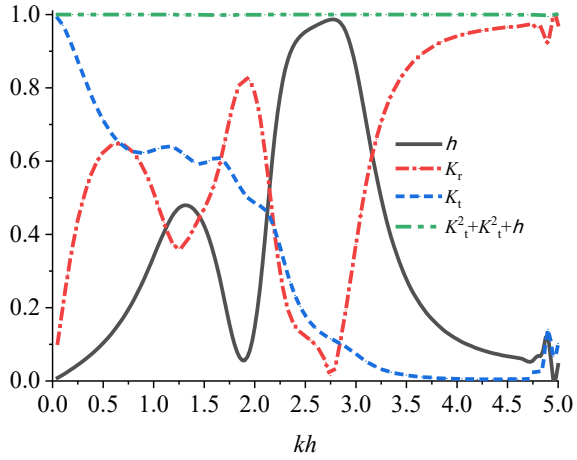

Fig. 2. Variations of reflection coefficient K_r, transmission coefficient K_t, capture width ratio η and $K_r^2+ K_t^2+\eta$ versus dimensionless wave number kh.

4 RESULTS AND DISCUSSIONS

In this section, we invesitigated the effect of locations of a heaving body on the hydrodynamic performance of the integrated system. The geomentrical dimensions are set as B/h=1, b_2/h=1/3, d_2/h=1/3, $w_1/h=w_2/h$=1/3 and d_1/h=1/6. Fig. 4 shows the variations of capture width ratio η, reflection coefficient K_r, transmission coefficient K_t and dimensionless wave exciting force $F_z/4\rho gAb_2w_2$ with the dimensionless wavenumber for different cases of b_1/b_3=3, 1 and 1/3. There exhibit some oscillations of η and K_r in the whole frequency domain. The η and F_z approaches the first peak in the region 1.0<kh<2.0. The frequency of the peak value shifts to the lower-frequency region with an increase in b_1/b_3. For the region of 1.5<kh<2.5, a valley of η can be found, which corresponds to spiked values of K_r and the wave exciting force F_z. The maximum of η approaches the 100% for cases of b_1/b_3=1 in the middle-frequency region, which reflects the total incident wave energy is absorbed by a heaving body. However, a dramatic change can be found for the case of b_1/b_3=3 in the high-frequency region. A symptom of η=0 accompanies the occurrence of F_z=0, and the device remains stationary which results in the strong reflection phenomenon. The changes of location have little influence on transmission coefficients. But it exhibits multiple small pike values in 1.5<kh<4.0. The effective frequency bandwidths can be defined as K_t≤50% and η>20% (Ning et al. (2017)). Therefore, the effective frequency region for b_1/b_3=3, 1 and 1/3 are 1.8≤kh≤4.4, 2.0≤kh≤3.6 and 2.6≤kh≤4.5, corresponding to bandwidths of 2.6, 1.6 and 1.9, respectively. The better wave energy capturing and attenuation performance can be realized simultaneously, when the device is located at the windward side of the wave chamber..

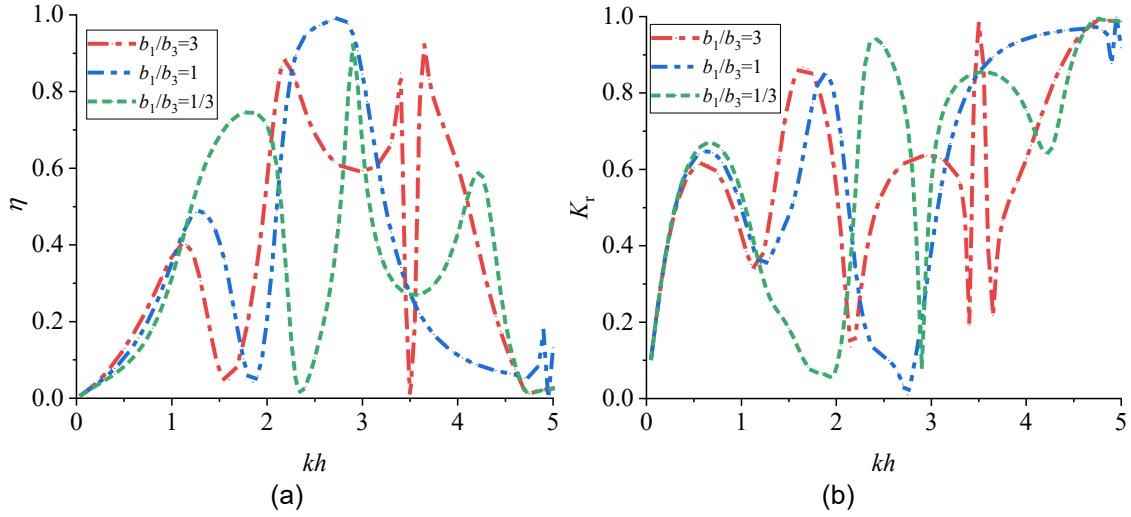

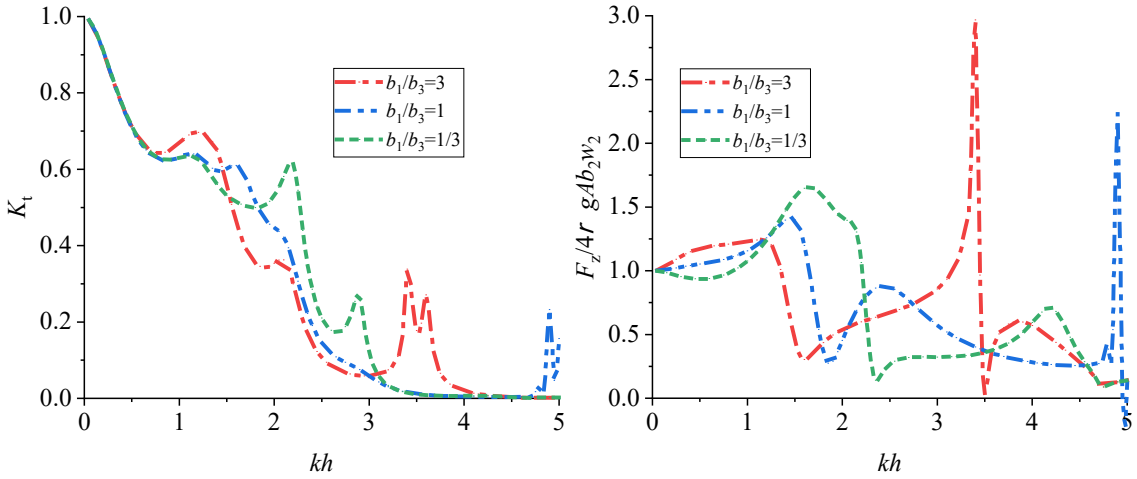

Fig. 4. The Varations of (a) capture width ratio η, (b) reflection coefficient K_r, (c) transmission coefficient K_t and (d) dimensionless wave exciting force $F_z/4\rho gAb_2w_2$ with the dimensionless wavenumber kh for cases of b_1/b_3=3, 1 and 1/3.

In order to futher analyze the physical explanation of some special phenomena, results of dimensionless added mass $\mu/4\rho gb_2w_2d_1$ and damping coefficient $\lambda/4\rho\omega gb_2w_2d_1$ are shown in Fig. 5 for cases of b_1/b_3=3, 1 and 1/3. For the case of b_1/b_3=1/3, the trend of the added mass versus kh experiences a dramatic decrease from a positive value in range of $2.0<kh<2.5$. Correspondingly, a peak value of radiated damping emerges, and the CWR nearly approaches the first peak value. As was reported in Ohkusu (1969), the near-resonant standing waves occur between the maximum and minimum of damping coefficient (i.e., the range of $2.0<kh<2.5$ in the present case). The negative added mass is related with the piston mode of water motion between a heaving body and the flange, which was known as Helmholtz or pumping mode (Faltinsen, 2006). As the b_1/b_3 decreases, the occurrence of the piston mode shifts to the high-frequency. This is due to that the water mass of the piston mode decreases, which corresponds to an increase in the natural frequency of water body. From the point view of wave theory, the superposition of incident and reflected waves from the flange may lead to the standing waves between a heaving body and the flange (Sarkar et al., 2015). The locations of $2kb_1\approx n\pi$ and $2kb_1\approx(n+0.5)\pi$ corresponds to the antinodes and nodes of the standing wave field. Therefore, the spike value of hydrodynamic coefficients is found at kh=3.38 for the case of b_1/b_3=3. The trend of the dimensionless added mass and radiated damping is significantly severe than that of the piston mode. The device is located at the wave antinodes of the wave field, accompanying the sloshing mode resonance. In addition, the zeros of μ and λ occur at kh=3.5, which results in no energy radiated to the far-field. The device is located at the wave node of the wave field, and a heaving body remains stationary, which accompanies the strong reflection phenomenon. For the capture width ratio η at the case of b_1/b_3=1, the first peak accompanies the piston mode, and the second peak corresponds to the matching between the incident wave and natural frequency of a heaving body.

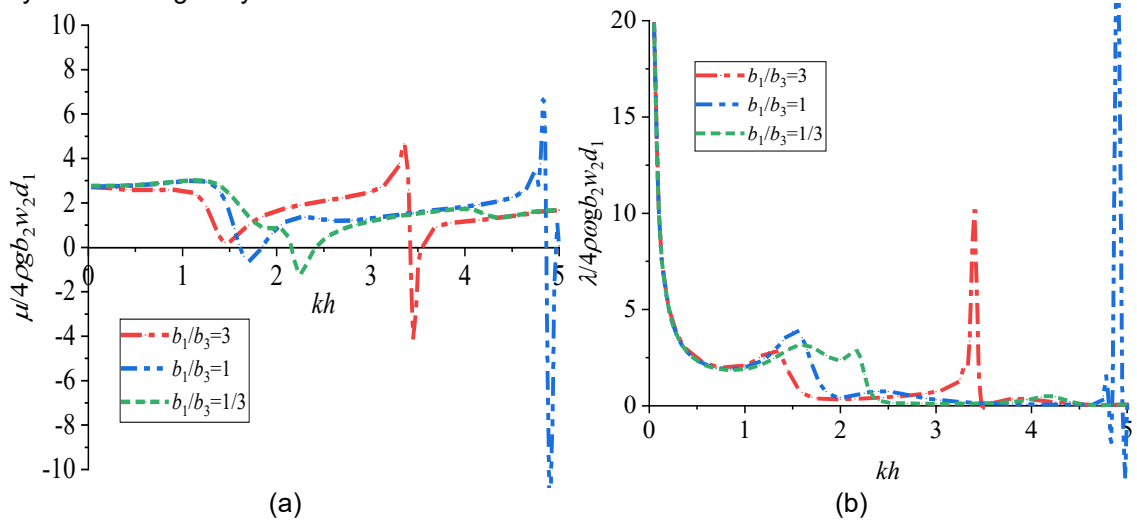

Fig. 5. The results of the dimensionless added mass $\mu/4\rho gb_2w_2d_1$ and damping coefficient $\lambda/4\rho\omega gb_2w_2d_1$ with the dimensionless wavenumber for different locations.

5 CONCLUSIONS

In this paper, hydrodynmic performance of the integrated system was investigated analytically. The velocity singularities at the tip of the flange was solved by using the Chebyshev polynomial. The location of device has significant influence on the capture width ratio and reflection coefficient of the integrated system. The maximum (i.e., 100%) of the CWR can be achieved for the integrated system, compared with that of an isloated heaving body-WEC (i.e., 50%, Zhao et al (2017)). The wave energy capturing performance is amplified, accompanying the piston mode and the sloshing mode resonance between a heaving body and the flange. The broader effective frequency bandwidth and the wave attenutaion peroformnce can be obtained by arranging the device close to the windside of the wave chamber. Besides we found that the synergies between the breakwater and wave energy devices can be achieved.

In this study, the incident wave angle was not considered. The performance of the system in oblique waves and multi-directional waves will be further investigated.

ACKNOWLEDGEMENTS

This work is supported by the following project grants, Fundamental Research Funds for the Central Universities, China (GK2010260303); Open Foundation of State Key Laboratory of Coastal and Offshore Engineering, China (LP1927); China Postdoctoral Science Foundation funded project (2019M661257); National Natural Science Foundation of China (51509056); Natural Science Foundation of Heilongjiang Province (E2017028); Fundamental Research Funds for the Central Universities (HEUCFG201813).

REFERENCES

Das, P., Dolai, D.P., Mandai, B.N., 1997. Oblique Wave Diffraction by Parallel Thin Vertical Barriers with Gaps. Journal of Waterway, Port, Coastal and Ocean Engineering. 123(4), 163-171.

Evans, D.V., Porter, R., 1995. Complementary Approximations to Wave Scattering by Vertical Barriers. Journal of Fluid Mechanics. 294, 155-180.

Falcão, A.F.D.O., 2010. Wave Energy Utilization: A Review of the Technologies. Renewable and Sustainable Energy Reviews. 14(3), 899-918.

Faltinsen, O.M., 2006. Hydrodynamics of High-Speed Marine Vehicles.

He, F., Zhang, H., Zhao, J., Zheng, S., Iglesias, G., 2019. Hydrodynamic Performance of a Pile-Supported OWC Breakwater: An Analytical Study. Applied Ocean Research. 88, 326-340.

Li Y. C., Teng B. Wave action on marine structures [M]. Bei-jing, China: China Ocean Press, 2015 (in Chinese).

Melikoglu, M., 2018. Current Status and Future of Ocean Energy Sources: A Global Review. Ocean Engineering. 148, 563-573.

Mustapa, M.A., Yaakob, O.B., Ahmed, Y.M., Rheem, C.K., Koh, K.K., Adnan, F.A., 2017. Wave Energy Device and Breakwater Integration: A Review. Renewable and Sustainable Energy Reviews. 77, 43-58.

Ning, D., Zhao, X., Göteman, M., Kang, H., 2016. Hydrodynamic Performance of a Pile-Restrained WEC-type Floating Breakwater: An Experimental Study. Renewable Energy. 95, 531-541.

Niu, E.Z., Ma, D.T., Sun, S.C., 2003. The Novel Comb-Type Breakwater. China Civil Engineering Journal. 36(10), 51-56.

Ohkusu, M., 1969. On the Heaving Motion of Two Circular Cylinders On the Surface of a Fluid.

Pérez-Collazo, C., Greaves, D., Iglesias, G., 2015. A Review of Combined Wave and Offshore Wind Energy. Renewable and Sustainable Energy Reviews. 42, 141-153.

Porter, R., Evans, D.V., 1996. Wave Scattering by Periodic Arrays of Breakwaters. Wave Motion. 23(2), 95-120.

Saadat, Y., Fernandez, N., Ghorbani, R., 2013. The Wave Energy Converter Based On Helmholtz Mode, Inspired by Nature. ASME 2013 32nd International Conference on Ocean, Offshore and Arctic Engineering, OMAE 2013, Nantes.

Saadat, Y., Fernandez, N., Samimi, A., Alam, M.R., Shakeri, M., Ghorbani, R., 2016. Investigating of Helmholtz Wave Energy Converter. Renewable Energy. 87, 67-76.

Sarkar, D., Renzi, E., Dias, F., 2015. Effect of a Straight Coast On the Hydrodynamics and Performance of the Oscillating Wave Surge Converter. Ocean Engineering. 105, 25-32.

Wang, X., Liu, Y., Liang, B., 2018. Analysis of Oblique Wave Interaction with a Comb-Type Caisson Breakwater. Journal of Ocean University of China. 17(2), 281-290.

Wang, X., Liu, Y., Lu, L., 2019. Analytical Solution of Oblique Wave Interacting with a Periodic Array of Specific Caissons Connected with Partially Immersed Thin Walls (Comb-Type). Ocean Engineering. 186, 106107.

Zang, Z., Fang, Z., Zhang, N., 2018. Flow Mechanism of Impulsive Wave Forces and Improvement On Hydrodynamic Performance of a Comb-Type Breakwater. Coastal Engineering. 133, 142-158.

Zhang, H., Zhou, B., Vogel, C., Willden, R., Zang, J., Geng, J., 2020. Hydrodynamic Performance of a Dual-Floater Hybrid System Combining a Floating Breakwater and an Oscillating-Buoy Type Wave Energy Converter. Applied Energy. 259

Zhang, H., Zhou, B., Vogel, C., Willden, R., Zang, J., Zhang, L., 2020. Hydrodynamic Performance of a Floating Breakwater as an Oscillating-Buoy Type Wave Energy Converter. Applied Energy. 257

Zhao, X., Ning, D., Zhang, C., Kang, H., 2017. Hydrodynamic Investigation of an Oscillating Buoy Wave Energy Converter Integrated into a Pile-Restrained Floating Breakwater. Energies. 10(5)

Zhao, X.L., Ning, D.Z., Zou, Q.P., Qiao, D.S., Cai, S.Q., 2019. Hybrid Floating breakwater-WEC System: A Review. Ocean Engineering. 186, 106126.

8th International Conference on the Application of Physical Modelling in Coastal and Port Engineering and Science
Dec. 9th - 12th, 2020, Zhoushan, China

TWO-DIMENSIONAL SIMULATION OF WATER AND SEDIMENT DYNAMICS ON THE YANGTZE RIVER ESTUARY

Zhao Hui-Ming(1), Zhang Yue-Feng(2), Tang Li-Qun(1), Wang Chong-Hao(1), Guo Chuan-Sheng(1), Liu Da-Bin(1), Feng Hao-Chuan(1), Wang Yu-hai(1) & Lu Jing(1)

(1) State Key Laboratory of Simulation and Regulation of River Basin Water Cycle, China Institute of Water Resources and Hydropower Research, Beijing 100048, China,
e-mail: zhaohuiming045@163.com

(2) Development Research Center of the Ministry of Water Resources of P. R. China, Beijing 100038, China,
e-mail: zhangyf513@163.com

ABSTRACT

With the economic development of estuarine and coastal areas, beach reclamation project has become the main reason for the change of coastline contour, which further affects the flood control pattern and the safety and stability of seawall. In this paper, regarding the Yangtze River Estuary and Hangzhou Bay as an organic whole, a two-dimensional mathematical model is established to study the influence of beach utilization on flood control and tide control focusing on the Yangtze River Estuary, which could simulate the movement of water and sediment and water exchange of the Yangtze River Estuary. The research scope covers the water areas from Jiangyin to the Yangtze River Estuary and Hangzhou Bay. Based on the existing research results and historical measured data, the tide level and tidal current of the established model are verified by the terrain data and synchronous hydrological observation data in 2012. The results show that the mathematical model is reasonable for boundary treatment and roughness selection, which can better reflect the dynamic characteristics of water and sediment in the Yangtze River Estuary, and can be used for the simulation study of the impact of beach use on flood control and tide control.

Keywords: two-dimensional mathematical model, water and sediment dynamics, the Yangtze River Estuary

1 INTRODUCTION

In recent decades, high-intensity beach development has changed the dynamic geomorphic pattern of channel and floodplain in estuaries and coasts, resulting in many problems such as coastal ecology, resources and environment, flood and tide disasters and economic and social problems (Auerbach et al., 2015; Maren, 2016). It is of great significance to establish a large-scale mathematical model of water and sediment in typical estuaries, to simulate the law of water and sediment movement and the trend of erosion and deposition in the corresponding estuary, and to carry out the research on the influence of beach utilization on flood control and tide control (Komar, 1998; McNeil& Lick, 2004; Foerstner, 2014). In this paper, regarding the Yangtze River Estuary and Hangzhou Bay as an organic whole, a two-dimensional mathematical model is established to simulate the dynamic characteristics of water and sediment and water exchange of the Yangtze River Estuary. The model is verified by the existing measured data. The results show that the mathematical model better reflect the movement of water and sediment on the Yangtze River Estuary, and can be used for the simulation study of the impact of beach use on flood control and tide control.

2 THE BASIC THEORY OF THE MODEL

2.1 Flow control equation

The flow equation of the model is Reynolds vertical average Navier-Stokes equation for incompressible fluid based on Boussinesq assumption and hydrostatic pressure assumption.

$$\frac{\partial h}{\partial t}+\frac{\partial h\bar{u}}{\partial x}+\frac{\partial h\bar{v}}{\partial y}=hS \qquad [1]$$

b. Momentum Equation in x direction

$$\frac{\partial h\bar{u}}{\partial t}+\frac{\partial h\bar{u}^2}{\partial x}+\frac{\partial h\bar{u}\bar{v}}{\partial y}=f\bar{v}h-gh\frac{\partial \eta}{\partial x}-\frac{h}{\rho_0}\frac{\partial p_a}{\partial x}-\frac{gh^2}{2\rho_0}\frac{\partial \rho}{\partial x}+\frac{\tau_{sx}}{\rho_0} \qquad [2]$$
$$-\frac{\tau_{bx}}{\rho_0}-\frac{1}{\rho_0}\left(\frac{\partial s_{xx}}{\partial x}+\frac{\partial s_{xy}}{\partial y}\right)+\frac{\partial}{\partial x}(hT_{xx})+\frac{\partial}{\partial y}(hT_{xy})+hu_sS$$

c. Momentum Equation in y direction

$$\frac{\partial h\overline{v}}{\partial t}+\frac{\partial h\overline{u}\overline{v}}{\partial x}+\frac{\partial h\overline{v}^2}{\partial y}=-f\overline{u}h-gh\frac{\partial \eta}{\partial y}-\frac{h}{\rho_0}\frac{\partial p_a}{\partial y}-\frac{gh^2}{2\rho_0}\frac{\partial \rho}{\partial y}+\frac{\tau_{sy}}{\rho_0} \quad [3]$$
$$-\frac{\tau_{by}}{\rho_0}-\frac{1}{\rho_0}(\frac{\partial s_{yx}}{\partial x}+\frac{\partial s_{yy}}{\partial y})+\frac{\partial}{\partial x}(hT_{xy})+\frac{\partial}{\partial y}(hT_{yy})+hv_sS$$

where, x, y are Cartesian coordinates; t is time; η is water level; d is still water depth; $h=\eta+d$ is total water depth; u and v are velocity components in x and y directions respectively; f is Coriolis force coefficient, $f=2\omega\sin\varphi$, ω is earth rotation velocity, φ is local latitude; g is gravitational acceleration; ρ is water density; s_{xx}, s_{xy} and s_{yy} are radiation stress components; S is source term; (u_s, v_s) is flow velocity of source term.

2.2 Sediment motion equation

The sediment transport process is also a convection-diffusion problem of mass conservation, which can be described by convection-diffusion equation:

$$\frac{\partial \overline{c}}{\partial t}+\overline{u}\frac{\partial \overline{c}}{\partial x}+\overline{v}\frac{\partial \overline{c}}{\partial y}= \quad [4]$$
$$\frac{1}{h}\frac{\partial}{\partial x}(hD_x\frac{\partial \overline{c}}{\partial x})+\frac{1}{h}\frac{\partial}{\partial y}(hD_y\frac{\partial \overline{c}}{\partial y})+\frac{1}{h}Q_LC_L-S_b$$

where, c is vertical average sediment concentration (kg/m^3); D_x and D_y are diffusion coefficient of sediment (m^2/s); Q_L is source flow per unit horizontal area (m^3/s/m^2); C_L is sediment concentration of source term (kg/m^3); S_b is increase of sediment concentration or erosion of bed surface (kg/m^3/s).

3 MODEL BUILDING

3.1 Calculation range

Taking the Yangtze River Estuary and Hangzhou Bay as an organic whole, a two-dimensional hydrodynamic mathematical model is established to reflect the hydrodynamic characteristics and water exchange of the Yangtze River Estuary. The calculation range of the model includes the water area from Jiangyin to the Yangtze River Estuary and Hangzhou Bay, namely the upper boundary is Jiangyin, the east boundary is 123°00'E, the south boundary is near Xiangshan Port, i.e. 29°45'N, and he northern boundary is in the north of lvsi Port, i.e. 32°15'N. The calculation range is shown in Figure 1.

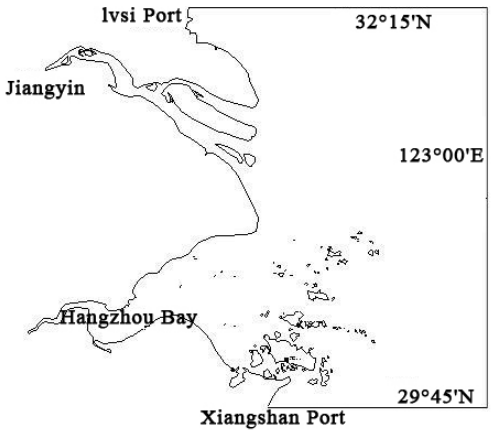

Figure 1. Schematic diagram of calculation range

The Heading 1 should be set in 10pt “Arial” boldface, with a leading (interline spacing) of 10pt and a single spacing of respectively, before and after.

3.2 Calculation conditions

(1) Topographic data

Within the calculation range, the topographic data from Jiangyin to the Yangtze Estuary and Hangzhou Bay consists of six parts:

Topography of Chengtong reach of the Yangtze River: 1:10000 topographic map (National 85 elevation) measured by Yangtze Estuary Bureau of Hydrology and Water Resources measured in 2001 is adopted.

Topography of the South Branch and the South-North-Channel of the Yangtze River Estuary: 1:25000 measured topographic map (National 85 elevation) in 2002 is adopted.

Topography of the South-North-Passage: 1:60000 underwater topographic map (theoretical lowest tide level) measured in February 2002 is adopted.

Topography of the North Branch: 1:25000 underwater topographic map (National 85 elevation) measured in November 2001 is adopted.

Topography outside the Yangtze River Estuary: 1:250000 nautical chart from Ivsi Port to Huaniao Mountain (No. 13100, theoretical lowest tide level) is adopted, which is compiled by the Navigation Assurance Department of the Navy Command of the people's Liberation Army of China in 1994.

Topography of Hangzhou Bay and Zhoushan Islands: 1:250000 nautical chart of Zhoushan Islands and its vicinity in the East China Sea (No. 13300, theoretical lowest tide level) is adopted, which is compiled by the Navigation Assurance Department of the Navy Command of the people's Liberation Army of China in December 1999.

The elevation base of the Yangtze Estuary and Hangzhou Bay is complex. Here the national 85 elevation base is adopted for the calculation. The topographic map of the calculated water area after unifying the elevation base is shown in Figure 2.

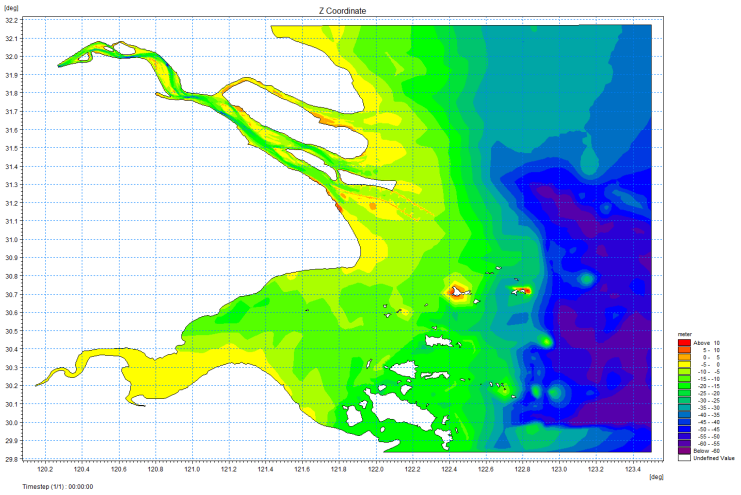

Figure 2. The underwater topographic map of the calculated water area

(2) Hydrological verification condition

According to the data, the water level and flow velocity from September 22 to 30, 2002 are selected as the hydrological data for model verification. There are 16 verification sections of water level and 15 verification points of velocity and sediment concentration in September 2002 (Figure 3).

(3) Boundary condition

The discharge process of Jiangyin section in the same period is used as the upper boundary of the model uses, as shown in Figure 4.

The harmonic constants of 11 tidal components of Q1、O1、P1、K1、N2、M2、S2、K4、M4、MS4、M6 at 13 stations (the location is shown in Figure 3) calculated by the ocean model of Hehai University have been determined, and the change process of tide level at the outer boundary from September 20 to 30, 2002 is shown in Figure 5. The tide level process of the outer boundary is obtained by the tide level interpolation of these stations.

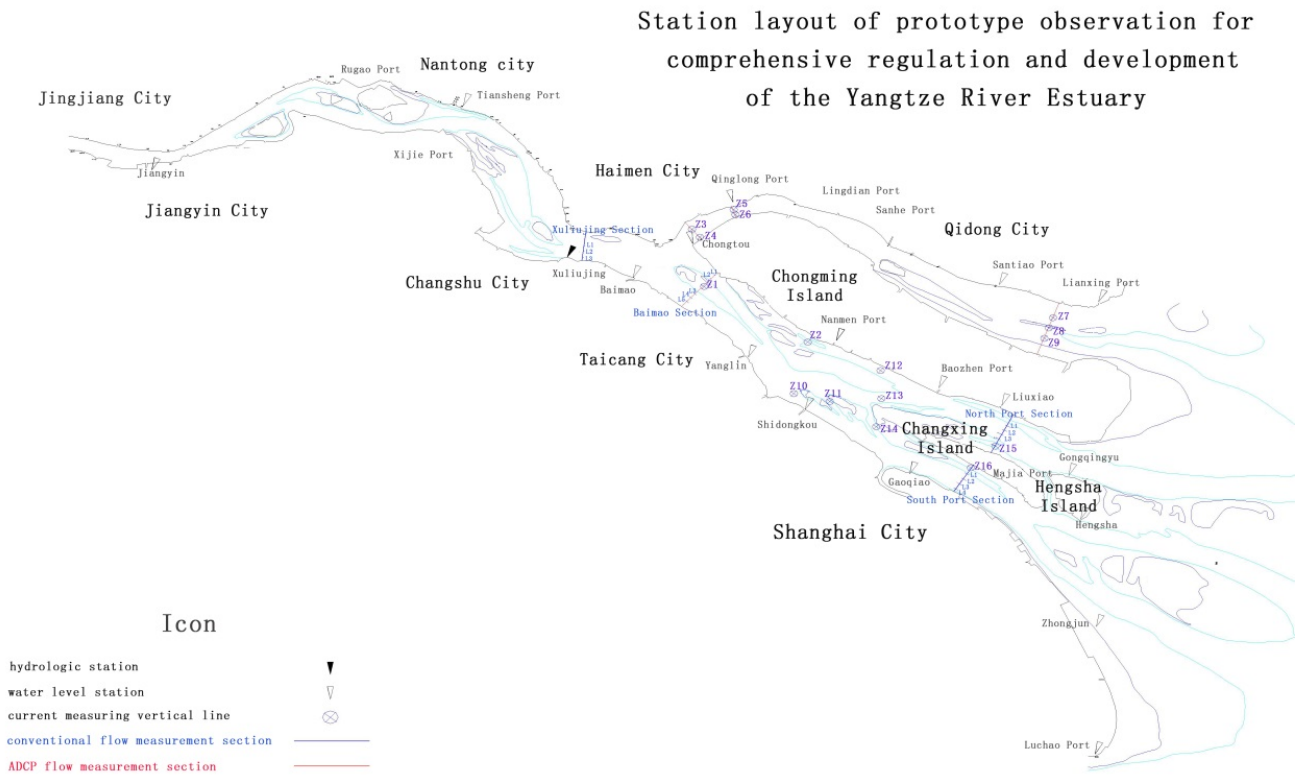

Figure 3. Schematic diagram of survey stations at the Yangtze River Estuary

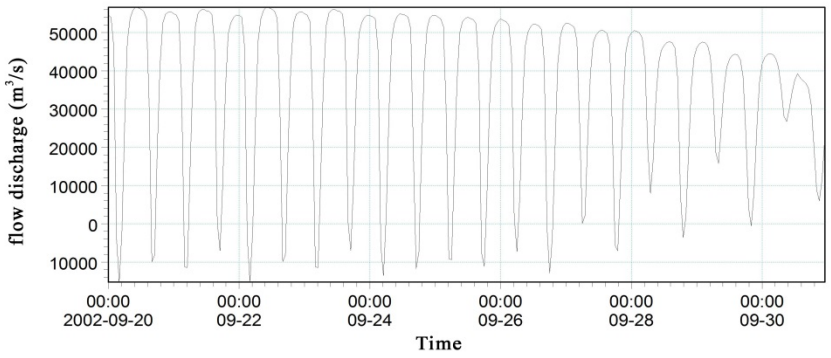

Figure 4. The flow process of the entrance boundary at Jiangyin

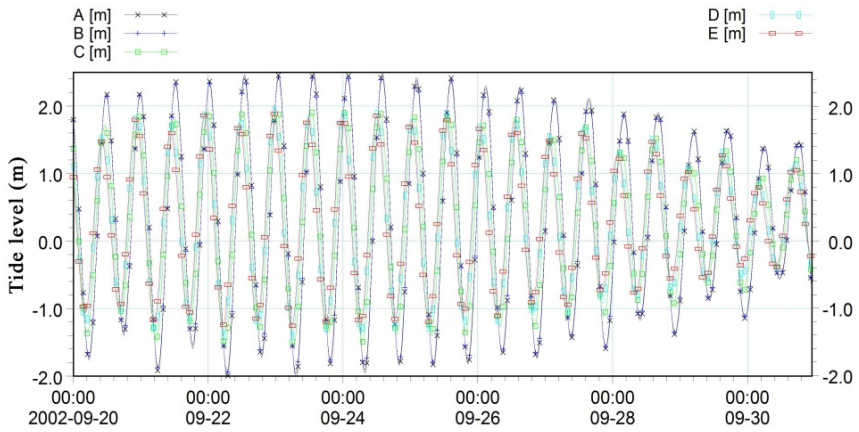

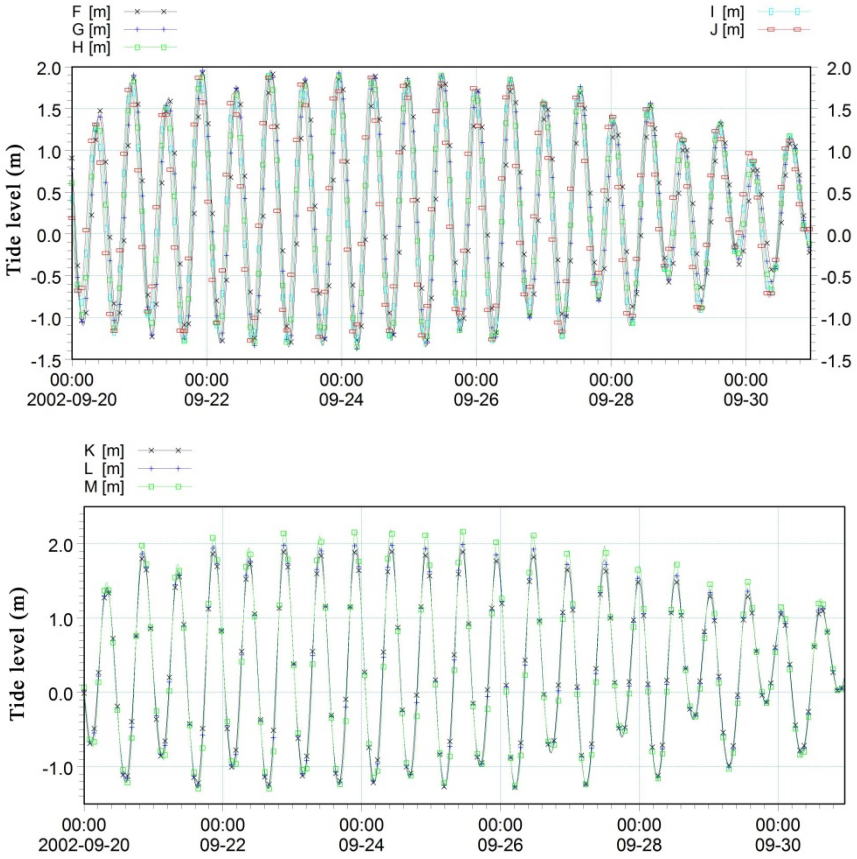

Figure 5. Tide level process of outer boundary control station

3.3 Calculation scheme

The calculation area is divided into 1508600 calculation units. There are 826200 calculation nodes in total, of which, there are 397942 water nodes, accounting for 48.17%.

The simulation period is 11 days from September 20 to 30, 2002. The time step is 30 seconds, and the Courant number is 2.77.

Boundary condition: The upper boundary is the flow discharge process of Jiangyin section, as shown in Figure 4. The outer sea boundary is obtained by the tide level interpolation of the 13 stations with known harmonic constants, as shown in Figure 5.

Dynamic boundary treatment of dry and wet discrimination method: Water depth less than 0.2m is considered as dry unit, and wet unit with water depth greater than 0.3m.

Eddy viscosity coefficient is calculated by Smagorinsky formula.

Manning resistance coefficient $n = 0.02 - 0.012$.

Wave and wind effects are not considered here.

4 MODEL VERIFICATION

4.1 Tide level verification

The tide level verification of four representative stations (Xuliujing, Chongtou, Luchaogang and Qinglonggang) is shown in Figure 6-Figure 9. The calculation results show that the calculated water level of each station is consistent with the measured value in a large range of the Yangtze River Estuary. The calculation of tide level from Xuliujing to Luchaogang in the reach of the South Branch is in good agreement with the actual measurement. The tide level of each station in the South Branch is generally consistent with the calculation, but the tidal range is small in spring tide, and the difference is slightly big at Luchaogang. The reason may be related to the terrain base, grid size and roughness. Lianxinggang in the North Branch is in good agreement. Chongtou Station is in good agreement in neap tide, and the tidal range is small in spring tide, existing the same problem as the South Branch, which shows that tide level at Chongtou is mainly affected by the South Branch. the verification of tide level at Qinglonggang is a little poor, the calculated values of tidal range and tidal time are both a little different from the measured values. The analysis shows that the main reason is that the river section has been silted up and shrunk in recent years, the water depth is

small, and the grid is not dense enough, resulting in the calculation results not completely consistent with the measured values.

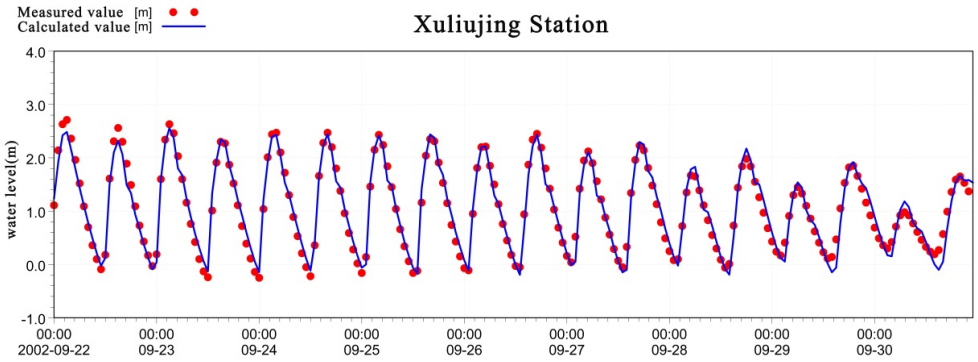

Figure 6. Verification of tide level process at Xuliujing Station

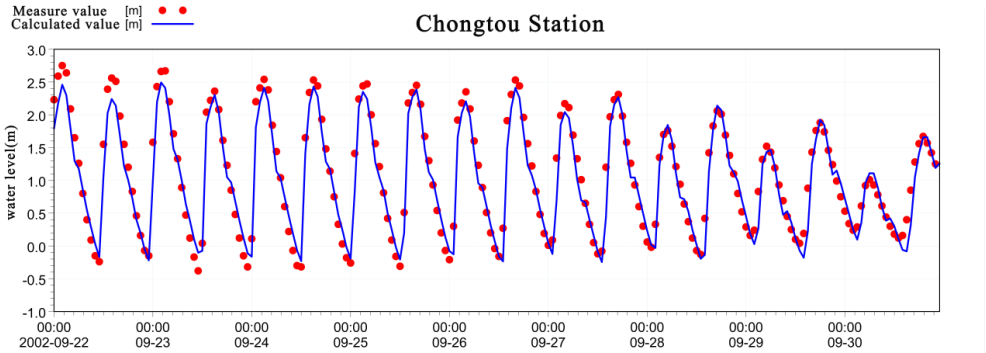

Figure 7. Verification of tide level process at Chongtou Station

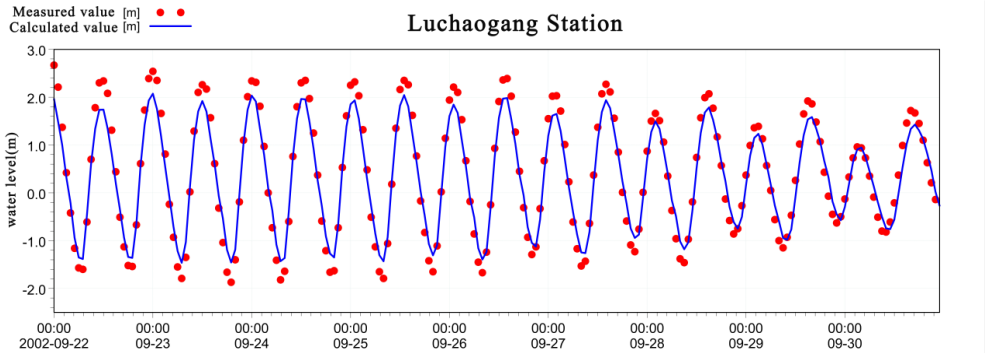

Figure 8. Verification of tide level process at Luchaogang Station

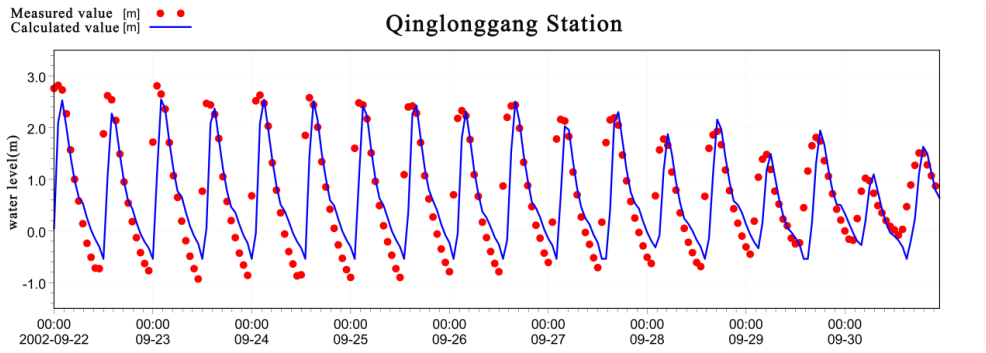

Figure 9. Verification of tide level process at Qinglonggang station

4.2 Tidal current verification

As there is no 9 day continuous data of the water period for the measured flow velocity and flow direction, and only some discontinuous data of the corresponding spring, middle and neap tides, the comparison is also conducted separately based on spring, middle and neap tides. The comparison between the calculation and measurement of flow velocity and flow direction at three representative vertical measuring lines (B2, Z3, Z14) are shown in Figure 10-Figure 12.

The flow direction calculated in the figure is specified as follows: 0° to the north, 90° to the east, 180° to the south and 270° to the west, clockwise rotation. Therefore, in the North and South Branch River section, the ebb current is about 120° and the flood current is about 300°. So the flow direction in the figure is about 120° during ebb tide and about 300° during flood tide.

The verification results of flow velocity and flow direction show that: Generally speaking, the calculated values of each representative velocity and flow direction are in good agreement with the measured values, and the calculated values of flow velocity and flow direction of individual stations are different from the measured values. In the Baimao section of the upper reach of the South Branch, the calculated velocity of the vertical line at B2 is larger, but the flow direction is in good agreement, which reflects the complexity of river regime in this reach. The flow in the north side of Baimaosha is affected not only by the upstream runoff and tidal current, but also by the back flow of the North Branch, which indicates that a more precise calculation grid is needed to accurately simulate the flow pattern of the Yangtze River Estuary. The calculated velocity of the North and South Branch estuaries is basically the same as the measured value, and the flow direction is in good agreement, which shows that the model can well simulate the reciprocating flow of the ebb and flood current at the North and South Branch. Similarly, the vertical calculation results of Z14 are basically consistent with the measured values, which can be inferred that the model can better reflect the diversion ratio of the North and South Channel. Due to the small diversion of the North Branch, the outlet flow of the North Branch is mainly affected by the tide current, tracing up and down with the form of reciprocating flow, and the flow pattern is relatively simple, so the model simulated well the process of flow velocity and flow direction. Near Chongtou and Qinglonggang at the North Branch entrance, due to the extremely complex flow, the calculated velocity of Z3 vertical lines is obviously smaller than the measured value, but the flow direction is basically the same, which directly leads to the smaller calculated velocity of B2 Section. It can be said that the current terrain and model calculation results may cause the calculated diversion ratio of the North Branch to be smaller. On the one hand, the local flow conditions are complex, which affects the simulation accuracy; on the other hand, the terrain processing is not precise, the mesh size of the model is 300m, the section near Qinglonggang is very narrow, due to years of siltation and shrinkage, development of side shoals and shallow water depth, the number of grids is too small to accurately reflect the existence of the main channel, namely the terrain is flattened and the flow in and out is blocked. It also reminds of the necessity of using more refined grid or nested model to study the flow characteristics of the Yangtze River Estuary in depth. But on the whole, the mathematical model can simulate the flow characteristics of the Yangtze River Estuary well, and can get more real tide level and tidal process.

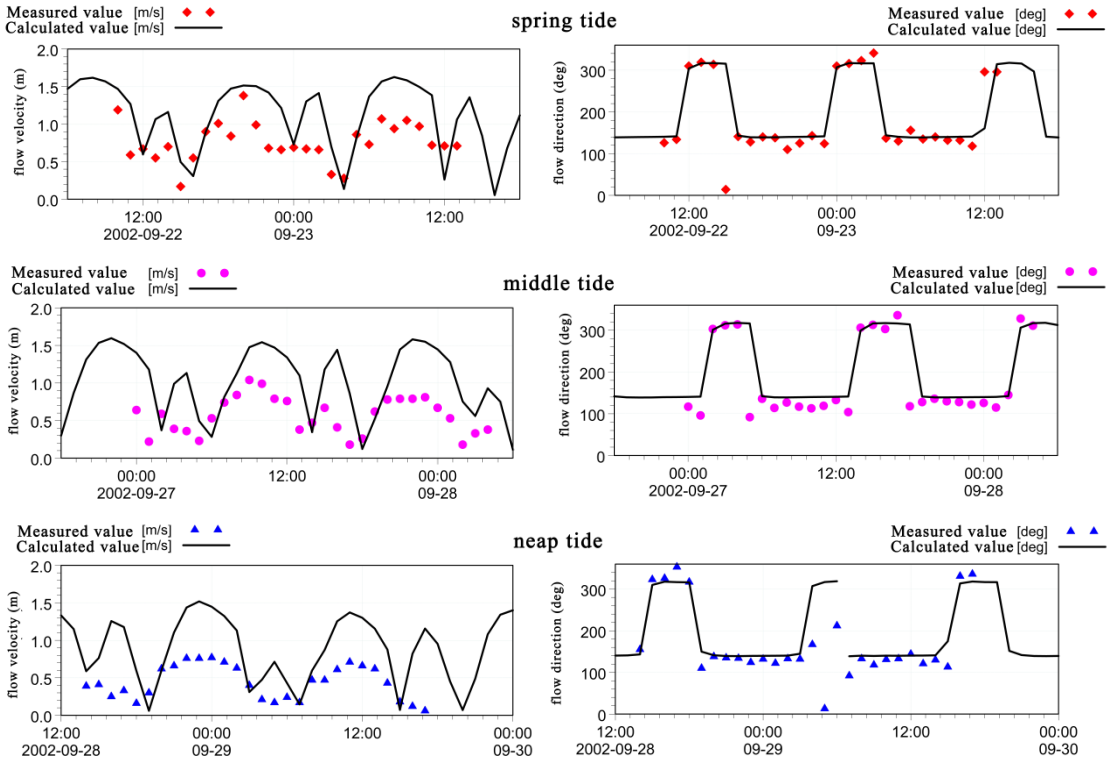

Figure 10. Verification of vertical average flow velocity and flow direction at B2

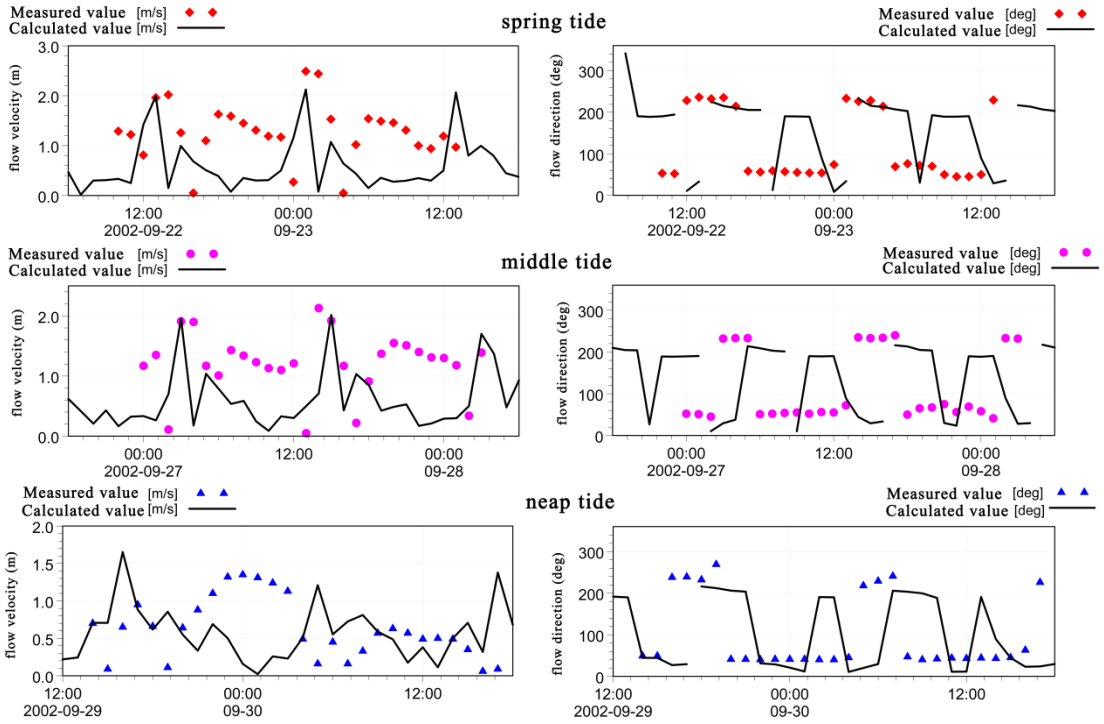

Figure 11. Verification of vertical average flow velocity and flow direction at Z3

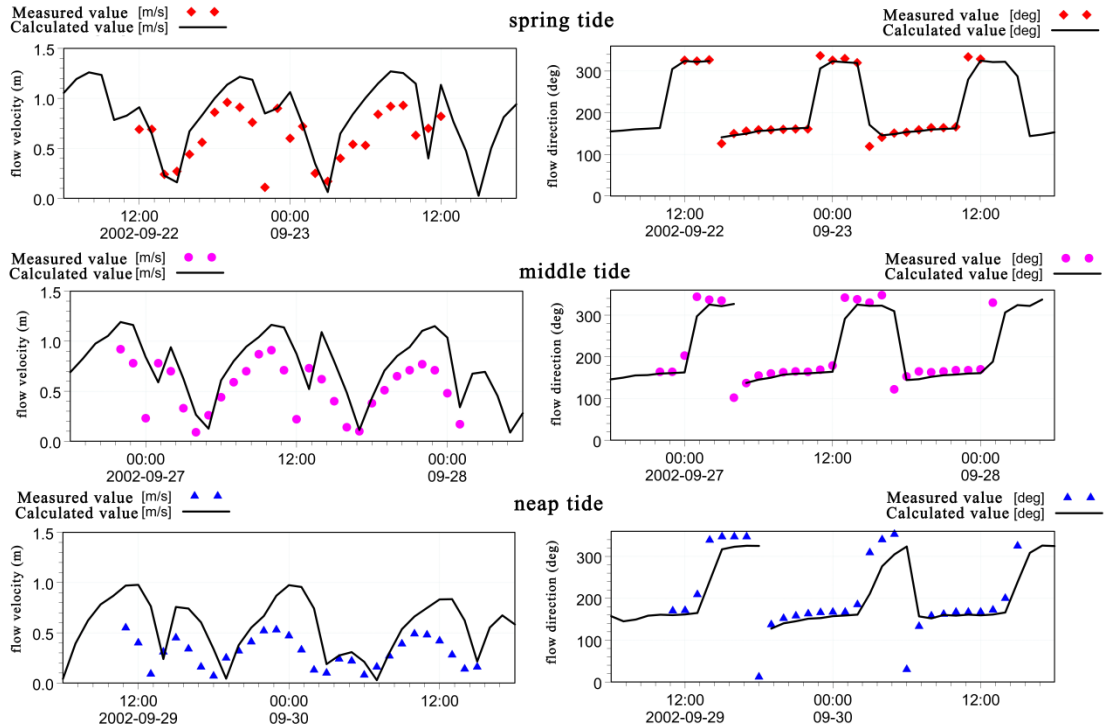

Figure 12. Verification of vertical average flow velocity and flow direction at Z14

4.3 Sediment concentration verification

The comparison between the calculation and measurement of sediment concentration at the three representative vertical measuring points (B2, Z3, Z14) are shown in Figure 13-Figure 15. Generally speaking, in the South Branch, South and North Channel, the fine sediment process calculated by this model is basically consistent with the actual situation, which better reflects the scouring and settling process of sediment particles in the different tidal processes of spring, middle and neap tide, and reflects the change of sediment concentration with the change of tidal current intensity. Near the bifurcation of the South and North Branch in the upper part of the North Branch, as Z5 vertical line, there is a big difference between the calculated and measured sediment concentration and the calculated value is obviously smaller. This is related to the complex

flow conditions in this reach. It is necessary to encrypt the computing grid, deal with the terrain data carefully, and make further and more detailed research.

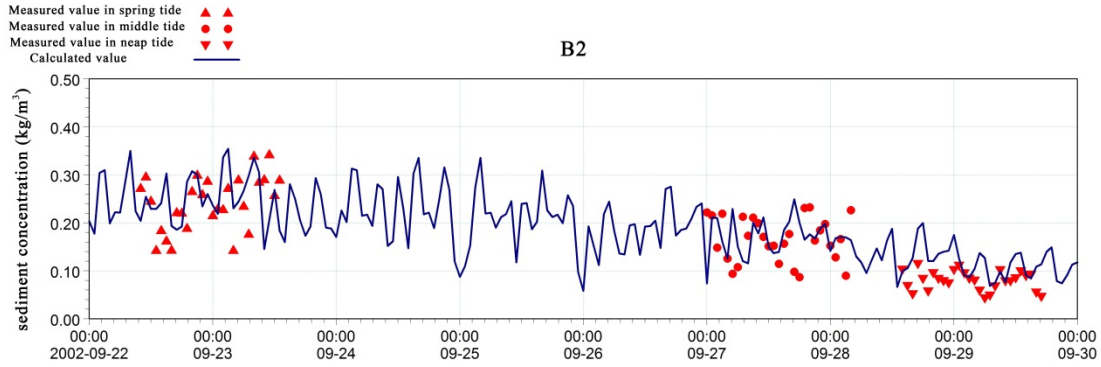

Figure 13. Verification of sediment concentration at B2

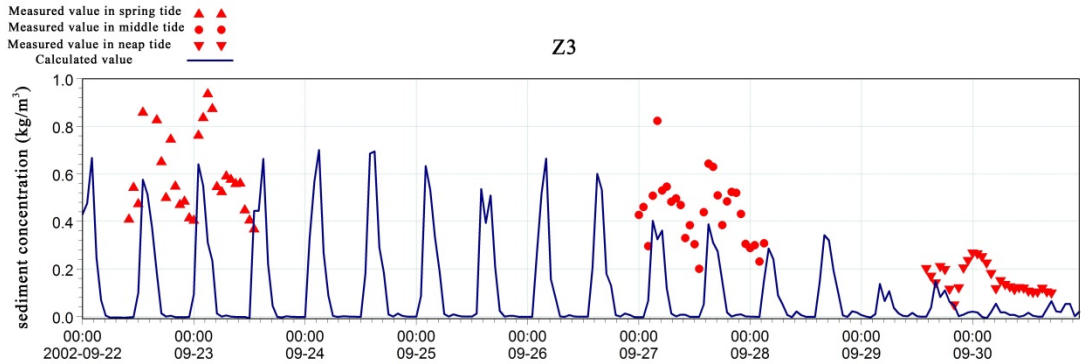

Figure 14. Verification of sediment concentration Z3

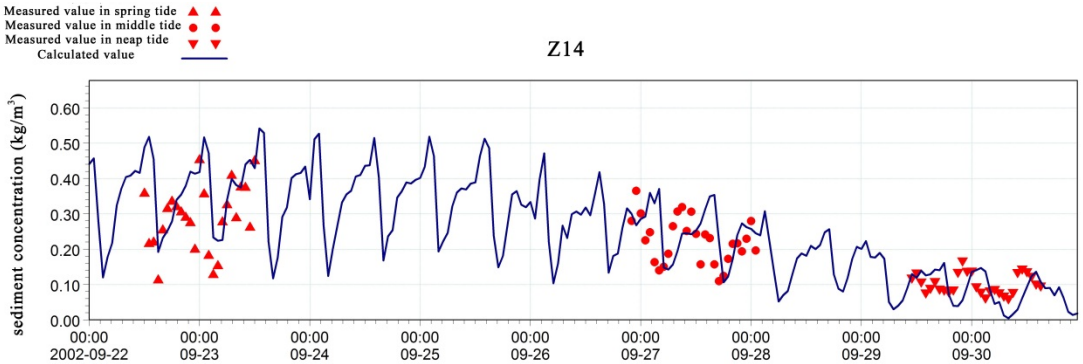

Figure 15. Verification of sediment concentration at Z14

5 CONCLUSIONS

In this paper, a two-dimensional mathematical model covering the water areas from Jiangyin to the Yangtze River Estuary and Hangzhou Bay has been established to simulate the dynamic characteristics of water and sediment and water exchange of the Yangtze River Estuary. The verifying results show that the calculated water level, flow velocity, flow direction and sediment concentration are consistent with the measured values in a large range of the Yangtze River Estuary on the whole, demonstrating that the established can better reflect the movement law of water and sediment on the Yangtze River Estuary. However, there are still some details to be improved, such as the computational grid needs to be further refined where the topography and flow is complex.

ACKNOWLEDGEMENTS

This work was supported by the National Key Research and Development Program of China (2018YFC0407503), IWHR Research&Development Support Program (SE0145B142017), Program for

Innovative Research Groups During 13th Five Year Plan Period of IWHR (No. NJBKYKY1785), the National Natural Science Foundation of China (No. 51479213).

REFERENCES

Auerbach, L.W., Goodbred, S.L., Jr.,Mondal, D.R., et al. (2015). Flood risk of natural andembanked landscapes on the Ganges-Brahmaputra tidal delta plain. *Nature Climate Change,* 5 (2), 153-157.

Foerstner U., Heise S., et al. (2014). Historical contaminated sediments and soils at the river basin scale. *Journal of Soils and Sediments,* 4, 247-260.

Komar PD. (1998). The mechanics of sand transport on beaches. *Journal of Geophysics Research,* 76 (3), 713-721.

McNeil J., Lick W. (2004). Erosion rates and bulk properties of sediments from the Kalamazoo River. *Journal of Great Lakes Research,* 30, 407-418.

van Maren, D.S., Oost, A.P., Wang, Z.B., et al. (2016). The effect of land reclamations and sediment extraction on the suspended sediment concentration in the Ems Estuary. *Marine Geology,* 376 (6), 147-157.

8th International Conference on the Application of Physical Modelling in Coastal and Port Engineering and Science
Dec. 9th - 12th, 2020, Zhoushan, China

NUMERICAL ANALYSIS OF THE INFLUENCE OF SEA LEVEL RISE ON SEDIMENT DEPOSITTION IN THE YELLOW RIVER ESTUARY

GUO CHUANSHENG(1); WANG CHONGHAO(2); TANG LIQUN(3); WANG YUHAI(4) & ZHAO HUIMING(5)

(1,2,3,4,5) State Key Laboratory of Simulation and Regulation of Water Cycle in River Basin,
China Institute of Water Resources and Hydropower Research, Beijing, P. R. China
guoliu1982@126.com; chwang@iwhr.com; liquntang@126.com; yhwang@iwhr.com; zhaohuiming045@163.com

ABSTRACT

To explore the influence of sea level rise on sediment deposition in the Yellow River Estuary, this article has simulated the change of flow velocity in Yellow River Channel in different situations of sea level rise with FVCOM and calculated the threshold motion velocity of sediment in main channel. The results show that as sea level rise, average velocities in the Yellow River Estuary increase. Average velocity increase by 12.66% at observation of C4. During the period of sea level rising, the suspended sediment diffusion played a significant role in the sediment transport. The largest turbidity zone in the north of Laizhou Bay moved eastward. In the nearshore zone, the suspended sediment increase in observation sites of C1, C2 and C3 with different situations of sea level rise.

Keywords: Suspended sediment transport; numerical model; level rise; Yellow River Estuary; sediment deposition

1 INTRODUCTION

The 5464 km-long Yellow River, originates from the Qinghai-Tibet Plateau and flows into the Bohai Sea, is the second longest river in China. The suspended sediment concentration (SSC) of The Yellow River is high, and the sediment injected into the sea is the main source of the bohai Sea geological deposition, which plays an important role in the development and evolution of the Yellow River delta (HBYRWCC, 2019). Therefore, the sediment problem in the Yellow River estuary has been concerned by many researchers in dometic and abroad.

The issue of sea level rise has a significant impact on estuaries. Sea level rise leads to increased nearshore wave and tidal energy, enhanced storm surge, aggravated coastal erosion and subshoal erosion, and increased the difficulty of repairing the eroded coast. From 1980 to 2019, China's coastal sea level rose at a rate of 3.4 mm/year. According to the latest results released by the intergovernmental Panel on Climate Change (IPCC), the World Meteorological Organization (WMO) and other international authorities, China's coastal sea level rise rate is higher than the other countries of the world (DMEWMMNR, 2020). Therefore, it is important to study the influence of suspended sediment at the mouth of Yellow River due to sea level rise.

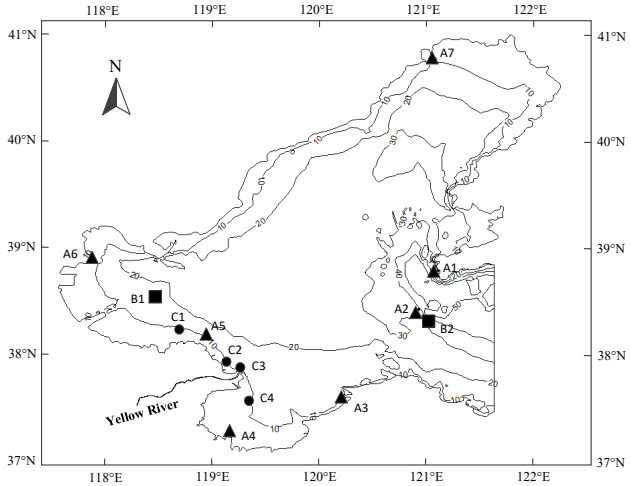

Figure 1. Sketch of study area and location of measurement stations.

Many of researches have been studied on sediment transport (Wang Hailong et al., 2009; Shi Hangxing, 2009) in bohai Sea from the Yellow River, and great progress has been made in the study of estuary tidal

current and sediment transport in the Yellow River by mathematical model. However, there are few studies on the influence of sea level rise on the Yellow River, and this article will research it by using numerical analysis.

2 STUDY AREA

The Yellow River estuary, located in the Bohai Sea, is a famous delta for its rapid erosion-deposition (Wang Kairong et al., 2004). The Yellow River has changed its course many times in history due to natural floods or human activities. In the past 150 years, the river has shifted its course more than 50 times. The channel of the Yellow River into the sea has been changed for many times due to flood, silt, tide, current and other reasons.

For example, in 1976, the estuary of the Yellow River was diverted from diaokou River to the Qingshuigou channel. In August 1996, the drainage channel was diverted from The drainage channel to Qing Shuigou channel. After 2008, a new drainage channel was created on the basis of the drainage channel.

3 NUMERICAL MOEDL

3.1 FVCOM numerical model

FVCOM tidal current and sediment model (Chen C. et al., 2006) is applied to establish the tidal current calculation model of the Yellow River estuary, which covers the whole Bohai Sea and the northern Part of the Yellow Sea, as shown in Figure 1. The model grid adopts the non-orthogonal triangular grid constructed by SMS, which is a good fit for the Yellow River port line. The grid in river channel area is encrypted with the grid step length of 20~1000m.

The boundary of the upper reaches of the Yellow River is located in Lijin, and the boundary condition is the measured flow and sediment concentration data of Lijin hydrological station. The tidal boundary provided by the T-TIDE model is adopted for the outer sea boundary.

3.2 Model Validation

The data of 7 tide levels, 3 flow rates and 4 sediment test stations measured on late August in 2018, were used as verification data. The locations of hydrological test stations are shown in Figure 1.

The verification results are shown in figure 2 to Figure 4. It can be seen from the figures that the tidal level, tidal current and sediment concentration calculated by the model are consistent with the measured values.

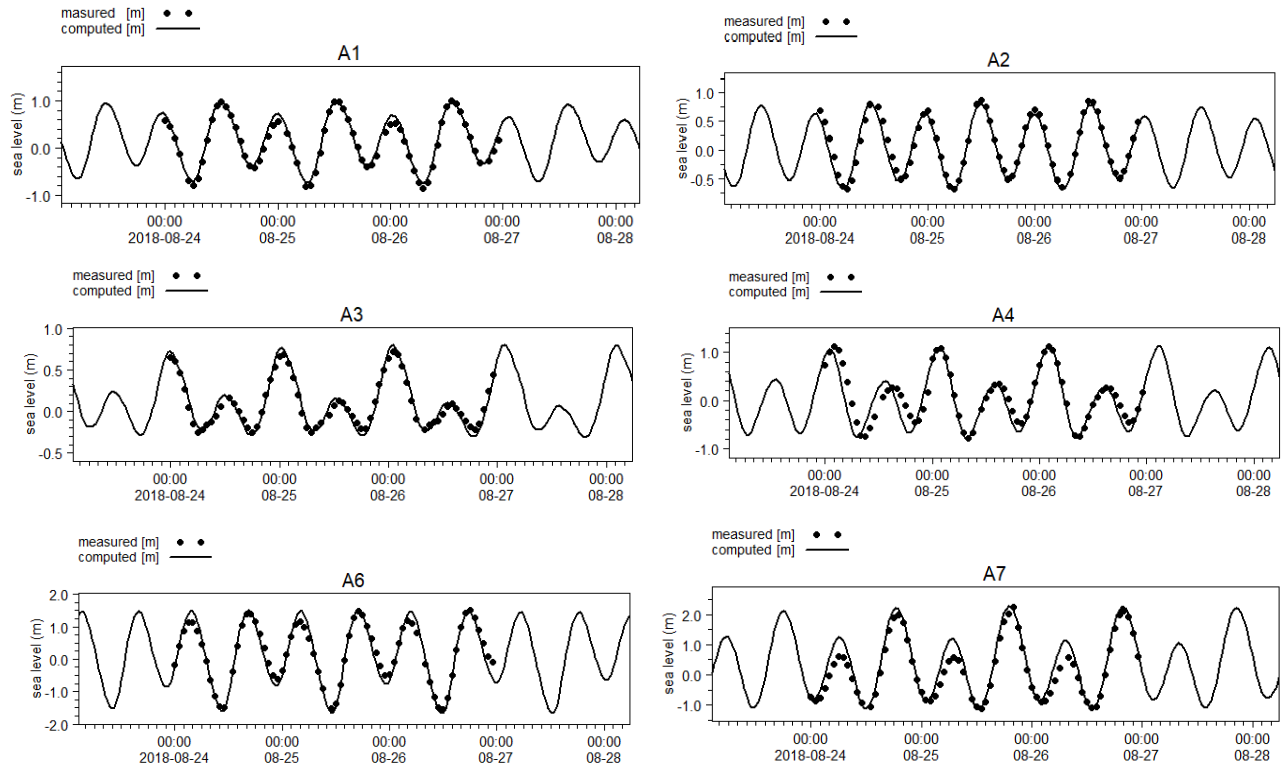

Figure 2. The verification of measured and computed sea level

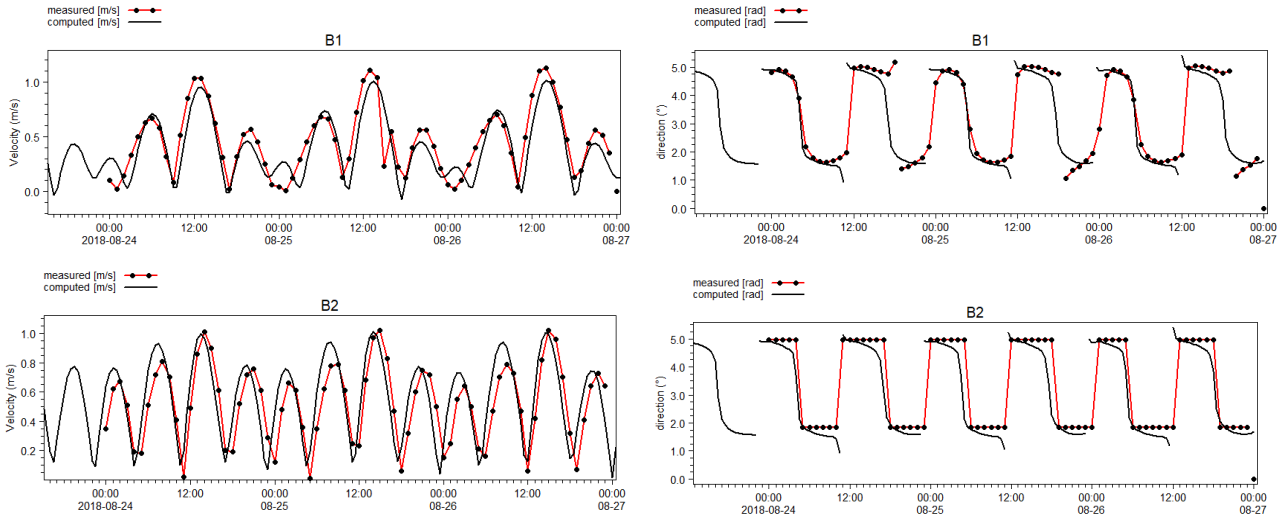

Figure 3. Comparison of velocity between simulation and observation

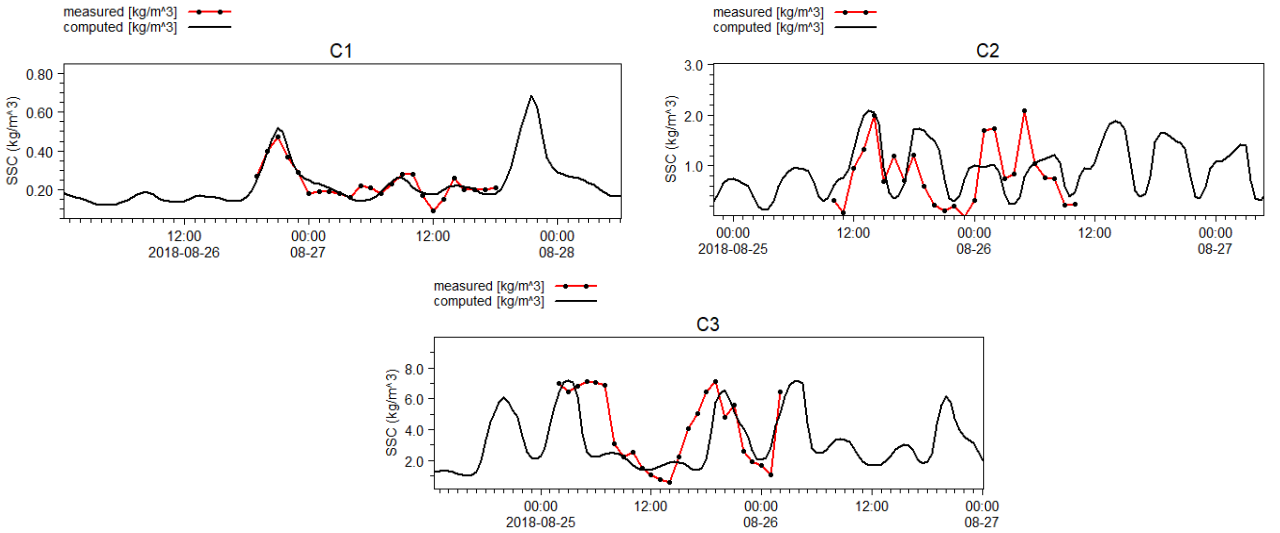

Figure 4. Comparison of suspended sediment concentration between simulation and observation

4 ANALYSIS OF CALCULATION RESULTS

To investigate the impact of sea level rise on suspended sand in the Yellow River Estuary, four sea-level rise schemes were selected and numerical simulation was carried out: no sea level rise, 0.30m sea level rise, 0.60m sea level rise and 1.0m sea level rise.

The calculation time of the model is consistent with that of the validation data, i.e., August 2018.

4.1 Influence of sea level rise on current speed

Table 1 shows the influence of different sea level rises on average velocity of measured stations. The current speed of C1 site increased with the sea level rise. When the sea level rose by 1m, the average flow rate increased from 0.536m/s to 0.566m/s, with an increase of 5.61%. The C2 site velocity increased with sea level rise. When sea level rose by 1m, the average velocity increased by 9.55%. The flow rate at C3 sites increased with sea level rise. When sea level rose by 1m, the average speed rate increased by 5.57%. The flow rate at C4 site increased with sea level rise. The average flow rate increased by 12.66% when sea level rise by 1m.

Table 1. Change of average velocity in observation in different situations of sea level rise

Site	Situation of sea level rise			
	0m	+0.3m	+0.6m	+1.0m
C1	0.536	0.546	0.557	0.566
C2	0.286	0.295	0.304	0.313
C3	0.515	0.527	0.538	0.544
C4	0.416	0.439	0.458	0.469

4.2 Influence of sea level rise on SSC

Figure 5 shows the sediment concentration distribution near the Yellow River Estuary. It can be seen that the sediment is mainly distributed near the Yellow River Estuary, and as far as the offshore distance is, the sediment concentration decreases sharply.

Before the sea level rise, the maximum SSC is distributed near the mouth of the Yellow River, which reflects that a large amount of sediment carried by the Yellow River first falls into silt near the mouth of the River, and some sediment is transported to the nearby zone such as Laizhou Bay along with the current.

The SSC in the south side of Yellow River Reservoir (Laizhou Bay) is higher than that in the north and east side. Figure 5b shows the distribution of SSC around the Yellow River Estuary by sea level rise of 1.0m. Due to the current sea level, the high sediment concentration area in the north of Laizhou Bay moves eastward after sea level rise, while the sediment concentration in the north of the Yellow River estuary increases.

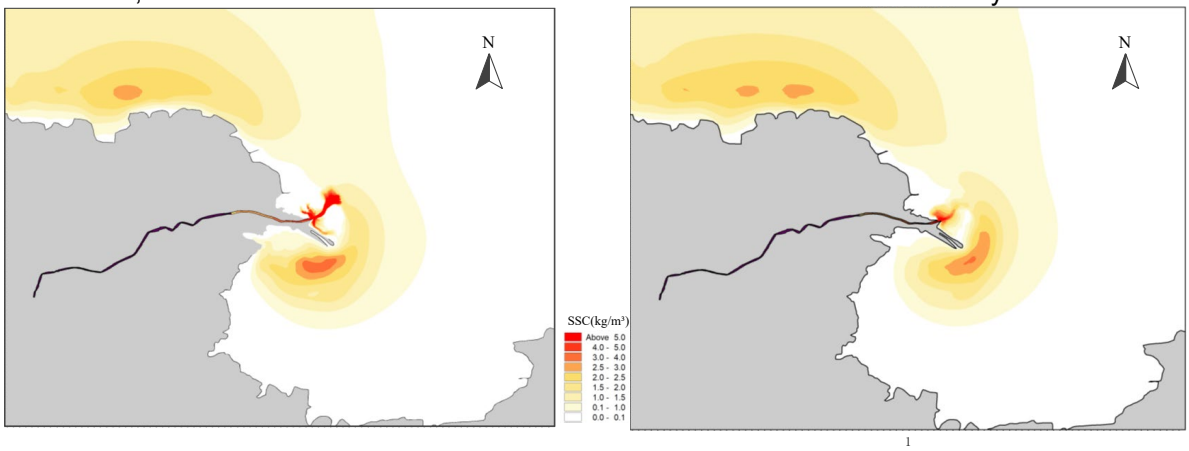

(a) Sea level rise 0.0m (b) Sea level rise 1.0m

Figure 5. Distribution of SSC in Yellow River Estuary

Figure 6 shows the influence of different sea level rise on the SSC at the observation stations. The SSC at C1, C2 and C3 sites increases with sea level rise. The suspended sediment concentration of site C4 increases slightly with the sea level rise, the maximum value of SSC appears at situation of the sea level rose by 0.3m.

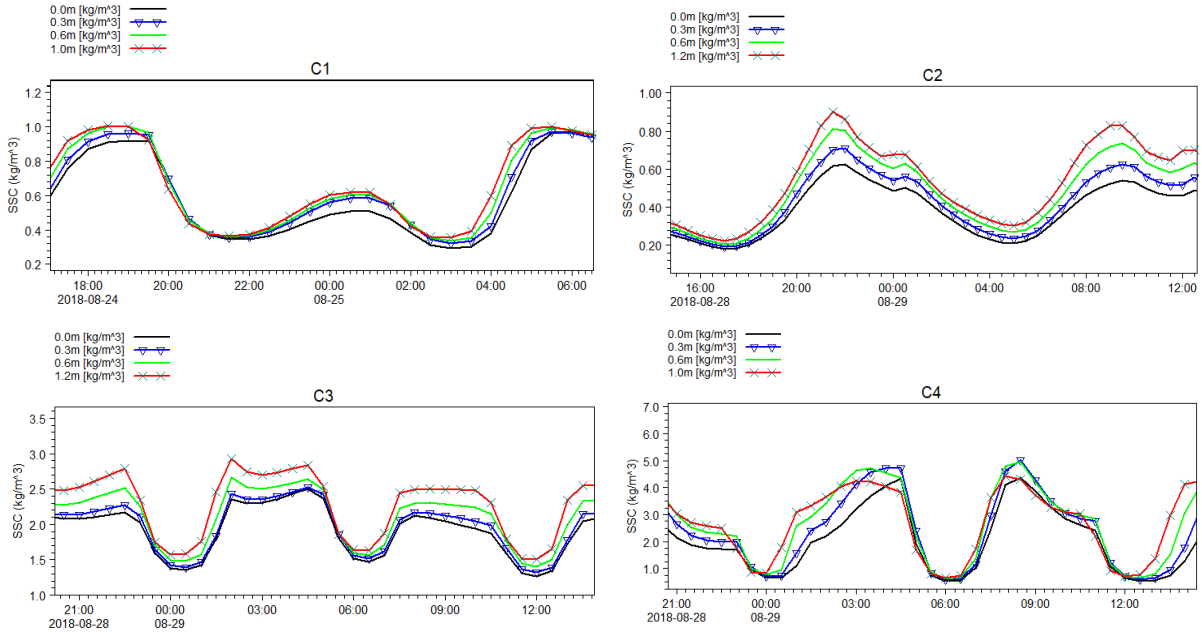

Figure 6. Change of SSC in observation sites in different situations of sea level rise (unit: kg/m³)

5 CONCLUSION

In this paper, the hydrodynamic and sediment coupling numerical model was established by FVCOM, and the model was verified by the measured data, and the sediment transport process of the Yellow River into the sea in August 2018 was simulated. Analysis shows that current speed and SSC changes at Yellow River Estuary. The current speed increases with the rise of sea level. After sea level rise, the largest turbidity zone in the north of Laizhou Bay moved eastward. The SSC of C1, C2 and C3 near the Yellow River estuary

increased with the sea level rise, while the sediment concentration at the C4 point did not change significantly before and after the sea level rise.

ACKNOWLEDGEMENTS

This research was supported financially by National Key Research and Development Program of China (2017YFC0405504) and IWHR Research & Development Support Program (SE0145B142017).

REFERENCES

Hydrological Bureau of Yellow River Water Conser-vancy Committee. (2019). *Yellow River sediment bulletin. Zhengzhou*. Yellow River Water Conser-vancy Committee, Book, Chapter1.

Department of Marine Early Warning and Monitoring Ministry of Natural Resources. (2020). *China Sea Level Bulletin*. China Oceanic Administration, Book, Chapter2.

Wang Hailong, LI Guosheng. (2009). Numerical simulation on seasonal transportation of suspended sediment from the Yellow River to Bohai Sea. *Oceanologiaet Limnolo-gia Sinica*, 40(2), 129-136.

Shi hangxing. 2009. Analysis of sediment dispersion of the Huanghe (Yellow) river mouth; a case of Diaokouhe Lobe. *Scientia Geographica Sinica*, 29(1), 83-88.

Wang Kairong, LI Ping, Zheng Chunmei. (2004). Regression analysis on sediment transportation-deposition pattern in Huanghe River Estuary. *Marine Sciences*, 28(12), 22-25.

Chen C, Beardsley R, Cowles G. (2006). An Unstructured Grid, Finite-Volume Coastal Ocean Model FVCOM User manual. Smast/Umassd, pp. 6-8.

8th International Conference on the Application of Physical Modelling in Coastal and Port Engineering and Science
Dec. 9th - 12th, 2020, Zhoushan, China

RHEOLOGY AND ITS MECHANISM OF CLAY SEDIMENT

YUAN LIN[1,2], HUAITAO QIN[1,2], JIN GUO[1,2], JIAWANG CHEN[1,2]

[1] Institute of Ocean Engineering and Technology, Ocean College, Zhejiang University, Zhoushan, China
[2] The Engineering Research Center of Oceanic Sensing Technology and Equipment, Ministry of Education, Zhoushan, China
arwang@zju.edu.cn

ABSTRACT

Clay sediments are the main component of the seabed sediment. The interactions between the nano-sized, disk-shaped and charged clay particles are complicated, which controls the flowing and the transportation criteria of the sediment. The rheological behavior of the clay sediment modeled by laponite-water (LW) mixtures is studied experimentally by a rotational rheometer. The yield stress of the LW system decreases with increasing water content. Meanwhile, the yield stress first increases and then decrease with increasing salinity. It is considered that the face-face repulsive electrostatic interaction between clay platelets dominates the yield behavior. A yield stress model is developed to describe the change of the yield stress with both the water content and the salinity. When the LW system starts to flow, the viscosity decreases with increasing shear. A master curve of viscosity is composed from the viscosity-stress curves at different water contents if the applied shear stress is normalized by the yield stress and the viscosity normalized by a characteristic viscosity. This study is to provide the basal understanding of the clay sediment rheology and its mechanism for the subsequent investigation on the transportation of the sediment systems with strong interparticle interaction.

Keywords: clay sediment; rheology; particle interaction.

1 INTRODUCTION

The deep-sea sediment is composed of sand, silt and clay, and the content of clay is commonly found to be more than 50% in, for example, South China Sea (Fuyuan Zhang et al., 2012). Due to the strong interaction between clay particles, the rheological properties of the sediment are determined by the clay sediment, which is a multiphase flow system composed of cohesive clay minerals (e.g., kaolinite, montmorillonite and illite) and water. Therefore, understanding the flowing behavior of the clay suspensions is important in the study of sediment transportation et al, where the viscosity and the yield stress are important factors. Clay particles are disk-shaped particles; their faces carry permanently negative charges, and their edges are positively charged in acidic condition, while negatively charged in alkaline condition. As a result, when suspended in water, clay platelets interact strongly with each other by a face-to-edge attractive electrostatic interaction or a face-to-face repulsive electrostatic interaction. Consequently, the clay sediment forms a gel with a card-house (face-edge) or a face-face microstructure, complicating the rheology behavior. (Lin et al., 2015; Paineau et al., 2011; Baird et al., 2007; Abou et al., 2003; Cocard et al., 2000; Pignon et al., 1998;). The system is solid at the static state (gel state) while becomes liquid (flowing state) that approaching a low viscosity when a shear stress larger than a yield stress is applied. At the gel state, Laxton et al. (2006) and Teh et al. (2009) studied the change of yield stress with pH for the clay system. Both groups observe a decreasing yield stress with increasing pH. The change of the yield stress is proportion to the square of the zeta potential of the system. Leong et al. (2012) find that the yield stress of the kaolinite suspension is changed by adding of citric acid and monophosphate. Sakairi et al. (2005) discover that the yield stress of the montmorillonite suspension decreases with increasing concentration of sodium chloride. Lin et al. (2015) find that yield stress of the kaolinite suspensions is strongly affected by the clay concentration and the microstructure changes with the concentration due to the packing effect. Also, the yield stress increases with increasing temperature (Lin et al., 2016). At the flowing state. Michot et al. (2008) find that the orientation of particles is affected by the electrostatic interactions between platelets, which is better for smaller particles and for lower ionic strength. For smectite and montmorillonite suspensions, Paineau et al. (2011) find particle alignment at high shear rates, which reduces the hydrodynamic drag, making the plateau viscosity at high shear rates insensitive to the clay concentration. Philippe et al. (2011) study the shear-thinning behavior of montmorillonite and beidellite suspensions. Based on the knowledge of the average orientation of the particles from the SAXS measurement, they are able to calculate the evolution of viscosity as a function of shear rate. Based on a master viscosity curve from the normalization of the applied shear stress by the yield stress of the system, Lin et al. (2019) developed a model for clay suspensions, indicating that electrostatic interaction, measured by the yield stress, also dominates at high shear rates.

At the current stage, the study on rheological behavior of clay suspensions is still insufficient. A rheological model for practical application, such as in the simulation of sediment transportation and erosion, is left to be developed. In this paper, we focus on the rheological behavior of an artificial laponite-water system to model the sea sediment. The yield stress of the system is studied as a function of the clay concentration, as well as the ionic strength (*IS*, or salinity), and the mechanism is proposed.

2 EXPERIMENT

A commercial laponite clay (BYK Additives & Instruments, UK) are used in the experiments. The clay suspensions are made by mixing the clay powder with deionized water. Samples are homogenized by an over-head stirrer for 60 mins at the rotation rate of 600 rpm. After mixing, samples are sealed and set for 24 hrs. The ionic strength (*IS*), or salinity is changed by the adding of NaCl powder. A DHR-1 rotational rheometer (TA Instrument, US) is used in the rheological measurement, with a 40 mm diameter cone-plate geometry. Both control-stress and control-shear-rate modes are adopted in the test. The temperature is kept at 25 ℃. A pre-shearing period of 30 s with the shear rate of 1000 s^{-1} is applied, after which the sample is rest for another 30 s before the former test is carried out. During the test of the laponite system, an obvious transition behavior can be observed (Lin et al., 2019), the duration of which is about 10 s. Therefore, in the ramp up (or step-up) test as shown in Figure 1, the shearing time in each step is set to 10 s in order to obtain the data at the equilibrium state. And the total time spent for one test to complete is about 12 mins, during which the influence caused by water evaporation is negligible.

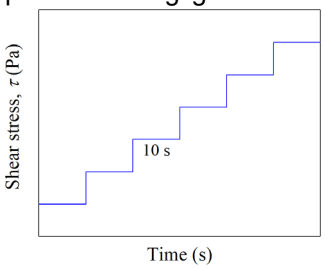

Figure 1. The ramp-up (step-up) shear test applied in the rheological experiment.

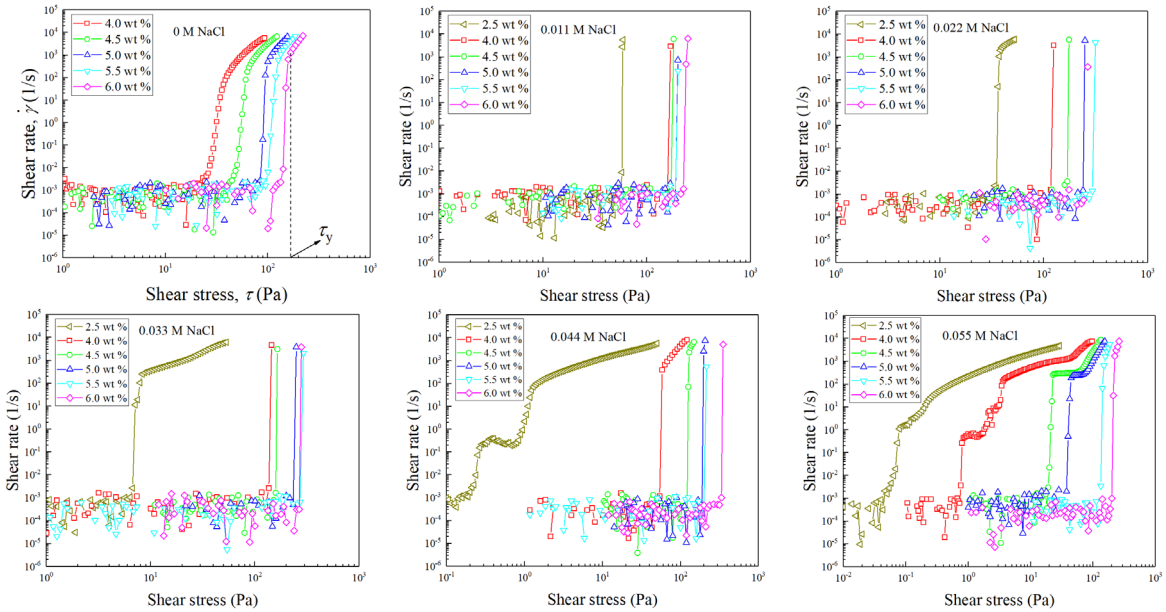

Figure 2. shear rate versus shear stress curves at different clay concentrations with the influence of ionic strength.

3 RESULT AND DISCUSSION

The shear rate curves as a function of shear stress using the stress-control mode is shown in Figure 2, from which the yield stress, τ_y, can be determined at the first point in the steady shear-rate curve after the shear rate increases significantly (e.g., several orders of magnitude), and the system starts to flow, as shown in Figure 2(a). Obviously, at all salinities (ionic strength), as shown in Fig.3(a), τ_y increases with clay concentration due to the decreasing of separation between clay platelets, which result in a higher electrostatic inter-particle force. As shown in Figure 2, the influence of the *IS* is also investigated. It is well accepted that τ_y should decreases with increasing *IS* due to the weakening of the electrostatic interaction. However, it is

observed from Figure 3(b) that, at a determined mass fraction, with increasing *IS*, τ_y first increases and then decreases above a critical *IS*. We consider the increment should be due to the local structure refinement. Since both face-to-face repulsive and face-to-edge attractive inter-particle interactions play roles in the gelation of the system (Lin et al., 2015), the increment of *IS* at the early stage may induce a local rearrangement of the structure for the ease of a single form of interaction, e.g., face-to-face repulsive interaction, by suppressing the face-to-edge interaction, and with further increase of *IS*, τ_y decreases due to the overall descending of the electrostatic potential.

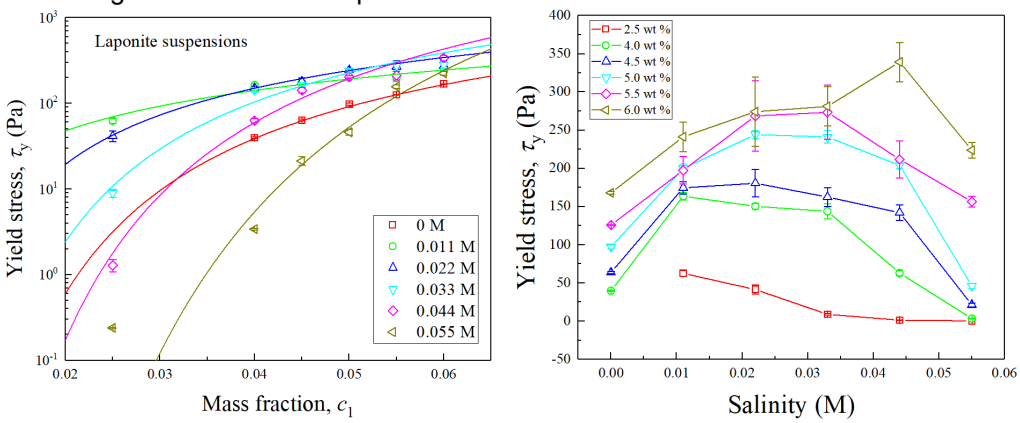

(a) (b)

Figure 3. Change of the yield stress as a function of clay concentration at different ionic strength with solid curves representing the fitting of the data using Eq.[4]; (b) change of the yield stress as a function of ionic strength at different clay concentrations.

Table 1. Parameters adopt for the fitting of experimental data in Figure 3.

NaCl concentration	0.011 M	0.022 M	0.033 M	0.044 M	0.055 M
B	7.03	26.96	55.46	88.04	173.25
$A\tau_0$	87.83	741.71	3617.37	16338.03	302752.7

The yield stress of the gel system may be estiamted as (Larson et al., 1999)

$$\tau_y \propto -\frac{\phi^2}{a^2} W'(D), \qquad [1]$$

and according to the DLVO theory,

$$W(D) = W_{\text{vdw}}(D) + W_{\text{e}}(D), \qquad [2]$$

where, *a* is the particle effective radius, *D* is the particle distance, and ϕ is the volume fraction of clay; $W_{\text{vdw}} = -aA_H/12D$ is the van de Waals potential with A_H the Hamaker constant; $W_{\text{e}} = 2\pi\varepsilon_r\varepsilon_0 a\psi_s^2 \ln[1-\exp(-\kappa D)]^{-1}$ is the electrostatic potential. ε_r and ε_0 are the permittivity of space and the dielectric constant of the medium, respectively. ψ_s is the surface electrostatic potential of clay particles and κ^{-1} is the Debye screen length, which decreases with increasing ionic strength. Consequently, the yield stress may be estimated as

$$\tau_y \propto -\frac{\phi^2}{a}\left(\frac{A_H}{12D_0^2} - \frac{2\pi\varepsilon_r\varepsilon_0\zeta^2\kappa}{e^{\kappa D_0}-1}\right). \qquad [3]$$

The above equation estimates the yield stress of the system considering the influence of clay concentration and ionic strength.

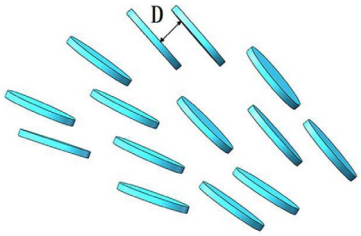

Figure 4. Diagram of the face-to-face structure by the face-to-face repulsive electrostatic interaction.

It is proposed that the face-to-face repulsive inter-particle interaction dominates, which results in a face-to-face structure, as shown in Figure 4. Therefore, the volume fraction can be related to the distance between clay platelets, $\phi \approx \delta/(\alpha D+\delta)$ and also the term from van de Waals interaction can be neglected (Lin et al., 2015), giving rise to

$$t_y = At_0 \frac{\left[\left(\frac{c}{r}\right)^{-1} + (1-r)^{-2}\right]}{\exp\left[\left(\frac{c}{r}\right)(c^{-1}-1)\right]-1}, \qquad [4]$$

where, $B = d/ak^{-1}$, and $t_0 = 2pe_0ey_s^2/ak^{-1}$ is a stress constant; A is a constant; c is the mass fraction of clay in the system; a is a correction factor of the volume fraction and ρ is the density of clay particles. At_0 and B are parameters to be determined through the fitting of the experimental data. As shown by the curve fitting using Eq.[4] shown in Figure 3(a), this theory well describes the change of yield stress as functions of both clay concentration and ionic strength. The value of At_0 and B are listed in Table 1, both of which increases with increasing IS. Since the two parameters are both linear with k, therefore increases with increasing IS.

As shown in Figure 5(a), a significant shear thinning of viscosity can be observed after yielding of the system, which is due to the deformation and disaggregation of the gel structure formed by clay platelets. The resistant force against the flow is induced by the interparticle interaction between clay platelets, e.g., face-to-edge attractive forces, which previously cause the gelation of the system at the static state. Therefore, it is proposed that $t \mu t_y$. We take the viscosity-stress curves at the natural salinity in Figure 5(a) for example, the stress is normalized by τ_y,, and the viscosity is also normalized by the corresponding characteristic viscosity, η_y at τ_y from the viscosity curves. As shown in Figure 5(b), a master curve of the normalized viscosity is achieved. Therefore, the viscosity of the system, $h \mu h_y$. It is noted that the characteristic viscosity, η_y, generally decreases with increasing mass fraction. It can be deduced that the plateau viscosity, η_∞, at high shear stress or rate (not shown in Figure 5(a) due to the up limitation of the shear rate of the rheometer) is proportion to η_y. Therefore, η_∞ also decreases with the mass fraction. For laponite suspensions with strong electrostatic inter-particle interaction at low salinity, the increasing concentration results in a more oriented structure at high shear rates due to the face-to-face repulsive interaction, thereby reducing the plateau viscosity.

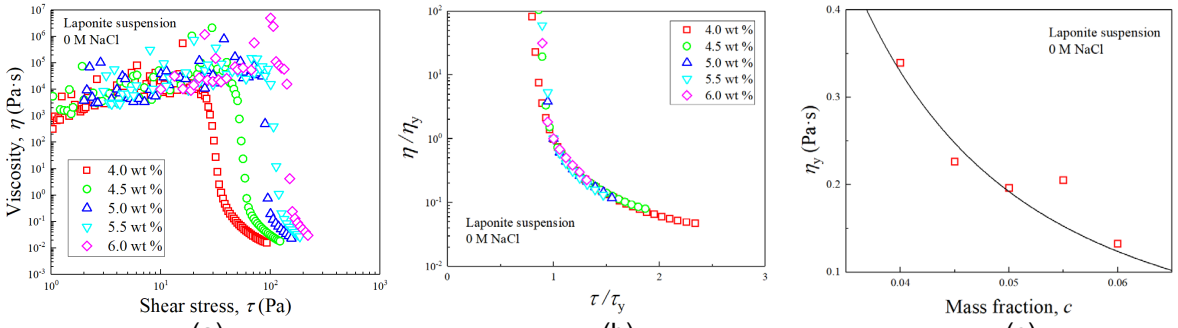

(a) (b) (c)

Figure 5. (a) Viscosity as a function of shear stress, (b) normalized viscosity as a function of normalized stress, and (c) change of the characteristic viscosity with mass frication of clay for laponite suspensions at the natural salinity with the solid line showing an empirical power-law curve fitting.

Obviously, the master curve in Figure 5(b) is independent of the clay concentration, and can be easily fitted by an empirical constitutive model such as Herschel-Bulkley model. This allows us to capture the non-Newtonian behavior of the LW system at different concentrations from the master curve, once the yield stress and the characteristic viscosity is known. As mentioned previously, τ_y can be estimated by Eq.[4]. And as shown in Figure 5(c), the evolution of η_y with the mass fraction can be approached by $h_y = 0.00014c^{-2.41}$.

4 CONCLUSION

The rheological behavior of artificial laponite-water suspensions is investigated at different clay concentration and salinity. It is found that the yield stress increases with increasing clay concentration due to the decrease of the distance between clay platelets which induces a larger electrostatic inter-particle force. Meanwhile, the yield stress first increases and then decrease with increasing salinity, which is proposed to be due to the local refinement of the structure. A master curve of viscosity can be obtained by normalizing the stress and viscosity by the yield stress and the corresponding viscosity at the yielding point, based on the viscosity curves at different clay concentration and salinity can be estimated once the yield stress and the characteristic viscosity is known.

ACKNOWLEDGEMENTS

This study is supported by the National Natural Science Foundation of China (NNSFC, No. 11702246), the Zhejiang Provincial Natural Science Foundation of China (Grant No. LY20A020008), and the Fundamental Research Funds for ZheJiang Provincial Colleges & Universities (No.2019XZZX003-07).

REFERENCES

Abou, B., Bonn, D. and Meunier, J. (2003). Nonlinear rheology of Laponite suspensions under an external drive, The Society of Rheology. *J. Rheol.*, 47(4), 979-988.

Baird, J.C. and Walz, J.Y. (2007). The effects of added nanoparticles on aqueous kaolinite suspensions: II. Rheological effects, Elsevier. *J. Colloid Interface Sci.*, 306(2), 411-420.

Cocard, S., Tassin, J.F. and Nicolai, T. (2000). *Dynamical mechanical properties of gelling colloidal disks*, The Society of Rheology. *J. Rheol.*, 44(3), 585-594.

Lin, Y., Zhu, H., Wang, W., Chen, J.W., Nhan, P.T. and Pan, D.Y. (2019). Rheological behavior for laponite and bentonite suspensions in shear flow. *AIP Advances*, 9(12), 125-233.

Lin, Y., Cheah, L.K.J., Nhan, P.T. and Khoo, B.C. (2016). Effect of temperature on rheological behavior of kaolinite and bentonite suspensions. *Colloids and Surfaces A: Physicochemical and Engineering Aspects*, 506, 1-5.

Lin, Y., Nhan, P.T., Lee, J.B.P. and Khoo, B.C. (2015). Concentration Dependence of Yield Stress and Dynamic Moduli of Kaolinite Suspensions. *Langmuir*, 31(16), 4791-4797.

Leong, Y.K., Teo, J., Teh, E., Smith, J., Widjaja, J., Lee, J.X., Fourie, A., Fahey, M. and Chen, R. (2012). Controlling attractive interparticle forces via small anionic and cationic additives in kaolin clay slurries, Elsevier. *Chem. Eng. Res. Des.*, 90(5), 658—666.

Laxton, P.B. and Berg, J.C. (2006). Relating clay yield stress to colloidal parameters, Elsevier. *J. Colloid Interface Sci.*, 296(2), 749-755.

Larson, R.G. (1999). The structure and rheology of complex fluids, *Oxford university press New York*.

Michot, L.J., Baravian, C., Bihannic, I., Maddi, S., Moyne, C., Duval, J.F., Levitz, P. and Davidson, P. (2009). Sol- Gel and Isotropic/Nematic Transitions in Aqueous Suspensions of Natural Nontronite Clay. Influence of Particle Anisotropy. 2. Gel Structure and Mechanical Properties, ACS Publications. *Langmuir*, 25(1), 127—139.

Philippe, A.M., Baravian, C., Imperor-Clerc, M., De, S.J., Paineau, E., Bihannic, I., Davidson, P., Meneau, F., Levitz, P. and Michot, L.J. (2011). Rheo-SAXS investigation of shear-thinning behaviour of very anisometric repulsive disc-like clay suspensions. *J Phys Condens Matter*, 23(19), 194112.

Paineau, E., Michot, L.J., Bihannic, I. and Baravian, C. (2011). Aqueous suspensions of natural swelling clay minerals. 2. Rheological characterization, ACS Publications. *Langmuir*, 27(12), 7806-7819.

Pignon, F., Magnin, A. and Piau, J.M. (1998). Thixotropic behavior of clay dispersions: combinations of scattering and rheometric techniques, The Society of Rheology. *J. Rheol.*, 42(6), 1349-1373.

Sakairi, N., Kobayashi, M. and Adachi, Y. (2005). Effects of salt concentration on the yield stress of sodium montmorillonite suspension, Elsevier. *J. Colloid Interface Sci.*, 283(1), 245—250.

Teh, E., Leong, Y.K., Liu, Y., Fourie, A.B. and Fahey, M. (2009). Differences in the rheology and surface chemistry of kaolin clay slurries: the source of the variations, Elsevier. *Chem. Eng. Sci.*, 64(17), 3817—3825.

Zhang, F.Y., Zhang, W.Y., Zhang, X.Y., Feng, X.L., Lin, L., Zhu, K.C., Chen, K.Y., Meng, Y. and Feng, X.W. (2012). Key Technique and Scheme of Classification and Nomenclature for Deep Sea Sediments. *Earth Scinence-Journal of China University of Geoscinences*, 37(1), 93-104.

8th International Conference on the Application of Physical Modelling in Coastal and Port Engineering and Science
Dec. 9th - 12th, 2020, Zhoushan, China

A STUDY ON THE APPLICATION OF WASTE GLASS SAND AND ALKALI-ACTIVATED SLAG MORTAR TO MARINE ENGINEERING STRUCTURAL MATERIALS

CHUN-LING HO [1],KAI-LIN HSU [2], HER-YUNG WANG [3]&YU-WEN CHEN [4]

[1]College of Civil Engineering, Huaqiao University, Intelligence and Automation in Construction Fujian ProvinceHigher-educational Engineering Research Centre,Xiamen, China
holling0712@gmail.com
[2] Department of Construction Engineering, National Kaohsiung University of Science and Technology, Kaohsiung City, Taiwan, ROC
vichsu@nkust.edu.tw,
[3,4] Department of Civil Engineering, National Kaohsiung University of Science and Technology, Kaohsiung City, Taiwan, ROC
wangho@nkust.edu.tw;F107141103@nkust.edu.tw

ABSTRACT

As the world advocates sustainable and cyclic development, recycling of industrial byproducts has been extensively adopted, such as slag powder and waste LCD glass sand. The disposal and recycling of waste can be solved, and the policy objective for the sustainable development of resources can be implemented. Moreover, Taiwan is located in the subtropical zone and surrounded by the sea. Coastal structures are prone to corrosion due to the intrusion of marine salt. The development of marine engineering structure materials in Taiwan should be the direction of vigorous development. This study applies industrial by-products to marine engineering structures Exploration of materials. Waste LCD glass sand is combined with alkali-activated cementitious paste as the main material of mortar specimens, and different liquid-solid ratios (L/S=0.45, 0.50, 0.55 and 0.60) are used. The base equivalent is fixed at 1%, and slag powder is replaced by glass sand (0, 20 and 40%). The fresh properties (slump, slump flow and setting time), hardened properties (compressive strength and ultrasonic pulse velocity) and durability (thermal conductivity and sulfate resistance) are determined after aging for 3, 7 and 28 days.
The results show that as the glass sand replacement level increases, the workability becomes better, the slump is increased by 11.6%~39.4%, the slump flow is increased by 19.5%~51.2%, the initial and final setting times are increased by 7.9~79.4% and 25.8~53.3%, respectively, the compressive strength is increased by 2.53%~180.73%, the ultrasonic pulse velocity is increased by 59.8%~101.2%, the thermal conductivity is 0.8769~1.1873 W/m*K and the sulfate resistance is good, thereby indicating that waste LCD glass sand has good engineering properties.

Keywords: waste LCD glass sand; alkali-activated cementitious paste; compressive strength; Marine engineering

1 INTRODUCTION

With the rapid development of industry and high-tech industry, industrial waste is an inevitable product of the present society. In 2016, Taiwan produced approximately 20 million MT business waste with the industry accounting for the largest proportion, followed by the construction industry, and slag and waste LCD glass are common waste products. As environmental considerations increase, it is necessary to design green products using the concepts of energy savings, carbon reduction and 4R (reduce, reuse, recycle, and replace) (Lin,2009) . Alkali-activated material is made by using alkaline solutions (sodium silicate solution and sodium hydroxide solution) to activate industrial waste (e.g., slag and fly ash). Alkali-activated material is a green energy material used to replace cement and has excellent engineering properties such as a high compressive strength, low weight, good thermal insulation properties, good erosion resistance and quick hardening in comparison to general cement material.If it can be applied to large-span structures, high-rise buildings and maritime engineering have broad application prospects.

Waste LCD glass contains much silicon and calcium, and its properties are similar to those of natural sand. In addition to its good particle shape, high hardness, good water permeability and good durability, waste LCD glass has excellent fire prevention, heat insulation and sound insulation characteristics (Xiao,2014). Extensive attention has been paid worldwide to the excellent chemical resistance, thermal performance and stability of industrial waste. As a polymer, precursor and activator, recycled waste glass in the preparation of alkali-

activated material seems to be a feasible way to efficiently use waste and to reduce the cost of alkali-activated material. Waste glass is recycled as an aggregate, precursor and activator.

Waste glass is used as the activator in alkali-activated slag mortar. The mixed liquor of $NaOH/Na_2CO_3$ and glass as an activator can increase the compressive strength (Wang et al.,2017; Puertas et al.,2014). The addition of waste glass to fine aggregates can enhance the workability, thermal conductivity and sulfate resistance. Using waste glass in alkali-activated material is feasible from the perspectives of the mechanical properties and fire resistance. The alkali-activated mortar prepared using glass powder as a precursor shows a significant fire resistance (Lu et al.,2019; Wang et al.,2016). Using glass powder and glass cullet in alkali-activated mortar for nonbearing partitions is feasible (Lu et al.,2018). Based on the aforementioned material characteristics, the disposal and recycling of waste can be solved, and the policy objective for the sustainable development of resources can be implemented.

The air temperature rises annually due to global warming, and conventional normal-weight concrete materials have different heat-insulating properties. Therefore, future objectives are to enhance the heat-insulating properties of concrete material and to improve the energy efficiency. In the present heat insulation engineering, the heat-insulating properties of heat-insulating materials are noni deal; a portion of the material cannot be recycled, and the natural environment is severely polluted (Chen,2014;Hung,2009;Wang et al.,2009). Common thermal insulating materials include bricks, ceramics, glass and lightweight aggregates. Light expanded clay aggregates are a type of lightweight aggregate, and the material is porous with a light unit weight that is applicable to structural and nonstructural engineering. In addition, the material has a low thermal conductivity and is often used for making lightweight masonry bricks and lightweight floor slabs or rooftops to improve the thermal insulating properties of buildings, thereby saving energy (Tsai,2014).

2 Experimental program

2.1 Experimental material

(a) Slag powder: The ground granulated blast furnace slag is from CHC Resources Corporation, and its properties meet the CNS12549 standards; the specific gravity is 2.89, the fineness is 4000 cm^2/g, its physicochemical properties are shown in Table 1, and the slag powder appearance is shown in Figure 1 (a).

(b) Sodium silicate solution: The commercially available #3 solution is used, which is generally known as water glass and is a viscous, colorless and tasteless liquid.

(c) Sodium hydroxide solution: Commercially available 98% pure caustic soda is used that is mixed with distilled water into a 5 M sodium hydroxide solution, which is encapsulated in a clean acid- and alkali-resistant barrel. As the reaction process releases much heat, the solution is stored for 24 h before use.

(d) Waste LCD glass sand: The waste LCD glass sand is ground in the dry state by a crusher and ball mill using 50 zirconia balls with Ø=10 mm, a speed of 400 rpm, one forward (backward) rotation every 5 min, and a milling time of 30 min into fine LCD glass sand with a homogeneous particle size; the specific gravity of the glass sand is 2.42, the fineness is 3850 cm2/g, the physicochemical properties are shown in Table 1 and the appearance is shown in Figure 1 (b).

(e) Natural sand: The aggregates are from Ligang district, and the natural sand is passed through a #8 sieve, while the specific gravity is 2.63. The water absorption is 0.80%, and its appearance is shown in Figure 1 (c).

(a) Slag powder	(b) Waste LCD glass sand	(c) Natural sand

Figure 1. Experimental material.

Table 1. Physical and chemical properties of the materials.

Materials	Slag	Water glass	NaOH	LCD glass
Physical properties				
Specific gravity	2.89	41.89	2.13	2.42
Water absorption (%)	—	—	—	0.45
Chemical contents (%)				
SiO_2	33.57	29.43	—	64.28
Al_2O_3	14.71	—	—	16.67
Fe_2O_3	0.36	0.01	—	9.41
CaO	41.18	—	—	2.70
MgO	6.42	—	—	0.20
SO_3	0.57	—	—	—
K_2O	0.29	—	—	1.37
Na_2O	0.19	9.51	—	0.64
TiO_2	0.52	—	—	0.01
P_2O_5	0.01	—	—	0.01
L.O.I	0.58	—	—	—
NaOH	—	—	98.2	—
$NaCO_3$	—	—	0.165	—
NaCl	—	—	0.0135	—
Fe	—	—	0.0004	—

2.2 Experimental material

Different liquid-solid ratios (L/S-s) of 0.45, 0.50, 0.55 and 0.60 are used, but the base equivalent is fixed at 1%; slag powder is replaced by glass sand by weight, and different levels of glass sand replacement (G) of 0%, 20% and 40% are used to determine the fresh properties (slump, slump flow and setting time). A 5 cm×5 cm×5 cm cubic specimen is prepared, and the hardened properties (compressive strength and ultrasonic pulse velocity) and durability (thermal conductivity and sulfate attack) are tested after aging for 3, 7 and 28 days. The mortar mix proportions are shown in Table 2.

Table 2. Physical and chemical properties of the materials.

L/S	N	Replace(%)	Slag	Water glass	NaOH	LCD glass
0.45	1	0	754	267	72	-
		20	603	267	72	151
		40	452	267	72	302
0.50	1	0	717	308	51	-
		20	573	308	51	143
		40	430	308	51	287
0.55	1	0	683	327	48	-
		20	547	327	48	137
		40	409	327	48	274
0.60	1	0	652	345	46	-
		20	522	345	46	130
		40	392	345	46	260

2.3 Experimental methods

(a) The fresh properties, slump and slump flow are determined according to ASTM D6103. The initial setting time is determined according to ASTM C403.
(b) The hardened properties and the compressive strength are determined according to ASTM C39, and the ultrasonic pulse velocity is determined according to ASTM C597.
(c) The durability and the sulfate resistance are tested according to ASTM C1012, and the thermal conductivity is tested according to ASTM E1225-13.

3 Results and Analysis

3.1 Slump

As shown in Figure 2, when L/S=0.50, the slump successively is 90 mm, 99 mm and 121 mm, and the replacement level of 40% is higher than that of the control group (0%) by 34.44%. When L/S=0.55, the slump is 105 mm, 123 mm and 135 mm, and the replacement level of 40% is higher than that of the control group (replacement 0%) by 28.57%. When L/S=0.60, the slump values are 125 mm, 138 mm and 142 mm, and the replacement level of 40% is higher than that of the control group by 13.60%. The slump increases with increasing glass sand replacement level and increases with increasing liquid to solid ratio. Because glass sand has repellent qualities, it may not have to completely be polymerized in the fresh state. Therefore, the mortar slump increases with increasing glass sand replacement level. In addition, when the liquid to solid ratio increases, the water content in the cementing material increases, and the workability of alkali-activated material is enhanced.

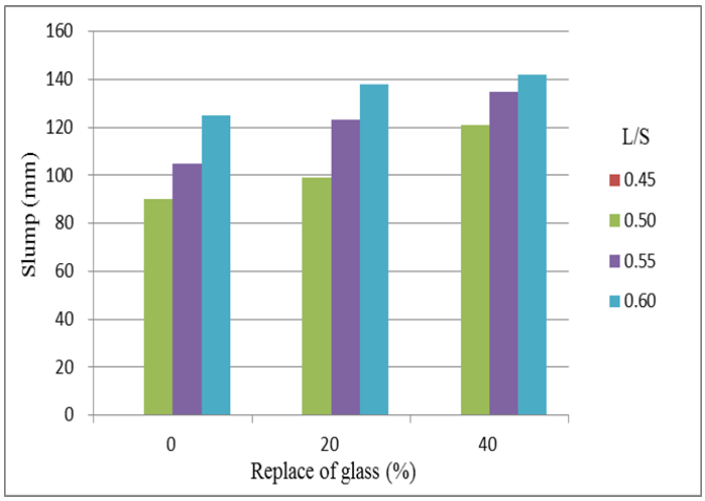

Figure 2. Slump of different liquid-solid ratios and glass sand alkali-activated mortar.

3.2 Slump flow

As shown in Figure 3, when the glass sand replacement is 0%, 20% and 40% and L/S is 0.50, 0.55 and 0.60, respectively, the slump flow of the three L/S levels of the control group is 121 mm, 177 mm and 246 mm, respectively; when the glass sand replacement level is 20% and 40%, the slump flow is 147 mm, 225 mm and 294 mm, respectively, and 183 mm, 248 mm and 327 mm, respectively. It is observed that the slump flow of the waste glass alkali-activated mortar material increases with increasing glass sand replacement level and liquid-solid ratio.

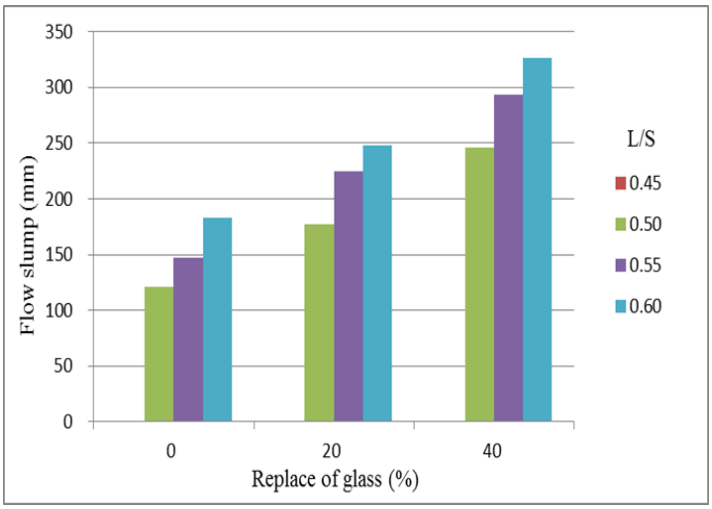

Figure 3. Slump flow of different liquid-solid ratios and glass sand alkali-activated mortar.

3.3 Setting time

As shown in Figure 4, when L/S=0.50 and the glass sand replacement level is 0%, the initial setting time and final setting time are 127 min and 362 min, respectively. When L/S=0.60 and the glass sand replacement level is 0%, the initial setting time and final setting time are 269 min and 549 min, respectively, indicating that when L/S increases from 0.50 to 0.60, the initial and final setting times increase by 111.81% and 51.66%, respectively, which means that the setting time increases as the liquid to solid ratio increases. When L/S=0.50 and the glass sand replacement level is 0%, the initial and final setting times are 127 min and 362 min, respectively, but when the glass sand replacement level is 20%, the initial and final setting times are 243 min

and 559 min, respectively; when the sand replacement is 40%, the initial and final setting times are 393 min and 68 min, respectively. The setting time increases as the glass sand replacement level increases, and the L/S=0.55 and L/S=0.60 mixtures exhibit the same trend. This phenomenon may be because glass sand is coarser than slag powder. When the glass sand replacement level increases, the overall fineness of the substrate containing silicon and aluminum decreases, the polymerization rate is low, and the setting time is prolonged.

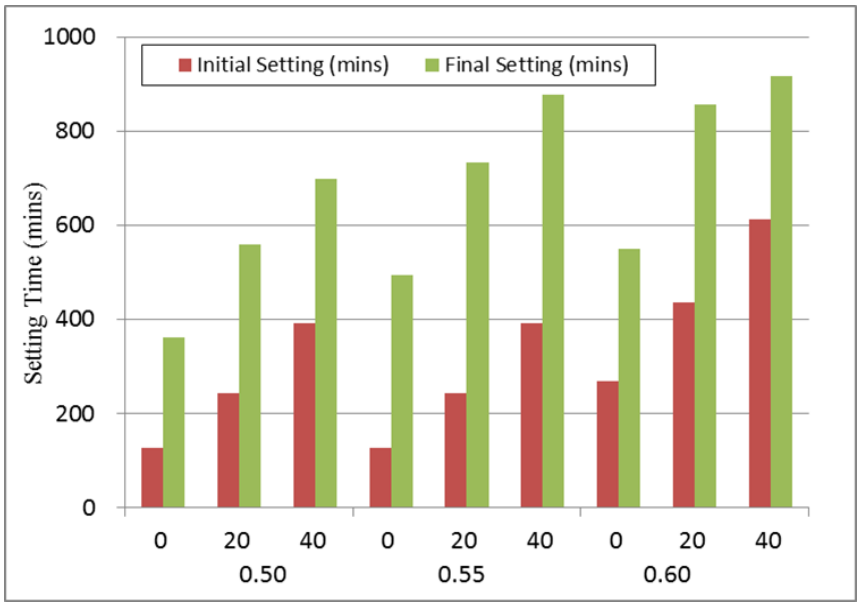

Figure 4. Setting time of different liquid-solid ratios and glass sand alkali-activated mortar.

3.4 Compressive strength

As shown in Figure 5, the compressive strength of the alkali-activated mortar increases with age and decreases as the liquid to solid ratio increases. When L/S increases from 0.45 to 0.60, the compressive strength is reduced by 33.08~63.70% because the base equivalent concentration is reduced when the liquid to solid ratio increases; an excessive or insufficient alkali content will reduce the compressive strength, and many pores are formed after water has evaporated, leading to strength reduction. When the glass sand replacement level increases from 0% to 20%, the compressive strength increases, but when the glass sand replacement level increases from 20% to 40%, the compressive strength decreases.

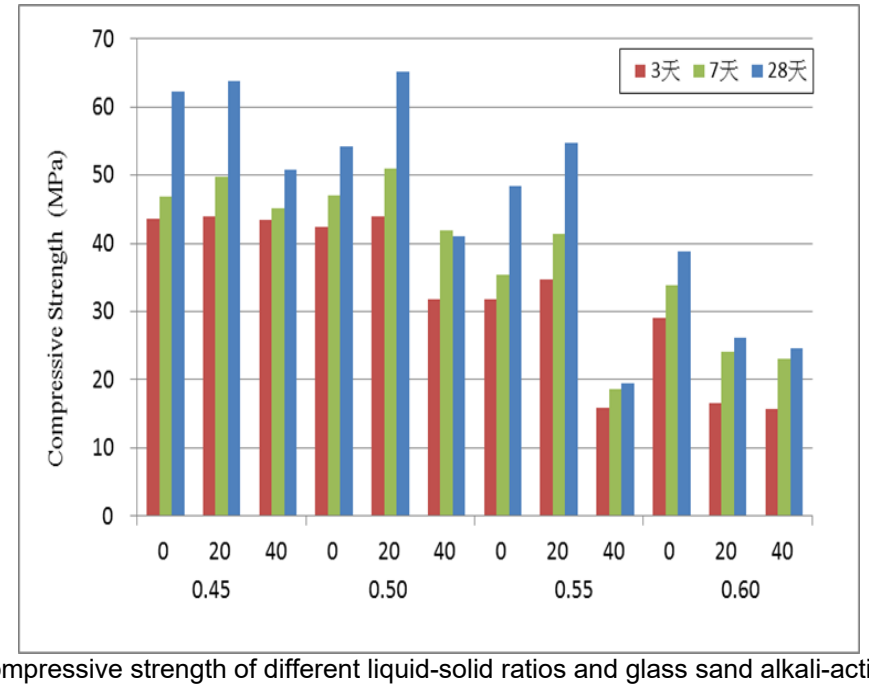

Figure 5. Compressive strength of different liquid-solid ratios and glass sand alkali-activated mortar.

3.5 Ultrasonic pulse velocity

Figure 6 shows the changes in the ultrasonic pulse velocity of the alkali-activated mortar with different glass sand replacement levels (L/S=0.50). The ultrasonic pulse velocity decreases as the glass sand replacement level increases. The ultrasonic pulse velocity decreases notably when the glass sand replacement level is 40%. At 28 days, the ultrasonic pulse velocities of the alkali-activated mortar are 3876 m/sec, 3788 m/sec and 3145 m/sec. At the same age, the ultrasonic pulse velocity decreases significantly in comparison to that of the alkali-activated mortar with the same glass sand replacement level when L/S=0.45. The internal organization of the material is relatively loose as the liquid to solid ratio increases, and thus the ultrasonic pulse velocity decreases, which is coincident with the result of the compressive strength.

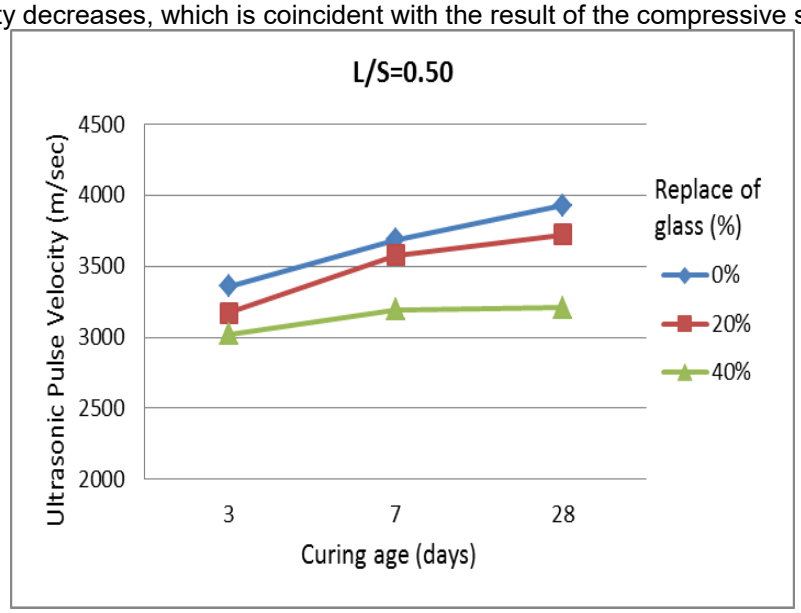

Figure 6. Ultrasonic pulse velocity of alkali-activated mortar of liquid to solid ratio 0.50.

3.6 Thermal conductivity

As shown in Figure 7, the thermal conductivity of the alkali-activated mortar increases with age and glass sand content, possibly because waste glass sand has a lower fineness than slag powder. When the waste glass replacement level increases, the polymerization rate is lower than when slag powder is used, and the actual content being polymerized is lower than when slag powder is used The thermal conductivity of glass before polymerization is 1.4 W/m*K, whereas that of the pure slag powder-based alkali-activated mortar is 0.8~1.1 W/m*K; so, when the glass sand replacement level increases, the glass sand that has not yet reacted increases the thermal conductivity of the alkali-activated mortar.

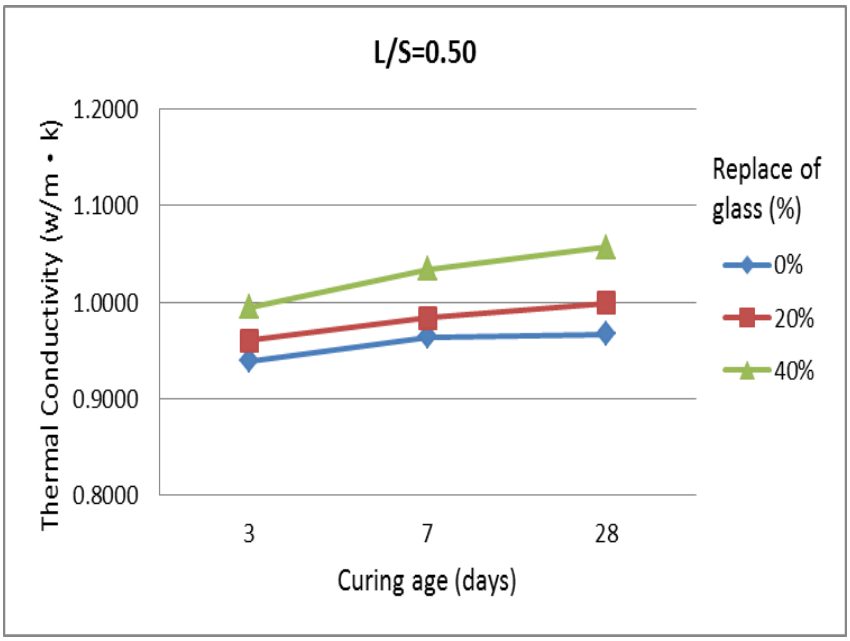

Figure 7. Thermal conductivity of alkali-activated mortar of liquid to solid ratio 0.50

3.7 Sulfate resistance

As shown in Figure 8, when the glass sand replacement level of slag is 0%, 20% and 40%, the weight loss is 0.29~1.60%, -0.86~-3.89% and -2.46~-5.97%, respectively. The weight loss due to sulfate attack decreases as the glass sand replacement level of slag increases; as glass sand contains much silicon and aluminum, polymerization is more complete, the specimen is more compact, and the resistance to corrosion is better. The weight increases with increasing liquid to solid ratio, and as there are pores inside the specimen, the sulfate solution permeates into the specimen to form crystals, which leads to the weight increasing. When L/S=0.50 and the glass sand replacement level is 40%, a more notable effect is observed, and the weight loss rate is -5.97%.

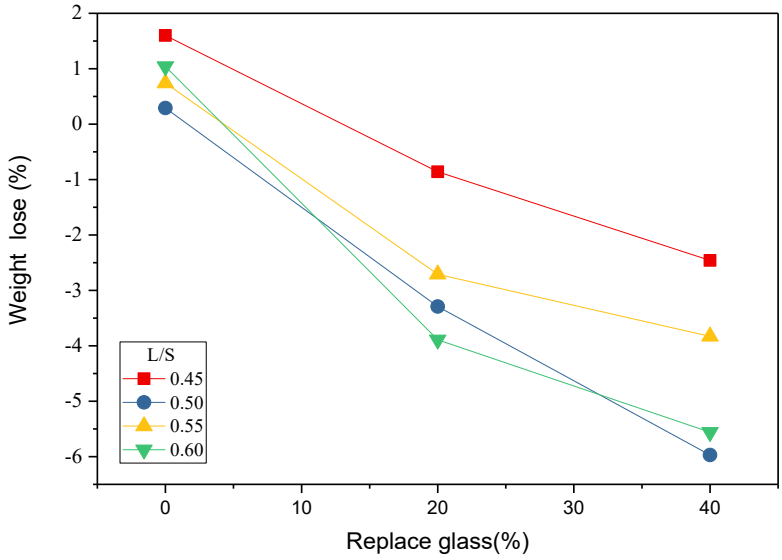

Figure 8. Sulfate soak weight loss of alkali-activated mortar of different liquid-solid ratios.

4 CONCLUSIONS

(a) Waste glass sand replacement of slag powder can enhance the workability of alkali-activated mortar. The slump and slump flow are the best when the glass sand replacement level is 40%; the slump and slump flow increase by 38.89% and 51.24%, respectively, as the liquid to solid ratio increases from 0.50 to 0.60.
(b) The alkali-activated mortar setting time is prolonged when slag powder is replaced by waste glass sand. When the replacement level increases to 40%, the initial setting time and final setting time increase by 142~219 min and 187~298 min, respectively.
(c) The compressive strength is higher when the glass sand replacement level is 20%, and the compressive strength at 28 days is 65.15 MPa.
(d) The thermal conductivity at 28 days of the waste glass alkali-activated mortar is 0.8069~1.4793 W/m*K; the thermal conductivity increases with increasing waste glass sand replacement level.
(e) The weight loss rate due to sulfate attack decreases as the glass sand replacement level increases, and the weight increases with increasing liquid to solid ratio. The effect is notable when L/S=0.50 and the glass sand replacement level is 40%, namely, the weight loss rate is -5.97%.

REFERENCES

Hsin-Ying Huang,(2009). Study of Insulation Performance Using Multi-layer Material on Roof, Master's thesis, National Taipei University of Science and Technology, Institute of Architecture and Urban Design.
Wei-lun Lin.(2009). Study on Engineering Properties of Alkali-Activated Slag Pastes, PhD thesis ,National Taiwan University of Science and Technology ,Department of Construction Engineering.
Shun-Yuan Wang,Wen-Po Tsai, De-Hong Liu,(2009). Application and introduction of lightweight aggregate concrete at home and abroad, Water conservancy and civil engineering information quarterly,45,.11-18.
Zh-Xiang Xiao.(2014). A feasibility study of using waste glass for light weight formed glass energy-saving bricks, Master's thesis, Feng Chia University, Department of Industrial Engineering and Systems Management.

Chien-Kuo Chen,(2014). The Research on Critical Impacts of Insulation Performance of Lightweight Concrete : The Case Study of Three Lightweight Aggregates, Master's thesis,.China University of Technology, Institute of Architecture.

F. Puertas and M. Torres-Carrasco,(2014). Use of glass waste as an activator in the preparation of alkali-activated slag. Mechanical strength and paste characterization, *Cement and Concrete Research*, 57, 95-104.

Ming-Feng Tsai,(2014). The Study of Thermos Insulation Effect to Cement Brick with Insulation Materials at Different Locations in the Brick,Master's thesis,Kunshan University of Science and Technology, Mechanical Engineering Research Institute.

Wei-Chien Wang , Bo-Tsun Chen , Her-Yung Wang , Hsien-Chih Chou,(2016). A study of the engineering properties of alkali-activated waste glass material (AAWGM), *Construction and building Materials*, 112, 962-969.

Chien-Chih Wang, Her-Yung Wang, Bo-Tsun Chen, Ya-Chi Peng,(2017). Study on the engineering properties and prediction models of an Alkali-activated mortar material containing recycled waste glass, *Construction and Building Materials* ,132, 130-141.

Jian-Xin Lu, Chi Sun Poon,(2018). Use of waste glass in alkali activated cement mortar, *Construction and building Materials*, 160, 399-407.

Jian-Xin Lu, Chi Sun Poon,(2019). An overview on the reuse of waste glasses in alkali-activated materials, Resources, *Conservation & Recycling*, 144, 297-309.

8th International Conference on the Application of Physical Modelling in Coastal and Port Engineering and Science
Dec. 9th - 12th, 2020, Zhoushan, China

RESEARCH ON THE PROPERTIES AND MICROSTRUCTURE OF GREEN RECYCLED LIGHTWEIGHT AGGREGATE CONCRETE (GRLAC) IN MARINE ENGINEERING STRUCTURAL MATERIALS

CHANG-CHI HUNG [1], HONG-CHUNG CHEN [2], CHIEN-CHIH WANG [3] & HER-YUNG WANG [4] *

[1] School of Architecture and Civil Engineering, Huizhou University, Huizhou, Guangdong, P.R. China
A0266@hzu.edn.cn

[2] Department of Naval Architecture and Ocean Engineering, National Kaohsiung University of Science and Technology, Kaohsiung City, ROC
hcchen@nkust.edu.tw

[3] Department of Civil Engineering and Geomatics, Cheng Shiu University, Kaohsiung City, ROC
ccw@gcloud.csu.edu.tw

[4] * Department of Civil Engineering, National Kaohsiung University of Science and Technology, Kaohsiung City, ROC
wangho@nkust.edu.tw

ABSTRACT

Taiwan is located in the subtropics and is surrounded by the sea. Coastal structures are prone to corrosion due to the intrusion of marine salt. The development of marine engineering structural materials in Taiwan should be the direction of vigorous development. This study applies industrial by-products to marine engineering structural materials Inquiry.This study was based on green materials applied to lightweight concrete. Waste rubber particles from tires and waste LCD glass sand passed through a #30 sieve were used to replace part of the fine aggregate in amounts of 0%, 5% and 10% with W/B=0.4, after curing for 7, 28 and 56 days for compressive strength, ultrasonic pulse velocity and micro-interface analysis. The results showed that a lightweight concrete specimen with replacement amount of 5% waste LCD glass sand had high flowing ability and the higher compressive strength, which after 28 days, reached 46 MPa; the wave velocity of normal concrete is higher than that of GRLAC. The weight loss of GRLAC is greater than that of normal concrete, Loss on Ignition display 28 days curing period of weight loss the greatest change, because more complete hydration, hydration products inside and gel more. X-ray powder diffraction analysis (XRD) at about 15 °~ 20 ° between can be found in Ca $(OH)_2$ wave front, the reaction of pozzolanic may be displayed by content degree. Scanning electron microscope (SEM) observation that, microstructure observation of the green lightweight aggregate and mortar are dandified compared to normal concrete. A variety of green recycled lightweight aggregate concrete, can not only be used effectively in recycling of waste resources but can also be part of the sustainable cycle of development.

Keywords: rubber particles; furnace slag; engineering properties; green recycled lightweight aggregate concrete (GRLAC); Marine engineering

1 INTRODUCTION

With respect to environmental protection, the reduction of carbon footprints has become a nationwide movement, and green building materials are widely used. Thus, sustainable development has become an important topic at present moment.

The number of typhoons and rainfall in Taiwan increase yearly, resulting in severe silting in many reservoirs. Thus, water storage is decreased sharply, and the reservoir life is shortened, which affects people's livelihood and limits industrial water use. If sludge is discarded and piled on good soil, the soil will be destroyed and a considerable amount of reservoir sludge is increasingly difficult to dispose of in landfills, creating some serious environmental problems (Chang et al.,2016). Furthermore, as it is difficult to construct legal dumping grounds, the sludge may be piled up at will or be thrown into the sea, thus causing secondary pollution. If the sludge is made into lightweight aggregates applied to structures, the insufficiency of urban space can be remedied, and it would become advantageous to the construction of high-rise buildings. Lightweight aggregate concrete (LWAC) has been used for structural applications for many years in long-span bridges, floating structures, high-rise buildings, and buildings where soil conditions are poor (Dulsang et al.,2016; Bogas et al.,2015). If it can be applied to large-span structures, high-rise buildings and maritime engineering, it has broad application prospects. In addition, Taiwan needs a large amount of sandstone for public constructions. Lightweight aggregates (LWA) can replace part of the sandstone and the decreasingly short natural aggregates, thus solving the severe sludge problem (González.et al.,2016)

LWA is not an exception in addition to reducing the self-weight of concrete and reducing the deadweight of the structure, the member size, steel bar consumption, and the effect of earthquakes on structures greatly. Lightweight concrete has become a popular building material. It has good compressive strength, durability and the most important advantage - low density and improved thermal conductivity. The main disadvantage of LWAC is its compressive brittleness compared with ordinary density concrete in material level. LWAC has attracted significant interest because of its advantages of being low-weight, improved thermal and acoustic insulation and better resistance to frost and fire (Cheng et al.,2018;Øverli et al.,2014). Moreover, LWAC can increase fireproofing, sound insulation and heat insulation efficiency (Altun et al.,2013; Liguori et al.,2014; Hunag et al.,2015; Kwon et al.,2018; Lv et al.,2015; Altun et al.,2013).These studies have been carried out at constant w/c ratio and it was shown that compressive strength decreases as the amount of rubber particle increases (Qu. et al.,2018; Real et al.,2018; Ganesan et al.,2013). In low w/c concretes, several researchers have concluded that the use of pre-wetted lightweight aggregates can improve overall concrete performance(Zhu,et al.,2017; Aslam,et al.,2016 ;Qu et al.,2018) , there by reducing micro-cracking, enhancing hydration, decreasing autogenously shrinkage and creep(Yu et al.,2013), improving durability(Yu et al.,2015), and enhancing the structure and properties in the Interface Transition Zone (ITZ) (González.et al.,2016). The goal is to improve the major structural performance and attain safety, environmental protection and economic benefit.

2 Experimental program

2.1 Experimental material

This study tests general cement made by the Taiwan Cement Corp., which is Type I Portland cement according to ASTM C150. The cement was sealed with impervious plastic to ensure quality. Water-quenched slag powder was produced by China Steel Corp. and was ground into a fine powder by China Hi-Ment Corporation. And according to CNS 12549. F-class fly ash was acquired from Tai-Power Hsin-Ta Thermal Power Plant and was to CNS 3036 standard. Waste LCD glass sand was crushed and passed through a No. #4 sieve to obtain a particle size close to that of natural fine aggregates. Table 1 shows the chemical properties of cement, fly ash, slag and waste liquid crystal glass. Waste tire rubber powder with #30 fineness was obtained from Taiwan Water-jet Technical Co.; its particle-size distribution and physical properties are shown in Table 2. Taiwan Shi-men Reservoir silt was dehydrated pelletized and sintered to obtain lightweight aggregate particles. Sieve analysis was conducted as per ASTM C33 to filter off some overly large and small particles and to decrease the influence of particle size on water absorption. The aggregates were granules from the Li-Gng region meeting the CNS 1240 concrete requirements. Aggregates physical properties are shown in Table3. The mixing water was normal tap water.

Table 1. Cement, fly ash, furnace powder and waste LCD glass of Chemical Composition. unit : %

Item	SiO_2	Al_2O_3	Fe_2O_3	CaO	MgO	SO_3	K_2O	Na_2O	TiO_2	P_2O_5	LoI
Cement	20.74	4.65	3.1	62.85	3.43	2.36	-	-	-	-	2.11
Fly ash	48.27	38.23	4.58	2.84	-	-	1.16	0.2	1.42	-	5.38
Slag	35.47	13.71	0.33	41	6.6	-	-	-	-	-	-
LCD glass	62.48	16.67	9.41	2.7	-	-	0.2	0.64	0.01	0.01	-

Table 2. Analysis of waste rubber powder sieve and physical properties.

Sieve NO.	#30	#50	#100	Chassis	Fineness modulus	Specific gravity
#20~40	121	56.9	65.5	9.6	2.17	0.95
#50~100	2.1	165.5	135	1.8	1.56	0.95

Table 3. Physical properties for aggregate.

Properties of Aggregates	Coarse Aggregates	Lightweight Aggregates	Fine Aggregates
Specific Gravity	2.65	1.35	2.61
Water Absorption in 30min (%)	-	4.6	-
Water Absorption in 24hr (%)	0.87	10	2.67
Maximum size(in)	1/2"	3/8"	-
Finesse Modulus (FM)	6.66		2.84
Dry-rodded unit weight (kg/m^3)	1572	901	1750

2.2 Experimental variables and mixtures

This study discussed the difference between the energy GRLAC and normal concrete. The water-binder ratio was fixed (W/B=0.4), and the general river sand was replaced by renewable resource materials (0%, 5%, 10%) to make GRLAC. Experiments were carried out at the curing age of 7, 28 and 56 days. The proportioning unit weight is shown in Table 4.

Table 4. Mixture proportions of GRLAC. unit：kg/m^3

NO.	Binding materials			Coarse	Substation	Fine aggregate			Water
	Cement	Fly ash	Slag	aggregate	%	Sand	Glass	Rubber	
L	398	32	32	545	0	690.0	-	-	185
LG5					5	655.5	34.5	-	
LG10					10	621.0	69.0	-	
LR5					5	655.5	-	34.5	
LR10					10	621.0	-	69.0	
LGR5					2.5	655.5	17.3	17.3	
LGR10					5	621.0	34.5	34.5	
N	398	32	32	872	0	885.0	-	-	185
NG5					5	840.7	44.2	-	
NG10					10	796.5	88.5	-	
NR5					5	840.7	-	44.2	
NR10					10	796.5	-	88.5	
NGR5					2.5	840.7	22.1	22.1	
NGR10					5	796.5	44.3	44.3	

2.3 Experimental methods

The hard-solid and durable nature follows ASTM C39 and C192 standards. The durability follows ASTMC597 standard. For the ignition loss experiment, 10g specimen is treated at different high temperatures, and the weight loss is measured to observe the change in internal hydration degree. The hydrated cementation is further discussed based on the principle of chemical decomposition at different temperatures, measured at 105℃, 400℃, 580℃ and 800℃, and after a time delay of one hour. The internal temperature reaches the design temperature. As for the micro-structure properties, after the compression resistance experiment for concrete, mortar fragments are soaked in methanol solution to terminate hydration, so as to observe micro items. The scanning electron microscope concentrates electron beams to scan the piece surface characteristics. Since the test piece is coated with a gold film, it conducts electricity when contacting the electron beam, and signals are generated and collected by the receiver and displayed in the CRT. The principle of X-ray powder diffraction is that the wavelength is less than that between atoms in crystals, and there will be diffraction that reflects lattice atom arrangement and structure. The X-ray passes through a slit forming parallel light waves irradiating the specimen with flat surface; the Bragg's Law calculates the distance between crystals, which can stand on the optimism for evaluation of concrete.

3 Results and Analysis

3.1 green lightweight materials

All the green lightweight materials used in this study are local materials. The fly ash is low calcium fly ash grade F, the CaO content is 2.84%, the F grade fly ash content should be less than 10% as defined in general mineralogy[45] and contain a lot of SiO_2 and $Al2O_3$ (48.27% and 38.23%). The physico-chemical properties of hearthstone are influenced by different manufacturing processes and raw material sources, generally, the main components are 41% CaO and 35.47% SiO_2, this composition is relatively related to forming glassiness, and the Al_2O_3 content is 13.71%. The LCD glass panel contains a lot of SiO_2 (62.48%) and fly ash, the furnace slag has the same effect, it can be regarded as pozzolanic admixture and added in concrete. The waste rubber mainly consists of carbon element, the fineness is determined by sieve #30 and #50, the content is (121g and 165.5g), and the specific gravity is about 0.95.

3.2 Fresh properties

The particle density of GRLAC is low, the load of particle piling is light, the downward force is small, and the horizontal side thrust is small. Therefore, high mortar content is designed to avoid the LWA floating, so that there is enough mortar covering the aggregate surface. This study uses the design slump of 150~180 mm. Table 5 shows that various groups of concrete have no apparent bleeding or separating after mixing. The slump value of normal-weight concrete is 150~173 mm, and the slump value of lightweight concrete is 151~175 mm.

All the groups conform to the designed slump range. When 5% and 10% waste glass sand are added, the slump increases by 6~15 mm. This increase might be because the waste glass sand is a flaky grain. In irregular shapes with edges and corners, the grains influence each other. Although it is unlikely to flow, moisture is lubricating, and the slump is increased greatly. When the waste rubber powder is added, the slump is less than that of the control group. The slump value decreases as the addition of waste rubber powder increases. The addition of rubber powder reduces the concrete workability. Because the specific gravity of waste glass sand (2.42) and waste rubber powder (0.95) are lower than normal sand, the concrete fresh property unit weight decreases as the replacement increases.

Table 5. Physical properties for aggregate.

NO.	Slump (mm)	Unit Weight (kg/m^3)
N	157	2330
NG5	160	2290
NG10	173	2242
NR5	153	2238
NR10	150	2221
NGR5	154	2218
NGR10	150	2208
L	160	1808
LG5	166	1782
LG10	175	1778
LR5	156	1765
LR10	152	1752
LGR5	154	1748
LGR10	151	1739

3.3 Compressive strength

As shown in Fig 1, the strength of GRLAC of the control group at the curing age of 28 days is higher than that of normal concrete by approximately 10.2% (4.4 MPa), and that of GRLAC at the curing age of 56 days is higher than normal concrete by approximately 4.9% (2.2 MPa). As for the specimens with 5% glass sand replacement, the compressive strength of normal concrete is 32.6~48.9 MPa, and the compressive strength of GRLAC is 35.7~51.0 MPa. Both of these values are greater than 42.6 MPa and 33.4~44.8 MPa of the control group. Because of the smoothness of the glass surface, the glass sand and the grout cannot bond tightly.

For the specimens with 10% rubber particle replacement, the compressive strength of normal concrete is approximately 18.1~26.4 MPa, and the compressive strength of GRLAC is 23.9~34.6 MPa. The compressive strength is lower than all the other specimens. Because the rubber is a high molecular weight material, the

material bonding interface is weak. When 5% glass sand and 10% rubber particles are mixed, the compressive strength is better than when only rubber particles are used as the added material.

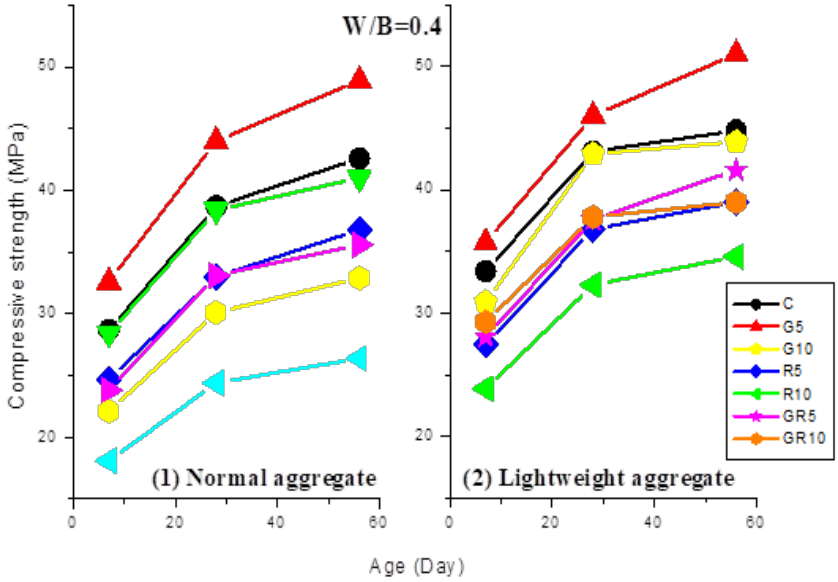

Figure 1. Growth trend of compressive strength of GRLAC.

3.4 Ultrasonic pulse velocity

The ultrasonic pulse velocity is likely to be influenced by the age, water-binder ratio, cement, water consumption and aggregate characteristics. The wave velocity reflects the compactness and homogeneity inside the concrete. Fig 2 shows the ultrasonic pulse velocity of normal concrete at the curing age of 7 days are 3552~4034 m/s. The value is 3719~4204 m/s at the curing age of 28 days, and the ultrasonic pulse velocity of GRLAC at the curing age of 7 days is 3310~3728 m/s, while the values is 3531~3926 m/s at the curing age of 28 days. The wave velocity of normal concrete is higher than that of GRLAC, because the GRLA has more pores and particles that interfere with the pulse wave transmission.

The material with 10% glass sand has the best wave velocity among the replacements of various green admixtures. When the hydration is completed on the 28th day, the wave velocities of the control group of normal weight and GRLAC are 4125 m/s and 3704 m/s respectively. The wave velocities of normal weight and GRLAC with 10% glass sand are 4204 and 3958 m/s, respectively, higher than the control group by 1.8% and 5.5%.

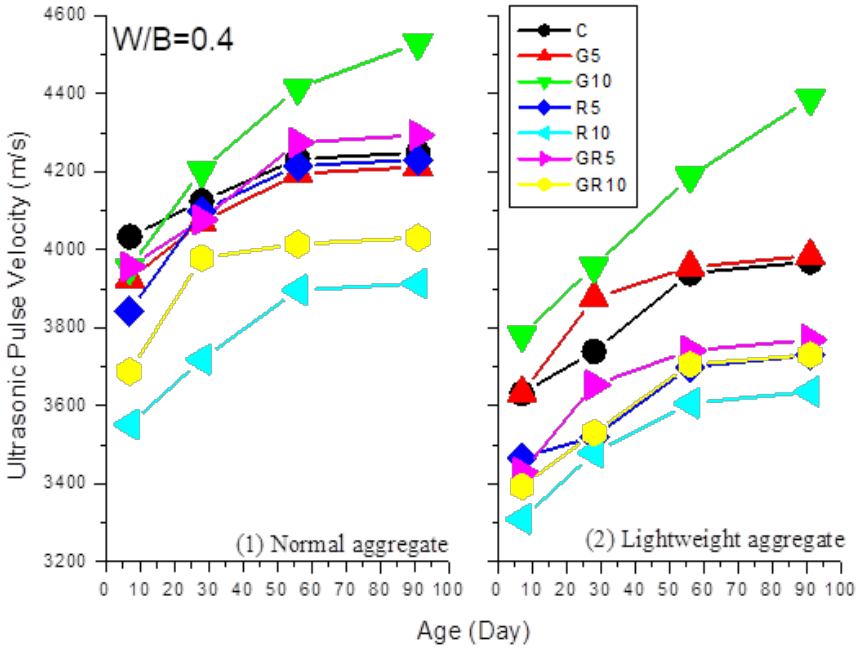

Figure 2. Ultrasonic pulse velocity of GRLAC.

3.5 Loss ignition

Fig 3 shows that the hydration of normal concrete was not been completed after 7 days. The weight loss is approximately -0.6~-1.4 g, and at the curing age of 28 days the weight loss is approximately -0.5~-1.3 g. The development of the internal strength of concrete becomes stable after 56 days. The loss is less than that after 28 days, and the weight loss is approximately -0.3~-0.8 g.

The weight loss of GRLAC is greater than that of normal concrete, the weight loss after 7 days is approximately -1.76~-1.98 g, while the weight loss after 28 days is approximately -1.37~-1.87 g, and the weight loss after 56 days is approximately -1.13~-1.84 g. The generation of hydrate is related to the variation of age. The weight loss decreases as the age increases, meaning that the internal hydration is complete, and the resultant stops growing gradually.

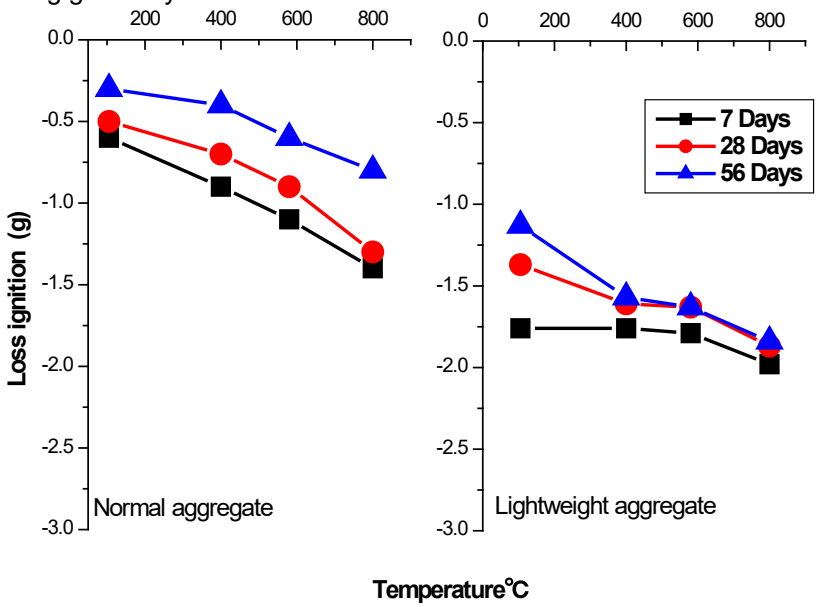

Figure 3. Ignition loss of GRLAC.

3.6 X-Ray Diffract meter, XRD

Fig 4 shows that the peak value of Ca $(OH)_2$ occurs in the rapid hydration at the curing age of 7 days, but the Ca $(OH)_2$ peak decreases when the hydration is almost completed at the curing age of 28 days. The longer the age of the hydration product C3S, is, the longer the reaction time will be. The concrete is filled up mostly with products that have not participated in hydration at an early age, but the peak of C3S can be found at the curing age of 28 days, while the C_3A peak rises at the curing age of 56 days.

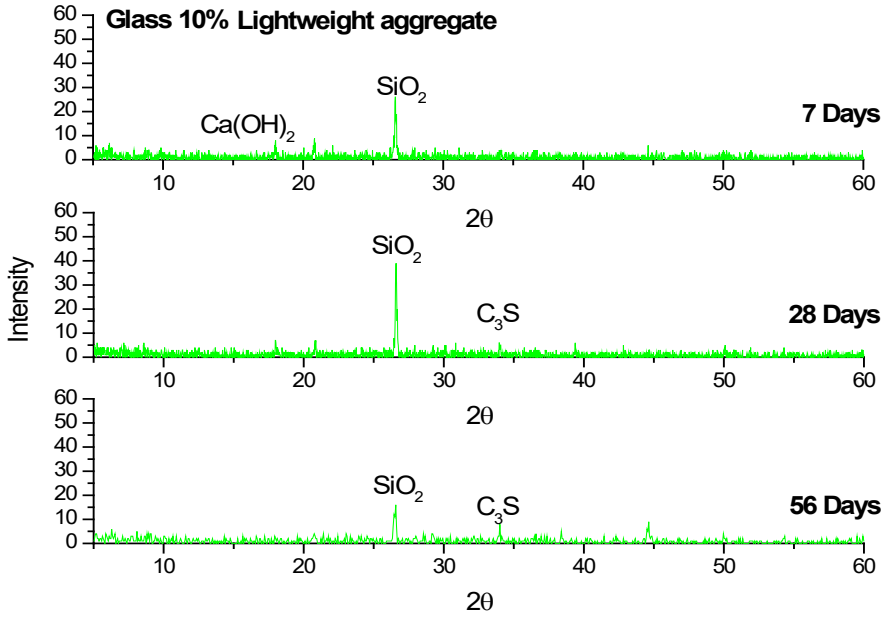

3.4 **Figure 4.** X-ray powder diffraction of GRLAC

3.7 Scanning Electron Microscopy, SEM

Fig5 shows that the overall structure inside the normal concrete is dense with a few pores, and the hydration process is not completed at the age of 7 days. There are many hydration products in disorder, but the fly ash balls and the grout bond well; a partial CH crystal begins to form. Many pores inside the concrete are filled up after the pozzolanic reaction between fly ash and furnace slag at the age of 28 days so that the overall microstructure becomes denser.

The coarse surface of lightweight aggregate enables the resultants to accumulate on the aggregate surface, so that there is good interface bonding with the mortar. Many hydration products adhere to the places near lightweight aggregate pores at the age of 7 days. There are an irregular CH crystals, needle tube-shaped C-S-H gel and rose-shaped AFt gelatin products.

An interface transition zone approximately 15~20 μm thick occurs between the cement and lightweight aggregate at the age of 28 days. The C-S-H gel connection into a network forms a surface colloid with high density.

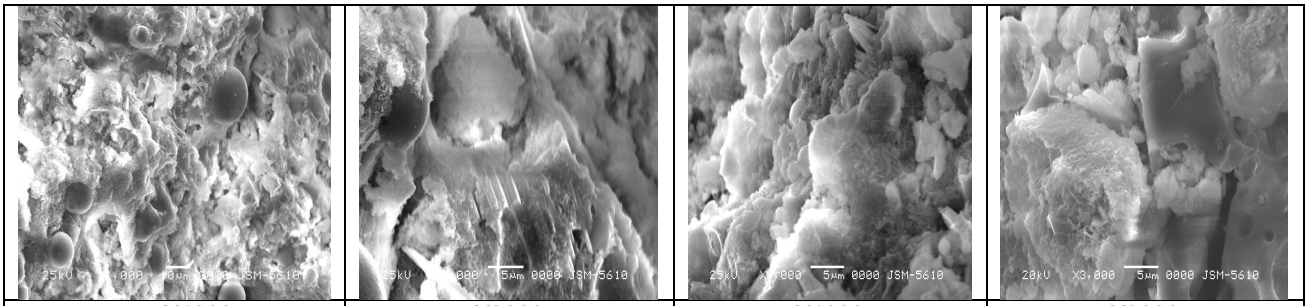

X1000	X3000	X1000	X3000
Normal aggregate		Lightweight aggregate	
(1) 7 days			

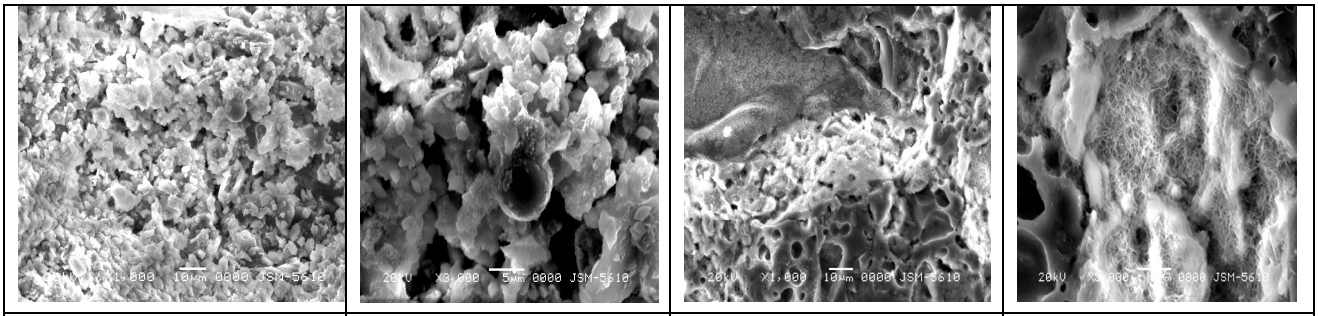

X1000	X3000	X1000	X3000
Normal aggregate		Lightweight aggregate	
(2) 28 days			

Figure 5. SEM images (×3000) of GRLAC. (Glass sand 10%) at the age of (1)7 days, (2) 28 days.

4 CONCLUSIONS

(a) The recycled green materials are local materials. The fly ash is low calcium fly ash grade F, containing 48.27%SiO_2 and 38.23%Al_2O_3, the hearthstone contains 41%CaO and SiO_2, and the LCD glass contains as high as 62.48% SiO_2. The waste rubber particles should pass through #30 and #50 sieves.

(b) The slump value of normal concrete is approximately 150~173 mm. The slump value of GRLAC is approximately 151~175 mm. The slump can be increased by approximately 3%~8% (6~15 mm) by adding 5% and 10% waste LCD glass sand, meaning the addition of waste LCD glass can enhance the slump and fluidity effectively. GRLAC that high flowing ability.

(c) GLWC that the compressive strength is 24 MPa at the curing age of 7 days, and it can reach 46 MPa at the curing age of 28 days. The 5% glass sand replacement has a good strength development trend.

(d) The ultrasonic pulse velocity of normal concrete is 3719~4204 m/s at the curing age of 28 days, higher than 3531~3926 m/s of GRLAC. The 10% glass sand replacement is optimal.

(e) The ignition loss shows the trend of overall weight loss is higher than normal concrete. The GLWC has many aggregate pores containing a high content of moisture and hydration products. The greater the age, the lower the weight loss, meaning that the hydration becomes stable as the age reaction time increases. New hydrates seldom occur.

(f) X-ray powder diffraction shows that the Ca $(OH)_2$ peak response occurs at 15~20°. The pozzolanic reaction will be reduced with the extension of age. The pozzolanic reaction degree can be obtained from the Ca $(OH)_2$ content.

It is observed through SEM that the LWA bonds with the mortar more tightly than the general aggregate does for its rough texture and pores, and the pozzolanic reaction can be enhanced by adding fly ash furnace slag, resulting in aggregate interface reinforcing reaction, which is advantageous to the long-term strength development.

REFERENCES

Yu, Q. L., Spiesz, P., & Brouwers, H. J. H. (2013). Development of cement-based lightweight composites – Part 1: Mix design methodology and hardened properties. *Cement and Concrete Composites*, 44, 17–29.

Øverli, J. A., & Jensen, T. M. (2014). Increasing ductility in heavily reinforced LWAC structures. *Engineering Structures*, 62-63, 11–22.

Bogas, J. A., de Brito, J., & Figueiredo, J. M. ,(2015). Mechanical characterization of concrete produced with recycled lightweight expanded clay aggregate concrete, *Journal of Cleaner Production*, 89, 187–195.

Chang, Y.H., Huang, P.-H., Chuang, T.F., & Chang, S.W.,(2016). A pilot study of the color performance of recycling green building materials, *Journal of Building Engineering*, 7, 114–120.

Dulsang, N., Kasemsiri, P., Posi, P., Hiziroglu, S., & Chindaprasirt, P. (2016). Characterization of an environment friendly lightweight concrete containing ethyl vinyl acetate *waste. Materials & Design*, 96, 350–356.

González-Corrochano, B., Alonso-Azcárate, J., Rodríguez, L., Lorenzo, A. P., Torío, M. F., Ramos, J. J. T., Muro, C ,(2016). Valorization of washing aggregate sludge and sewage sludge for lightweight aggregates production,*Construction and Building Materials*, 116, 252–262.

Cheng, S., Shui, Z., Sun, T., Huang, Y., & Liu, K. ,(2018). Effects of seawater and supplementary cementitious materials on the durability and microstructure of lightweight aggregate concrete. *Construction and Building Materials*, 190, 1081–1090.

Altun, F., & Aktaş, B. ,(2013). Investigation of reinforced concrete beams behavior of steel fiber added lightweight concrete, Construction and Building Materials, 38, 575–581.

Liguori, B., Iucolano, F., Capasso, I., Lavorgna, M., & Verdolotti, L.,(2014). The effect of recycled plastic aggregate on chemical-physical and functional properties of composite mortars. *Materials & Design*, 57, 578–584.

Hunag, L.J., Wang, H.Y., & Wang, S.Y. (2015). A study of the durability of recycled green building materials in lightweight aggregate concrete ,*Construction and Building Materials*, 96, 353–359.

Kwon, S.J., Yang, K.H., & Mun, J.-H. (2018). Flexural tests on externally post-tensioned lightweight concrete beams*. Engineering Structures*, 164, 128–140.

Lv, J., Zhou, T., Du, Q., & Wu, H. (2015). Effects of rubber particles on mechanical properties of lightweight aggregate concrete. *Construction and Building Materials*, 91, 145–149.

Altun, F., & Aktaş, B. (2013). Investigation of reinforced concrete beams behavior of steel fiber added lightweight concrete. *Construction and Building Materials*, 38, 575–581.

Qu, Z. Y., & Yu, Q. L. (2018). Synthesizing super-hydrophobic ground granulated blast furnace slag to enhance the transport property of lightweight aggregate concrete. *Construction and Building Materials*, 191, 176–186.

Real, S., & Bogas, J. A. (2018). Chloride ingress into structural lightweight aggregate concrete in real marine environment. *Marine Structures*, 61, 170–187.

Ganesan, N., Bharati Raj, J., & Shashikala, A. P. (2013). Flexural fatigue behavior of self-compacting rubberized concrete. *Construction and Building Materials*, 44, 7–14.

Zhu, C., Niu, J., Li, J., Wan, C., & Peng, J. (2017). Effect of aggregate saturation degree on the freeze–thaw resistance of high performance polypropylene fiber lightweight aggregate concrete. *Construction and Building Materials*, 145, 367–375.

Aslam, M., Shafigh, P., Jumaat, M. Z., & Lachemi, M. (2016). Benefits of using blended waste coarse lightweight aggregates in structural lightweight aggregate concrete. *Journal of Cleaner Production*, 119, 108–117.

Qu, Z. Y., & Yu, Q. L. (2018). Synthesizing super-hydrophobic ground granulated blast furnace slag to enhance the transport property of lightweight aggregate concrete. *Construction and Building Materials*, 191, 176–186.

Yu, Q. L., Spiesz, P., & Brouwers, H. J. H. (2015). Ultra-lightweight concrete: Conceptual design and performance evaluation. *Cement and Concrete Composites*, 61, 18–28.

8th International Conference on the Application of Physical Modelling in Coastal and Port Engineering and Science
Dec. 9th - 12th, 2020, Zhoushan, China

RESEARCH ON THE DURABILITY OF SSLAC IN MARINE ENGINEERING STRUCTURAL MATERIALS

JACK HUANG[1], WEN-DUO YANG[2], HER-YUNG WANG [3]

[1] President FSAB materials Science and Technology, Kaohsiung City, 807, ROC, color.jackhuang@gmail.com

[2] Department of Chemical and Materials Engineering, National Kaohsiung University of Science and Technology, Kaohsiung City, 807, ROC, ywd@nkust.edu.tw

[3] Department of Civil Engineering, National Kaohsiung University of Science and Technology, Kaohsiung City, 807, ROC, wangho@nkust.edu.tw

ABSTRACT

Improving the durability of marine engineering structural materials and achieving circular economy of energy saving and carbon reduction and effective use of resource materials have been the goals of the world. Lightweight aggregates are characterized by a low thermal conductivity, seismic resistance and fire resistance. This study uses the sedimentary sludge lightweight aggregate material of Taiwan and uses a densified mixture design algorithm to examine the influence of the lightweight aggregate density (normal density and 800 and 1600 kg/m^3) on the concrete engineering properties under the effect of a high temperature. The mixing water content is fixed at 170 kg/m^3, the W/B ratios are 0.28, 0.32 and 0.40, and the admixtures are fly ash, slag and superplasticizer; the designed lightweight aggregate concrete can meet the requirements of a high workability, and the cement content and mixing water consumption are reduced to improve the economy and durability.

The heating rate of the high-temperature furnace is fixed at 4°C/min, and three temperatures (250, 500, and 750°C) and two delay times (1 h and 2 h) are used for the fire-damage tests. Compared with room temperature conditions (25°C), the changes in engineering properties are examined, and SEM testing is conducted to observe the microstructural changes under the effect of a high temperature.

The findings show that the densified mixture design algorithm can provide high-flow Sedimentary sludge lightweight aggregate concrete (SSLAC). Lightweight aggregate concrete under the effect of a high temperature still has a high compressive strength residual ratio (56~99%), resistivity residual ratio (40~93%) and ultrasonic pulse velocity residual ratio (45~86%). The crack width is 86~398 μm, but the sulfate resistance is poor; after the specimen is heated, the initial temperature is low, and the thermal insulating properties are good. Lightweight aggregate concrete still has good engineering properties under the effect of a high temperature and is suitable for fire-resistant buildings, but the durability problem resulting from micro cracks requires further study. The research results can be used to solve a large number of industrial by-products, to achieve the circular economy of energy conservation and carbon reduction and environmental sustainability goals.

Keywords: rubber particles; furnace slag; engineering properties; green recycled lightweight aggregate concrete (GRLAC); Marine engineering

1 INTRODUCTION

With global efforts to conserve natural resources and address the depletion of natural aggregates, many different types of lightweight aggregates have been used, e.g., waste materials such as fly ash, bottom ash, dredged soil, reservoir sludge, and oil palm shells (Ahn et al.,2016; Hwang et al.,2012; Ahmmad et al.,2016) . Lightweight aggregates generally occupy more than 50% of the concrete volume; therefore, it is important to use appropriate aggregates to achieve the target performance of concrete materials (Chung et al.,2018; Yu et al.,2016; Lukic et al.,2017) While the unit weight of conventional LWAC materials has been successfully achieved within the stipulated guidelines, traditional LWAC has exhibited a lower mechanical strength and reduced performance, such as impaired durability and brittle failure (Zhou et al.,2019; American Society for Testing and Materials,2017). There are 86 reservoirs in Taiwan, and among these reservoirs, 16 are located in Central and South Taiwan and have an average decrease of 13% in the water storage capacity (Lin, 2012). The existing important reservoirs universally have deposition problems. If the reservoir sediment can be made into lightweight aggregates for engineering, the original water storage function of the reservoirs can be restored, and the sandstone shortage can be solved. The beneficial use of dredged materials in construction applications as coarse or fine aggregates in concrete production has been studied by several researchers (Natalia et al., 2017; Said et al., 2015). Pre-wetted lightweight aggregates (PLWA), especially fine aggregates, have been shown by numerous studies to provide an increased degree of hydration, reduced shrinkage, and

general improvement in concrete properties (John et al., 2013; O.M.Jensen, 2013). Natural or artificial lightweight aggregates can be used for producing lightweight concretes.
Concrete is the most widely used construction material in the world. There are several types of concrete in use, including structural lightweight concrete, shrinkage-compensating concrete, and heavyweight concrete for radiation shielding. Lightweight concrete is widely used as a supplementary building material due to its low density and effective insulation (Aslam et al., 2016; Roberz et al., 2017; Chung et al., 2017).Moreover, lightweight cement has an excellent performance in terms of fire prevention and fire insulation and has energy-saving and disaster prevention functions in comparison to normal concrete structures or steel skeleton structures. Lightweight cement is favorable for high-rise buildings, shock insulation structures and energy-saving buildings, and in the uniform and stable production mode, the concrete quality can be controlled, contributing to quality. Lightweight concrete has many favorable engineering properties, such as a light weight, high strength, low expansibility, good heat insulation, sound-dampening qualities, water and fire resistance, durability, stable volume, ease of use for construction, and low cost (Hague et al.,2004; Wang et al.,2010).

2 Experimental program

2.1 Experimental material

(a) In this study, general cement made by the Taiwan Cement Corp. is tested, which is Type I ordinary Portland cement according to ASTM C150. The cement was sealed with impervious plastic to ensure the quality.
(b) The water-quenched slag powder was produced by China Steel Corp. and was ground into a fine powder by the China Hi-Ment Corporation according to CNS 12549.
(c) F-class fly ash was acquired from the Tai-Power Hsin-Ta thermal power plant and was used according to the CNS 3036 standard.
(d) Taiwan Shi-men Reservoir silt was dehydrated, pelletized and sintered to obtain lightweight aggregate particles. Sieve analysis was conducted as per ASTM C33 to remove overly large and small particles and to decrease the influence of the particle size on water absorption.
(e) The aggregates were granules from the Li-Gng region that met the ASTM C127 concrete requirements.
(f) The mixing water was normal tap water.

Table 1 shows the chemical properties of the cement, fly ash and slag. The aggregate physical properties are summarized in Table 2.

Table 1. The chemical and physical properties of cement fly ash and Slag. unit：%

Test project		Cement	Fly Ash	Slag
Chemical properties	SiO_2 (S)	21.41	48.27	33.35
	Al_2O_3 (A)	5.53	38.23	14.76
	Fe_2O_3 (F)	2.66	4.58	0.59
	S+A+F	29.6	91.08	48.7
	CaO	62.92	2.84	40.64
	MgO	1.25	2.92	7.12
	SO_3	3.18	0.75	0.50
	f-CaO	1.05	-	-
	TiO_2	0.52	1.42	-
	Na_2O	0.41	0.21	-
	K_2O	0.78	1.16	-
	V_2O_5	0.06	-	-
	Loss on ignition	0.91	5.38	0.16
	Insoluble residue	0.13	-	-
	C_3S	43.41	-	-
	C_2S	28.64	-	-
	C_3A	10.15	-	-
	C_4AF	8.09	-	-
Physical properties	Fineness (m^2/kg)	365	435	405
	specific gravity	3.14	2.00	2.89
	Initial setting time (min)	135	-	-
	Final setting time (min)	260	-	-
	Amount Retained on #325 Sieve (%)	9.4	-	2.0

Table 2. The physical properties for aggregate.

property	unit	Coarse aggregate			Fine aggregate
		Lightweight Aggregates of Reservoir Sediment（Ⅰ）	Lightweight Aggregates of Reservoir Sediment（Ⅱ）	Normal-weight Aggregates	Sand
specific gravity	-	0.84	1.61	2.44	2.64
30min Water absorption rate	%	4.7	3.6	-	-
24hr Water absorption rate	%	7.8	6.5	1.2	2.35
Float rate	%	92	8	-	-
Maximum particle size	in	1/2 "	3/8 "	3/4 "	#4
Fineness simulation	-	6.65	6.50	7.12	2.81
particle cylindrical crushing strength	MPa	7.6	16	-	-
Unit weight	kg/m^3	508	826	1562	1649
Note	·Lightweight Aggregates of Reservoir Sediment（Ⅰ）density collectively referred to as 800 kg/m^3. ·Lightweight Aggregates of Reservoir Sediment（Ⅱ）density collectively referred to as 1600 kg/m^3. ·Normal-weight Aggregates density collectively referred to as 2440 kg/m^3.				

2.2 Experimental variables and mixtures

In this study, a densified mixture design algorithm, three W/B ratios (0.28, 0.32, and 0.40), three aggregate densities (800 kg/m^3, 1600 kg/m^3 and normal density) and a fixed mixing water content (170 kg/m3) are used to design nine mix proportions to make 385 cylindrical specimens, and a forced horizontal double shaft mixer is used for mixing. The cast cylindrical concrete specimens, Ø10 cm×20 cm, were used in compressive strength tests (ASTM C39). SSLAC was tested at three temperatures (250, 500, and 750°C) and two delay times (60 and 120 min) after curing for 28 days. The unit weight proportions are shown in Table 3.

Table 3. Mix proportions of lightweight aggregate concrete. unit：kg/m^3

Numbering	w/c	w/b	w/s	Paste	Binder			Aggregate		Mix Water	
					Cement	Slag	Fly Ash	Coarse aggregate	Sand	Water	Super plasticizers
LWC0828	0.345	0.28	0.108	2.885	493	26	88	315	646	158	12
LWC0832	0.407	0.32	0.111	2.668	418	22	91	327	671	160	10
LWC0840	0.544	0.40	0.115	2.363	312	16	96	344	706	163	7
LWC1628	0.355	0.28	0.090	2.334	478	25	104	529	760	154	16
LWC1632	0.422	0.32	0.091	2.154	403	20	108	550	789	156	14
LWC1640	0.574	0.40	0.093	1.902	296	16	113	578	830	158	12
NWC28	0.332	0.28	0.079	1.874	512	27	68	1058	501	155	15
NWC32	0.389	0.32	0.079	1.737	437	23	71	1098	520	158	12
NWC40	0.511	0.40	0.080	1.544	333	17	75	1155	547	162	8
Note The coarse aggregate of LWC0828~LWC1640 is lightweightaggregate. The coarse aggregate of NWC28~NWC40 is normal-weight aggregate.											

2.3 Experimental methods

The fresh concrete slump test was conducted as per ASTM C143. The cast cylindrical concrete specimens, Ø10 cm×20 cm, were used in compressive strength tests (ASTM C39). The ultrasonic pulse velocity test was conducted as per ASTM C597; the signals detected using an ultrasonic-echo sensor (EPOCH4) were filtered and processed, and vertical waves were converted into horizontal waves. In other words, the energy of the vertical axis was 100% released. The horizontal axis represents the travel time or distance of the energy, and the waveform reveals the locations of flaws. The signals detected by the ultra-sonic-echo sensor were analyzed according to the damped harmonic method. Energy will decay when

transmitted between two media, and the reflection generated in each medium is variable. Hence, the cyclic transmission of energy yields an energy peak at the interface of the two media, which can be used to determine the homogeneity of the material.

The surface resistivity and sulfate resistance were determined as per ASTM C876 and ASTM C1012, respectively, and the specimens were cured in saturated limewater for 7 days, dried for 24 h in an oven at 100±5°C, and immersed in saturated sulfate solution for 24 h. The dry-wet sulfate-attack tests were repeated for 5 cycles to evaluate the influence of sulfate attack on lightweight concrete. After the SSLAC was heated, the engineering properties and durability were tested, and the residual ultrasonic pulse velocity was measured by high-level ultrasonic flaw detection tests.

The specimens before and after heating are sampled. The detectable wave band of the infrared image analyzer (TVS-110) was 3-5.4 μm, and the temperature resolution was 0.2°C. The texture and morphology of the pellet fragments were determined by scanning electron microscopy (SEM) on a Philips XL30 microscope (Philips, Amsterdam, and the Netherlands). The scanning electron microscope uses concentrated electron beams to scan the surface characteristics of specimens. Since the specimen is coated with a gold film, it conducts electricity when contacted by the electron beam, and signals are generated and collected by the receiver and displayed in the CRT.

3 Results and Analysis

3.1 Fresh concrete properties

The lightweight aggregate floating phenomenon shall be considered during the mixing of concrete specimens, the mix proportion shall be adjusted, and the uniformity of concrete is balanced by the paste concentration. The paste content for the desired aggregate characteristics is prepared according to the aggregate proportion. To avoid aggregate flotation and segregation, the viscosity must be increased to enhance the overall coagulability. Figures 1 and Figures 2 show that the slump and slump flow are 265~280 mm and 570~630 mm, respectively, when the aggregate density is 800 kg/m^3 and are 275~285 mm and 610~670 mm, respectively, when the aggregate density is 1600 kg/m^3. The densified mixture design algorithm for SSLAC can result in high-flow concrete. As the specific gravity is higher than that of the cement mortar, the required paste content is lower than 800 kg/m3; the material is easily flattened after pouring, and attention must be paid to the addition of a superplasticizer to avoid bleeding.

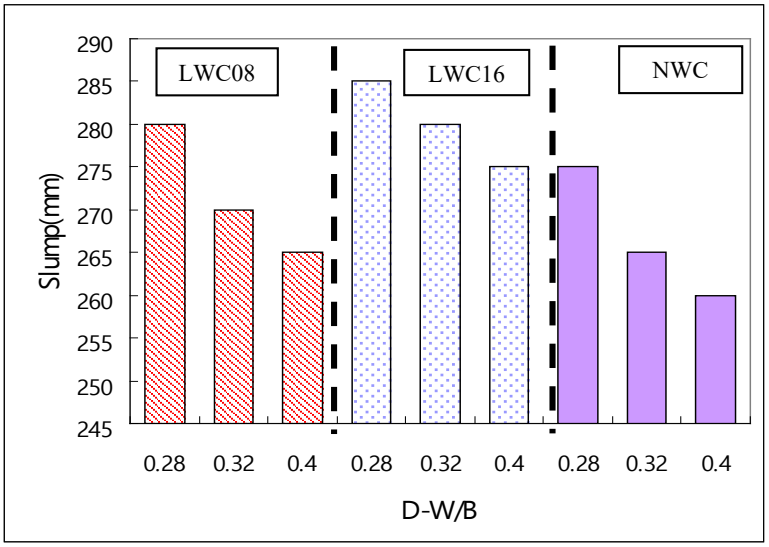

Figure 1. Slump of fresh SSLAC.

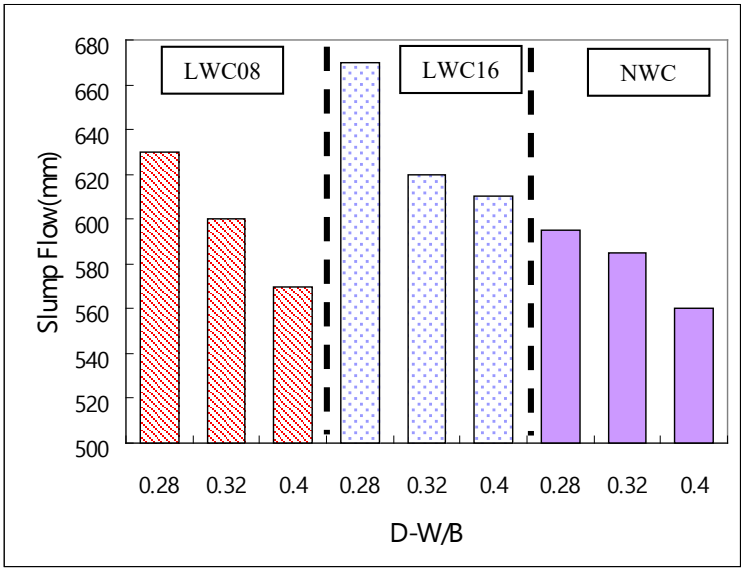

Figure 2. Slump flow of fresh SSLAC.

3.2 Compressive strength

Figure 3 shows that the compressive strength of SSLAC is 240~673 kg/cm^2; the compressive strength of LWC is lower than that of the control group (41~92%), but the compressive strength is lower than that of normal-weight aggregate, and the compressive strength of LWC increases with increasing aggregate density. The compressive strength decreases (13~25%) as the W/B ratio increases.

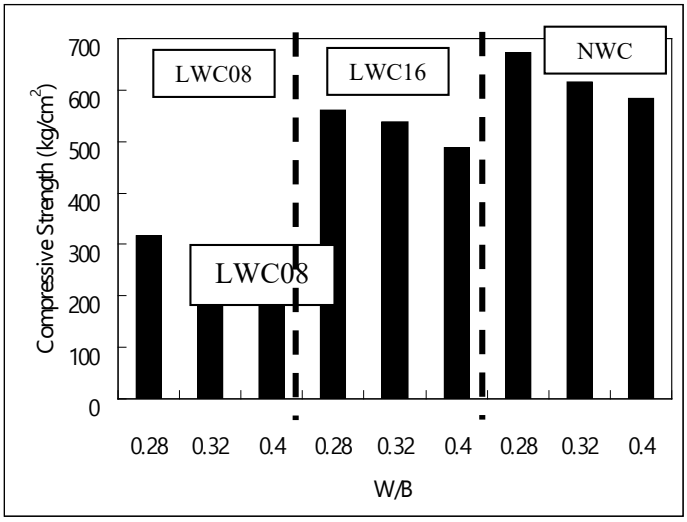

Figure 3. Compressive strength of l SSLAC at room temperature (25℃).

3.3 Ultrasonic pulse velocity

Lightweight aggregate particles have many pores and interfaces, and pulse transfer is subject to disturbance, so the pulse velocity is lower than that in normal-density concrete. The cement slurry and hydration product volumes decrease as the W/B ratio increases, the interfaces between the aggregates and paste are weak, there are more defects, and the ultrasonic pulse velocity development is influenced.

Figure 4 shows that the ultrasonic pulse velocity at various temperatures is 1552~3842 m/s, the W/B ratio and aggregate density increase and the ultrasonic pulse velocity decreases with the temperature. Figure 5 shows that R2 = 0.81~0.95 after regression of the ultrasonic pulse velocity and compressive strength data under various temperature effects; the two straight-line dependences are relatively close.

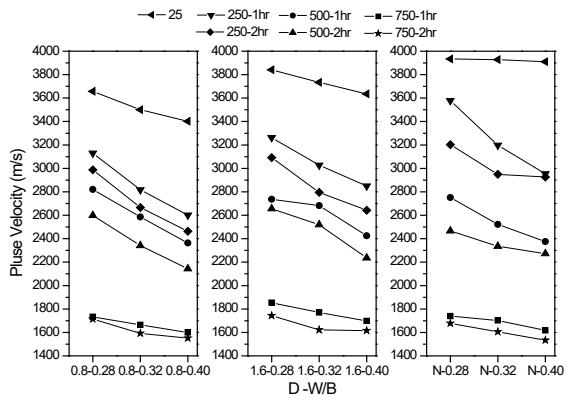

Figure 4. Flaw detection ultrasonic pulse velocity of SSLAC at different temperature

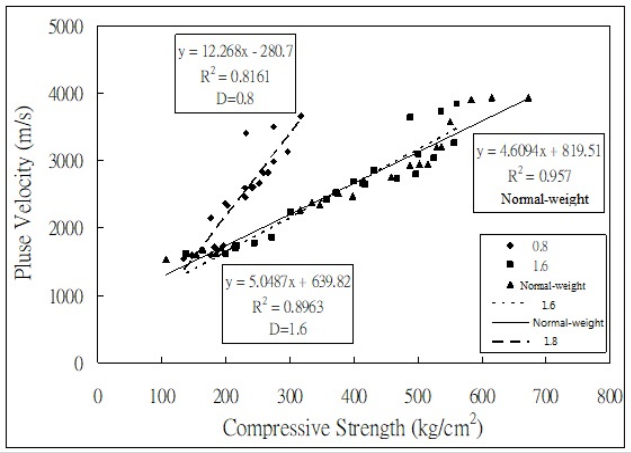

Figure 5. Correlation between flaw detection ultrasonic pulse velocity and compressive strength of SSLAC.

3.4 Electrical resistance

Figure 6 shows that the resistivity of the various groups is reduced by 3.2~5 kΩ-cm (19~23%) as the W/B ratio increases. The resistivity of SSLAC fired at 250°C for 1 h and 2 h decreases (10~30%). Lightweight aggregate concrete with a density of 1600 kg/m^3 and a low W/B ratio has the highest resistivity (increased by 5~12%). SSLAC with a density of 800 kg/m^3 has a large cement slurry volume, and many micro cracks disappear after hydration products are generated, so the surface resistivity is the lowest. The resistivity is reduced by 30~40% after having been fired at 500°C, and the interfacial strength decreases as the W/B ratio and temperature increase. As expansion inside the aggregate is inconsistent after having been fired at 750°C, there are more cracks, the interior of the concrete is more vulnerable, and the resistivity is lower.

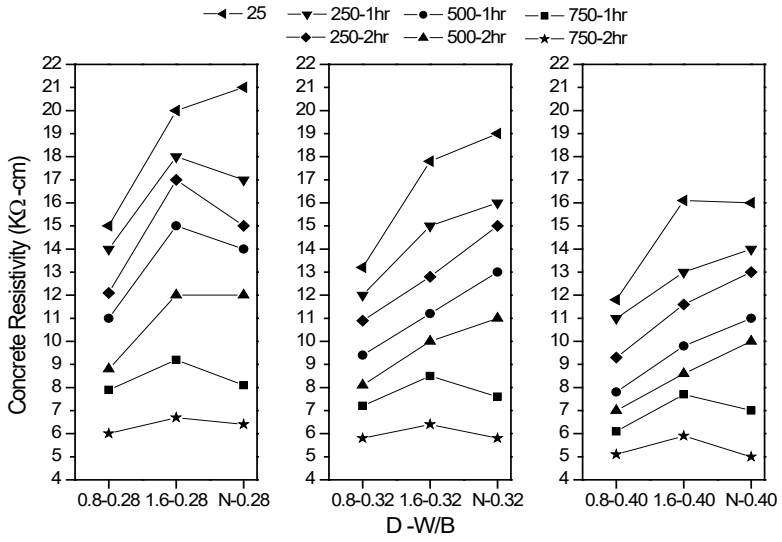

Figure 6. Surface resistivity of SSLAC under different aggregate densities with temperature change.

3.5 Sulfate resistance

Figure 7 shows SSLAC with a density of 800 kg/m^3 at a normal temperature and having been fired at 250°C. The weight loss rate is close to that of the SSLAC with a density of 1600 kg/m^3. The weight loss rate is higher (7%) at 500°C, and the SSLAC with a density of 800 kg/m3 at 750°C cannot be tested after the third cycle, thereby indicating that SSLAC with a higher aggregate density has a better erosion resistance. Moreover, at room temperature or high temperature, the weight loss of SSLAC induced by sulfate attack is larger than that of normal-weight aggregate concrete.

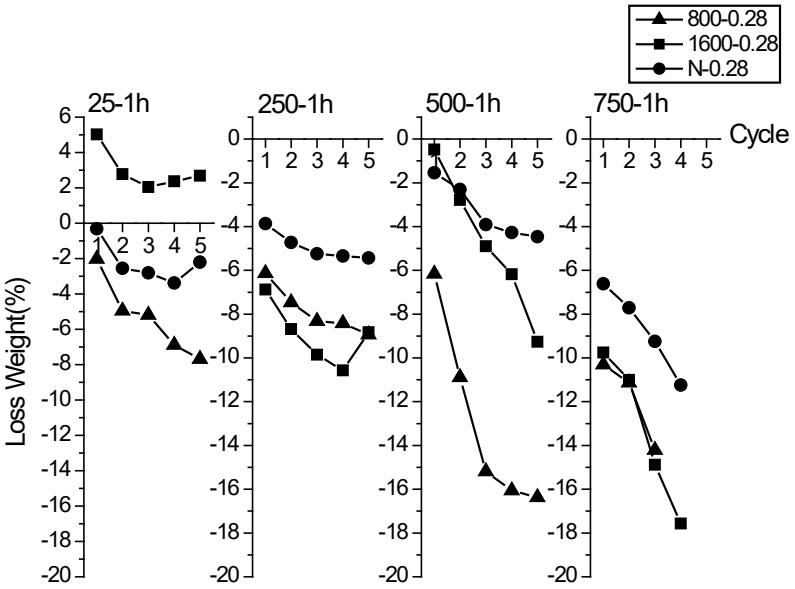

Figure 7. Weight loss from test for sulphate resistance of SSLAC under different aggregate densities with temperature change (W/B=0.28) .

3.6 Infrared thermography testing

Under the effect of a high temperature, the initial temperature of SSLAC is lower (62~71°C), validating the good thermal insulating properties of the lightweight aggregate particles.

Figure 8 shows normal-weight aggregate concrete and SSLAC. The initial temperature is lower, and the temperature decreases rapidly. The heat sinking rate of SSLAC is close to that of normal-weight aggregate concrete with time. Normal-weight aggregate concrete and SSLAC have similar heat sinking rates after heating.

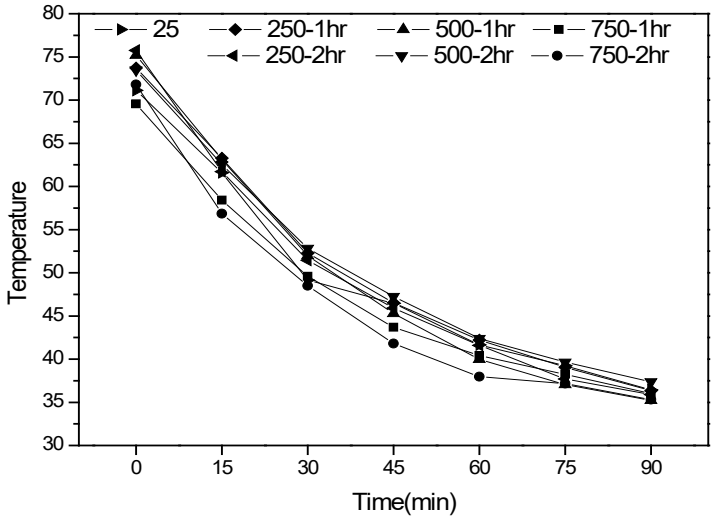

Figure 8. Temperature change of normal-weight aggregate concrete (NWC32) .

3.7 Microstructure

Figures 9 (1) and (2) show the crystalline phase of the SSLAC with an aggregate density of 800 kg/m^3; there are more initial monosulfate crystal and ettringite hydrates; the lightweight aggregate concrete with an aggregate density of 1600 kg/m^3 has a C-S-H gel with a compact structure. This result may be because the

aggregate density of 800 kg/m3 is lower; the aggregate is likely to float during mixing, and the cement slurry volume is increased to avoid floating of the aggregate, but the high paste content reduces the cement hydration rate; as a result, incomplete hydration occurs between the aggregates and cement, and the internal structure and strength of the concrete are influenced. Figure 9 (3) shows the crystalline phase of normal-weight aggregate concrete. It is observed that the C-S-H gel forms a continuous matrix with fewer distributed pores, and partial tabular monosulfate crystals and CH crystals are stacked, which makes the material more compact than SSLAC.

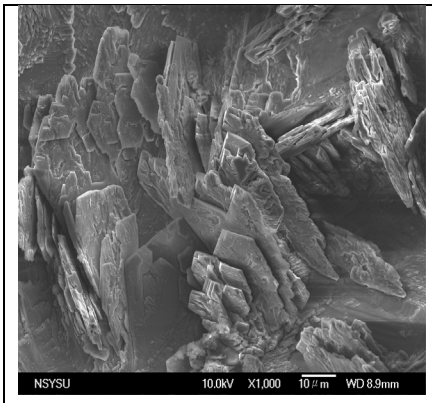

（1）LWC0832（×1000）

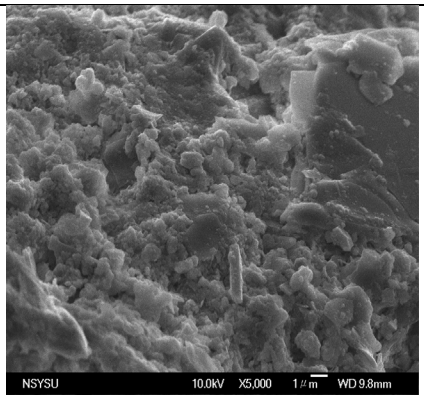

（2）LWC1632（×5000）

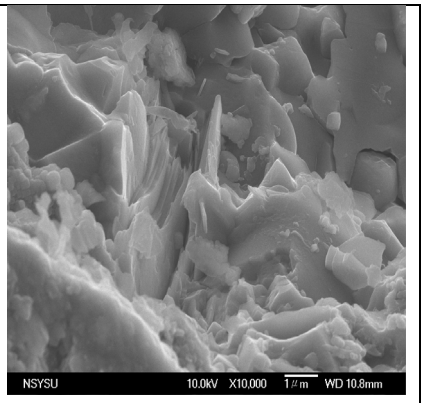

（3）NWC32（×10000）

Figure 9. SEM crystalline phase diagram of SSLAC (at the age of 28 days).

3.8 Interfacial cracking under the effect of a high temperature

Figure 10 shows SSLAC with the same W/B ratio (0.32) and aggregate density (1600 kg/m^3), and the micro crack width increases with the sintering temperature and delay time, proving that the temperature is one of the factors influencing the formation of cracks. Figures 10 (1) and (2) show that at a sintering temperature of 250°C, part of the C-S-H gel, the pore water and other components likely decompose, resulting in interfacial cracking. The crack width is only 86~106 μm, and the crack formation is not distinct.

Figures 10 (3) and (4) show that when the sintering temperature is 500°C, the C-S-H gel and other components have been completely decomposed, while a portion of the CH begins to decompose; the crack width increases (86~116 μm), and the interface between the aggregates and the paste is damaged and weakened. Figures 10 (5) and (6) show that when the sintering temperature is 750°C, all of the hydration products have decomposed, and cracking has increased substantially. The bonding between the aggregates and the paste is weakened. There are wider cracks, and the crack width is 265~398 μm. Higher temperatures and long heat energy transmission times will weaken the bonding between the aggregates and the cement paste, thereby influencing the concrete properties, the thermal properties, and the aggregate density, while the temperature and water content will influence the internal structure; these parameters are the primary causes for the high-temperature effect on concrete.

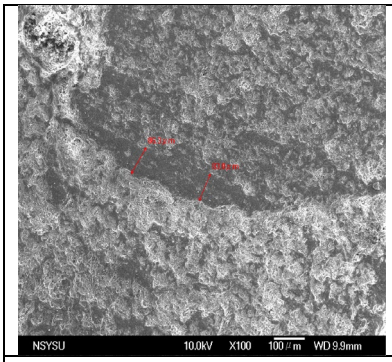

（1）250-1 LWC1632
（crack width 86.3；83）

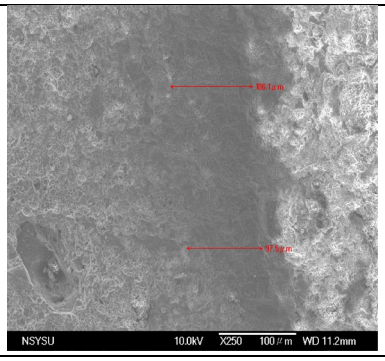

（2）250-2 LWC1632
（crack width 106.1；97.5）

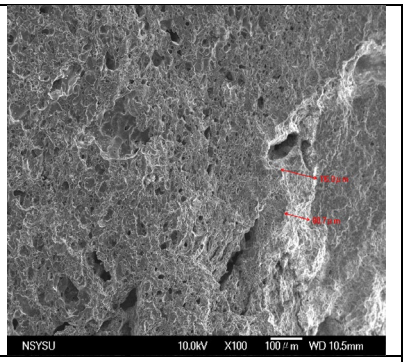

（3）500-1 LWC1632
（crack width 116；80.7）

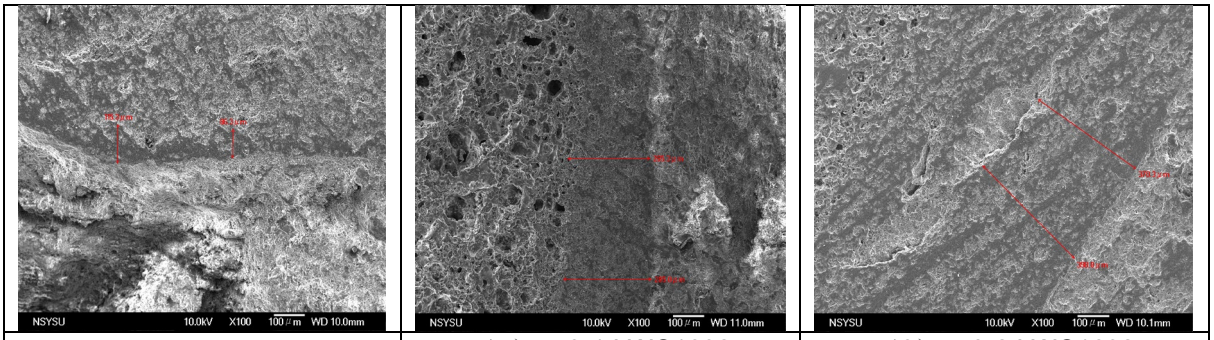

(4) 500-2 LWC1632 (crack width 115.3 ; 86.3)	（5）750-1 LWC1632 （crack width 265.3；285）	（6）750-2 LWC1632 （crack width 370.3；398）

Figure 10. SEM crystalline phase diagram of crack width of SSLAC with aggregate density 1600 kg/m3 under the effect of high temperature

4 CONCLUSIONS

(a) The slump and slump flow of SSLAC with a density of 800 kg/m3 are 265~280 mm and 570~630 mm, respectively, while those of SSLAC with a density of 1600 kg/m3 are 275~285 mm and 610~670 mm, respectively. The densified mixture design algorithm can result in high-flow SSLAC.

(b) For SSLAC with a density of 1600 kg/m3 at any high-temperature delay, the compressive strength at 750°C is higher than that of normal-weight aggregate concrete (31~54 kg/cm2), and the residual ratio is high (10~16%); the compressive strength (residual ratio) exceeds the reference value of 55~227 kg/cm^2 (4~40%).

(c) SSLAC has a lower ultrasonic pulse velocity than normal-weight aggregate concrete (86~92%) at day 28. The ultrasonic pulse velocity decreases by 349~399 m/s (8~10%) as the W/B ratio increases. The ultrasonic pulse velocity after heating as measured by the flaw detection ultrasonic meter is relatively reasonable, and R2 = 0.81~0.95 after regression of the ultrasonic pulse velocity and compressive strength data; these parameters have relatively similar straight-line dependences.

(d) Concrete with a low W/B ratio and an aggregate density of 1600 kg/m3 under the effect of a high temperature has a higher resistivity (5~12%); the resistivity after having been fired at a high temperature of 500°C is 30~40% lower, and the resistivity decreases as the W/B ratio increases. The resistivity is only 30~40% after having been fired ta 750°C.

(e) The initial temperature of lightweight aggregate concrete under the effect of a high temperature results in the highest heat sinking rate (lower than that of normal-weight aggregate concrete by 2~9°C), and the higher the temperature is, the more apparent the specimen delay time is. Lightweight aggregate concrete has a low thermal conductivity; when the temperature decreases, the aggregate structure results in a temperature difference.

(f) At 250°C, the hydration products decompose, micro cracks are formed, sulfate is formed internally, and the performance is influenced. Under the effect of a high temperature, SSLAC is subjected to sulfate attack, and the specimen notably collapses and flaking off occurs.

(g) SEM shows that a higher W/B ratio corresponds to a lower paste content, which requires more aggregates and causes a slower hydration. The concrete structure at a low W/B ratio is more compact, with fewer pores and a more complete hydration. At a high temperature and with increased time-lag action, the bonding between the aggregates and the cement paste is weakened, and the crack width is 86~398 μm, while the micro cracks will influence the concrete properties.

ACKNOWLEDGEMENTS

This is where one acknowledges funding bodies, etc. Note that section numbers are not required for Acknowledgements and References.

We appreciate the cooperation and efforts of all authors in producing the Proceedings. This will be a great congress following the tradition of our sponsoring organizations.

REFERENCES

Y.B.Ahn, J.G.Jang, H.K.Lee (2016).Mechanical properties of lightweight concrete made with coal ashes after exposure to elevated temperatures, *Cement and Concrete Composites*, 72, 27-38.

C.L.Hwang,A.T.Bui,K.L.Lin,C.T.Lo (2012).Manufacture and performance of lightweight aggregate from municipal solid waste incinerator fly ash and reservoir sediment for self-consolidating lightweight concrete, *Cement and Concrete Composites*,34(10),1159-1166 .

R. Ahmmad, M.Z. Jumaat, U.J. Alengaram, S. Bahri (2016), M.A. Rehman, H.B.Hashim,Performance evaluation of palm oil clinker as coarse aggregate in high strength lightweight concrete", *Journal of Cleaner Production*,112,566-574.

Sang-YeopChung,MohamedAbdElrahman,DietmarStephan,PaulH.Kamm (2018),The influence of different concrete additions on the properties of lightweight concrete evaluated using experimental and numerical approaches, *Construction and Building Materials*,189,314-322.

R. Yu, D.V. van Onna, P. Spiesz, Q.L. Yu, H.J.H (2016),Brouwers Development of ultra-lightweight fibre reinforced concrete applying expanded waste glass, *Journal of Cleaner Production*,112(1),690-701.

Lukic, M. Malesev, V. Radonjanin, V. Bulatovic(2017), Basic properties of structural LWAC based on waste and recycled materials", *Journal of Materials in Civil Engineering*, 29 (1),1-5.

Hongyu Zhou,Adam Brooks (2019),Thermal and mechanical properties of structural lightweight concrete containing lightweight aggregates and fly-ash cenospheres", *Construction and Building Materials*,98,512-526.

American Society for Testing and Materials. (2017), Standard Specification for Lightweight Aggregates for Structural Concrete". doi: 10.1520/C0330.

J.J. Lin (2002), View on dredging the silt in Taiwan area reservoirs, workshop on dredging reservoir silt, Taichung.

NataliaJunakova, JozefJunak (2017), Recycling of Reservoir Sediment Material as a Binder in Concrete, *Procedia Engineering*, 180, 1292-1297.

Said, A. Missaoui, Z. Lafhaj (2015),Reuse of Tunisian marine sediments in paving blocks: factory scale experiment",*Journal of Cleaner Production*,102,66-77.

JohnT.Kevern,QiweiC.Nowasell(2018),Internal curing of pervious concrete using lightweightaggregates,*Construction.and.Building.Materials*,161,229-235.

O.M.Jensen (2013), Use of superabsorbent polymers in concrete", *Concrete international*, 35 (1), 48-52.

M. Aslam, P. Shafigh, and M.Z. Jumaat (2016), Oil-palm by-products as lightweight aggregate in concrete mixture: a review, *Journal of Cleaner Production*, 126, 56-73.

F. Roberz, R.C.G.M. Loonen, P. Hoes, J.L.M. Hensen (2017),Ultra-lightweight concrete: energy and comfort performance evaluation in relation to buildings with low and high thermal mass,*Energy and Build*, 138,432-442.

S.Y. Chung, M.A. Elrahman, P. Sikora, T. Rucinska, E. Horszczaruk, D.Stephan (2017), Evaluation of the effects of crushed and expanded waste glass aggregates on the material,properties,of,lightweight,concrete,using,image-based,approaches ,*Materials*, 10(12),1354.

M.N.Hague, H.Al.Khaiat, O.Kayali (2004), Strength and, Durability of Lightweight Concrete, *Cement and Concrete Composites*, 26(4) pp.307-314.

H.Y. Wang, Y.N. Sheen, M.F. Hung (2010),Performance characteristics of dredged silt and high-performance lightweight aggregate concrete, *Journal of Computers and Concrete* ,7(1),53-62.

8th International Conference on the Application of Physical Modelling in Coastal and Port Engineering and Science
Dec. 9th - 12th, 2020, Zhoushan, China

EVALUATION OF THE ULTRASONIC PULSE VELOCITY OF ALKALI-ACTIVATED SLAG PASTES

CHIEN-CHIH WANG (1), HER-YUNG WANG (2), CHANG-CHI HUNG (3) *

[1] Department of Civil Engineering and Geomatics, Cheng Shiu University, Kaohsiung City, 83347, Taiwan; ccw@gcloud.csu.edu.tw

[2] Department of Civil Engineering, National Kaohsiung University of Sciences and Technology, Kaohsiung City, 80778, Taiwan; wangho@nkust.edu.tw

[3*] School of Architecture and Civil Engineering, Huizhou University, Huizhou, Guangdong, 516007, P.R. China; a0266@hzu.edu.cn

* Correspondence: a0266@hzu.edu.cn; Tel.: +886-7-735-8800

ABSTRACT

Coastal structures are prone to corrosion due to the intrusion of marine salt. Taiwan is located in the subtropics and is surrounded by the sea. For sustainable development, the development of environmentally friendly and economical material is worth encouraging. This study used different liquid-solid ratios and alkaline solutions as well as slag to produce pastes. Three liquid-solid ratios (L/S of 0.50, 0.55 and 0.60) and three alkali agent contents (N of 0.5%, 0.75% and 1.0%) are used in mixed proportions. The ultrasonic pulse velocity (UPV) are tested at the ages of 3, 7 and 28 days. The results show that the UPV increase with increasing alkali agent content and with age but decrease as the liquid-solid ratio increases. The UPVs for various alkali agent contents increase by 1.52-12.10 and 1.06-1.84 times, respectively, during aging from day 3 to day 28. Besides, the prediction models of the UPV of alkali-activated slag paste with alkali agent content are deduced in this study. According to the comparisons between the predicted values and the test results, the MAPE values of UPV are only 0.023-0.050%, respectively. Thus, the proposed analysis models achieve satisfactory forecasting accuracy for the UPV of alkali-activated slag pastes.

Keywords: paste; slag; alkali-activated; ultrasonic pulse velocity; prediction model

1 INTRODUCTION

Owing to the rapid industrialization and economic development during the century, overutilization of land will result in severe environmental damage and deterioration of the greenhouse. Therefore, it is an important environmental objective worldwide to reduce the atmospheric CO2 concentration of greenhouse gases (Chen, el al., 2010; Torres-Carrasco et al. 2015), and waste recycling in an environment with limited resources in recent years (Australian Government 2012; Bolden et al. 2013; Martínez-Barrera et al. 2016). CO2 emissions will also rapidly increase due to the significant growth of cement production. Chen et al. (2010) reported that the total CO2 emissions from the cement manufacturing industry account for 5-7% of the total global greenhouse gas emissions. Thus, to reduce the impact on the environment, cement consumption must be reduced. In concrete production, several techniques have been introduced for reducing CO2 emissions. Yang et al. (2013) reported that these technologies include the capture and storage of CO2 emissions and the reduction in the amount of clinker by replacing supplementary cementitious materials obtained from by-products such as fly ash and ground granulated blast furnace slag. Thus, alkali-activated inorganic polymer materials have become a developing trend in recent years. Alkali cementation is activated using an alkaline agent and industrial by-products such as slag and fly ash to achieve satisfactory economic and engineering performance and can be used as a green energy material to replace cement (Gu et al. 2015; Abdalqaderet. al. 2016; Ding et al., 2016; Ellis et al. 2016; Kim et al. 2017; Wang et al. 2014, 2015; Jeong et al. 2017). Wang et al. (2017, 2018) indicated that alkali cementitious material is a new type of environmentally friendly material, besides, it also has many excellent engineering performances, including high compressive strength, lightweight and low thermal conductivity.

Fly ash (FA) and ground granulated blast furnace slag (GGBFS) are the most frequently used raw materials in the production of alkali-activated binders. Aydin and Baradan (2014) reported that the activation process of the slag affected by some factors, including the chemical properties and phase compositions of the slag and the type and concentration of the activators. The property and composition of slags depend on the raw materials and the industrial process; hence, each slag reacts differently to the activation process. Therefore, before each

slag is applied, it is necessary to plan a research program for determining the most suitable type and amount of activator. Aydin and Baradan (2014) also indicated that sodium hydroxide and sodium silicate (water glass) are the most commonly used activators. Thus, for sustainable development and the reuse of waste materials, the applications of slag powder that is mixed with an alkali agent to replace some of the raw materials in concrete or cement mortar constitute a research topic that is worthy of study.

In this study, a series of ultrasonic pulse velocity (UPV) tests are conducted on alkali-activated slag pastes with three types of liquid-solid ratios and three different alkali agent contents. The engineering properties of an alkali-activated slag paste are discussed and a hyperbolic function is adopted to build predictive models for the UPV, as an evaluation reference for future studies.

2 EXPERIMENTAL PLAN

2.1 Test materials

This study tests general cement made by the Taiwan Cement Corp., which is Type I Portland cement according to ASTM C150. The cement was sealed with impervious plastic to ensure quality. GGBFS (Ground-granulated blast-furnace slag) is produced by the CHC Resources Corporation, and its properties conform to ASTM C989. The main chemical constituents are CaO (41.61%), SiO2 (33.47%) and Al2O3 (14.79%), as shown in Table 1. Sodium hydroxide solution is that 98% pure NaOH solid alkali is mixed with distilled water to prepare a 5 M NaOH solution, which is kept still for 24 hrs and then sealed in a clean acid- and alkali-resistant barrel. The chemical properties are shown in Table 2. Sodium silicate solution: this is the so-called “water glass.” The main constituents are 28-30% SiO2 and 9-10% Na2O, and it is a viscous, colorless and tasteless liquid. The chemical properties are shown in Table 3.

Table 1. The chemical properties of slag powder.

Oxide	Results (%)
SiO_2	33.47
Al_2O_3	14.79
Fe_2O_3	0.40
CaO	41.61
MgO	6.11
SO_3	0.65
L.O.I.	0.58
Sulfide sulfur	0.65

Table 2. The chemical properties of alkali-agent composition analysis.

Pilot project	Results (%)
NaOH	98.2
$NaCO_3$	0.165
NaCL	0.0135
Fe	0.0004

Table 3. The chemical properties of alkali metal silicate solution.

Element	Weight ratio (%)
SiO_2	28-30
Na_2O	9-10
Fe	0.02
Water-insoluble matter	0.2
SiO_2/Na_2O	2.8-3.3

2.2. Test variables and method

In this study, the specimens were cast with variable liquid-solid ratios (L/S=0.50, 0.55 and 0.60) of the sodium silicate solution with the alkali agent content (N) equal to 0.5%, 0.75% and 1.0%, respectively. The amount of alkali agent is the ratio of the equivalent of sodium oxide (Na2O) to the weight of slag in sodium

hydroxide (NaOH) solution. The L/S is the ratio of liquid (alkaline solution) to solid (slag) by weight. The mix proportion unit weights are shown in Table 4. In the specimen manufacturing process, the NaOH is mixed thoroughly with the sodium silicate solution and kept still. The GGBFS is mixed with the alkali solution and then poured into a 5 cm × 5 cm × 5 cm specimen mold. The forms are removed 24 hours after making the sample and the specimens are continuously placed and cured at room temperature (23-25°C). The compressive strength and ultrasonic pulse velocity (UPV) are tested at the ages of 3, 7 and 28 days. Ultrasound wave velocity can be transmitted through solid or liquid, and the propagation time will be prolonged when cracks or voids are encountered in the process of ultrasonic wave velocity transmission. Therefore, it can be used to judge the compactness and internal defects of the internal structure of the test body, as a basis for non-destructive testing. The experimental results are shown in Table 5.

Table 4. The properties of alkali-activated pastes mixture ratio.

Unit:kg/m^3

Liquid-soild ratio (L/S)	Alkali-agent (%) (N)	Slag powder	Sodium silicate solution (water glass)	Sodium hydroxide (NaOH)
0.50	0.50	1377	640	49
	0.75	1371	613	73
	1.00	1365	586	97
0.55	0.50	1312	675	46
	0.75	1306	649	69
	1.00	1301	623	92
0.60	0.50	1252	707	44
	0.75	1247	682	66
	1.00	1242	657	88

Table 5. Ultrasonic wave velocity of alkali-activated slag paste.

Unit: m/s

Liquid-soild ratio (L/S)	Alkali-agent (%) (N)	Days		
		3	**7**	**28**
0.50	0.50	2105	3876	3876
	0.75	3779	3876	4032
	1.00	3876	3980	4135
0.55	0.50	2078	2795	3764
	0.75	2196	3876	3901
	1.00	3828	3980	4032
0.60	0.50	1996	2102	3514
	0.75	2105	3597	3876
	1.00	3395	3779	3980

3 RESULTS AND DISCUSSION

In general, the Ultrasonic pulse velocity (UPV) is closely related to the compressive strength of concrete, mortar, and paste. The higher the compactness inside the specimen, the higher the compressive strength and the higher the ultrasonic pulse velocity. The test results show that the UPV increases with increasing alkali agent content (N) and with age but slightly decreases as the liquid-solid ratio (L/S) increases, as shown in Figure 1. This trend is the same as that of the compressive strength. When the L/S=0.50, the UPV is approximately 3870-4130 m/s for the curing age of 28 days. When the alkali agent contents are 0.75% and 1.0%, the UPVs are 3880-4030 m/s and 3980-4140 m/s, respectively. Besides, when the L/S=0.50, the UPV at the age of 28 days is higher than at 3 days by 1.06-1.84 times. The UPV has the same trend for other liquid-solid ratios. The UPV at the age of 28 days is higher than that at 3 days by 1.07-1.84 and 1.13-1.80 times for L/S values of 0.55 and

0.60, respectively. Thus, the change of UPV is not apparent with increasing liquid-solid ratio; however, an increase in UPV with increasing alkali agent content is observed, as shown in Figure 1.

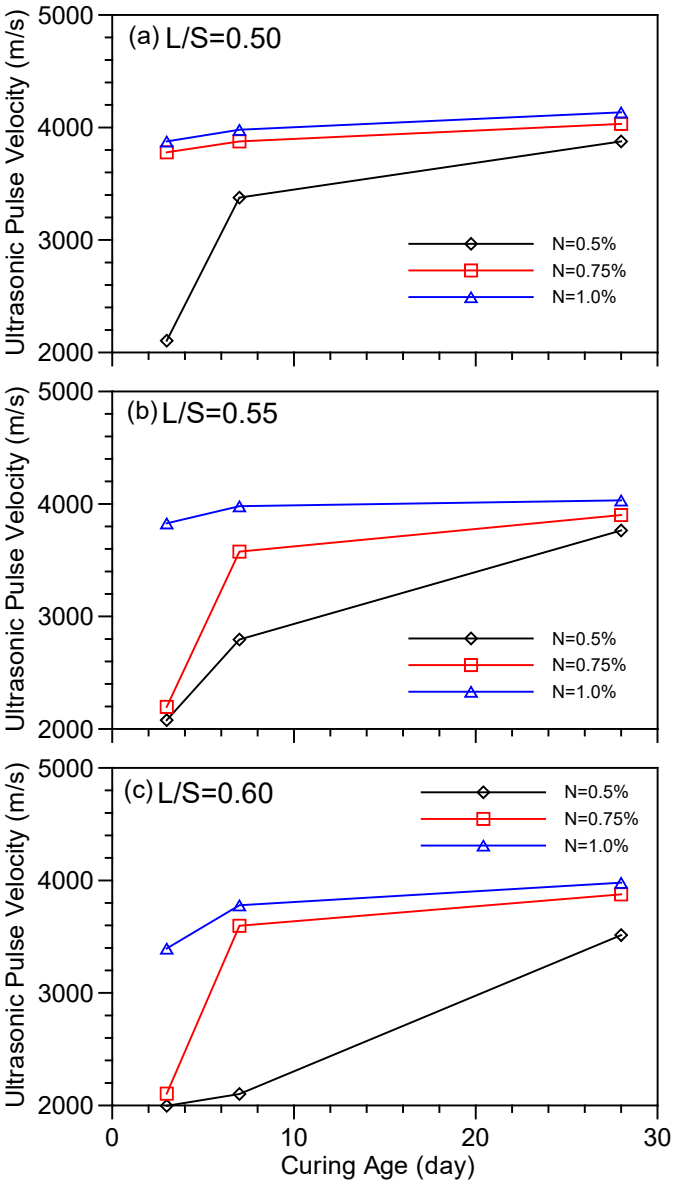

Figure 1(a)(b)(c). The relationship between the UPV and the curing time.

4 DEVELOPMENT OF PREDICTION MODELS AND COMPARISON BETWEEN THE ANALYSIS AND TEST RESULTS

Wang et al. (2017) indicated that for the ultrasonic pulse velocity (UPV) and age relationship curve for an alkali-activated mortar material that contains recycled waste glass, a hyperbolic function could be used for simulation analysis when the translation of the coordinate axes from the origin point was considered, as shown in Eq. (1).

$$V_s = (k + \gamma G) + \frac{(t - t_0)}{(a_{v1} + a_{v2}G + a_{v3}G^2) + (b_{v1} + b_{v2}G + b_{v3}G^2)(t - t_0)} \quad (1)$$

where t is the age, t_0 is the initial reference time, G is the glass sand replacement, and a_{v1}, a_{v2}, a_{v3}, b_{v1}, b_{v2}, b_{v3}, k and γ are model coefficients.

In this study, the characteristics of UPV versus curing age have a similar tendency to the compressive strength. The early UPV also increased rapidly in some mix proportions, as shown in Figure 1. Thus, the prediction formula of Eq. (1) could not be directly applied to the alkali-activated slag paste and should be used only after being appropriately modified. According to the method of translation of the coordinate axes, the relationship between UPV and curing age also has the trend of a hyperbolic function when the liquid-solid ratio is 0.55, as shown in Figure 2. The same trend is observed for other liquid-solid ratios. Hence, the UPV could be evaluated by Eq. (2).

The values of parameters a_v and b_v are established by hyperbolic function regression, as shown in Figures 3(a) and 3(b). The figures show the relationship between the value of parameter a_v and the alkali agent content (N) for different liquid-solid ratios. The trend of the value of parameter a_v with the alkali agent content is not consistent for different liquid-solid ratios. However, the relationship follows an approximately quadratic polynomial function, which is expressed as Eq. (3). The relationship between parameter b_v and the alkali agent content also increases according to an approximately quadratic polynomial function, which is expressed as Eq. (4). Furthermore, Figure 4 shows the ultrasonic pulse velocity V_{s0} that corresponds to the initial reference time (t_0) also increases nonlinearly with the alkali agent content and follows a quadratic polynomial function, which is expressed as Eq. (5). Thus, from Eqs. (2) to (5), the ultrasonic pulse velocity, which is denoted as V_s, can be expressed as Eq. (6) and the model parameters are shown in Table 6.

$$V_s - V_{s0} = \frac{(t - t_0)}{a_v + b_v \times (t - t_0)} \tag{2}$$

$$a_v = a_{v1} + a_{v2}N + a_{v3}N^2 \tag{3}$$

$$b_v = b_{v1} + b_{v2}N + b_{v3}N^2 \tag{4}$$

$$V_{s0} = c_{v1} + c_{v2}N + c_{v3}N^2 \tag{5}$$

$$V_s = (c_{v1} + c_{v2}N + c_{v3}N^2) + \frac{(t - t_0)}{(a_{v1} + a_{v2}N + a_{v3}N^2) + (b_{v1} + b_{v2}N + b_{v3}N^2) \times (t - t_0)} \tag{6}$$

where t is the age; t_0 is initial reference time, which is 3 days in this study; N is the alkali agent content; and a_{v1}, a_{v2}, a_{v3}, b_{v1}, b_{v2}, b_{v3},c_{v1}, c_{v2}, and c_{v3} are model coefficients.

Figure 5 shows a comparison between the UPV assay values and test results for different liquid-solid ratios at different ages that are analyzed by Eq. (6). The analysis results show that the calculated values are also close to the test results. The MAPE values are as follows: when L/S=0.50, MAPE=0.023%; when L/S=0.55, MAPE=0.006%; and when L/S=0.60, MAPE=0.050%, as shown in Figure 5(c). Thus, this proposed model also exhibits excellent predictive ability.

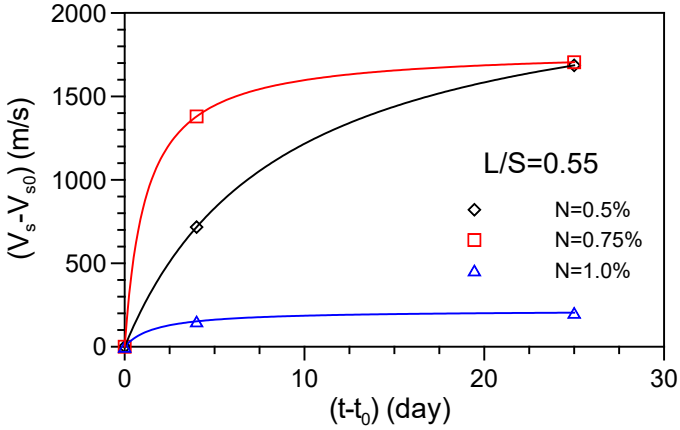

Figure 2. Relationship between the UPV and curing time after translation of coordinate axes.

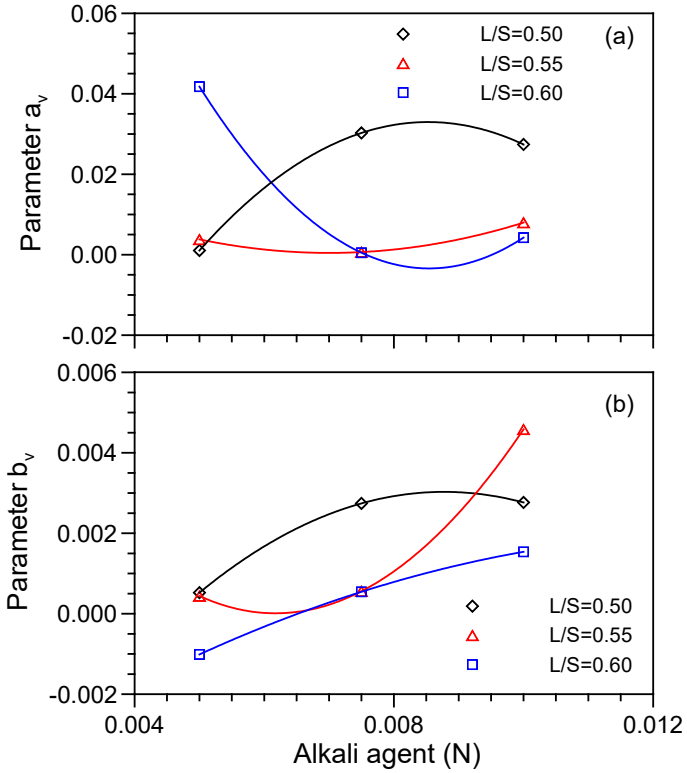

Figure 3(a)(b). The parameter characteristics versus alkali agent content for the UPV prediction model.

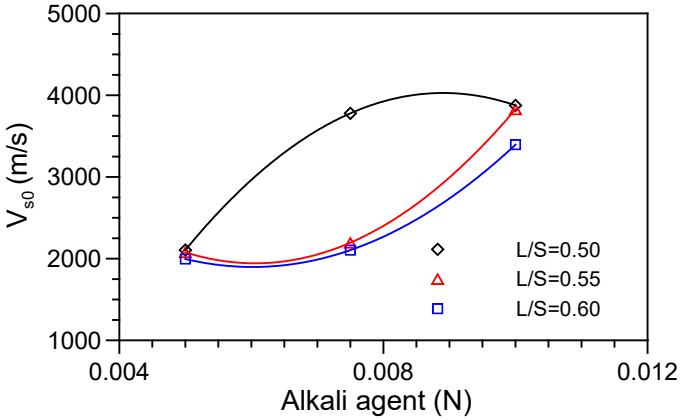

Figure 4. Relationship between the UPV corresponding to the initial reference time and alkali agent content.

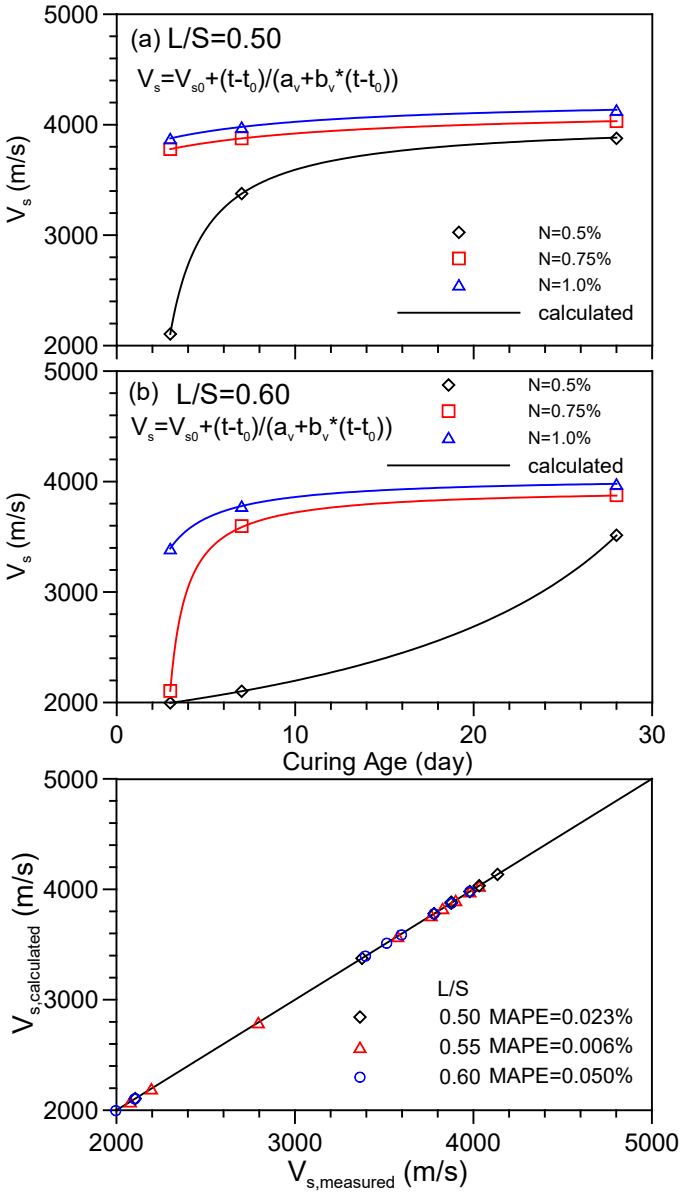

Figure 5 (a)(b)(c). Comparison of the UPV and the MAPE values for the calculated and tested results.

Table 6. Coefficients of the ultrasonic pulse velocity model

L/S	a_{v1}	a_{v2}	a_{v3}	b_{v1}	b_{v2}	b_{v3}	c_{v1}	c_{v2}	c_{v3}
0.50	-0.1536	43.767	-2566.6	-0.0105	3.0846	-175.74	-5974	2.2476×106	-1.2616×108
0.55	0.0416	-11.751	839.0	0.0119	-3.8551	312.24	6384	-1.4668×106	1.2112×108
0.60	0.2595	-61.556	3603.4	-0.0058	1.1856	-45.02	5321	-1.1374×106	9.4480×107

5. CONCLUSION

(a) The UPV increases with increasing alkali agent content and with age but decreases as the liquid-solid ratio increases. Moreover, the compressive strength and UPV for various alkali agent contents are increased by 1.52-12.10 and 1.06-1.84 times during the aging from day 3 to day 28, respectively.

(b) The test results show that the UPV increases significantly with increasing alkali agent content, especially for lower liquid-solid ratios. A possible cause of this phenomenon is that the alkali sodium silicate solution induces pozzolanic reactions of the slag, which results in the formation of a C-S-H gel, which causes the strength to still increase with age. Thus, the development of strength and UPV with higher alkali agent content is faster than when lower alkali agent content is utilized.

(c) The prediction models for the UPV of alkali-activated slag paste according to alkali agent content are deduced based on a hyperbolic function in this study. In addition, another compressive strength prediction model that is based on the UPV is proposed. This evaluation method is helpful for the safety assessment of structures with similar mix proportions using nondestructive testing of UPV.
(d) According to the comparisons between the simulations predicted values (calculated by Eqs. (6)) and the test results, the MAPE values of UPV is only 0.023-0.050%, respectively. The MAPE values are much lower than 10%. Thus, the proposed simulation analysis models achieve satisfactory forecasting accuracy for the alkali-activated slag paste.

REFERENCES

Chen, C.; Habert, G.; Bouzidi, Y.; Jullien, A. (2010). Environmental impact of cement production: Detail of the different processes and cement plant variability evaluation. *J. Clean. Prod.* 18(5), 478-485.

Torres-Carrasco, M.; Rodriguez-Puertas, C.; Alonso, M. M.; Puertas, F. (2015). Alkali activated slag cements using waste glass as alternative activators: Rheological behavior. Boletin De La Sociedad Espanola De, Ceramica Y Vidrio. , 54, 45–57.

Australian Government, (2012). Construction and demolition waste guide-recycling and re-use across the supply chain; Dept. Sustainability, Environment, Water, Population and Communities, Australian Government.

Bolden, J.; Abu-Lebdeh, T.; Fini, E. (2013). Utilization of recycled and waste materials in various construction applications. Amer. *J. Envi. Sci.*, 9(1), 14-24.

Martínez-Barrera, G.; González-Rivas, N.; Vigueras-Santiago, E.; Martínez-López, A.; Tello-González, J. A.; Menchaca-Campos, C. (2016). Waste and recycled materials and their impact on the mechanical properties of construction composite materials. In Composites from Renewable and Sustainable Materials; Chapter 9, 161-176.

Yang, K.H.; Jung, Y.B.; Cho, M.S.; Tae, S.H. (2015). Effect of supplementary cementitious materials on reduction of CO2 emissions from concrete. *J. Clean. Prod.* 103, 774-783.

Yang, K.H.; Song, J.K.; Song, K.I. (2013). Assessment of CO2 reduction of alkali-activated concrete. *J. Clean. Prod*. 39, 265-272.

Aydin, S.; Baradan, B. (2014). Effect of activator type and content on properties of alkali-activated slag mortars, *Composites: Part B*, 57, 166–172.

Abdalqader, A.F.; Jin, F.; Al-Tabbaa, A. (2015). Characterization of reactive magnesia and sodium carbonate-activated fly ash/slag paste blends. *Constr. Build. Mater*, 93, 506–513.

Gu, Y.M.; Fang, Y.H.; You, D.; Gong, Y.F.; Zhu, C.H. (2015). Properties and microstructure of alkali-activated slag cement cured at below- and about-normal temperature. *Constr. Build. Mater*. 79, 1–8.

Abdalqader, A.F.; Jin. F.; Al-Tabbaa, A. (2016). Development of greener alkali-activated cement: utilization of sodium carbonate for activating slag and fly ash mixtures. *J. Clean. Prod.* 113, 66-75.

Ding, Y.; Dai, J.G.; Shi, C.J. (2016). Mechanical properties of alkali-activated concrete: A state-of-the-art review. *Const. Build. Mater*. 127, 68–79.

Ellis, K.; Silvestrini, R.; Varela, B.; Alharbi, N.; Hailstone, R. (2016). Modeling setting time and compressive strength in sodium carbonate activated blast furnace slag mortars using statistical mixture design. *Cement and Concrete Composites*, 74, 1-6.

Kim, G.M.; Khalid, H.R.; Kim, H.J.; Lee, H.K. (2017). Alkali activated slag pastes with surface-modified blast furnace slag. *Cement and Concrete Composites*, 76, 39-47.

Wang, W.C.; Wang, H.Y.; Lo, M.H. (2014). The engineering properties of alkali-activated slag pastes exposed to high temperatures. *Constr. Build. Mater*. 68, 224-229.

Wang, W.C.; Wang, H.Y.; Lo, M.H. (2015). The fresh and engineering properties of alkali-activated slag as a function of fly ash replacement and alkali concentration. *Constr. Build. Mater*. 84, 224-229.

Jeong, Y.; Yum, W.S.; Jeon, D.; Oh, J.E. (2017). Strength development and microstructural characteristics of barium hydroxide-activated ground granulated blast furnace slag. *Cement and Concrete Composites*, 79, 34-44.

Wang, C.C.; Wang, H.Y., Chen, B.T.; Peng, Y.C. (2017). Study on the engineering properties and prediction models of an alkali-activated mortar material containing recycled waste glass. *Constr. Build. Mater.* 132, 130-141.

Wang, C.C.; Chen, T.T.; Wang, H.Y.; Huang, C. (2014a). A predictive model for compressive strength of waste LCD glass concrete by nonlinear-multivariate regression. *Comput. Concrete*, 13(4), 531-545.

Wang, C.C., Wang, H.Y.; Huang, C. (2014b). Predictive models of hardened mechanical properties of waste LCD glass concrete. *Comput. Concrete*, 14(5), 577-597.

8th International Conference on the Application of Physical Modelling in Coastal and Port Engineering and Science
Dec. 9th - 12th, 2020, Zhoushan, China

COUPLING SIMULATION OF WAVES AND STORM SURGES IN A WAVE-CURRENT FLUME

PAN JUNNING(1), CHEN MAOWEN(2), SUN TIANTING(3), WANG DENGTING(4), SUN ZHONGBIN(5)

(1,2,3,4,5) State Key Laboratory of Hydrology-Water Resources and Hydraulic Engineering, Nanjing Hydraulic Research Institute, Nanjing, China

e-mail: jnpan@nhri.cn

ABSTRACT

The coupling simulation technology of waves and storm surges is introduced, which can provide a new physical modelling method for wave-storm surge co-action on seawalls and disaster evaluation in coastal areas. In order to simulate the combined effect of storm surges and waves, the wave flume was modified to simulate water level change by installing a tide generator. The wave and storm surge processes were discretized into many time segments, and wave parameters of each time segment were calibrated at the corresponding water level. With wave-maker and tide generator controlled simultaneously, the dynamic coupling simulation of waves and storm surges was realized by simulating wave and water level variation process synchronously and continuously. In an application example, the storm surge and wave process of Typhoon Winnie was simulated in the wave flume, and the measured data of water level, wave parameters and wave spectra in the model test were compared with the target values. It is shown that the simulation results of this coupling simulation method are of relatively high accuracy. The wave overtopping of a typical seawall section in Beilun area under the dynamic coupling simulation and the fixed water level were measured and compared.

Keywords: storm surges, waves, coupling simulation, wave overtopping

1 INTRODUCTION

In recent years, global climate change causes the trend of increasing extreme ocean disasters, such as storm surges and huge typhoon waves. As storm surges usually occur with a rough sea, it is important to research on the co-action of storm surges and waves on coastal structures.

Schüttrumpf et al. (2001) studied the relationship between overflowing and overtopping in the case of storm surge and wave coaction, and added the wave-only overtopping and surge-only overflow discharge to estimate the combined wave and surge overtopping discharge based on their laboratory tests. Reeve et al. (2008) studied overflowing and overtopping considering the coupling effect of storm surge and wave by use of a numerical wave tank based on the RANS equation, and developed equations for dimensionless average discharge of combined wave and surge overtopping. Suzuki et al. (2014) analyzed hydraulic characteristics of overflowing and overtopping under combined action of storm surge and wave based on N-S equations by using the VOF numerical wave tank. ASCE (2015) explored inner slope erosion characteristics of seawall in the case of storm surge and wave coaction. Hughes (2008), Li et al. (2012) and Pan et al. (2013) studied on combined action of storm surge and wave on roller-compacted concrete (RCC), articulated concrete block (ACB) and high-performance turf reinforced mat (HPTRM). However, most researches on coupling action of storm surge and wave on seawall using constant water level, ignoring the effects of water level variation of storm surges. Van Gent et al. (2016) carried out physical model tests on the seawall erosion mechanism considering water level change of storm surges in a wave flume. Although storm surge level hydrograph used in the experiment is ladder-shaped rather than continuously varying, it is shown by the model test results that the water level variation of storm surges plays an important role in siltation and scour on the front slope of seawall. Chen et al. (2019) realized the coupling simulation of wave and tide in the wave flume by using wave generator and tide generating equipment to generate wave and tide continuously. So it is necessary to simulate actual variation process of storm surge and wave in a wave tank to consider the coupling effects of storm surges, astronomical tides and waves.

2 COUPLING SIMULATION TECHNIQUE OF WAVES AND storm surges

1.1 2.1 Instruments and equipment

Wave and tidal coupling simulation was carried out in the long wave tank of State key laboratory of hydrology-water resource and hydraulic engineering (see Figure 1). This tank can produce waves, current and

wind simultaneously. The tank is 175m long, 1.2m wide and 1.8m deep and equipped with a piston irregular wave generator produced by Nanjing Hydraulic Research Institute. The working section of the tank was divided into two portions, one of 0.6m width used to place the model section and conduct model test, and the other portion used for diffusing the secondary reflection wave of the wave paddle.

In order to simulate the combined effect of storm surges and waves, the wave tank was modified to simulate tidal level change by controlling the tail gate height to adjust the variation of water level. The schematic diagram of wave tank is shown in Figure 2.

Figure 1. Wave tank

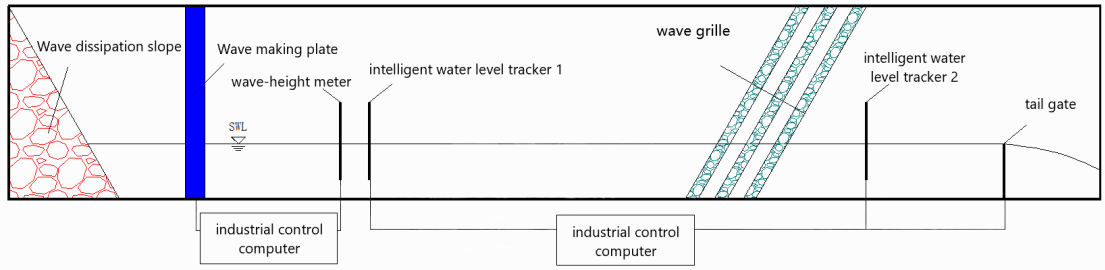

Figure 2. A schematic diagram of wave tank

The storm surge measurement and control system is composed of the tail gate, electric motor, water level control system and water level tracker, as shown in Figure 3.

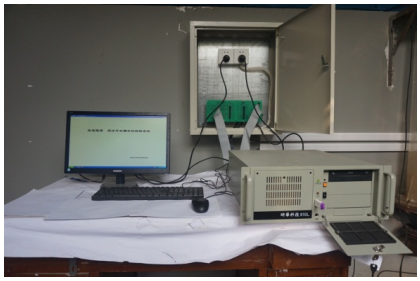

(a) Water level control system

(b) Electric motor

(c) Water level tracker

Figure 3. Tide generator

1.2 2.2 Coupling simulation technique

First, the water level process was inputted to the computer to generate storm surge in the flume and the water level data of the control station was measured and compared with the given value, to obtain a difference △h. The deviation △h was made to approach zero by controllable speed governor driving a DC servo motor to adjust the opening degree of the tail gate to control the variation of water level. The water level process was calibrated and the mean error of the simulated water level was controlled within 2mm (model value).

When simulating the wave process, the storm surge and wave processes were discretized, i.e., water levels and waves were divided into several small segments. In each time segment, the water level and wave conditions were considered nearly constant, and wave parameters of different time segments were calibrated at the corresponding water levels. Then the calibrated wave generation file elements were connected to get the whole continuous wave generation file, in which wave parameters vary with the water level during the simulation period. In the process of calibration, wave height and period simulation results were measured and analyzed in real time by wave-height meter, and compared with the target value, the mean error of the measured value of wave height and period and the target value were controlled within 5%.

Finally, storm surge simulation and wave simulation must be synchronized. In the experiment, the wave-maker was used to produce the wave with the connected wave generation file, and meanwhile the tide

generation system was utilized to adjust the water level, so as to realize the synchronous change of water level and wave. In the process of coupling simulation, it is necessary to monitor the water level in real time. The multi-point moving average method is used to calculate the water level based on the data collected by the water level tracker.

3 APPLICATION EXAMPLE

3.1 The coupling simulation of storm surge and wave

The study area is located at Beilun coast in Ningbo, Zhejiang province, which is severely affected by storm surge disasters in China. The typical seawall section of the study area shown in Figure 4 was selected as the experimental section. The thickness of concrete panel on the land side is 16cm. The core material in seawall section is 10~100kg block stone, which is simulated according to gravity similarity and considering seepage similarity. The physical model experiment was conducted to simulate the dynamic process of the co-action of storm surges, waves and tides on the seawall. The model scale was set at 1:16.

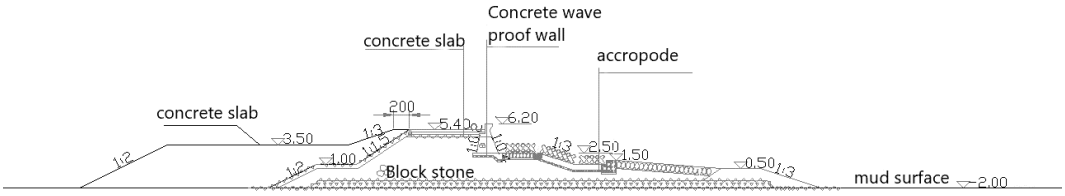

Figure 4. Typical seawall section in Beilun, Ningbo

The Institute of Oceanology Chinese Academy of Sciences calculated wave and storm surge process of Typhoon Winnie (No. 9711), which was the most severe storm surge in Ningbo area in the past 100 years. Figure 5 shows the calculated variation procedures of the storm surge water level, the significant wave height and the mean wave period at the site during Typhoon Winnie and the red frame range in Figure 5 is the simulated time period selected in this example.

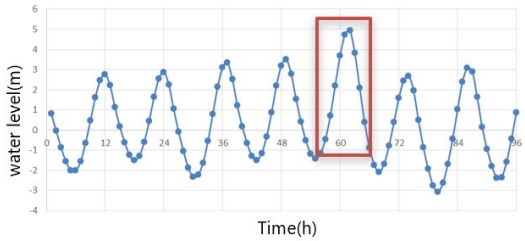

(a) Water level

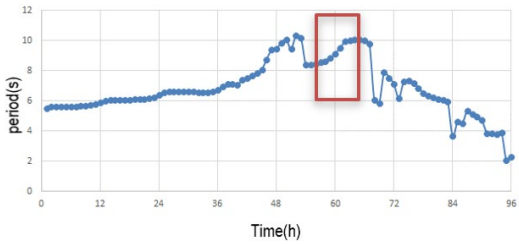

(b) Mean wave period

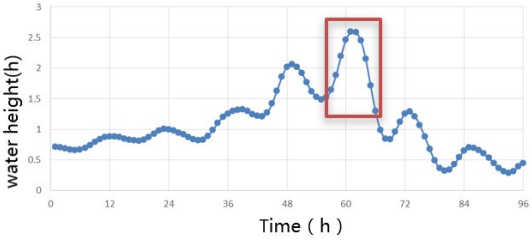

(c) Significant Wave height

Figure 5. Water level, significant wave height and mean wave period procedure of Typhoon Winnie

In this experiment, the wave and water level procedures were divided into many segments of 20-minute interval in prototype (see Figure 6). The calibrated wave-making files of all segments were connected into a total wave generation file, which was applied to simulate the variation of wave parameters along with the continuously changing water level during the modelling period (9 hours).

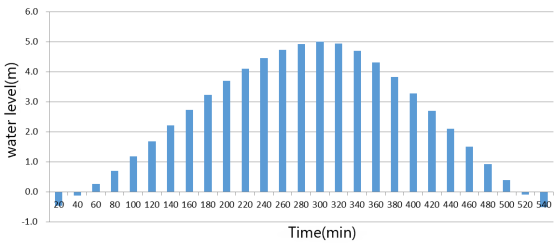

(a) Water level

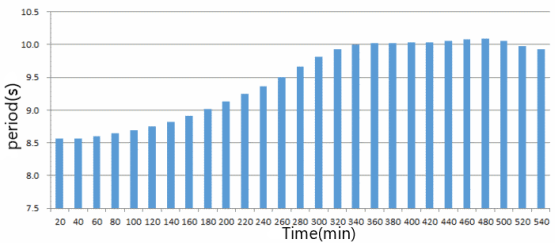

(b) Mean wave period

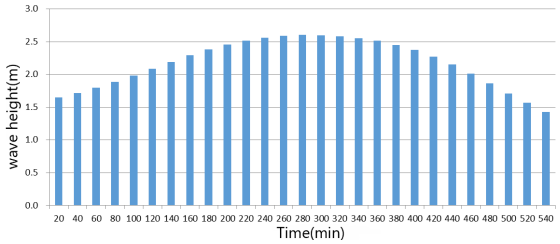

(c) Significant Wave height

Figure 6. The discrete map of water level, significant wave height and mean wave period

As the wave tank is 175 meters long, there may be a time lag in water level variation between the middle and the end of the tank. Therefore, water level meters were set in the vicinity of the tide generation system and in the middle of the tank respectively. The water level data measured by the water level meter near the tail gate was used for the tide generation system to control the opening of the tail gate, so as to ensure the water level of the tank varying according to the preset process. The water level meter in the middle of the tank was used to test whether the water level process at the model position met with the target one. The test shows that the hydrographs of the two water level meters were in good agreement, and the tide generator could well simulate the required changing process of tidal level. Figure 7 shows the comparison between simulation results and the target process of water level. The mean error of storm surge process simulation is -0.41mm (model value), which meets the accuracy requirement.

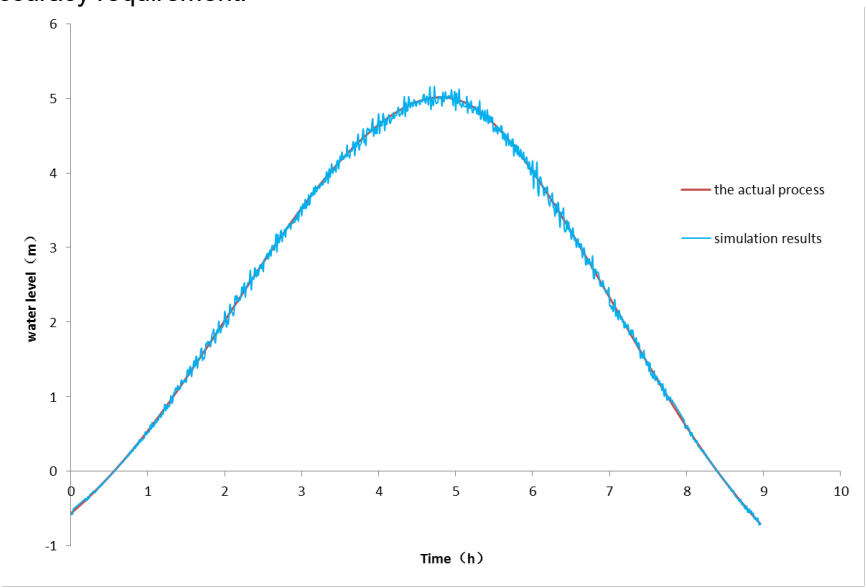

Figure 7. The comparison between simulation results and the target process of the storm surge water level

The simulation results of significant wave height and mean wave period at different water levels are shown in Figure 8. It can be seen from the Figure 8 that the mean error of the significant wave height and the mean wave period compared with the target values at different times in the test process are 0.98% and -0.29% respectively, which meets the precision requirements. Figure 9 shows the comparison between the measured wave spectra in the model test and the target ones in 220-240 minutes and 320-340 minutes respectively. It can be seen from the Figure 9 that the maximum relative error of spectral variance does not exceed 10%. In the frequency domain, the wave-tide coupling system can simulate the target wave process well. In the period of relatively large change of water level (eg. 320-340 minutes), the result of spectral simulation is relatively different from the target value affected by the change of water level.

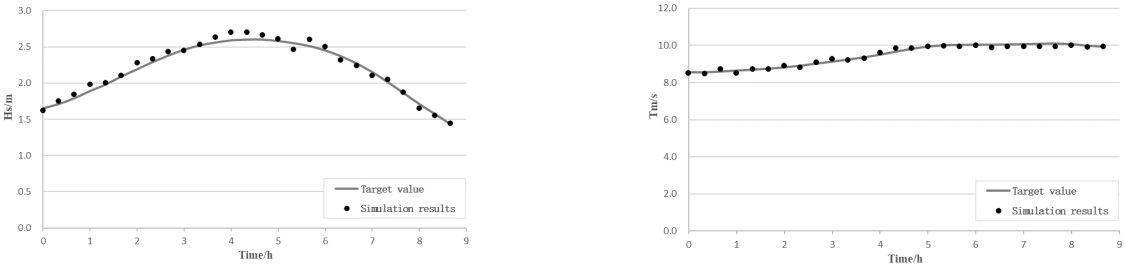

(a) Significant wave height (b) Mean wave period

Figure 8. Simulation results of significant wave height H_S (m) and mean wave period T_m (s)

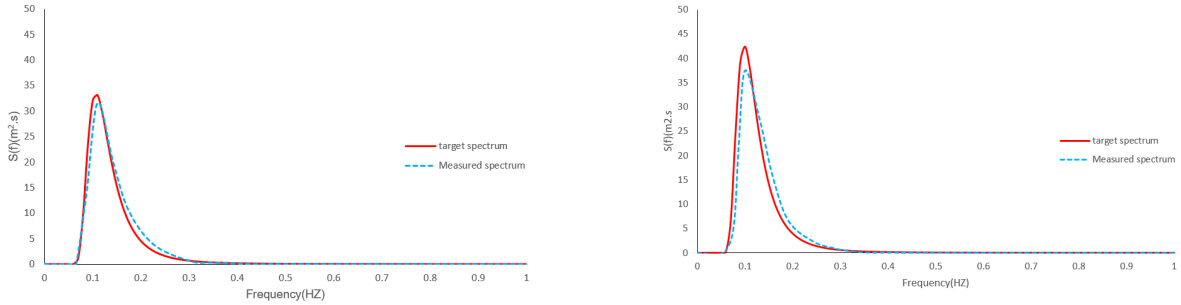

(a) 220-240 minutes (b) 320-340 minutes

Figure 9. The comparison of the simulated and the target spectra

During the experiment, according to the pre-set wave and tidal level process, the wave maker and tide generator generated synchronous storm surge and waves simultaneously. Figure 10 illustrates the superposed water level process of waves and storm surge. The moving average method was adopted to the wave surface elevation data collected from the wave-height meter to obtain a smooth storm surge water level hydrograph, and compared it with the target water level process and the simulation results measured by water level meter near the tail gate (Water level tracker 2 in Figure 2). The comparisons are shown in Figure 11. The mean errors of simulated water level calculated with moving average method and measured directly by water level tracker 2 are -1.4mm and -0.4mm respectively (model value), which meet the accuracy requirement.

After coupling, the simulation results of significant wave height H_S (m) and mean wave period T_m (s) are obtained. The errors between the measured wave parameters and the target values were controlled within 5% in accordance with the test accuracy requirement (see Table 1).

To sum up, the means of segmented calibration and then wave-making signal splicing is feasible for the simulation of wave and storm surge coupling action, with high-accuracy simulation results. Therefore, this simulation technology can be applied to model the dynamic co-action of wave and storm surge (or tide) on coastal structures.

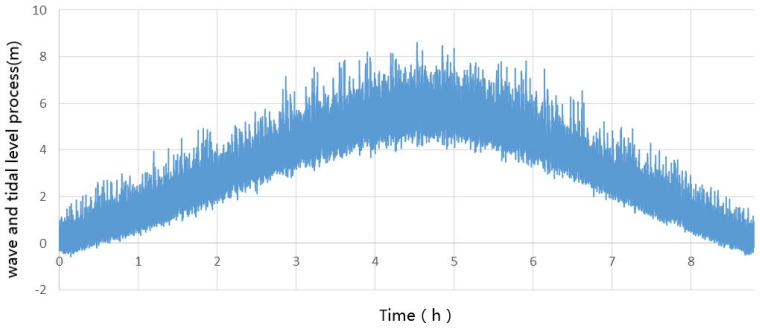

Figure 10. The hydrograph of laboratory simulation of wave + tidal level changes

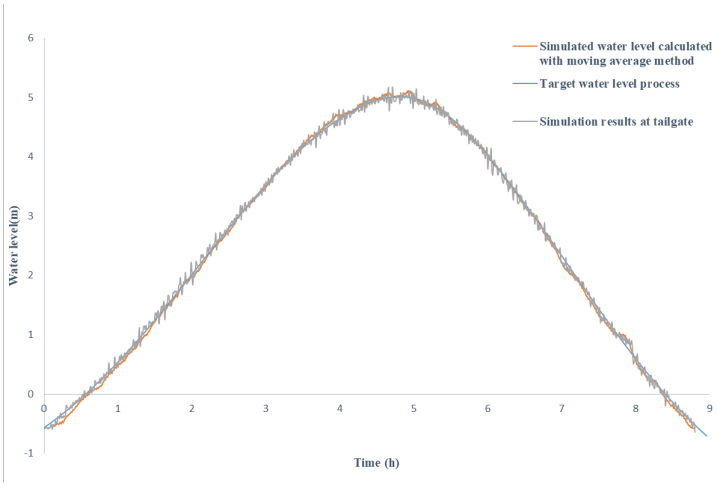

Figure 11. The comparison of simulated water level results calculated with sliding average method, measured results and the target process

Table 1. Coupling simulation results of significant wave height H_S (m) and mean period T_m (s)

Time (min)	Water level (m)	Target value		Simulation results			
				Hs		Tm	
		Hs(m)	Tm(s)	measured value (m)	Error value (%)	measured value (m)	Error value (%)
80-100	1.19	1.98	8.70	2.02	2.02	8.48	-2.53
180-200	3.70	2.46	9.13	2.46	0.00	9.11	-0.22
280-300	5.01	2.60	9.81	2.58	-0.77	9.61	-2.04
380-400	3.28	2.37	10.03	2.4	1.27	9.82	-2.09
480-500	0.40	1.71	10.06	1.63	-4.68	9.56	-4.97

3.2 Experimental results of wave overtopping discharge

Two physical model test cases are carried out: case 1 is the dynamic coupling action of storm surge and wave and case 2 is under the condition of a fixed water level combined with corresponding wave parameters. The fixed water level is 5.01m, 4.11m, 2.73m and 0.71m. i.e. the maximum water level is 5.01m, and the corresponding significant wave height and mean wave period are 2.60m and 9.81s, respectively.

In the model tests, the wave overtopping of seawalls was measured. The measurement results of overtopping discharge are shown in Table 2. The average period used in the calculation of mean overtopping discharge in the dynamic coupling test was defined within the period when overtopping can occur, the measured results of overtopping discharge under the dynamic coupling of storm surge and wave is 0.0593m^3/(m·s). The overtopping discharge measured at the 5.01m fixed water level and at the 4.11m fixed water level is 0.1214 m^3/(m·s) and 0.0087m^3/(m·s) respectively.

The measured results of overtopping discharge under the dynamic coupling of storm surge and wave are about 50% of the measured results of overtopping discharge at the fixed water level of 5.01m. Therefore, the results of overtopping discharge measured by the traditional test method of constant water level tend to be conservative and will lead to the increase in the levee crown and wave wall crest elevation, thus increasing project costs.

Table 2. Results of overtopping discharge (m^3/(m·s))

Case	Water level	Overtopping discharge
Fixed water level	5.01m	0.1214
	4.11m	0.0087
	2.73m	0.0006
	0.71m	No overtopping discharge
Dynamic coupling of storm surge and wave	/	0.0593

4 CONCLUSION

In this study, the wave and storm surge processes were discretized into many segments, and wave parameters were calibrated on corresponding water levels in a wave flume. With wave-maker and tide generator controlled simultaneously, the dynamic coupling simulation of waves and storm surges was realized by simulating wave and water level variation process synchronously and continuously.

In an application example, the dynamic processes of storm surges and waves of Typhoon Winnie were simultaneously simulated in a wave tank, and the measured data of water level, wave parameters and wave spectra in the model test are compared with the target values. It is shown that the simulation results of this technology are of high accuracy. The dynamic coupling simulation technique of waves and storm surges can be applied to model wave and storm surge co-action on coastal structures and improve the marine disaster forecasting and evaluation technology.

With regard to the wave overtopping discharge, the measured results of overtopping discharge under the dynamic coupling of storm surge and wave are about 50% of the measured results of overtopping discharge at the fixed water level of 5.01 m. Therefore, the results of overtopping discharge measured by the traditional test method of constant water level tend to be conservative, and will lead to the increase in the levee crown and wave wall crest elevation, thus increasing project costs.

ACKNOWLEDGMENTS

We acknowledged the support received from the National Key R&D Program of China (Grand No.2016YFC1402002), the Fifteenth Session Program between China and Bulgaria Scientific and Technological Cooperation Committee(No.15-13), the Major Project of Nanjing Hydraulic Research Institute Funds (Grand Nos. Y220002 and Y220013).

REFERENCES

ASCE. (2015). *The New Orleans Hurricane Protection System: What Went Wrong and Why*. ASCE, 84 pp.

Chen, M.W., Pan, J.N., Wang, D.T., Sun, Z.B., and Sun, T.T. (2019). Coupling simulation technology of wave and tide. *Port and Waterway Engineering*, 1, 29-34. (in Chinese with English abstract)

Hughes S.A. (2008). Combined Wave and Surge Overtopping of Levees: Flow Hydrodynamics and Articulated Concrete Mat Stability. *US Army Corps of Engineers*, 169 pp.

Li, L., Amini, F., Rao, X., and Tang, H.W. (2012). SPH Modeling of Surge Overflow over RCC Strengthened Levee. *International Journal of Ocean System Engineering*, 2 (4), 200-208.

Pan, Y., Li, L., Amini, F., and Kuang C. (2013). Influence of Three Levee-Strengthening Systems on Overtopping Hydraulic Parameters and Hydraulic Equivalency Analysis between Steady and Intermittent Overtopping. *Journal of Waterway, Port, Coastal, and Ocean Engineering*, 139 (4), 256-266.

Reeve, D.E., Soliman, A., and Lin, P.Z. (2008). Numerical study of combined overflow and wave overtopping over a smooth impermeable seawall. *Coastal Engineering*, 55 (2), 155-166.

Schüttrumpf, H., Moller, J., Oumeraci, H., Grune, J., and Weissmann, R. (2001). Effects of natural sea states on wave overtopping of sea dikes. *Proceedings of the 4th international Symposium Waves 2001, Ocean Wave Measurement and Analysis*, 1565–1574.

Suzuki, T., Shibaki, H., and Suzuyama, K. (2014). The numerical analysis of wave overtopping and water overflow over the coastal levee in the storm condition. *Coastal Engineering Proceedings*, 1 (34), 9.

Van Gent, M.R.A., Wolters, G., And Van der Werf, I.M. (2016). Rock Slopes with Open Filters under Wave Loading: Effects of Storm Duration and Water Level Varitions. *Proceedings of 35th Conference on Coastal Engineering*.

8th International Conference on the Application of Physical Modelling in Coastal and Port Engineering and Science
Dec. 9th - 12th, 2020, Zhoushan, China

THE PROPERTIES OF RATIONAL FUNCTION WAVE SPECTRUM (RWS) AND ITS APPLICATION TO ISLAND WAVES IN THE SOUTH CHINA SEA

ZHI ZONG(1), YIGENG WANG(1), LIZHOU(1)

(1)School of Naval Architecture, Dalian University of Technology, Dalian, China
zongzhi@dlut.edu.cn; wang_yigeng@163.com; zhouli@dlut.edu.cn

ABSTRACT

To describe stochastic properties of waves near atolls we arranged in-situ measurements near an atoll in the South China Sea. Analysis of the measured data shows that there exist four basic forms of wave spectra in the area. They are unimodal, bimodal, platykurtic characterized by a wide flat peak and uniform. Basing on the complex forms we introduce Rational function Wace Spectrum (RWS) form. The form can be described by four parameters which all have special meaning. They are A- amplitude parameter, C- frequency parameter, α- moment parameter, γ- self-similarity parameter. And they have a relationship with spectrum moments or semi-moment. By comparing 236 groups of data, we demonstrate that the RWS form can better describe the atoll wave which are characterized by the presence of breaking waves producing high-frequency waves, swells concentrated at low-frequency and storm waves creating complicated spectral form.

Keywords: Wave spectrum; RWS; parameter; spectral semi-moment.

1 INTRODUCTION

Protection of precious atolls requires a better understanding of wave properties inside/outside the atoll. Although shallow water theory is applicable to atoll waves, breaking waves and swells around the atoll are much more frequent than in an ordinary coast. Breaking waves produce high-frequency wave components, and swells are usually composed of very low-frequency waves. Therefore, the atoll wave power spectrum, the most powerful tool for describing stochastic properties of water waves (Newman, 1977), should be somewhat different from those employed for deep and shallow water waves.

One more factor to be considered is that atolls are heavily populated in the Pacific Ocean, where they are more frequently exposed to storms. Fully-developed wave power spectra like JONSWAP may not cover all the cases to be encountered. Therefore, there is a need to study the wave spectrum forms around atolls.

Worldwide efforts over several decades led to well-studied wave spectrum forms for deep water, among which are single-peaked spectrum NEUMANN and Pierson-Moskowitz spectrum (Pierson, 1964) in early 1960s, ITTC(ITTC, 1966) and JONSWAP spectra (Hasselmann, 1973) slightly later. P-M spectrum are proposed for fully developed wind seas based on the similarity theory of S.A. Kitaigorodskii. The parameters of P-M spectrum include wind speed and two dimensionless parameters. The P-M spectrum is experience spectrum. The JONSWAP is obtained by fitting the relatively systematic and reliable observation data. The spectrum contains five parameters, which can describe the flow pattern in different growth stages in detail. And much research has been performed on the statistical distribution of nonlinear random waves regarding the shapes of wave components (Akpınar et al., 2016; Alkhalidi and Tayfun, 2013; Izadparast and Niedzwecki, 2013).

Modifications based on these wave spectrum forms have been proposed by some authors so that these wave spectra may be applied to more cases. Chang(Wen and Zhang, 1990) generalized the JONSWAP spectrum applicable to the wind wave growth phase. Liu discussed the relationship between parameters in the spectrum and characteristic wave heights (Liu et al., 2015). Another important generalization is to include swell effects as well as wind waves. This features two peaks in a spectrum (bimodal spectrum)(Lee and Kim, 2006; Toffoli et al., 2010; Xueying et al., 1994). A double peaked spectrum may be described simply using combination of two simple spectra such as JONSWAP or Pierson-Moskowitz spectra (Panahi et al., 2015), or by modifying well-known spectra like Pierson-Moskowitz or JONSWAP to form a new double peaked spectral form. The latter is well exemplified by Ochi-Hubble model and Torsethaugen model(Haver, 2020; Mackay, 2011; Ochi and Hubble, 1976; Panahi et al., 2015; Soares, 1984; Torsethaugen, 1993; Violante-Carvalho et al., 2004). Mackay introduced additional parameters besides the wave height and period to tune the separate contributions of swell and wind sea components in the spectrum(Mackay, 2016). To include shallow water effects (Liao et al., 2014; Liu et al., 2004; Xie and Liu, 2013; Zhai et al., 2013), which increases nonlinearity and weakens dispersion, a TMA spectral form is often employed. The form is obtained by multiplying the deep water JONSWAP spectrum with a depth-dependent function (Bouws et al., 2020; Kitaigordskii et al., 1975). The spectrum, however, overestimates the significant wave heights in shallow waters.

As waves travel from deep to shallow waters, dispersion effects become weaker and nonlinearity increases. Therefore, long and short waves tend to travel at nearly equal phase speeds. Often their amplitudes are increased to such extent that breaking may appear. This is more prominent as waves evolve near a coral atoll. It is important to describe stochastic behaviour of water waves inside or outside an atoll because waves are decisive factor to influence atoll protection. A literature search shows that there are large numbers of on-site wave observations near islands, reefs and atolls, but there remains a lack of well-established wave spectrum form to describe waves inside or outside atolls.

In this paper, we report our one and half year in-situ measurements around an island in an atoll in the South China Sea. During the period, both storms and hurricanes were observed. This led us to realize that spectral form of waves around atolls might be somewhat different from those in the open sea or along coast. So we try to find the wave spectrum capable to describe the properties of atoll waves in this paper. In the same time we descries the properties of the new form and proposed a method to determine the parameters of it by measurement data.

2 IN-SITU MEASUREMENTS

The in-situ measurements were initiated from 2014 through arranging wave buoys around an atoll in the South China Sea. The measurement locations were located at the southeast of the atoll, 2 km away from the coast and local water is 100 m deep, as shown in Fig. 1. Wave Rider II buoy (also called MKII) is used for the measurements. The measurement data stored in Wave Rider II consist of three different types: displacement data, spectral data and wave data. The significant wave height (Hs) measured by wave rider buoy is the average in every 3 minutes. No filtering is applied to the data to remove outliers. The data used herein had been recorded from June 26th, 2014 to January 14th, 2015.

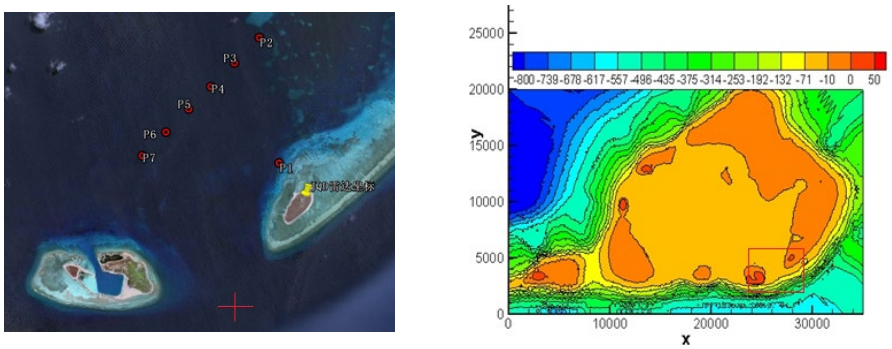

Figure 1. The measurement locations in South China Sea, which are around 16°26′48″N and 111°44′46″E in DMS

A wave train is a stochastic process, which is usually regarded as stationary narrow-banded one within half to three hours. If we took 3 hour records as a stationary process, we totally ob-tained 236 effective observational data in August, 2014. Here we take this month as an example. Simple analysis shows that these data can be described by four categories of wave spectra. They are unimodal, bimodal, platykurtic and uniform spectra, respectively.

(a) Unimodal spectrum: It has similar shape of the often-used ocean wave spectrum for deep water waves, as shown in Figure 2 (a). It occurs most frequently, occupying 50% within one month as demonstrated in Table 1. A slight difference observable here is that more energy is distributed at high frequency end. This is probably due to wave breaking.

(b) Bimodal spectrum: Two peaks can be observed as shown in Figure 2 (b). Its occurrence probability is about 10% given in Table 1. In this case, more wave energy is distributed around the two peaks. It is believed that two-peaked spectrum arises from swells.

(c) Platykurtic spectrum: it is characterized by a flat peak within a certain frequency range. Unimodal spectrum features one sharp peak while platykurtic spectrum has a much wider peak as shown in Figure 2 (c). What is surprising is that such spectrum has a higher occurrence probability up to 20% as given in Table 1. Platykurtic spectrum fea-tures storm waves. Their high occurrence probability corresponds to frequent occur-rences of storms in August in the South China Sea.

(d) Uniform spectrum: the energy is uniformly distributed throughout the frequency range as shown in Figure 2 (d). There does not exist typical frequency around which energy is localized. Their occurrence probability is 22%. Even so, a careful examination of Figure 2 (d) shows that the vertical axis of the wave power spectrum, that is, energy density, is very low compared with the rest three.

Comparing the power spectra in Figure 2, we observe that the vertical coordinate values of uniform

spectrum are of the order of 0.007 against 1, implying that uniform spectrum represents white-noise-like small waves. Although their occurrence probability is high (22%), they will not be considered here for their negligible energy. We will restrict ourselves to the rest three spectra in the following.

Table 1. Caption heading for a table s

Wave spectrum	Number	Percentage
Unimodal spectrum	105	49%
Bimodal spectrum	22	10%
Platykurtic spectrum	40	19%
Uniform spectrum	48	22%
total	215	100%

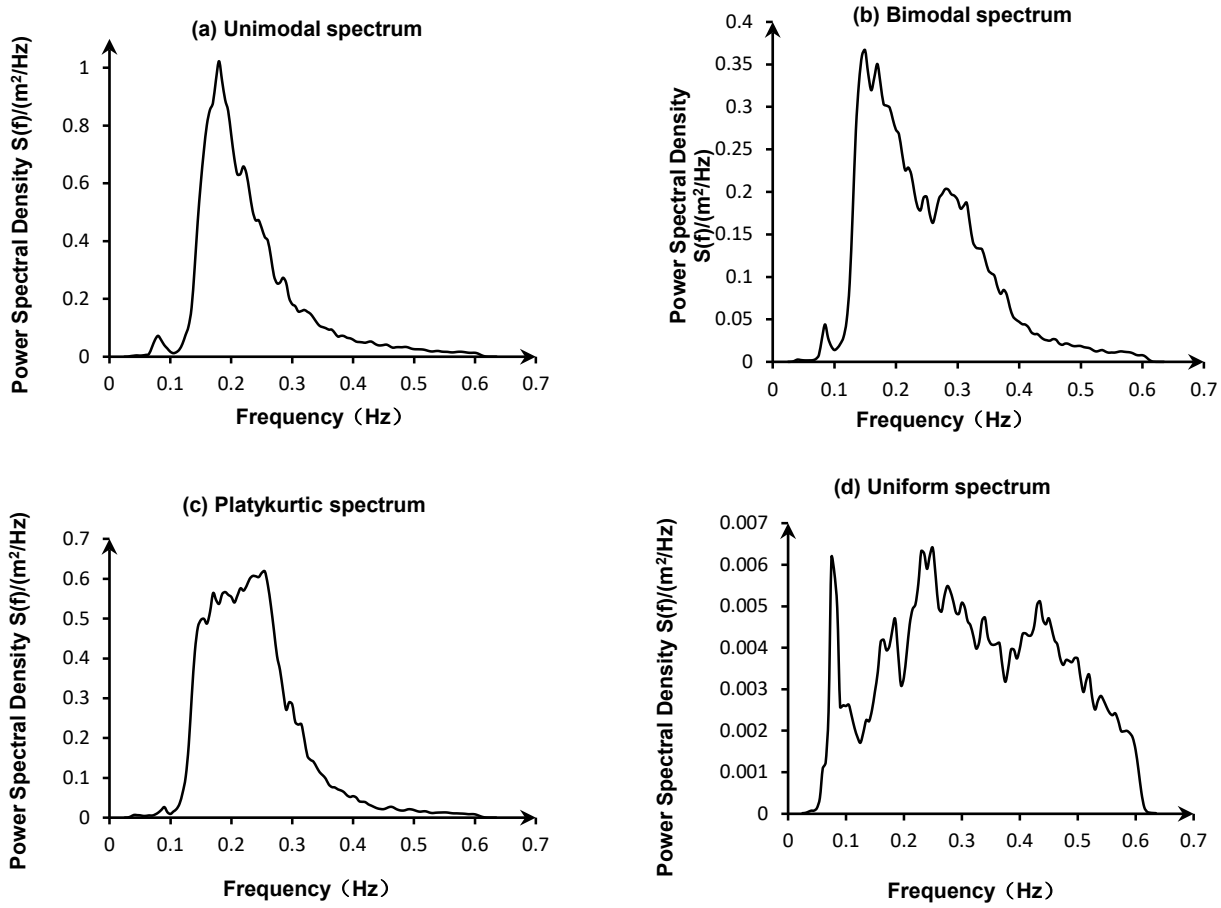

Figure 2. Four types of typical wave spectra present in our study

3 RATIONAL WAVE SPECTRUM (RWS)

Waves near atolls are affected by terrains, exhibiting nonlinearity and week dispersion. So, wave spectra near atoll are characterized by self-similarity arising from nonlinearity, long tail arising from breaking waves and swells, and flat and wide peak arising from balance between swells and wind waves. Therefore, the well-known wave spectra may not accurately describe waves around atolls. RWS has self-similarity and long tail, able to accurately capturing the properties of wave spectra around peak frequency, high- and low-frequency ends.

The RWS near atoll form is(Zong et al., 2019):

$$S(\omega) = A\frac{\omega^{\alpha}}{\omega^{\beta} + C} \quad [1]$$

Where, S(ω) represents power spectral density, ω is frequency, the other parameters are undetermined parameters.

As $\omega \to 0$, the denominator in Eq.[1] tends to constant C , so $S(\omega):\ \omega^{\alpha}$; as ω is large, the denominator in Eq. (1) can be ignored, and spectrum form behaves in the way of $S(\omega):\ \omega^{\alpha-\beta}$. In both cases, the RWS possesses self-similarity.

4 THE PARAMETERS OF RWS

By taking the derivative of Eq.[1], we can get:

$$S'(\omega) = A\frac{(\alpha-\beta)\omega^{\alpha+\beta-1} + \alpha C\omega^{\alpha-1}}{(\omega^{\beta}+C)^2} \quad [2]$$

The unimodal wave spectrum has a maximum value on $[0,+\infty]$, so there should be $\beta > \alpha$. Set the maximum value point to (ω_p, S_p). We can get:

$$\begin{cases} S(\omega_p) = S_p \\ S'(\omega_p) = 0 \end{cases} \rightarrow \begin{cases} S_p = A\dfrac{\omega_p^{\beta}}{\omega_p^{\beta}+C} \\ A\dfrac{(\alpha-\beta)\omega_p{}^{\alpha+\beta-1} + \alpha C\omega_p{}^{\alpha-1}}{(\omega_p{}^{\beta}+C)^2} = 0 \end{cases} \quad [3]$$

To solve the Eq. [3], we can get:

$$\begin{cases} A = \dfrac{\beta}{\alpha} S_p \omega_p^{\beta-\alpha} \\ C = \dfrac{\beta-\alpha}{\alpha}\omega_p^{\beta} \end{cases} \quad [4]$$

By referring to classical spectra, *α* and *β* value are generally given as constant values. Similarly, the shape of wave spectrum can be determined by S_p and ω_p when *α* and *β* are given. According to the Eq. [4], it can be seen that the parameter *C* is directly related to ω_p and not affected by S_p. So we use the parameter *C* to represent the spectral peak frequency ω_p. Similarly, on the basis of determining *α* and *β*, parameter *A* determines the amplitude of wave spectral density. So we call parameter *A* as amplitude parameter and parameter *C* as frequency parameter. We can use the parameter C to estimate the main concentrated frequency of the wave spectrum and use the parameter A to estimate the meaning energy.

Through the measurement data, we found that the range of spectral peak amplitude is from 0.21 to 1.68 (m2/Hz), and the range of spectral peak frequency is from 0.065 to 0.22 (Hz). For spectral peak amplitude, the different between maximum value and minimum value is nearly 7 times. For spectral peak frequency, the variation range of spectral peak frequency reaches 23.8% of the total observation frequency (0.65Hz). It is often deficient to use a single wave spectrum to describe such varied sea conditions. The parameters C and A of the RFWS can intuitively represent the main frequent and wave energy information of the wave spectrum, so we believe that the RFWS is suitable for local waters and has advantages.

Table 2. RFWS parameters values

(1)	(2)	(3)
β=13	α=7	β-α=3
f_p =0.15	f_p=0.15	f_p=0.15
S_p =1	S_p =1	S_p =1

In order to analyze the influence of parameter α and β on RFWS, we compare different values of α and β with each other. The comparison data is shown in Figure 3, and the parameters are shown in Table 2.

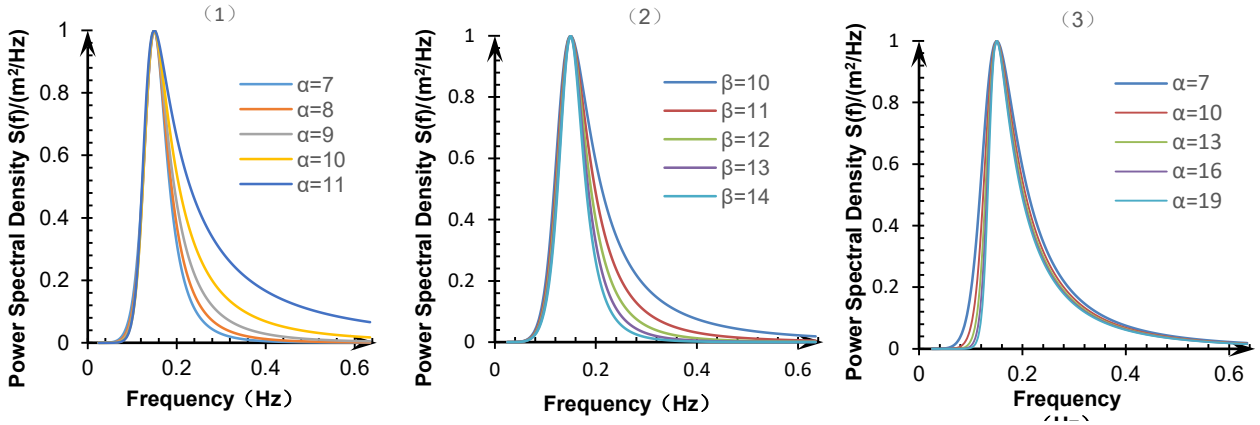

Figure 3. The contrast for parameters

The diagram in Figure 1 shows the influent of α, β and the difference between β and α in Eq. [1]. According to Eq. [1] and [4], RWS can be uniquely determined when α, β, fp, Sp are confirmed. In Figure 3- (1), the effects of α on the function are compared. The other three parameters are identical, and the values are shown in Table 1. Similarly, parameter β is compared in Figure 3- (2) and parameter β-α is constant in Figure 3 -(3). By comparing Figure 3- (1) and (2), it can be found that when one of α and β changed, the influence on RWS function is consistent. They mainly affects the trend on [fp, ∞]， which is the right half of the peak in the unimodal spectrum. In the shallow water near atoll, the long tail is affected by the self-similarity. Set *γ=β-α*, we may call *γ* the self-similarity parameter. The energy density decreases faster in the right half of the peak as *γ* increase.

The spectral moments are an important method to express the wave parameters like the zero-crossing, wave heights and periods. The *n-th* order moment of wave spectrum is $m_n = \int_0^\infty \omega^n S(\omega) d\omega$. To study the influent of α, we set the form like this:

$$M(n,\alpha) = m_n = \int_0^\infty \omega^n S(\omega) d\omega = A \int_0^\infty \frac{\omega^{\alpha+n}}{\omega^\beta + C} d\omega \quad [5]$$

we can get:

$$M(n+m,\alpha) = m_{n+m} = \int_0^\infty \omega^{n+m} S(\omega) d\omega = A \int_0^\infty \frac{\omega^{\alpha+n+m}}{\omega^\beta + C} d\omega = M(n,\alpha+m) \quad [6]$$

According to Eq. [6], it can be seen that α has the same status with n. So, we call the parameter α as the spectral moment parameter.

5 PROPERTIES OF RWS

5.1 symmetry

The Eq. [1] can be easy transform to the form like this:

$$S(v) = A'' \frac{v^\alpha}{v^\beta + 1} \quad [7]$$

We can get the *n-th* order moment like that:

$$M_n = \int_0^\infty A'' \frac{\omega^{\alpha+n}}{\omega^\beta + 1} d\omega \quad [8]$$

If set $\omega = 1/\xi$, we can get:

$$M_n = A'' \int_\infty^0 \frac{(1/\xi)^{\alpha+n}}{(1/\xi)^\beta + 1} d(1/\xi) = A'' \int_0^\infty \frac{\xi^{\beta-\alpha-n-2}}{\xi^\beta + 1} d\xi \quad [9]$$

So we get the relationship like that:

$$n_1 + n_2 = \beta - 2\alpha - 2 \quad [10]$$

We can find that the *n-th* moment of RFWS is symmetric with $\beta/2-\alpha-1$. This means that in some cases, negative moment can be converted to positive moments.

5.2 The spectral moment

It is a common method to study wave spectrum properties by using spectral moments. In the traditional classical spectrum, people associate the zero-order moment of the spectrum with the significant wave height of the wave. At the same time, many researches have proposed different spectral moment functions to determine the average period of waves.

According to the integral formula of the function:

$$\int_0^\infty \frac{x^{\alpha-1}}{1+x^\beta}dx = \frac{\pi}{\beta \sin\frac{\alpha\pi}{\beta}} \quad [11]$$

So from the Eq. [7] and Eq. [11], we can get:

$$\int_0^\infty A\frac{x^\alpha}{x^\beta + C} = A\frac{C^{\frac{\alpha-\beta+1}{\beta}}\pi}{\beta \sin\left(\frac{\alpha+1}{\beta}\pi\right)} \quad [12]$$

$$M_n = A\int_0^\infty \omega^n \frac{\omega^\alpha}{\omega^\beta + C}d\omega = AC^{\frac{\alpha-\beta+1+n}{\beta}} \frac{\pi}{\beta \sin\left(\frac{\alpha+1+n}{\beta}\pi\right)} \quad [13]$$

So, the relationship between parameters of RFWS and spectral moments can be obtained as follow (The derivation is in appendix A):

$$\begin{cases} \alpha = f_1(M_1, M_0, M_{-1}, M_{-2}) \\ \beta = f_2(M_1, M_0, M_{-1}, M_{-2}) \\ A = f_3(M_1, M_0, M_{-1}, M_{-2}) \\ C = f_4(M_1, M_0, M_{-1}, M_{-2}) \end{cases} \quad [14]$$

We select the observation data at 4:00 AM on August 17th, 2014. The recording period of the observation spectrum is 2hour, with 0.7m significant wave height (Hs) and 3.5s mean period. Using Eq. [14] to calculate these data, we obtain these estimated parameters given in Table 3. Where, Fr (Hz) represents wave spectrum frequency and PSD (m^2/Hz) represent power spectral density.

Table 3. Parameters of RWS

parameter	value
M_1	2.0340E-02
M_0	8.6099E-02
M_{-1}	4.0100E-01
M_{-2}	2.0889E+00
A	1.0033E-04
C	2.9162E-07
α	3.86
β	10.28
R^2	95.50%

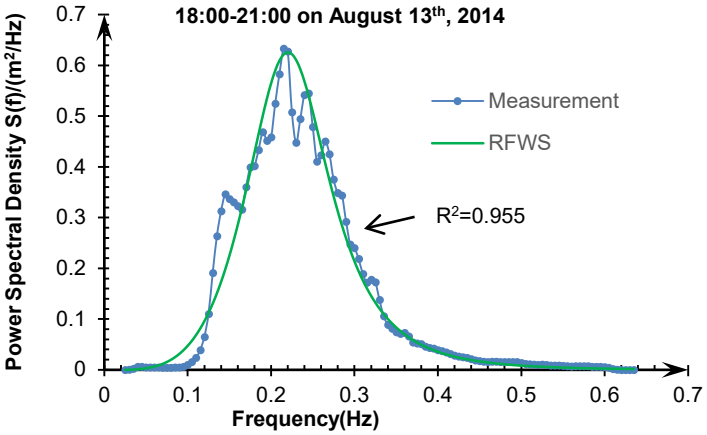

Figure 4. The coparison of measurement data and RWS data

The comparison between measured data and RWS data is shown in Figure 4. It can be seen from the figure that the RWS is well fitted to the measurement spectrum in peak and frequency. The predicted spectrum variation trend from trough to peak is basically consistent with the measured spectrum with a reliability index R^2=0.955.

5.3 Spectral semi-moment

The moment method can be used to express the relation between the moment and the parameters. But this method is calculated for the entire spectrum. In this way, the high and low frequency distribution characteristics are neglected in the estimation. From the previous analysis of parameters α and β for the RWS function, it can be found that parameters α and β control the change trend before and after the peak. And many scholars often introduced spectral peaks as important parameters. This inspire us to divide the spectrum into two parts. This may better reveal the characteristics of the wave spectrum.

The spectral semi-moment is defined as:

$$M^{-}=\int_{0}^{\omega_p} S(\omega)d\omega=\int_{0}^{\omega_p} A\frac{\omega^{\alpha}}{\omega^{\alpha}+C}d\omega \qquad [15]$$

$$M^{+}=\int_{\omega_p}^{\infty} S(\omega)d\omega=\int_{\omega_p}^{\infty} A\frac{\omega^{\alpha}}{\omega^{\alpha}+C}d\omega \qquad [16]$$

We can get the dimensionless zero-order moment of wave spectrum like this:

$$\begin{aligned} M'=\frac{M}{S_p\omega_p}&=\int_{0}^{\infty}\frac{1}{S_p\omega_p}\times\frac{S_p\dfrac{\beta}{\alpha}\omega_p^{\beta-\alpha}\omega^{\alpha}}{\omega^{\beta}+\omega_p^{\beta}\left(\dfrac{\beta-\alpha}{\alpha}\right)}d\omega \\ &=\left(\frac{\beta-\alpha}{\alpha}\right)^{\frac{\alpha-\beta+1}{\beta}}\times\frac{\pi}{\alpha\sin\left(\dfrac{\alpha+1}{\beta}\pi\right)} \end{aligned} \qquad [17]$$

Similarly, the dimensionless spectral semi-moment of RWS can be obtained as follows:

$$M^{-\prime}=\frac{M^{-}}{S_p\omega_p}=\frac{\beta}{\alpha}\int_{0}^{1}\frac{\omega^{\alpha}}{\omega^{\beta}+\dfrac{\beta-\alpha}{\alpha}}d\omega \qquad [18]$$

$$M^{+\prime}=\frac{M^{+}}{S_p\omega_p}=\frac{\beta}{\alpha}\int_1^{\infty}\frac{\omega^{\alpha}}{\omega^{\beta}+\frac{\beta-\alpha}{\alpha}}d\omega \quad [19]$$

$M^{-\prime}$ the energy sum of the left half-peak moment; $M^{+\prime}$ the energy sum of the right half-peak moment. The cut-off point is spectral peak frequency. After a lot of numerical experiments, we propose a method to estimate α and β based on the semi-moment as fellow:

$$\begin{cases}\gamma=\beta-\alpha=k_1\dfrac{M^{-\prime}}{M^{+\prime}}\\ \alpha=k_2\gamma^{k_3}M^{-\prime k_4}\end{cases} \quad [20]$$

Where, k_1=10, k_2=0.9489, k_3=-0.442, k_4=-1.89.

We select the observation data at 4:00 AM on August 17th, 2014. The recording period of the observation spectrum is 2hour, with 0.7m significant wave height (Hs) and 3.5s mean period. Using Eq. [20] to calculate these data, we obtain these estimated parameters given in Table 4. Where, Fr (Hz) represents wave spectrum frequency and PSD (m^2/Hz) represent power spectral density.

Table 4. Parameters of RWS

parameter	value
$M^{-\prime}$	0.162
$M^{+\prime}$	0.345
A	3.46E-04
C	1.02E-13
α	14.86
β	19.57
R^2	97.30%

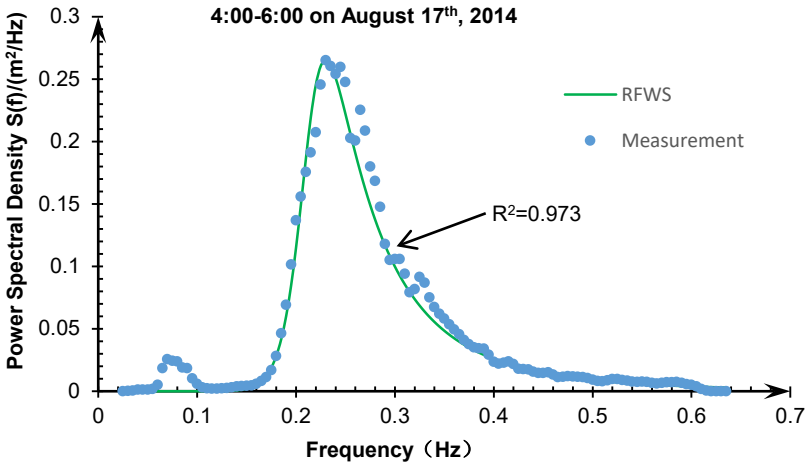

Figure 5. The comparison of measurement data and RWS data

The comparison between measured data and RWS data is shown in Figure 5. It can be seen from the figure that the RWS is well fitted to the measurement spectrum in peak and frequency. Small sub-peak disturbance occurs in the interval [0, fp] of the observation spectrum, and this method can still obtain a good fitting effect. The predicted spectrum variation trend from trough to peak is basically consistent with the measured spectrum with a reliability index R^2=0.973.

6 CONCLUSIONS

Waves near atolls are affected by terrains, exhibiting nonlinearity and week dispersion. So, wave spectra near atolls are characterized by (1) self-similarity arising from nonlinearity, (2) long tails arising from breaking waves and swells, (3) bimodal arising from swells and wind waves, and (4) flat and wide peaks arising from

balance between swells and wind waves. Therefore, the well-known wave spectra may not accurately describe waves around atolls.

In this paper, we proposed a new form of wave spectrum, Rational function Wave Spectrum to describe waves around the atoll. RSW has self-similarity and long tail, which can accurately capture the properties of wave spectra around peak frequency, high- and low-frequency ends. We also discussed the physical meaning of the RWS's four parameters liking A amplitude parameter, C frequency parameter, α moment parameter, γ self-similarity parameter. The correlation of its parameters and moment, semi-moment are present here, which may help we find a new way to make sure the parameters of spectrum.

ACKNOWLEDGEMENTS

The current research is financially supported by the Key Program (Grant No. 51639003) and the Normal Project (Grant No. 51679037) of the National Natural Science of China. This is also supported by the Ministry of Science and Technology with the research project No. 2013CB36101 and The Ministry of Industry and Information Technology with the research project in the fields of high-tech ships ([2016]22).

APPENDIX A

According to Eq. [1] and Eq. [13], and set $x_1 = \frac{\alpha}{\beta}\pi$, $x_2 = \frac{1}{\beta}\pi$, we get:

$$\frac{M_1}{M_0} = C^{\frac{1}{\beta}} \frac{\sin\left(\frac{\alpha+1}{\beta}\pi\right)}{\sin\left(\frac{\alpha+2}{\beta}\pi\right)} = C^{\frac{x_2}{\pi}} \frac{\sin(x_1+x_2)}{\sin(x_1+2x_2)} = a_0 \quad [A.1]$$

$$\frac{M_0}{M_{-1}} = C^{\frac{1}{\beta}} \frac{\sin\left(\frac{\alpha}{\beta}\pi\right)}{\sin\left(\frac{\alpha+1}{\beta}\pi\right)} = C^{\frac{x_2}{\pi}} \frac{\sin x_1}{\sin(x_1+x_2)} = a_1 \quad [A.2]$$

$$\frac{M_{-1}}{M_{-2}} = C^{\frac{1}{\beta}} \frac{\sin\left(\frac{\alpha-1}{\beta}\pi\right)}{\sin\left(\frac{\alpha}{\beta}\pi\right)} = C^{\frac{x_2}{\pi}} \frac{\sin(x_1-x_2)}{\sin x_1} = a_2 \quad [A.3]$$

If we set $\begin{cases} z_1 = \sin x_1 \\ z_2 = \sin x_2 \end{cases}$, we could get:

$$\frac{a_1}{a_2} = \frac{\sin^2 x_1}{\sin(x_1+x_2)\sin(x_1-x_2)} = \frac{z_1^2}{z_1^2 - z_2^2} \quad [A.4]$$

Set $z_1 = kz_2$, get: $k = \sqrt{\frac{a_1}{a_1 - a_2}}$,then:

$$\begin{aligned} \frac{a_0}{a_1} &= \frac{\sin(x_1+x_2)\sin(x_1+x_2)}{\sin x_1 \sin(x_1+2x_2)} \\ &= \frac{\sin^2 x_1 \cos^2 x_2 + 2\sin x_1 \cos x_1 \sin x_2 \cos x_2 + \sin^2 x_2 \cos^2 x_1}{\sin^2 x_1 \cos^2 x_2 - \sin^2 x_1 \sin^2 x_2 + 2\sin x_1 \cos x_1 \sin x_2 \cos x_2} \\ &= \frac{z_1^2\left(1-z_2^2\right) + 2z_1 z_2 \sqrt{1-z_1^2}\sqrt{1-z_2^2} + z_2^2\left(1-z_1^2\right)}{z_1^2\left(1-z_2^2\right) - z_1^2 z_2^2 + 2z_1 z_2 \sqrt{1-z_1^2}\sqrt{1-z_2^2}} \\ &= \frac{k^2 + 2k\sqrt{1-z_2^2}\sqrt{1-k^2 z_2^2} + \left(1-k^2 z_2^2\right)}{k^2 - 2k^2 z_2^2 + 2k\sqrt{1-z_2^2}\sqrt{1-k^2 z_2^2}} = g^2 \end{aligned} \quad [A.5]$$

We will get the function:

$$z_2^2\left(2k^2g^2-k^2\right)+\sqrt{1-z_2^2}\sqrt{1-k^2z_2^2}\left(2k-2kg^2\right)+\left(k^2+1-k^2g^2\right)=0 \quad [A.6]$$

If we set $\begin{cases} y=z_2^2 \\ d=2k^2g^2-2k^2 \\ e=k^2+1-k^2g^2 \\ h=2kg^2-2k \end{cases}$, we will get a unitary quadratic equation like this:

$$y^2+\frac{2de+h^2+h^2k^2}{d^2-h^2k^2}y+\frac{e^2-h^2}{d^2-h^2k^2}=0 \quad [A.7]$$

It is easy to solve the system of Eq. [B.7], Eq. [B.4], Eq. [13] to obtain:

$$\begin{cases} \alpha=f_1\left(M_1,M_0,M_{-1},M_{-2}\right) \\ \beta=f_2\left(M_1,M_0,M_{-1},M_{-2}\right) \\ A=f_3\left(M_1,M_0,M_{-1},M_{-2}\right) \\ C=f_4\left(M_1,M_0,M_{-1},M_{-2}\right) \end{cases} \quad [A.8]$$

REFERENCES

Akpınar, A., Bingölbali, B. and Van Vledder, G.P., 2016. Wind and wave characteristics in the Black Sea based on the SWAN wave model forced with the CFSR winds. Ocean Engineering, 126: 276 - 298.

Alkhalidi, M.A. and Tayfun, M.A., 2013. Generalized Boccotti distribution for nonlinear wave heights. Ocean Engineering, 74(6): 101-106.

Bouws, E., Gunther, H., Rosenthal, W. and Vincent, C., 2020. Similarity of the wind wave spectrum in finite depth water.

Hasselmann, K.E.A., 1973. Measurements of wind-wave growth and swell decay during the Joint North Sea Wave Project (JONSWAP). Deutche Hydrological Institute Hamburg, Germany, Reiche(A(8°),No. 12.).

Haver, S., 2020. Simplified double peak spectral model for ocean waves.: {}.

ITTC, 1966. Recommendations of the 11th International Towing Tank Conference. In: Proceedings of 11th ITTC, Tokyo.

Izadparast, A.H. and Niedzwecki, J.M., 2013. Four-parameter Weibull probability distribution model for weakly non-linear random variables. Probabilistic Engineering Mechanics, 32: 31 - 38.

Kitaigordskii, S., Krasitskii, V. and Zaslavskii, M., 1975. On Phillips' Theory of Equilibrium Range in the Spectra of Wind-Generated Gravity Waves. Journal of Physical Oceanography - J PHYS OCEANOGR, 5: 410-420.

Lee, H.S. and Kim, S.D., 2006. A comparison of several wave spectra for the random wave diffraction by a semi-infinite breakwater. Ocean Engineering, 33(14): 1954 - 1971.

Liao, B., Cao, D. and Liu, H., 2014. Wave transformation by a dredge excavation pit for waves from shallow water to deep water. Ocean Engineering, 76: 136-143.

Liu, H., Lin, P. and Shankar, N.J., 2004. An analytical solution of the mild-slope equation for waves around a circular island on a paraboloidal shoal. Coastal Engineering, 51(5): 421-437.

Mackay, E., 2011. Modelling and Description of Omnidirectional Wave Spectra.

Mackay, E., 2016. A unified model for unimodal and bimodal ocean wave spectra. International Journal of Marine Energy, 15: 17-40.

Newman, J.N., 1977. Marine hydrodynamics. Cambridge, Mass.: MIT Press.

Ochi, M.K. and Hubble, E.N., 1976. Six-parameter wave spectra. Proc. 15th Coastal Eng. Conf: pp. 301-328.

Panahi, R., Ghasemi K., A. and Shafieefar, M., 2015. Development of a bi-modal directional wave spectrum. Ocean Engineering, 105: 104-111.

Panahi, R., K., A.G. and Shafieefar, M., 2015. Development of a bi-modal directional wave spectrum. Ocean Engineering, 105: 104 - 111.

Pierson, W.J.M.L., 1964. Based on the Similarity Theory of S. A. Kitaigorodskii. Journal of Geophysical Research: 5181–5203.

Soares, C.G., 1984. Representation of double-peaked sea wave spectra. Ocean Engineering, 11(2): 185 - 207.

Toffoli, A., Onorato, M., Bitner-Gregersen, E.M. and Monbaliu, J., 2010. Development of a bimodal structure in ocean wave spectra. Journal of Geophysical Research: Oceans (1978--2012), 115.

Torsethaugen, K., 1993. Two peak wave spectrum model. Proceedings of the International Conference on Offshore Mechanics and Arctic Engineering - OMAE, 2: 175-180.

Violante-Carvalho, N., Ocampo-Torres, F.J. and Robinson, I.S., 2004. Buoy observations of the influence of swell on wind waves in the open ocean. Applied Ocean Research, 26(1): 49 - 60.

Wen, S.C. and Zhang, D.C., 1990. Improvement theory of wind wave spectrum. Acta Oceanologica Sinica, 03: 271-283.

Xie, J. and Liu, H., 2013. Analytical study for linear wave transformation by a trapezoidal breakwater or channel. Ocean Engineering, 64: 49-59.

Xueying, C., PeijiHu, H. and Zejian, 1994. The Statistical Characteristics of Sea Waves with Double-peaked Spectra in Jiaozhou Bay. Journal of Oceanograpgy of Huanghai & Bohai Seas.

Zhai, X., Liu, H. and Xie, J., 2013. Analytic study to wave scattering by a general Homma island using the explicit modified mild-slope equation. Applied Ocean Research, 43: 175-183.

Zong, Z. et al., 2019. Proposal of a Rational Function Wave Spectrum (RFWS) form for atoll waves. Ocean Engineering, 189: 106402.

8th International Conference on the Application of Physical Modelling in Coastal and Port Engineering and Science
Dec. 9th - 12th, 2020, Zhoushan, China

WAVE OVERTOPPING AT SEAWALLS WITH BULLNOSE

TANG XUAN THO(1), LE HAI TRUNG(2), DANG THI LINH(3), NGUYEN TRUONG DUY(4)& TRAN THANH TUNG

(1,2,3,4,5)Thuyloi University
trung.l.h@tlu.edu.vn

ABSTRACT

For years, seawalls have protectedan increasing number of towns and tourism areas stretching along the coast of Viet Nam. During storm surges or even high tides, wave overtopping and splash-up would often threaten the safety of infrastructures, traffic and residents behind the seawalls. Therefore, the paper studies the wave-wall interactions using hydraulic small scale model tests. We conducted experiments on model seawalls with different faces and bullnoses. The obtained data shows that bullnoses help to considerably reduce wave overtopping discharg. Therefore, the magnitude of these decreasing effects is quantitatively ascertained.

Keywords: bullnose, overtopping, seawall, wave flume.

1 INTRODUCTION

Historically, seawalls have been built along the coastlines to protect the land from erosion and flooding and sometimes provide additional amenity value. Typically structures are either massive vertical retaining walls or very steep face ones. For example, Chinese people constructed a steep stone seawall running along Hangzhou Bay several centuries ago. The structure had served to protect people and their property under many recorded hazards from sea and river (Wang et al 2012).

In severe weather conditions, big waves would attack and generate significant overtopping and splashing up. Wave overtopping at seawall has been intensively investigated in many works including physical models (Goda et al 1975, Napp et al 2004), numerical simulations (Gotoh et al 2005) and even in situ tests and field measurements (Pullen et al 2009). To reduce wave overtopping, the design would often consist of a seaward overhang in forms of recurve, parapet, return wall, bullnose. Notably, Pearson et al (2005) investigated the recurve/ parapet which give significant reductions of wave overtopping. Based on research, knowledge has been gradually accumulated thus leading to proper and economical design of seawalls as published in a large number of handbooks and guidelines (Besley1998, Hunt1958,Thomas& Hall2015).

Along the coast of Viet Nam, seawalls have become more and more popular and reliable to protect an increasing number of towns and tourism hotspots, especially since 2000s. In fact, seawalls would be newly constructed or upgraded from existing protection structures. In the latter case, concrete blocks of various shapes are built or placed on the crest of a revetment/ dike. By doing so, the crest is leveled up significantly while the landscape is not violently affected. However, the practice of design is very much dependent on experience with dikes and revetments, which have been long applied in Viet Nam.

Therefore, the paper aims to determine the performance of seawall blocks on a steep base, focusing on wave overtopping. To this end, physical experiments were conducted on four different cross-sections of seawall in a wave flume. Remarkably, the models are tested with and without bullnose. Section 2 describes the experimental setup including wave flume, cross-sections of the structure to be tested, wave conditions, measurement devices and test scenarios. Section 3 presents the test results and discusses how effectively the bullnoses prevent and reduce wave overtopping.

2 PHYSICAL MODEL

2.1 Holland wave flume

We performed all experiments in the Holland wave flume at the Integrated Hydraulic Laboratory at Thuyloi University. The flume measures 45 m long (effective), 1.0 m wide and 1.2 m high. The wave maker is equipped with an advanced automated system of Active Reflection Compensation (ARC) and may generate irregular waves with height of up to 30 cm and a peak period of 3.0 seconds. Measurement devices were manufactured and installed by HR Wallingford.

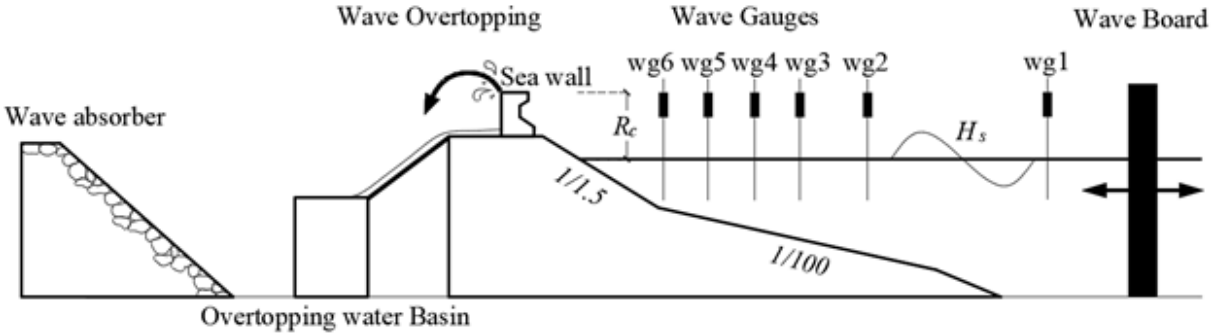

Figure 1.Experimental setup in the wave flume including a wave board, a foreland, a base, a sea wall, aovertopping water tank and a wave absorber (not to scale).

The model structures and wave parameters are selected according to a length scale of 1/15, a scale ratio (Hughes 1993) of 15. A foreland made of fine sand is shaped with an inclination of 1/100. The seawall is positioned on the top of a steep base (cotα = 1.5). Figure 1 sketches the experiment configuration and the arrangement of all measurement devices.

2.2 Measurement devices

We used capacitance-type wave gauges to record wave signals at sampling frequency of up to 100 Hz. Four gauges were used to separate reflected waves and thus determine incident waves at the front of the structures. The distances between these gauges are carefully selected so that singularities in the wave separation can be properly avoided. Two other gauges are utilised to determine waves in front of the board (deep water) and at the middle of the foreland, respectively (Fig. 1).

A tank was placed right behind the wall to collect all water produced by overtopping wave and splashing up. A pumping system was set-up to keep transferring the water to a bucket for measuring the volume. Besides, a digital camcorder is deserved to capture the splashing-up height with regard to a vertical ruler on side of the flume. Additionally, we used another camcorder to record the overview of every experiment.
In short, three groups of parameters were measured including wave characteristics, overtopping volumes and splash run-up height.

2.3 Cross-sections of the seawall model

The cross-section of any structure plays a vital role in the wave-structure interaction, especially overtopping and splashing up. Therefore, we investigated the performance of different seaward faces including curved (Fig 2a), steep (Fig 2b), straight (Fig 2c) and stepped (Fig 2d). In general, the studied structural configurations would be found similar to coastal structures of complex geometries as described in Zanuttigh (2016).

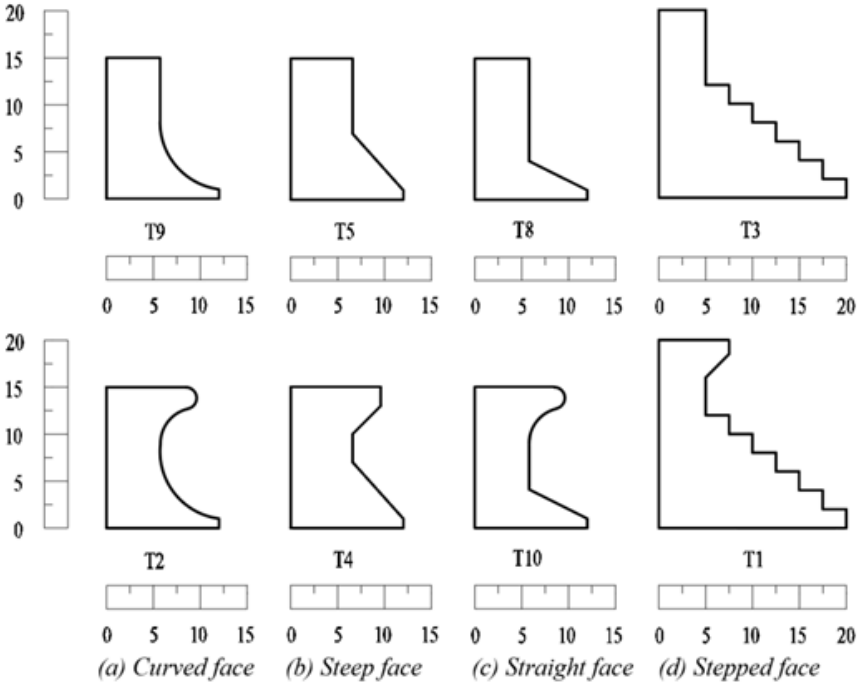

Figure 2. Different cross-sections of seawall with and without bullnose

Each type of wall was shaped with and without bullnose, e.g T2 is curved one with bullnose and T9 without bullnose. Remarkably, the bullnose is relatively large with regard to the dimension of the entire wall. These seawall models are made of mica plastic. The first three blocks are all 150 mm high while the stepped on is 200 mm.

2.4 Test scenaros

We conducted a series of experiments under two wave conditions which have standard JONSWAP spectrum. In which, the wave heights were 0.15, 0.17 m while wave period were 1.5 and 1.6 s, respectively (Table 1). Each wave condition was generated in the flume filled with two depths of 0.50 and 0.55 m in order to assess the influence of water level (especially low tide and high tide) on wave overtopping and splashing up. Every test consists of at least 500 waves in order to reproduce the entire spectra and to generate wave overtopping with stable discharges.

Table1. Wave conditions in the wave flume

d [m]	H_{m0}[m]	T_p [s]
0.60	0.15	1.9
0.60	0.16	1.5
0.65	0.16	1.9
0.65	0.17	1.6

For every cross-section, all tests were carried out twice to check the consistency of the measured results. A test name consists of four parts including water depth d, wave height H, wave period T, and its order (the 1st test is denoted as 'i' and 'ii' for the 2nd one). In practice, several tests were repeated three or four times in case of suspecting the results.

3 RESULTS AND DISCUSSION

3.1 Wave overtopping discharge

We directly measured the total wave overtopping volume V [m^3] and test duration t [second]. As the wave flume is 1 m wide, the averaged unit overtopping discharge q [m^3/s per m] is therefore simply derived from these two parameters

$$q = \frac{V}{t} \tag{1}$$

Table 2, 3, 4 and 5 provide all values of V, t and q for curved seawall models (T2 and T9); steep ones (T4 and T5); straight ones (T10 and T8) and stepped ones (T1 and T3). Due to the small amount of overtopping taking place, discharge q is expressed with a constant of 10^{-3}.

Table 2. Wave overtopping discharge on curved seawalls

Scenarios	T2			T9			K_{bn} (q_{meaT2}/q_{meaT9})
	V	t	q_{meaT2}	V	t	q_{meaT9}	
	m^3	s	10^{-3} m^3/s/m	m^3	s	10^{-3} m^3/s/m	
d60H15T19 i	0.003	1800	0.002	0.030	950	0.032	0.053
d60H15T19 ii	0.004	1800	0.002	0.030	950	0.032	0.062
d60H16T15 i	0.003	1800	0.002	0.010	750	0.013	0.142
d60H16T15 ii	0.003	1800	0.002	0.008	750	0.011	0.156
d65H16T19 i	0.020	1800	0.011	0.270	950	0.284	0.039
d65H16T19 ii	0.023	1800	0.013	0.265	950	0.279	0.046
d65H17T16 i	0.015	1800	0.008	0.155	800	0.194	0.043
d65H17T16 ii	0.014	1800	0.008	0.150	800	0.188	0.041

Table 3. Wave overtopping discharge on steep seawalls

Scenarios	T4			T5			K_{bn} (q_{meaT4}/q_{meaT5})
	V	t	q_{meaT4} 10^{-3} m³/s/m	V	t	q_{meaT5} 10^{-3} m³/s/m	
	m³	s		m³	s		
D60H15T19 i	0.003	950	0.003	0.07	950	0.074	0.043
D60H15T19 ii	0.004	950	0.004	0.07	950	0.074	0.057
D60H16T15 i	0.002	750	0.002	0.04	750	0.051	0.039
D60H16T15 ii	0.001	750	0.002	0.04	750	0.047	0.040
D65H16T19 i	0.022	950	0.023	0.42	950	0.442	0.052
D65H16T19 ii	0.023	950	0.024	0.42	950	0.440	0.055
D65H17T16 i	0.006	800	0.008	0.26	800	0.329	0.023
D65H17T16 ii	0.006	800	0.008	0.26	800	0.330	0.023

Table 4.Wave overtopping discharge on straight seawalls

Scenarios	T10			T8			K_{bn} (q_{meaT10}/q_{meaT8})
	V	t	q_{meaT10} 10^{-3} m³/s/m	V	t	q_{meaT8} 10^{-3} m³/s/m	
	m³	s		m³	s		
D60H15T19 i	0.02	950	0.016	0.02	950	0.021	0.750
D60H15T19 ii	0.02	950	0.018	0.02	950	0.019	0.944
D65H16T19 i	0.05	950	0.053	0.21	950	0.221	0.238
D65H16T19 ii	0.05	950	0.053	0.21	950	0.223	0.236
D65H17T16 i	0.03	800	0.036	0.10	800	0.123	0.296

Table 5. Wave overtopping discharge on stepped seawalls

Scenarios	T1			T3			K_{bn} (q_{meaT1}/q_{meaT3})
	V	t	q_{meaT1} 10^{-3} m³/s/m	V	t	q_{meaT3} 10^{-3} m³/s/m	
	m³	s		m³	s		
D60H15T19 i	0.03	950	0.036	0.06	950	0.063	0.567
D60H16T15 ii	0.01	750	0.013	0.022	750	0.029	0.455
D65H16T19 i	0.30	1800	0.167	0.37	950	0.389	0.428
D65H16T19 ii	0.38	1800	0.208	0.32	950	0.337	0.618
D65H16T19 iii	0.27	1800	0.151	0.62	1800	0.344	0.437
D65H17T16 i	0.30	1800	0.167	0.21	900	0.233	0.714
D65H17T16 ii	0.29	1800	0.163	0.22	900	0.244	0.666

From the measured values, we plot the dimensionless crest freeboard against R_c / H_{m0} dimensionless discharge $q / \sqrt{g H_{m0}^3}$ in Fig. 3, Fig. 4, Fig. 5, Fig. 6, Fig. 7.

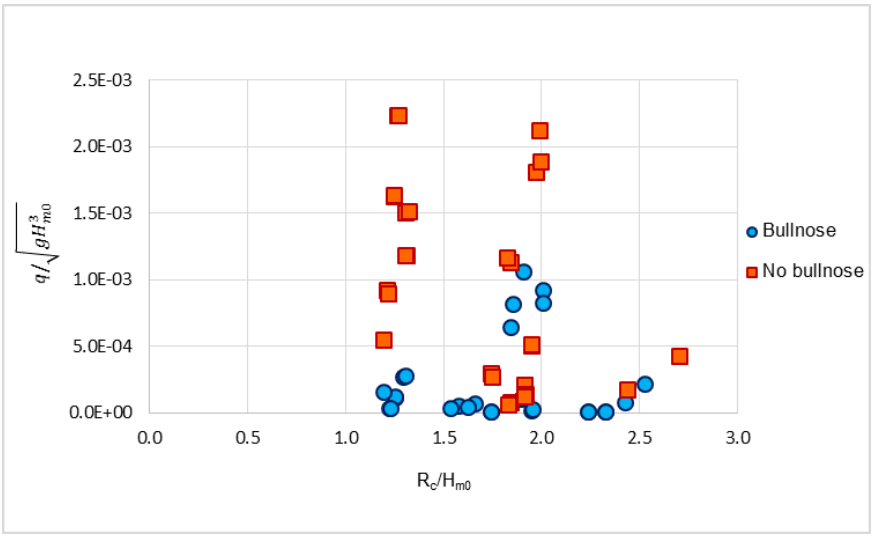

Figure 3. Dimensionless discharge vs. cress freeboard, seawalls with bullnose and without bullnose

It is clear that the higher the freeboard the smaller the discharge despite having a bullnose or not. In general, steep face models (T5 and T4) would produce highest overtopping discharge while straight ones generate lowest overtopping rate (T8 and T10).

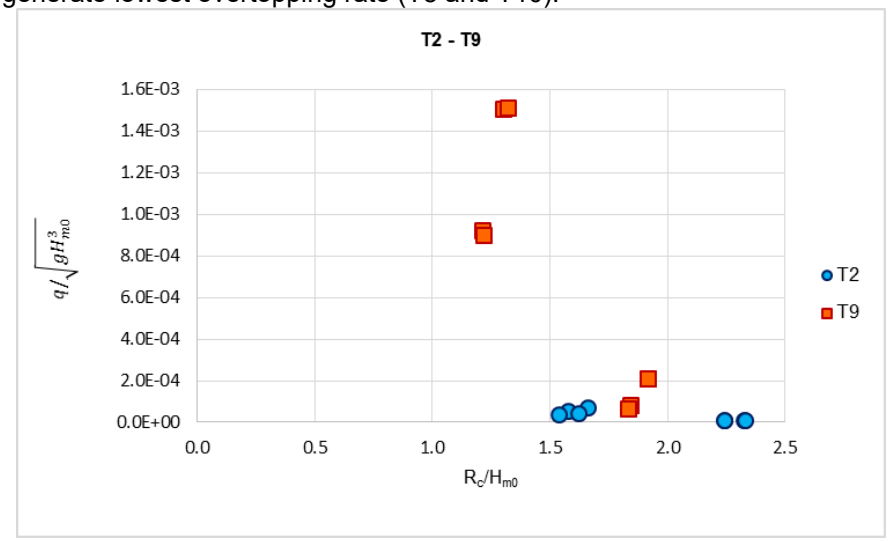

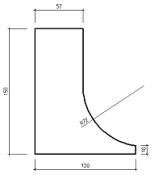

T9 no bullnose

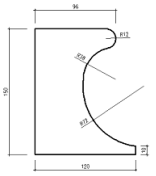

T2 bullnose

Figure 4. Dimensionless discharge vs. cress freeboard, curved face models T2 and T9

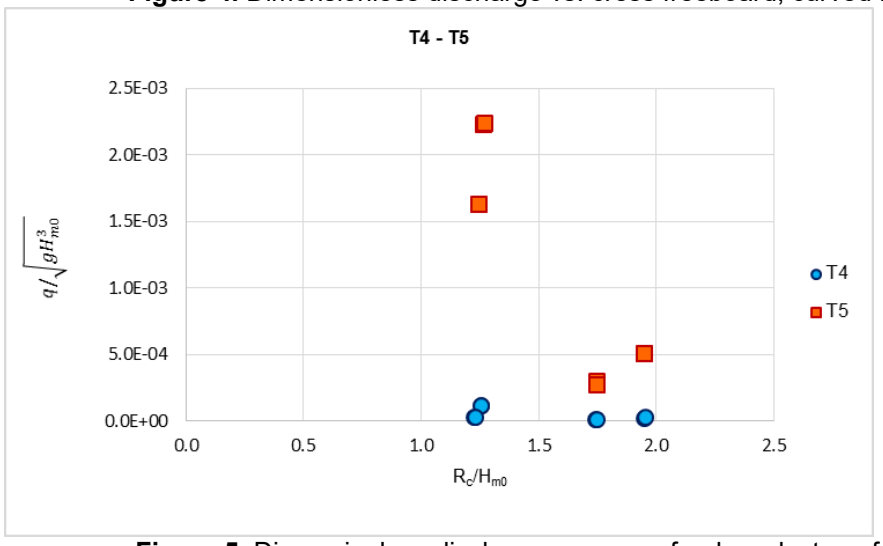

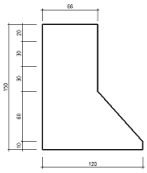

T5 no bullnose

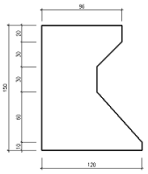

T4 bullnose

Figure 5. Dimensionless discharge vs. cress freeboard, steep face models T4 and T5

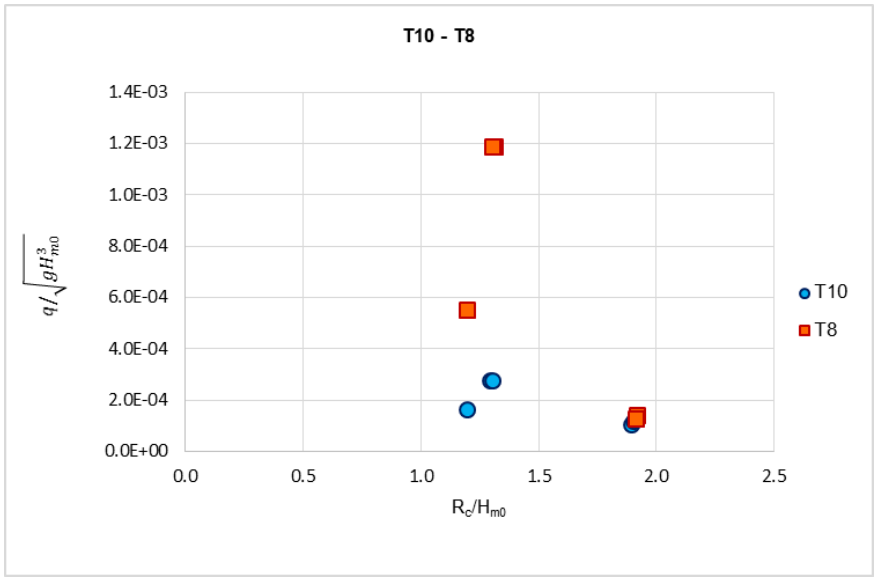

Figure 6. Dimensionless discharge vs. cress freeboard, straight face models T10 and T8

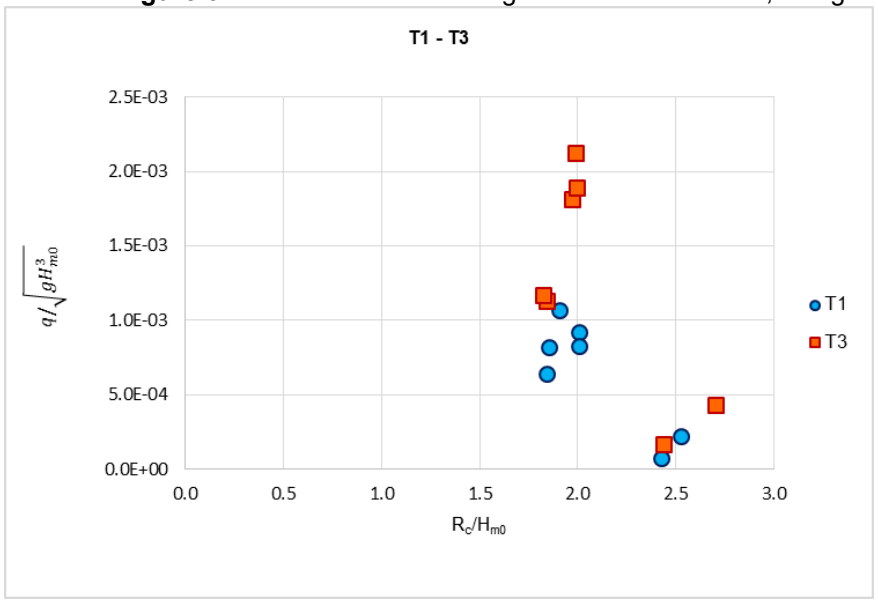

Figure 7. Dimensionless discharge vs. cress freeboard, stepped face models T1 and T3

Having no bullnose, overtopping discharges are similar between models T9, T8 slightly less than T3 and T5. It would be due to the steep face that stimulates water run-up to reach higher than in case of a straight and curved one. Maximum value of $q/\sqrt{g H_{m0}^3}$ is up to about 0.0022 for T5, 0.0021 for T3 while that is 0.0015 and 0.0011 for T9 and T8, respectively.

Interestingly, bullnose shows the most significant effect on steep face models when $q/\sqrt{g H_{m0}^3}$ drop from (0.27 ~ 2.24)×10^{-3} for T5 to (0.01 ~ 0.12) ×10^{-3} for T4, (0.17 ~ 2.13) ×10^{-3} for T3 to (0.08 ~ 1.07) ×10^{-3} for T1. In the mean while, overtopping rates reduce from (0.07 ~ 1.51) ×10^{-3} for T9 to (0.01 ~ 0.07) ×10^{-3} for T2 and $q/\sqrt{g H_{m0}^3}$ are (0.013 ~ 1.19) ×10^{-3} and (0.08 ~ 0.28) ×10^{-3} on T8 and T10, respectively.And for rather high freeboard, there would be hardly any water overtopping the curved seawall T2.

3.2 Reduction factor due to bullnose effect

It is the bullnose that considerably reduces the overtopping discharge on all seawall models to be tested. Based on EurOtop Overtopping Manuals, Bruce et al (2010) described the mean overtopping rates for various configurations of vertical and composite structures. Inspired by these existing theories, a discharge reduction factor is proposed to quantitatively estimate the effect of bullnose as:

$$k_{bn} = \frac{q_{bn}}{q_{no\ bn}} \quad (2)$$

in which, $q_{bn}$and $q_{no\ bn}$ are overtopping rates on seawall model with and without bullnose, respectively. The smaller the factor the greater amount of discharge which is decreased due to the bullnose.

In Tables 6, overtopping rates without bullnoses $q_{no\ bn}$ are assigned to q_{T9}, q_{T5}, q_{T8} and q_{T3} while those with bullnoses q_{bn}corresponding to q_{T2}, q_{T4}, q_{T10} and q_{T1}. And the calculated values ofk_{bn} cover a comparable range for curved (0.039 ~ 0.156) and straight (0.236 ~ 0.944) seawalls. Not surprisingly, the straight face model has the most scattering k_{bn}which fluctuates. For comparison, Pearson et al (2004) paid attention to seawalls with high freeboard and under wave breaking conditions. In their study, recurve/ parapet shows significant effect with reduction factor larger than 0.95.

Four sections all have smallest k_{bn} with water depth of 0.65 m in the wave flume. Curved, steep and straight ones get maximum value of the factor with 0.6 m water deep while it is 0.65 for stepped wall (Table 6). Interestingly, bullnoses seem possibly cause more obvious effect with higher water level in the wave flume. This is the opposite of what was observed in a series of experiments with a foreland of 1/50 (Hai Trung et al 2020). For curved, steep and straight seawalls, higher waves lead to smaller k_{bn}, i.e the influence of bullnose becomes more effective. In contrast, bullnose of stepped ones reduce less overtopping discharge when wave are higher.

Table 6. Comparison of k_{bn} among different seaward faces

k_{bn}	Curved	Steep	Straight	Stepped
Max	0.156	0.057	0.944	0.714
	d60H16T15ii	d60H15T19ii	d60H15T19i	d65H17T16i
Min	0.039	0.023	0.236	0.428
	d65H16T19i	d65H17T16i	d65H16T19ii	d65H16T19i
Averaged	0.073	0.042	0.493	0.555

Therefore, we are analysing the data set further in order to establish the relationship between k_{bn} and the configuration of the seawall as well as the bullnose shape. For example, Kortenhaus et al (2004) first discussed systematically a huge volume of data on overtopping at seawalls with recurves/ wave return walls/ parapets. And the authors did introduce a simple reduction factor depending on geometrical dimensions of the parapets.

4 CONCLUSIONS

The paper has explored the wave – seawall interaction including overtopping and splashing up based on experiments in a wave flume. We considered different structure models such as straight, curved, steep and stepped seaward faces and all cross-sections were built with and without bullnose. Measured data indicates the obvious effect of bullnose in decreasing wave overtopping discharge. The influence of bullnose becomes larger with higher waves at curved, straight and steep seawalls; but it is the other way around with stepped ones. These opposite effects encourage us to explore much further how bullnose geometry governs the wave overtopping at seawalls.

ACKNOWLEDGEMENTS

The research project ‘A study on producing seawall units with wave-returning bullnose to protect islands, resorts and urban coasts’ funded by the Vietnamese Ministry of Construction is acknowledged for providing data.

REFERENCES

Besley, P. (1998). Wave overtopping of seawalls, design and assessment manual. R&D technical report W178.

Bruce, T., Van Der Meer, J., Pullen, T., & Allsop, W. (2010). Wave overtopping at vertical and steep structures. In Handbook of coastal and ocean engineering (pp. 411-439).

Goda, Y., Kishara, Y., & Kamiyama, Y. (1975). Laboratory investigation on the overtopping rate of seawalls by irregular waves. Report of the Port and Harbour Research Institute, vol 14, nr. 4.

Gotoh, H., Ikari, H., Memita, T., & Sakai, T. (2005). Lagrangian particle method for simulation of wave overtopping on a vertical seawall. Coastal Engineering Journal, 47(2-3), 157-181.

Hughes, S. A. (1993). Physical models and laboratory techniques in coastal engineering (Vol. 7). World Scientific.

Hunt, I. A. (1958). Design of seawalls and breakwaters. US Lake Survey.

Kortenhaus, A., Pearson, J., Bruce, T., Allsop, N. W. H., & Van der Meer, J. W. (2004). Influence of parapets and recurves on wave overtopping and wave loading of complex vertical walls. In Coastal Structures 2003 (pp. 369-381).

Hai Trung, L., Linh, D. T., Tho, T. X., Duy, N. T., & Tung, T. T. (2020). Wave overtopping and splash-up at seawalls with bullnose. *Vietnam Journal of Marine Science and Technology*, *20*(3), 333-342.

Napp, N., Pearson, J., Bruce, T., & Allsop, W. (2004). Violent overtopping of vertical seawalls under oblique wave conditions. In Coastal Structures 2003 (pp. 528-541).

Pearson, J., Bruce, T., Allsop, W., Kortenhaus, A., &van der Meer, J.W. (2005). Effectiveness of recurve walls in reducing wave overtopping on seawalls and breakwaters. In Coastal Engineering 2004: (In 4 Volumes) (pp. 4404-4416).

Pullen, T., Allsop, W., Bruce, T., & Pearson, J. (2009). Field and laboratory measurements of mean overtopping discharges and spatial distributions at vertical seawalls. Coastal Engineering, 56(2), 121-140.

Pullen, T., Allsop, N. W. H., Bruce, T., Kortenhaus, A., Schüttrumpf, H., & Van der Meer, J. W. (2007). EurOtop wave overtopping of sea defences and related structures: assessment manual.

Thomas, R. S., & Hall, B. (2015). Seawall design. Butterworth-Heinemann.

Van der Meer, J. W., Allsop, N. W. H., Bruce, T., De Rouck, J., Kortenhaus, A., Pullen, T., ...& Zanuttigh, B. E. (2016). Manual on wave overtopping of sea defences and related structures. An Overtopping Manual Largely Based on European Research, but for Worldwide Application.

Wang, L., Xie, Y., Wu, Y., Guo, Z., Cai, Y., Xu, Y., & Zhu, X. (2012). Failure mechanism and conservation of the ancient seawall structure along Hangzhou Bay, China. Journal of Coastal Research, 28(6), 1393-1403.

Zanuttigh, B., Formentin, S. M., & van der Meer, J. W. (2016). Prediction of extreme and tolerable wave overtopping discharges through an advanced neural network. Ocean Engineering, 127, 7-22.

8th International Conference on the Application of Physical Modelling in Coastal and Port Engineering and Science
Dec. 9th - 12th, 2020, Zhoushan, China

Numerical simulation of force and deformation of a SPM deep-water aquaculture cage

XIAOHUA HUANG(1), LIUYANG SUI(2) & HAIYANG LIU (3)

(1,3) Key Lab. of Open-Sea Fishery Development, Ministry of Agriculture; Guangdong Cage Engineering Research Center; South China Sea Fisheries Research Institute, Chinese Academy of Fishery Sciences, Guangzhou 510300,China; huangx-hua@163.com; liuhaiyang@scsfri.ac.cn

(2) State Key Laboratory of Coastal and Offshore Engineering, Dalian University of Technology, Dalian 116024, China 18842632117@163.com

ABSTRACT

Based on the finite element method, a numerical model of a deep-water cage system with single-point mooring (SPM) is established. The whole cage system is modeled by a combination of line elements, three and six degree of freedom buoys. To verify the accuracy of the numerical model, we have conducted a series of physical model tests for the SPM cage in pure waves and wave-current combined conditions, in which the model scale is set as 1:15. We calculate the mooring force, heave and pitch of the cage collar and compare it with the experimental results, in which the relative error is within 10%. Afterwards, based on the numerical model, the force and deformation of the prototype SPM cage under various sea conditions of combined waves and current are simulated and analyzed, Furthermore, we consider three kinds of wall thickness of floating pipe (23.5, 29.4 or 36.4mm) and three kinds of mooring line length (60, 90 or 120 m), and discuss the effects of them on the mooring force and collar deformation of the cage system. The results of this study provide theoretical basis and data support for optimizing design of cage collar and mooring system.

Keywords: *S*ingle point mooring; deep-water net cage; floating collar; force and deformation; finite element simulation

1 INTRODUCTION

Since the 1980s, the production of capture fisheries in the world has remained relatively stable whiling aquaculture production has increased rapidly to meet the growing population's demand for high-quality aquatic products (FAO, 2018). In 2018, China's total aquaculture production was 49.91 million tons, accounting for 77.3% of the country's total aquatic product output, of which mariculture production was 20.31 million tons, making outstanding contributions to ensuring the supply of high-quality protein and reducing the utilization of aquatic biological resources in natural waters (China Fishery Statistics Yearbook, 2019). Due to the large-scale and disorderly development of inshore aquaculture in China in the past decades, the aquaculture space has gradually become saturated. Moreover, the rapid development of coastal tourism and heavy industry will inevitably occupy further coastal water resources. Therefore, it is an inevitable trend to move marine aquaculture towards much deeper water in open sea areas by using of efficient farming facilities and advanced equipments (Xu et al., 2016; Mai et al., 2016).

Deep-water cage aquaculture has significant advantages of high production and good economic efficiency. For instance, the annual output of farmed fish for a HDPE (high-density polyethylene) net cage with a circumference of 80 m is 40-70 tons. Deep-water cage has become an important and effective facility for expanding marine aquaculture space (Huang et al., 2018; Liu et al., 2017). Owing to severe sea conditions in open areas, especially the typhoon that having a great impact on net cage and farmed fish, the cage system must have adequate security against natural risks to ensure farming benefits (Jia et al., 2014). As an important part of cage system, the mooring plays a significant role in resisting the impact of wind, waves and current on cage structure. Meanwhile, by connecting the cage collar with mooring lines, cage movement is restricted within a certain range. Cage mooring systems include multiple-point mooring system (MPM) and single-point mooring system (SPM). The multiple-point mooring system is a traditional fixed mooring system, which is convenient for the daily management of cage farming because net cage always remain in a relatively fixed position in spite of wave/current impacting in any direction. Many researchers in the marine aquacultural community have conducted extensive studies related of the dynamic response of MPM cage by using of numerical method (Hou et al., 2019; Huang et al., 2018; Kristiansen et al., 2015; Zhao et al., 2013), physical model test (Fredriksson et al., 2006; Gui et al., 2006; Huang et al., 2011; Zheng et al.,2007) and in-situ measurement (Decew et al., 2010; Decew et al., 2013; Gansel et al., 2018; Guo et al., 2010). However, as the increasing of water depth, the installation of the MPM cage will become more and more difficult, which causes

mooring costs sharply increases. Compared with the MPM system, a SPM cage drifts within the scope of water areas at the center of the mooring point in the seabed, which increasing the distribution area for fish waste to reduce the probability of fish infections. Futhermore, it can save mooring cost of 2/3 and the marine installation for SPM system is simple and convenient (Goudey et al., 2001). The safety performance has also attracted the interest of some scholars. Decew et al. (2010) studied the dynamic response of a SPM trapezoidal cage under pure current through a numerical model. Shainee et al. (2013) and Xu et al. (2014) analyzed the self-submerging characteristics of a SPM cage under the combined waves and current condition using mathematical modeling. Li et al. (2018) conducted a numerical investigation on the dynamic response of a SPM ship-type fish farm in waves. Huang et al. (2019) used physical model tests with a scale of 1:30 to investigate the hydrodynamic performance of a SPM semi-submersible offshore fish farm with truss structure under various wave conditions.

In this study, we develop a finite element numerical model for simulating a SPM deep-water cage (see Figure 1), and carry out wave-current tank tests with scale of 1:15 to verify the accuracy and efficiency of the cage's model. On this basis, the structure deformation and mooring force of the prototype cage in waves and current are simulated, and the influence of the wall thickness of the floating pipe and the length of the anchor rope on the force and deformation of the cage are also analyzed, which aims to provide theoretical basis and data support for the optimal design of cage collar and mooring system.

Fig 1. The scene of SPM net cage

2 Numerical model

The numerical model tool used for the research is the professional hydrodynamic analysis software OrcaFlex 10.0d (Orcina Ltd. 2015; Yang et al., 2015). The software can perform system-wide static and dynamic analysis of various offshore facilities, including finite element modeling of ships, buoys and pipeline structures, and can handle a variety of nonlinear problems, such as marine riser vibration, mooring response, and platform drag force, displacement and deformation of unit structure, etc. The cage system is mainly composed of floating collar, fishing net and mooring lines. The finite element method is used to discretize the cage system into a series of line elements and lumped-mass buoys. Lumped-mass buoys are divided into three and six degree of freedom buoys. Both of them are assigned to the node at that end of line segment. For the surface collar, the pipe segments are connected by buoys with six degrees of freedom, which transfer rotational and translational motion to represent the bending stiffness of the material. For the fishing net and mooring lines connecting the collar, the line segments are connected by buoys with three degrees of freedom, but with no moment contributions considering that the bending stiffness is insignificant, which can be set to zero. All of the loads related to each line segment, such as the weight, buoyancy, hydrodynamic drag, added mass, tension and shear, and bending moment, are lumped and assigned to the node. The equation of motion is then formulated for each line node as follows (Orcina Ltd. 2015):

$$M(\mathrm{p},\mathrm{a}) + \mathrm{C}(\mathrm{p},\mathrm{v}) + K(\mathrm{p}) = \mathrm{F}(\mathrm{p},\mathrm{v},\mathrm{t}) \qquad [1]$$

where *M(p,a)* is the inertia load, *C(p,v)* is the damping load, *K(p)* is the stiffness load, *F(p,v,t)* is the external load.

For cage collar, fishing net and mooring lines, the effective tension of line element can be expressed using the following formula:

$$T_e = T_w + \left(P_0 A_0 - P_i A_i\right) \qquad [2]$$

where T_w is wall tension

$$T_w = EA\varepsilon - 2\mu\left(P_0A_0 - P_iA_i\right) + EAC\left(dL/dt\right)/L_0 \quad [3]$$

where EA is axial stiffness of line, ε is total mean axial strain, L is instantaneous length of segment, λ is expansion factor of segment, L_0 is unstretched length of segment, μ is Poisson ratio, P_i and P_o is internal pressure and external pressure, respectively, A_i, A_o is internal and external cross sectional stress areas, respectively, C is damping coefficient, dL/dt is rate of increase of length.

$$C = \left(\lambda_a/100\right)C_{crit} \quad [4]$$

where λ_a is target axial damping, the value is set as 0.4.

For the floating collar, the calculation expression of the bending moment and the shear force of the line segment are given by:

$$M = EIk + kd\left(\lambda_b/100\right)D_c/dt \quad [5]$$

$$Q = S_Z \times \left(M_2 - M_1\right)/L \quad [6]$$

where EI is the bending stiffness of a segment, k is the curvature, λ_b is the target bending damping ratio, D_c is the bending critical damping value equal to $L_0(mEIL_0)^{1/2}$, S_Z is the axial unit vector of the line element; M_1 and M_2 are the bending moments of the particles at both ends of the line element, L is the instant length of the line element.

The Morison equation is used to calculate the hydrodynamic load of the structural line elements of each component of net cage (Morison et al., 1950)

$$F_w = \frac{1}{2}\rho C_d S V_r\left|V_r\right| + \rho\forall_w a_f + \rho\forall_w C_a a_r \quad [7]$$

where ρ is the density of seawater, S is the drag area, V_r is water particle velocity relative to the segment, $\forall_w$ is the volume of water displaced by the segment, a_f is the water particle acceleration, a_r is the water particle acceleration relative to the segment, C_d and C_a are the drag coefficient and added mass coefficient, which are set as1.2 and 1.0, respectively.

3 Model validation

In order to verify the accuracy of the numerical model of the cage, a large-scale model cage with a scale of 1:15 is made to conduct its hydrodynamic experiments which have been performed in a wave-current tank at Rudong Experimental Base of Chinese Academy of Fishery Sciences in east China's Nantong city. The wave-current tank is 50 m long, 26 m wide and 1.2 m deep, which is equipped with a servo motor-driven piston-type wave-maker and a current generation system. The main parameters of the cage model are listed in Table 1. The physical model configuration of the SPM net cage is demonstrated in Figure 2. The floating pipes constitute three trapezoids connected by three pipes with a length of 0.51 m, which is the same as the length of the bottom edge of each trapezoid. The three pipes combine with the bottom edge of each trapezoid to form a regular hexagon, where the length of each side is 0.51 m.

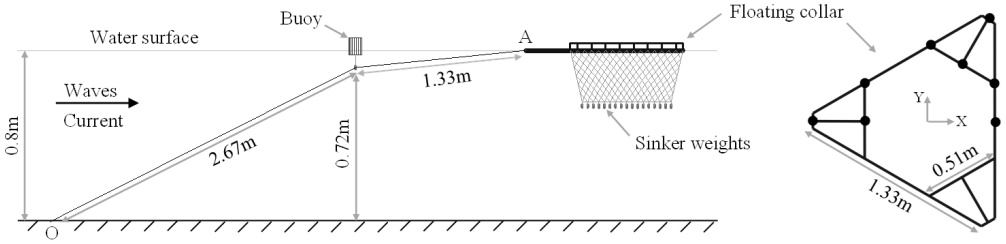

Fig 2. Physical model configuration of the SPM net cage.

Table 1. Parameters of net cage

Component	Parameters	Model value	Prototype Value
Floating pipe	Pipe diameter/mm	26.67	400
	Wall thickness/mm	1.57	23.5
	Shape	triangle	triangle
	Length/m	1.33	20
Net	Mesh size/mm	45	45
	Twine diameter/mm	2	2
	Height/m	0.4	6
	Material	PE	PE
Mooring line	Length/m	4	60
	Diameter/mm	2.67	40
	Material	PE	PE
Buoy	Height/m	0.13	2
	Diameter/m	0.1	1.5
Sinker	Mass/g	20×5.93	20×20000
	Material	concrete	concrete

The load cell connecting the mooring line and the point A of the floating collar is used for measuring the mooring force. The relative error in measurements is less than 1%. We have used an untouched 6-D measurement system to measure the motion responses. The relative error is less than 0.5%. Considering the capacity of the wave-current generation system and the test conditions of water tank, the regular waves with different heights (16, 20, or 24 cm), periods (1.64 or 2.01 s) and current velocities (10.3 or 12.9 cm/s) in the experiment are set as the environmental conditions. Before starting on the experiment, the test waves and current were calibrated to guarantee the accuracy of the experimental data. The error between the measured data and test data for the wave/current parameters is required to be less than 2% in the repeated wave/ current generation process.

Figure 3 shows the comparison between the calculated results and the experimental data for the mooring force, heave and pitch of the net cage under pure waves. The wave period is 1.64s. It can be seen from that the calculated results of the dynamic response of the cage are very close to the measuring data in which the relative errors are all within 10%. The comparison of mooring force for the net cage under different wave-current conditions is given by Figure 4, which indicates the peak value of calculated results have good agreement with the experimental data. Based on the above analysis, the finite element model of the SPM cage is feasible in simulating the dynamic response of cage in pure waves or combined wave-current.

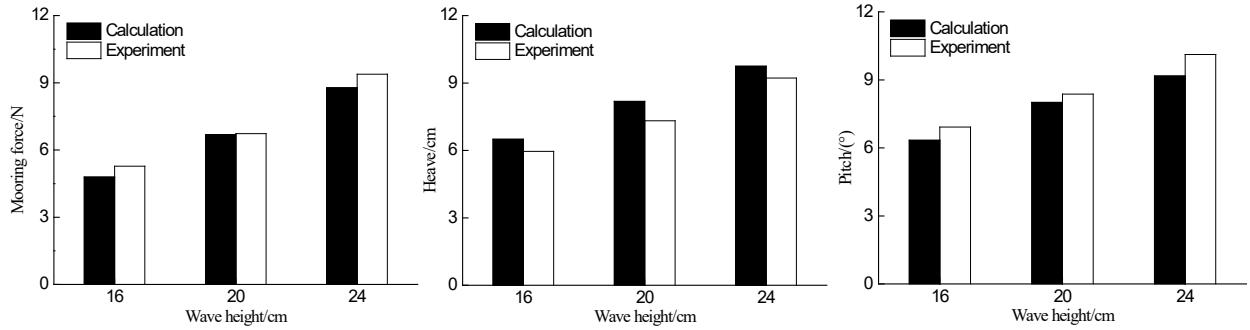

Fig 3. Comparison of dynamic responses between calculated and experimental results of the net cage under pure waves

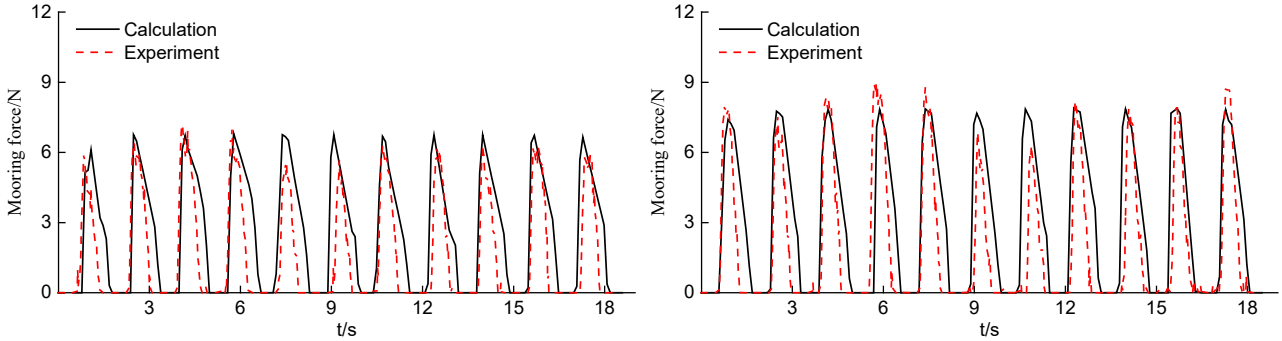

a. H=16cm, T=1.64s, V=10.3cm/s

b. H=20cm, T=1.64s, V=10.3cm/s

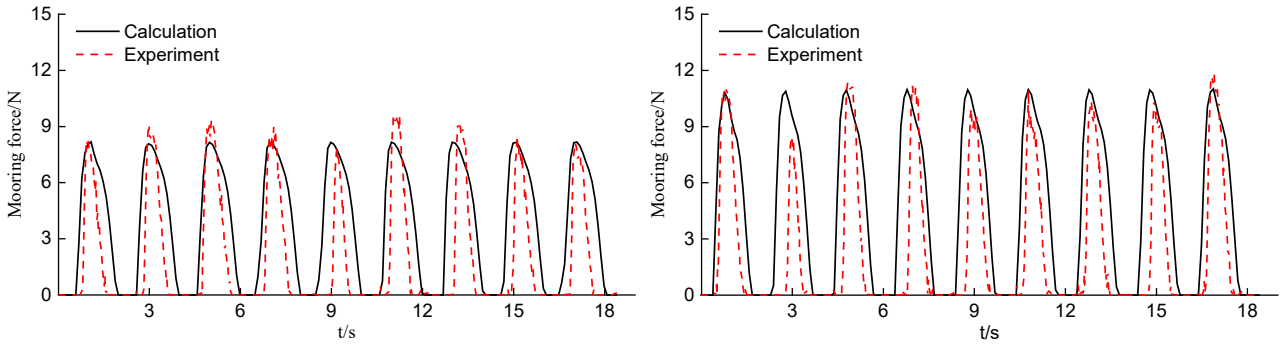

c. H=20cm, T=2.01s, V=12.9cm/s d. H=24cm, T=2.01s, V=12.9cm/s

Fig 4. Comparison of mooring force for the net cage under waves and current

4 Results and discussion

Considering that it is very difficult to use small-scaled model test to measure the deformation of cage collar exposed to waves and current, because the deformation of a small-scale cage collar is too small to be observed easily as the stiffness similarity is not likely to be appropriate for a small-scale, prototype cage collar (Huang et al., 2018). However, it is feasible by using numerical simulation method to investigate the dynamic deformation of cage collar in prototype. Based on the finite element numerical model established in this study, considering sea conditions in practice, the collar deformation and mooring force of the SPM cage are simulated and analyzed. In addition, the effects of the floating pipe thickness and the mooring line length on the dynamic response of the cage are discussed. The main parameters for each cage component are shown in Table 1. The calculated conditions for regular waves and current are setting as follows: wave height 4, 5, or 6 m, wave period 9 s, current velocity 0.5, 1.0 or 1.5 m/s, water depth 20m.

4.1 Deformation of the floating collar

Fig. 5 shows the instantaneous deformed shape of the floating collar when the wave height = 6 m and current velocity = 1.5m/s at different times during one wave period. The top line denotes water surface. It can be found that significant deformation occurs to the collar when t=T/4 and t=T/2. The safety performance of cage structure could be challenged in case of the severe deformation of floating collar. We select multiple points at different positions of the floating collar to analyze the deformation circumstance. Since the floating collar is a symmetrical structure, A-H points in Y positive axis are chosen which is demonstrated in Figure 6. The strain and stress can be written as follows:

$$\varepsilon_{vm} = \sqrt{\varepsilon_{zz}^2 + \varepsilon_{cc}^2 - \varepsilon_{zz}\varepsilon_{cc}} \quad [8]$$

$$\sigma_{vm} = \sqrt{\frac{(\sigma_1 - \sigma_2)^2 + (\sigma_2 - \sigma_3)^2 + (\sigma_3 - \sigma_1)^2}{2}} \quad [9]$$

where σ_1, σ_2, σ_3 are the principal stresses in the three directions, respectively, ε_{zz} is the axial strain, and ε_{cc} is the hoop strain.

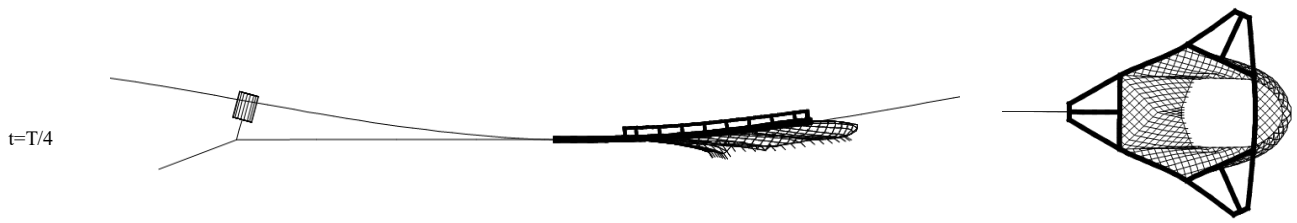

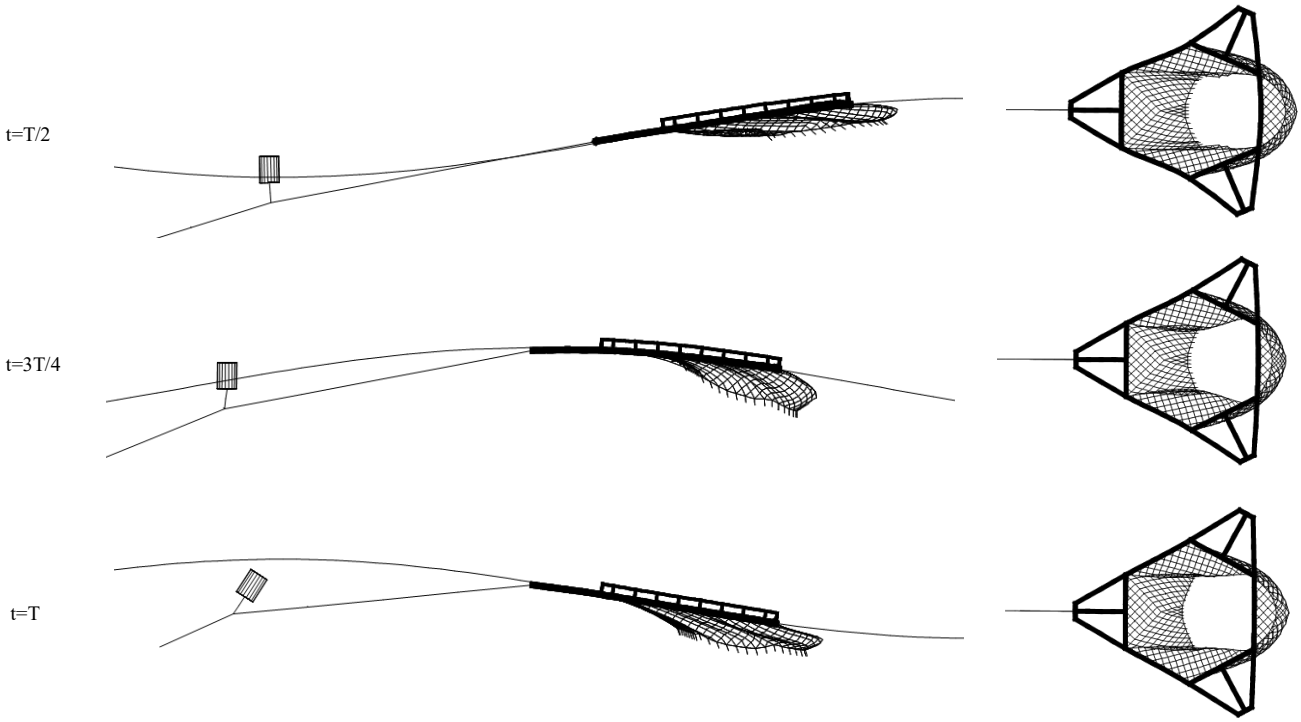

a. Side view b. Top view

Fig 5. Dynamic deformation of the SPM net cage in waves and current at different times （H=6m, T=9s, V=1.5m/s）

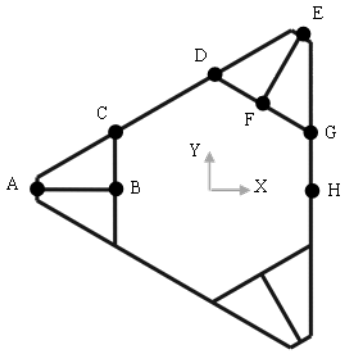

Fig 6. Different points of the floating collar

Table 2 lists the maximum values of stress and strain as well as bending moment for different points A-H on the floating collar under sea conditions with a wave height of 6 m, wave period of 9 s and a current velocity of 1.5 m/s. We can see that the deformation of point D is the highest with 19.5 MPa for the maximum stress, followed by point C with a peak value of 14.99 MPa. For the point F, the maximum stress is only 2.11 MPa, which is the lowest among all of the points attached at the collar. The severe deformation of point D on the floating collar can also be further illustrated in Figure 5. Especially when t = T/4 and t = T/2 during one wave period, large bending deformation occurs at the position of point D reflected from Figure 5. Fredriksson et al. (2007) used the yield stress of 24 MPa as a failure criterion to evaluate the plastic deformation of a floating pipe. Although the maximum stress shown in Table 2 reaches up to 19.5 MPa, which is lower than the yield critical value of 24 MPa, reasonable measures need to be taken to strengthen the weakest position of the point D at the floating collar in case of installing this kind of cage in the more open areas with severe sea conditions.

Table 2. Deformation at different points of the floating collar

Point of the collar	Stress/MPa	Strain/%	Bending moment (kN.m)
A (-11.78, 0.0, 0.0)	11.07	1.14	24.33
B (-6.58, 0.0, 0.0)	3.44	0.36	5.95
C (-6.58, 3.80, 0.0)	14.99	1.58	34.82
D (0.0, 7.60, 0.0)	19.50	2.05	46.40
E (5.89, 10.20, 0.0)	2.34	0.25	5.09
F (3.29, 5.70, 0.0)	2.11	0.42	8.00
G (6.58, 3.80, 0.0)	3.16	0.33	7.67
H (6.58, 0.0, 0.0)	7.37	0.78	17.92

4.2 Mooring line force

Figure 7 shows the results calculated for the maximum mooring force for the SPM cage under different combined conditions of waves and current. It can be seen that the mooring force becomes greater significantly as an increasing wave height or current velocity. Under the condition with a current velocity of 1.0 m/s, the mooring force increases from 30.71 kN to 44.28 kN with a growth of 44.2% as wave height varies from 4 m to 6 m. As a increasing current velocity from 0.5 m/s to 1.5 m/s at a wave height of 6 m, the mooring force increases from 25.33 kN to 68.94 kN with a growth of 172.2%. Figure 8 provides force time-series within 90 s for the upper and lower mooring line under sea conditions with a wave height of 6 m and a current velocity of 1.0 m/s. Clearly, the force for the upper line is slightly smaller than for the lower line, but the difference is very small, which the maximum value is only 13 kN. This is mainly the reason that the presence of the buoy can help to reduce the tension in the upper mooring line.

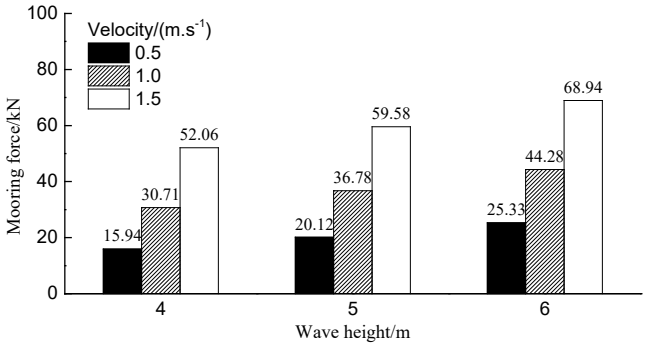

Fig 7. Maximum mooring force under various sea conditions

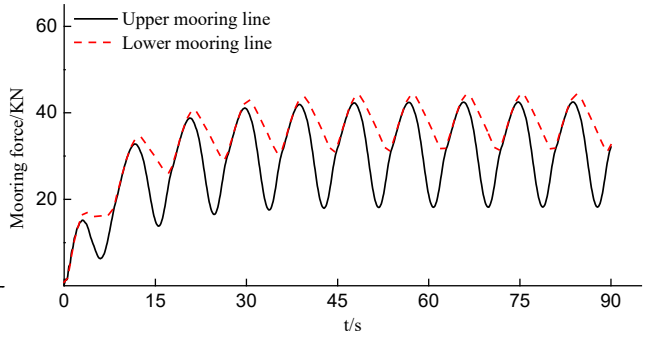

Fig 8. Time-series of force for the upper and lower mooring line（H=6cm, V=1.0m/s）

4.3 Effect of wall thickness of the floating pipe

Floating pipe is the core component of the cage collar. It not only provides buoyancy to enable the cage to drift on the water surface, but also plays an important role in supporting fishing net and resisting the action of wind, waves and current on cage structure with mooring system together. The wall thickness of floating pipe is an important factor for considering the safety behavior of net cage, which has a strong link with the extent of deformation of cage collar. Therefore, we chose to investigate the dimension impact of three wall thickness (23.5, 29.4, and 36.4mm) for the floating pipe on the deformation and force of cage collar exposed to waves and current. Figure 9 shows the time-series of mooring force and strain at point D attached to the floating pipe with various values for wall thickness, where the sea conditions are setting as follows: wave height 6 m, period 9 s and current velocity 1.5 m/s. Here, we select point D to represent the deformation of the floating collar because the deformation of point D is highest based on the previous analysis, and the position for point D is likely to happen failure by yield. As seen from Figure 9, as an increasing pipe thickness, the mooring force increases at some extent. The peak value of mooring force increases from 65.85 kN to 72.1 kN as a pipe thickness climbs up from 23.5 mm to 36.4 mm, but the maximum strain at point D decreases from 2.05% to 1.68%, which greatly reduces the failure risk of the floating pipe due to excessive deformation of the floating cage collar.

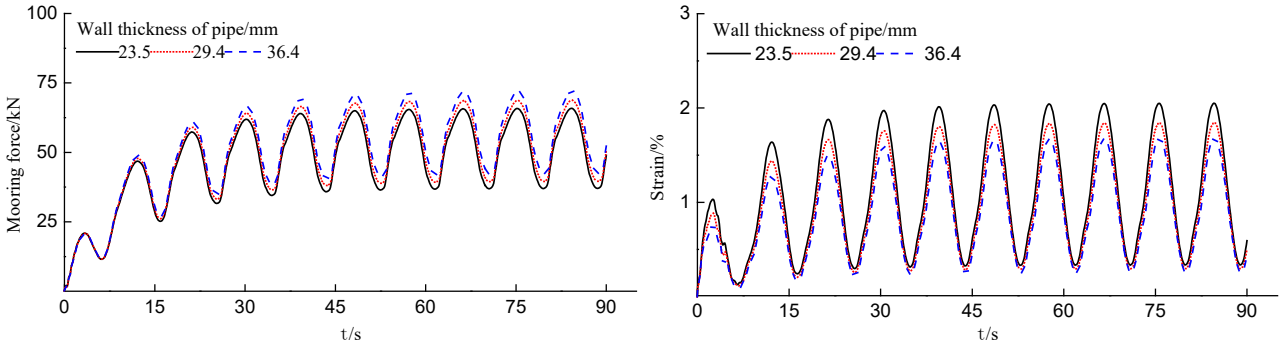

Fig 9. Time-series of mooring force and strain at point D attached to the floating pipe with various values for wall thickness (H=6m, T=9s, V=1.5m/s)

4.4 Effect of mooring line length

Moving cage aquaculture towards more open sea area becomes an inevitable trend. Whether the selection of length for mooring line is reasonable often directly related to the safety of net cage. Analyzing the influence of mooring line length on the force and deformation of cage has important practical significance. For this purpose, we select various length of mooring line (60, 90, and 120 m) and other parameters related to the cage remain unchanged (see Table 1). Figure 10 shows the time-series of mooring force and strain for the floating collar with varied length of mooring line under the conditions with wave height of 6m, wave period of 9 s and current velocity of 1.5 m/s. It can be seen from the figure that the mooring force and collar deformation decreases as a mooring line length increased. When the mooring length is set to 60 m, the values for the mooring force and the strain are 65.85 kN and 2.05%, respectively. When the mooring line length climbs up to 120 m, the force and strain reduce to 57.61 kN and 1.85%, which indicates that increasing the length of mooring line could effectively reduce the failure risk for the mooring system and the floating collar.

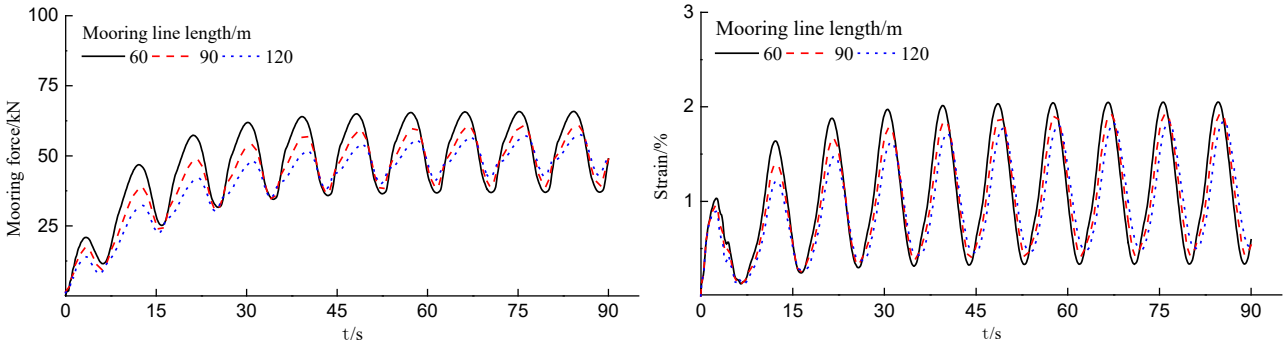

Fig 10. Time-series of mooring force and strain for the floating collar with varied length of mooring line (H=6m, T=9s, V=1.5m/s)

5 CONCLUSIONS

This study has conducted a numerical investigation related to the force and deformation of a SPM deep-water cage exposed to strong waves and current, and the effects of wall thickness of floating pipe and the mooring line length on the mooring force and the collar deformation for the net cage are analyzed. The following conclusions could be obtained:

1) Based on the finite element method, a numerical model simulated for single-point mooring cages under the combined conditions of waves and current is established, and the efficiency and accuracy of the numerical model are verified by carrying out a series of experiments on dynamic response of the cage, in which the relative errors are all within 10%.

2) Under the combined sea conditions with wave height of 6 m, wave period of 9 s period and current velocity of 1.5 m/s, obvious bending deformation occurs to the floating collar and the highest deformation take place in the position of point D attached to the cage collar, of which the peak value for stress is 19.5 MPa. The mooring force increases as wave height or current velocity climbs up.

3) Increasing the wall thickness of floating pipe is helpful to reduce the collar deformation, but the mooring force will increase to a certain extent. When the mooring line length from 60 m to 120 m, the mooring force and the strain reduce as much as 12.51% and 9.75%, respectively, which help to reduce the failure risk of the SPM cage.

ACKNOWLEDGEMENTS

This study was supported by the National Natural Science Foundation of China (Nos. 31772897 and 31902424), Demonstration Project of Marine Economy Innovation and Development (No. Bhsfs012), and Guangdong Provincial Special Fund for Modern Agriculture Industry Technology Innovation Teams (Grant No. 2019KJ143) as well as Central Public-interest Scientific Institution Basal Research Fund, CAFS (No. 2020TD77)

REFERENCES

DeCew, J., Fredriksson, D.W., Lader, P.F., Chambers, M., Howell, W.H., Osienki, M., Celikkol, B., Frank, K., Høy, E. (2013). Field Measurements of Cage Deformation Using Acoustic Sensors. *Aquacultural Engineering*. 57, 114-125.

DeCew, J., Tsukrov, I., Risso, A., Swift, M.R., Celikkol, B. (2010). Modeling of Dynamic Behavior of a Single-point Moored Submersible Fish Cage under Currents. *Aquacultural Engineering.* 43(2),38-45

FAO. (2018). The State of World Fisheries and Aquaculture 2018 - Meeting the sustainable development goals. Rome.

Fishery Administration of the Ministry of Agriculture and Rural Affairs. (2019). *China Fishery Statistics Yearbook*. China Agriculture Press, Beijing

Fredriksson, D.W., Swift, M.R., Irish, J.D., Tsukrov, I., Celikkol, B. (2003). Fish Cage and Mooring System Dynamics Using Physical and Numerical Models with Field Measurements. *Aquacultural Engineering*. 27(2),117-146

Fredriksson, D.W., DeCew, J.C., Tsukrov, I., (2007). Development of Structural Modeling Techniques for Evaluating HDPE Plastic Net Pens Used in Marine Aquaculture. *Ocean Engineering*. 34(16),2124-2137

Gansel, L.C., Oppedal, F., Birkevold, J., Tuene, S.A. (2018). Drag Forces and Deformation of Aquaculture Cages—Full-scale Towing Tests in the Field. *Aquacultural Engineering*. 81, 46-56.

Goudey, C.A., Loverich, G., Kite-Powell, H., Costa-Pierce, B.A. (2001). Mitigating the Environmental Effects of Mariculture through Single-Point Moorings (SPMs) and Drifting Cages. *ICES Journal of Marine Science*, 58: 497–503

Gui F.K. (2006). Hydrodynamic Behaviors of Deep-water Gravity Cage. Dalian: Dalian University of Technology. (in Chinese with English abstract)

Guo, G.X, Huang, X.H, Hu, Y., Tao, Q.Y, Gu, H.G. (2010). In-situ measurement on the forces of mooring lines of circular net cages with high density polyethylene. *Journal of Fishery Sciences of China*. 17(4), 847-852.

Hou, H.M, Dong, G.H, Xu, T.J., Zhao, Y.P. (2019). System Reliability Evaluation of Mooring System for Fish Cage Under Ultimate Limit State. *Ocean Engineering*. 172,422-433

Huang, X.H., Liu, H.Y., Hu, Y., Tao, Q.Y., Wang, S.M., Yuan, T.P. (2018). Deformation simulation and structural improvement design for floating collar of deep-water aquaculture net cage. *Transactions of the Chinese Society of Agricultural Engineering*. 34(15), 44-49.

Huang, X.H., Wang, F.F., Liu, H.Y., Hu, Y., Wang, Z.X., Wang, S.M., Zhao, Y.P. (2019). Effects of mooring systems and ballast status on dynamic behaviors of semi-submersible offshore fish farm. *Transactions of the Chinese Society of Agricultural Engineering*. 35(15), 48-53.

Huang, X.H., Guo, G.X., Tao, Q.Y., Hu, Y., Liu, H.T., Wang, S.M., Hao, S.H. (2018). Dynamic Deformation of the Floating Collar of a Net Cage Under the Combined Effect of Waves and Current. *Aquacultural Engineering*, 83,47-56

Huang, L.Y., Liang, Z.L., Wan, R., Mu, X.J., Zhao, F.F., Song, W.H., Wang, X.X., Shi, J.G. (2011). Tension of anchor lines of single gravity grid mooring cage under combining effects of wave and current. *Journal of Fishery Sciences of China*. 18(03), 636-645.

Jia, J.D., Jiang, D.P., Yang, H.S., Chen, Z.B. (2014). *Research on Innovation Strategy of Modern Marine Agriculture Technology*. China Agricultural Science and Technology Press, Beijing, China.

JTS 145-2-2013, Code of Hydrology for Sea Port Harbour

Kristiansen, T., Faltinsen, O.M. (2015). Experimental and Numerical Study of an Aquaculture Net Cage with Floater in Waves and Current. *Journal of Fluids and Structures*. 54, 1-26.

Li, L., J, Z.Y., Andreas, V.H., Muk, C.O. (2018). Numerical Analysis of a Vessel-Shaped Offshore Fish Farm. *Journal of Offshore Mechanics and Arctic Engineering*. 140, 0441201-1-11

Liu, H.Y., Wang, S.M., Huang, X.H., Tao, Q.Y., Hu, Y., Guo, G.X., Song, L.M. (2017). Mechanical property analysis and optimization of deep-water net cage guardrail. *Transactions of the Chinese Society of Agricultural Engineering*. 33(4), 248-257.

Mai, K.S., Xu, H., Xue, Z.H., Gu, W.D., Zhang, W.B., Li, Z.J., Yu, B. (2016). Study on strategies for developing offshore as the new spaces for mariculture in China. *Engineering Sciences*,18(3), 90-95.

Morison, R., J., Johnson, W., J., Schaaf, A., S. (1950). The Force Exerted by Surface Waves On Piles. Journal of Petroleum Technology. *Journal of Petroleum Technology*, 2 (5): 149-154.

Orcina Ltd. (2015). *OrcaFlex Manual Version 10.0a*. Ulverston,Cumbria, UK.

Shainee, M., DeCew, J., Leira, B.J., Ellingsen, H., Fredheim, A. (2013). Numerical Simulation of a Self-Submersible SPM Cage System in Regular Waves with Following Currents. *Aquacultural Engineering*. 54,29-37.

Xu, T.J., Dong, G.H., Li, Y.C., Guo, W.J. (2014). Numerical Study of a Self-Submersible Single-Point Mooring Gravity Cage in Combined Wave-Current Flow. *Applied Ocean Research*. 48,66-79.

Xu, H., Chen, Z.X., Cai, J.Q., Huang, Y.X., Liu, H. (2016). Research on the development of deep sea aquaculture engineering equipment in China. *Fishery modernization*. 43(3), 1-6.

Yang, R.Z., Zhu, K.Q., Jing, B., Zhang, D.P., Tang, Z.C. (2015). Dynamical analysis of submersible cage array. *Chinese Journal of Hydrodynamics*. 30(01), 83-91.

Zhao, Y.P., Gui, F.K., Xu, T.J., Chen, X.F, Cui, Y. (2013). Numerical Analysis of Dynamic Behavior of a Box-Shaped Net Cage in Pure Waves and Current. *Applied Ocean Research*. 39(1),158-167

Zheng, G.F., Huang, G.F., Wei, G.Y., Ding, L., Zhu, J.K. (2007). Study on the characters of tension in mooring lines of anti-stormy-wave cage with cylindrical net under the combined action of waves and currents. *Journal of Fisheries of China*. 1, 84-89.

Coastlab 20
Dec 10-12, Zhoushan, China

8th International Conference on the Application of Physical Modelling in Coastal and Port Engineering and Science
Dec. 9th - 12th, 2020, Zhoushan, China

HIGH-SPEED SOFT ROBOTS ENABLED BY COMBUSTION FOR STRUCTURAL HEALTH MONITORING IN OCEAN ENGINEERING

HAIPENG WANG[(1)], YANG YANG[(1)], GUANZHENG LIN[(1)], XINGHONG YE[(1)], WENTAO LI[(1)], LUQIN HONG[(1)], ALI MATIN NAZAR[(1)], KING-JAMES I. EGBE[(1)], ZHIGUO HE[(1), (2)], PENGCHENG JIAO[(1), (2)]

(1) Institute of Port, Coastal and Offshore Engineering, Ocean College, Zhejiang University, Zhoushan 316021, Zhejiang, China
(2) Engineering Research Center of Oceanic Sensing Technology and Equipment, Zhejiang University, Ministry of Education, China
Email: pjiao@zju.edu.cn

ABSTRACT

Soft robots have recently been extensively studied for applications in a variety of environments, accomplishing multifunctional tasks. Here, we develop a novel type of soft robots driven by mixed gas (i.e., oxygen and propane) combustion in a chamber sealed by expandable silicon- rubber membrane. The reported soft robots are able to jump out of the water with a high-speed of ~6 times body length per second on average and up to ~9 times body length per second at the most. Experiments are conducted to investigate the motion process of the soft robots under different driving conditions (i.e., gas ratio r, water depth D_w, and gas amount A). Numerical simulations are carried out to compare with the experimental results, and good agreements are obtained. Taking advantage of the high-speed movement through the multiphase environments, we envision the application of the soft robots for structural health monitoring (SHM) in ocean engineering by detecting the damages of underwater structures and wirelessly transmitting data when jumping out of water.

Keywords: Soft robots; High-speed; Combustion; Structural health monitoring

1. INTRODUCTION

The researches on soft robots are getting more and more attentions (Lee et al., 2017). However, the previous researches on soft robots mainly focus on structural design and manufacturing materials. The practical application of soft robots and the interaction of multiphase environments lack profound research. Moreover, because of the properties of the structural material, high-speed motion is a complicated problem in the research of soft robots.

Combustion driving method is one of the most effective techniques for soft robots to achieve high-speed motion. Shepherd et al. used premixed gas (e.g., CH_4-O_2) to develop combustion-driven actuators for on-land high-speed soft robots (Tolley et al., 2014; Stokes et al., 2014; Shepherd et al.,2012;Shepherd et al.,2011), such as the tri-pedal soft robots (Shepherd et al.,2012) and the soft combustion-driven pump for soft robots (Stergiopulos et al.,2014). At present, the research on the dynamic process of combustion is relatively insufficient, leading to the lack of research on quantitative analysis of the motion of combustion-driven soft robots. It makes it difficult to control the motion of combustion-enabled soft robots. Combustion is a transient physical phenomenon that occurs with the release of high energy. The process of combustion is complex and hard to control. As a consequence, combustion-driven soft robots have not been used in multiphase environments for multifunctional applications in reality.

In order to improve the controllability of the combustion-driven soft robot, we report a new type of untethered combustion-driven underwater soft robots. The combustion-enabled driving actuator comprises a silicon-rubber membrane, which could significantly expand by igniting the combustion of oxygen-propane mixed gas. Thus, enabling the soft robot to jump out of the water and reach 2.5 times body lengths from the water-air interface, 4.5 times body length from the initial position in 0.4s. By precisely manipulating the jumping motions, the untethered combustion underwater soft robots can be potentially used for different purposes in different environments.

2. DESIGN AND FABRICATION

2.1. Design Principle

In this section, we introduce the design principle of combustion-driven, high-speed soft robots. Figure 1 illustrates the detailed structures of the soft robots and the details of the series units, including the control unit, the weight unit, and the reaction unit. The control unit contains various circuit components. The weight unit is designed with a weight box to balance the buoyancy. The extreme energy-releasing phenomenon is designed to occur in the reaction unit. The size (D = 140 mm, L = 200 mm) and the actuation principle of the soft robot are illustrated in Figure 2. The gas source delivers the premixed gas (oxygen and propane) in a particular ratio. The power source consists of a power supply that provides a DC voltage about 9 V, and a spark generator to trigger the voltage release process when the voltage difference reaches~200 V (Oisin et al.,2018; Meuller et al., 2012). After the premixed gas is completely injected into the reaction unit, the spark generator in the soft robot is used to ignite the reactant. After that, the soft membrane swells rapidly from 0 to 1 ms in the shape of a volcano (Wang et al., 2020). It can be regarded as an acceleration process of the soft robot. Several cycles of the expansion process later, the soft membrane reaches the highest deformation at the end of the acceleration phase. Combustion-driven underwater soft robots can achieve various types of applications by effective control methods.

2.2. Fabrication and Experimental Setup

3D additive manufacturing technique (e.g., Acrylic 3D printing technique) is used to fabricate the components of the soft robots (i.e., Heads, Chambers, and Holders), and the ultra-expandable membrane was manufactured using silicon-rubber. In previous studies (Oisin et al.,2018; Zou et al., 2018; Hao et al., 2016), the membrane of soft robots is fabricated by Dragon Skin 30 silicon rubber. To ensure consistent quality of the soft robot, we particularly chose this kind of silicon rubber as raw material to fabricate the soft membrane. To compare the kinematic response of the soft robots with the previous studies (Oisin et al.,2018; Zou et al., 2018; Hao et al., 2016), we particularly chose Dragon Skin 30 silicon rubber as the raw material to fabricate the soft membrane (Smooth-on Inc.) (Yang et al., 2020). Figure 3(a) illustrates the fabrication process of the soft membrane. The manufacturing process includes mixing, stirring, reversing, defoaming, and cure. In the first step, we mixed the gel A and B together with the same volume (70 ml). The second step was implemented to mix gel well. We used a stirrer to mix the gel for 2-minutes

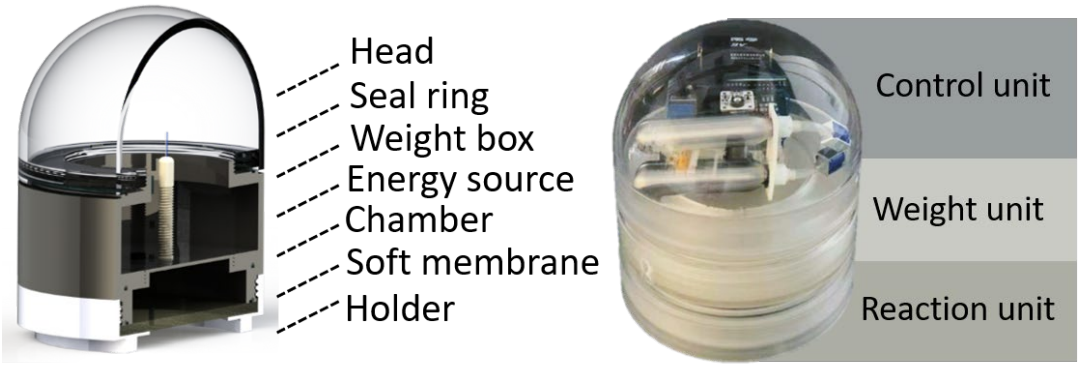

Figure 1. Illustrative demonstration of the soft robots' structure of the series units.

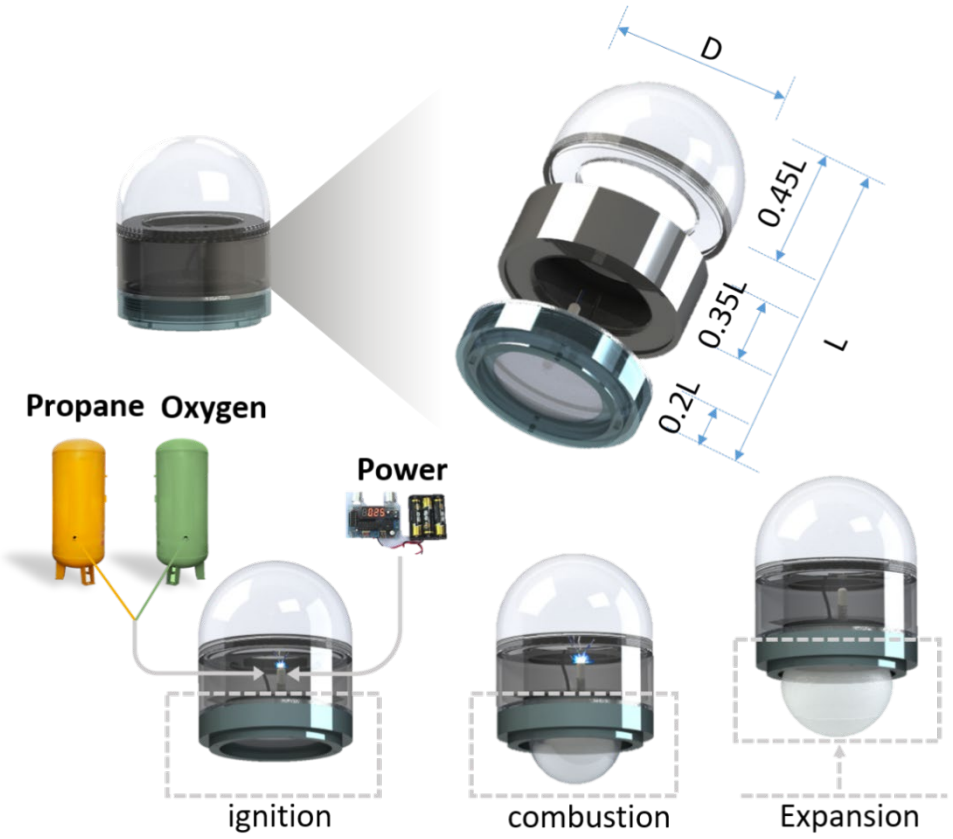

Figure 2. Combustion process of the robots: illustration of deformation and actuation principle..

to get the full mixed gel. In the third step, in order to get the fit shape of the soft membrane, we poured the gel into the 3D printed mold. In the fourth step, we provide a 15-minutes negative pressure environment through a vacuum generator to make bubbles defoaming and make the film evenly formed. In the final step, we fixed the mold under constant temperature environments (i.e., 25℃) for more than 8 hours. Figure 3(b) shows components of the soft robots manufactured by Acrylic 3D printing technique and silicone molding technology (Wang et al., 2020). The head was designed with two holes to assemble the gas tube and spark generator, the weight box designed with a hollow to set weight balancing the buoyancy force, soft membrane, and the chamber were connected in order.

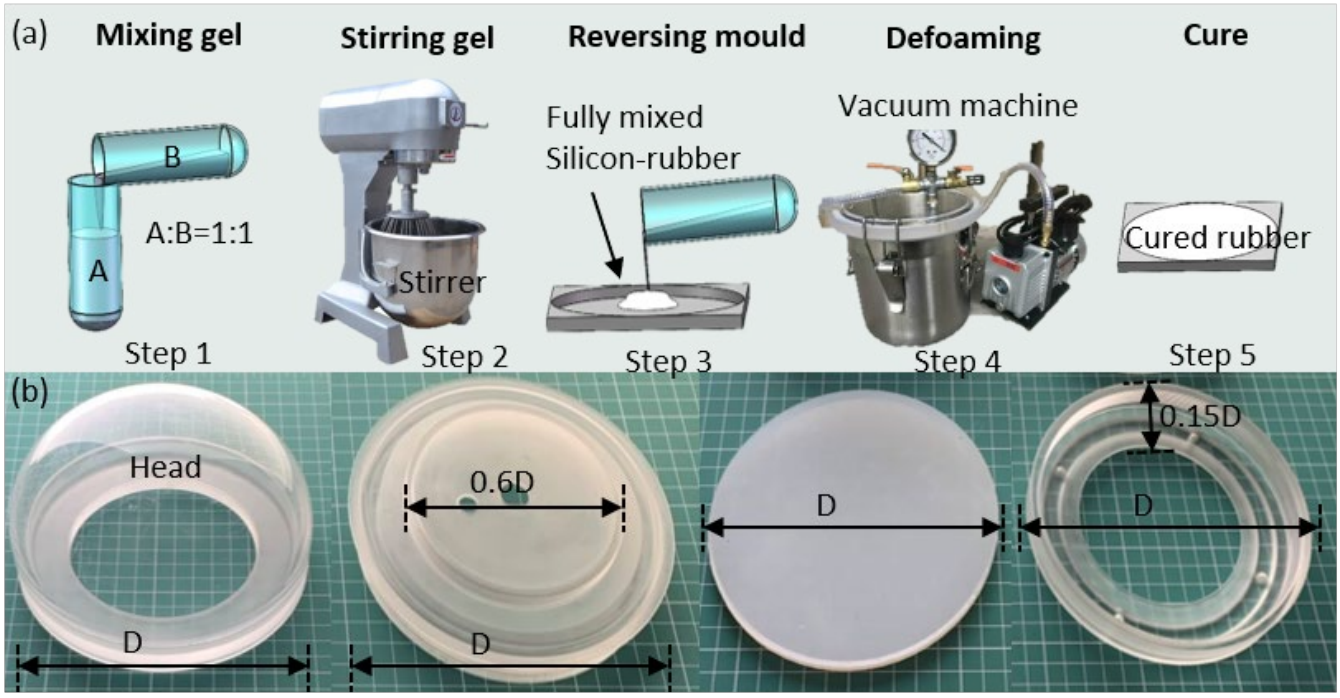

Figure 3. Fabrication process of the soft underwater robots: (a) the five fabrication processes of the soft membrane, and (b) the 3D printed components to assemble the soft underwater robots.

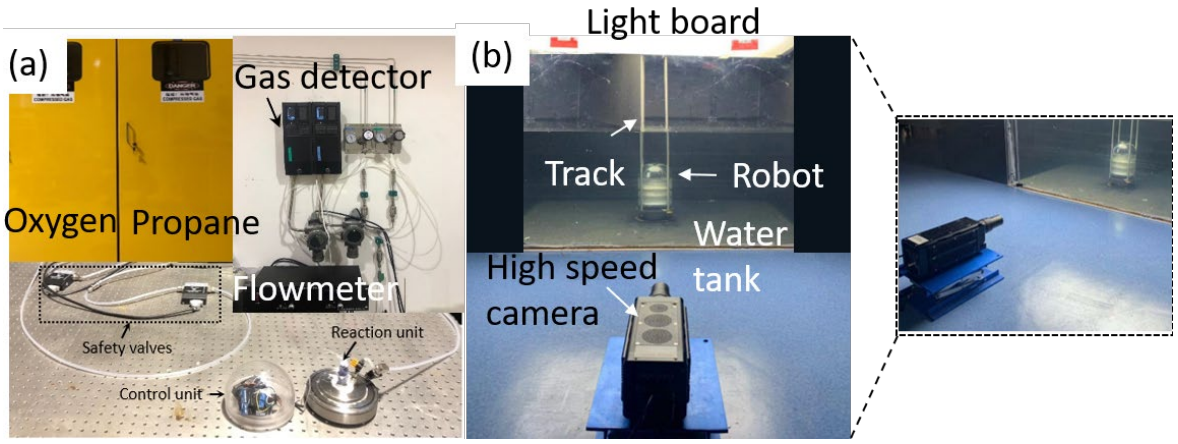

Figure 4. The experiment system of the soft underwater robots: (a) the setup for gas input and (b) the setup for the underwater testing platform.

Figure 4(a) details the gas supply setup. To ensure the security of this experiment setup systems the gas explosion proof cabinet, gas detector and safety valves were installed in the gas circuit. Oxygen and propane are fully mixed in a certain ratio and controlled by an electronic flowmeter to sustain the velocity and gas ratio. The premixed gas was input into the chamber of the reaction unit, which is sealed by the soft membrane, and this input process called well-developed out-body-source injection technology (Yang et al., 2020; Keithly et al., 2018; Tolley et al.,2014; Shepherd et al., 2012). After premixed gas is injected, the chamber unit is completely sealed. Figure 4(b) illustrates the experimental setup of the underwater test platform. Due to the transient fast movement of the

soft robot, the optical high-speed camera with a capture speed of 12000 FPS was placed in front of the experimental test tank. To create a clear shooting environment, the light board was installed on top of the water tank.

Table 1. Statistical analysis results of the experiments.

Ratio r	Depth D_w (m)	Amount A (ml)	Height H (m)	Ratio r	Depth D_w (m)	Amount A (ml)	Height H (m)
3	0.30	20	0.450	5	0.30	20	0.32
		25	0.565			25	0.439
		30	0.605			30	0.515
		35	0.59			35	0.562
	0.35	20	0.447		0.35	20	0.243
		25	0.488			25	0.362
		30	0.553			30	0.442
		35	0.571			35	0.487
	0.40	20	0.309		0.40	20	0.205
		25	0.412			25	0.31
		30	0.505			30	0.365
		35	0.531			35	0.443
4	0.30	20	0.380	6	0.30		
		25	0.526			25	0.325
		30	0.598			30	0.4
		35	0.653			35	0.418
	0.35	20	0.335		0.35		
		25	0.459			25	0.283
		30	0.548			30	0.365
		35	0.568			35	0.394
	0.40	20	0.25		0.40		
		25	0.39			25	0.259
		30	0.488			30	0.341
		35	0.528			35	0.374

3. OUT-OF-WATER JUMPING TESTING

In this section, we tested the out-of-water performance of the soft robots. A series of underwater jumping experiments have been done in order to get the relationship between the jumping height, gas volume, and premixed gas ratio, and the relationship between the results is shown in Table 1. The experimental premixing ratio design are 3, 4, 5, 6; the pre-mixed gas volumes are 20 ml, 25 ml, 30 ml, and 35 ml respectively; the water depths are 0.3 m, 0.35 m, and 0.4 m respectively. We generally specify the maximum displacement as the maximum jump height from the origin position. When the water depth and premixed gas radio is constant, the height of the soft robots is positively correlated with the gas volume. At the same time, we can find that the jumping height decreases as the water depth increase. This shows that the water-air multiphase movement of the soft robots is mainly affected by the water environment.

It is found that when the amount of premixed gas is 20 ml-25 ml, and the ratio is 3, the combustion rates are approximately 0%. When the gas volume is 35 ml and the premixed gas ratio is 3, the soft robots can obtain the maximum jumping height. But at the maximum jump height, the soft robots are in an excessive combustion state,

Table 2. Detailed information in the numerical simulations.

Mesh	Nodes	3529
	Elements	17912
	Minimum size (mm)	0.795
	Maximum face size (mm)	79.477
	Maximum Tet size (mm)	158.950
Multiphase model	Model	Volume of fluid
	Number of Eulerian phases	2
	Volume fraction parameters	Implicit
	Volume fraction cutoff	1×10^{-6}
Viscous model	Model	Standard $k-\varepsilon$
	C_{μ}	0.090
	$C_{1\varepsilon}$	1.440
	$C_{2\varepsilon}$	1.920
	σ_k	1
	σ_{ε}	1.300
Solution Methods	Scheme	PISO
	Neighbor Correction	1
	Skewness Correction	1

and the soft membrane can sustain about only ten explosions. Therefore, in order to accurately control the kinematics of the soft robots, we found a suitable range of premixed gas volume and gas ratio. The jumping motion of the soft robots at the water-air interface is shown in Figure 5. The jumping motion process of the soft robots can be divided into four processes: driving, swimming, jumping out of the water and falling. During the driving process, the soft robots move due to the large acceleration generated by the combustion of the premixed gas. The acceleration time of the soft robots is about 9 ms. After 9 ms, the soft robots stop accelerating and start swimming underwater. When the soft robots reach the water-air interface, it starts the jumping process. During the jumping

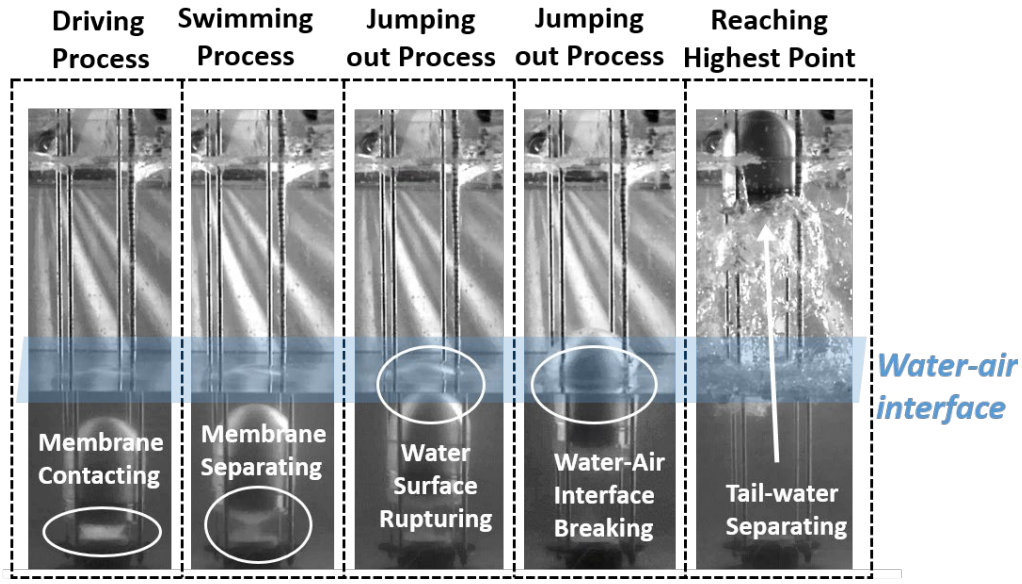

Figure 5. The underwater jumping tests experimental observations of the out-of-water, multiphase jumping response for the soft robots.

process, the soft robots are still moving, the surrounding water becomes turbulent, and the water surface begins to break. The soft robots quickly rush out of the water and cause the water-air interface rupture. Finally, during the falling, the tail of the soft robots gradually separates from the water-air interface. All experiments are carried out under the condition that the soft robots jump vertically out of the water.

4. MODEL VALIDATION

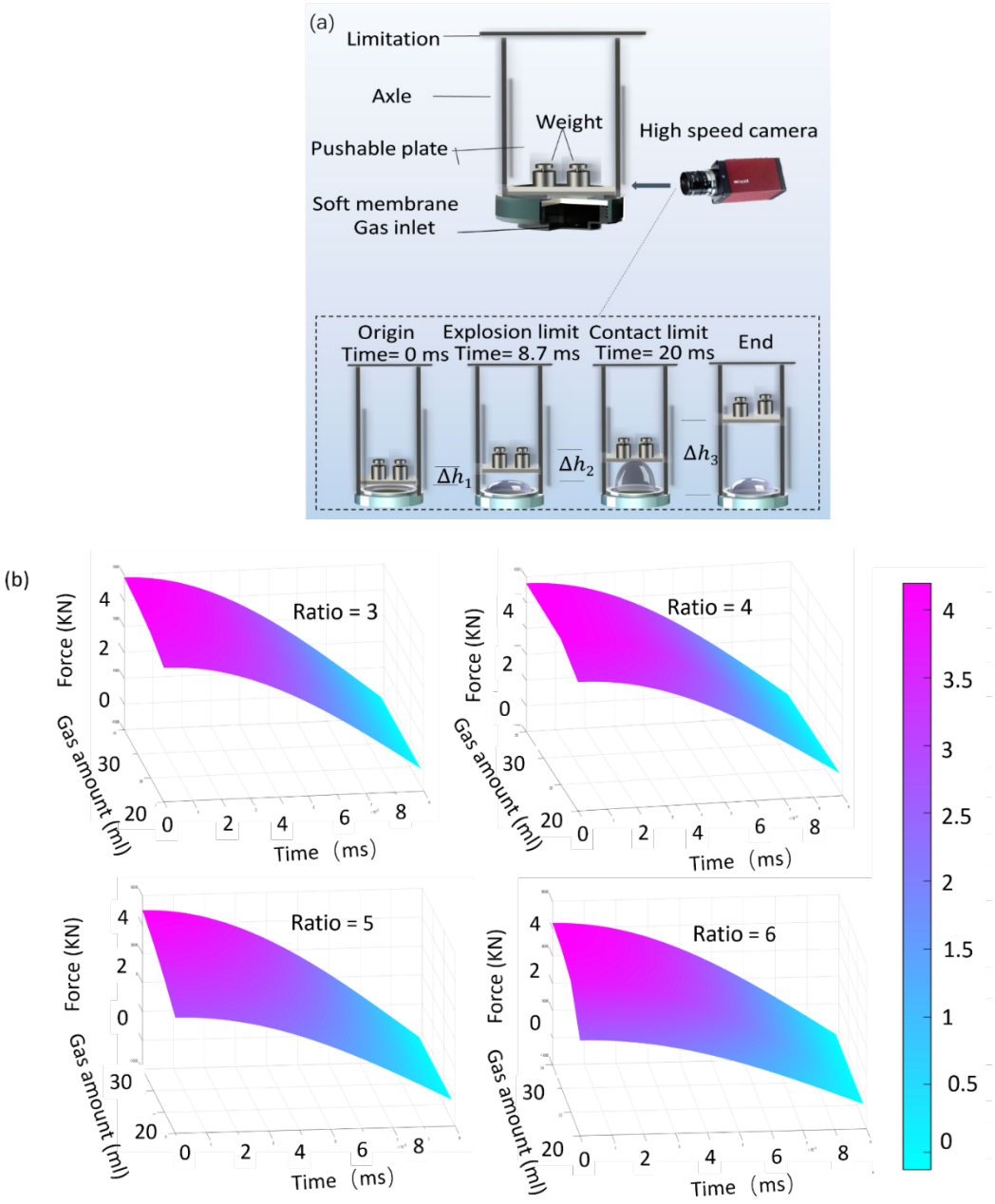

Figure 6. The combustion load experiments for force measurement: (a) experimental setup, actuation process, and displacement results of the pushable plate and (b) force results.

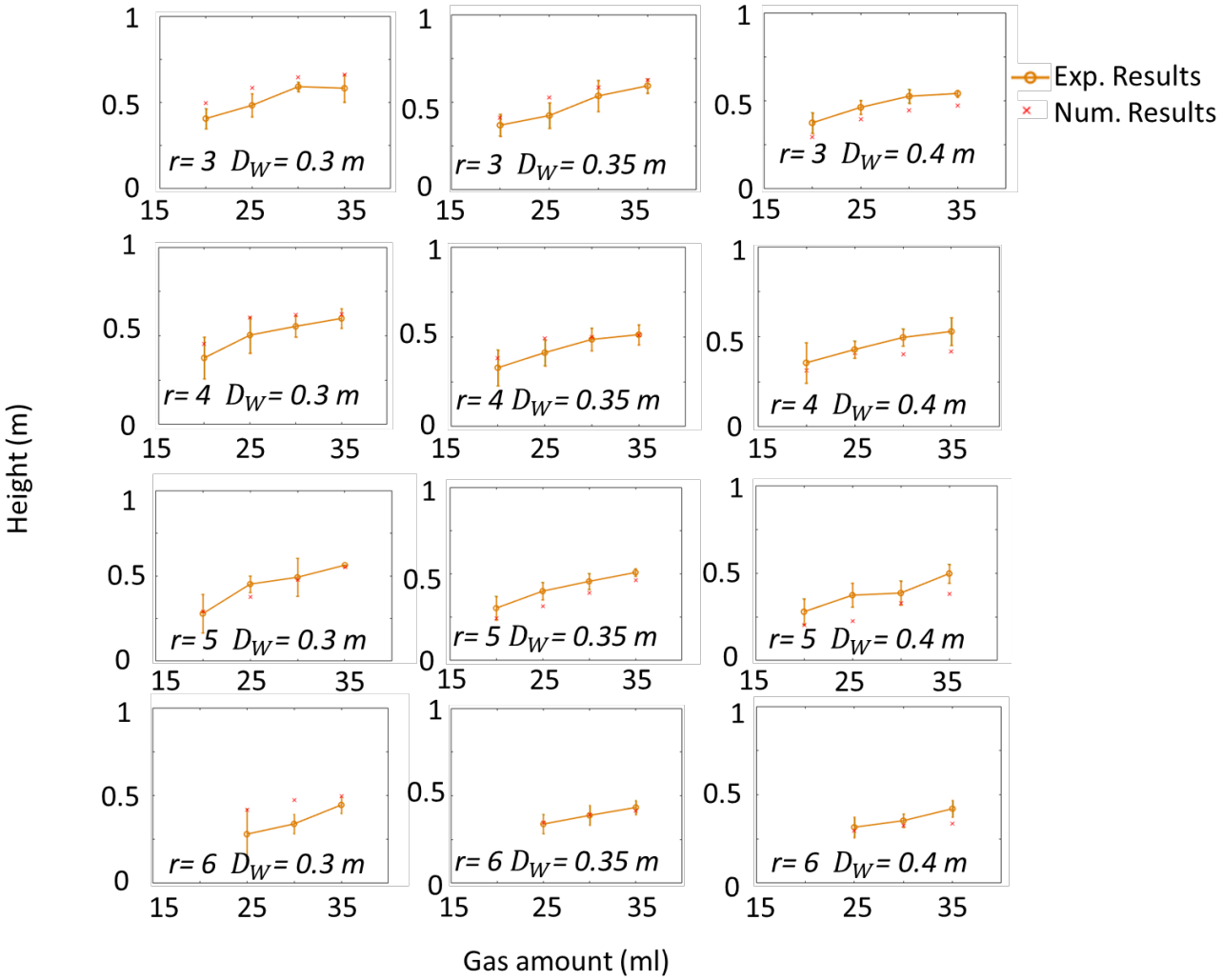

Figure 7. The relation between gas ratio, gas amount, water depth and displacement.

4.1. Numerical Modelling

The FLUENT, ANSYS is used to numerically simulate the jumping process of the soft robots. We use fluid-solid coupling technology, the multiphase flow model, and dynamic mesh method. Since the fluid field will be severely disturbed by the soft robots jumping out of the water at high speed, it is necessary to apply the transient thrust generated by the combustion to the bottom of the soft robots to achieve the water-air multiphase fluid field movement. The reaction force composed of resistance, additional mass force and gravity prevents the soft robots from jumping out of the water. The dynamic mesh method is applied in the numerical simulation, using spring performance assumptions to allow element deformation. When the deformation of the element reaches the maximum, the mesh will be automatically re-divided, which can make the calculation more accurate. For the hydrodynamic simulation, a 3D numerical model is developed, and the governing equations are the time-averaged incompressible continuity equation and Navier-Stokes (N-S) equation. The volume of phases (VOF) model is used to solve the multiphase fluid dynamics phenomenon. The standard k-ε viscous model is used to ensure the

calculation stability. The semi-implicit method for the pressure-linked equation (SIMPLE) algorithm is used to solve the coupling problem between the pressure and velocity. Table 2 shows the detailed information in the numerical simulations.

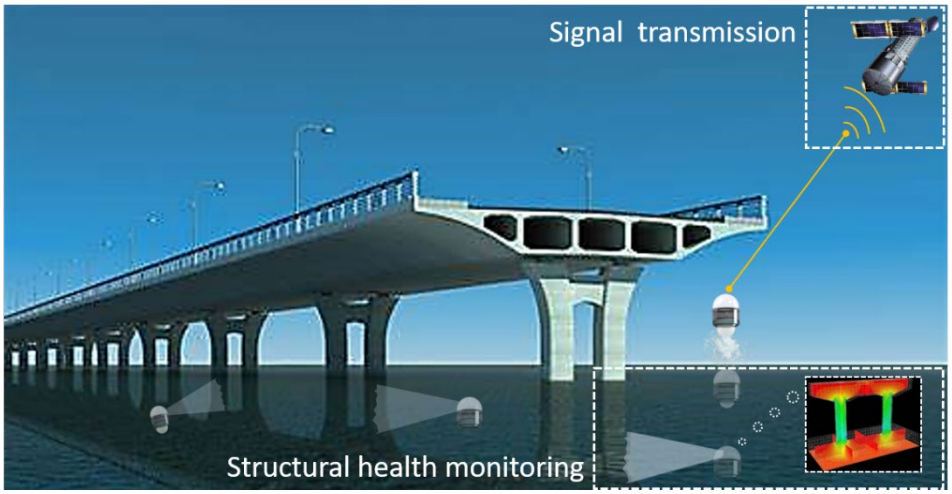

Figure 8. The application of the soft jumpers to monitor structure health and transmit.

4.2. Comparisons and Validation

Then the jumping height is compared with the experimental and numerical results, as shown in Figure 7. Under different pre-mixed air ratios, water depths and air volume, the results of maximum displacement in the multiphase environment are compared. The soft robots generally can jump out of the water surface 0.5 m on average, and the maximum jumping out of the water surface is 0.6 m. The relationship between the maximum jumping height and air volume indicates the quadratically increasing pattern. The amount of gas selected in this study is sufficient to provide accurate displacement control for the soft robots. Under the same pre-mixed air ratio, the maximum displacement decreases with the increase of water depth. Under the same water depth, as the pre-mixed air ratio increases, the maximum displacement gradually decreases. Unstable combustion under extreme conditions, guide shaft and interface assumptions are the main reasons for some of the differences in Figure 7. The combustion of a small amount of premixed gas is typically unstable. For example, when the amount of gas is 25 ml, the amount of reactant reaches the minimum limit of the amount of combustion. Although these factors have an effect on the accuracy of the experimental results, the overall difference in the comparison in this study is less than 15%, which is acceptable, especially for the reported transient motion under extremely strong combustion. The reported soft robots can generally jump to the maximum height point within 0.4 s, the longest can reach 0.5 s, and the time consumption to reach the highest position increases linearly with the gas volume. In all cases, the difference was less than 15%, and a good agreement was reached. We compared the maximum jumping heights under different water depths and obtained relevant principles. According to this rule, when the water depth is 0 m, that is, there is only a single phase, the jumping height is the largest; when the water depth tends to infinity, that is, there is only a single phase of water, the jumping height is the lowest. Therefore, we can conclude that the multiphase motion of the soft robots is dominated by the water phase.

5. FUTURE TRENDS OF THE SOFT ROBOTS

Based on the soft robots' multiple functions, the reported soft robots can be applied in different scenarios.

However, soft robots still have many technical problems that need to be addressed. For example, to solve the disadvantages that soft robots only can jump once time and move a short distance, we need to install a convenient gas source to sustain the soft robots to perform continuous jumping. Second, the expandable soft membranes need to be further optimized to sustain higher stiffness and better recoverability after the extremely larger deformation. Moreover, multiple equipment (e.g., monitoring equipment) can be coupled with these soft robots to monitor the conditions of the submarine environments or marine structures.

6.CONCLUSIONS

This research developed an untethered underwater soft robot which is driven by combustion. The robot can reach 2.5 times body lengths from the water-air interface, 4.5 times body length from the initial position in 0.4s. We conducted experiments to obtain the relationship between the jump height H, gas volume A, the premixed gas ratio r, and the water depth D_{W}. Numerical models were developed to compare with experimental results, and we obtained a satisfactory agreement. Finally, we obtained the interaction performance between the robot and the air-water interface in this study. The transient driving method (TDM) enabled by combustion is a potential method to realize high-speed movements of soft robots, especially underwater. The untethered soft robots can be put into engineering practice, such as structural health monitoring, as is shown in Figure 8, for their property of high-speed motion in multiphase environments. The soft robot can monitor the certain position of the structure quickly and accurately, then jump out of the water to transmit signals. However, we need more innovative designs to get rid of the bulky fuel cylinders and valves.

REFERENCES

Hao, Y., Gong, Z., Xie, Z., Guan, S., Yang, X., Ren, Z., Wang, T. & Wen, L. (2016) Universal soft pneumatic robotic gripper with variable effective length. *IEEE*, *Proceedings of the 35th Chinese Control Conference*, 6109-6114.

Keithly, D., Whitehead, J., Voinea, A., Horna, D., Hollenberg, S., Peck, M., Pikul, J. & Shepherd, R. F. (2018). A cephalopod-inspired combustion powered hydro-jet engine using soft actuators. *Extreme Mechanics Letters*, 20, 1-8.

Lee, C., Kim, M., Kim, Y. J., Hong, N., Ryu, S., Kim, H. J. & Kim, S. (2017). Soft robot review. *International Journal of Control*, *Automation and Systems*, 15, 3-15.

Meuller, B. O., Messing, M. E., Engberg, D. L. J., Jansson, A. M., Johansson, L. I. M., Norlen, S. M., Tureson Nina & Deppert, K. (2012). Review of spark discharge generators for production of nanoparticle aerosols. *Journal Aerosol Science and Technology*, 46, 1256-1270.

Oisin, B., Fergal, C., Mark, G., James, F. J., Aisling, N. A., Eoin, D. O. & Donal, P. H. (2018). Additive manufacture of composite soft pneumatic actuators. *Soft Robotics*, 5, 726-736.

Shepherd, R. F., Llievski, F., Choi, W., Morin, S. A., Stokes, A. A., Mazzeo, A. D., Chen, X., Wang, M. & Whitesides, G. M. (2011). Multigait soft robot. *Proceeding of the National Academy of Sciences of the United States of America*, 108, 20400-20403.

Shepherd, R. F., Stokes, A. A., Freake, J., Barber, J., Snyder, P. W., Mazzep, A. D., Cademartiri, L., Morin, S. A. & Whitesides, G. M. (2012). Using explosions to power a soft robot. *Angewandte Chemie International Edition*, 52, 2892-2896.

Stokes, A. A., Shepherd, R. F., Morin, S. A., Llievski, F. & Whitesides, G. M. (2014). A hybrid combing hard and soft robots. *Soft Robotics*, 1, 70-74.

Stergiopulos, C., Vogt, D., Tolley, M. T., Wehner, M., Barber, J., Whitesides, G. M. & Wood, R. J. (2014). A soft combustion-driven pump for soft robots. *Smart Materials, Adaptive Structures and Intelligent Systems*, 2, 1-6.

Tolley, M. T., Shepherd, R. F., Mosadegh, B., Galloway, K. C., Wehner, M., Karpelson, M., Wood, R. J. & Whitesides, G. M. (2014). A resilient, untethered soft robot. *Soft Robotics*, 1, 214-237.

Wang, H., Yang, Y., Lin, G., Jiao, P. & He, Z. (2020). Untethered, High-Speed Soft Jumpers Enabled by Combustion for Motions through Multiphase Environments. *Smart Materials and Structures*, (Accepted).

Yang, Y., Hou, B., Chen, J., Wang, H., Jiao, P. & He, Z. (2020). High-speed soft actuators based on combustion-enabled transient driving method (TDM). *Extreme Mechanics Letters*. 37, 10037.

Zou, J., Lin, Y., Ji, C. & Yang, H. (2018). A reconfigurable omnidirectional soft robot based on caterpillar locomotion. *Soft Robotics*. 5, 164-174.

8th International Conference on the Application of Physical Modelling in Coastal and Port Engineering and Science
Dec. 9th - 12th, 2020, Zhoushan, China

SMARTPHONE-ENABLED STRUCTURAL HEALTH MONITORING USING MAGNETIC FIELD INTENSITY

ALI MATIN NAZAR[1], KING-JAMES I. EGBE[1], YANG YANG[1], HAIPENG WANG[1], PENGCHENG JIAO[1,2]

1 Institute of Port, Coastal and Offshore Engineering, Ocean College, Zhejiang University, Zhoushan 316021, Zhejiang, China,
2 Engineering Research Center of Oceanic Sensing Technology and Equipment, Zhejiang University, Ministry of Education, China
Email: pjiao@zju.edu.cn

Abstract

In this study, a smartphone is idealized for use in the structural health monitoring (SHM) of infrastructures using magnetic field intensity detection. Experimental and numerical studies are performed on a steel plate with different damage states. The damages states are cracks and holes. The damages are in various combinations to determine the effectiveness of the proposed method. The magnets' magnetic field intensity variations are detected using the smartphone, with numerical simulations showing good agreements with the experimental results. The proposed smartphone-based SHM approach is considered a cost-effective and user-friendly platform for damage detection of coastal and offshore infrastructures.

Keywords: Magnetic field intensity; Structural health monitoring; Smartphone; Coastal and offshore structures.

1. INTRODUCTION

Degradation resulting from aging, deferred maintenance, natural disasters, and human-made hazards pose a significant threat to the world's structural systems. Degradation of civil infrastructure systems results in massive losses and failures (Gandomi et al., 2013). The challenges associated with age-related degradation have heightened the need for robust structural health monitoring (SHM) methods to identify and evaluate various structural damage types (Wang et al., (2014), Guo et al., (2008). Several studies exist on the power of new technologies such as wireless sensors (Lynch, (2006), Sabato et al., (2017), Li et al., (2015), fiber optic sensors, and radar system interferometry (Gentile & Bernardini, 2009) for improving traditional SHM systems. In spite of the efficiency of the existing SHM methods, they have their disadvantages and unique limitations. Currently, the installation and maintenance of SHM systems pose technical difficulties and economic issues. Moreover, the continuous collection of information about the structural system's health status is costly and requires remarkable human resources. These issues imply a need for cost-effective SHM methods that still offer reliable functionalities (Jiao et al., 2020). In recent years, citizen science projects have provided employment opportunities. Research shows that smartphones can provide an avenue for crowdsourced environmental information. Smartphones come equipped with

sensors that apply to purposes other than those designed initially. Some examples are GPS, accelerometer, magnetometer, and proximity sensors to provide useful information to users (Fig. 1). In general, the smartphone systems support three main groups of sensors, as shown in Fig. 1. Acceleration, gravity, and rotational sensors apply to motion-sensing; Environmental sensors include a temperature control system, humidity, lighting, and air pressure gauge, while orientation and magnetometer sensors belong to the position sensors cluster. The sensing framework of smartphones is composed of hardware and software. The hardware components are the smart device's physical structure that transmits environmental information processed by the software components. Table 1 summarizes the type, description, and expected uses of smartphone sensors.

Table 1. A summary of the features of smartphone sensors.

Cluster	Sensor	Description	Application
Motion	Accelerometer	Measures the acceleration force that is applied to a device on all three physical axes (x, y, and z)	Motion detection (Shake, tilt, etc.)
	Gravity	Measures the force of gravity that is applied to a device on all three physical axes (x, y, z)	Motion detection (Shake, tilt, etc.).
	Gyroscope	Measures a device rate of rotation around each of the three physical axes (x, y, and z)	Rotation detection (Spin, turn, etc.)
	Rotation Vector	Measures the orientation of a device by providing the three elements of the rotation vector	Motion detection and rotation detection
Environment	Temperature	Measures the ambient room temperature	Monitoring air temperature
	Humidity	Measures the relative ambient humidity	Monitoring dewpoint, absolute, and relative humidity
	Light	Measures the ambient light level	Controlling screen brightness
	Pressure	Measures the ambient air pressure	Monitoring air pressure changes
Position	Orientation	Measures degrees of rotation that a device makes around all three physical axes (x, y, z)	Determining device position
	Magnetometer	Measures the ambient geomagnetic field for all three physical axes (x, y, z)	Magnetic field, compass
	Proximity	Measures the proximity of an object relative to the view screen of a device	Phone position during a call

There has been a significant rise in interest in the use of smartphones for SHM purposes in recent years. For example, researchers have used accelerometer sensors from smartphones to collect structural integrity data at a low cost (Ozer & Feng, (2017), Matin Nazar (2021). A comprehensive review of the smartphone technology for citizen-centered civil infrastructure monitoring can be found in Alavi & Buttlar,(2019). In this study, we explore using a smartphone magnetometer to sense magnetic fields' fluctuation due to damage progression. A series of experimental and numerical studies are performed on undamaged and damaged steel plates to study the proposed monitoring approach. The key to more efficient damage detection in this method is to enhance the magnetic field around the steel plates. To this aim, permanent magnets are placed on the corners of the plates. The developed method offers promising results and can provide a basis for various SHM methods in a crowdsourcing platform empowered by citizens.

2. METHOD

2.1. SENSING MAGNETIC FIELD INTENSITY VARIATION USING SMARTPHONE

Strides to assess smartphone magnetic sensors' use for expanded reality biometric applications and geomagnetic storm location are in progress (Blum et al., (2013), S. Odenwald, (2019). However, the proposition of deploying smartphones for engineering applications is still in its infancy. Smartphones use their magnetometer to sense their orientation in space, achieved via a chip that contains a 3-axis magnetometer. The body outline framework has a +Z-axis opposite to the smartphone's front face and expanding upwards when a smartphone is in a normal position with the back/front cameras found at the top. Aside from the smartphone magnetometers' primary application, several smartphone applications can interface to measure magnetic field intensity. As an example, Fig. 1b-c shows the app used in this study, installed on a Vivo smartphone (model V1901A), a "Magnetic Field Detector" app developed by the "Mobile Develop Team." This app uses the three axes X, Y, and Z. The display of the magnetic field in this software is in micro-Tesla per second.

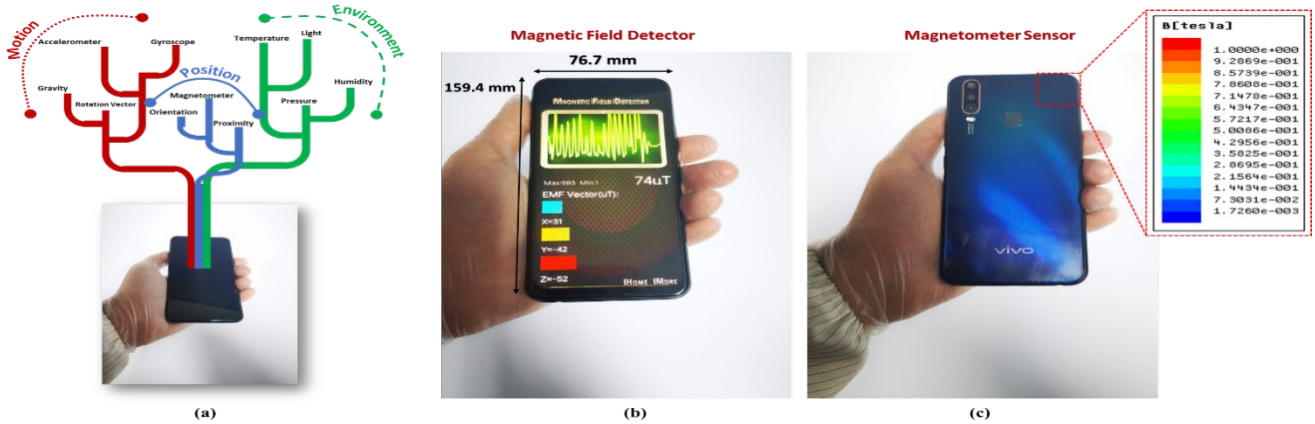

Fig. 1. (a) Smartphone sensors (b) Magnetic detector software and (c) Vivo smartphone (model V1901A).

2.2. SHM OF STRUCTURE USING MAGNETIC FIELD INTENSITY CHANGES

The proposed SHM technique, anchored on the magnetic field flux changes and intensity over metallic structures, demonstrates magnetic flux variation over a damaged and undamaged steel plate, as shown in Fig. 2(a). The magnetic flux is distributed over the intact steel plate evenly, whereas, in a cracked steel plate, results show a sharp fluctuation of the magnetic flows over the damaged region. By monitoring the magnetic field intensity changes, it is possible to infer the structural health status as in Fig. 2(b).

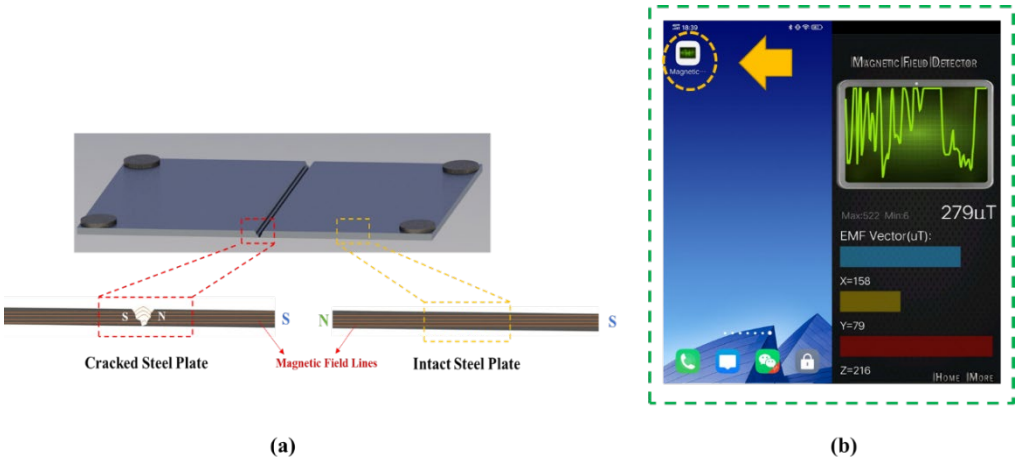

Fig. 2. (a) Demonstration of the magnetic flux over a damaged and undamaged steel plate, (b) Screenshot of the magnetometer app used for damage detection.

In today's structural systems, the prevailing magnetic field around steel plates is not strong enough. Therefore, it cannot be used as the proposed SHM method. The only way to strengthen it is to use the magnetic force of the magnet. A magnetic field is created by the interaction between two electric fields on top of each other (positive and negative charges). In this research, tests were performed on a steel sheet of 300 mm × 210 mm with a thickness of 0.8 mm. This steel plate is equipped with four neodymium magnets with a radius of 15 mm and a thickness of 3 mm in its four corners. The magnetic field at the center of each disc (B_0) can be calculated using the following equation:

$$B_0 = k\frac{2\pi I}{r} \quad [1]$$

where I is the effective current, r is the radius of the loop (disc), μ_0 magnetic constant, and k is a constant depending on the system of units:

$$k = \frac{\mu_0}{4\pi} \quad [2]$$

The magnetic dipole of the disc is denoted by m :

$$m = I\pi r^2 = \frac{B_0 r^3}{2k} \quad [3]$$

Assuming the magnetic field of a dipole on the point of distance R from the dipole and in a plane normal to the dipole is, then we will have:

$$B = -k\frac{m}{R^3} \quad [4]$$

The minus sign merely indicates that the magnetic field's direction is opposite to that of the magnetic dipole. Expressing m in terms of B_0:

$$B = -\frac{B_0}{2}\left(\frac{r}{R}\right)^3 \quad [5]$$

The center of the plane is at equal distances from four identical magnetic discs. Therefore, the magnetic field is four times the above equation and can be represented by B_t:

$$B_t = -2B_0\left(\frac{r}{R}\right)^3 \quad [6]$$

The magnetic field at height *z* from the center of the plate (B_z) can be calculated using the following equations:

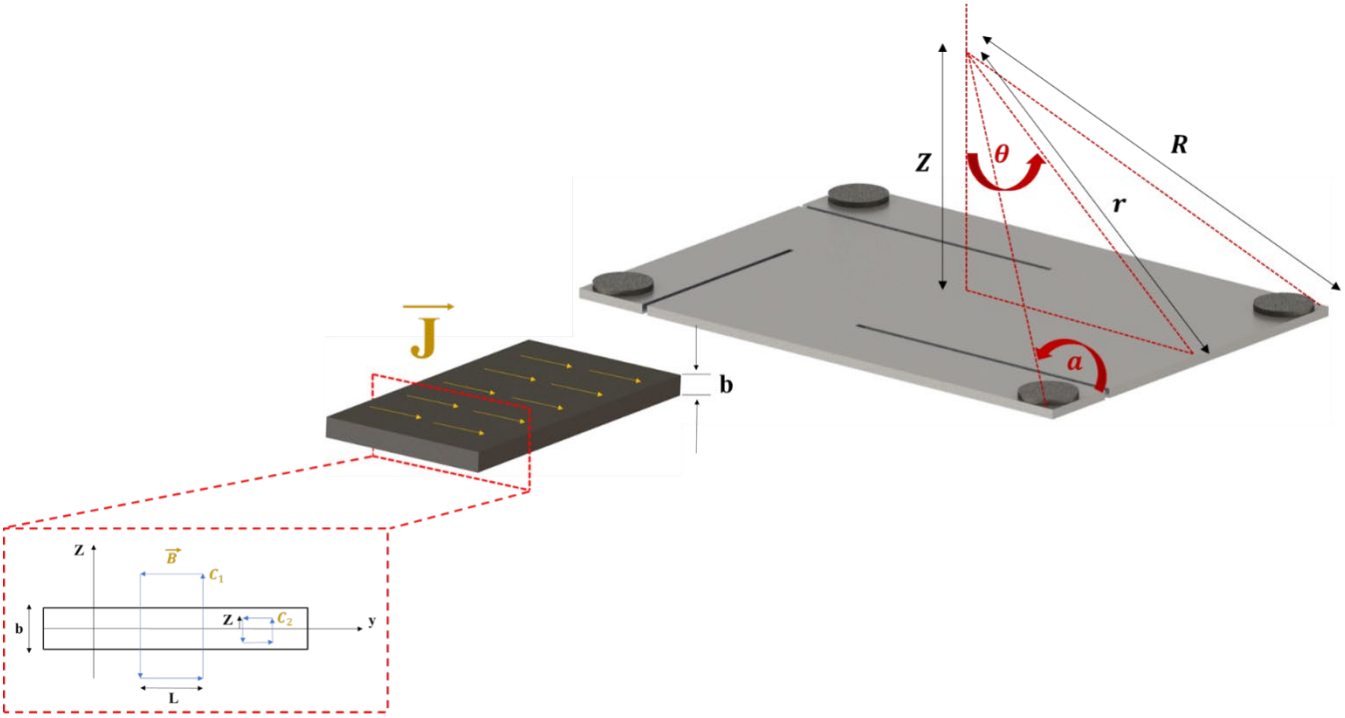

Fig. 3. Mathematical calculations of the magnetic field at altitude.

$$\text{Cos}\,\alpha = \frac{a/2}{R},\ \text{Sin}\theta = \frac{a/2}{r} \quad [7]$$

$$a^2 + (a/2)^2 = r^2 \ \rightarrow\ r = \frac{\sqrt{5}}{2} \quad [8]$$

$$r^2 + (a/2)^2 = R^2 \ \rightarrow\ R = \frac{\sqrt{6}}{2}a \quad [9]$$

$$B_1 = \frac{\mu_0 I}{4\pi r}\left(\text{Cos}\,\alpha - \text{Cos}\,(\pi - \alpha)\right) = \frac{\mu_0 I}{4\pi\frac{\sqrt{5}}{2}a}\left(2\frac{\frac{a}{2}}{\frac{\sqrt{6}}{2}a}\right) = \frac{\mu_0 I}{\pi a\sqrt{30}} \quad [10]$$

$$B_z = B_1\,\text{Sin}\theta = \frac{a}{2\left(\frac{\sqrt{5}}{2}a\right)}\frac{\mu_0 I}{\pi a\sqrt{30}} = \frac{\mu_0 I}{5\pi a\sqrt{6}} \times \frac{\sqrt{6}}{6} = \frac{\sqrt{6}\mu_0 I}{30\pi a} \ \rightarrow\ B_t = 4B_z = \frac{2\sqrt{6}\mu_0 I}{15\pi a} \quad [11]$$

$$B_z = B_1 \, Cos\left(\frac{\pi}{2} - \theta\right) = B_1 \, Sin\theta \quad [12]$$

According to Figure 3, If the thickness of the steel plate is b. The uniform current density is equal to:

$$\vec{j} = J.\,\hat{\imath} \quad [13]$$

C_1 and C_2 are the magnetic current path governing the metal plate. Therefore, according to the law of amps:

$$I = \iint \vec{j}.\,d\vec{A} = J_0(b.l) \quad [14]$$

I The Magnetic current enclosed in the steel plate, J is the uniform current density, b is thickness, and l is the length.

Law of amps for C_1:

$$\oint \vec{B}\,d\vec{s} = B(2l) = \mu_0 I = \mu_0(J_0.b.l) \quad [15]$$

$$B = \mu_0.J_0.b/2 \quad [16]$$

Law of amps for C_2:

$$\oint B.ds = B(2l) = \mu_0.I = \mu_0.J_0(2.|Z|.l) \quad [17]$$

$$B = \mu_0.J_0.|Z| \quad [18]$$

$$\vec{B} = \begin{cases} \frac{-\mu_0.J_0.b}{2}\hat{\jmath} \;, & Z > b/2 \\ -\mu_0.J_0.Z.\hat{\jmath} \;, & -\frac{b}{2} < Z < \frac{b}{2} \\ \frac{\mu_0.J_0.b}{2}\hat{\jmath} \;, & Z < -b/2 \end{cases} \quad [19]$$

3. EXPERIMENTAL AND NUMERICAL STUDIES

In this study, a series of experiments were performed on a steel plate. For this purpose, four circular neodymium magnets (radius 15 mm and thickness 3 mm) have been used to induce a magnetic field in the steel plate. Fig. 4 presents the experimental setup. The magnetic field created by magnets were measured on an intact steel plate and plates with one crack (158.5mm×3mm), two Cracks (158.5mm×3mm), three cracks, including two Cracks (158.5mm×3mm) and one Crack (112 mm × 3mm) and with Holes (Radius=10mm). In each cracking scenario, one, two, three cracks, and also holes were created on the steel plate to study the effect of damage on the magnetic field intensity (MFI). In this research, the magnetic field intensities were measured at 200 mm, 350 mm, and 500 mm height from the center of the steel plates. Measurements were done for one crack (158.5mm×3mm), two Cracks (158.5mm×3mm), three cracks, including two Cracks (158.5mm×3mm) and one Crack (112 mm × 3mm) and with Holes (Radius=10mm). Fig. 4 also shows the experimental design and damage progression for steel plates with two cracks, three cracks, and holes.

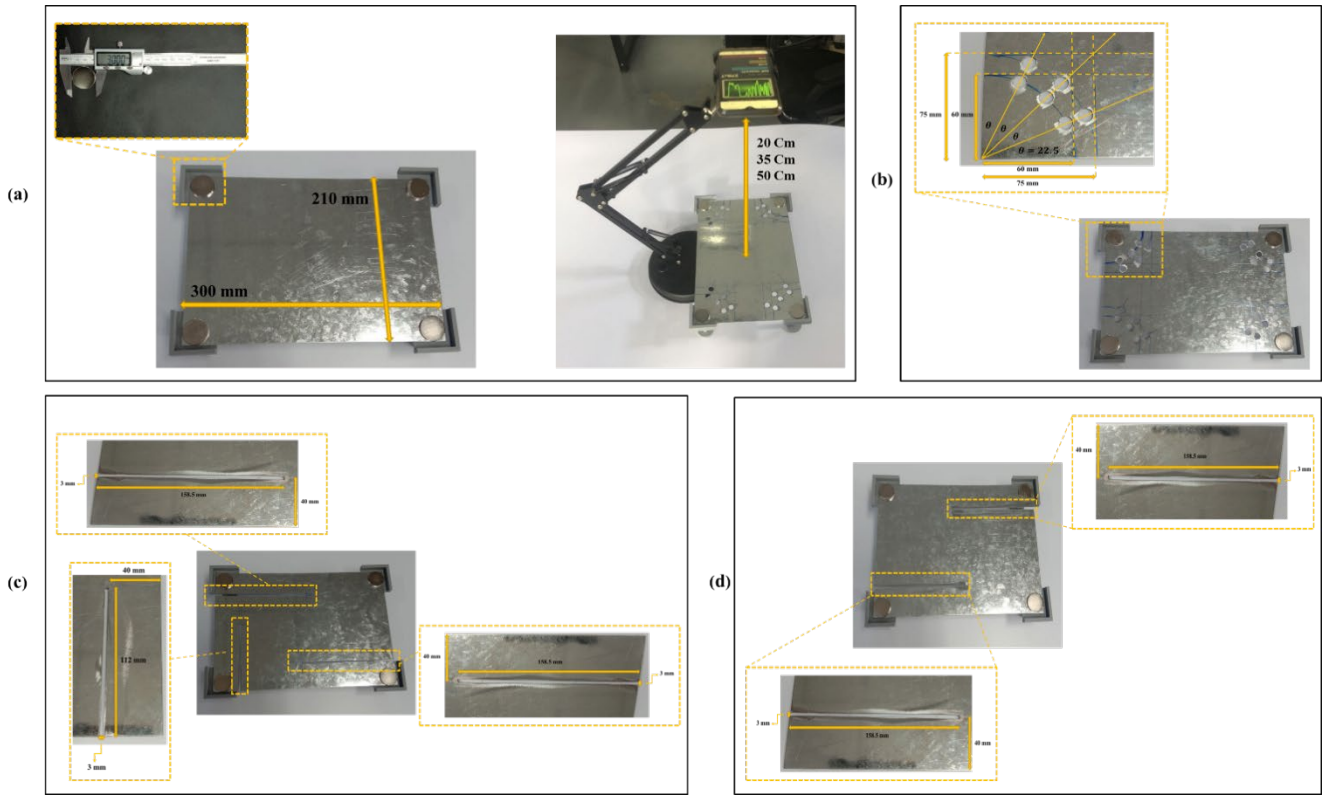

Fig. 4. (a) Smartphone setup considered to measure the magnetic field at a different height (b) Steel plate with holes. (c) Steel plate with three cracks. (d) Steel plate with two cracks.

Table 2 presents the smartphone-based detected magnetic field intensities for various defined damage states. According to the results, the magnetic field intensity (MFI) varies with the type, direction, and length of the plate's damage. In the case of damage state 1, the magnetic field increases relative to the intact plate because the steel plate volume decreased while the magnet's field lines at corner 1 are not significantly disrupted, as shown in figure 5. In case of damage state 2, the magnetic field increases relative to the intact plate but decreases relative to damage case 1 because the nature of the crack is such that it disrupts the magnets' magnetic field lines at corners 1 and 3 while reducing the volume of the plate. As a result, the increase in MFI resulting from a decreased volume is countered by a disrupted magnetic field line. In case of damage state three, the magnetic field decreases relative to the intact plate and damage case 2 because the nature of the crack is such that it disrupts the magnets' magnetic field lines at corners 1, 2, and 3 while reducing the volume of the plate. As a result, the increase in MFI resulting from a decreased volume is countered by a significantly disrupted magnetic field line. In case of damage state 4, with holes around the magnet (6 holes in that area), the magnet is being cut off from the steel plate, thus reducing the flux lines penetrating into the center of the plate and reducing the magnetic field relative to the intact plate, as observed in damage state 3.

Table 2. Smartphone-based detected magnetic field intensities for various damage states.

Damage State	Cracks	Distance (mm)	Magnetic Field (μT)
Intact	None	200 350 500	287 89 44
Damage State 1	1 Crack (158.5mm×3mm)	200 350 500	292 92 47
Damage State 2	2 Cracks (158.5mm×3mm)	200 350 500	290 88 43
Damage State 3	3 Cracks, including: 2 Cracks (158.5mm×3mm) & 1 Crack (112 mm × 3mm)	200 350 500	283 85 37
Damage State 4	With Holes (Radius=10mm)	200 350 500	285 87 43

A numerical study was performed for validating experiments. The numerical simulations were conducted using steel plates with the same size and properties as the experimental study. Tables 3 and 4, respectively, show the properties of the plates and magnets used in this study. Ansys Maxwell software was used for the simulations. The finite element model and mesh structure are shown in Fig. 5. In this study, linear quadrilateral shell elements of type S4R were used. Fig. 6 shows the effect of damage on the steel plate's magnetic field in numerical modeling. Besides, Fig. 7 presents the effect of measurement distance on the numerical study's detected magnetic field.

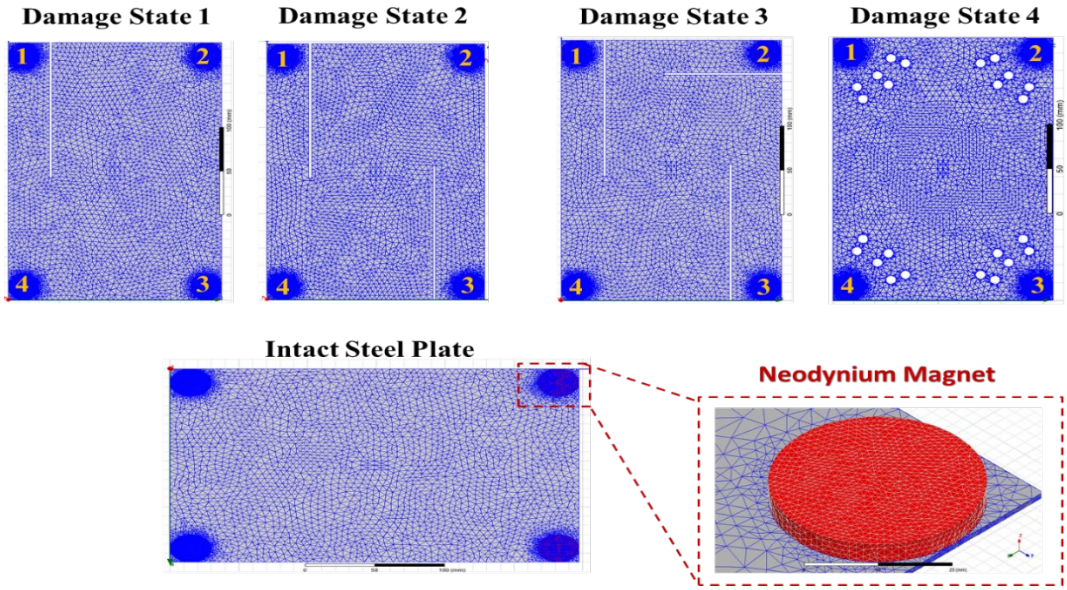

Fig. 5. The mesh structure of steel plate and magnet.

Table 3. Steel plate properties.

Name	Type	Value	Units
Relative Permeability	Nonlinear	B-H Curve	
Bulk Conductivity	Simple	2000000	Siemens/m
Magnetic Coercivity	Vector		
Magnitude	Vector Mag	0	A/m
X component	Unit Vector	1	
Y component	Unit Vector	0	
Z component	Unit Vector	0	
Composition		Solid	

Table 4. Magnet Property.

Name	Type	Value	Units
Relative Permeability	Simple	1.0997785406	
Bulk Conductivity	Simple	625000	Siemens/m
Magnetic Coercivity	Vector		
Magnitude	Vector Mag	-1060000	A/m
X component	Unit Vector	0	
Y component	Unit Vector	0	
Z component	Unit Vector	-1	
Composition		Solid	

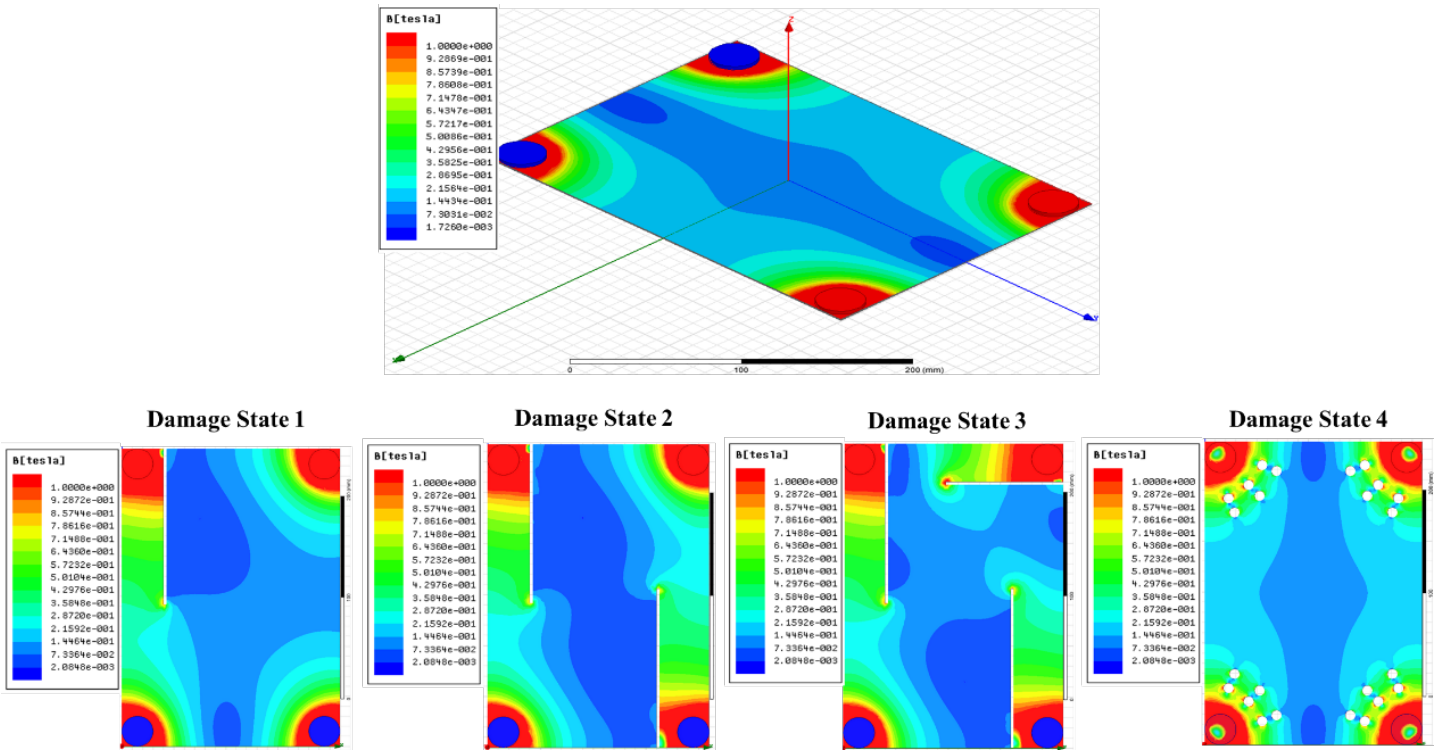

Fig. 6. Effect of damage on the magnetic field of the steel plate in the numerical modeling.

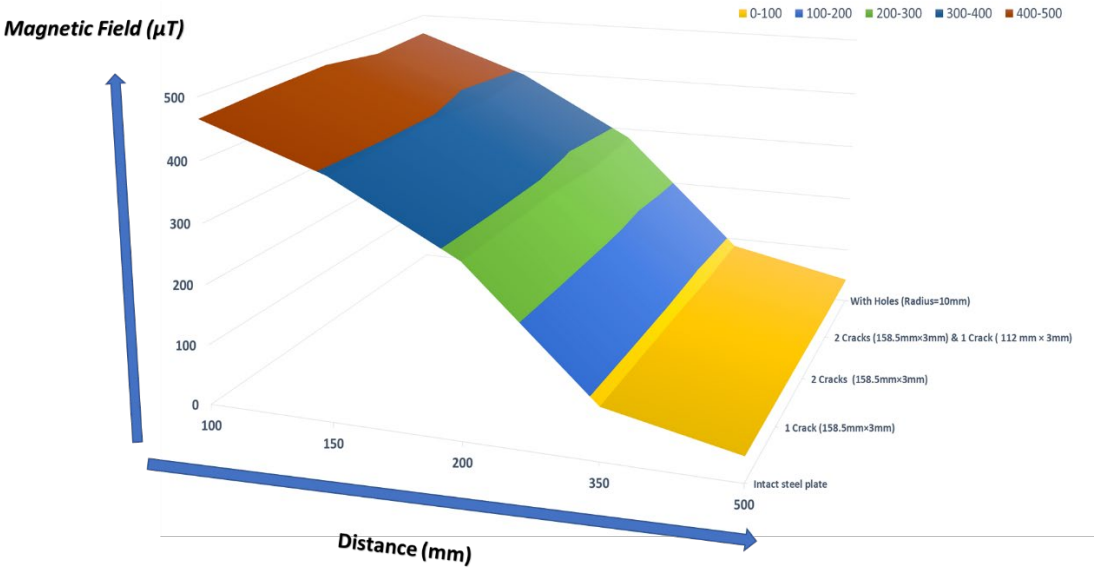

Fig. 7. Effect of measurement distance on the detected magnetic field in the numerical study.

Table 5 shows the numerical simulation results. According to the result, the magnetic field decreases as the smartphone's distance increases from the steel plate surface. The magnetic field intensity (MFI) varies with the type, direction, and length of damage in the steel plate.

Table 5. Detected magnetic field intensities for various damage states in the numerical study.

Damage State	Cracks	Distance (mm)	Magnetic Field (μT)
Intact	None	200 350 500	283.8675 86.1008 41.4903
Damage State 1	1 Crack (158.5mm×3mm)	200 350 500	284.9696 86.3568 41.6059
Damage State 2	2 Cracks (158.5mm×3mm)	200 350 500	284.3410 86.0541 41.4523
Damage State 3	3 Cracks, including: 2 Cracks (158.5mm×3mm) & 1 Crack (112 mm × 3mm)	200 350 500	275.1551 83.3154 40.1355
Damage State 4	With Holes (Radius=10mm)	200 350 500	283.0072 85.8556 41.3602

Figure 8 shows the comparison of the results obtained in the experimental and numerical studies. It is seen that the detected magnetic field intensities are within the same range in both experimental and numerical studies for various damage states. It is worth specifying that the cracks' dimension is not precisely the same as those designed within the numerical study due to manufacturing challenges. The little difference between the detailed experimental and numerical values may well be due to this issue.

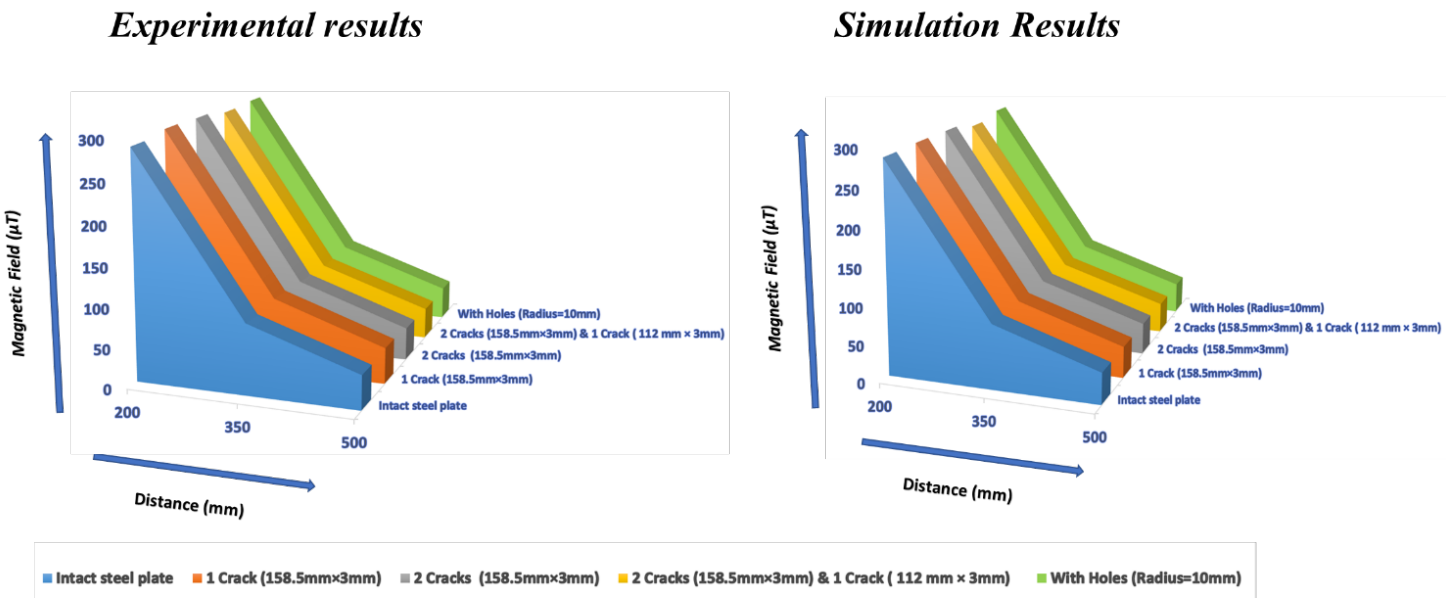

Fig. 8. A comparison of the results obtained in the experimental and numerical studies

4. CONCLUSION

This study focuses on a magnetic sensing technique for SHM of steel plates based on smartphone magnetometer sensors to measure the MFI. A series of experimental and numerical studies are carried on steel plates to validate the proposed approach's performance. Numerical simulations are carried out in Ansys Maxwell software to validate the experimental results. Comparison of the results obtained in the experimental and numerical studies. It is seen that the detected magnetic field intensities are within the same range in both experimental and numerical studies for various damage states. Future research can focus on cracks and holes in different directions. In this paper, we used Neodynium magnets to increase the magnetic field around the steel plates and, consequently, detect damage. The magnificence of the proposed smartphone-based approach is that it can be modified for different SHM tasks at the crowdsourcing stage enabled by everyday citizens.

References

Alavi, A. H., & Buttlar, W. G. (2019). An overview of smartphone technology for citizen-centered, real-time and scalable civil infrastructure monitoring. *Future Generation Computer Systems*, *93*, 651–672. https://doi.org/10.1016/j.future.2018.10.059

Matin Nazar. A., P Jiao, Q Zhang, KJI Egbe, AH Alavi. A new structural health monitoring approach based on smartphone measurements of magnetic field intensity. IEEE Instrumentation & Measurement Magazine, in press, 2020.

Blum, J. R., Greencorn, D. G., & Cooperstock, J. R. (2013). Smartphone Sensor Reliability for Augmented Reality Applications. *Lecture Notes of the Institute for Computer Sciences, Social Informatics and Telecommunications Engineering*, 127–138. https://doi.org/10.1007/978-3-642-40238-8_11

Gandomi, A. H., Alavi, A. H., Asghari, A., Niroomand, H., & Nazar, A. M. (2013). An innovative approach for modeling of hysteretic energy demand in steel moment resisting frames. *Neural Computing and Applications*, *24*(6), 1285–1291. https://doi.org/10.1007/s00521-013-1342-x

Gentile, C., & Bernardini, G. (2009). An interferometric radar for non-contact measurement of deflections on civil engineering structures: laboratory and full-scale tests. *Structure and Infrastructure Engineering*, *6*(5), 521–534. https://doi.org/10.1080/15732470903068557

GUO, T., LI, A., & WANG, H. (2008). Influence of ambient temperature on the fatigue damage of welded bridge decks. *International Journal of Fatigue*, *30*(6), 1092–1102. https://doi.org/10.1016/j.ijfatigue.2007.08.004

Jiao, P., Egbe, K.-J. I., Xie, Y., Matin Nazar, A., & Alavi, A. H. (2020). Piezoelectric Sensing Techniques in Structural Health Monitoring: A State-of-the-Art Review. *Sensors*, *20*(13), 3730. https://doi.org/10.3390/s20133730

Li, J., Mechitov, K. A., Kim, R. E., & Spencer, B. F. (2015). Efficient time synchronization for structural health monitoring using wireless smart sensor networks. *Structural Control and Health Monitoring*, *23*(3), 470–486. https://doi.org/10.1002/stc.1782

Lynch, J. P. (2006). A Summary Review of Wireless Sensors and Sensor Networks for Structural Health Monitoring. *The Shock and Vibration Digest*, *38*(2), 91–128. https://doi.org/10.1177/0583102406061499

Odenwald, S. (2019). Smartphone Sensors for Citizen Science Applications: Radioactivity and Magnetism. *Citizen Science: Theory and Practice*, *4*(1), 18. https://doi.org/10.5334/cstp.158

Odenwald, S. F. (2018). The Feasibility of Detecting Magnetic Storms With Smartphone Technology. *IEEE Access*, *6*, 43460–43471. https://doi.org/10.1109/access.2018.2863949

Ozer, E., & Feng, M. Q. (2017). Biomechanically influenced mobile and participatory pedestrian data for bridge monitoring. *International Journal of Distributed Sensor Networks*, *13*(4), 155014771770524. https://doi.org/10.1177/1550147717705240

Sabato, A., Niezrecki, C., & Fortino, G. (2017). Wireless MEMS-Based Accelerometer Sensor Boards for Structural Vibration Monitoring: A Review. *IEEE Sensors Journal*, *17*(2), 226–235. https://doi.org/10.1109/jsen.2016.2630008

Wang, H., Li, A., Guo, T., & Tao, T. (2014). Establishment and Application of the Wind and Structural Health Monitoring System for the Runyang Yangtze River Bridge. *Shock and Vibration*, *2014*, 1–15. https://doi.org/10.1155/2014/421038

8th International Conference on the Application of Physical Modelling in Coastal and Port Engineering and Science
Dec. 9th - 12th, 2020, Zhoushan, China

IMPACT OF TOE SCOUR ON WAVE OVERTOPPING OVER A VERTICAL WALL

ZHONG PENG(1) & QING HE(1)

(1) State Key Laboratory of Estuarine and Coastal Research, Shanghai, China
zpeng@sklec.ecnu.edu.cn
qhe@sklec.ecnu.edu.cn

ABSTRACT

This study uses a combination of a RANS-VOF wave model and measured bed profiles to study the impact of toe scour on wave overtopping over a vertical wall. Model data analysis has been carried out to examine mean wave overtopping discharges, and ultimately identify the physical processes behind wave overtopping in the presence of toe scour. Results show that the toe scour reduces the wave overtopping through enhancing wave breaking over the considerable deposition associated with toe scour. However, with a scenario of negligible deposition and large toe scour, it increases the wave overtopping by enabling more giant waves to reach the wall.

Keywords: *w*ave overtopping; vertical wall; toe scour; wave model; wave breaking;

1. INTRODUCTION

Vertical and nearly vertical coastal structures such as seawalls are often designed and constructed to protect coastal regions against flooding. Concurrent coastal processes, e.g., wind, wave, storm surge, tide, sediment transport, can cause natural hazards, such as the collapse of vertical walls and coastal flooding, simultaneously due to wave overtopping and toe scour (EurOtop, 2018).

Mean overtopping discharges can roughly represent wave overtopping at coastal structures during the peak of a storm. In past decades, different approaches such as empirical, process-based, and data mining (van Gent et al., 2007) approaches have been used for the prediction of the overtopping discharge. However, Lykke Andersen (2006) performed almost 600 tests on wave overtopping and found there is a large scatter between results obtained from different approaches and the measurements, especially for low overtopping discharge. While plenty of data on wave overtopping is available at various research institutes and universities, these data have not yet been integrated into a single, generic design method. De Rouck et al. (2009) summarized the EU-project CLASH project, in which a generic prediction method for crest height design or assessment has been derived. Pullen et al. (2009) measured wave overtopping at the vertical seawall at Samphire Hoe and comparing against laboratory tests in 2 & 3 dimensions. They found that there are no scale effects between the measured field and laboratory overtopping discharges, and the effect of wind is negligible when overtopping discharge increases. Etemad-Shahidi et al. (2016) applied scaling arguments and model tree approaches to derive formulae for estimating mean overtopping discharge at fully vertical and nearly vertical impermeable structures. However, there is little work on the impact of toe scour on wave overtopping.

Another distinguished coastal process is the toe scour in front of coastal structures. Sutherland and Gouldby (2003) claimed that the failure of coastal structures often occurred due to the toe scour. Müller et al. (2007) presented an overview of experimental research on toe scouring at vertical structures with sandy foreshore. Besides experimental studies, numerical studies have been carried out to examine the scouring patterns at coastal structures in past years, for example, Jayaratne et al. (2016), Peng et al. (2018). It is widely known that there is a strong correlation between the toe scour depth and relative water depth at the structure. For example, Müller et al. (2007) illustrated a trend line describing the development of non-dimensional toe scour depth (S_t/H_s) to the breaker type (h_b/L_m) for the vertical seawalls on a sandy beach. Further, Sutherland et al. (2008) demonstrated a new empirical relationship between non-dimensional toe scour depth (St/Hs) and relative toe water depth (h_t/L_m), for the conservative prediction of scour depth at a plain vertical seawall with a sandy foreshore slope. Salauddin and Pearson (2019) investigate the wave overtopping and toe scouring at a plain vertical wall with a shingle foreshore. They found that the relative toe scour depth at a plain vertical wall on a shingle beach is related to the relative toe water depth and Iribarren number. However, they mainly focused on the impact of shingle beach on wave overtopping discharge and toe scour depth, respectively. There is no conclusion on the impact of toe scour on wave overtopping.

One of the major concerns in designing coastal structures is mean wave overtopping discharge, in which predictions are derived from empirical formulae fitted to specific laboratory measurements (EurOtop, 2018). Most of the empirical expressions (TAW (2002), EurOtop (2018), Gallach Sanchez (2018) for mean overtopping

discharges at dikes can be rewritten using the following shape:
where, q is the mean wave overtopping discharge ($m^3/s/m$), g is the acceleration due to gravity (m/s^2), $\xi_{m-1,0}$ is the breaker parameter ($\xi_{m-1,0} = \tan\alpha/(2\pi H_{m0}/gT_{m-1,02})^{0.5}$) based on the significant wave height and the spectral wave period $T_{m-1,0}$ (s), Rc is the crest height relative to the still water level (m), α is the slope angle of the structure (°), γ denotes the influence factor for various effects such as those by berms (γ_b), the roughness of the slope (γ_f), angle of wave attack (γ_β), crest elements (γ_v) and crossing seas ($\gamma_\#$), and a, a', b, b 'and c are coefficients that are calibrated based on physical model tests.
While these structures may be efficient in the mitigation of wave overtopping, they may be subject to severe toe scour or over-washing simultaneously, leading to the invalidity of empirical formulae used in the design of coastal structures. Equation 1 demonstrates that the mean overtopping discharge depends on significant wave height at the toe of the structure, breaker parameter, $\xi_{m-1,0}$, and influence factor by berms, γ_b. In the presence of toe scour, an increasing toe depth for a fixed tide level would enable more giant waves to reach the structure, which in turn affects the wave overtopping discharge and its landward spatial distribution. The sediment from toe scour often settles down away from the vertical wall and might lead to more wave breaking. Moreover, the influence factor by a berm in Eq.1 is limited to the positive elevation of berms, and cannot handle the circumstance of toe scour. So far, there is little work available to account for the impact of toe scour on wave overtopping, and the physical processes behind remain unknown. Tofany et al. (2016) found that there are smaller scour depths at the toe of the breakwater as overtopping occurs. However, their study only accounts for the flat bottom in front of a vertical wall, and there is no wave breaking occurred.
The aim is to examine the impact of toe scour on wave overtopping over a vertical wall and identify the relevant physical processes. This study has employed the partial cell technique based RANS-VOF model described in Peng et al. (2018) and makes use of measured bed profiles collected in physical tests by Sutherland et al. (2006). The numerical model would be validated against empirical formulae by EurOtop (2018) for wave overtopping simulations. Mean overtopping discharges are often essential to determine the crest height of structures and enable them to account for the effects of oblique waves, roughness, and berms in the design and evaluation of flood defense structures (van Gent, 2020). Therefore, in this study, the mean overtopping discharges has been used to study the impact of toe scour on wave overtopping.

2. METHODOLOGY

This study investigates wave overtopping over a vertical wall using the coupled wave-sediment transport-morphological model developed by Peng et al. (2018), which was an extension of the RANS-VOF model initially developed by (Lin and Liu, 1998). It solves the 2D Reynolds Averaged Navier–Stokes equations by decomposing the instantaneous velocity and pressure fields into the mean and turbulent components. An algebraic non-linear k–ε turbulence model describes Reynolds stresses. A Volume of Fluid (VOF) method developed by Hirt and Nichols (1981) was used to capture the free surface. This model has been widely validated for wave overtopping studies (Peng and Zou, 2011; Zou et al., 2013).
There are 1160 cells in the horizontal direction and 90 cells in the vertical direction. The cell size varies in the z-direction from 0.02 m near the sea bed to 0.01 m around the free surface. The cell size in the x-direction ranges from 0.01 m to 0.05 m. Waves are generated by an internal wave-maker (Lin and Liu, 1999) at x=5 m using stokes second-order wave theory. The front face of the sea wall is concrete and hence considered to be impermeable. For numerical modelling purposes, the surface of the sea wall is also assumed to be hydraulically smooth, which will provide a conservative (i.e., worst-case) estimate of overtopping. Fig. 1 shows the comparison of the predicted mean overtopping discharge and the estimation by the empirical formulae of EurOtop (2018) over a plain vertical seawall. The predicted mean overtopping discharge agrees with estimations by the empirical formulae, and the scatter in RANS-VOF model predictions is due to the uncertainty and random nature in overtopping events as well as model truncation errors. The overtopping discharge is underestimated for large freeboards because small overtopping discharges have significant uncertainties, and the model also neglects the entrained air effect (Peng and Zou, 2011). Therefore, the present RANS-VOF model works well for wave overtopping simulation over a plain vertical wall.
The bed profiles representing the toe scour in the model were sourced from a laboratory experiment in Sutherland et al. (2006). They collected a series of bed profiles over a sandy beach with a 1:30 slope in front of a vertical wall, with particular attention to the effect of wave breaking and relative water depth. The vertical wall located at x=24 m, and the wavemaker locates at x=0 m. More details could be referred to Sutherland et al. (2006). In this study, we make use of the measured bed profiles because those bed profiles are realistic ones under the specific wave and hydrodynamic conditions. Since the experimental tests were designed to study the toe scour developments and no wave overtopping data were collected, therefore, the assumption of no impact of wave overtopping on toe scour is automatically applied in this study. Furthermore, only regular wave overtopping has been considered in this study as it provides better ways to study the impact of each parameter and relevant physical processes.

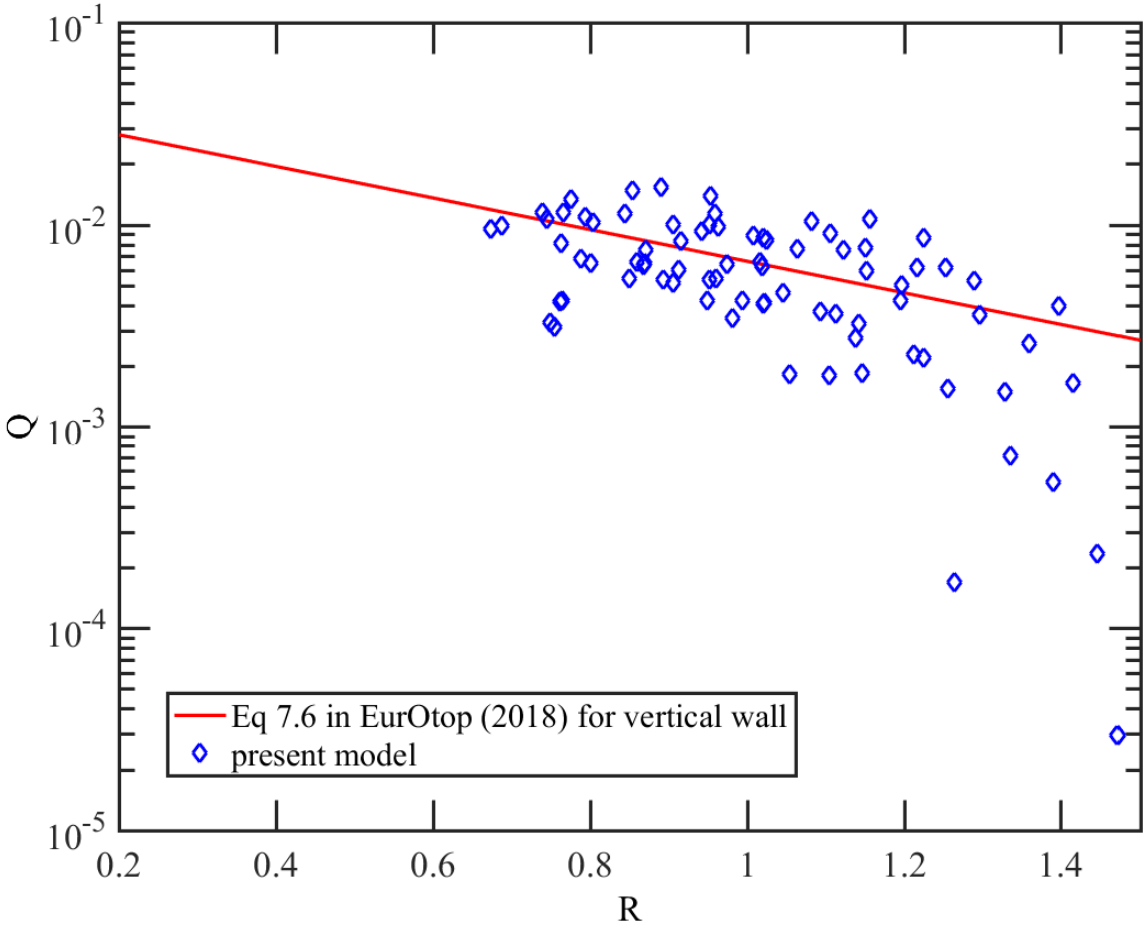

Fig. 1 Comparisons of dimensionless overtopping discharge, $Q = q/\sqrt{gH^3}$, against the relative freeboards, R = R_c/H, between the numerical model and empirical formulae. q is the mean wave overtopping discharge, R_c is the freeboard, H is the wave height. Diamond dots and solid line represent the wave overtopping over a vertical wall by the present RANS-VOF model and by Equation 7.6 in EurOtop (2018), respectively. Revised from Figure 11 in Zou et al. (2013)

3. MODEL DATA ANALYSIS

This study selected two cases to study the impact of toe scour on wave overtopping over a vertical wall. These cases represent different characteristics of bed profiles and wave features, consequently corresponding to different physical processes behind wave overtopping. Table 1 presents an overview of those two cases.

Table 1. Overview of selected two cases

Case No. (In Exp.)	H [m]	h_{toe} [m]	T [s]	BED PROFILES	WAVE FEATURES
5	0.2	0.2	4.58	considerable toe scour and deposition	wave breaking far from the wall
12	0.2	0.2	3.24	large toe scour and negligible deposition	wave breaking near the wall

3.1. Case 5: considerable deposition and wave breaking

This case studies wave overtopping with four bed profiles (Fig. 2), representing four different stages in the experimental test. The feature of toe scouring is with an increasing scour depth, and an increasing deposition offshore toe scour. The relative water depth at the toe of the vertical wall is 0.0315, indicating that the area at the toe is a shallow water region. The ratio of wave height, H, to the toe depth, h_{toe}, is 1; thus, this case has significant wave breaking. Furthermore, the toe scour and deposition would affect the wave breaking by modifying the local water depth.

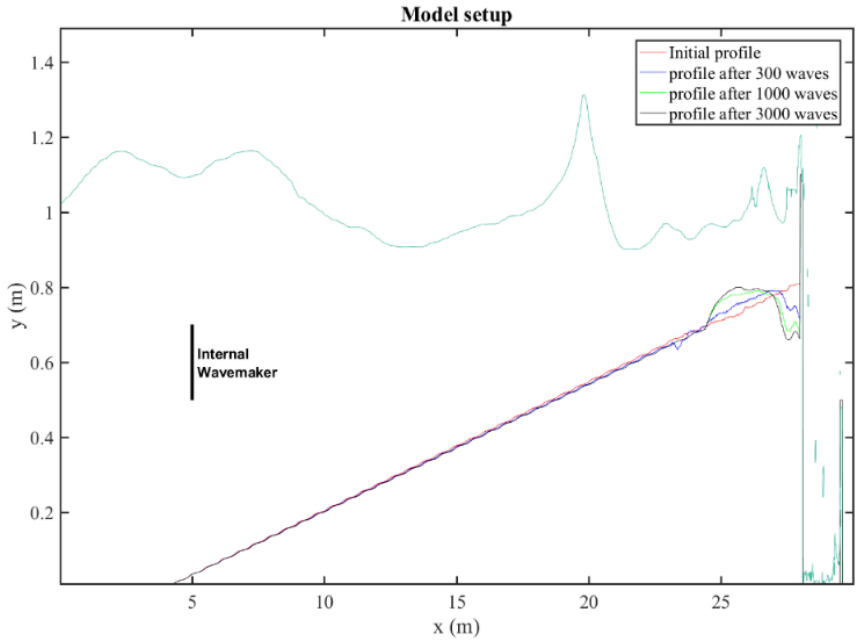

Fig. 2 The model setup with four different bed profiles in front of the vertical wall. Incoming waves are H=0.2 m, h_{toe}=0.2 m, T=4.58 s.

Fig. 3 displays the instantaneous wave overtopping discharge, normalized by local wave height. The instantaneous wave overtopping discharge becomes stable after the first several individual waves (spin-up). The mean wave overtopping discharge is then calculated by averaging the overtopping discharge over a certain number of waves. Results show that the scenario with the initial profile has the largest mean overtopping discharge. In contrast, other scenarios with toe scour have smaller mean overtopping discharge, indicating the toe scour significantly affects the wave overtopping over a vertical wall.

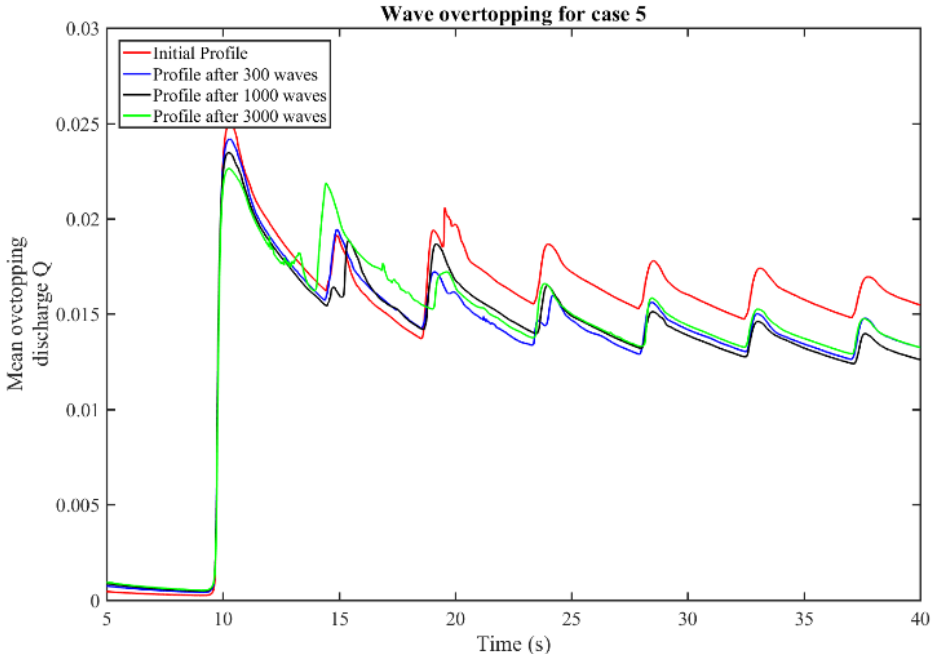

Fig. 3 Wave overtopping discharge, $Q = q/\sqrt{gH^3}$ for case 5

Turbulence kinetic energy is often treated as a measure of wave breaking, and a high value means significant wave breaking. Fig. 4 illustrates the turbulence kinetic energy (TKE) at 31 s, 32 s, and 33 s with the initial profile and profile after 300 waves. Results show that the case with profile after 300 waves always has larger TKE than the case with the initial profile. The deposition next to toe scour reduces the local water depth significantly, causing more wave breaking and more wave energy dissipated, consequently resulting in less wave energy for wave overtopping. Moreover, wave starts deshoaling in the toe scour area, while waves on the initial profile undertake the shoaling effect constantly, and become peaky, which increase the probability of wave overtopping

and mean overtopping discharges.

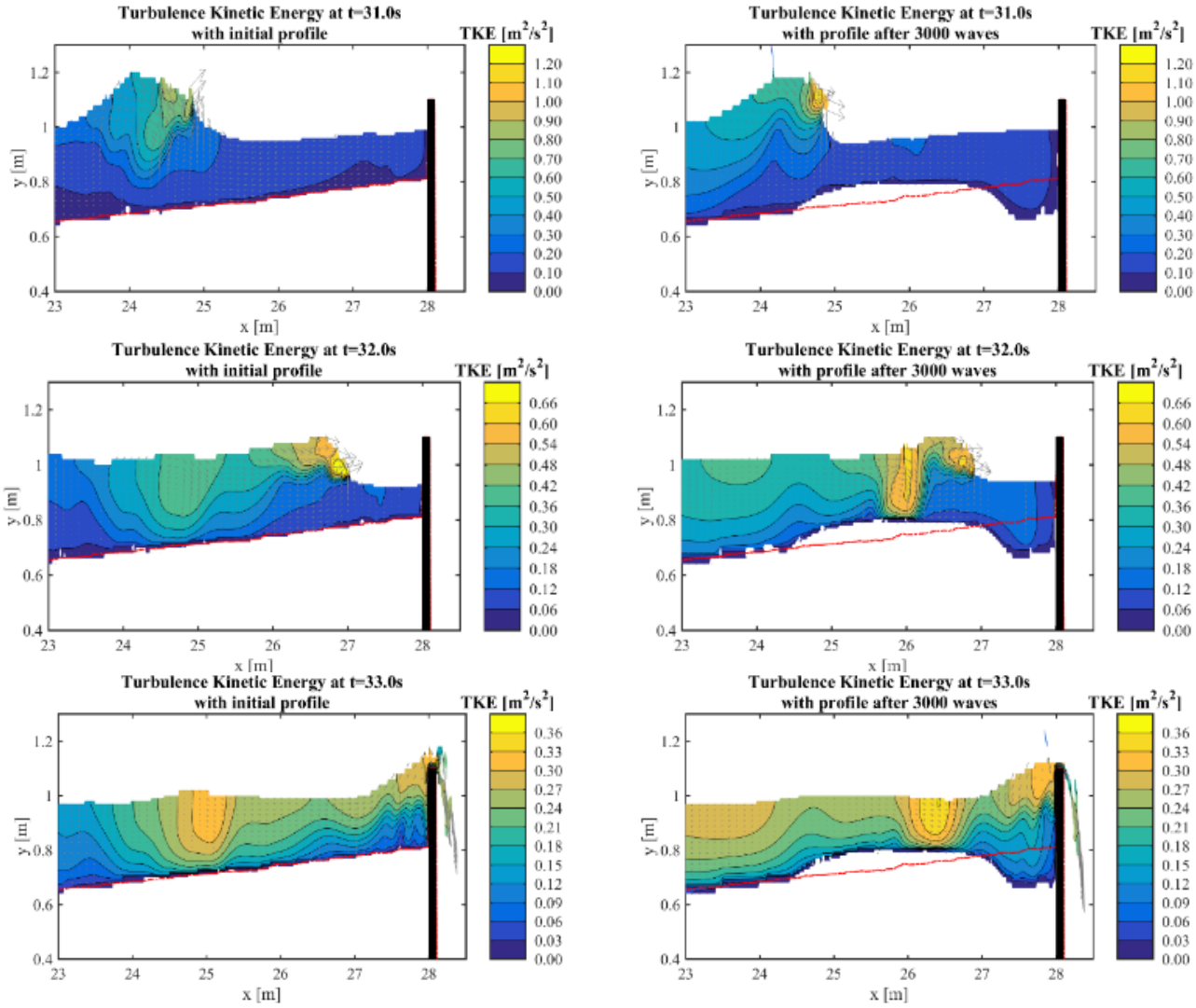

Fig. 4 Snapshots of turbulence kinetic energy (TKE) in front of the vertical wall, without toe scour (left) and with toe scour (right) under the same incoming wave conditions. Red line stands for the initial profile.

This process could also be observed by Fig. 5, which presents the surface elevation and near-surface wave orbital velocities at two locations in front of the vertical wall. Results show that the case with a profile after 3000 waves has smaller horizontal wave orbital velocities than the one without toe scour at 27 m and 27.9 m, indicating that the deposition next to the toe scour leads more wave breaking and more wave energy dissipation. The scenario without toe scour has higher horizontal velocity than the scenario with toe scour, and consequently causes more wave overtopping. The surface elevation shows that the wave is pitch forward and has high-frequency wave components (the wiggly feature). All those phenomena indicate there is intense wave nonlinearity in waves in front of the wall, mainly due to the shallow water depth.

A conclusion can be drawn that the deposition from toe scour reduces the local water depth, and consequently enhances wave breaking and dissipates more wave energy. Therefore, there is less wave energy for wave overtopping.

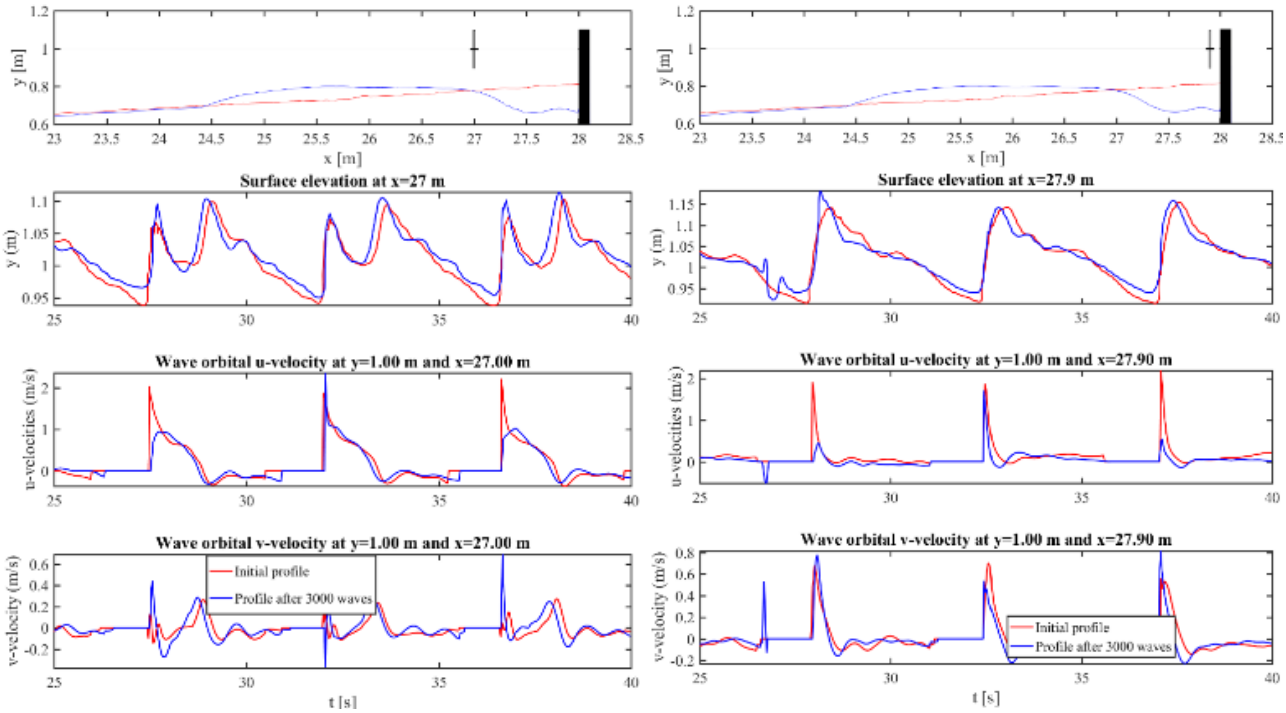

Fig. 5 Surface elevation and wave orbital velocities near the still water surface at (left) x=27 m and (right) x=27.9 m, between initial profile and profile after 3000 waves.

3.2. Case 12: negligible deposition and wave breaking

Fig. 10 shows the model setup for case 12 with three bed profiles, representing different stages in the experimental test (Sutherland et al., 2006). The feature of toe scour is with a large extent of toe scour and negligible deposition. This is because in the experiment the sediments moved far away from the toe scour, rather than deposited next to the toe scouring. In reality, the longshore sediment transport could also mitigate the deposition, given a big toe scour depth. The relative water depth at the toe of the vertical wall is 0.0461, indicating that the area at the toe is a shallow water region. This case has considerable wave breaking.

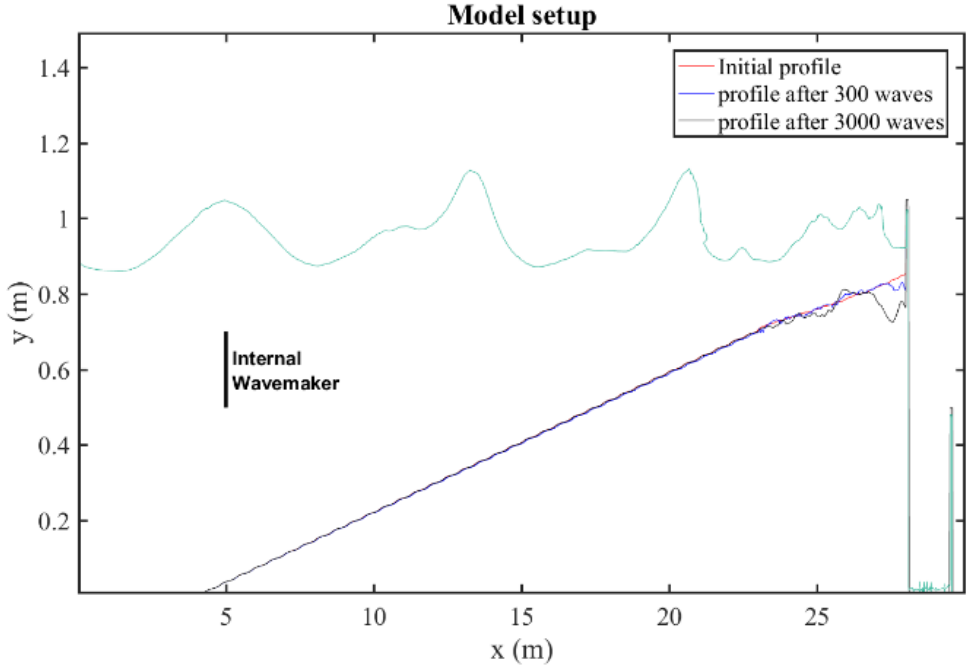

Fig. 10 The model setup with four different bed profiles in front of the vertical wall. Incoming waves are H=0.2 m, h_{toe}=0.2 m, T=3.24 s.

Fig. 11 displays the instantaneous wave overtopping discharge, normalized by local wave height. Results show that the scenario with severe toe scour (profile after 3000 waves) has the largest mean overtopping discharge. In contrast, the scenario with the initial profile has a relatively small mean overtopping discharge.

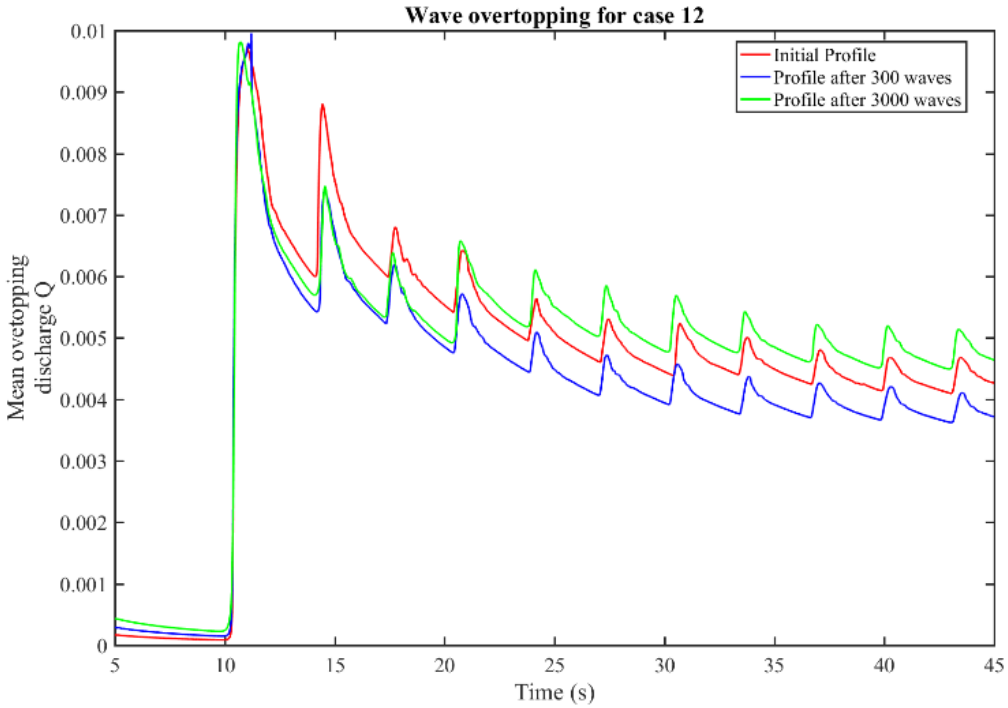

Fig. 11 Mean wave overtopping discharge, $Q = q/\sqrt{gH^3}$ for case 12

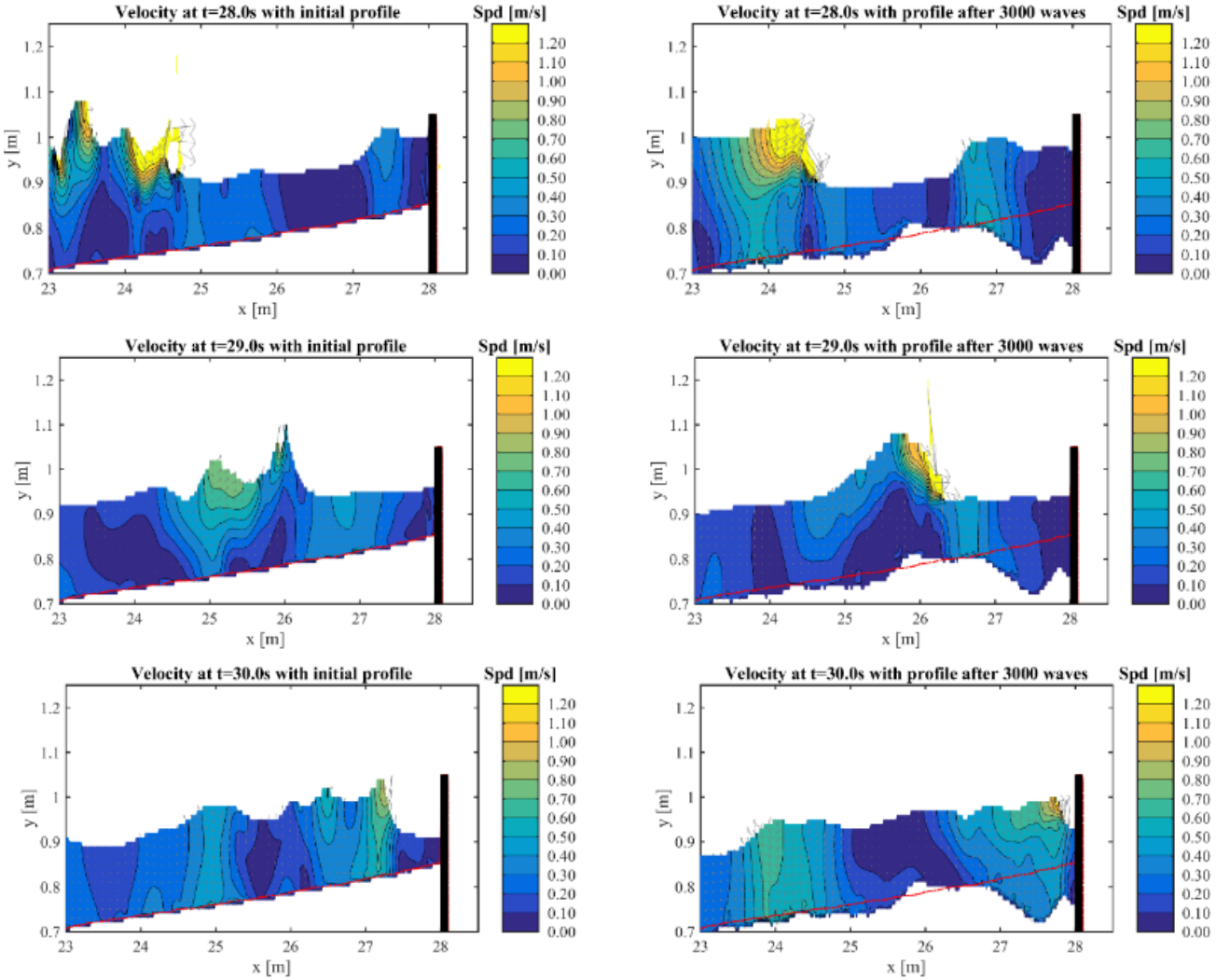

Fig. 12 Snapshots of wave velocities in front of the vertical wall, without toe scour (left) and with toe scour (right) under the same incoming wave conditions. Red line stands for the initial profile.

Fig. 12 presents the case with a large extent of toe scour in front of the vertical wall. Results show that for the case with initial profile, most of the waves break between 23 m and 25 m, while the case with profile after 3000 waves break at locations closer to the vertical wall. It also shows that waves with profile after 3000 waves travel faster than the one with initial profile, e.g., wave velocities at t=30 s.
Fig. 13 also present similar phenomena to Fig. 12. Wave phase and magnitude with profile after 3000 waves agree well with those with initial profile at 23.4 m. However, there are small differences in surface elevation and wave orbital velocities due to wave nonlinearity. However, wave data at 27.9 m shows that wave with profile after 3000 waves travels faster than one with initial profile. The former also has a larger horizontal velocity near the crest of a vertical wall, and this explains why it has a larger wave overtopping discharge. All those phenomena are mainly because the profile after 3000 waves has larger water depths from 23.5 m to the vertical wall; hence waves could travel faster and accommodate more giant waves close to the vertical wall. The more considerable water depths also help reduce wave dissipation by wave breaking and bottom friction; thus, there is more wave energy left for wave overtopping.

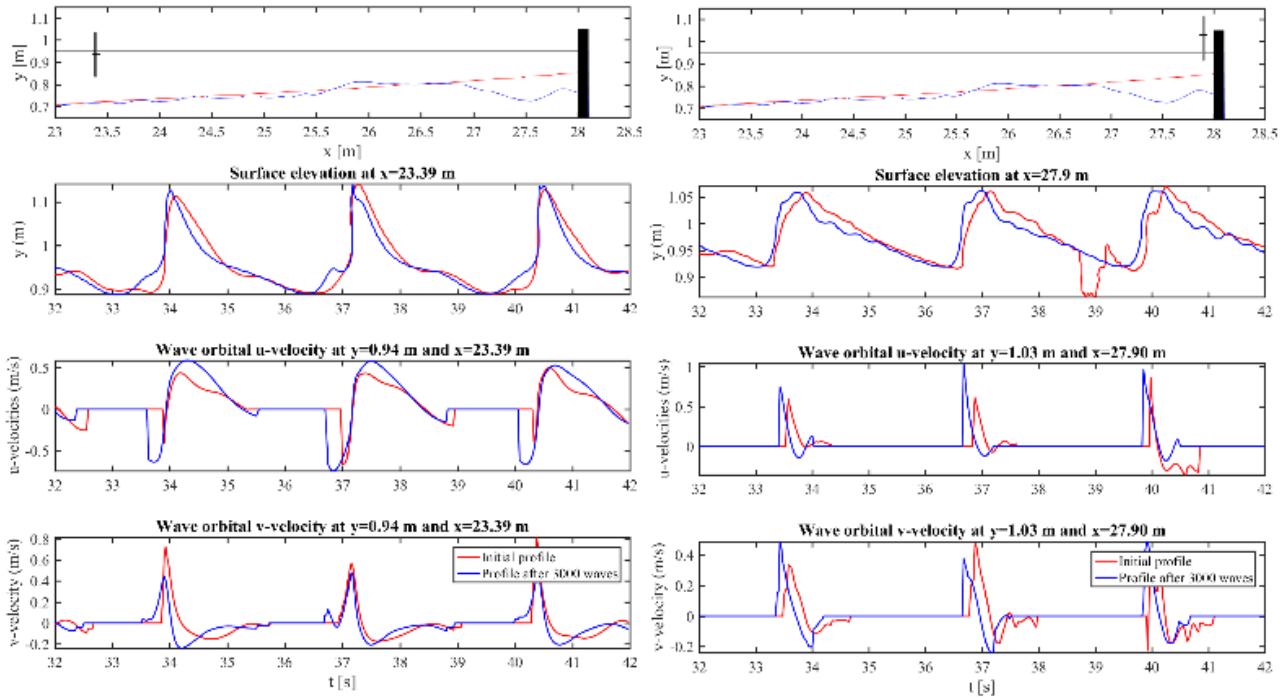

Fig. 13 Surface elevation and wave orbital velocities at (left) x=23.5 m and (right) x=27.9 m, with initial profile and profile after 3000 waves.

4. SUMMARY

A new approach, combining the numerical model for wave overtopping and the measured bed profiles, was proposed to study the impact of toe scour on wave overtopping over a vertical wall. This study analyzed the mean wave overtopping discharge and wave field, and ultimately identified the physical processes behind wave overtopping as below:

- Enhances wave breaking over the deposition area: the large deposition reduces the local water depth, thus, enhances the wave breaking process and dissipates more wave energy. Therefore, there is less wave energy for wave overtopping.
- Accommodates more giant waves over the scour area: the toe scour results in substantial water depths and enables more giant waves in front of the vertical wall, given negligible deposition. Hence, the toe scour leads to a larger wave overtopping discharge over a vertical wall than the scenario without toe scour. Because of the nonlinearity and wave breaking, the partial standing wave pattern does not exist.

Although this study successfully identified the physical processes behind the impact of toe scour on wave overtopping over a vertical wall, it is worth to mention that there are a few limitations of this study. It assumes that there is no impact of wave overtopping on the toe scour, and only takes into account regular wave overtopping on a constant beach slope. Future work would consider those two aspects and ultimately improve empirical formula in the EurOtop (2018) to account for the impact of toe scour on wave overtopping.

REFERENCES

De Rouck, J., Verhaeghe, H., Geeraerts, J., 2009. Crest level assessment of coastal structures - General

overview. Coast. Eng. 56, 99–107. https://doi.org/10.1016/j.coastaleng.2008.03.014
Etemad-Shahidi, A., Shaeri, S., Jafari, E., 2016. Prediction of wave overtopping at vertical structures. Coast. Eng. 109, 42–52. https://doi.org/10.1016/j.coastaleng.2015.12.001
EurOtop, 2018. EurOtop Manual on wave overtopping of sea defences and related structures An overtopping manual largely based on European research, but for worldwide application Second Edition 2018.
Gallach Sanchez, D., 2018. Experimental study of wave overtopping performance of steep low-crested structures. University of Ghent.
Hirt, C.W., Nichols, B.D., 1981. Volume of fluid (VOF) method for the dynamics of free boundaries. J. Comput. Phys. 39, 201–225. https://doi.org/10.1016/0021-9991(81)90145-5
Jayaratne, M.P.R., Premaratne, B., Adewale, A., Mikami, T., Matsuba, S., Shibayama, T., Esteban, M., Nistor, I., 2016. Failure mechanisms and local scour at coastal structures induced by Tsunami. Coast. Eng. J. https://doi.org/10.1142/S0578563416400179
Lin, P., Liu, P.L.-F., 1999. Internal Wave-Maker for Navier-Stokes Equations Models. J. Waterw. Port, Coastal, Ocean Eng. 125, 207–215. https://doi.org/10.1061/(ASCE)0733-950X(1999)125:4(207)
Lin, P., Liu, P.L.F., 1998. A numerical study of breaking waves in the surf zone 359, 239–264. https://doi.org/10.1017/S002211209700846X
Lykke Andersen, T., 2006. Hydraulic Response of Rubble Mound Breakwaters: Scale Effects - Berm Breakwaters | TU Delft Repositories. Aalborg University.
Müller Dipl-Ing, G., Allsop, W., Bruce, T., Kortenhaus Dr-Ing, A., Pearce, A., Sutherland, J., n.d. The occurrence and effects of wave impacts. https://doi.org/10.1680/maen.2007.160.4.167
Peng, Z., Zou, Q.-P., 2011. Spatial distribution of wave overtopping water behind coastal structures. Coast. Eng. 58, 489–498.
Peng, Z., Zou, Q.-P., Lin, P., 2018. A partial cell technique for modeling the morphological change and scour. Coast. Eng. 131, 88–105. https://doi.org/10.1016/j.coastaleng.2017.09.006
Pullen, T., Allsop, W., Bruce, T., Pearson, J., 2009. Field and laboratory measurements of mean overtopping discharges and spatial distributions at vertical seawalls. Coast. Eng. 56, 121–140. https://doi.org/10.1016/j.coastaleng.2008.03.011
Salauddin, M., Pearson, J.M., 2019. Wave overtopping and toe scouring at a plain vertical seawall with shingle foreshore: A physical model study. Ocean Eng. 171, 286–299. https://doi.org/10.1016/J.OCEANENG.2018.11.011
Sumer, B.., Fredsøe, J., 2000. Experimental study of 2D scour and its protection at a rubble-mound breakwater. Coast. Eng. 40, 59–87. https://doi.org/10.1016/S0378-3839(00)00006-5
Sutherland, J.;, Obhrai, C.;, Whitehouse, R.J.S.;, Pearce, A.M.C., 2006. Laboratory Tests of Scour at a Seawall, in: Proceedings 3rd International Conference on Scour and Erosion (ICSE-3). Amsterdam, pp. 622–631.
Sutherland, J., Brampton, A.H., Obhrai, C., Dunn, W., Whitehouse, R.J.S., 2008. Understanding the lowering of beaches in front of coastal defence structures, stage 2. London, UK.
Sutherland, J., Gouldby, B., 2003. Vulnerability of coastal defences to climate change. Proc. Inst. Civ. Eng. Water Marit. Eng. 156, 137–145. https://doi.org/10.1680/wame.2003.156.2.137
TAW, 2002. Guidelines for Hydraulic Structures.
Tofany, N., Ahmad, M.F., Mamat, M., Mohd-Lokman, H., 2016. The effects of wave activity on overtopping and scouring on a vertical breakwater. Ocean Eng. 116, 295–311.
van Gent, M.R.A., 2020. Influence of oblique wave attack on wave overtopping at smooth and rough dikes with a berm. Coast. Eng. 160, 103734. https://doi.org/10.1016/j.coastaleng.2020.103734
van Gent, M.R.A., van den Boogaard, H.F.P., Pozueta, B., Medina, J.R., 2007. Neural network modelling of wave overtopping at coastal structures. Coast. Eng. 54, 586–593. https://doi.org/10.1016/j.coastaleng.2006.12.001
Zou, Q.-P., Chen, Y., Cluckie, I., Hewston, R., Pan, S., Peng, Z., Reeve, D., 2013. Ensemble prediction of coastal flood risk arising from overtopping by linking meteorological, ocean, coastal and surf zone models. Q. J. R. Meteorol. Soc. 139, 298–313. https://doi.org/10.1002/qj.2078

8th International Conference on the Application of Physical Modelling in Coastal and Port Engineering and Science
Dec. 9th - 12th, 2020, Zhoushan, China

DEVELOPMENT OF COUPLING PROGRAM AND DYNAMIC RESPONSE OF ARTICULATED OFFSHORE WIND TURBINE

ZHANG PEI[1] [2] [3], TANG YOUGANG[1] [2] [3] , YANG SHUGENG[1] [2] [3] & LI YAN[1] [2] [3]

[1] State Key Laboratory of Hydraulic Engineering Simulation and Safety, Tianjin University, Tianjin, 300354
[2] Tianjin Key Laboratory of Port and Ocean Engineering, Tianjin University, Tianjin,300354
[3] School of Civil Engineering, Tianjin University, Tianjin, 300354

ABSTRACT

A new-type articulated offshore wind turbine (AOWT) is proposed for the water depth of 50 m, and an analytical model for the swing motion of AOWT was established. Through adopting the aerodynamic-hydrodynamic coupling analysis method and programing MATLAB code, the dynamic response of the structure under the action of different environmental loads such as wind, wave and flow was analyzed. Besides, the influence of the steady and turbulent wind models on the overall movement and load response of the structure was conducted. The results show that AOWT has great movement and load performance under the rated wind condition, the structure design meets the requirements of safe operation. Compared with the steady wind, the amplitude changes greatly under the action of the turbulent wind, but the mean value significantly decreases, and a large coupling resonance is induced in the low frequency range.

Keywords: Articulated Offshore wind turbine; Dynamic response; The time domain; Turbulent wind; Resonance

1 INTRODUCTION

At present, for water depths less than 30m, fixed basic wind turbines are mainly used, and for water depths greater than 100m, different types of floating basic wind turbines are used. Our country's submarine continental shelf is different from European and American countries. The landform is relatively flat. When the water depth exceeds 100m, the distance from the shore is often more than 50km, causing the cost of laying cables and related supporting facilities to increase sharply. And the water depth is greater than 30m, the construction cost of fixed wind turbines also increases significantly. Therefore, considering China's national conditions and market demand, it is particularly important to develop a wind power foundation suitable for water depth around 50m.

In recent years, domestic and foreign researchers have carried out relevant research on how to reduce the water depth of wind turbines and improve the applicability of shallow water. (Le C.H et al., 2019) put forward a new type of full submersible floating wind turbine suitable for 50m water depth. A wind turbine-tower-floating platform-mooring system model was established, and FAST software was used to study the dynamic response characteristics of the overall system under different wind conditions. A conceptual design scheme of a reinforced concrete semi-submersible floating wind turbine platform is proposed by (Deng L et al., 2016) for the medium and shallow water area. The hydrodynamic characteristics of the semi-submersible floating wind turbine platform are studied using SESAM software, and the structural stability and overall strength are analyzed.

Based on the characteristics of the articulated tower platform and the floating wind turbine, an articulated foundation wind turbine structure is proposed. A scheme for semi-floating articulated wind turbines suitable for medium and shallow waters is proposed by (Njomo W, 2016; Natara J.A, 2016). The finite element software Abaqus is used to carry out reliability analysis and fatigue load calculation of the structure, and the numerical response calculation of the rocking motion under operating sea conditions is carried out. A three-leg articulated foundation design for a 5MW wind turbine is proposed. The dynamic response of the upper wind turbine structure and the articulated foundation under the combined action of wind, waves and currents is studied by (Philip V, 2015; Jsoeph A,2015) using the finite element software NAOS and the wind turbine simulation software FAST.

This paper proposes a new type of articulated offshore wind turbine (AOWT) structure. Based on the theory of aerodynamics and hydrodynamics, a single-degree-of-freedom rigid body swaying motion analysis model of articulated wind turbines is established to analyze its dynamic response under the combined action of wind, wave and currents.

2 Calculation model of articulated wind turbine

This paper takes NREL5WM wind turbine as the research object, and applying for 50m water depth. The articulated wind turbine is improved and optimized, as shown in Figure 1(a). The foundation tower column of the wind turbine is connected to the seabed foundation through an articulated joint. A ballast tank is set at the bottom to reduce the center of gravity of the structure. A buoyancy chamber is set near the waterline surface to compensate for the structural stability. The part of the tower column above the water surface is left with a certain air gap height and is connected to the wind turbine tower. The hinged foundation and the upper wind turbine swing around the hinged joint with wind and waves.

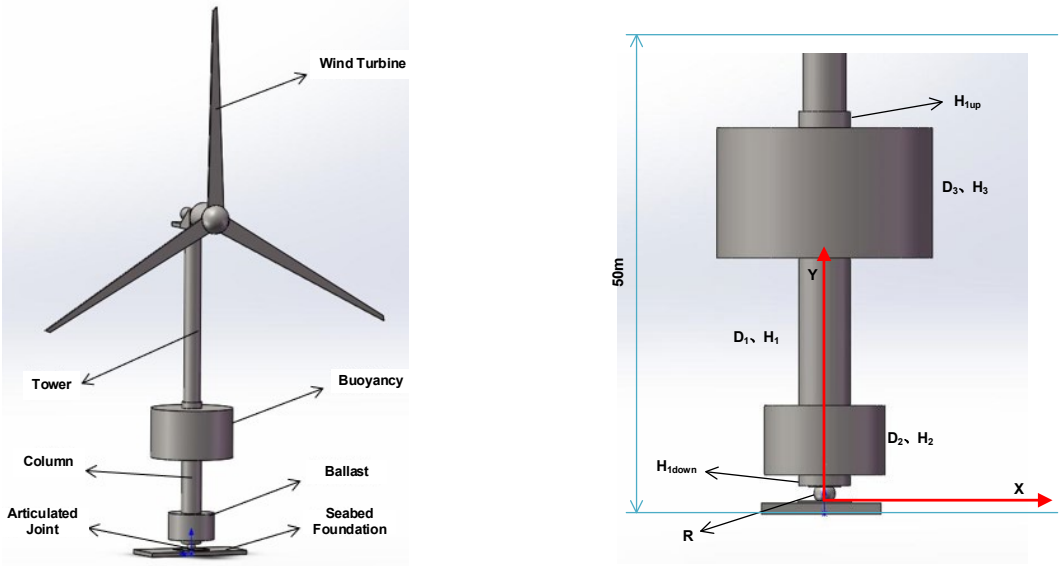

(a) Geometric model of AOWT (b) Structure of the articulated foundation

Figure 1. Basic structure of the articulated wind turbine (AQWT).

2.1 Structural model and parameters

The hinged foundation can be assumed as segmented column structures. In order to meet the requirements of water depth, the size of the middle tower column is shortened. At the same time, to compensate for the structural stability, the diameter of the buoyancy cabin at the waterline surface is increased. Radius of the joint ball is 1.5m which is used at the bottom, considering the influence of internal friction. The basic parameters of the articulated foundation are given in Table 1, and the structure is shown in Figure 1(b). The basic structure is mainly composed of three parts: a ballast tank with a height of H_2=8m at the bottom, and internal ballast concrete to lower the center of gravity of the structure. A buoyancy tank with a height of H_3=15m close to the waterline, which provides restoring force for the overall structure. The height of the column between the two is H_1=17m, which is used to connect the upper and lower tanks. At the same time, there are H_{1down}=2m and H_{1up}=5m left at the bottom of the ballast and the top of the buoyancy to ensure that the bottom ballast will not hit the bottom and the buoyancy tank will not lose buoyancy under the condition of large angle inclination.

Table 1. Parameters of the articulated foundation

ITEM	VALUE
Middle Column Diameter D_1/m	6.0
Ballast Tank Diameter D_2/m	14.0
Ballast Tank Diameter D_3/m	25.0
Articulated ball radius R/m	1.5
The air gap height /m	10.0
Mass of foundation (ballast)/t	4535.5
Center of Gravity (ballast)/m	(0,0,16.6)

The upper wind turbine of the model in this paper adopts the 5MW wind turbine developed by the American Renewable Energy Laboratory (NREL). The specific parameters and overall design parameters of the wind turbine are shown in Table 2 below.

Table 2. Main design parameters of the AOWT

ITEM	VALUE
Design water depth/m	50.0
Hub height/m	90.0
Wind speed (cut in/rated/cut out)/ m·s^{-1}	25.0
Rated speed/rpm	12.1
Total weight of upper wind turbine /t	670.3
Total mass /t	5205.8
Center of Gravity /m	(0,0,29.47)
Inertia of pitch / t·m^2	1.14e7
Initial tension at hinged joint /KN	4.23e4
Pitch natural frequency / rad·s^{-1}	0.29

2.2 Model Analysis

The calculation model of the articulated foundation wind turbine is established with reference to the dynamic model of the articulated tower platform (Zaheer M, 2017; Islam N, 2017), considering that the articulated foundation and the upper wind turbine are both rigid structures, the foundation tower column and the wind turbine tower are rigidly connected. The overall structure makes a single-degree-of-freedom swing motion around the hinged joint at the bottom. At the same time, the hinged point is defined as the origin of the system coordinates. The positive direction of the wind wheel is the positive direction of the X axis, and the vertical direction from the hinge point to the hub is the Y axis. In this paper, the environmental load is mainly considered along the positive direction of the X axis.

3 COMPUTATIONAL ANALYSIS THEORY

3.1 Motion governing equation

The hydrodynamic parameters such as the additional moment of inertia, the potential flow damping and the first-order wave force transfer function are calculated by using the hydrodynamic software SESAM. Since the hydrodynamic parameters corresponding to any frequency cannot be directly substituted into the time-domain equation in irregular waves, the additional rotational moment of inertia and potential flow damping are converted into hysteresis functions by the convolution integral method. The first-order wave force transfer function is converted into the wave load at each moment according to the wave frequency component and substituted into the governing equation. Finally, we use the fourth order runge-kutta numerical method to solve each time step motion, and the time domain motion response is obtained. The time-domain motion governing equation of the structure can be expressed as:

$$\left(I + I_A(\infty)\right)\ddot{\theta} + \int_0^t h(t-\tau)\dot{\theta}(\tau)d\tau + C_2\dot{\theta} + M_{fr}\left(\dot{\theta}\right) + M_{gb}(\theta) = F_{wave} + F_{wind} + F_{cur} \quad [1]$$

Where I is the moment of inertia of whole system, $I_A(\omega)$ is the additional moment of inertia, h is the damping hysteresis function, $C_2(\dot{\theta})$ is the viscous damping, $M_{fr}(\dot{\theta})$ is the friction moment of articulated joint, $M_{\mathrm{gb}}(\theta)$ is the system restoring moment, $F_{\mathrm{wave}}$is the wave force, F_{wind} is the aerodynamic force of impeller and wind force on tower, F_{cur} is the current force.

3.2 Wind loading

Before conducting the aerodynamic performance analysis of the wind turbine, it is necessary to simulate the random wind field. In this paper, the wind field under two characteristics of constant wind and turbulent wind are mainly considered. In the case of the constant wind, the wind shear model is used to calculate the wind speed changing with height. Based on the wind speed of the hub, the wind speed at each blade element can be obtained. The turbulent wind is simulated by NPD wind spectrum. For strong wind condition, the design wind speed $u(z,t)$ (t≤t_0=3600s) (China Classification Society, 2005) is calculated as follows:

$$u(z,t) = U_z\left[1 - 0.41 \cdot I_u(z) \cdot \ln\left(\frac{t}{t_0}\right)\right] \quad [2]$$
$$I_u(z) = 0.061 + 0.043 \cdot U_0\left(\frac{z}{10}\right)^{-0.22}$$
$$U_z = U_0\left[1 + C \cdot \ln\left(\frac{z}{10}\right)\right]$$
$$C = 5.73 \times 10^{-2}(1 + 0.15 \cdot U_0)^{0.5}$$

Where U_z is the 1-hour average wind speed at z meters above sea level, $I_u(z)$ is the turbulence intensity factor, U_0 is the 1-hour average wind speed at 10 meters above sea level, the following spectrum functions are used to generate the time-varying wind speed.

$$S(f) = \frac{320 \cdot \left(\frac{U_0}{10}\right)^2 \cdot \left(\frac{z}{10}\right)^{0.45}}{(1 + f_m{}^n)^{\frac{5}{3n}}} \quad [3]$$
$$f_m = 172 \cdot f \cdot \left(\frac{U_0}{10}\right)^{-0.75} \cdot \left(\frac{z}{10}\right)^{0.66}$$

Where,$n = 0.468$;$S(f)$ is the spectrum density function; f is the frequency, and the range of value is: $1/600H_z \le f \le 0.5H_z$ .Therefore, turbulent wind at z meters above sea level can be interpreted by superposition of design wind speed and time varying wind speed. It is calculated by the following formula:

$$U_{tur} = u(z,t) + \sum_{j=1}^{k}\sqrt{2 \cdot S(f) \cdot df} \cdot \cos(2\pi \cdot f \cdot t_j + \theta) \quad [4]$$

Where,θ is the random phase, and the simulation time t is 3600s. In this paper, we take the rated wind speed (11.4m/s) for example, considering the wind shear effect, the design wind speed amplitude at the hub is calculated according to the Eq. [2], and the time-varying wind speed was generated by combining the spectrum density function according to the Eq. [3]. The 1-hour simulation result was taken to draw the diagram, and the turbulent wind time history curve was obtained below.

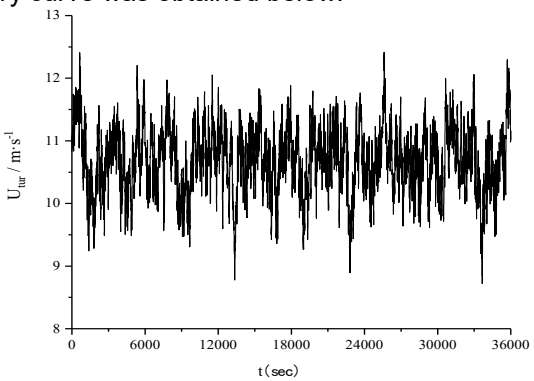

Figure 2. Time history curve of the turbulent wind at the hub

The wind load of the system includes the aerodynamic load on the impeller and the wind pressure load on tower. The aerodynamic load is calculated by using blade element momentum theory, and the blade is divided into many segments along the spreading direction, which are called as blade elements. For each blade element, the momentum theory is used to solve the force and moment, and results are integrated along the spreading direction to obtain the axial thrust and rotational moment on the whole blade (Li Y, et al., 2018).

The computational formula of total velocity seen by blade element and induction factors are equivalent to:

$$dT = 4\pi r\rho v_0^2 a(1-a)Fdr \quad [5]$$
$$dM = 4\pi r^3 \rho v_0 \omega_0 (1-a)a'Fdr$$
$$F = \frac{4}{\pi^2}\arccos\left(\exp(-\frac{B}{2}\frac{R-r}{r\sin\varphi})\right)\arccos\left(\exp\left(-\frac{B}{2}\frac{r-R_{\text{hub}}}{R_{\text{hub}}\sin\varphi}\right)\right)$$

Where, a is the axial induction factor, a' is the tangential induction factor, r is the local radius, c is the chord length, R_{hub} is the hub radius, w is the rotor rotational speed, v_0 is the inflow speed, φ is the local flow angle. The solution of the induction coefficient is an iterative process until it converges to a reasonable value. F is the prandtl coefficient which combined tip-loss and hub-loss, it is a modification of the assumption that the number of blades is infinite.

The wind load on tower is calculated according to the CCS document, as is shown in Eq. [6] below.

$$F_{\text{tower}} = 0.613\sum_{\text{j=1}}^{\text{n}}\left(C_{\text{h}}C_{\text{s}}A_{\text{i}}(\alpha)V_{\text{r}}{}^2\right) \quad [6]$$

In the formula, j is the number of component; n is the quantity of components; C_h is the height coefficient of component; C_s is the shape coefficient of component; $A_i(\alpha)$ is the projected area of component i on the α wind direction; V_r is the relative velocity between the wind and component.

3.3 Wave loading

The wave load of articulated wind turbine is solved by using three-dimensional potential flow theory considering the diffraction and radiation effect. Velocity potential can be divided into: the incident potential, the diffraction potential, and the radiation potential. Velocity potential on each element can be solved by the surface element method. The water pressure of the fluid is solved according to Bernoulli equation, and the wave load of the floating body is integrated along the whole surface.

3.4 Current loading

Current load on the foundation column is calculated in accordance with CCS document from the following formula:

$$F_{cur} = \frac{1}{2}C_D\rho_W A V_{cur}{}^2 \quad [7]$$

Where, C_D is the drag force coefficient;ρ_W is the density of sea water;A is the projected area of the component on the plane perpendicular to the current velocity.

3.5 Friction moment of articulated joint

For the articulated wind turbine, when the whole structure rotates around the hinged joint, the internal friction of the articulated joint produces corresponding friction damping. For the articulated joint in this paper, the articulated ball-type connection structure is selected (Hao J.S,2008). Its friction moment can be calculated by the formula below：

$$M_{fr} = \mu NR\left[sign(\dot{\theta})\right] \quad [8]$$
$$N = \sum N_x + \sum N_y$$
$$\sum N_x = M\omega^2 h_g \sin(\theta) - Mah_g\cos(\theta) + Q_x$$
$$\sum N_y = (F_{buoy} - Mg) + M\omega^2 h_g\cos(\theta) + Mah_g\sin(\theta) + Q_y$$

Where,μ is the friction coefficient, in this paper $\mu = 0.1$; N is the normal force; R is the radius of articulated joint; $sign|\theta|$ represents the unit vector in the same direction with the velocity vector. N denotes the reaction force, it can be divided into two parts, N_x in x direction and Ny in y direction. M is the total mass, θ, ω, a represent the pitch angle, angular velocity, and angular acceleration respectively. h_g is the height of center of gravity relative to the hinged joint, F_{buoy} represents the buoyancy, Q_x represents the external environmental loads in the x direction, including the thrust on the rotor, wind pressure on the tower, wave load and current load in the surge direction. Q_y represents the environmental forces in the heave direction.

3.6 Numerical program development

Based on the theory of aerodynamics and hydrodynamics, this paper establishes a single-degree-of-freedom rigid body swaying analysis model for articulated wind turbines. Using the hydrodynamic software WADAM and MATLAB, a numerical simulation program for aerodynamic-hydrodynamic-structure coupling of articulated wind turbines has been developed. The calculation flowchart of the program is shown below.

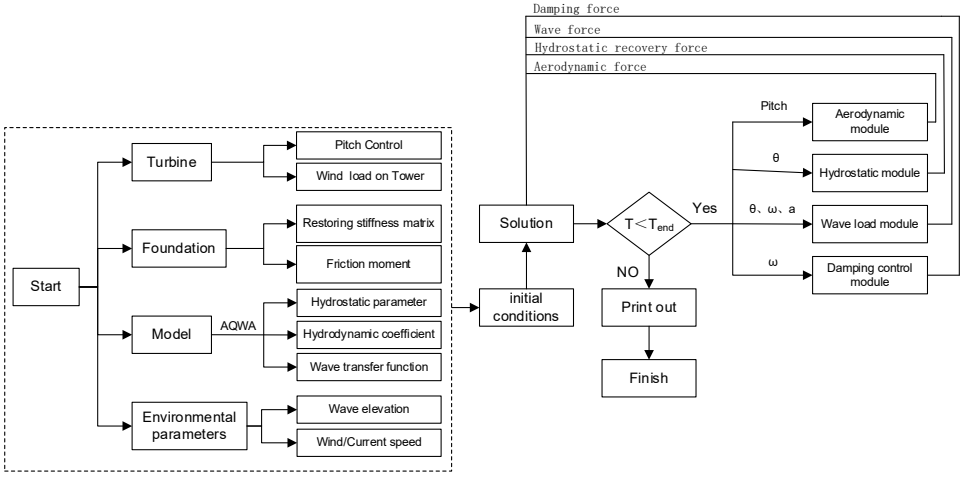

Figure 3. Flow chart of numerical calculation program for AOWT.

Among them, AQWA is mainly used in the calculation of hydrodynamic coefficients of articulated foundations in the frequency domain, including the hydrostatic matrix with six degrees of freedom, the additional mass matrix, the potential flow damping matrix, and the first-order wave transfer function. These parameters are edited into the program through the external interface, combined with the initially generated environmental parameters such as wind, waves and currents, and brought into the coupled dynamic response equation to solve the displacement and velocity at the center of gravity of the system. Then transfer the obtained structural displacement and speed to the load solving module to calculate the load change under the structural rocking motion, and then apply the updated load as the external load of the next time step to the system until the simulation time is over. The numerical results are analyzed through the post-processing module.

4 CALCULATION RESULTS AND ANALYSIS

4.1 Conditions

Considering the co-directional operation of wind, wave and current loads, wave is described by random wave generated by the JONSWAP wave spectrum. The incident direction of the wave is along the positive direction of the X-axis. Simultaneously, steady wind and turbulent wind are simulated. The turbulent wind is simulated using NPD wind spectrum, and the sea state corresponding to the rated wind speed of 11.4m/s is used for the analysis. The current is considered as a steady flow. The specific sea parameters are shown in Table 3 below.

Table 3. Condition Parameters

SEA CONDITIONS	WIND SPEED		WAVE HEIGHR	PEAK PERIOD	CURRENT
LC1	Constant	11.4 $m \cdot s^{-1}$	3.0 m	6.3 s	0.4 $m \cdot s^{-1}$
LC2	Turbulent		3.0 m	6.3 s	0.4 $m \cdot s^{-1}$

Two sea conditions of LC1/2 are selected to compare and study the influence of turbulent wind and steady wind on the dynamic response of the wind turbine foundation pitch angle θ, power generation P and joint tension Ten. The simulation time is 3600s. Take the 30~40min stable phase data as an example for graphing, and then use Fourier transform FFT to convert the time history result to the frequency domain for comparative analysis.

4.2 Pitch response

The following figure is based on the time history curve and amplitude response spectrum of pitch motion under steady wind and turbulent wind and sea conditions.

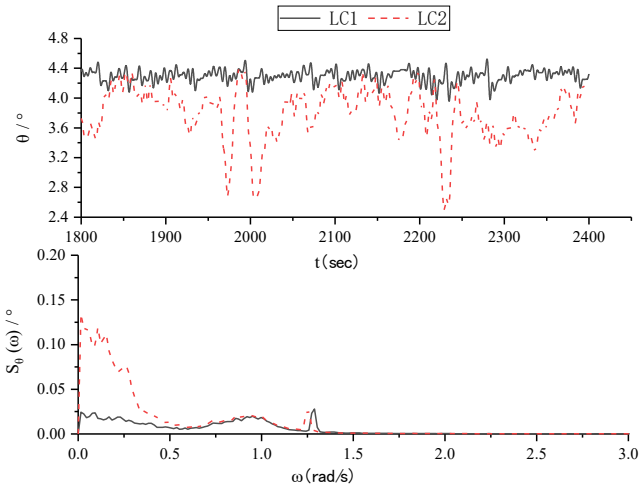

Figure 4. Time history curves and response spectra of pitch

It can be seen from the figure that under the action of steady wind, the pitch response is shown as a cyclical reciprocating motion around the equilibrium position, and the amplitude of the sway changes continuously within a certain limited range. The maximum value of the pitch motion does not exceed 5°, and the average value is about 4.3°. Under the action of turbulent wind, the pitch motion changes more drastically than the steady wind amplitude, and the standard deviation increases significantly, but the overall average value is reduced, about 3.8°.

It can be seen from the amplitude response spectrum that under the action of steady wind, there are mainly three response peaks in the pitch motion response spectrum. Corresponding to the low frequency response below 0.3 rad/s, the wave frequency response near 0.99 rad/s, and the 1P response of the wind wheel at 1.27 rad/s. Compared with the steady wind, the turbulent wind induces a greater low-frequency response at low frequencies, especially in the natural frequency range less than 0.3rad/s, the swing response peak value increases significantly. At the same time, the peak at the 1P frequency shifts to a certain extent to the low frequency, and the movement energy is mainly concentrated in the low frequency range.

4.3 Power response

The following figure is based on the time history curve and amplitude response spectrum of power generation under steady wind and turbulent wind and sea conditions.

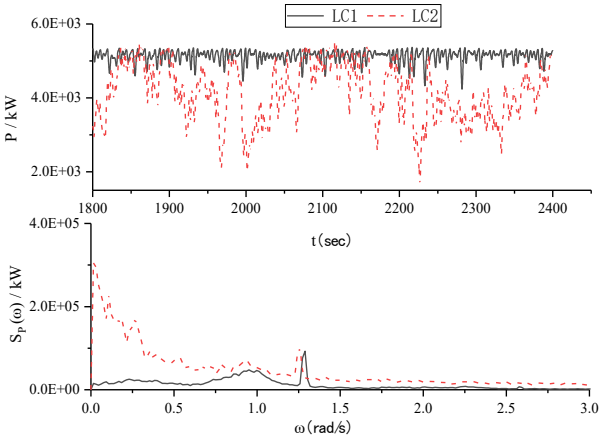

Figure 5. Time history curves and response spectra of power

It can be seen from the time history graph that the power generation of the wind turbine fluctuates around 5MW under the rated wind speed and constant wind and sea conditions, indicating that the simulation effect of the aerodynamic load program is good, and the structural design meets the normal power generation requirements of the wind turbine. Under turbulent wind and sea conditions, the power generation efficiency is significantly reduced, the amplitude changes drastically, and the power generation state is unstable. At the same time, the overall power generation average value is also greatly reduced, about 4.2MW. It can be seen from the amplitude response spectrum that, compared with the steady wind and sea conditions, the turbulent wind induces a larger resonance response at low frequencies, and the peaks at the wave frequency and 1P frequency increase. The overall change trend of the dynamic response of the power generation is consistent with the pitch response.

4.4 Tension response of the hinge joint

The following figure shows the time history curve and amplitude response spectrum of the combined tension of the bottom hinge joint under steady wind and turbulent wind and sea conditions.

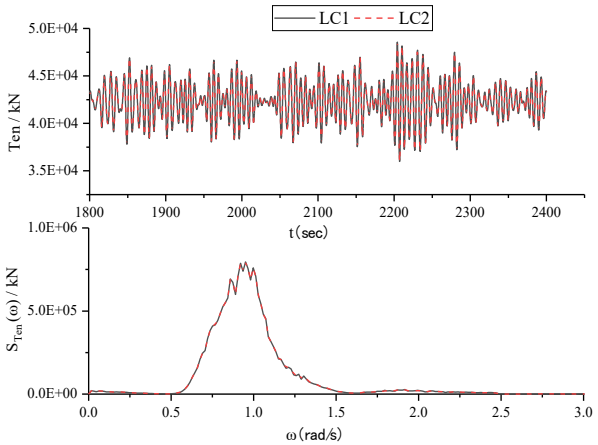

Figure 6. Time history curves and response spectra of hinge joint tensions

It can be seen from the figure that the maximum joint tension value of the hinge joint under the two sea conditions does not exceed 50000KN, which meets the requirements of the maximum bearing capacity value of the hinge joint. The peak amplitude response is mainly concentrated near the wave frequency, indicating that the hinge joint tension is mainly affected by the wave load, and the wind load has little effect on it, while the turbulent wind and steady wind have limited effect on the hinge joint tension. In the two wind field modes, the tension force response of the hinge joint does not change significantly.

5 CONCLUSIONS

In this paper, aiming at the design depth of 50m, an articulated foundation wind turbine is proposed. Based on the theory of aerodynamics and hydrodynamics, a single degree of freedom rigid body analysis model of the articulated wind turbine is established. In this paper, a calculation program is developed to consider the effects of turbulent wind and steady wind on the dynamic responses of pitch Angle, power generation and hinge point tension of the wind turbine respectively under the rated wind speed condition. The main conclusions are as follows:

(a) Under the rated wind speed condition, the wind turbine is subject to steady wind, and the basic motion performance is good, which can meet the normal power generation requirements, and the structural design meets the requirements of safe service.

(b) Compared with the steady wind condition, under the action of turbulent wind, the basic pitch motion and the average amplitude of the generated power are significantly reduced, but the range of response changes is increased, and the overall response is more intense. At the same time, in the amplitude response spectrum, change trends of the pitch motion and power generation response are basically the same. Compared with the steady wind, the turbulent wind induces larger resonance in the low frequency range of, and significantly improves the low frequency response.

(c) The tension force of the hinge joint is mainly affected by the wave load, while the wind load including turbulent wind have little effect on it.

ACKNOWLEDGEMENTS

This work is financially supported by the Natural Science Foundation of China (Grant No. 51879188 and 51779109) and the Innovative Foundation of Tianjin University (No. 2006).

REFERENCES

Deng Lu, Wang Biao, Xiao Zhiying, et al. Conceptual design and performance analysis of a reinforced concrete platform for floating wind turbines[J]. *Journal of huazhong university of science and technology*,2016, 000(001):11-15,21

Hao Jiashu. Dynamic response analysis of articulated tower platform [D]. *Harbin engineering university*, 2008.

Le Conghuan, Teng Lixia, Li Yan, et al. Dynamic Response Analysis of a New Type Submersible Floating Wind Turbines Under Different Wind Conditions [J]. *Journal of ocean university of China (natural science)*, 2019(S1).

Li Y, Zhu Q, Liu L, Tang Y. Transient response of a SPAR-type floating offshore wind turbine with fractured mooring lines. *Renew. Energy 2018,* 122, 576–588.

Njomo W, Natarajan A, Dimitrov N. Development and design of a semi-floater substructure for multi-megawatt wind turbines at 50 m water depths[J]. *Ocean Engineering*, 2016, 125:226-237.

Philip V, Jsoeph A, Joy C M. Three-Legged Articulated Support for 5 MW Offshore Wind Turbine [J]. *Aquatic Procedia*, 2015, 4:500-507.

Zaheer M, Islam N. Dynamic response of articulated towers under correlated wind and waves[J]. *Ocean Engineering*, 2017, 132:114-125.

8th International Conference on the Application of Physical Modelling in Coastal and Port Engineering and Science
Dec. 9th - 12th, Zhoushan, China

ENERGY PROPERTIES FOR HIGHER-ORDER STOKES WAVES OVER HORIZONTAL BOTTOM

XIANG GAO(1), XIAOZHOU MA(2), YUXIANG MA(3), GUOHAI DONG(4) , JUNLIANG GAO(5)

(1,2,3,4) The State Key Laboratory of Coastal and Offshore Engineering, Dalian University of Technology, Dalian, 116024,China
maxzh@dlut.edu.cn

(5) School of Naval Architecture and Ocean Engineering, Jiangsu University of Science and Technology, Zhenjiang, 212003, China
gaojunliang880917@163.com

ABSTRACT

The energy in the surface water waves is a very important concept. The most common method for calculating the wave energy is based on the linear or the first-order Stokes wave theory, where the phase-averaged potential, kinetic and total energy of waves is a function of just the amplitude or the height of the waves and the kinetic energy is equal to the potential energy. Because of its simplicity, this method is used for nonlinear waves as well. In this paper, the phase-averaged energy properties, i.e., potential, kinetic and total energy of very nonlinear waves in finite water depth and deep water over horizontal bottoms are studied. The analytical expressions of the wave energy properties are derived based on the nonlinear wave theories, such as the second-, third- and fifth-order Stokes wave theories. The energy are accurate to fourth order, sixth order and tenth order respectively. The results show that, for the nonlinear wave, the energy is no longer a single-variable function of wave height and varies with the wave parameters such as wave height and wave number. Besides, the kinetic energy and potential energy are not equal, the kinetic energy is larger than potential energy. Comparison between the energy of Airy waves and that of nonlinear waves has shown that cautions should be taken to calculate the energy of waves of high nonlinearity.

Keywords: Energy, Nonlinear wave, Analytical solution.

1 INTRODUCTION

The energy in the surface water waves is a very important concept as the waves basically are a propagation of certain amount of mechanical energy by transferring between kinetic and potential energy. The wave energy is used extensively to index the strength of the waves, to calculate the radiation stress and to evaluate the wave field for exploiting wave power [1]. The most common method for calculating the wave energy is based on the linear or the first-order Stokes wave theory. Dean and Dalryple [1] and Sorensen [2] calculate the average potential energy and kinetic energy per unit water by integrating over a wavelength range. Mei et al. [3] and Zou [4] calculate the energy by integrating over a wave period. The result is a univariate function of the wave height, proportional to the square of the wave height, and the kinetic energy is equal to the potential energy. Because of its simplicity, this method is used for nonlinear waves as well. The nonlinear wave theories have been well developed and many researchers have proposed expressions of higher order wave theories. However, there are a few studies on the properties of nonlinear wave energy. Longuet-Higgins [7] first derived the exact relations between the integral properties of steady water waves. Jonsson and Arneborg [8] derived the energy properties of fifth-order Stokes wave based on Fenton (1985) and the energy expression is accurate to the fourth order. Jonsson and Steenberg [9] calculated the potential and kinetic energy in deep water, which lead to the energy density correct to sixth order.

This paper derive the analytical expressions of nonlinear wave energy density in finite water depth and deep water, including second-, third- and fifth-order Stokes wave theories, and the results are accurate to fourth order, sixth order and tenth order respectively. The result shows that for the nonlinear wave, the kinetic energy and potential energy of the wave are no longer equal, and the total energy is no longer a univariate function of wave height and varies with the wave parameters such as wave height and wave number. Therefore, for the wave with nonlinearity, using wave energy formulas based on the linear wave theory will cause some errors. The results of this paper have certain research significance for the calculation of nonlinear wave energy.

2 ENERGY CALCULATION OF NONLINEAR WAVES

2.1 Energy Analytical Expression of Second-order Stokes Wave

The wave-induced potential energy per unit horizontal area under the free surface is taken into account, as shown in Figure 1. The potential energy must be measured relative to a horizontal level, which the mean water level (MWL) is naturally chosen as $z = 0$, x is the coordinate in the direction of wave propagation.

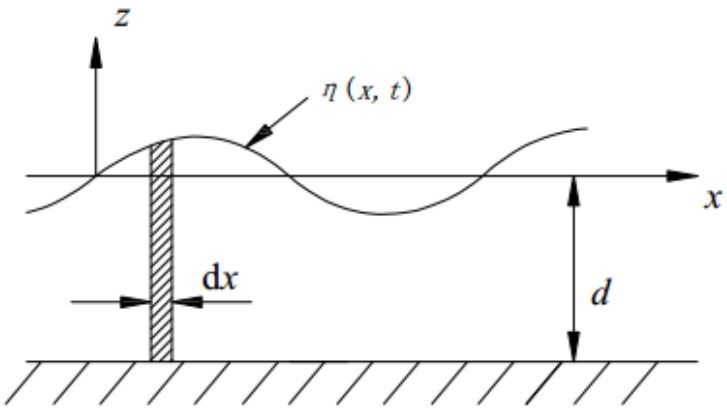

Figure 1. Definition sketch for determination of potential energy

The phase-averaged potential energy E_p over a wavelength is given [2]:

$$E_p = \frac{1}{L}\int_x^{x+L}\int_0^{\eta} \rho g z \, \mathrm{d}z\mathrm{d}x \,. \tag{1}$$

The phase-averaged kinetic energy E_k over a wavelength is given [2]:

$$E_k = \frac{1}{L}\int_x^{x+L}\int_{-d}^{\eta} \frac{1}{2}\rho\left(u^2 + w^2\right)\mathrm{d}z\mathrm{d}x \,. \tag{2}$$

where L is the wave length, ρ is the water density; g is the gravitational acceleration; η is the wave profiles; d is the mean water depth; u and w represent horizontal and vertical velocity.

The expressions of velocity potential and wave profile of second-order Stokes wave are given as follows [1]. Noting that there is no constant term in the expression of wave profile, for we choose the mean water level as origin of coordinates, the mean of η is zero. According to Dean and Dalrymple (1991), the constant term is related to Bernoulli constant, so the constant term vanishes.

$$\phi = \frac{A\omega}{k}\left[\frac{\cosh k(z+d)}{\sinh(kd)}\sin\theta + \frac{3}{8}Ak\frac{\cosh 2k(z+d)}{\sinh^4(kd)}\sin 2\theta\right], \tag{3}$$

$$\eta = A\left[\cos\theta + \frac{Ak}{4}\frac{\cosh kd\left(\cosh 2kd + 2\right)}{\sinh^3 kd}\cos 2\theta\right], \tag{4}$$

where θ represents the wave phase, $\theta = kx - \omega t$.

The second-order horizontal and vertical velocity can be obtained by the spatial derivative of velocity potential ϕ:

$$u = \frac{\partial\phi}{\partial x},\ w = \frac{\partial\phi}{\partial z}. \tag{5}$$

Considering the second-order Stokes wave profile, substituting Eq. 4 into Eq. 1, we can obtain the potential energy as follows:

$$E_p = \frac{1}{4}\rho\frac{g}{k^2}\varepsilon^2\left\{1 + \varepsilon^2\left(\frac{1}{4} + \frac{16S^4 + 21S^2 + 9}{16S^6}\right)\right\}, \tag{6}$$

where $S = \sinh kd$.

As for deep water, $kd \to \infty$, Eq. 6 is simplified and obtain expression of potential energy in deep water:

$$E_p = \frac{1}{4}\rho\frac{g}{k^2}\varepsilon^2\left(1 + \frac{1}{4}\varepsilon^2\right). \tag{7}$$

Considering the second-order velocity and wave profile, substituting Eqs. 3-4 into Eq. 2. The integral process is divided into two parts: the bottom to the mean water level, and the mean water level to the wave surface. The second-order Stokes wave kinetic energy can be obtained as follows:

$$E_k = \frac{\rho}{2}\overline{\int_{-d}^{0} u^2 \mathrm{d}z} + \frac{\rho}{2}\overline{\int_{0}^{\eta} u^2 \mathrm{d}z} + \frac{\rho}{2}\overline{\int_{-d}^{0} w^2 \mathrm{d}z} + \frac{\rho}{2}\overline{\int_{0}^{\eta} w^2 \mathrm{d}z}, \tag{8}$$

where the bar represent the mean value over a wavelength.

For the first term of Eq. 8:

$$u^2 = \left(u_{(1)} + u_{(2)}\right)^2 = u_{(1)}^2 + 2u_{(1)}u_{(2)} + u_{(2)}^2, \tag{9}$$

where $u_{(1)}$ and $u_{(2)}$ respectively represent first- and second-order term of horizontal velocity, and substituting the second-order dispersion relations,

$$\omega = \left(gk \tanh(kd)\right)^{1/2}. \tag{10}$$

The result of the first term of Eq.8 is given:

$$E_{k1} = \frac{1}{4}\rho\frac{g}{k^2}\varepsilon^2\left\{\frac{kdN}{2S^2} + \frac{1}{2} + \frac{9\varepsilon^2}{16}\left(\frac{kdN}{2S^8} + \frac{2C^2-1}{2S^6}\right)\right\}, \tag{11}$$

where $C = \cosh kd$, $N = \tanh kd$.

For the second term of Eq.8, the upper limit of integral is variable. Using Taylor expansion to expand the velocity at the mean water level (z = 0). For the second-order Stokes wave, expanding the velocity to the first derivative term can meet the accuracy requirements, the expression is as follows:

$$\frac{\rho}{2}\overline{\int_{0}^{\eta} u^2 \mathrm{d}z} = \frac{\rho}{2}\overline{\int_{0}^{\eta}\left[u^2(0) + (u^2(0))'z\right]\mathrm{d}z}. \tag{12}$$

Making necessary calculation, the result accurate to ε^4 is given:

$$E_{k2} = \frac{1}{4}\rho\frac{g}{k^2}\varepsilon^2\left\{\varepsilon^2\left(1 + \frac{17C^2-8}{8S^4}\right)\right\}. \tag{13}$$

In the same way, we can obtain the third and fourth term of Eq. 8:

$$E_{k3} = \frac{1}{4}\rho\frac{g}{k^2}\varepsilon^2\left\{-\frac{kdN}{2S^2} + \frac{1}{2} + \frac{9\varepsilon^2}{16}\left(-\frac{kdN}{2S^8} + \frac{2C^2-1}{2S^6}\right)\right\}, \tag{14}$$

$$E_{k4} = \frac{1}{4}\rho\frac{g}{k^2}\varepsilon^2\left(\varepsilon^2 - \frac{9}{8S^2}\right). \tag{15}$$

Over all, adding Eq.11 and Eqs.13-14 together, the kinetic energy of second-order Stokes wave is given:

$$E_k = \frac{1}{4}\rho\frac{g}{k^2}\varepsilon^2\left\{1 + \varepsilon^2\left(1 + \frac{52S^4 + 36S^2 + 9}{16S^6}\right)\right\}. \tag{16}$$

As for deep water, $kd \to \infty$, Eq. 16 is simplified and obtain expression of kinetic energy in deep water:

$$E_k = \frac{1}{4}\rho\frac{g}{k^2}\varepsilon^2(1+\varepsilon^2). \tag{17}$$

The total energy per unit area under the free surface of the second-order Stokes wave is:

$$E = E_p + E_k = \frac{1}{2}\rho\frac{g}{k^2}\varepsilon^2\left\{1 + \varepsilon^2\left(\frac{5}{8} + \frac{68S^4 + 57S^4 + 18}{32S^6}\right)\right\}. \tag{18}$$

As for deep water, the total energy is:

$$E = E_p + E_k = \frac{1}{2}\rho\frac{g}{k^2}\varepsilon^2\left(1 + \frac{5}{8}\varepsilon^2\right). \tag{19}$$

The expressions of potential and kinetic energy (Eq.6, Eq.16) in finite water depth are the same as Zou (2005), just expressed in another forms. Given wave period T = 4s, water depth d = 10m, within the range of application of finite water depth. Comparing the analytical results with the numerical integral results in the range of application of second-order Stokes wave [10]

As shown in the Figure 2, the analytical results are in good agreement with the numerical integral results. Besides, with the increase of the wave steepness, the kinetic energy is larger than the potential energy for the second order Stokes wave.

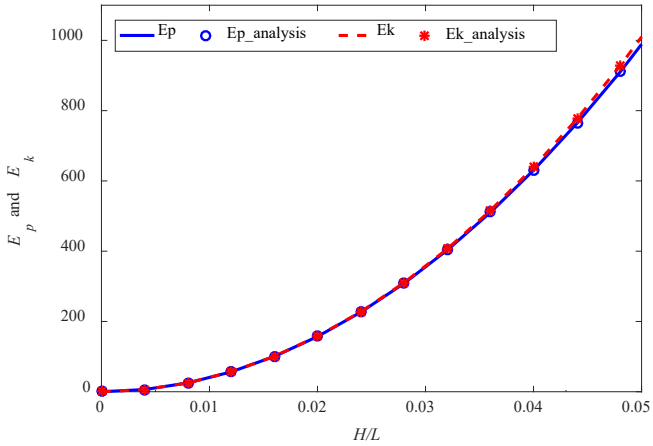

Figure 2. The comparison of analytical results and numerical integral results in the range of application of second-order Stokes wave

2.2 Energy Analytical Expression of Third-order Stokes Wave

As for the third-order Stokes wave theory, according to the Skjelbreia's (1959) results, the wave profile and velocity potential expression of third-order Stokes wave [5] are given:

$$\eta = E_1 \cos\theta + E_2 \cos 2\theta + E_3 \cos 3\theta\,, \tag{20}$$

$$\phi = \frac{\omega}{k}\left(F_1 \sin\theta + F_2 \sin 2\theta + F_3 \sin 3\theta\right), \tag{21}$$

in which,

$$\begin{cases} E_1 = A \\ E_2 = A\varepsilon \dfrac{C(2C^2+1)}{4S^3} \\ E_3 = A\varepsilon^2 \dfrac{3(8C^6+1)}{64S^6} \\ F_1 = A\left(\dfrac{1}{S} - \dfrac{\varepsilon^2\left(5S^4+11S^2+6\right)}{8S^5}\right)\cosh k(z+d) \\ F_2 = A\varepsilon \dfrac{3}{8S^4}\cosh 2k(z+d) \\ F_3 = A\varepsilon^2 \dfrac{9-4S^2}{64S^7}\cosh 3k(z+d) \end{cases}.$$

The third-order horizontal and vertical velocity can be obtained by the spatial derivative of velocity potential ϕ by Eq.5. Considering the third-order Stokes wave profile, substituting Eq. 20 into Eq. 1, we can obtain the potential energy as follows:

$$E_p = \frac{1}{4}\rho\frac{g}{k^2}\varepsilon^2\left(1+\varepsilon^2 P_1 + \varepsilon^4 P_2\right), \tag{22}$$

where,

$$P_1 = \frac{1}{4} + \frac{16S^4+21S^2+9}{16S^6},\quad P_2 = \frac{9(8C^6+1)^2}{64^2 S^{12}}.$$

As for deep water, $kd \to \infty$, Eq.22 is simplified and obtain expression of potential energy in deep water:

$$E_p = \frac{1}{4}\rho\frac{g}{k^2}\varepsilon^2\left(1+\frac{1}{4}\varepsilon^2 + \frac{9}{64}\varepsilon^4\right). \tag{23}$$

Considering the kinetic energy of third-order Stokes wave, substituting Eqs. 20-21 into Eq. 2. Using the same method as calculating the kinetic energy of second-order Stokes wave, substituting the third-order dispersion relations [5],

$$\omega = \left(gk\tanh(kd)\right)^{1/2}\left\{1+\varepsilon^2\left(\frac{8S^4+8S^2+9}{16S^4}\right)\right\}. \tag{24}$$

A considerable amount of calculation is involved in obtaining the expression of kinetic energy of third-order Stokes wave. The kinetic energy of third-order Stokes wave accurate to ε^6 is as follows:

$$E_k = \frac{1}{4}\rho\frac{g}{k^2}\varepsilon^2\left(1+\varepsilon^2 K_1+\varepsilon^4 K_2\right), \tag{25}$$

in which,

$$K_1 = \frac{3}{4}+\frac{24S^4+30S^2+9}{16S^6},\ K_2 = \frac{9}{64}+\frac{11904S^{10}+42304S^8+56064S^6+34416S^4+9720S^2+729}{4096S^{12}}.$$

As for deep water, $kd \to \infty$, Eq. 25 is simplified and obtain expression of kinetic energy in deep water:

$$E_k = \frac{1}{4}\rho\frac{g}{k^2}\varepsilon^2\left(1+\frac{3}{4}\varepsilon^2+\frac{9}{64}\varepsilon^4\right). \tag{26}$$

The total energy per unit area under the free surface of the third-order Stokes wave is:

$$E = E_p + E_k = \frac{1}{2}\rho\frac{g}{k^2}\varepsilon^2\left(1+\varepsilon^2 T_1+\varepsilon^4 T_2\right), \tag{27}$$

where,

$$T_1 = \frac{1}{2}\left(P_1+K_1\right),\ T_2 = \frac{1}{2}\left(P_2+K_2\right).$$

As for deep water, total energy is:

$$E = E_p + E_k = \frac{1}{2}\rho\frac{g}{k^2}\varepsilon^2\left(1+\frac{1}{2}\varepsilon^2+\frac{9}{64}\varepsilon^4\right). \tag{28}$$

In order to justify the correctness of the analytical expression, given wave period T = 4s, water depth d = 10m, within the range of application of finite water depth. Comparing the analytical and the numerical integral results in the range of application of third-order Stokes wave [10].

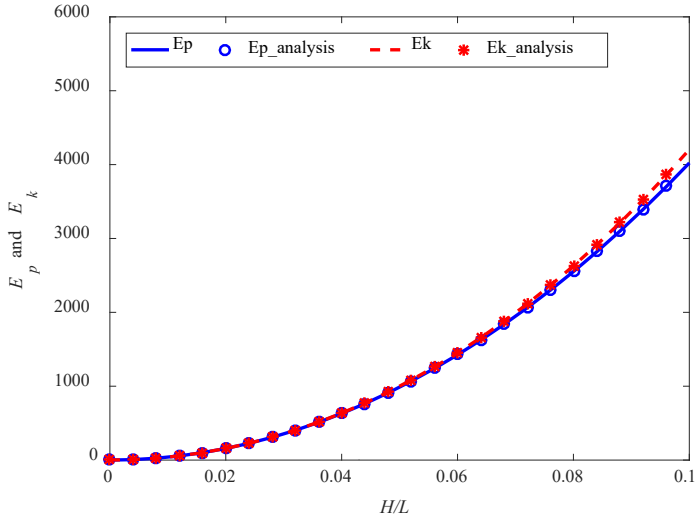

Figure 3. The comparison of analytical results and numerical integral results in the range of application of third-order Stokes wave

As shown in Figure 3, both of the potential and kinetic energy, the analytical results are in good agreement with the numerical integral results. Besides, with the increase of the wave steepness, kinetic energy and potential energy are not equal, the former is larger than the latter. Compared with the second-order Stokes wave, the difference between the two kinds of energy is more significant.

2.3 Energy Analytical Expression of Fifth-order Stokes Wave

The expressions of wave profile and velocity potential of fifth-order Stokes wave in fixed coordinate system can be found from Equation (28) and Equation (27) of Fenton (1985):

$$\eta = \eta_{(1)}+\eta_{(2)}+\eta_{(3)}+\eta_{(4)}+\eta_{(5)}, \tag{29}$$

where,

$$\begin{cases} \eta_{(1)} = A\cos\theta \\ \eta_{(2)} = A\varepsilon B_{22}\cos 2\theta \\ \eta_{(3)} = A\varepsilon^2 B_{31}\left(\cos\theta - \cos 3\theta\right) \\ \eta_{(4)} = A\varepsilon^3\left(B_{42}\cos 2\theta + B_{44}\cos 4\theta\right) \\ \eta_{(5)} = A\varepsilon^4\left\{-(B_{53}+B_{55})\cos\theta + B_{53}\cos 3\theta + B_{55}\cos 5\theta\right\} \end{cases},$$

$$\phi(x,z,t)=\left(c_a - c_r\right)x + C_0\left(\frac{g}{k^3}\right)^{1/2}\sum_{i=1}^{5}\varepsilon^i\sum_{j=1}^{i}A_{ij}\cosh jk(z+d)\sin j\theta \tag{30}$$

where $C_0 = (\tanh kd)^{1/2}$, A_{ij}, B_{ij} is a series of coefficients can be found from TABLE 1 of Fenton (1985); c_a is the absolute phase velocity; c_r is the phase velocity relative to a frame moving with the same velocity as the mean(Eulerian) velocity c_E below wave trough level. According to Stokes' first definition of wave celerity ($c_E = 0,\ c_a = c_r$) [9], the first term on the right-hand side in Eq.30 vanishes. Here, we calculate the wave energy in this situation.

Substituting Eq.29 into Eq.1, we can obtain the potential energy as follows:

$$E_p = \frac{1}{4}\rho\frac{g}{k^2}\varepsilon^2\left(1+\varepsilon^2 FP_1 + \varepsilon^4 FP_2 + \varepsilon^6 FP_3 + \varepsilon^8 FP_4\right), \tag{31}$$

in which,

$$\begin{cases} FP_1 = {B_{22}}^2 + 2B_{31} \\ FP_2 = 2{B_{31}}^2 - 2B_{53} - 2B_{55} + 2B_{22}B_{42} \\ FP_3 = {B_{42}}^2 + {B_{44}}^2 - 4B_{31}B_{53} - 2B_{31}B_{55} \\ FP_4 = 2{B_{53}}^2 + 2{B_{55}}^2 + 2B_{53}B_{55} \end{cases}.$$

As for deep water, substituting the expressions of coefficients B_{ij} and simplifying the Eq.31, we can obtain expression of potential energy in deep water:

$$E_p = \frac{1}{4}\rho\frac{g}{k^2}\varepsilon^2\left(1-\frac{1}{2}\varepsilon^2 - \frac{19}{12}\varepsilon^4 + \frac{7495}{4608}\varepsilon^6 + \frac{140959}{73728}\varepsilon^8\right). \tag{32}$$

Considering the kinetic energy of fifth-order Stokes wave, substituting Eqs. 29-30 into Eq. 2. Using the above method and the kinetic energy is accurate to ε^{10}, making the necessary (very extensive) calculation, the following expression is obtained:

$$E_k = \frac{1}{4}\rho\frac{g}{k^2}\varepsilon^2\left(1+\varepsilon^2 FK_1 + \varepsilon^4 FK_2 + \varepsilon^6 FK_3 + \varepsilon^8 FK_4\right). \tag{33}$$

The parameters in the expression Eq.33 are as follows:

$$\begin{cases} FK_1 = -\dfrac{3\left(4-2C_2+C_4\right)}{32S^6} \\ FK_2 = \dfrac{11083+20313C_2+17532C_4+10679C_6+4656C_8+473C_{10}+108C_{12}-25C_{14}-19C_{16}}{8192S^{12}\left(8+11C_2+6C_4\right)} \\ FK_3 = -\dfrac{\begin{array}{l}259553808+492963498C_2+397241624C_4+278483866C_6+153988226C_8+74995000C_{10}+\\ 29981381C_{12}+13918486C_{14}+3769740C_{16}+1061304C_{18}-56973C_{20}-39114C_{22}-846C_{24}\end{array}}{37748736S^{18}\left(2+3C_2\right)^2\left(1+4C_2\right)} \\ FK_4 = \dfrac{\begin{array}{l}55637835104856+104631811394372C_2+91080833890657C_4+69876133995462C_6+\\ 49637692964642C_8+30507459945542C_{10}+17222621624907C_{12}+7983631472872C_{14}+\\ 3350311001372C_{16}+1009016838672C_{18}+263561949377C_{20}+12427567930C_{22}-\\ 7755942978C_{24}-6098843910C_{26}-149520493C_{28}+78720900C_{30}+5435820C_{32}\end{array}}{773094113280S^{24}\left(8+11C_2+6C_4\right)^2} \end{cases},$$

where $C_j = \cosh(jkd)$.

The expression of kinetic energy in finite water depth is extremely complicated. As for the deep water, the expression of kinetic energy can be simplified as follows:

$$E_k = \frac{1}{4}\rho\frac{g}{k^2}\varepsilon^2\left(1-\frac{19}{12}\varepsilon^4 + \frac{47}{72}\varepsilon^6 + \frac{30199}{4608}\varepsilon^8\right). \tag{34}$$

There is no fourth-order term in the kinetic energy expression. It is also seen by comparing Eq.32 and Eq.34 that the kinetic energy is larger than the potential energy. The conclusion is the same as that obtained by the second and third order Stokes wave.

The total energy per unit area under the free surface of the fifth-order Stokes wave is:

$$E=\frac{1}{2}\rho\frac{g}{k^2}\varepsilon^2\left(1+\varepsilon^2 FT_1+\varepsilon^4 FT_2+\varepsilon^6 FT_3+\varepsilon^8 FT_4\right), \tag{35}$$

in which,

$$FT_j=\frac{1}{2}\left(FP_j+FK_j\right)\ \ (j=1,2,3,4).$$

As for deep water, the total energy is:

$$E=\frac{1}{2}\rho\frac{g}{k^2}\varepsilon^2\left(1-\frac{1}{4}\varepsilon^2-\frac{19}{12}\varepsilon^4+\frac{1167}{1024}\varepsilon^6+\frac{624143}{147456}\varepsilon^8\right). \tag{36}$$

The first three terms of potential energy in deep water Eq.32 and the first two terms of kinetic energy in deep water Eq.34 (in which the factor on ε^2 in the parentheses is zero) turn out to be agreement with Jonsson and Steenberg (1999), who presented sixth-order expressions for potential and kinetic energy in deep water. Compared with Longuet-Higgins (1975), who presented eighth-order expressions of potential and kinetic energy in deep water based on the findings by Schwartz (1974), similarly, the present expressions of energy are the same as his results until sixth order. However, the factors of eighth-order term are different. Given wave period T = 4s, water depth d = 20m, within the range of application in deep water. Compared the ratio of different analytical results to the numerical integral result as follows. As shown in the figures, both the present potential and kinetic energy is more consistent with the numerical integration results, especially near the extreme wave steepness.

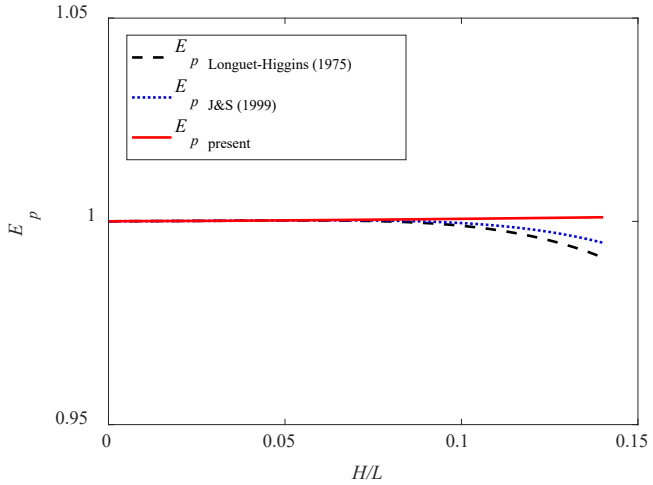

Figure 4. The ratio of analytical result to numerical integral result of potential energy E_p

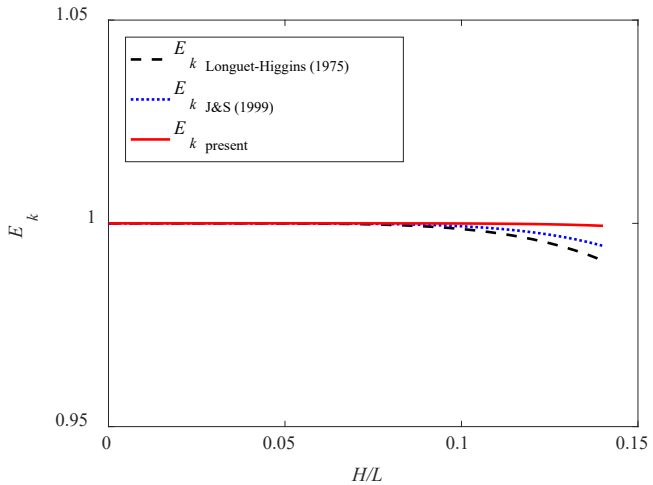

Figure 5. The ratio of analytical result to numerical integral result of kinetic energy E_k

3 RESULTS AND DISCUSSIONS

Based on the nonlinear Stokes wave theory, we obtain the energy density analytical expressions of different order nonlinear Stokes wave theory in finite water depth and deep water. For the second-order Stokes wave, the energy density expression is accurate to ε^4 and is the same as that of Zou (2005), just expressed in another forms. For the third-order Stokes wave, the analytical expression is accurate to ε^6. Compared with the numerical integration results, they are in good agreement. For the fifth-order Stokes wave, we obtain the energy expression which is accurate to the ε^{10} in the finite water depth and deep water. And the result in deep water is the same as that obtained by Jonsson and Steenberg (1999), who derived energy expression that is accurate to the ε^6 in deep water. Compared with Longuet-Higgins's (1975) eighth-order results of energy in deep water, we obtain different factors on eighth-order term and the present expression of energy is more consistent with the numerical integration result.

4 CONCLUSIONS

In this paper, the energy density in finite water depth and deep water of each order nonlinear wave is obtained by theoretical derivation. Some major conclusions can be obtained as follows:

1. As for second- and third- order Stokes wave, the energy expressions are accurate to fourth- the sixth-order respectively, and the results are in good agreement with the numerical integral results. As for fifth order Stokes wave, higher order energy expressions are proposed and is more consistent with the numerical integration results than previous expressions.

2. With the increase of nonlinearity, the kinetic energy and potential energy of the wave are no longer equal, the former is larger than the later. The energy is no longer a univariate function of wave height and varies with the wave parameters such as wave height and wave number.

ACKNOWLEDGEMENTS

This research is supported financially by the National Key Research and Development Program (2017YFC1404200), National Nature Science Foundation of China (Grant Nos. 51720105010, 51979029)

REFERENCES

R.G. Dean, R.A. Dalrymple. Water Wave Mechanics for Engineers and Scientists. Singapore: World Scientific, 1991: 94-97.

R.M. Sorensen. Basic Coastal Engineering (3rd Ed). the United States of America: Springer Science+Business Media, 2006: 36-37.

C.C. Mei. Theory and Applications of Ocean Surface Waves. World Scientific, 2005: 18-19.

Z.L. Zou. Water Wave Theories and Their Applications. Dalian: Science Publishing Company, 2005: 22-23. (in Chinese)

L. Skjelbreia. Gravity waves: Stokes' third order approximation; tables of functions. Engineering Foundation Council of Wave Research. 1959.

J.D. Fenton. A fifth-order Stokes theory for steady waves. Journal of Waterway Port Coastal and Ocean Engineering, 1985: 216-234.

M.S. Longuet-Higgins. Integral properties of periodic gravity waves of finite amplitude. Proc. R. Soc. Lond. 1975: 157–174.

I.G. Jonsson, L. Arneborg. Energy properties and shoaling of higher-order Stokes waves on a current. Oc. Engrg. 1995: 22(8), 819–857.

I.G. Jonsson, C.M. Steenberg. Characteristic velocities of higher-order Stokes waves in deep water. J. Waterway, Port, Coastal Ocean Engng ASCE 125, 1999: 109–117.

B. Le Mehaute. An Introduction to Hydrodynamics and Water Waves. 1976: 205-206.

8th International Conference on the Application of Physical Modelling in Coastal and Port Engineering and Science
Dec. 9th - 12th, 2020, Zhoushan, China

SIMULTANEOUS MEASUREMENT OF HORIZONTAL AND VERTICAL VELOCITIES AND FORCES BENEATH A TIDAL BORE

MUHAMMAD ZAIN BIN RIAZ(1), SHU-QING YANG(2) & MUTTUCUMARU SIVAKUMAR(3)

(1,2,3) School of Civil, Mining and Environmental Engineering, University of Wollongong, Wollongong, Australia
mzbr518@uowmail.edu.au, shuqing@uow.edu.au, siva@uow.edu.au

ABSTRACT

The development of a bore is a sudden change in water surface elevation represents the leading edge of the tidal wave propagating upstream. The impact of different types of forces under bores on sediment transport is not clear, hence specially designed experiments were conducted to clarify the mechanism of sediment initiation, although some physical experiments were performed during last two decades. In this study, a laser Doppler anemometer (LDA), a highly sensitive force sensor and ultrasonic displacement meters accompanied by video recordings were used to investigate simultaneously the incipient motion of sediment under tidal bores. No sediment motion was observed during the initial steady flow, but a transient sediment sheet flow motion was observed advected upstream during the breaking bore. The initiation of sediment motion was closely related to the passage of the breaking roller. According to the experimental results, upward vertical force due to swelling in free water surface before the roller toe was the main force in destabilizing the particles. Later, a large upstream longitudinal force was found to be the dominant cause promoting upstream particle motion during the breaking roller passage.

Keywords: Tidal bore, Incipient motion, Horizontal force, Vertical force, Physical modelling

1 INTRODUCTION

It is common that when a tide starts to rise, a series of waves propagate upstream in some river mouths as a tidal bore. During different tidal periods and distinct hydraulic conditions, various types of bores can occur at the same location. The shape and intensity of the bore is characterized by its Froude number (Eq. 1) (Bonneton et al. 2015), defined for a rectangular channel as:

$$Fr = \frac{V_0 + U}{\sqrt{gh_0}} \quad [1]$$

where V_0 is the initial river flow velocity positive downstream, U is the tidal bore celerity positive upstream for an observer standing on the bank, g is the gravitational acceleration and h_0 is the initial river flow depth. Khezri and Chanson (2015) observed that for smaller Froude numbers (Fr<1.3), an undular bore is a smooth wave without bubbles followed by a wave train, while with higher Froude numbers (Fr>1.35) a breaking bore is observed with marked roller and bubbles across the channel width (Figure 1).

The phenomenon of sediment incipient motion occurs, when instantaneous entraining forces are larger than the instantaneous stabilizing forces on a particle. This effect is also called the threshold of sediment motion (Van Rijn 1993). Bagnold (1963) recognized firstly the importance of wave-induced accelerations. Some field observations and physical modelling highlighted that sediment incipient motion is likely to occur due to horizontal pressure gradient introduced by free stream velocity gradient (Foster et al. 2006, Frank et al. 2015, Madsen 1975). However, the physical mechanisms that produces force on the particle due to streamwise pressure gradient were not discussed. Khezri and Chanson (2015) investigated the incipient sediment motion beneath the tidal bore by comparing longitudinal velocity and visual observation. They predicted only the longitudinal forces that are responsible for sediment entrainment and took no account of the role of vertical forces, i.e., buoyancy force and lift force. Furthermore, at the onset of motion, before the bed load they observed that some particles were lifted up and they commented simply “the apparent upward motion of some particles was likely caused by some intergranular reaction force”. Furthermore, vertical pressure gradient effects are also known to be important for bed destabilization (Liu et al. 2007, Scholtès et al. 2015). In waves, the vertical pressure gradient is mostly associated with variations in water depth. However, how the uplift force caused by the vertical pressure gradient modifies sediment transport still needs to be investigated (Berni et al. 2017). The non-hydrostatic pressure induced by the breaking bore in the free water surface can generate some upward force, for which Francalanci et al. (2008) introduced a parameter of “apparent density of the fluid” to modify the Shields

number. Similarly, Lamb et al. (2017) infer that non-hydrostatic pressure can affect the buoyancy force direction and magnitude. However, there is no direct force measurement in the literature to verify these assumptions.

To understand the actual phenomena of incipient motion during the tidal bore, more in situ comprehensive study is required which simultaneously measures free water surface, velocities and both horizontal and vertical forces, and which also uses visualization. This was not conducted to date. In order to understand how surface bores affect sediment transport on the bed, this study designed a delicate experiment to simulate the tidal bore, so that the instantaneous phenomena of sediment incipient motion and hydraulic parameters could be correlated. The main aim of this study is to ascertain the capability of the current experimental setup and relative impact of instantaneous horizontal and vertical forces during a tidal bore.

2 EXPERIMENTAL SETUP & INSTRUMENTATION

The incipient motion of sediment beneath a tidal bore was physically investigated in new laboratory experiments conducted in a 10.5 m long, 0.4 m deep and 0.3 m wide with glass sidewalls flume (Figure 1). The laser Doppler anemometer (LDA) was used to measure point instantaneous velocity and turbulence (Figures 2 & 3). In both steady and unsteady flows, removal of communication errors, low signal to noise ratio were done by the BSA processor software. More detail of flume and LDA system can be found in Yang et al. (2020). A fast-fully closing Tainter gate was installed downstream of the channel (at x=10 m) where x is the distance from the channel upstream inlet end. A forc el upstream inlet end (Figure 2a).

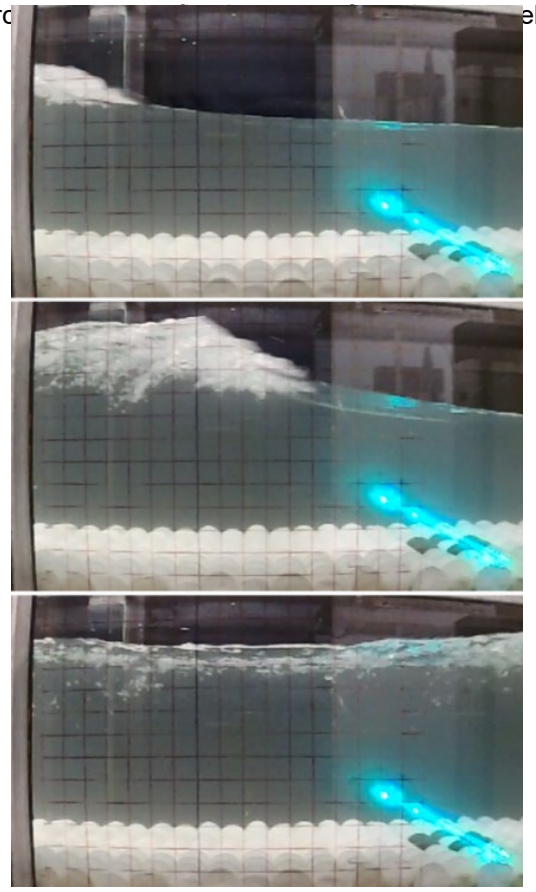

Figure 1. Breaking bore propagating upstream from left to right, with t=t_i, t_i + 0.20s, t_i + 0.60s between each photograph from top to bottom (h_0 = 0.135 m, Q = 0.03 m^3/s, Fr = 1.45, 60 fps photographs).

A contrived bed was made to compensate for the height of the force sensor by introducing river pebbles over the flume bed (see Figure. 2b). Spheres of 38 mm diameter were fixed by glue into a Perspex sheet in a hexagonal-shaped structure over a 10 m length of the flume. One layer of fixed spheres comprised most of the bed. In the test section a target ball of 36.6 mm diameter was surrounded by a group of 3D printed green balls filled with small steel spheres which were not glued (Figure 1), in order to allow them to stay in place due to their own weight. Such a bed configuration had previously been used by Dwivedi et al. (2010) in steady flows to study the hydrodynamic forces during sediment entrainment in a bed of comparable roughness to that used in the present experiments. Adjacent to the target sphere at downstream side, a mobile bed was placed for 0.5 m length to capture the movement of movable particles, covered by the river pebbles, which were sieved between 3 mm to 5 mm used for mobile bed configuration. The flow of the flume was generated using a pump

of maximum 50 L/s capacity connected to the head tank. To monitor the flow rates in the channel, an electromagnetic flow meter (F-2000 from Blue White Industries Ltd) was fixed to the plumbing system. The flow rate through the flume was controlled by the variable frequency driven pump. In steady flows, the water depths were measured using rail mounted pointer gauges. The unsteady water depth were recorded non-intrusively using a series of Ultrasonic displacement meters (UDM) (Microsonic™ Mic+25/IU/TC). The ultrasonic displacement meters were calibrated in steady flow using the pointer gauges.

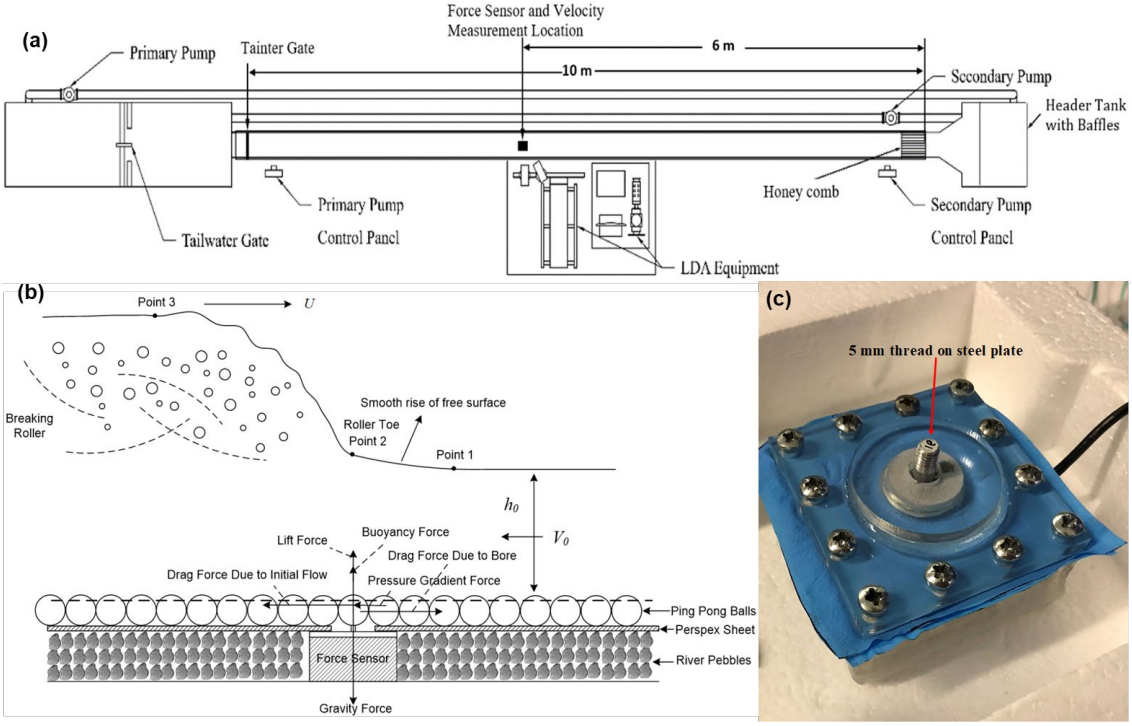

Figure 2. (a) Schematic diagram of the laboratory flume. (b) Breaking bore propagation and major forces. (c) Force sensor water proofing box with supporting rod (not to scale).

The three axis force sensor (a BesTech force sensor specially built and calibrated for this study) was used to measure the load imposed on metal foil strain gauges. The strain gauge signals were connected to the external amplifier (specially made for the strain gauge base force sensor and calibrated for the force sensor used in current study) and signal conditioning equipment through the sensor cable. In the external electronic system, the sensor signals were amplified and combined to produce signals representing the forces.

A box with a 7 mm diameter hole at its center (Figure 2c) was made from Perspex sheet to cover the sensor body, in order, to waterproof the force sensor. A space of 2 mm all round was kept between the sensor body and the Perspex box. The remaining hole clearance in the center of the box was 1 mm after the 6 mm supporting rod was fixed on the flat steel plate. A small amount of white petroleum jelly (Shell Snow) was applied in the gap, sealing the gap perfectly and allowing flexibility for small movement of the threaded rod. The target sphere attached to the supporting rod was arranged in such a way as to prevent it from touching the surrounding particles. According to this setup, the force sensor recorded the hydrodynamic forces on the sphere due only to water flow. Since the force sensor measures lift and drag plus any effects from the tidal bore water surface, any non-hydrostatic effects in buoyancy force are considered part of the lift and drag forces.

The static calibration of the waterproofed force sensor was done by first recording the output of known hanging weights in both horizontal and vertical directions in air. Then force sensor was fixed into the flume bed and the calibration was verified by pushing the targeted test particle with carefully calibrated springs into the water-filled flume. Figure 3 shows that the applied static force is directly proportional to the output voltages of the force sensor. The voltage output data were multiplied by the calibration matrix provided by the manufacturer to obtain the corresponding forces. The sensitivity of the force sensor is 0.98 mN in both x and z directions (where x is the positive downstream coordinate and z is the positive upward, normal coordinate to the flume bed). The crosstalk from x to z and z to x is <0.5 % and <1% of full scale respectively. Two separate processors (computers) were used to record LDA data, and forces sensor and UDM data to avoid any data loss. It was essential to synchronize all recordings. An analog pulse signal was sent from the LDA system to the National Instrument, to start the force sensor and UDM for obtaining the data. The camera was physically synchronized with the LDA by introducing a green light in front of the camera frame. All instruments were synchronized to within ±0.5 ms.

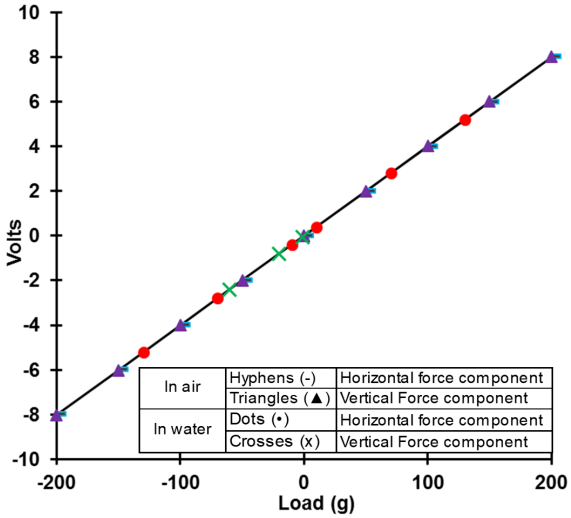

Figure 3. Response of installed force sensor calibration curves.

For all observations, the initial flow conditions were Q = 0.033 m^3/s, h_0 = 0.135 m and V_0 = 0.815 m/s where h_0 and V_0 are the flow depth and depth averaged velocity measured at x = 6m. No sediment motion was observed in the initially steady flow. The simultaneous measurements of velocities and forces were conducted at x = 6 m, and free water surface was measured at x = 6 and 6.5m. Videos were recorded between x = 6 and 7 m with a handy camera Zoom™ (60 fps) for a tidal bore, for which the bore celerity was U ≈ 0.85 m/s, corresponding to a Froude number = 1.35 to 1.45.

3 RESULTS

3.1 General observations

In all experimental series the instantaneous free-surface, velocity and force records were repeated twenty five times, and the data were synchronized in terms of the time. Usually ensemble average (EA) and variable interval time average (VITA) techniques were used to analyse the data in unsteady flows. Practically, the ensemble average (EA) technique is more suitable for repeated experiments because it requires less processing. Noticeably, the ensemble average and median ensemble average have slightly changed trends (see Figure 4) so the median EA technique was used in this study.

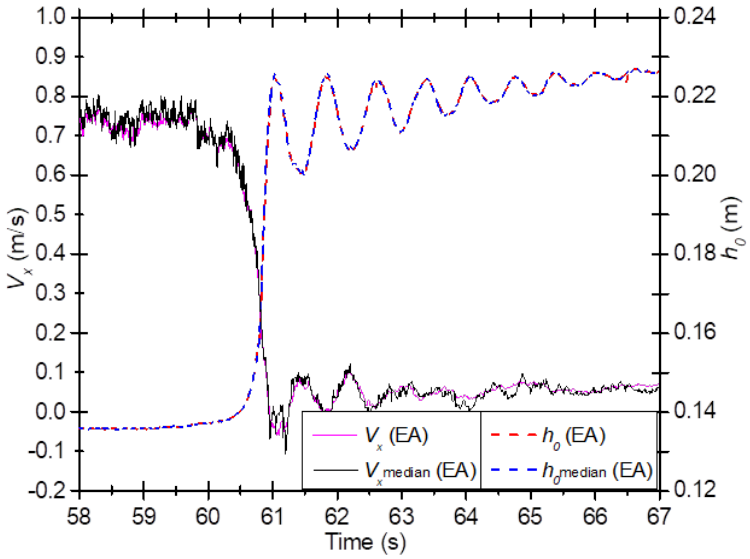

Figure 4. Ensemble Average and median EA (Run 1-25) water depth and horizontal velocity component of breaking bore at x=6 m, LDV sampling volume elevation: z/h_0=0.16

From the video recordings, it was observed that no gravel particle motion had occurred before the bore passage. Before the arrival of the roller toe, few particles moved and a large number of particles were set in motion and moved upstream behind the bore, similar to the results of Khezri and Chanson's (2015) experiments during the passage of a breaking bore. There was negligible sediment suspension close to the bed while the majority of particle motion was by sliding and rolling. A significant number of pebbles were set into motion by

the bore passage in the form of sheet flow. The experimental observation revealed that the incipient motion of a pebble was symptomatic predominantly, but not always, with the roller toe (Point 2, Figure 2b). In addition, dislodgement of a few particles occurred due to a rise in free surface as a result of deceleration in flow. According to visual observation, for a short duration a sheet flow motion occurred due to the passage of the breaking bore in upstream direction.

To verify the newly developed experimental setup of current study, measured drag force was compared with previously estimated drag force of Khezri and Chanson (2015). Figure 5 show the measured and estimated instantaneous drag force subjected to breaking bore. The measured data indicated the rapid increased in drag force along the breaking bore in upstream direction. The maximum measured drag force was found after $(T-T_t)(g/h_0)^{1/2} = 3$ whereas, estimated maximum drag force was found at $(T-T_t)(g/h_0)^{1/2} = 2.5$. However, very similar trend was observed between present study measured, and Khezri and Chanson's estimated drag force.

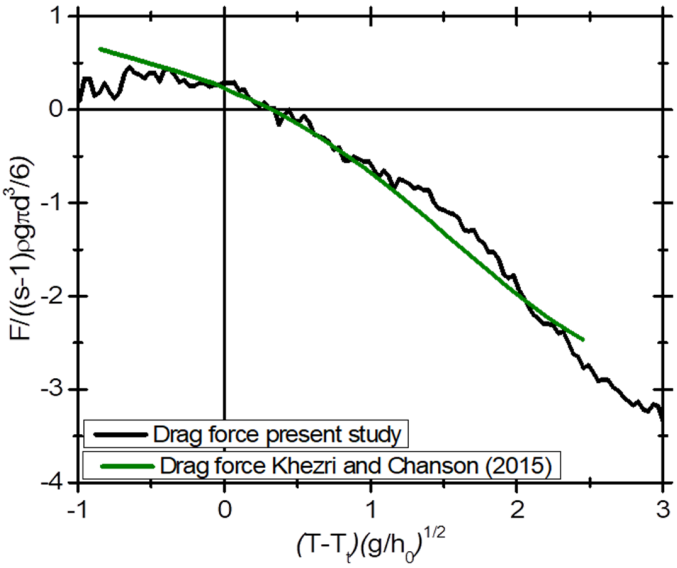

Figure 5. Comparison between measured (present study) and estimated drag force (Khezri & Chanson 2015) beneath breaking bore, where T_t=roller toe passage absolute time and d is target sphere diameter.

3.2 Instantaneous forces and velocities acting on target particle

The instantaneous velocity and force components were sampled at x = 6m over the fixed bed configuration above the target particle. The strong longitudinal deceleration and the negative vertical velocities were linked with the propagation of the bore roller for a short period, as reported by Reungoat et al. (2018). A transient recirculation was highlighted by the longitudinal velocity data as illustrated in Figure 6a beneath the breaking bore for $530<T(g/h_0)^{1/2}<550$ where T is time in seconds, and it is believed to be a characteristic feature of breaking bores. Figure 6a shows time-variations of the free water surface depth h and longitudinal velocity component V_x, where V_x is positive along the initial flow towards downstream and vertical velocity component V_z, where V_z is positive upward normal to the bed.

Both drag and lift forces acted on the particle in the negative direction due to flow reversal through transient recirculation and the sudden increase in free water surface at the arrival of the breaking bore. Almost all the particles stopped once the maximum lift force was reached 0.4 s after the roller toe, however during that time drag force tended to increase towards positive (point 3, see Figure 6b). At that moment lift force was negative (towards bed) with three times more in magnitude as compared to the drag force. All particle movement suddenly stopped due to former force effect. The same trend was observed via visual observation. Furthermore, the maximum lift force was observed beneath the peak of the first wave crest.

The forces acting on the target particle were median ensemble-averaged over 25 test runs to find the main trend, which is shown in Figure 6. The findings suggests that the lift force before and at the roller toe has an important role in incipient motion of pebbles. Furthermore, experimental data implies that the upstream advection of pebbles was due to the predominance of drag force. With the drag force, longitudinal pressure gradient force due to sudden change in free water surface and lift force before and at the roller toe are responsible for the onset of motion.

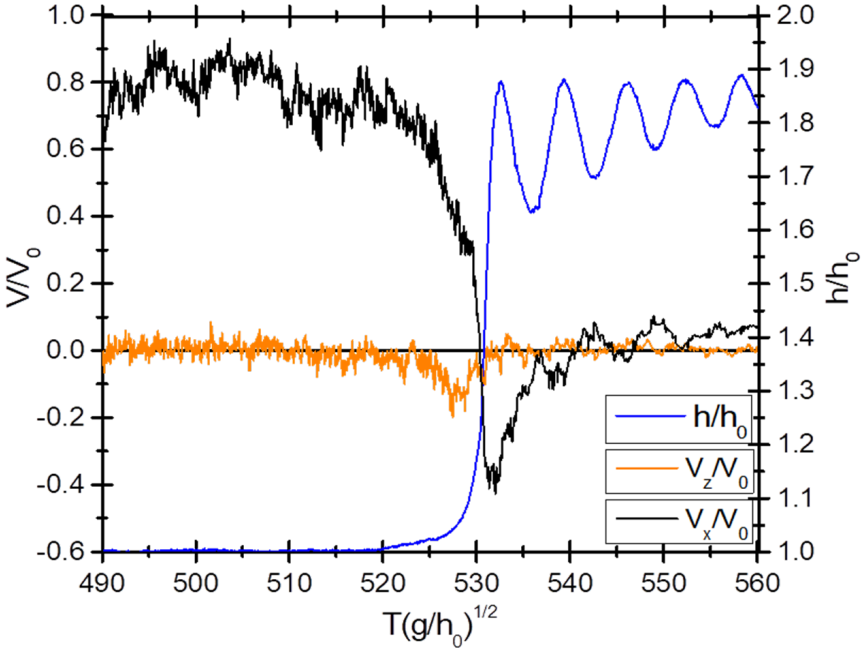

(a) Instantaneous measured velocity components with water depth

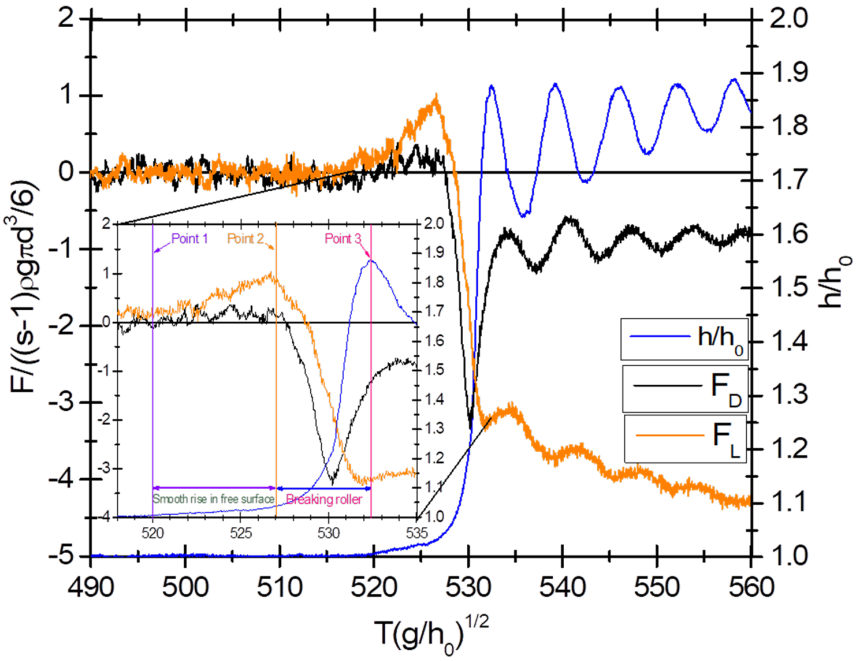

(b) Instantaneous measured force components with water depth

Figure 6. Dimensionless Median EA water depth, horizontal velocity and vertical velocity components, drag force and lift force components beneath breaking bore at x=6 m, z/h_0=0.037, Fr= 1.45.

4 DISCUSSION

Overall, the present measurements demonstrate some key findings. The lift force increased upward on the arrival of the bore and then decreased and was directed into the bed followed by an increase in drag force along the bore direction with the abrupt decrease in velocity. During the transient recirculation, the local flow reversal induced a drag force acting on the particle in the upstream direction along the bore. The lift force (≈ 85% of submerged weight) was the predominant force during the inception stages of particle motion along with the longitudinal pressure gradient force caused by the sudden change in free surface profile. Behind the bore, the increasing trend of drag force (i.e., along the bore, upstream) had a significant role in maintaining pebble motion and determining its extent. Yet the increasing trend of upward drag force did not last long and the pebble motion ended after some time while, the negative lift force was twice the drag force. To our knowledge, no study has reported simultaneous direct measurement of fluctuating force in combination with instantaneous velocities and water depth during the passage of rolling tidal bores. The directly measured drag force findings were consistent with Khezri and Chanson's (2015) estimated drag force data. Figure 7 shows a comparison between Khezri and Chanson's (2015) estimated forces with directly measured forces of the present study. During the passage of

the breaking bore, the results of estimated lift to relative weight forces was less than 0.05 as reported by Khezri and Chanson (2015) while, the physically measured lift force fluctuated from 0.25 to -3.4 between $+6<(T-T_t)(g/h_0)^{1/2}<-6$ where T_t is roller toe passage absolute time (see Figure 7). Between $+2<(T-T_t)(g/h_0)^{1/2}< 0$ the measured lift to weight force ratio was above 0.7 which cannot be ignored. Moreover, Khezri and Chanson (2015) concluded that longitudinal pressure force was the main driving force during the breaking bore which was insufficient before roller toe for suspension of particles (Figure 7).

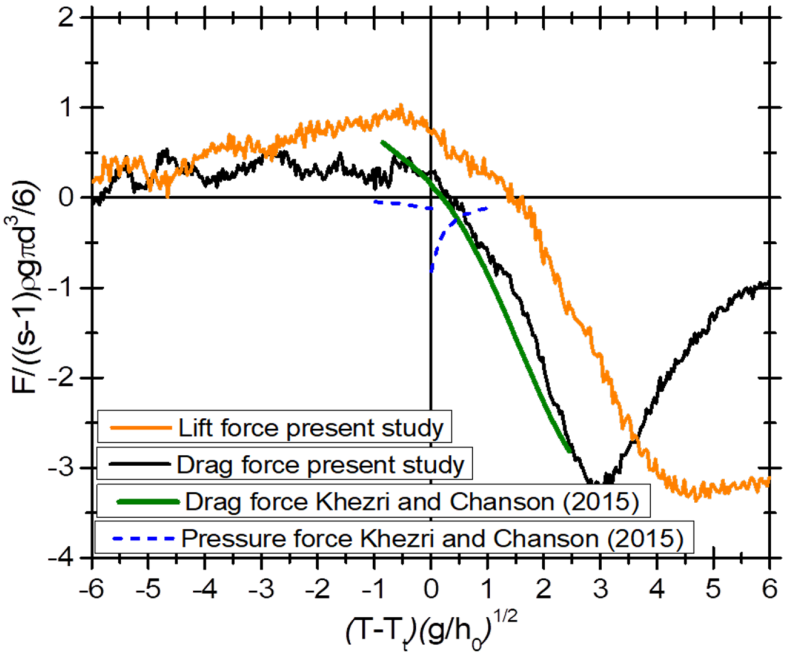

Figure 7. Comparison of dimensionless forces beneath breaking bore between measured for Fr=1.45 (present study) and estimated forces for Fr=1.4 (Khezri & Chanson 2015).

On the other hand, during the swelling of the free water surface, the predominance in lift force may cause suspension of sand and silt which is consistent with the field observation of Fan et al. (2012), Fang et al. (2018), and Pan and Huang (2010). Furthermore, a vast amount of sediment was deposited rapidly after the tidal bore passage (Fan et al. 2012). The field observation data of Reungoat et al. (2018) indicated that the maximum instantaneous shear stress was 150 Pa and maximum instantaneous tangential stress magnitudes were up to 100 Pa in the Garonne and Selune River tidal bores.

The study shows the role of hydrodynamic forces in eroding a river bed and causing upstream sediment motion due to tidal bores. The fluctuating forces, velocities and onset of sediment motion provide quantitative data from the present measurements that help explain some of the massive channel incision events reported in the literature.

5 CONCLUSIONS

A physical investigation was conducted into the phenomenon of incipient sediment motion. A laser Doppler anemometer (LDA), force sensor, ultrasonic Doppler meter and video recorder beneath the tidal bore were synchronize to monitor the flow field, force and particle's reaction. In initial steady flow, no discernible pebble motion occurred. During the experiments, the upward/downward velocities, the variation of free surface, horizontal/vertical forces were closely measured and the instantaneous sediment responses were recorded. Therefore, the cause-effect of sediment transport and the most important parameters can be established.

Beneath the breaking bore, transient sheet flow motion was seen and the inception of pebble motion was closely associated with the passage of a marked roller supplemented with onset of motion of pebbles with the rise in free surface. Generally, results showed that during the smooth rise of free-surface in a tidal breaking bore, the increase in forces indicates the importance of lift force which is necessary for particle movement and increases particle movement during the passage of the roller toe. For the most part, drag force was the main influencing force prompting the inception of upstream particle motion. During a tidal breaking bore, the forces that cause incipient motion are not only due to velocity but also to a sudden discontinuity in the free surface. The entire sheet flow motion was brief. The present data provided some quantitative data in terms of drag and lift force acting on sediment particles beneath a tidal bore.

ACKNOWLEDGEMENTS

The authors acknowledge the technical assistance of Gavin Bishop, Travis Marshall and Jordan Wallace. Furthermore, Peter Ihnat's assistance in LabView programming for data collection and synchronization is highly appreciated and the financial support provided by the Higher Education Commission (HEC) of Pakistan and the University of Wollongong, Australia.

REFERENCES

Bagnold R (1963): Mechanics of marine sedimentation. The sea 3, 507-528

Berni C, Michallet H, Barthélemy E (2017): Effects of horizontal pressure gradients on bed destabilization under waves. Journal of Fluid Mechanics 812, 721-751

Bonneton P, Bonneton N, Parisot JP, Castelle B (2015): Tidal bore dynamics in funnel-shaped estuaries. Journal of Geophysical Research: Oceans 120, 923-941

Dwivedi A, Melville BW, Shamseldin AY, Guha TK (2010): Drag force on a sediment particle from point velocity measurements: A spectral approach. Water Resources Research 46

Fan D, Cai G, Shang S, Wu Y, Zhang Y, Gao L (2012): Sedimentation processes and sedimentary characteristics of tidal bores along the north bank of the Qiantang Estuary. Chinese Science Bulletin 57, 1578-1589

Fang H, Han X, He G, Dey S (2018): Influence of permeable beds on hydraulically macro-rough flow. Journal of Fluid Mechanics 847, 552-590

Foster D, Bowen A, Holman RA, Natoo P (2006): Field evidence of pressure gradient induced incipient motion. Journal of Geophysical Research: Oceans 111

Francalanci S, Parker G, Solari L (2008): Effect of seepage-induced nonhydrostatic pressure distribution on bed-load transport and bed morphodynamics. Journal of Hydraulic Engineering 134, 378-389

Frank D, Foster D, Sou IM, Calantoni J (2015): Incipient motion of surf zone sediments. Journal of Geophysical Research: Oceans 120, 5710-5734

Khezri N, Chanson H (2015): Turbulent velocity, sediment motion and particle trajectories under breaking tidal bores: simultaneous physical measurements. Environmental Fluid Mechanics 15, 633-650

Lamb MP, Brun F, Fuller BM (2017): Direct measurements of lift and drag on shallowly submerged cobbles in steep streams: Implications for flow resistance and sediment transport. Water Resources Research 53, 7607-7629

Liu PL, Park YS, Lara JL (2007): Long-wave-induced flows in an unsaturated permeable seabed. Journal of Fluid Mechanics 586, 323

Madsen OS (1975): Stability of a sand bed under breaking waves, Coastal Engineering 1974, pp. 776-794 Pan C, Huang W (2010): Numerical modeling of suspended sediment transport affected by tidal bore in Qiantang Estuary. Journal of Coastal Research 26, 1123-1132

Reungoat D, Lubin P, Leng X, Chanson H (2018): Tidal bore hydrodynamics and sediment processes: 2010–2016 field observations in France. Coastal Engineering Journal 60, 484-498

Scholtès L, Chareyre B, Michallet H, Catalano E, Marzougui D (2015): Modeling wave-induced pore pressure and effective stress in a granular seabed. Continuum Mechanics and Thermodynamics 27, 305-323

Van Rijn LC (1993): Principles of sediment transport in rivers, estuaries and coastal seas, 1006. Aqua publications Amsterdam

Yang S-Q, Riaz MZB, Sivakumar M, Enever K, Miguntanna NS (2020): Three-Dimensional Velocity Distribution in Straight Smooth Channels Modeled by Modified Log-Law. Journal of Fluids Engineering 142

8th International Conference on the Application of Physical Modelling in Coastal and Port Engineering and Science
Dec. 9th - 12th, 2020, Zhoushan, China

TWO-LAYERED LIQUID SLOSHING IN A RECTANGULAR TANK UNDER VERTICAL EXCITATION

DONGMING LIU[1], PENGZHI LIN[2], DONGYI YAN[3] & JIJIAN LIAN[4]

[1,3,4] State Key Laboratory of Hydraulic Engineering Simulation and Safety, Tianjin University, Tianjin 300072, China
[1,2] State Key Laboratory of Hydraulics and Mountain River Engineering, Sichuan University, Chengdu 610065, China
[4] School of Water Conservancy and Hydropower, Hebei University of Engineering, Handan 056038, China
hpeliudm@tju.edu.cn; cvelinpz@scu.edu.cn; 1018205067@tju.edu.cn; jjlian@tju.edu.cn

ABSTRACT

An in-house numerical model called NEWTANK, which solves filtered NSEs on a non-inertial coordinate for external excitations, has been developed to study two-layered parametric sloshing under vertical oscillation. The two-step projection method is adopted in numerical solutions, and the Poisson equation for pressure field is solved by Bi-CGSTAB technique. A multi-layered volume-of-fluid (ML-VOF) method is introduced to track the interface between layered liquids and the free surface at the same time. In order to validate the accuracy of the model, experiment of layered parametric sloshing has been conducted to excite the resonance of the upper layer liquid. The simulated results for both layers favorably match those from experiments. The validated model will used to study energy transfer among modes and layers.

Keywords: parametric sloshing; Faraday waves; two-layered sloshing; Rayleigh-Taylor instability; resonance.

1 INTRODUCTION

In recent years, a growing number of Floating Production Storage and Offloading (FPSO) systems and ocean-going vessels have been produced and utilized to exploit offshore oil and natural gas, so the study of layered sloshing inside tanks is needed to ensure the safety of containers. For example, the layered liquids can be found in ballast tanks or free water knockout (FWKO) vessel, in which water, oil and emulsion, etc., coexist and form layered liquid system (Molin et al., 2012). Liquid sloshing under vertical external excitation is also called the parametric sloshing, which was first observed and studied in laboratory by Faraday (1831), who discovered that when the frequency of vertical external excitation is twice the natural frequency of the liquid, resonance occurs and the generation of standing waves on the free surface is called Faraday waves. One century later, McLachlan (1947) obtained the stable and unstable region of Mathieu equation by using mathematical analysis and Benjamin and Ursell (1954) found the governing equation of Faraday waves, which is equivalent to Mathieu equation, by using potential flow theory. From then on, many researchers have devoted their efforts to investigate single-layered parametric liquid sloshing by adopting theoretical solution, experiments and numerical models. For example, Jiang et al. (1996, 1998) conducted a series of experiments and also analyzed mild to steep standing waves generated in a rectangular tank undergoing vertical excitations with frequencies of 3.15-3.34 Hz. They showed that increasing the excitation amplitude can lead to breaking waves in three recurrent modes, i.e., sharp crest with breaking, dimpled or flat crest with breaking, and round crest without breaking. Frandsen and Borthwick (2003) and Frandsen (2004) utilized a 2-D σ-coordinate transformation model based on potential flow theory and conducted a series of numerical simulation in a tank which moved both horizontally and vertically. Zhao et al. (2018) adopted boundary element method and test resonant Faraday waves in different instability regions. However, in order to solve viscous liquid sloshing with rotational motion, one should approach Navier-Stokes equation, instead of Laplace equation. Murakami and Chikano (2001) examined standing surface waves on a viscous fluid driven parametrically by a vertical harmonic oscillation based on direct numerical simulations of the 2D Navier-Stokes equation. Sanapala et al. (2018) compared their numerical results of Faraday waves with mode 1 to mode 5 with available experimental data and proposed the optimal design of baffles to control the amplitude of parametric sloshing.

Two-layered Faraday waves with an upper free surface have not been studied until recent five years. Pototsky and Bestehorn (2016) studied the linear stability of a two-layer liquid film under the vertical external excitation. The conditions of in-phase and the anti-phase displacements are determined. In addition, the location of the stability threshold of two-layered liquid film has been acquired numerically. Li et al. (2018a, 2018b) conducted experiment of two coupled Faraday waves in a Hele-Shaw cell under periodic vertical vibration and observed that the upper surface vibrates vertically while the lower one oscillates horizontally with the same

wave height. They also discussed the influence of depth of upper and lower liquids on the standing waves at both surfaces. However, so far there has been no report that has systematically studied various resonant conditions under which different layers respond to external excitations, as well as the energy transfer between different modes and different layers in a two-layered parametric sloshing motion.

In this study, we shall present a numerical model called NEWTANK to study the two-layered parametric liquid sloshing under vertical periodic excitations. The computational domain is constructed in a moving non-inertial frame to simulate the external excitation. A multi-layered VOF (ML-VOF) method is employed to track both free surface and the interface between different liquids simultaneously. For 2-D sloshing problems with multiple layers, the model will be validated by comparing the numerical results with experimental data. The phenomena of upper layer resonance, lower layer resonance, and both layer resonances will be investigated with the validated numerical model. The nonlinear effects on energy transfer between different modes and different layers will be analyzed and discussed.

2 MATHEMATICAL MODEL AND NUMERICAL IMPLEMENTATION

When the parametric sloshing response of layered liquid is considered, the spatially averaged Navier-Stokes equations are employed as the governing equations under the assumption of incompressible fluid. In addition, the coordinate system fixed on the moving tank and the non-inertial reference frame, which follows the tank motion, is adopted. Therefore, the NSEs are modified as:

$$\frac{\partial \bar{u}_i}{\partial x_i} = 0 \qquad [1]$$

$$\frac{\partial \bar{u}_i}{\partial t} + \bar{u}_j \frac{\partial \bar{u}_i}{\partial x_j} = -\frac{1}{\rho}\frac{\partial \bar{p}}{\partial x_i} + \frac{1}{\rho}\frac{\partial (\tau_{ij}+R_{ij})}{\partial x_j} + g_i - \frac{\mathrm{d}w_e}{\mathrm{d}t} \qquad [2]$$

where *i*, *j* = 1, 2, 3 for three dimensional flow, $\bar{u}_i$ is the *i*th component of the spatially averaged velocity, *t* the time, ρ the density ($\rho = \rho_1$ in lower liquid, $\rho = \rho_2$ in upper liquid, $\rho = \rho_a$ in air, see Fig. 1), $\bar{p}$ the filtered pressure, gi the gravitational acceleration, w_e the vertical velocity of external excitation, $\tau_{ij} = 2\rho\nu S_{ij}$ the molecular viscous stress tensor with ν being the kinematic viscosity, and R_{ij} the stress induced by the filtering process for spatial flow variation that is mainly caused by small-scale turbulence. To be more specific, $S_{ij} = \frac{1}{2}\left(\frac{\partial \bar{u}_i}{\partial x_j} + \frac{\partial \bar{u}_j}{\partial x_i}\right)$ is the rate of strain of the filtered flow. The stress R_{ij} can be simulated by Smagorinsky sub-grid scale (SGS) model from the concept of large eddy simulation (LES) (Smagorinsky, 1967), i.e.,

$$R_{ij} = 2\rho\nu_t S_{ij} \qquad [3]$$

where $\nu_t = L_s^2\sqrt{2S_{ij}S_{ij}}$ is the eddy viscosity and L_s is the characteristic length scale, which equals to $C_s(\Delta x\Delta y\Delta z)^{1/3}$ with $C_s = 0.15$ (Lin and Li, 2003). The symbol for space filtering, '¯', will be omitted from herein for simplicity.

The transport equation of density can be expressed as,

$$\frac{\partial \rho}{\partial t} + u_i \frac{\partial \rho}{\partial x_i} = 0 \qquad [4]$$

which implies that the incompressibility of fluid is imposed in the entire multiphase flow field.

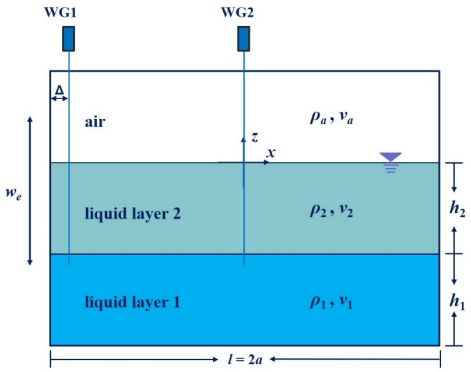

Figure 1. The sketch of two-layered sloshing system in a rectangular tank partially filled with two layers of liquids and one layer of air, and the positions of two wave gauges.

In order to track both free surface and the interface between two liquids simultaneously, a multi-layered volume-of-fluid (ML-VOF) method proposed by Liu et al. (2020) is employed and will be briefly summarized here. Two sets of VOF function F_1 and F_2 are defined as volumetric fraction of lower liquid and upper liquid, respectively, so the volumetric fraction of air can be expressed as $(1 - F_1 - F_2)$. Therefore, $F_1 = 1$ in lower liquid and $F_1 = 0$ in upper liquid and air; similarly, $F_2 = 1$ in upper liquid and $F_2 = 0$ in lower liquid and air (Fig. 1). If substituting the definition of F_1 and F_2 into Eq. [4], we can obtain the transport equations of F_1 and F_2.

$$\frac{\partial F_1}{\partial t} + u_i \frac{\partial F_1}{\partial x_i} = 0 \quad [5]$$

$$\frac{\partial F_2}{\partial t} + u_i \frac{\partial F_2}{\partial x_i} = 0 \quad [6]$$

Therefore, the average density and kinematic viscosity of fluid in each grid can be updated as

$$\rho = F_1\rho_1 + F_2\rho_2 + (1 - F_1 - F_2)\rho_a \quad [7]$$

$$\nu = F_1\nu_1 + F_2\nu_2 + (1 - F_1 - F_2)\nu_a \quad [8]$$

For each set of VOF interface tracking method, the normal vector of the interface in each grid is calculated by using Youngs' least square method (Gueyffier, 1999). The detailed numerical treatment for volume flux calculation and the VOF update scheme can be found in Liu (2008).

3 NATURAL FREQUENCIES OF TWO-LAYERED LIQUID SYSTEM

For the natural frequency of two-layered parametric sloshing, each mode of the two-layered system is characterized by two natural frequencies (Veletsos and Shivakumar, 1993), i.e., ω_{m1} and ω_{m2}. It should be noted that the first subscript 'm' of ω refers to the *m*th mode of natural frequency and the second subscript '1' or '2' means whether the natural frequency is related to the first layer (i.e., the lower layer) or to the second layer (i.e., the upper layer). In other words, the existence of two natural frequencies for each mode arises from the presence of two moving surfaces; the one with larger value ω_{m2} (hence sometimes denoted as ω_{m+}) is related to the movement of free surface, while the one with smaller value ω_{m1} (hence sometimes denoted as ω_{m-}) is related to the movement of interface between two liquid layers. Actually, if there are *n* interfaces/free surface, there should exist *n* natural frequencies for each mode.

The two natural frequencies for each mode of two-layered liquid system can be expressed as

$$\omega_{m1} = \frac{-B_m - \sqrt{B_m^2 - 4A_mC_m}}{2A_m} \quad [9]$$

$$\omega_{m2} = \frac{-B_m + \sqrt{B_m^2 - 4A_mC_m}}{2A_m} \quad [10]$$

in which $A_m = 1 + \rho_{21}\tanh\lambda_m\frac{h_1}{a}\tanh\lambda_m\frac{h_2}{a}$, $B_m = -\tanh\lambda_m\frac{h_1}{a} - \tanh\lambda_m\frac{h_2}{a}$, and $C_m = (1 - \rho_{21})\tanh\lambda_m\frac{h_1}{a}\tanh\lambda_m\frac{h_2}{a}$, where $\rho_{21} = \frac{\rho_2}{\rho_1}$, $\lambda_m = (2m-1)\frac{\pi}{2}$, and *a* is half length of the tank.

From the analysis of Benjamin and Ursell (1954), when the frequency of vertical external excitation is equal to the natural frequency, twice the natural frequency, or two-thirds of the natural frequency, etc., and the amplitude of excitation is large enough, instability of free surface will develop for single-layered parametric sloshing. Therefore, it is naturally assumed that for two-layered liquid system, instability or resonant response may also occur under similar conditions.

4 EXPERIMENTAL SETUP

In order to validate the performance of our numerical model, a series of experiments were conducted by utilizing the dynamic triaxial apparatus in State Key Laboratory of Hydraulic Engineering Simulation and Safety in Tianjin University, China. A rigid liquid tank, which is 0.25 m in length, 0.10 m in width and 0.45 m in height, is hanged up on the triaxial apparatus (Fig. 2). The vertical movement of the tank can be precisely controlled by the motor in triaxial apparatus. The chosen lower liquid is fresh water with density of 998.0 kg/m3 and the upper one is diesel oil with density of 826.0 kg/m3, so the density ratio ρ_{21} = 0.8277. The diesel oil was dyed with dark green color and the movement of free surface and the interface between oil and water was video-recorded. Standard image processing is used to track the movement of free surface and interface simultaneously. In the experiment, a CCD camera with 60 Hz and a spatial resolution of 1920×1080 pixels were used to record the sloshing process. However, it is unavoidable that the tank in the frame is visually tilted due to the squint of the camera view. Therefore, four control points are fixed on front side of the tank and are used to rectify the errors.

In the experiment, the depth of both layers $h_1 = h_2 = 0.05$ m. Therefore, the first and second natural frequencies related to the upper layer $\omega_{12} = 10.1480\ s^{-1}$, $\omega_{22} = 15.5817\ s^{-1}$. Two numerical wave gauges near the left boundary of tank (Δ = 0.01 m) and at the center of the tank (Fig. 1) were selected to compare the displacement of free surface and the interface between water and diesel oil with the results from the experiments. The vertical velocity of the tank movement follows the sinusoidal function, i.e., $w_e = -b\omega_e\cos\omega_e t$, in which b and ω_e are the amplitude and frequency of the external excitation, respectively.

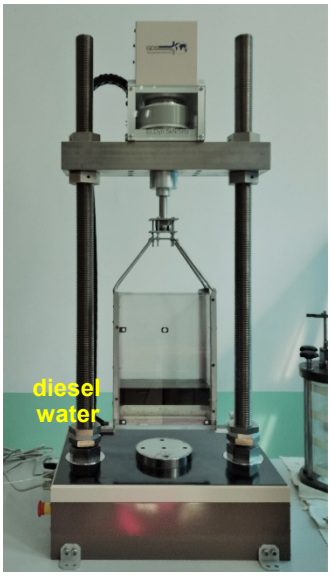

Figure 2 Experimental apparatus of two-layered liquid sloshing under vertical external excitation with upper layer diesel dyed dark green.

5 RESONANCE OF 2-D LAYERED PARAMETRIC SLOSHING

In the experiment, the frequency of external excitation is set to be twice the first mode natural frequency related to the upper layer, i.e., $\omega_e = 2\omega_{12} = 20.2960\ s^{-1}$, so it is expected that the first mode resonant response of upper layer will occur. The amplitude of external excitation b = 0.003 m. In the computation, the length of the computational domain is 0.25 m, and the height of the domain is 0.225 m. The employed mesh system has 200 uniform horizontal and 180 uniform vertical grids with mesh size $\Delta x = \Delta z$ = 0.00125 m. The simulation runs up to t = 45 s and the time step is automatically adjusted to ensure the stability of the numerical model. Special attention should be paid to the initial condition of surfaces in simulation. If no perturbation is preset on the profiles of surfaces, the displacement of free surface and interface in the calculation will be zero forever during parametric sloshing and only pressure distribution will be altered under vertical external excitation. Therefore, in order to predict the resonant response of the surfaces, the initial slope of free surface and interface is set to be a small value, which is equal to -1.0×1.0^{-5} instead of 0, so the disturbance includes all the modes of the layered liquid system, which will not affect the final results significantly as long as the initial slope is kept very small.

The comparisons of the snapshots of free surface and interface profiles from experiment and numerical simulation at t = 20.00, 35.22, 40.18, 42.00, 42.38 and 44.55 s are shown in Fig. 3, in which we can observe that the elevation of surfaces becomes increasingly larger and obvious resonance occurs during the parametric sloshing. In addition, the results of both free surface and interface profiles from numerical simulation (right column) favorably match those from experiment (left column), indicating that the hydrodynamic characteristics of layered sloshing can be well reproduced and predicted by NEWTANK. The numerical results of free surface and interface displacement at the position of WG1 (Fig. 1) are also compared with the experimental data. It can be seen from Fig. 4(A) and 4(B) that fairly good agreements are obtained for both free surface and interface between the numerical results and experimental data. From Fig. 4(A) and 4(B) we can also observe that before 25 s, the responses of both free surface and interface are very small. However, after 25 s, resonant response gradually develops and the free surface displacement is as large as 0.1 m at t = 42.5 m. It should also be noted that the wave crest becomes sharper and the trough becomes flatter after t = 35 s, indicating that nonlinearity begins to take effects. Furthermore, after t = 42.5 s, the effect of nonlinearity restricts the wave amplitude to become infinity along with time. Instead, the response begins to become smaller. Nonlinearity can be further confirmed from the spectral analysis using fast Fourier transform (FFT) method in Fig. 4(a) and 4(b). We can see that the dominant frequency of the energy density is 10.15 s^{-1}, which is equal to the first mode of natural frequency related to free surface ω_{12}. The second peaks, which are probably excited by nonlinearity (La Rocca et al., 2002), are equal to $2\omega_{12}$.

In order to investigate the energy transfer mechanism among different modes, wavelet transform (WT) technique is employed to study the change of energy density along with time. As can be seen from Fig. 5(A) and 5(B), we can also observe two main bands which correspond to ω_{12} and $2\omega_{12}$ in time-frequency domain. Five energy density spectra at specific time t = 25, 30, 35, 40, 42.5 s are also drawn in Fig. 5(a) and 5(b). It can be seen from these figures that after t = 25 s, energy transferred from external excitation becomes obvious and the dominant frequency corresponding to ω_{12} can be observed in the energy density spectrum. In addition, it can be seen from Fig. 5(a) and 5(b) that the energy density becomes larger along with time. Furthermore, after

t = 35 s, the second peak corresponding to $2\omega_{12}$ is excited, which means that some of the energy absorbed from external excitation has been transferred to this frequency because of nonlinearity. From WT analysis in Fig. 5(A) and 5(B), we can confirm that the second peak in FFT analysis, which is equal to ω_e and $2\omega_{12}$, is excited not directly by external excitation, but by nonlinearity developed during sloshing since this second peak does not appear until the nonlinearity becomes distinct.

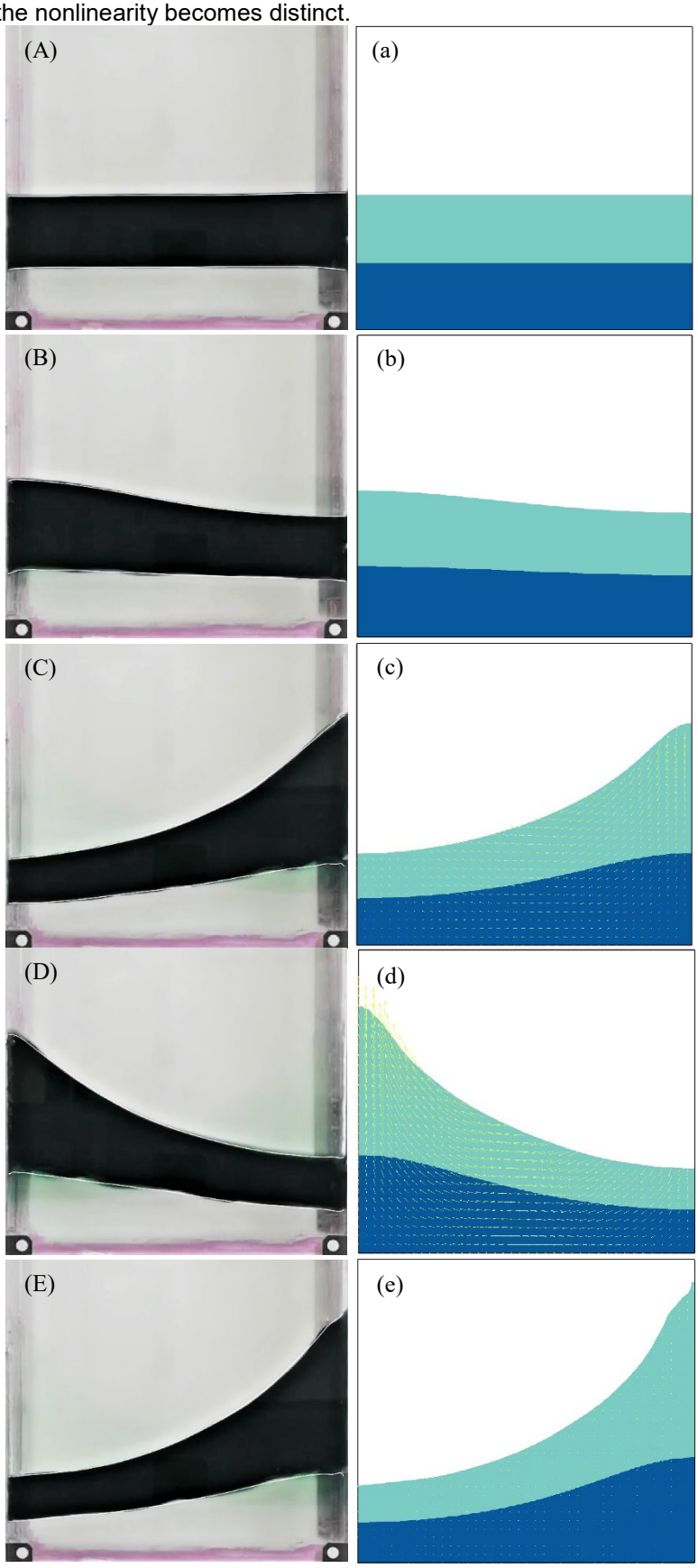

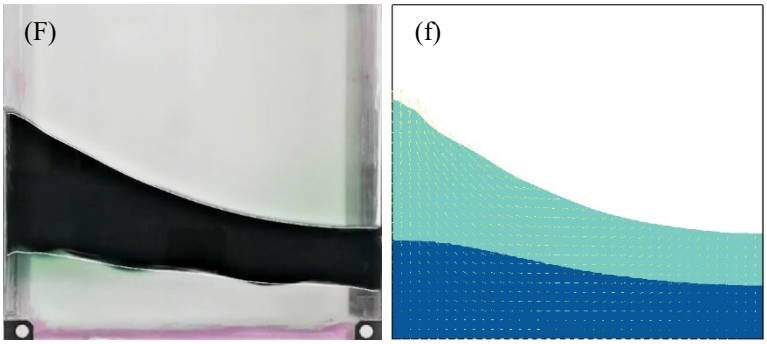

Figure 3. Comparisons of snap shots of free surface and interface during parametric sloshing with external excitation b = 0.003 m and $\omega_e = 2.0\omega_{12}$ at t = 20.00, 35.22, 40.18, 42.00, 42.38 and 44.55 s between experimental results (A-F) and present numerical results (a-f).

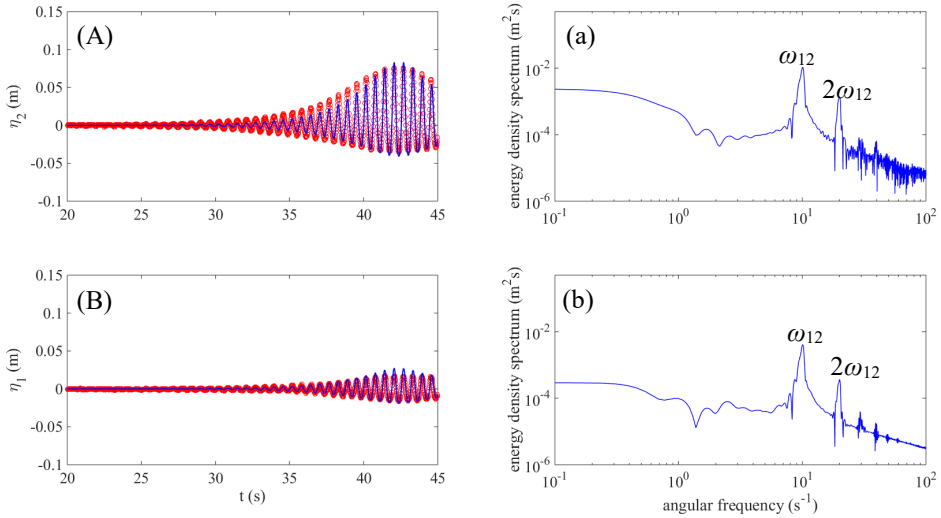

Figure 4. Left column: comparisons of displacement of (A) free surface and (B) interface at the position of WG1 in a vertically excited tank with b = 0.003 m and $\omega_e = 2.0\omega_{12}$ between the present numerical results (solid line) and the experimental data (circles); right column: the corresponding energy density spectra of numerical results (solid line).

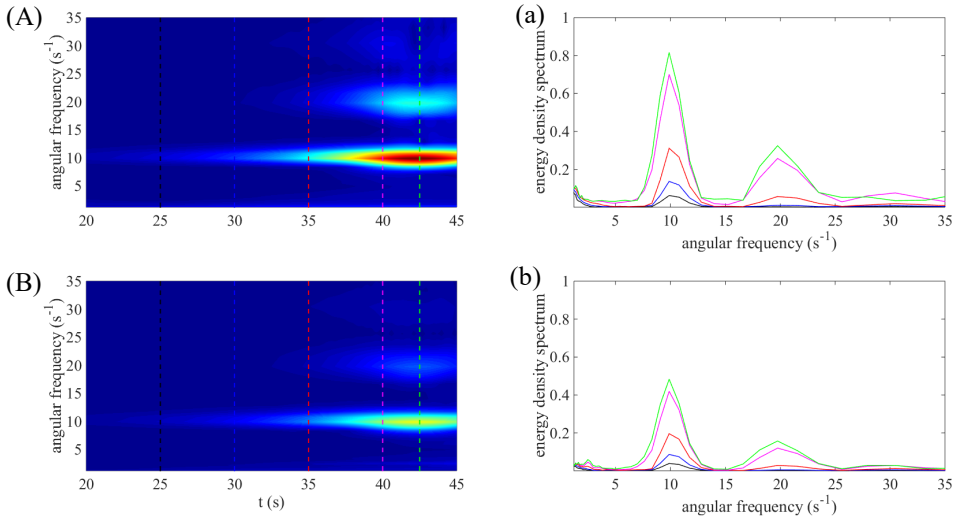

Figure 5. Wavelet transform analysis of time series of (A) free surface elevation and (B) interface elevation when b = 0.003 m and $\omega_e = 2\omega_{12}$ and the energy density spectra obtained from WT at t = 25 (black), 30 (blue), 35 (red), 40 (magenta), 42.5 (green) s.

6 CONCLUSIONS

In this study, a 3-D multiphase fluid flow model NEWTANK has been developed by solving the spatially averaged NSEs. In order to simulate layered parametric sloshing under vertical external excitations, the multi-layered volume-of-fluid (ML-VOF) method has been utilized to track the free surface and interface between different immiscible liquids. The model has been employed to study two-layered parametric liquid sloshing in rectangular tanks and has the capability of simulating nonlinear sloshing processes. Laboratory experiment is also conducted for layered sloshing under the external excitation of heave motion in order to provide the data for model validation.

It has been proved in this paper that for two-layered liquid, when the frequency of vertical external oscillation is equal to twice the natural frequency of the system, resonant response can be excited, a condition similar to single-layered resonant sloshing. Spectral analysis of the corresponding energy density is made by employing fast Fourier transform (FFT) and wavelet transform (WT) technique. Upper layer resonance has been studied. When resonance occurs and the amplitude grows, more peaks corresponding to integral times of external excitation frequency can appear, but such additional frequencies do not emerge from the beginning of parametric sloshing. Only when the nonlinearity becomes obvious enough will the energy start to transfer from lower modes to higher modes.

ACKNOWLEDGEMENTS

The research was supported by the Open Fund of State Key Laboratory of Hydraulics and Mountain River Engineering (SKHL1720).

REFERENCES

Molin, B., Remy, F., Audiffren, C., Marcer, R., Ledoux, A., Helland, S., Mottaghi, M., 2012. Experimental and Numerical Study of Liquid Sloshing in a Rectangular Tank with Three Fluids. The 22nd International Offshore and Polar Engineering Conference, Greece.

M. Faraday, “On a peculiar class of acoustical figures; and on certain forms assumed by groups of particles upon vibrating elastic surfaces,” Philos. Trans. R. Soc. London **121**, 299-340 (1831).

N. W. McLachlan, Theory and application of Mathieu functions. Oxford University, London. 1947

T. B. Benjamin and F. Ursell, “The stability of the plane free surface of a liquid in vertical periodic motion,” Proc. R. Soc. A **225**, 505-515 (1954).

Jiang, L., Ting, C., Perlin, M., Schultz, W.W., Moderate and steep faraday waves: instabilities, modulation and temporal asymmetries. J. Fluid Mech. 329, 275-307 (1996).

Jiang, L., Perlin, M., Schultz, W.W., 1998. Period tripling and energy dissipation of breaking standing waves. J. Fluid Mech. 369, 273-299.

J. B. Frandsen and A. G. L. Borthwick, “Simulation of sloshing motions in fixed and vertically excited containers using a 2-D inviscid σ-transformed finite difference solver,” J. Fluids Structs 18(2), 197-214 (2003).

J. B. Frandsen, “Sloshing motions in excited tanks,” J. Comput. Phys 196(1), 53-87 (2004).

Zhao, D., Hu, Z., Chen, G., Lim, S., Wang, S., 2018. Nonlinear sloshing in rectangular tanks under forced excitation. International Journal of Naval Architecture and Ocean Engineering. 10(5), 545-565.

Murakami, Y., Chikano, M., 2001. Two-dimensional direct numerical simulation of parametrically excited surface waves in viscous fluid. Physics of Fluids. 13(1), 65-74.

Sanapala, V.S., M, R., Velusamy, K., Patnaik, B.S.V., 2018. Numerical simulation of parametric liquid sloshing in a horizontally baffled rectangular container. Journal of Fluids and Structures. 76, 229-250.

X. Li, X. Li, and S. Liao, “Observation of two coupled Faraday waves in a vertically vibrating Hele-Shaw cell with one of them oscillating horizontally,” Phys. Fluids 30, 012108 (2018).

Li, X., Li, J., Liao, S., Chen, C., 2018. Effect of depth on the properties of two coupled faraday waves in a Hele-Shaw cell. Phys. Fluids 30(10), 102103.

D. Liu, P. Lin, M. Xue, L. Cheng, and J. Lian, “Numerical simulation of two-layered liquid sloshing in tanks under horizontal excitations,” Ocean Engineering. (submitted in 2020)

Smagorinsky J., 1963. General circulation experiments with the primitive equations. Monthly Weather Review. 91, 99-164.

Lin, P., Li, C.W., 2003. Wave-Current Interaction with a Vertical Square Cylinder. Ocean Engineering. 30(7), 855-876.

Liu, D., Lin, P., 2008. A Numerical Study of Three-Dimensional Liquid Sloshing in Tanks. Journal of Computational Physics. 227(8), 3921-3939.

Liu, D., 2007. Numerical modeling of three-dimensional water waves and their interaction with structures, Ph.D. thesis, National University of Singapore.

Gueyffier, D., Li, J., Nadim, A., Scardovelli, R., Zaleski, S., 1999. Volume-of-Fluid Interface Tracking with Smoothed Surface Stress Methods for Three-Dimensional Flows. Journal of Computational Physics. 152(2), 423-456.

Veletsos, A.S., Shivakumar, P., 1993. Sloshing Response of Layered Liquids in Rigid Tanks. Earthquake Engineering & Structural Dynamics. 22(9), 801-821.
La Rocca, M., Sciortino, G., Boniforti, M.A., 2002. Interfacial Gravity Waves in a Two-Fluid System. Fluid Dynamics Research. 30(1), 31-63.

Coastlab20
Dec 9-12, Zhoushan, China&Online

8th International Conference on the Application of Physical Modelling in Coastal and Port Engineering and Science
Dec. 9th - 12th, 2020, Zhoushan, China

NUMERICAL SIMULATIONS FOR BODY HYDRODYMATIC RESPONSES WITHIN UNEVEN SEABED CONDITIONS

AICHUN FENG[a,b], KE CHEN[b,c]

[a]School of Naval Architecture, Ocean and Civil Engineering, Shanghai Jiao Tong University, Shanghai 200240, China
[b]State Key laboratory of Ocean Engineering, School of Naval Architecture, Ocean and Civil Engineering, Shanghai Jiao Tong University, Shanghai 200240, China
[c]Shanghai Jiao Tong University Yazhou Bay Institute of Deepsea Technology, Sanya 572000, China

Abstract

Three dimensional Rankine source model is developed to investigate the hydrodynamic responses for oscillatory body within uneven seabed conditions. The free surface, seabed surface and body surface are presented by layer of continuous panels. The accuracy of the numerical solutions are validated by comparison with published data for flat seabed conditions. The influences of ellipsoid shape seabed and sloping seabed are investigated. Numerical simulations demonstrate that various seabed profiles have significant and complicated effects on the body hydrodynamic response characteristics.

Keywords: Rankine source, uneven seabed, hydrodynamic responses

1. Introduction

The wave-structure interaction problem within a potential flow framework, can be solved theoretically by eigenfunction method, or numerically investigated by either a free surface Green function or a Rankine source approach. The free surface Green function model is very limited to investigate various seabed conditions (Wehausen and Laitone, 1960). The Rankine source approach only needs to calculate the integral of Rankine sources and is very flexible to deal with various boundary conditions problems (Feng and Price, 2018).

The importance of finite water depth on the hydrodynamic responses has been demonstrated using different mathematical models (Clauss et al., 2009). The numerical techniques for infinite water depth problem can be directly applied for finite water problems by mirror image technique (Mei et al., 2019). However this method can only deal with flat seabed and is not valid for arbitrary seabed profile. Belibassakis (2005) introduced an extra term called the sloping-bottom mode to modify the incident wave potential to satisfies the sloping seabed condition.

One key numerical technique in the boundary integral method is the evaluation of Rankine source on the surface panel. The analytical expression of Rankine source integral was first derived for arbitrary bodies in unbounded fluid domains by Hess and Smith (1964). By using constant-strength distributions on quadrilateral flat panels, the panel integral can be analytically expressed as a superposition of integral over four parallel strips. Each strip is defined by one side of the quadrilateral panel. The value of corresponding integral depends only on the coordinates of each side and therefore the contribution from each side can be evaluated independently. This method is demonstrated very robust and accurate in hydrodynamic analysis (Cao et al., 1991; Zhou et al., 2014). The source points distribution on the free surface is vital for the accuracy and efficiency of the boundary integral method. Feng et al. (2014, 2019) developed an ever increasing spaces between source points to replace the even space method. This method places a higher density of source points near the floating body and, at distant from the body, a distribution of lesser density. Through this method, the number of source points is reduced and therefore the computational effort is significantly reduced.

In this paper, layer of Rankine source panels is distributed to simulate three dimensional flat, uneven and sloping seabed profiles. The source panel distance ever increasing method is applied to

*Corresponding Author: Aichun Feng; Email, fengaichun@sjtu.edu.cn

arrange the source panel on both the free surface and seabed surface. The accuracy and efficiency of the numerical solutions are validated by comparison with flat seabed cases. The influences of various uneven seabed profiles, and sloping seabed with different slope angles are investigated. Numerical simulations demonstrate that various seabed profiles have significant and complicated effects on the body hydrodynamic characteristics.

2. Boundary Element Formulation

2.1. Fluid motion governing equation and boundary conditions

A coordinate frame of reference OXY Z is defined with origin O at the centre of a three dimensional body floating in a fluid domain. The fluid domain Ω is bounded by a free surface S_f , body surface S_b, seabed surface S_0 and enclosing surface at infinity, S_∞. Figure 1 shows the sketch of a three dimensional wave-body interaction problem in arbitrary seabed condition.

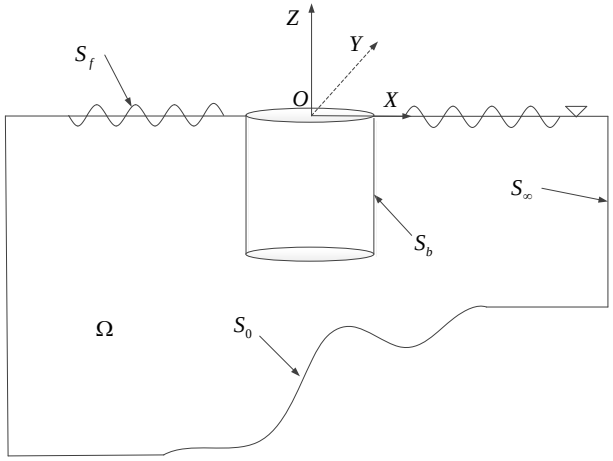

Figure 1: Sketch of a three dimensional wave-body interaction problem in finite water depth condition.

The fluid flow is assumed irrotational and therefore the velocity potential φ satisfies Laplace equa-tion as

$$\frac{\partial^2\phi}{\partial x^2}+\frac{\partial^2\phi}{\partial y^2}+\frac{\partial^2\phi}{\partial z^2}=0 \text{ in } \Omega. \tag{1}$$

The kinematic body boundary condition is given by

$$\frac{\partial\phi}{\partial \mathbf{n}_b}=\mathbf{v}_b\cdot\mathbf{n}_b \text{ on } S_b, \tag{2}$$

where n_b, t and g denote the body surface unit normal vector, time and gravitational acceleration respectively.
The linear kinematic and dynamic free surface boundary conditions are given respectively by

$$\frac{\partial\hat{\eta}}{\partial t}-\frac{\partial\phi}{\partial z}=0 \text{ on } S_f, \tag{3}$$

and

$$\frac{\partial\phi}{\partial t}+g\hat{\eta}=0 \text{ on } S_f, \tag{4}$$

where $\hat{\eta}$ denotes the wave elevation and g is the gravitational acceleration.
The far field boundary condition requires that the disturbance vanishes at infinity such that:

$$\nabla\phi\to 0 \text{ on } S_\infty. \tag{5}$$

It is assumed that no flow penetrates the solid seabed boundary and therefore For the solid seabed boundary condition, non-permeable conditions is applied as

$$\frac{\partial \phi}{\partial \mathbf{n}_0} = 0 \ \text{ on } S_0, \tag{6}$$

where n_0 is the unit normal vector on the seabed surface pointing into the fluid domain.

The velocity potential φ as a boundary integral of Rankine sources distributed on the fluid boundary surface $S = S_b \cup S_f \cup S_0$ can be expressed in the form

$$\phi(\mathbf{x}', t) = \int_{S_b} \sigma^b \frac{1}{|\mathbf{x}' - \mathbf{x}|} ds_{\mathbf{x}} + \int_{S_f} \sigma^f \frac{1}{|\mathbf{x}' - \mathbf{x}|} ds_{\mathbf{x}} + \int_{S_0} \sigma^0 \frac{1}{|\mathbf{x}' - \mathbf{x}|} ds_{\mathbf{x}}. \tag{7}$$

Here we denote control point $x' = (x', y', z')$, source point $x = (x, y, z)$, body source strength $\sigma^b = \sigma(x, t)$, free surface source strength $\sigma^f = \sigma(x, t)$ and seabed source strength $\sigma^0 = \sigma(x, t)$ and variable of integration ds_x.

2.2. Fluid domain surface discretization

In this simulation, the fluid domain surface S is discretized by Rankine source panels rather than isolated Rankine source points. These source panels are located exactly on the fluid domain surface S. Let the integral surfaces S_b, S_f and S_0 be approximated as sums of panels N_b, N_f and N_0 respectively

such as $S_b = \cup_{i=1}^{N_b} S_i^b$, $S_f = \cup_{j=1}^{N_f}$. S_j^f and $S_0 = \cup_{k=1}^{N_0} S_k^0$

Therefore, the discretization of equation (7) is given by

$$\phi(\mathbf{x}', t) = \sum_{i=1}^{N^b} \sigma_i^b \int_{S_i^b} \frac{1}{|\mathbf{x}' - \mathbf{x}_i|} ds_{\mathbf{x}} + \sum_{j=1}^{N^f} \sigma_j^f \int_{S_j^f} \frac{1}{|\mathbf{x}' - \mathbf{x}_j|} ds_{\mathbf{x}} + \sum_{k=1}^{N^0} \sigma_k^f \int_{S_k^0} \frac{1}{|\mathbf{x}' - \mathbf{x}_k|} ds_{\mathbf{x}}. \tag{8}$$

Let $\mathbf{x}_i^b, \mathbf{x}'^b_i \in S_b$, $\mathbf{x}^f, \mathbf{x}'^f_j \notin S_f$ and $\mathbf{x}_k^0, \mathbf{x}'^0_k \in S_0$ be source points and control points respectively for $i = 1, ..., N^b$, $j = 1, ..., N^f$ and $k = 1, ..., N^k$. These control points are located at the centre of three dimensional surface panels. With the use of the body boundary conditions (2) and the boundary integral equation (8) with its normal derivative, we solve the source strengths σ_i^b, σ_j^f on S_i^b, and σ_k^0 S_j^f and S_k^0 from the following equations

$$\begin{aligned}\frac{\partial \phi(\mathbf{x}'^b_i, t)}{\partial \mathbf{n}_b} = &\sum_{i=1}^{N^b} \sigma_i^b \frac{\partial}{\partial n_b^i} \int_{S_i^b} \frac{1}{|\mathbf{x}'^b_i - \mathbf{x}_i^b|} ds_{\mathbf{x}} + \sum_{j=1}^{N^f} \sigma_j^f \frac{\partial}{\partial n_b^i} \int_{S_j^f} \frac{1}{|\mathbf{x}'^b_i - \mathbf{x}_j^f|} ds_{\mathbf{x}} \\ &+ \sum_{k=1}^{N^0} \sigma_k^0 \frac{\partial}{\partial n_b^i} \int_{S_k^0} \frac{1}{|\mathbf{x}'^b_i - \mathbf{x}_k^0|} ds_{\mathbf{x}}.\end{aligned} \tag{9}$$

$$\begin{aligned}\frac{\partial \phi(\mathbf{x}'^0_k, t)}{\partial \mathbf{n}_0} = &\sum_{i=1}^{N^b} \sigma_i^b \frac{\partial}{\partial n_0^k} \int_{S_i^b} \frac{1}{|\mathbf{x}'^0_k - \mathbf{x}_i^b|} ds_{\mathbf{x}} + \sum_{j=1}^{N^f} \sigma_j^f \frac{\partial}{\partial n_0^k} \int_{S_j^f} \frac{1}{|\mathbf{x}'^0_k - \mathbf{x}_j^f|} ds_{\mathbf{x}} \\ &+ \sum_{k=1}^{N^0} \sigma_k^0 \frac{\partial}{\partial n_0^k} \int_{S_k^0} \frac{1}{|\mathbf{x}'^0_k - \mathbf{x}_k^0|} ds_{\mathbf{x}}.\end{aligned} \tag{10}$$

$$\begin{aligned}\phi(\mathbf{x}'^f_j, t) = &\sum_{i=1}^{N^b} \sigma_i^b \int_{S_i^b} \frac{1}{|\mathbf{x}'^f_j - \mathbf{x}_i^b|} ds_{\mathbf{x}} + \sum_{j=1}^{N^f} \sigma_j^f \int_{S_j^f} \frac{1}{|\mathbf{x}'^f_j - \mathbf{x}_j^f|} ds_{\mathbf{x}} \\ &+ \sum_{k=1}^{N^0} \sigma_k^0 \int_{S_k^0} \frac{1}{|\mathbf{x}'^f_j - \mathbf{x}_k^0|} ds_{\mathbf{x}},\end{aligned} \tag{11}$$

Equations (9) and (10) form a Neumann boundary condition whereas Equations (11) is formulated as Dirichlet boundary condition. These two kinds of boundary conditions formulate a mixed Neumann-Dirichlet boundary conditions for the velocity potential in the whole domain. The intersection points between free surface and body surface have to satisfy both Neumann and Dirichlet boundary conditions. The fluid domain surface is composed of a body surface S_b, free surface S_f and seabed surface S_0. In present study, the free surface is divided into inner and outer domains. In the inner and outer domains, the source panel distribution method discussed by Feng et al. (2014) is adopted.

2.3. Hydrodynamic force and coefficient calculation

With strengths σ^b_i, σ^f_j and σ^0_k determined, the velocity potentials on the body surface S_b are derived from equation (7) in the form:

$$\begin{aligned}\phi(\mathbf{x'}^b_i,t) = &\sum_{i=1}^{N^b}\sigma^b_i\int_{S^b_i}\frac{1}{|\mathbf{x'}^b_i-\mathbf{x}_i|}ds_{\mathbf{x}}\\ &+\sum_{j=1}^{N^f}\sigma^f_j\int_{S^f_j}\frac{1}{|\mathbf{x'}^b_i-\mathbf{x}_j|}ds_{\mathbf{x}}+\sum_{k=1}^{N^0}\sigma^0_k\int_{S^0_k}\frac{1}{|\mathbf{x'}^b_i-\mathbf{x}_k|}ds_{\mathbf{x}}.\end{aligned} \tag{12}$$

The dynamic pressure on the body surface, $p = p(\mathbf{x'}^b_i, t)$, is calculated by Bernoulli's equation as

$$\frac{p(t)}{\rho} = -\frac{\partial\phi}{\partial t}, \tag{13}$$

where ρ denotes the fluid density. The temporal derivative of the potential is calculated by a finite difference method using the values of the velocity potential at two consecutive time steps.

The dynamic force $\hat{F}(t)$ applied on the body surface is investigated by integrating the dynamic pressure $p(\mathbf{x'}^b_i, t)$ over the wet body surface as given by

$$\hat{F}(t) = \int_{S_b} p(\mathbf{x'}^b_i, t)\mathbf{n}_b ds. \tag{14}$$

By adopting Fourier transforms, the added mass $\hat{A}_{kk}(\omega)$ (k = 1, 2, 3, 4, 5, 6 for surge, sway, heave, roll, pitch and yaw motion respectively) and damping coefficient $\hat{B}_{kk}(\omega)$ can be obtained as:

$$\hat{A}_{kk}(\omega) = \frac{2}{\xi\omega^2 T_0}\int_0^{T_0}\hat{F}_{kk}(t)\sin(\omega t)dt, \tag{15}$$

$$\hat{B}_{kk}(\omega) = -\frac{2}{\xi\omega T_0}\int_0^{T_0}\hat{F}_{kk}(t)\cos(\omega t)dt, \tag{16}$$

where ξ, ω and T_0 denote body motion amplitude, angular velocity and period. For direct comparison, the results will be presented in nondimensional form as:

$$A_{kl}(\omega) = \hat{A}_{kl}(\omega)/m, \qquad B_{kl}(\omega) = \hat{B}_{kl}(\omega)/m\omega,$$

where m denotes body mass.

3. Numerical validation and simulation

3.1. Numerical validation

Numerical simulations are performed to validate the proposed numerical model. Two truncated cylinders are applied in the numerical simulations. The first truncated cylinder has ratio H/a = 2.0 and d/a = 1.0 while the second one has H/a = 2.0 and d/a = 1.5. Figure 2 demonstrates comparison between proposed method data and Yeung (1981) analytical data for heave added mass coefficient $A_{33}(\omega)$ (a) and heave damping coefficient $B_{33}(\omega)$ (b) for both two cylinders. It is noticed that both $A_{33}(\omega)$ and $B_{33}(\omega)$ obtained by proposed model agree with published data favourably well. These numerical tests validate the proposed numerical model to investigate body oscillation problem within seabed condition.

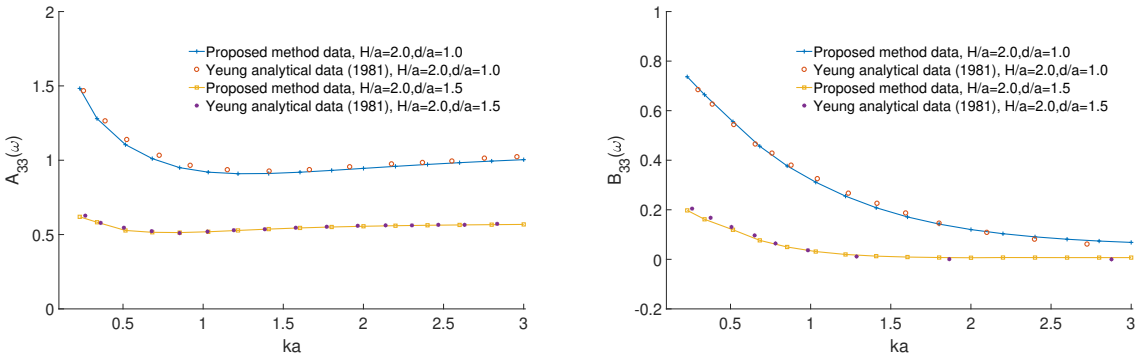

(a) Heave added mass (b) Heave added mass

Figure 2: Comparison between proposed method data and Yeung (1981) analytical data for heave added mass coefficient $A_{33}(\omega)$ (a) and heave damping coefficient $B_{33}(\omega)$ (b).

3.2. Semi-ellipsoid seabed effects

Numerical simulations are conducted to demonstrate the uneven seabed effects for the hydrodynamic characteristics of body experiencing forced oscillatory motion problem. Concave and convex shaped undulations are two basic seabed topographies and widely exist in the marine environment. For example, a sediment scour or a buried pipeline can form a concave and convex seabed topography. Figure 3 shows the convex semi-ellipsoid seabed profile applied in present study. The seabed model is constructed by the ellipsoid equation:

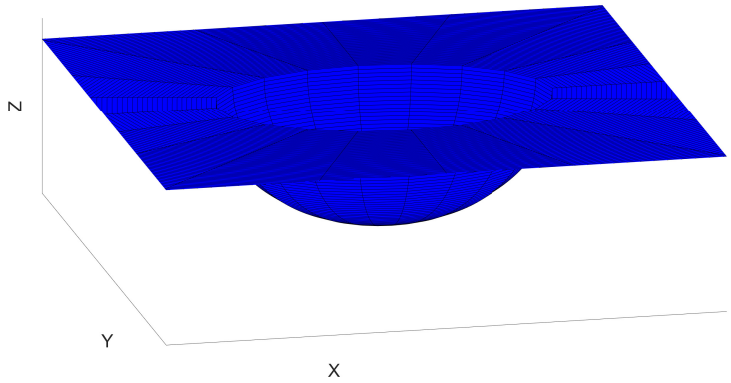

Figure 3: The convex semi-ellipsoid seabed profile.

$$\frac{x^2}{x_1^2}+\frac{y^2}{y_1^2}+\frac{z^2}{z_1^2}=1, \tag{17}$$

here x_1, y_1 and z_1 denote half length of the principal axes. x and y axes form flat seabed surface. Positive and negative z denote concave and convex seabed profile. A truncated cylinder with water depth H to cylinder radius a ratio H/a = 1.0 and cylinder draft d to cylinder radius a ratio d/a = 0.5 is applied in the numerical simulation.

Figure 4 shows comparison of heave added mass $A_{33}(\omega)$ (a) and damping $B_{33}(\omega)$ (b) coefficients for ellipsoid seabed with z_1 = 0.4H, z_1 = 0.2H, z_1 = 0, z_1 = −2H respectively. z_1 = 0 refers to flat seabed essentially. In this numerical simulation, the seabed profile has x_1 = 3H and y_1 = 2H. It is noticed that both added mass coefficient $A_{33}(\omega)$ and damping coefficients $B_{33}(\omega)$ significantly increase as z_1 increasing. This is especially true for the added mass coefficient $A_{33}(\omega)$. This hydrodynamic

coefficient is almost tripled as z_1 increases from −2H to 0.4H across the frequency range. Figure 5 demonstrates comparison of surge added mass $A_{11}(\omega)$ (a) and damping $B_{11}(\omega)$ (b) coefficients for ellipsoid seabed with $z_1 = 0.4H$, $z_1 = 0.2H$, $z_1 = 0$ and $z_1 = -2.0H$ respectively. The value of z_1 effects both added mass $A_{11}(\omega)$ and damping $B_{11}(\omega)$ coefficients significantly. Surge added mass coefficient $A_{11}(\omega)$ increases with z_1 going up in lower frequency range ka < 0.8 while this coefficient decreases in higher frequency range ka > 0.8. Surge damping coefficient $B_{11}(\omega)$ increases with z_1 increasing when the frequency ka is smaller than 1.7 and keeps constant when the frequency ka is bigger than 1.7.

Figure 6 shows oblique views of free surface profile generated by heave motion (a) and surge motion (b) for ka = 2.0 and $z_1 = 0.4$ at time $t = 6T_0$. It should be noticed the wave elevation is in a radiated way around the body for heave motion and it is approximately symmetric along y axis for body experiencing surge motion.

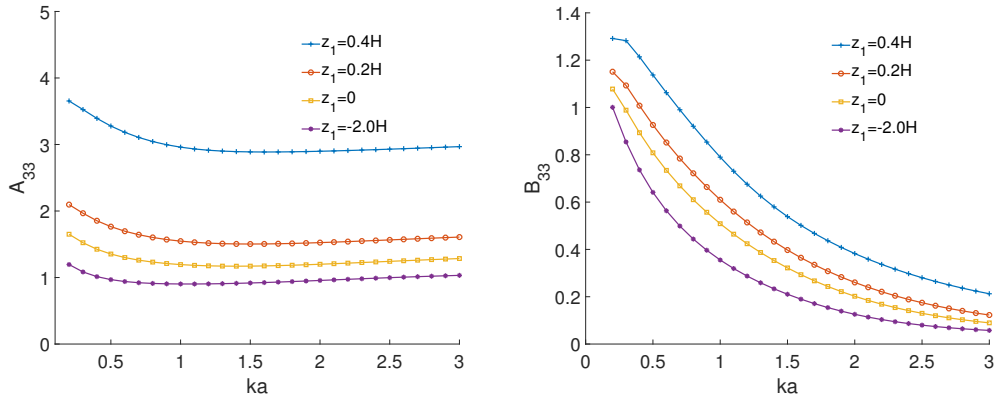

(a) added mass (b) damping

Figure 4: Comparison of heave added mass $A_{33}(\omega)$ (a) and damping $B_{33}(\omega)$ (b) coefficients for ellipsoid seabed with $z_1 = 0.4H$, $z_1 = 0.2H$, $z_1 = 0$ and $z_1 = -2.0H$ respectively.

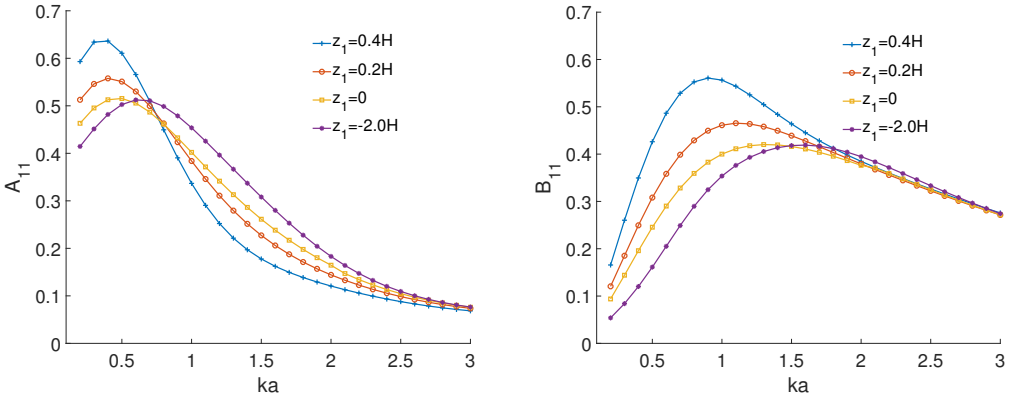

(a) added mass (b) damping

Figure 5: Comparison of surge added mass $A_{11}(\omega)$ (a) and damping $B_{11}(\omega)$ (b) coefficients for ellipsoid seabed with $z_1 = 0.4H$, $z_1 = 0.2H$, $z_1 = 0$ and $z_1 = -2.0H$ respectively.

3.3. Sloping seabed effects

One major concern about sloping seabed effects is the reflection caused by the sloping seabed side (Feng et al., 2017). In proposed model, large area of free surface and seabed surface are covered by Rankine source panel according to the proposed source distributed method. The sloping seabed side causes reflected wave and this reflected wave travels into fluid domain in another side. As very large

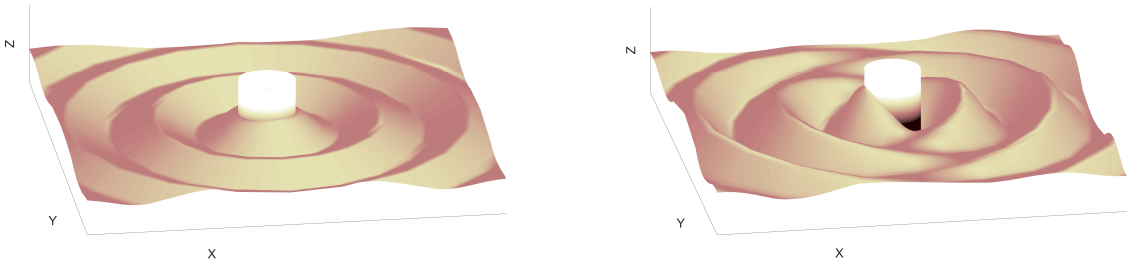

(a) Heave motion (b) Surge motion

Figure 6: Oblique views of free surface profile generated by heave motion (a) and surge motion (b) for ka = 2.0 and z_1 = 0.4 at time t = $6T_0$.

area is covered by Rankine source panel, the reflected wave can travel towards far field without suffering second reflection. Numerical simulations are performed to demonstrate the sloping seabed effects for cylinder experiencing forced oscillatory motions. The seabed inclination is indexed by seabed sloping angle β which is defined as tan β = L_x/L_z. Here L_x and L_z denote the horizontal and vertical distance of sloping seabed part in the X and Z direction respectively. Figure 7 shows the illustration of sloping seabed sloping.

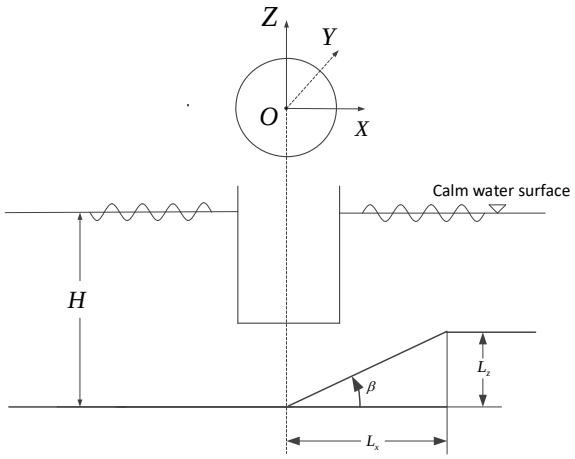

Figure 7: Illustration of sloping seabed.

A cylinder with a/d = 6 is applied in the numerical simulation and this cylinder is located in mean water depth H/d = 1.6. To give a direct comparison, the flat seabed condition is also included in the numerical simulation. Figure 8 shows comparison of heave added mass $A_{33}(\omega)$ (a) and damping $B_{33}(\omega)$ (b) coefficients for flat seabed, sloping seabed with sloping angle tanβ = 4%, tanβ = 6%and tanβ = 8% respectively. It is noticed that the sloping seabed increases the heave added mass $A_{11}(\omega)$ significantly across the frequency range. The heave damping coefficient $B_{33}(\omega)$ also increases noticeably as the slope angle increases. Figure 9 shows top view of wave profile for body experiencing forced heave motion with ka = 2.1 at time t = $6T_0$ for flat seabed (a), sloping seabed with sloping angle tanβ = 4% (b), tanβ = 6% (c) and tanβ = 8% (d) respectively. For flat seabed case, the wave is in a radiated symmetrical profile along the body. For sloping seabed, the wave profile becomes more and more unsymmetrical as the slope seabed angle β increases. Also with the increasing of angle β, the wave length on the slope side becomes more and more less but for the wave length on the flat seabed, the wave length keeps roughly constant.

Figure 10 illustrates the top view of wave profile for body experiencing forced surge motion with ka = 2.1 at time t = $6T_0$ for flat seabed (a), sloping seabed with sloping angle tanβ = 4% (b), tanβ = 6% (c) and tanβ = 8% (d) respectively. For flat seabed, the wave profile is roughly symmetric

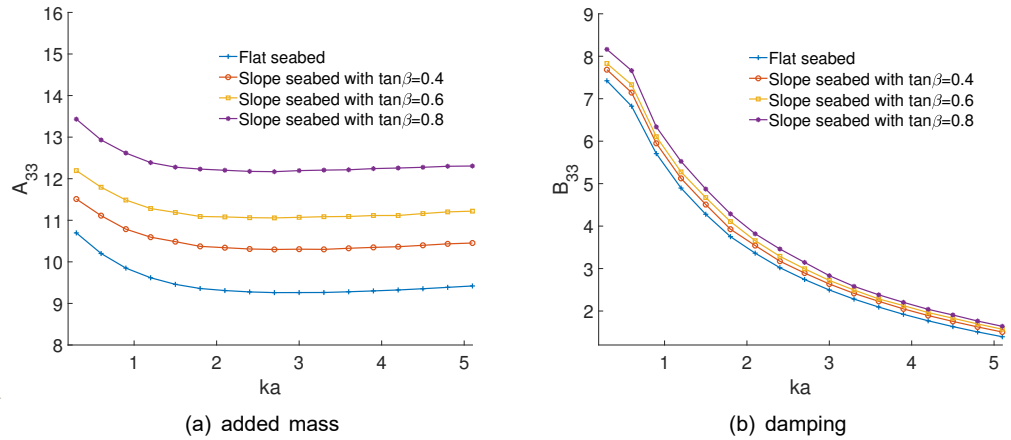

Figure 8: Comparison of heave added mass $A_{33}(\omega)$ (a) and damping $B_{33}(\omega)$ (b) coefficients for flat seabed, sloping seabed with sloping angle tanβ = 4%, tanβ = 6% and tanβ = 8% respectively.

along the y-axis but the seabed inclination alters this symmetric characteristics and shortens the generated wave length on the sloping seabed side. For the wave on the flat seabed side, the wave length keeps roughly constant.

4. Conclusions

Three dimensional Rankine source model is utilized to study the hydrodynamic responses for forced oscillatory body in arbitrary seabed condition. The free surface, seabed surface and body surface are presented by layer of continuous panels. The free surface and seabed surface boundary conditions fea-ture a Neumann boundary condition whereas body surface boundary condition constructs a Dirichlet boundary condition. These mixed Neumann-Dirichlet boundary conditions formulate a closed bound-ary element model to investigate hydrodynamic responses for forced oscillatory problem within various seabed conditions. As very large area free surface and seabed surface are covered by Rankine source panel, the reflected wave produced by sloping seabed side can travel towards far field without further reflection caused by truncated boundary. The proposed model are validated by comparison with flat seabed conditions.

The ellipsoid equation is applied to represent the concave and convex seabed shapes. With z_1 increasing, both the heave hydrodynamic coefficients A_{33} and B_{33} increase dramatically across the frequency range. The surge hydrodynamic coefficients A_{11} and B_{11} also change noticeable but demon-strate different trends across the frequency range. The wave elevation η_3 increases along the frequency range while the wave elevation η_1 increases first and then decreases with the value of z_1 going up. With x_1 increasing, both the heave hydrodynamic coefficients A_{33} and B_{33} increase dramatically across the frequency range but the surge hydrodynamic coefficients A_{11} and B_{11} show different trends across the frequency range.

The sloping seabed inclination has remarkable and complicated effects to the floating body hydro-dynamic coefficients. Both the heave added mass coefficient A_{33} and B_{33} increase significantly across the whole frequency range as seabed sloping angle increases. The increasing of seabed inclination also increases the heave force amplitudes but has no effects on the force phase. The sloping seabed alters the symmetrical characteristics of the seabed profile and causes wave profile become more and more unsymmetrical as the slope seabed angle β increases. With the increase of sloping angle, the surge added mass coefficient A_{11} decreases while surge damping coefficient B_{11} increases across the frequency range noticeably. Due to the change of seabed profile, the wave profile becomes unsymmetrical and the generated wave has shorter wave length on the sloping seabed side for body experiencing both forced heave and surge motions.

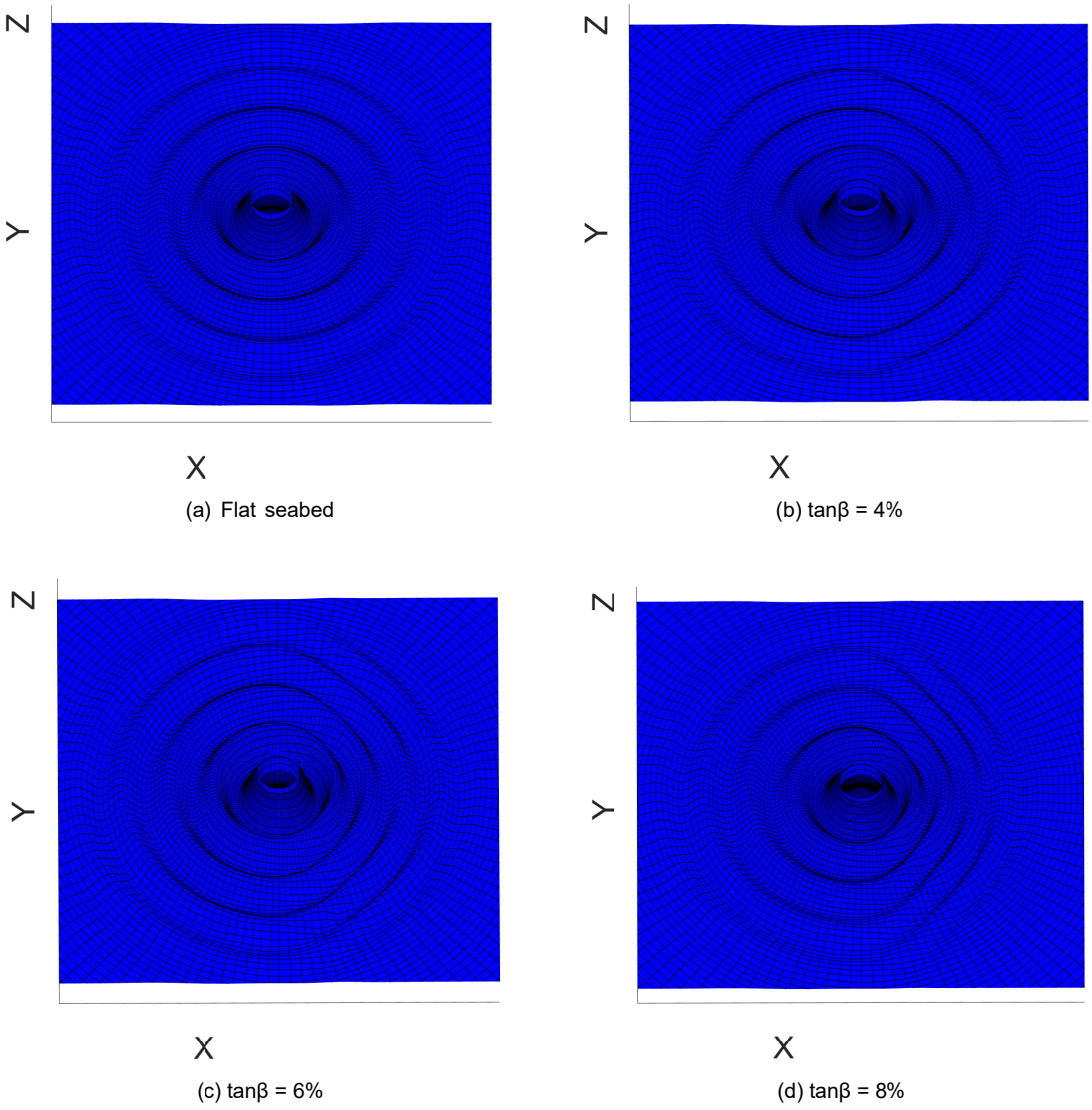

Figure 9: Top view of wave profile for body experiencing forced heave motion with ka = 2.1 at time t = $6T_0$ for flat seabed (a), sloping seabed with sloping angle tanβ = 4% (b), tanβ = 6% (c) and tanβ = 8% (d) respectively.

Acknowledgements

This work is supported by the Sci-tech Project of Sanya Yazhou Bay Science and Technology City Administration (Grant No.SKJC-KJ-2019KY08) and the National Natural Science Foundation of China with Grant No. 51909027.

References

Belibassakis, K., 2005. Hydrodynamic analysis of floating bodies in general bathymetry, in: Proceeding
of the 24th International Conference on Offshore Mechanics and Arctic Engineering, pp. 449–456.
Cao, Y., Schultz, W., Beck, R., 1991. Three-dimensional desingularized boundary integral methods for potential problems. International Journal for Numerical Methods in Fluids 12, 785–803. Clauss, G., Stempinski, F., Dudek, M., Klein, M., 2009. Water depth influence on wave–structure-interaction. Ocean Engineering 36, 1396–1403.

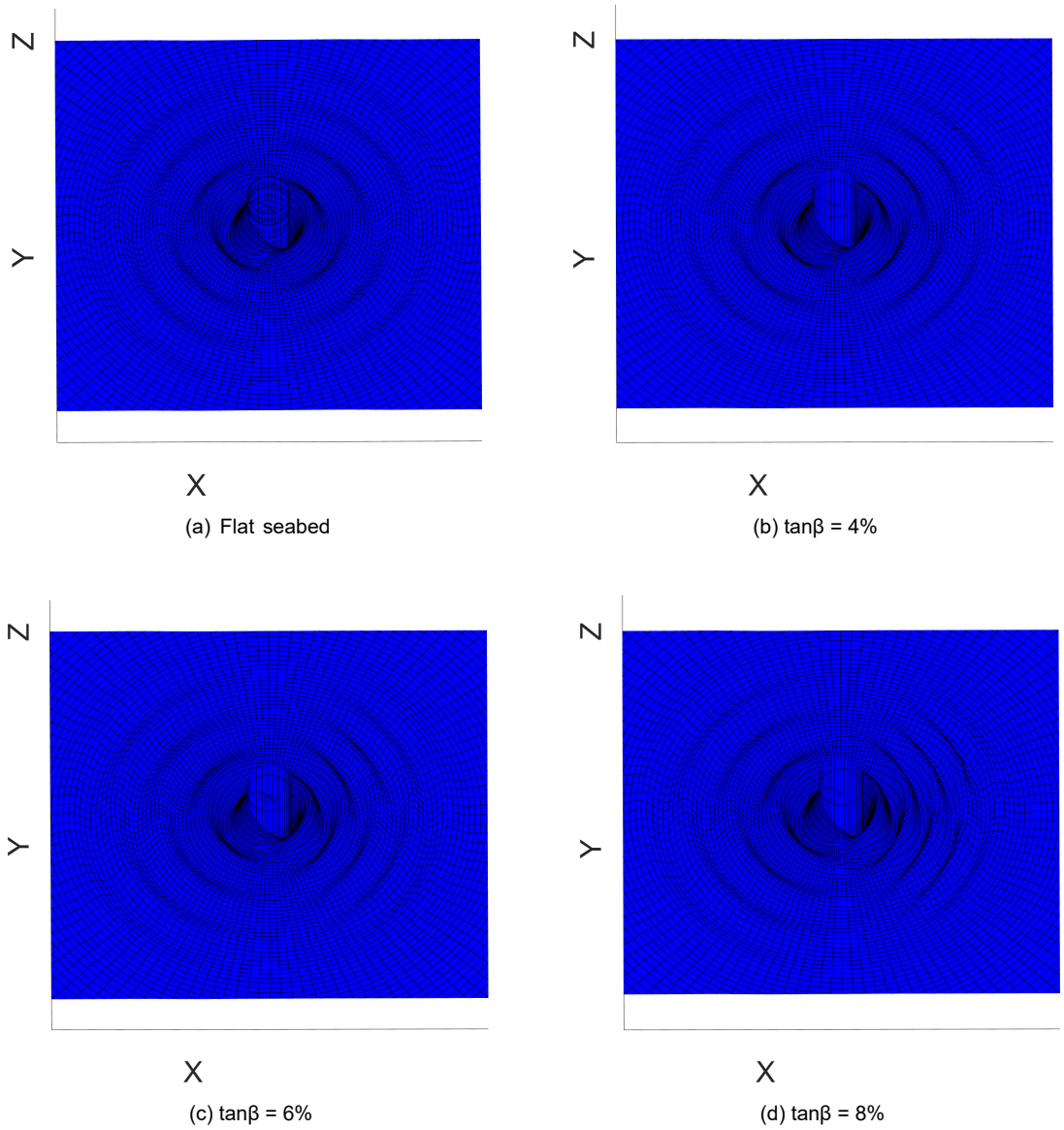

Figure 10: Top view of wave profile for body experiencing forced surge motion with ka = 2.1 at time t = $6T_0$ for flat seabed (a), sloping seabed with sloping angle tanβ = 4% (b), tanβ = 6% (c) and tanβ = 8% (d) respectively.

Feng, A., Bai, W., Price, W., 2017. Two-dimensional wave radiation and diffraction problems in a flat or sloping seabed environment. Journal of Fluids and Structures 75, 193–212.
Feng, A., Chen, Z., Price, W., 2014. A Rankine source computation for three dimensional wave–body interactions adopting a nonlinear body boundary condition. Applied Ocean Research 47, 313–321.
Feng, A., Magee, A., Price, W., 2019. Two dimensional wave-current-structure interaction with flat or sloping seabed environment in a linearized framework. Ocean Engineering 174, 296–306.
Feng, A., Price, W., 2018. Numerical simulations of the hydrodynamic responses of a body interacting with wave and current over a sloping seabed. Applied Ocean Research 79, 184–196.
Hess, J., Smith, A., 1964. Calculation of non-lifting potential flow about arbitrary three dimensional bodies. Journal of Ship Research 8, 22–44.

Mei, T., Delefortrie, G., Ruiz, M., Lataire, E., Vantorre, M., Chen, C., Zou, Z., 2019. Numerical and experimental study on the wave-body interaction problem with the effects of forward speed and finite water depth in regular waves. Ocean Engineering 192, 106366.

Wehausen, J., Laitone, E., 1960. Surface Waves. Springer.

Yeung, R., 1981. Added mass and damping of a vertical cylinder in finite-depth waters. Applied Ocean Research 3, 119–133.

Zhou, X., Sutulo, S., Soares, G., 2014. Computation of ship-to-ship interaction forces by a three-dimensional potential-flow panel method in finite water depth. Journal of Offshore Mechanics and Arctic Engineering 136.

8th International Conference on the Application of Physical Modelling in Coastal and Port Engineering and Science
Dec. 9th - 12th, 2020, Zhoushan, China

COMBINED ENERGY HARVESTING AND DATA COMPRESSION APPROACHES FOR EFFICIENT EXTREME EVENTS MONITORING IN CIVIL INFRASTRUCTURE

TALAL SALEM1, NIZAR LAJNEF1*, PENGCHENG JIAO2*

1: Department of Civil and Environmental Engineering, Michigan State University, East Lansing, MI 48824, USA
2: Ocean College, Zhejiang University, Zhoushan 3216021, Zhejiang, China.
* Corresponding authors email: lajnefni@msu.edu (N.L) and jiao@zju.edu.cn (P.J).

ABSTRACT

Wireless sensors and sensor networks have been widely used recently to monitor structures. In general, the longevity, and hence the efficacy, of these sensors are severely limited by their stored power. In addition, systems that are deployed to monitor extreme events, such as earthquakes, hurricanes, or impacts, will most probably miss the event of interest either due to power blackouts or due to the inefficient approach of data collection. The typical continuous sampling and recording of structure responses is impractical when targeting rare extreme events. This paper addresses these two shortcomings. First, the ability to convert abundant ambient energy into electric power would eliminate the problem of drained electrical supply, and would allow indefinite monitoring thus eliminating the risk of power blackouts. This paper focuses on vibration in civil engineering structures as a source of ambient energy. Earthquake, wind and traffic loads are used as realistic sources of vibrations. In addition, novel data storage and analysis approaches are discussed. These methods allow to reduce the needed storage and computational requirements by more than 1000% for rare events monitoring. Thus, extending the longevity and efficacy of any monitoring system.

Keyword: Energy harvesting; wireless sensor; structural health monitoring; vibrations.

1 INTRODUCTION

A recurring lesson that we have learned from the past natural and man-made structural disasters is that the first responders, occupants, and authorities lack accurate actionable information on the systems resilience during and in the aftermath of a disaster. For example, during the 9/11 attacks on the World Trade Center (WTC) towers [1-3], rescuers and firefighters were instructed to start evacuation and rescue operations despite the fact that officials did not have adequate information on the damage scale and overall stability of the towers. The buildings were prone to collapse within 60 minutes of impact [1, 3]. Another recent example is the fire in the residential tower in London (Grenfell Tower) where the poor coordination of the rescue operations due to the lack of structural information served as one of the reasons for the high number of casualties [4, 5]. It took days for the search and rescue operations to clear all the 24 stories of the building while being assisted by structural engineers monitoring the structural stability. Fukushima [6], the impact of wildfires on communities' infrastructure [7], hurricanes Katrina [8] and Laura constitute a long-list of incidents that highlight infrastructure vulnerabilities and the need for access to structural integrity assessment tools for coordinating intervention and evacuation operations under independent, concurrent, or cascading multi-hazard conditions. Unfortunately, current structural monitoring tools and techniques focus primarily on maintenance [9-13] and thus lack the ability to provide actionable intelligence during such extreme events.

2 ENERGY HARVESTING

It is commonly known that material defects, long-term environmental degradation and wear are important factors in the complex process that guides the life-cycle performance of a structural system. Nonetheless, several recent studies have shown that external factors account for the higher rate of failure causes. For example, studies of bridges failures in the U.S. over the last three decades [14-17] have shown that the top reasons of failures are flood, scour, collisions, overload, environmental degradation, fire, earthquakes, and wind. Most of these external factors will manifest at the component level as a propagating crack failure or a change of boundary conditions. Figure 1. presents the vibration energy for different structure types, under such extreme loading conditions (i.e., earthquake, wind, traffic). As it is shown, the maximum earthquake event (labeled 'blue' in Figure 1) is for the Llolleo earthquake which occurred in Chile in 1985. Moreover, the maximum energy that would be harvested for tall buildings (labeled 'red') is for a 44-story building subjected to a small earthquake [18]. Labeled yellow in Figure 1 is the maximum energy that would be harvested from the flexible tower subjected to 100 km h^{-1} wind gusts; this wind speed exceeds 50% of the design wind capacity. The energy harvesting values are sufficient to power embedded sensing devices.

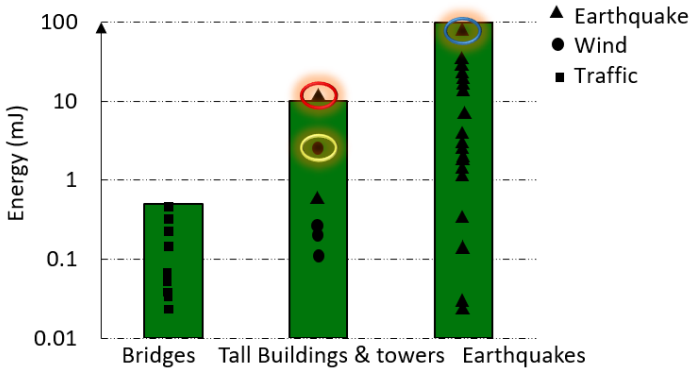

Figure 1. *Maximum theoretical vibration energy for various structures and loading conditions.* [18].

3 DATA COMPRESSION AND ANALYSIS

In our previous work focusing, we have tested and validated the damage detection capabilities of a self-powered sensing platform [19-24]. In this work, the focus is on harsh environments (high temperatures and high loading rates). Typically, damage monitoring systems rely on the measurement of strain or vibration time histories, and then correlate the response with mechanistic and empirical models (including constitutive models) in order to track and predict damage. In contrast, this methodology is a different approach based on the long-term monitoring of response statistics changes that are indicative of damage. The physical response signal is compressed in real time in the sensor devices, before being recorded on onboard memories, using the scheme shown in Figure 3. This is made possible thanks to the unique design of our previously reported sensing system [25, 26]. The sensor has a series of memory cells that cumulatively store the duration of strain events at preselected levels of discretization.

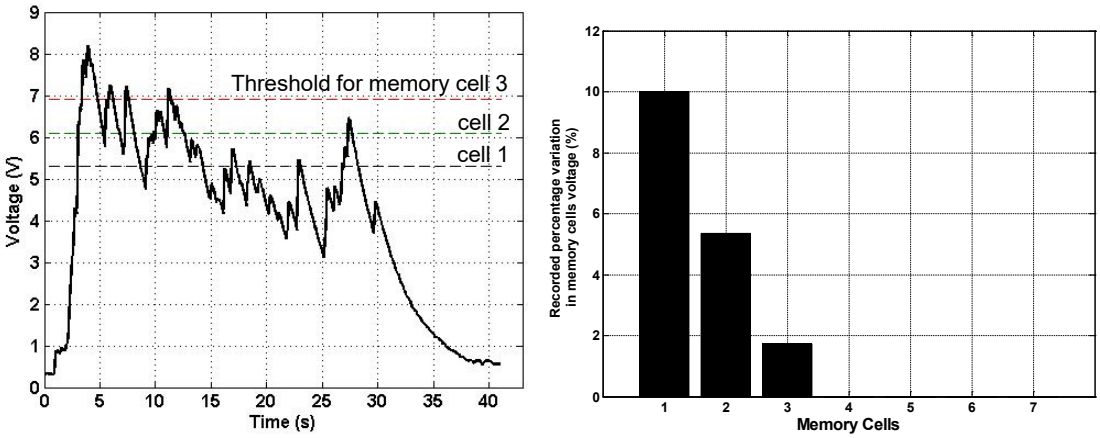

Figure 2. (a) Voltage generated by a piezoelectric transducer in response to large deformations during an extreme high loading event – Simulated earthquake loading; (b) Voltage variation in the sensor memory cells (proportional to energy) in response to the event.

The sensing system measures the duration of events when the amplitude of the input signal exceeds the preset thresholds (Figure 2(a)). The signal is thus stored as probability distribution functions instead of lengthy time histories (Figure 2(b)). Changes and shifts over time in the probability distributions are directly correlated to abnormalities in the monitored structure response (damage accumulation or boundary conditions change). This scheme allows to avoid using complex constitutive or FEM models, it also statistically eliminates the effects of external parameters, and allows the use of low computation environments for post processing. Only the distribution functions are transmitted wirelessly.

The performance of the sensing and data analysis platform has been experimentally validated on different laboratory test-beds as shown in Figure 3. The unique properties of the sensing platform, means that the output of each self-powered sensing node at a specified location is a histogram where each bin represents the cumulative time of an event (strain or acceleration levels) occurrences at predetermined thresholds.

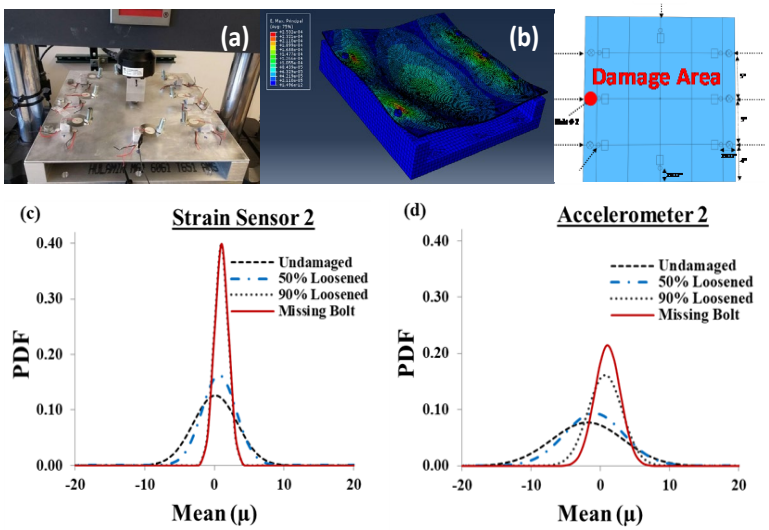

Figure 3. (a) plate specimen instrumented with self-powered sensors in both strain and acceleration monitoring modes; (b) example vibration response of the plate under dynamic loading; damage (red dot) is introduced as a boundary condition change – connecting bolt loosening. (c-d) The plots show real data collected from sensors periodically (each 1 million load cycle). The shifts in PDFs for each sensor are used to locate and quantify the damage level. A hybrid global to local monitoring method was demonstrated.

The experimental setup shown in Figure 3 evaluated the capability of the data management approach to detect

damage progression in different structural materials under dynamic loadings. Data were collected from 16 sensor nodes and also from conventional strain gages to compare the observed measurements [24]. Figure 3b) show the effect of the damage progression on the response of the sensors placed in the damage area. The data is collected from the sensors once every one million cycles. The extracted data per reading is a probability density function (PDF) as shown in Figure 3(c-d). The changes in the statistical parameters of the curves between readings is

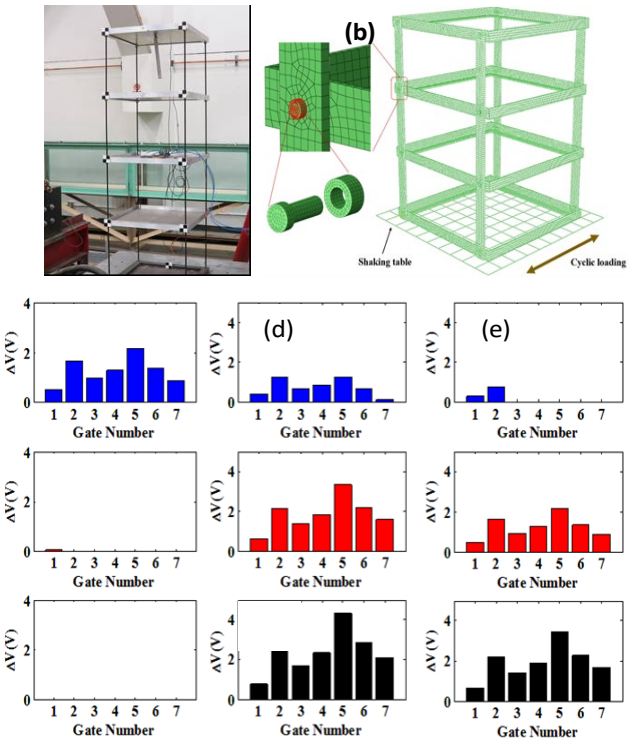

Figure 4. (a) Test setup for a three-story frame structure on a shake table; (b) Damage is introduced as changes in the second-floor connection; (c-k) sample data extracted from different sensing locations. For example, a sensor on the second floor (f,g,h) shows increased response after damage. If the damage threshold is crossed for that location, the component is marked as damaged.

correlated to damage progression. This also clearly shows how data is compressed on chip before wireless transmission. For each reading, a single PDF is extracted from the sensor data, aggregating one million cycles of collected structural response, thus significantly reducing the data transmitted over the wireless link and allowing for self-powered operation. The influence of damage is evaluated based on relative shifts of PDFs over time. When the sensors are placed in a network, those with higher loosening ratio experienced higher shifts in the functions. The sample results discussed here show tests undertaken to develop a data analysis framework that is based on a multilevel strategy for damage identification through: (a) analysis of individual self-powered strain sensors, (b) data fusion in a network of self-powered strain sensors, and (c) data analysis in a hybrid network of self-powered accelerometers and strain sensors. The novel algorithms combine genetic programming and logistic regression for multistate damage classification. The data from the self-powered accelerometers (global indicators) are used to identify the probability of damage in a region, while the combined strain energy response reported on the second layer of self-powered sensors, are used to identify the type and location of damage. This hybrid strategy significantly reduces the computational time. The data recorded on the sensors are collected in real time during the loading event and is used to quantify the resiliency of the structure. Post event analysis is used for the purpose of failures re-construction and visualization. Results showed that data collected at a sensor node from an extreme vibration event are proportional to the energy absorbed by the structural element where the sensor is located. This can be directly correlated to damage in order to generate real data damage maps of each structural component. An example data sample is shown in Figure 2. The data shows the output from an acceleration self-powered sensor node attached to a steel column subject to extreme deformations simulating a near failure event. Each memory cell on the sensor records the duration for which the response voltage (proportional to strain/vibration) is higher than a corresponding preset threshold. The total distribution recorded by the sensor in all the memory cells is thus a

representation of the energy absorbed by the monitored structure at the sensor location (Figure 3(b)). The curated compressive data as shown in Figure 3(b) is directly compared to the damage thresholds established using the combined pre-installation and long-term data. A binary decision parameter is assigned to the specific sensor location. Combining the binary data generated in real time at all the critical locations on the structure allows to predict and visualize the real-time structural integrity (see example below). A three-story steel frame structure (Figure 4(a)) is tested and analyzed using the proposed algorithms. The validated methods can be applied in the future to large scale structures.

Figure 4 shows numerical results from the considered setup. A failure scenario, with a broken connection bolt, is considered as shown in Figure 4(b). Plots in Figure 4(c-k) show the treated real time data from different sensors. The data is directly compared to the damage thresholds established using the pre-event algorithms described above. A network of self-powered strain and acceleration sensors is used. The temperature, acceleration, and strain data, as well as corresponding features for the data acquisition nodes, can be added as additional features in large-scale deployments. Data is extracted for various extreme damage scenarios. While the piezo-based self-powered accelerometers are expected to detect changes in the global characteristics of the structure, the damage details and the approximate damage location are identified by the strain sensors. Kalman filters are used to estimate the states of the system using the features extracted from the heterogeneous sensors. The data shown in Figure 4(c-k) is compared to the damage thresholds derived from the pre-event algorithms and transformed into simplified statistics as shown in Figure 5(a). The changes in slope are indicative of damage. In this

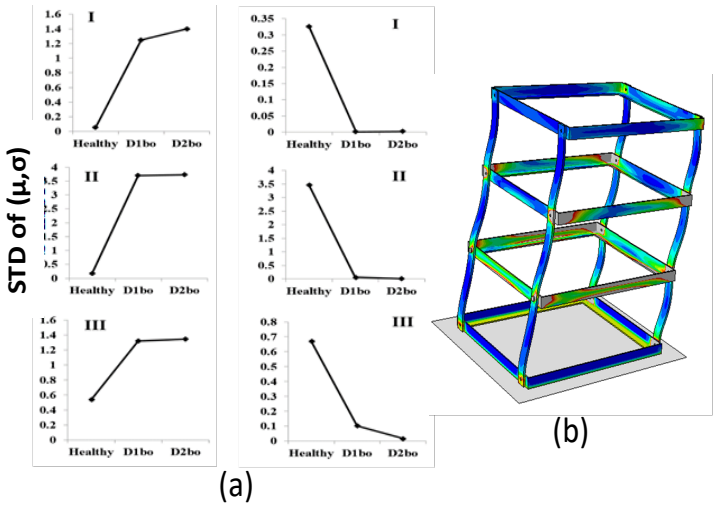

Figure 5. (a) Data compared to damage threshold and transformed into the shown probabilistic parameter variations. This information is directly related to the level of damage at each location; (b) Illustration of damage data from measured sensor responses. Red means a damage threshold was crossed. The illustration is generated from real data (Not FEM).

context, verification of the long-term performance of the proposed approach for real-life structure and other multi-hazard environmental conditions is an interesting topic for the future study. Figure 5(b) shows an example of color-coded data generated based on the different slopes for each sensor location. Figure 5(b) is NOT generated from finite element data, but only from sensor data. In this illustration, red indicates severe damage.

ACKNOWLEDGMENT:

The presented work is supported in part by a research grant from the National Science Foundation (NSF) (CNS# 1645783).

REFERENCES:

[1] W. Langewiesche, American ground: Unbuilding the world trade center, North Point Press, 2010.

[2] M. P. Kwan and J. Lee, "Emergency response after 9/11: the potential of real-time 3D GIS for quick emergency response in micro-spatial environments," Computers, Environment and Urban Systems, vol. 29, p. 93–113, 2005.

[3] V. Kodur, “Role of Fire Resistance Issues in the Collapse of the Twin Towers”, Proceedings of the CIB-CTBUH International Conference on Tall Buildings, 8-10 May 2003, Malaysia

[4] Grenfell firefighters “hampered by equipment”, (retrieved 08/15/2020) http://www.bbc.com/news/uk-40535417

[5] Grenfell Tower Fire Community Safety Committee, West Yorkshire Fire and Rescue Authority, Community Safety Committee, 07/21/2017

[6] M. Siegrist and V. H. M. Visschers, “How a nuclear power plant accident influences acceptance of nuclear power: Results of a longitudinal study before and after the Fukushima disaster,” Risk Analysis, vol. 33, no. 2, pp. 333-347, 2013.
[7] Andrew M. Fraser, Mikhail V. Chester & B. Shane Underwood (2020) Wildfire risk, post-fire debris flows, and transportation infrastructure vulnerability, Sustainable and Resilient Infrastructure, DOI: 10.1080/23789689.2020.1737785.
[8] T. Litman, “Lessons from Katrina and Rita: What major disasters can teach transportation planners,” Journal of Transportation Engineering, vol. 132, pp. 11-18, 2006.
[9] Y. N. Lien, H. C. Jang and T. C. Tsai, “A MANET based emergency communication and information system for catastrophic natural disasters,” in 29th IEEE International Conference on Distributed Computing Systems Workshops, Montreal, QC, Canada, 2009.
[10] S. M. Fang, J. M. Niedzwecki, M. C. Ozbey and T. J. Cummis, “A Brief Review of Structural Health Monitoring with Special Focus on Damage Detection and Sensor Optimization,” Encyclopedia of Maritime and Offshore Engineering, DOI: 10.1002/9781118476406.emoe328
[11] J. Collins, G. Mullins, C. Lewis and D. Winters, “State of the Practice and Art for Structural Health Monitoring of Bridge,” Federal Highway Administration-HRT-09-040, 2014.
[12] J. Seo, J. Hu and J. Lee, “Summary Review of Structural Health Monitoring Applications for Highway Bridges,” Journal of Performance of Constructed Facilities, 2015.
[13] R. Chen, X. Zhang, C. Peng and H. Zhang, “A Study on Design and Implementation of Remote Fire Monitoring System for Buildings,” Procedia Engineering, 2013.
[14] G. Lee, S. Mohan, C. Huang and B. Fard, “A Study of U.S. Bridge Failures (1980-2012)” Technical Report MCEER-13-0008, June 15, 2013.
[15] W. Cook, “Bridge Failure Rates, Consequences, and Predictive Trends,” Doctor of Philosophy, Utah State University, 2014.
[16] M. Stearns and J. E. Padgett, “Impact of 2008 Hurricane Ike on bridge infrastructure in the Houston/Galveston region.” Journal of Performance of Constructed Facilities, vol. 26, no. 4, pp. 441-452, 2011.
[17] A. S. Nowak and K. R. Collins, Reliability of Structures. CRC Press, 2nd Ed., Boca Raton, FL, 2013.
[18] N.G., Elvin, N., Lajnef, A.A. Elvin. Feasibility of structural monitoring with vibration powered sensors. Smart materials and structures (2006)15(4) 977.
[19] A. H. Alavi, H. Hasni, P. Jiao, W. Borchani and N. Lajnef, “Fatigue Cracking Detection in Steel Bridge Girders through a Self-Powered Sensing Concept,” Journal of Constructional Steel Research, vol. 128, pp. 19-38, 2017.
[20] H. Hasni, A. H. Alavi, P. Jiao and N. Lajnef, “Detection of Fatigue Cracking in Steel Bridge Girders: A Support Vector Machine Approach,” Archives of Civil and Mechanical Engineering, vol. 17, no. 3, pp. 609-622, 2017.
[21] H. Hasni, A. H. Alavi, N. Lajnef, M. Abdelbarr, S.F. Masri and S. Chakrabartty, “Self-powered piezo-floating-gate sensors for health monitoring of steel plates,” Engineering Structures, vol. 148, pp. 584-601, 2017.
[22] A. H. Alavi, H. Hasni, N. Lajnef, K. Chatti and F. Faridazar, “An Intelligent Structural Damage Detection Approach Based on Self-Powered Wireless Sensor Data,” Automation in Construction, vol. 62, pp. 24-44, 2016.
[23] A. H. Alavi, H. Hasni, N. Lajnef, K. Chatti and F. Faridazar, “Damage Detection Using Self-Powered Wireless Sensor Data: An Evolutionary Approach,” Measurement, vol. 82, pp. 254-283, 2016.
[24] H. Hasni, P. Jiao, A.H. Alavi, N. Lajnef, N., Masri, S. F. (2018). Structural health monitoring of steel frames using a network of self-powered strain and acceleration sensors: A numerical study. Automation in Construction, 85, 344-357.
[25] C. Huang, N. Lajnef and S. Chakrabartty, “Calibration and Characterization of Self-powered Floating-gate Usage Monitors with Single Electron per Second Operational Limit,” IEEE Transactions of Circuits and Systems I, vol. 57, no. 3, pp. 556–567, 2010, DOI: 10.1109/TCSI.2009.2024976.
[26] C. Huang and S. Chakrabartty, “An Asynchronous Analog Self-powered Sensor-Data-Logger with a 13.56MHz RF Programming Interface,” IEEE Journal of Solid-State Circuits, vol. 47, no. 2, 2012, DOI:10.1109/JSSC.2011.2172159.

8th International Conference on the Application of Physical Modelling in Coastal and Port Engineering and Science
Dec. 9th - 12th, 2020, Zhoushan, China

NECESSITY OF USING A WAVE FRICTION FACTOR IN TSUNAMI NUMERICAL SIMULATION

HITOSHI TANAKA(1) & NGUYEN XUAN TINH(2)

(1, 2) Department of Civil Engineering, Tohoku University, Sendai, Japan
e-mail hitoshi.tanaka.b7@tohoku.ac.jp; nguyen.xuan.tinh.c5@tohoku.ac.jp

ABSTRACT

In most of the existing tsunami numerical models, a steady flow friction factor such as Manning's *n* or Darcy-Weisbach's *f* has commonly been applied for accessing the tsunami-induced bottom shear stress. However, it has theoretically been proved by the authors that a wave friction law is valid, rather than a steady flow friction law in almost the entire computational domain from tsunami source to shallow area (Tinh and Tanaka, 2019). In this study, a k-ω model is used to calculate velocity profile, turbulent kinetic energy and resultant sea bottom shear stress under shoaling hypothetical tsunami propagating over a uniformly sloping bathymetry. Numerical solution is obtained by applying a finite difference method with finer grid spacing in the vicinity of the bottom to achieve accurate numerical analysis. It is found that the behavior of tsunami-induced bottom boundary layer has an unsteady characteristic and acting similar to that induced by wind-generated waves even under a long period tsunami. Therefore, the conventional steady flow friction law gives underestimated value for tsunami-induced bottom shear stress. In addition, a calculation method of tsunami-induced bottom shear stress using a wave friction factor is proposed.

Keywords: Tsunami, bottom boundary layer, bottom shear stress, current friction factor, wave friction factor, numerical simulation

1 INTRODUCTION

It is well known that the bottom boundary layer under wave motion is totally different from that induced steady current. Generally, the thickness of wave boundary layer is extremely thin as compared with water depth, resulting high shear stress due to its steep velocity gradient near the bottom. Moreover, another distinct difference as compare with steady current can be found in phase difference between the free-stream velocity and the bottom shear stress.

Considering these remarkable differences between steady and wave boundary layers, a significant question arises for friction law under tsunami; whether steady current friction law or wave fiction law. Usually, steady flow friction law has commonly been applied in numerical simulation of tsunami, simply assuming that the period of tsunami is long enough as compared with wind-generated waves (e.g., Imamura, 1996; Liu et al., 1998). However, there have been almost no detailed investigations on this topic.

According to a field observation of Lacy et al. (2012) during the 2010 Chilean Earthquake Tsunami in the U.S. Monterey Bay mouth, the thickness of tsunami bottom boundary layer was about 40cm, which is much smaller than the water depth, 10m. In addition, Williams and Fuhrman (2016) and Tinh and Tanaka (2019) carried out investigation on the bottom boundary layer under tsunami by using a two-equation turbulence model, and confirmed the result obtained by Lacy et al. (2012).

In this paper, detailed turbulent structure of tsunami boundary layer, such as velocity profile, turbulent kinetic energy and bottom shear stress, at the depth of h=100 m will be described from the numerical computation of Tinh and Tanaka (2019) obtained by a k-ω model computation. In addition, a method is proposed how to apply a wave friction factor to 2-D tsunami numerical simulation.

2 Method of Numerical Simulation

In the study of Tinh and Tanaka (2019), the height of a tsunami in source area is assumed to be H=1m, and tsunami shoaling process over a uniformly sloping bottom has been calculated using Green's law, as depicted in Figure 1. In addition, the grain size of bottom sediment is assumed to be d= 0.3 mm. The characteristics of tsunami at the depth of h=100m is summarized in Table 1.

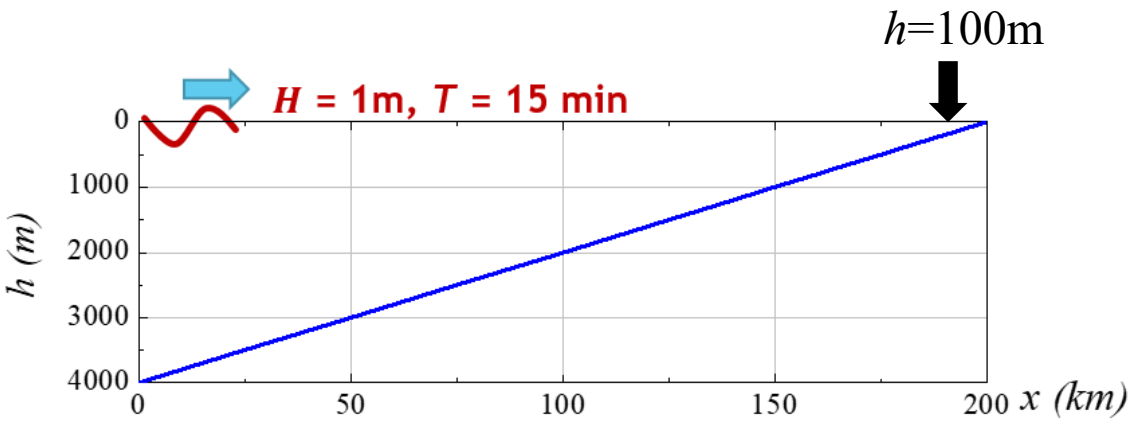

Figure 1. Cross-section of sea bottom.

Table 1. Computational condition.

h(m)	H(m)	T(min)	U_m(m/s)	d (mm)	a_m/k_s	Re
100	2.51	15	0.394	0.3	7.52×10^4	2.22×10^7

In the numerical computation of a turbulent boundary layer, a k-ω model is applied and solved numerically using a method propose by Sana et al. (2009). The governing equations is a linearized boundary layer equation given by the following equation.

$$\frac{\partial u}{\partial t} = -\frac{1}{\rho}\frac{\partial p}{\partial x} + \frac{1}{\rho}\frac{\partial \tau}{\partial z} \qquad [1]$$

where u: the flow velocity in the boundary layer, t: the time, p: the pressure, x, z: the horizontal and vertical coordinates, ρ: the fluid density, and τ: the shear stress. The pressure gradient term in Eq. [1] can be obtained from the acceleration of the free-stream velocity under tsunami.

The numerical computation of the tsunami bottom boundary layer was carried out by solving Eq. [1] along with governing equations for k and ω. Accurate computation in the vicinity of the bottom was achieved near the bottom by using finer grid spacing. More details of the calculation method can be found in Sana et al. (2009).

The calculation condition described above is summarized in Table 1, in which H: the wave height, U_m: the amplitude of free-stream velocity in the tsunami boundary layer, a_m: the amplitude of excursion length of water particle outside the boundary layer (=U_m/σ), σ: the angular frequency (=$2\pi/T$, T: the wave period), k_s: Nikuradse's equivalent roughness (= 2.5d), Re: the wave Reynolds number, and ν: the kinematic viscosity of the fluid, and U_m and a_m are calculated using the linear long wave theory.

The transitional behavior in a wave boundary layer has been investigated by many researchers such as Tanaka and Shuto (1984), Tanaka and Sana (1994), and Sumer and Fuhrman (2020). According to Tanaka and Thu (1994), the critical Reynolds number for transition to turbulence in a wave boundary layer is given by

$$Re = 2.5 \times 10^5 \qquad [2]$$

where the wave Reynolds number is defined by the following equation.

$$Re = \frac{U_m\, a_m}{\nu} \qquad [3]$$

It is confirmed that the Reynolds number shown in Table 1 is much higher than the critical value of transition given by Eq. [2].

The closed circle in Figure 2 illustrates the computational case in term of h/L and H/h, in which L: the wavelength computed by the linear long wave theory. From Figure 2, it is confirmed that the calculated case is classified into long wave condition, and that H/h is sufficiently smaller than the breaking limit.

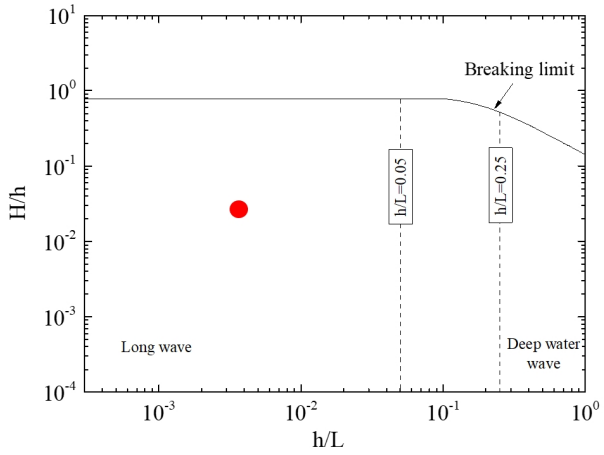

Figure 2. Computational condition in terms of *H/h* and *h/L*.

3 RESULTS OF k-ω MODEL COMPUTATION

3.1 Velocity distribution

The time-variation of free-stream velocity $U(t)$ is assumed to be expressed by a sinusoidal function as shown in Figure 3(a). Vertical distribution of the horizontal velocity inside the boundary layer is illustrated to Figure 3(b), in which the vertical axis and the velocity are normalize by the water depth h and the maximum of the free-stream velocity U_m, respectively. Although the computed case satisfies long wave condition as shown in Figure 2, the flow velocity distribution is totally similar to that in a wave boundary layer, characterized by the uniform velocity distribution outside the boundary layer along with gradual decrease of the velocity in the immediate vicinity of the bottom below z*=0.02 (z=2m). In addition, an over-shooting of the velocity can be observed under the wave crest, which is another characteristic of a wave boundary layer.

Recently, Tanaka et al. (2020a) proposed a full-range equation for wave boundary layer thickness by improving the previous version of estimation method by Sana and Tanaka (2007, 2019). The definition of Jensen at al. (1989) based on the height of overshoot under the wave crest is employed by Tanaka et al. (2020a) for wave boundary layer thickness δ. Using the equation proposed by Tanaka et al. (2020a), the boundary thickness δ for the present computational case is estimated to be δ=0.70m (δ/h=7.0x10^{-3}), which is in highly good agreement with the k-ω computation depicted in Figure 3(b).

Hence, it is highly clear that the flow velocity distribution shown in Figure 3 totally differs from steady current, although it satisfies the long wave condition.

3.2 Turbulence intensity distribution

The vertical and temporal variation of turbulence intensity k is shown in Figure 3(c). It is seen that its distribution is confined in a very thin wave layer in the vicinity of the bottom below z*=0.02. Moreover, the time-variation of k value is almost corresponding to the change of the free-stream velocity.

3.3 Bottom shear stress

The calculated result of the bottom shear stress τ_0 by the turbulent model is depicted in Figure 4. Moreover, the calculation result using Manning's roughness coefficient is also plotted in this diagram. The bottom shear stress from the present computation shows a slight phase difference ahead the free-stream velocity. Meanwhile, in computation result using the steady flow friction law, the phase difference does not exist between the shear stress and the free-stream velocity. Moreover, it is highly interesting to note that the calculation value by the steady flow friction factor is about a half as compared with the value from the k-ω model computation. The difference between two computation methods can be easily understood from the steep velocity gradient near the bottom observed in Figure 3(b).

From Figure 4, it is clear that in order to estimate precise bottom shear stress under tsunami, it is necessary to use a wave friction factor rather than steady friction factor until transition occurs from ordinary wave boundary layer to depth-limited boundary layer (Tanaka et al., 1999).

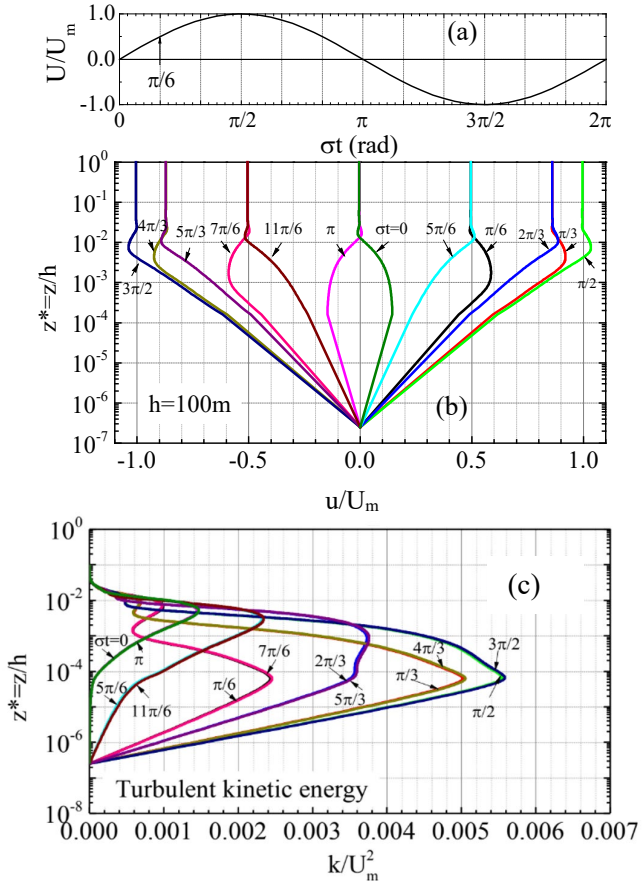

Figure 3. (a) Free-stream velocity, (b) velocity profile and (c) turbulent kinetic energy.

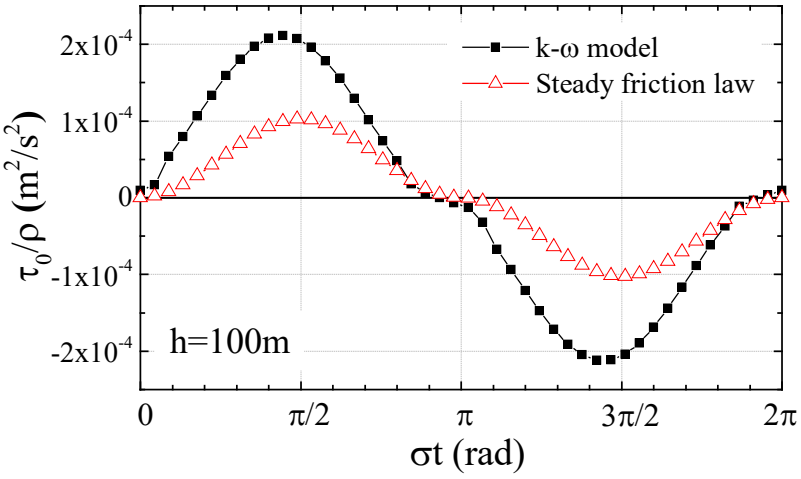

Figure 4. Time-variation of bottom shear stress

4 PROPOSAL OF A NEW FRICTION COEFFICIENT FOR TSUNAMI SIMULATION

Tinh and Tanaka (2019) applied a new correction method for the hypothetical tsunami shoaling case and the obtained bottom shear stress result highly comparable with the results from the *k-ω* turbulent model.

The bed shear stress in a numerical modelling based on shallow water equation is normally assessed by using the Manning's equation, assuming a conventional steady friction law.

$$\tau_0(t) = \tau_c(t) = \frac{\rho g n^2}{h^{1/3}} \bar{u}(t)|\bar{u}(t)| = \rho \frac{f_c}{2} \bar{u}(t)|\bar{u}(t)| \quad [4]$$

where $\tau_c(t)$ is the steady bed shear stress, n is the Manning roughness coefficient, f_c is the steady flow friction factor obtained from the logarithmic law.

$$f_c = \frac{2\kappa^2}{[\ln(\frac{h}{z_0})-1]^2} \quad [5]$$

where κ is the von Karman constant (= 0.4), and z_0 is the roughness length.

Under wave motion, the bed shear stress is estimated using a wave friction factor.

$$\tau_0(t) = \tau_w(t) = \rho \frac{f_w}{2} U(t)|U(t)| \quad [6]$$

where $\tau_w(t)$ is the bottom shear stress induced by wave motion, $U(t)$ is the free-stream velocity, f_w is the wave friction factor. Recently, Tanaka et al. (2020b) discussed transitional behavior of flow regime in tsunami boundary layers, though, it is simply assumed rough turbulent in this study. According to Tanaka (1992) and Tanaka and Thu (1994), the wave friction factor for rough turbulent regime is calculated by;

$$f_w = exp\left\{-7.53 + 8.07(\frac{30a_m}{k_s})^{-0.100}\right\} \quad [7]$$

where $k_s = 30z_0$. Afterwards, Humbyrd (2012) theoretically obtained almost the same form of wave friction coefficient for a rough bottom.

Based on Eqs. [4] and [6], and assuming $\bar{u}(t) = U(t)$, Tinh and Tanaka (2019) proposed a new roughness coefficient, n_0, as

$$n_0 = an \quad [8]$$

in which the coefficient a is expressed by

$$a = \frac{n_0}{n} = \sqrt{\frac{f_w}{f_c}} \quad [9]$$

When tsunami propagates in a shallow region the wave friction factor approaches the steady friction factor, hence the *a*-value becomes 1.0 point due to transition to depth-limited condition (Tinh and Tanaka, 2019). From that location, the Manning method can be applied to the shore direction. Therefore, the calculation method for the correction *a*-parameter is summarized by the following equation.

$$a = \begin{cases} \sqrt{\frac{f_w}{f_c}} & \text{if} \quad f_w > f_c \\ 1.0 & \text{if} \quad f_w \le f_c \end{cases} \quad [10]$$

Larsen and Fuhrman (2019) used a similar method to recognize the location where the depth-limited condition is satisfied in their numerical simulations for propagation and run-up of full-scale tsunamis using a Reynolds-Averaged Navier-Stokes model.

5 CONCLUSIONS

In the present study, detailed turbulent structure of tsunami boundary layer obtained from k-ω model computation is shown. It is noted that, although the computational case satisfies long wave condition, the bottom boundary layer under tsunami is highly similar to that under wave motion, resulting in underestimation of bottom shear stress using a steady friction coefficient, as assumed in a conventional tsunami simulation method.

ACKNOWLEDGEMENTS

The authors would like to express their sincere gratitude to the Taisei Scientific Foundation for their financial support during the course of the present study.

REFERENCES

Humbyrd, C.J. (2012) Turbulent combined wave-current boundary layer model for application in coastal waters. *Master's thesis, Massachusetts Institute of Technology*, Cambridge, MA, USA, 157pp.

Imamura, F. (1996) Review of tsunami simulation with a finite difference method. *Long-wave runup models,* Ed: H. Yeh, P. Liu and C. Synolakis. World Scientific, Singapore, 25-42.

Jensen, B.L., Sumer, B.M., Fredsøe, J. (1989) Turbulent oscillatory boundary layers at high Reynolds numbers. *J. Fluid Mech*., 206, 265-297.

Lacy, J.R., Rubin, D.M. and Buscombe, D. (2012). Currents, drag, and sediment transport induced by a tsunami. *J. Geophys. Res*., 117 (C9).

Larsen, B.E. and Fuhrman, D.R. (2019) Full-scale CFD simulation of tsunamis. Part 2: Boundary layers and bed shear stresses. *Coast. Eng*., 151, 42-57.

Liu, P.L.F., Woo, S.B. and Cho, Y.S. (1998). Computer programs for tsunami propagation and inundation. *Technical Report, Cornell University*, NY, USA.

Sana, A, Ghumman, AR and Tanaka, H. (2009). Modeling of a rough-wall oscillatory boundary layer using two-equation turbulence models. *J. Hydr. Eng*., 135 (1), 60-65.

Sana, A. and Tanaka, H. (2007) Full-range equation for wave boundary layer thickness. *Coast. Eng*., 54, 639-642.

Sana, A. and Tanaka, H. (2019) Corrigendum to "Full-range equation for wave boundary layer thickness" [Coast. Eng. 54 (2007) 639-642], *Coast. Eng*., 152.

Sumer, M.B. and Fuhrman, D.R. (2020) *Turbulence in Coastal and Civil Engineering*. World Scientific, Singapore, 758p.

Tanaka, H. and Shuto, N. (1984) Friction laws and flow regimes under wave and current motion. *J. Hydr. Res*., 22(4), 245-261.

Tanaka, H. (1992) An explicit expression of friction coefficient for a wave-current coexistent motion. *Coastal Eng. in Jap.*, 35 (1), 83-91.

Tanaka, H. and Sana, A. (1994) Numerical study on transition to turbulence in a wave boundary layer. *Sediment Transport Mechanisms in Coastal Environments and Rivers*, Ed. M. Bélorgey, D. Rajaona and J.F.A. Sleath, World Scientific, Singapore, 14-25.

Tanaka, H. and Thu, A. (1994). Full-range equation of friction coefficient and phase difference in a wave-current boundary layer. *Coastal Eng*., 22, 237-254.

Tanaka, H., Sana, A., Kawamura, I. and Yamaji, H. (1999) Depth-limited oscillatory boundary layers on a rough bottom. *Coastal Eng. Jap*., 41(1), 85-105.

Tanaka, H., Tinh, N.X. and Sana, A. (2020a) A. Improvement of the full-range equation for wave boundary layer thickness. *J. Marine Sci. Eng*., 8(8), 573.

Tanaka, H., Tinh, N.X. and Sana, A. (2020b) Transitional behavior of flow regime in shoaling tsunami boundary layers. *J. Marine Sci. Eng*., 8(9), 700.

Tinh, N.X., and Tanaka, H. (2019). Study on boundary layer development and bottom shear stress beneath a tsunami. *Coast. Eng. J.*, 61 (4), 574-589.

Williams, I.A. and Fuhrman, D.R. (2016). Numerical simulation of tsunami-scale wave boundary layers. *Coastal Eng.*, 110, 17-31.

8th International Conference on the Application of Physical Modelling in Coastal and Port Engineering and Science
Dec. 9th - 12th, 2020, Zhoushan, China

THE CONTACT MEASUREMENT METHOD OF MOTION RESPONSE FOR A CONSTRAINED FLOATING OBJECT UNDER WAVE ACTION

TENGXIAO WANG(1) , HENG JIN(2), RUIYIN SONG(3)

(1,2,3) Ningbo Institute of Technology, Zhejiang University, Ningbo, China
e-mail jinheng@nit.zju.edu.cn
(2) Ningbo Institute of Dalian University of Technology, Ningbo, China

ABSTRACT

The motion of the floating object is an important indicator in the ocean hydrodynamic experiment. And a reduced-dimensional motion system is usually easier to capture and study. In this study, a simple restraint device was proposed to constrain the six-degree-of-freedom motion of the floating object in a two-dimensional plane. A contact measurement method based on two rope displacement sensors and one inclination sensor was used to measure the motion response of the floating object. The experimental validation of the present restraint device and the corresponding measurement demonstrated the feasibility and accuracy of the restraint-measurement system. The above system may be helpful to the experimental investigation of the motion response of the floating objects in the hydrodynamic test.

Keywords: Contact measurement, restraint device, motion response, floating object

1 INTRODUCTION

Ships are a common floating structure in the ocean. The resistance, maneuverability, and motion response are several considerations for the design of the ship. In addition to ships, a number of new floating structures such as deep-water breakwaters, floating platforms, offshore wind turbines and ocean energy converter have appeared in recent years. Different from fast moving ships, the motion response and hydrodynamic analysis of these new types of offshore structures are more important. Among them, the motion response is the basis for understanding the working mechanism of the floating object, optimizing the structure design, and carrying out the coupled dynamic analysis. Therefore, it is of great significance to understand and capture the motion response of the floating bodies under the ocean wave.

In the hydrodynamic experiments of ocean engineering, the six-degree-of-freedom (6DoF) motion responses (surge, sway, heave, pitch, roll, and yaw) of the three-dimensional (3D) floating object is the most frequently investigated parameter (Mitra et al., 2012; Bayati et al., 2014; Lee et al., 2015). As the experimental research about the 6DoF motion of the floating object usually require complex environmental conditions and therefore to bring a large amount of original data, which will lead to increased errors and costs. Many scholars simplified the experimental conditions was to limit the floating objects to two-dimensional (2D) planes or even one-dimensional lines (Pessoa et al., 2015; Chen et al., 2016; Lei et al., 2017; Fang et al., 2020). Based on this method, not only the test process can be simplified, but also the test conclusions were more concentrated, which is beneficial to the analysis of motion response. Since 3D numerical simulation usually required more time and computing resources, it may be a meaningful method to reduce the system dimension for hydrodynamic testing. To constraint the 6DoF motion of the floating objects under the ocean wave, one common way was to set the horizontal dimension of the floating object equal to the width of the wave tank (He et al., 2012). Another way was to design a special restraint device to constraint the motion of the floating object in a specific direction or plane (Elsherbiny et al., 2019). Once the dimension of the motion was reduced, it became easy to capture the motion of the floating object. For example, the researcher can easily obtain the heave and pitch responses of the ship through a laser displacement sensor fixed on the trailer and an inclination sensor installed on the ship, when the ship is towed for fast sailing in order to measure the resistance of the ship.

According to the above requirements,this paper proposed a simple restraint device to constraint the 6DoF motion of the floating box to a 2D plane. Meanwhile, a motion measurement method suitable for such a plane motion was given. The feasibility of the above restraint device and the accuracy of the measurement method was carefully confirmed. With the present restraint-measurement system, the hydrodynamic experiments such as floating breakwater, wave energy converter or LNG-FLNG coupling interaction can be carried out in 2D plane. And the corresponding motion can also be obtained.

2 STRUCTURE AND EXPERIMENT DESIGN

In order to satisfy the requirement of the 2D hydrodynamic test of floating bodies, a simple restraint device was introduced in this paper. The above device was used to constraint a floating object with 6DoF on the 2D plane. It was composed of a pair of slots plates and two rigid restraint rods (see Figure 1). The bottom of the slots plates was fixed on the floating object and the rods were installed on the outer fixed frame. The layout of the structure and the restraint device in the wave tank can refer to Figure 2.

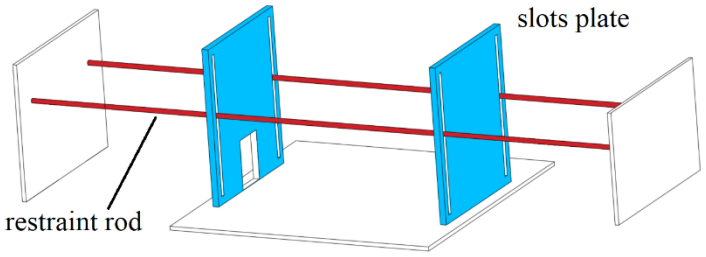

Figure 1 Sketches of the restraint device

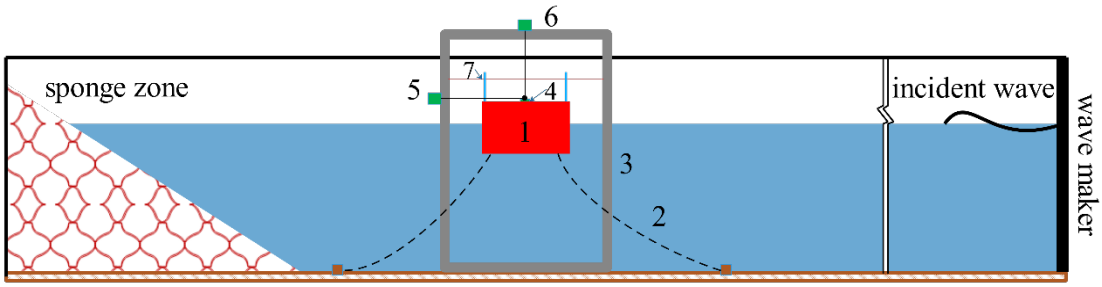

Figure 2 The layout of the experimental wave tank and the floating box with a restraint device, 1, floating box, 2, mooring line, 3, outer fixed frame, 4, inclination sensor, 5, side sensor, 6, top sensor, 7, restraint device.

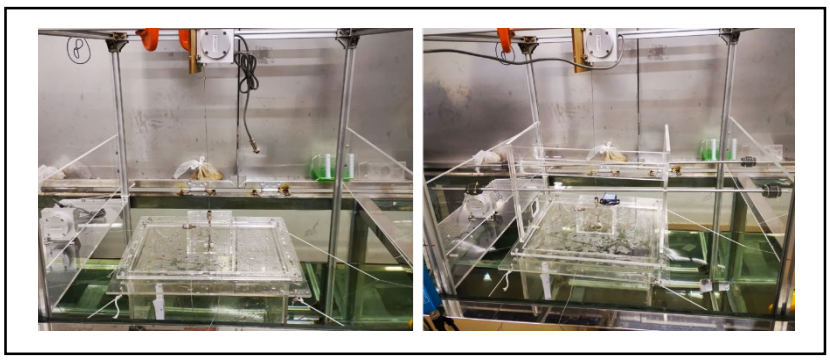

Figure 3 The experimental snapshot of the floating box without (Left) and with (Right) the restraint device.

With the restraint device, the floating box under ocean wave then was allowed to sway along the wave direction and heave along the vertical direction in Figure 3. Also, the rotation around the axis perpendicular to the above directions was allowed. In the right of Figure 3, the layout of three sensors were shown. One rope displacement sensor was installed on the top of the floating box and the other one was installed at the lee side of the floating box. With the inclination sensor fixed on the floating box, the motion of the floating box then can be captured.

3 MEASUREMENT METHOD

3.1 Measurement algorithm

With the above captured data, the position of the floating box in *Oxz* plane can be expressed by Figure 4. As a rigid body, the initial position of the floating box was set as I, with the distance to the top sensor was $L1_1$ and the distance to the side sensor was $L1_2$. $L1_i$ and $L2_i$ were the distance from any position *i* of the floating box to the two sensors. Once the motion occurred, the position of the floating object changes to II, III and so on. The displacements of the floating box to two sensors were updated according to the new position. Each contact line can be decomposed into horizontal and vertical components. The locations then can be expressed by Eq. (1):

$$\begin{cases} L1z_i + L2z_i - L1_1 = 0 \\ L1x_i + L2x_i - L2_1 = 0 \\ L1x_i^2 + L1z_i^2 - L1_i^2 = 0 \\ L2x_i^2 + L2z_i^2 - L2_i^2 = 0 \end{cases} \quad (1)$$

with $L1x_i$ and $L1z_i$ were the horizontal and vertical components of the $L1_i$. $L2x_i$ *and* $L2z_i$ were the horizontal and vertical components of the $L2_i$.

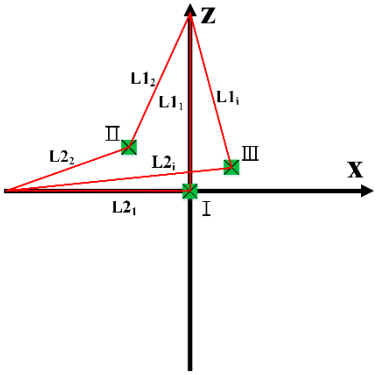

Figure 4 *Oxz* plane of the floating box motion

The horizontal and vertical displacements of the anchor point were present as $L2_x$ and $L2_y$. In Figure 5, it can be found that the above displacements were composed of translational displacement and rotational displacement. With the measured angle θ by inclination sensor, the horizontal and vertical displacement $L0_x$ and $L0_y$ caused by the rotational motion was present by $k\sin\theta$ *and* k-$k\cos\theta$ respectively, k was the distance between the anchor point and the center of gravity, θ was the rotational angle of the floating box from the initial position captured by inclination sensor. *Then the translation component of* $L1_X$ and $L1_y$ can be calculated by Eq. (2):

$$\begin{aligned} L1_x &= L2_x - L0_x \\ L1_y &= L2_y - L0_y \end{aligned} \quad (2)$$

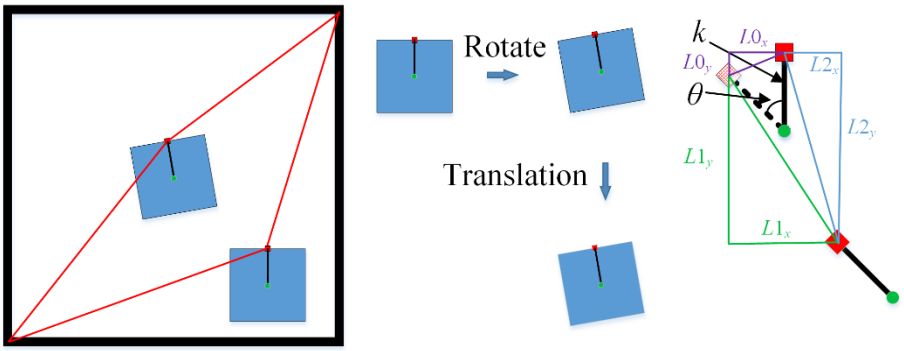

Figure 5 measurement algorithm of floating box translation motion, red rectangular was the anchor point, green ball was the center of gravity of floating object.

After the above transformation, the 2D translation and rotate motion in the *Oxz* plane can be expressed by $L1x$, $L1y$ and θ. After an iterative solution of the Eqs. (1-2), the distances from the anchor point in Figure 5 to the initial position can be obtained.

3.2 Validation

To validate the above algorithm, a experiment was carried out on a 6DoF platform (see Figure 6). The preset motion data series were input to the platform with $X(t)=A_1\sin(2\pi f_1 t)$, $Z(t)=A_2\sin(2\pi f_2 t)$ and $\theta(t)=A_3\sin(2\pi f_3 t)$, which were shown in Figure 7. A_1, A_2 and A_3 = 0.02m, 0.035m and 4°, f_1, f_2 and f_3=2.2 Hz, 1 Hz and 1.35Hz, respectively. Based on the above measurement method, the motion responses in *Oxz* plane were compared in Figure 7. The results show a good agreement between measured data and the original input

motions, with translation errors X: 4.75%, Z: 4.57% and the rotation error θ: 1.5%, respectively. It is practical to use the present method to obtain the plane motion of the floating objects.

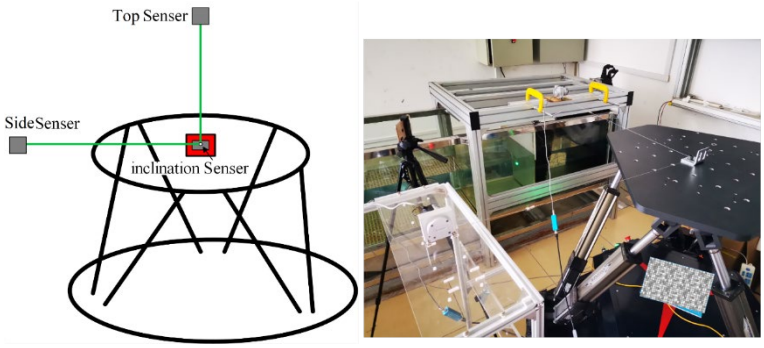

Figure 6 Arrangement of the 6DoF platform for validation

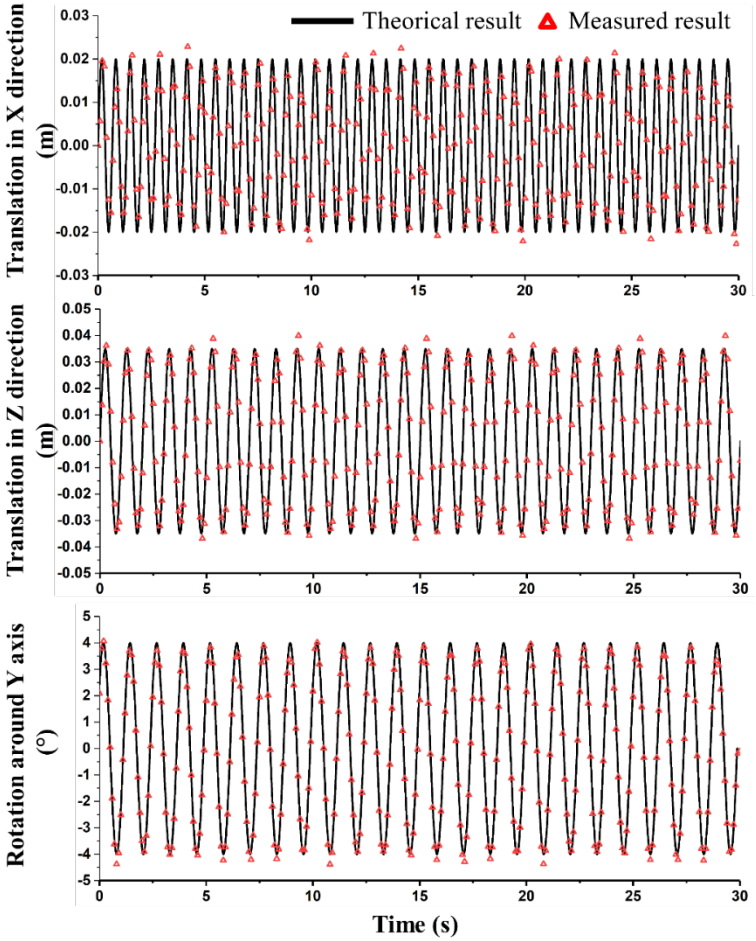

Figure 7 Validation of the motion response in *Oxz* plane.

4 RESULTS AND DISCUSSION

4.1 Problem description

The experimental test was conducted in the 2D wave channel in the Ningbo Institute of Technology. The wave tank (11m×0.6m×0.6m) was used to conduct the present experimental test. The parameters of the wave and floating box were listed in Table 1.

Table 1 Experimental setup of the wave tank.

Wave period (s)	1	**Water level (m)**	0.38
Wave height (m)	0.04	**Floating box size (m)**	0.35×0.3×0.21
Wave length (m)	1.45	**Draft (m)**	0.04
Wave steep (-)	0.0275	**Center of gravity (m)**	0.144 (without restraint device) 0.210 (with restraint device)

Based on the above measurement method, the translational displacement and the rotational angle, and the motion track of the floating box can be obtained. Then, the stability design and the motion response analysis of the floating object can be carried out.

In the following part, the effect of the restraint device was tested using the measurement algorithm in section 3.1.

4.2 Time history of the floating box motion

The time history of the translational and rotational motions of the floating box was shown in Figure 8. The results showed that the 6DoF motions of the floating box were constrained well by the restraint device. The translational displacements in X and Z directions and the rotational angle around the Y axis were allowed. The constrained and unconstrained motions in *Oxz* plane maintained a good consistency. Out of the *Oxz* plane, the motions of translation in Y axis and the rotation around X axis were well restrained. However, it should be noted that the constrained displacement in X direction was a little larger than that unconstrained. This may be because the motion in other directions was constrained, and more energy was concentrated in the wave direction. In Figure 8f, it can be found that the floating box had a significant offset under the wave action. The above phenomenon may be because there was no restoring force to restore the deflected floating box. Therefore, there was a deflection angle between the final position and the original position of the floating box.

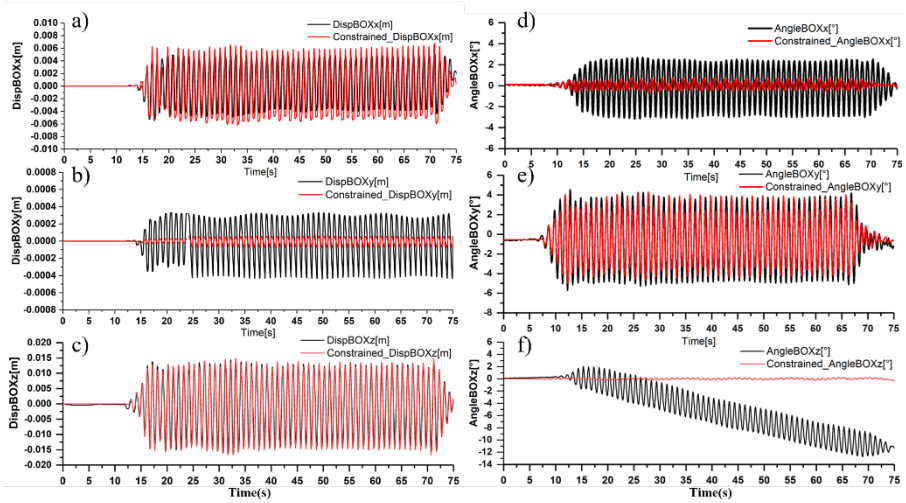

Figure 8 Translation response of the floating box in *Oxz* plane

4.3 The frequency response of the floating box motion

The motion responses of the floating box were then transferred to the frequency domain to further validate the present restraint device. It can be seen in Figure 9 that the primary frequency of the Fourier amplitude spectra was located at the wave frequency. Also, there were small motion responses at 2 and 3 times wave frequency. While, with the present restraint device, the motion responses of the floating box at the primary frequency were suppressed out of the *Oxz* plane.

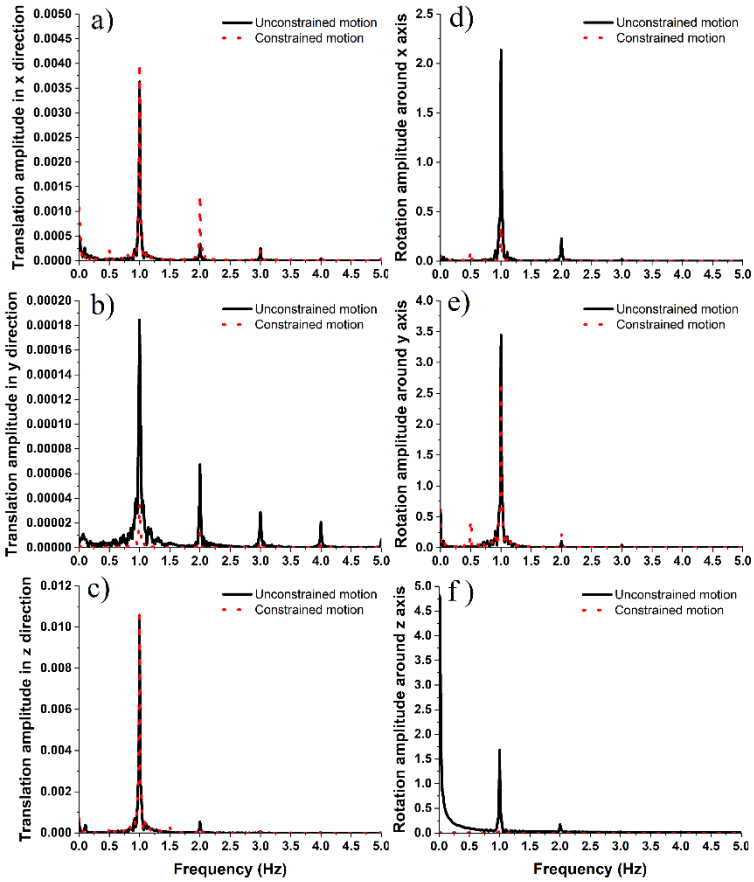

Figure 9 Fourier amplitude spectra of rotation response of the floating box in *Oxz* plane

In Figure 8f, the offset of the unconstrained rotation around the Z axis can be explained by the result in Figure 9f. There was an obvious DC component can be observed.

Due to the deflection of the floating box, the rotation response around the Z axis cannot be intuitively observed without restraint device. In order to understand the effect of the restraint device on the rotation around the Z axis, the time history of the rotation motion was filtered by a high-pass filter. The cutoff frequency was f_c=0.1 Hz so that the DC component can be filtered. Figure 10 gives the filtered time history and amplitude of the rotation motion. Also, a good suppression effect by restraint device can be obtained.

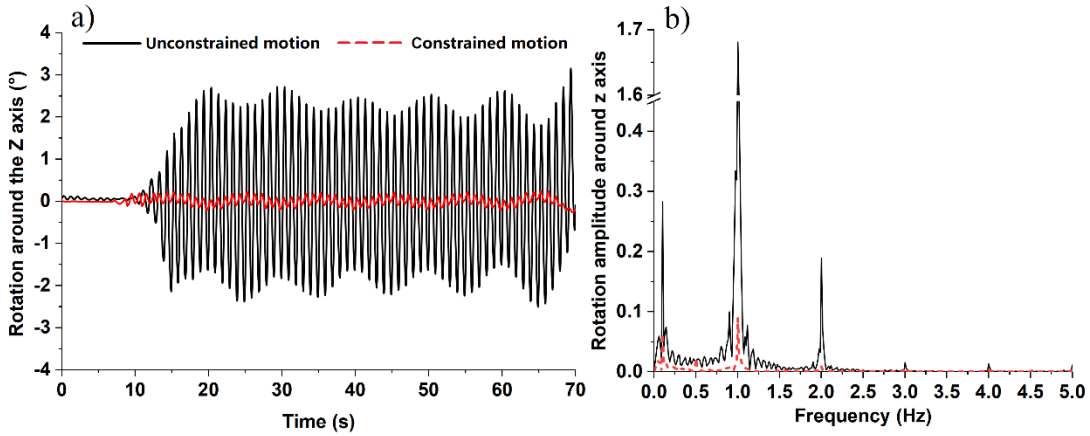

Figure 10 The time series and Fourier amplitude spectrum of the rotating motion of the floating box after high-pass filtering, with the cutoff frequency f_c=0.1 Hz

4.4 Control ability of the restraint device

Table 2 Control ability of the restraint device

Translation response	Restraint	Rotation response	Restraint
X	10.47%	**X axis**	-83.17%
Y	-80.86%	**Y axis**	-10.99%
Z	4.52%	**Z axis**	-82.71%

Finally, the control ability of the restraint device was summarized in Table 2. Out of the Oxz plane, the motion responses were reduced by about 80%. In the Oxz plane, the error between the constrained and the unconstrained motions were around 10%. Here, the increase of the motion response in X and Z direction maybe because the translation in Y direction was suppressed and then more energy was focus on these two directions. While the motion reduction around Y axis may be explained that a slight rotation around the X axis will cause a little resistance to the motion around the Y axis. And therefore, the motion response was suppressed.

5 CONCLUSIONS

In this paper, a simple restraint device for constraining the motion of the floating object in one plane was proposed and a contact measurement method for capturing the motion response of the floating object was given. Both the restraint device and the measurement method were easy to achieve. The accuracy of the present measurement method based two rope displacement sensors and one inclination sensor was more than 95%. The suppression effect of the present restraint device was about 80% and the error of motions in the allowed plane was about 10%. With the present restraint-measurement system, the hydrodynamic experiment of the floating bodies motion can be carried out in 2D plane and the motion track can be obtained directly.

ACKNOLEDGEMETNS

This study was supported by the Natural Science Foundation of China under Grant numbers 52001276, the Natural Science Foundation of Zhejiang under Grant numbers LQ19E090005 and Natural Science Foundation of Ningbo under Grant numbers 2019A610164.

REFERENCES

Bayati I, Belloli M, Ferrari D, et al. Design of a 6-DoF robotic platform for wind tunnel tests of floating wind turbines[J]. Energy Procedia, 2014, 53: 313-323.

Chen L, Sun L, Zang J, et al. Numerical study of roll motion of a 2-D floating structure in viscous flow[J]. Journal of Hydrodynamics, 2016, 28(4): 544-563.

Elsherbiny K, Tezdogan T, Kotb M, et al. Experimental analysis of the squat of ships advancing through the New Suez Canal[J]. Ocean Engineering, 2019, 178: 331-344.

Fang Y, Duan L, Han Z, et al. Numerical analysis of aerodynamic performance of a floating offshore wind turbine under pitch motion[J]. Energy, 2020, 192: 116621.

He F, Huang Z, Law A W K. Hydrodynamic performance of a rectangular floating breakwater with and without pneumatic chambers: An experimental study[J]. Ocean Engineering, 2012, 51: 16-27.

Lee S, You J M, Lee H H, et al. Experimental study on the six degree-of-freedom motions of a damaged ship floating in regular waves[J]. IEEE Journal of Oceanic Engineering, 2015, 41(1): 40-49.

Lei H, Zhou D, Bao Y, et al. Numerical simulations of the unsteady aerodynamics of a floating vertical axis wind turbine in surge motion[J]. Energy, 2017, 127: 1-17.

Mitra S, Wang C Z, Reddy J N, et al. A 3D fully coupled analysis of nonlinear sloshing and ship motion[J]. Ocean Engineering, 2012, 39: 1-13.

Pessoa J, Fonseca N, Soares C G. Numerical study of the coupled motion responses in waves of side-by-side LNG floating systems[J]. Applied Ocean Research, 2015, 51: 350-366.

8th International Conference on the Application of Physical Modelling in Coastal and Port Engineering and Science
Dec. 9th - 12th, 2020, Zhoushan, China

Preliminary Study on Tidal Defense Engineering of the Diaokou River

XIONGBO CHEN[1]LI ZHANG[1]SHENTANG DOU[2]

(1. Yellow River Engineering Consulting Co., Ltd., Zhengzhou, Henan, China, 450003; 2. Yellow River Institute of Hydraulic Research, Zhengzhou, Henan, China, 450003)

Abstract: The Diaokou River resumed running from 1964 to 1976. Now, it serves as the standby entrance course for the Yellow River, and it has a very small entrance flow rate. In the Comprehensive Control Planning for the Yellow River Estuary, a full-open scheme is used for the tidal defense engineering of the Diaokou River. That is to say, new tide embankments are not built within a certain range in front of the entrance, and the reserved width of entrance is consistent with the entrance width of Qingshuigou Course in principle. However, with the socio-economic development, most production facilities need to be protected within the tide embankment, to reduce the loss caused by storm tide disaster, and to effectively protect the life and property safety of the nation and its people. As the Qingshuigou Course can run for more than 50 years and considering that the area downstream of the branch point when the Diaokou River is running is within the tail wandering range, the space for estuary erosion shall be reserved to reduce the river length and mitigate the feedback influence on the lower reaches of the Yellow River. According to the combined utilization and study results of the Qingshuigou and the Diaokou River, the maximum discharge of the Diaokou River can be controlled at 30 m3/s. Therefore, estuary and course tide gates are built in the existing main river channel (i.e. the Sihe River), which is outside the Delta National Nature Reserve and to the south of the Zhuangcheng Highway. The tide gates are smoothly connected to the backwater dike along river. The gates have a water release capacity matched with their discharge. The gates extend to the Diaokou Wharf to the west and the tide embankment end of oil recovery team II of No. 5 pile to the east. The gates, together with the entrance road, production road and tide dam built for the oil filed, form a tide-prevention engineering system that can withstand 50-year storm tide disaster. At ordinary times, the system can delivery water, sands and nutritional ingredients to the places near the entrance, facilitating both utilization of water resource and protection of delta ecological environment.

Keywords: Diaokou River, tide gate, backwater dike along river, operation mode of course, tidal defense engineering

The Yellow River entered the sea through the Diaokou River in January 1964 and through the Qingshuigou Course in May 1976. The Diaokou River has stopped running for 44 years. At present, the river course downstream of the Luojiawuzi has a length of 49 km and a longitudinal gradient of about $1^0/_{000}$.

Within the range of the Diaokou River Course, approximate 5,300 hm^2 of cultivated lands, 3,300 hm^2 of forest lands and 6,600 hm^2 of stock farming and planting lands have been under cultivation. These lands are mainly distributed in the upper and middle reaches of the river course. In addition, 2,600 hm^2 of salt and breeding industry lands have also been put into operation, and these lands are mainly distributed on both banks of the Tiaohe River estuary.

1 Current Situation and Layout Scheme of Tidal Defense Engineering of the Diaokou River

Now, the issues about tide prevention of the reaches on the north bank of the Yellow River are relatively serious for the Dongying City, and the tide-prevention non-engineering system is incomplete. Firstly, the tidal defense engineering management organization of Dongying City is established a little late, and its personnel and auxiliary facilities both need to be further supplemented and completed. Secondly, the tidal and hydrological observation work is weak. Thirdly, there is no tide-prevention communication system or pre-warning system, lacking of effective warning before disaster, forecasting and real-time dispatching measures for post-disaster rescue.

Within the management range of the Diaokou River Course, the total length of tide embankment is 60.49 km, including 23.40 km with no slope protection and 37.09 km with stone masonry or concrete plate slope protection. SINOPEC SHENGLI OILFIELD'S offshore oilfield is arranged with open-type overflow road, entrance road (Fig. 1), entrance gate (Fig. 1) and other tide-prevention works, belonging to the partial self-protection project. The *Comprehensive Control Planning for the Yellow River Estuary* completed in 2011 does not include these works.

Fig. 1 Diaokou River Entrance Gate (Discharge Capacity of 5 m^3/s) of SINOPEC SHENGLI OILFIELD'S Entrance Road

According to the Dongying City's tide-prevention planning, works such as tide embankment, backwater dike, and tide gate are built to form a tide-prevention engineering system covering the area on the north of the Yellow River (Hekou District, Dongying Port District, and Gudong Border Dike District) and the Laizhou Bay District on the south of the Yellow River, thus reducing the 50-year storm tide disaster in the protection areas and 100-year disaster in the key areas of the tide embankments under administration of Dongying City.

2. Design of Future 100-year Course Utilization Scheme

(1) Topic of "entrance course scheme and control measures for 100-year stable Yellow River Estuary": The basic principles to be used for the Yellow River Estuary in the future are "stabilizing the estuary course, alleviating the sea bank scouring, and maintaining the regional ecology".

Stabilizing the estuary course: With comprehensive consideration of various factors, the Qingshuigou Course will be preferentially utilized in the future and the relative stability of course will be kept. The scheme maintaining the current situation and keeping the Qingshuigou Course and other courses relatively stable is in favor of the local social and economic development and ecological environmental protection. This scheme can fully utilize the potential of the Qingshuigou Course. At present, a large number of river protection works have been completed, and the investment in continuous construction of works guaranteeing running of the river is small.

Alleviating the sea bank scouring: On the premise of using the Qingshuigou Course to keep the general trend stable, giving consideration to the utilization time and mode of North Distributary can deliver the sediments from the Yellow River to the Gudong, thus alleviating the coastal erosion near Gudong. Meanwhile, the discussions on rational discharge capacity and utilization mode of Qingshuigou Course can reduce the coastal erosion near the Qingshuigou Course entrance.

Maintaining the regional ecology: The ecological water transfer channel function of the courses or branches that will not be put into use in a short term shall be improved to ensure that they have constantly flowing water with a certain discharge capacity as much as possible. The course utilization scheme shall maintain the basic water demand of the regional ecology.

(2) The emphasis is laid on "single course with planned river diversion" and "multiple courses in use at the same time", to complete the design of future 100-year course utilization option, clearly determine the development basis and index of option, and analyze both advantages and disadvantages of each utilization mode. See Tables 1~2 for details.

Table 1 "Single Course with Planned River Diversion" Option

Channeling Mode	Diversion Condition	Description	Analysis of Advantages and Disadvantages
Single course: 1. Use the Qingshuigou Course (existing Qing 8 Distributary, North Distributary, and original river course) and the Diaokou River in turns. 2. Keep a certain environmental flow for the courses not in use.	Option 1: Keep the water level at 12m when the discharge of the west estuary is 10,000 m^3/s.	In 2018, the water level was 10.87m when the discharge of the west estuary (II) station is 10,000 m^3/s. Therefore, the Qingshuigou Course has a relatively large channeling potential. Upon analysis, the Qingshuigou Course can be used for another 50 years and more.	Advantages: 1. Fully use the existing course functions. 2. Put the North Distributary in use in good time to allocate sediments, thus alleviating the scouring of Gudong border dike. 3. Ensure that the courses not in use have constantly flowing water and protect the ecological environment of key areas at the estuary. Disadvantages: 1. Wandering of courses is bad for the future layout of local productivity. 2. It cannot effectively protect the discharge and sediment flushing functions of the standby course of the Diaokou River in a short term.
	Option 2: Meet the stability index conditions of river course (results of Topics 1 and 2).	According to the relevant indexes of the tail river course, automatically judge the river course status and the time of diversion.	

Table 2 "Multiple Courses in Use at the Same Time" Option

Channeling Mode	Diversion Condition	Description	Analysis of Advantages and Disadvantages
1. Arrange the control works near the west estuary, and excavate the Diaokou River course. 2. Simultaneously use the Qingshuigou Course (existing Qing 8	Option 3: Based on a relatively small discharge capacity, perform the flood diversion as per the discharge of Diaokou River being 1,500 m^3/s in June ~ October (river discharge: over 3,000 m^3/s), and keep the constantly flow water with a discharge of 30 m^3/s in other time frames.	According to the studies, 1,500 m^3/s is the critical discharge for flushing of entrance course, and the discharge of flood diversion channel should not be too small.	Advantages: 1. It can alleviate the flood control pressure of estuaries and reaches in a short term, and realize the optimal dispatching of sea water and sediments. 2. It can protect the discharge and sediment flushing capacity of standby course of the Diaokou River, and improve both northern ecological environment and bank line of the delta area.

Distributary, North Distributary, and original river course) and the Diaokou River course, which are at the entrance.	Option 4: Perform the flood diversion as per the maximum discharge of Diaokou River being 3,000 m^3/s and water diversion ratio being 50% in June ~ October (river discharge: over 3,000 m^3/s), and keep the constantly flow water with a discharge of 30 m^3/s in other time frames.	An extremely large water diversion amount may affect the water taking downstream of the Qingshuigou Course water diversion port, thus causing river course sedimentation. Therefore, the flood diversion discharge of the Diaokou River is controlled not more than 3,000 m^3/s.	3. It can prolong the service life of the existing Qingshuigou Course. Disadvantages: 1. The demand of water and sediments diversion is small, so the flood diversion will not be performed often. 2. The quantities are large, so the workload of operation management and maintenance tasks increases. 3. The project influences the river course and the regional productivity layout.

(3) Calculated Results of Channeling Options

With the water and sediment series - "300 million t" of water and sediments coming from four stations as an example, the average annual sediment runoff of the Lijin Station in the water and sediment series is 200 million t/year. According to the calculated results, in the series years (100 years) mentioned in Option 1, the annual river course sedimentation is 3.6 billion t; 16.4 billion t of sediments are delivered to the estuary, including 20% of them delivered to the open seas; about 13.1 billion t (12.0 billion m^3) of sediments settle on the entrance and form the land, including 3.1 billion m^3 of deposits on the Qing 8 Distributary reaches of the Qingshuigou Course, and 8.9 billion m^3 of deposits on the North Distributary.

According to Fig. 2, the existing Qing 8 Distributary reaches operate for the 32nd year and the length of river downstream of the west estuary is 80 km. The North Distributary is then put into operation instead of the former. The North Distributary operate for the end of the 100th year and the length of river course is 69 km. The service life of the North Distributary is not end, and it can still be put into use.

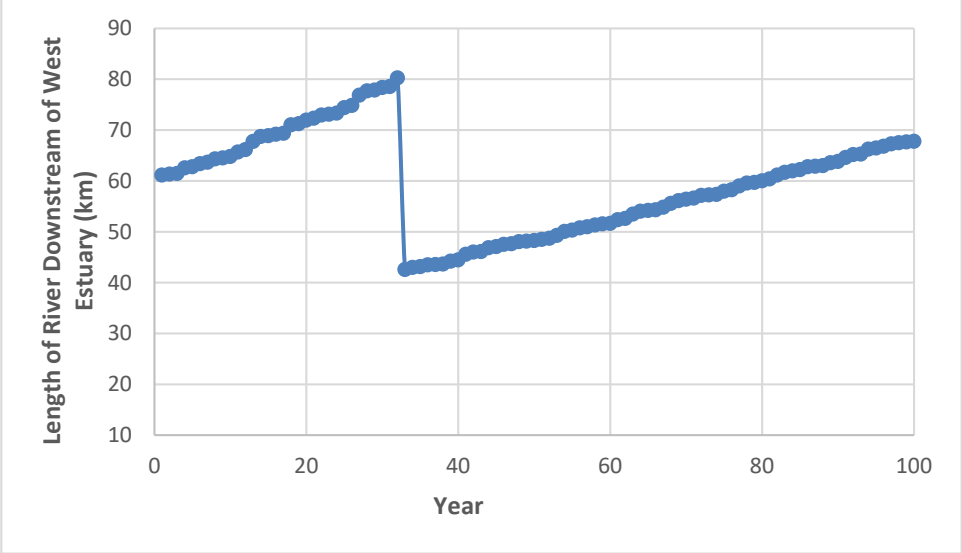

Fig. 2 Utilization of "300 Million t" Series Course

The Option 1 or 2 is better because the Qingshuigou Course can be used for more than another 100 years. At this stage, the discharge of the Diaokou River shall be controlled within 30 m^3/s.

3 Analysis of Tide-prevention Entrance Width of the Diaokou River

3.1 Analysis of Industrial and Agricultural Facilities within the Management Range of the Diaokou River

There are densely distributed oil wells and longitudinal and transverse roads inside the embankment lines within the management range of the Diaokou River. Vast stretches of WTGSs are distributed near the

coast. The Donggang Expressway, S310 and S312 provincial highways, and the Zhuangcheng Highway cross the planned course. In addition, a large number of buildings and vast stretches of forests and salt pans are distributed inside the planned embankment lines. According to the statistics, there are 175 big and small buildings inside the planned embankment lines, with a total occupied area of 7.388 million m2.

Outside the planned embankment lines, a large number of villages, oil fields, factories, agricultural facilities, and other facilities are distributed, involving the Hekou District, Lijin County, Kenli County, Bohai Farm, Dongying Port Economic Development Zone, and Shengli Oilfield. The area mainly covers the Bohai Farm Headquarters site, Diaokou Country, Lijin Coastal New Region, Dongying Port Economic Development Zone, 16 villages, and 30 main production and living facilities (dominated by oil fields, schools and factories), with a total occupied area of 20.524 million m2.

With the socio-economic development, most production facilities need to be protected within the tide embankment, to reduce the loss caused by storm tide disaster, and to effectively protect the life and property safety of the nation and its people.

3.2 Operation Practice of the Diaokou River

After the Yellow River migrated to the Qingshuigou Course in 1976, the original river course area of the Yellow River was continuously lack of water and sediments makeup, and eroded along the sea beach. Inwelling accelerated the salinization of soils, causing the land vegetation subject to retrogressive succession and severely endangering the safety of wetlands ecosystem.

During the water and sediments dispatching from the Yellow River in June ~ July 2010, the amount of water diverted to the Diaokou River was 36.28 million m^3 via gravity diversion and pumping vessel. The ecological water compensation was performed in most years after this period, and the maximum discharge was 30 m^3/s. See Table 3 for details.

Table 3 Statistics on Ecological Water Compensation for Wetlands along Entrance Course

Year	Discharge of Lijin during Water Compensation (m^3/s)	Days (d) of Water Diversion	Water Diversion of Qingshuigou Course (10^4 m^3)	Water Diversion of Diaokou River (10^4 m^3)	Total Water Diversion (10^4 m^3)
2008	3387	11	1356		1356
2009	3366	10	1508		1508
2010	3560	12.6	2041	3628	5669
2011	2689	15	2248	3619	5867
2012	2763	19	3036	3285	6321
2013	3300	19	2156	2620	4776
2014	2600	10	803	1325	2128
2015	2430	16	1679	1487	3165
2016	No water compensation				

2017	No water compensation				
2018	3500		2400	500	2900
2019		32			6370

3.3 Analysis of Stable River Width

The C.T.Алтунин formula is used to calculate the stable river width. The C.T.Алтунин formula is shown below.

$$B=AQ^{0.5}/J^{0.2}$$

Where, B means the width (m) of stable water flow, A means the coefficient that is 0.64~1.15 for a meandering channel, Q means the channel forming discharge that is taken as the maximum discharge capacity (30 m3/s) of the Diaokou River mentioned in Option 1, and J means the average longitudinal gradient (1.00/000) of river course.

According to the C.T.Алтунин formula, the stable river width is 22.1m ~ 39.7m.

In the Hydraulic Energy Manual, Tu Qihua and Zhang Junhua make statistics for and analysis of the hydraulic elements of sand riverbeds of both relatively small rivers and reservoirs, and obtain the following:

$$B=(17.5\sim25.8)Q^{0.31}$$

According to the Tu Qihua Formula, the stable river width is 50.2m~74.0m.

3.4 Determination of Entrance Width of the Diaokou River

In April 2019, a site survey was carried out for the Diaokou River, involving the bridge (about 45m long) on the mainstream (the Sihe River) of the Diaokou River at the Zhuangxi ~ Chengdong Highway, as shown in Fig. 3. The measured value is approximate to the calculated values obtained from the C.T.Алтунин formula and the Tu Qihua Formula. Considering that the discharge of the Diaokou River is controlled by the pump output (or flow output by gravity) of the head structure of Cuijiazhuang River Control Works, the current maximum discharge capacity of the Luojiawuzi gate is 30 m^3/s, and the Zhuangxi ~ Chengdong highway bridge will not be renovated temporarily, it can be determined that the entrance width of the Diaokou River is 45m.

Fig. 3 Sihe River Bridge on the Diaokou River at the Zhuangxi ~ Chengdong Highway

Therefore, according to the analysis of information that the Qingshuigou Course can still be used for a long time, the industrial and agricultural facilities within the management range of the Diaokou River need to be protected, and the maximum discharge of ecological water compensation after 2010 is 30 m^3/s, the entrance width of the Diaokou River is considered as 45m for the construction of ecological gate, which is equivalent to that of the Sihe River bridge at the Zhuangxi ~ Chengdong Highway.

4 Study on Layout of Tidal Defense Engineering of the Diaokou River

According to the *Comprehensive Control Planning for the Yellow River Estuary*, the main comments on the tide-prevention planning for the Diaokou River Course are as follows: The full-open layout scheme is adopted. The reserved width of entrance is consistent with the entrance width of Qingshuigou Course in principle. Both reserved width of entrance and scale of tidal defense engineering will be determined at the next stage.

According to the preliminary study, the basic layout of tidal defense engineering of the Diaokou River is as follows: The estuary and course tide gates are built in the existing main river channel (i.e. the Sihe River), which is outside the Delta National Nature Reserve and to the south of the Zhuangcheng Highway. The tide gates are smoothly connected to the backwater dike along river. The gates have a water release capacity matched with their discharge. The estuary and course tide gates and the backwater dike works are built as per the discharge (30 m3/s) of the Diaokou River. The gates extend to the Diaokou Wharf to the west and the tide embankment end of oil recovery team II of No. 5 pile to the east. The estuary is not closed but built with a tide gate and backwater dike along river course. In the aspect of the construction standards, the seawalls near the Diaokou River are built as per the 50-year standard. The seawalls, together with the entrance road, production road and tide dam built for the oil filed, form a tide-prevention engineering system that can withstand 50-year storm tide disaster. At ordinary times, the system can delivery water, sands and nutritional ingredients to the places near the entrance, facilitating both utilization of water resource and protection of delta ecological environment, as shown in Fig. 4.

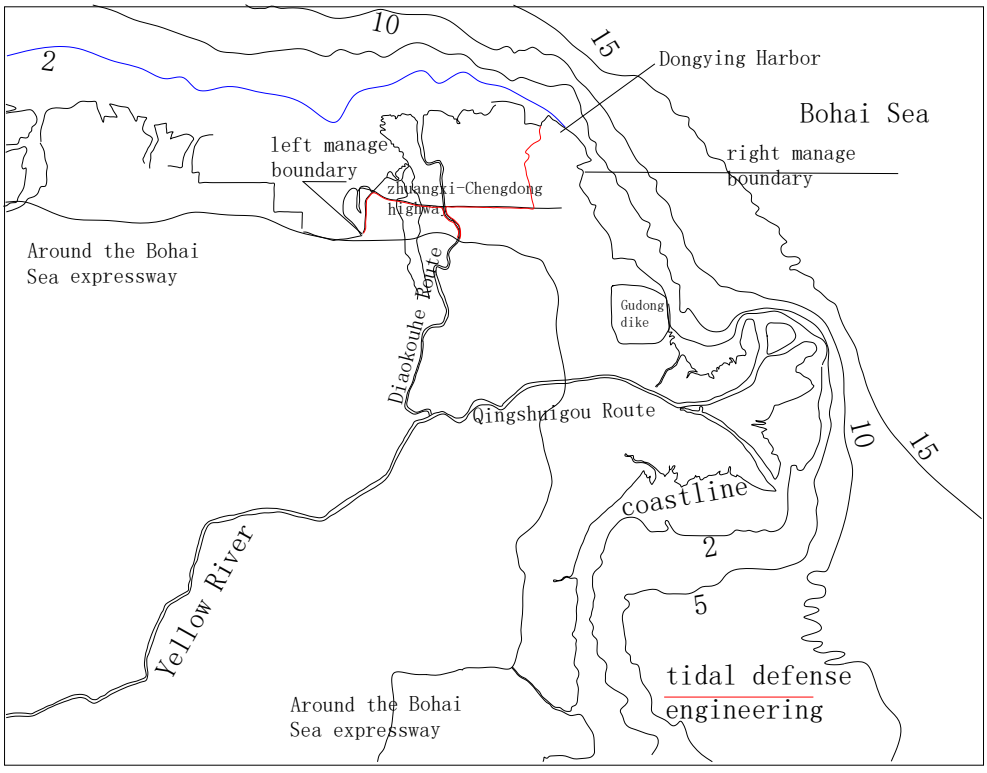

Fig. 4 Layout of Tidal Defense Engineering of the Diaokou River

The Flood Control Evaluation on the Diaokou River Course Bridge at the Yellow River and the Dongying Section of the Wudi ~ Laizhou Coastal Highway completed by YREC in 2018 analyzes the wandering range of the Diaokou River Course in use, deems that the Circum-Bohai Sea Expressway Bridge will be built near the Luo 9 section, and considers it as the starting point of river fork wandering after the Diaokou River is put into operation again, like the Qing 7 section of the Qingshuigou Course. Considering that the river regime wandering upstream of the highway upon the completion of the Circum-Bohai Sea Expressway will be more controlled artificially, the peak of backwater dike along river is preliminarily determined as the Diaokou River

Bridge of the Circum-Bohai Sea Expressway.

In addition, after the system is established, it will not affect the normal operation of the existing Dongying Port or reduce the natural ecological coastline of Dongying City, in conformity with the ecological protection and high-quality development concepts of the Yellow River Basin.

5 Conclusions

The conclusion that the Diaokou River with a discharge capacity of 30 m3/s is better is made by analyzing the "current situation and layout scheme of tidal defense engineering of the Diaokou River" and adopting the "design of future 100-year course utilization scheme". The recommended width of ecological gate is proposed by analyzing the "industrial and agricultural facilities within the management range of the Diaokou River". In addition, the layout scheme of tidal defense engineering of the Diaokou River is put forward.

(1) With the socio-economic development, most production facilities need to be protected within the tide embankment. Therefore, the study on the tidal defense engineering of the Diaokou River is necessary.

(2) The tidal defense engineering can be a semi-closed system, extending from the Diaokou Wharf to the tide embankment end of oil recovery team II of No. 5 pile. The ecological gates are built in the existing mainstream (the Sihe River) of the Diaokou River. The gates have a water release capacity matched with their discharge. The entrance width is considered as 45m for analysis. The construction is performed based on the 50-year standard.

(3) According to the river regime analysis and the actual situation of project construction in the river course, it is preliminarily determined that the peak of backwater dike along river is the Diaokou River Bridge of the Circum-Bohai Sea Expressway.

Fund project: supported by Topic Six - "Entrance Course Scheme and Control Measures for 100-Year Stable Yellow River Estuary" of National Key Research and Development Program - "Comprehensive Control and Study on the Yellow River Estuary Evolution and Course Stabilization" (No.: 2017YFC0405506)

REFERENCES

Ding Dafa, An Cuihua and Yao Tongshan et al. Comprehensive Control Planning for the Yellow River Estuary [R]. Yellow River Engineering Consulting Co., Ltd., Zhengzhou, October 2011: 50~106.

Qian Yu, Chen Xiongbo and Lin Dong et al. Flood Control Evaluation on the Diaokou River Course Bridge at the Yellow River and the Dongying Section of the Wudi ~ Laizhou Coastal Highway [R]. Yellow River Engineering Consulting Co., Ltd., Zhengzhou, May 2018: 31~50.

An Cuihua, Tang Meiying and Chen Xiongbo et al. Issues and Countermeasures about Comprehensive Control of the Yellow River Estuary [J]. YELLOW RIVER, 2013, 35(10): 60 -62.

Tang Meiying, Qian Yu and Peng Yanming et al. Development and Management Planning for Beach on Estuaries and Coastal Areas of the Yellow River [R]. Yellow River Engineering Consulting Co., Ltd., Zhengzhou, July 2013.

Chen Xiongbo, Chen Songwei and Dou Shentang et al. Current Situation and Trend of Study on Utilization Mode of Entrance Course at the Yellow River Estuary [J]. YELLOW RIVER, 2018. 49(10): 10-15.

Brief introduction of author: Chen Xiongbo (1973-), male, born in Tianmen Hubei, professor level senior engineer, mainly engaged in study on river dynamics numerical computation Mobile phone: 13838385309; E-mail: cxb73001@sina.com

8th International Conference on the Application of Physical Modelling in Coastal and Port Engineering and Science
Dec. 9th - 12th, 2020, Zhoushan, China

Preliminary Study on the Utilization and High-quality Development of Tidal Flat Resources in the Yellow River Estuary

LI ZHANG, JUAN JING, YUANLU YUN, JIWEI LI & YANMING PENG

(Yellow River Engineering Consulting Co., Ltd., Zhengzhou, Henan, China, 450003, alrps@163.com)

Abstract: The Yellow River Estuary is an important ecologically sensitive area and ecological protection area, and the tidal flats in the estuary are an important natural resource. The regulation of the Yellow River Estuary is of prominent strategic importance in the overall ecological protection and high-quality development of the river basin. Based on the analysis of the current situation of tidal flat resources in the estuary, this paper discusses the ways to utilize the tidal flat resources and proposes to divide function zones of the tidal flats, to realize rational utilization, scientific protection and effective management of the coastal tidal flat resources in the estuary and promote sustainable socio-economic development of the region and coordinated development of the economic society, resources and the environment.

Keywords: Yellow River Estuary; utilization of tidal flat resources; high-quality development

The lower reaches of the Yellow River flow through the North China Plain and flow into the Bohai Sea in Kenli County, Shandong Province. The Yellow River Estuary is located on the southwest coast of the Bohai Sea, between the Bohai Bay and Laizhou Bay. The Yellow River Estuary refers to the fan-shaped area and the determined sand-bearing area with Ninghai, Kenli County, Dongying City as the base point, up to Zhimaigou Estuary in the south and Tuhai Estuary in the north[1]. The Bohai Sea is a semi-closed inland sea, with only the narrow Bohai Strait (approximately 106 km wide) between the Liaodong Peninsula and the Shandong Peninsula connected with the Yellow Sea. The rest is surrounded by land, with weak influence of ocean currents and relatively significant influence of temperate monsoon climate. The Bohai Sea consists of Bohai Bay, Laizhou Bay, Liaodong Bay and the central area, and is a shallow sea facing northeast-southwest. The bottom elevation of the sea slopes from the three bays towards the center of the Bohai Sea. The terrain is flat and the average water depth is about 18m. Twenty-six percent of the sea area has a water depth of less than 10m and the deepest part of the central basin has a water depth of about 30m. The water depth near the Laotieshan Channel of the Strait is 80m.

The land part of the tidal flats of the Yellow River Estuary is bounded by the tide embankment or by the high tide line (if there is no tide embankment). The sea part is bounded by 3m isobath (elevation of the Yellow Sea). According to the calculated tidal flat resources along the Yellow River Delta by using the bathymetric chart and the topographic map of the coastal area of the Yellow River Delta, the current total area of the tidal flats above the mean low tide line is 802.74 km^2, and the total area above the 3m isobath is 2,380.67 km^2[2]. The water surface depth in the Yellow River Delta area is relatively shallow, and the seabed is relatively flat, but there are still significant differences in elevation among different bank sections. The sea area outside the Shenxiangou Mouth in the central part is the deepest area, with the 5m, 10m, and 15m isobaths being 3.3 km, 7.5 km, and 17 km from the shore. The maximum water depth is up to 20m.

The Yellow River Delta is an estuarine delta with the best ecological status and the most typical characteristics and of the most significant protection significance among the existing river estuaries in China[3]. The Shandong Yellow River Delta Wetland National Nature Reserve was set up there. The Yellow River Estuary is a depositary estuary with much sediment, weak tide and frequent wandering of the river course. Compared with the estuaries of other major rivers at home and abroad, the Yellow River Estuary is of unique complexity. The Yellow River features little incoming water, much sediment, and weak ocean dynamics. Therefore, it is not possible to transport the sediment to the open sea smoothly, resulting in frequent occurrence of estuary extension, wandering, deposition, and diversion change for a long time. The continuous change of the entrance course into the sea has a negative effect not only on the deposition and wandering of the lower reaches of the Yellow River, but also on the socio-economic development of the estuary area. Under the dual effects of human activities and climate change, the habitats of the tidal flats and wetlands in the Yellow River Delta have suffered long-term damage[4].

1 Historical Evolution of the Estuary

After the dyke breach of the Yellow River at Tongwaxiang in 1855, it was diverted from the Huang-Huai confluence to the current course into the Bohai Sea. The section below Yuwa is known as the estuary section. The Yellow River is a river with much sediment. A large amount of sediment from the Loess Plateau in the middle reaches flows into the estuary area. The river bottom gradient becomes gentle and the sediment cannot

be transported by the ocean dynamics. The sediment-carrying capacity at the junction of the river and the sea drops suddenly. Except for a small part of sediment which is transported to the deep sea area by tidal currents, sea currents, and residual currents, most of the rest sediment is deposited in the coastal area, filling the sea into fields and leading to continuous deposition and expansion of the estuary. The deposition and extension at the river channel tail causes the erosion basis of the channel to be uplifted continually. The gradient of the reaches near the estuary decreases, the sediment-carrying capacity becomes weaker, and the sediment is deposited at the bottom, uplifting the riverbed deposition and the erosion basis of the lower boundary of the adjacent upper channel. Continuous backward deposition effect is transmitted to the upper reaches of the estuary, which intensifies the trend of secondary elevated rivers downstream and increases the flood control pressure of the river channel. The long-term deposition and extension of the estuary slows down the flow velocity of the lower reaches, and at the same time, increases the water level of the channel and relatively shallows the main river channel, resulting in small beaches on the Yellow River and above-ground rivers constrained by the productive embankment of the beach lip. At the same time, it causes the problem of sediment deposition, and raises the main river channel to form secondary elevated rivers. The current entrance course into the sea is the Qingshuigou course artificially diverted in 1976. The channel is 65.0 km long and has been running for more than 40 years. The continuous extension, deposition and change of the Yellow River Estuary will change the entrance course into the sea accordingly. If no engineering measures are taken, the current entrance course into the sea will be blocked by deposition and the estuary will be diverted, affecting the lower reaches of the Yellow River.

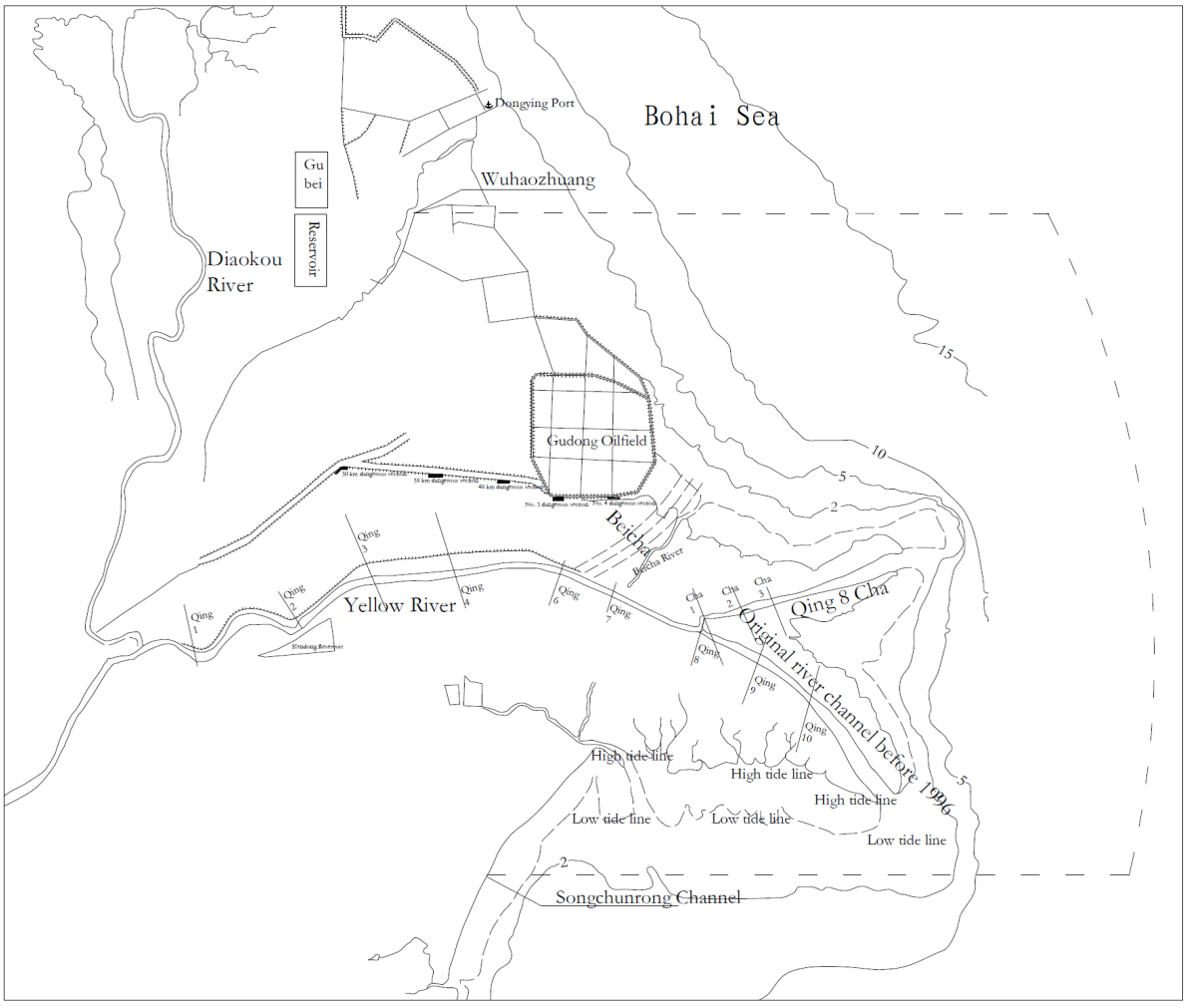

Fig. 1 Schematic Diagram of Qingshuigou Course at the Yellow River Estuary

Less water and more sediment in the Yellow River is the main reason for the instability of the entrance course into the sea, and the incoming water and sediment in the estuary are affected by the natural conditions and human activities in the Yellow River Basin. The recent Yellow River Delta starts from Yuwa. The coastal sections of the coastal area are largely subject to irregular semi-diurnal tides. Irregular diurnal tides only appear in the surrounding coastal sections of the Shenxiangou Mouth. The farther away from the Shenxiangou, the stronger the characteristics of semi-diurnal tides are. At present, the Qingshuigou Mouth shows characteristics

of semi-diurnal tides. The tidal range varies from place to place. The tidal range is the smallest in the vicinity of the tidal wave in the north of Shenxiangou - only 0.4m. The tidal range tends to increase southward along the eastern shoreline of the delta and westward along the northern shoreline of the delta. The tidal range is 1.6 ~ 2.0m in the Xiaoqing Estuary and the Tuhai Estuary.

Due to the synergistic superimposed effect of many dynamic systems such as ocean, river, land and human production activities, the Yellow River Delta interface has been formed where various energy and material systems converge. Meanwhile, due to the relatively late land formation, the development duration of soil and vegetation is relatively short, leading to a fragile ecological environment in the estuary area. The Yellow River Estuary area borders the Shandong Peninsula in the south and Beijing-Tianjin-Tanggu in the north. It is a transition belt between the Yellow River Economic Belt and the Circum-Bohai Sea Economic Zone. It is also an important sea-land link between the Northeast and Central Plains Economic Zones. The particularity of the Yellow River Estuary shows that it is one of the most complicated and difficult to control estuaries in the world. The estuary area is abundant in natural elements such as land, oil, and ocean, and has great potential for exploitation. There are 5 villages and nearly 1,000 residents living in the Yellow River beach. There are more than 200,000 *mu* of cultivated land and some related facilities of Shengli Oilfield in the beach. The scarcity of water resources and the fragile ecological environment severely restrict the economic development of the region.

2 Utilization of Tidal Flat Resources

The coastal tidal flats in the estuary have the functions of wave dissipation, flood detention, storm surge buffering, seawall stabilization, biodiversity maintenance, and environmental pollution degradation. They are extremely important wetland resources and are national reserve land resources of strategic significance[5]. The ecological system established in the marine tidal flats and wetlands has the highest ecological service value per unit area, and has important ecological functions such as water purification, food chain maintenance, flood and tide storage, local climate regulation, and cultural leisure. Tidal flats are a transition zone from ocean to land and have the natural characteristics of both ocean and land. Tidal flats are suitable for a variety of creatures to inhabit and can provide a suitable living space for plants and animals. Tidal flats can continuously supply food, salt, and energy, and build a springboard and platform for human beings to expand into the sea.

The tidal flats of the Yellow River Delta can be classified into coastal and riparian tidal flats. The riparian tidal flats are distributed within the area constrained by the embankments on both banks of the Yellow River below Xihekou. Coastal tidal flats are mainly distributed in the area from Zhimaigou in the south to Tuhai Estuary in the north, involving the west bank of Laizhou Bay and the south bank of Bohai Bay. The area of tidal flats is distributed along the shoreline. The section from Tuhai Estuary to the northern right boundary of the nature reserve has the largest area - 1,310.33 km^2 (3m isobath), accounting for 55.04% of the total tidal flat area. The section from Xiaodao Estuary to Zhimaigou Mouth has the smallest area - 222.56 km^2 (3m isobath), accounting for 9.35% of the total tidal flat area. The amount and distribution of tidal flat resources in the Yellow River Estuary are shown in Table 1.

Table 1 Current Situation and Distribution Statistics of Tidal Flat Resources Unit: km^2

Bank Section No.	Bank Section	Within Low Tide Line	Within 3m Isobath
I	From Tuhai River Estuary to the northern right boundary of the Yellow River Delta Reserve	586.30	1310.33
II	From the northern right boundary of the Yellow River Delta Reserve to Xiaodao River Estuary	133.01	847.78
III	From Xiaodao River Estuary to Zhimaigou Estuary	83.43	222.56
Total		802.74	2380.67

The riparian tidal flats below Xihekou of the Yellow River are newly deposited land after the Yellow River

was changed to the Qingshuigou course in 1976. They are within the range of the Yellow River Delta Nature Reserve[6]. There are five national special marine reserves in the sea area. The estuary delta has extensive land and ocean resources. There are vast land resources to be developed in the land area, and there are infrastructures such as fishing ports, seaports, wharves, and oil fields in the intertidal zone. In addition, salt pans and breeding ponds are scattered. At present, coastal tidal flats and estuarine waters near the Yellow River Estuary are classified as the Shandong Yellow River Delta National Nature Reserve and the Dongying Yellow River Estuary Special Ecological Marine Reserve. There are a few sea-utilization projects in the experimental area of the nature reserve and the environmental improvement area of the special marine reserve.

The current development and utilization methods of the tidal flat resources in the Yellow River Delta mainly include marine aquaculture, oil exploitation, ports and fishing ports, salt production, a small amount of cultivated land, and nature reserves. The Yellow River Delta has vast tidal flats and shallow seas. The Yellow River deposition plain is located in the supratidal zone, with a large intertidal zone area. The tidal flats in the subtidal zone are gentle and flat, with a relatively small gradient. The subtidal zone features large freshwater runoff, superior water quality and abundant food organism resources for fish, shrimp, crabs and shellfish. It is a good breeding site for such creatures. The coastal aquatic resources are rich in species and huge in amount. The land area and sea area under the jurisdiction of the Yellow River Delta is abundant in oil and gas resources. It is one of the key exploration and exploitation areas of Shengli Oilfield, the second largest oilfield in China. The offshore oilfield of Shengli Oilfield is mainly composed of the offshore oilfields of three oil production plants (Gudong, Zhuangxi and Hekou Oil Production Plants).

3 High-quality Development Model

The problems in the utilization of tidal flat resources in the estuary mainly include large-scale development and environmental fragility, inconsistency between the existing land utilization structure and land suitability, and shortage of water resources. The development of marine aquaculture industry causes intensified soil salinization, shallower groundwater depth, higher salinity, storm surges, etc., resulting in serious environmental pollution and a decrease in biological population. The petrochemical enterprises along the coastal tidal flats discharge industrial "three wastes", and the harmful substances from the land enter the Bohai Sea, destroying the weak ecological environment in the estuary and coastal areas. Dongying City is short of water resources. The annual rainfall of the Yellow River Delta is only 500 mm. The water supply mainly depends on the Yellow River, the eastern route of the South-to-North Water Diversion Project, the Xiaoqing River, and Zhimaigou, which limits the development of industry and agriculture and aggravates the impact of ecological damage.

The regulation of the Yellow River focuses on protection, with regulation as a key point. Considering the functional orientation, natural conditions, socio-economic development needs, and development and control of tidal flat resources, the tidal flats are classified into different characteristic areas from the perspective of water ecological environment protection, smooth entrance course into the sea, flood (tide) control safety in the estuary, water supply safety, and other water management contents, to determine their development and utilization conditions and management objectives, so as to meet the relevant requirements for seawall safety, Yellow River Estuary safety, sustainable development of tidal flat resources, and ecological protection, and provide the basis for scientific management.

According to the class definition and division principles of water conservancy function zones, as well as the current situation of the development and utilization of tidal flat resources, the coastal tidal flats in the Yellow River Estuary are classified into four categories: protected zone, reserve zone, controlled utilization zone, and development and utilization zone. According to the planning scope, the land part is bounded by the tide embankment or by the high tide line (if there is no tide embankment). The sea part is bounded by 3m isobath. The tidal flat protected zone includes the Qingshuigou course currently in operation for the Yellow River, the standby entrance course into the sea - Diaokou River course, and the national nature reserve. The tidal flat reserve zone includes the possible prospective standby entrance course into the sea - Maxin River course and Shibahu course, as well as the Yongfeng River and Zhanli River estuaries in the port-free area. The controlled utilization zone includes Binzhou Port area (in the east of the central line of Tuhan Estuary), Diaokou Port area (Caoqiaogou and Tiaohe Estuary), Guangli Port area (Zhimaigou, Yihong River, and Guangli River Estuary), and the areas other than estuary, course and port area. The development and utilization zone is Dongying Port area.

The core area of the national nature reserve is the tidal flat protected zone. Top priority is given to the protection of the Qingshuigou course currently in operation for the Yellow River and the standby Diaokou River course. Part of the management scope of Qingshuigou course and Diaokou River course is classified as tidal flat protected zone. The development and utilization zone refers to the zone where the development and utilization activities have no or slight impact on such aspects as the safety of water supply in the coastal tidal

flats, the smooth flow of the Yellow River into the sea, the safety of coastal flood (tide) control, and the regional water ecological environment . Protected zone and reserve zone are mainly for ecological protection and restoration, while controlled utilization zone and development and utilization zone are used for proper industrial construction. The industry should be based on the water situation to develop a green economy.

4 Conclusion

The Yellow River Delta should be properly protected to promote the health of river ecosystems and increase biodiversity. The principles of scientific planning, overall arrangement, highlighting key points, step-by-step advancement, subjecting regulation to development, and serving development with regulation should be adhered to realize a high degree of unity in ecological, economic and social benefits and the ultimate goal of sustainable development. The strictest system for ecological environment protection should be implemented to coordinate the holistic approach to conserving mountains, rivers, forests, farmlands, lakes, and grasslands. Restoration of the wetland ecosystem in the Yellow River Delta, zoning planning, and effective and standardized management of tidal flat development and regulation should be carried out to realize the orderly, rational, scientific development and utilization of coastal tidal flats, ensure the safety of flood (tide) control, drainage, navigation, ecological environment in the Yellow River Estuary area and the safe operation of important national economic facilities, and promote the sustainable development of the regional economy and society.

REFERENCES

Ding Dafa, An Cuihua, Yao Tongshan, et. al. Comprehensive Control Planning for Yellow River Estuary [R]. Zhengzhou: Yellow River Engineering Consulting Co., Ltd., 2011.

Tang Meiying, Qian Yu, Peng Yanming, et al. Development and Management Planning for Tidal Flats on Estuaries and Coastal Areas of the Yellow River [R]. Zhengzhou: Yellow River Engineering Consulting Co., Ltd., 2013.

Wang Jianhua, Hu Peng and Gong Jiaguo. Implementation of Yellow River Estuary Protection to Promote the Construction of Ecological Civilization in the Yellow River Basin [J]. Yellow River, 2019, 41 (10): 8-11.

Li Huai, Yan Baixing, Li Haiyan, et al. Distribution Characteristics of Nitrogen and Phosphorus in Wetland Soil in the Typical Salt Water and Freshwater Interaction Area of the Yellow River Estuary [J]. Wetland Science, 2018, 16 (5): 679-683.

Cao Duoqian, Yang Yonglin. Some Thoughts on the Development and Construction Management of Tidal Flats in the Haihe River Basin [J]. Haihe Water Resources, 2017 (3): 30-32, 35.

Chen Xiongbo, Qiu Weiguo and Liu Juan. Research on the "One Water, Three Streams" Flow Pattern of the Yellow River Estuary [J]. Coastal Engineering, 38 (3), 2019: 194-202

Zhang Li (1982 -), male, native of Tanghe County, Henan Province, engineer, his major research direction is water conservancy project planning. Mobile phone: 13783699810, E-mail: alrps@163.com

Fund Project: *Research on and Application of Key Technologies for Protection and Efficient Utilization of Coastal Tidal Flat Resources in the Estuary* (No. 2018YFC0407505) founded by National Key Research and Development Project.

8th International Conference on the Application of Physical Modelling in Coastal and Port Engineering and Science
Dec. 9th - 12th, 2020, Zhoushan, China

Research on Control Scheme in YuwaReach of the Yellow River Estuary

YANJIE LIANG & JUAN JING

(Yellow River Engineering Consulting Co., Ltd., Zhengzhou, Henan, China, 450003)

Abstract: There are only a few river channel regulation projects below Yuwain Yellow River estuary, and the control projects cannot play an effective control role and the river is unstable,the swing of the flow path is unfavorable to the development of the estuary area. At present, there are two schemes for river regulation near the Xihekou: "big bend" and "small bend". The "big bend" plan is formed by the combination of the Cuijiazhuang and the Xihekou control projects located in the left bank, forming a big bend. The "small bend" plan is from Cuijiazhuangcontrol projectin the left bank to Weigaizhacontrol project in the right bank and then to the Xihekou control project. The 2D mathematical model was used to simulate the flow patterns of the 24.4km section from Yuwa to Qing3 near the Xihekou under three different inflow conditions of 1,000m^3/s, 4,000m^3/s and 10,000m^3/s. The results showed that the control effect of Weigaizhaproject was not obvious when the flow rate was 1000m^3/s. At 10,000m^3/s, the water in the Xihekou were not able to slide well. At 4000m^3/s, the projects can control the water flow effectively. By the four cross sections of different flow velocity distribution arbitrage and river mainstream lines comparison, the characteristics of cross section velocity distribution under different inflow conditions and its adaptability to river regulation are analyzed. When the flow rate is 4000m^3/s, the main stream of the river fits with the "small bend " schemecontrol traverse, which is favorable for controlling the river flow. Considering the inflow and sediment situation of the Yellow River estuary, the small bend scheme is more suitable for medium and small flood, and also is conducive to the water diversion of Shengli oilfield in the Xihekou.

Keywords: Yellow River Estuary; Xihekou; stable river regime; small bend scheme

1 Background

The Yellow River Estuary features little incoming water, much sediment, and relatively weak ocean dynamics. Historically, most of the sediment transported to the estuary area in the Yellow River Basin was deposited in the estuary, causing continuous deposition and extension of the estuary course, increase of river channel length and decrease of gradient. The Yellow River Estuary has been in an unstable state of wandering and diversion for a long time. The section from Yuwa in the Yellow River Estuary to the sea estuary is about 65 km long, and the distance between the two banks with embankments is 5 ~14 km. The river control projects are insufficient, the river channel plane changes greatly, and the main channel is very unstable. Specifically, the Yuwa ~ Xihekou section is about 6.5 km long, between the narrow section and the section into the sea, the main channel is 300 ~ 500m wide, and the channel is slightly curved. The section below Xihekou is the section of Qingshuigou course into the sea. The embankment distance between the two banks is 6.0 ~ 14.0 km, in a trumpet shape from top to bottom. The section below Qing 4 river control works to the sea estuary is about 33 km and is a projects-free control section. It is restricted into the sea by the diversion dikes on both banks, and the number of river channel regulation projects in the estuary section is significantly less than that in the adjacent lower reaches of the Yellow River, so the river regime cannot be effectively controlled. In addition, the inflow of water from the Yellow River Estuary has been decreased greatly in recent years, and the river course has shrunk, which is not conducive to the stability of the current Qingshuigou course.

At present, in view of the ecological, economic and social development needs of the estuary area, it is very necessary to maintain the long-term stability of the estuary course. Many scholars have proposed ideas and methods for the stability of the estuary course[1-2]. Li Zegang proposed to design flood diversion sluice and

rubber dam at Xihekou, using the Diaokou River as a flood diversion channel[3-4]. Li Diankui proposed to build an elevated flood diversion sluice at Xihekou to DiaokouRiver[5].

Stabilizing the Yuwa-Xihekou river regime is of great significance for prolonging the service life of Qingshuigou course. By establishing a planar two-dimensional hydrodynamic model, the flow velocity distribution and changes in the main flow line of the river channel are studied for Yuwa-Xihekou under different inflow conditions, to further analyze the adaptability of floods at different flow levels to river channel regulation projects, and propose regulation schemes that are suitable for the current inflow conditions and conducive to the stability of the river regime.

2 Evolution Characteristics of Xihekou Channel

2.1 Current Situation of Xihekou Reach Regulation Projects

The existing river regulation projects below Yuwa in the Yellow River Estuary cannot control the river regime effectively. Since 1986, new river control projects such as Shibahu, Cuijiazhuang, Weigaizha, and Xihekou have been successively built (see Fig. 1). As these projects were built late, and most of them were built to avoid beach collapse or water diversion, the layout for some of them is unreasonable, the number and length of such projects cannot meet the requirements, resulting that the river regime cannot be effectively controlled. The flow receiving capacity of Shibahu river control projects is insufficient, and the first section of the beach bank collapsed severely, which has posed a threat to the old river control projects and Linhuangdi. Due to the insufficient flow direction capacity of Cuijiazhuangprojects, the Weigaizhaprojects downstream on the opposite bank has been out of flow since the flood season in 1993. The flow discharge trend of most projects below Weigaizha has also been raised or lowered, resulting in a situation of change of one bend leading to changes of multiple bends, causing collapse of river banks. The front of most river regulation projects are deposited into beaches. The Weigaizha river control projects were built in 1986, and were completely out of the reach of river at the end of the flood season in 1993. At the end of the flood season in 2011, they started to discharge flow again. Partial collapse occurred during the water and sediment regulation in 2014. Danger also occurred during the flood season of 2015 ~ 2016.

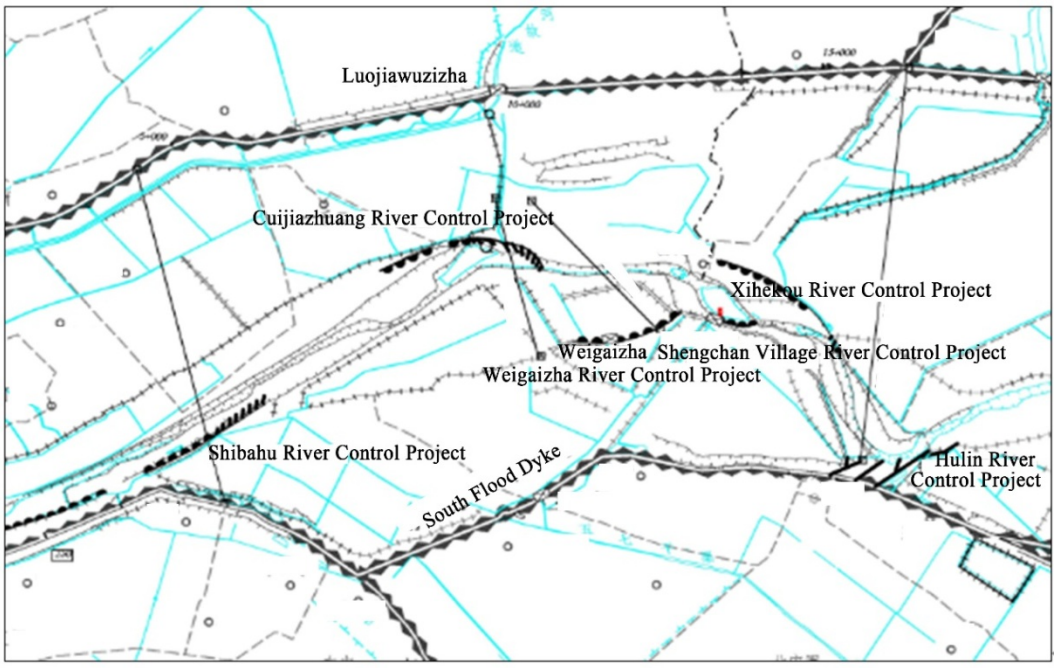

Fig. 1 Layout of Regulation Projects at Xihekou Reach

2.2 Historical Evolution of Xihekou Channel

As the inflow in the estuary has been small since the mid-1980s, the channel has deposited and shrunk, and the river regime has been adjusted accordingly. The river channel plane has changed to a certain extent, mainly including the rise or fall of flow potential at the projects. The river regime underwent major changes in the 1990s in some sections of the river due to the continuous formation of small bends and poor control of regulation projects over the river regime. For example, in the 1993 flood season, the Weigaizha river control projects were completely out of the reach of river and the deposited beach in front of the dam reached 1,200m. The Xiaolangdi Reservoir was put into operation in 2000, and the Xiaolangdi Reservoir began to carry out water and sediment regulation in 2002. Due to the regulation and control of the Xiaolangdi Reservoir, the regime of Xihekou River did not change significantly. The main flow line in different periods is shown in Fig. 2.

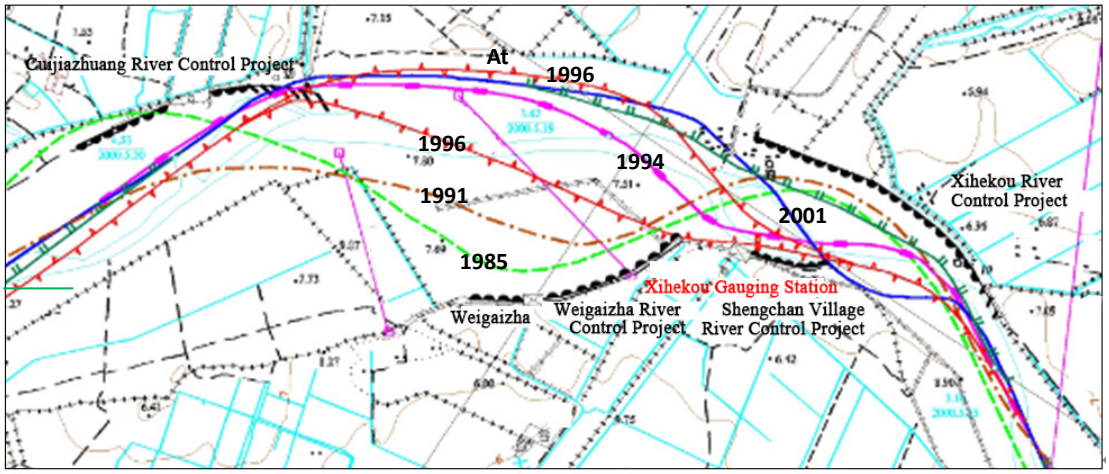

Fig. 2 Changes in the Main Flow Line of Xihekou Channel in Different Periods

3 Two-dimensional Hydrodynamic Model

3.1 Control Equation

Governing equation in the Cartesian coordinate system:

Continuity equation of flow:

$$\frac{\partial Z}{\partial t}+\frac{\partial (hu)}{\partial x}+\frac{\partial (hv)}{\partial y}=0 \quad (1)$$

x Directional water flow movement equation:

$$\frac{\partial (hu)}{\partial t}+\frac{\partial u(hu)}{\partial x}+\frac{\partial v(hu)}{\partial y}=-gh\frac{\partial Z}{\partial x}+D\left(\frac{\partial^2 (hu)}{\partial x^2}+\frac{\partial^2 (hu)}{\partial y^2}\right)-\frac{gn^2 (hu)\sqrt{u^2+v^2}}{h^{4/3}} \quad (2)$$

y Directional water flow movement equation:

$$\frac{\partial (hv)}{\partial t}+\frac{\partial u(hv)}{\partial x}+\frac{\partial v(hv)}{\partial y}=-gh\frac{\partial Z}{\partial y}+D\left(\frac{\partial^2 (hv)}{\partial x^2}+\frac{\partial^2 (hv)}{\partial y^2}\right)-\frac{gn^2 N\sqrt{u^2+v^2}}{h^{4/3}} \quad (3)$$

Where, z is the water level; *h* is the water depth; *u* and *v* are the flow velocities in the *x* and *y* directions; C is the Chezy coefficient; *n* is the roughness coefficient; D is the turbulent viscosity coefficient.

In order to fit the boundary of the irregular river channel, the orthogonal curve grid is used to mesh the river channel, and the equations (3) and (4) are converted into an orthogonal curve coordinate system:

$$\frac{\partial C_\xi C_\eta z}{\partial t}+\frac{\partial (C_\eta hu)}{\partial \xi}+\frac{\partial (C_\xi hv)}{\partial \eta}=0 \quad (4)$$

$$\begin{aligned}&\frac{\partial (C_\xi C_\eta hu)}{\partial t}+[\frac{\partial}{\partial \xi}(C_\eta hu\cdot u)+\frac{\partial}{\partial \eta}(C_\xi hv\cdot u)+hvu\frac{\partial C_\xi}{\partial \eta}-hV^2\frac{\partial C_\eta}{\partial \xi}]\\&+C_\eta gh\frac{\partial z}{\partial \xi}=-\frac{C_\xi C_\eta n^2 gu\sqrt{u^2+v^2}}{h^{1/3}}+C_\zeta C_\eta fhv\\&+[\frac{\partial}{\partial \xi}(C_\eta h\sigma_{\xi\xi})+\frac{\partial}{\partial \eta}(C_\xi h\sigma_{\eta\xi})+h\sigma_{\xi\eta}\frac{\partial C_\xi}{\partial \eta}-h\sigma_{\eta\eta}\frac{\partial C_\eta}{\partial \xi}]\end{aligned} \quad (5)$$

$$\begin{aligned}&\frac{\partial (C_\xi C_\eta hv)}{\partial t}+[\frac{\partial}{\partial \xi}(C_\eta hu\cdot v)+\frac{\partial}{\partial \eta}(C_\xi hv\cdot v)+huv\frac{\partial C_\eta}{\partial \xi}-hU^2\frac{\partial C_\xi}{\partial \eta}]\\&+C_\xi gh\frac{\partial z}{\partial \eta}=-\frac{C_\xi C_\eta n^2 gv\sqrt{U^2+V^2}}{h^{1/3}}-C_\zeta C_\eta fhu\\&+[\frac{\partial}{\partial \xi}(C_\eta h\sigma_{\xi\eta})+\frac{\partial}{\partial \eta}(C_\xi h\sigma_{\eta\eta})+h\sigma_{\xi\eta}\frac{\partial C_\eta}{\partial \xi}-h\sigma_{\xi\xi}\frac{\partial C_\xi}{\partial \eta}]\end{aligned} \quad (6)$$

Where, u and v are the velocity components in the ξ and η directions, respectively; z and h are water level and water depth, respectively; g is the gravity acceleration; υ_t is the turbulent viscosity coefficient of water flow; n is the roughness coefficient; f is the Coriolis Force coefficient; $f=2\omega\sin\Phi$, ω is the rotation angular velocity of the earth, Φ is the latitude of the calculated river reach; $\sigma_{\xi\xi}$, $\sigma_{\eta\eta}$, $\sigma_{\xi\eta}$, and $\sigma_{\eta\xi}$ are stress terms, and the expression is as follows:

$$\sigma_{\xi\xi}=2\upsilon_t[\frac{1}{C_\xi}\frac{\partial u}{\partial \xi}+\frac{v}{C_\xi C_\eta}\frac{\partial C_\xi}{\partial \eta}],\ \sigma_{\eta\eta}=2\upsilon_t[\frac{1}{C_\eta}\frac{\partial v}{\partial \eta}+\frac{u}{C_\xi C_\eta}\frac{\partial C_\eta}{\partial \xi}]$$

$$\sigma_{\xi\eta}=\sigma_{\eta\xi}=\upsilon_t[\frac{C_\eta}{C_\xi}\frac{\partial}{\partial \xi}(\frac{v}{C_\eta})+\frac{C_\xi}{C_\eta}\frac{\partial}{\partial \eta}(\frac{u}{C_\xi})]$$

3.2 Solving Method and Definite Solution Condition

According to the derivation, the basic equations of the model in the curvilinear coordinate system can be expressed in the following general form:

$$\frac{\partial(C_\eta hu\Phi)}{\partial\xi}+\frac{\partial(C_\xi hv\Phi)}{\partial\eta}=\frac{\partial}{\partial\xi}(\Gamma_\Phi h\frac{C_\eta}{C_\xi}\frac{\partial\Phi}{\partial\xi})+\frac{\partial}{\partial\eta}(\Gamma_\Phi h\frac{C_\xi}{C_\eta}\frac{\partial\Phi}{\partial\eta})+S_\Phi \quad (7)$$

The finite volume method is used to discretize the governing equation. The advantage of this method is that it can well guarantee the conservation of water volume and momentum in the water flow model. The equation is discretized in an automatic windward format, and the discrete equation is solved by using the SIMPLEC algorithm.

Given the solution conditions of inlet flow and outlet water level, an initial water level for the gradient assignment calculation area is assumed based on the outlet water level.

4 Flow Characteristics of Xihekou Channel

4.1 Calculation Conditions and Grid Layout

A planar two-dimensional mathematical model is used to calculate the 24.4 km river channel from Yuwa to Qing 3 section near Xihekou, including three cases of upstream flow at 1,000 m^3/s, 4,000 m^3/s, and 10,000 m^3/s, respectively. The calculation grid layout is shown in Fig. 3. A total of 1

6,000 grids are arranged.

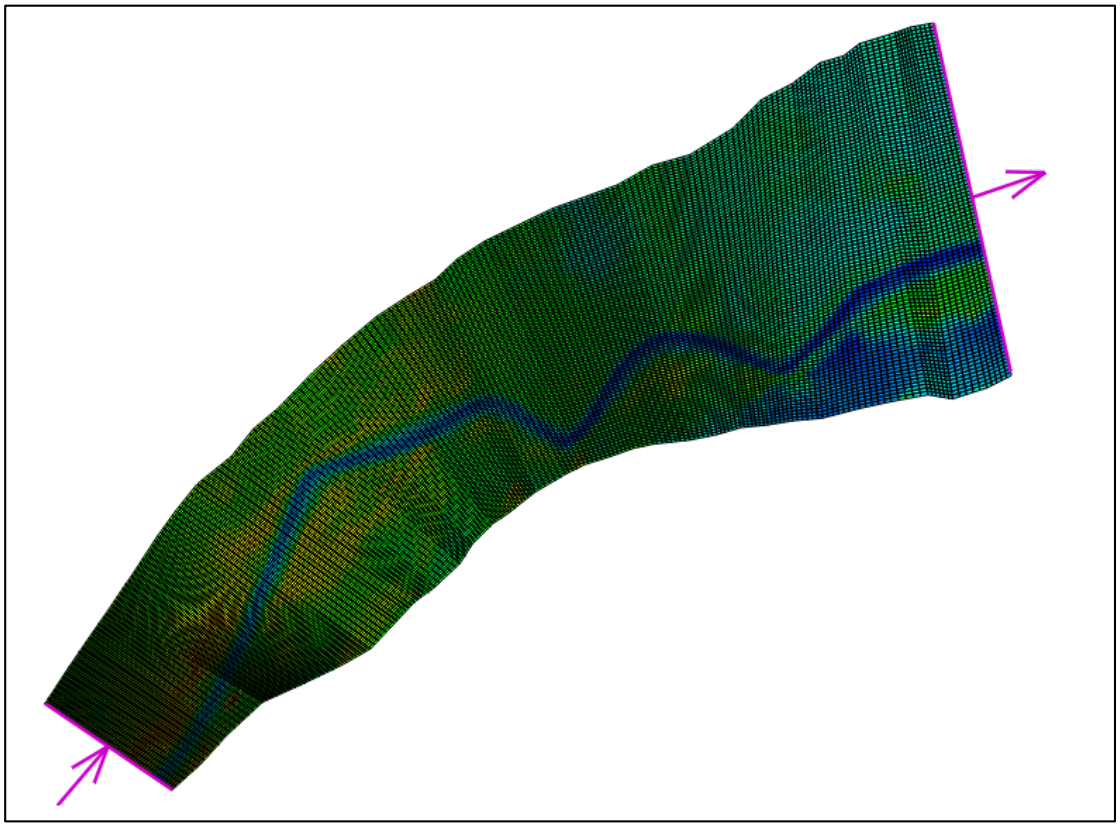

Fig. 3 Layout of Computing Grid

4.2 Flow Field Distribution

When the flow rate is 1,000 m^3/s, the upstream flow goes southeast along the river channel under the action of Cuizhuang river control projects. The Weigaizha river control projects only discharge flow at the tail. The flow velocity distribution is shown in Fig. 4. When the flow rate is 4,000 m^3/s, the Cuizhuang river control projects have a significant effect of flow deflection. The main flow deflects to the right bank, and most of

Weigaizha river control projects discharge flow. The flow velocity distribution is shown in Fig. 5. When the flow rate is 10,000 m^3/s, both the river floodplain and the main channel are overflowing. The Cuizhuang river control projects and the Weigaizha river control projects have a significant effect of flow deflection. The velocity distribution is shown in Fig. 6.

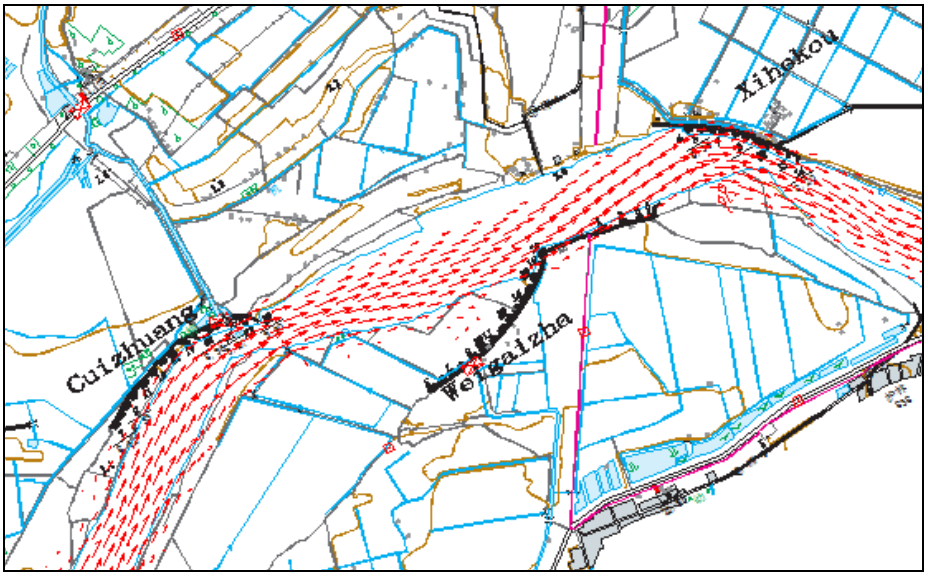

Fig. 4 Schematic Diagram of Velocity Distribution near Xihekou (Flow Rate at 1,000 m^3/s)

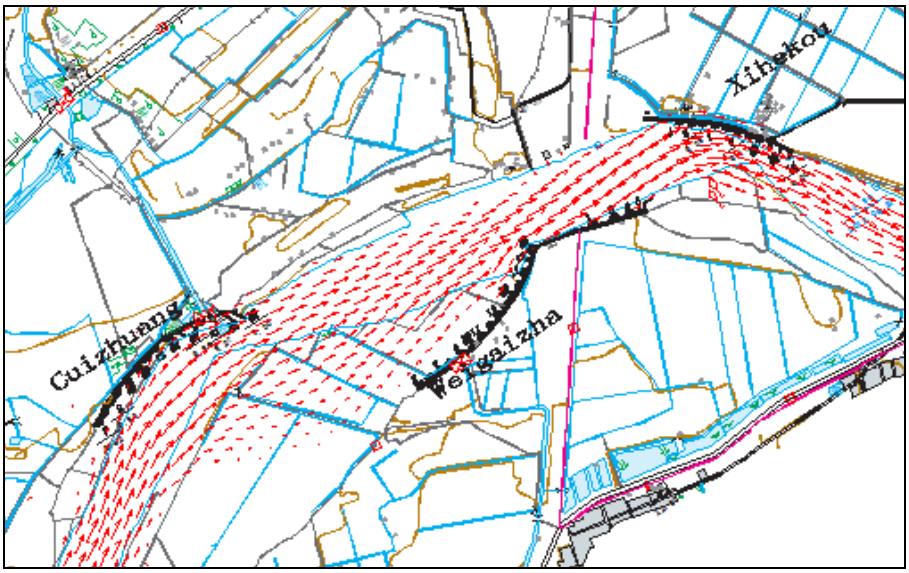

Fig. 5 Schematic Diagram of Velocity Distribution near Xihekou River Control Projects (Flow Rate at 4,000 m^3/s)

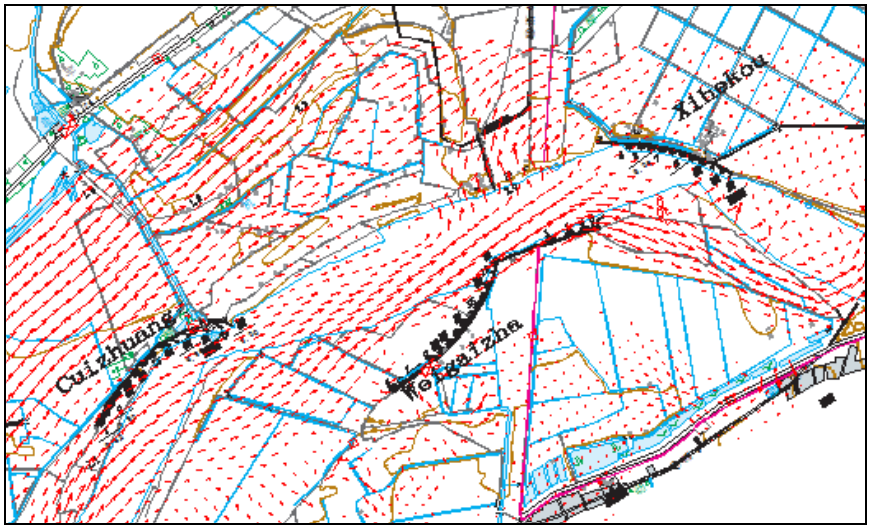

Fig. 6 Schematic Diagram of Velocity Distribution near Xihekou River Control Projects (Flow Rate at 10,000 m^3/s)

4.3 Cross-sectional Velocity Distribution

Four sections are arranged in the calculation area (Fig. 7). By analyzing the cross-sectional velocity under different inflow conditions, it can be seen from Fig. 8 to 11 that the cross-sectional velocity distribution is parabolic under three different inflow conditions. At 1,000 m^3/s, only the main channel overflows, and the maximum flow velocity position basically corresponds to thalweg. At 4,000 m^3/s, the maximum velocity position of Section 1 and Section 2 shifts to the left, and the flow range of Section 2 and Section 3 is increased. The river width of Section 4 is small, and it is a bayonet cross-section. The maximum flow velocity position is basically in the middle. At 10,000 m^3/s, the maximum flow velocity position of Section 1 and Section 2 is on the left side, close to Cuizhuang river control projects. The maximum flow velocity of Section 3 is on the right side, close to Weigaizha river control projects, and the maximum flow velocity of Section 4 remains unchanged.

It can be seen from the change in cross-sectional velocity that when the upstream flow is at 1,000 m^3/s, the water flow is adjusted to the middle of the channel under the action of the Cuizhuang river control projects. Due to the small flow rate, the overflow range has not reached Weigaizha, and most of the projects do not discharge flow. When the upstream flow is at 4,000 m^3/s, under the deflection action of the Cuizhuang river control projects, the flow is discharged near Weigaizha. When the upstream flow is at 10,000 m^3/s, the main flow of Section 3 is obviously deflected towards the right bank.

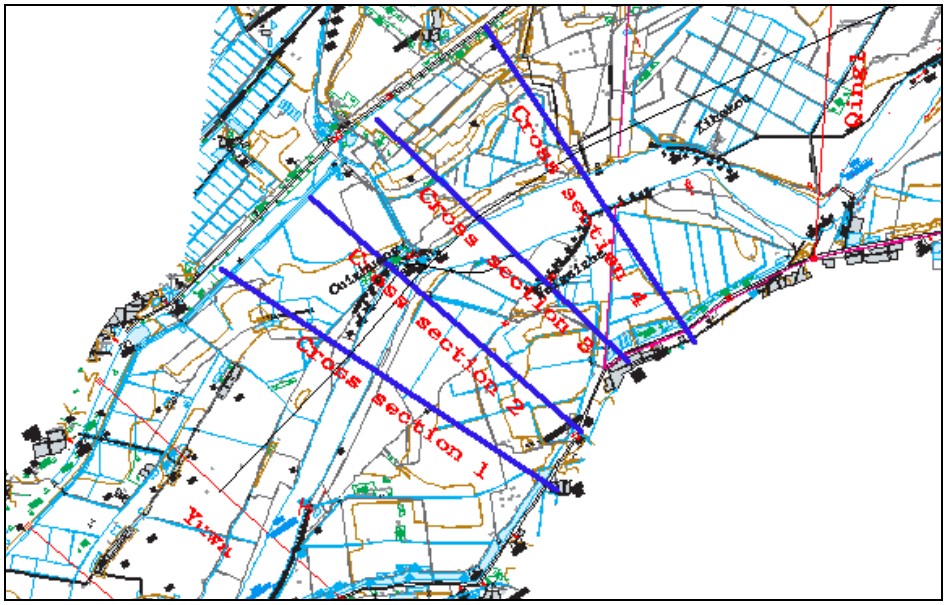

Fig. 7 Layout of Cross Section

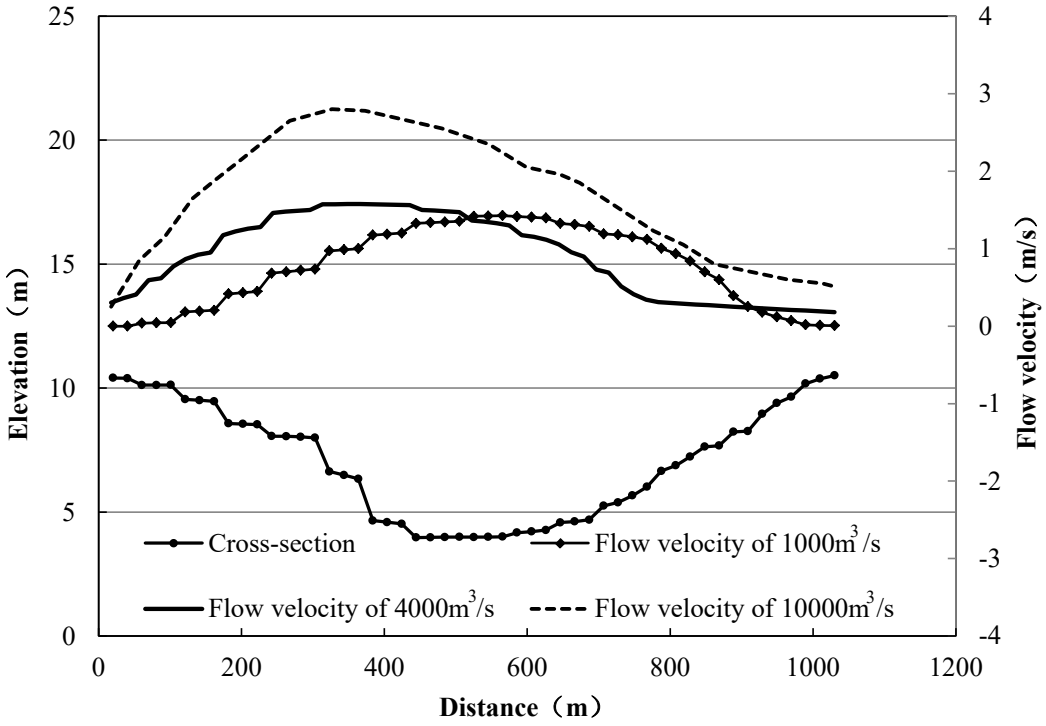

Fig. 8 Velocity Distribution of Section 1

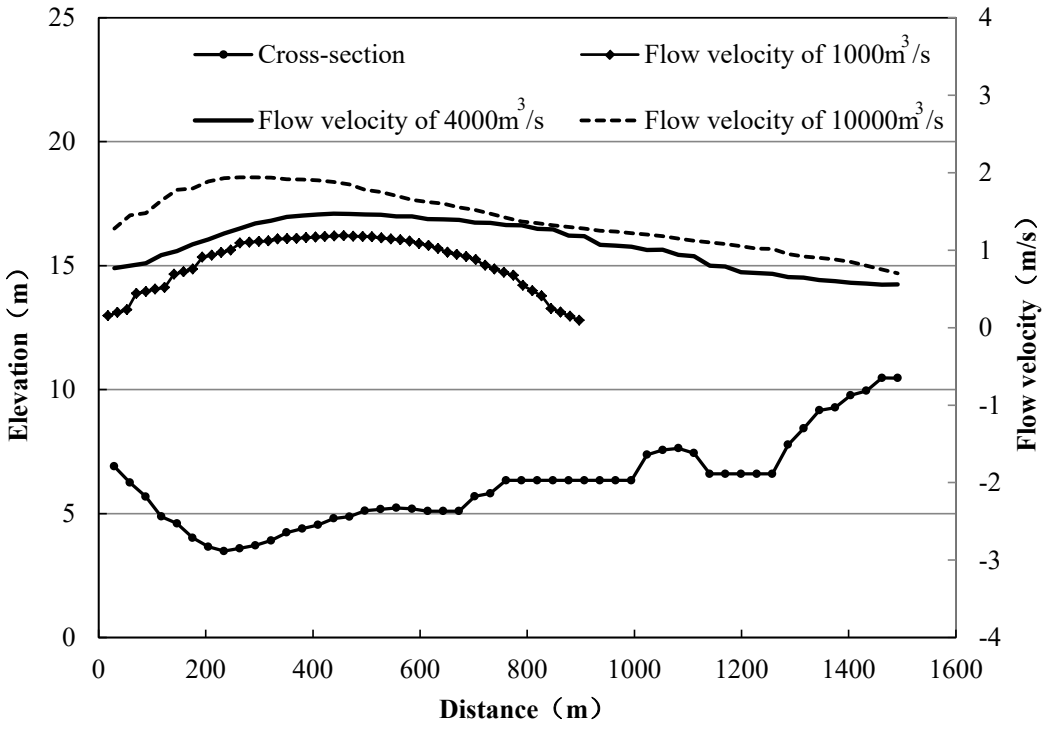

Fig. 9 Velocity Distribution of Section 2

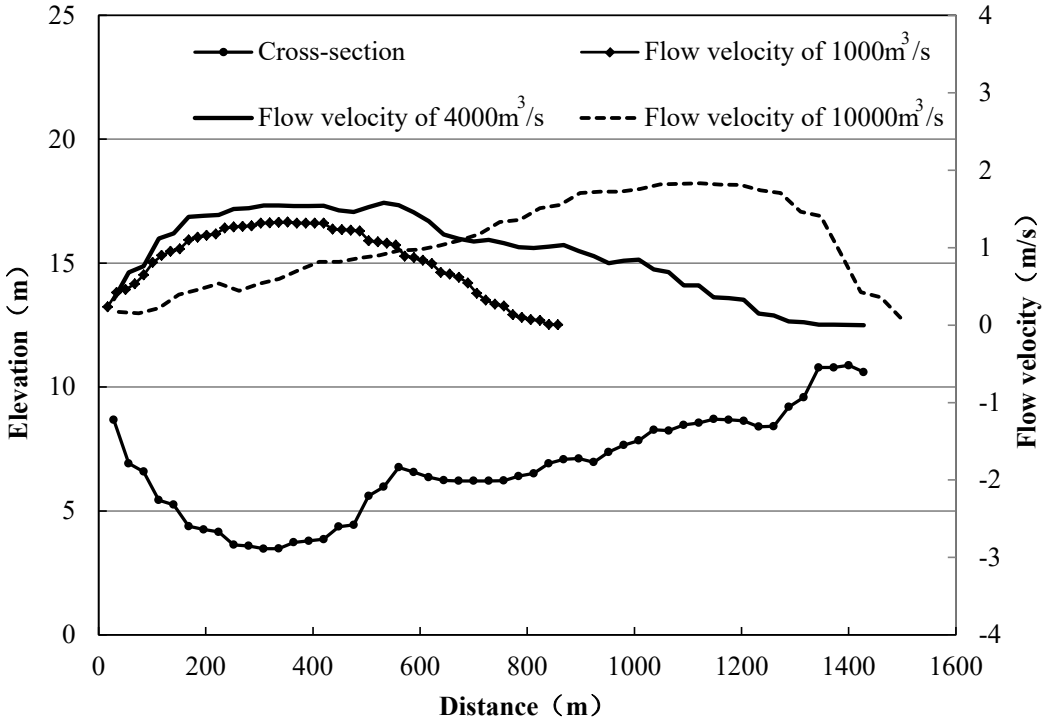

Fig. 10 Velocity Distribution of Section 3

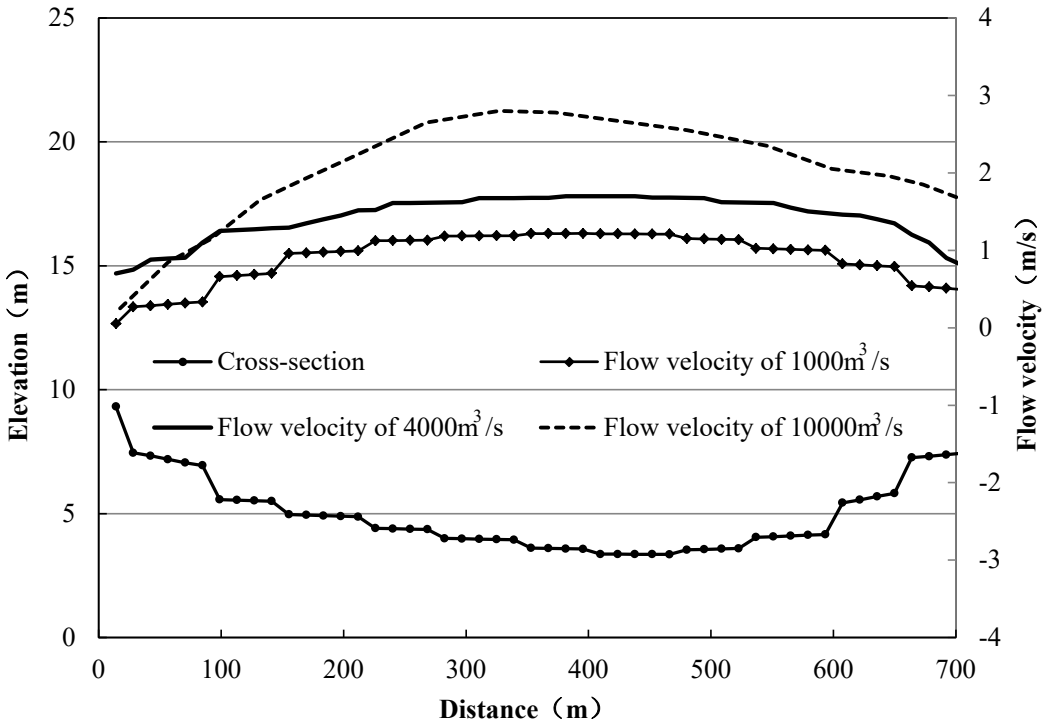

Fig. 11 Velocity Distribution of Section 4

4.4 Hydrodynamic Axis

Combined with the velocity distribution, the hydrodynamic axis under different inflow conditions are drawn (Fig. 12). When the inflow is at 1,000 m^3/s, the upstream main flow line is close to Cuizhuang river control projects, and the downstream main flow line is basically in the middle of the river channel. The Weigaizha river control projects do not discharge flow. When the inflow is at 4,000 m^3/s, the main flow line near Cuizhuang river control projects shifts to the middle of the channel, and the main flow line near Weigaizha river control projects shifts to the right. When the inflow is at 10,000 m^3/s,

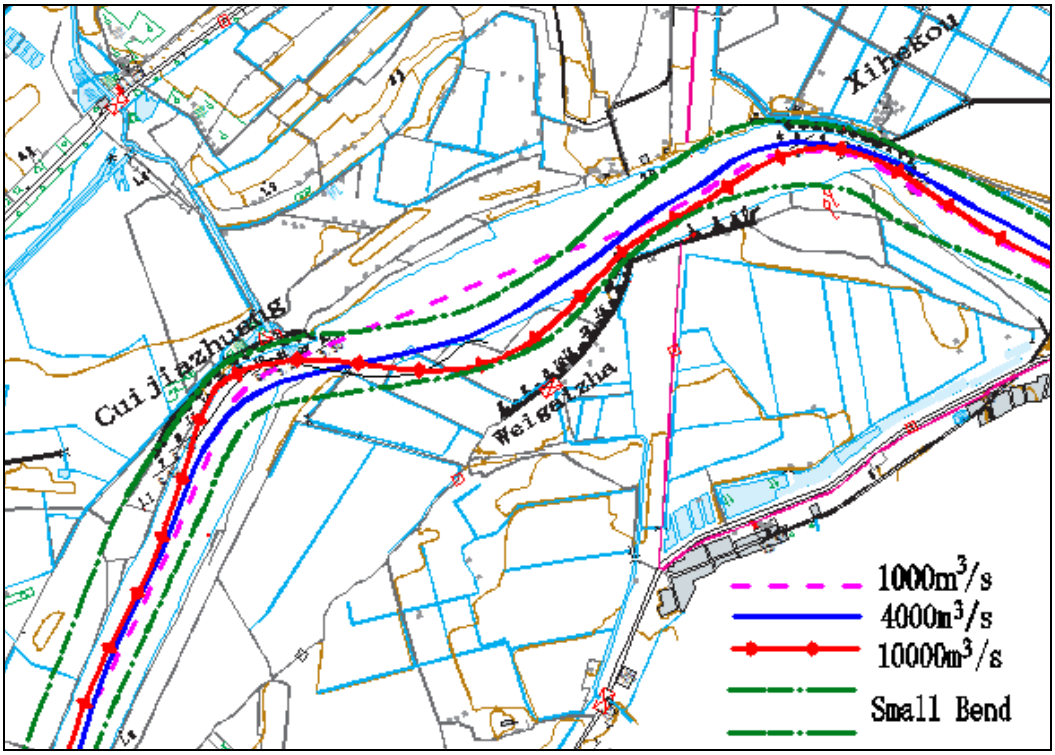

Fig. 12 Distribution Diagram of Hydrodynamic Axis

The main flow line of the river channel is in an "S" shape, close to Cuizhuang and Weigaizha river control projects. According to the distribution of hydrodynamic axis, it can be seen that the regulation line in the "small bend scheme" is consistent with the overall flow, which can divert the water to the channel, smooth the flow, reduce the scattered water flow and improve the sediment transport capacity of the river.

At present, there are two schemes for river channel regulation near Xihekou: "big bend" and "small bend". In the large bend scheme, the river control projects of Cuijiazhuang on the left bank and Xihekou are combined to form a big bend. In the "small bend scheme", the flow is deflected at Cuijiazhuang to the right bank for Weigaizha river control and then for Xihekou river control. In the "big bend scheme", it requires long projects. First, it needs to construct the apex of the bends at Cuijiazhuang and Xihekou. A large number of projects need to be constructed in the projects-free control area with a gap of about 4 km between Cuijiazhuang and Xihekou. In addition, the scale requirement of "big bend scheme" is higher than that of "small bend scheme". Combined with the flow characteristics of Xihekou reach, the "small bend scheme" has more advantages. It can smooth the flow and play the role of the existing river control projects, which is more conducive to the stability of river regime.

5 Conclusions

(1) There are only a few river channel regulation projects below Yuwa in the Yellow River Estuary, and the river regime is unstable. This paper analyzes the current situation of Xihekou regulation projects and the historical evolution of the river channel from the perspective of stabilizing the Yellow River Estuary course, and suggests the necessity of Xihekou regulation.

(2) A planar two-dimensional hydrodynamic model is used to simulate the flow pattern of the 24.4 km section from Yuwa to Qing 3 near Xihekou under the three different inflow conditions of 1,000 m^3/s, 4,000 m^3/s and 10,000 m^3/s. The results show that the Weigaizha river control effect is not obvious at the flow rate of 1,000 m^3/s, the flow discharge effect of Xihekou dangerous section is not ideal at the flow rate of 10,000 m^3/s, and all

the river control projects can play the role of controlling water flow at the flow rate of 4,000 m^3/s.

(3) By comparing the flow velocity distribution arbitrage and the main flow line of the channel for four cross-sections at different flow levels, this paper analyzes the characteristics of flow velocity distribution of the cross section under different inflow conditions and their adaptability to the river regulation projects. The main flow of the channel is consistent with the regulation line in the "small bend scheme" at the flow rate of 4,000 m^3/s, which is more beneficial for controlling the river regime.

Fund project: supported by Topic Six - "Entrance Course Scheme and Control Measures for 100-Year Stable Yellow River Estuary" of National Key Research and Development Program - "Comprehensive Control and Study on the Yellow River Estuary Evolution and Course Stabilization" (No.: 2017YFC0405506)

References:

Li Zegang and Wang Wanzhan. Thoughts on and Methods of Stabilizing the Course of the Yellow River Estuary into the Sea [J]. Yellow River, 2009, 31 (8), 13-14.

Zeng Qinghua, Zhang Shiqi, Hu Chunhong, et al. Evolution Laws and Regulation of the Yellow River Estuary [J]. [M]. Zhengzhou: Yellow River Water Conservancy Press, 1997: 102.

Li Zegang. Basic Evolution Laws of the Yellow River Estuary in Modern Times and Regulation of Stable Course [M]. Zhengzhou: Yellow River Water Conservancy Press, 2006:.

Li Zegang and Li Changxin. Creating a Relatively Stable Coast of the Yellow River Delta [J]. Yellow River, 2012, 34 (6), 13-15.

Li Diankui, Yang Yuzhen, Cheng Yijie, et. al. Study on Extension of Flood Discharge Period of Qingshuigou Course at the Yellow River Estuary [M], Zhengzhou: Yellow River Conservancy Press, 2002, 262-264.

Brief introduction of corresponding author: Liang Yanjie (1984 -), female, native of Luoyang City, Henan Province, senior engineer, her major research direction is river numerical simulation. Mobile phone: 18237125190, E-mail: iamlyj_2006@163.com

8th International Conference on the Application of Physical Modelling in Coastal and Port Engineering and Science
Dec. 9th - 12th, 2020, Zhoushan, China

CURRENT VELOCITY MEASURING SYSTEM OF RIVER MODEL BASED ON VIRTUAL INSTRUMENT TECHNOLOGY

ZHANG HONG-WEI

Estuarine and Coastal Science Research Center, Ministry of Communications, Shanghai, 201201, China.

ABSTRACT

As a kind of computer technology applied in automation industry, virtual instrument (vi) technology is a new direction of instrument designing. Based on the analysis of micro-propeller current meter, a new current velocity measuring system of hydraulic river model is developed. The system is designed with VI technology, merging some computer resources and the related hardware together. The paper focuses on the total architecture of the system virtual instrument, design pattern, data structure and hardware driving technology. IN contrast to the method of traditional text programming, the graphic programming of LabVIEW to design VI is clearer in logic and easier to simplify the system developing process. It is also more efficient to enhance the automatic level of the other river model instruments.

Keywords: virtual instrument; current velocity measuring; river model

1 Introduction of VI

Virtual Instrument (VI) technology , created by National Instruments（NI）corporation in USA, is an innovating concept for instrument design that combines universal computer technology with special test or measuring technology in some field. Contrasted with the traditional method, VI reserves only requisite sensors and necessary circuits to acquire physical signal, while separating the common functions including data analyzing and processing, test outcome output and showing, then transplanting them to the computer to complete. Due to the abundant resources on computer, VI can adjust most function architectures and total performances of the system to execute various automatic test and control tasks by optimizing the software conveniently[1]. As a kind of current velocity meter , micro-propeller has been widely applied in hydraulic model test .In order to probe how to adapt new instrument technology in hydraulic model, the paper explores a new current velocity system with LabVIEW technology based on micro-propellers to measure single point or multi-points of a hydraulic model.

2 Operating principles of current velocity meter

As a major measuring item in hydraulic model test, current velocity is usually obtained by a sensor called micro-propeller, which is shown in Fig.1. The two branches of optical fiber are used to conduct light, one is for transmitting light and the other is for receiving light. All the optical fibers are enclosed by stainless pipes, with three facets sealed by epoxy resin and polished. When the micro-propeller rotates with current, the electroplated facets of its tiny impeller will rotate in front of the light detector and the reflected light will be sensed by the receiver eventually through the light-guide fiber. In order to weaken the influence of the natural light, the optical fiber is changed into an infrared fiber and the parcel plating technology is adopted on the impeller facets.

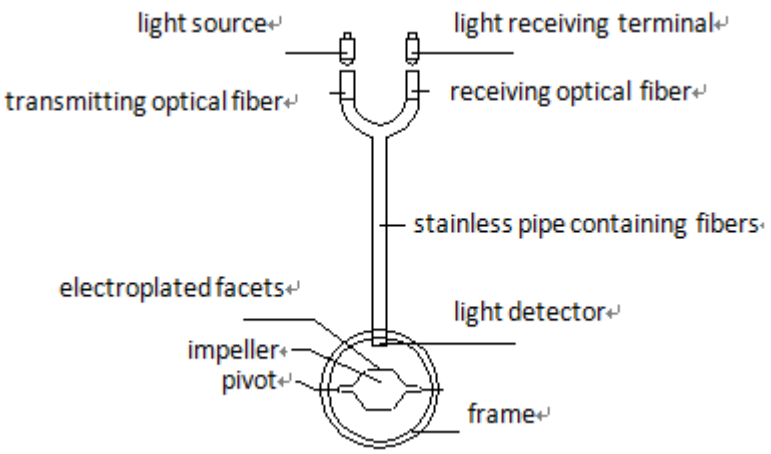

Fig.1 Structural diagram of the micro-propeller

The rotation rate of the impeller is proportional to the current velocity ,which can be described as v=Kn+c. Here, v is the velocity, n is the rotation rate, K、c are constants that can be calibrated in the standard tunnel. In this way, the rotation rate of the impeller can be got through the pulse numbers in an unit time, and the current velocity is got ,too.

3 Hardware architecture of the measuring system

The whole system is designed according to the modularization method, as the structure is shown in Fig.2, including PC control unit, multichannel micro-propellers with their amplifiers.

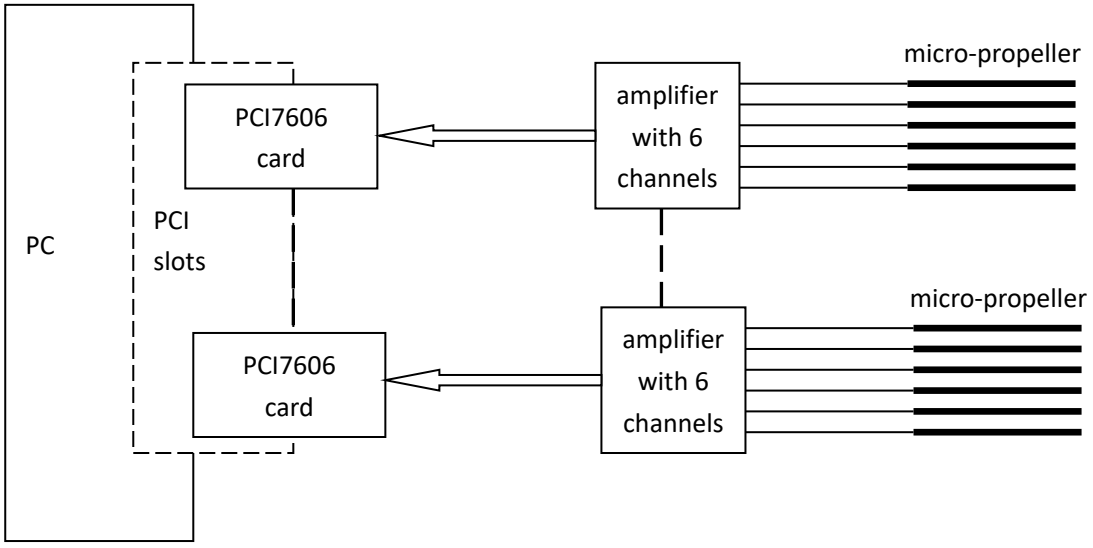

Fig.2 Hardware diagram of the system

Comprising PC and PCI7606 pulse numbering card, the PC control unit is the data acquiring and control center of the system. PCI7606 is a multichannel pulse numbering card presented by HongTuo Corporation, through which PC can obtain the rotation rate of the micro-propeller. PCI7606 is connected with PC through the PCI interface which can be configured directly on the motherboard or transferred indirectly from other interface, and the number of PCI interface depend on the number of micro-propellers contained in the system.

The PCI7606 is designed for industrial application with 12 channels of 16 digits programmable counter, and its main function part constitutes 4 chips of 82c53. After photoelectric conversion and Schmitt plastic circuit, most of the noise mixed in the signal is eliminated and the effective pulse signal is conveyed at 82c53 input pin.

A piece of PCI7606 installed in PC can connect 12 micro-propellers at most.

The amplifier provides working power supply to the scattered micro-propellers, reshape and amplify the pulse signal so as to convey it in a long distance. Each amplifier outputs 6 electric pulse signals of TTL level that are connected to PCI7606 directly.

4 Virtual Instrument Design of the system

4.1 LabVIEW Virtual Instrument

Virtual instrument is a new instrument design concept proposed by National Instruments in USA. Contrasted to the traditional instrument, VI utilizes the abundant resources in computer to complete tasks of data processing and results expressing, which often occupy a considerable hardware part in a traditional instrument. Due to the abundant computer resources, VI can optimize the software conveniently to adjust the function or overall performance of the instrument. As a graphic programmable language, every programs of LabVIEW has a suffix of ".vi", namely virtual instrument. This paper adopted LabVIEW8.6 to develop hydraulic model current velocity measuring system based on VI technology[2].

4.2 Overall architecture

One of the main design task of the system is to develop its virtual instrument, which is shown in Fig.3, including:①Parameter set. There are two classes of parameter to set, one to choice the functions of PCI7606 to determine its working mode as pulse counting mode, the other is to set beat time and its timing unit of the system to determine the display parameters of the acquired data.②Measuring of the micro-propeller rotation rate. During running period, the system counts the number of pulses in a unit time produced from rotating impellers and stores it.③Function call. During the process of developing virtual instruments, it is necessary to call a large number of sub-VIs provided by LabVIEW development environments, some called in a direct way of static mode, some called in an indirect way of dynamic mode which needs to set input parameters.④according to the above parameters set, the system will collect the data of current velocity to

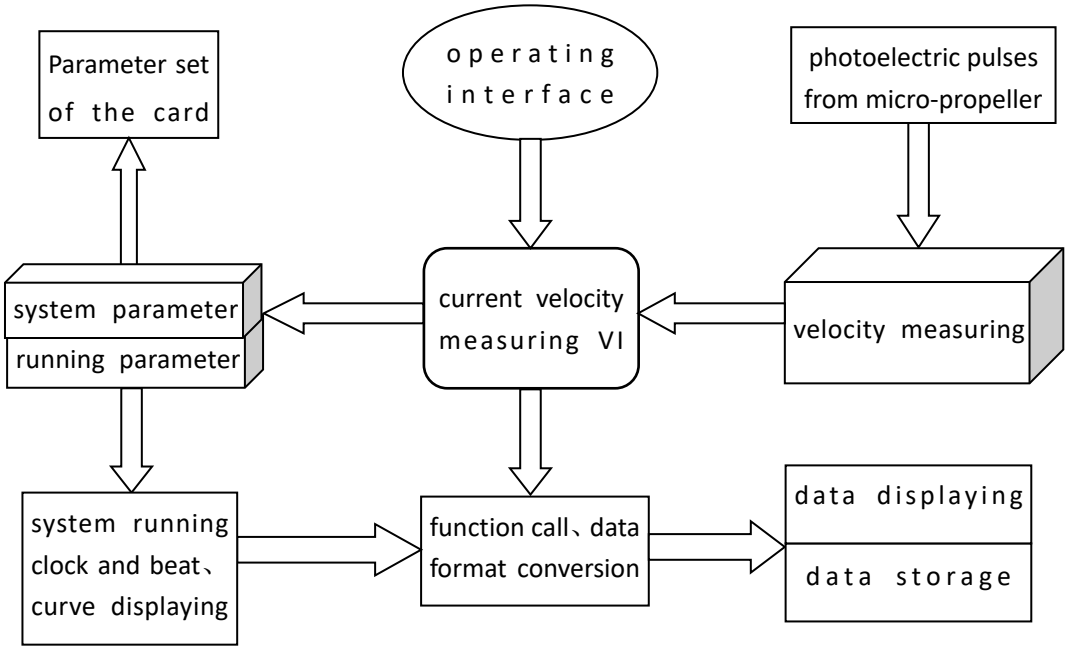

Fig.3 Architecture diagram of system VI

display and store in real time during the whole running period. The modular programming method is adopted to develop virtual instruments of the system. So in this way, the top VI is generated by integrating all sub-VIs in the end after each VI is developed and debugged individually.

4.3 Function realizing of the virtual instruments

4.3.1Design mode of the top VI

When current velocity measuring system VIs are in working state, it is necessary to operate several bottom hardware resources of the computer and to execute multi tasks at the same time. Hence, some issues relating to VI design such as program optimizing, program running efficiency and so on should be paid more attention to. In this paper, the design pattern of event driven state machine is adopted to organize each function VI to develop the top VI. The concrete realization is that the running states of the top VI is divided into five definite statuses, including Initialize, Idle, PCI7606, Report and Shutdown. Here, the status of Initialize executes parameter setting function, while the status of PCI7606 executing micro-propeller pulses counting function, the status of Report executing data logging function, the status of Shutdown executing system closing function. The status of Idle is inserted into the event structure of LabVIEW to process GUI(Graphic User Interface) events initiated by the operator. In order to manage the alternate shift among all the statuses efficiently, the paper adopts queue functions of LabVIEW8.6 to deal with data correspondence operation of each status, such as entering queue, departing from queue and so on. The queue functions used in the part of the top VI shown in Fig.4 are ObtainQueue, EnqueElement, DequeElement and ReleaseQueue.

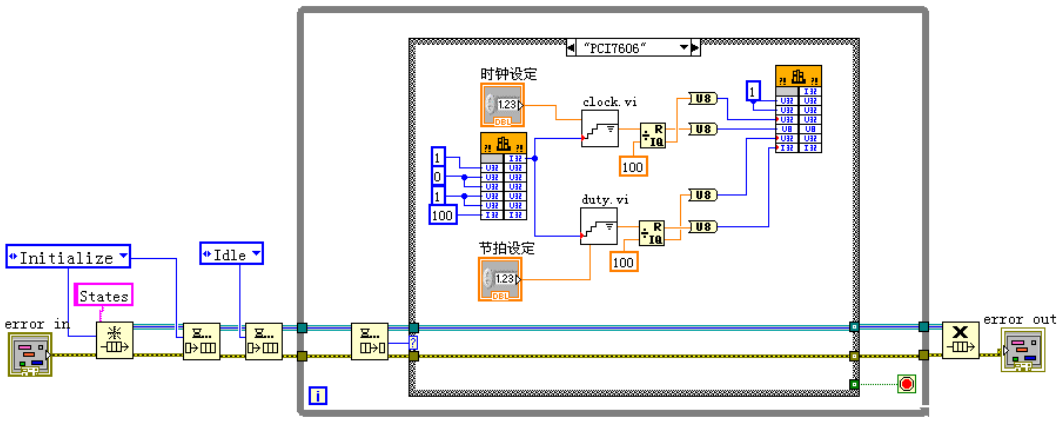

Fig.4 Part graphic programming of the top VI

4.3.2 DLL call of hardware Driving

To control the bottom hardware installed in the computer, it is appropriate to adopt DLL(Dynamic Link Library) method to design VIs related to hardware operating. In LabVIEW8.6, a node named Call Library Function can identify driving function in DLL modules to exchange data with LabVIEW conveniently to realize hardware programming. The PCI7606 card provides DLL driving library of PCI7606.dll, which can be called after the card has been installed. The graphic program shown in Fig.4 calls PCI7606js function of PCI7606.dll to read data from six counting channels.

4.3.3 Data structure

In order to reduce the quantities of linking wires in the back panels of VIs and enhance the readability and maintainability of VIs, the paper adopts array and array functions to organize data items of the same class with various values, while adopting cluster to organize data items of different classes. In this way, the relations between data hierarchies can be indicated clearly and the data exchange between sub-VIs are concise and efficient. In a sub-VI with its Report status graphic programming as shown in Fig.5, array is used to transfer parameters between ReadFromSpreadsheet.vi and prcsData.vi, while cluster is used to assemble data to input horizontal axis and vertical axis of XYGraph control named gCurrVelocity.

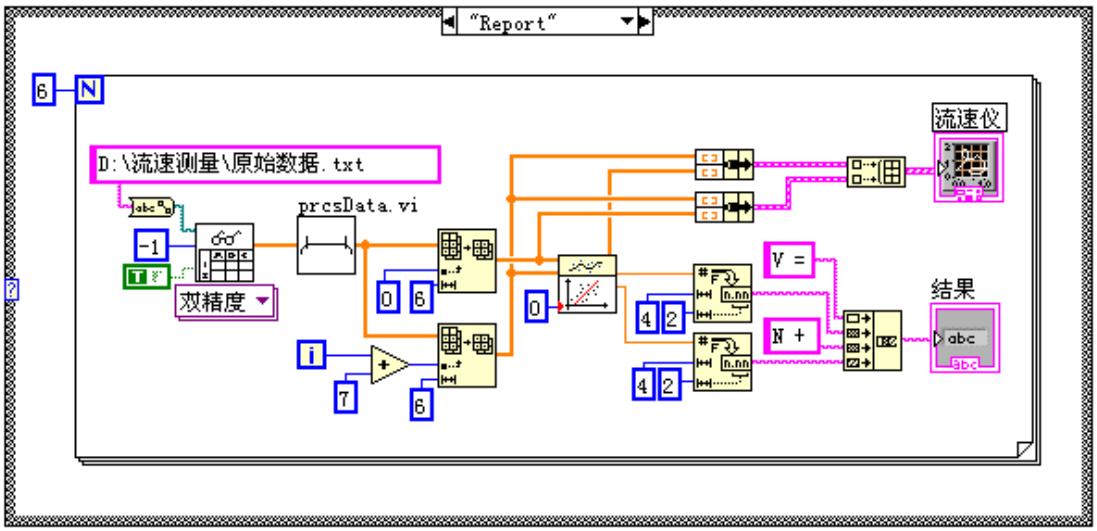

Fig.5 VI program organizing data with array and cluster

The system is required to store data measured to analyze the whole flow field, and therefore it is important to program an efficient data storage VI. Here, a method of main-VI calling sub-VI is adopted to simplify the structure of the main-VI and enhance its running efficiency. In the concrete programming, the VI nodes supplied by the LabVIEW Database Tools in LabVIEW8.6 are called to program VIs relating to database linking and data operating, including Database Connection.vi, Database Insert.vi, Database Logging.vi and Database Transantion.vi.

5 Application of the system

It is through the monitoring graph that the operator checks the working condition of micro-propellers and analyze the hydraulic model experiment progress, and the monitoring graph design is a significant point that VI graphic programming surpasses the traditional text programming . Fig.6 is the monitoring interface of the current velocity measuring system, displaying data acquired from the field micro-propellers and storing them in the background.

There are two types of data displayed in the monitoring graph. One is overall data of the all measured points in the model, and the other is a curve displayed of a single measured point with its time from the moment the data acquisition started. Velocity values measured at the same time of all micro-propellers and their working statuses can be displayed succinctly through programming multi-list controls and boolean controls provided by LavVIEW8.6. When the propeller is driven by water and the current velocity is measured, the correspondent lamp in Fig.6 turns on otherwise it turns off. In order to conveniently observe the current velocity varying process of a designated position where a micro-propeller is placed, the monitoring interface provides the option operation to select the micro-propellers of a velocity measuring node and the correspondent measuring period. The Wavegraph control in Fig.6 displays the data curve of the second micro-propeller of the third measuring node in the second period.

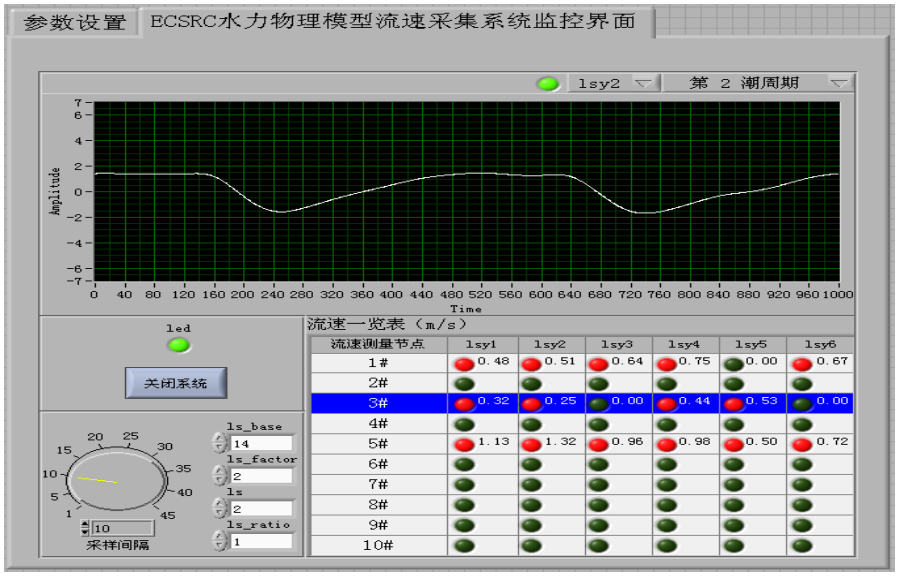

Fig.6 User interface of the current velocity measuring system

6 Conclusions

The hydraulic model current velocity measuring system adopting VI technology can store and analyze the measuring data completely, display the acquired data and status data of the micro-propellers in real time. In a whole, the system has evident features such as interface friendly, operating conveniently, running stably and so on. The application results show that the method to develop instruments with graphic programming language LabVIEW has clearer logic hierarchies and more abundant graphic resources to call in contrast to the traditional text programming, which is helpful to enhance the automatic level of hydraulic model instruments more conveniently.

References

[1] Zhou Nanquan, Quan Xiaoli, “Deign of virtual experiment system for digital circuit based on LavVIEW”, *Electronic Test,* 2018, 22, 14-16.

[2] Huang Zhijun, “Design of replacing traditional electronic belt scale based on virtual instrument technicality”, *Electric Engineering*, 2018,12,144-146.

8th International Conference on the Application of Physical Modelling in Coastal and Port Engineering and Science
Dec. 9th - 12th, 2020, Zhoushan, China

MORPHODYNAMIC RESPONSES OF PINGSHUIQIAO BEACH TO A STORM SURGE USING ARGUS IMAGES

ZILONG XIA [1], CUIPING KUANG [2]，LEI ZHU[3]，YUHUA ZHENG[4] & YUNLONG WU[5]

[1,2,4,5] College of Civil Engineering, Tongji University, 200092, Shanghai, China. Email: cpkuang@tongji.edu.cn
[3] The Eighth Geological Brigade, Hebei Geological Prospecting Bureau, No.221, Yanshan Road, Qinhuangdao, Hebei, 066001, China. Email: siriusn@126.com

ABSTRACT

During a storm event, such as tropical cyclone and cold front, sea surface in coastal water will experience a significant increase due to storm surge. The high wind-waves therefore may break on the beach and strongly stir up local sediment, resulting in an erosion. The morphological impact of these extreme events has drawn great interest of coastal community, however, a real-time in-site observation is still hard to be conducted considering the devastating forcings. The Argus monitoring system, a real-time and omnibearing image observation, is able to record the image information during the storm event with high-definition cameras mounted in a high and safe place. In combined with some post-processing tools, the recorded image can be converted and provide the information of shoreline location and the digital elevation model (DEM) for intertidal zone. It is therefore considered to be a robust technique to estimate the coastal morphological evolution in recent years. The Pingshuiqiao beach is located in the west of Beidaihe district, Hebei province, China. To maintain local ecotourism value, the Argus monitoring system is applied to the beach to monitor shoreline movement, morphological evolution of intertidal zone and berm profile, with six high-definition cameras. In this study, we firstly extract the location of shoreline by processing time exposure images every 30 minutes based on the improved Canny edge detector, which uses a conventional “derivative of Gaussian” filter to detect step edges, i.e., shoreline. Then, the coordinates of shoreline are derived by establishing coordinate relation based on the control points fixed on the beach. Finally, the multi-temporal shoreline coordinates in one day are inputted into ArcGIS for interpolation to set up a DEM. We adopt the above method to process 11-day Argus monitoring results during a storm event on 15-25, July, 2016. The results indicate that the most severe erosion appeared in the western beach with the loss of beach volume per unit width of 132.50m^3/m by the storm. After the storm surge, sediment gradually comes back to the beach and deposits there due to the restorative effect of wave in normal weather conditions. Generally, the strong erosion occurs in the supratidal zone and the upper part of intertidal zone, while the deposition in the lower part of intertidal zone during the storm surge in such a wave-dominated low tidal range sandy coast. This study clearly presents the morphological change processes at Pingshuiqiao beach based on the Argus monitoring system that can be taken as a practical technique to study on coastal morphology.

Keywords: Argus monitoring system; storm surge; morphological evolution; short-term change.

1 INTRODUCTION

Beach is a valuable tourism resource, which is composed of beach landform, water body, biology, climate, meteorology, humanities and other resources. Due to its rich resources and beautiful scenery, the beach has become the first destination of coastal tourism. The economic, social and cultural development of coastal cities such as Qinhuangdao is often based on the beach. However, in recent years, severe beach erosion caused by storms occurred frequently around the world, posing a serious threat to the safety of people's lives and property and the destruction of the ecology. Quantifying the impact of storms on beaches is a challenging issue as extreme weather increases. The evolution of Pingshuiqiao beach for years is complex as there are a submerged rubble-mound breakwater in the offshore and two natural headlands at its east end, thereby increasing the complexity and uncertainty associated with the morphological evolution of intertidal zone.

Research on the morphological evolution of intertidal zone is one of the key scientific issues pertaining to the long-term sustainability of intertidal ecosystems and related coastal defense issues(Bouma et al., 2014). Previous researches had found that the recovery processes are not the same for the beach suffered different storm events. The mixed gravel beach after a storm event, as pointed by Bramato (2014), under the condition

of low energy sea state, the responses of the beach experience were different, i.e., the beach recovery process showed a large spatial variability due to wave direction and wave height change. In addition, some studies have shown that the change of tide level has a certain impact on the recovery of beaches, and the difference of wave energy conditions in the sea adjacent to the beach makes the transportation of beach sediments after the storm different, and the recovery degree of different parts of the beach is also different after the action of severe storm events (Archetti, Paci, et al., 2015). As a relatively advanced technology, the Argus monitoring system is able to acquire high-accuracy surface data over a large area. Sancho (2013) used Argus video image data to study the response characteristics of three cove beaches in Barcelona, Spain, to the storm after the construction of breakwaters. Guo (2019) used Argus video image data to analyze the response characteristics of Dongsha beach in Zhoushan to continuous storms.

The objective of this work was to study the response of beach to a storm surge by employing a video system to monitor the intertidal zone variation in the three-dimensional topography (Elko, Gelfenbaum, 2005). To meet this object, the coordinates of the shorelines at different times were first proposed as the indicator; then, a method for extracting shorelines from video imagery was adopted (Bergsma, et, al. 2019). Finally, the daily topographic changes recorded by a coastal video system are presented and studied.

2 METHODS

2.1 Study area

Pingshuiqiao beach is located in the west of Beidaihe district, Hebei province, China, and consists of coarse sediment with median grain size of 0.29 - 0.35 mm, which is an important tourism source for Qinhuangdao. The beach is near the amphidromic point, indicating weak tidal flow, with an average tidal range of 60 cm and a maximum tidal range of 154 cm. Figure 1 shows the installation components of Agrus System and profiles of the study area. There are a submerged rubble-mound breakwater in the offshore and two natural headlands at its east end (Figure 1e), resulting in the complex geometry and topography of Pingshuiqiao beach. In order to maintain local eco-tourism value, a number of beach nourishment projects had been implemented and the Beidaihe Beach In-situ Monitoring Station was established in June 2011, which was located right at the Pingshuiqiao beach. This station has been equipped with many advanced equipment, such as the Argus system, the detailed location of the system was shown in Figure 1e.

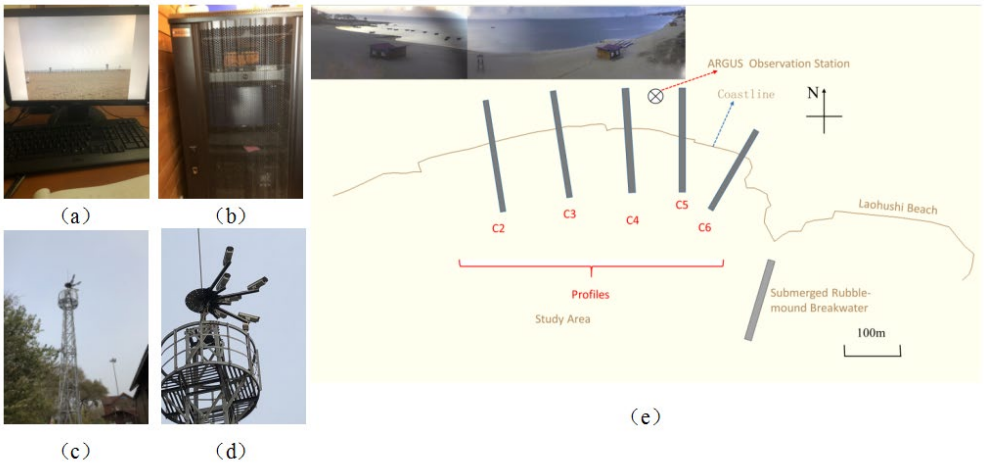

Figure 1. Snapshots of the Argus system (a, b, c, d) and study area (e).

According to the website of the North Sea Forecast Center of the State Oceanic Administration (2016), there were nine storm surges in the whole year of 2016, three of which occurred in the summer. Among them, the storm surge on July 20 had a significant impact to Pingshuiqiao beach. This storm surge caused the local water level to rise by 50-150cm, making the port of Qinhuangdao reaching the warning level of 218cm with the highest level of 220cm. The Argus system recorded videos of the process of this storm surge from July 15 to July 25, a total of 11 days.

2.2 Video data

The Argus system consists of 6 high-resolution cameras with resolution of 2048×1536 pixels (Figure 1c, d) and corresponding terminal equipment (Figure 1a, b,). The study area is covered by cameras No.2 - No.6 (corresponding profiles c2-c6). The rectified images extended from nearly 230 m in the cross-shore direction and 750 m in the alongshore direction. For further analysis, the beach morphology images were collected during

and post the storm surge. The basic data were processed in three steps. First, image noise was filtered out using a Gaussian filtering algorithm, which avoids the destruction of edge information while filtering the noise in the image. Second, Canny edge detector (image abstraction algorithm) was applied to extract the shoreline. The interface of shoreline extraction was showed as Figure 2. The shoreline was marked with red lines, and its pixel coordinates were extracted and displayed at the bottom of the image. After that, the cameras were calibrated by using the control points fixed on the beach and pixel coordinates of the shoreline were transformed into three-dimensional (3D) coordinates (Stockdon and Holman, 2000).

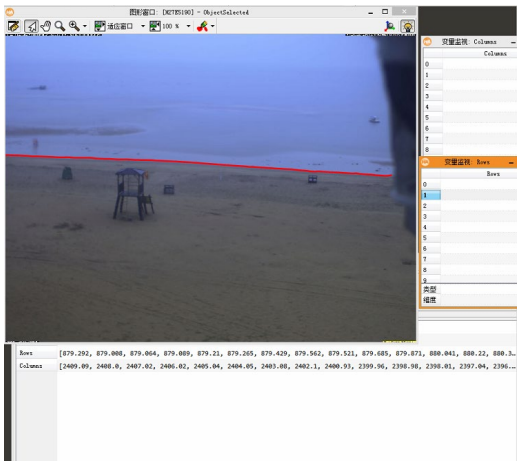

Figure 2. Pixel coordinates of shoreline extraction interface

2.3 Mathematical solution of the camera model

The Argus system captures images every half an hour. Images are classified as two types of image, i.e. snapshot and time exposure image. The time exposure image is from 600 snapshot images averaged within 10 minutes, which is able to effectively decrease the "visual noise" generated by random changes (Shi, et, al. 2019). The basic data were processed by three steps. First, image noise was filtered out by a Gaussian filtering algorithm, which avoided the destruction of edge information while filtering the noise in the image. Second, Canny (Gonzalez and Richard, 2011) edge detector (image abstraction algorithm) was applied to extract the shoreline (Figure2). After that, the cameras were calibrated by using the control points fixed on the beach and pixel coordinates of the shoreline are transformed into three-dimensional coordinates (Stockdon and Holman, 2000; Zhou, et al. 2006; Holman, Stanley, 2007). Figure 3 shows that the in-situ three-dimensional coordinates are reflected in the image by optical conversion. It can be seen that the correspondence between pixel coordinates and in-situ three-dimensional coordinates is linear, and the transformation from three-dimensional coordinates to pixel coordinates can be implemented by the following collinear equation [1].

$$\begin{cases} u = \dfrac{l_1(x-x_c)+l_2(y-y_c)+l_3(z-z_c)}{l_7(x-x_c)+l_8(y-y_c)+l_9(z-z_c)} \\ v = \dfrac{l_4(x-x_c)+l_5(y-y_c)+l_6(z-z_c)}{l_7(x-x_c)+l_8(y-y_c)+l_9(z-z_c)} \end{cases} \quad [1]$$

where u and v respectively correspond to the transverse and longitudinal coordinates of the pixels in the video imagery, and (x, y, z) denote the three-dimensional coordinates of the corresponding real-world points, (x_c, y_c, z_c) represent the three-dimensional coordinates of cameras location. After solving above 9 unknown parameters (l_i, $i \in$ [1,9]), the post-processed plane view of video imagery represents an important and basic component of video-based coastal monitoring systems resulting in the available access for accurate quantitative information of the monitoring area. Furthermore, the coordinates of the extracted shoreline at any time could be calculated accurately by coupling with the tidal data (Shen, 2009).

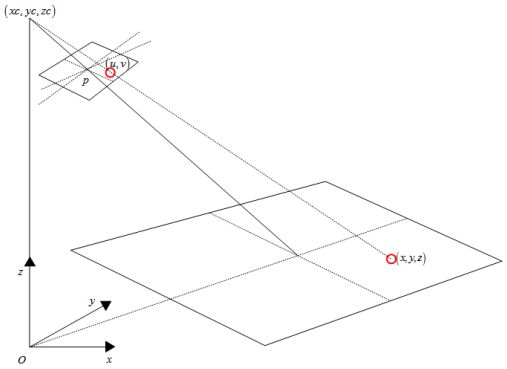

Figure 3. Linear transformation schematic diagram

2.4 DEM acquisition

The shoreline regarded as contour line (Shen, 2009) is the basic hypothesis for obtaining the intertidal zone using digital elevation model (DEM). On this basis, the DEM of intertidal zone was acquired after two steps. Firstly, the 3D coordinates of shorelines at different times of one day were extracted by using linear transformation equation combined with tidal model. After that, the DEM was obtained by interpolation of several shorelines. The kriging interpolation was used, and the terrain spacing was 10m × 10m. We established the beach DEMs on July 19 (the day before the storm surge) and July 22 (the day after the storm surge), 2016. The response of the beach to the storm surge was evaluated by analyzing the DEM modeling results.

3 Results

3.1 General variation

By extracting the position of coastline of each profile, the coastlines on July 19 and July 22, 2016 were posted by Figure 4. It turns out that the storm surge caused the western and eastern parts of coastline to be retreated with an average of 3 m, while the middle part was in silted. DEMs on July 19 and July 22, 2016 were shown in Figure 5. The elevation of intertidal zone was demonstrated here. By comparing the DEM on July 19 (Figure 5a) with the DEM on July 22 (Figure 5b), it was observed that the overall trend of the beach was towards erosion. The most severe erosion appeared in the western beach. Generally, the storm surge took a considerable effect on Pingshuiqiao beach shape.

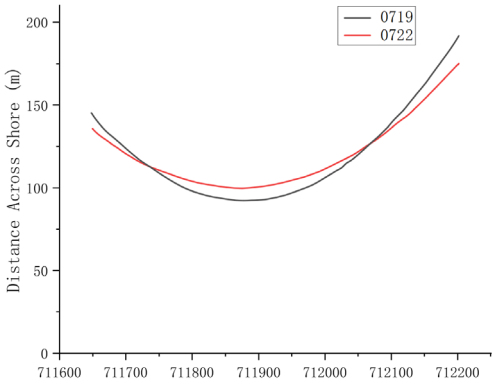

Figure 4. Coastline variations from July 19 to July 22, 2016

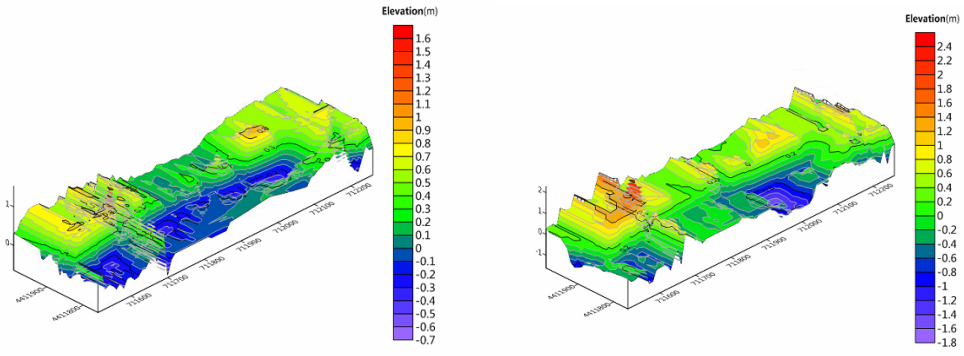

(a) July 19 (b) July 22

Figure 5. DEMs of intertidal zone on July 19 (a) and July 22 (b), 2016

3.2 Erosion and silting of beach profile and morphological changes during storm

The profiles volume variation caused by the storm surge were shown in Figure 6. According to Figure 6a, there was only profile c2 in erosion during this storm surge, while other profiles showed slight deposition or remained unchanged. This was related to the existence of a submerged rubble-mound breakwater in the offshore and two natural headlands at its east end. For more precise analysis, the beach was divided into three parts: the headland sheltering part (profile c5, profile c6, Figure 6e, f), the straight part (profile c3, profile c4, Figure 6c, d) and profile c2 (Figure 6b). Profiles c5 and c6 are shaded by the headland, both of them deposited slightly. The deposition gradually increased from c6 to c5. Profiles c3 and c4 are located in the straight part of the beach, where c4 was affected more severely by the storm: the part above the mean sea level was in erosion, and the part below the mean sea level was in deposition. The beach slope in profile c3 is gentler than other profiles and there was no obvious volume change in profile c3. Furthermore, for the profile c2 represented the most drastic erosion, we extracted the Argus image data of camera No.2 on July 20 (Figure 7) and observed the change of shoreline during the storm surge. It could be seen that the area monitored by camera No.2 showed different status during the storm surge. At 9:10 am (Figure 7b), the sea water began to flood the beach were eroded. The sea water even overflowed the house on the beach at 19:10 (Figure 7d). The beach slope here was steeper than other profiles, and there was no protection from headland, which contributed a lot to erosion. According to Figure 6a, the beach volume per unit width here was decreased by 132.50m^3/m during the storm.

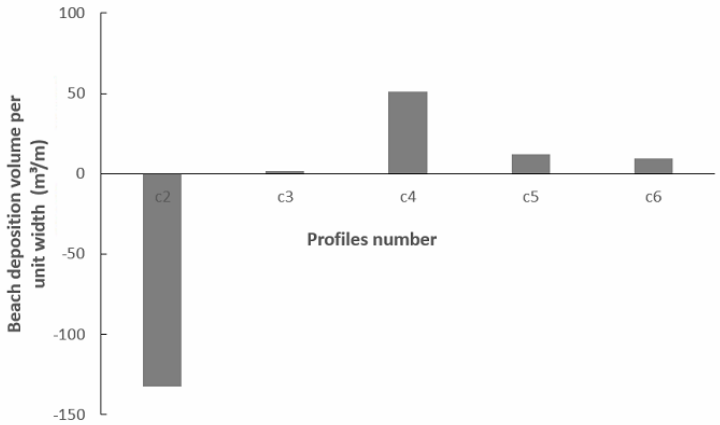

(a) Profiles volume variation

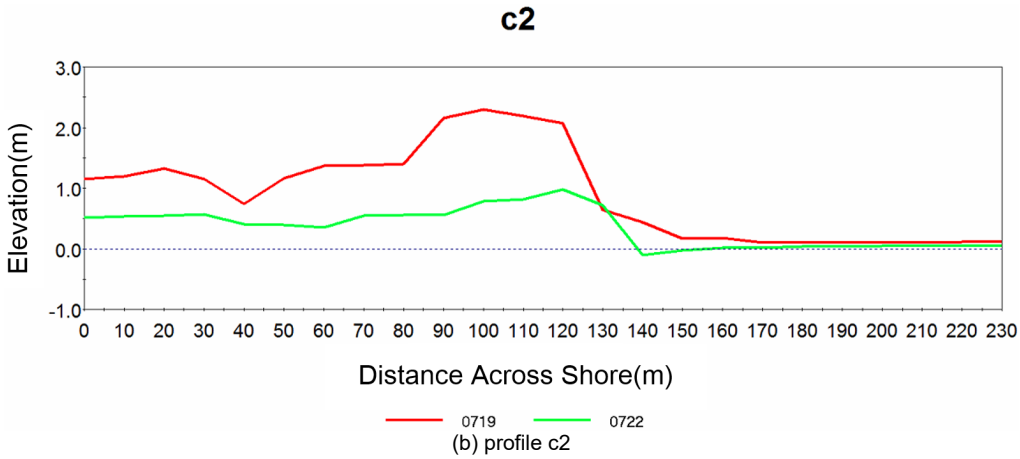

(b) profile c2

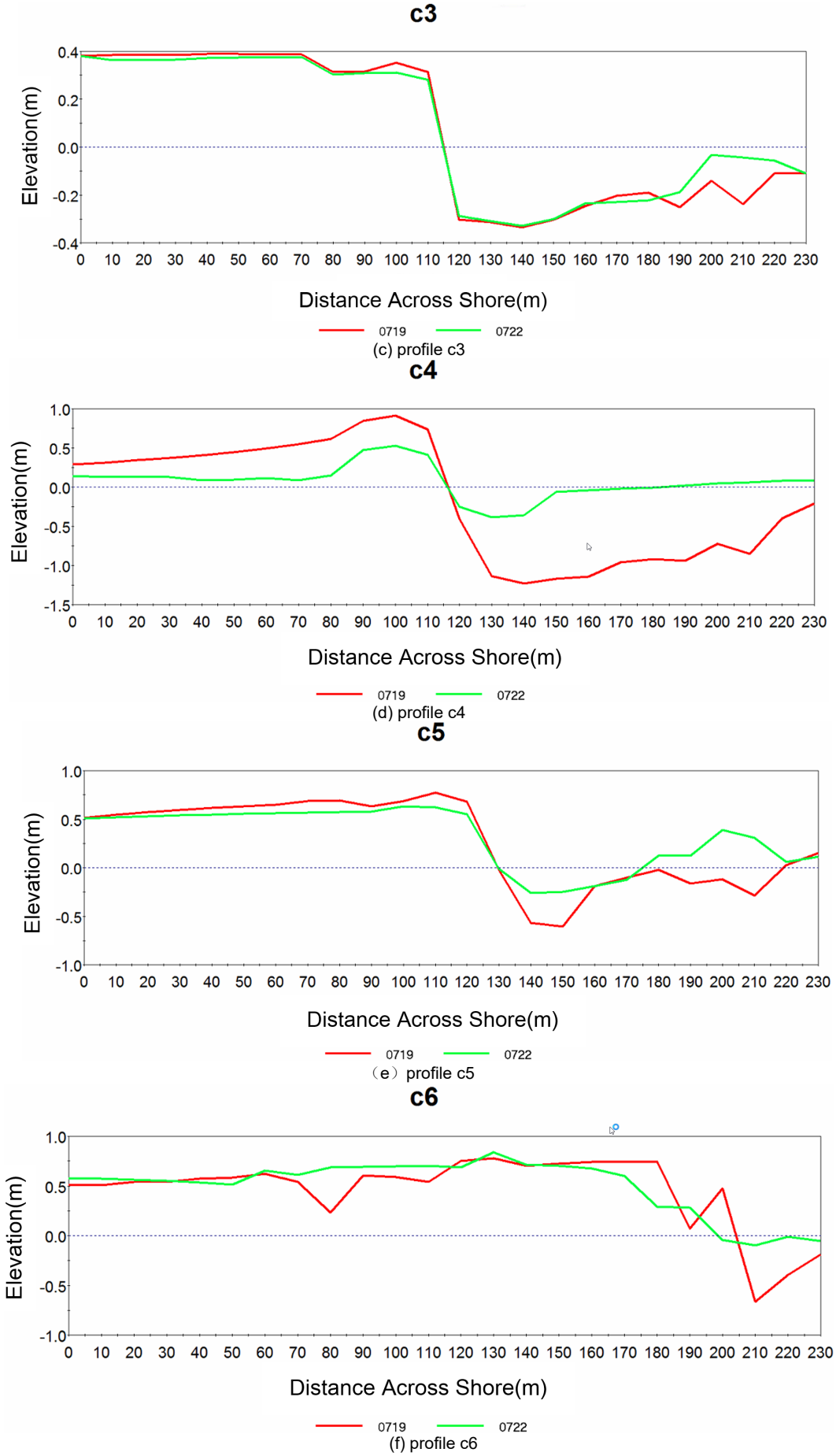

Figure6. Beach volume change (a) and beach elevation variation of profiles (b-f)

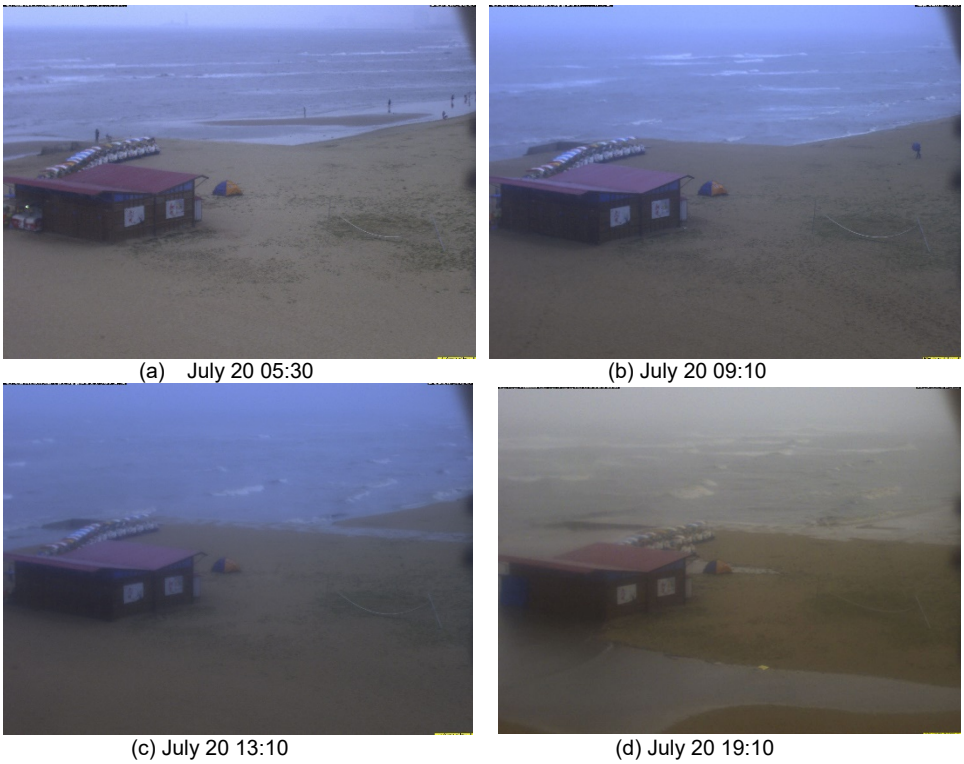

Figure 7. Argus images of camera No.2 during the storm surge

4 CONCLUSIONS

This work reported the morphodynamic changes at Pingshuiqiao beach, China using the coastal video monitoring system during a storm surge. The Argus system used in this study is an advanced measurement technology for long-term monitoring of shoreline, which is able to support continuous and sustainable monitoring, even in some extreme weather conditions. Therefore, it is more convenient than traditional field measurements. Additionally, since the measurement range of Argus system is intertidal zone and the basic assumption of treating the shoreline as contour line, it is more suitable to measure the beach with relatively gentle slope. As a result, by combining the Argus system with the tidal model, the DEM of intertidal zone was acquired, in order to examine the response pattern of the beach to the storm surge.

The images captured by Argus were processed to extract the pixel coordinates of shorelines at different time in one day. The pixel coordinates of shorelines images were converted into 3D coordinates of shorelines via linear transformation. On this basis, the response of the beach to the storm surge was analyzed by comparing the DEMs built for daily intertidal with different days. The results showed that the storm surge generally had a negative impact on the morphology evolution of the beach. As a whole, the beach of Pingshuiqiao was eroded continuously during the storm surge, especially, the most severe erosion appeared in the western beach with the loss of beach volume per unit width of 132.50m^3/m. However, the eastern beach was partly well protected due to the existence of the submerged breakwater and natural headlands on the east side of the beach. Generally, the strong erosion occurs in the supratidal zone and the upper part of intertidal zone, while the deposition in the lower part of intertidal zone during the storm surge in such a wave-dominated low tidal range sandy coast. In order to protect eco-tourism resources, the sediment loss caused by storm surge need to be replenished by artificial measures.

ACKNOWLEDGEMENTS

The authors thank The Eighth Geological Brigade, Hebei Geological Prospecting Bureau for providing the Argus data.

REFERENCES

Archetti R., Paci A., Carniel S., and Bonaldo, D (2015). Optimal index related to the shoreline dynamics during a storm: the case of Jesolo beach. Natural Hazards and Earth System Sciences, 3(11):7089-7134.

Bergsma, E., Conley, D. , Davidson, M. , O'Hare, T. and Almar, R. (2019). Storm event to seasonal evolution of nearshore bathymetry fervid from shore-based video imagery. Remote Sensing, 11(5):519.

Bouma, T.J., Belzen, J., Balke, T., Zhu, Z.; Airoldi, L., Blight, A.J., Davies, A.J., Galvan, C., Hawkins, S.J., Hoggart, S.P.G., Lara, J.L., Losada, I.J., Maza, M., Ondiviela, B., Skov, M.W., Strain, E.M., Thompson, R.C., Yang, S., Zanuttigh, B., Zhang, L. and Herman,P.M.J., (2014). Identifying knowledge gaps hampering application of intertidal habitats in coastal protection: Opportunities & steps to take. Coastal Engineering, 87, 147–157.

Elko N. A., Gelfenbaum H. G. (2005). Quantifying the rapid evolution of a nourishment project with video imagery. Journal of Coastal Research, 21(4):633-645.

Gonzalez R. C., Woods R. E. (2011). Digital Image Processing, third edition. Publishing house of electronics industry:445-467.

Guo J. L., Shi L. Q., Chen S. L., Ye Q. H. (2019). Responese of Dongsha beach in Zhoushan to continuous storms based on Argus. Oceanologia et Limnologia Sinica, 50(4):728-739 (in Chinese).

Guo J. L., Shi L. Q., Tong X. L., Zheng Y. J., Xu D. L. (2018). The response to tropical storm Nakri and the restoration of Dongsha Beach in Zhujiajian Island,Zhejiang Province[J]. Acta Oceanologica Sinica, 040(009):137-147 (in Chinese).

Holman R. A., Stanley J. (2007). The history and technical capabilities of Argus. Coastal engineering, 54(6-7): 477-491.

North Sea Forecast Center of the State Oceanic Administration, (2016). Storm surge III alarm. http://www.nmfc.org.cn.

Sancho-García A., Guillén J., Ojeda E. (2013). Storm-induced readjustment of an embayed beach after modification by protection works [J]. Geo-Marine Letters, 33(2-3): 159-172.

Shen J. S., Zhai J. S., Guo H. T. (2009). Study on coastline extraction technology. Hydrographic Surveying and Charting, 29(6):74-77.

Shi L. Q., Guo J. L., Liu H. J., Ye Q. H. (2019). Application progress and prospect of Argus system in beach research in China. Advances in Earth Science (05), 552-560.

Stockdon H. F., Holman R. A. (2000). Estimation of wave phase speed and nearshore bathymetry from video imagery. Journal of Geophysical Research, 105(C9):22015.

Zhang S. P., Zhang C. T.(2006). An introduction to nearshore video imaging observations. Journal of Ocean Technology (01), 15-23 (in Chinese).

8th International Conference on the Application of Physical Modelling in Coastal and Port Engineering and Science
Dec. 9th - 12th, 2020, Zhoushan, China

STUDY ON MEASURES TO STABILIZE COURSES OF THE YELLOW RIVER ESTUARY

SONGWEI CHEN XIONGBO CHEN YANJIE LIANG & YU QIAN

(Yellow River Engineering Consulting Co., Ltd., Zhengzhou, Henan, 450003)

ABSTRACT

The purposes of the Yellow River Estuary improvement are toensure the flood control safety at the estuarine area, stabilize courses and extend the service life. Great achievements have been made, since Chinese people set out to regulate the Yellow River, in terms of flood control works construction, water resources development & utilization and tide-prevention project construction, thanks to economic and social development of the estuarine areas. Measures taken, at present, to regulate the Yellow River Estuary include dyke building, river regulation, sea embankments, diversion dikes, river dredging for dikes reinforcing, artificial diversion of river channel or distributary, bar dredging and ecological water diversion. Course stability, in fact, is affected by various complicated factors. Moreover, the Yellow River Estuary still features a large amount of silt and weak ocean dynamic. As a result, estuary improvement is now plagued by such problems as estuary backward deposition and incomplete flood control works in the courses in use. This paper summarizes the measures already taken to improve the Yellow River Estuary and their effects in a systematic way. Based on analysis of current situation and existing problems of estuary improvement, improving flood control works, carrying out artificial diversion of distributary and building sea embankments are considered effective in ensuring stable courses of the Yellow River Estuary. Measures for improvement of the Yellow River Estuary in the near future are also proposed with consideration given to the application mode of the courses.

Keywords: Yellow River Estuary Course stabilization Artificial diversion of distributary Flood control works River dredging and excavation Sea embankments

At the Yellow River Estuary, course change and river fork swing have a great impact on the stability of the downstream channel of the Yellow River, and frequent course change is detrimental to social and economic development of the estuarine areas. Measures suitable for management of the Yellow River Estuary courses are explored by analyzing the current situation and the problems of the engineering measures taken at the estuary. Drawing up improvement measures that facilitate course stability in the light of existing engineering measures, course topography and sea area features is important in promoting sustainable economic and social development of the estuarine areas.

1 Major Problems of the Yellow River Estuary Improvement

(1) Extension of deposits at the river mouth gives rise to backward deposition at the downstream river channel. The Yellow River Estuary evolves in the rule of deposition, extension, swing and course change. From 1976 to 1996, Qingshuigou Course became the new course where the Yellow River enters the sea. The estuary has an average annual incoming sediment load of 630 million tons and an average extension speed of 1.96km/year. From 1996 to 2018, the estuary saw an average annual incoming sediment load down to 130 million tons, but the extension speed fell by only 0.33 km each year on average and the deposition stretched for 63 km. Influenced by the backward deposition at the end of the tail-end river channel, the erosion basis of the river channel rises relatively. With the gradient of the reach close to the estuary becomes gentle, the sediment carrying capability of the flow decreases, causing deposition and higher riverbed which then leads to higher erosion basis at the lower boundary of the adjacent upstream river channel. In this way, the effect of backward deposition is conveyed to the upper reaches of the river mouth, complicating flood control and deposition reduction work at the downstream river channels[1].

(2) Large traverse gradient at bench land is likely to induce cross river and other unfavorable river regimes, which may cause flood along the dyke and towards the dyke directly. Since 1985, back silting at main channel of the Qingshuigou Course have become prominent gradually. The inflow of Qingshuigou is small in the past decade or so because of the single straight river channel. In most cases, the deposition found is bench lip deposition, while beach face deposition is rarely seen, forming relatively large traverse gradient. This may lead to bursting or flood along the dyke, a passive situation unfavorable in flood control, in the case of overbank flood and sudden change of river regime.

(3) The river regulation works now in place cannot control river regime effectively, so great river regime

change is possible and the river channel is still unstable. Dykes along the reach of the estuary are wide apart. Most of the works are built to avoid bench land collapse or water diversion. Some of the works are of unreasonable layout and both their number and length are below the requirements. Given the poor adaptability and strength of the works, river regime cannot be controlled in an effective manner.

(4) With incomplete system of tide-prevention projects, storm surge is still a great threat. Dongying is prone to storm surge disaster as the Dongying sea area is semi-enclosed and the tide of most coastal segments is of irregular semi-diurnal tide. With the development of the Shengli Oilfield and given other demands of economic construction, governments at all levels and relevant units attach increasingly more importance on prevention of coastal storm surge disasters. Measures including strengthening storm surge monitoring and prediction and building sea embankments are taken for tide prevention and disaster alleviation, significantly reducing the land inundated and ships and boats damaged in the disasters. The economic losses caused by storm surge, however, are not reduced since there are many economic enterprises.

2 Overview of Improvement Measures of the Yellow River Estuary

Since 1950, river channel of the estuary has been diverted artificially for three times to reduce deposition at the downstream river channel and ensure flood control security at the estuarine area. Dyke building, river regulation works and other works were carried out during artificial diversion, creating favorable conditions for economic and social development of the estuarine area. In 1953, artificial diversion was carried out so that water in the Yellow River emptied into the sea through the Shenxiangou only, instead of through Tianshuigou, Songchunronggou and Shenxiangou, simultaneously; in January 1964, as water level rose due to river channel deposition, blasting was implemented at Luojiawuzi during ice run period, diverting the estuary from Shenxiangou Course to Diaokou River; in May 1976, a planned artificial diversion was performed at Xihekou, after which the Yellow River estuary was diverted to Qingshuigou Course. Much improvement work was done during diversion; in 1988, a dredging test aiming at “extending the service life of the Qingshuigou Course as long as possible” was conducted at the estuary; from 1988 to 1992, a project was executed to increase the inflow of the main stream by diverting water from the tributaries downstream of the Qing 7 cross section in combination with river dredging and excavation, reducing the quantity of tail-end channels, forming a main stream of large water flow and realizing better sand flushing performance. By 1996, river length downstream of Xihekou was up to 65km. To facilitate oil exploitation at the Shengli Oilfield, Qing 8 Distributary diversion was carried out along the east by slightly north direction, and phase 1 project of estuary improvement was conducted. In 2011, Qing 8~Cha 2 reach was improved by curve cut-off. The successive governments of Dongying and the Shengli Oilfield has built 217.73 km sea embankment of high standard since 1970s, safeguarding development of the Shengli Oilfield and construction of the coastal industrial economic belt in Dongying. Dyke building, river regulation works and sea embankments jointly play an important role in improving flood control capability of the estuary reach, stabilizing river channel upstream of Qing 7, reducing deposition at downstream river channels and protecting industrial and agricultural production and people’s life and property safety at the estuarine area. Refer to Table 1 for major improvement measures taken at the Yellow River Estuary.

Table 1 Major Existing Measures of Yellow River Estuary Improvement

Measures	Targets	Time	Location	Description
Artificial diversion of river channel	Reducing estuaries to only one, Shenxiangou	July 1953	Xiaokouzi	Artificial curve cut-off
	Diverting water to the sea through Diaokou River	January 1964	Luojiawuzi	Artificial blasting during ice run period
	Diverting water to the sea through	May 1976	Xihekou	Artificial closure and diversion of river channel

Measures	Targets	Time	Location	Description
	Qingshuigou			
Artificial diversion of distributary	Reclamation for oil exploitation with sludge	Before flood season in 1996	Qing 8 cross section	A closure dam was built in the original river channel, an approach channel was excavated and a diversion dike was built at the left bank of the approach channel
Curve cut-off	Improving distorted river bends	May 2011	Qing 8~Cha 2 reaches	Artificial curve cut-off
Flood control works	Improving flood control capability of the estuary reach and stabilizing the river regime	Long Term	Downstream of Yuwa	Dyke building, critical levee sections and river control works
River dredging and excavation	Reducing deposition of the river channel and improving flow release of the tail-end channels	May 1988	Qing 6 cross section	The main channel was widened and deepened
		November 1997~June 1998	Zhujiawuzi cross section~CS6 section	River dredging for dikes reinforcing
		2001~2002	Yihe critical levee section~Qing 3 cross section	River dredging for dikes reinforcing
		2004	Jifeng critical levee section~Yihe critical levee section	River dredging for dikes reinforcing
Blocking the tributaries and enhancing the main stream	Diverting water from the tail-end channels to the main stream	1988~1992	Downstream of Qing 7 cross section	Distributary closure was carried out
Diverting flood with high sediment content for warping	Reducing deposition at the estuary	1970~1979	Shibahu Warping Area	A test of flood diversion and warping
Tide-prevention project	Reducing the risk of storm surge disaster	Since 1970s	Coastline of Dongying	Sea embankment construction

3 Effects of Improvement Measures of the Yellow River Estuary

3.1 Artificial Diversion of Distributary

Under the influence of human activities, the Yellow River still evolves in the rule of “deposition, extension, swing and course change” in a long period, but the evolving period is extended. The swing vertex will move upward to the area close to Ninghai after the sediment at Qingshuigou and other courses reaches the upper limit, starting the major circulation of estuarine delta. Compared with natural swing, diverting and regulating the Yellow River Estuary according to plan is conducive to the development of headward scouring, extending the service life of the course[2].

To realize oil exploitation with artificial land, before the flood season of 1996, a distributary diversion project was carried out 950m upstream of the Qing 8 cross section of the Yellow River Estuary. Water of the new distributary enter the sea along the east by slightly north direction, forming an angle of 29.5° with the original river channel. The estuary is about 14km from that of the North Distributary, imposing no impact on the North Distributary sea area. The project commenced on May 11 of the year, during the dry season of the Yellow River. The works were completed before the flood season and the inflow was discharged from the approach channel. After the flood peak in August, a river channel developed in the Qing 8 artificial distributary. The main works include excavating the approach channel of 5.0km long, building a closure dam of 4.1km in the original channel and constructing a diversion dike of 5.5km long at the left bank of the approach channel. The distance to the sea is reduced by 16 km after distributary diversion compared with the original course[3].

From 1976 to 1995, or from the year when the original channel of Qingshuigou Course was put into use to the year of Qing 8 Distributary diversion, sand spit at the estuary stretched for 65km from Xihekou, extending 1.96km each year on average. At the early stage after Qing 8 Distributary diversion (before the flood season of 1996), the river length downstream of Xihekou was 49 km. The 0m isobath behind the estuary moved outward by 5.5 km after flood because of the large amount of incoming sediment load that year. The position of 0m isobath changes little as inflow and incoming sediment load of the following years were small. The amount of sediment entering the estuary dropped in 2000 after the Xiaolangdi Reservoir was put into operation. Deposition and erosion of the sand spit was basically balanced. Before 2001, river length downstream of Xihekou maintained at 56km. After 2002 when water and sediment regulation tests were carried out, sediment conveyed to the estuary increased and sand spit at the estuary extended to the sea again. In 2007, the course bifurcated towards north near the Cha 3 cross section, but the sediment pile still belonged to the Qing 8 Distributary sea area. In 2011, Qing 8~Cha 2 reach was improved by curve cut-off. At present, the Qing 8 Distributary downstream of Xihekou is 54~60km long and in good conditions, showing relatively large operation potential[4]. Before the flood season of 2017, the water level of Xihekou is 10.37m when the flow rate is 10,000 m3/s, far below the diversion standard.

3.2 Flood Control Works

(1) Dyke Building

Currently, various embankments of 206.331 km long can be found in the estuarine area, including north dyke, south flood dyke and other dykes totaled 77.466 km long. The embankment at the left bank is 49.731 km long, composed of 44.631 km north dyke and 5.100 km south-east border dike of Gudong Oilfield; the south flood dyke at the right bank is 27.735 km long.

(2) Critical Levee Sections

Since 1985, to prevent flood along the dyke, dyke inundation and flood overflow in flood seasons, 4 critical levee sections of 22 km, 30 km, 38 km and 42 km, respectively, have been built one after another at the turns of dykes from upstream to downstream at the dyke sections previously without critical levee sections on the left bank, to prevent overflow and scouring with groyne and to protect embankments. The 4 critical levee sections are 3.101 km long in total, with protection body of 3.294 km and 23 dam buttresses.

(3) Channel Improvement Works

At the early stage after the diversion of Qingshuigou Course, the estuary reach of the Yellow River barely had any control works except the river improvement works at Zhonggudian, Hulin and Shisigongli. Since 1986, river control works have been built at Weigaizha, Xihekou, Balian, Shibahu, Cuijiazhuang and Shengchancun. By the end of 2015, there were 11 river improvement works stretching for 21,476m at the estuary reach, with 203 dam buttresses and 19,485m protection body. Among them, 5 improvement works totaled 10,776m were on the left bank—the Zhonggudian, Cuijiazhuang, Xihekou, Balian and Qing 3 river improvement works—with

99 dam buttresses and 10,138m protection body; 6 improvement works totaled 10,700m were on the right bank—the Shibahu, Weigaizha, Shengchancun, Hulin, Shisigongli and Qing 4 river improvement works—with 104 dam buttresses and 9,347m protection body.

The embankments were raised and strengthened with the construction of the flood control projects, improving their flood resistance capability; new works for river improvement played a great role in preventing beach land and bank collapse, stabilizing river regime and protecting embankment. Refer to Fig. 1 for current layout of the flood control works.

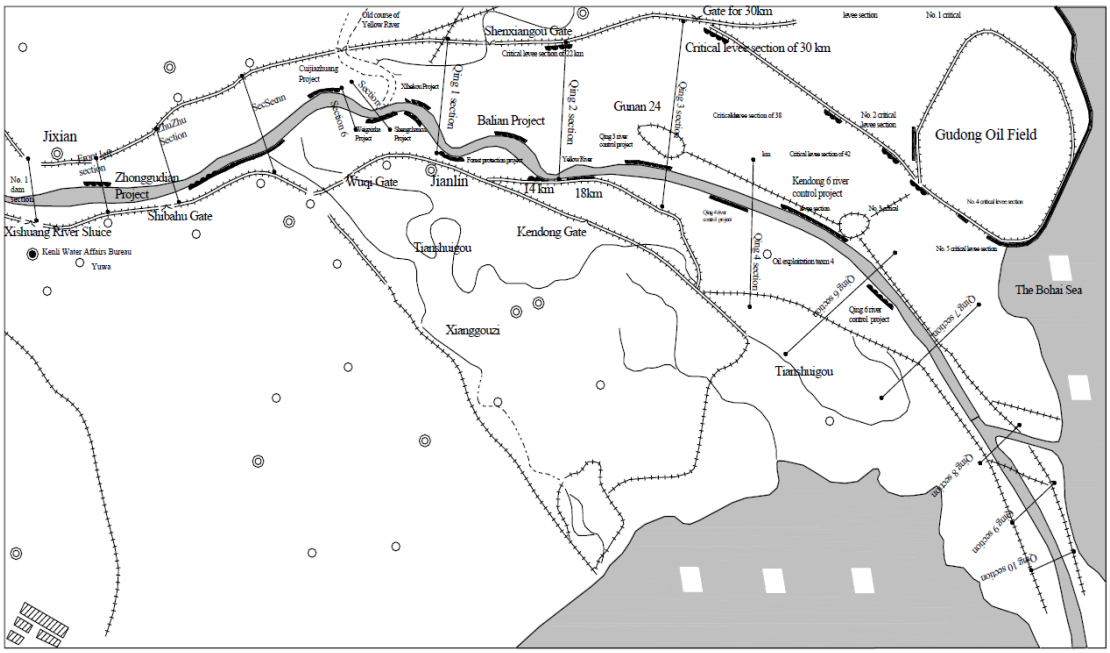

Fig. 1 Schematic Diagram of Flood Control Works at the Yellow River Estuary

3.3 Tide-prevention Project

Up to now, Dongying has built 212.5 km sea dyke of high standard, consisting of the north dyke of the Gudong Oilfield (two sections), 17 km, the east border dike of Gudong Oilfield, 88.9 km, lower reach dyke of Guangli River at Dongying District, 1.4 km, Laizhou Bay coastal dyke to the east of Guangrao County, 4 km, border dike of Kendong, 47.3 km, Chengdong sea embankment, 41.4 km, east bank dyke of Diaokou River, 5.2 km, 50-year flood sea dyke of the Central Fishing Port of Dongying Harbor, 7.3 km. Construction of sea embankments greatly mitigates the damage caused by storm surge.

3.4 River Dredging and Excavation

In 1987, the 12th year in operation of the Qingshuigou Course, river channel downstream of Lijin was 29 km longer compared with years before diversion, and had much deposition at the river channel, making it difficult for flow release. This caused overflow during both ice run period and flood season of that year, forcing the oilfield at the beach land to cease production twice. From 1988 to 1993, Dongying City, the Shengli Oilfield and the Yellow River Estuary Administration Bureau performed dredging test at the estuary to block the tail-end river channels and enhance the main stream, reversing the unfavorable flood control situation at the estuary reach.

River dredging for dikes reinforcing was conducted in three times at 1997 ~1998, 2001~2002 and 2004 at the estuary reach. The first river excavation project was conducted in the segment from Zhujiawuzi to Qing 2 cross section, 24.4 km in total, with the 11 km section from Zhujiawuzi to the CS6 cross section being excavation section, while the 13.4 km section from CS6 cross section to Qing 2 cross section being dredging section. The work was finished with both excavators and combined sludge pumps. In the project, 5,479,600 m^3 sediment was excavated and 10.0 km embankment was reinforced.The second river excavation project was conducted in the 41 km river channel from Yihe critical levee section to Qing 3 cross section. The section, 9.7 km long, from Yihe critical levee section to Zhujiawuzi was the excavation section, while the section, 10.9 km long, from Zhujiawuzi to CS6 cross section was the dredging section. From CS6 cross section to the Qing 3 cross section, 20.4 km in total, 5 sections which were discontinuous and totaled 9.16 km, were dredged. Excavation was conducted with 80 m^3/h dredgers and combined sludge pumps. In the project, 3,495,600 m^3

sediment was excavated and 8.0 km embankment was reinforced. The third project of river dredging for dikes reinforcing was conducted from Yihe critical levee section to Jifeng critical levee section. The river segment was 12.5 km long and the river channel excavated was 9.8 km long. Only 120 m^3/h dredgers were employed for excavation. In the project, 1,594,200 m^3 sediment was excavated and 6.8 km embankment was reinforced. In the three projects, 53.6 km river channel was excavated or dredged, 10.57 million m^3 sediment was excavated and 24.8 km embankment was reinforced[5]. The embankments were of higher flood resistance capacity upon completion of the three projects, during which 24.8 km dyke was reinforced and the sediment filling width was 80~100m. This reduced deposition at the downstream narrow reaches of the Yellow River, and also facilitated embankment construction. Therefore, this is a reasonable and important measure of handling and utilizing sediment in the Yellow River.

3.5 Blocking the Tributaries and Enhancing the Main Stream

The Yellow River Estuary, in natural state, is prone to develop several tributaries with low sediment transporting capacity, creating conditions for natural swing and course change. On that account, the engineering measure of “blocking the tributaries and enhancing the main stream” was taken at the estuary. The tributaries were blocked locally with mechanical measures, while the main river channel was dredged to improve its discharge capacity. “Clearing sands with converging flow” proved an effective measure. From 1988 to 1992, this measure was taken, in combination with river dredging and excavation, downstream of Qing 7 cross section. Over 80 tributaries and distributaries were blocked, reducing the quantity of tail-end channels, forming a main stream of large water flow and realizing better sand flushing performance.

3.6 Diverting Flood with High Sediment Content for Warping

In 1969, a flood diversion and warping sluice and the supporting works of the silt area were completed at Shibahu. From 1970 to 1979, a total of 5 warping tests were conducted. The cumulative time of warping was 105 days, the sluice discharge rate 15~382 m^3/s, the average sediment concentration 54 kg/m^3, the total water diversion amount 1.68 billion m^3 and the sediment release amount 79.63 million m^3. During the tests, it was found that trying to conduct the tests as per the design indexes was not practical, because there were only 4.2 days and 20 days with sluice discharge rate higher than 3,000 m^3/s and 2,000 m^3/s each year, respectively, at the Lijin Station of the Yellow River. Later work was not finished according to the initial design. Problems like dispersed water flow, uneven sediment release and large difference in benefits were encountered during the tests, preventing the warping tests from proceeding. In addition, two flood diversion and warping tests were conducted at the South Bank Widening Project carried out in 1970s.

Only limited sediment was diverted with the warping works built at the Yellow River Estuary. The Shibahu Warping Area, for example, diverted sediment accounting to 3% at most, or generally 1%~2%, of the incoming sediment load at the Lijin Station each year. In terms of the South Bank Widening Project, flood diversion and warping were conducted at the Caodian sluice in August 1979. The average sediment concentration was 73.7 kg/m^3 and the total sediment diversion load was 46 million tons, accounting to as low as 6.3% of 733 million tons, the sediment entering the sea through Lijin that year. Moreover, the sediment amount diverted in warping dropped year by year. Upon completion of the water-sediment regulation system of the Yellow River, the sediment concentration of water entering the estuary fell, so the sediment diversion load under the same conditions decreased as well. Apparently, it is not an effective way to reduce estuary deposition and extend service life of the courses by depending on flood diversion and warping which divert only a few percent of the sediment. Warping on a large scale, however, is not possible in short term since it involves problems including warping position determination, resettlement of inhabitant and project investment.

4 Measures for improvement of the Yellow River Estuary in the Near Future

4.1 Operation Method of the Course

For estuary courses of the Yellow River, operation modes of “fixed course in operation”, “multiple courses in operation in turn” and “multiple courses in operation at the same time” are available [6]. In this study, the mode of “multiple courses in operation at the same time” is considered, which means that water enter the sea through both Qingshuigou (current Qing 8 Distributary, North Distributary and the original river channel) and Diaokou River Courses. Two alternatives are drafted for the operation of Diaokou River:

Perform the flood diversion as per the discharge of Diaokou River being 1,500 m^3/s in June ~ October (river discharge: over 3,000 m^3/s), and keep the constantly flow water with a discharge of 30 m^3/s in other time frames.

Perform the flood diversion as per the discharge of Diaokou River not exceeding 3,000 m^3/s and water

diversion ratio being 50% in June ~ October (river discharge: over 3,000 m^3/s), and keep the constantly flow water with a discharge of 30 m^3/s in other time frames.

4.2. Measures for Improvement of the Yellow River Estuary in the Near Future

Given the effects and problems of the improvement measures taken, it is believed that building flood control works, carrying out artificial diversion of distributary and building sea embankments are effective in stabilizing the courses of the Yellow River Estuary. Building flood control works can improve flood resistance capacity of embankments and stabilize river regime. Artificial diversion of distributary shortens the distance to the sea, reducing headward scouring and thus extending the service life of the courses. Construction of sea embankments improves our capabilities against storm surge. The measures for the Yellow River Estuary improvement are proposed on the basis of the Comprehensive Control Planning for the Yellow River Estuary, the Shandong Sea Dyke Construction Planning, and the Feasibility Study Report of Comprehensive Control of the Yellow River Downstream Channels[7].

(1) Artificial Diversion of Distributary

For the Qingshuigou Course, Qing 8 Distributary will continue to be used. Water of Qing 8 Distributary will be diverted to North Distributary when the discharge of 10,000 m^3/s reaches a water level of 12m downstream of the Xihekou, and then to the original river channel of Qingshuigou Course in operation before 1996 when the discharge of 10,000 m^3/s reaches a water level of 12m at Xihekou. Diverting water in Qing 8 Distributary to North Distributary means to excavate an approach channel on the left bank near the Qing 7 cross section to connect North Distributary. Major engineering measures: approach channel excavation, as per the 800 m^3/s flow rate standard; closure work; removal of diversion dyke and other facilities at the diversion mouth.

(2) Flood Control Works

Raise the height of the dyke sections over 0.5m lower than the required height, and widen the dyke sections over 1m less than the required width. Reconstruct the critical levee sections of 22 km, 30 km, 38 km and 42 km. Extend the river control works of Shibahu, Cuizhuang, Xihekou, Balian and Qing 3 upward by 1,300m, 300m, 800m, 400m and 1,200m, respectively, and those at Weigaizha and Qing 4 downward by 400m and 500m, respectively.

（3） Flood Diversion Works

If the Diaokou River Course is adopted again as one of the courses in the “multiple courses in operation at the same time” mode, a flood diversion sluice shall be built near Xihekou and a main river channel with a discharge capacity of 3,000 m^3/s (or 1,500 m^3/s) shall be excavated. If it is used as the geological water supplement channel with a constant discharge of 30 m^3/s, it shall be dredged at regular intervals according to the deposition conditions.

5 Tide-prevention Project

According to the Dongying City's tide-prevention planning, works such as tide embankment, backwater dike, and tide gate are built to form a tide-prevention engineering system covering the area on the north of the Yellow River (Hekou District, Dongying Port District, and Gudong Border Dike District) and the Laizhou Bay District on the south of the Yellow River, thus reducing the 50-year storm tide disaster in the protection areas and 100-year disaster in the key areas of the tide embankments under administration of Dongying City. It is necessary to build or reconstruct 241.2 km dyke, including 44.1 km sea dyke to be reinforced and 197.1 km new dyke (129.9 km of sea dyke and 67.2 km of sea dyke at the estuary).

6 Conclusions

(1) This paper summarizes the measures already taken to improve the Yellow River Estuary and their effects in a systematic way. It is believed that improving flood control works, carrying out artificial diversion of distributary and building sea embankments are considered effective in ensuring stable courses of the Yellow River Estuary. Measures for improvement of the Yellow River Estuary in the near future are also proposed with consideration given to the application mode of the courses.

(2) For rationality analysis of the improvement measures, mathematic models are needed to simulate the long-term and short-term effects of the measures, analyze the effects of the measures on the services life of the course and decide the controlling effects of river regime change of tail-end channels, so as to evaluate their effects from all aspects.

References

[1] Yellow River Engineering Consulting Co., Ltd., China Institute of Water Resources and Hydropower Research, et al. Study on Key Technologies for Comprehensive Improvement of the Yellow River Estuary [R], 2010.

[2] Cao Wenhong. Study on Evolution of the Yellow River Delta and Its Feedback Influence [J]. Journal of Sediment Research, 1997, (4):1-6.

[3] GuYuanze, Jiang Mingxing et al. Effects of the Qing 8 Bifurcating Project and Its Influence on Estuary Evolution [J]. Journal of Sediment Research, 2000, (5):57-61.

[4] Chen Xiongbo. Prediction on River Channel Scouring and Silting of Qing 8 Distributary [J]. YELLOW RIVER, 2009, 31(6):30-33.

[5] Yellow River Engineering Consulting Co., Ltd..Comprehensive Control Planning for the Yellow River Estuary [R], 2011.

[6] Chen Xiongbo, Chen Songwei et al. Current Situation and Trend of Study on Utilization Mode of Entrance Course at the Yellow River Estuary [J]. YELLOW RIVER, 2018, 40(9): 10-15.

[7] Yellow River Engineering Consulting Co., Ltd. Feasibility Study Report of Comprehensive Control of the Yellow River Downstream Channels [R], 2018.

Fund project: supported by Topic Six - "Entrance Course Scheme and Control Measures for 100-Year Stable Yellow River Estuary" of National Key Research and Development Program - "Comprehensive Control and Study on the Yellow River Estuary Evolution and Course Stabilization" (No.: 2017YFC0405506)

Author: Chen Songwei (1983-), male, born in Lingbao City, Henan Province, senior engineer, mainly engaged in study on sediment.

E-mail: chensongwei_x@163.com Mobile phone: 15003805378

8th International Conference on the Application of Physical Modelling in Coastal and Port Engineering and Science
Dec. 9th - 12th, 2020, Zhoushan, China

PRACTICE AND EXPLORATION OF CHINESE LIVING SHORELINES

AIFENG TAO1,2, JINYAN2, WEIXU2, JIAN SHI1,2

1 Key Laboratory of Ministry of Education for Coastal Disaster and Protection, Hohai University, China, aftao@hhu.edu.cn
2.College of Harbour, Coastal and Offshore Engineering, Hohai University, China, xw1102@foxmail.com

Abstract: Living shorelines are defined as shoreline stabilization techniques that use as many natural habitat elements as possible to protect shorelines from erosion while also providing critical habitat for wildlife. They can improve the abilities for both ecology system and disaster reduction. This concept will be introduced to China officially with launch of Coastal Zone Protection and Restoration Projects, which are proposed by president Xi, from this year. The main works of Coastal Zone Protection and Restoration Projects include two parts: natural ecosystem restoration and ecological construction of artificial protection engineering. This paper expounds the connotation, measures and practice of this series of projects, and puts forward some suggestions by summarizing engineering cases at home and abroad, so as to provide reference for further development of Chinese Living Shorelines.

Key Words: Chinese living shorelines, coastal zone, protection and restoration, ecological hazard mitigation

1 INTRODUCTION

With the development of social productivity, the ecological environment of the earth has been seriously damaged. The 21st century can be called the century of repairing the earth. In the 21st century, China has carried out some major projects, such as ecological restoration of some river basins, ecological protection and restoration of grassland, and returning farmland to forest and grassland, and achieved remarkable results. The report of the 19th National Congress of the Communist Party of China pointed out that it is necessary to strengthen the protection of ecosystems, implement major projects for the protection and restoration of important ecosystems, optimize the ecological security barrier system, build ecological corridors and biodiversity networks, and improve the quality and stability of ecosystems. With the deepening of ecological civilization construction in China, the concept of green and ecological coastal zone protection has been further developed, and marine ecosystem damage has been paid more and more attention.

Coastal zone is the habitat of many creatures, is a valuable natural resource of human beings, and is also the most seriously affected area by marine disasters. China has more than 18000 km of continental coastline, which is seriously affected by marine disasters such as storm surge. In order to resist marine disasters such as typhoon storm surge, by the end of 2015, 14500 km seawalls have been built[1]. These seawalls have played a crucial role in ensuring the production and living of coastal residents and promoting regional economic development. However, gray and hard seawalls certainly have an effect on ecological environment of coastal zone which is brittle and weak.

In October 2018, general secretary Xi Jinping proposed the implementation of the coastal protection and restoration project at the Third Meeting of the Central Finance and Economic Commission, building ecological seawalls, and enhancing the ability to withstand such marine disasters as typhoons and storm surges. In order to implement the spirit of general secretary Xi Jinping's important instructions, all departments responded quickly and actively, making top-level design, organizing relevant standards, establishing and improving the technical method system, and effectively guiding the implementation of coastal protection and restoration projects. The local government is actively working out the relevant plans for coastal zone protection and restoration projects. Some regions have carried out the coastal zone protection and restoration projects first, and the synergy between ecological and disaster reduction functions is remarkable. However, considering the long coastline, coastal zone protection and restoration project of China is still in its infancy.

2. CONNOTATION OF COASTAL ZONE PROTECTION AND RESTORATION

Foundation item: This research work is funded by the Fundamental Research Funds for the Central Universities (Grant No.2017B633X14), the Postgraduate Research & Practice Innovation Program of Jiangsu Province (Grant No.KYCX17_0453).

To carry out the coastal zone protection and restoration project, we should first establish the faith of ecological protection, adjust measures to local conditions, combine green and ecological means with gray and most-pollutional engineering. Secondly, we should take ecological restoration as an important starting point and take multiple measures simultaneously to create a safe, ecological and harmonious comprehensive protection system for coastal ecological disaster reduction, so as to achieve the goal of improving disaster reduction ability and habitat quality. The coastal ecological rehabilitation for hazard mitigation refers to the activities of ecological protection and disaster prevention and mitigation through the protection and restoration of coastal ecosystem, consolidation and enhancement of its disaster reduction functions such as tidewater and wave resistance and bank protection or ecological construction of coastal protection engineering facilities to promote the synergy of ecological protection and disaster prevention and mitigation[2]. Generally speaking, the restoration project mainly includes two parts: one is the protection and restoration of natural ecosystem, the other is the ecological construction of artificial protection project.

In terms of spatial distribution, the coastal zone can be divided into seashore zone, sea dike zone and continental zone, and sea dike zone or continental zone are not within some coastal zones. The seashore zone is generally the area where the sea dike protection area is close to the sea (with sea dike) or the average high tide line (without sea dike) extending to the outer boundary of coral reef and seaweed bed. The sea dike zone is generally the area between the sea dike side boundary and the seaward side boundary. The continental zone is generally the area with sea dike side boundary (with sea dike) or average high tide line of high tide (without sea dike) extends land to the area suitable for coastal shelterbelt planting boundary line[2]. The corresponding ecological restoration measures should be taken for different spatial regions to enhance the disaster prevention and mitigation capacity and ecological service function of coastal zone.

3. MEASURES OF COASTAL ZONE PROTECTION AND RESTORATION

The measures of coastal zone protection and restoration can be divided into natural ecosystem restoration and ecological construction of artificial protection engineering. The natural ecosystem restoration includes typical coastal ecosystem restoration such as mangrove, salt marsh, coral reef, seaweed bed, oyster reef and sandy shoreline, and coastal forest protection. Ecological construction of artificial protection engineering includes ecological sea dike reforming and renovation of island-connecting seawall and coastal engineering.

3.1 NATURAL ECOSYSTEM RESTORATION

(1) Ecological restoration of mangrove. Mangrove refers to the biological community with mangrove plants as the main body[3]. It mainly grows in the shoal at the junction of land and sea, and is widely distributed in the global tropical and subtropical coasts. Mangrove not only can resist the wind and waves, purify the sea water and air, but also has the function of promoting silt to build land, consolidating dike and protecting bank. It is also an important gas station for birds migration in Southeast Asia. In the process of ecological restoration, mangrove ecosystem restoration can be achieved by restoring water environment, improving micro landform and improving sediment environment.

(2) Ecological restoration of salt marsh. Salt marsh refers to the wetland containing a lot of salt[4]. Coastal salt marsh is distributed in estuaries or coastal shoals, which is important channel for biological migration, fish migration, nutrient exchange, material and energy transfer. Remediation measures include removing threat factors, restoring water environment, improving micro topography, improving sediment environment and vegetation restoration.

(3) Ecological restoration of coral reef. Coral reef is a special seabed habitat composed of living coral and dead coral skeleton[5]. It is a typical marine ecosystem on the earth, mainly distributed in tropical and subtropical areas. Coral reef can protect the coast, slow down erosion, and has a positive effect on energy dissipation and bank protection. In the process of ecological restoration, human activities should be strictly controlled. Specifically, ecological restoration of coral reef can be realized by means of habitat restoration, coral larval cultivation and artificial reef.

(4) Ecological restoration of seaweed bed. Seaweed bed is a seaweed community composed of one or more kinds of seaweeds[6]. It grows in the intertidal zone or subtidal zone. It has the important functions of regulating climate, settling sediment, preventing waves and consolidating dykes, providing nutrients and spawning places for organisms. At present, the ecological restoration of seaweed bed can be achieved by controlling pollution sources, improving sediment conditions, cultivating seaweed seedlings and transplanting

seaweed plants.

(5) Ecological restoration of oyster reef. Oyster reef is a kind of aggregation composed of living oysters, dead oyster shells and other reef area organisms[7]. It is distributed in temperate estuaries and coastal areas, and is called coral reef in temperate zone. Oyster reef can effectively improve water quality and reduce the incidence of red tide. It is a habitat for many fish and crustaceans. The three key technologies for the ecological restoration of oyster reef are site selection, reef construction and population multiplication.

(6) Ecological restoration of sandy coast. Sandy coast refers to the coast mainly constructed by wave action and mainly composed of sand (gravel)[8]. It is distributed in coastal provinces and cities of China, mainly concentrated in Liaodong Peninsula, Shandong Peninsula and South China coast. Sandy coast can effectively resist storm surges. It is the habitat of many coastal organisms and an important place for tourism and leisure. At present, they are the main measures that sand dune restoration, sand fixation vegetation restoration, artificial sand supplement and construction of underwater sand bar to carry out ecological restoration of sandy coast.

3.2 ECOLOGICAL CONSTRUCTION OF ARTIFICIAL PROTECTION ENGINEERING

(1) Ecological sea dike reforming. It refers to the maintenance, renewal, reinforcement and other activities of the existing seawall by optimizing the dike structure, using ecological building materials, planting vegetation and other measures to maintain the seawall's ability of dampproof and disaster prevention and restore the coastal ecological function[2]. The ecological construction of seawall is mainly carried out by optimizing the structure of dike body, using ecological materials, planting vegetation, retreating to build dams and adding tidal channels.

(2) Renovation of island-connecting seawall and coastal engineering. Island-connecting seawall refers to the seawall connected islands with land or other islands. In order to improve the marine dynamic conditions, restore the integrity of the marine ecosystem and enhance the service function of the marine ecosystem, the historical island-connecting seawall and coastal engineering can be retreated to the sea, the seawall opening or permeable reconstruction can be carried out, and the construction projects can be removed that seriously affect the marine ecosystem and are not conducive to disaster prevention.

4. PRACTICE OF COASTAL ZONE PROTECTION AND RESTORATION

In early 2019, Ministry of Natural Resources and Ministry of Water Resources of the People's Republic of China organized the preparation of Coastal Zone Protection and Restoration Projects Work Plan. In February 2020, it was jointly issued and implemented by Ministry of Natural Resources, Ministry of Water Resources, Ministry of Finance of the People's Republic of China and National Development and Reform Commission. In June 2020, the first batch of coastal zone protection and restoration projects were approved. According to the task planning and designing, the project was divided into three stages that the first stage (2019) was the preparation and start-up stage, the second stage (2020-2022) was the implementation stage, and the third stage (medium and long-term) was the summary and promotion stage. From the content, the project was carried out in three stages which were suitability evaluation, project construction and effect evaluation. In July 2020, 21 series of group standards were issued by China Association of Oceanic Engineering, including technical guideline for investigation and assessment of coastal ecosystem and technical guideline on coastal ecological rehabilitation for hazard mitigation, which provided technical support for standardizing engineering project construction and improving standardization level.

For coastal zone protection and restoration projects, it is gradually systematized on top-level design, specification compilation and project implementation in China. At home and abroad, coastal ecological protection projects are worth learning and referencing in some countries.

4.1 INTERNATIONAL COASTAL ECOLOGICAL PROTECTION

In the 1970s and 1980s, some developed countries, such as Holland and Germany, made changes in the concept of coastal zone protection, put forward the concepts of "natural restoration" and "building with nature", and carried out ecological restoration projects (Table 1), which provided habitat for organisms, improved the habitat quality and the function of coastal zone disaster prevention and mitigation , to a certain extent.

Table 1 international coastal ecological protection cases

Number	Region	Case	Content
1	Holland	Delta Engineering[9]	In order to protect the habitat of animals and plants in the east Schelde estuary, the open tide gates were built to replace the solid dam.
2	Germany	Coastal protection projects in Mecklenburg-Vorpommern and Lower Saxony[10]	Sand dune, wooden spur dike, mobile seawall and salt marsh are used to establish coastal protection system.
3	America	“Living shorelines” project in Sapelo Island, Georgia	Establishing the dynamic shorelines and providing habitat for organisms by gabions containing oyster shells, oyster shell bags and stones.
4	Indonesia	"Building with nature Indonesia" project in Java Island	The coastal erosion can be reduced by mangrove restoration, sediment conservation and permeable wave dissipation structures.
5	Australia	Ecological reconstruction project of McMahon sea dike	Construction of platform, restoration of aquatic environment, and improvement of aquatic environment.

4.2 DOMESTIC COASTAL ECOLOGICAL PROTECTION

In recent years, Zhejiang, Guangxi, Fujian and other regions have also actively carried out coastal ecological protection projects (Table 2). According to local conditions, natural ecosystems such as mangroves, oyster reefs, salt marshes and other natural ecosystems have been restored, and the projects that seriously affect the regional ecosystem have been reconstructed or even demolished, which provide reference for next stage of coastal zone protection and restoration projects in China.

Table 2 domestic coastal ecological protection cases

Number	Region	Case	Content
1	Guangxi	Hong sha huan ecological seawall project in Fangchenggang[11]	According to the combination of seawall and mangrove, the protection function is improved and the habitat space for marine organisms is provided.
2	Zhejiang	oyster reef restoration project in Sanmen	In order to increase biodiversity and improve the function of ecological disaster reduction, the restoration aquaculture of oyster was carried out.
3	Liaoning	estuary wetland regulation project in Xingcheng[12]	The coastal ecological protection zone was formed by raising low-lying land, planting Suaeda salsa and dredging tidal ditches.

4	Fujian	Beach restoration project of Convention and Exhibition Center	In order to reduce the loss of sediment, layered sand filling and jetty construction are adopted.
5	Zhejiang	Reconstruction project of Lingni levee in Wenzhou	The ecological trench formed by the opening reconstruction of the seawall connecting islands is conducive to restore seawater exchange channel, promote the migration of fishes and shrimps and improve seawater quality.

5 SUGGESTIONS

On the basis of international coastal ecological protection concept and engineering experience, combined with the types and characteristics of China's coastal zone, scholars put forward coastal zone protection and restoration schemes which are suitable for different regional construction and carried out, which is of great significance to enrich the theoretical system of coastal zone ecological disaster reduction and guide projects in China. There are six suggestions for the protection and restoration of coastal zone in the next stage. Firstly, in order to realize the orderly integration and development of land and sea, we should make overall planning and adjust measures to local conditions. Secondly, we should strengthen the publicity of marine science popularization and improve the marine science popularization education system. Thirdly, natural restoration and artificial restoration should be carried out simultaneously and maximize the self recovery function of marine ecosystem. Fourthly, relevant standards and specifications for coastal zone protection and restoration project should be formulated and improved to ensure scientific and orderly construction of projects. Fifthly, we should carry out coastline monitoring and investigation vigorously, and establish coastal zone data platform. Last but not least, We should speed up the research on key technologies and effect evaluation of ecological restoration, and accelerate the transformation of application achievements.

Coastal zone protection and restoration projects are important measures to improve the ability of coastal zone disaster prevention and mitigation and promote the construction of marine ecological civilization. The 21st century is not only a century to repair the earth, but also to build a community of human and natural life. Practice the ecological concept of lucid waters and lush mountains are invaluable assets, adhere to unified deployment, suit measures to local conditions, and carry out scientific restoration, it will be able to improve the ability of disaster prevention and mitigation, restore the ecological service function of coastal zone, build safe ecological and beautiful coastal barrier, and realize the harmonious coexistence of human and nature in the end.

REFERENCES

[1] National Development and Reform Commission, Ministry of water resources. National seawall construction plan [Z]. 2017.
[2] China Association of Oceanic Engineering. Technical guideline on coastal ecological rehabilitation for hazard mitigation-Part 1: General [EB/OL]. [2020.09.06] http://www.caoe.org.cn/nr/cont.aspx?itemid=209&id=3038.
[3] China Association of Oceanic Engineering. Technical guideline on coastal ecological rehabilitation for hazard mitigation-Part 2: Mangroves [EB/OL]. [2020.09.06] http://www.caoe.org.cn/nr/cont.aspx?itemid=209&id=3038.
[4] China Association of Oceanic Engineering. Technical guideline on coastal ecological rehabilitation for hazard mitigation-Part 3: Salt marshes [EB/OL]. [2020.09.06] http://www.caoe.org.cn/nr/cont.aspx?itemid=209&id=3038.
[5] China Association of Oceanic Engineering. Technical guideline on coastal ecological rehabilitation for hazard mitigation-Part 4: Coral reef [EB/OL]. [2020.09.06] http://www.caoe.org.cn/nr/cont.aspx?itemid=209&id=3038.

[6] China Association of Oceanic Engineering. Technical guideline on coastal ecological rehabilitation for hazard mitigation-Part 5: Seagrass bed [EB/OL]. [2020.09.06] http://www.caoe.org.cn/nr/cont.aspx?itemid=209&id=3038.
[7] China Association of Oceanic Engineering. Technical guideline on coastal ecological rehabilitation for hazard mitigation-Part 6: Oyster reef [EB/OL]. [2020.09.06] http://www.caoe.org.cn/nr/cont.aspx?itemid=209&id=3038.
[8] China Association of Oceanic Engineering. Technical guideline on coastal ecological rehabilitation for hazard mitigation-Part 7: Sandy Coast [EB/OL]. [2020.09.06] http://www.caoe.org.cn/nr/cont.aspx?itemid=209&id=3038.
[9] Yuanzhi Liao, Hongzhi Liao. Discussion on coordinated development of water conservancy project construction and ecological environment in Netherlands [J]. Express Water Resources and Hydropower Information, 2007 (16): 7-9.
[10] Jinhai Zheng, Xiangbo Feng, Aifeng Tao, et al. New concept and style of coastal protection in Mecklenburg-Vorpommern and Lower Saxony, Germany [A]. Marine engineering branch of Chinese ocean society. Proceedings of the 15th China Ocean (Shore) Engineering Symposium (c) [C]. Chinese society of Ocean Engineering: marine engineering branch of Chinese society of Oceanography, 2011: 1089-1095.
[11] Hangqing Fan, Binyuan He, Xin Wang, et al. The conception and practices of ecological sea dyke [J]. Guangxi Sciences, 2017, 24 (5): 427-434, 440.
[12] Wei Xu, Aifeng Tao, Jianhui Liu, et al. The enlightenment of international coastal zone ecological protection for China's ecological sea dike construction [J]. Ocean Development and Management, 2019, 36 (10): 12-15.

Coastlab 20

Dec 9-12 Zhoushan, China

Abstracts

8th International Conference on the Application of Physical Modelling in Coastal and Port Engineering and Science
Zhoushan, China - Dec. 9th - 12th, 2020

PHYSICAL MODEL TESTS FOR SEAWATER INTAKE PUMPING STATION

ABBAS MORTAZAVIPOUR[1], SAEED GOUDARZI[2]

1 Petropars Ltd., Iran,
mortazavipour@ppars.com 2 Petropars Ltd.,
Iran, Goudarzi.sa@ppars.com

This paper presents the result of the physical model testing for the South Pars seawater intake pump station located in the North coast of the Persian Gulf. The Inlet Screening Plant and Pumping Station have been designed to provide a facility to pump 20,000 m3/hour seawater through gas plant as cooling water of process units. The basin is required to be designed to ensure a steady flow approach to the pumps. This is very essential to prevent a very uneven flow approach which may lead to significant pre-rotation in the pumps and therefore increases the likelihood of establishing surface and/or subsurface vortices entering the pumps.

Model tests are carried out in a Froude scaled model applying a linear scale 1:9.26. The original design of seawater intake consisted of two band screen and eight cooling water pumps with rated capacity of 2500m3/hour each. The seawater intake model was constructed mainly in plywood, however, the downstream wall is built in Plexiglas in order to facilitate observations of pre-rotation and vortex action close to the pumps. The model pumps and bellmouths were built in Plexiglas. The flow through the model pumps were established by means of siphons which allowed an accurate representation of the complex flow patterns caused by the physical geometry of the approach bay and pump bays.

The water levels in the intake pump house and flow through the individual pump intake were measured. In addition, pre-rotation in the individual pump intakes and current profiles of the approaching flow in one of the pump chambers for selected load cases were monitored. The surface and subsurface vortices close to the pumps and flow conditions in the distribution chamber were observed.

The design of the screen area and pump bay performance were evaluated through physical model testing and some modifications were proposed to optimize the flow conditions in the intake by considering the head-losses, uniformity of the approach flow, evenness of pump throat velocity distribution, and free and subsurface vortex formation

Key Words: Physical Model Test, Seawater Intake, Pumping Station, Vortex

8th International Conference on the Application of Physical Modelling in Coastal and Port Engineering and Science
Zhoushan, China - Dec. 9th - 12th, 2020

EXPERIMENTAL STUDY OF LOCAL SCOUR AROUND POROUS PILES IN STEADY CURRENTS

Fan YANG[1], Lili QU, Lin LU, Liang CHENG

[1] State Key Laboratory of Coastal and Offshore Engineering, Dalian University of Technology, Dalian 116024, China
Email: fanyang@dlut.edu.cn

As one of the key factors resulting to structural failure, local scour around subsea structures attracts substantial interests in the past decades. Most of studies focus on the local scour around a slender vertical pile due to its significant engineering application. The present work focus on the local scour around porous piles, looking into the following questions: 1) what is the mechanism of porosity on the local scour; 2) does the distribution of porosity plays the key role in the local scour; 3) how does the incident angle of the flow affect the cylinder.

The current laboratory-based tests were carried out under steady flow current with a series of configurations of porous plies. The plane shape of model piles is square and the dimension is 15 cm × 15 cm with the height of 120 cm, over the top of the water surface. The aim of this study is focused on the variation of scour depth and time scale with the different porosity rate of the pile. The influence of three parameters on the local scour has been presented, which is the porosity along the flow direction $\eta 1$, the porosity perpendicular to the flow direction $\eta 2$ and the incident angle α.

Experimental testings were carried out in the O-Tube facility at The State Key Laboratory of Coastal and Offshore Engineering. The dimensions of the water flume are 30m in length, 4m in width and 2.5m in height. A sand basin with length of 6m and deep of 0.3m is built in the middle and the sand is extended to the whole flume to provide sand supply to the test section for its excessive loss during the experiments. The model pile was setup up in the middle of the sand basin in Fig 1. θ/θ_{cr} was set to
1.138 to minimize the influence of ripples on the results.

It was found from experimental results that horseshoe vortex was weaken due to the presence of the porosity along the flow direction, $\eta 1$. And the porosity perpendicular to the flow direction $\eta 2$ plays less significant influence on the flow contraction at the two sides of piles comparing with $\eta 1$ in the front in Fig 2. Velocity gradients were measured to validate the above indications. The incident angle of flow ($\alpha > 30^{o}$) dramatically improved the maximum scour depth of piles, comparing with the less influence of incident angle ($\alpha < 30^{o}$). Two scour modes, A&B, induced by the incident angles were quantified in the specific cases of the present study. Mode A was the regular scour with time. Mode B was initial with a regular scour following by a secondary local scour as the depth of previous scour reached 70% of the maximum scour depth.

Key Words: local scour; porosity; piles; steady current

8th International Conference on the Application of Physical Modelling in Coastal and Port Engineering and Science
Zhoushan, China - Dec. 9th - 12th, 2020

SEASONAL VARIATION OF SURFACE CURRENTS AT THE WEST COAST OF IRELAND BASED ON HIGH FREQUENCY RADARS

LEI REN[1,2,3*], GUANGWEI PAN[2,3], MANMAN WANG[4], QINGSHU YANG[1,2,3], MICHAEL HARTNETT[5]

1 Southern Marine Science and Engineering Guangdong Laboratory (Zhuhai), P. R. China, renlei7@mail.sysu.edu.cn 2 School of Marine Engineering and Technology, P. R. China, pangw6@mail2.sysu.edu.cn
3 Institute of Estuarine and Coastal Research, P. R. China 4 Ocean Networks Canada, Canada, manmanw@uvic.ca
5 National University of Ireland Galway, Ireland, michael.hartnett@nuigalway.ie

To investigate variation characteristics of coastal circulation in fine temporal and spatial resolution, the High Frequency Radar (HFR) network was expanded and has been operated since 2011 at the west coastal of Ireland. Hourly surface current velocities are combined in rectangular grid points of 300-metre interval for the inner Galway Bay. Tide and wind are dominant forces that driving surface currents in research domain, which result in significant difference of coastal circulation among different seasons over the year due to their variation. In order to study seasonal variation characteristics and patterns of surface circulation, raw HFR data and de-tided currents are used to discuss contribution mechanism of driving forces. Three observation points with high coverage density during analysis period are selected. Zonal and meridional surface velocity components were studied separately based on harmonic analysis. Moreover, spatial patterns of surface circulation were extracted using self-organizing map for each season. Comparison was undertaken to illustrate effects of driving forces on changing processes of surface circulation.

Key Words: coastal circulation, surface currents, high frequency radar, seasonal variation, self-organizing map,

8th International Conference on the Application of Physical Modelling in Coastal and Port Engineering and Science
Zhoushan, China - Dec. 9th - 12th, 2020

STEPWISE VARIATION OF SPRING-NEAP CHANGE IN TIDAL HYDRODYNAMICS IN THE LINGDINGYANG BAY OF THE PEARL RIVER DELTA

PING ZHANG[1], HUAYNAG CAI[2]

1 Institute of Estuarine and Coastal Research, School of Marine Engineering and Technology, Sun Yat-sen University, China, E-mail:zhangp@mail2.sysu.edu.cn

2 Institute of Estuarine and Coastal Research, School of Marine Engineering and Technology, Sun Yat-sen University, China, E-mail:caihy7@mail.sysu.edu.cn

Assessing the impacts of natural (e.g., rising sea-level) and human-induced (e.g., land reclamations) changes on estuarine hydrodynamics is essential for the healthy of estuarine environment and sustainable water resources management. In this study, the enhanced harmonic analysis model for nonstationary tide (S_Tide) was used to extract the amplitudes and phases of different tidal constituents (M2, K1, O1 and S2) in a daily scale in four tidal gauging stations (i.e., Chiwan, Sishengwei, Dasheng and Huangpu) in order to explore the daily alternation of tidal hydrodynamics (e.g., tidal wave celerity and tidal damping rate) in the Lingdingyang Bay. Subsequently, the evolution with regard to the relationship between the tidal wave celerity and the tidal damping rate at three distinct periods, in the pre-human (e.g., from 1965-1997), transitional (e.g., from 1998-2007) and post-human periods (e.g., from 2008-2016) were identified. It was shown that the spring-neap change in tidal hydrodynamics was mainly impacted by the highly-modified geometry (including deepening and narrowing) in the Lingdingyang Bay. To quantify the effects of estuarine morphological alterations in terms of deepening and narrowing on tidal hydrodynamics, we adopted an analytical hydrodynamics model to assess the stepwise variations in estuarine shape and bottom friction, which are two controlled factors for hydrodynamics in the Lingdingyang Bay. The merit of contribution lies in that it offers a simple yet powerful approach for understanding the evolution of estuarine tidal hydrodynamics over past 50 years, which may provide scientific guidelines for potential uses of water resources in this region.

Key Words: Tidal hydrodynamics; S_Tide; Spring-neap change; Lingdingyang Bay; Analytical model

8th International Conference on the Application of Physical Modelling in Coastal and Port Engineering and Science
Zhoushan, China - Dec. 9th - 12th, 2020

INTERNAL SOLITARY WAVE BREAKING AND TURBULENT DISSIPATION IN FRONT OF A GAUSSIAN RIDGE

JUNYANG YU[1], YUANYE LUO[2], YEPING YUAN[3], YINTIEN LIN[4]

1 Ocean College, Zhejiang University, China, junyang-yu@zju.edu.cn 2 Ocean College, Zhejiang University, China, luoyuanye@outlook.com 3 Ocean College, Zhejiang University, China, yyping@zju.edu.cn

4 Ocean College, Zhejiang University, China, kevinlin@zju.edu.cn

The breaking of internal solitary waves (ISWs) are common phenomenon in continental shelf margin areas or seamount areas; these breaking events are important to the mixing and dissipation process in global ocean. Despite several decades of research, it remains an active topic about the life cycle of internal waves, because the mechanisms and detailed turbulent structure of breaking and wave-induced dissipation are still unclear. In this study, laboratory experiments were conducted to investigate the breaking of ISWs in front of a submerged Gaussian ridge and resulting turbulent dissipation. Gravitational collapse methods were used to generated ISWs with different amplitudes. Image series were obtained by Particle Image Velocimetry system, and processed by PIVlab to reconstructe a two-dimensional plane flow field. Based on velocity field data from the experiments, we could analyze the breaking process and calculated turbulent dissipation rate. During the breaking events, when ISW was approaching the ridge, a rapid flow along the slope was induced, the flow rushed to the region below the wave trough in front of ridge, the interface near trough was deformed and eventually a vortex was produced. Then the vortex split into many smaller ones, which dissipated energy continuously -and interface recovered after the waves. Results showed that both breaking of ISWs and just local mixing could occur, and it depends amplitudes and the distance between interface and ridge top. Dissipation rate in breaking runs could reach the order of 10^{-5} m^2/s^3, while in local mixing runs it was only in the order of 10^{-6} m^2/s^3. It was also found that ISWs were prone to break in a suitable condition, the amplitudes, stratification and ridge height were main factors affecting the breaking process. In addition, maximum turbulent dissipation was related to the ridge and stratification in breaking runs. These results will be helpful in relevant research, such as ocean model parameterization.

Key Words: internal solitary waves; turbulent dissipation rate; ridge; stratification

8th International Conference on the Application of Physical Modelling in Coastal and Port Engineering and Science
Zhoushan, China - Dec. 9th - 12th, 2020

EFFECT OF STRATIFIED ENVIRONMENT AND RIGID VEGETATION ON HYDRODYNAMIC CHARACTERISTICS OF DOWNSLOPE GRAVITY CURRENTS

Yayu LIU, Yingtien LIN

Ocean College, Zhejiang University, China, 21734077@zju.edu.cn

A series of lock-exchange experiments are carried out in uniform and linear stratified environments created by the "two tank method". In this study, the development process of gravity currents is recorded by digital camera, and the local flow field structure is obtained by Particle Image Velocimetry (PIV). The experimental results show that the head velocity of gravity currents with submerge vegetation experienced "acceleration, deceleration, second acceleration, and second deceleration" processes. As the stratification level becomes greater, the transition points among the four stages move ahead but are not significantly impacted by the vegetation density. In the stratified water with the submerged vegetation (α<1) patches, the head of the gravity current splits, so there are two separation processes. Compared with the case without vegetation, the vegetation delayed the separation of gravity current. At the same slope, the separation depth of gravity current under the condition of submerged vegetation is greater than emergent vegetation. With the increase of vegetation density and slope, the final separation depth of the gravity current increases. Vegetation can restrain the development of vorticity fields of gravity currents. When the vegetation density turns into denser, the vorticity fields decrease more obviously. Both stratified environments and submerged vegetation patches can inhibit the development of vorticity fields of gravity currents, and the stratified water environment plays a more important role on this inhibition．.

Key Words: gravity current; slope; vegetation; stratification; separation

8th International Conference on the Application of Physical Modelling in Coastal and Port Engineering and Science
Zhoushan, China - Dec. 9th - 12th, 2020

AN IMPROVED METHOD FOR REAL-TIME WAVE FORCE RECONSTRUCTION ON A CYLINDER BY USING MONITORED WATER SURFACE ELEVATION

JIABIN LIU[1,2], ANXIN GUO[1,2]

1 Key Lab of Structures Dynamic Behavior and Control of the Ministry of Education, Harbin Institute of Technology, Harbin, 150090, China, liujiabin@hit.edu.cn

1 Key Lab of Structures Dynamic Behavior and Control of the Ministry of Education, Harbin Institute of Technology, Harbin, 150090, China, guoanxin@hit.edu.cn

An improved method is presented for reconstructing wave forces on a circular cylinder at the real-time. Assisted by the historical data of measured wave elevation, a novel approach is built to ameliorate the accuracy of nonlinear wave force reconstruction. Similar to the linear method, wave forces in the improved method are reconstructed directly by integrating the transformed wave elevation along the side surface of the cylinder. Hydrodynamic tests were carried out in the wave flume on a circular cylinder to examine the reconstructed results of the improved method. Comparative results demonstrate that the accuracy of real-time reconstructed wave forces are significantly enhanced. The over prediction errors at force crests and under prediction errors at force troughs have been reduced. Two different algorithms, Fast Fourier Translation (FFT) and Recursive Least Squares (RLS), for the real-time reconstruction are conducted. Comparative results show that the improved method performed by FFT algorithm provides the most accurate results. Time cost analysis for the linear method and improved method is investigated with different input data. The efficiency of RLS algorithm makes the real-time wave force reconstruction has great potential in practical applications.

Key Words: wave force; wave elevation; cylinder; real-time reconstruction.

8th International Conference on the Application of Physical Modelling in Coastal and Port Engineering and Science
Zhoushan, China - Dec. 9th - 12th, 2020

EXPERIMENTAL DERIVATION OF THE FLOW DRAG COEFFICIENT OF COASTAL WOODEN FENCES

H.T. DAO[1,2]; B. HOFLAND[1]; M.J.F. STIVE[1]

[1] *Faculty of Civil Engineering and Geosciences, Delft University of Technology, Stevinweg 1, Delft, The Netherlands, H.T.Dao-1@tudelft.nl, B.Hofland@tudelft.nl, M.J.F.Stive@tudelft.nl*

[2] *Faculty of Marine Sciences, Hanoi University of Natural Resources and Environment, 41A Phu Dien, Bac Tu Liem, Hanoi, Vietnam, H.T.Dao-1@tudelft.nl*

Wooden fences are being applied as a natural-based solution to create a low-energy environment for mangrove restoration along the Mekong Delta coast. The simple structure contains vertical bamboo poles as the frame to storing horizontal bamboo and tree branches (brushwood). Even though previous studies present field and simulation data to determine the expected wave energy reduction, the understanding of fence resistance is hindered by the limited knowledge on the drag coefficient of the fence material. The drag coefficient is a crucial input parameter for numerical models (Dao et al., 2018; Mendez and Losada, 2004) that should be known a-priori, and small scale models are often influenced by scale effects. It is not straightforward to predict the drag coefficient, because the density of branches in a fence is rather high, such that the wakes behind the branches influence the drag on other branches (Nepf, 1999). Moreover, the arrangement of branches is random and possibly inhomogeneous. Therefore, tests were conducted to determine the drag coefficient for various branch arrangements. In these experiments, a constant flow of water is forced through the fence material, and the hydraulic pressure loss over the fence sample is measured. The fence configurations that were tested are presented in Figure 1 with an inhomogeneous arrangement (Figure a) and a staggered arrangement of cylinders (Figure b, c, and d). Two diameters were applied, i.e. small scale and large scale. Several conclusions from the experimental results will be presented. Firstly, the bulk of drag coefficient ($\overline{C_D}$) is influenced by the flow regime representing for Reynold number. While C_D converges at high Re for all fence thicknesses and all diameters for turbulent conditions, scale effects are nearly absent in contrast to those for low Re numbers. Secondly, the experimental findings point out that the increase of porosity relating to cylinder arrangement is inversely proportional to $\overline{CD}$. Finally, a comparison of experimental results with previous findings, such as Forchheimer coefficients, is discussed. The results will be used in future research to upscale small-scale tests, and to conduct numerical simulations with realistic drag values.

Figure 1. a: Inhomogeneous spacing small scale; b: staggered small scale; c: staggered large scale, high density; d: staggered large scale, low density.

References

Dao, T., Stive, M.J.F., Hofland, B., Mai, T., 2018. Wave Damping due to Wooden Fences along Mangrove Coasts. Journal of Coastal Research 1317–1327. https://doi.org/10.2112/JCOASTRES-D-18-00015.1

Mendez, F.J., Losada, I.J., 2004. An empirical model to estimate the propagation of random breaking and nonbreaking waves over vegetation fields. Coastal Engineering 51, 103–118.

Nepf, H.M., 1999. Drag, turbulence, and diffusion in flow through emergent vegetation. Water resources research 35, 479–489.

8th International Conference on the Application of Physical Modelling in Coastal and Port Engineering and Science
Zhoushan, China - Dec. 9th - 12th, 2020

EXPERIMENTAL STUDY ON THE MOORING TENSION OF SUBMERGED TUNNEL ELEMENT SUSPENDED FROM A TWIN- BARGE

CAN YANG [1*], CHANG WAN [2]

1 College of Shipbuilding Engineering, Harbin Engineering University, China, cyangdlut@163.com

2 College of Shipbuilding Engineering, Harbin Engineering University, China, changwan96@hrbeu.edu.cn

A moored tunnel element suspended by a twin-barge model is experimentally tested to study the effect of the sea states on the mooring tension of coupled tunnel-barge system during immersion installation. The experimental investigations were carried out in the State Key Laboratory of Coastal and Offshore Engineering at Dalian University of Technology (DUT). The mooring and cable tensions of the tunnel-barge system with different wave heights, wave periods and immersion depths are investigated in this paper. The dynamic behavior of the mooring system and the phrase relationships between the mooring tension, suspension cable tension and tunnel element motions are analyzed, we observed that the maximum mooring tension and slack of suspension cable tension alternately occur during immersion stage, which was not highlighted in the past. In addition, the maximum mooring tensions of the tunnel element are discussed after comparing for different mooring configurations, which help to minimize the sinking risk of the tunnel element during immersion installation.

Key Words: immersed tunnel; mooring tension; twin-barge; coupled system; suspension cable

8th International Conference on the Application of Physical Modelling in Coastal and Port Engineering and Science
Zhoushan, China - Dec. 9th - 12th, 2020

QUANTIFYING THE INFLUENCE OF THE THREE GORGES DAM ON THE SPATIAL-TEMPORAL WATER LEVEL DYNAMICS IN THE YANGTZE RIVER ESTUARY

HUAYANG CAI[1]

1 School of Marine Engineering and Technology, Sun Yat-sen University, China, caihy7@mail.sysu.edu.cn

Water level dynamics is an important factor for estuarine environment as they influence the hydrological, ecological, and biogeochemical processes in many ways (e.g., flood control, water quality, carbons and nutrients cycles etc.). In this study, we propose a simple triple linear regression model linking the water level variation on daily scale to hydrodynamics at the both ends of an estuary. The model was applied to the Yangtze River estuary for examining the influence of the world's largest dam, the Three Gorges Dam (TGD), on the spatial-temporal water level dynamics along the estuary. It was shown that the regression model can satisfactorily reproduce the water level dynamics along the Yangtze River estuary with root mean squared error (RMSE) ranging 0.063-0.23 m in the 5 gauging stations for the pre-TGD period, which confirms our hypothesis that the response of water level dynamics to hydrodynamics at the both ends is mostly linear. The obtained linear regression coefficients from 5 gauging stations were spatially interpolated to predict the water levels at arbitrary locations together with to provide insights into the spatial-temporal water level dynamics. The regression model calibrated during the pre-TGD period was successively applied to the case for the post-TGD period, keeping the same coefficients obtained before. The simulated water levels were compared with the actual measurements and the differences between them indicate the alterations caused by the overall impacts of human interventions, which is primarily attributed to the TGD's operation.

Key Words: river discharge, triple linear model, hydrodynamics, rive-tide interaction, human interventions

8th International Conference on the Application of Physical Modelling in Coastal and Port Engineering and Science
Zhoushan, China - Dec. 9th - 12th, 2020

EXPERIMENTAL DEVELOPMENT OF A HYBRID WAVE ENERGY CONVERTER FOR RUBBLE MOUND BREAKWATERS

P. ROSA-SANTOS, F. TAVEIRA-PINTO, T. CABRAL, D. CLEMENTE

Interdisciplinary Centre of Marine and Environmental Research (CIIMAR) of the University of Porto, Portugal.
Faculty of Engineering of the University of Porto (FEUP), Department of Civil Engineering, Hydraulics, Water Resources and Environment Division, Rua Dr. Roberto, Frias, S/N, 4200-465, Porto, Portugal.
pjrsantos@fe.up.pt, fpinto@fe.up.pt, tcabral@fe.up.pt, ec10140@fe.up.pt

The harvesting and use of marine renewable energy at sea ports is a promising option to put these important and also energy intensive infrastructures on the right track to energy self-sufficiency and environmental sustainability, reducing their carbon footprint. The protection of sea ports against wave action is usually provided by breakwaters, which are designed to withstand extreme wave actions and to dissipate wave energy, reducing wave refection and overtopping. The exposure of these structures to wave action makes them suitable for the installation of wave energy converters (WEC), exploring the dual mind-set of wave energy production and sheltering of harbor basins. On the other hand, this application also allows sharing the construction costs and may improve the recirculation of water in the harbor and the performance of the breakwater reducing wave overtopping and wave reflection, due to a more efficient absorption of energy.

The paper presents the main conclusions of the project SE@PORTS – Sustainable Energy at Sea PORTS, recently concluded, and recent developments on two other related projects: PORTOS – Ports Towards Energy Self-Sufficiency and WEC4Ports – A hybrid Wave Energy Converter for Ports. The three projects are focused on the development of a hybrid technology that combines the overtopping and the oscillating water column principles (h-WEC). The paper describes the experimental study carried out in the wave basin of the Hydraulics Laboratory of the Hydraulics, Water Resources and Environment Division of the Faculty of Engineering of the University of Porto, Portugal, in order to assess the performance of the h-WEC integrated in the rubble-mound structure that was proposed for the extension of the North breakwater of the Port Leixões, Portugal (case study). A special attention is given to the assessment of the effects of the h-WEC integration in the breakwater, both in terms of its stability and functionality, since these important topics received very little attention in recent years. The physical model included the reproduction of the seabed bathymetry in front of the breakwater and the generation of a wide range of sea states, including extreme wave conditions. The results have shown that the integration of the hybrid WEC in the breakwater impacts mostly the stability of its toe berm blocks and might reduce significantly the magnitude of overtopping events. The conclusions obtained are therefore favorable to the integration of this type of devices on breakwaters. The research works regarding the development of the h-WEC within PORTS and WEC4Ports are also presented.

Key Words: Overtopping WEC, Oscillating Water Column, Stability of breakwaters, Blue Ports, Energy Self-Sufficiency.

Acknowledgements

The project SE@PORTS – Sustainable Energy at Sea PORTS (OCEANERA/0004/2016) was funded under the frame of FCT, the Portuguese Foundation for Science and Technology. The project PORTOS – Ports Towards Energy Self-Sufficiency (EAPA 784/2018) is co-financed by the Interreg Atlantic Area Programme through the European Regional Development Fund. The project WEC4Ports – A hybrid Wave Energy Converter for Ports (OCEANERA-NET COFUND) is funded under the frame of FCT.

8th International Conference on the Application of Physical Modelling in Coastal and Port Engineering and Science
Zhoushan, China - Dec. 9th - 12th, 2020

STUDY ON LOADING DIFFERENCE ON COASTAL STRUCTURE BETWEEN EMPIRICAL FORMULA AND TEST UNDER SWELL WAVE ACTION

JIANG YUNPENG[1], CHEN HANBAO[1], LIU CHAO[2]

1 Tianjin Research Institute for Water Transport Engineering, National Engineering Laboratory for Port Hydraulic Construction Technology, Ministry of Transport, China, jyp1220@163.com

2 Engineering College, Ocean University of China, China, chaoliu_ouc@163.com

Wave loading on coastal structure is an important issue in design process of project, which determines the safety and economy. The traditional method is to calculate the wave loading by empirical formula in Design Code. Physical model test is the effective method to verify the loading in detailed design. Some designers did not put enough attention on that and only empirical formula is used without model test. Thus, many damages occurred when rough wave hit on the structure.

Physical model test was carried out to study wave load of crest wall under impulsive action by swell wave. The result of test was compared with China Design Code and American Coastal Engineering Manual (CEM). For example, a new breakwater was designed in Pakistan, with design wave period 14 second. Wave loading was calculated by empirical formula and then physical model test was done. The wave load by China Design Code and CEM was 70kN/m, but 350kN/m by physical model test. It was indicated that China code and CEM had very close results but much smaller than that of test, with ratio of 1:5. Some experts doubt the result because of the obvious difference and said the ratio of results by formula and test was usually 1:1.5~1:2.5.

Verification test was adopted to prove the obvious difference between them. The crest wall was put on the top of structure with no support of soil in front or back, it is isolated. The gravity force was 330kN/m and frictional force was 200kN/m. It failed in stability under swell wave because the wall moved from the initial position under wave action. Thus the wave loading is surely larger than 200kN/m, impossible to be 70kN/m. The fact from the test revealed that the empirical formula is not suitable for swell wave condition and there is obvious difference between formula and test. When wave period is larger than 8 second, wave load on crest wall would be much larger than the designer's expectation.

Impulsive action by swell wave on crest wall should be paid more attention in project design. Only calculation by Code formula is not enough and safe. Physical model test is indispensable for the reliability of structure.

Key Words: swell wave; wave load; pressure distribution; experimental test

8th International Conference on the Application of Physical Modelling in Coastal and Port Engineering and Science
Zhoushan, China - Dec. 9th - 12th, 2020

TSUNAMI-INDUCED SCOUR AROUND STRUCTURES

IOAN NISTOR[1], RAZIEH MEHRZAD[2], COLIN RENNIE[3],

1 Dept, of Civil Engineering, University of Ottawa, Canada, inistor@uottawa.ca
2 Dept, of Civil Engineering, University of Ottawa, Canada, sansa048@uottawa.ca 3 Dept, of Civil Engineering, University of Ottawa, Canada, crennie@uottawa.ca

In recent years, extreme natural phenomena such as tsunamis have affected communities located on coastal regions around the Indian and Pacific Oceans, causing significant loss of life and extensive damage to coastal communities. At present, limited information and guidance about tsunami loads and effects on coastal communities exist. This study presents results of a comprehensive experimental program focusing on scour mechanisms around a structures due to an inland-propagating, tsunami-like bore using physical modelling and analytical investigation. The experiments were conducted on the basis of the demonstrated analogy between overland-propagating tsunami bores and dam-break waves (Chanson, 2006). A series of hydraulic bores were simulated in the Hydraulic Flume in the Hydraulics Laboratory of the University of Ottawa, Canada. The dam-break wave was generated by releasing water impounded behind a rapidly-opening swing gate. A novel video-recording system and data processing algorithm was used to record the time and spatial evolution of the scour and vortex around two (circular and square) structures. Image processing allowed the accurate tracking the time and spatial evolution of the scour around the structure using fine (sand) and course (gravel) sediments. Different characteristics of a generated bore, final scour topography, and the relationship between scour depth and bore characteristics will be presented.

One of the main findings of this experimental program is that the high velocity and relatively short duration of a tsunami-like bore can generate a rapid scour process with important magnitude. Significant scour depths were observed at the front of structure while distinct sediment deposition patterns were observed and measured at the back of structure. Similar to the some of the post-tsunami forensic engineering field surveys, a scour hole was observed to have formed at the seaward corners of the structure while scour at the shoreward corner was found to be insignificant. Moreover, it was found that the presence of an initial water depth (following a first tsunami inundation) can greatly influence both the behavior of a hydraulic bore and the resulting local scour.

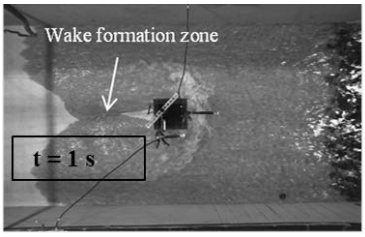

a) Top view

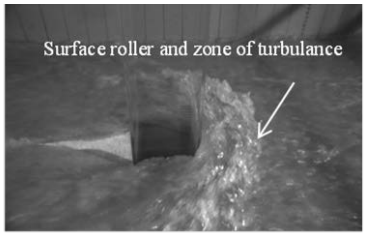

b) Side view

c) Front face

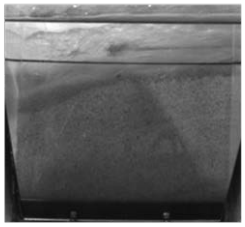

d) Side face

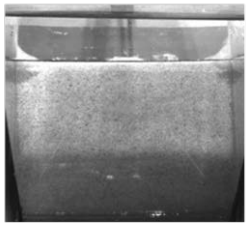

e) Back face

Key Words: tsunami, scour, dam-break, ASCE7 Chapter 6,

8th International Conference on the Application of Physical Modelling in Coastal and Port Engineering and Science
Zhoushan, China - Dec. 9th - 12th, 2020

A BRIEF ANALYSIS OF MEASURES TO IMPROVE THE MOORING STABILITY IN SUIZHONG PORT

GAO Feng[1], WANG Yue[2], TANG Guoming[3], LIU Zhen[1], ZHANG Ciheng[1]

1 Tianjin Research Institute of Water Transport Engineering, National Engineering Laboratory for Port Hydraulic Construction Technology&Key Laboratory of Engineering Sediment of Ministry of Communications, Tianjin, China, Seal326@163.com

2 Hohai University, Nanjing, China, sdwfwye@163.com

3 Suizhong port group Co. LTD, Huludao, China, tangguoming1982@163.com

ABSTRACT: Berthing stability condition is one of the key factors that determine the success of port design and normal operation. The covering condition, the position of the entrance and the orientation of the breakwater play an important role in the law of wave propagation in the harbor. In this study, aiming at the problem of mooring stability in the current layout of Suizhong Port and the layout plan of improvement measures, the 3-D wave physical model test was carried out, and optimization suggestions were given, which provided theoretical support and scientific basis for the implementation of the next stage. The results show that the lack of effective cover for SSW~SE direction is caused by the lack of full cover layout in the port at the present stage, and the wave can directly act on the wharf, which leads to the increase of downtime, which is the main reason for the poor mooring stability condition. Specially, 104 # and 105 # pier in phase ii, wave conditions in the basin will worsen. Therefore to extend the west breakwater, east cofferdam extended and the construction of the temporary dam at the entrance could effectively reduce the harbor wave height, combined with the basin angle area partially perforated caisson arrangement etc can improve the wave conditions, reduce the downtime and improve the berthing conditions.

Key Words: Mooring Stability; Wave; Breakwater; Berthing condition; Downtime.

ACKNOWLEDGEMENTS

The authors would like to acknowledge the support of Central Commonweal Research Institute Basic R&D Special Foundation of TIWTE (Grant No. TKS170217，TKS180402).

8th International Conference on the Application of Physical Modelling in Coastal and Port Engineering and Science
Zhoushan, China - Dec. 9th - 12th, 2020

EXPERIMENTAL STUDY ON HYDRODYNAMIC CHARACTERISTICS OF DUAL-PONTOON BREAKWATER IN TRANSIENT WAVES

XIAOTONG SUN [1], CHONGWEI ZHANG[2, *], DEZHI NING[3]

1 State Key Laboratory of Coastal and Offshore Engineering, Dalian University of Technology, Dalian, China, tong1996tong@mail.dlut.edu.cn

2 State Key Laboratory of Coastal and Offshore Engineering, Dalian University of Technology, Dalian, China, chongweizhang@dlut.edu.cn.

*3 State Key Laboratory of Coastal and Offshore Engineering, Dalian University of Technology, Dalian, China, dzning@dlut.edu.cn*Corresponding author.*

Breakwaters are widely used for the creation of a calm water area from attacking waves. For the deep-water condition or temporary works, pontoon-type floating breakwaters are more popular than conventional rubble mound ones in terms of economic cost, construction process and environmental impact. However, for certain sea states such as long wave conditions, the wave transmission through the breakwater is non-neglectable. The floating breakwater itself may also work as a wavemaker for the downstream water area. A possible solution to increase the wave protection efficiency is to deploy multiple floating breakwaters in parallel, so that transmitted waves behind the front breakwater can be reflected by the rear one. The distance between neighbour breakwaters is an essential element to consider. With a large distance, breakwaters normally occupy a large area of sea surface that may affect ship routes. On the other hand, if the distance is too small, standing waves at resonance may occur between neighbour breakwaters after multiple reflections, which may harm the global performance of the breakwater system. This study considers a dual-pontoon breakwater, as the simplest deployment of multiple breakwaters. A series of physical experiments is conducted in the wave flume at Dalian University of Technology, China. Hydrodynamic performance of dual-pontoon breakwaters in various regular waves is studied. Free-surface elevation histories around the breakwaters are recorded, with which the reflection and transmission coefficients are calculated. Effects of the distance between two pontoons on two coefficients are analysed in detail. The wave response around each dual-pontoon breakwater in transient waves is also investigated. More results will be shown in the full-length paper and presentation in the future.

Key Words: breakwater, dual-pontoon, water wave, reflection coefficient, transmission coefficient

Acknowledgement: This study is supported by the National Natural Science Foundation of China (Grant Nos. 51709038, 51739010, and 51679036), and the Project funded by China Postdoctoral Science Foundation (No. 2018M630289 and 2019T120209).

8th International Conference on the Application of Physical Modelling in Coastal and Port Engineering and Science
Zhoushan, China - Dec. 9th - 12th, 2020

EXPERIMENT ON VORTEX-INDUCED VIBRATION RESPONSE OF SUBMARINE FLEXIBLE PIPELINE NEAR SEABED

HONGJUN ZHU[1,2], HONGLEI ZHAO[3], NARAKORN SRINIL[4]

1 State Key Laboratory of Oil and Gas Reservoir Geology and Exploitation, Southwest Petroleum University, China, zhuhj@swpu.edu.cn

2 State Key Laboratory of Coastal and Offshore Engineering, Dalian University of Technology, China

3 Petroleum Engineering School, Southwest Petroleum University, China, 201811000091@stu.swpu.edu.cn

4 Marine, Offshore & Subsea Technology Group, School of Engineering, Newcastle University, United Kingdom,

Offshore oil and gas are commonly transported by submarine pipelines that are generally laid on or shallowly buried in the seafloor. Free spans are easily formed due to the complex topographic conditions and local scour, posing a risk to the safety of pipelines. In the past decades, significant research efforts have been devoted to investigating the scour process beneath submarine pipelines and the forces exerted on pipelines' surface. A gap between the pipeline and the seabed is observed to be a key parameter determining the hydrodynamic lift/drag forces and the pipe vibration response. If the gap is sufficiently small, the pipeline may collide with the seabed and bounce back after the collision, influencing the vibration characteristics due to the time-varying gap. However, quite a few studies in the literature have investigated the bounce mechanism of the free-hanging suspended pipeline and its effect on the vortex-induced vibration (VIV) phenomenon. In this work, VIV of a flexible pipeline span is experimentally investigated in a water flume. The pipeline made of silica gel has an aspect ratio of about 87 and fixed supports, subject to approaching flow with an angle of attack of 30°. A non-intrusive measurement technique is employed to record the spanwise vibration displacements in both in-line/cross-flow directions through high-speed cameras. Displacements of 26 markers evenly located along the pipe span are captured with the sampling frequency of 100 Hz. The VIV and seabed beating characteristics in the reduced velocity range of 3–15 are compared in terms of time-space varying response amplitudes, frequencies, trajectories, equilibrium positions, collision location and its occurrence likelihood. A mode transition in in-line versus cross-flow directions is out of synchronization as the reduced velocity increases. Depending on the dominant vibration mode and beating-type response feature, the tank bottom-pipeline interaction is classified into four types including single-point, single-segment, two-point alternating and two-segment alternating contacts. A switching of such response patterns contributes to a reconfiguration of the pipe equilibrium position and hence an abrupt change of vibration amplitudes. A beating frequency is found to be associated with the time-space varying gap. Overall, experimental findings improve our understanding in the flexible pipe-seabed interaction involving VIV and associated fluid-structure-solid interaction.

Key Words: vortex-induced vibration (VIV); submarine pipeline; pipe-seabed interaction; flexible cylinder; non-intrusive measurement

8th International Conference on the Application of Physical Modelling in Coastal and Port Engineering and Science
Zhoushan, China - Dec. 9th - 12th, 2020

WAVE DISSIPATION BY VEGETATION IN COMBINED WAVE AND CURRENT FLOW

ZHAN HU[1], SIMEI LIAN[2], XIONGHUI ZHANG[3], TOMOHIRO SUZUKI[4], DIRK RIJNSDORP[5]

1 School of Marine Sciences, Sun Yat-sen University, huzh9@mail.sysu.edu.cn 2 School of Marine Sciences, Sun Yat-sen University, liansm@mail2.sysu.edu.cn
3 School of Marine Sciences, Sun Yat-sen University, zhangxh57@mail2.sysu.edu.cn 4 Flanders Hydraulics Research, tomohiro.suzuki@mow.vlaanderen.be
5 Ocean Graduate School, University of Western Australia, dirk.rijnsdorp@uwa.edu.au

Coastal vegetation such as mangroves and salt marshes can dissipate wave energy and reduce shoreline erosion effectively. Most previous studies have investigated how canopy traits and incident wave conditions affect wave dissipation by vegetation (hereafter referred as WDV) in pure wave condition. However, mangroves are often found in the inter-tidal zone, where waves and currents coexist. To explore the effect of currents on WDV, flume experiments with stiff plant mimics were carried out in combined wave-flow conditions with both following and adverse current. Laboratory experiments were conducted in a 26-m-long, 0.6-m-wide, 0.6-m-high wave and recirculating flume. Stiff wooden rods (0.01m in diameter) fixed to a false bottom were used to mimic a 6-m-long, 0.6-m-wide, 0.25-m-high canopy area. We considered two mimic stem densities (N), 124 and 550 stems/m^2, as well as a control test (0 stem/m^2). Seven wave gauges were used to measure the free surface elevation along the flume. Three ADVs and force sensors in the same cross section were used to measure the fluid velocities inside the canopy and the in-phase force of the mimic plant. Additionally, we chose two water depths (h=20/33 cm) to mimic emergent and submerged canopies. Drag coefficients (C_D), a key parameter for calculating the force of rigid vegetation, were obtained in both pure wave and combined current–wave flows using the direct measurement approach. Results of this study showed that opposite currents lead to larger WDV compared to following currents. This was especially obvious for submerged canopies. The drag coefficient C_D under following currents and opposing currents follow an empirical pattern, with reducing C_D for increasing Reynolds number that asymptotes at 1 for fully turbulent conditions. Drag coefficients obtained in this study are in line with the empirical relationship between C_D and Reynolds number in previous study. There is no obvious difference between the pattern and value of C_D under following and opposite currents. We will further study the wave and velocity field in the wave-current environment using the SWASH model.

Key Words: laboratory experiment; wave dissipation; vegetation; wave; currents

8th International Conference on the Application of Physical Modelling in Coastal and Port Engineering and Science
Zhoushan, China - Dec. 9th - 12th, 2020

STEPWISE ADJUSIMENT OF RIVER-TIDE DYNAMICS IN RESPONSE TO HUMAN INTERVENTIONS IN THE EAST RIVER NETWORKS OF THE PEARL RIVER, CHINA

HAO YANG[1], HUAYANG CAI[2]

1 *Institute of Estuarine and Coastal Research, School of Marine Engineering and Technology, Sun Yat-sen University, China, yangh236@mail2.sysu.edu.cn*

2 *Institute of Estuarine and Coastal Research, School of Marine Engineering and Technology, Sun Yat-sen University, China, caihy7@mail.sysu.edu.cn*

Many estuaries worldwide are subject to both natural (e.g., tidal forcing from the ocean and global sea level rise) and human-induced (e.g., dam construction, sand excavation, and land reclamation). However, the impact of these interventions on the spatio-temporal river-tide dynamics is insufficiently understood. In recent decades, due to the intensive human interventions the patterns of river-tide dynamics in the East River networks of the Pearl River have changed a lot. In this study, we used a MATLAB-based T_TIDE toolbox to extract tidal constituents from water level records collected over the past 40 years at two gauging stations (Shilong and Sishengwei) in this river network system. The results show that the M_2 tide has the largest amplitude, followed by K_1 and O_1, while the S_2 tide has the least amplitude at two stations. The M_2 tide has the largest tidal damping rate along the channel, followed by the S_2 and K_1 tides, while the O_1 tide has the least tidal damping rate. The amplitudes for the four predominant constituents were significantly amplified in the Shilong station owing to the intensive human interventions caused by sand excavations and dam constructions. Using the double mass curve approach, we identified three stepwise phases (i.e. 1975–1989 representing the pre-human intervention period, 1990–1998 representing the transitional period, and 1999–2016 representing the post-human intervention period) corresponding to residual water level slopes, and qualitatively matched the river-tide dynamics shift observed in the East river networks. It was shown that the enhancement of tidal dynamics was primarily due to the reduction in residual water level slope (and thus the weakening of the tidal damping effect) caused by the channel deepening along the East river networks where the residual water level slope was decreased by 68%, while the absolute value of the tidal damping rate was decreased by 48% after intensive human interventions.

Key Words: human interventions, tidal damping rate, residual water level slope, river discharge

8th International Conference on the Application of Physical Modelling in Coastal and Port Engineering and Science
Zhoushan, China - Dec. 9th - 12th, 2020

A BOTTOM-SITTING WAVE ENERGY CONVERTER: CHARACTERISTICS OF LOCAL FLOW FIELD AND SCOUR

ZHENHUA HUANG[1], SHIJIE HUANG[1], CONGHAO XU[1],
YING-MIN LOW[2], ZHIXUN ZHANG[2], JUNCHENG CHEN[2]

[1] *Department of Ocean and Resources Engineering, School of Ocean and Earth Science and Technology, University of Hawaii at Manoa, Hawaii, USA*

[2] *School of Civil and Environmental Engineering, National Singapore University, Singapore*

Most existing studies on wave energy converters (WECs) focused on the hydrodynamics and conversion efficiency of various designs. For the foundation safety of a bottom-sitting wave energy converter, wave-induced scour around the device is an important factor to consider. There is a rich literature in wave or current induced scour around circular cylinders or bridge piers. However, published results on the local scour around WECs is scarce. Compared to circular cylinders or bridge piers, wave energy converters have much more complicated geometry and near-field flow conditions. Incident waves, diffracted waves and radiated wave all contribute to this complicated flow-structure-seabed interaction problem. This talk will focus on an OWC-pile, which is a pile integrated with an oscillating-water-column (OWC) type wave energy converter (WEC). We discuss flow field characteristics around the WEC and present a set of preliminary experimental results of wave-induced local scour at the WEC. The tests were performed in a wave flume of 36 m long, 2 m wide and 1.3 m deep. The OWC-pile was installed in a sand bed built in the middle of the wave flume. Development of the scour hole depth and the final scour hole profile around the OWC-pile will be presented. Two-phase (air-water) flow simulations were also performed on XSEDE's Stampede2 supercomputers to reveal the local flow structure and understand the experimental results. The data will be used to tune a three-phase (solid-gas-liquid) flow model developed to study sediment transport in geophysical flows and sediment transport around marine structures.

Acknowledgement

This work was partially supported by the US National Science Foundation under grant no. CBET-1706938. The National University of Singapore is acknowledged for supporting the experimental work reported here through a MSc student project under the supervision of Dr. Low. Extreme Science and Engineering Discovery Environment (XSEDE) is also acknowledged for providing computing resources through two grants (OCE170015 and ENG180008). Any opinions, findings, and conclusions or recommendations expressed in this material are those of the author(s) and do not necessarily reflect the views of the National Science Foundation.

Key Words: Local scour; Wave-energy converter; Vortex; Two-phase flow simulation

8th International Conference on the Application of Physical Modelling in Coastal and Port Engineering and Science
Zhoushan, China - Dec. 9th - 12th, 2020

NUMERICAL STUDY ON INFLUENCE OF WIDTH OF VEGETATED ZONE ON WAVE ATTENUATION

JUN TANG[1]

1 State Key laboratory of Coastal and Offshore Engineering, Dalian University of Technology, Dalian 116023, China, jtang@dlut.edu.cn

The study numerically investigates vegetated zone width effects on wave attenuation. The numerical model is based on a parabolic mild slope equation for wave refraction-diffraction in which wave energy dissipation module due to vegetation is implemented. Before the model is firstly tested to model wave propagation on vegetated planes to examine the extent to which it can be applied to quantify wave attenuation due to vegetation. Next, the model is applied to investigate waves with different period propagation in vegetated water zones. The sensitivities of wave attenuation due to vegetation at one wavelength to wave period and water depth are investigated in comparison to the numerical results of wave height attenuation in vegetated zones.

Key Words: Wave, Vegetation, Attenuation, numerical study

8th International Conference on the Application of Physical Modelling in Coastal and Port Engineering and Science
Zhoushan, China - Dec. 9th - 12th, 2020

APPROACH COASTAL CHANGE ANALYSIS AT THE NORTHERN CUA DAI RIVER MOUTH BY ADOPTING DIGITAL SHORELINE ANALYSIS SYSTEM

VU HUONG NGAN [1], NGUYEN NHAT MINH [2], NGUYEN KHANH LINH [2], DINH NHAT QUANG [2], HO SY TAM [2] & NGUYEN TRUNG VIET [2]

1 International Center of Tropical Agriculture, Pham Van Dong, Hanoi, Vietnam,vuhuongngan235@gmail.com

2 Thuyloi University, 175 Tay Son, Dong Da, Hanoi, Vietnam minhnn6nk@wru.vn; quang.dinh@tlu.edu.vn, tamhs.cttl@tlu.edu.vn, nguyentrungviet@tlu.edu.vn

3 Former student, Thuyloi University, 175 Tay Son, Dong Da, Hanoi, Vietnam linhnk5nk@wru.vn

Coastal change analysis is one of the controversial issues in water resources fields since this greatly impacts coastal management. The case study of this research is the coastline at the Northern Cua Dai river mouth, where witnessed the significant morphological change in recent years. To approach coastal change analysis in this region, the authors adopted DSAS - Digital Shoreline Analysis System, an addi-in to ArcGIS software, to calculate rate-of-changes statistics in the long-term process. Satellite scenes in 1990, 1995, 2000, 2005, 2010, 2015, 2017 and 2019 were collected and processed to extract representative coastlines, which were the inputs to implement DSAS calculation. The results indicate the case study experience both erosion and accretion phenomenon, where 8 km coastline in Hoi An had been eroded most seriously with the highest rate reached to -45 m/yr and retreat distance was more than 1 km. Importantly this methodological approach provides not only visual coastline change information (Net Shoreline Movement, End Point Rate, Linear Regression Rate) but also relating indicators (Uncertainty, Standard Error, Correlation Coefficient and Confidence Interval) for checking the accuracy of the application. Three primary reasons leading to the severe situation of erosion and accretion in the Northern Cua Dai river mouth are natural factors, constructions and tourism industry. The local authorities can base on the results of this research to offer suitable and optimal methods in cover the damage in this area.

Key Words: coastal change analysis, satellite images, Digital Shoreline Analysis System, Quang Nam province.

8th International Conference on the Application of Physical Modelling in Coastal and Port Engineering and Science
Zhoushan, China - Dec. 9th - 12th, 2020

REAL TIME MONITORING OF DESTABILIZATION RISK FOR NEAR SHORE INFRASTRUCTURE

YI XU[1], MANOUSOS VALYRAKIS[1]

[1]*School of Engineering, University of Glasgow, G12 8QQ, UK (2421380x@student.gla.ac.uk)*

During extreme weather events, the risk of underscouring of near or off-shore infrastructure such as monopoles supporting wind farm turbines, oil transport pipelines and power grid or telecommunications cables, may significantly increase. Sufficiently energetic flow structures, shed downstream a monopole and typically scaling with its cross-sectional length-scale, may lead to the removal of coarse bed material and lead to the critical failure of its protective layer against scour (typically a naturally formed armor layer or implemented rip-rap protection, comprising of cobbles and rocks).

The goal of this study is to assess the risk of critical failure of the protective layer in the vicinity of a monopole by directly monitoring the seabed destabilization through an instrumented particle appropriately positioned on its surface. A set of flume experiments under a range of well-controlled increasing flow conditions is undertaken to assess the increase in entrainment frequencies of an instrumented particle, laying downstream a physical model of a bridge pier. Highly resolved time series of the instrumented particle's entrainment for the tried flow conditions, are acquired with micro-electromechanical sensors (MEMS) embedded within it and validated with synchronous recordings of a visual assessment method. Flow profiles at different distances downstream the model pier are obtained with Acoustic Doppler Velocimetry (ADV) in a preliminary attempt to further link the driving mechanisms for particle entrainment to the phenomenologically relevant bulk flow and pier characteristics (such as pier length-scale, average flow velocity and depth, median size of armor layer particles).

Key Words: coastal infrastructure, instrumented particle, turbulent flow

8th International Conference on the Application of Physical Modelling in Coastal and Port Engineering and Science
Zhoushan, China - Dec. 9th - 12th, 2020

INFLUENCE OF ROCK BERM AND REVETMENT ON WAVE OVERTOPPING AT DIKES

WEIQIU CHEN[1,2], ALBERTO MARCONI[2,3], MARCEL R.A. VAN GENT[2], JORD J. WARMINK[1], SUZANNE J.M.H. HULSCHER[1]

1University of Twente, Netherlands, w.chen-6@utwente.nl, j.j.warmink@utwente.nl; s.j.m.h.hulscher@utwente.nl

2 Deltares, Netherlands, marcel.vangent@deltares.nl

3 University of Roma Tre, Italy, alb.marconi@stud.uniroma3.it

Nowadays, due to climate change and sea level rise, storm surges occur more frequently. During extreme events, the probability of wave overtopping over dikes increases significantly, which might lead to dike breaching. With this background, some existing dikes might not satisfy the safety standards and therefore require reinforcement. Berms and roughness elements are widely used around the world to reinforce a dike by reducing the overtopping discharge. Rock armour is often combined with other types of roughness elements at the waterside slope to protect a dike. Chen et al. (2019) showed that existing guidelines such as the EurOtop Manual (2018) overtopping equations do not perform very well when taking the combination of berms and roughness into account. New equations were developed to estimate the berm and roughness influence factors. However, the applicability of the new equations for rock armour is still unclear. Therefore, this study aims at extending the applicability of the new equations to quantify the influence of a rock berm and rock slope protection on wave overtopping at dikes.

Physical model tests were conducted in the Pacific Basin at Deltares (Figure 1). Various dike configurations by changing the applied location of rock armour on the slope were tested to investigate the effect of the location of rock armour along the slope on the overall roughness influence factor. Both straight and bermed slopes were included to study the rock berm influence on the overtopping discharge. Applying the new equations for the berm and roughness influence factors, the empirical coefficients were recalibrated for rock. Additionally, the equation for varying roughness along the slope was improved by taking the berm width into account. These new equations for rocks significantly improved the predictive accuracy of average overtopping discharge at dikes.

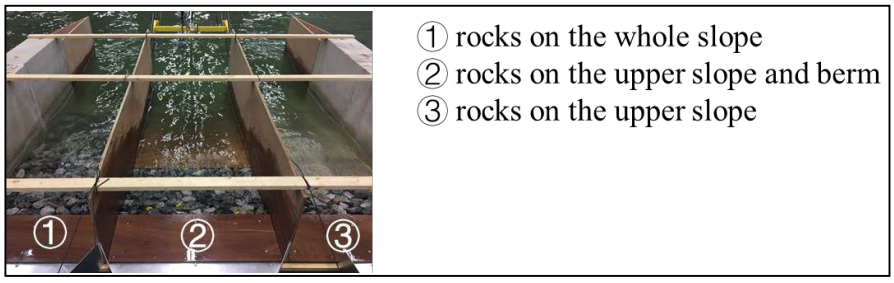

Figure 1 Three sections with rocks applied on different parts of the slope

Key Words: overtopping discharge, experiments, rocks, berms, roughness

8th International Conference on the Application of Physical Modelling in Coastal and Port Engineering and Science
Zhoushan, China - Dec. 9th - 12th, 2020

NUMERICAL SIMULATION AND EXPERIMENTAL INVESTIGATION ON THE CAVITY DYNAMICS AND MULTIPHASE FLOW FIELD EVOLUTION FOR WATER ENTRY OF THE DOUBLE CYLINDERS

ZHOU Bo1, LIU Hui1, WANG Jie1, HAN Xiaoshuang2,3,*

1.State Key Laboratory of Structural Analysis for Industrial Equipment, School of Naval Architecture Engineering, Dalian University of Technology, Dalian 116024, P.R. China.
2. State Key Laboratory of Coastal and Offshore Engineering, Dalian University of Technology.
3.Marine Engineering College, Dalian Maritime University, Dalian 116026, P.R.China Corresponding author.*
Email: xhan@dlmu.edu.cn

Water entry means the process that the structure enters water through free liquid surface from the air, which is an instantaneous and strong nonlinear process with complicated phenomenon including turbulent flow, free liquid surface and vortices evolution, and it widely exist in engineering applications such as ship slamming, seaplane landing, torpedo airdrop and marine floating platform. Therefore, the combination of experiment and numerical simulation is used to study the effects of entry angle, entry velocity, cylinder spacing, synchronization and other factors on the characteristics for water entry of the double cylinders under various working conditions. For experiments, the cylinder motion characteristics and the wall pressure changes of the experimental system are recorded based on the force and acceleration sensors, and the evolution of cavity and structural characteristics of multi-phase flow field are captured based on high-speed camera and PIV technology, respectively. For numerical simulation, the N-S equations are solved based on the finite volume method and the RANS SST k-ω viscous model, and the complex motion is simulated based on the DFBI and six-degree-of-freedom solver. Meanwhile, the numerical results can be verified by comparison with the experimental results. Through the summary and analysis of the above results, the complicated water entry phenomena and mechanisms can be further studied and revealed.

Key words： Double cylinders water entry; Six degrees of freedom; Cavity evolution; Multiphase flow field structure; Dynamics characteristics

8th International Conference on the Application of Physical Modelling in Coastal and Port Engineering and Science
Zhoushan, China - Dec. 9th - 12th, 2020

PERFORMANCE ASSESSMENT OF TWO ACTIVE ABSORPTION SYSTEMS IN A LARGE WAVE FLUME

PEDRO LOMONACO[1], UNA SAVIC[1,2], TIMMOTHY MADDUX[3]

1 O.H. Hinsdale Wave Research Laboratory, Oregon State University, USA, Pedro.lomonaco@oregonstate.edu 2 Currently at GHD, USA, Una.Savic@ghd.com
3 O.H. Hinsdale Wave Research Laboratory, Oregon State University, USA, Tim.maddux@oregonstate.edu

The quality of most coastal or ocean laboratory experiment depends on the accuracy, uniformity and stability of the generated waves. Generation of waves in the laboratory seems simple, but it should consider the spatio-temporal variability of the wave profile. As they propagate, waves interact with the boundaries, i.e. changes in water depth, lateral walls, test specimens, instrument supporting structures, passive absorbers, etc., as well as with varying hydrodynamic conditions (wave-induced currents, wave-wave interactions, or nonlinear energy transfer, among others).

Theoretically, for weakly nonlinear unidirectional waves propagating over relatively small number of wavelengths, and as long as the still water depth and facility width does not change, the wave properties should remain constant in space and time, also identified as the uniformity and stability of the waves. Under these conditions, nonuniform or unsteady wave properties are associated to wave reflection and the performance of the active wave absorption system. In other words, it can be said that the performance of the active wave absorption control system is an indicator of the quality of the generated waves.

Many laboratories have implemented different passive and active wave absorption systems, but the performance on the uniformity and stability of the generated waves, as well as the active wave absorption system used, have not been assessed in a systematic way, and related published data and information is quite scarce.

This paper presents a thorough study on the performance assessment of two different active wave absorption control systems as a means to establish the quality of the experiment in terms of the uniformity (space) and stability (time) of generated wave parameters (descriptors) in the laboratory. The experiments have been conducted in the Large Wave Flume at O.H. Hinsdale Wave Research Laboratory (HWRL), Oregon State University. The flume is equipped with a piston-type dry-back wave generator manufactured in 2009 by MTS Systems Corp. It includes a built-in wave generation and active absorption control system based in simple linear superposition. Waves are synthesized with in-house routines incorporating second-order wave generation and evanescent modes. More recently, in 2016, the HWRL acquired Awasys7, a state-of-the-art wave generation system, developed by Aalborg University, that includes second-order wave generation and nonlinear wave absorption, among other features.

Different tests were executed with regular and irregular waves, comprising a wide range of wave periods and wave heights, where the absorbing beach has been removed and the bottom remained flat and horizontal, aiming the full reflection of waves at the opposing end of the flume, while propagating over a constant depth. Both generation and absorption methods were used, and measurements of the surface elevation were made along the flume to assess the performance of the absorption systems.

The methodology was not only able to comparatively assess the performance of both active wave absorption control systems, but also to identify the parameters to describe the uniformity and stability of the generated waves.

Key Words: wave generation, active absorption, wave reflection, wave uniformity, wave stability

8th International Conference on the Application of Physical Modelling in Coastal and Port Engineering and Science
Zhoushan, China - Dec. 9th - 12th, 2020

ISPH SIMULATION OF WAVE BREAKING AND SEDIMENT TRANSPORT

Dong Wang1,2

1 College of Environmental Sciences and Engineering, Dalian Maritime University, China
2 Department of Civil & Environmental Engineering, National University of Singapore, Singapore
Email: ceewadg@nus.edu.sg

Extreme waves may destroy the coast-protection structures through continuous scour around them. A 3D incompressible Smoothed Particle Hydrodynamics (ISPH) erosion model is proposed to simulate the scouring process around coastal structures. The erosion model is based on the turbidity water particle concept and the sediment motion is initiated when the fluid bottom shear stress exceeds the critical value. To validate the developed model, a laboratory flume experiment was carried out to study the clear water scouring around a vertical cylinder under unidirectional current, in which high-speed video cameras were used for the real-time monitoring of sediment movement. Recently, the Incompressible Smoothed Particle Hydrodynamics (ISPH) method solving the 2D RANS (Reynolds Averaged Navier-Stokes) equations with the k–ε turbulence closure is constructed. The concept of "massless ISPH" utilizing the definition of "particle density" (number of computational particles within unit volume) is stressed. The skills of this numerical model are tested by applying to two laboratory experiments: (1) A non-breaking solitary wave propagating over a bottom-mounted barrier and (2) a solitary wave breaking on a 1 on 50 slope.

Keywords: ISPH; k–ε model; sediment transport; wave breaking

8th International Conference on the Application of Physical Modelling in Coastal and Port Engineering and Science
Zhoushan, China - Dec. 9th - 12th, 2020

WAVE PRESSURES ON A CAISSON THAT IS ARMORED WITH RUBBLE STONES AND TETRAPODS

SANG-HO OH[1], SUKJIN AHN[2]

1 Korea Institute of Ocean Science and Technology, Republic of Korea, ohsangho@kiost.ac.kr 2 GeoSystem Research Corporation, Republic of Korea, sjahn@geosr.com

This study reports experimental and numerical investigation on the horizontal wave force acting on a solid caisson that is armored with double-layer Tetrapods and core-layer of rubble stones. The main focus of this study was to evaluate the effects of crest level of the armor layers on the measured wave pressures. The experiment was carried out in a two-dimensional wave flume. The wave pressures were measured by using miniscule disk-type pressure transducers. The measurement was conducted with four different models in terms of the coverage of the front face of the caisson: no coverage, full coverage up to the crest of the caisson, and two different partial coverages where the crest level of the armor layers were lower than the crest of the caisson.

OpenFOAM modeling was also conducted to numerically simulate the wave pressure on the upright caisson. Then the simulation result was compared with the physical experiment, which showed fairly good agreement with the measurement. This implies the feasibility of OpenFOAM model for reproducing wave pressure on the structure. Based on the simulation results, the combination of porous media coefficients to reproduce the properties of tetrapod was suggested in this study.

Key Words: Wave force, Tetrapods, OpenFOAM, Physical experiment

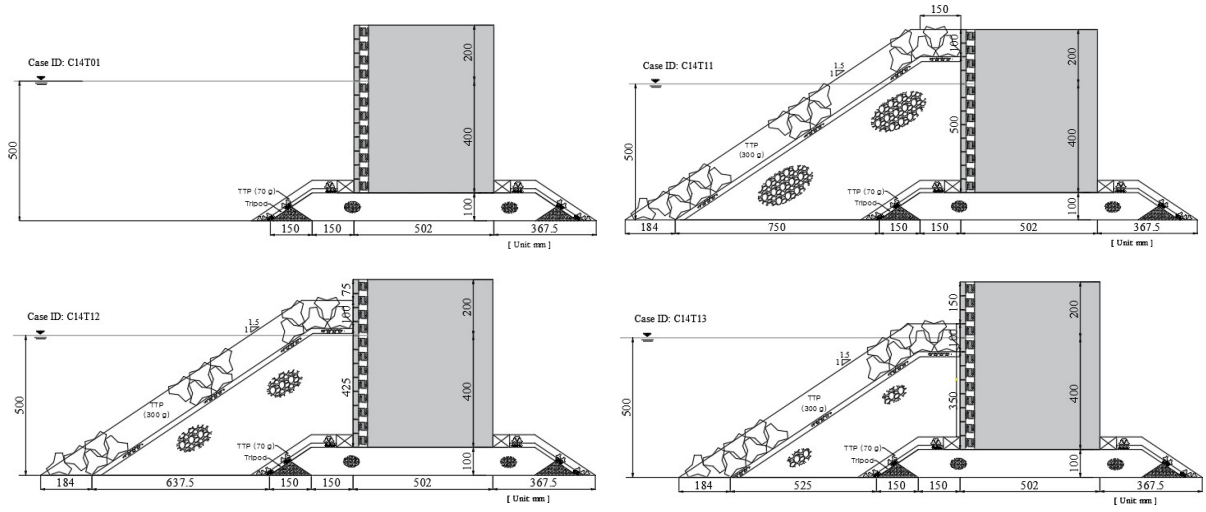

Figure 1. Side views of the four different models that were used in this study

8th International Conference on the Application of Physical Modelling in Coastal and Port Engineering and Science
Zhoushan, China - Dec. 9th - 12th, 2020

A PRELIMINARY STUDY ON THE GENERATION OF RIP-CURRENT SYSTEMS AT YEN-LIAU COAST SUBJECTTO MORPHOLOGICAL VARIATIONS, TAIWAN

PEI-HSIAN HSU[1], TING-CHIEH LIN[2], CHIH-MIN HSIEH[3]

1 Graduate student, Department of Harbor and River Engineering, National Taiwan Ocean University, Taiwan, 10852031@email.ntou.edu.tw

2 Assistant Professor, Department of Harbor and River Engineering, National Taiwan Ocean University, Taiwan, tclin@mail.ntou.edu.tw

3 Professor, Department of Maritime Information and Technology, National Kaohsiung University of Science and Technology, Taiwan, chihmin_623@yahoo.com.tw

The morphological variations on the generation of rip-current systems were investigated using a well-known Boussinesq model (FUNWAVE-TVD). The comprehensive bathymetry measurements were also carried out along the YEN-LIAU coast to quantitatively realize the variation of water depths. It was found that several reef rocks were existed within the nearshore regions; the nearly parallel topography was found along the coast line. The FUNWAVE-TVD model was validated against published data of wave-induced rip-currents/longshore currents in the shallow water regions subject to morphological variations for justifying the model setups. Based on the measured bathymetry and reliable model setups, the FUNWAVE-TVD was applied to a case study of rip-current generation along Yen-Liau coast. The results discuss where/when rip-current occurred based on the effects of morphological variations of nearshore regions. The future strategy for studying the rip- current/longshore currents to this study was also reported.

Key Words: rip-current; longshore current; Boussinesq model; FUNWAVE-TVD.

8th International Conference on the Application of Physical Modelling in Coastal and Port Engineering and Science
Zhoushan, China - Dec. 9th - 12th, 2020

HAVE WE MISUNDERSTOOD THE SHIELDS CURVE?

THOMAS PÄHTZ[1]

1 Institute of Port, Coastal and Offshore Engineering, Ocean College, Zhejiang University, China, 0012136@zju.edu.cn

The Shields curve, which compiles measurements of fluvial sediment transport thresholds in terms of the nondimensionalised threshold fluid shear stress and shear Reynolds number, is a standard reference in geophysics and hydraulic and coastal engineering and commonly thought to describe the critical flow conditions that are required for flow-driven entrainment of bed sediment. However, recent findings from several independent research groups have challenged this belief on various grounds: (i) particle-bed impacts predominately trigger sediment entrainment; (ii) such impact-triggered entrainment can sustain continuous transport even when flow-driven entrainment events are completely absent; and (iii) extrapolating the transport rate of such impact-sustained continuous transport to zero yields transport thresholds that still fall on the Shields curve. The question that thus emerges from these findings is, if not flow-driven entrainment, then what is the physics behind the thresholds shown in the Shields curve? In my presentation, I will provide an answer to this question based on my latest research.

Key Words: Shields curve, Shields diagram, sediment entrainment, sediment transport threshold

8th International Conference on the Application of Physical Modelling in Coastal and Port Engineering and Science
Zhoushan, China - Dec. 9th - 12th, 2020

GENERALIZED BUCKINGHAM'S THEOREM FOR DIMENSIONAL ANALYSIS ON BREAKWATERS

MªVICTORIA MORAGUES [1], PILAR DÍAZ-CARRASCO[1], MARÍA CLAVERO [1], MIGUEL Á. LOSADA[1]

[1] *Andalusian Institute for Earth System Research (IISTA) - University of Granada, Spain.*
mvmorague s@ugr.es, pidiazc@ugr.es, mclavero@ugr.es, mlosada@ugr.es

Breakwaters are the principal structure for the protection of ports and beaches. Their study should analyze the consequences that the loss of structural attributes has on their operativity, functionality and reliability so to came up with calculus methodologies that can guaranty his useful life. A breakwater analysis has to take into account three laws: (1) energy conservation, use to estimate the wave energy transformation when it interacts with the structure, (2) the conservation of mass, applicable for the estimation of run-up, run-down or overtopping, and (3) conservation of momentum that is used for the calculus of forces and momentums (ROM 1.1-18).

While designing experiments on a physical model of a breakwater the geometrical characteristics are chosen (breakwater type, porous material, main armor layer, etc.) and then the wave conditions (wave height, wave period and water depth). Each of the parameters to study is usually non- dimensionalized with different variables: run-up through the wave height, eroded area with the diameter of the pieces, etc. Is there a global dimensional analysis for estimating all breakwater failure modes in the same way?

Dimensional analysis offers a simple methodology to describe physical processes establishing the dependence of physical quantities by using their dimensions. The advantages of dimensional analysis are: (1) the dimension reduction, and (2) scalability of the developed model (Díaz-Carrasco et al. 2019).

Four steps are necessary for the dimensional analysis once the dependent quantities are defined: (1) choose a complete set of n independent variables, (2) list a complete dimensionally independent subset of k quantities, (3) define the dimensionless forms of the n-k remaining independent variables, and (4) application of the Buckingham's Π theorem to state the dimensionless dependent quantities as a function of the (n-k) dimensionless independent quantities.

The generalization of the Buckingham's Π theorem can be defined as: once the dependent quantities are identified and determined by a set of n independent quantities, of which k are dimensionally independent, if nf of these quantities have fixed values and of those, kf are dimensionally independent, the dimensionless dependent variable can be determined by $(n-k)-(nf-kf)$ dimensionless similarity parameters. If these quantities with fixed values are chosen as base quantities and used for non-dimensionalize the rest, then this base quantity can be used as the principal variable. This allows a combined dimensional analysis of all the involved variables.

At the conference it will be discussed how this methodology permits to choose which tests are necessary for an investigation, saving time and money from unnecessary experiments. Furthermore, done in the same way, this analysis would allow researchers to effectively compare or extrapolate experimental results although the different laboratories.

Key Words: Breakwater, hydraulic performance, dimensional analysis, experimental design, Buckingham theorem

8th International Conference on the Application of Physical Modelling in Coastal and Port Engineering and Science
Zhoushan, China - Dec. 9th - 12th, 2020

EFFECTIVENESS OF DUMMY WATER LEVELS IN PHYSICAL MODELS TO OPTIMIZE THE TOE AND THE CREST LEVELS

D.P.L.RANASINGHE[1], I.G.I.K.KUMARA[2], N.L.ENGILIYAGE[3], K.RAVEENTHIRAN[4]

1 Engineering Manager, Lanka Hydraulic Institute Ltd., Sri Lanka, prasanthiranasinghe@gmail.com

2 Research Engineer, Lanka Hydraulic Institute Ltd., Sri Lanka, indika.kumara@lhi.lk

3 Research Engineer, Lanka Hydraulic Institute, Sri Lanka, nalika.engiliyage@lhi.lk

4 Senior Engineering Manager, Lanka Hydraulic Institute, Sri Lanka, ravi@lhi.lk

To design a stable coastal structure, empirical equations would be sufficient if the design parameters are well defined and fully obtained. However, physical models are necessary to optimize coastal structures while assessing hydraulic performance. Even though it is cost and time consuming than the other design techniques, physical models can save a substantial amount from the actual construction as it reproduces actual phenomenon in a small scale without any schematization. The objective of this study was to use the constructed physical model to represent the different toe and the crest levels by adjusting the water levels during the model testing. The crest optimization has been done for a deep breakwater at -26m CD (Chart Datum) depth by changing the water levels to represent the effective freeboard for the overtopping. The same design waves were applied for the different water levels as deep water wave conditions are not much varying at the adjacent water depths. Since the toe stability is assessed by considering maximum wave height that can be generated at the critical low water level, effective water depth at the toe has been considered while optimizing the toe elevation using adjusted water levels. Application of dummy water levels in toe optimization has been adopted for the various 2D models done in Lanka Hydraulic institute Ltd for shallow and deep water coastal structures.

Initially, the deep water breakwater section was designed with +5.0m CD crest and -5.0m CD of toe berm. The overtopping and wave transmission through the main armour created an unfavourable wave disturbance at the harbour side during the design wave condition with design high water level of +3.95m CD. Therefore, the structure was modified with crest level of +7.0m CD and the observed wave height at the harbour side was reduced to 0.03m. Hence, a dummy water level of +4.95m CD was utilized over the +7.0m CD crest to represent the +6.0m CD crest for
+3.95m CD. The observed wave height of 0.06 m confirms the sufficient calmness at the harbour side. Finally, the design waves were applied for modified section with +6.5m CD crest. The results depicted that the structure was stable when its crest raised above the +6.0m CD.

The design waves were hardly created any impacts for both toe levels at -5.0m CD and -4.0m CD during 0.0m CD critical low water level (CLWL). Therefore, -2.0m CD dummy level has been used as the CLWL for -4.0m CD toe to represent the -2.0m CD toe for 0.0m CD CLWL. Based on the results, it was recommended to increase the toe up to -2.0m CD as the damage observed using dummy water level gave the acceptable results for the toe stability.

The full paper will include the further discussion on the toe stability for deep and shallow water sections as well as the suitability of dummy water levels for the engineering judgments while optimizing the crest and toe levels of the coastal structures.

Key Words: Crest level, Dummy water levels, Physical models, Toe stability

8th International Conference on the Application of Physical Modelling in Coastal and Port Engineering and Science
Zhoushan, China - Dec. 9th - 12th, 2020

QUANTIFICATION OF FLOW VELOCITY AND WAVE DAMPING IN A PHYSICAL MODEL OF A MANGROVE FOREST INCLUDING SECONDARY ROOTS

PIEDRAHITA, M.A.[1], OSORIO, A.F.[1], HUGUENARD, K.[2], URREGO, L.E.[1], OSORIO-CANO, J.D.[1]

1 Research Group in Oceanography and Coastal Engineering, OCEANICOS, Department of Geosciences and Environment, Universidad Nacional de Colombia, Sede Medellin.

2 Department of Civil and Environmental Engineering, University of Maine, USA

In order to promote the use of trees as a natural solution for coastal protection, the aim of this study was to improve the understanding of flow velocity under oscillatory flow conditions in an artificial Rhizophora mangle population (ARmP). The effectiveness of mangrove forests as a wave and velocity-damping structure and sediment retention structure was studied through physical modeling under laboratory experiments at Universidad Nacional de Colombia - Medellín in a wave - current flume that is able to reproduce linear and 2nd-order stokes waves. Eight wave gauges were implemented along the flume to record the free surface elevation, and a 3-D Acoustic Doppler Velocimeter (ADV; Nortek Vectrino) to measure velocity time series at different vertical positions. The mangrove trees were scaled (1:10) and constructed in stainless steel using a morphometric model to which secondary roots were added. A set of wave scenarios were run for a fixed wave height and several wave periods (H = 0.07 m, T = 0.5 s - 1.5 s) and 0.28 m still water level, in order to analyze different non-linearity cases. In most cases, there was a considerable reduction of the steady component velocity inside the ARmP of approximately 30%, where high velocities were associated with the higher periods. During the experiments, wave damping was 14% lower compared with no mangrove trees condition. Thus, it can be inferred that the mangrove structure could be helpful protecting the coastline and reducing erosional processes by reducing the incoming wave energy. Our experiments showed the capability of prop roots to reduce the velocity, irrespective of variations in the period, its capability to increment the TKE and its capability to reduce wave amplitude.

Key Words: Oscillatory flow, physical model, mangrove forest, primary roots, secondary roots

8th International Conference on the Application of Physical Modelling in Coastal and Port Engineering and Science
Zhoushan, China - Dec. 9th - 12th, 2020

EXPERIMENTAL STUDY OF SOLITARY WAVES PROPAGATING OVER A SUSPENDED PLATE

XUYANG NIU[1], YUXIANG MA[2*], GUOHAI DONG[3], KUANG-AN CHANG[4]

1 Dalian University of Technology, China, niuxuyang@mail.dlut.edu.cn
2 Dalian University of Technology, China, yuxma@dlut.edu.cn*
3 Dalian University of Technology, China, ghdong@dlut.edu.cn
4 Texas A&M University, USA, kchang@tamu.edu

Characteristics of velocity fields on a solitary wave impacting on a suspended horizontal plate are investigated experimentally. In the experiments, a rigid horizontal plate is fixed above the free surface in a two-dimension wave flume and the incident relative wave height (H/h) varies from 0.23 to 0.43. A high-speed camera is used to capture images during the wave-structure interaction and the particle image velocimetry (PIV) is adopted to measure the detailed velocity fields in regions without bubble. Additionally, the flow fields in the aerated regions are measured using the bubble image velocimetry (BIV). The results show that the flow structure evolution can be divided into three stages with respect to the profile of free surface: wave overtopping, water slamming and surface separation. At the wave overtopping stage, with the dropping down of water tongue, bubbles are trapped into the water and break up above the plate. Meanwhile, the air-water mixture at lee side is squeezed out and pushed forward. After the wave crest passing over the plate, the high-speed flow jet slams into the water and splashes upward at the rear of plate, causing a mass of air entrapped. During surface separation stage, air is drawn into the water along the edge of the vortex at weather-side while intense interface separation is observed at the plate bottom.

Key Words: Suspended plate; Solitary waves; PIV; BIV; Wave overtopping

8th International Conference on the Application of Physical Modelling in Coastal and Port Engineering and Science
Zhoushan, China - Dec. 9th - 12th, 2020

OPTIMIZATION OF MOORING LINES AND FENDERS SYSTEM IN A PHYSICAL MODEL OF A BULKCARRIER

RAQUEL COSTAS[1], ANDRÉS FIGUERO[2], JOSÉ SANDE[3], ENRIQUE PEÑA[4], DELIA REGUEIRA[5], ALEXANDRE PRADA[6]

1 University of A Coruña, Spain, raquel.costas.gomez@udc.es
2 University of A Coruña, Spain, andres.figuero@udc.es
3 University of A Coruña, Spain, jose.sande@udc.es
4 University of A Coruña, Spain, enrique.penag@udc.es
5 University of A Coruña, Spain, delia.regueiram@udc.es
6 University of A Coruña, Spain, alexander.prada.varela@udc.es

The movements of a ship at berth during port operations are responsible for ensuring that they are carried out under appropriate safety and performance conditions. Therefore, to optimize the process it is essential to know the relationship between the movement of the ship, the forcer (hydrodynamics at berth) and the restrictor (the system of mooring lines and fenders).

For that purpose, in the wave basin of the CITEEC (R&D Technological Innovation Centre in Construction and Civil Engineering), University of A Coruña (Spain), tests were carried out to analyse the behaviour of the ship moored in its six degrees of freedom, as well as the response of the moorings and fenders system for different wave climate combinations. The final objective was to find the optimum layout of the restrictor to ensure that the ship movements are as minimal as possible.

With this goal, short and long wave energy has been quantified for different wave parameters under different tidal, tension of the mooring lines, divers fender elasticity and configuration of the mooring-fender system. Additionally, tests of two lines breakage are planned to be done in order to analyse the effect on the motions with a method that shows the energy in the frequency-time domain, the wavelet transform.

To obtain the records of the movements in its six degrees of freedom, the necessary instrumentation consisted of three video cameras with the corresponding targets, one zenithal, one frontal and one lateral, which were processed with an image tracking program. On the other hand, the mooring lines and fenders were simulated by a system of four pulleys and four rocker arms that simulate elasticity with non-deformable thread and springs of defined elastic constant. As for the waves, there were 10 level probes located in the generation area and next to the berth.

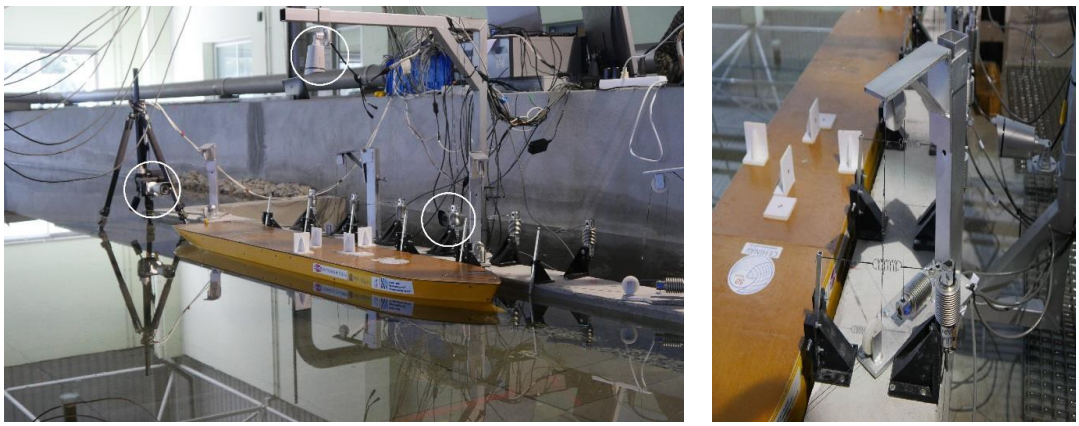

Figure 1. Vessel at berth with camera positions (left) and instrumentation to measure mooring line and fender loads (right)

Key Words: physical model, vessel motions, moored line, fender, wavelet.

8th International Conference on the Application of Physical Modelling in Coastal and Port Engineering and Science
Zhoushan, China - Dec. 9th - 12th, 2020

ANALYSIS ON THE CURRENT SITUATION OF WATER ENERGY RESOURCES DEVELOPMENT IN CHINA'S MAJOR RIVERS

LANG YONGYUAN[1], MENG CHANGQING[2], ZHONG DEYU[3,4]

1 School of Water Resources and Electric Power, Qinghai University, China, yongyuan_lang@163.com

2 School of Renewable Energy, North China Electric Power University, China, mcq789@foxmail.com

3 State Key Laboratory of Plateau Ecology and Agriculture, Qinghai University, China, zhongdy@tsinghua.edu.cn 4 State Key Laboratory of Hydroscience and Engineering, Tsinghua University, China, zhongdy@tsinghua.edu.cn

The development of hydropower resources and ecological protection is still under fierce debate. This paper selects 8 main rivers with abundant hydropower resources, and its total installed capacity accounts for 42.36% of the total hydropower installed capacity of the country by the end of 2018. These 8 main rivers is the Yangtze River, the Yellow River, the Pearl River, the Lancang River, the Nujiang River and the Yalong River, Dadu River and Wujiang River. Using the technology development degree and water consumption rate to measure the development and utilization rate of water resources respectively of the main 8 rivers in China by the end of 2018.The first analysis result is that the technology development degree of the major 8 rivers are 53.66%. 55.69%, 63.34%, 88.83%, 0%, 59.58%, 57.50%, 85.10%. Except the Nujiang River, the technology development degree of the other seven rivers all exceeds 50% and the Pearl River leads with 88.83%, which far surpasses the country's technology development degree of water energy resource of 49.84% (including pumped storage power stations). The second analysis result is that half of the rivers' water consumption rate transcends 1kW·h/m³ , of which the Yellow River is the highest and water consumption rate is 1.73kW·h/m³ . Undoubtedly, the actual power generation produced by unit volume of water of the Yellow River is the highest. It is the most high-quality river for the development of hydropower resources, followed by the Lancang River, the Dadu River and the Yalong River, their water consumption rate are 1.48kW·h/m³ , 1.39kW·h/m³ and 1.22kW·h/m³ separately. By 2018, the Nujiang River has not been developed yet, so water consumption rate is 0. The remaining 3 rivers —the Wujiang River, the Yangtze River and the Pearl River has the water consumption rate of less than 1kW·h/m³ , the value is 0.69kW·h/m³ ,0.63kW·h/m³ and 0.42kW·h/m³ . What needs to be clear is that the higher the development of hydropower resources, the higher the water consumption rate for the one river. Exploring the current status of cascade hydropower development in China's major river basins will provide scientific guidance and policy basis for China's ecological protection and water supply. At present, although some scholars have analyzed the reasons for selecting the indicators on the degree of development of hydropower resources and they have made suggestions, indicators selection are still relatively chaotic.

Key Words: Hydropower Resources; Technology Development Degree; Water Consumption Rate

8th International Conference on the Application of Physical Modelling in Coastal and Port Engineering and Science
Zhoushan, China - Dec. 9th - 12th, 2020

HIGH-RESOLUTION BATHYMETRY MEASUREMENT AND 3D SHAPE RECONSTRUCT USING AFFORDABLE 3D SCANNER DEVICE, MICROSOFT® KINECT CAMERA

YANJUN MAO[1], XIAOZHOU MA[2],JUNLIANG GAO[3]

1 Da Lian University of Technology, CHINA, myj@mail.dlut.edu.cn

2 Da Lian University of Technology, CHINA, maxzh@dlut.edu.cn
3 Jiangsu University of Science and Technology, CHINA, gaojunliang880917@163.com

In many cases during the physical model tests in laboratories, high-resolution bathymetry data can be necessary and useful to both scientific measurement and visualization. For example, the measurement of the dynamic cross section of the berm breakwater under wave action. Numerical modeling often needs bathymetry data from physical experiments.

Kinect is a motion sensing input device by Microsoft for the Xbox 360 video game console and Windows PCs. Though it was designed for video games, It has great potential for other applications. It has a depth sensor which can obtain the depth data of a surface with relative accuracy which means it can be converted into a low cost 3D scanner easily.

We use Kinect to scan the dynamic cross-section of a berm breakwater under long period wave action and reconstruct the entire surface of the cross-section.then we compare the shape of the cross-section before wave action and after that to evaluate the difference. It can get the 3D point cloud rather than a line of points using Point laser rangefinder. So it has large information to check the 3D deformation of the surface. We give calibration tests and present the workflow of using Kinect as a 3D scanner in physical model tests. It shows Kinect can be quiet useful and competent in some specific cases in laboratory tests.

Key Words: Kinect, 3D scanner, cross-section measurement, geometric reconstruction

8th International Conference on the Application of Physical Modelling in Coastal and Port Engineering and Science
Zhoushan, China - Dec. 9th - 12th, 2020

NUMERICAL SIMULATION OF SAND SPIT ELONGATION AT CUA LO RIVER MOUTH, QUANG NAM PROVINCE, VIETNAM

NGUYEN QUANG DUC ANH[1], DUONG CONG DIEN[2], HITOSHI TANAKA[3], NGUYEN TRUNG VIET[4], HO SY TAM[5]

1 Thuyloi University, Vietnam, ducanh.cte@gmail.com

2 Institute of Mechanics, Vietnam, duongdienim@gmail.com

3 Tohoku University, Japan, hitoshi.tanaka.b7@tohoku.ac.jp

4 Thuyloi University, Vietnam, nguyentrungviet@tlu.edu.vn

5 Thuyloi University, Vietnam, tamhs.cttl@tlu.edu.vn

In recent decades, serious problems of sedimentation and erosion in Cua Lo River Mouth, in Quang Nam province, Vietnam have occurred. One of the main causes that pointed out for this phenomenon had considered by the elongation of up-drift sand spit, which leads to the severe erosion of the south bank of the river mouth. The morphological changes of the sand spit highly depend on the topographic - geomorphological conditions and the interactions between the change of wave elements, tidal exchange through the estuaries and the long-shore sediment transport rates and river discharges. Based on topographic and hydrographical survey data conducted in 2019, this research will focus on developing the numerical model (Delft 3D) to simulate and investigate the hydrodynamic regime in response to sand spit elongation in Cua Lo River Mouth area. The model has been calibrated using river discharges, tidal currents, offshore and nearshore wave parameters. Then, its results of the sand spit elongation progress are validated by using historical shoreline evolution data. Last but not least, the relationship between the hydrodynamic conditions and the sand spit elongation progresses will be discussed to find out the main influencing factors.

Key Words: Cua Lo River Mouth, long-shore sediment transport rates, river discharges, tidal currents, nearshore wave parameters.

8th International Conference on the Application of Physical Modelling in Coastal and Port Engineering and Science
Zhoushan, China - Dec. 9th - 12th, 2020

PHYSICAL MODEL INVESTIGATION OF THE BANGABANDHU RAILWAY BRIDGE OVER THE RIVER JAMUNA, BANGLADESH

MD.LUTFOR RAHMAN

Director, Hydraulic Research Directorate, River Research Institute
BSc Engg.(Civil), M.Engg.(Water Resources), PGD (PPR.Engg., PhD.(Civil)
Professional Engineering,Bangladesh, E-mail: lutforntf@gmail.com

For further enhancement of the capacity and to overcome the loading restriction of Bangabandhu Bridge, it would be necessary to go for the construction of a parallel Bangabandhu Railway Bridge, dedicated to railway, while the existing Bangabandhu Bridge could carry road traffic only. In this context, Bangladesh Railway has decided to construct Bangabandhu Railway Bridge over the River Jamuna which will be located 300m upstream of the existing Bangabandhu Bridge. Therefore, a study was undertaken by River Research Institute (RRI) to support the design required for the proposed Bangabandhu Railway Bridge over the River Jamuna using physical modelling. The study includes to assess the bridge-to-bridge and bridge to River Training Works (RTW) interaction; to find out local scour along the RTW as well as around the bridge piers as influenced by the presence of the new railway bridge piers and to provide hydraulic design parameters for the detailed design of the proposed structure. For this purpose, an indoor undistorted model (mobile bed) having scale 1:100 is designed by fulfilling the Froude's model law. After calibration of the model, application test runs are conducted with existing and proposed structure under different test scenarios and discharge conditions. Within the framework of the study, two sectional models (West Guide Bund & East Guide Bund) covering a reach of about 3.0 km and part width of about 1.0 km of the Jamuna River have been reproduced. The findings of the test results of WGB model study are presented in this paper.

Key Words: Bangabandhu Bridge, Bangabandhu Railway Bridge, Jamuna, BangladeshPle

8th International Conference on the Application of Physical Modelling in Coastal and Port Engineering and Science
Zhoushan, China - Dec. 9th - 12th, 2020

HARBOUR WAVE AGITATION ANALYSIS IN THE PORT OF MANTA, ECUADOR

WILLIAM JAEN[1]

1 Superior Polytechnic School of the Litoral, ESPOL, Ecuador, wjaen@espol.edu.ec 2 University of Cantabria, UC, Spain, wjs229@alumnos.unican.es
3 FARMINMOBILIE S.A., Ecuador, farminmobilie@gmail.com

Ecuador is a country located in the northwestern region of South America. The economic dynamism that is achieving the country is reflected in economic growth of 5.2% year on year, according to data from the Central Bank of Ecuador. It features a high growth in the aquaculture sector, which is also reflected in a significant increase in employment in the fisheries sector. Ecuador is one of the countries with greatest biodiversity and mineral resources in the world, with unique plant and animal species and the only one in the world that has in its constitution the right to environment (Denis, 1976). Seaports are a remarkable point in trade and tourism, that is why its modernization in recent years has allowed to ports like Manta can reach large cruise and cargo ships and others. The importance of increasing the operation of the port of Manta, fulfills a fundamental factor to increase the local economy of the country, and this can be achieved by guaranteeing the minimum wave agitation within the port.

Harbour wave agitation is a physic phenomenon of the waves found inside a harbour. It becomes important when the incident waves have a big height, and a frequency close to that of the harbor basins. This phenomenon, that affects harbors around the world, can generate violent oscillatory movements of the semi-closed waters. Consequences can be damage to structures or boats, and operativity problems, generating important economic losses. Working with the wave predictions, together with the harbor agitation predictions, we can avoid damage, as well as guarantee the user's safety. The methodology of the analysis of the harbour wave agitation begins with the analysis of the hindcast data of the maritime climate in deep waters, and continues with the propagation of the waves by means of the hybrid downscaling technique from a GOW point located in deep waters towards the area of the analysis, using this information, a numerical mild slope model is employs to analyze the port agitation in the internal area.

Key Words: Manta, Harbour, Wave Agitation, Mild Slope.

8th International Conference on the Application of Physical Modelling in Coastal and Port Engineering and Science
Zhoushan, China - Dec. 9th - 12th, 2020

EXPERIMENTAL STUDY OF WAVE-DRIVEN TRANSPORT OF WOODY DEBRIS AND DEBRIS-SHORE INTERACTIONS

ENDA MURPHY[1,2], ALISTAIR RAYNER[1], SCOTT BAKER[1], IOAN NISTOR[2], ANDREW CORNETT[1], JACOB STOLLE[2], JESSICA WILSON[2]

1 National Research Council Canada, enda.murphy@nrc-cnrc.gc.ca 2 University of Ottawa, Canada, inistor@uottawa.ca

Woody debris originating from natural and anthropogenic sources is ubiquitous in North American coastal waters and on shorelines. Logs and driftwood are thought to play a vital role in coastal and global ecosystems, providing habitat, structure, nutrients and carbon storage. The quantity, effects and fate of woody debris at coastal sites are determined by sources, pathways, weathering processes, and interactions with physical features and shorelines. This debris can provide valuable data to support studies of oceanography, geomorphology, ecology and human occupation. However, there is limited knowledge of the processes underlying woody debris interactions with shorelines and coastal structures, and/or how debris influences the stability of sediments and shore-based vegetation. The majority of research on physical transport of woody debris is limited to tsunami and inland (riverine) environments, where spatio-temporal scales and driving processes are significantly different from typical climatic or even extreme (storm) conditions in coastal waters.

Scale physical model tests were conducted at the National Research Council of Canada's Ocean, Coastal and Engineering Research Centre in Ottawa, to provide insight to debris transport processes in coastal waters under a range of controlled wave and water level conditions. The experiments were conducted in a 50-metre by 30-metre wave basin in which a 1/30 scale model of a natural shoreline comprised of a shallow sloping foreshore, a sandy shoreline, and series or small coastal structures (groins and breakwaters) was constructed. Wooden dowels, scaled to replicate the size distribution of woody debris observed on Pacific Northwest shorelines, were released in the model. An optical tracking technique was used to detect the movement and dispersion of the model debris and interactions with waves and shoreline features. The results of the physical model tests will inform the parameterization of important physical processes (e.g. beaching, mobilization, longshore transport) in a numerical model that is being developed to predict the fate and transport of woody debris in coastal waters.

Key Words: Debris, physical modelling, coastal engineering, fate and transport, numerical modelling

8th International Conference on the Application of Physical Modelling in Coastal and Port Engineering and Science
Zhoushan, China - Dec. 9th - 12th, 2020

EXPERIMENTAL STUDY ON THE IMPACT EFFECT ON A SHALLOW-BURIED PIPELINE BY A FALLING ANCHOR

YUXIN SUN[1], CIHENG ZHANG[1,2], HAIYUAN YAO[1,3], ZHIPENG ZANG[1]

1 State Key Laboratory of Hydraulic Engineering Simulation and Safety, Tianjin University, 300350, China, 2 Tianjin Research Institute for water transport Engineering, Ministry of Transport, Tianjin, 30000, China, 3 Transport planning and Research Institute, Ministry of Transport, Beijing 100028, China
Email: Zhipeng.Zang@tju.edu.cn

Submarine pipelines are key infrastructures in offshore oil and gas engineering. They are widely used for transportation of the oil and gas from production wells to onshore facilities. With the development of the port engineering and the exploitation of ocean oil and gas resources, overlap may occur between the harbor channel area and the landfall area of submarine pipelines. There is an occurrence that a shallow-buried submarine pipeline below a channel is collided by a falling object from third party activities, e.g., a falling anchor or a sliding container from a ship. In order to seek reasonable protection measures to ensure the safe operation of the pipeline, it is necessary to experimentally study the dynamic response of the pipeline caused by the falling objects. In this study, different protective measures on the pipeline, including pure rock layer, concrete mattress + rock layer, concrete mattress + rock layer + rubber pad and compound flexible pad + rock layer, are physically modelled in the tests to protect a buried pipeline below a seabed from the collision by a falling anchor. The dynamic responses of the pipeline are measured with a series of Fiber Bragg Grating (FBG) sensor on the surface of the pipeline to analyze its maximum value and the distribution of the strain. For each test case, ten attempts were repeated to ensure the most severe condition can be captured. A statistic method is applied to analyze the randomness and probability of the impact effect on the pipeline. The time duration of each impact was also obtained from the time history of the FBG data to explain the impact effect from the aspect of momentum conservation. The most effective protective measures and its thickness can be determined based on the experiments. The results indicate that the protective method of compound flexible pad + rock layer is most suitable to protect the buried pipeline from a falling anchor. The present work can provide technical supports for the design and maintenance of submarine pipelines.

Key Words: Submarine pipeline; impact effect; falling anchor; dynamic response; protective layers.

8th International Conference on the Application of Physical Modelling in Coastal and Port Engineering and Science
Zhoushan, China - Dec. 9th - 12th, 2020

MOTION RESPONSES OF MOORED FLOATING TANK UNDER THE ACTION OF INTERNAL AND EXTERNAL FLOW

LIN CHENG, MIAN XUE, XIN LIU, JINHAI ZHENG*

College of Harbour, Coastal and Offshore Engineering, Hohai University Nanjing, Jiangsu, PR China, xochenglin@qq.com

A series of experiments were conducted at the Offshore Engineering Laboratory of the Hohai University to study the motion response of a moored floating tank under the action of internal and external flow. The motion response of the floating tank and the sloshing of the liquid in the tank are analyzed under the different wave actions with the same water depth, different wave heights and different periods. An in-house two-phase model (NEWTANK) is also used to study these problems. In this numerical model, the interaction between water wave and structure is simulated by the virtual boundary force (VBF) method which is used to satisfy the no-slip condition on the rigid body surface. The motion of the free surface is tracked by a second-order accurate volume-of-fluid (VOF) method. The large eddy simulation (LES) is used to model the effect of turbulent flows. In this study, the model is firstly validated by a linear wave impact on a free-floating box. The validated numerical model is then employed to investigate the different wave impacts on the moored floating tank and the sloshing state in the tank. We will discuss the variation of wave form around the floating tank and the impact wave force on it. The numerical results will also be compared with the available experimental data.

Key Words: moored floating tank, motion responses, sloshing, virtual boundary force method

8th International Conference on the Application of Physical Modelling in Coastal and Port Engineering and Science
Zhoushan, China - Dec. 9th - 12th, 2020

EXPERIMENTAL STUDY OF SPRAY FROM WAVE RUN-UP

XUEXUE CHEN[1,2], IRENE RIVERA-ARREBA[3], BAS HOFLAND[1]

1 Delft University of Technology, The Netherlands, E-mail: x.chen-2@tudelft.nl 2 Royal Haskoning DHV, The Netherlands

3. Norwegian University of Science and Technology, Norway

Spray from wave run-up is relevant to coastal defence for overtopping analysis of sea walls, levees, and gates, and for marine applications (Bodaghkhani, 2016). Improved insight into this phenomenon will further enhance the prediction of wave overtopping and its induced hazard, e.g., erosion, saltwater ingress and hindrance to traffic. To characterize the wave run-up on a vertical structure and the spray jet break up in droplets as a function of the type of wave impact, a series of small-scale experiments has been carried out in the WaterLab at TU Delft. Focused waves were generated by the piston-type wavemaker to control the wave breaking point on the wall, which allowed to create different types of wave impact (see Hofland et al. 2010). In the experiments, three types of wave impacts were investigated respectively: slosh, flip-through, and air pocket. All the stages of the spray formation after the wave impact were filmed using a highspeed camera at a frame rate of 500fps. This allows for the characterization of the spray formation at a small scale, including both the wave runup and the water sheet breakup. The tests indicate that, depending on the type of impact, the front of the uprising water sheet presents different patterns. Finally, the droplet size distributions are analyzed, as well as the velocity and the height reached by the droplets, so that a relation between the three variables can be established. These characteristics are needed to estimate the influence of wind on the overtopping amount and distance behind the structure.

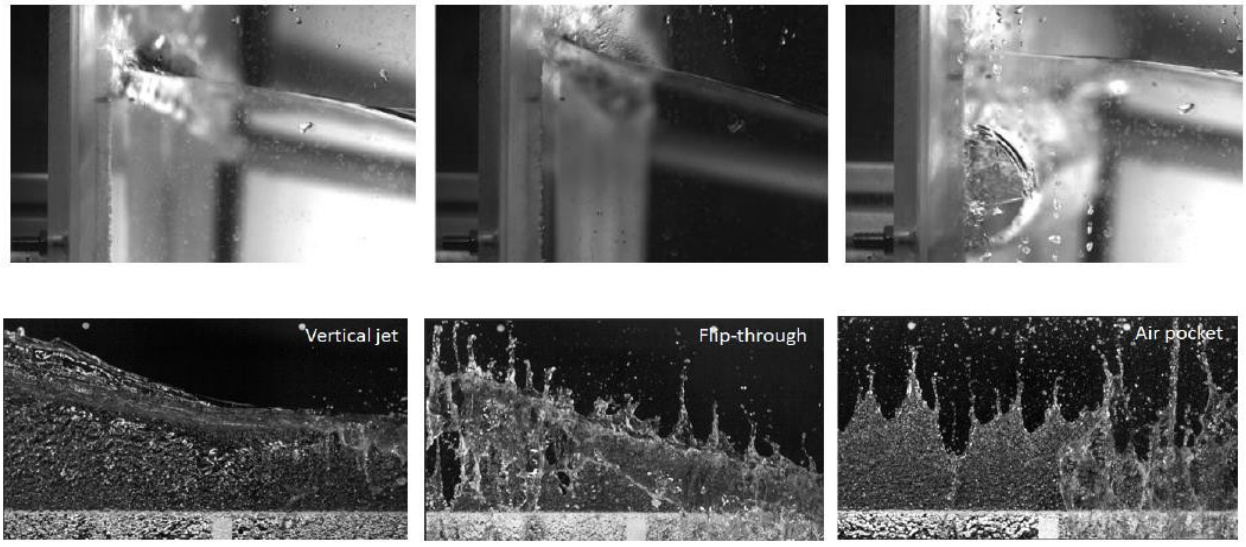

Figure *1*. Top: close up side view of types of wave impact at the time the wave crest hits the vertical wall on the left of the picture (left: vertical jet; center: flip-through, right: air pocket). Bottom: water sheet runup for the three types of impact (view from the sea towards the wall).

Keywords: spray-water, droplets, wave focusing theory, wave-wall interaction, physical modeling.

8th International Conference on the Application of Physical Modelling in Coastal and Port Engineering and Science
Zhoushan, China - Dec. 9th - 12th, 2020

EVALUATION OF TSUNAMIS AMPLIFICATION AT COASTAL AREAS USING A MODAL DECOMPOSITION METHOD

GIORGIO BELLOTTI[1]

[1] *Roma Tre University, Italy, giorgio.bellotti@uniroma3.it*

When tsunamis attack a coastal area, the local shape of the bottom and of the coast strongly affects the amplification of the waves and resonance phenomena can play a relevant role on the level of inundation (Rabinovich, 1997; Yamazaki & Cheung, 2011; Bellotti et al., 2012a; Cortés et al., 2017), as natural modes of free surface oscillation can be excited. These phenomena are related to bathymetric features and to specific shapes of the coastline. The more relevant effects due to the bathymetry are the continental shelf resonance and the generation of trapped edge waves (Romano et al., 2013). As far as coastal features are concerned, bays with regular shapes appear to be prone to the risk of harbour-like resonance phenomena. Given that the typical frequency spectrum of tsunamis is broad banded, multiple scale (i.e. regional and local) bathymetric and coastal features can have importance.

Given the importance of the natural modes of oscillation, efforts have been spent recently, to develop models (Sobey, 2006) and analysis techniques (Tolkova & Power, 2011), to better understand their role and properties. Within this context, this paper presents a model for the evaluation of long waves amplification at coastal areas, based on a modal decomposition method. It is able of modelling the growth and the decay of the natural modes of the area under investigation, and their contribution to the total wave field. The model is an improvement of that developed by Bellotti, et al. (2012b), that was able of calculating the frequencies and the shapes of the natural modes, but not their amplification under the action of the forcing waves.

Some test cases are used for the validation and to show the capabilities of the model. The first considers the long waves resonance into a regular shape bay, for which a high degree of wave trapping is induced by the specific shape of the coastline. The second case involves the interaction of tsunamis propagating around a conical island, for which laboratory data are available. In this test, a low degree of trapping exists, but it is interesting for the present aims as the propagation of the waves around the island can take the form of edge waves modes, partially trapped by the bathymetry.

Key Words: Tsunamis, Edge waves, Modal analysis, Harbour resonance, Long waves

References

Bellotti, G., Briganti, R., Beltrami, G., 2012a. The combined role of bay and shelf modes in tsunami amplification along the coast. Journal of Geophysical Research: Oceans 117.

Bellotti, G., Briganti, R., Beltrami, G., Franco, L., 2012b. Modal analysis of semi-enclosed basins. Coastal Engineering, 64:16–25

Cortés, P., Cataln, P., Ar´anguiz, R., and Bellotti, G., 2017. Tsunami and shelf resonance on the northern Chile coast. Journal of Geophysical Research: Oceans, 122(9):7364–7379.

Rabinovich, A., 1997. Spectral analysis of tsunami waves: Separation of603source and topography effects.Journal of Geophysical Research: Oceans,604102(C6):12663–12676.

Romano, A., Bellotti, G., Di Risio, M., 2013. Wavenumber-frequency analysis of the landslide-generated tsunamis at a conical island. Coastal Engineering 81, 32-43.

Sobey, R., 2006. Normal mode decomposition for identification of storm tide and tsunami hazard. Coastal Engineering 53, 289-301.

Tolkova, E., Power, W., 2011. Obtaining natural oscillatory modes of bays and harbors via Empirical Orthogonal Function analysis of tsunami wave fields. Ocean Dynamics 61(6), 731-751.

Yamazaki, Y. and Cheung, K. (2011). Shelf resonance and impact of near-field639tsunami generated by the 2010 Chile earthquake.Geophys. Res. Lett., 38(12).

8th International Conference on the Application of Physical Modelling in Coastal and Port Engineering and Science
Zhoushan, China - Dec. 9th - 12th, 2020

OPEN FILTERS ON SAND-COVERED ROCK MOUNDS

DAAN VAN DE VEN[1], BAS HOFLAND[1], DENNIS VAN KESTER[2], GREG SMITH[2], ALESSANDRO ANTONINI[1]

1 Delft University of Technology, Netherlands, b.hofland@tudelft.nl

2 Van Oord, Netherlands, dennis.vankester@vanoord.com

When constructing rock bunds for land reclamations, often sand is placed on top of the coarse rock of the bund, see Fig. 1. Making a geometrically closed filter between the bund and the sand can be laborious. Hence the use of a geometrically open filter could be cost effective. Due to the low hydraulic gradients in the lower corner between bund and sand layer, it is expected that the geo- metrically open filter might be stable due to the arching mechanism (De Graauw, 1983). For such an open filter the hydraulic attack was studied by Polidoro et al. (2015), but the actual stability of such a "negative" open filter is unknown. Hence this study is focussed on the stability of a negative geometrically open filter under cyclic loading. This paper mainly describes the development of the test setup. First the numerical model OpenFOAM was used to extract the gradients from a representative case study (Fig. 1). A test setup was developed to generate these low-magnitude loads at full-scale (Fig. 2). Various sand-filter combinations were tested, with a range of ratios of the diameters of the gravel filter (D15F) and the sand base layer (D85B). They were tested for both parallel (i//) and perpendicular (i⊥) gradients. Critical gradients as derived from the results will be presented (see e.g. Fig. 2 for i//).

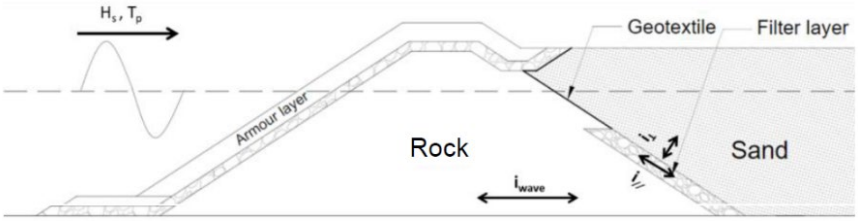

Figure 1. Example of a breakwater/reclamation section with negative open filter.

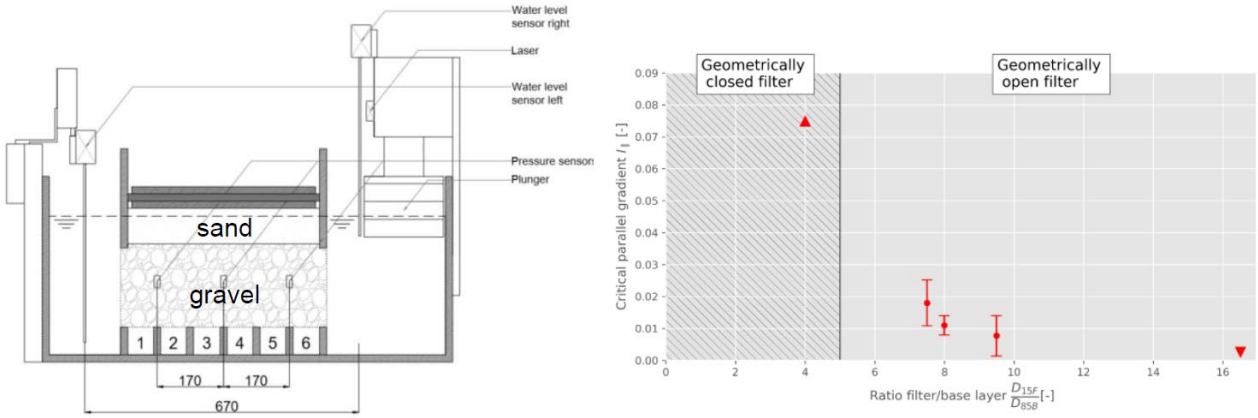

Figure 2. Left: Setup for testing parallel loads. Right: critical parallel gradients as determined from the setup.

REFERENCES

De Graauw, A., T. van der Meulen, and M. van der Does de Bye. (1983) Design criteria for granular filters. Technical Report January 1983, Delft Hydraulics (Deltares). 1983.

Polidoro, A., W. Allsop, and T. Pullen. (2015) Exploring the Need for Geotextile Filters for Rubble Bunds Retaining Sand-Fill Islands.
Proc. Coastal Structures and Solutions to Coastal Disasters 2015, pages 763–773, 2015.

Key Words: geometrically open filter, breakwater core

8th International Conference on the Application of Physical Modelling in Coastal and Port Engineering and Science
Zhoushan, China - Dec. 9th - 12th, 2020

EXPERIMENTAL INVESTIGATIONS ON NEAR-FIELD CHARACTERISTICS OF INTERNAL WAVES GENERATED BY SUBMARINE LANDSLIDE

Dongyi Yan, Jijian Lian, Dongming Liu

(State Key Laboratory of Hydraulic Engineering Simulation and Safety, Tianjin University, Tianjin 300350, China)

A two-dimensional laboratory experiment has been performed in an enclosed rectangle tank to investigate the internal waves generated by the submarine landslide in a system of two-layered miscible fluid. Image recognition technology is used to track the interface between the upper fresh-water layer and the dyed lower saline layer. Both scenarios in which the slide passes through the interface and starts moving from the lower layer are studied. Experimental parameters including slope inclination, slide shape, sliding velocity and initial submergence of slide are considered in 146 tests. The near-field features of internal waves, such as the amplitude and period affected by these parameters, are inspected. Furthermore, the energy transfer from slide into internal waves and the energy dissipation are also investigated and discussed.

Key words: laboratory experiment; submarine landslide; internal waves; energy conversation

8th International Conference on the Application of Physical Modelling in Coastal and Port Engineering and Science
Zhoushan, China - Dec. 9th - 12th, 2020

LARGE-SCALE LABORATORY EXPERIMENTS ON MUSSEL DROPPER LINES

REBEKKA GIESCHEN[1], JANNIS LANDMANN[2], LUKAS FRÖHLING[2], ARNDT HILDEBRANDT[2], NILS GOSEBERG[2,3]

1 Technische Universität Braunschweig, Germany,r.gieschen@tubraunschweig.de
2 Leibniz Universität Hannover, Germany
3 Coastal Research Center, Germany

The rapid growth of marine aquaculture around the world accentuates issues of sustainability and environmental impacts of large scale farming systems (FAO 2018). These issues range from reliability of technical equipment, stakeholder conflicts regarding the space occupied by near shore farm systems, the biological demands of bivalves regarding nutrients, different methods of spat recruiting, issues regarding decomposition and pseudo-faeces or socio-economic issues (McVey, 1996; Buck and Krause, 2012). One potential mitigation avenue is to relocate to more energetic offshore locations (Buck et al., 2010). However, research regarding the forces which waves and currents impose on aquaculture structures in such conditions is still scarce (Plew et al., 2005; Stevens et al., 2008; Gagnon and Bergeron 2017). The present study aims at extending the knowledge related to live blue mussels, cultivated on dropper lines, as well as at surrogates, by unique, large-scale laboratory experiments. Dropper lines grown with blue mussels were hence tested in extreme wave conditions to determine wave-induced forces, associated mussel drop-off, and the comparability of the surrogates.

The experiments were conducted in the Large Wave Flume of the Coastal Research Center, Hannover, Germany. Two live blue mussel and one surrogate dropper lines of 2.0 m length were mounted next to each other between a concrete block at the bottom and a steel beam at the top of the flume. The still water level was 3.5 m, resulting in the dropper lines to be submerged by 1.0 m at rest. Four force transducers were attached to the top and the bottom of each wire holding a dropper line. Incident wave conditions were measured with two wave gauge arrays as well as two single wave gauges, 0.35 and 3.0 m in front of the mussel line setup. The impact area was monitored with a video camera. The dynamics of the water mass were measured with a 2D laser scanner recording a transect along the middle of the flume as well as by two electromagnetic current meters positioned at the two single wave gauges at a height of 1.0 and 2.5 m above the flume bottom.

In total, eight live blue mussel dropper lines were tested for 14 regular waves with wave heights between 0.2 and 1.0 m and periods between 1.5 and 8.0 s. Furthermore, maximum adhesion forces of single mussels were determined by pull-off tests to correlate wave-induced forces with occurring mussel drop-off in waves.

Measurements of the hydrodynamics and forces on the dropper lines were combined to describe the droppers' behavior in extreme wave conditions. Comparisons showed the surrogates ability to model a live blue mussel dropper line. Total mussel drop-off was quantified and correlated to the observed maximum shear forces. The results allow to examine drag and inertia coefficients of live blue mussel dropper lines as well as first predictions of mussel drop-off in extreme wave conditions. These results will offer knowledge to improve design tools for offshore aquaculture structures.

Key Words: Aquaculture, Bivalves, Waves, Dropper line forces, Physical model tests, Large Wave Flume

8th International Conference on the Application of Physical Modelling in Coastal and Port Engineering and Science
Zhoushan, China - Dec. 9th - 12th, 2020

OVERTOPPING BORE IMPACT LOADS ON A DIKE MOUNTED WALL - A ROBUST STATISTICAL ANALYSIS

MAXIMILIAN STREICHER[1], ANDREAS KORTENHAUS[1]

1 Dept. of Civil Engineering, Ghent University, Technologiepark 904, B-9052 Zwijnaarde (Ghent), Belgium; email: Maximilian.Streicher@UGent.be

Key Words: overtopping bore, storm wall, impact force, statistical analysis, prediction

1 INTRODUCTION AND OBJECTIVE

Coast protections of low lying countries are often comprised of a mild foreshore and shallow waters, followed by a sloping structure (e.g. a dike) and a promenade, with a dike mounted vertical wall on top (building or storm wall). In this setting, waves can overtop the dike, form a bore type wave and impact the vertical wall. Design guidance for the bore impact force is scarce. Furthermore, the turbulent nature of the overtopping bore and the interaction with reflected bores prior to impact result in a stochastic behavior of the measured impact forces at the wall (Streicher et al. 2019). For this reason Chen et al. (2016) and Van Doorslaer et al. (2017) proposed statistical prediction methods. They noticed that the derived statistical fitting parameters for a Weibull and Generalized Pareto distribution were not stable, probably due to too few data points available for the fitting. Hence, the key objective of this study is to further elaborate on a statistical prediction method, e.g. by investigating the required sample size, to arrive at a robust statistical fitting method.

2 DATASET

For the purpose of this study the timeseries of bore impact forces and pressures on a vertical sea wall were measured in small- and large-scale wave flume experiments for extreme storm wave conditions. Small-scale experiments were conducted at the Ghent University wave flume facility, Belgium (dataset UGent1-UGent3) and large-scale experiments in the Deltares Delta Flume (dataset DeltaFlume). The timeseries from all datasets were filtered and the peak force per impact event derived.

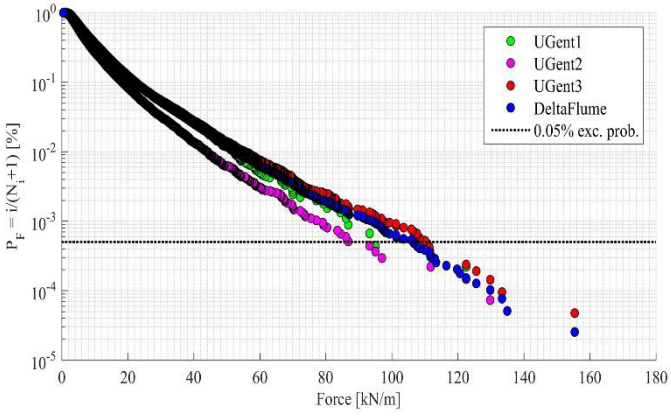

The peak forces from each dataset were combined (see Figure 1), to form a large enough dataset of maximum impact forces for robust statistical analysis.

3 RESULTS AND DISCUSSION

Figure 1: Plotting positioning of the force peaks from data-set 'UGent1'-'UGent3' and 'DeltaFlume'.

The total dataset was divided in sub-samples based on the non-dimensional average overtopping discharge. A Weibull distribution was further fitted to these sub-samples. Shape and scale parameter were derived. Based on these findings a statistical impact force prediction method was proposed. Sensitivity analysis revealed that at least 50 data points were required for robust statistical fitting. More findings will be included in the full length paper and presented at the conference.

8th International Conference on the Application of Physical Modelling in Coastal and Port Engineering and Science
Zhoushan, China - Dec. 9th - 12th, 2020

ON THE FROUDE NUMBER IN TSUNAMI-LIKE WAVES

DAVIDE WÜTHRICH[1]

[1] *The University of Queensland, Australia, d.wuthrich@uq.edu.au*

Tsunamis, impulse waves and storm surges have afflicted coastal areas for centuries. Physically, these phenomena are associated with a sudden increase in flow depth, resulting into damages to critical infrastructures and human losses. Because of climate change, the last decades have seen an increasing number of catastrophic events, including, among others, the Indian Ocean tsunami in 2004, the Japan Tōhoku tsunami in 2011 and Sulawesi (Indonesia) in 2018. Even though these events were responsible for destruction and human losses, post-event surveys showed that measures can be taken to save people lives and limit reconstruction costs. For this, a comprehensive understanding of the physical process is necessary, thus explaining the large number of studies on tsunami-related issues conducted in the recent years. Because of the complexity of these unsteady flows, most studies rely on physical modelling and dam-break waves are commonly employed to reproduce tsunami-like waves. Nevertheless, limited comparison is available between laboratory and prototype data and discrepancies in the wave generation techniques still exist among the facilities throughout the world.

In coastal and and hydraulic engineering, physical modelling is commonly based on a Froude similitude, implying that the ratio between gravitational and inertial forces is maintained at all scales. The Froude number is also a critical parameter to describe the air-water flow properties, the energy dissipation process and for the comparison between different flows, *i.e.* breaking waves, bores, surges and hydraulic jumps. In highly unsteady flows propagating inland on both dry and wet surfaces, the definition of the Froude number is not trivial and disagreement still exists in literature. In this context, the present study presents an overview on the different values of the Froude number used in multiple tsunami-related studies throughout the world, comparing them with values estimated during real events at prototype scale. Through the support of experimental data acquired in a large-scale facility, the temporal development of the Froude number in tsunami-like waves is presented and discussed. It is believed that a comprehensive discussion on the main hydrodynamic properties of tsunami-like waves can lead toward a deeper understanding of the physical process and to a better reproduction of the real phenomena in laboratory environments.

Key Words: Tsunami, Froude number, Physical modelling, Wave generation, Unsteady flows.

8th International Conference on the Application of Physical Modelling in Coastal and Port Engineering and Science
Zhoushan, China - Dec. 9th - 12th, 2020

PROTECTING RESIDENTIAL BEACHES FROM FLOODING AND EROSION THROUGH NUMERICAL & PHYSICAL MODELLING

JUNNING PAN [1,4], VALERI PENCHEV [2], JINSHAN ZHANG [1,4], PHILIP PENCHEV [2], MENGJIE XIONG [1,4], SHIRIN SHUKRIEVA[2], DORINA DRAGANCHEVA [2]

1 Key Lab of Port, Waterway and Sedimentation Engineering of the Ministry of Transport, Nanjing Hydraulic Research Institute, PR of China; e-mails: jnpan@nhri.cn; jszhang@nhri.cn; mjxiong@nhri.cn
2 Black Sea Danube Association for Research and Development, Bulgaria; e-mail: office@bdcabg.org 3 Centre of Hydro- and Aero- Dynamics, IMST – BAS, Bulgaria; e-mail: d.dragancheva@bshc.bg
4 International Joint Research Center of Water Science and Engineering, PR of China

A study on various numerical tools for simulation of coastal flooding and beach erosion has been carried out within the framework of a bilateral research project supported by the National Science Fund of Bulgaria and the Ministry of Science & Technologies of the PR of China. Based on preliminary analysis, two different numerical approaches have been demonstrated by Bulgarian and Chinese research teams to simulate coastal flooding, and evaluate inundation hazard and beach erosion, and their interaction.

As a first stage of the study, a high resolution digital elevation model has been established for Asparuhovo - Karantina area in Varna, Bulgaria, located at Black Sea coast (a closed sea, with negligible tidal variations). This is a residential area that includes a sandy beach and a small river (gulley) in the neighborhood. The residential area behind the beach is considered with high risk of flooding, being at low elevation above the sea-level. A MIKE FLOOD/ MIKE21 FM approach was used to simulate inundations in the beach area under various scenarios for compound flooding: coastal flood (storm surge) in combination with pluvial/flash flood (heavy rainfall in the urban area), and/or fluvial flood (river overflow due to excessive rainfall over an extended period). In parallel, short and long-term predictions of shoreline evolution has been carried out with MIKE 21 Shoreline Morphology software to gain greater insight into the nature of the erosion and the effectiveness of possible management options. Concurrently a SWASH model has been elaborated by the Chinese part to study wave transformation for the same geographical area, for the same scenarios for water levels and wind-wave climate conditions. SWASH is referred to a non- hydrostatic wave-flow model aimed to simulate wave transformation in coastal area. As a second stage, the above approach has been applied also for the coastal zone of Beilun city in China, where different environmental conditions are present (tide variations, open sea). Numerical simulation results have been compared and verified versus some field survey data and previous physical model tests, building on the conclusions and recommendations of the first stage research.

Results obtained by two different numerical approaches - compared versus physical model data - have shown a good matching, and more important - they complement each other. MIKE approach provides good overview on hydrodynamics, as well as understanding on beach evolution processes. The SWASH results indicate that, the shoaling effect near shore and wave run-up and breaking in the swash zone may aggravate the flooding disaster on the beach, especially when a severe storm generate intense water level rise.

The results of the joint bilateral study encourage authors for further research and improvement of the demonstrated approach of combining various numerical simulation and physical modelling tools. Further recommendations on the use of the selected numerical models, in combination with physical modeling and field observations data (composite modeling approach) are suggested.

Key Words: coastal, beach, numerical, physical, modeling

8th International Conference on the Application of Physical Modelling in Coastal and Port Engineering and Science
Zhoushan, China - Dec. 9th - 12th, 2020

DESIGN OF THE MAIN WAVE ENERGY ABSORBER FOR THE IMARES WAVE TANK

GOVAERE G.[1], ALFARO H.[2] AND MURILLO R.

1 University of Costa Rica, Costa Rica, georges.govaere@ucr.ac.cr 2 University of Costa Rica, Costa Rica, henry.alfaro@ucr.ac.cr

3 University of Costa Rica, Costa Rica, rafael.murillo@ucr.ac.cr

The IMARES group of the University of Costa Rica moves to its new facilities in 2018 that include a wave tank, with 24 box-type paddles with active energy absorption, but that did not include its main energy absorber, which is one of its principal components. Using a small 11m x 0.3m wave flume, different configurations of the absorber were tested.

The design parameters that were taken into account were that the wave reflection coefficient has to be close to 20%, that it could be built with materials found in Costa Rica, had a long service life, could be easily repaired and finally, that kept within a reasonable budget.

The configurations tested were the following:

A layer of the material used to absorb and dissipate the waves that occur behind the paddles (between the generator and the walls). This material evidenced to work very well in the facilities, but its own cost and the cost of transportation to Costa Rica do not make it a viable option for the tank; however, we tested it to use it as a baseline of comparison.

Another option that was studied was to build a smooth ramp as a breakwater, with the coronation just above the level of rest of the water in order to generate a large overflow, and the wave energy would dissipate behind that structure. The idea is very simple and generated good results in regular waves (adjusting the height of the coronation according to the wave height), but turn out very inefficient in irregular waves.

The next option studied was using the same principle of concentrating the energy behind the structure to be dissipated. The structure was constructed by a combination of "Torricellli trumpets" joined in a hexagonal pattern. The model showed interesting results, although with many variables to adjust that would require much more study, but the configuration was ruled out due to its very high complexity of metal construction with the existing industrial limitations in Costa Rica (although quite easy using plastic in 3D printers).

The last configuration was a "traditional" series of meshes that gradually dissipated the energy. Up to 20 series of plastic meshes with decreasing openings on rigid frames were used. To reduce costs, high strength meshes used in construction and soil stabilization were sought.

The final configuration remained as 11 blocks (1,0m width x 1,40m high and 1,50m deep) with 22 frames each, for a total of 242 frames of 1,0m x 1,40m. The entire structure is made of aluminum to reduce weight and avoid corrosion problems (stainless steel was discarded due to its cost). Each frame can carry two meshes (one front and one back) and can be filled with porous materials if necessary. All frames are interchangeable and can be removed individually in case of repair.

The final installation in the tank is expected to generate slightly better results than the model. The installation is scheduled in mid November 2019 and the first tests at the end of 2019 or January 2020.

Key Words: wave absorber, design, wave tank

8th International Conference on the Application of Physical Modelling in Coastal and Port Engineering and Science
Zhoushan, China - Dec. 9th - 12th, 2020

INTEGRATED APPROACH TO PHYSICAL MODELLING OF MAJOR PORT UPGRADE IN CYCLONIC REGION

FRANCOIS FLOCARD[1], BEN MODRA[2], ANTHONY FOLAN[3], DAN HOWE[4], KATE MACLEAN[5]

1 University of New South Wales, Water Research Laboratory (WRL), Australia, f.flocard@wrl.unsw.edu.au 2 University of New South Wales, Water Research Laboratory (WRL), Australia, b.modra@wrl.unsw.edu.au 3 SMEC Pty Ltd, Australia, anthony.folan@smec.com
4 University of New South Wales, Water Research Laboratory (WRL), Australia, d.howe@wrl.unsw.edu.au
5 Port of Townsville Limited, Australia, kclean@townsville-port.com.au

The Port of Townsville Limited (POTL) in Northern Queensland (Australia) is seeking to increase the capacity of its existing shipping channel through dredging activities by increasing the depth and width along the approach channel. Due to Townsville's proximity to the Great Barrier Reef Marine Park, the option of offshore placement of dredged material generated by the channel capacity upgrade works was not available. Consequently, the construction of a new rock bund wall has been selected to provide a new basin, which will be used to safely accommodate the dredge material.

An integrated approach to physical modelling was adopted, which enabled a more accurate assessment of the following key coastal processes as well as design optimisation and validation, including:

1. 3D physical modelling of the outer harbour and approach channel, in order to provide wave climate information as a design input for the bund seawall. Specifically, this component of the study showed that channel reflection and channel concentration can significantly transform the local waves, resulting in multidirectional wave fields and higher design wave conditions. These complex processes should be an important consideration for infrastructure and coastal management in regions with dredge channels.
2. 2D physical modelling of a representative cross-section of the proposed bund wall to investigate structure design and armour stability under a wide range of extreme environmental conditions. Modelling allowed optimisation of armour gradings as well as crest geometry to mitigate the risk of large overtopping flows associated with cyclonic specific conditions (i.e. storm surge and bi-model spectra).
3. Quasi-3D modelling of the bund wall corner to provide an assessment of the armour stability of the structure under design wave loading. This modelling validated the design of the 3D section of the structure. Specific modelling of 3D structural elements, such as heads or corners, is important as they respond differently to straight trunk sections of seawalls and often require larger armour units or flatter slopes.

Key Words: physical modelling, basin, flume, seawall, channel

8th International Conference on the Application of Physical Modelling in Coastal and Port Engineering and Science
Zhoushan, China - Dec. 9th - 12th, 2020

INDUSTRY 4.0 TECHNOLOGY FOR SUSTAINABLE SMART LOGISTICS AT NORDIC SEAPORTS

WEI DENG SOLVANG

Faculty of Engineering Science and Technology, UiT the Arctic University of Norway, Norway, wei.d.solvang@uit.no

Industry 4.0, ever since the concept was initiated in 2011 by German federal government, has becoming synonym of powerful set of enablers for technological innovation and new value generation for sustainable development of industries at global base, including port industry. The benefit of utilizing industry 4,0 technologies at seaports are apparently limitless. Many large seaports worldwide have already documented considerable benefits by utilizing industry 4.0 technologies in its fullscale (i.e., Smart Ports). And positive gains in terms of environmental, economical and social sustainability are clearly stated. However, Nordic seaports are mainly small- and medium-sized and limited in resource. Infrastructure at these ports and their spheres can be insufficient. How to conduct sustainable port development by benefiting from Industry 4.0 technology becomes a critical question.

The paper starts with establishing a general overview of Industry 4.0 and its extending concept in logistics (i.e., Logistics 4.0 and Smart Logistics) that are relevant to seaport management. A literature review on the application of Industry 4.0 technologies at seaports are conducted. Further, the author explores the concept of sustainable development with emphasis on its significance at seaport management. The uniqueness and importance of SMPs are explored, especially in the context of Nordic perspective. The potential of using Industry 4.0 technologies to enable sustainable development at seaports is discussed. Moreover, the author conducts a qualified evaluation on levels of applying Industry 4.0 technologies at Norwegian SMPs. This further leads to suggestions on types of Industry 4.0 technologies that could applied to Norwegian SMPs to enable sustainable development with necessary level of smartness.

Key Words: Industry 4.0, Sustainable development, Smart logistics, SMP, Nordic seaports

8th International Conference on the Application of Physical Modelling in Coastal and Port Engineering and Science
Zhoushan, China - Dec. 9th - 12th, 2020

MEASUREMENT OF WAVE OVERTOPPING AT SEAWALLS WITH LARGE BULL NOSE

HAI TRUNG LE[1], TUNG TRAN THANH[2], LINH DANG THI[3]

1 Thuyloi University, Viet Nam, trung.l.h@tlu.edu.vn

2 Thuyloi University, Viet Nam, T.T.Tung@tlu.edu.vn

3 Thuyloi University, Viet Nam, linhdt05@wru.vn

Seawalls have become more popular in protecting many towns and tourism areas located in 28 coastal provinces and cities of Viet Nam. During storm surges and high tide events, wave overtopping at this kind of structure is the most dangerous phenomenon that would often threaten infrastructures, traffic and residents in the land strip behind. Therefore, the paper investigates the wave-seawall interaction using physical model tests in a wave flume. The experimental set-up uses different combinations of water depth, foreshore inclination and wave characteristics. We measure the quantity of wave overtopping (total volume and unit discharge) at seawall with seaward faces of vertical, steep and curved. The data analysis indicates that the three cross-sections are relatively comparable in reducing wave overtopping. Furthermore, the model seawalls are shaped without and with bull noses of large dimension. As a result, we propose a discharge ratio k_{bn} of wall with to which without the bull nose. The higher incoming wave, the larger k_{bn} becomes for seaward faces of steep and vertical. In contrast, the curved wall shows less effectively with smaller ratio.

Key Words: curved, steep, vertical, overtopping, seawall

8th International Conference on the Application of Physical Modelling in Coastal and Port Engineering and Science
Zhoushan, China - Dec. 9th - 12th, 2020

LABORATORY MEASUREMENT OF WAVE-DRIVEN CURRENT AROUND THE REEF SURF ZONE UNDER THE EFFECT OF TIDAL CURRENT

Yu Yao a,b,*, Menjun Jia, Yicheng Liua, Changbo Jianga,b

a School of Hydraulic Engineering, Changsha University of Science and Technology, Changsha, Hunan, 410114, China.

b. Key Laboratory of Water-Sediment Sciences and Water Disaster Prevention of Hunan Province, Changsha 410004, China

A series of innovative laboratory experiments are performed in a wave-current flume to investigate the wave-driven current around the reef surf zone. Experimental results are reported for an idealized barrier reef model subjected to a typical plugging breaker. A pipe is constructed to connect both the lagoon and the offshore, and a pump is set on the middle of the pipe to generate the designed steady current in the pipe and force a circulation in the flume. The vertical distributions of undertow current associated with the breaking waves at different cross-shore locations are measured by a sophisticated Laser Doppler Velocimeter (LDV) system. Results are reported for the undertow profiles under both effects of a shoreward current and a seaward current, and they are compared to those without the effect of current.

Key words: undertow, tidal current, surf zone, barrier reef

8th International Conference on the Application of Physical Modelling in Coastal and Port Engineering and Science
Zhoushan, China - Dec. 9th - 12th, 2020

DETERMINING VERTICAL DISTRIBUTION OF EROSION PARAMETERS BY IN SITU MEASUREMENTS

QIN ZHU[1], BRAM C. VAN PROOIJEN[2]

1 Guangdong University of Technology, China, qin.zhu@gdut.edu.cn
2 Delft Univerity of Technology, Netherlands, B.C.vanProoijen@tudelft.nl

Predictions of the morphological evolution of mudflats are not straightforward, as it is a complex outcome of tidal currents, waves, bed and suspended sediment properties, and even ecological processes. Various steps have been taken to overcome shortcomings of the mudflats' morphodynamic models. The erosion rate in these models is often calculated based on the so-called Partheniades' erosion equation $E=M(\tau_b - \tau_e)$ or $E=M'(\tau_b/\tau_e - 1)$ for $\tau_b > \tau_e$, with the erosion rate E, erosion coefficient M, bed shear stress τ_b and critical shear stress for erosion τ_e. However, the estimation of the erosion threshold and erosion coefficient has remained a challenge, as these two parameters vary with the sediment composition, bulk density, consolidation state and biological interaction.

To investigate how τ_e and M vary over the natural sediment bed, comprehensive observations of the sediment properties, hydrodynamics and bed-level changes were conducted on an intertidal flat in the Western Scheldt Estuary, the Netherlands. A storm event induced erosion at low water line revealed a vertical distribution of τ_e and M over a sediment bed of 12 cm. We find that the erosion coefficient M can be regarded as being constant with depth in the linear erosion equation $E=M(\tau_b - \tau_e)$ for $\tau_b > \tau_e$. Whereas a clear vertical variation of τ_e was found: τ_e increased significantly downward from 0.10 Pa at the sediment surface to 1.13 Pa at 12 cm below the surface. Such a significant variation of τ_e over a limited depth indicates that erosion rates can be overestimated if a uniform τ_e is used. Additionally, there was a strong indication that the presence of diatoms enhanced τ_e in the upper 2 mm of sediment by five times of the abiotic τ_e (from 0.09 Pa to 0.46 Pa). It means that an appropriate description of the effect of diatoms should be considered as part of the bottom boundary condition, especially a seasonal variation of sediment budget is considered. These, however, would have serious consequences for the computation times.

Key Words: Erosion threshold; Erosion coefficient; In situ measurement; Mudflat; Diatoms

8th International Conference on the Application of Physical Modelling in Coastal and Port Engineering and Science
Zhoushan, China - Dec. 9th - 12th, 2020

NUMERICAL SIMULATION OF HYDRODYNAMIC RESPONSES OF A MULTI-BODY FISH CAGE WITH SINGLE-POINT MOORING SYSTEM IN WAVES

CHAO MA [1], YUN-PENG ZHAO [1], CHUN-WEI BI [1], HANG-FEI LIU [1], QIU-PAN CHEN [1]

1 State Key Laboratory of Coastal and Offshore Engineering, Dalian University of Technology, Dalian 116024, China，dlutmc@mail.dlut.edu.cn

As fish farming gradually migrates to the deep sea, farming facilities that can withstand harsh sea conditions become more important. Compared with traditional high density polyethylene gravity cages, a multi-body ship type floating net cage has numerous advantages. Combined with a single-point mooring system, the special structural form of the ship type can greatly reduce the wave load transmitted from the bow. In this study, a numerical model is established to study the hydrodynamic responses of a single-point moored ship type floating net cage in waves. Three different numerical models of the net cage with two, three and four frames were established and calculated to find the difference in the motion and mooring force responses between the ship type floating net cages with different numbers of frames. The difference in the motion responses between different frames of the same net cage and between different wave conditions were compared. The difference in the hinge joint force between hinges at different positions of the same net cage is also analyzed.

Key Words: Floating net cage; Single-point mooring system; Numerical simulation; Hydrodynamic responses

8th International Conference on the Application of Physical Modelling in Coastal and Port Engineering and Science
Zhoushan, China - Dec. 9th - 12th, 2020

NECESSITY OF USING A WAVE FRICTION FACTORIN TSUNAUMI NUMERICAL SIMULATION

HITOSHI TANAKA[1], NGUYEN XUAN TINH[2], NGUYEN TRUNG VIET[3]

1 Professor, Tohoku University, Japan, hitoshi.tanaka.b7@tohoku.ac.jp
2 Assistant Professor, Tohoku University, Japan, nguyen.xuan.tinh.c5@tohoku.ac.jp
3 Professor, Thuyloi University, Vietnam, nguyentrungviet@tlu.edu.vn

In all of existing tsunami numerical models, steady flow friction factor, such as Manning's *n* or Darcy-Weisbach's *f*, has commonly been applied for accessing the tsunami-induced bottom shear stress. However, it has theoretically been proved by the authors that the wave friction law is valid, rather than the steady flow friction law in almost the entire computational domain from tsunami source to shallow area (Tinh and Tanaka, 2019). In the present, we propose a correction method for tsunami-induced bottom shear stress. Subsequently a numerical implementation of this correction method into the one-dimensional shallow water equation model of tsunami propagation is presented. As a result, comparison results indicate that the simulated maximum tsunami wave height and tsunami-induced velocity by the new method and conventional one are almost similar. However, the bottom shear stress estimated by the present method is found to be about 10 times higher than that from a conventional method in the source area, and the difference decreases as the water depth decreases. Two methods give almost same shear stress from the location of water depth around 6m to the shoreline.

Key Words: tsunami, bottom boundary layer, bottom shear stress, numerical simulation

8th International Conference on the Application of Physical Modelling in Coastal and Port Engineering and Science
Zhoushan, China - Dec. 9th - 12th, 2020

MECHANICAL METAMATERIALS PIEZOELECTRIC NANOGENERATOR (MM-PENG)

PENGCHENG JIAO[1], XIAOYUN XIE[1], HAIPENG WANG[1], KINGJAMES IDALA EGBE[1], ALI MATIN NAZAR[1], YANG YANG[1], ZHIGUO HE[1]

1 Institute of Port, Coastal and Offshore Engineering, Ocean College, Zhejiang University, Zhoushan 316021, Zhejiang, China

Traditional energy sources, e.g., disposable batteries, typically suffer severe limitations given the difficulty, if not impossible, of regular replacement. Therefore, it is of desire to develop new energy solutions that continuously generate reliable electrical power. Lack of reliable blue energy is one of the most critical challenges in electrical devices and thus, research efforts have been dedicated to addressing such power issue. Here, we develop a novel energy harvesting technique under quasi-static excitations using piezoelectric materials (PENG) enhanced by mechanical metamaterials (MM). Piezoelectric nanogenerator (PENG) has been reported as the blue energy solution that converts mechanical energy into electrical power. As a vibration-based energy harvesting technique, the mechanical characteristics of PENG critically affect the output performance, especially when the input is low-frequency excitation. While the studies on PENG have mainly been reported on the material perspective (i.e., fabrication and experiment), it is necessary to investigate the output electrical energy from the mechanical perspective.

In this study, we fabricate the MM in the plate shape using the photolithography and atomic layer deposition (ALD) techniques and the piezoelectric layer was grown by the PVDF-TrFE material using the spin-coating technique. A sliding cell is designed to convert low-frequency excitations into high-frequency motions through postbuckling mode transitions of the piezo-MM. As a consequence, the PVDF-TrFE is triggered to generate electrical power. In this process, the environmental input (<1Hz) is transformed into mechanical energy, which is then converted into electrical power. Fabrication and testing of the MM-PENG are conducted at the microscale, and the theoretical and numerical models are developed to validate the experimental results with satisfactory agreements. Parametric studies are carried out to investigate the enhancement of MM on the output electrical power of the MM-PENG by considering the pattern, geometric and scaling ratios. According to the systematic studies, we find that the most dominant ratios of the MM-PENG are the geometries of their microstructures. In particular, the piezo layer thickness and piezo-MM height can be used to control the output electrical power. The material length scale factor l tends not to affect the energy harvesting performance, which outlooks exciting applications of the MM-PENG at the macroscale. In the end, we outlook that the MM-PENG opens an exciting path to green energy by generating electrical power for multifunctional applications. Throughout years of space travel, for example, electrical energy of nanodevices in the nanocraft are likely to be severely reduced and thus, it is of significance to automatically charge those devices via the energy harvester. Moreover, fluctuation of ocean surface provides periodically vibrated wave. Increasing the MM-PENG to millimeter-scale and placing in ocean, the periodic wave can be used as axial excitation to trigger the energy harvester to generate electrical power.

Key Words: Piezoelectric nanogenerator (PENG); Plate-shaped mechanical metamaterial (MM); Bilaterally sliding constraints; Mechanical energy harvesting; Low-frequency excitations

8th International Conference on the Application of Physical Modelling in Coastal and Port Engineering and Science
Zhoushan, China - Dec. 9th - 12th, 2020

PHYSICAL MODELING OF REGULAR WAVE INDUCED HORIZONTAL CIRCULATION OVER A REEF-LAGOON-CHANNEL SYSTEM

Shubin Chen[1], Songgui Chen[1,2], Jian Shi[1], Yu Yao[3], Qiming Zhang[3], Jinhai Zheng[1*]

1 Hohai University, Nanjing, P.R. China, 181303020029@hhu.edu.cn; jianshi@hhu.edu.cn

2 Tianjin Research Institute of Water Transport Engineering, Tianjin, P.R. China, chensg05@ 163. com

3 Changsha University of Science and Technology, Changsha, Hunan 410114, P.R China, yaoyu821101@163.com

Among the forces that affect the hydrodynamic process of coral reefs, current is the primary dynamic factor that impacts nutrient transport and coral sediment movement.

Based on the topography configuration of the Paopao Bay, Moorea, French Polynesiain, an idealized 3D reef-lagoon-channel system was built in a wave basin. Using the current meter array and surface velocity measurement system (SVM), a series of physical model tests are carried out to study the horizontal circulation characteristics of the coral reef coast in regular waves. The SVM method can get detailed velocity distribution over the basin. Comparison to results by ADV flow meters shows that SVM method has reliable accuracy.

A counterclockwise circulation and a offshore jet were observed in the middle channel. Results revealed that the flow field pattern highly depended on the incident wave height and initial water depth. With increasing wave height and decreasing water depth, velocity and offshore outflow velocities

Results revealed that the flow field pattern highly depended on the incident wave height and initial water depth. With increasing wave height and decreasing water depth, velocity and offshore outflow velocities were found to increase, and the position of the maximum offshore velocity in the longitudinal profile of the channel is advanced. The formation mechanism of the horizontal circulation was also analyzed based on the changes of coastal radiation stress and pressure gradients.

Key Words: Horizontal circulation, Reef-lagoon-channel system, SVM, Regular waves.

8th International Conference on the Application of Physical Modelling in Coastal and Port Engineering and Science
Zhoushan, China - Dec. 9th - 12th, 2020

VALIDATION OF TSUNAMI-INDUCED CURRENT USING A NON-HYDROSTATIC NUMERICAL MODEL

BING CHEN[1]

1 Shandong Jiaotong University, Jinan, Shandong province, China. E-mail: chenbing@sdjtu.edu.cn

Strong currents have been observed in America's west and China's east coastal area during the Tohoku tsunami event occurred in Japan in 2011. The strong currents caused collapse to maritime facilities, scour at the head of groyne, and deposition inside the port. While such impacts have been observed in the field, the hazard from tsunami-induced current remains an underappreciated risk in the port and maritime community, studies about this phenomenon were quite limited. The National Tsunami Hazard Mitigation Program (NHTMP) organized a benchmark workshop to evaluate the numerical modeling of tsunami currents in 2015. Five benchmark cases were adopted for validation, and thirteen tsunami models were used for modeling tsunami-induced current. Results showed that accurate simulation in the areas affected by eddies is still a big challenge to those numerical models. In this study, the SST *k-w* turbulence model was introduced to the original 3D un-structured grid non-hydrostatic model SUNTANS (Stanford Unstructured Non-hydrostatic Terrain-following Adaptive Navier-Stokes Simulator). The modified model was validated by two benchmark cases including an experimental data of shallow flows around a submerged conical island with small side slopes and a field survey of tsunami-induced current near Hilo harbor provided in the tsunami current workshop. Results showed that the model could reproduce the lee vortices street in the laboratory case and large eddies in the field case well. The computed velocities consist with experimental observed values in the observation station. As a result of the analyses in this study, it is expected that the non-hydrostatic model had a deeper awareness of ability to accurately capture the physics of tsunami currents, and therefore be a useful simulation tool for hazard assessment and mitigation efforts.

Key Words: tsunami-induced current, non-hydrostatic model, large eddies, turbulence model

8th International Conference on the Application of Physical Modelling in Coastal and Port Engineering and Science
Zhoushan, China - Dec. 9th - 12th, 2020

MODELING WAVE PROCESSES OVER FRINGING REEFS WITH LARGE SURFACE ROUGHNESS

Menjun Jiaa,*, Yu Yaoa,b, Xiaoxiao Yanga, Yichen Liua

a. School of Hydraulic Engineering, Changsha University of Science and Technology, Changsha, Hunan, 410114, China.

b. Key Laboratory of Water-Sediment Sciences and Water Disaster Prevention of Hunan Province, Changsha 410114, China

A number of field studies have reported that the surface roughness of coral reefs is one or two magnitude larger than that of sandy beaches. Aside from wave breaking, a substantial portion of incident wave energy can be dissipated by bottom friction. In this study, the effect of reef roughness on wave transformation over reefs is simulated based on two approaches: One is to use the Boussinesq equations by adding a drag term and the other is to use the Volume-averaged Reynolds-averaged Navier–Stokes (VARANS) equations by incorporating a porous media model. Both models are validated by the laboratory experiments in view of such wave processes as wave breaking near the reef edge, bore prorogation across the reef flat as well as wave run-up on the back- reef beach. Model comparison for both solitary waves and monoharmonic waves are reported.

Key words: Roughness, drag force, porous media, fringing reef, wave transformation

8th International Conference on the Application of Physical Modelling in Coastal and Port Engineering and Science
Zhoushan, China - Dec. 9th - 12th, 2020

FLOC SIZE DISTRIBUTIONS OF SUSPENDED COHESIVE SEDIMENTS IN ESTUARINES AND COASTAL WATERS

XIAOTENG SHEN [1, 2, 3], ERIK A. TOORMAN [4], JEROME P.-Y. MAA [5], JINFENGZHANG [6], QING HE [7], YULIANG ZHU [2], YIXIN YAN [2]

1 Key Laboratory of Coastal Disaster and Defence of Ministry of Education, Hohai University, China Email: xiaoteng_shen@163.com

2 College of Harbour, Coastal and Offshore Engineering, Hohai University, China

3 State Key Laboratory of Hydrology-Water Resources and Hydraulic Engineering, Hohai University, China

4 Hydraulics Laboratory, Department of Civil Engineering, KU Leuven, Belgium

5 Virginia Institute of Marine Science, School of Marine Science, College of William and Mary, USA

6 State Key Laboratory of Hydraulic Engineering Simulation and Safety, Tianjin University, China

7 State Key Laboratory of Estuarine and Coastal Research, East China Normal University, China

To manage coastal and estuarine waters, it is critical to accurately predict the movements of suspended material (e.g., cohesive and non-cohesive sediments, micro-plastics, etc.). There are well-established methods to estimate the behavior of non-cohesive sediments; however, without extensive knowledge on flocculation processes it remains difficult to predict the behavior of others, especially for cohesive sediments. Flocculation is one of the main processes (e.g., erosion, deposition, settling, consolidation and flocculation) in cohesive sediment dynamics. The study of flocculation is an interdisciplinary work since it relates to various physical (e.g., transport, settling and deposition), chemical (e.g., contaminant uptake and transformation), and biological (e.g., community structure activities and metabolism) activities. Nevertheless, a widely-accepted flocculation model that can quantitatively simulate the Floc Size Distributions (FSDs) for a relatively large study domain has not yet been fully developed.

In this study, the observed FSD by LISST (Laser In Situ Scattering and Transmissometry) instrument were decomposed into subordinate lognormal distributions for microflocs, macroflocs and megaflocs. The three-class Population Balance Equation (PBE) was developed to illustrate the characteristic sizes and mass fractions of these three particle groups to match the observations. This PBE based flocculation model has also been successfully implemented in the open-source TELEMAC system. Assuming that the microflocs are the building blocks of the macroflocs and megaflocs, only five tracers are tracked in the system: (1) the number concentration of microflocs N_P, (2) the number concentration of macroflocs N_{F1}, (3) the number concentration of megaflocs N_{F2}, (4) the number of microflocs in all macroflocs per unit volume N_{T1}, and (5) the number of microflocs in all megaflocs per unit volume N_{T2}, which enables better settling flux estimates and better addresses the occurrence and concentration of larger megaflocs. This three-class flocculation model was validated with both laboratory data of a settling column experiment and field data collected at the Port Zeebrugge at the Belgian coast. Results show that the flocculation properties of cohesive sediments can be reasonably simulated in both environments. This model has the potential to better illustrate the sediment dynamics in nearshore regions such as the Yangtze River Estuary and the Pearl River Estuary in China coast.

Key Words: cohesive sediments; flocculation; floc size distributions; population balance model; estuaries

8th International Conference on the Application of Physical Modelling in Coastal and Port Engineering and Science
Zhoushan, China - Dec. 9th - 12th, 2020

TESTING TECHNOLOGY OF FIBER ROPES FORMARINE RENEWABLE ENERGY APPLICATIONS

YUSHUN LIAN [1], JINHAI ZHENG [2], HAIXIAO LIU [3], XIAOTENG SHEN [2]

1 Key Laboratory of Coastal Disaster and Defence, Hohai University, Ministry of Education, Nanjing 210098, China e-mail: yushunlian@hhu.edu.cn

2 College of Harbour Coastal and Offshore Engineering, Hohai University, Nanjing, 210098, China e-mail: jhzheng@hhu.edu.cn Haixiao Liu, third author

3 State Key Laboratory of Hydraulic Engineering Simulation and Safety, Tianjin University, Tianjin 300072, China e-mail: liuhx@tju.edu.cn

As the occurrence of utilization of fiber mooring ropes for marine renewable energy devices (MRED) including wave energy converters, wind farms and macro-algae (kelp) farms, dynamic responses of marine renewable energy devices with fiber mooring ropes should be investigated. However, capturing the responses of MREDs' mooring system is still challenge due to the material nonlinearity of mooring lines and highly nonlinear motions of MRED. In the present study, to address the nonlinear issues in the application of fiber ropes in marine renewable energy devices, the dynamic stiffness and damping behaviors of synthetic fiber ropes are investigated by performing cyclic loading tests. To perform these tests, the experimental equipment of fiber mooring ropes has been developed. The key testing technology of synthetic fiber ropes is developed. The detailed experimental procedure and method are introduced. The method of analyzing the test results is presented. The present test technology will contribute to develop the test machine of full-scale synthetic fiber ropes and aid the industry to capture the test procedure and method of full-scale ropes. Based on the present test technology, the mechanical behavior of fiber ropes can be investigated and aid to the application of fiber ropes in marine renewable energy devices.

Key Words: Mooring; Fiber ropes, Wave energy converters, Macro-algae (kelp) farms, Test technology

8th International Conference on the Application of Physical Modelling in Coastal and Port Engineering and Science
Zhoushan, China - Dec. 9th - 12th, 2020

ANALYSIS ON THE POWER FLUCTUATION OF TIDAL STREAM TURBINE IN THE TURBULENCE FLOW COMBINED WITH REGULAR WAVES

Yuquan Zhang 1,2, Jinhai Zheng 2, Yuan Zheng 1, Jisheng Zhang 2 and Wei Zang 1

1 College of Energy and Electrical Engineering, Hohai University, Nanjing 210098, China;

2 College of Harbor, Coastal and Offshore Engineering, Hohai University, Nanjing 210098, China;

The structure of the wave-induced turbulence-driven power fluctuation of a tidal turbine is described from the experiments with basic concepts. A model horizontal tidal stream turbine (HTST), of diameter D=0.3 m, was installed at half-depth of the water column. Water-tunnel experiments, with a blockage ratio of 9.8%, were performed to inspect the impact of a variety of linear waves on the instantaneous power output and turbine wake. For comparison, measurements were also performed in current-only flow with an ambient turbulent intensity around 8%. Acoustic doppler velocimeter (ADV) probes were used to obtain the spectral scaled velocities and the turbulent intensities. Results show that the mean power-output slightly increased with influence of wave turbulence and the power fluctuation exhibited an extreme peak more than 2 times of the averaged value (P_0) in turbulence flow. Duo to the turbulence diffusion of large-scaled wave structure, the spectral content of the power-spectrum represented a sharp peak with the frequency of the wave and it proved a power-law decay with different rate in the near wake corresponding to the turbine-induced turbulence and far wake region at relatively large scales from the wave.

8th International Conference on the Application of Physical Modelling in Coastal and Port Engineering and Science
Zhoushan, China - Dec. 9th - 12th, 2020

A SYSTEM SHIFT IN HYDRODYNAMICS DUE TO THE CONSTRUCTION OF YANGSHAN HARBOR, SHANGHAI, CHINA

GUO WEN YUN [1], GE JIAN ZHONG [2], SONG DE HAI [3], DING PING XING [2], WANG XIAO HUA [4]

1 Shanghai Maritime University, China, wyguo@shmtu.edu.cn
2 East China Normal University, China, jzge@sklec.ecnu.edu.cn; pxding@sklec.ecnu.edu.cn
3 Ocean University of China, China, songdh@ouc.edu.cn
4 University of New South Wales, Australia, x.h.wang@unsw.edu.au

The Yangshan Harbor was constructed on an archipelago with high-concentration mud suspension. The construction engineering had closed three major channels from 2002 to 2008, causing intense morphological changes in the Yangshan sea area. But the physical mechanisms for the morphological changes remains further research.

In this study, we focus on the shift in tidal current and circulation induced by the construction of Yangshan Harbor. Observations and a high-resolution numerical model based on FVCOM are used to provide a comprehensive understanding on these shifts. Its impacts on sediment transport is also discussed. Results show that the harbour's construction has reinforced the tidal currents in the passages and in most of the harbor basins. The bathymetry in the passages is thus deeper after the harbour's construction. A large horizontal circulation is formed in the Inner Harbour Area, which may contribute to the sedimentation in the middle and southern harbor area. The harbour's construction also induced stronger tidal asymmetry in the Yangshan area. The stronger tidal asymmetry contributes much to the suspended sediment transport. That is why the Kezhushan Passage is advised to be reserved.

Key Words: Yangshan Harbor, tidal asymmetry, circulation, FVCOM

8th International Conference on the Application of Physical Modelling in Coastal and Port Engineering and Science
Zhoushan, China - Dec. 9th - 12th, 2020

MAPPING TIDAL CURRENTS AT A TIDAL CHANNEL JUNCTION USING FLUVIAL ACOUSTIC TOMOGRAPHY SYSTEM

CONG XIAO[1], KIYOSI KAWANISI[2], MOHAMAD BASEL AL SAWAF[3]

1 Department of Civil and Environmental Engineering, Graduate School of Engineering, Hiroshima University, Higashi-Hiroshima, Japan, d180047@hiroshima-u.ac.jp

2 Department of Civil and Environmental Engineering, Graduate School of Engineering, Hiroshima University, Higashi-Hiroshima, Japan, kiyosi@hiroshima-u.ac.jp

3 Department of Civil and Environmental Engineering, Graduate School of Engineering, Hiroshima University, Higashi-Hiroshima, Japan, mbasel@hiroshima-u.ac.jp

In a tidal channel network, there are many branches/ junctions that are commonly bifurcated asymmetrically. An investigation of hydrodynamics at the tidal channel junction related to the interaction between the tidal wave, upstream river, and the geometrical shape of branches has been carried out by a few researchers. The Fluvial Acoustic Tomography (FAT) System is developed at Hiroshima University is a technique that is able to measure tidal currents in shallow waters, one fascinating application of FAT is continuous visualizing 2D flow pattern. Herein, we present an example application of an array of FAT in a shallow tidal junction in conjunction with numerical inversion schemes.

The horizontal distributions of the tidal currents and the residual currents were well calculated by inverse analysis of FAT data. Although the salt-wedge intrusion had a strong effect on sound propagation patterns that led to a multitude of arrival times, the reconstructed flow patterns agreed favorably with ADCP data. Moreover, we analyzed the main dynamic processes responsible for the residual currents by using the averaged horizontal momentum equation. The predominant terms in balancing the momentum equation of the residual currents are advection of the tidal currents, horizontal pressure gradient, and advection of the residual currents.

Key Words: Shallow water tomography, tidal channel junction, tidal current, residual current

8th International Conference on the Application of Physical Modelling in Coastal and Port Engineering and Science
Zhoushan, China - Dec. 9th - 12th, 2020

DOWNSTREAM HYDRAULIC GEOMETRY OF THE YELLOW RIVER DELTA

HAOCHUAN FENG[1], CHONGHAO WANG[1], CHUANSHENG GUO[1]

1 Department of Sediment Research, China Institute of Water Resources and Hydropower Research, China, haochuanfeng@sina.com

Delta channels influenced by mixed river tidal dynamics may features complex, composite scaling of geometrical properties, which have not yet been thoroughly understood. The effect of tide has long been ignored in discussing the hydraulic geometry of the Yellow River Delta, where the flow changes its path and carves a new channel frequently. Due to intensive climate change and anthropogenic activities, the river discharge that debouch into this river dominant delta has been dramatically decreased in recent years, which amplifies the tidal dynamics relatively. Several measurements was operated to depict the channel variation at a list of cross sections from Lijin to the outlet, in 2000 and 2015. The widths and depths for these cross sections are further exhibited to depict the geometrics characters along the main channel in this delta. A 2D hydrodynamic models is applied to reproduce the river tide dynamics in 2000 and 2015. This model is validated based on the deltaic bathymetry and hydrological data that measured in these two years. By incorporating the tidal prism into the empirical power law relations between the channel geometry and the discharge transported in the channel, the hydraulic geometry concept, which was originally defined for fluvial channels, was extended to tidal influenced channels. Therefore, the tidal signature was quantified on delta morphology in the Yellow River Delta, the tidal impacts on the hydraulic geometry relations in this delta was theoretically analysed. In general, the effects of tide in this river delta is reflected by the along channel variation of downstream hydraulic geometry exponents from 2002 to 2015.

Key Words: hydraulic geometry; bathymetric evolution; tidal impacts; Yellow River Delta

8th International Conference on the Application of Physical Modelling in Coastal and Port Engineering and Science
Zhoushan, China - Dec. 9th - 12th, 2020

DEPTHS ESTIMATION OF A SANDY BEACH FROM X-BAND RADAR OBSERVATION

WANG DI[1] AND TAKAWAKA SATOSHI[2]

1 Graduate School of Systems and Information Engineering, University of Tsukuba, Japan, wangdi0103@outlook.com 2 Graduate School of Systems and Information Engineering, University of Tsukuba, Japan, takewaka@kz.tsukuba.ac.jp

Bathymetric data is one of the most crucial elements for understanding the morphodynamic processes along shorelines and forecasting some environmental phenomena such as beach erosion, sea-level rise, and subsidence. In this study, a recently developed depths estimation algorithm cBathy (Holman, 2013) is applied to a set of continuous data from X-band marine radar observation during a stormy period at Hasaki Coast, Japan. Radar images are collected every 2 seconds, in which wave propagations from the offshore to the onshore are captured. The function of this algorithm is to process the input stack information of a set of continues radar images then obtain the depths. In phase 1, individual data sets are first calculated to derive the wavenumber over selected tiles. In phase 2, the wavenumber is used to estimate the depths of each pixel point by using the linear dispersion relationship. The result of depths estimation by cBathy agreed reasonably well with the survey results. Temporal variation of the results suggests that the depths of shallow water was increasing during the first half of the storm due to attack of high waves, and then recovered back.

Key Words: Remote sensing, X-band marine radar, cBathy, typhoon, seabed deformation.

8th International Conference on the Application of Physical Modelling in Coastal and Port Engineering and Science
Zhoushan, China - Dec. 9th - 12th, 2020

MEASURING HYDRODYNAMICS IN AQUATIC VEGETATION CANOPIES: CHALLENGES AND OPPORTUNITIES

ARNOLD VAN ROOIJEN[1], MARYAM ABDOLAHPOUR[2], MARIO CONDE-FRIAS[3], LIMING TAN[4]

1 University of Western Australia, Australia, Arnold.vanRooijen@research.uwa.edu.au 2 University of Western Australia, Australia, maryam.abdolahpour@uwa.edu.au
3 University of Western Australia, Australia, mario.conde-frias@research.uwa.edu.au 4 Zhejiang University, China, tanliming@zju.edu.cn

Marine ecosystems (e.g., salt marshes, mangrove forests, seagrass meadows) are known to play an important role in the nearshore by dissipating wave energy and reducing current magnitudes, and thereby help to provide coastal stability and safety from flooding. Natural and nature-based flood defences have consequently become increasingly popular in the past decade as an alternative to traditional coastal protection. However, quantifying and predicting wave dissipation and flow reduction by aquatic vegetation canopies in the field is challenging as it depends on the hydrodynamic conditions (e.g., Reynolds number), species morphology, spatial variability etc. Therefore, many researchers have placed natural or artificial vegetation canopies in experimental facilities (e.g., unidirectional flow flumes, wave flumes and basins) with the aim to improve general understanding in wave- and current-vegetation interaction processes.

However, obtaining accurate hydrodynamic measurements in and around vegetation canopies is often not trivial due to the lack of spacing in between canopy elements, as well as the complexity in local hydrodynamics introduced by the canopy itself. This talk will highlight some of the challenges and opportunities for measuring hydrodynamics in aquatic vegetation canopies based on a large number of recent experiments in unidirectional and oscillatory flow tanks carried out at the University of Western Australia and Zhejiang University. It provides an overview of traditional and novel techniques for measuring water levels, wave heights, velocities, and drag and inertia forces in vegetation canopies. Specifically, we will address some of the challenges in obtaining accurate velocity measurements inside canopies using ADV and PIV systems. We also discuss a novel technique for measuring the vegetation drag and inertia forces using a low-cost load cell. Finally, based on our recent experiences, we present opportunities and recommendations for future laboratory experiments with aquatic vegetation canopies.

Key Words: ecohydraulics, wave attenuation, ecosystems, physical modelling, lab experiments

8th International Conference on the Application of Physical Modelling in Coastal and Port Engineering and Science
Zhoushan, China - Dec. 9th - 12th, 2020

EXPERIMENTAL STUDY OF THE DUCT-EFFECTS OF TIDAL CURRENT TURBINES IN MULTI-ROW-STAGGERED LAYOUT

YALING CHEN[1], BINLIANG LIN[2], JINXI GUO[2]

1 College of Earth and Environmental Sciences, Lanzhou University, Lanzhou 730000, China
2 State Key Laboratory of Hydro-science and Engineering, Tsinghua University, Beijing 100084, China
**Corresponding author. Email address: chenyaling@lzu.edu.cn*

Tidal turbine array was optimized to increase the power production in order to improve the commercial competitivity of tidal current energy with other forms of energy generation. Due to duct-effects, the power performance of turbines in the staggered layout was better than that of the aligned layout. However, shear layer with enhanced turbulence occurred between the duct zone and isolated wake zone downstream, which had influence on the performance stability and increased the fatigue failure of tidal turbines. The study conducted a series of laboratory experiments to investigate the duct-effects of tidal turbines located in multi-row array with staggered layout. The turbine rotor was represented by porous disc. The flow thrust and time-varying velocity were measured using micro strain gauge and acoustic doppler velometer, respectively. Results showed that the flow was accelerated between turbines with the increment around 20% behind the first row, while the duct-effects were weakened as distance increased downstream. The shear-induced turbulence was enlarged by the duct-effect when it diffused mainly towards individual wake zone at the initial stage. As the turbulence filled the whole individual wake zones, it diffused rapidly to lateral sides and jointed together, and the turbulence intensity across the array wake was significantly higher than that of the free flow. Correspondingly, the performance of turbine rotor located downstream was improved limitedly by the duct-effects, and the stability was reduced clearly. It indicated that the advantage of the duct-effect induced in the staggered layout was limited in the near wake as the lateral interval between two turbine centres was 2 times of rotor diameter.

Key Words: Turbine rotor array; Staggered layout; Duct-effects; Turbine performance; Shear-induced turbulence

8th International Conference on the Application of Physical Modelling in Coastal and Port Engineering and Science
Zhoushan, China - Dec. 9th - 12th, 2020

SIMULATION OF DAM-BREAK FLOW THROUGH POROUS MEDIA BY WC-MPS MESH-FREE METHOD

TIBING XU[1], YIQUN YE[1], YEE-CHUNG JIN[2]

1 School of Civil and Environmental Engineering, Ningbo University, China, E-mail: xutibing@nbu.edu.cn
2 Faculty of Engineering and Applied Science, University of Regina, Canada, E-mail: yee-chung.jin@uregina.ca

The mesh-free method discretizes the fluid and boundaries by a set of movable particles/points instead of fixed meshes. The free surface or interface can be automatically captured without introducing additional equations such as volume of fluid (VOF). Therefore, the mesh-free method is good at handling interface problems. Over decades' development, there are many improved techniques for the mesh-free method including particle shifting technique, stabilization technique, improved gradient and Laplacian models, which make it capable of satisfying requirements for engineering applications. Thus, it has been applied into simulating free-surface flows in ocean engineering, coastal engineering and hydraulic engineering.

In this study, the Weakly-Compressible Moving Particle Semi-implicit method (WC-MPS) is employed to simulate the dam-break flow through porous media, which is characterized with violent free-surface variations. In the method, a stabilization technique is used to reduce the pressure noise caused by the equation of state in calculating the pressure field. The spatial operators including the gradient model and Laplacian model are modified by using the porosity with a smooth transition at the interface between porous and non-porous domain in the simulations. In the porous domain, the resistive force composed of the linear Darcy and nonlinear Forchheimer forces is adopted while the SPS turbulence model is implemented in the method to capture the turbulence. The mesh-free method is validated by using a dam-break flow through porous media. The simulated free-surface profiles are in good agreement with the experimental measurements and smooth pressure field is obtained. The validated mesh-free method is then applied to simulate a series dam-break wave impacting different porous media with different porosities and mean diameters for the solids. To investigate the effect from porosity, by defining a constant mean diameter for the material, the dam-break flow is modeled by varying the porosity to be 0.25-1.0. The effect from the grain size for the porous media is also examined by simulating the dam-break flow through the porous media with mean diameter of 0.01m-0.12m. The impacting pressure on the interface between the porous and non-porous regions is plotted for the different porosity values and mean diameters for comparison. It is found that both the porosity and grain size for the porous material can greatly affect the impacting pressure on the interface between porous and non-porous regions. The impacting pressure can be greatly eliminated by using larger porosity or larger mean diameter materials since these materials easily facilitate more water penetrating into the porous media. This study also shows that the mesh-free method can be applied into simulation of flow through porous media with aid in design of coastal structures.

Key Words: mesh-free method, porous media, free surface, impacting pressure.

8th International Conference on the Application of Physical Modelling in Coastal and Port Engineering and Science
Zhoushan, China - Dec. 9th - 12th, 2020

PRELIMINARY STUDY ON TIDAL DEFENSE ENGINEERING OF DIAOKOU RIVER

Chen Xiongbo, Zhang Li

（Yellow River Engineering Consulting Co.Ltd, Zhengzhou 450003, China）

Abstract: Diaokou river ran from 1964 to 1976, and now it is the standby channel for the Yellow River to enter the sea. The flow into the sea is very small. In the comprehensive management plan of the Yellow River Estuary, the fully open scheme is adopted for the tidal defense project of Diaokou River, i.e. the tidal dike will not be newly built within a certain range of the entrance, and the reserved width of the entrance is in principle the same as the width of the entrance of the current clear water ditch flow road. However, with the development of economy and society, it is necessary to protect most of the production facilities within the tidal dike, reduce the losses caused by storm surge disaster, and effectively protect the safety of life and property of the country and people. Since Qingshuigou River can run for more than 50 years, and considering that the downstream of Diaokou river is the swing range of the tail end after the

channel is opened, the space for erosion and retreat of the river mouth should be reserved to shorten the river length and reduce the feedback impact on the lower Yellow River. According to the research results of joint application of Qingshuigou River and Diaokou River, the maximum flow of Diaokou River can be controlled as 30m3 / s. Therefore, a tide gate is built in the existing main channel (i.e. the fourth river) outside the National Nature Reserve of the Delta and to the south of Zhuangcheng road. The gate discharge scale matches with the flow. It is smoothly connected with the backwater dike along the river to the West and to the second oil production team of pile 5 to the East At the end of tide dike, a tidal defense engineering system which can resist the storm surge once in 50 years is formed together with the sea access road, production road and tidal dam built by the oilfield. The system can transport water, sand and nutrients near the mouth gate at ordinary times, which is conducive to the utilization of water resources and the ecological environment protection of the delta.

Key words: Diaokou River, tide gate, backwater dike along the river, operation mode of flow path, tidal defense engineering

8th International Conference on the Application of Physical Modelling in Coastal and Port Engineering and Science
Zhoushan, China - Dec. 9th - 12th, 2020

LABORATORY MEASUREMENTS OF OVERTOPPING SPATIAL DISTRIBUTIONS UNDER THE EFFECT OF WIND

T Pullen[1], E Silva[1] and JG Zhou[2]

1 HR Wallingford, Wallingford, UK

2School of CMTD, Manchester Metropolitan University, UK

Wind effects on wave overtopping is an unresolved challenge in engineering practice due to lack of reliable assessment tools, which has become an increasing concern under climate change. Methods that enable engineers and practitioners to establish the extent of hazardous zones behind the crest of a seawall where overtopping is anticipated are therefore needed.

We report the results obtained during 2D physical modelling tests to collect spatial overtopping data under the influence of a range of wind velocities and discharges. The tests examined a generic section where waves lead to overtopping discharges becoming airborne and subsequently influenced by wind.

A bank of three phase wind generators were placed in the flume in-line with the test structure. They were positioned so that they could directly affect overtopping discharges as they exceeded the structure crest, causing the discharges to be blown leeward of the crest. A multi-chamber overtopping tank collected the discharges (see Figure 1), which recorded the spatial distribution in the lee of structure.

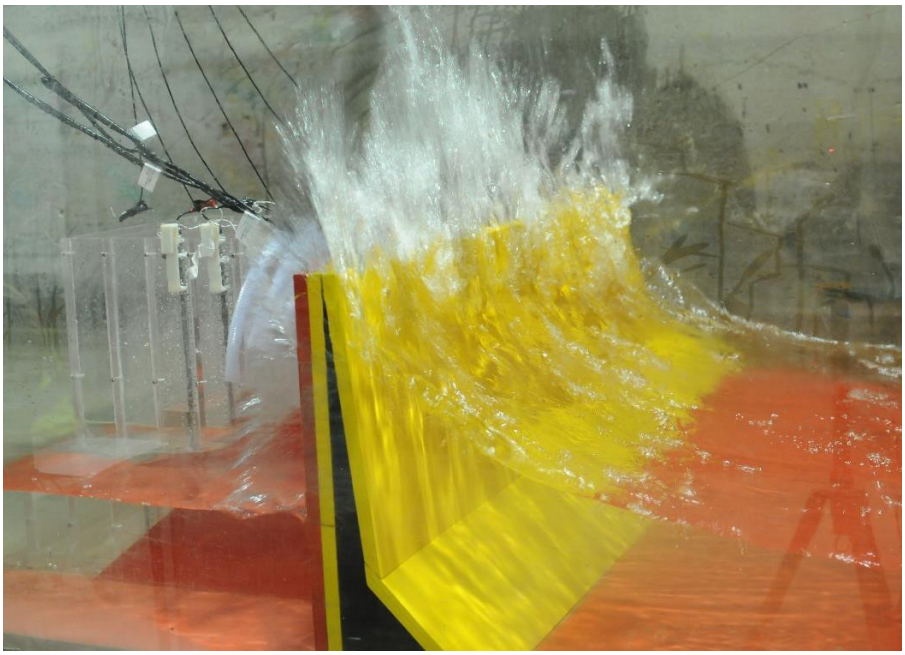

Figure 1. Airborne wave overtopping during flume tests and multi-chamber tank in the lee of the structure

Test conditions were selected so that only those waves impacting against the seawall were choosen. Impacting waves ensured that the discharges were directed vertically and would subsequently be effected by the wind.

Test conditions were selected from parametric and real wave data. A typical battered seawall, found on many UK seafronts vulnerable to overtopping, was chosen for the investigation. A total of

57 tests with different combinations of wave conditions and wind speeds were performed. Wave heights, Hm0, varied from 1.13 to 2.08m and peak wave periods, Tp, from 9 to 12s with four different sea water levels. Tests without wind, and two or three different wind velocities were performed.

The detailed analysis of the physical modellling data recorded is currently underway, but on an initial review, the influence of wind effecting the distribution of overtopping discharges leeward of the crest of the seawall, for one of the conditions tested, is shown in Figure 2. It is expected that the increase on overtopping due to wind is larger for low overtopping discharges, and this effect will decrease as the discharges increase.

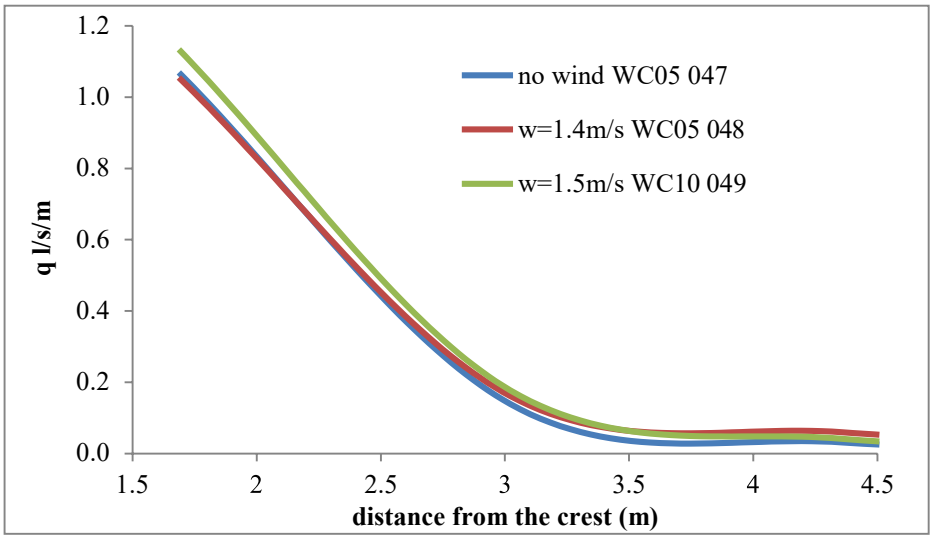

Figure 2. Spatial distribution of mean overtopping discharges for one of the tested conditions

Wave overtopping on a 2D physical model of a near-vertical seawall capturing the effect of wind on the measurements and distribution of the discharges has been measured successfully. The collected data should allow increased confidence in a method for assessing the extent of any potential hazards in the lee of a vertical or near- vertical seawalls. Scaling wind remains a challenge especially with regards to its effect on air-spray mixtures, where surface tension, viscosity and droplet size are the same for both prototype and model.

The physical model tests were part of a joint research developed with Manchester Metropolitan University (MMU). These model tests were further used in combination with numerical modelling simulations developed at MMU (also submitted as an abstract to this conference.

AKNOWLEDGEMENTS

The 2D physical model tests have been developed at HR Wallingford funded by the NERC Quantitative Assessment Tool for Concurrent Effect of Wind and Sea Level Rise on Wave Overtopping Seawalls.

REFERENCES

T. Pullen, W. Allsop , T. Bruce, J. Pearson, " Field and laboratory measurements of mean overtopping discharges and special distributions at vertical seawalls" Coastal Engineering, vol. 56, pp. 121-140, 2009.

Keywords: Laboratory measurements, Wave overtopping, Wind effect, Vertical-seawalls, Spacial distrubution.

8th International Conference on the Application of Physical Modelling in Coastal and Port Engineering and Science
Zhoushan, China - Dec. 9th - 12th, 2020

PHYSICAL AND NUMERICAL MODELING OF TSUNAMI AND STORM SURGE INUNDATION IN A COASTAL CITY

ZHONGDUO ZHANG[1], ANDREW KENNEDY[2], ANDREW COPP[3], NOBUKI FUKUI[4], NOBUHITO MORI[5], CHE-WEI CHANG[6], TOMOHIRO YASUDA[7], TAKASHI YAMAMOTO[8], YU CHIDA[9]

1 University of Notre Dame, USA, zzhang24@nd.edu
2 University of Notre Dame, USA, andew.kennedy@nd.edu
3 University of Notre Dame, USA, acopp@nd.edu
4 Disaster Prevention Research Institute, Kyoto University, fukui.nobuki.22s@st.kyoto-u.ac.jp
5 Disaster Prevention Research Institute, Kyoto University, mori@oceanwave.jp
6 Disaster Prevention Research Institute, Kyoto University, chang.chewei.5z@kyoto-u.ac.jp
7 Kansai University, tomo@oceanwave.jp
8 Kansai University, k198781@kansai-u.ac.jp
9 Port and Airport Research Institute, chida-y@p.mpat.go.jp

In the past decades, multiple devastating tsunami and storm surge event has shown that modern coastal cities are facing increased risk of coastal inundation hazards. It is necessary for researchers to study the behavior of water flow and inundation within a coastal urban area, to further accommodate the need for pre-disaster preparation and prevention of further casualties. This experiment used a physical model of a coastal city to simulate various wave conditions which may lead to city inundation. The goal of the experiment is to provide a better understanding on the variation of tsunami or storm surge inundation level at different locations of the city, and to develop an effective numerical model to increase the accuracy of current hazard maps and evacuation plans, eventually reducing casualties and financial losses.

The experiment was conducted in the Hybrid Tsunami Open Flume in Ujigawa Open Laboratory (HyTOFU) at Kyoto University. The physical model used in the experiment was a 1/250 model of the city center of Kainan, Wakayama, with a width of 4.0m and a length of 8.0m. The wave generator in the laboratory could produce various wave conditions to accommodate different flooding situation. In this experiment, the applied conditions were solitary waves with wave height of 5cm and 6cm, constant water flows with flow rate of 0.015, 0.020, 0.035, and 0.080 m3/s, and Nankai trough tsunami conditions with normal estimated wave height and wave height $\sqrt{2}$ times greater than the estimate. In total 8 wave gauges were set up at different locations across the city such as port, industrial and residential zones. After the experiment, LIDAR scanning was conducted on the physical model to obtain the topography of the model.

The results from wave gauges provided the time variation of water level in the inundation event. The maximum inundation, as well as the time to reach maximum inundation of each wave gauge location was collected. The wave gauge results display that the maximum inundation and the required time to reach that may depend on various factors, including the distance from the location to coastline, density as well as height of buildings surrounding the location, etc. The DEM data from the LIDAR scanning further provided ground elevation of each wave gauge location, which was useful for wave gauge data calibration, and the relationship between the maximum inundation and the building pattern. Based on the initial wave input and elevation data, numerical modeling using a sub-grid model based on shallow water equation was also conducted, and the results from physical experiment and numerical modeling were compared to examine the accuracy of the numerical model. More results and information will be available at the conference.

Key Words: coastal inundation, numerical modeling, sub-grid model, tsunami, storm surge

8th International Conference on the Application of Physical Modelling in Coastal and Port Engineering and Science
Zhoushan, China - Dec. 9th - 12th, 2020

DYNAMICS OF SUSPENDED SEDIMENTS IN THE YELLOW RIVER ESTUARY

Yueying Zha[1], Li Li[1,2*], Zhiguo He[1,2], Yuezhang Xia[1,2]

1 Ocean College, Zhejiang Univ., Zhoushan 316021, China

2 State Key Lab. of Satellite Ocean Environment Dynamics (Second Institute of Oceanography, SOA, Hangzhou, 310058, China

Email: lilizju@zju.edu.cn

Suspended sediment dynamics played a key role in estuarine ecological environment and morphological evolution. The three dimensional sediment dynamics is studied using a fully calibrated numerical model. The model considers the contribution of sediment on stratification, sediment flocculation and sediment bottom boundary layer. The results showed that the velocity distribution of the Yellow River Estuary is closely related to the morphology. The estuary coastline protruded more sharply towards the sea, leading to more intensive convergence and higher speed of the tidal currents, under the interaction of tides and morphology. The spatial and temporal distribution of sediment concentration in the Yellow River Mouth changed periodically with tidal dynamics. The resuspended sediments would be re-spreaded due to the tidal currents and shear fronts, which were important for the formation of the erosion and deposition pattern in the Yellow River Delta.

Keywords：Yellow river estuary, FVCOM，sediments, transport , numerical simulation,

8th International Conference on the Application of Physical Modelling in Coastal and Port Engineering and Science
Zhoushan, China - Dec. 9th - 12th, 2020

LARGE EDDY SIMULATION OF THE HORIZONTAL-AXIS TIDAL CURRENT TURBINE BASED ON ACTUATION LINE MODEL

RENWEI JI[1], KE SUN[1*], ZHIJIA SUO[1], YANG YI[1], QIHU SHENG[1]

1 College of Shipbuilding Engineering, Harbin Engineering University, Harbin 150001, China
** Corresponding Author: Ke Sun*
** Corresponding Email: sunke@hrbeu.edu.cn*

This paper introduces the actuation line model(ALM) of the horizontal-axis tidal current turbine(HACT) with high accuracy and low calculation cost. The core idea of the ALM is to simplify the HACT into a line with radial force distribution in the flow field. The ALM is used to simulate the effect of the HACT on the flow field, and the Navier-Stokes equation is solved to obtain the hydrodynamic characteristics of the wake field. Compared with the three-dimensional CFD numerical simulation of the full geometry real blade, the ALM combines the blade element momentum theory(BEM) with the CFD method. This method does not need to model the blade, avoids solving the surface boundary layer of the real blade, greatly reduces the number of meshes required, and saves the computing resources and computing time. Firstly, This paper is based on the OpenFOAM open source software platform, self-compiled ALM library functions, and combined with the pisoFoam solver to form a custom solver pisoFoam-ALM-HEU that can solve the HACT wake field. Combined with the large eddy simulation method, the numerical simulation of S809 type HACT independently designed by HEU is carried out by using the solver. The simulation results of the ALM model are compared with the experimental data of the real HCAT pool model. The results show that the thrust and power are in good agreement, which proves the correctness of the solver. Secondly, the effects of different parameter selections on the numerical simulation results in the pisoFoam-ALM-HEU solver are explored in detail. Finally, the hydrodynamic characteristics and the difference in wake field of the HACT at different blade tip speed ratios are analyzed. The research results can provide basis and reference for the numerical simulation of large-scale tidal energy array farm.

Key Words: Actuation line model(ALM); Large eddy simulation; Horizontal-axis tidal current turbine(HACT); Wake field; Hydrodynamic performance

Acknowledgement

The authors would like to acknowledge the support of National Natural Science Foundation of China (Projects No. 11572094, No. 51761135013 and No. 51979062). In addition, One of the author (Renwei Ji) wants to acknowledge the CFD-China community for the fruitful OpenFOAM-related discussions.

8th International Conference on the Application of Physical Modelling in Coastal and Port Engineering and Science
Zhoushan, China - Dec. 9th - 12th, 2020

EXPERIMENTAL AND NUMERICAL INVESTIGATION OF WAVE DEFORMATION AROUND HEAVING HORIZONTAL PLATE BREAKWATER

HENG JIN[1,2,*], RUIYIN SONG[3]

1 Ningbo Institute of Technology, Zhejiang University, China, jinheng@nit.zju.edu.cn.

2 Ningbo Research Institute, Zhejiang University, China, jinheng@nit.zju.edu.cn.
3 Ningbo Institute of Technology, Zhejiang University, China, ruiyinsong@163.com.

In recent years, floating breakwaters are considered for protecting the offshore engineering structures in the deep sea. Further, expand the capabilities of the horizontal plate breakwater, an elastic supported horizontal plate (ESHP) breakwater is carried out as an eco-friend and high energy dissipation structure. A submerged horizontal plate can reduce the transmission coefficient of the structure significantly by utilizing the shallow water deformation of the wave [1]. However, allowing the horizontal plate to move vertically could be more efficient in wave-blocking than the fixed structure [2].

As the additional layer of breakwater may improve the wave dissipation ability for low-frequency and wideband waves [3]. To further understand the wave blocking mechanism of ESHP breakwater for different wave frequencies. In this study, the wave dissipation effect of two submerged layers of ESHP breakwater is investigated firstly with experimental tests. After careful verification, OpenFOAM (version v1906) solvers interFoam and its variant overInterDyMFoam are used to produce the wave motion in this work. Then the hydrodynamic coefficients and the wave force acting on the breakwater are analyzed numerically with a variable stiffness of support spring and wave conditions. The movement of the heaving plate can be simulated by the dynamic mesh and multi-body coupling connection. The experimental study shows that the interaction between the radiation wave of the heaving plate and scattered waves causes additional vortex flow, and the wave height reduced rapidly at the lee side of the breakwater. With the numerical investigation of the wave deformation and velocity field distribution around the structure. Then the wave dissipation mechanism of ESHP breakwater for incident waves with different frequencies is discussed. At last, the wave force changes due to plate motion are also revealed to ensure the robustness of the structure.

Key Words: breakwater; wave deformation; heaving horizontal plate; wave dissipation; wave force

References:

[1] YU, X., 2002, "Functional Performance of a Submerged and Essentially Horizontal Plate for Offshore Wave Control: A Review," Coast. Eng. J., **44**(02), pp. 127–147.

[2] He, M., Xu, W., Gao, X., and Ren, B., 2018, "SPH Simulation of Wave Scattering by a Heaving Submerged Horizontal Plate," Int. J. Ocean Coast. Eng., **1**(2), p. 1840004.

[3] Fang, Z., Xiao, L., Kou, Y., and Li, J., 2018, "Experimental Study of the Wave-Dissipating Performance of a Four-Layer Horizontal Porous-Plate Breakwater," Ocean Eng., **151**(January), pp. 222–233.

8th International Conference on the Application of Physical Modelling in Coastal and Port Engineering and Science
Zhoushan, China - Dec. 9th - 12th, 2020

NUMERICAL INVESTIGATION OFTHE LOCAL SCOUR PROCESS ROUND BRIDGE PIERS

YIZHOU XIAO[1], GUILIN PAN[2], XIANDAO FENG[3]

1 CCCC Second Harbor Engineering Company LTD, Key Laboratory of Large-span Bridge Construction Technology China, Research and Development Center of Transport Industry of Intelligent Manufacturing Technologies of Transport Infrastructure, CCCC Highway Bridge National Engineering Research Centre Co. LTD, China, xiao_yizhou@163.com

2 CCCC Second Harbor Engineering Company LTD, Key Laboratory of Large-span Bridge Construction Technology China, Research and Development Center of Transport Industry of Intelligent Manufacturing Technologies of Transport Infrastructure, CCCC Highway Bridge National Engineering Research Centre Co. LTD, China, 1368539596@qq.com

3 CCCC Second Harbor Engineering Company LTD, Key Laboratory of Large-span Bridge Construction Technology China, Research and Development Center of Transport Industry of Intelligent Manufacturing Technologies of Transport Infrastructure, CCCC Highway Bridge National Engineering Research Centre Co. LTD, China, 1403438483@qq.com

Scour of sediments around bridge piers by the flow is the most significant contributing factor for bridge failures. The aim of this study is to assess the simulation and prediction of scour processes, both hydrodynamically and morphologically, around vertical round ended piers. The RNG $k-\varepsilon$ turbulent model is employed to capture turbulent performances. Firstly, the simulations at previous experimental flow conditions in the literatures are conducted, and results obtained from simulations agree well with the experimental data, thus validating the numerical reliability. The hydrodynamic and morphological characteristics are acquired, including the velocity distributions of cross-sections, turbulent characteristics and the scour depth near bridge pier. Additionally, the instantaneous scour process around piers are evaluated. This study indicated that a 3D hydromophological model can predict effectively the scour depth around bridge piers.

Key Words: scour of bridge piers; numerical simulation; scouring-depth

8th International Conference on the Application of Physical Modelling in Coastal and Port Engineering and Science
Zhoushan, China - Dec. 9th - 12th, 2020

EXPERIMENTAL STUDY OF PHYSICAL INTERACTION ACROSS THE AIR-SEA INTERFACE USING COUPLED PARTICLE IMAGE VELOCIMETRY

BYOUNGJOON NA[1], SANGYOUNG SON[2], KUANG-AN CHANG[3]

1 Research Institute for Mega Construction, Korea University, South Korea, bjna420@gmail.com
2 School of Civil, Environmental and Architectural Engineering, Korea University, South Korea, sson@korea.ac.kr 3 Zachry Department of Civil Engineering, Texas A&M University, USA, kchang@tamu.edu

Ocean waves play major role in setting the global and local climate as they influence the heat and mass transfer between the oceans and the atmosphere, are strongly affected by extreme weather events, and have tremendous impact such as on safety of maritime transportation, coastal structures, leisure activities, maritime agriculture. Alleviating atmospheric climate change by absorbing and storing heat strongly depends on the exchange processes of mass, momentum, and energy at the ocean surface boundary layer (OSBL; upper ~50 m of the ocean). However, in coupled ocean-atmosphere models (e.g. HadCM3, EdGCM, GFDL CM2.X, ARPEGE-Climat), it is usually assumed that the momentum flux into ocean is equal to the flux from the air (i.e. wind stress) neglecting the effects of small-scale dynamics at the wavy air-sea interface. Recent studies have questioned this assumption and revealed that drag depends not only on the wind speed but also the surface wave conditions (e.g. wave height, wave slope, wave age, fetch, gustiness). Moreover, in the aforementioned climate models, turbulence parametrizations on the water side are missing the key component: the surface-wave driven processes. In a changing climate, the distributions of both wind and waves, and their relative importance in driving ocean mixing, are likely to change. Thus, there is a clear need to provide observational evidence of wind-wave-turbulence processes. As a crucial step toward this goal, a series of laboratory and field experiments are to be conducted.

The technical objectives of the current study include the design, test, and application of a field-ready coupled air-sea boundary Particle Image Velocimetry (PIV) system, which is capable of simultaneously measuring the flow structure in the air and in the water. The desired system will reliably resolve the wavy water surface, which then allows the profiles of turbulence parameters to be obtained on both sides. To achieve simultaneous measurement, the system will essentially consist of two synchronized PIV systems to each side of the air-sea interface. The light sources will be two high-performance lasers with different wave lengths considering different temporal resolutions sufficient to provide accurate estimations of turbulent kinetic energy in air and water flow. Narrow band optical filters with corresponding laser wave lengths will be used to eliminate background light and the laser light from the other side of the interface. Once the PIV system has been developed and proven in the laboratory, the system is subsequently morphed to in-situ coupled PIV which is capable of measuring velocity fields in the field.

The experiment is to be conducted in the new Environmental Fluid Dynamics Laboratory (EFDL) housed in the Department of Civil Engineering at Texas A&M University, USA by the support of Korea Research Foundation (Grant number: KRF R1915701). The wind-wave-current flume is 28 m long, 0.8 m wide, and 1.0 m height with a piston-type wavemaker of ±0.3 m stroke and a 1:5 sloping beach covered with horsehair are placed at each end of the flume. EFDL is equipped with a Dantec 6-channel hotwire system with one 3-D probe and three 1-D probes for air-flow velocity measurements. The lab also has four lasers (a 5W and a 15W diode lasers, a 5W Argon-Ion laser, and a dual-head 400 mJ/pulse Nd:YAG laser) and three high-speed cameras (all Vision Research M340).

Key Words: PIV, Air-sea interaction, momentum flux, turbulence, EFDL

8th International Conference on the Application of Physical Modelling in Coastal and Port Engineering and Science
Zhoushan, China - Dec. 9th - 12th, 2020

FREAK WAVE IMPACT ON A FLOATING PLATFORM IN THE SMALL-AIR-GAP CONDITION

MIN LUO[1], XIN WANG[1], SAIYU YUAN[2], PENGZHI LIN[3]

1 Zienkiewicz Centre for Computational Engineering, College of Engineering, Swansea University, United Kingdom, min.luo@swansea.ac.uk, 1914744@swansea.ac.uk

2 State Key Laboratory of Hydrology-Water Resources and Hydraulic Engineering, Hohai University, China, yuansaiyu@hhu.edu.cn

3 State Key Laboratory of Hydraulics and Mountain River Engineering, Sichuan University, China, cvelinpz@126.com

Freak waves, also known as rogue or monster waves, are characterized by unusually large wave height and can appear suddenly in most of the places in the sea. The most spectacular sighting in recent years is the "New Year Wave", which hit Statoil's Draupner gas platform in the North Sea on New Year's Day of 1995 with a wave height of nearly 26 m. Freak waves can cause large slamming forces and massive overtopping, posing a great danger to the operational safety of marine structures like oil/gas platforms and ships. Such damaging effects are exacerbated by the global climate change and the accompanied more frequent occurrence of extreme ocean events. In this context, this study looks into the freak wave impact on a floating platform structure.

For offshore/deep-water platforms, the air gap is an important parameter in affecting the wave impact loads and overtopping. Some researchers studied the regular/irregular wave actions on fixed box-shape structures in different deck elevations. To name just one, the work in [1] found that the horizontal force increased with the decrease of the deck elevation from air to water, while the maximum vertical force occurred when the structure was positioned at the still water level. Recently, the freak wave impacts on a fixed box-shape structure have been investigated, focusing on the peak pressure/force [2] and the negative pressure (suction effect) [3]. Although significant findings have been made for fixed structures, researches on floating structures are still limited especially those related to freak waves. Another practical issue is that the floating platform may suffer from the operation weight beyond design. This combined with the water level run-up during an extreme wave event will lead to a lower air gap than the design. Special attention should be paid to this situation because a small air gap may result in more intensive wave loads, structural motions and overtopping.

Therefore, this study examines the freak wave impact on a floating platform in the small-air-gap condition, through carefully controlled wave flume experiments. The wave profiles during the wave impact process, the wave impact pressures on the vertical, bottom and top walls of the upper deck of the platform, the six-degree-of-freedom structural motions and the forces in the platform tethers will be measured simultaneously. The characteristics of these measurements including the overall trend and magnitude will be discussed and compared with those in normal air-gap conditions.

Key Words: freak wave; floating platform; air gap; wave impact; platform motion; tether force

References

[1] Park H, Tomiczek T, Cox DT, van de Lindt JW, Lomonaco P. Experimental modeling of horizontal and vertical wave forces on an elevated coastal structure. Coastal Engineering. 2017;128:58-74.

[2] Yan B, Luo M, Bai W. An experimental and numerical study of plunging wave impact on a box-shape structure. Marine Structures. 2019;66:272-87.

[3] Sun P-N, Luo M, Le Touzé D, Zhang AM. The suction effect during freak wave slamming on a fixed platform deck: Smoothed particle hydrodynamics simulation and experimental study. Physics of Fluids. 2019;31:117108.

8th International Conference on the Application of Physical Modelling in Coastal and Port Engineering and Science
Zhoushan, China - Dec. 9th - 12th, 2020

SALINITY INTRUSION RESPONSE TO DIFFERENT DYNAMIC MECHANISMS IN THE PEARL RIVER DELTA

ZHOU RONGXIANG[1], ZHANG WEI[2], JI XIAOMEI[3]

1College of Harbor, Coastal and Offshore Engineering, Hohai University, China, zrx@hhu.edu.cn

2State Key Laboratory of Hydrology-Water Resources and Hydraulic Engineering, Hohai University, zhangweihhu@126.com

3College of Harbor, Coastal and Offshore Engineering, Hohai University, China, vastocean@hhu.edu.cn

The topography of the Pearl River Estuary has mixed features of channels, shoals, deep trough and tidal flats, impacted by multichannel river system with many intersections and bifurcations. In recent years, with the rapid development of economy, the intensive human activities led to dramatic morphological changes. Under the influence of climate change and human activities, salinity intrusion in the Pearl River Delta (PRD) has obviously been intensified. In this study, a coupled 1-D river networks and 3-D estuarine combined numerical model has been established to evaluate the influence of different dynamic mechanisms on salinity intrusion in the river networks. The variation of salinity intrusion length (SIL) was analyzed under a series of upstream discharge at the main control nodes of the Pearl River networks. Moreover, the changes of salinity intrusion in PRD under the impacts of topography change and sea level rise are compared. It manifested that SIL has the negative correlation with river discharge, which means that SIL decreases with increasing river discharge. Furthermore, it is quite interesting to notice that the SIL is also quite relative to the flow division ratio at the delta apex. Under the same upstream discharge, the higher the flow division ratio, the smaller the SIL, which would be quite useful to the authority to transfer the water to control the salinity intrusion in Pearl River networks. The set of bathymetry data of 2001 and 2010 have been used to simulate the SIL, which in 2010 was 24 km further upstream than that in 2001. Meanwhile, the SIL increases only about 3 km when sea level rises by 30 cm. It displays that the impacts of human induced topography change overwhelm the effects of sea level rise considerably under the same boundary conditions. Besides, SIL depicts a positive correlation with the tidal range. Our research may expand and deepen the understanding of the salinity intrusion in the PRD, which has important practical significance.

Key Words: salinity intrusion; the Pearl River networks; bathymetry change; sea level rise; flow division ratio

8th International Conference on the Application of Physical Modelling in Coastal and Port Engineering and Science
Zhoushan, China - Dec. 9th - 12th, 2020

STUDY ON INTERACTION BETWEEN WAVE AND DENSE-ROW PILE BREAKWATER

YIFENG ZHANG[1], CHUNGUANG YUAN[1] HUALIANG XIE [1]

1 Tianjin Research Institute for Water Transport Engineering of Ministry of Transport, China, haizhongniao163.com

Dense-row pile breakwater is a common type in ocean engineering in recent years. In order to analyze the interaction between wave and dense-row pile breakwater, the wave transmission coefficient of breakwater with different pile spacing is studied by physical model method. and the influence of pile spacing, wave height, period and water depth on the wave permeability coefficient is clarified. At the same time, the wave force distribution of piles is studied, and it is pointed out that under certain conditions, the wave trough pressure is greater than the wave peak pressure.

Key Words: Dense-row pile; breakwater; physical model; wave transmission

8th International Conference on the Application of Physical Modelling in Coastal and Port Engineering and Science
Zhoushan, China - Dec. 9th - 12th, 2020

THE 3-D NUMERICAL SIMULATION SAND DATA ASSIMILATION OF THE SEATEMPERATURE IN THE NORTHERN SOUTH CH IN A SEA

Hui Shen1, Zhiguo He1,3*, Jianlong Li2, Li Li1,3

1 Institute of Port，Coastal and Offshore Engineering,Ocean college, Zhejiang University, Zhoushan, 316021, China
2 College of Information Science and Electronic Engineering, Zhejiang University,Hangzhou 310027, China
3 State Key Laboratary of Satellite Ocean Environment Dynamics (Second Institute of Oceanography, MNR), Hangzhou, 310058, China Corresponding author : hezhiguo@zju.edu.cn*

The three-dimensional structure of temperature and salinity plays an important role in understanding the heat and mass balance, mixing, diffusion and stratification of ocean water. ENKF and4DVARS were used to fuse multi-source observation data into the ocean dynamic models to systematically adjust the model parameters and to minimize the errors between the observed and simulated values. The results suggest that the relative error of SST in the entire model domain decreased by 0.2%, from 6.28% to 6.08%, after the assimilation was adopted in the ocean dynamic model. In the field work areas, the relative error was reduced from 5.76% to 5% after data assimilation.

Keywords: Data Assimilation; water temperature; South China Sea; Glider; FVCOM

8th International Conference on the Application of Physical Modelling in Coastal and Port Engineering and Science
Zhoushan, China - Dec. 9th - 12th, 2020

EXPERIMENTAL AND NUMERICAL STUDY ON A NOVEL DOUBLE-CYLIDER DOUBLE-PLATE BREAKWATER

XIAOYUN CHEN[1], DANJUAN FU[2], BIJIN LIU[3], ZHENWEI ZHANG[4]
HEPING YUAN[5]

1 Xiamen University of Technology, Xiamen, China, xychen_xmut@163.com
2 Xiamen University of Technology, Xiamen, China, fudanjaun@xmut.edu.cn
3 Xiamen University of Technology, Xiamen, China, 94709585@qq.com
4 Xiamen University of Technology, Xiamen, China, zwzhang@live.cn
5 Xiamen University of Technology, Xiamen, China, yuanhp@xmut.edu.cn

Experimental and numerical investigations of regular waves interacting with a double-cylinder double-plate breakwater are presented in this paper. The physical model test is carried out in a 35m long, 0.7m wide and 0.8m deep wave flume in the laboratory of Port and Coastal Engineering, Xiamen University of Technology. Based on the Navier-Stokes equations for viscous, incompressible fluid and Volume of Fluid (VOF) method, a numerical wave tank is established. The wave is generated on the basis of boundary values and absorbed by employing a wave-damping function. Both the experimental and numerical results show outstanding wave attenuation performance of the proposed breakwater, where the transmission coefficient could be lower than 0.4 under short waves. Furthermore, the influences of wave height, wave period, submerged depth and cylinder diameter on the wave forces are discussed in detail. The results have demonstrated the wave elimination ability and stability of double-cylinder double-plate breakwater, which ensures its application in ocean engineering.

Key Words: double-cylinder double-plate breakwater, experimental test, numerical wave tank, wave attenuation performance, wave force

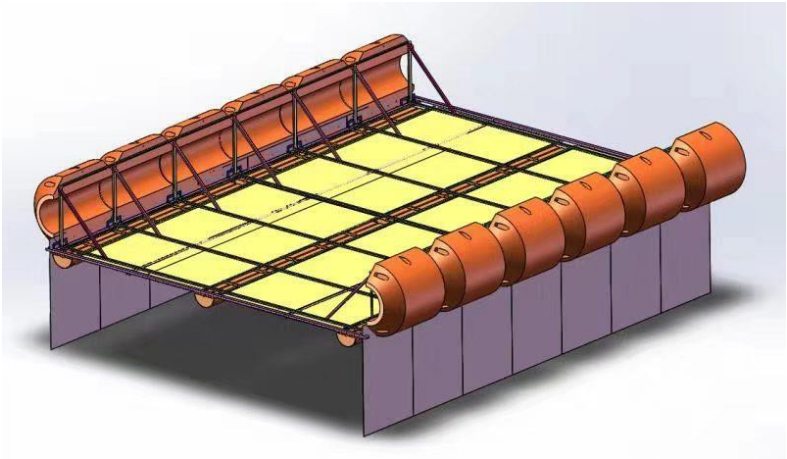

Fig. Model of a double-cylinder double-plate breakwater

8th International Conference on the Application of Physical Modelling in Coastal and Port Engineering and Science
Zhoushan, China - Dec. 9th - 12th, 2020

PROPAGATION AND TURBULENCE CHARACTERISTICS OF CONTINUOUS-FLUX RELEASE GRAVITY CURRENTS OVER ROUGH BEDS

Dongrui Han[1], Yintien Lin[2], Zhiguo He[3]

1 zhejiang university, china, 21734097@zju.edu.cn

2 zhejiang university, china, kevinlin@zju.edu.cn

3 zhejiang university, china, hezhiguo@zju.edu.cn

In both nature environment and hydraulic engineering, the phenomenon of gravitycurrent exists widely. In practical conditions, most riverbeds and seabeds are covered with sediment particles, which can be regarded as rough beds conditions. Therefore, it is of practical scientific significance and engineering application value to study the dynamic characteristics of gravity current flowing over rough beds. Through flume experiments for continuous-flux saline and turbidity currents, the propagation characteristics such as the current front position and entrainment coefficient, the turbulence characteristics such as turbulent kinetic energy (TKE) and turbulent bursting were analyzed. The velocity profiles and concentration profiles were also discussed to further understand the time-averaging characteristics of those currents. The results showed that the presence of rough bed had no significant influence on the buoyant jet phase of the current, but the duration of the inertial phase was shortened. For particle-driven type (turbidity currents), it was easier to enter the viscous phase than composition-driven type (saline) with the same conditions. In our study, the measurement of concentration was replaced by the backscatter acoustic intensity of particles in the sample volume of acoustic doppler velocimetry (ADV). When currents flowing over the rough beds, some influencing mechanisms such as “additional friction”, “additional mixing”, “concentration redistribution”, will jointly determine the mixing level between gravity current and ambient fluid. With the same initial current concentration and bed roughness, the overall TKE value of turbidity currents was less than that of saline, which indicated that sediment deposition inhibited the generation of turbulence. With the increase of bed roughness, the minimum point of TKE profiles gradually rose and its value aggrandized. The vorticity values in the upper part of the gravity current were positive. However, the vorticity value in the the lower part was positive and negative alternately. The combined influence of the wall boundary conditions and the friction of the bed resulted in the appearance of negative values, while the positive values was due to the rough beds influenced the distribution of the flow field and changed the local turbulent structure of the gravity current which illustrated by the power spectral density. The study of turbulence bursting revealed that intermittent bursting events played an important role in the momentum and component exchange process of gravity current. The presence of rough bed could result in a more complicated motion and fluid structure of the gravity currents.

Key Words: gravity current; rough bed; propagation characteristics; turbulence characteristics

8th International Conference on the Application of Physical Modelling in Coastal and Port Engineering and Science
Zhoushan, China - Dec. 9th - 12th, 2020

THE CHARACTERISTICS ON PROCESS OF RUNOFF AND SEDIMENT AT DATONG STATION AND BED EVOLUTION IN THE SOUTH AND NORTH CHANNEL OF THE YANGTZE ESTUARY

WENTAO LEI[1], GENG QU[1], WEINA KONG[2], ZHAOHUI CHAI[1]

1 Changjiang River Scientific Research Institute, China, leiwt86@163.com

2 Hubei Provincial Water Resources and Hydropower Planning Survey and Design Institute, China

In this study, investigations on the characteristics of runoff and sediment transport process in the the Yangtze Estuary are conducted, based on observed runoff and sediment transport time series data from representative hydrological station of Datong during 1952-2018. Non-parameter statistical methods such as the moving average statistics, Mann-Kendall test, Spearman order correlativity and wavelet analysis are all employed. Therefore, the trend, variability and periodicity characteristics are investigated, respectively. The trend and variability analysis results show that the annual runoff volume (ARV) decreased significantly in several years during 1950s to 1970s and generally slightly increased during 1980s to 1990s as well as significantly increased in 1998. In recent years, ARV slightly increased after 2006. The annual sediment load (ASL) decreased slightly from 1964 and showed significantly decrease after 1998. The average annual ASL during 1952-1998 was around 4.36×10^8t and decreased 62% during 1999-2018. The Morlet wavelet analysis results indicate that significant periodicities of 4-5 years, 8-11 years and 19-24 years at different scales in ARV time series, as well as periodicities of 3-5 years, 9-14 years and 21-24 years at different scales in ASL time series. Then topographic maps surveyed in several years are also collected to generate DEM and evaluate the change feature of the thalweg and channel planform during the recent years in 1997-2017. It can be seen that the main thalweg in the South Channel tended to move towards the south bank in 1997, then the middle reach of the thalweg moved north at about 300 meters in 2004, and the thalweg evolved generally towards south during 2010-2017 under influences of artificial dredging and fluvial process. Besides, the bed evolution analysis on the North Channel shows that north side of the main course in the upper reach was scoured whereas deposition occurred in the south side during 2012-2017, while the lower reach was generally scoured towards downstream.

Key Words: Yangtze Estuary; North and South Channel; runoff and sediment transport; bed evolution

8th International Conference on the Application of Physical Modelling in Coastal and Port Engineering and Science
Zhoushan, China - Dec. 9th - 12th, 2020

THE KEY TECHNOLOGY OF TIDAL LEVEL CONTROL IN THE YELLOW RIVER ESTUARY PHYSICAL MODEL

FAN YAOSHEN[1,2], DONG NIANHU[1,2], DOU SHENTANG[1,2], YU SHOUBING[1,2]

1. Yellow River Institute of Hydraulic Research, YRCC, Zhengzhou 450003, China;
2. Key Laboratory of Yellow River sediment, Ministry of water resource, Zhengzhou 450003, China

The simulation and control of tidal dynamics are the key part of the Yellow River estuary physical model. The tidal types of the Yellow River estuary are very complex, including irregular semidiurnal tide and irregular diurnal tide, with an average tidal range of about 1 m, belonging to the weak tidal estuary. The tide level changes rapidly with time, and has the properties of strong unsteady and non-uniformity. In addition, the observation data are few and unsystematic. How to improve the reliability and accuracy of tide level control technology according to these characteristics is the key problem of the Yellow River estuary physical model. Based on the characteristics of the hydrodynamic and sediment transport in the Yellow River estuary, the physical model was made according to the horizontal scale of 1:600 and the vertical scale of 1:60. By analysing the tidal parameters at the boundary of the physical model, such as tidal level, tidal phase and tidal period, which represent the tidal dynamic process in the Yellow River estuary, we determined the layout scheme of reversible pump and the roughening mode of the transitional moving bed, and put forward reasonable key technologies of tidal level control in model area. It is found that 8 constant-frequency reversible pumps are arranged on the boundary parallel to the coast, 12 variable-frequency reversible pumps are arranged on the left and right boundaries perpendicular to the coast, and the roughness of moving bed is changed by laying model sand of different grain size, which can realize the simulation of tidal level control in the Yellow River estuary physical model.

Key words: Yellow River estuary; physical model; tidal level control; tidal dynamic

8th International Conference on the Application of Physical Modelling in Coastal and Port Engineering and Science
Zhoushan, China - Dec. 9th - 12th, 2020

FREQUENCY DOMAIN ANALYSIS OF HYDRODYNAMIC CHARACTERISTICS OF MARICULTURE SHIP WITH TRUSS AND PLATE FRAME HYBRID STRUCTURE

WANG SHAOMIN[1], YANG XIEQIU[1], YUAN TAIPING[1]

1 South China Sea Fisheries Research Institute， Chinese Academy of Fishery Sciences， Guangzhou, Guangdong，China， E-mail：wagnshaomin2013@163.com

In recent years, mariculture in deeper and farther waters has attracted much attention, and the optimal design and development of large-scale aquaculture facilities has become an urgent need. To study the hydrodynamic performances of a mariculture ship composed of truss structure and several floating bodies with plate and frame structures, we analyzed the hydrodynamic characteristics of the ship based on three-dimensional potential flow theory and Morison theory. Through the analysis of hydrodynamic parameters and motion responses, we get the changing trend of the main performance of mariculture ship. The results show that the added mass and radiation damping of mariculture ship are sensitive to the change of frequency, and the sensitivity is obviously different in all motion directions. The added mass and radiation damping of rotational motion are larger than those of plane motion, which are closely relate to the structural type of mariculture ship. Under the action of incident waves in different directions, the first-order wave force on mariculture ship increases at first and then decreases with the increase of frequency, and the first-order wave force curve in high frequency section tends to be stable under the action of incident waves in different directions. There is a great difference in the medium and low frequency section. Under the conditions of high frequency and low frequency, the ship motion is small, but it resonates when encountering medium and short period waves. The surge and pitch of mariculture ship are the main motion modes in head or follow wave condition, and the roll and heave are the main modes of motion in the beam wave. This study lays the theoretical basis for optimal design of subsequent mariculture ship and the safe implementation of marine aquaculture facilities afterwards.

Key Words: Truss and plate frame hybrid structure; mariculture ship; hydrodynamic performance; Motion response

8th International Conference on the Application of Physical Modelling in Coastal and Port Engineering and Science
Zhoushan, China - Dec. 9th - 12th, 2020

HYDRODYNAMICS WITHIN NATURALAND RESTORED MANGROVES IN SOUTHEAST CHINA

YINING CHEN[1], TINGLU CAI[2], YANG CHANG[3]

1 Second Institute of Oceanography, MNR, China, yiningchen@sio.org.cn

2 Second Institute of Oceanography, MNR, China, caitlu@sio.org.cn
3 State Key Laboratory of Estuarine and Coastal Research, East China Normal University, China, YChang1994@outlook.com

Natural coastal wetlands, such as mangroves and saltmarshes, are now widely recognized as potential buffers to hydrodynamic forces, in addition to their global importance in ecosystem services. Mangrove trees have been reported to change the flows and dissipate turbulent energy due to the presence of aboveground biomass and aerial roots, although direct field observations are still limited.

Despite the valuable services that mangroves provide, human activities are gradually altering the area of mangroves worldwide. Mangroves in China are mainly distributed in the southeast coasts of the tropical and subtropical regions. The total area of mangrove plants in China declined significantly over last serval decades but rehabilitation work is currently being conducted in many locations to restore degrading, or create new mangroves.

Understanding the ability of mangroves to modify hydrodynamics allows the evaluation of coastal protection function, mechanism of degradation and the optimum condition of restoration. Therefore, in this study, we carry out *in situ* observations to investigate the influences of mangroves on hydrodynamics, within both natural and restored mangroves.

Two sites were selected for this study to deploy Acoustic Doppler Velocimeters and pressure sensors: a natural mangrove forest located in Zhangjiang Estuary and a restored mangrove forest in Yueqing Bay. In the former site, comparative observations between a mangrove edge and a bare mudflat were conducted to reveal the effects of mangroves on the hydrodynamics. For the latter one, lifting systems were invented to examine the influences of mangroves (mature stands and seedlings) on the vertical profiles. Both sites are sheltered from waves and thus we mainly look into tidal flows.

Field observations found that: 1) at a planar interface between natural mangroves and bare mudflat, the plants not only reduce flow speed and suppress turbulent energy, but also deflect tidal flows in a considerable magnitude; 2) the presence of mature mangroves in the restored site causes an ‘S’ shape in vertical velocity profile, differing remarkably from bare mudflats and saltmarshes; 3) planting mangrove seedlings has minimal influence on flow speed in comparison with bare mudflats, but a similar ‘S’ shape in vertical velocity profile has also been found; and 4) restored mangroves show less efficiency in decreasing flow magnitude compared with natural mangroves, however, they have considerable abilities in turbulent energy dissipation, even for small seedlings.

In summary, this study covers natural mangroves and restored mangroves in order to understand the influences of mangroves on hydrodynamics. The observations tell that the presence of mangroves have markedly changed the hydrodynamics, although difference exists between natural and restored mangroves. Turbulent energy dissipation is possibly an important process throughout the life cycle of grown mangroves and should be taken into account for future restoration.

Key Words: Hydrodynamics; Flows; Turbulent energy; Mangroves; Restoration

8th International Conference on the Application of Physical Modelling in Coastal and Port Engineering and Science
Zhoushan, China - Dec. 9th - 12th, 2020

EXPERIMENTAL AND NUMERICAL INVESTIGATION OF WAVE ATTENUATION BY FLEXIBLE VEGETATION

KAI YIN[1], SUDONG XU[2]

1 Department of Port, Waterway and Coastal Engineering, School of Transportation, Southeast University, China, yinkai@seu.edu.cn

2 Department of Port, Waterway and Coastal Engineering, School of Transportation, Southeast University, China, sudongxu@seu.edu.cn

The dynamic interactions between wave and flexible vegetation play an important role in coastal processes. Since coastal vegetation has a well-known effect on attenuating waves, investigating wave attenuation by flexible vegetation is fundamental to enhance the ability of disaster prevention and mitigation, promote ecological carrying capacity and build ecological security shelters. However, the interaction between flexible vegetation and wave has not been fully characterized up to now, especially when integrated into a wave propagation model. Therefore, it is essential to carry on more profound research in the force and motion of ecological vegetation as well as its principle of energy dissipation. To quantitatively examine the attenuation ability of flexible vegetation on wave height, wave flume experiment and numerical simulation are conducted in this study. Firstly, experimental studies on wave attenuation by flexible vegetation are carried out based on a wave flume at Hohai University. This wave flume is 80 m long, 1 m wide and 1.2 m deep. Three different types of vegetation as well as 26 regular wave conditions are utilized. Through comparing with measured data of experiments without vegetation, wave attenuation under cases of varying vegetation as well as wave conditions were determined. Furthermore, influence of different vegetation and wave parameters on wave attenuation is investigated. Secondly, force balance equation and its numerical solving algorithm for submerged single flexible vegetation forced by wave action are established, thus developing a flexible vegetation dynamic model under the effect of waves. Based on this model, a coupled flexible vegetation and wave interaction model is developed. Developed models are validated against measured data of wave flume experiments. Investigating results from this study would be conducive to advance the understanding of wave attenuation by flexible vegetation, thus promoting the development of ecological vegetation revetment.

Key Words: Wave attenuation; Flexible vegetation; Flume experiment; Numerical simulation

8th International Conference on the Application of Physical Modelling in Coastal and Port Engineering and Science
Zhoushan, China - Dec. 9th - 12th, 2020

HIGH-FIDELITY SIMULATION OF SOLITARY WAVE PROPAGATION AND EVOLUTION

YICHEN HUANG[1], ZHILIANG LIN[2], BIN XIE[3]

1 Shanghai Jiao Tong University, China, syuico@sjtu.edu.cn
2 Shanghai Jiao Tong University, China, xie.b.aa@sjtu.edu.cn
3 Shanghai Jiao Tong University, China, linzhiliang@sjtu.edu.cn

Solitary wave propagation and run-up is a critical issue of coastal hydrodynamics and coastal processes, which has been routinely used as a wave paradigm to study the hydrodynamic characteristics of tsunami wave and its devastating impact on coastal infrastructures, such as cylinders, breakwaters, seawalls, platforms and beachfront houses. However, it is a great challenge for numerical simulations based on the multiphase model that is required to capture the topologically deforming interface, to resolve the rapid jump in fluid properties such as density and to represent the complicated geometry of coastal structure. Moreover, most of the industry-standard solvers for wave problems are constructed from second-order schemes, which suffer from excessive numerical dissipation and dispersion for accurately resolving some important flow structures, like vortices, eddies and turbulence, and their influence to the coastal infrastructures. From the perspective of practical applications, a numerical solver which integrates the solution accuracy, computational efficiency and numerical robustness for high-fidelity simulations is still highly demanding.

Aiming at high-fidelity wave simulations, we have developed a sophisticated numerical model called MARS (MultiphAse solver based on high-fidelity Reconstruction Schemes) by solving Navier–Stokes equations on polyhedral unstructured grids. It is constructed based on our newly developed FVMS3 [1] (Finite Volume method based on Merged Stencil with 3rd-order reconstruction) and THINC/QQ [2] (Tangent of Hyperbola for INterface Capturing method with Quadratic surface representation and Gaussian Quadrature) schemes along with some attractive features such as consistent formulation of mass and momentum transport equation and balanced-force algorithm between pressure and gravity forces. Compared with conventional interFoam solver in OpenFOAM package, the present model provides high-fidelity simulations for free surface flows which undergo complicated topological changes and involve strong air/water interactions.

It is demonstrated by various numerical examples that this model can carry out high-fidelity simulations for solitary wave propagations on plane and sloping beaches with a great superiority in controlling numerical dissipation and dispersion. Energy loss is significantly restrained and waveforms are highly consistent with the reference solutions. Furthermore, the runup heights of the present model fully approach the reference solution for the two-dimensional inviscid flow, outperforming the previous results. Besides, we also simulate solitary wave problems involving complex geometries such as submerged plates or porous structure to explore the interactions between waves and solid structure in detail.

Key Words: high-fidelity; solitary wave; MARS; interface capturing

References

[1] B. Xie, X. Deng, S.J. Liao, High-fidelity solver on polyhedral unstructured grids for low-Mach number compressible viscous flow, Comput. Appl. Mech. Engrg. 357 (2019) 112584.

[2] B. Xie, F. Xiao, Toward efficient and accurate interface capturing on arbitrary hybrid unstructured grids: The THINC method with quadratic surface representation and Gaussian quadrature, J. Comput. Phys. 349 (2017) 415-440.

8th International Conference on the Application of Physical Modelling in Coastal and Port Engineering and Science
Zhoushan, China - Dec. 9th - 12th, 2020

SHORELINE CHANGE ALONG THE NAM DINH COAST (VIETNAM), INDUCED BY SUBSIDENCE AND SEA LEVEL RISE

NGUYEN HAO QUANG[1], SATOSHI TAKEWAKA[2]

1 Department of Engineering Mechanics and Energy, University of Tsukuba, 1-1-1 Tennodai, Tsukuba, Ibaraki, JAPAN, ri.nguyenri@gmail.com

2 Department of Engineering Mechanics and Energy, University of Tsukuba, 1-1-1 Tennodai, Tsukuba, Ibaraki, JAPAN, takewaka@kz.tsukuba.ac.jp

During the last hundred years, several sections along the Nam Dinh Coast, located in the Red River Delta of Vietnam, has been undergoing severe erosion. Vital agricultural area has vanished into the sea and families have been forced to abandon their houses due to the action of waves, leading to the loss of land along the coastline. Numerous studies have been done to finding out the major causes governing erosion problems, and several hypotheses are proposed: (i) the gradients in the longshore sediment transport rate, (ii) sea level rise (SLR) and increase of typhoons, and (iii) construction of dams upstream of the Red River system. This paper aims to examine another hypothesis that land subsidence combined with SLR is contributing to erosion in the middle portion of the Nam Dinh Coast, based on the one-line model. The simulated shorelines agree well with the measured shorelines from satellite data, Landsat images. Projections of future shoreline change are made further using SLR projections of the Intergovernmental Panel for Climate Change (IPCC), along with Representative Concentration Pathways (RCPs) 2.6 and 8.5. Results of sensitivity analyses show that most sections of the coast are expected to be slightly eroding to 2200 with the best-case scenario (RCP2.6), and severely eroding with the worst-case scenario (RCP8.5), except the northern and southern ends at estuaries where the shorelines are predicted to be continuously moving seaward.

Key Words: Nam Dinh Coast, shoreline, erosion, accretion, sea level rise, subsidence

8th International Conference on the Application of Physical Modelling in Coastal and Port Engineering and Science
Zhoushan, China - Dec. 9th - 12th, 2020

NUMERICAL SIMULATION OF CHLORIDE ION DIFFUSIONIN CONCRETE BASED ON STOCHASTIC CONVEX POLYGON COARSE AGGREGATE MODEL

YUANZHAN WANG[1], ZHEHUI ZHOU[1], ZHEN LIU[1], DUO WANG[2]

1 Tianjin University, china,yzwang@tju.edu.cn Tianjin University, china, 472195343@qq.com Tianjin University, china, zliu@tju.edu.cn

2 China Academy of Building Research, china, duowang1994@163.com

In the marine environment, the corrosion of steel in the reinforced concrete (RC) structure caused by chloride ion diffusion is one of the most significant factors affecting the durability of RC structures. Using physical model experiment method to explore the natural diffusion of chloride ion in concrete not only needs a lot of manpower, material resources, financial resources and time, but also is difficult to carry out long-term experimental research. Using numerical model simulation method is an efficient research method to save a lot of physical experiment costs. In this paper, a mesoscopic numerical model of chloride ion diffusion in concrete is established. In the mesoscopic numerical model, the concrete is regarded as a three-phase composite composed of cement mortar, coarse aggregate and interfacial transition zone (ITZ). Compared with the widely used extended convex algorithm, a more computationally efficient method, namely interpolation sorting algorithm, is proposed. This method can consider the influence of ITZ and generate convex polygon coarse aggregate randomly. The accuracy and reliability of the numerical model are verified by the comparison between the proposed model and the experimental data.

Key Words: concrete, chloride ion diffusion, mesoscopic numerical model, interpolation sorting algorithm

8th International Conference on the Application of Physical Modelling in Coastal and Port Engineering and Science
Zhoushan, China - Dec. 9th - 12th, 2020

SWASH FLOWS GENERATED BY BORES WITH VARIABLE LENGTH

Ignacio Barranco1 and Philip L.-F. Liu1,2,3

1Department of Civil and Environmental Engineering, National University of Singapore, Singapore
2School of Civil and Environmental Engineering, Cornell University, USA
3Institute of Hydrological and Oceanic Sciences, National Central University, Taiwan

Bores are ubiquitous in nature. For example, tidal bores can be found in upstream of many large river mouths (e.g. Qiantang River in China). Tsunamis have also been observed to reach coastal areas in the shape of undulating or broken bore. Large tsunamis are very long waves that can produce large inundations in coastal areas. It is expected that the crest length of tsunami-like bores will have an important role on the inundation and swash flows. The aim of this study is to analyze the flooding produced by bores with different bore lengths. Both laboratory experiments and numerical simulations are conducted with the aim to better understand the relations between the bores length and the swash flows, in terms of runup heights and inundation depths.

In this study we generate bores in a wave flume with a dam-break system in which the reservoir length varies. The total length of the flume is 36m and it is 0.9m high and 0.9m wide. At one end of the flume a 6m glass beach (1:10 slope) is installed. The maximum length of the reservoir is 17.6 m. To measure the swash flows, including the run- up and inundation depth, the flume is equipped with capacitance gauges, ultrasound sensors and a full HD camera.

Experiments are conducted using different bore strength and bore length. The inundation depth at the still water shoreline and the heights of moving shoreline are recorded. They are plotted against the bore strength and the normalized bore length in Figure 1. Since only a limited number of laboratory experiments can be performed in the parameter space, a numerical model, SWASH, is used to obtain additional data for a wider range of parameters. As shown in Figure 1, the agreement between experimental data and numerical results for the current laboratory set-up is quite good.

Based on the experimental and numerical results, the bore length has a significant influence in the swash processes. The results also suggest that for a specified bore strength there is a minimum bore length for which the inudation depth only depends on the bore strength and slope. More discussions on the findings will be presented in the meeting.

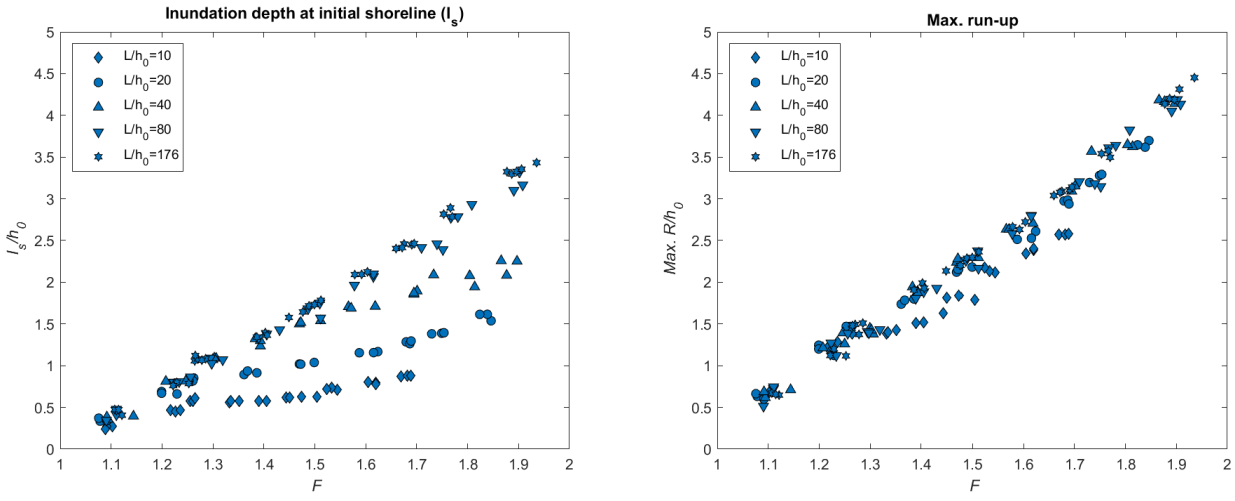

Figure 1. Dimensionless maximum inundation depths at the initial shoreline (left panel), and maximum dimensionless run-up (right panel), for bores generated with different reservoir length (Diamonds L_r = 1 m, circles L_r = 2 m, triangles L_r = 4 m, upside-down triangles, L_r = 8 m, and hexagrams, L_r = 17.6 m).

8th International Conference on the Application of Physical Modelling in Coastal and Port Engineering and Science
Zhoushan, China - Dec. 9th - 12th, 2020

STUDY ON THE RESPONSE MECHANISM OF SILTATION AND SLOPE IN THE DEEP WATER CHANNEL OF THE SILT COAST

XIAOTIAN DONG[1], WENJIN ZHU[1], XIAOFEI CHENG[1]

1 JiangSu Ocean University, China, 2018000040@jou.edu.cn 1 JiangSu

1 Ocean University, China, 377068140@qq.com

1 JiangSu Ocean University, China, 24267473@qq.com

The construction of deepwater navigation channel of the silt coast is faced with the problems of shallow slope, large digging deep navigation channel, short maintenance period and large silting amount, and it is of practical reference value to the construction of waterway engineering.

Based on the hydrodynamic equilibrium equation of sediment-laden flow, the formula of sediment carrying capacity is derived, which could be used in nearshore water. Fullly verification of sediment carrying capacity formula is conducted utilizing measured data, which means that the formula can be used in the calculation of marine sediment carrying capacity. Because the sediment carrying capacity formula takes account of seabed slope factor, it has unique advantage in the problem of silting of marine projects such as navigation channel and harbor construction.

According to suspended sediment transport equation and the deformation equation of the seabed, the formula of seabed erosion and deposition is derived combining sediment carrying capacity derived, and the different forms of the seabed erosion and deposition formula under different flow regions are discussed. The formula of seabed scouring and deposition is applied on calculation of silting in the ideal channel of various slope, and verifies the applicability of the sea-bed erosion and deposition formula. Using the obtained seabed silting formula, the back siltation of the channel of the Lianyun Port 300,000-ton waterway was calculated, compared with the measured data, the reliability of the formula was verified, and the back-silting characteristics of the deep water channel were further analyzed.

Key Words: nearshore sediment carrying capacity; seabed erosion and deposition; suspended sediment transport; numerical simulation;

8th International Conference on the Application of Physical Modelling in Coastal and Port Engineering and Science
Zhoushan, China - Dec. 9th - 12th, 2020

EFFECTS OF THREE GORGES DAM AND SEA LEVEL RISE ON TIDAL CURRENT ASYMMETRY IN THE YANGTZE RIVER ESTUARY

CHEN TING[1], ZHANG WEI[2]

1 College of Harbor,Coastal and offshore Engineering, Hohai University, China, 15150687661@163.com 2 State Key Laboratory of Hydrology-Water Resources and Hydraulic Engineering , Hohai University, China, zhangweihhu@126.com

Characterized by large seasonal discharges, Yangtze River Estuary (YRE) is of high interest due to its representative tidal estuarine network and increasing human activities, meanwhile, tendency of sea level rise is also obvious in the Yangtze River Delta. Different from the research conducted by predecessors, a two-dimensional flow model including the YRE and adjacent Hangzhou Bay was employed to simulate tidal currents of the estuary. Based on the information abstracted from the model, non-stationary harmonic analysis (NS_TIDE) was applied to analyse the variations of tidal amplitudes and tidal phases along the YRE. Tidal current asymmetry including peak current asymmetry (PCA) and slack water asymmetry (SWA) which are related to coarse and fine sediment transport was discussed then in this study. Taking the interactions of O1/K1/M2, M2/S2/MS4, and M2/M4 into consideration, we could find that the SWA presented flood dominance, consistent with tidal asymmetry, indicating the landward transport of fine sediments. However, the PCA transformed to ebb dominance, favoring the seaward transport of coarse sediment, reasons which could be used to explain this phenomenon are that when we took PCA into account, contributions of the residual flow could not be neglected and the YRE was famous for its large variable riverine discharge. For the PCA, it first increased, and then decreased upwards, the trends between dry and wet were somewhat different. For the SWA, the value was smaller in the dry than in the wet, indicating slower friction dissipation in the dry season. Discharge regulation of Three Gorges Dam led to seasonal alterations of tidal current asymmetry in the YRE. In the dry season, increasing river discharge led to increase of the PCA and decrease of the SWA in magnitude, while in the wet, the reduction of discharge led to slightly decrease of the PCA and increase of the SWA in magnitude. The rising sea level also led to variations of tidal asymmetries along the YRE as it could increase mean water depth significantly while change the amplitudes of tidal waves little. In dry season, stations downwards Xuliujing showed decrease in PCA and SWA in magnitude, while stations upwards Jiangyin showed increase of PCA, due to relative large river discharge in the wet season, the effect of SLR on the PCA was negligible, the changing sea level led to some significant changes of SWA.

Key Words: Yangtze River Estuary; tidal current asymmetry; Three Gorges Dam; Sea Level Rise

8th International Conference on the Application of Physical Modelling in Coastal and Port Engineering and Science
Zhoushan, China - Dec. 9th - 12th, 2020

TWO-PHASE SPH SIMULATIONS OF EROSIONAL DAM-BREAK FLOODS USING GRAPHICS PROCESSING UNITS

HUABIN SHI[1, 2]

1 State Key Laboratory of Internet of Things for Smart City and Department of Civil and Environmental Engineering, University of Macau, Macau S.A.R., China, HuabinShi@um.edu.mo

2 School of Engineering, University of Liverpool, Liverpool, UK, shihb180520@gmail.com

A two-phase SPH model based on a continuum description of solid-fluid mixtures is proposed for violent surface water flows induced by dam breaks on erodible beds. In the model, the water and the sediment are governed by t e conservative laws of mass and momentum. A constitutive law based on the rheology of dense granular flow is employed for the inter-granular stresses of sediment phase. An integrated formulation of the Ergun equation for dense solid-liquid mixtures and the power law for dilute suspensions is adopted for the inter-phase drag. The solid-liquid mixture is represented by a single set of Lagrangian SPH particles, which move with the water velocity while carry the quantities of both phases. The computations are conducted in parallel using Graphics Processing Units (GPU). The model is applied to erosional dam-break floods on movable beds of different initial configurations. The temporal evolutions of the water surface, the bed profiles, and the dam-break wave front are in good agreement with the measured data. Scaling laws of the wave front propagation with the water depth and the bed compositions are discussed. It is shown that the proposed model performs well in the simulations of intense sediment transport by violent free surface water flows.

Key Words: Two-phase SPH model; GPU computing; Erosion dam-break floods; Intense sediment transport; Free surface flows

8th International Conference on the Application of Physical Modelling in Coastal and Port Engineering and Science
Zhoushan, China - Dec. 9th - 12th, 2020

NONUNIFORM SUSPENDED SEDIMENT TRANSPORT EQUATION FOR COMBINED WAVE-CURRENT FLOWS

BAOZHEN JIA[1], DEYU ZHONG[1, 2]

1 State Key Laboratory of Hydroscience and Engineering, Tsinghua University, China, laojia@mail.tsinghua.edu.cn

2 Joint-Sponsored State Key Laboratory of Plateau Ecology and Agriculture, Qinghai University, China, zhongdy@mail.tsinghua.edu.cn

The combined interactions of wave and currents act as the main driven force for sediment transport in coastal areas, which still remains unclear and needs further investigation. This paper aims to present a new non-uniform sediment transport equation to apply for combined wave and current situation. On basis of two-phase flow theory, mass and momentum conservation equations for both of flow and sediment in different grain sizes are first presented, including the interactions between wave-current flow and particles and different particles themselves. Then a two-phase mixture model is further developed in combination of the equations for the different phases, retaining the basic flow and sediment characteristics. For closure of the equations, drift velocity is introduced as the relative velocity between each phase and the mixture flows. Rather than the direct numerical simulation, with the perturbation asymptotic method applied, the constitutive relation of drift velocity is explicitly derived. Transport equation is further developed in combination of mass conservation equation and the constitutive relation of drift velocity. Then the new transport equation is applied for wave-current flows to compute the vertical distribution of time-averaged concentrations for sediment mixtures over the plane bed. Compared to the classic Rouse equation, the suspension of the particles is not only attributed to the turbulent diffusion, but also to the particle inertia, inter-phase interaction and other forces. The turbulent diffusivity, as well as other driven forces are described as the compound function of the wave-related and current-related variables, which are determined with the aids of reasonable semi-empirical formulations for simplicity. To further verify the new transport equation, the calculated concentration profiles are compared with several experimental data. Results indicate well consistency between the simulations and observations, which proves the validity of the new equations for sediment suspension simulation. In this paper, the new equation is proposed to provide a theoretical tool for investigation of sediment transport in coastal engineering, more delicate flow and sediment dynamics modelling will be conducted in follow-up research.

Key Words: wave-current flow, suspended sediment transport, two-phase mixture model, concentration profile

8th International Conference on the Application of Physical Modelling in Coastal and Port Engineering and Science
Zhoushan, China - Dec. 9th - 12th, 2020

EXPERIMENTAL INVESTIGATION ON REGULARWAVES INTERACTING WITH FLEXIBLE VEGETATION

YANXU WANG[1], DECHUN LIU[2], ZEGAO YIN[3,*], XIUTAO JIANG[4]

1 Engineering College, Ocean University of China, China, wangyanxu@stu.ouc.edu.cn

2 Engineering College, Ocean University of China, China, liudechun@stu.ouc.edu.cn

3, Engineering College, Ocean University of China, China, yinzegao@ouc.edu.cn*

4 Engineering College, Ocean University of China, China, 21180911066@stu.ouc.edu.cn

Wave interaction with flexible vegetation is crucial in supporting a highly bio-diverse and protecting against coastal erosion. In this work, artificial low density polyethylene (LDPE) was selected to model the flexible vegetation, a series of physical experiments were conducted to study the wave attenuation over the emergent/submerged flexible vegetation. The wave height reduction was evaluated by using relative wave height attenuation (K_v). A bulk drag coefficient (C_D) was obtained based on linear wave theory and conservation of energy equation. A group of dimensionless parameters were obtained by using wave and vegetation parameters, and their relationships were explored with K_v and C_D in detail. As a result, simple prediction formulas were proposed with respect to K_v and C_D with high correlation coefficient values. In particular, the emergent cases had much higher C_D values than submerged cases, indicating that C_D increased with the increasing water depth. Wave attenuation by flexible vegetation is a highly dynamic process and its quantification plays a significant role in understanding shore protection and providing instructions for future engineering.

Key Words: physical experiments, flexible vegetation, wave attenuation, bulk drag coefficient

8th International Conference on the Application of Physical Modelling in Coastal and Port Engineering and Science
Zhoushan, China - Dec. 9th - 12th, 2020

EXPERIMENTAL INVESTIGATONS OF HYDRAULIC BORE INDUCED SEDIMENT TRANSPORT AROUND A SQUARE STRUCTURE LOCATED ON HORIZONTAL AND INCLINED SLOPES

MARIEH RAJAIE[1], AMIR H. AZIMI[2], IOAN NISTOR[3], COLIN D. RENNIE[4]

1 University of Ottawa, Canada, mraja091@uottawa.ca

2 Lakehead University, Canada, azimi@lakeheadu.ca

3 University of Ottawa, Canada, inistor@uottawa.ca

4 University of Ottawa, Canada, crennie@genie.uottawa.ca

Tsunami waves are extreme natural hazards that often claim human lives and damage coastal infrastructure due to significant impact force and excessive erosion. Experimental research on tsunami effects has been hampered by a lack of adequate methods to replicate, at scale, the action of tsunami waves. Chanson (2004) demonstrated the similarity between the hydraulic characteristics of tsunami waves (water surface elevation and bore velocity) and the propagation of a hydraulic bore generated by sudden release of impounded water. This similarity enables physical modeling of tsunami wave inundation on erosion around buildings.

In this study, a comprehensive program of laboratory experiments was conducted in the large flume (30 m long, 1.5 m wide, and 0.8 m deep) in the Hydraulic Laboratory of the University of Ottawa. Hydraulic bores replicating tsunami waves were generated using a rapidly opening swing gate that released an impounded volume of water. Scour formations around a square structure were investigated on two different bed slopes under various still to impoundment water depth ratios. Four different impoundment depths of 0.4 m, 0.35 m, 0.3 m, and 0.25 m and two different still water depths of 0.1 m and 0.03 m were used in these tests. A sediment section with a length of 3.15 m and a thickness of 0.2 m was used to investigate the erosion characteristics around a model 20 cm x 20 cm square Plexiglas structure placed in the center of the test section. The sediment was uniform sand with a median size of 0.5 mm, and the two tested bed slopes were horizontal and an inverse slope of +5%. The time-histories of wave height and velocity were measured using ultrasonic and Acoustic Doppler Velocimeter probes. Bore front velocities were extracted using an image analysis technique and results were validated with semi-theoretical solutions.

The results of these experimental investigations indicated that the deepest scour holes were formed in the case of the horizontal bed tests and occurred at the front corners of the structure. In addition, the bore front and wave velocities increased with decreasing still-to-impoundment depth ratio. The results of this novel experimental program are expected to contribute to the elaboration of design guidelines and are presently incorporated into the revised ASCE/SEI7 Chapter 6 (Tsunami Loads and Effects).

Key Words: Dam-break wave, horizontal bed, inclined bed, bore front velocity, sediment erosion, scour

8th International Conference on the Application of Physical Modelling in Coastal and Port Engineering and Science
Zhoushan, China - Dec. 9th - 12th, 2020

PHYSICAL MODELLING AS A TOOL TO OPTIMISE BREAKWATER DESIGN OF THE LARGEST PLEASURE PORT IN ALGERIA

S. WICKRAMARATNE[1], MOHAMED AMARI [2]

1 Lanka Hydraulic Institute(LHI), Sri Lanka, sanjeewa@lhi.lk

2 Hydro Marine Ingénierie (HMI), Algeria, contact@hmi.dz

Development of pleasure ports has picked its momentum over last decade primarily to accommodate growing interests for marine recreation. Mediterranean region in particular is home to a range of picturesque cruising grounds namely St Tropez, Cannes, and Antibes; and is in need of more such venues. Algeria, in line with such developments is eager to provide its best services for recreational travelers. Thus, plans are afoot to develop a brand new pleasure port in Ain Adjroud of Tlemcen Wilaya: approximately 155km west of Oran. The port is expected to receive about 1017 vessels and to be the largest pleasure port of Algeria.

In this context, Lanka Hydraulic Institute Ltd (LHI) was commissioned to provide a range of numerical & physical modeling services by Hydro Marine Ingénierie (HMI), Algeria: the main design consultant of Ain Adjroud Pleasure Port development project. The physical modeling work that includes both flume (2D) and basin (3D) assessment of breakwater performance of two proposed layouts is presented in this paper.

Numerical simulations of wave tranquility inside the port basin as well as the sediment transport simulations that assessed the littoral impacts have preferred one layout over the other, as such the physical modeling was used to further attest the preference via flume modelling and to fine-tune the corresponding breakwater design via basin modelling. In particular, the flume modeling helped to identify relative stability and overtopping performances of the two layouts, and established the best layout which is optimized via a basin physical model. The project posed many challenges as the project aims at converting a rugged and cliffy terrain and sediment deficit beach into an attractive, sustainable pleasure port. Given the restricted options available in Algeria for the selection of concrete armour type, traditional Antifer (BCR) units constituted the design. In addition, unavailability of reliable long-term wave and wind information is remedied through data adopted from Wave Watch III global wave model. During the process, a continuing practice of using a wave data source based on ship observations is successfully challenged. The project, in this context, provides a frontier example as to how to negotiate challenges in developing pleasure ports in Algeria and even beyond.

Key Words: extreme analyses, 2D and 3D physical modelling, pleasure port development

8th International Conference on the Application of Physical Modelling in Coastal and Port Engineering and Science
Zhoushan, China - Dec. 9th - 12th, 2020

NUMERICAL MODELING OF WAVE PROPAGATING THROUGH FISH AGGREGATING DEVICES

TONGZHENG ZHANG[1], RONG WAN[2*], CHENG ZHOU[3], FENFANG ZHAO[4], ZENGGUANG LI[5], WEIJIE WANG[6]

1 College of Fisheries, Ocean University of China, China, zhangtongzheng7@163.com

2 College of Marine Sciences, Shanghai Ocean University, China, rwan@shou.edu.cn

3 College of Marine Sciences, Shanghai Ocean University, China, c-zhou@shou.edu.cn

4 College of Fisheries, Ocean University of China, China, zhaoff@ouc.edu.cn

5 College of Marine Sciences, Shanghai Ocean University, China, zgli@shou.edu.cn

6 College of Marine Sciences, Shanghai Ocean University, China, weijiewang@shou.edu.cn

Fish Aggregating Devices (FADs) are increasingly used by tuna purse-seine fleets and fishers to aggregate pelagic fishes, like tuna and other tropical species, enhance the catchability of these species. FADs are deployed in tropical oceans around the world. Understanding the hydrodynamic characteristics of Fish Aggregating Devices (FADs) in waves is essential to evaluate the drifting behavior of FADs and its effect of fish attraction in mid-ocean. In this study, the numerical modelling (k-ε turbulence) with was used to explore the hydrodynamic interactions between FADs and waves with different characters (e.g., angle and height). The numerical solutions from this Computational Fluid Dynamics (CFD) model were obtained using a three-dimensional (3D) numerical wave tank based on both the Navier–Stokes solver (N-S) and mixed two-phase Eulerian volume of fluid (VOF) method. The movement tracks of FADs were estimated by the Dynamic Fluid Body Interaction (DFBI). The motions and wave resistance of FADs, considering the effect of relative wave angle and relative wave height, would be also investigated. The numerical simulation would make important contribution to the scientific understanding of FADs. This information has significant meaning for improved conservation and management of pelagic fisheries.

Key Words: Fish Aggregating Devices; wave propagating; numerical; VOF.

8th International Conference on the Application of Physical Modelling in Coastal and Port Engineering and Science
Zhoushan, China - Dec. 9th - 12th, 2020

MONSOON–FACILITATED OFF–SHELF TRANSPORT OF DISSOLVED ALUMINUM ACROSS THE EAST CHINA SEA DURING SUMMER

ZHAOWEI WANG[1], JILIANG XUAN[2], JINGLING REN

1 Innovation Center for Ports and Maritime Safety, Dalian Maritime University, China, wzw1128@dlmu.edu.cn

2 State Key Laboratory of Satellite Ocean Environment Dynamics, Second Institute of Oceanography, Ministry of Natural Resources, China, xuanjl@sio.org.cn

3 Key Laboratory of Marine Chemistry Theory and Technology, Ministry of Education, Ocean University of China, China, renjingl@ouc.edu.cn

Continental shelf pump is believed to be important for transporting terrestrial materials across the East China Sea (ECS). Here we use samples of dissolved aluminum collected from the ECS and a numerical model to identify the cross–shelf exchanges of dissolved aluminum along the ECS. With dissolved aluminum as a tracer, evidences were found about the cross–shelf transport behavior of aluminum across the ECS. Numerical model results indicated that Ekman transport promoted by monsoon and geostrophic in summer is the key physical mechanisms controlling the off–shelf transport of dissolved aluminum. Quantitative calculation showed that the ECS is the net source of dissolved aluminum to adjacent waters, of which nearly 65% of the output enters into the East/Japan Sea, while the remaining 36% enters into the Kuroshio currents. Resolving the cross– shelf transport process is a key issue for the investigation of marine biogeochemical cycles of trace metals.

Key Words: Dissolved Aluminum; Continental Shelf Pump; Shelf Export; East China Sea; Marginal Seas

8th International Conference on the Application of Physical Modelling in Coastal and Port Engineering and Science
Zhoushan, China - Dec. 9th - 12th, 2020

INTERACTION BETWEEN THREE-DIMENSIONAL TOPOGRAPHY AND DIFFERENT REGIONS OF GRAVITY CURRENTS

CHEN JINGYAO[1], CHEN YANAN[2], HE ZHIGUO[3], BENJAMIN KNELLER[4], YUAN YEPING[5]

1 Institute of Coastal and Offshore Engineering, Ocean College, Zhejiang University, China, 11834012@zju.edu.cn 2 Institute of Coastal and Offshore Engineering, Ocean College, Zhejiang University, China, cynwddt@zju.edu.cn 3 Institute of Coastal and Offshore Engineering, Ocean College, Zhejiang University, China, hezhiguo@zju.edu.cn 4 Department of Geology and Petroleum Geology, University of Aberdeen, UK, b.kneller@abdn.ac.uk

5 Institute of Physical Oceanology, Ocean College, Zhejiang University, China, yyping@zju.edu.cn

In the deep ocean, there is a range of complex topography such as seamounts, submarine canyons and faults. Gravity currents originating from the land or from shallower water pass may interact with this topography, leading to variations of flow propagation process, settling and resuspension of sediment, and erosion or accumulation of the topography. This process may have a significant impact on the evolution of submarine topography and present a major hazard to underwater engineering. There have been many studies related to the interaction between gravity currents and topography. However, most of them focus mainly on the head, interfaces and boundary layers. Few studies have considered the gravity current's velocity structure, which can be divided into a jet region and a wall region; the response to the topography of each of these two regions is different.

A series of laboratory experiments has been devised to isolate the interactions of each region with an obstacle, and to examine their separate influence of the wall region and jet region on mixing and propagation processes of gravity currents. We investigate the dynamics of interaction between inverted obstacles and positively buoyant plumes that represent the jet region of the flow, while the interaction between the wall region and the obstacle is investigated by the experiments with negatively buoyant gravity currents whose wall region is thicker than the height of the topography. We use a symmetrical Gaussian bump of various heights as the obstacle. Since the body of the gravity current is more important for long-distance movement, we focus on continuous flows with a stable flow structure. A particle image velocimetry (PIV) system and a high-speed camera are used to obtain the instantaneous velocity and vorticity fields, while the density field is assessed using conductivity as a proxy. Fluids of different density are prepared using sodium chloride and ethyl alcohol solutions, thus precisely matching the refractive indices (within 0.0001) to prevent optical distortion. The height of bumps and the velocity profile are regarded as variables. By varying the height with respect to the thickness of the layer in question, scale-independent descriptors of the interaction between gravity currents and topography are developed.

Key Words: Gravity currents; Topography; PIV; Obstacle;

8th International Conference on the Application of Physical Modelling in Coastal and Port Engineering and Science
Zhoushan, China - Dec. 9th - 12th, 2020

NUMERICAL SIMULATION OF THE INFLUENCE OF THE DISTANCES AMONG ARTIFICIAL REEFS ON ARTIFICIAL REEF FLOW EFFECTS

XINXIN WANG[1], YANLI TANG[2], LIUYI HUANG[3], FENFANG ZHAO[4]

1 Fisheries College, Ocean University of China, Qingdao, China, wxinxin@ouc.edu.cn
2 Fisheries College, Ocean University of China, Qingdao, China, tangyanli@ouc.edu.cn
3 Fisheries College, Ocean University of China, Qingdao, China, huangly@ouc.edu.cn
4 Fisheries College, Ocean University of China, Qingdao, China, zhaoff@ouc.edu.cn

Artificial reefs have been deployed worldwide in marine environments to enhance attraction and capture of fish, but, despite the potential as an artificial reef management option, few studies addressed whether fish assemblages will change with the distance among the reefs. Typically, the way for reefs deployment is often the crucial factor that determines whether reef sets or reef assemblages demonstrate their maximum function of fish aggregation. We experimentally assessed the relationship between the fluid effect and the distances among the artificial reefs. Simultaneously, CFD flow simulation was conducted to investigate the effects of distance changes on the flow field surrounding reefs. The main purpose of this paper is to provide suggestions for the construction and management of the deployment of the artificial reef based on the simulation results.

Key Words: Artificial reef, CFD simulation, reef deployment

8th International Conference on the Application of Physical Modelling in Coastal and Port Engineering and Science
Zhoushan, China - Dec. 9th - 12th, 2020

A DYNAMIC MODEL PREDICTING THE RECONFIGURATION AND DRAG FORCE OF SALT MARSH PLANTS WITH LEAVES

Xiaoxia Zhang[1,2], Zhilin Peng[1],Heidi Nepf[2]

1 State Key Laboratory of Hydraulics and Mountain River Engineering, Sichuan University, Chengdu, Sichuan, China

2 Department of Civil and Environmental Engineering, Massachusetts Institute of Technology, Cambridge, Massachusetts, USA

Salt marshes are important ecosystems in the coastal regions. Among many of their ecosystem services, they provide context-dependent protection from erosion, storm surge, and potentially small tsunami waves. Researches have conducted field surveys and experiments using simplified model stem from which difference between the salt marsh plants and rigid cylinders was observed. In this study, we build physical dependent theoretic model to describe the dynamics of salt marsh plant with both leaves and stem. Laboratory experiments were conducted to measure the drag force and wave height simultaneously on the leaf, the stem, the model plant and, the fresh salt marsh plant. Comparing plants with both leaves and stem to the stem alone cases, the leaf associated drag force was found to contribute to 50 to 90% of the plant scale drag. The percentage varies with water depth and wave intensity. This important role of the leaves of salt marsh plant on resisting flow and damping waves has not being highlighted yet. The model proposed can be applied to explore the span of dynamic behavior among varies of marsh plant species. Further, with this theoretic model on single plant, the flow resistance and wave attenuation of marsh plant meadows can also be predicted.

8th International Conference on the Application of Physical Modelling in Coastal and Port Engineering and Science
Zhoushan, China - Dec. 9th - 12th, 2020

PHYSICAL MODELLING OF SCOUR AROUND PILES OF MARINE WIND POWER UNDER A COMBINED WAVE-CURRENT ENVIRONMENT IN PRE

CHENG LIU[1], XIAOJIAN LIU[2], QISONG WANG[3]

1 Pearl River Hydraulic Research Institute, Pearl River Water Resources Commission of the Ministry of Water Resources, Guangzhou, Guangdong, jacklc2004@163.com
2 Pearl River Hydraulic Research Institute, Pearl River Water Resources Commission of the Ministry of Water Resources, Guangzhou, Guangdong, lxiaojian2010@163.com
3 Pearl River Hydraulic Research Institute, Pearl River Water Resources Commission of the Ministry of Water Resources, Guangzhou, Guangdong, lxiaojian2010@163.com

This paper presents a study on scour around the pile-type structure foundations, representative of those commonly used for offshore wind farms in Pearl River Estuary (PRE), namely the monopile, offshore substation, and the suction bucket. The local scour around those structures in combined irregular waves and current have been physically modeled with a specially-designed flow–structure–sand interaction flume. In the series of experiments, the developments of the wave surface, velocity and scour depth in the proximity of the model structures were measured simultaneously. The measured maximum scour-depth was plotted as a function of Ucw = Uc/(Uc+Um) for various Keulegan-Carpenter number (KC), in which Uc is the undisturbed current velocity and Um is the undisturbed orbital velocity at the seabed. Experimental results indicated that the superimposition of the irregular waves on a constant current had much effect on the time development of local scour pattern and the resulting equilibrium scour depth. The scour-depth around larger diameter monopile under the combined waves and current was smaller than the pure current, but in some cases an order of magnitude larger than the scour caused by pure waves. For the more slender piles, such as the foundation of offshore substation, the scour was approximately the same for the combined wave-current and pure current environment. The scour around the suction bucket foundation was not remarkable, which was attributed to the shelter effect of bucket top surface on the down welling induced by structure central slender pile. Finally, the scour around the monopile under combined waves and current in PRE was discussed by comprising the published empirical expressions.

Key Words: Local scour; Marine wind power structures; combined waves and current; Pearl River Estuary

8th International Conference on the Application of Physical Modelling in Coastal and Port Engineering and Science
Zhoushan, China - Dec. 9th - 12th, 2020

MORPHODYNAMIC RESPONSES OF PINGSHUIQIAO BEACH TO A STORM SURGE USING ARGUS IMAGES

ZILONG XIA[1], CUIPING KUANG[1*], JIE GU[2*], HONGLIN SONG[1], YUHUA ZHENG[1], LEI ZHU[3], YUNLONG WU[1]

1College of Civil Engineering, Tongji University, 200092, Shanghai, China. Email: cpkuang@tongji.edu.cn
2 College of Marine Ecology and Environment, Shanghai Ocean University, 201306, Shanghai, China. Email: jgu@shou.edu.cn
3 The Eighth Geological Brigade, Hebei Geological Prospecting Bureau, No.221, Yanshan Road, Qinhuangdao, Hebei, 066001, China. Email: siriusn@126.com

During a storm event, such as tropical cyclone and cold front, sea surface in coastal water will experience a significant increase due to storm surge. The high wind-waves therefore may break on the beach and strongly stir up local sediment, resulting in an erosion. The morphological impact of these extreme events has drawn great interest of coastal community, however, a real-time in-site observation is still hard to be conducted considering their devastating forcings. The Argus monitoring system, a real-time and omnibearing image observation, is able to record the image information during the storm event with high-definition camera(s) mounted in a high and safe place. In combined with some post-processing tools, the recorded image can be converted and provide the information of shoreline location and the digital elevation model (DEM) for intertidal zone. It is therefore considered to be a robust technique to estimate the coastal morphological evolution in recent years. The Pingshuiqiao beach is located in the west of Beidaihe district, Hebei province, China, and consists coarse sediment with median grain size of 0.29 - 0.35 mm. The geometry and topography of Pingshuiqiao beach is complex as there are a submerged rubble-mound breakwater in the offshore and two headlands at its east end. To maintain local ecotourism value, the Argus monitoring system is applied to the beach to monitor shoreline movement, morphological evolution of intertidal zone and berm profile, with six high-definition cameras. In this study, we firstly extract the location of shoreline by processing time exposure images every 30 minutes based on the improved Canny edge detector, which uses a conventional “derivative of Gaussian” filter to detect step edges, i.e., shoreline here. Then, the coordinates of shoreline is derived by establishing coordinate relation based on the control points fixed on the beach. Finally, the multi-temporal shoreline coordinates in one day are input into ArcGIS for interpolation to set up a DEM. We adopt the above method to process 11-day Argus monitoring results during a storm event on 15-25, July, 2016. The results indicate that the beach volume per unit width is decreased by an average of 8.2 m^3/m with the shoreline retreat of about 5 m by the storm. After that, sediment gradually comes back to the beach and deposit there, with the restorative effect of wave in normal weather. Generally, the strong erosion occurs in the supratidal zone and the upper part of intertidal zone, while the deposition in the lower part of intertidal zone during the storm surge in such a wave- dominated low tidal range sandy coast. This study clearly presents the morphological change processes at Pingshuiqiao beach based on the Argus monitoring system that can be taken as a practical technique to study on coastal morphology.

Key Words: Argus monitoring system; storm surge; morphological evolution; short-term change.

8th International Conference on the Application of Physical Modelling in Coastal and Port Engineering and Science
Zhoushan, China - Dec. 9th - 12th, 2020

A NEW METHOD FOR GENERATING CURRENT IN A LARGE-SCALE INTERMEDIATE DEPTH BASIN WITH LATERAL INLET BOUNDARY

ZHIWEN YANG[1], HUAQING ZHANG[1], CHUNGUANG YUAN[1], HUA YANG[1]

1 National Engineering Laboratory for Port Hydraulic Construction Technology, Tianjin Research Institute for Water Transport Engineering, M.O.T., China, E-mail: oyangzhiwen@126.com

Physical scale model testing is an important part of the development process for coastal offshore engineering or utilization of ocean energy. The newly-built Ocean Research Facility at Tianjin Research Institute for Water Transport Engineering, M.O.T. (TIWTE) is designed to recreate the complex ocean environment and conduct hydrodynamic model tests for the development of ocean technologies. Unlike the traditional ocean research facility which generates tidal current from the bottom, the new basin in TIWTE creates current from its lateral boundary due to space constraints. This paper introduces a new method to generate uniform and stable current in a large-scale intermediate depth basin with lateral inlet boundary.

A CFD model was used to compare different vertical and horizontal design schemes and confirm the final design parameters. A series of current generation tests were performed and assessed to extend the characterisation of this new facility, aiming to highlight what can be learnt from testing at scale with complex conditions in a controlled environment. In this work, flow measurements taken throughout the test volume of the basin, allowed spatial and temporal variations in the currents to be determined. Outputs from this research are being used to help both academic and commercial tests at TIWTE new basin. The test area in currents was shown to be >1500m2 with <10% variation in flow. Results are important when designing client test plans.

Key Words: New method; Current generation; Intermediate depth basin; Lateral inlet boundary

8th International Conference on the Application of Physical Modelling in Coastal and Port Engineering and Science
Zhoushan, China - Dec. 9th - 12th, 2020

THE LA YARADA COASTAL AQUIFER, AFTER 100 YEARS OF EXPLOITATION AS A SUSTENANCE FOR AGRICULTURE IN ARID ZONES

PINO V., EDWIN[1], CHÁVARRI V., EDUARDO[2], MONTALVAN D., ISAAC [3], ASCENSIOS T., DAVID[4]

1 Jorge Basadre Grohmann National University, Tacna, Perú, epin o68@hotmail.com, isaac.montalvan1992@gmail.com

2 Agrarian National University, Lima, Perú, echavarri@ lamolina.edu.pe, dascensios@lamolina.edu.pe

This article is a historical review of the events that occurred in the exploitation of the La Yarada coastal aquifer, located in an arid zone, located at the head of the Atacama Desert. The period in which the exploitation has been in a balanced regime (recharge - extractions) until the 1970s and unbalanced after the 80s has been identified. Likewise, favorable and unfavorable management measures are identified in the conservation of the aquifer system Future engineering measures were identified, leading to the recovery and conservation of the aquifer that consist of the incorporation of hydraulic barriers.

Key Words: La Yarada aquifer, balanced exploitation, unbalanced exploitation

8th International Conference on the Application of Physical Modelling in Coastal and Port Engineering and Science
Zhoushan, China - Dec. 9th - 12th, 2020

NUMERICAL STUDY OF THE HYDRODYNAMIC CHARACTERISTICS OF A SEMI-SUBMERSIBLE AQUACULTURE FACILITY IN WAVES

HANG-FEI LIU[1], YUN-PENG ZHAO[1], CHUN-WEI BI[1], CHAO MA[1]

1 State Key Laboratory of Coastal and Offshore Engineering, Dalian University of Technology, Dalian, China, liuhf@mail.dlut.edu.cn

The destruction of aquaculture facility is easily caused by extreme wind and waves in open sea, so it is essential to analyze the hydrodynamic response of aquaculture facility based on a numerical method. In order to ensure the accuracy of calculation and avoid the huge computational resources needed by computational fluid dynamics-CFD, this paper adopts a new method which combines boundary element method based on the potential flow theory with Morison equation to simulate the dynamic response of semi-submersible aquaculture facility in pure waves. The pontoon and thick column are modeled by surface element, and the net and thin column are modeled by the Morison element. The hydrodynamic response including mooring line tension and motion response is simulated in pure waves and compared with experimental values. The results show that the numerical data is agree well on the experimental data. Based on the above work, the numerical model presented here can be used to analyze the hydrodynamic response of semi-submersible aquaculture facility. The effects of wave length and wave steepness on the mooring line tension and motion response are studied. Additionally, with the increase of working draught, the force on the mooring line has a reduction. It is an effective way for the aquaculture facility to avoid damage due to the severe wave loads through increasing draught properly.

Key Words: aquaculture facility, mooring line tension, motion response, boundary element method

8th International Conference on the Application of Physical Modelling in Coastal and Port Engineering and Science
Zhoushan, China - Dec. 9th - 12th, 2020

SAND SPIT BREACHING AND SUBSEQUENT REFORMATION AT LAI GIANG RIVER MOUTH, CENTRAL VIETNAM

NGUYEN QUANG DUC ANH[1], NGUYEN TRUNG VIET[2], HITOSHI TANAKA[3], TRAN THANH TUNG[4] AND NGUYEN XUAN TINH[5]

1 Researcher, Thuyloi University, Vietnam, ducanh.cte@gmail.com
2 Professor, Thuyloi University, Vietnam, nguyentrungviet@tlu.edu.vn
3 Professor, Tohoku University, Japan, hitoshi.tanaka.b7@tohoku.ac.jp
4 Associate Professor, Thuyloi University, Vietnam, T.T.Tung@tlu.edu.vn
5 Assistant Professor, Tohoku University, Japan, nguyen.xuan.tinh.c5@tohoku.ac.jp

Sand spit elongation is remarkable at the mouth of Lai Giang river mouth, located in central Vietnam, and sudden migration of the river mouth has been induced by sand spit breaching. In order to understand the frequency of spit breaching and subsequent spit reformation process, a series of Landsat and Google Earth images which has been accumulated since 1976 were analyzed to clarify the characteristic change of the estuary topography. In order to quantitatively investigate such characteristics, the tip coordinate and the area of the sand spit on the left of the estuary were calculated. From the satellite analysis, it is found that the river opening has been moved consistently to the down-drift direction, and its traveling speed has reached 150m/year. In particular, the area of the sandbar has increased remarkably, and the increasing rate is almost constant. Using this value, the rate of sand volume intruded into the river mouth by waves was estimated and it is almost consistent with longshore sediment transport rate along the surrounding sandy beach.

Key Words: sand spit, elongation, breaching, Lai Giang river mouth, longshore sediment transport rate

8th International Conference on the Application of Physical Modelling in Coastal and Port Engineering and Science
Zhoushan, China - Dec. 9th - 12th, 2020

NUMERICAL STUDY OF SCOUR DEVELOPMENT AROUND TWO TANDEM PIPELINES USING CFD-DEM METHOD

DAN HU[1], LIANG SUN[2]

1 School of Transportation, Wuhan University of Technology, China, hudan1989.happy@163.com
2 School of Transportation, Wuhan University of Technology, China, l.sun@outlook.com

In the field of offshore oil and gas engineering, the arrangement of multiple pipelines are becoming more common. The spacing between the pipelines and the incoming stream velocities will affect the scour development around the pipelines significantly. In this study, the effect of space ratio (G/D) and the stream velocities on the local scour around two pipelines in tandem are investigated using the coupled approach of computational fluid dynamics (CFD) and discrete element method (DEM). Here G is the spacing between the pipelines and D is the diameter of the pipeline. The coupling algorithm between CFD and DEM is summarized. Numerical model is verified by comparing numerical results of equilibrium scour profile with experimental measurements. In the further analysis, the effect of space ratio and the stream velocities are discussed by simulating the gap ratio (G/D) between two pipelines ranging from 1 to 3 with an interval of 1, under the stream velocity U=0.5, 1 and 2 m/s. The corresponding results indicate that when G/D$\leqslant$2, the equilibrium scour depth below the upstream pipeline (S1) is slightly larger than that under the downstream pipeline (S2). The equilibrium scour depth S1 and S2 slightly increase as the gap ratio increases. Whereas for G/D>2, the equilibrium scour depth beneath the upstream pipeline is slightly smaller than that under the downstream pipeline. The equilibrium scour depth S1 and S2 slightly decrease as the gap ratio increases. Furthermore, the scour depths are highly dependent on and positively related to the incoming stream velocities. The equilibrium bed profiles are similar under the same incident stream velocity with different gap ratios.

Key Words: Local scour, Two pipelines in tandem, Computational fluid dynamics (CFD), Discrete element method (DEM), Coarse grain method (CGM)

8th International Conference on the Application of Physical Modelling in Coastal and Port Engineering and Science
Zhoushan, China - Dec. 9th - 12th, 2020

MORPHOLOGICAL EVOLUTION OF A TYPICAL CHANNEL-SHOAL SYSTEM IN THE CHANGJIANG ESTUARY AND A DISCUSSION ON THE CONTROLLING COUNTERMEASURES

HUALONG LUAN[1], GENG QU[2], WENTAO LEI[3], TONGHUAN LIU[4]

1 Changjiang River Scientific Research Institute, China, luanhualong@126.com
2 Changjiang River Scientific Research Institute, China, qugeng0516@163.com
3 Changjiang River Scientific Research Institute, China, leiwt86@163.com
4 Changjiang River Scientific Research Institute, China, liuth@mail.crsri.cn

The Changjiang Estuary is an important carrier of regional socio-economic development, and the stability of the channel-shoal pattern is related to flood control safety, water supply security, shipping safety and ecological environment protection. Channel-shoal systems with different spatial scales, as a morphological element, can be found in the bifurcated estuarine channels. These multiple channel systems are characterized by interlaced ebb and flood channels with a shallow shoals between them as observed in the many other tidal-influenced estuaries around the world. Under the combined river-tidal forces, the evolution of a channel-shoal system interacts within each other as a whole. This study takes the Biandan Shoal as a typical example, to analyse the morphological evolution processes in the past half century, and discuss the controlling countermeasures to stabilize the channel-shoal pattern.

Observed bathymetry data during 1958-2016 are collected and quantitatively analysed using GIS techniques. The results indicate that the Biandan Shoal experienced overall accretion and extension in terms of the sand area and sediment volume above the -5m isobath. The effect of fluvial sediment decline on the Biandan Shoal seems to be limited. The geometry of the sand body gradually tends to align with the flow direction, suggesting that the shoal was approaching towards equilibrium. As the Lower Biandan Shoal gradually moved downstream, the Xinqiao Channel and Zhongyang Shoal was squeezed and moved downstream simultaneously. The Biandan Shoal experienced a periodic evolution process of downstream moving, shoal incision and downstream moving. This changed the bifurcation site of the North and South Channel and influenced the evolution of downstream channels. In recent years, several connecting channels formed across the Biandan Shoal. The observed lowest bed level of a connecting channel in 2016 was -9 m. This is probably due to the construction of the Qingcaosha Reservoir and thereby fixing the downstream boundary of the Xinqiao Channel. The erosion of connecting channels will probably continue since the downstream moving of the Lower Biandan Shoal and the Xinqiao Channel was stopped. In order to stabilize the overall pattern of this large-scale channel-shoal system, it is proposed to strengthen the control of the Biandan Shoal from three aspects, (1) to strengthen the in-site observation of connection channel evolution and analyse the reasons of shoal incision; (2) to protect the head of the Qingcaosha Reservoir against erosion by engineering measures; (3) to strengthen the feasibility study of blocking the connection channel and optimize the present plan considering the ecological environment needs.

Key Words: channel-shoal system; Biandan Shoal; morphological evolution; incision; Changjiang Estuary

8th International Conference on the Application of Physical Modelling in Coastal and Port Engineering and Science
Zhoushan, China - Dec. 9th - 12th, 2020

A COMPARISON BETWEEN COASTAL SURFACE FEATURES OBSERVED BY X-BAND RADAR AND NUMERICAL COMPUTATION AT KASHIMA COAST, JAPAN

YANG ZHEN[1], SATOSHI TAKEWAKA[2]

1 Graduate School of Systems and Information Engineering, University of Tsukuba, Japan, yzhen777@gmail.com
2 Graduate School of Systems and Information Engineering, University of Tsukuba, Japan, takewaka@kz.tsukuba.ac.jp

A comparison is made at Kashima Coast in Japan between X-band radar observation, which captures ocean surface features like ocean fronts, and results of numerical computation on coastal flows. X-band radar is installed at a straight sandy coastline which is facing the Pacific Ocean. It collects hourly data of coastal surface of approximately 5 km in the longshore. In the X-band radar images, migrations of so-called fronts are captured frequently. They travel either in the cross-shore and in the longshore, and in this study, their alongshore traveling speeds are estimated. Numerical results on coastal flows, which is a down-scaled data set computed from ocean reanalysis data set FORA. Temperature and velocities variations and distributions along the coast are compared with temporal variations of coastal surface features observed in the radar images. We analyzed data of 12 months in 2006, and found that the migration speeds of ocean fronts can be correlated with numerical results to some extent.

Key Words: X-band radar, front, coastal surface feature, coastal flow, numerical result.

8th International Conference on the Application of Physical Modelling in Coastal and Port Engineering and Science
Zhoushan, China - Dec. 9th - 12th, 2020

THE OPPORTUNITIES AND CHALLENGES OF COASTAL RESERVOIR STRATEGY FOR SUSTAINABLE WATER RESOURCES DEVELOPMENT- INDIAN PERSPECTIVE

RAMESH HONNASIDDAIAH

National Institute of Technology Karnataka, India,
E-mail: ramesh.hgowda@gmail.com; hramesh@nitk.ac.in

Abstract: Any country to become prosperous, developed and strengthen economy is mainly depend on its sufficient amount of water resources to meet the demand. In the present days, due to climate change, global warming, etc. the amount of rainfall altered and hence experiences frequent extreme events such as droughts, floods and cyclones. India is one of the emerging countries in the field of development, economy, agriculture, industries, import and export, etc. and it is predicted that India will become developed country in the in the near future. Attention has been given to upgrade all basic infrastructures such water, sanitation, transportation, housing, irrigation, etc. to the international standards. India is a vast country with wide diversified culture having a population of
1.35 billion experiences all six seasons and the weather ranging from very cold to very hot, flood plains to desert, and annual rainfall ranging from as low as 200 mm to as high as 11800 mm, which is the highest in the world. So the average rainfall over Indian geographical terrain is ranging from 300 mm to 750 mm. India has built more than 5000 large dams to store and supply water for domestic, industries, irrigation, power generation etc. and ranks third in the world after USA and China. No more dams can be built across any streams or rivers as lot of environmental, social, and economic degradation. So the only path way is to build dams with minimum environmental and social degradation is near coastal plains or nearshore in the sea to store flood water and use it for the any purpose for which is intended during summer months. Such reservoirs are called coastal reservoirs. India faces sever water crisis studied by many global researchers including United Nations. Presently many cities and rural areas find difficult to get sufficient quantity of drinking water during summer months. Hence the present paper explores the opportunity and challenges of coastal reservoir to meet such demand for future sustainable water supply through coastal reservoir technology.

Key Words: Indian water resources, coastal reservoir, water demand and supply, rainfall

8th International Conference on the Application of Physical Modelling in Coastal and Port Engineering and Science
Zhoushan, China - Dec. 9th - 12th, 2020

WAVES AND SEDIMENT TRANSPORT GENERATED BY GRANULAR LANDSLIDE IMPACTING RESERVOIR: APPLICATION TO REAL AND POTENTIAL EVENTS

JI LI [1, 2], ZHIXIAN CAO[1]

1 State Key Laboratory of Water Resources and Hydropower Engineering Science, Wuhan University, China

2 College of Engineering, Swansea University, UK

Granular landslides impacting reservoirs usually generate large water waves and active sediment transport, of which enhanced understanding is important to public safety and effective sediment management. In this work, a coupled two-dimensional double-layer shallow water hydro-sediment-morphodynamic (SHSM) model is used to investigate granular landslides impacting reservoirs. The model is benchmarked against laboratory experiments of landslide-generated waves in both two and three dimensions. Then, it is applied to study the real and potential events of large-scale landslide impacting reservoir. Generated wave amplitude, wave run-up and depositional area of landslide are estimated under different scenarios, including high-intensive rainfall-induced or earthquake-induced landslides. Especially, the results show that the landslide-generated waves cannot overtop the dam and cause damages to dam body. Moreover, the deposition of the landslide would not block the intake and the emptying culvert of the hydropower station. Based on extended numerical tests, the amplitude of generated wave is shown to correlate closely with the water-enter velocity of landslide, depending on the initial landslide volume, friction coefficient and particle size.

Key Words: Granular landslide; Reservoir; Waves; Sediment transport; Case study

8th International Conference on the Application of Physical Modelling in Coastal and Port Engineering and Science
Zhoushan, China - Dec. 9th - 12th, 2020

A THEORETICAL MODEL FOR DESCRIBING CHANNEL AXIS DEVIATION AND CROSS-SECTION CHANGE UNDER THE ACTION OF CROSS FLOW IN COASTAL REGION

WENJIN ZHU[1], NA WANG[2]， XIN CONG[3],XIAOTIAN DONG[4]

1. *Jiangsu Ocean University , China , zhuwj@hhit.edu.cn*
2. *Jiangsu Ocean University , China , 1098577677@qq.com*
3. *Tongji University , China , congxin@tongji.edu.cn*
4. *Jiangsu Ocean University , China , dongxt@hhit.edu.cn*

The mechanism of coastal sediment transport is: wave stirs up sediment and current transports the sediment. The waterway of the coastal region is subject to current and waves. Usually, currents are perpendicular to the longitudinal axis of the waterway. The currents are called as cross flow. The phenomenon of channel axis deviation and cross-section change will occur under the action of the cross flow. The velocity of cross flow comprises the residual velocity and main tidal constituents velocity. It is assumed that waves only act as stirring when the channel axis deviation and cross-section change. Moreover, it is also assumed that the morphological time is larger compared to the tidal period. The seabed deformation equations caused by the motion of bed load and suspended load are averaged over the tidal period separately. For the bed load, Bagnold transport formula is used for bottom boundary condition. For the suspended load, the bottom net sediment flux equation is used and the reference concentration is proportion to the square velocity. The higher order terms are retained for the results, while lowed order terms are neglected. Then, a theoretical model is established for describing the law of channel axis deviation and cross-section change in the coastal region. The new theoretical model has the form of one-dimensional convection-diffusion equation which has constant convection-diffusion coefficients. By analyzing the new equation, the migration rate of channel axis and the law of channel cross-section change under the action of cross flow are obtained. The channel axis deviation and cross-section change is a function of residual velocity. The Gauss function is used to describe the waterway cross-section. According to the theoretical solution of the one-dimensional convection-diffusion equation, the quantitative description of channel axis deviation and cross-section change under the action of cross flow is obtained. The new method is applied to evaluate channel axis deviation and cross-section change under the action of cross flow in the 300000-ton deep-water channel of Lianyungang Port in the Southern Yellow Sea. Under natural conditions, the shifting distance of channel axis in Lianyungang Port is about 5 m yr^{-1}, and the change rate of waterway cross-section shape is 292.69m^2 yr^{-1}. What's more, it is also applied to the waterway of the Port of Hai'an at Qiongzhou Strait. The shifting distance of channel axis in Hai'an Port is about 10 m yr^{-1}, and the change rate of waterway cross-section shape is 294.22m^2 yr^{-1}. This research has important engineering value for designing channel and dredging maintenance.

Key Words: cross flow, residual velocity, one-dimensional convection-diffusion equation, Gauss function, migration rate

8th International Conference on the Application of Physical Modelling in Coastal and Port Engineering and Science
Zhoushan, China - Dec. 9th - 12th, 2020

MAJOR CHALLENGE FOR COASTAL RESERVOIRS: WATER QUALITY

GUANGQIU JIN[1,2], YUMING MO[1,2], KAI JIN[3], HONGWU TANG[1,2,*], LING LI[4], D. A. BARRY [5]

1 State Key Laboratory of Hydrology-Water Resources and Hydraulic Engineering, Hohai University, Nanjing, China, jingq@hhu.edu.cn yuming_m@hhu.edu.cn hwtang@hhu.edu.cn
2 College of Water Conservancy and Hydropower Engineering, Hohai University, Nanjing, China
3 Zhejiang Design Institute of Water Conservancy and Hydro-electric Power 279889914@qq.com
4 School of Engineering, Westlake University, Hangzhou, Zhejiang, China liling@westlake.edu.cn
5 Laboratoire de technologie écologique (ECOL), Institut d'ingénierie de l'environnement (IIE), Faculté de l'environnement naturel, architectural et construit (ENAC), Ecole Polytechnique Fédérale de Lausanne (EPFL), Station 2, 1015 Lausanne, Switzerland andrew.barry@epfl.ch

There is a serious shortage of fresh water in coastal zones of economically developed areas in China. Coastal reservoirs are normally constructed in coastal zones. Compared with inland reservoirs, coastal reservoirs have the advantage of reduced farmland use and larger storage capacity, and so they can be an effective way to solve water shortage problems. However, due to salinization, the quality of water in coastal reservoirs can be difficult during reservoir operation, which limits normal functions.

To investigate water quality degradation in a controlled setting, laboratory experiments and associated numerical modelling were performed. The major results are as follows: (1) There is a complex interplay evident in the dynamics of coupled surface water-groundwater interactions. The physical model and numerical model regarding the coupled surface water-groundwater in coastal reservoir are developed. Coastal reservoirs greatly changed groundwater discharge pathways to sea. Without coastal reservoir, groundwater discharge to sea directly, while with coastal reservoir, part of groundwater would firstly discharge to coastal reservoir, desalinate the reservoir water, and then to sea. Storm surge significantly increased the flow velocity of coastal reservoir. (2) The salt transport process and seawater intrusion in coastal reservoirs under complex dynamic conditions were explored. We analyzed the desalinization process in coastal reservoir, found that with the groundwater discharge rate increased, residual saltwater distribution result from intruded fresh groundwater was further moderated. The effects of surface water and groundwater on the seawater intrusion in coastal reservoirs are considered respectively. Deep pool have greatly increased the salinization of coastal reservoir because it acts as the additional saltwater source, the existence of high-salinity water at the deep pool were may owing to the dominant channel from sea to deep pool. (3) The suggestions to prevent seawater intrusion in coastal reservoir were given in this project. Based on the researches about the complex hydrodynamics of coupled surface water-groundwater and the saltwater transport process in coastal reservoir. With the depth of dam increased, the salinization of coastal reservoir saw an reduced trend, relevant dimensionless number regarding the major hydrodynamics in coastal reservoir was designed, and the optimal depth of the dam to prevent seawater intrusion while considering the project cost was received.

Results of this paper improved the theory of hydrodynamics and pollutant transport in coastal reservoir and provided feasible measures for the major challenge faced by coastal reservoirs – salinization. Further studies regarding the other major challenges of water quality, such as eutrophication, were also needed to push in future. These results enrich the theoretical and methodological foundations for the management of coastal reservoirss.

Key Words: Coastal reservoir; Groundwater; Seawater intrusion; Tide; Salt transport process

8th International Conference on the Application of Physical Modelling in Coastal and Port Engineering and Science
Zhoushan, China - Dec. 9th - 12th, 2020

STUDY OF SOLITARY WAVE INTERACTION WITH A ROW OF VERTICAL SLOTTED PILES ON A SLOPING BEACH

XIAOJIAN LIU[1], CHENG LIU[2], CHANGBO JIANG[3], YU YAO[4]

1 Pearl River Hydraulic Research Institute, Pearl River Water Resources Commission of the Ministry of Water Resources, Guangzhou, Guangdong, lxiaojian2010@163.com

2 Pearl River Hydraulic Research Institute, Pearl River Water Resources Commission of the Ministry of Water Resources, Guangzhou, Guangdong, jacklc2004@163.com

3 School of Hydraulic Engineering, Changsha University of Science and Technology, Changsha, Hunan, jiangchb@csust.edu.cn

4 School of Hydraulic Engineering, Changsha University of Science and Technology, Changsha, Hunan, yaoyu821101@163.com

To improve our current understanding of tsunami-like solitary waves interacting with a row of vertical slotted piles on a sloping beach, a series of laboratory experiments were conducted in wave tank considering three different typical situations: slope beach with installing no additional structure, a single pile or a row of piles. Both the slope and the piles were made of PVC materials. The surface elevations were measured at five locations (S1-S5) across the flume by using non-intrusive ultrasonic sensors (Sinfotek, China). The current was measured by an Acoustic Doppler Velocimetry (Nortek, Norway). The dynamic pressure around the pile was measured by four pressure transducers (TEST, China), which were installed on the front, rear, and two side faces of the most-centered pile in the flume. All above instruments were sampling with a frequency of 50 Hz by a data acquisition system. Additionally, a video camera (Logitech, Switzerland) was put on the top of the pile model to capture the free surface run-up during the process of wave impact. The measured water elevations, current speed, impacting pressure, and maximum run-up are systematically discussed in detail. Besides, a 3D numerical wave tank based on OpenFOAM® was established to supplement the physical results. The results show that maximum run-up was found to increase almost linearly with the increasing of wave height, water depth, spacing distance between piles, and beach slope, as well as the maximum breaking wave force increased with the increasing incident wave height and water depth, and but decreased with the increasing pile space and beach slope. Finally, the empirical equation accounting for predicting the maximum runup and slamming coefficients are proposed for pile structures. This study will help to improve our understanding in the wave interaction with the pile row structures during the tsunami wave events.

Key Words: Solitary wave; slotted piles; impact force; maximum runup

8th International Conference on the Application of Physical Modelling in Coastal and Port Engineering and Science
Zhoushan, China - Dec. 9th - 12th, 2020

NUMERICAL STUDY ON LOCAL SCOUR AROUND CYLINDER UNDER RECIPROCATING TIDAL FLOW

XIA YUE-ZHANG[1],YANG SHI-YU[2], WANG SHAO-HUA[3]

1 Ocean college, Zhejiang University, Zhoushan 316021, China,E-mail：yzxia@zju.edu.cn

2 Ocean college, Zhejiang University, Zhoushan 316021, China,E-mail：21834069@zju.edu.cn

3 Ocean college, Zhejiang University, Zhoushan 316021, China,E-mail：wagshaohua@zju.edu.cn

Despite cross-sea bridges and offshore wind farms being mostly situated in tidally dominated waters, only limited research on the effects of tidal flow on the scour process around offshore foundation structures has been carried out so far. Therefore, there is an urgent need to conduct in-depth research on structural scour in the estuary and bay area dominated by the tide. In this paper, the local scour process of a cylinder subjected to bidirectionally reversing currents was studied by a coupled numerical model, which includes the hydrodynamics and sediment transport model. The model uses the RNG k-ε turbulence equation to close the N-S equation, and the governing equation is discretized using the finite difference method. The numerical results show that the local scour profile is nearly symmetrical around the cylinder, and the position of its maximum scouring depth swings due to the turning of the water flow velocity. The maximum scour depth increases as the water depth increases. But the scour rate is smaller than the incoming water depth growth rate. When the incoming water depth is greater than a certain limited water depth, the maximum scour depth of the cylinder has nothing to do with the incoming water depth. Besides, the scour depth caused by bidirectionally reciprocating flow is reduced by about 20% compared with the case of unidirectional constant flow.

Key Words: Scour; Unidirectional and tidal currents; Sediment transport

8th International Conference on the Application of Physical Modelling in Coastal and Port Engineering and Science
Zhoushan, China - Dec. 9th - 12th, 2020

EFFECTS OF PEAKEDNESS OF BIMODAL WAVES ON OVERTOPPING OF SLOPING SEAWALLS

STEPHEN ORIMOLOYE[1], JOSE HORRILLO-CARABALLO[2], HARSHINIE KARUNARATHNA[3], DOMINIC E. REEVE[4]

1 Swansea University, United Kingdom, stephen.orimoloye@swansea.ac.uk
2 Swansea University, United Kingdom, j.m.horrillo-caraballo@swansea.ac.uk
3 Swansea University, United Kingdom, h.u.karunarathna@Swansea.ac.uk
4 Swansea University, United Kingdom, d.e.reeve@swansea.ac.uk

Prediction of wave overtopping is an essential component of coastal seawall designing and management. Not only that excessive overtopping is reported for impermeable seawalls under bimodal waves (Reeve et al., 2015), but overtopping is also showing a high sensitivity to the peakedness of the random wave propagation patterns (Figure 1). In present study, we present a comprehensive analysis of the effects of peakedness of bimodal wave patterns of the overtopping of sloping seawalls.

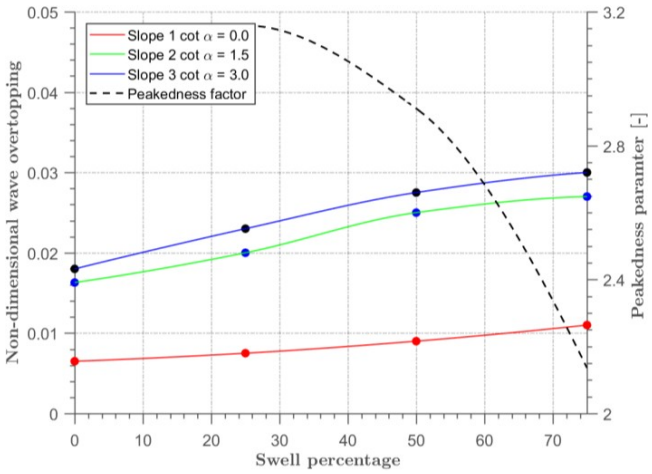

Figure 1. Influences of peakedness parameters on the wave overtopping of sloping seawall under different bimodal sea states of different swell percentages (Orimoloye et al., 2019).

An energy-conserved bimodal spectrum with four different spectra peak periods and swell percentages was applied to estimate wave overtopping in both numerical and experimental flumes. Results of incident surface elevations and bimodal spectra were accurately captured across the flume domain using sets of well-positioned resistant-type wave gauges. Peakedness characteristics of the wave patterns were extracted to derive a relationship between the non-dimensional overtopping and the peakedness across the wave groups in the wave series.

The full paper will briefly describe the development of the spectrum and present comprehensive results analysis leading to the derivation of relationship between dimensionless overtopping and peakedness of bimodal waves.

Key Words: wave overtopping, peakedness, bimodal waves, swell percentages.

References

Orimoloye, S., Horrillo-Caraballo, J., Karunarathna, H., and Reeve, D. E., 2019. "Experimental investigation of the sensitivity of bimodal overtopping on spectral shape". Journal of Water, (Under Review).

Reeve, Chadwick, and Fleming (2015), 'Coastal engineering: Processes, theory and design practice', A textbook on Coastal Engineering p. 518, Spon Press, London.

8th International Conference on the Application of Physical Modelling in Coastal and Port Engineering and Science
Zhoushan, China - Dec. 9th - 12th, 2020

SEDIMENT TRANSPORT DURING REGULATION SEASON OF WATER AND SEDIMENT IN THE LOWER YELLOW RIVER

YUANFENG ZHANG[1], PING WANG[1], MING WANG[1]

1 Yellow River Institute of Hydraulic Research, YRCC. Zhengzhou, China, Zhangdut@hotmail.com

Since Xiaolangdi Reservoir (XLD) impoundment in 2000, approximately 80% of the sediment load has deposited in the XLD reservoir, and only about 0.06 billion t of sediment have been flushed out into the Lower Yellow River (LYR) during each annual season for regulation of sediment (RSWS) and water. The bed of the LYR has scoured markedly, and the main channel bed elevation has been lowered by about 1-2.5 m. The bed material below XLD has become noticeable coarser, with a median diameter of 0.2 mm on average in the wandering reach, as compared to a pre-XLD value of
0.095 mm. with Multi-Beam Echo Sounding (MBES), series bathymetric surveys were conducted in the vicinity of the Huayuankou hydrological station (HYK) in the LYR during RSWS. The bedforms are characterised by two scales of dune, i.e., dunes with small superimposed dunes, at less sediment concentration flow conditions. Large-scale dune height and length in average are 2.45m, 770 m respectively with 21 data sets. Small-scale dune height length in average are 0.55m, 9.5m respectively with 756 data sets. The large-scale dunes make more contribution to flow resistance than the small scale dunes. As serious deposition take place during high sediment concentrated flow, the compound bedforms would disappear and become single ones. A bedform discriminator is proposed to describe formative conditions for bedforms in this study. Different bedform phases group well in regard to the phase boundary curves of the discriminator against a control factor based on a new method to calculate energy slope, for both flume and LYR data. The relationship between the bedform discriminator and relative equilibrium sediment concentration can be characterized by three segments. Very high sediment transport capacity is caused mainly by large form drag associated with the two- scale dunes. Very low sediment transport prevails when the dunes wash out corresponding to heavy and fine sediment load flows.

Key Words: bedforms, flow resistance, compound dunes, sediment transport, the lower Yellow River

8th International Conference on the Application of Physical Modelling in Coastal and Port Engineering and Science
Zhoushan, China - Dec. 9th - 12th, 2020

STUDY ON TREATMENT MEASURES TO STABILIZE THE YELLOW RIVER ESTUARY

SONGWEI CHEN[1]

1 Yellow River Engineering Consulting Co., Ltd., Zhengzhou 450003, China

The purpose of regulating the Yellow River estuary is to ensure the flood control safety, stabilize the flow road and improve the service life of the flow road. Since the people began to regulate the Yellow River, with the economic and social development of the estuary area, great achievements have been made in the construction of flood control works, the development and utilization of water resources, and the construction of tidal defense engineering, which greatly promoted the regional economic and social development. At present, the existing measures for regulating the Yellow River estuary include embankment, river regulation engineering, sea embankment, diversion dike, river dredging for embankment reinforcing, artificial diversion of river course, dredging of gate sand, ecological water diversion and other measures. Due to the complexity and diversity of factors affecting the stability of the flow road, and the characteristics of heavy sediment and weak ocean dynamics in the Yellow River estuary remain unchanged, there are still some problems in estuary management, such as the influence of back silting in estuary and the imperfection of current flood control works. Analysis of the present situation and existing problems of engineering measures in estuary area, to evaluate its role and limitations on slowing down the extension length of the flow road and increasing the service life of the flow road, combined with existing engineering measures layout, river topography and waters features, setting up treatment measures conducive to the stability of the flow road, it plays an important role in promoting the sustainable development of economy and society in the estuary area. The treatment measures of the Yellow River estuary and implementation effect was systematically induced. On the basis of analyzing the current situation and existing problems of estuarine regulation, the paper holds that the improvement flood control projects construction, implement artificial diversion of river course, river dredging and sea embankment construction are effective treatment measures to stabilize the Yellow River estuary. Considering the operation mode of the channel into the sea, the layout of recent control measures for the Yellow River estuary is proposed.

Key words: Yellow River estuary; channel stability; artificial diversion of river course; flood control project ; river dredging; sea embankment

8th International Conference on the Application of Physical Modelling in Coastal and Port Engineering and Science
Zhoushan, China - Dec. 9th - 12th, 2020

GEOMORPHOLOGICAL RESPONSE OF THE YELLOW RIVER (HUANGHE) MOUTH TO THE CHANGES IN ITS BOUNDARY CONDITIONS

NAISHUANG BI[1, 2], HOUJIE WANG[1, 2], XIAO WU[1, 2], ZUOSHENG YANG[1], CONGLIANG XU[3]

1 Key Laboratory of Submarine Geosciences and Prospecting Technique, MOE, Ocean University of China, China, E- mail: binaishuang@ouc.edu.cn

2 Laboratory for Marine Geology, Qingdao National Laboratory for Marine Science and Technology, China

3. Institute of the Yellow River Estuarine and Coastal Science, China

Evolution of the river mouth is the result of interactions among terrestrial material supply, fluvial and coastal dynamics. The Yellow River mouth used to be the most rapid land-building river mouth in the world. Its evolution has become a global concern because the sediment load of the Yellow River has decreased sharply in recent decades. This study examined the geomorphological evolution of the Yellow River mouth in response to the changes in conditions of both fluvial and marine boundaries. The result indicated that the temporal evolution of the Yellow River mouth had a four-phase pattern in both subaerial and subaqueous deltas since 1976, with quite close but different relationships with sediment load. In addition to sediment load, evolution of the Yellow River mouth was largely controlled by grain size of the sediment supplied from the river which had been significantly coarsened since the operation of the Water-sediment Regulation Scheme in 2002. Not only fluvial sediment supply but also coastal boundary conditions have changed in recent decades. Velocities of the tidal currents off the present river mouth had increased by 60%–90% compared with those in 1976 as the Yellow River mouth prograding seawards. The enhanced tidal currents favored sediment dispersal away from the river mouth, with increased dispersal extent. Consequently, the subaqueous delta lobe rapidly prograded seaward, while the accretion range of the subaerial delta shrank obviously. Moreover, sediment dispersal pattern has shifted from hyperpycnal to hypopycnal flow as the decrease in sediment load of the Yellow River. As a result, along-shore sediment transport delivered by tidal currents (hypopycnal flow) dominated instead of cross-shore sediment transport driven by gravity (hyperpycnal flow), which would affect spatial deposition of the Yellow River- delivered sediment in the river mouth.

Key Words: Yellow River mouth, geomorphological response, river sediment supply, coastal hydrodynamics

8th International Conference on the Application of Physical Modelling in Coastal and Port Engineering and Science
Zhoushan, China - Dec. 9th - 12th, 2020

MODEL TEST OF JETTING ARM SUBSEA TRENCHER AND STUDY ON SEDIMENT DEPOSITION CHARACTERISTICSIN THE TRENCH

ZOU LI[1,2,*], WANG ZIWEI[1], YUE CAIXING[1], WANG ZHEN[3], PEI YUGUO[1], WANG AIMIN[1]

1 School of Naval Architecture, State Key Laboratory of Structural Analysis for Industrial Equipment, Dalian University of Technology, Dalian 116024, PR China

2 Collaborative Innovation Center for Advanced Ship and Deep-Sea Exploration, Shanghai 200240, PR China

3 School of Mathematic Science, Dalian University of Technology, Dalian 116024, P.R. China

** Email: zoulidut@126.com*

The subsea trencher is an important equipment for laying submarine pipelines and cables. In this paper, the model test of a self-developed jetting arm subsea trencher is carried out, the influence of the angle θ between the jetting arm and the ground on the effect of trenching is studied and the sediment deposition characteristics in the trench are also studied. The test pool is 9m long, 2.5m wide and 2m deep. The gravity similarity criterion is adopted in the test and the scale ratio of the model is 1:4. In the test, the main pipeline flow is 48m³/h, the sediment layer is 1m thick, the shear strength of the sediment is 8kPa, and the water depth is 50cm. During the test, the trencher model is completely submerged. A self-made sounding rod system is used to record the cross-section shape of the trench. The distance between two adjacent sounding rods is 5cm and the total number of sounding rods is 37. The test results show that the shape of the trench is inverted trapezoid, the initial slope angle varies between 50° and 56°, the width of the bottom of the trench does not change with the change of θ, and the depth of the trench increases with the increase of θ, showing a linear relationship. After the completion of trenching, the trench shape at a certain position is measured many times and the corresponding time points of each measurement are also recorded to explore the sediment deposition characteristics in the trench. The results show that the width of the top of the trench does not change with time, the depth of the trench decreases with time and the decrease is fast first and then slow. The depth of the trench can be expressed by the formula H=A/(T+C)+B, where H is the depth of the trench, T is the time, B is the final depth of the trench, A/C is the change of depth between the initial trench and the final trench, A is related to the rate of sediment deposition and the angle of the final trench slope is 45°.

Key Words: subsea trencher; model test; sediment deposition characteristics

8th International Conference on the Application of Physical Modelling in Coastal and Port Engineering and Science
Zhoushan, China - Dec. 9th - 12th, 2020

NUMERICAL SIMULATION OF WINTER WAVE FIELD IN THE SOUTH CHINA SEA FIELD BASED ON SWAN

ZOU LI[1,2,*], WANG WEI[1], JIANG SHENGCHAO[1], WANG PEIZHENG[1], ZHAO JIAN[1]

1 School of Naval Architecture, State Key Laboratory of Structural Analysis for Industrial Equipment, Dalian University of Technology, Dalian 116024, PR China

2 Collaborative Innovation Center for Advanced Ship and Deep-Sea Exploration, Shanghai 200240, PR China

** Email: zoulidut@126.com*

Studying the wave fields in the South China Sea is of great significance for maritime shipping and energy development in the South China Sea. Under the influence of the winter monsoon, the change of the South China Sea wave field becomes more complicated. This paper utilizes the internationally advanced third-generation wave mode SWAN (Simulating Waves Nearshore) on the numerical simulation of the South China Sea wave field for three months from November 1, 2014 to January 31, 2015, adopting nested grid technology, structured grid and triangular grid respectively. The numerical simulation results are compared with the measured wave height and period from the local buoy, and the results show that the numerical results using the nested grid technique agree well with the measured data, and the error statistics of wave height and period are within a reasonable range. Therefore, using the nested grid technology of the SWAN wave pattern can more accurately simulate the winter wave fields in the South China Sea, which is of great significance to the numerical prediction of long-term wave fields in the South China Sea.

Key Words: South China Sea; SWAN; Nested grid technology; Winter wave field; The measured data.

8th International Conference on the Application of Physical Modelling in Coastal and Port Engineering and Science
Zhoushan, China - Dec. 9th - 12th, 2020

NUMERICAL SIMULATION OF TYPHOON WAVES BASED ON THREE COMMON GRIDS OF SWAN

ZOU LI[1,2,*], WANG PEIZHENG[1],JIANG SHENGCHAO[1],WANG WEI[1], ZHAO JIAN[1]

1 School of Naval Architecture, State Key Laboratory of Structural Analysis for Industrial Equipment, Dalian University of Technology, Dalian 116024, PR China

2 Collaborative Innovation Center for Advanced Ship and Deep-Sea Exploration, Shanghai 200240, PR China

** Email: zoulidut@126.com*

The third-generation wave model SWAN was used to numerically study the wave fields in a certain area of the South China Sea during the effects of Typhoon "Doksuri" in 2017 and Typhoon "Ewiniar" in 2018, respectively using nested grids, structured grids and unstructured grids to simulate the wave height changes and compare it with the measured data of the local buoys. And average absolute error value and the average relative error value between the number of numerical results and the measured data under the influence of different grids are analyzed. The results show that under the same grid conditions, SWAN self-nested grids have better grid accuracy than un-nested structured grids and unstructured grids, and agree well with the measured results. This also shows that the SWAN self-nested grid can perform accurate numerical simulation in the South China Sea area. Furthermore, the wind speed process at the measurement point is compared with the wave process, and the dependence between the maximum wind speed and the maximum wave height during the typhoon is analyzed. The above results have reference significance for the numerical prediction and analysis of typhoon waves in the South China Sea.

Key Words: SWAN; Nested grids; Typhoon waves; Measured data; Accuracy

8th International Conference on the Application of Physical Modelling in Coastal and Port Engineering and Science
Zhoushan, China - Dec. 9th - 12th, 2020

RESEARCH ON CONTROL SCHEME IN YUWA REACH OF YELLOW RIVER ESTUARY

YANJIE LIANG[1], XIONGBO CHEN[1]
1 Yellow River Engineering Consulting Co.Ltd, Zhengzhou 450003, China

There are few river regulation projects below Yuwa of Yellow River estuary, and the control project can not play an effective control role and the river is unstable, the swing of the flow path is unfavorable to the development of the estuary area. At present, there are two schemes for river regulation near the Xihekou: "big bend" and "small bend". The "big bend" plan is formed by the combination of the Cuijiazhuang and the Xihekou control projects located in the left bank, forming a big bend. The "small bend" plan is from Cuijiazhuang control project in the left bank to Weigaizha control project in the right bank and then to the Xihekou control project. The 2D mathematical model was used to simulate the flow patterns of the 24.4km section from Yuwa to Qing3 near the Xihekou under three different inflow conditions of 1000m3/s, 4000m3/s and 10000m3/s. The results showed that the control effect of Weigaizha project was not obvious when the flow rate was 1000m3/s. At 10000m3/s, the water in the Xihekou were not able to slide well. At 4000m3/s, the projects can control the water flow effectively. By the four cross sections of different flow velocity distribution arbitrage and river mainstream lines comparison, the characteristics of cross section velocity distribution under different inflow conditions and its adaptability to river regulation are analyzed. When the flow rate is 4000m3/s, the main stream of the river fits with the "small bend " scheme control traverse, which is favorable for controlling the river flow. Considering the inflow and sediment situation of the Yellow River estuary, the small bend scheme is more suitable for medium and small flood, and also is conducive to the water diversion of Shengli oilfield in the Xihekou.

Key words: the Yellow River estuary ; the Xihekou; stabilizing river regime ;the "small bend " scheme

8th International Conference on the Application of Physical Modelling in Coastal and Port Engineering and Science
Zhoushan, China - Dec. 9th - 12th, 2020

CFD INVESTIGATION OF WAVE DAMPING PERFORMANCE OF A PNEUMATIC BREAKWATER

XU TIAO-JIAN[1], WANG XIAO-RONG[2]

1 State Key Laboratory of Coastal and Offshore Engineering, Dalian University of Technology, Dalian 116024, China, tjxu@dlut.edu.cn

2 Southwestern Research Institute of Water Transport Engineering, Chongqing Jiaotong University, Chongqing 400016, China, xrwang2017@163.com

Breakwaters are widely used to reduce the intensity of wave action on the coastal structures. In the past decades, the pneumatic breakwater was proposed as an alternative to the traditional breakwaters due to several advantages, such as mobility, temporality, and low cost. A numerical model is proposed to analyze the wave damping performance of pneumatic breakwater. The Reynolds Averaged Navier-Stokes equations combined with the Shear Stress Transport (SST) k-omega turbulence model is adopted to analyze the flow field around the pneumatic breakwater. An existing experimental model test conducted in a wave flume equipped with Particle Image Velocimetry (PIV) system is used to validate the numerical model, indicating that the numerical model can be applied to investigate the wave damping performance of the pneumatic breakwater. The flow field around the pneumatic breakwater in static water is investigated firstly, and then the wave damping performance of pneumatic breakwater is also analyzed considering different wave parameters, airflow rates and layout patterns. In addition, the combining effect of the joint breakwater of pneumatic breakwater and submerged breakwater is discussed in details. The results indicate that the airflow rates, wave periods and wave heights have obviously influences on the wave dissipation capacity of pneumatic breakwater. The joint breakwater can dramatically improve the wave dissipation capacity when the aerial barrier is located at the downstream of the submerged breakwater.

Key Words: Numerical simulation; Bubble dynamics; Wave damping; Two-phase flow.

8th International Conference on the Application of Physical Modelling in Coastal and Port Engineering and Science
Zhoushan, China - Dec. 9th - 12th, 2020

RESPONSE OF PLUM IN LINGDING BAY DURING AN VARING WIND EVENT

LIRONG YAUN[1], OUYANG LITING[1], ZHANGGUANG[1], GONWENPING[1],SUBO[2]

1 School of Marine Sciences, Sun Yat-Sen University, Guangzhou, China, yuanlr@mail.sysu.edu.cn

2 The Pearl River Hydraulic Research Institute, Guangzhou, China, 68422909@qq.com

The transport pathways of estuarine plume has important impacts on shelf water quality and productivity level. Due to the lack of observation data, most of the studies on wind impact on Lingding Bay plume transport pathways are based on remote sensing and digital-analog results, using steady-state theoretical model analysis, lack of response research on the hourly scale.

A large-scale observation was carried out in Lingding Bay from August 13th to 17th, 2007; On August 19th, typhoon "Sanpa" landed on Huian County, Fujian Province. The observation caught the response of estuary under the action of strongly changing wind. Based on the observation data and a 3D numerical simulation, the variation of estuary stratification structure, plume pattern and freshwater transport direction under the action of wind and tide is analyzed in this paper. Model results confirmed that the Lantau channel beside Dayu island is a key section which dominates the freshwater transport pathways, and can be affected by wind dramatically.

Key Words: Plume. Wind. Pearl River. Linding Bay.

SEDIMENT TRANSPORT IN A SHALLOW COASTAL REGION FOLLOWING SEVERE FLOOD EVENTS

Severe floods usually result in harmful sediment and pollutant dispersion in shallow coastal regions. This study therefore presents a three-dimensional hydrodynamic and transport model investigation into the sediment transport behaviour following severe flooding which occurred in the Brisbane River catchment. It was found that the flood-driven sediment plume formed in the adjacent Moreton Bay and then spread into the northern part of the bay. Based on analysis of the variations in horizontal sediment flux, four distinct characteristics of sediment transport were identified, corresponding to the combined effects of flooding runoff and tidal currents. Firstly, within the estuary, sediment was driven by the flood discharge and primarily transported in the seaward direction. Secondly, at the river mouth, the transport pattern of the sediment was similar that of the first region, however, the horizontal flux was significantly smaller by 50%. Thirdly, a short distance from the river mouth, variations occurred not only in magnitude but also in transport pattern. Lastly, within the coastal bay, the sediment transport was mainly driven by tides, resulting in the changing direction of sediment movement. The results would be used to assist the implementation of coastal management strategies.

8th International Conference on the Application of Physical Modelling in Coastal and Port Engineering and Science
Zhoushan, China - Dec. 9th - 12th, 2020

CONFIGURATION OPTIMIZATION OF A FLOATING BREAKWATER BY DYCORS ALGORITHM

YUANYUAN TAO[1], CHRISTINE A. SHOEMAKER[2,*],PENGZHI LIN[1]

1 State Key Laboratory of Hydraulics and Mountain River Engineering, Sichuan University, Chengdu 610065, China; tyyscu@126.com (Y.T.); cvelinpz@126.com (P.L.)

2 Department of Civil and Environmental Engineering and Operations Research Cluster, National University of Singapore, Singapore, Singapore, shoemaker@nus.edu.sg

In this paper, we optimize the configuration of a floating breakwater which has high performance of protecting a harbour basin from incoming waves in a wide range of wave lengths.For this purpose, an optimization method called DYCORS(Rommel G. Regis & Christine A. Shoemaker,2013)combined with 2D numerical models is employed as the main calculation method.The objective function and constraints are expressed in terms of geometrical parameters of the floating breakwater as mathematical expressions assembled in DYCORS algorithm which is good at HEB(High-dimensional, Expensive, and Black-box) optimization problems.The satisfactory results are obtained demonstrating the capability and effectiveness of this method.

Key Words: configuration optimization,floating breakwater, DYCORS algorithm,wave height

8th International Conference on the Application of Physical Modelling in Coastal and Port Engineering and Science
Zhoushan, China - Dec. 9th - 12th, 2020

A C2 CONSISTENCY INCOMPRESSIBLE SPH MODEL FOR WAVE TRANSFORMATION OVER A SUBMERGED BREAKWATER

YARU REN[1], HAIHUA XU[2], PENGZHI LIN[1]

1 Sichuan University, China, renyaru818@163.com (Y.R.); cvelinpz@126.com (P.L.)

2 Keppel Offshore & Marine Technology Centre, Singapore, xuhaihua@outlook.com

Submerged breakwaters are usually designed in coastal regions to reduce the incident wave energy before waves reach shore. When a periodic wave train propagates over an un-even bottom, it may decomposes into several smaller or isolated waves and experiences significant nonlinear energy transfer. This problem is an important phenomenon and its study has a practical implication in the coastal engineering. To validate the capability of the C2-ISPH model in simulating the problem, the numerical experiment is conducted in the current study and compared with available physical experimental results and previously published numerical results using a σ-coordinate finite difference model. The overall agreements between experimental and simulated results are reasonable.

Key Words: C2-ISPH; breakwater; wave transformation

8th International Conference on the Application of Physical Modelling in Coastal and Port Engineering and Science
Zhoushan, China - Dec. 9th - 12th, 2020

STUDY ON HYDRODYNAMICS OF ECOLOGICALLY VEGETATED HONEYCOMB-TYPE REVETMENT UNDER WAVES

JINFENG ZHANG[1], YIHANG WANG[1], FANGQIAN JIAO[1], NA ZHANG[2], QINGHE ZHNAG[1]

1 State Key Laboratory of Hydraulic Engineering Simulation and Safety, Tianjin University, Tianjin, China, 300072 jfzhang@tju.edu.cn
2 Tianjin Research Institute for Water Transport Engineering, Key Laboratory of Engineering Sediment, Ministry of Transport, Tianjin, China, 300456, sunrain79516@163.com

In estuary and coastal areas, the ecological slope protection is proposed in order to protect the slope erosion and avoid the drawbacks of traditional revetment as it destroys the ecological environment of the water area. For the ecological revetment, the vegetations are introduced into the construction of revetment projects, which can weaken waves and enhance the stability of bank slopes. The ecological slope protection can control the environmental problems to achieve both ecological and economic benefits.

A physical model of ecologically vegetated honeycomb-type revetment with a slope of 1:3.5 is selected and built in the wave flume, then this model is used to study the wave runup, wave overtopping, the near-bed velocity, and the stability of the slope under the action of various regular waves. Furthermore, based on OpenFOAM, an open source computational fluid dynamics software, a three-dimensional numerical wave tank was established which took into account particle movement and flexible plant deformation. Numerical simulation investigation on wave run up and overtopping on honeycomb type ecological revetment with vegetation was carried out.

Based on the experimental data, it can be concluded that vegetations can enhance the stability of revetment under regular wave action, reduce the regular wave runup and overtopping. Furthermore, the wave runup and overtopping decreases with the plant density and height increasing. But vegetations cannot decrease the near-bed flow velocity, and the near-bed velocity tends to increase slightly with the increase of vegetations density.

Key Words: Ecologically vegetated honeycomb-type revetment; Experiments; OpenFOAM; Discrete particle model; Overtopping

8th International Conference on the Application of Physical Modelling in Coastal and Port Engineering and Science
Zhoushan, China - Dec. 9th - 12th, 2020

RESEARCH ON WAVE ENERGY CAPTURE FOR JIGGING SHIP

HANBIN GU[1,3], ZHAODE ZHANG[2], GUANGNIAN LI[1], GUOQIANG LI[2] , YAN ZHANG[2]

1 Institute of Ocean Engineering, Ningbo University, China, guhanbin@nbu.edu.cn; guangnianli@nbu.edu.cn

2 School of Naval Architecture & Mechanical-electrical Engineering, Zhejiang Ocean University,China, zhangzhaode@163.com,qiang_zi168@126.com, zhangyan@zjou.edu.cn

3 Hande Renewable Energy Limited, Zhuji, Shaoxing, China, hanbin.gu@163.com

A device conception of wave energy capture for jigging ship is brought up, which is numerical simulated and tested in experiment. The device is using floats relatively motion with ship to converter wave energy into mechanical energy.

The paper presents the current research of the numerical analysis of the wave energy capture conception of one float connected with the ship, in which wave period in the range of 4s to 12s, wave energy capture ratio is calculated and based on these ratios annual power is estimated about 135kW in North Pacific fishing fields where wave energy density is 10~120kW/m.

Two floats are connected with the ship symmetrically which is tested in experiment. The experimental result is similar to analytical. Result is presented in the paper. The research indicated that the conception is worth to be implemented which may save more than 20% energy for owner of a jigging ship.

Key Words: Wave energy capture, Jigging ship, Simulation, Experiment

8th International Conference on the Application of Physical Modelling in Coastal and Port Engineering and Science
Zhoushan, China - Dec. 9th - 12th, 2020

EXPERIMENTAL STUDY ON SLOSHING IN A TANK WITH DIFFERENT BAFFLES UNDER HORIZONTAL AND ROTATION EXCITATIONS

AIMENG ZHU[1], MI-AN XUE[2]

1 College of Harbour Coastal and Offshore Engineering, Hohai University, China, 15150687681@163.com

2 Key Laboratory of Coastal Disaster and Defence (Hohai University), Ministry of Education, China, mi-anxue@163.com

In the actual situation, no matter ships travelling in sea, or liquid storage tanks building on shore, the external excitation applied to them is not one type or single degree of freedom load. Nowadays, most of the studies on external excitation only discuss the influence of single degree of freedom load on liquid sloshing, but ignore the characteristics of liquid sloshing under the coupling of multiple degrees of freedom excitation. In this study, experiments are carried out to analyze the damping sloshing mechanism under the external excitation of horizontal and rotation in rectangular tank with different shape of baffles, which are vertical baffle, T-shaped baffle and double-side curved baffle, respectively. Besides, software ADINA is used to simulate liquid sloshing of rectangular tank with different baffles under horizontal, rotation and the combine of horizontal and rotation excitation. By analyzing flow field showed by software ADINA and data obtained by experiments and numerical simulation, the anti-sloshing mechanism of different baffles is studied.

Key Words: anti-sloshing mechanism; vertical baffle; T-shaped baffle; double-side curved baffle.

8th International Conference on the Application of Physical Modelling in Coastal and Port Engineering and Science
Zhoushan, China - Dec. 9th - 12th, 2020

STUDY ON HYDRODYNAMIC CHARACTERISTICS OF A LARGE-SPAN JACKET FISH CAGE IN WAVES AND CURRENT

QIU-PAN CHEN[1], CHUN-WEI BI[1], YUN-PENG ZHAO[1], CHAO MA[1], HANG-FEI LIU[1]

1 State Key Laboratory of Coastal and Offshore Engineering, Dalian University of Technology, Dalian 116024, China, chenpan@mail.dlut.edu.cn

In coastal and offshore engineering, the jacket was widely used as basic structure, and it would have a good application prospect in combination with marine fisheries as the jacket fish cage. However, the hydrodynamic force of the structure is more complicated under the action of wave and current loads. In this study, the jacket and the jacket fish cage model were taken as the research objects. Through a series of wave and current tests, the hydrodynamic characteristics of the models were studied. The corresponding numerical models were established to obtain preliminary calculation results, based on the experimental and numerical results, the least square method was used to fit the hydrodynamic coefficients of the jacket and the netting, and the corresponding drag and inertia force are calculated. The research results showed that the additional netting significantly increased the wave force and flow resistance of the jacket. The horizontal wave force of the jacket was greatly affected by the drag and inertial force, and the horizontal wave force of the netting was dominated by drag force. For large-span offshore structures, due to the large wave phase difference between the structural components, the wave period greatly affected the total force of the structure.

Key Words: Jacket; jacket fish cage; hydrodynamic coefficients; Morison equation

8th International Conference on the Application of Physical Modelling in Coastal and Port Engineering and Science
Zhoushan, China - Dec. 9th - 12th, 2020

RESEARCH ON HARBOUR RESONANCE UNDER EDGE WAVES INDUCED BY METEOROLOGICAL DISTURBANCES

QIUYI SUN[1], XIAOJING NIU[2]

1 Department of Hydraulic Engineering, Tsinghua University, Beijing 100084, China. E-mail: sqy19@mails.tsinghua.edu.cn

2 State Key Laboratory of Hydroscience and Engineering, Department of Hydraulic Engineering, Tsinghua University, Beijing 100084, China. E-mail: nxj@tsinghua.edu.cn

Edge waves, which are of great significant to the near-shore hydrodynamic process, can be generated by a moving atmospheric pressure disturbance under certain circumstances. Their frequencies and amplitudes are related to the scale and the central pressure deviation of the pressure disturbance as well as the speed and direction of its movement. This research focuses on the response of a harbour to a group of edge waves generated by meteorological disturbances. Whether edge waves can excite harbour resonance has been investigated.

Numerical simulation is conducted based on the nonlinear shallow water equations. First, the occurence conditions of edge wave induced by moving pressure disturbances are discussed. And then, the response of an idealized harbour to a group of edge waves is analyzed. A series of numerical experiments are carried out considering different ratios between the frequency of edge wave and the natrual frequency of the harbour. The wave pattern in the harbour basin and the energy transfer at the entrance are discussed. When edge waves pass a harbour entrance, part of wave energy will be transferred into the harbour. Harbour resonance might be excited when the frequency of edge wave is close to the harbour's natural frequency. The effect of aspect ratio of the harbour basin and width of the harbour entrance are also shown. Finaly, a relationship between meteorological factors and harbour resonance is given, and representative events of harbour resonance caused by meteorological disturbances in history are discussed.

Key Words: edge wave; meteorological disturbance; harbour resonance; wave energy.

8th International Conference on the Application of Physical Modelling in Coastal and Port Engineering and Science
Zhoushan, China - Dec. 9th - 12th, 2020

HYDRODYNAMIC STUDY OF OSCILLATING FLOAT-TYPE WAVE ENERGY EXTRACTION DEVICE

BINGTAO YIN[1], HANBIN GU[2], ZHAODE ZHANG[1]

1 School of Naval Architecture & Mechanical-electrical Engineering, Zhejiang Ocean University, China, aaa17858804594@163.com, zhangzhaode@163.com

2 Institute of Ocean Engineering, Ningbo University, China, guhanbin@nbu.edu.cn

In this paper an oscillating float-type wave energy extraction device is presented which absorbs wave energy through oscillating float in heave under waves. In the device system, the left side is a storage tank, and the right side is connected with a hydraulic cylinder. The hydraulic cylinder driven by a float under wave converts wave energy into water circulation motion through valves. High pressure water flow to drive a turbine to generate electricity at the top of the storage tank, Main research objectives of this paper are to establish the mathematical model, construct the hydrodynamic equation of the energy extraction device and solve it. Based on the knowledge of fluid mechanics, different sections of the extraction device were energy conserved. The relationship between the velocities of different sections is obtained by using the continuity equation. Bernoulli equation is established for different sections, and the relationship of pressure and velocity between different sections can be obtained. By solving the equation through transformation, it can be concluded that the driving force of the extraction device to the floating body is a function of the change of the floating body's position. Finally, based on Newton's second law, the equilibrium equation of floating body is given, and extracted wave power can be evaluated by the force multiplying the speed of float motion.

Key Words: Wave energy extraction device, Bernoulli equation, Continuity equation, Extracted wave power

8th International Conference on the Application of Physical Modelling in Coastal and Port Engineering and Science
Zhoushan, China - Dec. 9th - 12th, 2020

ASSESSMENT OF MACROSCOPIC RESISTANCE-TYPE POROSITY IMPLEMENTATIONS FOR CFD MODELLING OF THIN POROUS STRUCTURES EXPOSED TO OCEAN WAVES

A. Feichtner1*, E. Mackay1, G. Tabor2, P. R. Thies1, L. Johanning1
1 University of Exeter, CEMPS, Renewable Energy, Penryn Campus
2 University of Exeter, CEMPS, Engineering, Streatham Campus
**Corresponding author: af506@exeter.ac.uk*

One of the key engineering challenges of floating offshore wind turbines is the stability of the platform. Equipping the platforms with porous outer shrouds has the potential to function as a passive motion damping mechanism. Attenuation of the motion responses entails reduced mooring loads and longer turbine operation phases. As a first step towards this complex wave-structure-interaction problem, this work evaluates potential options for a macroscopic representation of thin porous structures exposed to regular ocean waves. For this work, OpenFOAM is used in combinations with and modifications of the OlaFlow and waves2Foam libraries.

In general, for macroscopic porosity implementations in Navier-Stokes models, resistance terms are applied in the momentum equation to account for the pressure drop for flow through the porous material and porosity is often taken into account in a volume-averaged manner for a geometrically defined region. This removes the need to explicitly resolve the openings in the porous material in the computational mesh and results in lower computational costs compared to a microscopic approach where the openings are resolved explicitly. For thin porous structures such as perforated steel plates in oscillatory fluid flow, the flow regime tends to be turbulent. Hence, the dominant porosity term is a turbulent drag term with the drag coefficient described as a function of porosity. Inertial effects due to fluid acceleration through the openings have a smaller effect, mainly influencing the phase of the force relative to the incident wave.

This work uses a constant porous resistance term and presents the assessment of the main options of a macroscopic porosity implementation for CFD models: a representation as a porous pressure-jump across a baffle with zero thickness, a simplified assumption of isotropic porous material and representation as orthotropic or anisotropic porous material. For the latter two options, a thin volumetric porous zone is applied at defined mesh cells. The three options are evaluated for their ability to model wave loads on fixed porous plates and fixed porous cylinders as well as the fluid velocity profiles near the structures. The model development focuses on characteristic mesh cell dimensions and the number of cells across the porous barrier respectively. The CFD results are validated against wave tank results and have been shown to compare well.

The present CFD results aim to inform the setup of future models addressing wave interaction with floating wind turbine platforms equipped with porous outer layers. As the computational cost will drastically increase for these more complex models, one objective is to achieve a trade-off between accuracy and feasibility in terms of the number of mesh cells and computational cost respectively.

Key Words: thin porous structures, resistance-type porosity, wave structure interaction

8th International Conference on the Application of Physical Modelling in Coastal and Port Engineering and Science
Zhoushan, China - Dec. 9th - 12th, 2020

NUMERICAL ANALYSIS OFA MULTI-MODULE VLFS BASED ON A STRUCTURAL-HYDRODYNAMIC MODEL BY CONSIDERING GAP RESONANCES

MINGSHENG CHEN [1], HONGRUI GUO [2], MEIYAN ZOU [3], LING ZHU [4]

1 School of Transportation, Wuhan University of Technology, CHINA, mschen@whut.edu.cn 2 School of Transportation, Wuhan University of Technology, CHINA, hrguo@whut.edu.cn 3 School of Transportation, Wuhan University of Technology, CHINA, zmyeol@163.com

4 School of Transportation, Wuhan University of Technology, CHINA, lingzhu@whut.edu.cn

Very Large Floating Structure (VLFS) has attracted much attention in recent years as the ocean space utilisation becomes more demanding. This type of structure generally consists of multiple modules interconnected by either semi-rigid or hinged connectors. This flexible connection allows certain relative motion between the different modules to reduce the longitudinal loads. The floating airport is a typical example of VLFS, which has been extensively studied by Japanese scholars in 1990s and by Chinese scholars in the 21st century. This paper considers a simplified floating airport model consisting of three rectangular box interconnected by a flexible beam to study the dynamics of VLFS subjected to the waves. Frequency-domain hydrodynamic analyses are carried out for this multi-module floating structure by using both ANSYS-AQWA and DIFFRACT. Based on ANSYS-AQWA, different gap widths between the adjacent modules are considered to analyse the complex multi-body hydrodynamic interactions by introducing an artificial damping lid on the gap surfaces. A simplified structural-hydrodynamic model is established to study the dynamics of the multi-module with flexible connections, which condenses the mass and stiffness of the flexible beam onto the nodes connected on the modules, resulting in a constant parameter frequency-domain model. Parametric studies are carried out to investigate the effects of the gap width, artificial damping ration on the gap surface and the stiffness of the flexible beam on the dynamics and of the multi-module VLFS and the constraint forces at the connection nodes. Finally, recommendations for the design of the flexible connection and selection of the gap width are provided.

Key Words: VLFS; rigid-flexible coupling; static condensation; gap resonance; hydrodynamic interactions

8th International Conference on the Application of Physical Modelling in Coastal and Port Engineering and Science
Zhoushan, China - Dec. 9th - 12th, 2020

DYNAMICS OF FISH CAGES WITH ELASTIC NET IN CURRENT AND WAVES

ZITTI GIANLUCA, NOVELLI NICO, BROCCHINI MAURIZIO

Dipartimento Ingegneria Civile, Edile e dell'Architettura
Università Politecnica delle Marche, Ancona, Italy
g.zitti@univpm.it

Over the last decades the aquaculture sector increased significantly and constantly, moving fish-farm plants further from the coast, and exposing them to increasingly high forcing due to currents and waves. The performances of cages in currents and waves have been widely studied in literature, by means of laboratory experiments and numerical models, but virtually all the research is focused on the global performances of the system, i.e. on the maximum displacement, the volume reduction or the mooring tension.

In this work we propose a numerical model, derived from the net-truss model of Kristiansen and Faltinsen (2012), to study the dynamics of fish farm cages in current and waves. In this model the net is modeled with straight trusses connecting nodes, where the mass of the net is concentrated at the nodes. The deformation of the net is evaluated solving the equation of motion of the nodes, subjected to gravity, buoyancy, lift and drag forces. With respect to the original model, the elasticity of the net is included. Further, the net grid is not lumped into a reduced number of equivalent elements, as was done in many applications to reduce the computational cost. In this work the real size of the net is used for the computation mesh grid, this allowing the numerical model to reproduce the exact dynamics of the cage.

The numerical model is used to simulate a cage with fixed rings, based on the concept of mooring the cage to the foundation of no longer functioning offshore structures. The deformation and tension of the system subjected to currents and waves are studied, focusing also on the change in shape of the cage.

References:

Kristiansen, T. and Faltinsen, O.M. (2012). Modelling of current loads on aquaculture net cages. *Journal of Fluids and Structures* 34, 218-235. doi:10.1016/j.juidstructs.2012.04.001.

Key Words: fish-farm, cage dynamics, deformable net

8th International Conference on the Application of Physical Modelling in Coastal and Port Engineering and Science
Zhoushan, China - Dec. 9th - 12th, 2020

EXPERIMENTAL STUDY ON THE EVOLUTION OFSCOURING AND DEPOSITION IN YELLOW RIVER DELTA

XIANG ZHAO[1], ZUWEN JI[2],ANJUN DENG[3],DANGWEI WANG[4]

1,2,3,4 State Key Laboratory of Simulation and Regulation of Water Cycle in River Basin, China Institute of Hydropower & Water Resources Research, Beijing, China, zx_sedi@163.com; jzw@iwhr.com; denganj@iwhr.com; wangdw17@126.com

The Yellow River has the characteristics of less water and more sediment, and the distribution of water and sediment is uneven. The estuary is affected by runoff and ocean dynamics, the evolution of scouring and deposition is complicated. The flow path swings frequently and has experienced three stages and 11times major avulsions since 1855. Therefore, maintaining the stability of the Yellow River estuary flow path and prolonging the service life of the current flow path are important for the construction of the Yellow River Delta Highly Efficient Ecological Economic Zone. Based on the generalized model of the Yellow River estuary, the scouring and deposition of the Yellow River delta under different dynamic conditions and boundary conditions are studied. For the problem of large experimental area topographic survey, the traditional measurement methods are time-consuming and labor-intensive. 3D laser scanning technology was adopted to measure the experimental terrain, and the experimental data statistics and analysis such as contour drawing and scouring and deposition calculation were made by Arcgis software. The result shows that the runoff plays a dominant role in the evolution of scouring and deposition in the Yellow River delta, while the ocean dynamics is relatively weak. In addition, the relationship between the distribution of scouring and and deposition and the avulsion is discussed. The avulsion of the Yellow River estuary flow path is not only related to the dynamic conditions, but also important to the boundary conditions, and the formation of boundary conditions is mainly related to the dynamic conditions. Therefore, the study on the evolution of scouring and deposition under different dynamic conditions and boundary conditions can provide some references for the development process of the avulsion.

Key Words: river model, 3D laser scanning technology, scouring and deposition, avulsion

8th International Conference on the Application of Physical Modelling in Coastal and Port Engineering and Science
Zhoushan, China - Dec. 9th - 12th, 2020

FOCUSED WAVE SIMULATION BASED ON CONSTANT STEEPNESS METHOD

QIANLI GUO[1], HANBIN GU[2]

1 Zhejiang Ocean University, China, 1766088699@qq.com

2 Ningbo University, China, guhanbin@nbuedu.cn

It is well known that focused waves are generally generated using the principle of linear superposition. In 1998 Kway JHL et al. proposed the constant steepness method to generate focused waves in application. This paper will view the characteristics of the focused wave generated by the method. In the method, the steepness is constant, which is wave component amplitude multiplying its corresponding wave number. To implement the method, constant steepness can be given, component wave number related to water depth and can be solved by dispersion relation, after that corresponding wave amplitude is determined.

The article further observes the variation of the shape of the focused wave by changing the center frequency, constant steepness, and wave frequency range respectively in an environment where the constant water depth, focus time and focus point are not changed. The characteristic of focus wave include height of peaks, the ratio of the highest peak to the secondary peak and influence of constant steepness, center frequency, frequency range to shape of the focus wave.

Results of the study will be helpful to researchers who use the constant steepness method in their works.

Key Words: Focused wave; Constant steepness method; Focus wave shape

8th International Conference on the Application of Physical Modelling in Coastal and Port Engineering and Science
Zhoushan, China - Dec. 9th - 12th, 2020

MODELING THE FLOODING DEPTH AND TIME USING A DEPTH AVERAGED HYDRODYNAMIC MODEL IN COASTAL WETLANDS OF THE LIAO RIVER ESTUARY

YINI WANG[1], HUI XU[1], YARU KANG[1], HENGZHI JIANG[2], MINGLIANG ZHANG[1*]

1.College of Ocean Science and Environment, Dalian Ocean University, Dalian, China 2.National Marine Environment Monitoring Center, Dalian, Liaoning, 116023, China

Suaeda heteroptera is the most common indicator plant of solonchak in coastal wetlands of the Liao River Estuary, the change of the flooding depths and period in *Suaeda heteroptera* habitat is of growing interest. In this study, a depth-averaged hydrodynamic model was adopted to simulate the changing process of water level and tidal currents, with the distribution of water retention time in coastal wetlands of the Liao River Estuary. Remote sensing (RS) and geographic information system (GIS) were used to analysis the distribution of vegetation in coastal wetlands of the Liao River Estuary. The results showed that the hydrodynamic model could accurately simulate the water level and tidal currents process of the research area. During the ebb tide period, owing to the development of many shoals, the current at the mouth of the estuary is divided into many branches. This model was also used to analyze the flooding depth and time in wetland vegetation domain of the Liao River Estuary. In addition, the influence of wind on water retention time and flooding depth in tidal flat was explored according to the distribution of *Suaeda heteroptera* vegetation in Liao River estuary. The research results provide important reference and guidance for the analysis on the degradation of *Suaeda salsa* vegetation.

Key Words: Remote Sensing ; Numerical Modeling ; Suaeda Heteroptera ; Water Retention Time; Liao River Estuary.

8th International Conference on the Application of Physical Modelling in Coastal and Port Engineering and Science
Zhoushan, China - Dec. 9th - 12th, 2020

SIMULATION OF DEPOSITION AND EXTENSION PROCESS OF QINGSHUIGOU PATH IN THE PERIOD OF WATER AND SEDIMENT REGULATION

WANG ming[1], ZHANG Yuan Feng[1] , WANG Ping[1]

1 Yellow River Institute of Hydraulic Research，Key Laboratory of Yellow River Sediment Research of MWR, Zhengzhou 450003, China

The evolution of the Yellow River Estuary in modern times is characterized by frequent swings and diversions of flow paths，the basic reason is that the Yellow River estuary is continuously extending，so it has a feedback effect on the river course，it is of great significance to carry out the study on the law of deposition and extension in the Yellow River Estuary. This study is based on the analysis of historical data, a sediment erosion and deposition model suitable for the Yellow River estuary is established, and use two dimensional mathematical model of water and sediment i to simulate the process of deposition and extension in the estuary.First, use the measured data from 2007 to 2015，The model verification shows that the calculated results are in good agreement with the measured data；Then, under different water and sand condition，the deposition and extension process of the estuary in 30 years is predicted，the evolution law of the Yellow River estuary is analyzed，It provides technical support for the comprehensive management of the Yellow River Estuary flow path.

Key words: Qingshuigou path；Yellow River Estuary；two dimensional mathematical; water and sediment regulation model

8th International Conference on the Application of Physical Modelling in Coastal and Port Engineering and Science
Zhoushan, China - Dec. 9th - 12th, 2020

HYDRODYNAMICS AND SEDIMENTARY PROCESSES OF A TURBID ESTUARY UNDER THE CHANGING ENVIRONMENT

HONGYU JI[1,2], SHUNQI PAN[1,2], SHENLIANG CHEN[1]

1. State Key Laboratory of Estuarine and Coastal Research, East China Normal University, Shanghai 200062, China
2. Hydro-environmental Research Centre, School of Engineering, Cardiff University, Cardiff CF24 3AA, UK, 52152601006@stu.ecnu.edu.cn, PanS2@cardiff.ac.uk, slchen@sklec.ecnu.edu.cn

The interplay between riverine flow and tides are crucial for the land-ocean interactions and river-born sediment transfer and dispersal. Regulating the river discharge may have met the need for water demands in the river basin, but resulted in carrying less freshwater and sediment to the sea and inducing land degradation and shoreline retreat in worldwide mega-river-deltas. Tides response to the water discharge changes plays an important role in sediment retention and estuarine deposits.

The Yellow River Delta (YRD), which is under the increasing pressure of the new discharge regime of the Yellow River, has undergone drastic changes in sediment dynamics and morphologic evolution. To gain a better understanding of the overall fluvial and oceanic hydrodynamic and morphodynamic processes in the YRD, a full-scale numerical model was built to study the interaction and impacts of the changing environmental forcing and dynamics on flow and sediment transport in the estuary and adjacent coasts. The results show that the river discharge strongly affects the tidal dynamics and morphology of river deltas, particularly in the close vicinity of the outlet and the intertidal zone with a range of river discharges imposed. Tidal constituents M2 and K1, which are the most significant tidal constituents in the YRD, are found to be noticeably affected by the increase of river discharge with decreased tidal constituents.

The model results also show that the river discharge affects the location and intensity of the shear front around the YRD. Increased the flow discharge can reduce its width and increase the shear front intensity. The reverse of the velocity direction in each side of the shear front zone acts as a barrier for the sediment dispersal process, keeping suspended sediment concentration in the inner zone, thus to form a particular sediment deposition zone and the depo-center.

Key Words: Tides, river discharge, suspended sediment transport, depocenter, active Yellow River Delta

8th International Conference on the Application of Physical Modelling in Coastal and Port Engineering and Science
Zhoushan, China - Dec. 9th - 12th, 2020

MIXING AND PROPAGATING OF WEAKLY AND STRONGLY STRATIFIED TWO-LAYER LOCK-EXCHANGE GRAVITY CURRENTS

RUI ZHU[1], ZHIGUO HE[2], ECKART MEIBURG[3]

1 PhD Student, Ocean College, Zhejiang University, Zhoushan, China Email: zhurui@zju.edu.cn
2 Professor, Ocean College, Zhejiang University, Zhoushan, China Email: hezhiguo@zju.edu.cn
3 Professor, Department of Mechanical Engineering, University of California, Santa Barbara, Santa Barbara, California, USA Email: meiburg@engineering.ucsb.edu

A series of lock-exchange experiments and numerical simulations are carried out to investigate the hydrodynamics of gravity currents produced from weakly and strongly two-layer stratified buoyancy source on a flat bottom. A high-speed camera and a particle image velocimetry (PIV) system are applied to obtain the moving and the mixing behavior of the two layers. For a weakly stratified two-layer gravity current, the two layers mix thoroughly earlier with a higher initial height ratio and lock aspect ratio. For a strongly stratified two-layer gravity current, a higher initial height ratio and a smaller lock aspect ratio result in a shorter time for the upper layer to outrun the lower layer. After the upper layer outruns the lower layer, the current has a constant-velocity phase and a deceleration phase. Two- and three-dimensional Direct Numerical Simulations (DNS) are undertaken to get the data about the interface structure and energy budget. There is more intense turbulence at the interface of weakly stratified two layers. An energy analysis shows the energy transfer between the two layers.

Key Words: Mixing; separation; two-layer gravity current; vertical stratification

8th International Conference on the Application of Physical Modelling in Coastal and Port Engineering and Science
Zhoushan, China - Dec. 9th - 12th, 2020

EFFECTS OF HYDROID-FOULING ON THE HYDRODYNAMICS OF THE FISH CAGE NETTING

CHUN-WEI BI[1], YUN-PENG ZHAO[1], GUO-HAI DONG[1]

1 State Key Laboratory of Coastal and Offshore Engineering, Dalian University of Technology, Dalian 116024, China, bicw@dlut.edu.cn

With the steady growth of world population and the continuous improvement of living standards, the demands for high quality seafood continue to grow. To fulfill this goal, efforts must be paid to modern technology regarding to offshore aquaculture facilities and equipments. In the aquaculture industry, offshore net cages are becoming prevalent around the world. Biofouling is an inevitable problem in marine aquaculture and it is prone to cause many negative effects on the hydrodynamic behavior of the aquaculture facility. In this study, the dominant biofouling, hydroids, on the netting of fish farms in the Yellow Sea of China was determined by field sampling. Plane nets with various levels of hydroid-fouling were obtained by different submerged periods and depths.

Effects of hydroid-fouling on motion responses and hydrodynamic loads of an aquaculture net in waves were investigated using laboratory experiment. The results indicate that the hydrodynamic loads acting on the aquaculture net increases with increasing level of hydroid-fouling. Compared to the clean net, the accumulation of hydroid-fouling can lead to over 5 times more wave loads on net cages. As the level of hydroid-fouling increases, the motion responses of the aquaculture net increases continuously. The net with the greatest level of hydroid-fouling produces the largest motion amplitude which is approximately 4 times than that of the clean net. Overall, the solidity of the hydroid-fouling net is recommended to be a reliable index for describing the level of hydroid-fouled net with hydroid-type fouling.

There are many different kinds of biofouling organisms, which is primarily depending on location and season, related to marine aquaculture. The physical and geometrical characteristics as well as the distribution of various types of biofouling have different effects on the hydrodynamic characteristics of the net cage. Thus, it is essential to conduct researches into the hydrodynamic characteristics of the net cage considering the effect of various types of biofouling in currents and waves in the future work.

Key Words: aquaculture net; hydroid-fouling; motion response; wave loads; laboratory experiment

8th International Conference on the Application of Physical Modelling in Coastal and Port Engineering and Science
Zhoushan, China - Dec. 9th - 12th, 2020

ACOUSTIC OBSERVATIONS OF KELVIN-HELMHOLTZ BILLOWS ON AN ESTUARINE LUTOCLINE

Junbiao Tu[1*], Daidu Fan[1,2], Qiang Lian[3], Zhiyu Liu[3], Wei Liu[1], Alexis Kaminski[4], William Smyth[5]

1 State Key Laboratory of Marine Geology, Tongji University, Shanghai, China

2 Laboratory of Marine Geology, Qingdao National Laboratory for Marine Science and Technology, Qingdao 266061, China

3 State Key Laboratory of Marine Environmental Science, and Department of Physical Oceanography, College of Ocean and Earth Sciences, Xiamen University, Xiamen, China

4 Applied Physics Laboratory, University of Washington, Seattle, Washington, USA

5 College of Oceanic and Atmospheric Sciences, Oregon State University, Corvallis, Oregon, USA

**Corresponding author: Junbiao Tu (jtu@tongji.edu.cn)*

Kelvin-Helmholtz (KH) instability plays an important role in turbulent mixing in deep oceans and coastal seas. Though widely observed and studied in thermohaline-stratified waters, KH instability is scarcely observed in sediment-stratified environments. For the first time, we present direct observations of KH billows on an estuarine lutocline by combining echosounder images with velocity and density measurements. The interaction between velocity shear and the density stratification induced by suspended sediments initiated shear instabilities near the bed, indicated by gradient Richardson number (Ri) < 0.25 at the early stages of the observed billows. Once formed, the instabilities enhance vertical mixing of momentum, reducing vertical shear and elevating Ri. Linear instability analysis using measured velocity and density profiles well predicts the vertical location and spatial characteristics of the observed billows. These instabilities are believed to contribute to the vertical mixing, entrainment, and transport of estuarine and coastal sediments.

8th International Conference on the Application of Physical Modelling in Coastal and Port Engineering and Science
Zhoushan, China - Dec. 9th - 12th, 2020

EXPERIMENTAL STUDY ON THE INTERACTIONS BETWEEN COUNTERFLOWING GRAVITY CURRENTS

OKON SAMUEL UKPONG[1], HE ZHIGUO[2], CHEN YANAN[3]

[1]*Ocean College, Zhejiang University, Zhoushan 316021, China. E-mail: samukpong@zju.edu.cn*
[2]*Ocean College, Zhejiang University, Zhoushan 316021, China. E-mail: hezhiguo@zju.edu.cn*
[3]*Ocean College, Zhejiang University, Zhoushan 316021, China. E-mail: cynwddt@zju.edu.cn*

Interactions between counterflowing gravity currents are common in nature as observed between sea- breeze fronts. This interaction is an important triggering mechanism for deep moist convection. Severe precipitation associated with deep convection drives several high impact events such as flash flooding. Gaining a better understanding of the deep convection phenomenon is necessary for predicting severe weather events. We experimentally studied the dynamics of two counterflowing gravity currents with the aim of understanding the collision and convection processes which is difficult to study in nature. In a novel double-lock flume of horizontal bed and rectangular cross- section, eighteen (18) different experimental runs were performed in replicate by varying the density of the dense fluids in respective locks. Dense and ambient fluids were prepared using salt and aqueous ethanol solutions respectively, meticulously matching the refractive indices to enable accurate velocity field measurements without laser beam distortions. The evolution of the counterflowing gravity currents were recorded using a high-speed digital camera and detailed velocity fields were obtained with particle image velocimetry (PIV). Various image analysis techniques were applied to enable an easy understanding of its general dynamics and the collision process. Experimental results revealed four main stages of flow evolution: independent propagation of respective gravity currents, their approach with influence on each other, collision/ascending motion, and post-collision slumping of mixed collision front. Upon collision, a mixed front developed between the two currents. In symmetric cases, the mixed front was vertical and stationary, producing propagating hydraulic bores in the post-collision slumping stage. In asymmetric cases, the mixed front developed at an angle with the denser current intruding underneath the less dense current, producing a new gravity current at the bottom with Kelvin–Helmholtz billows visible in the post-collision slumping stage. Overall, the angle of the collision was dependent on the currents' buoyancy ratio and the amount of mixing along the collision front decreased with asymmetry. We present a detail description of the collision and convection processes. Our experimental observations are useful to the meteorological community whose major task is the development of improved weather forecasting models.

Key Words: Counterflowing gravity currents, sea breeze, collision, deep convection, fluid dynamics

JET FIELD DISTRIBUTION OF SHIP PROPELLER IN WATERWAY

During the ship's voyage, the propeller jet will affect the movement of sediment at the bottom of the bed. In order to study the influence of the bottom boundary on the propeller jet field, this paper takes the standard propeller DTRC4119 propeller as the research object, and uses the CFD software Star-ccm + to carry out the numerical simulation of the propeller jet uniformly. The flow velocity distribution of the jet under five operating conditions is mainly analyzed, including the axial, tangential, radial components and turbulence intensity of the jet velocity. The results show that the distance between the propeller and the boundary does not affect the magnitude and distribution of velocity on the initial plane, but affects the peak value of the axial velocity in the development zone and the magnitude of the velocity on the central axis. The tangential and radial velocity values generated by the rotation decrease, and the velocity change is no longer obvious at this time; for turbulence intensity, the closer the propeller is to the bottom boundary, the turbulent fluctuations due to the boundary, Incoming velocity mixing reduces the intensity of turbulence.

8th International Conference on the Application of Physical Modelling in Coastal and Port Engineering and Science
Zhoushan, China - Dec. 9th - 12th, 2020

THE WAVE ENVELOPE DYNAMICS FOR SURFACE GRAVITY WAVES OVER A VARYING BATHYMETRY IN A BACKGROUND FLOW

YAN LI [1, 2]

1 Department of Energy and process engineering, Norwegian University of Science and Technology, 7491 Trondheim, Norway, yan.li@ntnu.no

2 Department of Engineering Science, University of Oxford, United Kingdom, yan.li@eng.ox.ac.uk

This work focuses on weakly nonlinear waves over a varying bathymetry in a background flow. In contrast to most classical studies where the potential flow theory is employed, a theoretical model is developed in this study that relaxes the assumption of irrotational wave motions. Specifically, the surface waves are assumed of an envelope-type form, and thus the evolution equation of wave envelope is derived, taking into account a varying bathymetry and a background flow of gradients.

The variation of water depth is considered small compared to the variation of the primary wavelength in space and the horizontal gradients of a background flow is small relative to its depth dependent gradient. The effects of a varying seabed and a background flow on the wave envelope dynamics are examined. Moreover, the additional generation of free waves as a result of a flow over a varying seabed is also considered. The presented work has illustrated that the energy transfer of a background flow to surface waves can be made via two different ways: (1) the generation of free surface waves; and (2) the evolution of wave energy propagating at different speeds that depend on the properties of the primary wave.

Key Words: surface gravity waves; wave evolution; sheared current; varying bathyemetry

A LABORATORY STUDY OF CLASS III BRAGG RESONANCE

When moderately steep waves travel over a periodic rippled bed, class III Bragg resonance may occur due to the third-order quartet wave-bottom interaction among one bottom and three surface wave components. The theory, however, has not been experimentally confirmed. To verify the existence of class III Bragg resonance, we consider the simplest possible case involving a single incident wave, and conduct a series of physical experiments. The experiments show that as the theory predicts, class III Bragg resonance could generate not only the reflected waves (from sub- harmonic resonance) but also the transmitted waves (from super-harmonic resonance), and the reflection and transmission coefficients vary linearly along the rippled bottom patch. Furthermore, the experimental data of the reflected and transmitted waves (due to class III resonance) agree quantitatively well with the prediction of high-order spectral (HOS) method computations.

8th International Conference on the Application of Physical Modelling in Coastal and Port Engineering and Science
Zhoushan, China - Dec. 9th - 12th, 2020

AMPLIFICATION OF INFRAGRAVITY WAVES INDUCED BY UNDERWATER SHOALS

Z. L. LIAO[1], S. W. LI[2], Y. LIU[3]

1 State Key Laboratory of Hydraulic Engineering Simulation and Safety, Tianjin University, Tianjin, China, tju_lzl@tju.edu.cn

2 State Key Laboratory of Hydraulic Engineering Simulation and Safety, Tianjin University, Tianjin, China, lishaowu@tju.edu.cn

3 State Key Laboratory of Hydraulic Engineering Simulation and Safety, Tianjin University, Tianjin, China, liuye2009@tju.edu.cn

Infragravity waves (IGWs) are waves with frequencies remarkably lower than short waves (SWs), typically between 0.004 and 0.04 Hz in prototype, and have important effects on many aspects of coastal hydrodynamics, such as beach and dune erosion, nearshore sediment transport, and short-wave groupiness on coral-reef flat. Utilizing the non-hydrostatic wave model SWASH, the previously reported phenomenon of IGWs being amplified in the presence of an underwater shoal was investigated in detail under non-breaking conditions. Nonlinear energy transfer from SWs to IGWs was found to consistently occur in the shoal region, and the effect was more significant on a milder bottom slope. Energetic free IGWs that are weakly correlated with the wave group were found to transmit behind the shoal, constituting a potential source of nearshore IGWs.

Key Words: infragravity waves, shoal, non-hydrostatic model

8th International Conference on the Application of Physical Modelling in Coastal and Port Engineering and Science
Zhoushan, China - Dec. 9th - 12th, 2020

COMPARATIVE STUDY ON BREAKWATER EMERGENCY PROTECTIVE WAYS DURING CONSTRUCTION PROCESS

LIU HAICHENG [1], YANG HUILI [2]

1 Tianjin Research Institute for Water Transport Engineering, M.O.T. China, lhc_02@163.com
2 Tianjin Research Institute for Water Transport Engineering, M.O.T. China, yanghuili22@126.com

On strong wave sea area, emergency protection of breakwater during construction process is problem often faced. For different projects, there are many emergency protective measures. There are different risks and effects for different protective measures. In this paper, different measures were studied by physical model for Ashdod port breakwater project. The wave on project sea area is very strong during monsoon period. And breakwater construction will be suspended and it will be protected by interim protective measures. For the safety and success of the construction, the physical model test of different emergency protective measures during construction process will be studied. The safe and financial interim protective measures to keep breakwater head stable during monsoon season will be studied and recommended in order to guide the phases of the project construction. In this study, the interim protective effect of gabion, gabion chain and antifer units were studied. Compare the stability of gabion, gabion chain, antifer units. The study found that stable weight of gabion, gabion chain and antifer block was different. The potential risks of different protective measures were analyzed. For example, the production and construction of gabion and gabion chain was complicated, and once the gabions broken up into small rocks under strong wave action it would result in destruction of the entire breakwater. As a result of this study the interim protection of two layers antifer units was found to be superior to the other interim protective measures.

Key Words: Emergency protective measures, Strong wave, Antifer, Gabion chain

8th International Conference on the Application of Physical Modelling in Coastal and Port Engineering and Science
Zhoushan, China - Dec. 9th - 12th, 2020

EVALUATION OF COAST EROSION AND THE FORMED LAND AREA OF THE YELLOW RIVERESTUARY

SHOUBING YU[1], YAOSHEN FAN[2]

1 the Yellow River Institute of Hydraulic Research, Zhengzhou, Henan, P.R.C., 450003, yushoubing@163.com

2 the Yellow River Institute of Hydraulic Research, Zhengzhou, Henan, P.R.C., 450003, fysmyself@126.com

Abstract: The relation between land area and sediment load in the Yellow River Estuary has always been a significant focus of estuarine evolution, especially in the situation of long term low runoff and sediment load since the mid 1980s. However, the sediment transported by ocean dynamic has been few considered, and therefore the formed land area rate has been different from each other. It is necessary to evaluate the effect of ocean dynamic and acquire a new formula between the formed land area and sediment load. The annual land erosion of the Qingshuigou Course lobe formed before May, 1996 has been evaluated in the period of 1996~2015. The isobath of 2 m by National Vertical Datum is used to divide land and coast in the lobe, for its reflection of sediment transported by the runoff and advantages of many continuous field observation data. Thus, the annual land erosion of 0.038×10^8 t/km is obtained, according to retreat of 2 m isobath, mean high tide level, and dynamic balance depth, and bulk density. Then the relation between the lobe area and accumulative sediment load is fitted, considering the erosion intensity and the length of the lobe. Annual sediment erosion amount in the period of 1996~2003 and 2012~2015, with nearly the same land area of the lobe, are 1.2×10^8t and 1.0×10^8t, respectively, which approach the mean annual sediment load from the Lijin Station.

Key Words: the Yellow River Estuary, land area, sediment load, the Qingshuigou Course

8th International Conference on the Application of Physical Modelling in Coastal and Port Engineering and Science
Zhoushan, China - Dec. 9th - 12th, 2020

WAKE MODELING OF TIDAL STREAM TURBINES USING MACHINE LEARNING

LONG CHEN[1], REN-JIE CHIN[2]

1 Changsha University of Science & Technology, China,
logchan11@hotmail.com 2 Universiti Tunku Abdul Rahman, Malaysia,
chinrenjie@gmail.com

A novel framework that employs the machine learning and CFD (computational fluid dynamics) simulation to develop new wake velocity with high accuracy and good efficiency is proposed to improve the tidal turbine wake predictions. In this study, multilayer perceptron neural network (MLP-NN) and adaptive neuro-fuzzy inference system (ANFIS) are designed to build the underlying spatial relationship between the inflow conditions and the three-dimensional wake flows. RANS (Reynolds-averaged Navier-Stokes equations) simulations coupled with k-ε turbulence model is incorporated to provide big datasets of wake flow for training, testing, and validation of the MLP-NN and ANFIS model. Comparing the predicted values from the developed artificial intelligence model and the values obtaining through the empirical formula and experimental measurements, it was found that the developed model exhibits good performance in terms of accuracy, which indicates that the machine learning is capable of establishing the complex spatial relationship between inflow conditions and the wake flows.

Key Words: tidal turbine, wake, machine learning

8th International Conference on the Application of Physical Modelling in Coastal and Port Engineering and Science
Zhoushan, China - Dec. 9th - 12th, 2020

EXTRACTION OF HIGHER HARMONICS IN A FOCUSED WAVE GROUP BY A PHASE MANIPULATION APPROACH

XINGYA FENG[1], WEI BAI[2], DEZHI NING[3]

1 Southern University of Science and Technology, Shenzhen, China, fengxy@sustech.edu.cn

2 Manchester Metropolitan University, UK, w.bai@mmu.ac.uk

3 Dalian University of Technology, China, dzning@dlut.edu.cn

In this work we aim at extracting the higher harmonic wave profiles of nonlinear focused wave groups based on the assumption of a 'Stokes-type' harmonic structure. We present a methodology to generate high-quality nonlinear wave groups of a narrow-banded wave spectrum in a wave tank. The methodology manipulates the wave group phases by an active control of the wave paddle. Four phases with 90 degree shift each are prescribed – four runs for each case, in order to extract the harmonics up to fourth order. The input focused wave group is generated by the NewWave model, which represents an extreme wave in a random sea state. Experiments were carried out in the Kelvin Tank in Glasgow, UK. A fully nonlinear potential flow (FNPF) model is also employed to replicate the experiments. The results show clean separation of the first four harmonics in the elevation spectra. Comparisons between the experimental data and the FNPF model show remarkably good agreements for the higher harmonics. We confirm the Stokes-type underlying nonlinear structure of the harmonic elevations in wave groups. This is concluded by simulating wave groups with varying wave steepness and calculating the corresponding elevation coefficients of the higher harmonics. The harmonic coefficients are found almost constant against varying steepness. We are able to extract wave profiles of higher harmonics in space in the numerical simulation such that the evolution of the higher harmonics can be clearly demonstrated.

Key Words: Focused wave group, Higher harmonics, Stokes expansion, Nonlinear simulation

8th International Conference on the Application of Physical Modelling in Coastal and Port Engineering and Science
Zhoushan, China - Dec. 9th - 12th, 2020

PHYSICAL MODELLING STUDY OF LOCAL SCOUR AROUND PILE FOUNDATION IN RESPONSE TO REVERSING SEDIMENT TRANSPORT FLOW

HUANG LIBING, ZHU MIN

Yellow River Institute of Hydraulic Research, China, 223413865@qq.com

In estuary and offshore areas, wind turbines, sea bridges are increasing. By the influence of tide and reversing sediment transport flow, the course and mechanism of the flow regime and local scour around pile foundation has not yet fully revealed. In this study, it uses idealization model to research flow structure and the characteristics around pile foundation by reversing flow affecting.it researches the scouring development course around pile foundation, reveals the interaction mechanism between scour parameters (geometric features, spatial scales, and development rate of scour holes) and key factors.

Key Words: physical modelling; reversing flow; local scour; flow and sediment transport

8th International Conference on the Application of Physical Modelling in Coastal and Port Engineering and Science
Zhoushan, China - Dec. 9th - 12th, 2020

HOW TO DESIGN A COASTAL RESERVOIR

Shu-Qing Yang

School of Civil, Mining & Environ. Eng., Univ. of Wollongong, NSW 2522, Australia,

email: shuqing@uow.edu.au

Water cycle looks like a giant invisible machine creating life, one of its products is human being. Urbanization is possible only when large scale reservoirs can supply stable, sufficient, high-quality and affordable water to the nearby cities. As most people are migrating towards coastlines, more and more mega cities appear at deltaic regions, it has reached the point to develop large scales coastal reservoirs (CRs). A coastal reservoir is a freshwater reservoir displacing seawater. The statistics shows that the world discharges 42,800 km3/year of freshwater into the sea, most of it is floodwater. Human society only uses 5.6% of the surface runoff. Thus it is not that the world is running out of fresh water, it is that fresh water is running out of the world. This paper analyzes the existing water supply strategies and explains why CRs will dominate future water supply. This paper also compares the differences between inland dams and CRs in its design considerations. The past experience of CRs is summarized and methods to determine some critical parameters for CRs are proposed including CR's location selection, size, shape and layout plan as well as water quality control for desalinization and high quality management. The feasibility of IACRR's vision is justified, i.e., to provide sufficient, high-quality and affordable water to the world with minimum environmental/social impacts.

Key words: Site selection, seawater intrusion, water quality management, embankment design, layout plan

8th International Conference on the Application of Physical Modelling in Coastal and Port Engineering and Science
Zhoushan, China - Dec. 9th - 12th, 2020

RATIONAL WAVE SPECTRUM (RWS) WITH APPLICATIONS TO REEF ISLAND WAVES IN THE SOUTH CHINA SEA

Z. ZONG[1], Y.G.WANG[2] & L. ZHOU[3]

1 School of Naval Architecture, Dalian University of Technology, Dalian 116024, China,zongzhi@dlut.edu.cn
2 School of Naval Architecture, Dalian University of Technology, Dalian 116024, China,wang_yigeng@163.com
3 School of Naval Architecture, Dalian University of Technology, Dalian 116024, China,zongzhi@dlut.edu.cn

To describe stochastic properties of waves near reef islands we arranged in-situ measurements near an atoll in the South China Sea. Analysis of the measured data shows that there exist four basic forms of wave spectra in the area. They are unimodal characterized by single peak with occurrence probability around 50%, bimodal characterized by two peaks with occurrence probability around 10%, platykurtic characterized by a wide flat peak with occurrence probability around 20% and uniform describing white-noise-like small waves. Atoll waves are characterized by the presence of breaking waves producing high-frequency waves, swells concentrated at low-frequency and storm waves creating complicated spectral form. This makes widely-used wave spectra like Pierson-Moskowitz and JONSWAP spectra cannot capture well the energy distribution properties around peak frequency, high- and low-frequency ends. To be able to better describe the complex forms we introduce Rational Wave Spectrum (RWS) form in this paper. Based on 236 groups of data, 20 among which are presented here, we demonstrate the applicability of RWS to describe island waves in the south china sea.

A database of the worldwide seas is also introduced in this presentation which has been developed over the last few years in our research group.s.

Key Words: rational wave spectrum, high-low frequency, double-peak, swell, sea waves

8th International Conference on the Application of Physical Modelling in Coastal and Port Engineering and Science
Zhoushan, China - Dec. 9th - 12th, 2020

IMPACATS OF SEA LEVELRISE ON STORM SURGE INDUCED EXTREME SEA LEVEL ALONG JIANGSU COAST

JIE YANG[1,2], FENG YAN[2]

1 Key Laboratory of Coastal Disaster and Defence (Hohai University), Ministry of Education, Hohai University, Nanjing, China, jie_yang@hhu.edu.cn

2 College of Harbor, Coastal and Offshore Engineering, Hohai University, Nanjing, China

The extreme sea level contributed by tides, storm surges and other extreme weathers is a crucial index to assess the inundation risk and provide guidance for coastal mitigation and adaptation. Considering the risk exacerbated by land subsidence and global sea level rise, how extreme sea level respond to associate regional relative sea level rise (RSLR) when accounting for the tidal dynamics is investigated in the present study. We employ a high-resolution coastal storm surge model to simulate the top 20 cyclone events from 152 historical records that impacted Jiangsu coast off the Yellow Sea. The future RSLR scenario by the end of the century is projected from satellite altimeter data-based sea level analysis and is adjusted for the influence of the Glacial Isostatic Adjustment (GIA) using the ICE-6G/VM5a model. This spatial-varied RSLR, which incorporates the anomalies of both sea level trend and land subsidence rate, is implemented by elevating the present-day water depth on mesh nodes. We find that the extreme sea levels along Jiangsu coast are contributed mainly by both direct landfall and offshore cyclones; although the cyclones straight hit Jiangsu coast only add up to six times, they generate relative larger surge heights than offshore ones. Under the scenario of RSLR, the modulated bottom friction with increased water depth and introduced extra energy dissipation vary with tidal dynamics, and will result in increased or decreased extreme sea level variation locally. Tidal amplification is found especially in radial sand ridges, where is characterized with very shallow water depth and convergent shoreline and leads to corresponding attenuated surge heights in most regions. We also present the spatial distribution of nonlinear responses of storm surge induced extreme sea levels to RSLR, implicating the regions of exacerbation and attenuation, respectively, due to future sea level trend.

Key Words: Extreme sea level; storm surge; sea level rise; GIA; nonlinearity

8th International Conference on the Application of Physical Modelling in Coastal and Port Engineering and Science
Zhoushan, China - Dec. 9th - 12th, 2020

RESONANCE OF LONG WAVES AROUND A CIRCULAR ISLAND AND ITS RELATION TO EDGE WAVES

XIAOJING NIU[1]

1 State Key Laboratory of Hydroscience and Engineering, Department of Hydraulic Engineering, Tsinghua University, Beijing 100084, China. E-mail: nxj@tsinghua.edu.cn

As long waves propagate over an island, wave energy can be trapped in the shallow water near the coastline due to the effect of refraction and diffraction. However, in some particular situations extremely huge near-shore waves can be excited due to the resonance of edge waves. This study focuses on the occurrence conditions of the resonance phenomenon, and mainly investigates the effects of geometric parameters of underwater topography around island, especially the curvature of island profile. Based on an analytical solution of long waves over an idealized circular island, resonance of long waves around islands has been investigated. The profile of island is described as a constant plus a power function with arbitrary power. The influences of average slope and curvature of island profile on the resonance frequency and amplification factor have been discussed. It is found that not only the average slope but also the curvature parameter greatly affects the resonance frequency and amplification factor of resonance peaks. The resonance frequency shifts to lower frequency with the decrease of average slope and the increase of curvature parameter of island profile. And the milder slope and larger curvature parameter are associated with a larger resonance peak and a narrower resonance bandwidth. By comparison with the existing edge wave theory, the resonance peaks are confirmed to relate to edge waves. The resonance peaks appear when the frequency of incident long wave is close to the edge wave that the perimeter of island is an integral multiple of its wave length. An approach to estimate the resonance frequency considering the curvature of island profile is given, which agrees well to the result of the complex analytical solution.

Key Words: long wave; resonance; edge wave; analytical solution.

8th International Conference on the Application of Physical Modelling in Coastal and Port Engineering and Science
Zhoushan, China - Dec. 9th - 12th, 2020

A HIGH-ORDER BOUSSINESQ-TYPE MODEL FOR INTERNAL WAVES OVER A MILDLY-SLOPING TOPOGRAPHY IN A TWO-FLUID SYSTEM

ZHONGBO LIU[1], KEZHAO FANG[2], JIAWEN SUN[3], ZAIJIN YOU[1]

1 Transportation Engineering College, Innovation Center for Ports and Maritime Safety, Dalian Maritime University, China, *liuzhongbo@dlmu.edu.cn*, *b.you@dlmu.edu.cn.*

2 State Key Laboratory of Coastal and Offshore Engineering, Dalian University of Technology, China, *kfang@dlut.edu.cn*

3. National Marine Environmental Monitoring Center, China, *jwsun@nmemc.org.cn*

With a rigid lid assumption on the upper boundary in a two-fluid system, a new high-order Boussinesq-type model for internal waves over a mildly-sloping topography is derived. This model is formulated in terms of computational velocity vectors defined at mid water depth in each fluid. Stokes-type expansions are used to theoretically analyze the linear and nonlinear properties of the new Boussinesq-type model. The most attractive aspect of this work is that the newly developed model shows high accuracy in linear, nonlinear, shoaling and kinematic characteristics from deep to shallow water. For an equivalent water depth in upper and lower fluid, the model is applicable to up to $kh_2 \approx 10$ in linear dispersion, up to $kh_2 \approx 7.0$ in the second nonlinear property within 2% error, and up to $0 < kh_2 < 10$ in linear shoaling property. Compared with most existing Boussinesq-type models in a two-fluid system for internal wave, the accuracy of the velocity profiles of the new model along the water column is improved significantly, and the model can be applicable to up to $kh_2 \approx 4.48$.

Key Words: Boussineqs-type model; internal wave; dispersion; nonlinearity; shoaling property.

NUMERICAL STUDY OF BRISBANE RIVER ESTUARY AND MORETON BAY, AUSTRALIA: PROPOSED COASTAL RESERVOIR FOR FLOOD ADAPTATION AND WATER RESOURCE DEVELOPMENT

Floods are more likely to occur due to global warming and climate change. In Australia more than 85 %, the population is living in coastal areas, which are exposed to the impact of climate change. Brisbane, the capital city of Queensland has been selected as the study area to analyze the adaptation measures against flood through a Coastal Reservoir (CR) technique. Extreme weather events are one of the significant aspects of South East Queensland (SEQ). The floods history starts from 1806 to recent 2011, after a decade-long drought, the Brisbane River catchment experienced an extreme rainfall event during January 2011 that gave rise to the so-called '2011 Brisbane flood'. The catchment rainfall-runoff and flow releases from Wivenhoe Dam augmented and caused excessive flooding in the Brisbane city, causing significant damage to lives and property. The existing studies have considered flood mitigation measures upstream of the Wivenhoe dam. However, half the catchment of the Brisbane River lies above the Wivenhoe dam and almost half of the area below the dam, and the Wivenhoe dam for flood control cannot regulate catchment flows associated with the latter. The aim of this paper is to analyses lower Brisbane River flood dynamics for flood adaptation through a Coastal Reservoir technique at the mouth of the Brisbane River in the Moreton Bay, so when a significant climate event occurs in future, its effects on the regional community are lessened. A numerical model (MIKE-21) will be used to study the feasibility of proposed CR for flood adaptation. The gate operation of the CR will be analyzed under different flow conditions (riverine and tidal flows) to see how the flood levels can be reduced in the Brisbane city. The hydrodynamic simulation of the Brisbane River Estuary (BRE) will be performed with and without proposed CR. For this paper hydrodynamic model will be calibrated and validate of the Brisbane River and Moreton Bay, which will give the water levels variation inside the BRE. Further, CR gate operation will show the quantity (flood volume) of floodwater inside the CR. Thus, the paper would provide useful information for the feasibility and design of the CR technique for floodwater storage and water resource development in Brisbane River estuary. It will provide a practical solution for flood adaptation and also possible water resource development for water shortage areas affected by saltwater intrusion near estuaries.

8th International Conference on the Application of Physical Modelling in Coastal and Port Engineering and Science
Zhoushan, China - Dec. 9th - 12th, 2020

EFFECT OF SCOUR ON THE LATERAL BEARING CAPACITY OF THE MONOPILE UNDER CYCLIC AND STATIC LOADS

FEN LI[1], YU YANG[2], JIN PAN[3], LIANG SUN[4]

1 School of Transportation, Wuhan University of Technology, CHINA, jessilifen@whut.edu.cn
2 School of Transportation, Wuhan University of Technology, CHINA, 2414725770@qq.com
3 School of Transportation, Wuhan University of Technology, CHINA,okele1978@163.com
4 School of Transportation, Wuhan University of Technology, CHINA,l.sun@outlook.com

Nowadays offshore wind turbines have been widely used for wind energy exploitation. The lateral bearing capacity of monopile is important to ensuring the safe operation of the monopile based offshore wind turbines. As one of the most used forms of foundations for offshore wind turbines, the monopile is subjected to lateral loads engendered by winds and waves. Meanwhile, scouring is often formed by the flushing of sea currents, which may affect the lateral bearing capacity of the monopile. Thus, it is important to investigate the lateral bearing capacity of the monopile subjected to combined cyclic wave loads and scouring condition.Through the model test and numerical simulation, the effect of scour on the law of pile-soil interaction and deformation of the monopile head under cyclic load and static loads are studied. The results show that, under non- scour condition, the monopile head will produce accumulated deformation after cyclic loading, the first cyclic loading has greater effect on the development of the monopile head deformation, the foundation stiffness becomes larger, but the ultimate lateral bearing capacity of the monopile foundation has no significant change after cyclic loading. Under the scour condition, the accumulated deformation of the monopile head increases after cyclic loading, and the number of cycles has greater effect on the development of the monopile head deformation. Meanwhile, the foundation stiffness decreases, and the ultimate lateral bearing capacity of the monopile foundation decreases significantly after cyclic loading. The bearing capacity of the monopile foundation under cyclic loads is very sensitive to the change of scour depth, but insensitive to the change of scour width. Scour will significantly reduce the ultimate lateral bearing capacity of the monopile foundation and the bending moment along the monopile, and make the maximum bending moment point move down. It is advised that the effect of scour and cyclic loads should be considered simultaneously when evaluating the ultimate lateral bearing capacity of the monopile foundation.

Key Words: scour, monopile, cyclic load, pile-soil interaction, lateral bearing capacity

8th International Conference on the Application of Physical Modelling in Coastal and Port Engineering and Science
Zhoushan, China - Dec. 9th - 12th, 2020

INVESTIGATION ON DEAD WATER RESISTANCE ON A BARGE IN A TWO-LAYER FLUID

YING GOU[1], JINGWEI SUN[1], BIN TENG[1], NING DEZHI[1]

1 State Key Laboratory of Coastal and Offshore Engineering, Dalian University of Technology, China, gouying@dlut.edu.cn; jingweis94@sina.com; bteng@dlut.edu.cn; dzning@dlut.edu.cn

In the real ocean, due to the uneven distribution of temperature and salinity, the density of seawater is stratified along the depth of the ocean, in which the fluctuations will be generated when a structures is sailing on the free surface. Dead water resistance on a barge in a two-layer fluid is investigated by numerical simulation and experimental test in this research. A 3-D time-domain numerical model by higher-order boundary element (HOBEM) method in linearized theory is developed to investigate the dead water resistance on a barge moving with speed U along the upper layer of a two-layer fluid. The numerical results of the dead water resistance are compared with the experimental data which is obtained by a series of experimental test carried in a two-layer fluid wave flume. The internal Froude number $Fr=U/c_0$ is varied in the range 0.3 to 1.2. There is a local maximum of the dead water resistance. The Most of the numerical results of dead water resistance are smaller than the experimental date except the peak value, while the trend of numerical results and experimental test is identical. The discrepancy between the numerical and experimental results are analyzed. The effect of the draft and the scale of the barge on the dead water resistance are investigated and the Fr corresponding to the maximum dead water resistance is not changed with the draft and the scale of the barge. The wave patterns on the interface are also shown and the relations between the wave patterns and the dead water resistance are analyzed.

Key Words: two-layer fluid; dead water resistance; higher-order boundary element method

8th International Conference on the Application of Physical Modelling in Coastal and Port Engineering and Science
Zhoushan, China - Dec. 9th - 12th, 2020

TURBULENT BOUNDARY LAYERS OFNONLINEAR OSCILLATORY FLOWS ABOVE SLOPES

YULONG DING[1], LIAN TANG[1], PENGZHI LIN[1*]

1 Sichuan University, China, E-mail: cvelinpz@126.com

In coastal and offshore engineering, the seabed response under waves is an important research subject. Although the slope of the bottom bed greatly affects the characteristics of the wave boundary layer and shape of wave, the understanding of the interaction between bed slope and wave boundary layer has been still unclear. In this study, the oscillatory flows under different types of nonlinear wave conditions (including velocity and acceleration skewness or asymmetry) and bed slops are simulated with two-dimensional Reynolds-averaged Navier–Stokes (RANS) baseline (BSL) k–ω equations model. Through comparisons on the results of mean flow velocity, turbulence characteristics etc, the influences of slope and nonlinearity on wave boundary layer are also analyzed.

Key Words: turbulent boundary layer; nonlinear oscillatory flow; slope bed;

8th International Conference on the Application of Physical Modelling in Coastal and Port Engineering and Science
Zhoushan, China - Dec. 9th - 12th, 2020

THE EFFECT OF MARINE GROWTH ON THE HYDRODYNAMCIS OF SUBSEA PIPELINES

TERRY GRIFFITHS[1], MARIE-LISE SCHLAPPY[2], HONGWEI AN[3]

1 School of Engineering and Ocean Graduate School, UWA, Australia. terry.griffiths@research.uwa.eud.au
2 Ocean Graduate School, UWA, Australia. marie-lise.schlappy@uwa.edu.au
3 School of Engineering, UWA, Australia. hongwei.an@uwa.eud.au

In coastal and offshore engineering, marine growth or biofouling is referred to the accumulation of unwanted microorganisms, plants, algae, or small animals on wetted surfaces of engineering structures. The buildup of marine growth is a significant problem. Using subsea pipeline as an example, the accumulation of marine growth can increase the overall dimeter of pipelines and its surface roughness. Consequently, an increase of hydrodynamic load on the pipeline can be expected. The increase of surface roughness, will also modify the boundary layer separation, vortex shedding and vibrations of spanning pipelines. The marine growth is a very complicated problem. The distribution of marine growth is highly dependent on geographical location, water depth, seasons and many other factors. It is often characterized with irregularity in spatial distribution, variation of individual dimensions, mixing of verities, and difference in flexibility.

In current design guidelines for subsea pipelines, the effect of marine growth is simply treated as an increase of the overall diameter. There has been some research work carried out to assess the effect of hard marine growth on the hydrodynamics of subsea pipelines, but the effect of soft marine growth (such as kelp, algae and sea grass etc.) has not been studied, although they are often seen in the field and can grow to a significant dimension relative to pipeline diameter. In this work, the video footage of marine growth developed on an offshore gas pipeline in Tasmania, Australia is reviewed. It is found that the dominating growth is a kind of red algae, which grows to a height about 300mm and it mainly grows on the top side of the pipeline. To assess the effect of the marine growth, a model pipeline covered with soft marine growth with different density is tested in the O-tube facility at the University of Western Australia. The test results show that pipeline covered with soft marine growth can experience increased drag force, modified mean-lift forces, different vortex shedding frequency, reduced vortex shedding strength, and reduced potential for vortex induced vibration. It demonstrates that the effect of marine growth on subsea pipeline is far away from simply increasing the overall diameter of the pipeline.

Key Words: marine growth; subsea pipeline; hydrodynamic forces; vortex shedding

8th International Conference on the Application of Physical Modelling in Coastal and Port Engineering and Science
Zhoushan, China - Dec. 9th - 12th, 2020

DEVELOPMENT AND APPLICATION OF A FAST SHALLOW WATER MODEL BASED ON THE LOCAL-TIME-STEP APPROACH AND GPU-ACCELERATION

PENG HU[1], ZIXIONG ZHAO[2]

1Associate Professor, Institute of Port, Coastal and Offshore Engineering, Ocean College, Zhejiang University, Zhoushan 316021, China. Email: pengphu@zju.edu.cn

2Research Assisstant, Institute of Port, Coastal and Offshore Engineering, Ocean College, Zhejiang University, Zhoushan 316021, China. Email: 187477@zju.edu.cn

Shallow water model and its variants (e.g., coupling sediment transport, wave effects, vegetation effects etc) are widely used in river, coastal and near-shore flows. To capture the potential complex flow regimes, shock-capturing finite volume methods are widely used to solve the shallow water equations. Such models are computationally demanding due to the CFL constraint and the commonly adopted global minimum value of the locally allowable maximum time steps for variable updating. This paper reports an effort of improving the computational efficiency of such models, which take advantages of both the efficient local-time-step (LTS) method and the GPU parallel computing. Performance (accuracy and computational cost) of the model is demonstrated by preliminary applications to flows in the Yangtze river and estuary, urban flooding, as well as sediment transport modeling.

Key Words: shallow water model, computational cost, local-time-step, GPU-acceleration

8th International Conference on the Application of Physical Modelling in Coastal and Port Engineering and Science
Zhoushan, China - Dec. 9th - 12th, 2020

RIVER DELTA MORPHODYNAMIC RESPONSE TO SEDIMENT SUPPLY DECLINE AND SEA-LEVEL RISE

LEICHENG GUO[1], QING HE[2]

1 State Key Lab of Estuarine & Coastal Research, East China Normal University, E-mail: lcguo@sklec.ecnu.edu.cn

2 State Key Lab of Estuarine & Coastal Research, East China Normal University, E-mail: qinghe@sklec.ecnu.edu.cn

Global climate change has led to accelerated sea-level rise (SLR), which is a worldwide concern as regards to the consequent coastal flooding and erosion risk. Moreover, riverine sediment supply to coasts and deltas is also declining owing to dams and human activities in watershed. It is of particular interest to understand how river delta morphodynamics will respond and adjust to sediment decline and SLR, and whether their inter-tidal flats can survive SLR at the century time scale.

Field data is not readily available to assess SLR impact in the future. Long-term morphodynamic modelling provides an effective tool to evaluate SLR impact on coasts. Previous knowledge of SLR impacts on open coasts includes the Brune rule on costal profile changes. More recently, Dissanayake et al. (2012), van Maanen et al. (2013), van der Wegen (2013) had employed morphodynamic models to explore SLR impact on tidal lagoons and estuaries where river influence is excluded. It was reported that tidal flats in those systems were highly likely to be drowned under SLR. But it remains insufficiently understood to what degree and how system dynamics may adapt to combined impact of riverine sediment decline and SLR.

In this work we use a long-term morphodynamic model to explore large-scale morphodynamic evolution of a schematized delta system based on Delft3D. The model is river-dominated with micro- to macro-tide but not waves, mimicking a river-dominated delta environment. We first run the morphodynamic simulation to reproduce the development a river dominated delta, with channel bifurcation and avulsion achieved. Based on that, we continue the simulation for another 100 years considering sediment source decline and SLR of different rates. Model results suggest sediment decline leads erosion of the front shoreline of the delta. The impact of SLR is in submerging the tidal flats and drowning of the delta. Under the combined influence of sediment decline and SLR, the river delta will shrink as whole both horizontally and vertically. Including marine tides have effect in mitigating the SLR impact, and macro-tidal systems tend to have resilience to external forcing changes. The findings in this modeling study have implications for coastal and delta management in conserving flats and saltmarshes and for human adaptability.

Key Words: Delta; Morphodynamic; Sediment supply; Sea-level rise

8th International Conference on the Application of Physical Modelling in Coastal and Port Engineering and Science
Zhoushan, China - Dec. 9th - 12th, 2020

EFFECT OF ARTIFICIAL REEFS CONSTRUCTION ON PHYTOPLANKTON COMMUNITY

ZHANG ZHI-PENG[1], WANG MING-QI[2], LIU HONG-JUN[3]

1 Tianjin Research Institute for Water Transport Engineering, Ministry of Transport, China, zhipeng246@163.com
2 Tianjin Research Institute for Water Transport Engineering, Ministry of Transport, China, wangmingqi1991@163.com
3 Marine Biology Institute of Shandong Province, China, hongjunl@126.com

In this paper, the response of phytoplankton community to the artificial reefs construction in short term at the sea area of Xiaoheishan Island was investigated. Xiaoheishan Island is a typical island ecosystem, characterized by a simple structure and complete system. Based on the survey of 12 periods in this sea area from 2013 to 2016, A total of 75 species of phytoplankton were identified, Bacillariophyta was the most important phytoplankton in this sea area; The chlorophyll a concentration was from 0.22 to 9.46 μg/L, Shannon index (log_2) (H′) was from 0.76 to 3.06, Pielou index (J') was from 0.28 to 0.77. After the construction, the changes of sea environmental factors were minor, and there was no significant difference within and outside the reefs area. Following the construction, Pb and Hg were reduced, chlorophyll a, H′ and J′ were decreased, but there was no significant difference in chlorophyll a concentration within and outside the reefs area, and the H′ and J′ inside the reefs area were higher than those in the outside, the dominant species have a little change, however, there was no significant difference between the inner and outer reefs area. *Melosira sulcata* was the dominant specie in this sea area throughout this survey. The canonical correspondence analysis (CCA) shows that, instead of the construction of artificial reefs, the most important factor which affected the distribution of stations and phytoplankton species is seasonal variations.The phytoplankton community was mainly affected by dissolved oxygen, NO_3-N, water temperature, suspended solids and As. Although the concentration of As was well up to the state standards of the first grade of China, the distribution of phytoplankton community was significantly influenced by As.

Key Words: artificial reefs; phytoplankton; seasonal variations; Xiaoheishan Island; environmental factor

8th International Conference on the Application of Physical Modelling in Coastal and Port Engineering and Science
Zhoushan, China - Dec. 9th - 12th, 2020

NUMERICAL INVESTIGATION OF BREAKING TSUNAMI-LIKE WAVE RUNUP ON PERMEABLE SLOPED BEACH USING A NONHYDROSTATIC MODEL

K. QU[1], B. DENG[2], S. KRAATZ[3], C.B. JIANG[4]

1 School of Hydraulic Engineering, Changsha University of Science & Technology, Changsha, 410114, China, qukeforjc@126.com

2 School of Hydraulic Engineering, Changsha University of Science & Technology, Changsha, 410114, China, dengbin07@163.com

3 Department of Electrical and Computer Engineering, University of Massachusetts Amherst, Amherst, MA, 01003, USA, skraatz@umass.edu

4 School of Hydraulic Engineering, Changsha University of Science & Technology, Changsha, 410114, China, jcb36@163.com

The wave profile of solitary wave has been widely used as a tsunami paradigm for decades to capture the main features of actual tsunamis. Since most of the fatalities were attributed to overland flow of tsunamis, the runup and rundown processes of solitary waves have been extensively studied experimentally and numerically. Comparing to previous research, this study systematically investigates the hydrodynamic characteristics of breaking solitary wave runup on a permeable sloped beach using a nonhydrostatic model. Firstly, the computational capabilities of present numerical model in predicting solitary wave runup process and flow field in permeable media are well validated with experimental data. Then, a series of computational runs have been performed to study the breaking solitary wave on permeable sloped beach. Effects of three prominent factors on the maximum runup height of breaking solitary wave are considered in detail: the thickness, median diameter, and porosity of the permeable layers. The porosity of the beach has a substantial impact on the flow field for breaking waves running up a sloped beach. The maximum wave runup height can be substantially reduced if the permeability of the beach is considered. It is also found that the maximum wave runup height decreases with permeable layer thickness. However, the reduction rate gradually decreases. The influences of median diameter are very limited and can be ignored. In addition, based on our results, we also proposed a new empirical formula to calculate the maximum wave runup height of breaking solitary wave on permeable sloped beach. Results of this study are expected to be useful for developing an improved understanding on the runup processes of breaking solitary wave on sloped beach with some permeability.

Key Words: Solitary wave; Runup height; Permeable; Nonhydrostatic model; Porosity

8th International Conference on the Application of Physical Modelling in Coastal and Port Engineering and Science
Zhoushan, China - Dec. 9th - 12th, 2020

NUMERICAL INVESTIGATION OF TIDAL FLOW HYDRODYNAMICS IN A NEW TYPE FISHERY GROUND

XU DONG[1], GAO LINGHAN[1], YING CHAO[2], JI CHUNNING[1]

1 State Key Laboratory of Hydraulic Engineering Simulation and Safety, Tianjin University, China, xudong@tju.edu.cn

2 Zhejiang Institute of Hydraulics and Estuary, Zhejiang, China, xinqing928@126.com

As an important part of "Blue Economy", the construction of Marine Ranching is getting more and more popular along China's long coastlines since 2009. Aquacultures and fisheries usually have a requirement on aquatic habitat environment including hydrodynamics. Favored by the low flow velocity and water depth in the nearshore area, fishery industry grows rapidly in the coastal zones, where the waterbody is getting more and more crowded. Fishery cultivations in areas farther away from coastline are usually faced with high tidal flow velocities, which may endanger the survive of most fisheries. A new type of fishery ground is proposed to tackle this problem: it uses a series of ex-service bulk cargo ships to form a ring-shaped area, inside of which the flow velocities are greatly reduced owing to the shielding effects of ships.

In order to predict the peak flow velocity inside of the new type fishery ground and evaluate potential shielding effects of ships, numerical simulations are carried out in both 2D and 3D. In the 2D model, two-dimensional shallow water equations are solved using a Finite Volume Method to predict the tidal flow fields in a pilot coastal area in Zhoushan, Zhejiang, China. The 2D model provides necessary boundary conditions for the 3D model, which is restrained to the ring-shaped area formed by ships. The 3D model solves the Reynolds Averaged Navier-Stokes Euqations (RANS) using Finite Volume Method. A Realizable k-ε model is adopted as turbulent closure. Both the 2D and 3D models are verified using field measurement data or laboratory experimental data. The simulations provide both the detailed hydrodynamics of flow around ships, and the overall flow-velocity shielding effects. Results show that for the selected pilot area, ships can reduce tidal flow velocity by over 40% and the peak flow velocity can be reduced below 1.0m/s. Such flow conditions can be favorable for most marine fishery industries.

Key Words: numerical simulation; tidal flow, hydrodynamics, cargo ship, fishery ground

8th International Conference on the Application of Physical Modelling in Coastal and Port Engineering and Science
Zhoushan, China - Dec. 9th - 12th, 2020

LABORATORY MEASUREMENT OF BUBBLE SIZE DISTRIBUTION UNDER A PLUNGING BREAKING SOLITARY WAVE

LIAN TANG, PENG ZHI LIN

State Key Laboratory of Hydraulics and Mountain River Engineering, Sichuan University, China, tanglian.scu@163.com

The bubble size distribution under a plunging breaking solitary wave on a 1:20 sloping beach are investigated by the fiber optic reflectometer (FOR) measurement. A total of 22 repeated runs are conducted at each measurement point. The instantaneous FOR signals are obtained and analyzed to determine the bubble velocity and bubble residence time, then, the bubble size distributions in the aerated region are determined accordingly. The results will provide important basis for numerical modeling of the bubbly flow dynamics in the surf zone.

Key Words: Breaking solitary wave; FOR measurement; Bubble size distribution

8th International Conference on the Application of Physical Modelling in Coastal and Port Engineering and Science
Zhoushan, China - Dec. 9th - 12th, 2020

DEVELOPMENT OF THREE-DIMENSIONAL NUMERICAL WAVE FLUME BASED ON LATTICE BOLTZMANN METHOD

QINGHE ZHANG[1], GUANGWEI LIU[2], JINFENG ZHANG[1], XINFENG LI[1]

1 State Key Laboratory of Hydraulic Simulation and Safety, Tianjin University, China, coastlab@163.com

2 State Key Laboratory of Hydroscience and Engineering, Tsinghua University, China

Lattice Botzmann method (LBM) has been widely applied in many fields of hydrodynamic simulation due to its high efficiency for massive parallel computation. However, it application is limited in water wave simulation because of the unrealistic energy dissipation during water wave propagation. A three-dimensional numerical wave flume based on lattice Boltzmann method is developed by using the improved method of modified pressure term, and the numerical flume is free of unrealistic energy dissipation in traditional LBM model with free surface. Previous experimental data including wave propagation over submerged breakwater, submerged elliptic shoal are collected and compared with the simulated results of numerical wave flume. It is shown that the numerical wave flume by LBM has the capability to simulate the wave reflection, combined refraction and diffraction, and shoaling and breaking of waves.

Complex structure treatment and porous medium simulation are also developed for the LBM numerical wave flume. The wave reflection performance of perforated-wall caisson breakwater and the wave overtopping over permeable sloping breakwater armored by Accropode blocks due to irregular waves are simulated. The comparison between the numerical results and the experimental measurement shows good agreement.

The parallel computational efficiency of numerical wave flume by LBM is compared with the numerical flume of OpenFOAM. It is shown that the numerical flume by LBM has higher computational efficiency and parallel scalability.

It is indicated that the three-dimensional numerical wave flume based on LBM promises to be an effective simulation tool on interaction between waves and structures in the future.

Key Words: numerical wave flume; three-dimension; lattice Boltzmann method; parallel efficiency; interaction between waves and structures

8th International Conference on the Application of Physical Modelling in Coastal and Port Engineering and Science
Zhoushan, China - Dec. 9th - 12th, 2020

SIMULATING THREE-DIMENSIONAL MUDSLIDE KINEMATICS BY DISCONTINUOUS BI-VISCOUS MODEL

Tso-Ren Wu [1], Thi-Hong-Nhi Vuong [1], Chun-Yu Wang [2], Chia-Ren Chu [2], Chun-Wei Lin[1]

[1]*Graduate Institute of Hydrological and Oceanic Sciences, National Central University, Taiwan*
[2]*Department of Civil Engineering, National Central University, Taiwan*

Tsunamis can be generated by landslides. Different landslides, such as rock-slides, mudslides, and debris flows, can generate different tsunamis. This study intends to develop a brand new model to simulate flow slides and mudflow. The model was originated from the Bingham model. However, due to the intrinsic characteristic, the Bingham model wasn't able to offer a satisfactory illustration of the stratified material. Therefore, the Bingham model was extended by introducing the discontinuous rheology relationship between the solid and liquid phases. A newly non-Newtonian fluid model, Discontinuous Bi-viscous Model (DBM), was invented with a purpose reproducing closet mud material nature without many empirical coefficients as well as empirical formula. A yield strain rate was introduced as the indicator to identify the corresponding rheological prosperity. This new rheology model was integrated and coupled into the Splash3D model, which resolves the Navier-Stokes equations with PLIC-VOF surface-tracking algorithm. The DBM was carefully validated with the theoretical result and laboratory data with good agreements. In the end, the failure of the Gypsum Tailings dam in East Texas in 1966 was taken as an application case. Results reveal a comparison between the conventional Bingham model and the DBM in terms of the flood length, shape, and average velocity. The results declare that the DBM matches most of the field observations. The stratify between solid and liquid (or the plug zone and the liquefied zone) in a mudslide material depending on the strain rate can also be well described.

Key Words: Mudslide, Bingham model, Rheology mode, Landslide tsunami, Discontinuous Bi-viscous Model (DBM)

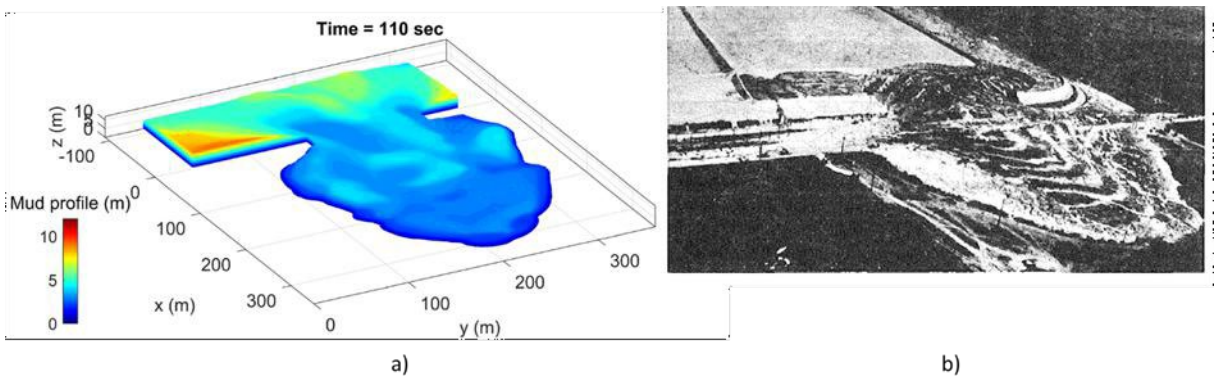

Figure 1. Failure of tailings dam at t = 110 s. a) A result from DBM-Splash3D b) Flow of liquefied tailings from Gypsum tailings impoundment, East Texas (1966) [1].

8th International Conference on the Application of Physical Modelling in Coastal and Port Engineering and Science
Zhoushan, China - Dec. 9th - 12th, 2020

PHOSPHORUS TRANSFER AND TRANSFORMATION DYNAMICS AT SEDIMENT-WATER INTERFACE UNDER PROPELLER JET FLOW

YU ZHI[1], HU XUYUE[2], SHENG XIAOXIONG[3], SUN SHIQUAN[4], WANGBO[5], SHANG GUANGQI[6]

1 School of Hydraulic Engineering,Chang sha University of Science & Technology, China, yuzhi2643@csust.edu.cn
2 School of Hydraulic Engineering,Chang sha University of Science & Technology, China, huxuyue62@163.com
3 School of Hydraulic Engineering,Chang sha University of Science & Technology, China, 418864786@qq.com 4 School of Hydraulic Engineering,Chang sha University of Science & Technology, China, 1175822625@qq.com
5 School of Hydraulic Engineering,Chang sha University of Science & Technology, China, 1402213098@qq.com

Sediments of rivers and lakes are the “source” and “sink” of water pollutants. Pollutants are transported and transformed between overlying waters and riverbed by sediment, which affects the water environment of rivers and lakes. The migration process is mainly affected by the sediment-water interface which is called environmental boundary layer. There are many research results related to the influence factors about the interface. However, the propeller wake caused by the ship in the voyage will flush the riverbed, causing the sediment incipient and resuspension, which promotes the release of pollutants into the overlying water body, research on the mechanism of the migration of pollutants under propeller wake flow is rarely reported at home and abroad. For this reason, this research is focused on the main limiting factor phosphorus based on the indoor sink test and theoretical analysis. The in-situ observation technique of diffusion gradient technique in thin film is applicated to clarify the dynamic mechanism of the sediment resuspension release of the riverbed caused by propeller wake flow, as well as to analyze the influencing factors of phosphorus at the sediment-water interface and calculate the vertical exchange flux of phosphorus.

The goal of this research is to reveal the migration and transformation of sediment-water interface of sediment phosphorus under the action of propeller wake flowl, which can provide a scientific basis for river navigation development and management and river water environment management protection.

Key Words: water-sediment transport; phosphorus in bottom sediment; water-sediment interface process; propeller wake flow; transfer and transformation dynamics

8th International Conference on the Application of Physical Modelling in Coastal and Port Engineering and Science
Zhoushan, China - Dec. 9th - 12th, 2020

EXPERIMENTAL STUDY ON GENERALIZED PHYSICAL MODEL OF YELLOW RIVER ESTUARY

ZUWEN JI[1], XIANG ZHAO[2], DANGWEI WANG[3]

1,2,3 State Key Laboratory of Simulation and Regulation of Water Cycle in River Basin, China Institute of Hydropower & Water Resources Research, Beijing, China, jzw@iwhr.com; zx_sedi@163.com; wangdw17@126.com

The distance from Lijin hydrologic station to the entrance is about 90 km, and the distance from T-junction gauging station to the entrance is about 20 km. The generalized physical model simulation area is below Xiheko. The reach from Xihekou to T-junction is the runoff dynamic simulation area, and the current flow path below the T-junction is the simulation area of runoff dynamic and ocean dynamic. The sea area outside the current flow path is the ocean dynamic simulation area. This model test generalizes the simulation object using the principle of "planar shape parameter generalization and dynamic characteristic parameter simulation". The generalized physical model includes three parts: runoff dynamic simulation area, runoff-ocean dynamic simulation area, and ocean dynamic simulation area. The runoff dynamic simulation area is a straight compound channel with the totally movable bed. And boundary conditions take into account factors such as discharge, sediment concentration and grain size of suspended sediment, mainly based on the measured data of Lijin hydrological station. The runoff-ocean dynamic simulation area is a rectangular area with the totally movable bed, which is mainly formed by the joint creation of runoff dynamic and ocean dynamic. The boundary conditions of ocean dynamic simulation area such as tide level, tidal current and flow direction, is mainly provided by mathematical models. Wind waves and storm surges are based on measured data. The model design takes into account the similarity criterion of flow motion, tide motion, wave motion and sediment motion. The physical model was completed in the daxing test hall. It was mainly a brick-concrete structure. The horizontal scale of the model is 500, while the vertical scale is 100. The model sediment selects fly ash of power plate. The automatic measurement and control system realizes the integration of clean water automatic control subsystem, muddy water automatic control subsystem, tide control automatic subsystem and wave automatic control subsystem. All devices realize wireless connection and feedback control through WIFI technology. According to the boundary conditions determined by the model design and preliminary tests, the underwater delta terrain naturally shaped by water and sediment processes, a total of 20 simulation tests under 4 natural cycles were performed, of which 11 branches were successfully simulated. The results provided basic data for the study on the development process and the branch mechanism of the alluvial estuary.

Key Words: generalized physical model, Yellow River estuary, automatic measurement and control system, branch

8th International Conference on the Application of Physical Modelling in Coastal and Port Engineering and Science
Zhoushan, China - Dec. 9th - 12th, 2020

MODEL TEST ON FLOATING OFFSHORE WIND TURBINE WITH AIR-CUSHIONASSISTED TRUSS BARGE PLATFORM

HONGBIN HAO[1], ZHIQUN GUO[2], KANGPING LIAO[3], SHULING CHEN[4], GUOCHUN XU[5]

1 Harbin Engineering University, China, haohongbin@hrbeu.edu.cn 2 Harbin Engineering University, China, guozhiqun2002@163.com

3 Harbin Engineering University, China, liaokangping@hrbeu.edu.cn

4 Jiangsu University of Science and Technology, China, chensl@just.edu.cn 5 Ningbo University, China, xuguochun@nbu.edu.cn

The Floating Offshore Wind Turbine (FOWT) is suitable to be worked in the seas with water depth more than 50m, and the main 4 types of supported platform for FOWT are Semi-submersible, Barge, Spar-buoy and TLP. It is considered that the least water depth for spar-buoy platform should be more than 100m and 70m for TLP, only the Semi-submersible and Barge platform can cover the water depth 50-70m. The Barge platform has simpler structure and is more adaptable to water depth, but its seakeeping motion in large waves is more significant, which can be improved by the new design of Air-cushion Assisted Truss Barge Platform (AATBP).

In model test, it is considered that the aerodynamic of wind turbine should satisfy the Reynolds similarity and the hydrodynamic of floating platform should satisfy the Froude similarity, they are contradictory and con not be satisfied at the same time. This question is solved by a new wind turbine model, which is designed base on the similar lift conditions of blade section. According to the result of wind tunnel model test, the thrust and torque of the new wind turbine model agree well to the simulation in CFD.

For FOWT system, the key of basin model test is how to generate a high quality wind. In this paper, a new wind generating system is designed and the wind speed at the plane of rotor distributes uniformly. Then, the FOWT with Air-cushion Assisted Truss Barge Platform is tested in regular and irregular waves.

Key Words: Floating Offshore Wind Turbine; Air-cushion Assisted Truss Barge Platform; Wind tunnel model test; Basin model test

8th International Conference on the Application of Physical Modelling in Coastal and Port Engineering and Science
Zhoushan, China - Dec. 9th - 12th, 2020

EFFECT OF THE WAVE RESONANCE IN THE GAP ON THE HYDRODYNAMICS CHARACTERISTICS OF A WEC DEVICE

Jing Geng[1], Yang Zhang[2], Xuanlie Zhao[3], Lars Johanning[4], Mingwei Li[5]

1 College of Shipbuilding Engineering, Harbin Engineering University, Harbin, China, gengjing@hrbeu.edu.cn
2 College of Shipbuilding Engineering, Harbin Engineering University, Harbin, China, zhyangchanges@hrbeu.edu.cn
3 College of Shipbuilding Engineering, Harbin Engineering University, Harbin, China, xlzhao@hrbeu.edu.cn
4 College of Engineering, Mathematics and Physical Sciences, Exeter University, Cornwall TR10 9FE, UK, L.Johanning@exeter.ac.uk
5 College of Shipbuilding Engineering, Harbin Engineering University, Harbin, China, limingwei@hrbeu.edu.cn
Corresponding author: Xuanlie Zhao

The Comb-Type Breakwater-WEC (Wave Energy Converter) system is characterized by a gap between the device and the flange. In this paper analytical model based on the linear potential flow theory was built to investigate the effect of the wave resonance in the gap on the hydrodynamics characteristics of a WEC device. For the purpose of improving the numerical convergence, the Galerkin method is used to solve the singularity in the velocity near the tip of the flange. Results showed that wave resonance (including piston and sloshing mode) modified the performance of the system significantly. It mainly reflected in that the occurrence of the piston response increases the capture width ratio of the device. When the sloshing resonance occurs, the device was located at the antinode of reflected waves from the flange. Thus, the occurrence of the sloshing resonance improves the efficiency of the device.

Key Words: Comb-type breakwater; capture width ratio; wave resonance; analytical method

8th International Conference on the Application of Physical Modelling in Coastal and Port Engineering and Science
Zhoushan, China - Dec. 9th - 12th, 2020

HYDRODYNAMIC CHARACTERISTICS OF ARTIFICIAL REEF IN JUEHUA ISLAND, LIAODONG BAY

JIPING QIN[1], ANPING SHU[1], MENGYAO WANG[1], SHU WANG[1],

1 School of Environment, Key Laboratory of Water and Sediment Sciences of MOE, Beijing Normal University, Beijing 100875, 18813177198@163.com

Artificial reefs are structures set up in the sea to improve the ecological environment and provide places for fish to breed, grow, catch and harbor enemies. At present, artificial reef construction has been widely carried out with good results. The flow field effect of artificial reefs is one of the main mechanisms to improve the marine ecological environment. The hydrodynamic characteristics of the flow field in the reef area are closely related to the type, structure, size and layout of the reef. Therefore, it is of great significance to study the flow field effect and its scale of the artificial reef. In order to optimize the spatial layout of artificial reefs in the coastal waters of Juehua Island, M-type breeding reefs are selected. On the scale of unit reef, the experimental models are made according to the geometric scale of 50:1. Five inflow velocities are designed, which are 0.085, 0.130, 0.170, 0.214 and 0.257 m/s. Using particle image velocimetry (PIV), the hydrodynamic characteristics of M-type artificial reef under different conditions were tested in flume. The results show that there are obvious upwelling and back vortex in the face and back of artificial reef, the scale of upwelling increases with the increase of velocity, and the scale of back vortex decreases with the increase of velocity; The drag force increases between the two reefs, and the drag force promotes the start-up of sediment and bait, indicating that the bait between the two reefs may be more abundant, which can provide more food for fish, etc.; The trend of drag force along the course is similar, and the velocity have little effect on it. The research on the hydrodynamic characteristics of M-type artificial reef can provide theoretical reference for the form of artificial reef in Juehua island.

Key Words: artificial reef; flow field effect; PIV experiment

8th International Conference on the Application of Physical Modelling in Coastal and Port Engineering and Science
Zhoushan, China - Dec. 9th - 12th, 2020

SPH SIMULATION OF DYNAMICAL FORCES ON TURBIDITY CURTAINS IN COMBINED WAVE-CURRENT FLOW

SHAOWU LI[1], XIAODONG LIU[2], QINGWEI WU[3]

1 State Key Laboratory of Hydraulic Engineering Simulation and Safety, Tianjin University, P. R. China, lishaowu@tju.edu.cn

2 State Key Laboratory of Hydraulic Engineering Simulation and Safety, Tianjin University, P. R. China, liuxiaodong@tju.edu.cn

3 CCCC First Harbor Consultants Co. Ltd, P. R. China, wuqingwei@fdine.net

Turbidity curtain is a commonly-used impermeable device for temporal or long-term control of suspended solids or turbidity in the water column generated during dredging operations and disposing dredged spoils. When fixed at its bottom end to the sea bottom, however, it will bear substantial tension of currents, waves or their combination. A Smoothed Particle Hydrodynamics (SPH) method is developed to simulate the dynamical forces of the curtain. An algorithm is proposed based on the dynamic boundary particles (DBPs) for preventing particle disorders of fluid particle movement around solid boundary. Then a 2D numerical wave-current flume is established with a piston-type wave generator and a current filling system. Simulation of the flexible curtain body is implemented by introducing a Rigid Module and Flexible Connector (RMFC) multi-body system. Different depths, waterheads and wave parameters are considered. The numerical solution of dynamical forces in the turbidity curtain are compared with the experimental results.

Key Words: silt curtain, SPH, tension

8th International Conference on the Application of Physical Modelling in Coastal and Port Engineering and Science
Zhoushan, China - Dec. 9th - 12th, 2020

THE YELLOW RIVER DELTA IN TRANSITION: INSIGHTS FROM LONG-TERM MORPHOLOGICAL EVOLUTION

YUTAO FU[1], SHENLIANG CHEN[1], SHUNQI PAN[1,2], HONGYU JI[1,2]

1. State Key Laboratory of Estuarine and Coastal Research, East China Normal University, Shanghai 200062, China
2. Hydro-environmental Research Centre, School of Engineering, Cardiff University, Cardiff CF24 3AA, UK, 52173904008@stu.ecnu.edu.cn, PanS2@cardiff.ac.uk, slchen@sklec.ecnu.edu.cn

Sustainable development of megadeltas worldwide has recently been the focus of international socioeconomic and environmental attention. Long-term erosion and deposition dynamics of deltas are crucial for sustaining coastal resources and marine ecosystems. The Yellow River Delta (YRD), one of the most famous deposition systems, is increasingly facing erosion threat under natural and human-induced changes. Although short to medium-term morphological adapt of the YRD has been sufficiently analyzed, the features of long-term delta change and transition mechanism of the YRD are still unclear. Knowledge of the long-term morphological evolution of deltas is urgently needed.

Utilizing long-term hydrological data, remote-sensing satellite images and bathymetric survey, the transition processes of the YRD during 1855-2015 from a perspective of geomorphology is examined, including both its subaerial and subaqueous deltas. The development of the Yellow River subaerial delta (YRAD) over the past 160 years has undergone five different sequential stages: rapid accretion in 1855-1976, stable accretion in 1976-1996, slow accretion in 1996-2000, rapid erosion in 2000-2007, and slow accretion in 2007-2015. The analysis demonstrated that the transition processes of the YRAD included three periods, and the riverine discharge had a critical influence on the transition of the YRAD. The time of reversal is about 1997 and 2003, which is agrees well with the rapid decrease of sediment load to the sea. Correspondingly, the Yellow River subaqueous delta (YRSD) also underwent different erosion-deposition patterns: moderate accretion (1855-2000), rapid erosion (2000-2007), and slow erosion (2007-2015). Since 2000, the subaqueous delta had turned from accretion into erosion, with a net volume change about -2.61 km^3.

The long-term morphological evolution of the YRD is closely related to water discharge and sediment load to the sea. Apart from the riverine discharge, avulsion of the river channel and the tidal shear front also influence the spatial difference in morphological evolution. To maintain the erosion-deposition balance of YRSD, an estimation of 0.22×10^9 t/yr sediment delivery should be kept, from the perspective of the deltaic sedimentary system. Due to the fluvial discharge change caused by human activities in the basin, the entire YRSD system is expected to be in erosive status since 2000 and will continue to exist in the future.

Key Words: The Yellow River Delta, Morphological evolution, Transition, Erosion and deposition, Water discharge and sediment load

8th International Conference on the Application of Physical Modelling in Coastal and Port Engineering and Science
Zhoushan, China - Dec. 9th - 12th, 2020

SPATIAL AND TEMPORAL CHARACTERISTICS OF WAVE ENERGY RESOURCES IN YELLOW AND BOHAI SEA BASED ON ERA5 DATASETS

SHI Hongyuan[1,2*], SUN Qingying[1], You Zaijin[1,2]

(1 Institute of Ports and Coastal Disaster Mitigation, Ludong University, Yantai 264025, China

2. The Center for Ports and Maritime Safety (CPMS), Dalian Maritime University, Dalian 116026)

Wave energy is an important marine renewable energy, the development and utilization of wave energy can effectively alleviate the energy problems caused by the shortage of conventional energy and environmental pollution. Scientific evaluation of wave energy resources is the prerequisite for the utilization of ocean energy resources. In this paper, based on the latest ERA5 data of ECMWF and the new wave energy evaluation formula to evaluate the wave energy resources in Yellow and Bohai sea during the period of 1980-2018. It mainly includes wave power density and evaluation indices such as usable level frequency, rich level frequency, variability index of wave energy resources and the available wave height proportion, etc. It can be concluded that the wave energy resources have obvious seasonal feature in Yellow and Bohai sea and resources are richer in winter and autumn and poorer in spring and summer. Winter is the best season for wave energy resource development. The wave energy enrichment areas are mainly concentrated in the outer part of the Bohai strait, the eastern part of Chengshantou and the offshore area of the Yangtze estuary. On this basis, the key development and utilization areas of wave energy resources are determined , and these data provide reference points for wave energy resource exploitation.

Key words: ERA5; wave energy assessment; power density; rich level frequency; usable level frequency

8th International Conference on the Application of Physical Modelling in Coastal and Port Engineering and Science
Zhoushan, China - Dec. 9th - 12th, 2020

TURBULENCE CHARACTERISTICSAND MASS TRANSPORT IN THE NEAR WAKE OF FISHING NET PANEL

DONGDONG SHAO [1], LI HUANG [1]

1 State Key Laboratory of Water Environment Simulation & School of Environment, Beijing Normal University, Beijing, 100875, China, ddshao@bnu.edu.cn

Cage-based aquaculture has been growing rapidly in recent years, which results in clustering of large quantities of cages in fish farms located in inland lakes and reservoirs and coastal embayment, and hence significantly affecting flow and mass transport in the surrounding waters. However, existing studies focus primarily on the macro-scale flow blockage effects of the fish cages, and the complex wake flow and associated mass transport in the presence of the cages are largely unclear. As a first step toward resolving this issue, this study employed the combined particle image velocimetry and planar laser induced fluorescence (PIV-PLIF) technique to measure the turbulence characteristics and the associated mass transport in the near wake of steady current through fishing net panel, as a key component of the fish cage, in flume experiments. In the near wake ~3M (mesh size) downstream of the net, the flow was observed to be highly inhomogeneous and anisotropic. The turbulent intensity followed a power law decay after the turbulence production region, albeit with a decay exponent much smaller than reported values for grid-generated turbulence. Overall, the presence of the net slightly enhanced the lateral spreading of the scalar plume, but the lateral distribution of the scalar concentration, concentration fluctuation and transverse turbulent scalar flux exhibited self-similarity from very near downstream where the flow is still strongly inhomogeneous. The apparent turbulent diffusivity estimated from the gross plume parameters was shown to be in reasonable agreement with the Taylor diffusivity calculated as the product of the transverse velocity fluctuation and integral length scale, even when the plume development is still transitioning from turbulent-convective to turbulent-diffusive regime. The findings of this study provide references to the near-field scalar transport of fish cages, which has important implications in the assessment of the environmental impacts and environmental carrying capacity of cage-based aquaculture.

Key Words: fishing net panel, near wake, turbulence characteristics, mass transport, PIV-PLIF

8th International Conference on the Application of Physical Modelling in Coastal and Port Engineering and Science
Zhoushan, China - Dec. 9th - 12th, 2020

EVOLUTION OF THE QINGSHUIGOU CHANNEL ON THE YELLOW RIVER DELTA THROUGH 1976 TO 2014: EVOLUTION STAGES AND ANTHROPOGENIC IMPACTS

Shan Zheng

State Key Laboratory of Water Resources and Hydropower Engineering Science, Wuhan University, Hubei 430072, China.

Tel: (86) 130 7278 6098

E-mail: zhengs@whu.edu.cn

Avulsion at the Yellow River delta (YRD) is very frequent and the average lifespan of channels is only about a decade due to the heavy sediment load and the subsequent rapid channel aggradation and progradation. Nevertheless, the Qingshuigou channel, the recent lobe on the delta, has been maintained for about four decades since an artificial avulsion in 1976. In this study, we comprehensively analyze the geomorphic adjustment of the channel at the downstream of the avulsion location during 1976-2014. Results showed that channel evolution processes may be divided into four phases: I (1976-1980) rapid aggradation, II (1980-1986) channel widening andenlargement, III (1986-1994) main channel aggradation and shrinkage, and IV (1994-2014) main channel incision and deepening. In Phase II, the channel experienced typical evolution sequences that have been observed for various incised channels, i.e. "channel bed incision—degradation and widening—aggradation and widening". These sequences are well included in the widely applied Channel Evolution Models (CEMs). By the end of Phase III, the normalized gradient advantage and superelevation at the lower channel reaches were close to or exceeded the critical values proposed by previous studies, implying that the channel was prone to avulsion. Nevertheless, avulsion was prevented mainly due to the lack of overbank flows and the construction of artificial dikes. Channel evolution processes at Qingshuigou channel in Phases I, II and III are similar with those observed at natural and experimental fluvial systems, and a possible evolution cycle is proposed for the fluvial systems with aggradational avulsions, i.e. "sediment rapidly deposits in a new, lower river channel and floodplains immediately following avulsion—a new channel starts to form and becomes deeper and wider by eroding the deposition—channel is backfilled and an alluvial ridge forms—avulsion occurs when critical conditions are attained". Nevertheless, allogenic controls can interrupt the cycle, such as in the case of the Qingshuigou channel, where overwhelming anthropogenic impacts, including damming, water and sediment regulation, artificial avulsion at the mouth channel, etc., caused incision at the channel in Phase IV and reversed the tendency towards avulsion. During the almost four decades, the bedslope decreased exponentially and has since relaxed to quasi-equilibrium value, and channel progradation decelerated with time.

The evolution of the Qingshuigou channel confirms previous arguments that superelevation and gradient advantage are not sufficient for avulsion, and multiple factors should be considered, including flood frequency, lateral mobility, sediment diameter and human interruptions.

Keywords: Yellow River delta; Qingshuigou channel; geomorphologic adjustment; avulsion; superelevation; human interruption.

8th International Conference on the Application of Physical Modelling in Coastal and Port Engineering and Science
Zhoushan, China - Dec. 9th - 12th, 2020

COMPARISON OF HYDRODYNAMIC CHARACTERISTICS OF DIFFERENT PLATE TYPE OPEN BREAKWATERS

Xueyan Li*, Lixue Wang, Tian Xie, Qin Li

a Coast Institute, Ludong University, Yantai 264025, China;
b Institute of Sea-Crossing Engineering，Ludong University ,Yantai,264024,P.R.China;

With the rapid development of the internationalized trade and the trend of the larger-sized vessels, port construction in China is gradually moving into the offshore area with deep water, large waves and complicated geological conditions. Due to their shortcomings, such as high engineering cost, poor seawater flow and difficulty in construction, the traditional gravitybreakwaters represented by the slope-type and the vertical-type breakwaters have been unable to meet the requirements of the modern port construction. As a new type of breakwater structure, the plate type open breakwaters are favored by many experts and scholars, since they have the advantages of low requirements for foundation conditions, free exchange of water bodies, ecological environment protection, simple structure, and so on. Among them, the arc-plate-type open breakwaters were newly proposed in recent years. To explore the characteristics of the arc-plate-type open breakwaters, comparative studies were conducted between the flat-plate type breakwater and arc-plate type open breakwater by performing hydrodynamic tests on the two type open breakwaters. The similarities and differences in wave attenuation performance and structural stress were analyzed, and the hydrodynamic characteristics of the two plate type open breakwaters were compared from the aspects of wave transmission coefficient, reflection coefficient, wave pressure, total wave force and structural flow field characteristics.

The results show that the wave elevation and the transmission coefficients of the two plate type open breakwaters are significantly different under different submergence conditions. When the breakwaters are above and located at the still water surface, the wave elevation of the arc-plate type breakwater is lower than that of the flat-plate type breakwater, and the transmission coefficient of the arc-plate type breakwater is significantly lower than that of the flat-plate type breakwater. The maximum reductions of the transmission coefficients for the conditions of the plate type breakwater above and located at the still water surface are 34.5% and 25%, respectively .However, the wave elevation and transmission coefficient of the flat-plate type breakwater are lower than that of the arc-plate type breakwater when the they are below the still water surface. Under different submergence conditions, the reflection coefficients of the flat-plate type breakwater are significantly higher than those of the arc-plate type breakwater with a maximum increase of 66.7%. Besides, studies in this paper have shown that the difference in the wave pressure between the two type breakwaters is also significant. Above the still water surface, the wave pressure on the upper plate of the arc-plate type breakwater is slightly greater than that of the flat-plate breakwater, and the maximum increase could be up to 32.3%, while the wave pressure on the lower plate of the arc-plate type breakwater is slightly smaller than that of the flat-plate type breakwater. Below and located at the still water surface, the wave pressure on the flat-plate type breakwater is slightly higher than that on the arc-plate type breakwater; the corresponding maximum increases are 5.8%and 19.6% , respectively. Above the still water surface, the vertical wave force on the arc-plate type breakwater is significantly larger than that on the flat-plate type breakwater. Below and located at the still water surface, the vertical wave force of the flat-plate type breakwater is larger than that of the arc-plate type breakwater. The horizontal wave force of the arc-plate breakwater is greater than that of the flat-plate breakwater. The impact of the two plate type breakwaters on the flow field

around the structure was also discussed. The wave turbulence around the arc-plate structure is more severe, and the waves acting on the arc-plate type breakwater are provided with a significant climbing process above the still water surface, so the arc-plate type breakwater has a greater resistance to the waves. In summary, above the still water surface, the wave attenuation performance of the arc-plate type breakwater is better than that of the flat-plate type breakwater, but its wave forces are significantly larger; Below and located at the still water surface, the wave attenuation performance of the flat-plate type breakwater is better than that of the arc-plate type breakwater, but its wave force is greater. For the practical engineering applications, it is recommended to adopt the arc-plate-type open breakwater when the structures are above the still water surface; while it is recommended to use the flat-plate type breakwater below and located at the still water surface.

8th International Conference on the Application of Physical Modelling in Coastal and Port Engineering and Science
Zhoushan, China - Dec. 9th - 12th, 2020

TWO-LAYER IMMISCIBLE FLUIDS SLOSHING IN A RECTANGULAR TANK

MI-AN XUE [1,2], OBAI KARGBO [1,2], JINHAI ZHENG[1,2]

1 *Key Laboratory of Coastal Disaster and Defence (Hohai University), Ministry of Education, Nanjing 210024, China, E-mail: coexue@hhu.edu.cn*

2 College of Harbour Coastal and Offshore Engineering, Hohai University, Nanjing 210024, China

Sloshing is the violent motion of the free surface of a fluid in a partially filled container, which is a classic problem in hydrodynamics. It has a wide range of applications in ocean and offshore engineering fields particularly in cargo ship carrying the partially filled container with fluids. Fluid sloshing motion in a liquid tank has thus been the subject of numerous studies in the past many years. However, lots of the previous investigations were devoted to the single fluid sloshing in containers. It was found from the industry that the density stratification may change the hydrodynamic properties of sloshing interfacial waves. Two kinds of fluids are considered to be immiscible in this study. This study will conduct the two-layer immiscible fluids sloshing in a rectangular liquid tank by varying the depth ratio of upper and lower fluids, excitation frequency and amplitude. Especially, effect of an immersed vertical baffle on interfacial wave evolution will be discussed detailed by varying its position under different excitation conditions.

Laboratory experiments will be conducted in a shaker table to further explore the sloshing characteristics when two layer liquids of different densities are presented. The tap water and diesel oil are adopted in the experiments. The pressure distribution inside liquid tank filled with different depth ratio of two-layer fluids will be obtained near the resonant frequencies. The fast Fourier transform analysis techniques will be used to present a spectral analysis of the time series of interfacial waves, which can reveal the relations between the sloshing frequency and surface sloshing mode and interfacial wave elevation. These studies will be used to explore the dependencies of layered sloshing behavior on depth ratio and density stratification.

Key Words: density stratification; two-layer sloshing; interfacial wave evolution; laboratory experiments

8th International Conference on the Application of Physical Modelling in Coastal and Port Engineering and Science
Zhoushan, China - Dec. 9th - 12th, 2020

TWO-DIMENSIONAL SIMULATION OF WATER AND SEDIMENT DYNAMICS ON THE YANGTZE RIVER ESTUARY

ZHAO HUI-MING[1], TANG LI-QUN[1], WANG CHONG-HAO[1], GUO CHUAN-SHENG[1], WANG YU-HAI[1], LIU DA-BIN[1], FENG HAO-CHUAN[1], ZHANG YUE-FENG2, LU JING[2]

1 State Key Laboratory of Simulation and Regulation of River Basin Water Cycle, China Institute of Water Resources and Hydropower Research, Beijing 100048, China, zhaohuiming045@163.com

2 Development Research Center of the Ministry of Water Resources of P. R. China, Beijing 100038, China, zhangyf513@163.com

With the economic development of estuarine and coastal areas, beach reclamation project has become the main reason for the change of coastline contour, which further affects the flood control pattern and the safety and stability of seawall. In this paper, regarding the Yangtze River Estuary and Hangzhou Bay as an organic whole, a two-dimensional mathematical model is established to reflect the dynamic characteristics of water and sediment and water exchange of the Yangtze River Estuary. Focusing on the Yangtze River Estuary, the simulation research on the influence of beach utilization on flood control and tide control has been carried out, and the research scope covers the water areas from Jiangyin to the Yangtze River Estuary and Hangzhou Bay. Based on the existing research results and historical measured data, the tide level and tidal current of the established model are verified by the terrain data and synchronous hydrological observation data in 2012. The results show that the mathematical model is reasonable for boundary treatment and roughness selection, which can better reflect the movement of water and sediment on the Yangtze River Estuary, and can be used for the simulation study of the impact of beach use on flood control and tide control.

Key Words: a two-dimensional mathematical model, water and sediment dynamics, the Yangtze River Estuary

8th International Conference on the Application of Physical Modelling in Coastal and Port Engineering and Science
Zhoushan, China - Dec. 9th - 12th, 2020

A NEW LAGRANGIAN DISCONTINUOUS GALERKIN SCHEME WITH MOVING UNSTRUCTURED TRIANGULAR MESH

WENBIN WU[1], MOUBIN LIU[2]

1 Institute of Ocean Research, Peking University, Beijing 100871, China, wuwenbin_fsi@pku.edu.cn
2 Department of Mechanics and Engineering Science, Peking University, Beijing 100871, China, mbliu@pku.edu.cn

Fluid flows with large deformations are common in free surface flow and fluid-structure interaction problems. When the fluid flow accompanies with large distortions, Lagrangian-based grid method usually suffers from a lack of accuracy and stability. In this paper, we present a new Lagrangian discontinuous Galerkin (LDG) scheme to simulate compressible flows on the unstructured triangular mesh. The new scheme can overcome the large distortions in the Lagrangian framework as it combines the advantage of the discontinuous Galerkin scheme and the adaptive mesh optimization technique. It consists of three phases, Lagrangian phase, remeshing phase and remapping phase. Firstly, the compressible Euler equation in the Lagrangian framework is solved by the discontinuous Galerkin method, while the nodal velocity and numerical fluxes are determined by the nodal solver. Secondly, the adaptive mesh optimization technique is employed to eliminate the ill-shaped triangular elements caused by the large distortions of fluid flow. The mesh subdivision, mesh simplification and mesh relaxation techniques are adopted to optimize the mesh topology and improve the mesh quality. Thirdly, the physical solutions on the original mesh are projected onto the newly remeshed mesh. The LDG scheme can preserve the conservation of mass, momentum and energy. Numerical examples demonstrate that the newly developed LDG is effective in modeling fluid flows with large deformations and it should also be attractive for free surface flows and fluid structure interaction problems in ocean and coastal engineering.

Key Words: compressible flow, discontinuous Galerkin, unstructured triangular mesh, mesh optimization technique

8th International Conference on the Application of Physical Modelling in Coastal and Port Engineering and Science
Zhoushan, China - Dec. 9th - 12th, 2020

APPLICATION OF A COUPLED MODEL IN SIMULATING WAVE DEFORMATION AND OVERTOPPING ON CORAL REEF

KUN LIU[1], SHAOWU LI[1,*], YE LIU[2]

1 State Key Laboratory of Hydraulic Engineering Simulation and Safety, Tianjin University, Tianjin 300072, People's Republic of China.

2 National Engineering Laboratory of Port Hydraulic Construction Technology, Tianjin Research Institute for Water Transport Engineering, M.O.T., Tianjin 300456, People's Republic of China.

Corresponding author, Email: lishaowu@tju.edu.cn

The present work validates a numerical model using a laboratory dataset of wave deformation over a coral reef topography and wave overtopping around vertical seawalls located on the reef flat. The numerical model is a newly-proposed model in which wave propagation over the off-reef region with deep depth is simulated by an Eulerian Finite Difference (FD) approach solving the Navier-Stokes equations, and wave propagation over the region from the reef edge to the seawalls is simulated with a Lagrangian approach based on the incompressible Smoothed Particle Hydrodynamics (ISPH) method. Numerical results were compared with experimental data and good agreement was achieved. It shows that the coupled model can be used as an efficient numerical tool in terms of providing reliable estimations of interaction between waves and structures built on the coral reef area.

Key Words: Coupled model; Finite Difference Method; Incompressible Smoothed Particle Hydrodynamics; wave overtopping; coral reef

8th International Conference on the Application of Physical Modelling in Coastal and Port Engineering and Science
Zhoushan, China - Dec. 9th - 12th, 2020

BOUNDARY LAYER FLOW APPROXIMATION FOR ASYMMETRIC OSCILLATORY SHEET FLOW

XIN CHEN[1], JIAXING LI[2], XINYU HU[3]

1 Professor, Beijing Engineering Research Center of Safety and Energy Saving Technology for Water Supply Network System, China Agricultural University , Beijing, 100083, China. Email: chenx@cau.edu.cn

2 PhD Candidate, Beijing Engineering Research Center of Safety and Energy Saving Technology for Water Supply Network System, China Agricultural University , Beijing, 100083, China, Email: 1309080227@cau.edu.cn

3 PhD Candidate, Beijing Engineering Research Center of Safety and Energy Saving Technology for Water Supply Network System, China Agricultural University , Beijing, 100083, China. Email: huxinyu@cau.edu.cn

Wave boundary layer is important for sand transport in oscillatory sheet flow because sand is mainly picked up and moved in the boundary layer. This study uses an analytical approximation for velocity distribution resulting from asymmetric wave theory and turbulent wave boundary layer theory over movable sandy bed. The phase residual and phase shift effects of sand movement are accounted into the movable bed, and the phase lead which denotes the time-lead of bottom shear stress to free stream velocity is considered into the velocity distribution. The asymmetry in wave friction factor, oscillatory flow orbital amplitude, roughness height, bed shear stress and wave boundary layer thickness are presented by dividing the boundary layer flow into four quarters of pseudo-sinusoidal flow. The velocity distribution for boundary layer beneath oscillatory sheet flow induced by asymmetric wave can be properly predicted with accuracy as that of a two-phase numerical model. The differences of onshore and offshore flow durations and acceleration and deceleration flow durations can be presented so that the net wave boundary layer flow of asymmetric oscillatory flow can be obtained.

Key Words: asymmetric wave, movable bed, oscillatory sheet flow, velocity distribution, wave boundary layer

8th International Conference on the Application of Physical Modelling in Coastal and Port Engineering and Science
Zhoushan, China - Dec. 9th - 12th, 2020

WAVELET COHERENCE ANALYSIS OF SHEAR INSTABILITIES OF LONGSHORE CURRENTS ON PLANE BEACHES

REN CHUNPING[1], LIU YU[2]

1 College of Water Resource Science and Engineering, Taiyuan University of Technology, Taiyuan, China, Chunpingren@163.com

2 College of Water Resource Science and Engineering, Taiyuan University of Technology, Taiyuan, China, 564924859 @qq.com

A detailed description is given of the results of laboratory experiments on wave-driven longshore currents on plane beaches of slopes 1:40 and 1:100. Unidirectional obliquely incident waves, both regular and random, were used. The current velocity measurements were located at one third of the water depth from the bottom. The objective is to investigate the development of shear instabilities of a wave-driven alongshore current in time frequency domain. The cross wavelet transform was used to compute the coherence between two horizontal velocity time series collected in two positions of same water depth. And the effects of the incident wave height, period and slope of the plane beach on the development of shear instabilities were examined using the wavelet coherence results.

Key Words: longshore current; shear instabilities; plane beach; wavelet coherence

8th International Conference on the Application of Physical Modelling in Coastal and Port Engineering and Science
Zhoushan, China - Dec. 9th - 12th, 2020

COUPLING SIMULATION OF WAVES AND STORM SURGES IN A WAVE-CURRENT FLUME

PAN JUNNING[1], CHEN MAOWEN[1], SUN TIANTING[1], WANG DENGTING[1], SUN ZHONGBIN[1]

1 State Key Laboratory of Hydrology-Water Resources and Hydraulic Engineering, Nanjing Hydraulic Research Institute, Nanjing, China, jnpan@nhri.cn

The coupling simulation technology of waves and storm surges is introduced, which can provide a new physical modelling method for wave-storm surge co-action on seawalls and disaster evaluation in coastal areas. Previous physical model test researches on seawall damage due to wave and storm surge action did not consider the effect of the dynamic variation process of water level and wave parameters enough, although it is important for modelling damage procedure of coastal structures accurately.

The simulation was carried out in a wave flume of 175m long, 1.2m wide and 1.8m deep. In order to simulate the combined effect of storm surges and waves, the wave flume was modified to simulate water level change by installing a tide generator. The wave and storm surge processes were discretized into many segments. In each time segment, the water level and wave conditions were considered nearly constant, and wave parameters of different time segments were calibrated at the corresponding water levels. Then the calibrated wave generation file elements were connected to get the whole continuous wave generation file, in which wave parameters vary with the water level during the simulation period. In the process of calibration, wave height and period simulation results were measured and analyzed in real time by wave-height meter, and compared with the target value, the mean error of the measured value of wave height and period and the target value were controlled within 5%. With wavemaker and tide generator controlled simultaneously, the dynamic coupling simulation of waves and storm surges was realized by simulating wave and water level variation process synchronously and continuously.

In an application example, the dynamic processes of storm surges and waves of Typhoon Winnie were simultaneously simulated in the wave flume, and the measured data of water level, wave parameters and wave spectra in the model test are compared with the target values. It is shown by the comparison analysis that the simulation results of this coupling simulation method are of relatively high accuracy.

Key Words: storm surges, waves, coupling simulation

8th International Conference on the Application of Physical Modelling in Coastal and Port Engineering and Science
Zhoushan, China - Dec. 9th - 12th, 2020

NUMERICAL INVESTIGATION INTO DYNAMIC POREWATER PRESSURE WITH COASTAL SEA DEFENCES FROM TIDAL CYCLES

RICHARD REES & SHUNQI PAN

School of Engineering, University of Cardiff, CF24 3AA, United Kingdom (Reesrs2@cardiff.ac.uk; pans2@cardiff.ac.uk)

Recent winters in the UK have demonstrated the susceptibility of the sea defences to increasingly powerful and more prevalent storm systems, resulting in major damage to defence themselves and the infrastructure it is designed to protect. This trend is expected to continue with climate change and exasperated by an increase in sea level. In the future, to ensure continued confidence that these defences are able to perform their task, modifications to old, and the construction of new defences will have to occur. Essential to the design resilience, would be how to mitigate the effect of previously unknown or under considered instability factors.

Pore water pressure (PWP) within a soil plays a vital role determining its stability, for a coastal structure, seepage can cause geo-hydraulic failure if not properly accounted for in the design though internal erosional processes (Vorogushyn, Merz and Apel, 2009). Several different researchers (Vorogushyn, Merz and Apel, 2009; Chen *et al.*, 2013) have been investigating the hydraulic action of cyclical events i.e. tides and wave impacts on stability of earthworks. A particular focus has been the fabric of the soil within the earthwork and the dynamic effect of varying seepage gradients and velocities. The hydraulic forcing in respect to tides has been initially investigated through the numerical modelling and physical experimentation by the previous authors.

This paper is to present the results of the numerically investigation of the effects of tidal action on two differing homogeneous embankments on the PWP, using both seepage only analysis and fully coupled stress-seepage analysis using an elasto-plastic soil model. A base line was established per model, with the main simulations employing transient seepage analysis. Within these simulations, the water level was varied using S2 and M2 tides over a 42-day period. The phase and PWP difference between the tidal cycle and migrating pressure pulse was established within the earthwork, by comparing the values of different vertical sections.

Initial results demonstrated that PWP were higher within the embankment for the flood tide but significantly, lower for the ebb, this is due to the ability of the later to simulate deformation of the embankment due to loading and unloading cycles. Further investigation revealed that a pressure pulse does exist between vertical sections and were found to occur at the higher reaches of the earthwork, which experience the greatest periods of saturation and unsaturation.

References

Chen, L. *et al.* (2013) 'Experimental study of seawall piping under water level fluctuation', *European Journal of Environmental and Civil Engineering*. Taylor & Francis, 17(sup1), pp. s1–s22. doi: 10.1080/19648189.2013.834582.

Vorogushyn, S., Merz, B. and Apel, H. (2009) 'Development of dike fragility curves for piping and micro-instability breach mechanisms', *Nat. Hazards Earth Syst. Sci*, 9(4), pp. 1383–1401. doi: 10.5194/nhess-9-1383-2009.

8th International Conference on the Application of Physical Modelling in Coastal and Port Engineering and Science
Zhoushan, China - Dec. 9th - 12th, 2020

STUDY OB THE EFFICIENCY OF COASTALPROTECTION BY ARC TYPE SUBMERGED BREAKWATERS

WEN-JUINN CHEN[1], HON WEI[2]

1 Department of Civil and Water Resources Engineering, Nation Chiayi University, Taiwan,wjchen@mail.ncyu.edu.tw
2 The Seventh River Management Office, WRA, Taiwan, cyuchi@kimo.com

In recent year, the consciousness of coastal sustainable development is promoted, so more environmentally friendly coastal protection methods are strongly advocated by the peoples. To improve the disadvantages of traditional rectangular submerged breakwater and to improve its aesthetics and to increase the landscape in coastal waters is planning now, the arc type submerged breakwater is one of our ideas. The main purpose of this paper is to study the effect of coastal protection by the arc type submerged breakwater (ASB) and the results were compared with the rectangular type submerged breakwater (RSB). A series of experiments were conducted in a 20m X 40 m wave basin and a regular wave with T=1.2 sec, H=6cm were generated by the wave generator. Several setups of submerged breakwater segments with different gap at various depth sites were tested to examine their effects on coastal erosion control. After the analysis, we found the arc type submerged detached breakwater has a better efficiency on mitigating the scour depth at the sea side of the breakwater, it could be reduced by about 15%~36% if compared with the rectangular type submerged breakwater. And shoreline recession for arc type submerged breakwater could be reduced by about 20%~32% if compare with the rectangular type submerged detached breakwater. However the efficiency on sand depositing behind the breakwater for arc type submerged breakwater is less than the rectangular type submerged detached breakwater. So how to select an effective submerged breakwater on coastal protection and reservation must rely on the purpose of needed.

Key Words: coastal erosion, submerged breakwater, sediment, shoreline

8th International Conference on the Application of Physical Modelling in Coastal and Port Engineering and Science
Zhoushan, China - Dec. 9th - 12th, 2020

NUMERICAL ANALYSIS OF THE INFLUENCE OF SEA LEVEL RISE ON SEDIMENT DEPOSITTION IN THE YELLOW RIVER ESTUARY

GUO CHUANSEHNG[1], WANG CHONGHAO[1], WANG YUHAI[1], ZHAO HUIMING[1], LIU DABIN[1]

1 State Key Laboratory of Simulation and Regulation of Water Cycle in River Basin, China Institute of Water Resources and Hydropower Research, Beijing, P. R. China, guoliu1982@126.com

To explore the influence of sea level rise on sediment deposition in the Yellow River Estuary, this article has simulated the change of flow velocity in Yellow River Channel in different situations of sea level rise with FVCOM and calculated the threshold motion velocity of sediment in main channel. The results show that as sea level rise, flooding and precipitating velocities in upside main channel increase. During the period of sea level rising, with the runoff emptying into the sea, the ebb tide dynamics were enhanced; the runoff was mixed up with the sea water as diluted water when it diffused into the open sea. The diffusion range of diluted water extended dramatically north 38°10′N, east to 119°30′E and south to 37°45′S. The suspended sediment diffusion played a significant role in the sediment transport. In the nearshore zone, the suspended sediment deposited rapidly because of the cutting off by the tidal shear front. More rapid deposition occurred where the frontal cutting off was with the ebb tide inside and flood tide outside.

Key Words: suspended sediment transport; 3-D numerical model; level rise; Yellow River Estuary; sediment deposition

8th International Conference on the Application of Physical Modelling in Coastal and Port Engineering and Science
Zhoushan, China - Dec. 9th - 12th, 2020

EXPERIMENTAL INVESTIGATION OF SCOUR AROUND A PERMEABLE PILE BREAKWATER

CONGHAO XU[123], ZHENHUA HUANG[2]

1 Key Laboratory of Water-Sediment Sciences and Water Disaster Prevention of Hunan Province, Changsha 410114,China, conghaox@csust.edu.cn

2 Affiliation, Country, E-mail Department of Ocean and Resources Engineering, School of Ocean and Earth Science and Technology,

University of Hawaii at Manoa, Honolulu HI, 96822, USA

3 School of Hydraulic Engineering, Changsha University of Science and Technology, Changsha 410114, China

Permeable pile breakwaters consisted of a row of closely spaced vertical piles are useful in ecological shoreline protection due to its ability to allow water flow passage and to reflect and dissipate wave energy. However, such structures inevitably induce flow contraction through the narrow gaps formed by adjacent pile members, which may enhance sediment scour around the structure. Although a relatively well understanding has been generated towards scour mechanisms around a single standalone pile or a row of loosely spaced piles, the characteristics of scour occurring around a row of closely spaced piles with significant flow contraction effect under regular waves is not well understood.

This study presents a set of laboratory experiments investigating the scour around a permeable breakwater consisted of a row of closely spaced vertical piles sitting on a quartz sand bed, under the effect of regular waves. Wave gauges are used to measure the wave propagation and scattering around the structure. High-resolution three-dimensional scour profiles are measured using precise 3D underwater laser scanner. The development of scour with increasing scour time under different incident wave conditions is examined. Focus is given to the identification and quantification of representative scour profile parameters that characterizes the onset of scour around a permeable pile breakwater with closely spaced pile members under the effect of regular waves.

Key Words: Sediment transport, Regular wave, Pile Breakwater, Foundation scour

8th International Conference on the Application of Physical Modelling in Coastal and Port Engineering and Science
Zhoushan, China - Dec. 9th - 12th, 2020

NUMERICAL SIMULATION OF STORM SURGE IN LAIZHOU BAY

GUO CHUANSEHNG[1], LIU DABIN[1], WANG CHONGHAO[1], WANG YUHAI[1], ZHAO HUIMING[1]

1 State Key Laboratory of Simulation and Regulation of Water Cycle in River Basin, China Institute of Water Resources and Hydropower Research, Beijing, P. R. China, guochsh@iwhr.com

Storm surge in Aug. 2018 was reproduced using a 3-D FVCOM nonlinear barotropic model. The hydrodynamic model was forced by using wind data obtained from the weather research forecasting model(WRF). The hindcast surge elevations agreed closely with in situ observations and the results showed the spatial-temporal features of the coastal water level fluctuation in Laizhou Bay. The surge level increment became greater at the coast of Laizhou Bay with an obvious water level fluctuation because of the Typhoon effects, The current changed in the storm surge. A series of numerical experiments were performed to study the impact of coastal engineering on storm surges. The results showed that the maximum surge level in-creased at South of Yellow River Estuary, which could potentially cause severe damages.

Key Words: storm surge; 3-D numerical model; water level fluctuation; Yellow River Estuary; sediment erosion

8th International Conference on the Application of Physical Modelling in Coastal and Port Engineering and Science
Zhoushan, China - Dec. 9th - 12th, 2020

INFLUENCES OF RECLAMATION ON THE HYDRODYNAMICS AND MORPHO-DYNAMICS OF THE QIANTANG ESTUARY

Wei Li[1,*], Zhuo Chen[1], Peng Hu[1], Zhiguo He[1]

1 Zhejiang University, Zhoushan Campus, China

Intense reclamation has greatly narrowed the coastalembankment in Qiantang River Estuary (QRE) since 1950s. In the last decade, there have been increasingly more and more numerical researches on how reclamation affects the hydrodynamic environment and sediment transport of the QRE but using idealized symmetrical triangular configuration. These investigations, however, have neglected the very important meandering aspect of the QRE. Aiming to further reveal the effects of reclamation, this paper presents a series of numerical case studies based on actual QRE plane shape. Specifically, three representative plane shape extracted from USGS Landsat satellite images (representing the year of 1984, 2004 and 2017) are considered. The initial bed level decreases linearly from 0 to -7 m from the landward end to seaward end to avoid influence of the river bed. Some preliminary understandings are obtained from this investigation. The tidal characteristics of the three plane shapes are compared in detail, the rise of tidal high level and the decline of tidal low level in Hangzhou Bay lead the increase of the tidal range along the QRE. Large scale coastal embankment intensifies the tidal asymmetry, so the ratio of tidal rise to fall duration become smaller especially from Ganpu to Wenyan section. The estuarine turbidity maximum in Hangzhou Bay (ETM1) tend to move upstream and a new estuarine turbidity maximum around Yanguan (ETM2) accounting for the high sediment concentration in this area is observed. The sediment exchange pattern along the QRE is well demonstrated and it plays a major role on the inside bar evolution. The net sediment fluxes pointing upstream in Ganpu become larger in a single tidal period due to the reclamation, a large amount of sediment deposition between Yanguan and Ganpu may contributed to the downstream development of the inside bar. Compared with the idealized model, the morphological evolution is well reproduced in the reclamation area based on actual QRE plane shape.

8th International Conference on the Application of Physical Modelling in Coastal and Port Engineering and Science
Zhoushan, China - Dec. 9th - 12th, 2020

RIPPLE FORMATION AT LARGE SCALE WAVE FLUME EXPERIMENTS

IV N C CERES[1], AGUST N S NCHEZ-ARCILLA[1], PETER THORNE[2], DAVID HURTHER[3]

1 Universitat Politècnica de Catalunya, Spain, i.caceres@upc.edu, agustin.arcilla@upc.edu
2 National Oceanography Center, UK, pdt@noc.ac.uk
3 Laboratoire des Écoulements Géophysiques et Industriels, France, david.hurther@legi.cnrs.fr

The development and improvement of reliable ripple formulations to predict ripple height and length, or its growth rate require a better understanding of the hydrodynamic conditions under which they grow and evolve. While current ripple formulations rely on wave height, period, grain size and water depth, little is known their interactions with the velocity skewness, re-suspension patterns and growth rate. Moreover that, there is limited information on the effect of mixed sediment conditions over the ripples features (height and length). Here a new data set of experiments is presented including the analysis of the collected data. The experiments were done at the CIEM large wave flume of Barcelona when considering three different wave conditions and three different sediments (fine sediment with d_{50}=0.25 mm, coarse sediment with d_{50} of 0.54 mm and a mixture of both sediments with d_{50} of 0.37 mm). The information of the ripples features has been collected by means of two different equipment: an array of echosounders and an acoustic ripple scanner. The velocity field data has been collected by means of standard 3D point measurement Norteck Vectrinos and by means of the Acoustic Current Velocity Profiler (ACVP) developed by Hurther et al. (2011). The suspended sediment information has been retrieved by means of Optical Backscattar Sensors, and by the Bedform And Suspended Sediment Imager (BASSI) an array of 60 Acoustic Backscatter Sensors (Moate et al. 2016).

The obtained ripple features, height and length, are compared to state of the art formulations. The formulation that obtains a better average approximation to the measured ripples is Grasmeijer 2002 despite it importantly under predict the larger ripples found for the coarser tested sediment. An important disagreement is found between the theoretical orbital velocities and excursion amplitudes computed by means of linear wave theory when compared to the measured values. These disagreements are up to 43 % and 50 % larger (orbital velocities and excursion amplitude respectively) for the larger tested period (9s waves). The ripple growth is studied by constantly measuring the bottom evolution along the 4 hours that each wave condition has been tested.

Figure 1 Different ripples obtained along the RIPCOM data set.

Key Words: ripples, large scale experiments, velocities, suspended sediment concentrations

8th International Conference on the Application of Physical Modelling in Coastal and Port Engineering and Science
Zhoushan, China - Dec. 9th - 12th, 2020

A MODIFIED BRAGG'S LAW FOR LINEAR LONG WAVE REFLECTION BY ARTIFICIAL BARS

HUAN-WEN LIU

School of Naval Architecture and Mechanical-electrical Engineering, Zhejiang Ocean University, Zhoushan, Zhejiang 316022, PR China E-mail: liuhuanwen@zjou.edu.cn

The Bragg resonance between artificial sandbars and ocean surface waves can greatly reflect incident waves thus plays an important role in coast protection. Because of this reason, the Bragg resonance in water waves has attracted many scholars to conduct related research. However, it is shown by almost all the experimental and computational results that the Bragg's resonance law is not correct in water wave reflection and the frequency of the peak Bragg reflection significantly shifts downward. The reason is that the traditional Bragg's law established for non-mechanical waves is not applicable for water waves which are mechanical and their propagation relies on the water body. In fact, Bragg resonance of water waves comes from the superposition of incident waves and reflected waves, which relies on the propagation velocity of waves, thus it is affected by the varying water depth caused by artificial bars. This means that the resonance condition relies on the configuration of bars and the bar number, bar height and bar width. In this study, by using various analytical solutions to the depth-averaged wave equations for waves over artificial bars, we are going to establish a modified Bragg's law for linear long wave resonant reflection caused by various artificial bars.

Key Words: modified Bragg's law, linear long wave, reflection, Bragg resonance, artificial bars.

8th International Conference on the Application of Physical Modelling in Coastal and Port Engineering and Science
Zhoushan, China - Dec. 9th - 12th, 2020

LARGE-EDDY SIMULATION OF BREAKING WAVES

ZHIHUA XIE[1], THORSTEN STOESSER[2], PENGZHI LIN[3]

1 School of Engineering, Cardiff University, Unite Kingdom, zxie@cardiff.ac.uk

2 Department of Department of Civil, Environmental and Geomatic Engineering, University College London, United Kingdom, t.stoesser@ucl.ac.uk

3 State Key Laboratory of Hydraulics and Mountain River Engineering, Sichuan University, China, cvelinpz@126.com

Wave breaking plays an important role in marine hydrodynamics, wave-structure interaction, air-sea interaction, surf zone dynamics, and nearshore sediment transport. A three-dimensional numerical study has been undertaken to investigate the turbulent structures under breaking waves, including wave pre-breaking, overturning, and post-breaking processes. A two-phase flow model has been developed and the large-eddy simulation (LES) approach has been adopted in the study, for which the filtered Navier–Stokes equations are solved and the dynnamic Smagorinsky sub-grid model is employed to compute the unresolved scales of turbulence. The governing equations have been discretised using the finite volume method, with the air–water interface being captured using a volume of fluid method. The cut cell method has been implemented to deal with complex geometry in the Cartesian grid with a moving body algorithm being employed to simulate moving bodies in the fixed Cartesian grid.

The LES code is validated with the help of various benchmark problems, and it is demonstrated that both the free-surface and velocity field are captured successfully by the code. Numerical results of breaking waves over a slope and a submerged object are presented and compared with the available experimental measurements. Detailed free surface profile, velocity fields and vortical structures during wave breaking are shown and discussed.

Key Words: breaking waves; large-eddy simulation; turbulence; volume-of-fluid method.

8th International Conference on the Application of Physical Modelling in Coastal and Port Engineering and Science
Zhoushan, China - Dec. 9th - 12th, 2020

INTEGRATING COASTAL DUNES DEGRADATION IN MARINE SUBMERSION RISK MODELING: APPLICATION TO AZEMMOUR SITE, MOROCCO

HASSAN AYAD[1], DALILA LOUDYI[2], MOHAMED CHAGDALI[1]

1 Hassan II University of Casablanca, Faculty of Sciences - Ben M'Sik, Morocco, ayadhassan01@gmail.com

2 Hassan II University of Casablanca, Faculty of Sciences and Technics -Mohammedia, Morocco, loudyi.d@gmail.com

The storm that hit Moroccan north Atlantic coast on the night of January 7th, 2014 has generated extremely intense submersion and erosion, causing significant damage. The peak of the storm coincided with high seas of a spring tide and strong swells between 8 and 9 m height.

In some areas like Azemmour, located 75 km southwest of Casablanca city on North Atlantic coast, coastal dunes degradation is responsible for a large part of the submersion extent. Visual observations show that the band of dunes was broken after marine submersion flooded the land behind the beach and was mainly responsible of dunes breaching.

Azemmour site is a highly vulnerable area as are all Moroccan coasts subject to long ocean swells. Indeed, many phenomena occur in this area such as predominant astronomical tide, storm surges and marine submersions occurring at extreme sea levels. The risk of flooding by the sea is currently high on this coast, particularly in areas where coastal dunes undergo anthropogenic disturbances. The realistic representation of degradations in coastal dunes is therefore a major issue in assessing the risk of submersion in sensitive areas.

This article presents a coupled numerical modeling system using Telemac2D and Tomawac to reproduce in a accurate way the submersion caused by the storm of January 2014 on Azemmour site. The model consists in the development of regional and local meshes that can represent the processes of tide, atmospheric pressure, wind, swell and specially the overtopping on dunes. The numerical model enables to calculate currents on the coast and also to evaluate the setup induced by waves and to integrate the overtopping by packets of water calculated on each zone.

Key Words: Marine submersion, Breaches, Sea packet crossing, Numerical modeling, Dunes degradation

8th International Conference on the Application of Physical Modelling in Coastal and Port Engineering and Science
Zhoushan, China - Dec. 9th - 12th, 2020

RIP CURRENTS BY INTERSECTING WAVE ON BARRED BEACH WITH RIP CHANNEL

WANG Yan[1,2], ZOU Zhili[3], LIU Zhongbo[1,2]

1. Innovation Center for Ports and Maritime Safety, Dalian Maritime University, Dalian 116026, *China*;

2. *College of Transportation Engineering, Dalian Maritime University, Dalian* 116026, *China*;

3. *State Key Laboratory of Coastal and Offshore Engineering, Dalian University of Technology, Dalian* 116024, *China*)

The study of rip currents by intersecting waves is helpful to thecomprehensive study of disaster mechanisms and risk assessment. To better understand the characteristics of rip currents controlled by hydrodynamic forcing and longshore topographical variability, an experimental study on rip currents by intersecting waves over barred beaches with rip channels is conducted. The investigation focuses on the distribution characteristics of rip currents resulting from intersecting waves and longshore topographical variability. Analytical results of velocity distribution measurements by acoustic Doppler velocimeters are presented for the distribution characteristics of rip currents on barred beaches with rip channel. The location and width of rip currents are controlled by rip channel and wave nodes, and the length of the rip currents depends on the wave height and coastal slope. The driving force of rip currents without rip channel is primarily determined by the alongshore pressure gradient of the wave setup caused by intersecting waves. By contrast, the driving force of rip currents with rip channel is determined by both the alongshore pressure gradient of the wave set-up and the radial stress gradient, and the relative magnitude of the two values depends on the wave period.

8th International Conference on the Application of Physical Modelling in Coastal and Port Engineering and Science
Zhoushan, China - Dec. 9th - 12th, 2020

A MULTI-PHASE SPH MODEL WITH THE APPLICATION ON SUBMARINE LANDSLIDES

Can Huang [1,2,3], Ting Long [1,2,3] and Moubin Liu[1,2,3*]

1 BIC-ESAT, College of Engineering, Peking University, Beijing 100871, China.

2 Institute of Ocean Research, Peking University, Beijing 100871, China.

3 State Key Laboratory for Turbulence and Complex systems, Peking University, Beijing 100871, China.

**Corresponding author: mbliu@pku.edu.cn*

In the oil and gas industry, the focus on onshore production has shifted to offshore production during the last 20 years, as the onshore and nearshore oil and gas production cannot meet the demand. In order to access the oil reserves in the sea, pipelines must travel through extreme terrains which are sometimes associated with various geohazards such as submarine landslides caused by hydrates dissociation.

Submarine landslides have gained tremendous attention. The initiation of submarine landslide is caused by the instability of seafloor slope, which is a consequence of a reduction in the resisting forces or an increase in driving forces. When the resistance is insufficient to balance the driving forces, slope failure occurs and leads to the flow of the debris materials. Submarine landslides pose not only a direct threat to offshore infrastructure but also an indirect threat to coastal communities through the generation of tsunamis. Therefore, a deep understanding of submarine landslide is a good way to mitigating the impact on offshore pipelines and offshore structures.

The simulation of submarine landslides has been a long-standing challenge majorly due to the strong coupling among sliding sediments, seawater and infrastructure. In order to understand the fundamental mechanism of submarine landslide movement, it is urgent to develop a good numerical model. SPH (smoothed particle hydrodynamics) method is a meshless Lagrangian particle method[1]. It has special advantages in simulating multi-phase flow and fluid-solid coupling problems, and has been widely used in the field of marine engineering fluid dynamics[2]. The objective of this thesis is to develop a multi-phase SPH to simulate the soil and water behavior in the process of the submarine landslides and predict the run-out distance and the final profile of submarine landslides.

Keywords: Smoothed particle hydrodynamics; Multi-phase flow; Fluid-solid coupling; Submarine landslides

References

[1] Ye, T., Pan, D. Y., Huang, C. and Liu, M. B. (2019) Smoothed particle hydrodynamics (SPH) for complex fluid flows: Recent developments in methodology and applications, *Physics of Fluids* **31**, 011301.

[2] Liu, M.B. and Zhang, Z.L. (2019) Smoothed particle hydrodynamics (SPH) for modeling fluid-structure interactions, *SCIENCE CHINA Physics, Mechanics & Astronomy* **62**:984701.

8th International Conference on the Application of Physical Modelling in Coastal and Port Engineering and Science
Zhoushan, China - Dec. 9th - 12th, 2020

PHYSICAL STUDY ON WAVE OVERTOPPING-INDUCED SAND DIKE BREACHING

YANQIAO WANG[1], DA XU[1], ZHIGUO HE[1], WEIMING WU[2]

1 Ocean College, Zhejiang University, Zhejiang Province, 316021, China, hezhiguo@zju.edu.cn

2 Department of Civil and Environmental Engineering, Clarkson University, NY 13699, USA, wwu@clarkson.edu

A physical study on dike breaching due to wave overtopping is carried out. The dike is constructed with noncohesive sand and has a clay layer covered on its upstream slope to prevent seepage. The breaching process is recorded using a 3D laser scanner. The effects of wave height, wave period and dike slopes are investigated. Results indicate the breach development to grow with wave height, wave period and dike slopes. Breach flow is approximated using the reservoir water balance equation and is found to increase at an accelerated rate until a peak breach flow is reached. The measured data enable prediction of breach development due to wave overtopping and add to the overall knowledge of the dike breaching process.

Key Words: dike; sand; breaching; wave overtopping; erosion

8th International Conference on the Application of Physical Modelling in Coastal and Port Engineering and Science
Zhoushan, China - Dec. 9th - 12th, 2020

FIELD OBSERVATION ON SEASONAL VARIATION OF THE FRESHWATER TRANSPORT AT YANGTZE RIVER PLUME REGION

HAOCHEN SONG[1], YEPING YUAN[2]

1 Ocean College, Zhejiang University, China,
21834018@zju.edu.cn
2 Ocean College, Zhejiang University, China, yyping@zju.edu.cn

Field observations in coastal and estuarine regions are important for studying physical and biological features. Measuring the transport of the Yangtze River plume is of great importance for understanding the fate of terrestrial materials from this large river into the open ocean. Even though several studies have been done to reveal the phenomenon and mechanism of Yangtze River plume, the seasonal variation of the freshwater transport at Yangtze River plume region still remain vacant.

In order to solve this issue, cruise surveys have been made to investigate seasonal variation mechanisms of Yangtze River plume in March(winter), July(summer) and October(fall) of 2019. During the field observations, several instruments were used to collect physical units. Temperature, salinity, dissolved oxygen and chlorophyll a were obtained by conductivity, temperature and depth (CTD). The magnitude and direction of the velocity were obtained by acoustic doppler current profiler (ADCP). Turbidity was obtained by optical backscatter (OBS). The rate of turbulent kinetic energy dissipation was obtained by vertical microstructure profiler (VMP). The VMP developed a statistical technique to estimate the rate of turbulent kinetic energy dissipation, ε, from the variance of du/dz data. Using this technique, we were able to estimate the turbulent kinetic energy dissipation rate associated with river outflow in the Yangtze River plume region. The results of the observations showed strong alongshore current driven by Yangtze River Diluted Water existed in the plume region accompanied with obvious thermohaline and halocline nearby. Besides, high ε values were also detected on the outside of the Yangtze River estuary which means strong turbulent mixing, generated by shear instability, occurs near Yangtze River plume region. The most obvious phenomenon appears in summer with strongest current and highest ε value which is consistent with recent numerical model studies.

Key Words: river plume; field observations; turbulent mixing

8th International Conference on the Application of Physical Modelling in Coastal and Port Engineering and Science
Zhoushan, China - Dec. 9th - 12th, 2020

RHEOLOGY AND ITS MECHANISM OF CLAYSEDIMENT

YUAN LIN[1], HAI ZHU[1], HUAITAO QIN[1]

1 Institute of Ocean Engineering and Technology, Ocean College, Zhejiang University, Zhoushan 316021, China, samylin@zju.edu.cn

Clay sediments are the main component of the seabed sediment. The interactions between the nano-sized, disk-shaped and charged clay particles are complicated, which controls the flowing and the transportation criteria of the sediment. The rheological behavior of the clay sediment modeled by the bentonite-water (BW) mixtures is studied experimentally by the rotational rheometer. The yield stress of the BW system decreases with increasing water content, as well as with decreasing temperature. It is considered that the face-face repulsive electrostatic interaction between the clay platelets dominates the yield behavior. A yield stress model is developed to describe the change of the yield stress with the water content. When the BW system starts to flow, the viscosity decreases with increasing shear. A master curve of viscosity is composed from the viscosity-stress curves at different water contents if the applied shear stress is normalized by the yield stress, which shows that the same mechanism controlling the yield behavior (at the static state) also controls the behavior of the system at the flowing state. A constitutive model is developed to predict the viscosity as a function of the normalized shear stress. This study is to provide the basal understanding of the clay particle interaction for the subsequent investigation on the transportation of the sediment systems with strong interparticle interaction.

Key Words: clay sediment, rheology, particle interaction

8th International Conference on the Application of Physical Modelling in Coastal and Port Engineering and Science
Zhoushan, China - Dec. 9th - 12th, 2020

EXPERIMENTAL AND NUMERICAL STUDY ON A NOVEL DOUBLE-CYLIDER DOUBLE-PLATE BREAKWATER

XIAOYUN CHEN[1], DANJUAN FU[2], BIJIN LIU[3], ZHENWEI ZHANG[4] HEPING YUAN[5]

1 Xiamen University of Technology, Xiamen, China, xychen_xmut@163.com 2 Xiamen University of Technology, Xiamen, China, fudanjaun@xmut.edu.cn 3 Xiamen University of Technology, Xiamen, China, 94709585@qq.com

4 Xiamen University of Technology, Xiamen, China, zwzhang@live.cn

5 Xiamen University of Technology, Xiamen, China, yuanhp@xmut.edu.cn

Experimental and numerical investigations of regular waves interacting with a double-cylinder double-plate breakwater are presented in this paper. The physical model test is carried out in a 35m long, 0.7m wide and 0.8m deep wave flume in the laboratory of Port and Coastal Engineering, Xiamen University of Technology. Based on the Navier-Stokes equations for viscous, incompressible fluid and Volume of Fluid (VOF) method, a numerical wave tank is established. The wave is generated on the basis of boundary values and absorbed by employing a wave-damping function. Both the experimental and numerical results show outstanding wave attenuation performance of the proposed breakwater, where the transmission coefficient could be lower than 0.4 under short waves. Furthermore, the influences of wave height, wave period, submerged depth and cylinder diameter on the wave forces are discussed in detail. The results have demonstrated the wave elimination ability and stability of double-cylinder double-plate breakwater, which ensures its application in ocean engineering.

Key Words: double-cylinder double-plate breakwater, experimental test, numerical wave tank, wave attenuation performance, wave force

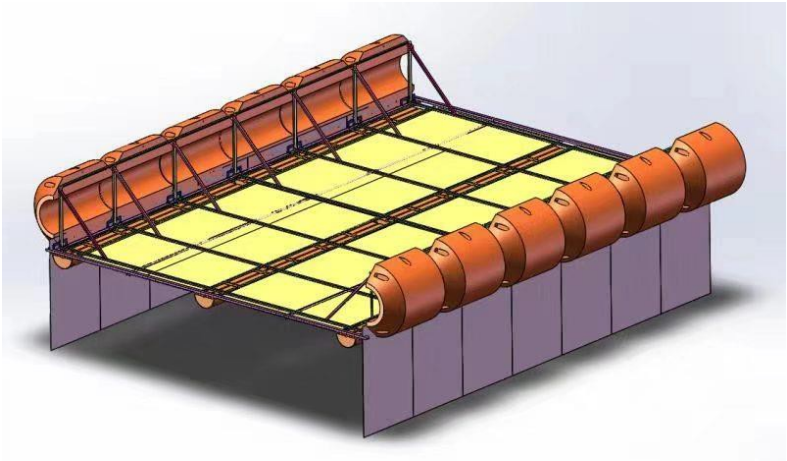

Fig. Model of a double-cylinder double-plate breakwater

8th International Conference on the Application of Physical Modelling in Coastal and Port Engineering and Science
Zhoushan, China - Dec. 9th - 12th, 2020

INTERACTIONS AND ALIGNMENTS OF TWO RIVER PLUMES

JUANJUAN DAI[1], HAOCHEN SONG[2],* YEPING YUAN

1 Ocean College, Zhejiang University, China, dai_jjuan@163.com
2 Ocean College, Zhejiang University, China, 21834018@zju.edu.cn
**Correspondence: Ocean College, Zhejiang University, China, yyping@zju.edu.cn*

River plumes are generated by the flow of buoyant river water into the coastal ocean where they have strong impacts on the coastal dynamics and ecosystems. We have had a general understanding of single plume's mixing and transport, but it's still unclear about how the two plumes interact exactly and their alignment situations. Interaction between two adjacent rivers (for example, Douro and Minho River system on the northwestern coast of the Iberian Peninsula or Ob and Yenisei River system in the Kara Sea), as well as their interaction with ambient sea water is a key issue in order to better understand the coastal circulation, the transport of pollutants and the fate of terrestrial materials. We propose a novel technique to simulate and measured the three-dimensional structure of the two-plume system on a rotating table. We then analyze how the upstream river discharge affects the evolution of each individual plume under the plume-to-plume interaction scenario by calculating the bulge center and the area of the downstream bulge. Previous study showed the ratio of the baroclinic Rossby radius of deformation (τ_1/ τ_2) and the Burger numbers (B_1/B_2) of the two buoyant fluids could determine the relative vertical and horizontal alignments of two buoyant fluids. In the present study, we used a simple analytical model and rotating table experiments to test this hypothesis in the two-plume coastal current system under geostrophic condition. We changed the value of B_2 to observe the position of the external front. We observed the situation of plumes collision and their freshwater downstream transport after reaching the geostrophic balance. This study will help us further study how the two plumes interact and their alignment situations in the complex coastal ocean, especially where there are multiple buoyant water outlets. The plume-to-plume interaction is of great significance to the study of social and ecological problems such as the fate of pollutant, the survival of harmful algal blooms, the dispersion of larvae and the connectivity of population.

Keywords: River Plumes, Rotating Table; Layered-PIV Method; Plume Interaction

8th International Conference on the Application of Physical Modelling in Coastal and Port Engineering and Science
Zhoushan, China - Dec. 9th - 12th, 2020

DISCUSSION OF INSTABILITY ANALYSIS FOR TRIAD RESONANCE AMONG FREE SURFACE WAVES,AMBIENT CURRENTS AND RIPPLED BOTTOMS

JUN FAN[1], AIFENG TAO[2], JINHAI ZHENG[3]

1 Hohai Univerisity, Nanjing P.R.China,
fanjun@hhu.edu.cn
2 Hohai Univerisity, Nanjing P.R.China,
aftao@hhu.edu.cn
3 Hohai Univerisity, Nanjing P.R.China, jhzheng@hhu.edu.cn

Continuous submarine sandbars were widely measured in many estuaries and coastal regions, which could induce the intensive resonant interactions on free surface with the existence of ambient current in these areas. And the corresponding free-surface wave field will be affected if these intensive resonances are triggered.

Based on the previous experimental observation of upstream-advancing waves induced by flow over rippled bottoms, the theoretical study of the resonant interaction among free-surface waves, ambient currents and rippled bottoms is well established by multiple-scale expansion perturbation analysis in the perspective of triad resonance. The quantitative wave temporal evolution properties are identified for up to six triad resonant types. It reveals different temporal growth features compared with regular wave instability analysis.

In this study, the mechanism of instability properties for triad resonance above is investigated in depth. Based on multiple-scale perturbation expansion, the effects of free-surface and bottom nonlinear resonant forcing terms on waves' temporal evolution properties are derived and compared for all six triad resonant types. Among these resonant types, three of them are distinguished from the regular instability analysis results. Then the explicit characteristics of inhomogeneous forcing terms corresponding to the free-surface and bottom nonlinearity are discussed in detail respectively. And the source of unstable resonant modes is acquired. Besides, the numerical model established by high- order spectral method (HOS) is utilized to validate the theoretical derivations. With the advantage of Zakharov equation and mode-coupling, the amplitude temporal evolution processes of resonant waves are simulated and compared well with multiple-scale expansion solution. This theoretical and numerical investigation of the instability properties of resonant waves for triad resonance among free- surface waves, ambient currents and rippled bottoms will give new insights to the interaction process in estuarial and coastal hydrodynamics.

Key Words: Triad resonance, Instability, Free surface waves, Rippled bottoms, Ambient current

8th International Conference on the Application of Physical Modelling in Coastal and Port Engineering and Science
Zhoushan, China - Dec. 9th - 12th, 2020

CFD SIMULATION OF SCOUR AROUND A MONOPILE IN COASTAL AREA USING OPENFOAM

JINZHAO LI[1,2], DAVID R. FUHRMAN[2], YILIN YANG[3]

1 Shandong University of Science and Technology, College of Transportation, Qingdao 266590, China, kingle@bjtu.edu.cn

2 Technical University of Denmark, Department of Mechanical Engineering, Section of Fluid Mechanics, Coastal and Maritime Engineering, DK-2800 Kgs. Lyngby, Denmark, drf@mek.dtu.dk

3 Beijing Jiaotong University, School of Civil Engineering, Beijing 100044, China, yilinyang@bjtu.edu.cn

A fully-coupled (hydrodynamic and morphologic) numerical model based on the open-source computational fluid dynamics (CFD) package OpenFOAM is presented and utilized to simulate flow and scour around a monopile in coastal area. The hydrodynamic model is based on Reynolds-averaged Navier-Stokes (RANS) equations together with k-ω turbulence closure and volume of fluid (VOF) method for capturing the free surface. These are then coupled with both bed load and suspended load transport descriptions, which drive resultant morphology of the bed. The present numerical model is validated against a large-scale laboratory experiments involving interaction of breaking solitary waves with a monopile and induced flow and scour. The hydrodynamic characteristics and flow features around the pile are described in detail, as well as the scouring mechanism at different locations of the pile is thoroughly analyzed. The hydrodynamic validation indicates that the numerical results agree quite well with the experimental results in terms of water surface elevation and velocity around the pile, particularly considering the complexity in the physical process involved. The scour simulation indicates that the present numerical model can reasonably reproduce the scour morphology around the pile, especially for the prediction of the maximum scour depth and its position. The temporal variation of scour depth at the side of the pile is satisfactorily predicted while those at the offshore and onshore are under-predicted. This is due to the underestimation of the horseshoe vortex in front of the pile and not accounting for pore water pressures. The scour at the onshore location of the pile starts to increase rapidly at the end of wave drawdown. The temporal scour depth at the side of the pile shows a double-peaked feature mainly due to the separation flow inducing high bed shear stress.

Key Words: CFD simulation; solitary wave; scour; monopile; sloping beach

8th International Conference on the Application of Physical Modelling in Coastal and Port Engineering and Science
Zhoushan, China - Dec. 9th - 12th, 2020

EXPERIMENTAL STUDY ON HORSESHOE VORTEX CHARACTERISTICS AROUND PILE GROUPS USING PIV

YILIN YANG[1], JINZHAO LI[2]

1 School of Civil Engineering, Beijing Jiaotong University, Beijing, 100044, China, yilinyang@bjtu.edu.cn

2 College of Transportation, Shandong University of Science and Technology, Qingdao, 266590, China, kingle@bjtu.edu.cn

Pile-group foundations are widely used in coastal and ocean engineering to support structures (e.g. bridge, oil platform and offshore wind farm), and the associated scour issue has received much attention because it may reduce the stability of these structures. The dynamic factors of local scouring around piles includes: (i) the horseshoe vortex (HV) system in front of the pile, (ii) the accelerated flow at the sides of pile, and (iii) the wake vortex shedding behind the pile. In particular, the HV is considered as the main factor causing local scour in front of the pile. In this study, the flow fields around pile groups mounted on a flatbed were measured by Particle Image Velocimetry (PIV) with the aim of identifying the mechanism responsible for scour initiating. The time-averaged characteristics of the HV were obtained, including the location, strength and scale. Furthermore, the influences of pile Reynolds number (Re_D), pile spacing (G/D) and pile arrangement on the HV characteristics were thoroughly discussed. The instantaneous evolution and periodic characteristics of the HV were described in detail. Additionally, the bed shear stress induced by HV was analyzed. It shows that the horizontal distance between the time-averaged HV and the pile decreases with Re_D in the range of $Re_D < 10^4$. The variation of the time-averaged HV position with G/D is not monotonically increasing or decreasing. The bed shear stress in front of the pile for the case of $G/D = 1.5$ is relatively larger compared with the cases of $G/D = 1$ and 2. The process of the transient evolution of the main horseshoe vortex mainly includes merging the weak vortex, annexation of the strong vortex and breaking up due to dissipation and diffusion. The present experimental results provide not only new insight into the complex flow fields around pile groups but also valuable experimental data to validate numerical simulations.

Key Words: pile group; PIV; horseshoe vortex; turbulence; bed shear stress

8th International Conference on the Application of Physical Modelling in Coastal and Port Engineering and Science
Zhoushan, China - Dec. 9th - 12th, 2020

RESEARCH PROGRESS OF ANTIFOULING TECHNOLOGY OF NETTING IN CHINA'S AQUACULTURE FACILITIES

JIANGAO SHI[1], WENWEN YU[2]

1 East China Sea Fisheries Research Institute, Chinese Academy Fishery Sciences, China, E-mail: jiangaoshi666@163.com
2 East China Sea Fisheries Research Institute, Chinese Academy Fishery Sciences, China, E-mail: yuwenwen666@163.com

This paper mainly introduces the new netting materials and research background of the antifouling technology of the netting in the aquaculture facilities in China. The antifouling technologies such as manual cleaning, mechanical cleaning, biological antifouling, metal alloy netting antifouling, special UHMWPE monofilament netting antifouling, gaudiness netting antifouling and antifouling coating protection are described. The results show that the netting anti pollution has a long way to go. Conclusion it can provide reference for the development of aquaculture.

Key Words: Netting; antifouling technology; agriculture facilities; research progress

8th International Conference on the Application of Physical Modelling in Coastal and Port Engineering and Science
Zhoushan, China - Dec. 9th - 12th, 2020

A STUDY OF THE EFFECT OF RECYCLED MATERIAL ON THE DURABILITY OF OCEAN ENGINEERING CONCRETE IN A HOT-SPRING ENVIRONMENT

JUNG-NAN CHANG [1], YU-LING CHANG [2], HER-YUNG WANG [3], BING-YANG CHAING [4]

1 Department of Tourism and Recreation Management, Fooyin University, Kaohsiung City, 831, Taiwan, ROC, t0910715493@yahoo.com.tw

2 Graduate Institute of tourism management, National Kaohsiung University of hospitality and tourism, Kaohsiung City, 812, Taiwan, ROC, defeg1230@gmail.com

3Department of Civil Engineering, National Kaohsiung University of Science and Technology, Kaohsiung City, 807, Taiwan, ROC,wangho@nkust.edu.tw

4 Department of Civil Engineering, National Kaohsiung University of Science and Technology, Kaohsiung City, 807, Taiwan, ROC,F107141112@nkust.edu.tw

There are many natural hot springs in Taiwan, and hot springs have many benefits, but hot-spring geology can change drastically, significantly influencing the durability of structural concrete. This study examines the durability of concrete according to the sulfate ion and chloride ion contents and pH of hot-spring water. Recycled materials such as fly ash, slag and waste LCD glass are added to concrete for energy savings, it is used in maritime engineering. In coastal structures, the steel bars are easily corroded by the intrusion of marine salt,use of waste materials to save energy and reducecarbon reduction and enhancement of the durability of concrete, has become an important goal in the world,This study uses a water-binder ratio (W/B) of 0.5 and fly ash, slag and waste glass sand as replacements (0, 40, and 80%) via soaking in different environments (tap water and hot-spring water), and examines the fresh properties, hardened properties and durability of concrete in hot-spring environments.

The results show that the addition of glass sand can reduce costs, and the material properties are close to those of the control group. An excessive addition of slag and fly ash is likely to increase the viscosity, and an excessive addition of glass sand will result in excessive no absorptive surfaces. The unit weight of the fresh concrete control group is 2411 kg/m^3, and those of the 40% and 80% slag-fly ash-glass sand specimens are 2345 kg/m^3 and 2303 kg/m^3, respectively; the unit weight decreases as the addition level increases. The final setting times are 451 min, 443 min and 446 min, respectively. The three groups have similar compressive strengths. In terms of the sulfate resistance, after 5 cycles at 56 days, the control group has fissures resulting from expansion, and the 40 and 80% slag-fly ash-glass sand specimens have no expansion fissures. The findings show that slag-fly ash-glass sand in concrete in a hot-spring environment can enhance the concrete workability and durability.

Key Words: Recycled material; Hot-spring environment; Ocean engineering concrete; Durability; Sulfate resistant

8th International Conference on the Application of Physical Modelling in Coastal and Port Engineering and Science
Zhoushan, China - Dec. 9th - 12th, 2020

A STUDY ON THE APPLICATION OF WASTE GLASS SAND AND ALKALI-ACTIVATED SLAG MORTAR TO MARINE ENGINEERING STRUCTURAL MATERIALS.

CHUN-LING HO [1], KAI-LIN HSU [2], HER-YUNG WANG [3], YU-WEN CHEN[4]

1College of Civil Engineering, Huaqiao University, Intelligence and Automation in Construction Fujian ProvinceHigher-educational Engineering Research Centre,Xiamen,361021, China, holling0712@gmail.com

2 Department of Construction Engineering, National Kaohsiung University of Science and Technology, Kaohsiung City, 807, Taiwan, ROC, vichsu@nkust.edu.tw

3 Department of Civil Engineering, National Kaohsiung University of Science and Technology, Kaohsiung City, 807, Taiwan, ROC,wangho@nkust.edu.tw

4 Department of Civil Engineering, National Kaohsiung University of Science and Technology, Kaohsiung City, 807, Taiwan, ROC, F107141103@nkust.edu.tw

As the world advocates sustainable and cyclic development, recycling of industrial byproducts has been extensively adopted, such as slag powder and waste LCD glass sand. The disposal and recycling of waste can be solved, and the policy objective for the sustainable development of resources can be implemented. Moreover, Taiwan is located in the subtropical zone and surrounded by the sea. Coastal structures are prone to corrosion due to the intrusion of marine salt. The development of marine engineering structure materials in Taiwan should be the direction of vigorous development. This study applies industrial by-products to marine engineering structures Exploration of materials. Waste LCD glass sand is combined with alkali-activated cementitious paste as the main material of mortar specimens, and different liquid-solid ratios (L/S=0.45, 0.50, and 0.60) are used. The base equivalent is fixed at 1%, and slag powder is replaced by glass sand (0, 20 and 40%). The fresh properties (slump, slump flow and setting time), hardened properties (compressive strength and ultrasonic pulse velocity) and durability (thermal conductivity and sulfate resistance) are determined after aging for 3, 7 and 28 days.

The results show that as the glass sand replacement level increases, the workability becomes better, the slump is increased by 11.6%~39.4%, the slump flow is increased by 19.5%~51.2%, the initial and final setting times are increased by 7.9~79.4% and 25.8~53.3%, respectively, the compressive strength is increased by 2.53%~180.73%, the ultrasonic pulse velocity is increased by 59.8%~101.2%, the thermal conductivity is 0.8769~1.1873 W/m*K and the sulfate resistance is good, thereby indicating that waste LCD glass sand has good engineering properties.

Key Words: waste LCD glass sand; alkali-activated cementitious paste; compressive strength; lightweight insulation brick; Marine engineering

8th International Conference on the Application of Physical Modelling in Coastal and Port Engineering and Science
Zhoushan, China - Dec. 9th - 12th, 2020

RESEARCH ON THE PROPERTIES AND MICROSTRUCTURE OF GREEN RECYCLED LIGHTWEIGHT AGGREGATE CONCRETE (GRLAC) IN MARINE ENGINEERING STRUCTURAL MATERIALS

CHANG-CHI HUNG[1],HONG-CHUNG CHEN[2],CHIEN-CHIH WANG[3],HER-YUNG WANG [4*]

1 School of Architecture and Civil Engineering, Huizhou University, Huizhou, Guangdong, 516007 P.R. China., A0266@hzu.edn.cn

2 Department of Naval Architecture and Ocean Engineering, National Kaohsiung University of Science and Technology, Kaohsiung City, 807, ROC, hcchen@nkust.edu.tw

3 Department of Civil Engineering and Geomatics, Cheng Shiu University , Kaohsiung City, 807, ROC, ccw@gcloud.csu.edu.tw

*4 * Department of Civil Engineering, National Kaohsiung University of Science and Technology, Kaohsiung City, 807, ROC, wangho@nkust.edu.tw*

Taiwan is located in the subtropics and is surrounded by the sea. Coastal structures are prone to corrosion due to the intrusion of marine salt. The development of marine engineering structural materials in Taiwan should be the direction of vigorous development. This study applies industrial by-products to marine engineering structural materials Inquiry.This study was based on green materials applied to lightweight concrete. Waste rubber particles from tires and waste LCD glass sand passed through a #30 sieve were used to replace part of the fine aggregate in amounts of 0%, 5% and 10% with W/B=0.4, after curing for 7, 28 and 56 days for compressive strength, ultrasonic pulse velocity and micro-interface analysis. The results showed that a lightweight concrete specimen with replacement amount of 5% waste LCD glass sand had high flowing ability and the higher compressive strength, which after 28 days, reached 46 MPa; the wave velocity of normal concrete is higher than that of GRLAC. The weight loss of GRLAC is greater than that of normal concrete, Loss on Ignition display 28 days curing period of weight loss the greatest change, because more complete hydration, hydration products inside and gel more. X-ray powder diffraction analysis (XRD) at about 15 °~ 20 ° between can be found in Ca (OH)2 wave front, the reaction of pozzolanic may be displayed by content degree. Scanning electron microscope (SEM) observation that, microstructure observation of the green lightweight aggregate and mortar are dandified compared to normal concrete. A variety of green recycled lightweight aggregate concrete, can not only be used effectively in recycling of waste resources but can also be part of the sustainable cycle of development.

Key Words: rubber particles ; furnace slag ; engineering properties ; green recycled lightweight aggregate concrete (GRLAC); Marine engineering

8th International Conference on the Application of Physical Modelling in Coastal and Port Engineering and Science
Zhoushan, China - Dec. 9th - 12th, 2020

CHARACTERISTIC LENGTH SCALE FOR EVALUATING WAVE- INDUCED PIPELINE SCOUR

NIAN-SHENG CHENG[1], MAOXING WEI[2], PUER XU[3], RANRAN MAO[4]

1 Professor, Ocean College, Zhejiang University, Zhoushan City, Zhejiang Province, 316021, China. Email: nscheng@zju.edu.cn

2 Post-doc Fellow, Ocean College, Zhejiang University, Zhoushan City, Zhejiang Province, 316 021, China. Email: mxwei@zju.edu.cn

3 Research Student, Ocean College, Zhejiang University, Zhoushan City, Zhejiang Province, 316021, China. Email: pexu@zju.edu.cn

4 Research Student, Ocean College, Zhejiang University, Zhoushan City, Zhejiang Province, 316021, China. Email: 21934106@zju.edu.cn

Based on the size of the vortex street formed on the lee-side of a pipeline, a characteristic length scale is proposed for evaluating the scour depth below the pipeline for wave and wave-plus- current conditions. It takes into account both wave properties and pipeline diameter. By analyzing experimental data available in the literature, it is shown that the scour depth scales well with the proposed length scale, provided that the current effect is not dominant.

Key Words: Pipeline scour; Length scale; Wave

8th International Conference on the Application of Physical Modelling in Coastal and Port Engineering and Science
Zhoushan, China - Dec. 9th - 12th, 2020

FORMULA DEVELOPMENT OF HYBRID-BASED FOAMED MATERIAL FOR FLOATING MARINE STRUCTURE

KAI-LIN HSU [1], HER-YUNG WANG [2]

1 Department of Construction Engineering, National Kaohsiung University of Science and Technology, Kaohsiung City, 807, Taiwan, ROC, vichsu@nkust.edu.tw

2 Department of Civil Engineering, National Kaohsiung University of Science and Technology, Kaohsiung City, 807, Taiwan, ROC,wangho@nkust.edu.tw

Global warming has caused severe changes in extreme weather and the environment. In addition, repeated record typhoons or hurricanes have led to flooding. In the future, all coastal land areas may experience the crisis of long-term inundation by sea water. Therefore, there is potential need to develop floating material having low density and high strength characteristics for floating marine structures due to land area reduction.

The application of foamed material on floating marine structure may be offered as a feasible construction alternative for land loss due to severe weather disasters. The foamed floating material has a good nature itself; therefore, it can be used as a kind of multifunctional material in construction, such as heat and sound insulation material as well as lightweight materials. However, the strength of the material itself is not high, so the application range is limited. In this study, cement was used as a cementing material. Also, epoxy resin was used to partially replace cement. The foaming agent, foam stabilizer, and strength synergist as material factors were applied to test mix proportions of the materials in accordance with regression orthogonal table planning. And the compressive strength, density and porosity were measured. The results of this study proved that the foamed test group could have compressive strength of 24.0 Mpa, density of 1.43 g/cm^3 and its weight could be 0.6 times that of ordinary concrete. With the regression analysis, the strength was predicted to be as high as 25.6 Mpa and the density prediction was 0.92 g/cm^3. By the mix proportion design, the material could have both excellent strength and density. The cement-based foamed floating material developed by this study had low-density, high-strength, and pore- independent structural characteristics, which may be a kind of indispensable floating material in the future.

Key Words: foamed concrete; floating material; engineering properties; regression orthogonal array method

8th International Conference on the Application of Physical Modelling in Coastal and Port Engineering and Science
Zhoushan, China - Dec. 9th - 12th, 2020

BENDING STIFFNESS ANALYSIS OF MAIN BODY OF FRAMEWORK OF PLASTIC FISHING RAFT

WEI SHENGJUN[1]，ZHENG GUOFU[1]

1 Fisheries Research Institute of Fujian,China,641984380@qq.com

The traditional Wooden-Foam fishing raft has been unable to meet the needs after decades of development and application of aquaculture industry.The Plastic Fishing Raft is one of the good choice which can replace the Wooden-Foam fishing raft, because of the good performance on wind and wave resistance and environmental protection.Tubular Fishing Raft and Plate Fishing Raft are the two typical forms of Plastic Fishing Raft. But it is less accepted by fishermen in practical application, due to the unsafe production problems such as frame tilting, twisting and rolling-over of the main frame of Plastic Fishing Raft. Our analysis shows although the Section moment of inertia of the two typs Plastic Fishing Raft are basically equal to the Wooden-Foam fishing raft, the Elastic Modulus of HDPE is less than a tenth of wood. So, the bending stiffness of Tubular Fishing Raft and Plate Fishing Raft main body of framework is only 8.5% and 6.16% of Wooden-Foam fishing raft on X-axis, 13.59% and 7.95% on Y-axis. The study also shows that the bending stiffness of Tubular Fishing Raft is better than Plate Fishing Raft, it is also consistent with the performance in practical application.In summary one of the key problem to improve the function of Plastic Fishing Raft is to up-grade the bending stiffness of the framework.

Key Words: Plastic Fishing Raft,Tubular Fishing Raft, Plate Fishing Raft,bending stiffness

8th International Conference on the Application of Physical Modelling in Coastal and Port Engineering and Science
Zhoushan, China - Dec. 9th - 12th, 2020

RESEARCH ON THE DURABILITY OF SSLAC IN MARINE ENGINEERING STRUCTURAL MATERIALS

JACK HUANG[1], WEN-DUO YANG[2], HER-YUNG WANG [3]

[1] *President FSAB materials Science and Technology, Kaohsiung City, 807, ROC, color.jackhuang@gmail.com*

[2] *Department of Chemical and Materials Engineering, National Kaohsiung University of Science and Technology, Kaohsiung City, 807, ROC, ywd@nkust.edu.tw*

[3] *Department of Civil Engineering, National Kaohsiung University of Science and Technology, Kaohsiung City, 807, ROC, wangho@nkust.edu.tw*

Improving the durability of marine engineering structural materials and achieving circular economy of energy saving and carbon reduction and effective use of resource materials have been the goals of the world. Lightweight aggregates are characterized by a low thermal conductivity, seismic resistance and fire resistance. This study uses the sedimentary sludge lightweight aggregate material of Taiwan and uses a densified mixture design algorithm to examine the influence of the lightweight aggregate density (normal density and 800 and 1600 kg/m^3) on the concrete engineering properties under the effect of a high temperature. The mixing water content is fixed at 170 kg/m^3, the W/B ratios are 0.28, 0.32 and 0.40, and the admixtures are fly ash, slag and superplasticizer; the designed lightweight aggregate concrete can meet the requirements of a high workability, and the cement content and mixing water consumption are reduced to improve the economy and durability.

The heating rate of the high-temperature furnace is fixed at 4°C/min, and three temperatures (250, 500, and 750°C) and two delay times (1 h and 2 h) are used for the fire-damage tests. Compared with room temperature conditions (25°C), the changes in engineering properties are examined, and SEM testing is conducted to observe the microstructural changes under the effect of a high temperature.

The findings show that the densified mixture design algorithm can provide high-flow Sedimentary sludge lightweight aggregate concrete (SSLAC). Lightweight aggregate concrete under the effect of a high temperature still has a high compressive strength residual ratio (56~99%), resistivity residual ratio (40~93%) and ultrasonic pulse velocity residual ratio (45~86%). The crack width is 86~398 μm, but the sulfate resistance is poor; after the specimen is heated, the initial temperature is low, and the thermal insulating properties are good. Lightweight aggregate concrete still has good engineering properties under the effect of a high temperature and is suitable for fire-resistant buildings, but the durability problem resulting from micro cracks requires further study. The research results can be used to solve a large number of industrial by-products, to achieve the circular economy of energy conservation and carbon reduction and environmental sustainability goals.

Key Words: marine engineering; durability; Sedimentary sludge lightweight aggregate concrete (SSLAC); carbon reduction.

8th International Conference on the Application of Physical Modelling in Coastal and Port Engineering and Science
Zhoushan, China - Dec. 9th - 12th, 2020

EVALUATION OF THE ULTRASONIC PULSE VELOCITY OF ALKALI-ACTIVATED SLAG PASTES

Chien-Chih Wang (1), Her-Yung Wang (2), Chang-Chi Hung (3) *

1 Department of Civil Engineering and Geomatics, Cheng Shiu University, Kaohsiung City, 83347, Taiwan; ccw@gcloud.csu.edu.tw

2 Department of Civil Engineering, National Kaohsiung University of Sciences and Technology, Kaohsiung City, 80778, Taiwan; wangho@nkust.edu.tw

3 School of Architecture and Civil Engineering, Huizhou University, Huizhou, Guangdong, 516007, P.R. China; a0266@hzu.edu.cn*

** Correspondence: a0266@hzu.edu.cn; Tel.: +886-7-735-8800*

Coastal structures are prone to corrosion due to the intrusion of marine salt. Taiwan is located in the subtropics and is surrounded by the sea. For sustainable development, the development of environmentally friendly and economical material is worth encouraging. This study used different liquid-solid ratios and alkaline solutions as well as slag to produce pastes. Three liquid-solid ratios (L/S of 0.50, 0.55 and 0.60) and three alkali agent contents (N of 0.5%, 0.75% and 1.0%) are used in mixed proportions. The ultrasonic pulse velocity (UPV) are tested at the ages of 3, 7 and 28 days. The results show that the UPV increase with increasing alkali agent content and with age but decrease as the liquid-solid ratio increases. The UPVs for various alkali agent contents increase by 1.52-12.10 and 1.06-1.84 times, respectively, during aging from day 3 to day 28. Besides, the prediction models of the UPV of alkali-activated slag paste with alkali agent content are deduced in this study. According to the comparisons between the predicted values and the test results, the MAPE values of UPV are only 0.023-0.050%, respectively. Thus, the proposed analysis models achieve satisfactory forecasting accuracy for the UPV of alkali-activated slag pastes.

Keywords: paste; slag; alkali-activated; ultrasonic pulse velocity; prediction model

8th International Conference on the Application of Physical Modelling in Coastal and Port Engineering and Science
Zhoushan, China - Dec. 9th - 12th, 2020

EXPERIMENTAL STUDY ON SOLITARY WAVE ATTENUATION BY RIGID EMERGED VEGETATION IN CURRENTS

CHUYAN ZHAO [1], JUN TANG [2]

1 State Key Laboratory of Coastal and Offshore Engineering, Dalian University of Technology, Dalian 116024, China, zhaocy@mail.dlut.edu.cn

2 State Key Laboratory of Coastal and Offshore Engineering, Dalian University of Technology, Dalian 116024, China, jtang@dlut.edu.cn

An experimental study was conducted to investigate the effects of positive and oppositive currents on solitary wave attenuation by vegetation. The experimental results show that for solitary wave propagating through vegetation zone in positive currents, wave height and wave energy before vegetation zone and wave attenuation in vegetation zone would increase with increase of positive current velocity. For solitary wave propagating through vegetation area in oppositive currents, the wave height and wave energy before vegetation zone decreases with increase in the oppositive current velocity, and the wave attenuation in vegetation zone is also decreased compared to that in the absence of currents in general but it does not vary monotonously with increase in the oppositive current velocity. Overall, the effects of currents on wave dissipation due to vegetation depend on not only the current direction and velocity but also the length of vegetation area. For a preset wave height and water depth, there is a specific vegetation length, when vegetation length is shorter than it, a larger wave attenuation is found in oppositive currents, and when vegetation length is longer than it, a larger wave attenuation is obtained in positive currents. Moreover, positive currents also increase the attenuation of solitary velocity in vegetation up to 46% while oppositive currents decrease it up to 23% compared to it in the absence of currents in the experiments.

Key Words: solitary wave; current effect on wave; vegetation; experimental study

8th International Conference on the Application of Physical Modelling in Coastal and Port Engineering and Science
Zhoushan, China - Dec. 9th - 12th, 2020

EXPERIMENTAL STUDY ON SEABED-MONOPILE INTERACTIONS UNDER CYCLIC LATERAL LOADING EFFECTS

Xingyu Ding [1,2], Dawei Guan [1,2], Jialong Li [1,2], Jinghai Zheng [1,2]

1 Key Laboratory of Coastal Disaster and Defense (Hohai University), Ministry of Education, Nanjing 210024,China
2 College of Harbour, Coastal and Offshore Engineering, Hohai University, Nanjing 210024, China

Offshore windfarm monopile foundations are subjected to cyclic lateral loading from periodic wind, waves, currents or rotor motions in the marine environments. The cyclic lateral loading can induce monopile vibrations and further lead to convective motions of sediment particles and seabed deformations nearby. Some studies have found this phenomenon or explain its mechanism, but few focused on the relationship between these sediment motions and the dynamic behavior of the vibrating monopile.

This paper experimentally investigates the seabed-monopile interactions under cyclic lateral loading conditions by using PTV (Particle Tracking Velocimetry) and Real-time photogrammetry techniques. The experiments were designed in 2D conditions and an aluminum plate with a dimension of 0.04 m wide, 0.10 m long, and 0.70 m high was used as the monopile model to simplify the process of seabed-monopile interaction. For the convenience of observation, the experiments were conducted in a rectangular box (internal size: 0.55 m long, 0.04 m wide, and 0.40 m high), whose front wall was a tempered glass plate. An eccentric wheel was installed on the electrical machinery and was pined to the top of the plate to exert the cyclic lateral loading with harmonic sinusoidal trends. In this experiment, the vibrating amplitude on the top of the plate was 2.33 mm, and the vibrating frequency was 5 Hz. The sand of different colors with same median grain size (D_{50}=0.48 mm) was compacted every 2 cm and carefully levelled before the experiment. A high-speed camera was used to record the temporal development of seabed deformations and the vibrating amplitude of the monopile at the original seabed level. The data were collected as a function of time with a frame rate of 125 fps during 72 hours of cyclic lateral loading.

The observation shows that a subsidence crater and two expanding sediment convective cells present around the monopile because of monopile vibration effects. The seabed was compacted around the vibrating monopile. The results show that under a steady vibrating frequency and amplitude input on the top of the monopile, the vibrating amplitude of the monopile at the original seabed level experiences a gradual decrease over time, and the intensity of sediment motions (seabed deformations and sediment convective motions) keeps increasing with a decreasing rate(see Fig. 1).

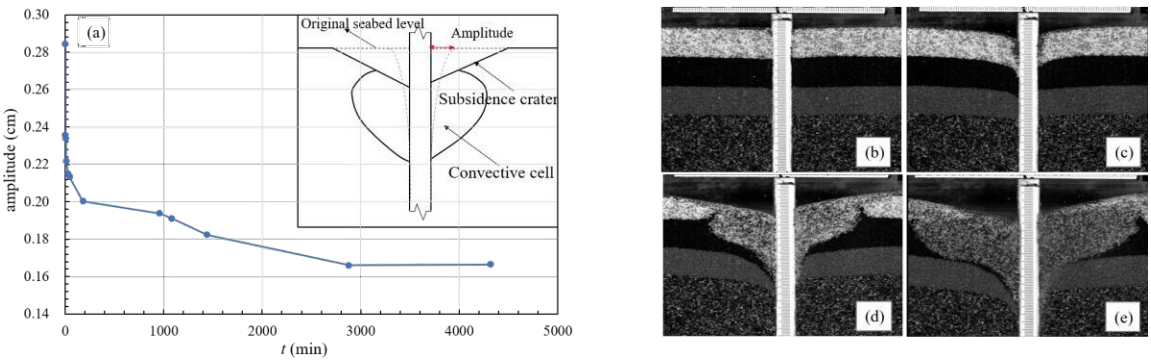

Fig. 1 The relationship between the sediment motions and the dynamic behavior of the vibrating monopile. (a) The vibrating amplitude of the monopile at the original seabed level; and the sand deformations for: (b) t = 0 min; (c) t = 1 min; (d) t = 960 min; (e) t = 4320 min

Keywords: amplitude; sediment motions; cyclic lateral loadings; monopile; PTV

8th International Conference on the Application of Physical Modelling in Coastal and Port Engineering and Science
Zhoushan, China - Dec. 9th - 12th, 2020

HOW PRECISE CAN WE CONDUCT THE LABORATORY EXPERIMENTS?

HAIJIANG LIU

College of Civil Engineering and Architecture, Zhejiang University, China, haijiangliu@zju.edu.cn

At present, laboratory experiment has become a key research approach in coastal engineering field. Nevertheless, precise experiment measurements are very much depended on the facilities, instruments, deployments, as well as personal experience. In this study, experiment measurements on several typical physical parameters in coastal engineering will be scrutinized with respect to their measurement accuracy to specify the question, how precise can we conduct the laboratory experiments? Attentions will be paid to the measurements of wave height, flow velocity, water pressure, sediment concentration, and groundwater pore pressure, respectively. Pros and cons in measuring these representative flow and sediment parameters will be discussed individually. Subsequently, some general problems in laboratory experiments will be raised, including the experiment repeatability, the instrument calibration, as well as the synchronization among various instruments. Upon which, personal understandings and suggestions will be summarized.

Key Words: Laboratory experiment; Accuracy; Repeatability; Calibration; Synchronization

8th International Conference on the Application of Physical Modelling in Coastal and Port Engineering and Science
Zhoushan, China - Dec. 9th - 12th, 2020

WAVE OVERTOPPING AT SEAWALLS WITH BULLNOSE

TANG XUAN THO(1), LE HAI TRUNG(2), DANG THI LINH(3), NGUYEN TRUONG DUY(4) & TRAN THANH TUNG(5)

(1,2,3,4,5)Thuyloi University trung.l.h@tlu.edu.vn

For years, seawalls have protected an increasing number of towns and tourism areas stretching along the coast of Viet Nam. During storm surges or even high tides, wave overtopping and splash-up would often threaten the safety of infrastructures, traffic and residents behind the seawalls. Therefore, the paper studies the wave-wall interactions using hydraulic small scale model tests. We conducted experiments on model seawalls with different faces and bullnoses. The obtained data shows that bullnoses help to considerably reduce wave overtopping discharge and splash run-up height. Furthermore, the magnitude of these decreasing effects is quantitatively estimated.

Keywords: bullnose, overtopping, seawall, splash up, wave flume.

8th International Conference on the Application of Physical Modelling in Coastal and Port Engineering and Science
Zhoushan, China - Dec. 9th - 12th, 2020

THE RESPONSE TO TYPHOON LIKEMAAND RESTORATION FOR THE BEACH OF CHUDAO ISLAND IN WEIHAI

LI-YANG WANG[1], ZAI-JIN YOU[1,2]

1 School of Civil Engineering, Ludong University, China, arguswangliyang@163.com
2 College of Transportation Engineering, Dalian Maritime University, China, b.you@dlmu.edu.cn

In order to explore the impact of the typhoon for the beach and the self-evolution process of the beach. In this paper, the field observation results and sediment sampling data are used to analyze the beach profile erosion and sediment changes before and after the landing of "likema" within three months, to explore the response characteristics of the beach to "likema" and the recovery after typhoon. The results show that the double overlap of shore waves and storm surges caused the erosion of the entire beach in Chudao, because the study area is located on the right side of the typhoon path. And the erosion areas are mainly concentrated in the high tide zone. In order to relieve the energy brought by the big waves, the beach shifted towards a more dissipated state, The mean particle size of sediments was coarsened as a whole, and the sorting becomes worse. The scour area is especially obvious. Due to the difference of profile shape, the beach profile was eroded more and more violently from south to north, and the profile of N06-N10 on the north side changed from beach shoulder type to sand bar type. Within three months after the typhoon, the eroded beaches recovered quickly, showing a trend of silting up in the upper part and scouring in the lower part as a whole, and the beaches on the south side recovered slowly, which is the result of the combined effects of sand transport along transversal and longitudinal and human factors.

Key Words: Beach response; Typhoon; Coastal erode; Beach restoration; Beach profile

8th International Conference on the Application of Physical Modelling in Coastal and Port Engineering and Science
Zhoushan, China - Dec. 9th - 12th, 2020

THE INFLUENCES OF BEACH BERM HEIGHT ON THE BEACH RESPONSE TO STORMS

JUN ZHU[1], FENGYAN SHI[2], FENGCAI[1*], HONGSHUAI QI[1]

1 Third Institute of Oceanography, MNR, Xiamen 361005, China, junzhu@tio.org.cn
2 Center for Applied Coastal Research, University of Delaware, Newark, DE 19716, USA

The field observation at two neighboring beaches with different berm heights shows significant effects of berm heights on beach profile changes during a storm. A fully nonlinear Boussinesq wave model, FUNWAVE-TVD, is applied to simulating the storm-induced waves, sediment transport and morphological processes in the neighboring-beach domain to compare the effects of berm height on the beach erosion during the storm. Model validations are made against in situ morphological data. The model results reveal that, for the beach with a higher berm, the wave forcing, wave-induced undertow, as well as the breaking-enhanced suspended sediment concentration, make more offshore sediment transport and cause significant beach profile changes. A group of test cases with various wave conditions and berm heights are carried out to investigate the nonlinear relationship between beach erosion and relative beach berm height. A nondimensional parameter and an empirical function are proposed based on test results to predict the beach erosion during storms.

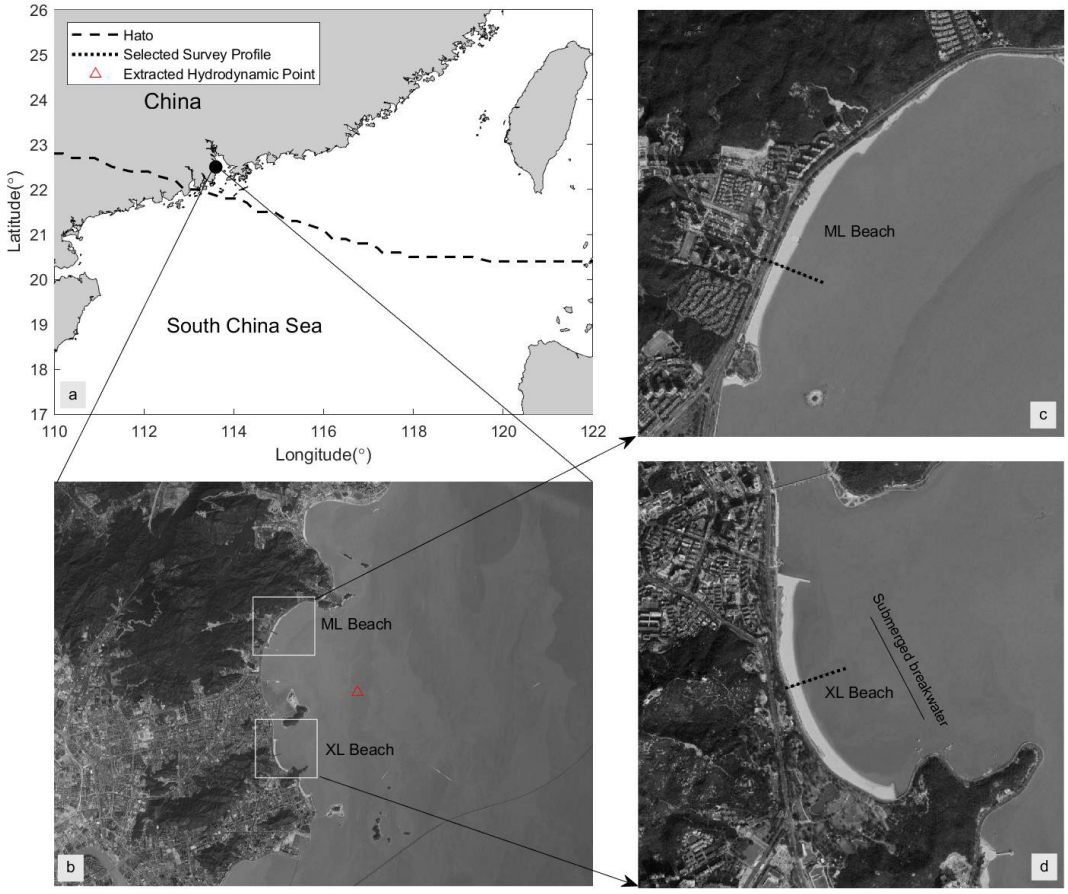

Key Words: FUNWAVE, berm height, undertow, beach erosion

8th International Conference on the Application of Physical Modelling in Coastal and Port Engineering and Science
Zhoushan, China - Dec. 9th - 12th, 2020

THE NUMERICAL SIMULATION OF WAVES AND ANALYSIS OF SHORELINE STABILITY IN HEADLAND-BAY

YI SUI[1], ZAIJIN YOU [1,2]

1 School of Civil Engineering,LuDong University, China, 1362391099@qq.com
2 School of Transportation Engineering, Dalian Maritime University, China, b.you@dlmu.edu.cn

The stability of headland-bay coast is an important research content of sandy coast, and the wave conditions are the most important factor affecting the stability of headland-bay coast. In practice, there is often a lack of powerful real wave measurement data for research. In this paper, the SW module in Mike21 is used to simulate the wave field in Jiahe Sea area of Yantai, so as to replace the real wave measurement data and study the stability of headland-bay coast. Delicate triangular mesh improved the spatial resolution of numerical calculation. The results of wave simulation are in good agreement with the measured data, and then more reliable wave conditions are obtained. The parabolic headland-bay coast shape model (MEPBAY) is adopt to analyze and predict the stability of flat shape. The results show that the simulated results of other positions are in good agreement with the actual shoreline except that the west shoreline is not balanced under the influence of artificial revetment, which indicates that the coastline of Jiahe Sea is basically in a stable state. If there is no extreme situation, the coastline of Jiahe Sea will not change greatly.

Key Words: Headland-bay Coast, Wave Simulation, The parabolic headland-bay coast shape model,Mepbay

8th International Conference on the Application of Physical Modelling in Coastal and Port Engineering and Science
Zhoushan, China - Dec. 9th - 12th, 2020

FULLY COUPLED ATMOSPHERE-HYDROLOGY SIMULATIONS FOR THE CHANGJIANG (YANGTZE) ESTUARY: SPATIOTEMPORAL EVALUATION OF FLOOD INUNDATION DURING A TROPICAL CYCLONE

ZHIYUAN WU[1,2], CHANGBO JIANG[1,2], JIE CHEN[1,2], BIN DENG[1,2], YUANNAN LONG[1,2], YIZHUANG LIU[1,2]

1 School of Hydraulic Engineering, Changsha University of Science & Technology, Changsha, 410114, China, zwu@csust.edu.cn

2 Key Laboratory of Dongting Lake Aquatic Eco-Environmental Control and Restoration of Hunan Province, Changsha 410114, China

The urban and rural area connecting to the Changjiang (Yangtze) Estuary is frequently flooded due to storm-induced coastal inundations. Establishing an advanced flood early-warning system requires a fully coupled atmosphere-hydrology-estuarine model capable of resolving the complex geometries of the Changjiang Delta. A fully coupled high-resolution atmospheric-hydrology-ocean model system is being developed under the framework of WRF-Hydro and FVCOM for the East China Sea coast. The WRF-Hydro is configured by two nested domains with horizontal resolutions of 9.0 and 3.0 km, respectively. FVCOM covers the coastal, estuarine and land area with a resolution up to ~50 m. As an initial pilot experiment, Typhoon Ampil (2018) is selected to test WRF-Hydro performance in the study area. This typhoon formed in the Western Pacific Ocean east of Luzon Island on 17 July 2018, landed in Chongming Island, Shanghai, on July 22 2018. The coastal inundation was caused by storm-induced heavy rainfall in the upper and middle regions of the Changjiang Delta Basin. Experiments were made for the two cases with coarse (~3 km) and fine (~50 m) bathymetric data. The preliminary results show that the model-predicted rainfall and streamflow significantly differ as the fine resolution bathymetry is used. The validation will be carried out through a direct comparison with precipitation measurement at local weather stations and streamflow at river monitoring sites in the Changjiang River.

Key Words: typhoon; storm-induced inundations; coupled atmosphere-hydrology modeling; the Changjiang Estuary; rainfall and streamflow

8th International Conference on the Application of Physical Modelling in Coastal and Port Engineering and Science
Zhoushan, China - Dec. 9th - 12th, 2020

A MODIFIED EXPRESSION OF BOTTOM FRICTION FACTOR BENEATH NONLINEAR NEARSHORE WAVES

MINGXIAO XIE[1], HUAQING ZHANG[1], CHI ZHANG[2]

1 National Engineering Laboratory for Port Hydraulic Construction Technology, Tianjin Research Institute for Water Transport Engineering, M.O.T., China, E-mail: crabsaver@163.com

2 State Key Laboratory of Hydrology-Water Resources and Hydraulic Engineering, Hohai University, China, E-mail: zhangchi@hhu.edu.cn

Bottom friction factor beneath waves (friction factor for brevity), which directly determines the bed shear stress, is particularly important in coastal research. Though a series of studies have been carried out in pre-existent studies, however, at present the expressions of which are still quite different in the literatures, without a unified form so far. The general recognized method for obtaining bottom friction factor is through constructing a relationship with maximum bottom shear stress and maximum free stream velocity. However, in most of practical engineering applications the value of maximum free stream velocity was usually calculated following linear wave theory, in which the wave nonlinearity was not thoroughly considered. Additionally, the limitation of experimental facilities also brought in uncertainties for investigating the boundary layer mechanism, in which the wave Reynolds number obtained in small wave flume tests were commonly restricted within 10^5, while the oscillatory tunnel experiments neglected the wave free surface and vertical velocity.

To better clarify the boundary layer process beneath real nonlinear waves, an experiment was designed and conducted in a super large wave flume. The experimental environment, essentially full- scale, was set to be equivalent to actual field condition in both water depth and wave parameters, and 24 cases including a wide range of wave nonlinearities were also considered in the experiment. The flow structure within the boundary layer were measured using a high-resolution acoustic Vectrino profiler. The effect of wave nonlinearity, as well as bed friction were discussed in depth. Results show that the the wave boundary layer thickness tends to be smaller compared with existing oscillatory tunnel experiments under similar flow intensities. Generally, the relationship between wave friction factor and relative roughness agrees with the traditional exponential law proposed in the literatures, however, the friction factor is proved to be larger because the thinner boundary layer induces a larger friction velocity. That means, the bed shear stress would be underestimated by pre- existent expressions in the literature derived from oscillatory tunnel experiments. Another fact is found that the value of friction factor would be several times larger if the free stream velocity is calculated using linear wave theory, which is questionable as the measured waves in the large wave flume were shown to be highly nonlinear. To compensate the nonlinear effect that significantly contributes to the maximum bed shear stress, a velocity asymmetry factor based on second order Stokes wave theory was introduced to modify the pre-existent expression of friction factor, which satisfactorily improves the prediction precision. This new expression has simple and explicit form that can be directly used in practical engineering applications, especially is advantageous for the nonlinear waves in the field.

Key Words: large wave flume; wave boundary layer; bottom friction; Stokes waves

8th International Conference on the Application of Physical Modelling in Coastal and Port Engineering and Science
Zhoushan, China - Dec. 9th - 12th, 2020

HUMAN-INDUCED IMPACTS ON FORMATION OF ESTUARINE TURBIDITY MAXIMA IN A MACRO-TIDAL ESTUARY

ZHIXIN CHENG[1], ISABEL JALON-ROJAS[3], XIAO HUA WANG[2]

1 College of Environmental Science and Engineering, Dalian Maritime Univeristy, Dalian, China.
2 School of Science, The University of New South Wales, Canberra, ACT, Australia.
3 UMR5805 EPOC, CNRS, OASU, University of Bordeaux, Pessac, France
Zhixin.Cheng@student.adfa.edu.au

During the past decades, extensive coastal areas have been reclaimed along the coastline of China, while the physical mechanisms of human pressures on estuarine-sedimentation are largely unknown. This study investigates the impacts of a land reclamation activity on the formation of estuarine turbidity maxima (ETM) in the Yalu River Estuary (YE), China. In order to explore physical drivers behind the change in ETM formation, 3-D hydro-sedimentary dynamics were simulated by Finite Volume Coastal Ocean Model (FVCOM) Then an improved Lagrangian particle-tracking model Sed-TrackMPD was developed for tracking the trajectories of resuspended sediment particles in coastal areas. Comparison between Sed-TrackMPD and field measurements agreed well, indicating this improved model is feasible and has wider applications. After the land reclamation, model results show that: (1) the degree of flood dominance decreased, and the tidal- choking effect was enhanced in the main branch. (2) The estuary became more well-mixed due to the stronger tidal current; (3) Suspended-sediment concentration (SSC), especially SSC in the bottom layer was increased. (4) The landward sediment flux caused by tidal pumping decreased significantly and the YE may turn into a sediment source instead of a sink if more land is reclaimed in the future. Furthermore, sediments in the main branch were likely from different sources before reclamation but became a homogenous mixture afterwards. This study qualitatively demonstrates the human-induced impacts on estuarine sedimentation using a multidisciplinary method.

Key Words: Yalu river estuary; Sediment transport; Particle tracking; Numerical simulation; Land reclamation

8th International Conference on the Application of Physical Modelling in Coastal and Port Engineering and Science
Zhoushan, China - Dec. 9th - 12th, 2020

REAL-TIME PHASE-RESOLVED OCEAN WAVE FORECAST WITH DATA ASSIMILATION

GUANGYAO WANG[1,2], JINFENG ZHANG[1], YULIN PAN[2]

STATE KEY LABORATORY OF HYDRAULIC ENGINEERING SIMULATION AND SAFETY, TIANJIN UNIVERSITY, CHINA

DEPARTMENT OF NAVAL ARCHITECTURE AND MARINE ENGINEERING, UNIVERSITY OF MICHIGAN, USA

The phase-resolved prediction of ocean waves is crucial for the safety of offshore operations. With the ocean surface obtained from radar measurements as the initial condition, nonlinear wave models such as the high-order spectral (HOS) method can be applied to predict the evolution of the ocean waves. However, due to the error in the initial condition (associated with the radar measurements and reconstruction algorithm) and the chaotic nature of the nonlinear wave equations, the prediction by HOS can deviate quickly from the true surface evolution. To address these issues, the capability to regularly incorporate measured data into the HOS simulation through data assimilation is desirable. In this work, we develop the data assimilation capability for nonlinear wave models, through the coupling of an ensemble Kalman filter (EnKF) with HOS. We also propose a strategy of modifying the Kalman gain to address the problem of the shrinking of the predictable zone. The validity of the developed scheme is benchmarked using both the synthetic data and radar measurements. We show that the EnKF-HOS coupled scheme achieves much higher accuracy in the long-term simulation of nonlinear waves compared to the HOS-only method.

Key Words: Ocean wave, data assimilation, ensemble Kalman filter, high-order spectral method

8th International Conference on the Application of Physical Modelling in Coastal and Port Engineering and Science
Zhoushan, China - Dec. 9th - 12th, 2020

LABORATORY INVESTIGATION OF BEACH PROFILE EVOLUTION UNDER SLOWLY VARYING STORM WAVES

Jun Wang[a], Zai-Jin You[b, c*], Bingchen Liang[a], Zhenlu Wang[a]

a Shandong Provincial Key Laboratory of Ocean Engineering, College of Engineering, Ocean University of China, Qingdao 266100, China
b Centre for Ports and Marine Safety, Dalian Maritime University, Dalian 116024, China
c School of Civil Engineering, University of Queensland, Brisbane, QLD 4072, Australia

Traditional experimental investigations are often undertaken by generating regular waves or random waves in wave flumes to simulate storm waves, but this approach generally fails to simulate field storm waves with slowly varying wave heights. Novel series of experiments are presented on sandy beaches to study the physical processes of sandy beach evolution under coastal storm conditions in a laboratory wave flume of 60m long, 3m wide and 1.5m high. Novel techniques were applied to simultaneously collect lab data on surface elevation and beach elevation profile. This lab experiment has the following new features that distinguish from traditional ones: 1) slowly varying wave height but constant wave period were generated by modifying wave maker piston stroke, to simulate storm waves over a period of storm event. To the authors' knowledge, this may be only the first lab experiment undertaken to enable us to simulate storm waves by using regular waves with slowly varying wave heights. 2) non-intrusive instrumentations, video cameras, were applied during the whole experiment to monitor the continuous beach profile evolution in a spatial resolution of 0.25cm and a temporal resolution of 0.1s, respectively. All data collected in this study are being analyzed. As continuous wave height change induces breaking point real-time change and further induce sediment transport direction vary before and after break point. Sediment moved onshore under initial smaller waves to make foreshore slope steeper, a sand bar was generated when storm waves were formed, and a certain portion of sediment also moved offshore during energetic wave conditions. Even the relationship between beach profile change or sediment flux and continue wave change is non-monotonic and nonlinear, breaker wave energy flux shows good promise in predicting beach mass change or storm erosion potential. Based on this study, it is found that initial slope and relative wave height have obvious influence on sediment transport direction and intensity.

8th International Conference on the Application of Physical Modelling in Coastal and Port Engineering and Science
Zhoushan, China - Dec. 9th - 12th, 2020

HIGH-SPEED SOFT ROBOTS ENABLED BY COMBUSTION FOR STRUCTURAL HEALTH MONITORING IN OCEAN ENGINEERING

HAIPENG WANG[1], YANG YANG[1], GUANZHENG LIN[1], XINGHONG YE[1], WENTAO LI[1], LUQIN HONG[1], ALI MATIN NAZAR[1], KING-JAMES I. EGBE[1], ZHIGUO HE[1,2], PENGCHENG JIAO[1,2]

1 Institute of Port, Coastal and Offshore Engineering, Ocean College, Zhejiang University, Zhoushan 316021, Zhejiang, China

2 Engineering Research Center of Oceanic Sensing Technology and Equipment, Zhejiang University, Ministry of Education, China

Email: pjiao@zju.edu.cn

Soft robots have recently been extensively studied for the applications in variety environments, accomplishing multifunctional tasks. Here, we develop a novel type of soft robots driven by mixed gas (i.e., oxygen and propane) combustion that occurring in chamber sealed by expandable silicon- rubber membranes. The reported soft robots are able to jump out of the water with a high-speed of~6 times body length per second on average and up to ~9 times body length per second at the most. Experiments are conducted to investigate the motion process of the soft robots under different driving conditions (i.e., gas ratio r, water depth D_W and gas amount A). Numerical simulations are carried out to compare with the experimental results and good agreements are obtained. Taking advantage of the high-speed movement through the multiphase environments, we envision the application of the soft robots for structural health monitoring (SHM) in ocean engineering by detecting the damages of underwater structures and wirelessly transmitting data when jumping out of water.

Key Words: Soft robots; High-speed; Combustion; Structural health monitoring

8th International Conference on the Application of Physical Modelling in Coastal and Port Engineering and Science
Zhoushan, China - Dec. 9th - 12th, 2020

WAVE OVERTOPPING MITIGATION BY A POROUS LAYER ON A ROCK SLOPE

GANCHENG ZHU[1], GUOYU WANG[2] HONGJIE WEN, WEIDONG CHEN, BING REN

1 State Key Laboratory of Coastal and Offshore Engineering, Dalian University of Technology, China, i191376645@mail.dlut.edu.cn

2 State Key Laboratory of Coastal and Offshore Engineering, Dalian University of Technology, China, wanggyu@dlut.edu.cn

This paper presents the experimental investigation of the wave overtopping mitigation by aporous layer. Due to more extreme storms and sea level rise, excessive wave overtopping may occur in the future. The porous layer of rock is considered as the possible measure to mitigate the wave overtopping. Model tests have been perforated in the nonlinear wave fume with the height of 2.5m in Dalian University of Technology. Two rubber mound structures of a slope of 1:3.0 with different porous layers were tested in the experiment. One porous layer is 0.14m thick with three layers of rock and the other one is 0.055cm thick with one layer of rock. Wave overtopping results of the two different porous layers were compared. It was found that the thicker porous layer has a positive effect on the mitigation of wave overtopping. The individual overtopping volume was found to be in accord with the Weibull distribution. The distributions of individual wave overtopping volume, overtopping thickness and overtopping flow velocity are analyzed.

Key Words: Wave overtopping, porous layer, Weibull distribution

8th International Conference on the Application of Physical Modelling in Coastal and Port Engineering and Science
Zhoushan, China - Dec. 9th - 12th, 2020

AN EXPERIMENTAL STUDY ON FLOW KINEMATIC CHARACTERISTICS OF DAM-BREAK FLOW

TING TAN[1], YUXIANG MA [2], GUOHAI DONG [2], XIAOZHOU MA [2]

1 Dalian University of Technology, State Key Laboratory of Coastal & Offshore Engineering , China, tanting@dlut.edu.cn

2 Dalian University of Technology, State Key Laboratory of Coastal & Offshore Engineering , China, yuxma@dlut.edu.cn

Experiments have been carried out to measure velocity fields of dam break flows over a horizontal dry bed and then impacting on a downstream vertical wall. Particle image velocimetry (PIV) techniques was used to quantify the flow kinematics before the impact process. Then impacting-induced aerated turbulent flows were measured by a modified particle image velocimetry technique. The turbulence intensity and vorticity were quantified through the ensemble average of 20 experiments. Furthermore, the experimental data of velocity fields, turbulence intensities and vorticities of overturning dam break aerated flows can be used to validate CFD models.

Key Words: dam break; particle image velocimetry; aerated flows

8th International Conference on the Application of Physical Modelling in Coastal and Port Engineering and Science
Zhoushan, China - Dec. 9th - 12th, 2020

SMARTPHONE-ENABLED STRUCTURAL HEALTH MONITORING USING MAGNETIC FIELD INTENSITY

ALI MATIN NAZAR[1], KING-JAMES I. EGBE[1], YANG YANG[1], HAIPENG WANG[1], PENGCHENG JIAO[1,2]

1 Institute of Port, Coastal and Offshore Engineering, Ocean College, Zhejiang University, Zhoushan 316021, Zhejiang, China,

2 Engineering Research Center of Oceanic Sensing Technology and Equipment, Zhejiang University, Ministry of Education, China

Email: pjiao@zju.edu.cn

In this study, smartphone is used for structural health monitoring (SHM) of coastal and offshore infrastructures using magnetic field intensity. Experimental and numerical studies are performed on the steel plates with one, two and three cracks with the length of 14 mm, 34 mm and 54 mm to evaluate the proposed method, and the magnetic field changes created by the magnets are observed. The numerical simulations are conducted and good agreements are obtained between the experimental and numerical results. The proposed smartphone-based SHM approach is considered as a cost-effective and user-friendly platform for damage detection of coastal and offshore infrastructures.

Keywords: Magnetic field intensity; Structural health monitoring; Smartphone; Coastal and offshore structures;

8th International Conference on the Application of Physical Modelling in Coastal and Port Engineering and Science
Zhoushan, China - Dec. 9th - 12th, 2020

ASYMMETRIC TIDAL DYNAMICS IN THE MARCO-TIDAL HANGZHOU BAY, CHINA

Li Li[1,2], Yihan Ren[1], Mingzhe Yang[3], Weibing Guan[2,1], Yuezhang Xia[1,2*]

1 Ocean College, Zhejiang University, Zhoushan 316021, China
2 State Key Laboratory of Satellite Ocean Environment Dynamics (Second Institute of Oceanography, MNR), Hangzhou, 310058, China
3 College of Civil Engineering and Architecture, Zhejiang University, Hangzhou 310058, China
Email: yzxia@zju.edu.cn

The asymmetric tidal currents and water fluxes in the marco-tidal Hangzhou Bay (HZB), China, was studied through a nested-grids three-dimensional numerical model. The model considered the tidal dynamics and sediment dynamics together through the two-way coupling of water density and suspended sediment concentration (SSC), as the bay was highly turbid. The model was fully calibrated using field data of tidal levels, currents. Anticlockwise residual currents and water fluxes occurs at both the surface and bottom in the bay. Residual currents and net water fluxes move towards the south bank at the bottom by lateral circulation generated by the combined effects of tides, morphology and the Coriolis force. Tides moves into the bay along the north bank and out of the bay along the south bank. The friction process and nonlinear advection dominate the water circulation in the bay, followed by the Coriolis force. Land reclamation increases the curvature and thus correlates positively to the southward circulations. The findings of this study are applicable to similar estuaries worldwide.

Key Words: sediment fluxes; tides; curvature; tidal flat; numerical modeling

8th International Conference on the Application of Physical Modelling in Coastal and Port Engineering and Science
Zhoushan, China - Dec. 9th - 12th, 2020

HYDROGEOLOGICAL CHARACTERIZATION OF COASTAL AQUIFERS AND BOREFIELD OPTIMIZATION

YE MA[1]

1 Centre for Ports and Maritime Safety, Dalian Maritime University, China, ye.mawater@outlook.com

Groundwater contained in coastal aquifers is a very important freshwater resource, which supplies freshwater to local township. The extraction of groundwater is managed by the pumping of borefield. Therefore, there is a need for efficient operation of the borefield to aid in reducing the potential risks of groundwater quality deterioration, such seawater intrusion and bore interference, and ensure long-term sustainable bore yields.

A hydrogeological conceptualisation of the site was developed and evaluated with the aim of providing an understanding of the aquifer and borefield operations which would inform the development of a borefield optimisation assessment for the site. Environmental factors such as climate, geology, potential contamination sources, groundwater quality and water levels were reviewed. All these factors were integrated to better understanding the hydrogeological conditions of the site including groundwater recharge, discharge, flow direction, water quality and aquifer characteristics. The primary groundwater aquifer is an unconsolidated sand, overlies bedrock. The sand deposits extent from ground surface to depths of approximately 10 to 50 metres with intercalated layers or lenses of medium to coarse sand. The coastal aquifer has high permeability and porosity and is recharged by rainfall infiltration. The sandy aquifers could support moderate to large-scale yields.

A borefield optimisation study has been conducted to further improve the understanding of the groundwater system at the coastal environment. Aquifer management and borefield optimisation would target solutions to reduce the potential need for replacement of production bores due to operational activities, limiting the need to large capital expenditure. Optimisation modelling was undertaken to assess borefield operations and operational costs, specially focused on bore submersible pumps for water supply, and the response of the local groundwater system to pumping. The groundwater table drawdown and interference between operating bores was then used to delineate bore capture zones and interaction with known sources of contamination within the vicinity of borefield. A numerical Modflow groundwater model was developed to assess the groundwater response to pumping with multi-objective optimization approach used to enable assessment of operational inputs, costs and aquifer response. This borefield optimization was suitable for assessing the aquifer responses to various pumping rate scenarios and how this response might influence groundwater migration pathways and groundwater quality. The borefield optimization provides information to assess the risks of a) bore interference and groundwater table response at various pumping rates; b) potential contamination of groundwater, and c) saline seawater intrusion.

Key Words: coastal sandy aquifer, borefield optimization, hydrogeological conceptualization

8th International Conference on the Application of Physical Modelling in Coastal and Port Engineering and Science
Zhoushan, China - Dec. 9th - 12th, 2020

MODELLING LONG-PERIOD WAVE IMPACTS ONTO SEASHORE AREAS INDUCED BY STORM SURGE BASED ON HYBRID NUMERICAL MODELS

MING XIAO[1], HANBIN GU[1], TINBIN XU[1]

1 School of Civil and Enviromental Engineering, Ningbo University, Ningbo, China E-mail: xiaoming@hotmail.com

A code solving the 2D shallow water equations by the smoothed particle hydrodynamics (SPH) scheme is used to simulate the severe storm surge caused by the typhoon No. 9711 -2013 in the town of Seaside, Oregon. Important theoretical and open boundary conditions have been implemented to handle a single long-period wave propagating up a piecewise linear slope of the city. The SPH scheme based shallow water equations compares well with free surface information recorded via resistance-type wave gauges and sonic wave gages in general. And the results show that the local flow can be drastically modified when the local flow regime is modified. By the assist of self-parameter adjustments based on comprehensively improved BP neural network to enhance the reliability, this 2D model can be used to help planning mitigation measures in a seashore area.

Key Words: Shallow water equations (SWEs); Storm surge; Improved BP neural network model

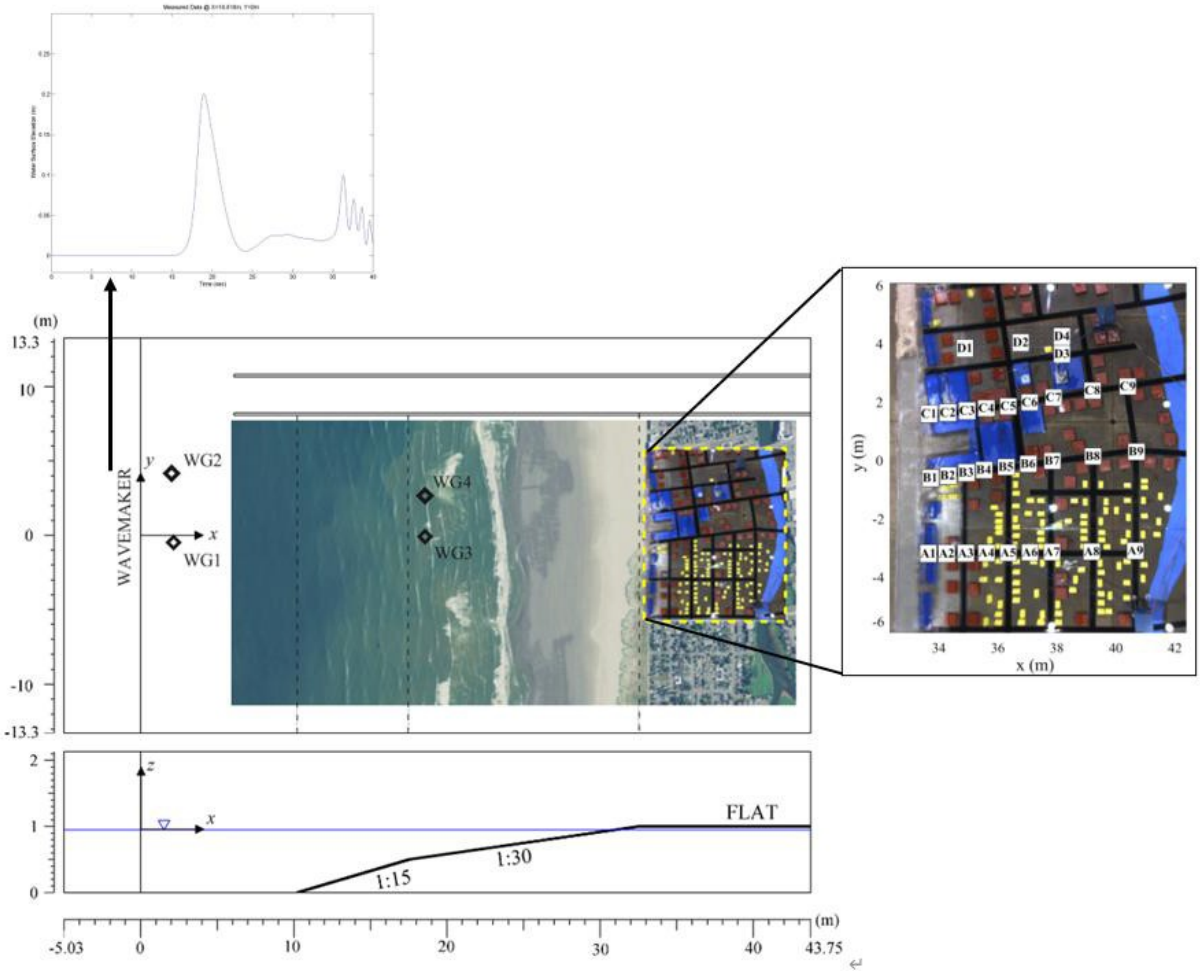

Figure 1. The location of USWG and ADV along the seashore city

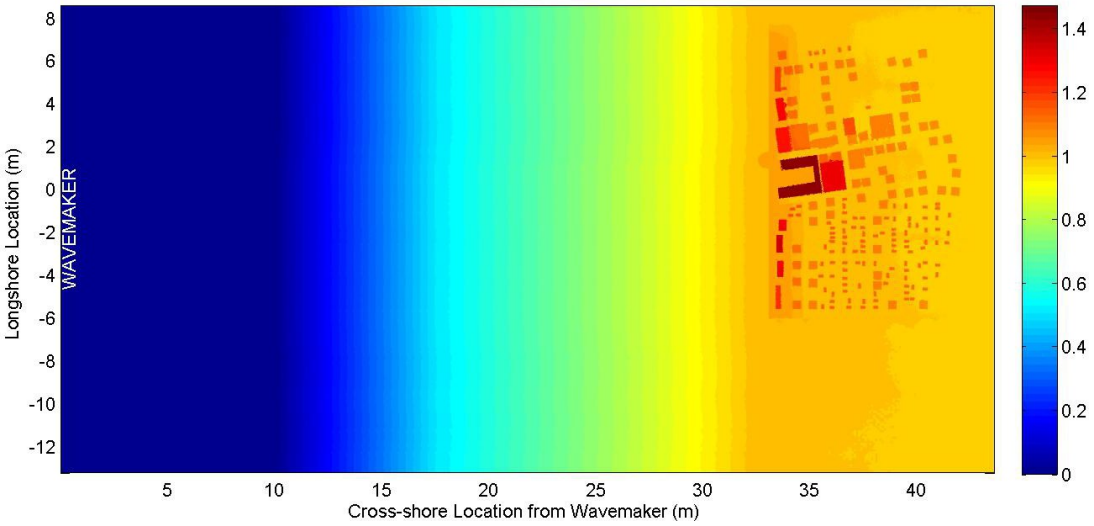

Figure 2. Water surface elevation

8th International Conference on the Application of Physical Modelling in Coastal and Port Engineering and Science
Zhoushan, China - Dec. 9th - 12th, 2020

A COMPUTATIONALLY EFFICIENT SUBGRID MODEL FOR COUPLED SURFACE AND GROUNDWATER FLOWS

YUJIE CHEN[1,2], FENGYAN SHI[2], BINGCHEN LIANG[1], JAMES T. KIRBY[2], GUOXIANG WU[1]

1 Ocean University of China, Qingdao, China,

2 University of Delaware, Delaware, U.S.

We present the development of a high-efficiency and high-resolution subgrid model for simulating surface water and groundwater interaction in coastal regions. The governing equations are derived from Saint-Venant equations, Richards equation and Darcy's law, and based on an assumption of the fully saturated subsurface flow and a phase-averaging method, in which two phase functions are defined respectively for the surface phase and subsurface phase at the subgrid level. Both the surface water and groundwater processes are modeled by solving the phase-averaged equations on a coarse grid, taking into account the subgrid effects. Model validation with laboratory data indicates that the subgrid model is capable of simulating flow processes within permeable structures.

The model was applied to simulate flooding and draining processes and the interaction of surface flows and groundwater flows in meso-tidal salt marshes on western coast of Delaware Bay, U.S., including the Brockonbridge Marsh and a part of the Bombay Hook Marsh. The model results indicate that the subgrid model can be used in a complex salt marsh system with numerous narrow channels, creeks and artificial ditches. On one hand, it is demonstrated the accuracy of subgrid model results is similar to that of the full model running directly on the high-resolution grid, but computational costs can be two orders of magnitude smaller than for the full grid model. On the other hand, compared to traditional surface flow model, the coupled surface and groundwater flow model is capable of providing more accurate results of hydrodynamic process on the marsh platform with many depressions. Tidal influence on the phreatic surface of the groundwater in the marsh system was discussed, as well as the impacts of interactions between surface and groundwater flows.

Key Words: Subgrid model, groundwater flow, surface water and groundwater interaction

8th International Conference on the Application of Physical Modelling in Coastal and Port Engineering and Science
Zhoushan, China - Dec. 9th - 12th, 2020

WAVE DISTRIBUTION CHARACTERISTICS OF HUASHAN LAKE

SHU YA XIE [1], AI FENG TAO [2]

1,2 Key Laboratory of Ministry of Education for Coastal Disaster and Protection , Hohai University, Nanjing, China

College of Harbour, Coastal and Offshore Engineering, Hohai University, Nanjing, China, Xieshuya@hhu.edu.cn; aftao@hhu.edu.cn

Huashan Lake is the core of Huashan Wetland, its wave characteristics have significant effects on construction of the lake ecosystem and the safety of cruise ships. In order to study the wave distribution characteristics of the lake area, the MIKE-21 Spectral Waves numerical models were established based on the design and extreme wind speed. At the same time, Putian formula method, SMB method and Wilson IV method were utilized to calculate wave elements. The simulation results were compared with the theoretical formula calculation results and verified in the absence of measured wave data in the Lake. Based on the verified and applicable numerical model, the wave distribution characteristics and changing laws of the lake area are analyzed. The results reveal that the mean wave period is between 1.01~1.62s.The significant wave heights under design wind speed and extreme wind speed are 0.19~0.35m and 0.36~0.79m respectively. The distribution of wave height shows the law of larger in the center of the lake and smaller in the near shore. The distribution of the wave height contour is basically consistent with the distribution trend of the depth contour, which can better reflect the process of waves propagating from the center of the lake to the shore. And the western part of the lake is the area with higher frequency of huge waves, followed by the eastern part of Huashan Mountain. There is a close relationship between waves and wind elements, and their size is related to water depth and wind fetch length. The wave characteristics of the lake provide a basis for the construction of water ecosystem and the design of ship berths.

Key Words: Huashan Lake; Numerical simulation; Theoretical formulas; Wave characteristics

8th International Conference on the Application of Physical Modelling in Coastal and Port Engineering and Science
Zhoushan, China - Dec. 9th - 12th, 2020

DEVELOPMENT OF COUPLING PROGRAM AND DYNAMIC RESPONSE OF ARTICULATED OFFSHORE WIND TURBINE

ZHANG PEI[1,2,3], TANG YOUGANG[1,2,3], YANG SHUGENG[1,2,3] & LI YAN[1,2,3]

1 State Key Laboratory of Hydraulic Engineering Simulation and Safety, Tianjin University, Tianjin, 300354
2 Tianjin Key Laboratory of Port and Ocean Engineering, Tianjin University, Tianjin,300354
3 School of Civil Engineering, Tianjin University, Tianjin, 300354

A new-type articulated offshore wind turbine (AOWT) is proposed for the water depth of 50 m, and an analytical model for the swing motion of AOWT was established. Through adopting the aerodynamic- hydrodynamic coupling analysis method and programing MATLAB code, the dynamic response of the structure under the action of different environmental loads such as wind, wave and flow was analyzed. Besides, the influence of the steady and turbulent wind models on the overall movement and load response of the structure was conducted. The results show that AOWT has great movement and load performance under the rated wind condition, the structure design meets the requirements of safe operation. Compared with the steady wind, the amplitude changes greatly under the action of the turbulent wind, but the mean value significantly decreases, and a large coupling resonance is induced in the low frequency range.

Keywords: Articulated Offshore wind turbine; Dynamic response; The time domain; Turbulent wind; Resonance

8th International Conference on the Application of Physical Modelling in Coastal and Port Engineering and Science
Zhoushan, China - Dec. 9th - 12th, 2020

WAVE ENERGY FOCUSING DUE TO THREE-DIMENSIONAL BRAGG RESONANCE WITH UNDULATING BOTTOM OF V-SHAPED LAYOUT

HAIMING ZHANG[1], AIFENG TAO[2], JUNWEI SU[2], JUN FAN[2], JUNHAO TU[2]

1 Key Laboratory of Ministry of Education for Coastal Disaster and Protection, Hohai University, Nanjing 210098, China3045192602@qq.com

2 College of Harbor, Coastal and Offshore Engineering, Hohai University, Nanjing 210098, China,aftao@hhu.edu.cn

Intensive wave reflection occurs when the incident waves and rippled bottoms satisfy the so-called Bragg resonance condition. At the same time, wave energy density will be enhanced at the incident side of rippled bottoms. This phenomenon could be utilized to improve the wave energy harvesting (e.g. by point absorbers) but still restricted to unidirectional 2D resonant scenarios. By taking the three-dimensional spatial-focusing effect into consideration, the wave energy will be spatially focused and concentrated to limited areas by Bragg resonance, which importantly relies on the optimization of spatial layout of rippled bottoms. In this paper, three-dimensional high-order spectral (HOS) method for wave-bottom interactions is applied to investigate the Bragg resonance processes induced by the spatial V-shaped rippled bottom layouts. And the wave characteristics on the focusing points for different V-shaped layout angles α are compared and analyzed. By optimizing the angle α of V-shaped layout, the wave energy focusing effects are improved. The results are specified as follows: i) When $145°<\alpha<180°$, the wave energy focusing effects are better and the wave amplitudes on the focusing points can reach more than 1.81 times of the initial incident waves; ii) When α=178.21°, the wave energy focusing area is approximately rectangular;iii) With the decrease of α from 178.21° to 162.24°, the reflected waves from both sides of V- shaped layouts gradually focus on the central axis, the wave energy focusing areas gradually present V-shaped distribution and extend to the side far away from V-shaped layout; iv) When α=162.24°, the wave energy focusing effect is the best and the maximum amplitude increases by 2.87 times of the initial incident wave amplitude.

Key Words: three-dimensional Bragg resonance; high-order spectral (HOS) method; bottom layout optimization; wave energy focusing

8th International Conference on the Application of Physical Modelling in Coastal and Port Engineering and Science
Zhoushan, China - Dec. 9th - 12th, 2020

FREAK WAVE IMPACT ON A FLOATING PLATFORM IN THE SMALL-AIR-GAP CONDITION

MIN LUO[1], XIN WANG[1], SAIYU YUAN[2], PENGZHI LIN[3]

1 Zienkiewicz Centre for Computational Engineering, College of Engineering, Swansea University, United Kingdom, min.luo@swansea.ac.uk, 1914744@swansea.ac.uk

2 State Key Laboratory of Hydrology-Water Resources and Hydraulic Engineering, Hohai University, China, yuansaiyu@hhu.edu.cn

3 State Key Laboratory of Hydraulics and Mountain River Engineering, Sichuan University, China, cvelinpz@126.com

Freak waves, also known as rogue or monster waves, are characterized by unusually large wave height and can appear suddenly in most of the places in the sea. The most spectacular sighting in recent years is the "New Year Wave", which hit Statoil's Draupner gas platform in the North Sea on New Year's Day of 1995 with a wave height of nearly 26 m. Freak waves can cause large slamming forces and massive overtopping, posing a great danger to the operational safety of marine structures like oil/gas platforms and ships. Such damaging effects are exacerbated by the global climate change and the accompanied more frequent occurrence of extreme ocean events. In this context, this study looks into the freak wave impact on a floating platform structure.

For offshore/deep-water platforms, the air gap is an important parameter in affecting the wave impact loads and overtopping. Some researchers studied the regular/irregular wave actions on fixed box-shape structures in different deck elevations. To name just one, the work in [1] found that the horizontal force increased with the decrease of the deck elevation from air to water, while the maximum vertical force occurred when the structure was positioned at the still water level. Recently, the freak wave impacts on a fixed box-shape structure have been investigated, focusing on the peak pressure/force [2] and the negative pressure (suction effect) [3]. Although significant findings have been made for fixed structures, researches on floating structures are still limited especially those related to freak waves. Another practical issue is that the floating platform may suffer from the operation weight beyond design. This combined with the water level run-up during an extreme wave event will lead to a lower air gap than the design. Special attention should be paid to this situation because a small air gap may result in more intensive wave loads, structural motions and overtopping.

Therefore, this study examines the freak wave impact on a floating platform in the small-air-gap condition, through carefully controlled wave flume experiments. The wave profiles during the wave impact process, the wave impact pressures on the vertical, bottom and top walls of the upper deck of the platform, the six-degree-of-freedom structural motions and the forces in the platform tethers will be measured simultaneously. The characteristics of these measurements including the overall trend and magnitude will be discussed and compared with those in normal air-gap conditions.

Key Words: freak wave; floating platform; air gap; wave impact; platform motion; tether force

References

[1] Park H, Tomiczek T, Cox DT, van de Lindt JW, Lomonaco P. Experimental modeling of horizontal and vertical wave forces on an elevated coastal structure. Coastal Engineering. 2017;128:58-74.

[2] Yan B, Luo M, Bai W. An experimental and numerical study of plunging wave impact on a box-shape structure. Marine Structures. 2019;66:272-87.

[3] Sun P-N, Luo M, Le Touzé D, Zhang AM. The suction effect during freak wave slamming on a fixed platform deck: Smoothed

8th International Conference on the Application of Physical Modelling in Coastal and Port Engineering and Science
Zhoushan, China - Dec. 9th - 12th, 2020

NUMERICAL SIMULATION OF AN OFFSHORE SINGLE-CHAMBER HEAVE-ONLY OSCILLATING WATER COLUMN DEVICE

PINJIE WANG[1], ZHENGZHI DENG[2]

1 Ocean College, Zhejiang University, Zhoushan, China, opinkwang@foxmail.com
2 Ocean College, Zhejiang University, Zhoushan, China, zzdeng@zju.edu.cn

For the sake of further accurate exploration of OWC structure, the hydrodynamic performance of an offshore single-chamber heave-only oscillating water column device is numerically simulated, with the open-source package OpenFOAM and its toolbox waves2Foam. The volume of fluid (VOF) method is employed to capture the free water surface. In the study, the spring force used to restrain heave motion of the structure and the geometric arrangement, that is, the chamber width and the rear wall draught, have been taken into full consideration to investigate the hydrodynamic performance of OWC device thoroughly.

The simulation results show that a proper stiffness coefficient of linear spring has a positive impact on the energy conversion performance. Besides, an excellent scheme of chamber width is obtained to reach high efficiency at as wide frequency domain as possible. What's more, according to the study, it is vital that a relatively deep draught of rear wall be selected, to get outstanding performance in full frequency domain.

Key Words: OpenFOAM, rigid-body dynamic, wave energy conversion, oscillating water column

8th International Conference on the Application of Physical Modelling in Coastal and Port Engineering and Science
Zhoushan, China - Dec. 9th - 12th, 2020

EFFECT OF SUBMERGED AND RIGID ARTIFICIAL VEGETATION DISTRIBUTIONS ON CURVED CHANNEL FLOW

YANG YU[1], LIN YING-TIEN[2]

1 Ocean College, Zhejiang University, China,
yangyu168@zju.edu.cn
2 Ocean College, Zhejiang University, China, kevinlin@zju.edu.cn

In natural river bend, the presence and distribution of submerged vegetation would change the flow hydrodynamics and subsequently affect the sediment transport and bathymetric changes. In this study, a 180° U-shaped curved open channel is used to simulate the natural river bend, and wood sticks are applied to simulate the submerged and rigid vegetation. The variations of longitudinal velocity distribution, turbulence kinetic energy (TKE), bend circulation and power spectral analysis are obtained using the measured data from the Acoustic Doppler Velocimeter (ADV). The results show that the longitudinal velocity is the largest at the top of vegetation. Different vegetation distribution and channel bend both strengthen the turbulence, especially around the top of vegetation. TKE is the largest below the top of vegetation and decays downward into the vegetation. There is also secondary flow within submerged vegetation, but the directions in vegetation area and non-vegetation area are opposite. Through power spectral analysis, vegetation and channel bends will increase the intensity of turbulence and small scale turbulence; the mixing among water bodies at the interface between vegetation and non-vegetation area (lateral and vertical direction) is stronger, also improving turbulence at the interface area.

Key Words: submerged and rigid vegetation; longitudinal velocity distribution; turbulence kinetic energy (TKE); bend circulation; power spectral analysis

8th International Conference on the Application of Physical Modelling in Coastal and Port Engineering and Science
Zhoushan, China - Dec. 9th - 12th, 2020

OBSERVATION OF WAVE OVERWASH ON AN ARTIFICIAL BEACH

ZHUBIN CAO[1], CHI ZHANG[1], SHANHANG CHI[1]

1 College of Harbour, Coastal and Offshore Engineering, Hohai University, Nanjing, China

Wave overwash is a discontinuous water flow overtopping the beach/berm crest. Investigation of this process is particularly important for the assessment of coastal hazards and flooding along the low-lying and densely populated coastal regions. Besides, overwash-driven onshore sediment transport is vital for the long-term stabilization of coastal landform. Although a large number of previous studies have been dedicated to the evaluation of wave-induced overwash processes along barrier islands, including the frequency, overwash flow dynamics, and the associated sediment transport processes, very few work have focused on the investigation of this process on an artificial beach. Beach nourishment indicates a large perturbation of the antecedent hydro-morphodynamic system of dynamic equilibrium. Wave overwash process occurring on a nourished beach, especially during the initial stage after construction, can lead to significant morphological change and thus affect the effectiveness of nourishment in terms of coastal resilience and recreational function.

In this study, we focus on wave overwash processes occurring on a newly artificial beach in Rizhao Coast, China. This nourishment project comprises 4.56×10^6 m^3 sand placement (median grain size of 0.3 ~0.8 mm), backed by a landward seawall, and laterally constrained by a northern breakwater and a southern breakwater. The artificial beach is characterized by a 1.8 km long shoreline, a ~100 m wide backshore with concave shape, and a ~150 m wide foreshore with an average slope of 1:10. The berm crest elevation is ~1.5 m high above the mean high water level. We established a video monitoring system consisting of four cameras to provide continuous imagery records. The high water level events, the overwash processes and the resulted beach morphology change, as well as the alongshore variability are quantified and analyzed, during both the storm and non-storm time periods. A medium-term total water level time series is constructed to evaluate the potential of overwash events, and to investigate the relative importance of various components of water level variability.

Key Words: Overwash; Beach nourishment; Video monitoring; Total Water Level

8th International Conference on the Application of Physical Modelling in Coastal and Port Engineering and Science
Zhoushan, China - Dec. 9th - 12th, 2020

SIMULATING THE MORPHOLOGICAL EVOLUTION OF DELTAIC LOBES IN THE YELLOW RIVER ESTUARY

LI WEI[1], ZHU LEHONG[2]

1 Institute of Port, Coastal, Offshore Engineering, Ocean College, Zhejiang University, China, lw05@zju.edu.cn
2 Institute of Port, Coastal, Offshore Engineering, Ocean College, Zhejiang University, China, 21934123@zju.edu.cn

The river delta grows with cyclic repeating of lobe development punctuated by channel avulsions. Like in the Yellow River delta, the combination of long-term north-south shifts and short-term evolution of river patterns associated with overladen sediments contribute to the delta progradation. Yet, the understanding of morphological processes and controlling factors in the lobe evolution remains immature. Herein, numerical experimental study has been conducted to unravel the short-term evolution of river patterns in a schematic Yellow River delta by a 2-D depth- averaged morphological model coupling the interactions between sediment-laden flow and river bed. Under constant discharge and sediment concentration, the typical process of wandering-merging-meandering patterns in nature can be reproduced by random disturbances on the initial topography. Moreover, a small bed slope and discharge favor the formation and long-lasting of the wandering pattern at the upstream, while a large bed slope and discharge may accelerate the merging and meandering processes. At the downstream, the flow routing may be facilitated by large tidal ranges. Besides, the increase of sediment concentration may change the channel evolution pattern from erosion dominance to the combination of channel erosion and levee lip sedimentation. The sediment transported to the river mouth helps the growth of subaqueous delta, but the extension of delta lobes on it needs a rather long time. It is also intriguing to mention that though the construction of artificial diverted trench may prompt the channel development in the early stage, it slows down the natural adaptation and thus requires longer time for morphological equilibrium.

Key Words: Morphological evolution; Yellow River Estuary; Delta lobes; Mathematical modelling

8th International Conference on the Application of Physical Modelling in Coastal and Port Engineering and Science
Zhoushan, China - Dec. 9th - 12th, 2020

EFFECT OF INCLINATION ANGLES ON THE LOCAL SCOUR AROUND A SUBMERGED CYLINDER

Shaohua Wang, Shiyu Yang, Zhiguo He, Li Li and Yuezhang Xia *

Ocean College, Zhejiang University, Zhoushan 316021, China;
**Correspondence: yzxia@zju.edu.cn*

In ocean engineering and coastal environmental studies, local scour around a submerged structure is a typical issue, which is affected by the inclination of the structure. To investigate the effect of inclination directions and angles on flow structure and the bed morphology, a three-dimensional numerical model of a submerged inclined cylinder was established. In this model, the hydrodynamics are solved from the RANS (Reynolds-averaged Navier–Stokes) equations closed with the RNG k-ε turbulence model, while the bed morphology evolution is captured by the sediment transport model. In the case of vertical-cylinder scour, the simulation results agree well with existing laboratory experiments. In the cases of inclined-cylinder scour, the results show that the inclination direction not only changes the intensity and the location of the downflow but also modulates the pattern of the horseshoe vortex in front of the cylinder, thus influencing the local scour depth and the morphology of the bed. Compared with the case of vertical cylinder, the scour around an upstream-inclined cylinder is deeper, mainly due to the enhancement of downflow in front of the cylinder. The scour around a downstream-inclined cylinder is shallower and broader due to the weakened downflow and accelerated incoming flow. The maximum scour depth decreases with the inclination angle in the downstream-inclination case. In the upstream-inclination case, the maximum scour depth does not vary monotonously with the inclination angle, which results from a competitive effect of the horseshoe vortex and downflow in the front of the cylinder.

Keywords: underwater structure; inclined cylinder; downflow; local scour; stability

8th International Conference on the Application of Physical Modelling in Coastal and Port Engineering and Science
Zhoushan, China - Dec. 9th - 12th, 2020

ENERGY PROPERTIES FOR HIGHER-ORDER STOKES WAVES OVER HORIZONTAL BOTTOM

XIANG GAO[1], XIAOZHOU MA[1], YUXIANG MA[1], GUOHAI DONG[1]
JUNLIANG GAO[2]

The State Key Laboratory of Coastal and Offshore Engineering, Dalian University of Technology, Dalian, 116024,China, maxzh@dlut.edu.cn

School of Naval Architecture and Ocean Engineering, Jiangsu University of Science and Technology, Zhenjiang, 212003, China

The energy in the surface water waves is a very important concept as the waves basically are a propagation of certain amount of mechanical energy by transferring between kinetic and potential energy. The wave energy is used extensively to index the strength of the waves, to calculate the radiation stress and to evaluate the wave field for exploiting wave power. The most common method for calculating the wave energy is based on the linear or the first-order Stokes wave theory, where the phase-averaged potential, kinetic and total energy of waves is a function of just the amplitude or the height of the waves and the kinetic energy is equal to the potential energy. Because of its simplicity, this method is used for nonlinear waves as well. However, there are few studies on the properties of nonlinear wave energy. In this paper, the phase-averaged energy properties, i.e., the potential, kinetic, total energy of very nonlinear waves in finite water depth and deep water over horizontal bottoms are studied. Using perturbation expansion method and Taylor expansion, the analytical expressions of the wave energy properties are derived based on the nonlinear Stokes wave theories such as the second-, third- and fifth-order Stokes wave theories， and the results are accurate to fourth order, sixth order and tenth order respectively. Compared with previous findings, the present fifth-order Stokes wave energy density is more consistent with the numerical integration result. The results show that, for the nonlinear wave, the phase-averaged energy is no longer a single-variable function of wave height and varies with the wave parameters such as wave height and wave number. Besides, the kinetic energy and potential energy are not equal, the kinetic energy is larger than potential energy. Comparison between the energy of Airy waves and that of nonlinear waves has shown that cautions should be taken to calculate the energy of waves of high nonlinearity.

Key Words: Energy, Nonlinear wave, Analytical solution.

8th International Conference on the Application of Physical Modelling in Coastal and Port Engineering and Science
Zhoushan, China - Dec. 9th - 12th, 2020

A PROBABILISTIC STORM SURGE PREDICTION SYSTEM BASED ON MULTI-SOURCE DATA FOR THE CHANGJIANG ESTUARY

GUOYU SONG1, WENYUN GUO2, JIANZHONG GE3, CHENG QIU4，HONGSHENG ZHANG5

1 Shanghai Maritime University, China, 598578794@qq.com
2 Shanghai Maritime University, China
3 State key laboratory of estuarine and coastal research, East China Normal University, China
4 Shanghai Marine monitoring and forecasting center, China
5 Shanghai Maritime University, China

Storm surge is a kind of severe natural disasters. Mainly due to the considerable errors in the pr edicted typhoon track, it is hard to improve the predicting skill in storm surge. In this study, we aim to establishing a probabilistic prediction system for the storms surges around the Changjiang Estuary. Since there are multiple forecasting offices (for xample, CMA,HKO,CWB,JTWC,RSMC_Tokyo, KMA) conduct operational forecast for the typhoons around the northwest Pacific Ocean, this syste m merges the six different forecasting tracks from these offices into one analytical track firstly. The weight coefficient is carefully determined according to the historical forecasting errors of each forec ast office. Based on the analytical typhoon track, a total of 45 (5 tracks, 3 maximum wind speeds an d 3 central pressure) typhoon samples were derived. The ability of the modeling system was invest igated simulating water levels in Changjiang Estuary coast of two tropical cyclones Lekima (2019) and Ampil(2018). The results show that the model has a good prediction accuracy of surge level. Th e system can offer the probabilities of each forecasted surge level, which is of great value for the dis aster prevention and reduction.

Key Words: storm surge ensemble forecast probability prediction FVCOM

8th International Conference on the Application of Physical Modelling in Coastal and Port Engineering and Science
Zhoushan, China - Dec. 9th - 12th, 2020

HYDRO-ENVIRONMENTAL MODELLING OF NORTH WALES TIDAL LAGOON USING TELEMAC-2D

BIN GUO[1], REZA AHMADIAN, ROGER A FALCONER

1 School of Engineering, Cardiff University, U.K. guob2@cardiff.ac.uk

Coastal reservoirs are also appropriate for tidal energy generation where ideal conditions exist, such as a large tidal range and suitable geographical conditions. The tidal range along the North Wales coast is one of the highest in the UK, and its generally shallow waters adjacent to deeper waters are suitable for situating turbines while minimising construction costs, making the North Wales coast an attractive site for tidal range impoundments. Furthermore, a coastal attached tidal energy impoundment project here can also act as a coastal protection system, as the North Wales seacoast has historically suffered from flooding.

The North Wales Tidal Lagoon (NWTL) is one of the latest proposed tidal range energy schemes proposed in the UK. The lagoon was planned to span from Llandudno to Prestatyn, with a breakwater stretching over 30 km in length and a water impoundment area of 150 km^2 . In the preliminary design stage, NWTL hosts 150 turbines with a diameter of 9 m which are averagely distributed into 10 blocks; 9 blocks of sluice gates are designed to contribute to the electricity generation and the water quality, with a total sluicing area of 20000 m^2. The numerical model TELEMAC-2D has been adopted to model the hydrodynamic impacts of NWTL. Domain decomposition was applied in the model and full momentum conservation between the subdomains was achieved in the model by implementing momentum source terms at the turbine locations. Furthermore, to study the relationship between lagoon operation and the water renewal capacity, a passive mass-conservative tracer was released in the NWTL impoundment basin for the scenarios of pre-construction and post-construction. The tracer was introduced instantaneously and uniformly dispersed at the high-water of a typical spring tide; then the residence time was calculated based on a commonly used method, that was defined statistically equal to the time when the concentration was reduced to 10% of its initial concentration.

The results showed that the estimated annual energy production values of the NWTL for the optimised flexible two-way generation with or without a pumping function were 4.80 TWh and 5.48 TWh respectively. The noticeable decrease in water levels inside the lagoon was the result of the two-way operation, which could provide extra protection for defences against flooding. The hydrodynamic influence of NWTL appeared in both near-fields (i.e. Colwyd Bay and Liverpool Bay) and far-fields (i.e. Cardigan Bay). Furthermore, the operation of the NWTL could also decrease the high water level in Liverpool Bay by 5–10 cm while slightly increase the high water level in Cardigan Bay. The residence time study in the NWTL impoundment basin indicated that the water renewal capacity was reduced by 61% with the operation of NWTL. This is believed due to the well natural water exchange rate in the proposed impoundment basin and the limited discharge volume of the sluice gates on the east side.

Key Words: Tidal energy; Tidal lagoon; Hydrodynamic impact; Hydro-environmental impact

8th International Conference on the Application of Physical Modelling in Coastal and Port Engineering and Science
Zhoushan, China - Dec. 9th - 12th, 2020

TWO-LAYERED LIQUID SLOSHING IN A TANK UNDER VERTICAL EXCITATION

DONGMING LIU(1), PENGZHI LIN(2), DONGYI YAN(3) & JIJIAN LIAN(4)

(1,3,4) State Key Laboratory of Hydraulic Engineering Simulation and Safety, Tianjin University, Tianjin 300072, China
(1,2) State Key Laboratory of Hydraulics and Mountain River Engineering, Sichuan University, Chengdu 610065, China
(4) School of Water Conservancy and Hydropower, Hebei University of Engineering, Handan 056038, China
hpeliudm@tju.edu.cn; cvelinpz@scu.edu.cn; 1018205067@tju.edu.cn; jjlian@ tju.edu.cn

An in-house numerical model called NEWTANK, which solves filtered NSEs on a non-inertial coordinate for external excitations, has been developed to study two-layered parametric sloshing under vertical oscillation. The two-step projection method is adopted in numerical solutions, and the Poisson equation for pressure field is solved by Bi-CGSTAB technique. A multi-layered volume-of-fluid (ML-VOF) method is introduced to track the interface between layered liquids and the free surface at the same time. In order to validate the accuracy of the model, experiment of layered parametric sloshing has been conducted to excite the resonance of the upper layer liquid. The simulated results for both layers favorably match those from experiments. The validated model will used to study energy transfer among modes and layers.

Keywords: parametric sloshing; Faraday waves; two-layered sloshing; Rayleigh-Taylor instability; resonance.

8th International Conference on the Application of Physical Modelling in Coastal and Port Engineering and Science
Zhoushan, China - Dec. 9th - 12th, 2020

EXPLORING THE POSSIBILITY OF MODELLING WAVE OVERTOPPING OVER SEA DIKES ON VERY GENTLY SLOPING AND VERY SHALLOW FORESHORES

THU-HA NGUYEN[1,2], BAS HOFLAND[1], H.T.DAO[1,3]
1 Faculty of Civil Engineering and Geosicences, Delft University of Technology, the Netherlands, H.Nguyen- 1@tudelft.nl; B.Hofland@tudelft.nl; H.T.Dao-1@tudelft.nl
2 Faculty of Coastal and Offshore Engineering, National University of Civil Engineering, Vietnam 3 Faculty of Marine Sciences, Hanoi University of Natural Resources and Environment, Vietnam

The research of wave overtopping behavior over very gently sloping and very shallow foreshores is not yet fully understood, especially for the slopes gentler than 1/500 as many Vietnamese coasts (Silke Tas, 2016). Furthermore, very gentle slopes associated with very wide shelfs makes their physical model simulations more difficult in wave flumes due to the limited effective length of flumes, so combining numerical models and laboratory results are chosen in this case. The physical experiments are planned to be carried out in the wave flume of Water Lab of Delft University of Technology, and the numerical model applied is the nearshore time domain model SWASH.

Wave parameters at the toe play a crucial role to define wave overtopping behavior over sea-dikes. It is indicated that (very) shallow waters associated with very gently sloping foreshores lead to significant changes of wave spectrum shape from offshore to foreshore. JONSWAP-shaped wave spectra at offshore transform into flattened spectra at the toe of sea defences in the SWASH model (Altomare et al., 2016; Suzuki et al., 2017). Moreover, it is complicated to simulate accurately and efficiently this kind of wave spectrum in a wave flume, due to the dominance of infragravity waves and nonlinear shape of the primary waves (Goring, 1979). The corresponding wave paddle control signal in the wave flume can be determined based on surface elevation of water particles at the toe of structures. Therefore, in this study we explore an approach to describe accurately the flattened wave spectra with piston wave makers in case of very gentle slopes. The key to the success of this composite modelling approach is prior analysis of the spectral wave periods and wave spectra at the toe of the sea-dikes, allowing the measurement of a rather wave overtopping discharges or/and volumes over the structures in the wave flume. The SWASH simulations will be used to explore the capabilities of a standard long-stroke piston-type wave maker with active absorption to create near-shore wave spectra.

REFERENCES

Altomare, C., T. Suzuki, X. Chen. T. Verwaest, A. Kortenhaus, 2016. Wave overtopping of sea dikes with very shallow foreshores. *Coastal Engineering 116 (2016), 236-257 (ISSN 0378-3839).*

Goring, D. G, 1979. Tsunamis - the propagation of long waves onto a shelf. *Report number KH-R-38, California Inst. of Tech., Pasadena, Calif.*

Goring, D.G., and Raichlen, F., 1980. The generation of long waves in the laboratory. *Proc. 17th Int. Conf. on Coastal Eng.*

Silke Tas, 2016. Coastal protection in the Mekong Delta: Wave load and overtopping of sea dikes as function of their location in the cross-section, for different foreshore geometries. *Master thesis, Delft University of Technology, Delft, the Netherlands, 17-18.*

Suzuki, T., C. Altomare, W. Veale, T. Verwaest, K. Trouw, P. Troch, M. Zijlema, 2017. Efficient and robust wave overtopping estimation for impermeable coastal structures in shallow

foreshores using SWASH. *Coastal Engineering 122 (2017), 108-123.*

Key Words: flattened wave spectra, very gentle slope, SWASH, wave overtopping

8th International Conference on the Application of Physical Modelling in Coastal and Port Engineering and Science
Zhoushan, China - Dec. 9th - 12th, 2020

APPLICATION OF THE DIGITAL SHORELINE ANALYSIS SYSTEMS IN DETECTING SHORELINE CHANGE: A CASE STUDY OF QUANG NAM PROVINCE, VIETNAM

VU HUONG NGAN[1], DINH NHAT QUANG[2], HO SY TAM[3], NGUYEN TRUNG VIET[4]

1 Thuyloi University, Vietnam, vuhuongngan235@gmail.com
2 Thuyloi University, Vietnam, quang.dinh@tlu.edu.vn
3 Thuyloi University, Vietnam, tamhs.cttl@tlu.edu.vn
4 Thuyloi University, Vietnam, nguyentrungviet@tlu.eduv.n

Shoreline erosion and accretion have become urgent problems in the world generally and in Quang Nam coast particularly. Moreover, they are enhancing exacerbated because of complicated climate change. Therefore, shoreline change should be taken into consideration to understand the reasons, as well as finding challenges and making essential solutions for better coastline management and protection. In this research, Digital Shoreline Analysis System (DSAS) software, an add-in to Esri ArcGIS desktop, is adopted to calculate rate-of-change statistics from multiple historical shoreline positions, which will be extracted from satellite images, i.e. Landsat and Sentinel images from 1985 to 2018. DSAS is a trustworthy tool to compare and digitize shoreline positions following chosen timeseries, specifically the trend of movement is also evaluated by the function of calculating parameters for each transects, comprising end point rate, shoreline change envelops, net shoreline movement and linear regression rate. The result performs that within 33 years, although both phenomena of erosion and accumulation occurred along the Quang Nam coast, erosion trend is obviously observed with the maximum rate change is 34.5 m/year and the minimum value is 0.01 m/year, whereas the average rate of accretion is lower, at 12.1 m/year.

Key Words: shoreline change, Quang Nam province, satellite images, Digital Shoreline Analysis System

8th International Conference on the Application of Physical Modelling in Coastal and Port Engineering and Science
Zhoushan, China - Dec. 9th - 12th, 2020

A MIXTURE THEORY BASED ISPH MODEL FOR SIMULATING SEDIMENT TRANSPORT AND EROSION PROCESS AROUND COASTAL STRUCTURES

Dong Wang[1]

1 Department of Civil & Environmental Engineering, National University of Singapore, Singapore
Email: ceewadg@nus.edu.sg

This paper proposes an incompressible smoothed particle hydrodynamics (ISPH) model to study the sediment transport and erosion process around coastal structures. The concept of mixture theory (Hsu et al., 2004) based on Favre averaged governing equations is adopted so that the ISPH particles simultaneously solve the two-phase flow equations with sediment concentration. To solve the two-phase flow equations with the ISPH scheme, we propose a new two-system framework. Turbid water particles (TWP) represent the numerical particles in the ISPH algorithm solving the fluid phase equations, while dummy sediment particles (DSP) denote the numerical particles in solving the sediment phase equations. These two continuums are coupled through interactions between fluids and sediments. The sediment concentration is updated in real time based on the location of DSPs. Two sets of $k-\varepsilon$ turbulence closure model are adopted for the fluid and sediment phases, which provide accurate turbulence kinetic energy and shear stress. Initiation of the sediment movement is judged based on the comparison between the critical value of shear stress for sediment incipient motion and the shear stress exerting on the interface wall particle (IWP) on the sand-bed (Wang and Li, 2016). Once the calculated shear stress of the IWP exceeds the critical shear stress, the IWP will be automatically flagged as TWPs and allowed to be peeled off from the bed. Benchmark examples of turbulence flows are first simulated to validate the single-phase model. Furthermore, the developed ISPH-MPM model is used for more challenging practical engineering issues, such as the sediment flushing caused by the dam-break, bed scouring around coastal structures due to the tsunami, and sand-water interface formation near the sea bed under waves.

8th International Conference on the Application of Physical Modelling in Coastal and Port Engineering and Science
Zhoushan, China - Dec. 9th - 12th, 2020

COMPARATIVE LABORATORY STUDYON ORIGINAL OWC BASED WAVE ENERGY CONVERTERS

LORENZO CAPPIETTI [1], VALERI PENCHEV[2],IRENE SIMONETTI [3], PHILIP PENCHEV[4]

1 University of Florence, Florence, Italy, lorenzo.cappietti@unifi.it
2 CORES, Black Sea Danube Association of Research and Development, Varna, Bulgaria, v.penchev@corebg.eu
3 University of Florence, Florence, Italy, irene.simonetti@unifi.it
4 Black Sea Danube Association of Research and Development, Varna, Bulgaria, f.penchev@bdcabg.org

This work compares results of two scale model tests on innovative Wave Energy Converters (WEC) based on Oscillating Water Column (OWC) principle. First, the results are presented of an experimental study of an original WEC in which the energy is harvested by means of an OWC in combination with an Overtopping structure. The studied WEC embodies a classical OWC device where the water column chamber is hydraulically connected to a second oscillating column though which water overtops into a reservoir above the mean sea level. The wave energy can thus be converted by an air turbine and a low-head water turbine. Scale-model test have been carried out in the wave flume of LABIMA at the University of Florence in 2018 in the framework of the EU-FP7 MARINET project. The OWC/overtopping WEC was investigated in a scale-model under regular waves for different wave height, period and steepness. The water column oscillation inside the two chambers, the overtopping of water and the free surface level in the reservoir were measured. Data analysis on terms of power extracted as air flux and water discharge was performed, and the capture width of the device was presented.

The results of the scale-model test were compared to those of a similar innovative WEC device where the air turbine is replaced by a closing valve, this way the OWC chamber is closed and remains under negative pressure. A large OWC chamber of this device can also utilise tidal variations in combination with wave oscillations in order to accumulate wave energy. Laboratory scale-model studies on such a device were also carried in the wave flume of LABIMA at the University of Florence in 2015. Hydraulic head generated by incoming waves was compared for the 2 devices mentioned - as a main parameter influencing the efficiency of use of the air turbine. The potential advantage of the air turbine for the first case was also analysed.

Further numerical test on both concepts will take place in order to optimise geometry of these devise, and prove (or decline) their potential for practical application.

Key Words: wave energy converter model test

8th International Conference on the Application of Physical Modelling in Coastal and Port Engineering and Science
Zhoushan, China - Dec. 9th - 12th, 2020

STORM SURGE AND WAVES SIMULATION FOR SUPER TYPHOON MANGKHUT (1822)

XIAOJIAN LIU[1], CHENG LIU[2], QISONG WANG [3]

1 Pearl River Hydraulic Research Institute, Pearl River Water Resources Commission of the Ministry of Water Resources, Guangzhou, Guangdong, lxiaojian2010@163.com

2 Pearl River Hydraulic Research Institute, Pearl River Water Resources Commission of the Ministry of Water Resources, Guangzhou, Guangdong, jacklc2004@163.com

3 Pearl River Hydraulic Research Institute, Pearl River Water Resources Commission of the Ministry of Water Resources, Guangzhou, Guangdong, wqisong@126.com

Typhoon Mangkhut (1822) is an extremely destructive tropical cyclone that caused widespread damage in the Philippines and South China in mid-September 2018. Statistically, it was the strongest typhoon to affect Luzon since Megi in 2010, and the strongest typhoon to strike Hong Kong since Ellen in 1983. In this study, a 3D fully wave-current coupled finite-volume community ocean model system was developed and applied to simulate and examine the coastal ocean responses to typhoon Mangkhut. The waves derived from the unstructured version of the third‐generation wave model (SWAN) simulating waves nearshore. The surge derives from the unstructured Finite-Volume Coastal Ocean Model (FVCOM), to which wave-induced forces are added based on radiation stress theory to the traditional forces by winds and atmospheric pressure. The accurate meteorology field was acquired by a combined usage of the empirical and the CCMP reanalysis results. Numerical results showed that the impact of wave-current interaction on surge elevation varied in space and in time, and quantified the contribution of wave to the total storm surge. Such strong interactions through coupling suggest that the waves should not be neglected in typhoon storm surge simulations, more significant over the shelf than inside the inner bays. Subsequently, this model was used to reveal distributions of storm surge and waves, as well as their time evolutions in South China Sea. Finally, the effect of radiation stress on causing both set-up and set-down in the storm surge events was discussed.

Key Words: Super Typhoon Mangkhut; Storm Surge; Wave; 3D fully wave-current coupled model

8th International Conference on the Application of Physical Modelling in Coastal and Port Engineering and Science
Zhoushan, China - Dec. 9th - 12th, 2020

ON THE OPTIMIZATION OF POWER GENERATION OF A NOVEL POINT ABSORBER INTEGRATED WITH A FLOATING SEMI-SUBMERSIBLE WIND TURBINE

MINGSHENG CHEN [1], PANPAN XIAO [2], REN WANG [3], LING ZHU [4]

1 School of Transportation, Wuhan University of Technology, CHINA, mschen@whut.edu.cn
2 School of Transportation, Wuhan University of Technology, CHINA, xiaopanpan@whut.edu.cn
3 School of Transportation, Wuhan University of Technology, CHINA, WHUT279338@whut.edu.cn
4 School of Transportation, Wuhan University of Technology, CHINA, lingzhu@whut.edu.cn

Offshore renewable energies such as the wind and wave energies have attracted vast interests worldwide, due to their abundance in quantity and easy applicability in coastal areas. Compared with the wave power generation, offshore wind power generation has achieved a much more mature stage and a large number of offshore wind farms have been installed worldwide in the last two decades. With intensive research work and technology development, offshore wind power generation has exhibited the trend for developing floating wind turbines in deep waters where the wind energy is stronger and more stable. Although much research has been dedicated to the wave power generation, the development of wave energy is still at the demonstration stage. The most important inhibitor to deploying the wave energy convertors is its vulnerable survivability and reliability subjected to the complex ocean environment. Therefore, many researchers have considered the idea of integrating the wave energy convertor with an offshore wind turbine since the robustness and structural integrity of offshore wind turbines have been well proven in the commercial projects. This study presents a novel concept that integrates a heaving Point Absorber Wave Energy Convertor (PAWEC) with a semi-submersible type floating wind turbine to achieve combined wind and wave power generation. The PAWEC is enclosed by the three legs of the semi-submersible foundation and its motions may be enhanced due to the near-trapping phenomenon arising from the complex hydrodynamic interactions between the PAWEC and the three large dimension legs of the semi-submersible. By this concept, the PTO device is mounted onto the floating wind turbine foundation such that the relative heaving motion between the PAWEC and floating wind turbine can be used for wave power generation. In this way, the PTO device will be placed above the water level to prevent damage caused by the waves and to facilitate control, maintenance, and inspection work during its lifetime services. The integrated system is numerically modeled by two hydrodynamics codes ANSYS-AQWA and DIFFRACT, which are based on the constant panel BEM and high-order BEM, respectively. The magnification of the free surface enclosed by the three legs of semi-submersible is investigated by ANSYS-AQWA. Due to its high computation efficiency, DIFFRACT is applied to investigate the influence of the PAWEC dimension on its dynamics and power generation. The mean wave power generation of the integrated device is further compared with that of a single PAWEC. In addition, parametric analyses are carried out to study the effect of the PTO parameters on the coupled dynamics of the integrated device and the mean wave power generation. Finally, suggestions for the optimized design of the integrated wind and wave power generation device are provided.

Key Words: floating semi-submersible wind turbine; PAWEC; hydrodynamic interaction; combined wind and wave power generation; mean power generation

8th International Conference on the Application of Physical Modelling in Coastal and Port Engineering and Science
Zhoushan, China - Dec. 9th - 12th, 2020

REVIEW ON THE DERIVATION AND APPLICATION OF BOUSSINESQ-TYPE EQUATIONS FOR WATER WAVES

ZHONGBO LIU[1], KEZHAO FANG[2], JIAWEN SUN[3], ZHAOCHEN SUN[2], ZAIJIN YOU[1]

1 Transportation Engineering College, Innovation Center for Ports and Maritime Safety, Dalian Maritime University, China, liuzhongbo@dlmu.edu.cn, b.you@dlmu.edu.cn.

2 State Key Laboratory of Coastal and Offshore Engineering, Dalian University of Technology, China, kfang@dlut.edu.cn, sunzc@dlut.edu.cn

3. National Marine Environmental Monitoring Center, China, jwsun@nmemc.org.cn

The Boussinesq-type equation is one of the important numerical tools for simulating the propagation and evolution of water waves. The theoretical derivation and numerical application of the Boussinesq-type water wave equation commonly used in 1967-2019 are reviewed. From the theoretical aspect, the derivation of such equations mainly starts from Euler equations or Laplace equations. Under the conditions of certain nonlinearity and gentle slope assumptions, the researchers have established various Boussinesq-type water wave equations. Through the comparisons with the related theories of Stokes waves, these models are investigated with respect to the properties such as phase velocity, group velocity, linear shoaling gradient, second-order nonlinearity, third-order nonlinearity, dispersion characteristics due to amplitude dispersion, velocity distribution along the vertical column, sub- and super harmonics etc. The Boussinesq-type equations can be divided into two categories such as horizontal two-dimensional and three- dimensional models. And the main derivation methods to obtain Boussinesq-type equations for wave are reviewed. In addition, the Boussinesq-type equations are briefly described and commented on the special cases involved with permeable media and the presence of fluid stratification. Finally, the application of these equations is summarized and analyzed to further promote the application of these Boussineq-type models in the hydrodynamic direction of coastal engineering.

Key Words: Boussinesq-type equations, dispersion, nonlinear property, linear shoaling property.

8th International Conference on the Application of Physical Modelling in Coastal and Port Engineering and Science
Zhoushan, China - Dec. 9th - 12th, 2020

DEPTH-AVERAGED TWO-DIMENSIONAL MODELING OF SUSPENDED SEDIMENT CONCENTRATION IN THE YANGTZE ESTUARY

JUNYU TAO[2], PENG HU[1]

1Institute of Port, Coastal and Offshore Engineering, Ocean College, Zhejiang University, Zhoushan 316021, China. Email:11734017@zju.edu.cn

2 Institute of Port, Coastal and Offshore Engineering, Ocean College, Zhejiang University, Zhoushan 316021, China. Email: pengphu@zju.edu.cn

This paper presents a two-dimensional depth-averaged hydro-sediment-tidal-morphodynamic model for the Yangtze Estuary, which considers the mixed cohesive and non-cohesive sediment transport, and the effects of salinity and SSC on the flocculation of cohesive sediment. The depth-averaged 2D governing equations are numerically solved on unstructured triangular meshes using a well-balanced shock-capturing finite volume method with the HLLC approximate Riemann solver and a hybrid local time step/global maximum time step (LTS/GMaTS) method to achieve better application to irregular computational domain and computationally efficient modeling of hydro-sediment-tidal-morphodynamic processes. The simulation results are consistent with the measured data in tidal level, current velocity, current direction and salinity, which indicates the accuracy of the numerical model. Based on the measured suspended sediment concentration at several stations in the Changjiang Estuary in July 2016 (including spring tidal and neap tidal), the effects of key factors on suspended sediment concentration in the Changjiang Estuary were studied. It is shown that the suspended sediment concentration in the North channel, the North passage and South passage of the Changjiang Estuary has obvious turbidity characteristics. The critical shear stress of erosion and deposition is one of the key factors controlling suspended sediment concentration in the Changjiang Estuary.

Key Words: Changjiang Estuary; suspended sediment concentration; cohesive; non-cohesive; critical shear stress

8th International Conference on the Application of Physical Modelling in Coastal and Port Engineering and Science
Zhoushan, China - Dec. 9th - 12th, 2020

EVALUATING THE ACCURACY OF ERA5 WIND AND WAVE REANALYSES IN THE CHINA SEA

Hongyuan Shi1,2, Jiacheng Sun1, Xuefeng Cao3, Delei Li4 ,Qingjie Li5 Zaijin You1,2*

1 School of Civil Engineering, Ludong University. Yantai 264025 P. R. China;
2 Institute of Ports and Coastal Disaster Mitigation, Ludong University, Yantai 264025 P. R.China;
3 National Marine Environmental Monitoring Center, Dalian 116023, China
4 Key Laboratory of Ocean Circulation and Waves, Institute of Oceanology, Chinese Academy of Sciences, Qingdao, China
5 Marine Environmental Monitoring Central Station, SOA, Yantai 264025 P.R. China;

Pairs of comparisons among measurements, satellite datasets and ERA reanalysis along China Sea are performed in this paper. Measurement is obtained by buoys and it is covered the whole year with the temporal resolution of 1h. ERA5 was developed by the European Centre for Medium-Range Weather Forecasts (ECMWF), adopting the wave model WAM, covering the whole globe. Satellite datasets was obtained from Jason-2, providing the wave data. The main analysis covers a detailed comparison of measurement and ERA5, followed by a comparison of ERA5 against satellite data. Wind speed and significant wave height are the two variables considered. The differences for the whole dataset and for extreme events (upper percentiles) are calculated. A spatial and time integration is applied to determine where and when the main differences between hindcasts occur. The results show a relatively good agreement between ERA5 and both measurement and satellite datasets for calm and moderate weather conditions. There is a large increase of the differences under extreme conditions. Although ERA5 data is larger than measured data on the whole, it is smaller in maximum wind speed and significant wave height simulation, if we adopt ERA5 to do marine engineering design, it maybe underestimate the destructive force of the wind and wave.

8th International Conference on the Application of Physical Modelling in Coastal and Port Engineering and Science
Zhoushan, China - Dec. 9th - 12th, 2020

MORPHOLOGICAL EVOLUTION ANALYSIS OF SOUTH TROUGH IN YANGTZE ESTUARY OVER PAST TENYEARS

GUO CHUANSEHNG[1], TANG LIQUN[1], WANG YUHAI[1], ZHAO HUIMING[1], LIU DABIN[1]

1 State Key Laboratory of Simulation and Regulation of Water Cycle in River Basin, China Institute of Water Resources and Hydropower Research, Beijing, P. R. China, guoliu1982@126.com

Based on the latest bathymetric data from July 2007 to February 2016, a time series of digital elevation model of the South Trough were established. This research analyzes the general erosion-silted characteristics of the South Trough, the spatio-temporal variations in different sub-regions, and temporal changes of elevation along the typical cross section. The results show that: (1) In general, the study area was silted during 2007~2016 in circulations of erosion- deposition. The spatial-temporal erosion and deposition characteristics of South Trough varied significantly. (2) The sandbars and gullies in the upper South Trough were frequently modified by the complicated erosion-accretion process. The evolution of the three sections of the sandbar was controlled by different mechanisms: the upper section has a noisy pattern of erosion and accretion alternation; the middle section was silted; the lower section was eroded. (3) The Jiuduansha shoal region showed a silting, widening and downward extending trend. Human activities took the leading role changing the erosion and accretion pattern by drastically reducing the sediment load. (4) The drastic reduction of sediment into the sea will continue the trend of scouring in the upstream section of the southern trough and the offshore section.

Key Words: South Trough; Yangtze River estuary; sediment load; sediment erosion; sediment deposition

8th International Conference on the Application of Physical Modelling in Coastal and Port Engineering and Science
Zhoushan, China - Dec. 9th - 12th, 2020

COMBINED ENERGY HARVESTING AND DATA COMPRESSION APPROACHES FOR EFFICIENT EXTREME EVENTS MONITORING IN CIVIL INFRASTRUCTURE

TALAL SALEM[1], NIZAR LAJNEF[1], PENGCHENG JIAO[2,3]

1 Department of Civil and Environmental Engineering, Michigan State University, East Lansing, MI 48824, USA
2 Institute of Port, Coastal and Offshore Engineering, Ocean College, Zhejiang University, Zhoushan 316021,Zhejiang, China
3 Engineering Research Center of Oceanic Sensing Technology and Equipment, Zhejiang University, Ministry of Education, ChinaEmail: pjiao@zju.edu.cn

Wireless sensors and sensor networks have been widely used recently to monitor structures. In general, the longevity, and hence the efficacy, of these sensors are severely limited by their stored power. In addition, systems that are deployed to monitor extreme events, such as earthquakes, hurricanes, or impacts, will most probably miss the event of interest either due to power blackouts or due to the inefficient approach of data collection. The typical continuous sampling and recording of structure responses is impractical when targeting rare extreme events. This paper addresses these two shortcomings. First, the ability to convert abundant ambient energy into electric power would eliminate the problem of drained electrical supply, and would allow indefinite monitoring thus eliminating the risk of power blackouts. This paper focuses on vibration in civil engineering structures as a source of ambient energy. Earthquake, wind and traffic loads are used as realistic sources of vibrations. In addition, novel data storage and analysis approaches are discussed. These methods allow to reduce the needed storage and computational requirements by more than 1000% for rare events monitoring. Thus, extending the longevity and efficacy of any monitoring system.

Key Words: Wireless sensor; energy harvesting; extreme events; structural health monitoring (SHM).

Dec 9-12, 2020
Zhoushan, China